

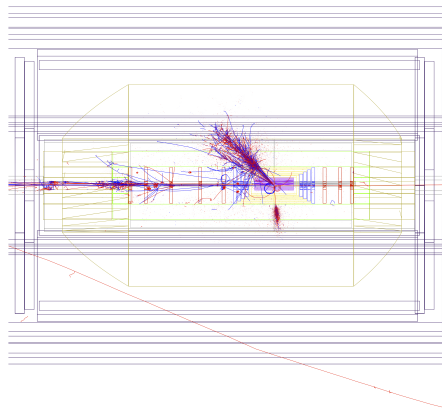
1 DRAFT 0.8
2 July 2, 2011
3 CERN report
4 ECFA report
5 NuPECC report
6



7 **A Large Hadron Electron Collider at CERN**

8 Report on the Physics and Design
9 Concepts for Machine and Detector

10 **LHeC Study Group**
11 THIS IS THE VERSION FOR REFEREEING, NOT FOR DISTRIBUTION



12 View of a (draft) leptiquark event in the LHeC Detector modelled in GEANT4

Abstract

14 The physics programme and the design are described of a new electron-hadron collider, the
15 LHeC, in which electrons of 60 to possibly 140 GeV collide with LHC protons of 7000 GeV.
16 The Large Hadron Electron Collider extends the kinematic range of HERA by nearly two
17 orders of magnitude in four-momentum squared, Q^2 , and in $1/x$, using a design luminosity of
18 $O(10^{33}) \text{ cm}^{-2} \text{ s}^{-1}$. The physics programme is devoted to an exploration of the energy frontier
19 complementing the LHC with high precision DIS measurements which are projected to solve
20 a number of fundamental questions in strong and electroweak interactions. The LHeC thus
21 becomes the world's cleanest high resolution microscope, designed to continue the path of
22 deep inelastic lepton-hadron scattering into unknown areas of physics and kinematics. This
23 includes electron-ion (eA) scattering into a range extended by four orders of magnitude as
24 compared to previous lepton-nucleus experiments. The LHeC may be realised as a ring-ring
25 or linac-ring collider. For both options the optics and beam dynamics studies are presented,
26 along with technical design considerations on the interaction region, magnets, cryo, rf, civil
27 engineering and further components. A design study is also presented of a detector suitable
28 to perform high precision DIS measurements in a wide range of acceptance using state-of-the
29 art detector technology, which is modular and of limited size enabling its fast installation. The
30 detector includes tagging devices for electron, photon, proton and neutron detection near to the
31 beampipe. The LHeC may be built and is designed to be operated while the LHC runs. It so
32 represents a major opportunity for particle physics to progress and for the LHC to be further
33 exploited.

34 LHeC Study Group

35 C.Adolphsen¹, S.Alekhin^{2,3}, H.Aksakal⁴, P.Allport⁵, J.L.Albacete⁶, V.Andreev⁷, R.Appleby⁸,
36 N.Armesto⁹, G.Azuelos¹⁰, M.Bai¹¹, D.Barber³, J.Bartels¹², J.Behr³, O.Behnke³, S.Belyaev⁴,
37 I.BenZvi¹¹, N.Bernard¹³, S.Bertolucci⁴, S.Bettoni⁴, J.Bluemlein³, H.Boettcher³, S.Brodsky¹,
38 A.Bogacz¹⁴, C.Bracco⁴, O.Bruening⁴, A.Bunyatian³, H.Burkhardt⁴, R.Calaga¹¹, E.Ciapala⁴,
39 R.Ciftci¹⁵, A.K.Ciftci¹⁵, B.A.Cole¹⁶, J.C.Collins¹⁷, J.Dainton⁵, A.De.Roeck⁴, D.d'Enterria⁴,
40 A.Dudarev⁴, A.Eide¹⁸, E.Eroglu¹⁹, K.J.Eskola²⁰, L.Favart²¹, M.Fitterer⁴, S.Forte²², P.Gambino²³,
41 T.Gehrmann²⁴, C.Glasman²⁵, R.Godbole²⁶, B.Goddard⁴, T.Greenshaw⁵, A.Guffanti²⁷, C.Gwenlan²⁸,
42 T.Han²⁹, Y.Hao¹¹, F.Haug⁴, W.Herr⁴, B.Holzer⁴, M.Ishitsuka³⁰, M.Jacquet³¹, B.Jeanerret⁴,
43 J.M.Jimenez⁴, H.Jung³, J.Jowett⁴, D.Kayran¹¹, F.Kosac¹⁹, A.Kilic¹⁹, K.Kimura³⁰, M.Klein⁵,
44 U.Klein⁵, T.Kluge¹², G.Kramer¹², M.Korostelev⁸, A.Kosmicki⁴, P.Kostka³, H.Kowalski³, M.Kuze³⁰,
45 T.Lappi²⁰, P.Laycock⁵, E.Levichev³², S.Levonian³, V.N.Litvinenko¹¹, C.Marquet⁴, B.Mellado²⁹,
46 KH.Mess⁴, S.Moch³, I.I.Morozov³², Y.Muttoni⁴, S.Myers⁴, P.R.Newman³³, T.Omori³⁴, J.Osborne⁴,
47 E.Paoloni³⁵, C.Pascaud³¹, H.Paukkunen⁹, E.Perez⁴, T.Pieloni³⁶, E.Pilic¹⁹, A.Polini³⁷, V.Ptitsyn¹¹,
48 Y.Pupkov³², V.Radescu³⁸, S.Raychaudhuri²⁶, L.Rinolfi⁴, R.Rohini²⁶, J.Rojo²², S.Russenschuck⁴,
49 C.A.Salgado⁹, K.Sampai³⁰, E.Sauvan³⁹, U.Schneekloth³, T.Schoerner Sadenius³, D.Schulte⁴,
50 N.Soumitra²³, H.Spiesberger⁴¹, A.M.Stasto¹⁷, M.Strikman¹⁷, M.Sullivan¹, B.Surrow⁴⁰, S.Sultansoy¹⁵,
51 Y.P.Sun¹, W.Smith⁴², I.Tapan¹⁹, P.Taels⁴³, H.Ten.Kate⁴, J.Terron²⁵, H.Thiesen⁴, L.Thompson⁸,
52 K.Tokushuku³⁴, R.Tomas.Garcia⁴, D.Tommasini⁴, D.Trbojevic¹¹, N.Tsoupas¹¹, J.Tuckmantel⁴,
53 K.Tywniuk⁽⁴⁴⁾, G.Unel⁴, J.Urakawa³⁴, P.VanMechelen⁴³, R.Veness⁴, A.Vivoli⁴, P.Vobly³²,
54 R.Wallny⁽⁴⁵⁾, G.Watt⁴, G.Weiglein¹², C.Weiss¹⁴, U.A.Wiedemann⁴, U.Wienands¹, F.Willeke¹¹,
55 V.Yakimenko¹¹, A.F.Zarnecki⁽⁴⁶⁾, F.Zimmermann⁴, F.Zomer³¹

56 ¹ *SLAC, Stanford Linear Accelerator, USA*

57 ² *Serpukhov Institute, Russia*

58 ³ *DESY, Hamburg, Germany*

59 ⁴ *CERN, Geneva, Switzerland*

60 ⁵ *Liverpool, UK*

61 ⁶ *IPhT Saclay, France*

62 ⁷ *LPIMoscow, Russia*

63 ⁸ *Cockcroft Institute, UK*

64 ⁹ *University of Santiago de Compostela, Spain*

65 ¹⁰ *Montreal University, Canada*

66 ¹¹ *Brookhaven National Laboratory, BNL, USA*

67 ¹² *Hamburg, Germany*

68 ¹³ *University of California in Los Angeles, UCLA, USA*

69 ¹⁴ *Jefferson Laboratory, USA*

70 ¹⁵ *Ankara University, Turkey*

71 ¹⁶ *Columbia University, USA*

72 ¹⁷ *Pennsylvania State University, USA*

73 ¹⁸ *NTNU, ??*

74 ¹⁹ *Uludag University, Turkey*

75 ²⁰ *Jyvaskyla University, Finland*

76 ²¹ *IHE Brussels, Belgium*

77 ²² *INFN Milano, Italy*

78 ²³ *INFN Torino, Italy*

79 24 *Zurich, Switzerland*
80 25 *Madrid, Spain*
81 26 *Tata Institute, India*
82 27 *Freiburg University, Germany*
83 28 *Oxford University, UK*
84 29 *Harvard University, USA*
85 30 *Tokyo Institute of Technology, Japan*
86 31 *Orsay, LAL, France*
87 32 *BINP, Russia*
88 33 *Birmingham, UK*
89 34 *KEK, Japan*
90 35 *Pisa, Italy*
91 36 *EPFL, Lausanne, Switzerland*
92 37 *Bologna, Italy*
93 38 *Heidelberg, Germany*
94 39 *Lyon, France*
95 40 *Massachusetts Institute of Technology, MIT, USA*
96 41 *University of Mainz, Germany*
97 42 *Madison, USA*
98 43 *Antwerpen, Belgium*
99 44 *Lund University, Sweden*
100 45 *ETHZ, Zurich, Switzerland*
101 46 *Warsaw, Poland*

102 Contents

103	I Introduction	11
104	1 Lepton-Hadron Scattering	12
105	2 Design Considerations	16
106	2.1 DIS and Particle Physics	16
107	2.2 Synchronous pp and ep operation	16
108	2.3 Choice of Electron Beam Energy	17
109	2.4 Detector Constraints	19
110	2.5 Two Electron Beam Options	19
111	2.6 Luminosity and Power	20
112	3 Executive Summary	23
113	II Physics	24
114	4 Precision QCD and Electroweak Physics	25
115	4.1 Inclusive Deep Inelastic Scattering	25
116	4.1.1 Cross Sections and Structure Functions	25
117	4.1.2 Neutral Current	26
118	4.1.3 Charged Current	27
119	4.1.4 Cross Section Simulation and Uncertainties	30
120	4.1.5 Longitudinal Structure Function $\mathbf{F_L}$	31
121	4.2 Determination of Parton Distributions	36
122	4.2.1 QCD Fit Ansatz	38
123	4.2.2 Valence Quarks	39
124	4.2.3 Strange Quarks	42
125	4.2.4 Top Quarks	45
126	4.3 Gluon Distribution	46
127	4.4 Prospects to Measure the Strong Coupling Constant	50
128	4.4.1 Status of the DIS Measurements of α_s	50
129	4.4.2 Simulation of α_s Determination	52
130	4.5 Electron-Deuteron Scattering	53
131	4.6 Electroweak physics	55
132	4.6.1 Determination of the Weak Mixing Angle	59

133	4.7	Charm and Beauty production	65
134	4.7.1	Charm and Beauty production at LHeC	65
135	4.8	High p_t jets	77
136	4.8.1	Jets in ep	77
137	4.8.2	Jets in γA	84
138	4.9	Total photoproduction cross section	85
139	5	New Physics at Large Scales	88
140	5.1	New Physics in inclusive DIS at high Q^2	88
141	5.1.1	Quark substructure	89
142	5.1.2	Contact Interactions	89
143	5.1.3	Kaluza-Klein gravitons in extra-dimensions	91
144	5.2	Leptoquarks and leptogluons	91
145	5.2.1	Phenomenology of leptoquarks in ep collisions	93
146	5.2.2	The Buchmüller-Rückl-Wyler Model	93
147	5.2.3	Phenomenology of leptoquarks in pp collisions	94
148	5.2.4	Current status of leptoquark searches	96
149	5.2.5	Sensitivity on leptoquarks at LHC and at LHeC	96
150	5.2.6	Determination of LQ properties	97
151	5.2.7	Leptogluons	102
152	5.3	Excited leptons and other new heavy leptons	103
153	5.3.1	Excited Fermion Models	104
154	5.3.2	Simulation and Results	105
155	5.3.3	New leptons from a fourth generation	109
156	5.4	New physics in boson-quark interactions	109
157	5.4.1	An LHeC-based γp collider	109
158	5.4.2	Anomalous Single Top Production at the LHeC Based γp Collider	109
159	5.4.3	Excited quarks in γp collisions at LHeC	113
160	5.4.4	Quarks from a fourth generation at LHeC	113
161	5.4.5	Diquarks at LHeC	114
162	5.4.6	Quarks from a fourth generation in Wq interactions	114
163	5.5	Sensitivity to a Higgs boson	114
164	5.5.1	Higgs production at LHeC	116
165	5.5.2	Signal and background Monte-Carlo samples	118
166	5.5.3	Observability of the signal	118
167	6	Physics at High Parton Densities	123
168	6.1	Physics at small x	123
169	6.1.1	Unitarity and QCD	123
170	6.1.2	Status following HERA data	131
171	6.1.3	Low- x physics perspectives at the LHC	139
172	6.1.4	Nuclear targets	141
173	6.2	Prospects at the LHeC	146
174	6.2.1	Strategy: decreasing x and increasing A	146
175	6.2.2	Inclusive measurements	146
176	6.2.3	Exclusive Production	154
177	6.2.4	Inclusive diffraction	169

178	6.2.5	Jet and multi-jet observables, parton dynamics and fragmentation	180
179	6.2.6	Implications for ultra-high energy neutrino interactions and detection . .	190

180 **III Accelerator** **193**

181	7	Ring-Ring Collider	194
182	7.1	Baseline Parameters and Configuration	194
183	7.2	Geometry	194
184	7.2.1	General Layout	194
185	7.2.2	Electron Ring Circumference	194
186	7.2.3	Idealized Ring	195
187	7.2.4	Different Bypass Options	196
188	7.2.5	Bypass Point 1	197
189	7.2.6	Bypasses Point 5	197
190	7.2.7	Matching Proton and Electron Ring Circumference	197
191	7.3	Layout and Optics	198
192	7.3.1	Arc Cell Layout and Optics	198
193	7.3.2	Insertion Layout and Optics	199
194	7.3.3	Bypass Layout and Optics	200
195	7.3.4	Chromaticity Correction	200
196	7.3.5	Working Point	200
197	7.3.6	Aperture	200
198	7.3.7	Complete Lattice and Optics	202
199	7.4	Layout	213
200	7.4.1	Beam Separation Scheme	214
201	7.4.2	Crossing Angle	216
202	7.4.3	Beam Optics and Luminosity	218
203	7.5	Design Requirements of the Electron Beam Optics	220
204	7.5.1	Optics Matching and IR Geometry	220
205	7.6	High Luminosity IR Layout	221
206	7.6.1	Parameters	221
207	7.6.2	Layout	221
208	7.6.3	Separation Scheme	221
209	7.6.4	Optics Matching and IR Geometry	222
210	7.7	High Acceptance IR Layout	224
211	7.7.1	Parameters	224
212	7.7.2	Layout and separation scheme	225
213	7.7.3	Optics Matching and IR Geometry	226
214	7.7.4	Comparison of Layouts	228
215	7.8	Beam-beam effects in the LHeC	249
216	7.8.1	Head-on beam-beam effects	250
217	7.8.2	Long range beam-beam effects	253
218	7.9	Performance as an electron-ion collider	254
219	7.10	Spin polarisation – an overview	255
220	7.10.1	Self polarisation	256
221	7.10.2	Suppression of depolarisation – spin matching	259

222	7.10.3	Higher order resonances	260
223	7.10.4	Spin rotators	260
224	7.10.5	Calculations of the e^\pm polarisation in the LHeC	261
225	7.10.6	Further work	263
226	7.10.7	Summary	265
227	7.11	Integration and machine protection issues	265
228	7.11.1	Space requirements	265
229	7.11.2	Impact of the synchrotron radiation on tunnel electronics	272
230	7.11.3	Compatibility with the proton beam loss system	272
231	7.11.4	Space requirements for the electron dump	273
232	7.11.5	Protection of the p-machine against heavy electron losses	273
233	7.11.6	How to combine the Machine Protection of both rings?	274
234	7.12	LHeC Injector for the Ring-Ring option	274
235	8	Linac-Ring Collider	277
236	8.1	Basic Parameters and Configurations	277
237	8.1.1	General Considerations	277
238	8.1.2	ERL Performance and Layout	278
239	8.1.3	Polarization	287
240	8.1.4	Pulsed Linacs	287
241	8.1.5	Highest-Energy LHeC ERL Option	289
242	8.1.6	γ - p/A Option	289
243	8.1.7	Summary of Basic Parameters and Configurations	292
244	8.2	Interaction region	293
245	8.2.1	Layout	293
246	8.2.2	Optics	293
247	8.2.3	Modifications for γp or γ -A	300
248	8.2.4	Synchrotron radiation and absorbers	300
249	8.3	Linac Lattice and Impedance	308
250	8.3.1	Overall Layout	308
251	8.3.2	Linac Layout and Lattice	309
252	8.3.3	Beam Break-Up	316
253	8.3.4	Imperfections	326
254	8.4	Polarized-Electron Injector for the Linac-Ring LHeC	326
255	8.5	Spin Rotator	328
256	8.6	Positron Options for the Linac-Ring LHeC	332
257	8.6.1	Motivation	332
258	8.6.2	LHeC Linac-Ring e^+ Requirements	332
259	8.6.3	Mitigation Schemes	333
260	8.6.4	Positron Production Schemes	337
261	8.6.5	Targets	338
262	8.6.6	Conventional Scheme based on e^- Beam Hitting Target	338
263	8.6.7	Compton Sources	341
264	8.6.8	Undulator Source	347
265	8.6.9	Source based on Coherent Pair Creation	348
266	8.6.10	Conclusions	348

267	9 Civil Engineering and Services	349
268	9.1 Overview	349
269	9.2 Location, Geology and Construction Methods	349
270	9.2.1 Location	349
271	9.2.2 Land Features	350
272	9.2.3 Geology	351
273	9.2.4 Site Development	351
274	9.2.5 Construction Methods	352
275	9.3 Civil Engineering Layouts for Ring-Ring	352
276	9.4 Civil Engineering Layouts for Linac-Ring	354
277	9.5 Summary	357
278	10 System Design	358
279	10.1 Magnets for the Interaction Region	358
280	10.1.1 Introduction	358
281	10.1.2 Magnets for the ring-ring option	358
282	10.1.3 Magnets for the linac-ring option	362
283	10.1.4 Dipole Magnets	364
284	10.1.5 BINP Model	367
285	10.1.6 CERN Model	369
286	10.1.7 Quadrupole and Corrector Magnets	369
287	10.2 Ring-Ring RF Design	374
288	10.2.1 Design Parameters	374
289	10.2.2 Cavities and klystrons	375
290	10.3 Linac-Ring RF Design	380
291	10.3.1 Design Parameters	380
292	10.3.2 Layout and RF powering	381
293	10.3.3 Arc RF systems	383
294	10.4 Crab crossing for the LHeC	385
295	10.4.1 Luminosity Reduction	385
296	10.4.2 Crossing Schemes	385
297	10.4.3 RF Technology	386
298	10.5 Vacuum	387
299	10.5.1 Vacuum requirements	387
300	10.5.2 Synchrotron radiation	388
301	10.5.3 Vacuum engineering issues	390
302	10.6 Beam Pipe Design	395
303	10.6.1 Requirements	395
304	10.6.2 Choice of Materials for beampipes	395
305	10.6.3 Beampipe Geometries	396
306	10.6.4 Vacuum Instrumentation	398
307	10.6.5 Synchrotron Radiation Masks	398
308	10.6.6 Installation and Integration	399
309	10.7 Cryogenics	400
310	10.8 Positron P for the Linac-Ring option	401
311	10.9 Beam dumps	403
312	10.10 Post collision line for 140 GeV option	403

313	10.11 Absorber for 140 GeV option	403
314	10.11.1 Energy deposition studies	404
315	10.12 Beam line dump for ERL Linac-Ring option	404
316	10.13 Absorber for ERL Linac-Ring option	406
317	10.14 Injection Region Design for Ring-Ring Option	406
318	10.14.1 Injection onto the closed orbit	406
319	10.14.2 Mismatched injection	407
320	10.14.3 Injection transfer line	409
321	10.15 60 GeV internal dump	412
322	IV Detector	415
323	11 Detector Requirements	416
324	11.1 Requirements on the LHeC Detector	416
325	11.1.1 Installation and Magnets	416
326	11.1.2 Kinematic reconstruction	418
327	11.1.3 Acceptance regions - scattered electron	419
328	11.1.4 Acceptance regions - hadronic final state	421
329	11.1.5 Acceptance at the High Energy LHC	425
330	11.1.6 Energy Resolution and Calibration	425
331	11.1.7 Tracking Requirements	426
332	11.1.8 Particle Identification Requirements	429
333	11.1.9 Summary of the Requirements on the LHeC Detector	430
334	12 Central Detector	432
335	12.1 Basic Detector Description	432
336	12.2 Baseline Detector Layout	438
337	12.2.1 An Alternative Solenoid Placement - Option B	440
338	12.3 Magnet Design	442
339	12.4 Tracking Detector	442
340	12.4.1 Tracking Detectors Layout - Baseline Detector	442
341	12.4.2 Tracking Detector Design Criteria and possible Solutions	448
342	12.5 Geant4 Event Simulations - General Detector Description	453
343	12.5.1 Introduction	453
344	12.5.2 Pythia6	453
345	12.5.3 1 MeV Neutron Equivalent	455
346	12.5.4 Nearest Neighbor	457
347	12.5.5 Cross Checking	459
348	12.5.6 Future Goals	462
349	12.6 Calorimetry	462
350	12.6.1 The Barrel Electromagnetic Calorimeter	463
351	12.6.2 The Hadronic Barrel Calorimeter	465
352	12.6.3 Endcap Calorimeters	467
353	12.7 Calorimeter Simulation	468
354	12.7.1 Liquid Argon Barrel Calorimeter Simulation	469
355	12.7.2 Electromagnetic (warm) and Hadronic Barrel (tile) Calorimeter Simulation	469

356	12.7.3 Energy Resolution of the Combined Calorimeter System	475
357	12.7.4 Longitudinal Shower Profiles	475
358	12.7.5 Transverse Shower Profiles	477
359	12.8 Electromagnetic and Hadronic Forward/Backward Insert Calorimeter Simulation	
360	for the LHeC Detector	477
361	12.8.1 The Forward and Backward Calorimeter Construction	477
362	12.8.2 Calorimeter Simulation Conclusion	489
363	12.9 Further Option	493
364	12.10 Calorimeter Summary	493
365	12.11 Muon Detector	494
366	13 Forward and Backward Detectors	495
367	13.1 Luminosity Measurement and Electron Tagging	495
368	13.1.1 Options	496
369	13.1.2 Use of the Main LHeC Detector	496
370	13.1.3 Dedicated Luminosity Detectors in the tunnel	497
371	13.1.4 Small angle Electron Tagger	498
372	13.1.5 Summary and Open Questions	500
373	13.2 Polarimeter	501
374	13.2.1 Polarisation from the scattered photons	502
375	13.2.2 Polarisation from the scattered electrons	502
376	13.3 Zero Degree Calorimeter	503
377	13.3.1 ZDC detector design	503
378	13.3.2 Neutron Calorimeter	503
379	13.3.3 Proton Calorimeter	504
380	13.3.4 Calibration and monitoring	504
381	13.4 Forward Proton Detection	505
382	V Summary	510

383

Part I

384

Introduction

Chapter 1

Lepton-Hadron Scattering

It is almost exactly 100 years since the birth of the scattering experiment as a means of revealing the structure of matter. Geiger and Marsden's experiment [1] and its interpretation by Rutherford [2] set the scene for a century of ever-deeper and more precise resolution of the constituents of the atom, the nucleus and the nucleon. Lepton-hadron scattering has played a crucial role in this exploration over the past 55 years. The finite radius of the proton of about 1 fm was first established through elastic electron-proton scattering experiments [3]. Later, through inelastic electron proton scattering at Stanford [4,5], proton structure was understood in terms of quarks, still the smallest known constituents of matter. With the discovery of the scaling with Q^2 of the proton structure function $F_2(x, Q^2)$ for the originally accessed values around $x \simeq 0.2$ and its quark model interpretation in terms asymptotic freedom [6, 7], deep inelastic scattering (DIS) became a field of fundamental theoretical importance [8] to the understanding of the strong interaction. Precise measurements of the parton momentum distributions of the nucleon became a major testing ground for the selection and development of Quantum Chromodynamics (QCD) [9] as the appropriate theory of the strong interaction.

QCD is a Yang-Mills Lagrangian gauge field theory, in which the interaction between confined quarks proceeds via coloured gluons. With improved resolution, as provided by increased Q^2 , quarks can be resolved as quarks radiating gluons, whilst gluons may split into quark-antiquark pairs or, due to the non-abelian nature of the underlying gauge field theory, into pairs of gluons. The development of QCD beyond leading order is one of the most remarkable recent achievements of particle physics theory and experiment. It leads to a consistent description of all perturbatively accessible strong interaction observables, including the complex violations of the scaling of F_2 away from $x \sim 0.2$, as has recently been precisely measured over a wide kinematic range at HERA [10].

As discussed in detail in Section II, several fundamental properties of nature could be explored more deeply than hitherto through a continued programme of scattering electrons from protons and nuclei at a Large Hadron electron Collider (LHeC), as is proposed in sections III and IV. A few of the most pressing questions are outlined briefly below.

- The Standard Model of particle physics contains a remarkable, but unexplained, symmetry between quarks and leptons [11], with three generations, in each of which two quarks and two leptons are embedded. It was pointed out long ago [12] that it appears somewhat artificial that the basic building blocks of matter share the electromagnetic and the weak interactions but differ in their sensitivity to the strong interaction. Many theories which

419 unify the quark and lepton sectors, such as E6 [13], R -parity violating supersymmetry [14]
420 and left-right symmetric extensions of the Standard Model [15], predict new resonant
421 states with both lepton and baryon numbers, usually referred to as leptoquarks. Although
422 some of the specific theories have not been supported by experiment, the search for
423 leptoquarks has been a prime motivation for high energy scattering experiments. An
424 LHeC, in combination with the existing LHC programme, can extend this search into
425 a previously unexplored mass region, with the prospect of deciphering the leptoquark
426 quantum numbers.

427 • The mass of baryons is almost entirely due to strong interaction field energy, generated
428 through the self-interaction of gluons in a manner which is not yet well understood, but
429 which may be accessible through a more detailed mapping of QCD dynamics, particularly
430 in the low x region of proton structure, where gluon densities become very large and
431 $g \rightarrow gg$ splittings dominate. The search for the Higgs boson, which explains the masses of
432 the electroweak bosons, is currently the central focus of particle physics and is expected
433 to be resolved within the next year by the ATLAS and CMS experiments. The question
434 of hadronic mass deserves similar exploration.

435 • No analytic proof yet exists that QCD should exhibit the property of colour confinement,
436 though it is reasonable to assume that it is a consequence of gluon dynamics, as reflected
437 for example in popular hadronisation models [16]. Studying the behaviour of gluons under
438 new extreme conditions and contrasting the conditions under which the proton stays intact
439 with those in which it is destroyed may help to shed light on the precise mechanism at
440 work.

441 • the strong coupling constant α_s decreases as energy scales increase, in contrast to the en-
442 ergy dependence of the weak coupling and the fine structure constant. It appears possible
443 that the three constants approach a common value at energies of order 10^{15} GeV, such
444 that the distinctions we make between the electromagnetic, weak and strong interactions
445 are merely a consequence of the low energy scale at which we live. The possible grand
446 unification of the known interactions has been one of the major goals of modern particle
447 physics theory and experiment. Progress in this area requires that we know α_s , by far
448 the most poorly constrained of the fundamental couplings, much more accurately than is
449 currently the case. The LHeC promises a factor of ten reduction in the uncertainty on α_s
450 based on a major renewal and extension of the experimental and the theoretical basis of
451 DIS.

452 • After quarks were discovered, a distinction was soon made between valence and sea
453 quarks [17]. However, it was not until the high energy colliding beam configuration
454 of HERA became available that the rich partonic structure of the proton was fully re-
455 alised. Despite the resulting fast development of our knowledge of the parton momentum
456 distribution functions (PDFs) in the proton, there are still many outstanding important
457 questions concerning quark-gluon interactions in hadronic matter, which cannot be an-
458 swered with currently available data.

459 – Modern determinations of PDFs assume that sea quarks and anti-quarks have the
460 same momentum distributions. Experimental constraints are required to test this
461 assumption.

- 462 – Similarly, the strange-quark density is often assumed to be a fixed fraction of the
463 down-quark density, for which there is no experimental verification.
- 464 – With no high energy DIS data available from deuteron scattering, the low x quark
465 content of the neutron is unresolved. It is important to test the assumption of
466 isospin symmetry, which relates for example the neutron down quark distribution to
467 the proton up-quark distribution.
- 468 – The gluon density is still not precisely determined, particularly at small and large x
469 values. This has implications for example to our knowledge of the Higgs boson cross
470 section at the LHC, since the dominant production mechanism is through gluon-
471 gluon fusion.
- 472 – With no data on the scattering of leptons from heavy ions with colliding beam
473 kinematics, our knowledge of the modifications to nucleon parton densities when
474 they are bound inside nuclei, rather than free, is restricted to high x values. This is
475 reflected in a lack of detailed understanding of shadowing phenomena, particularly
476 for the gluon density and a corresponding lack of knowledge of the initial state of
477 heavy ion collisions at LHC energies.
- 478 – The emission of partons is assumed in PDF fits to be governed by the linear DGLAP
479 evolution equations, an approximation to a full solution to QCD in which parton
480 cascades are ordered in transverse momentum. There are good reasons to believe
481 that the DGLAP approximation is insufficient to describe the Q^2 evolution of low
482 x partons, even within the x range to which the LHC rapidity plateau corresponds.
483 Inclusive DIS and jet data in an extended low x kinematic regime are required to
484 resolve this situation.
- 485 – The understanding of the role of heavy quarks in QCD is still at its infancy. Charm
486 may exist in an intrinsic state [18]. The b density, which plays an important role in
487 the production mechanisms for new particles in many LHC scenarios, is measured to
488 only about 20% accuracy and the role of top quarks in DIS is completely unknown
489 due to the limited energy and luminosity of HERA.
- 490 – While ordinary quark distributions correspond to an incoherent sum of squared am-
491 plitudes, a new approach has been developed, which uses quark amplitudes and
492 Generalised Parton Distributions (GPDs) to understand proton structure in a new,
493 three-dimensional way [19,20]. Our understanding of GPDs is limited by the relative
494 paucity of experimental data on exclusive DIS channels.
- 495 • The rapid rise of the proton gluon density as x decreases cannot continue indefinitely.
496 At x values within the reach of LHeC ep and eA scattering, a transition takes place
497 from the currently known DIS regime in which the proton behaves as a dilute system
498 to a new low x domain in which parton densities saturate and the proton approaches
499 a 'black disk' limit [21]. This latter region represents a fundamentally new regime of
500 strong interaction dynamics, for which a rich phenomenology has developed, but where
501 the detailed mechanisms and the full consequences are not yet known. Experimental data
502 at sufficiently low x with scales which are large enough to allow a partonic interpretation
503 are urgently required in order to test the models and fully understand the behaviour of
504 partons at high densities.

505 Despite its huge success in describing existing high energy data, the Standard Model is known
506 to be incomplete, not only due to the absence of an experimentally established mechanism

507 for electroweak symmetry breaking. As the exploitation of the TeV energy regime and the
508 high luminosities of the LHC era develops further, a full understanding can only be obtained
509 by challenging the existing theory through new precision measurements, as broad in scope
510 as possible, with initial states involving leptons as well as quarks and gluons. Furthermore,
511 many of the remaining open fundamental questions in our field are associated with the strong
512 interaction sector of the Standard Model, to which a future facility such as the LHeC provides
513 unique experimental sensitivity.

514 Chapter 2

515 Design Considerations

516 The following sections describe briefly which general considerations have determined the LHeC
517 design as presented in this report. Major changes to the underlying assumptions would naturally
518 require an appropriately changed variation of the design.

519 2.1 DIS and Particle Physics

520 Deep inelastic scattering experiments with charged leptons may be classified as low energy,
521 medium and high energy experiments. The pioneering low energy DIS experiment, which dis-
522 covered quarks, was performed at SLAC. Classic medium energy experiments were the BCDMS
523 and the NMC experiments at CERN, while HERA, the first ep collider ever built, had pushed
524 the DIS energy reach to the Fermi scale. This allowed the field of deep inelastic scattering to
525 develop as part of the energy frontier particle physics, complementary to the Tevatron and LEP.
526 In all three areas, the field of DIS is considering upgrade projects with the 12 GeV upgrade at
527 Jlab, the medium energy colliders at Jlab and/or BNL, possibly fixed target further neutrino
528 experiments and the LHeC.

529 The LHeC provides the only realistic possibility for an energy frontier ep programme in the
530 coming probably three decades. Owing to the LHC, there is one opportunity to complement
531 the TeV scale pp machine with a TeV energy ep collider, besides a pure lepton collider in this
532 energy range. It took about 30 years for HERA, LEP and the Tevatron to be built, operated
533 and analysed. The exploration of the tera energy scale is subject to similar time horizons.

534 2.2 Synchronous pp and ep operation

535 The intense, energetic hadron beams of the LHC provide the unique possibility to realise a
536 luminous experimental programme of deep inelastic scattering at TeV energies. The LHeC is
537 therefore by its nature an upgrade to the LHC, which gives it its site and in a way determines
538 its dimensions too. The first design consideration builds on the assumption that the LHC still
539 runs in pp mode when an electron beam becomes operational. This has several implications:

- 540 • The LHeC has to be built in the coming about 10 years.

- 541 • The design has to be adapted for synchronous pp and ep (or e.g. pA and eA) operation -
542 for example with magnets in the IR to steer three beams and with civil engineering and
543 detector modularity requirements to be compliant with the LHC operation and upgrade
544 programme.
- 545 • The synchronous operation of pp and ep allows to collect a high integrated luminosity and
546 makes the most efficient use of both the proton beams and the electron beam installation
547 too.

548 It can not realistically be assumed today, that the ep physics would commence only when the
549 pp programme was finished: because of the finite LHC lifetime, which nowadays is estimated
550 to be about 20 years.

551 The LHeC is thus thought and designed to accompany the proton and the ion physics
552 programme of the LHC in its high luminosity phase, now assumed to begin in 2023.

553 2.3 Choice of Electron Beam Energy

554 The centre of mass energy squared of an ep collider is $s = 4E_e E_p$. It determines the maximum
555 four-momentum transfer squared, Q^2 , between the electron and the proton because $Q^2 = sxy$,
556 where x is the fraction of four momentum of the proton carried by the struck parton while y
557 is the inelasticity of the scattering process which in the laboratory frame is the relative energy
558 transfer, with $0 < x, y \leq 1$.

559 HERA has operated with a proton beam energy of $E_p = 0.92$ TeV and an electron (and
560 positron) beam energy of $E_e = 27.5$ GeV. With Sokolov-Ternov build-up times of about half an
561 hour, the electron beam became polarised and mean polarisations of up to 40% were achieved.
562 HERA has not accelerated any hadron beam other than protons. The LHeC has to surpass
563 these parameters significantly for a unique and exciting programme to be pursued.

564 The LHeC can use an up to 7 TeV energy proton beam. For this design study the electron
565 beam energy is set to 60 GeV. This implies that the gain in s , or Q^2 at fixed (x, y) , as compared
566 to HERA will be a factor of 16.6, or about 4 in \sqrt{s} . The real gain in range of Q^2 and x will even
567 be larger as with the superior luminosity even the highest Q^2 values and x close to 1 become
568 accessible then. The kinematic range of the LHeC as compared to HERA at low x and at high
569 Q^2 is illustrated in Fig. 2.1.

570 The choice of a default $E_e = 60$ GeV for this design report is dictated by physics and by
571 practical considerations:

- 572 • New physics has been assumed to appear at the TeV energy scale. At the time of com-
573 pletion of this report, the LHC has excluded much of the sub-TeV physics beyond the
574 Standard Model (SM) but leaves the possibility open of resonant lepton-parton states
575 with masses of larger than about 500 GeV, for which the LHeC would be a particularly
576 suitable machine with a range of up to $M \lesssim \sqrt{s}$.
- 577 • High precision QCD and electroweak physics require a maximum range in $\ln Q^2$ and
578 highest Q^2 , respectively. The unification of electromagnetic and weak forces takes place
579 at $Q^2 \simeq M_Z^2$ which is much exceeded by the LHeC energies. Part of the electroweak
580 physics requires lepton beam polarisation which as is shown below may reach values (for
581 the ring) as at HERA at 60 GeV but much less at significantly larger E_e .

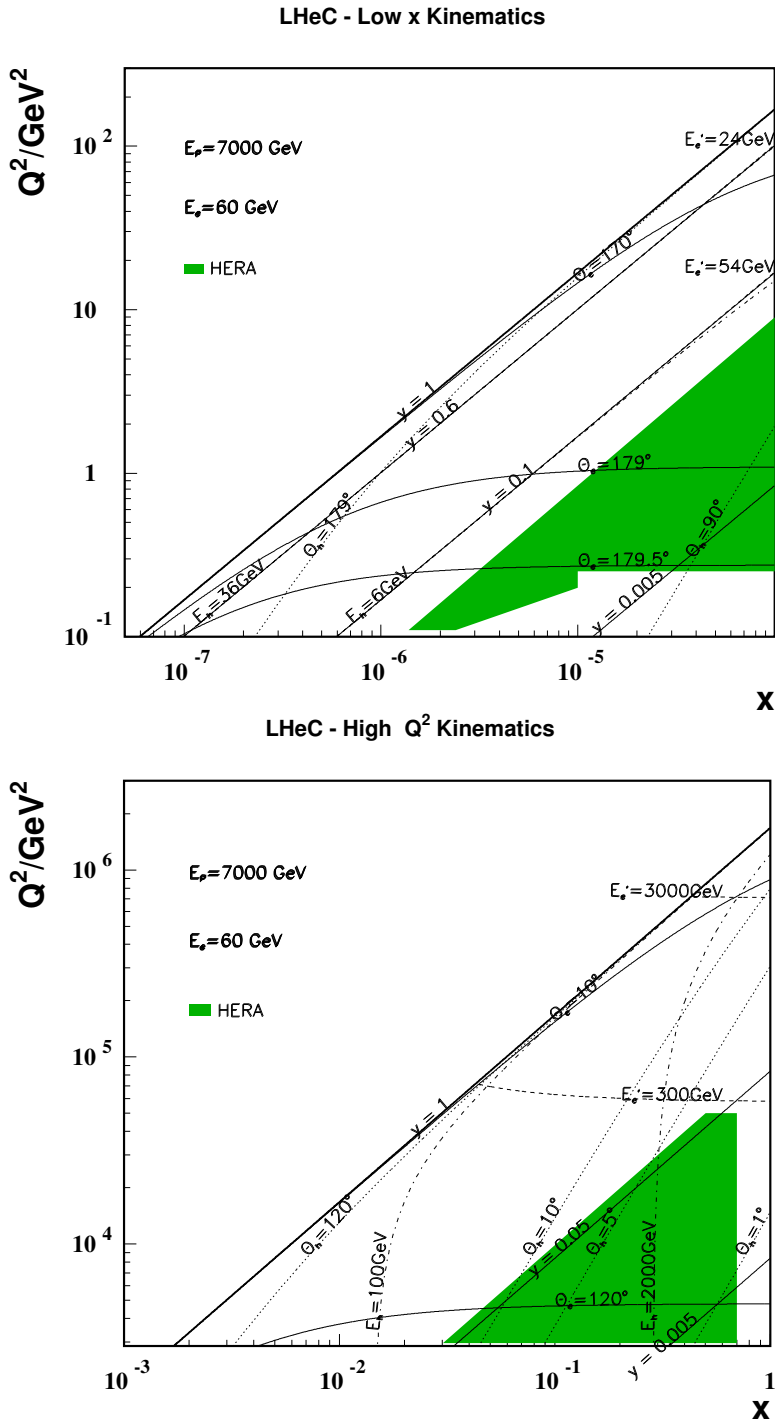


Figure 2.1: Kinematics of ep scattering at the LHeC at low x (top) and high Q^2 (bottom). Solid (dotted) curves correspond to constant polar angles θ_e (θ_h) of the scattered electron (hadronic final state). The polar angle is defined with respect to the proton beam direction. Dashed (dashed-dotted) curves correspond to constant energies E'_e (E_h) of the scattered electron (hadronic final state). The shaded area illustrates the region of kinematic coverage in neutral current scattering at HERA. The energy and angle isochrone lines are discussed in the detector design chapter in detail.

- 582 • The discovery of gluon saturation requires to measure at typical values of small $x \simeq 10^{-5}$
583 with $Q^2 \gg M_p^2$, where M_p is the mass of the proton. The choice of energies ensures this
584 discovery in ep collisions in the DIS region.
- 585 • Energy losses by synchrotron radiation, $\propto E_e^4$, both in the ring and the return arcs for
586 the linac, can be kept at reasonable levels, in terms of the power, P , needed to achieve
587 high luminosity and the radius of the racetrack return arcs for the linac too.

588 It so appears that 60 GeV is an appropriate and affordable choice. It yet is well possible that the
589 60 GeV may not be the final value of the electron beam energy, especially if the LHC would find
590 non-SM physics just above the now chosen energy range. The design therefore also considers
591 a dedicated high energy beam of 140 GeV as an option, which yet has not been worked out to
592 any comparable detail ¹.

593 2.4 Detector Constraints

594 One easily recognises, in Fig. 2.1, that the asymmetry of the electron and proton beam energies
595 poses severe constraints to the detector design: i) the “whole” low Q^2 and low x physics requires
596 to measure the electron, of energy $E'_e \lesssim E_e$, scattered in backward direction between about
597 170° and 179° , and ii) the forward scattered final state, of energy comparable to E_p , needs to
598 be reconstructed down to very small angles in order to cover the high x region in a range of
599 not too extreme Q^2 .

600 The current detector design considers an option to have split data taking phases, like HERA
601 I and II, with different interaction region configurations, a high acceptance phase, covering
602 $1^\circ - 179^\circ$, at reduced luminosity and a high luminosity phase, of acceptance limited to $8^\circ - 172^\circ$.
603 In the course of the study, however, an optics was found for the high acceptance configuration
604 with only a factor of two reduced luminosity. It is likely, therefore, that the TDR will lead to a
605 unification of these configurations and correspondingly weakened demands on the modularity
606 of the inner detector region.

607 Synchronous ep and pp operation implies that at least one of the four IPs, currently occupied
608 by experiments, will have to be free'd for an LHeC detector. It was decided to use for this report
609 IP2 as an example site and to limit the study of bypasses, in the ring option, to IP1 and IP5.
610 This does not imply that any decision was taken about which experiment one would favour to
611 stop in ten years.

612 2.5 Two Electron Beam Options

613 It was shown a few years ago [?] that an electron beam in the LHC tunnel would allow to
614 achieve an outstanding luminosity of about $10^{33} \text{ cm}^{-2} \text{ s}^{-1}$ in ep interactions for both electrons
615 and positrons. It is obvious, however, that while such a ring may be built without any major
616 technical obstacle, installing it on top of the LHC magnet ring would be a non-trivial engineering
617 task. For this reason it was decided to consider besides this “ring-ring (RR)” option also a
618 “linac-ring (LR)” configuration, with a linear electron accelerator tangential to the LHC. For

¹Such a large E_e would also fit better to a future HE LHC, when about 16 TeV proton beam energy might become available in the yet much farther future, as that would keep the $e - p$ beam energy asymmetry tolerable.

619 the comparison of RR and LR options, E_e was kept the same 60 GeV. The ring may extend to
 620 somewhat higher energies, while only a Linac would allow to exceed 100 GeV E_e largely.

621 This report presents all major components and considerations for both the RR and the LR
 622 configuration. A decision is envisaged soon after the appearance of the CDR. It is important
 623 to consider that the RR configuration delivers high electron and positron luminosity, with
 624 difficulties for high polarisation, while the LR configuration has a high potential for polarised
 625 electrons but difficulties to deliver an intense positron beam, yet offering also a photon beam
 626 option. A choice of one over the other option has primarily to be based on physics but as well
 627 technical, cost and further considerations, which is why considerable effort had been spent to
 628 develop both options to the required detail. No attempt is made in the report to favour one
 629 over the other configuration. In the period of this design study both options came into a very
 630 fruitful interaction and occasional competition which nicely boosted both designs.

631 2.6 Luminosity and Power

632 The relation of the luminosity, power and energy differs for the RR and the LR configurations.
 633 In the case of the ring accelerator, as for HERA, the luminosity for matched beams is determined
 634 by the number of protons per bunch (N_p), the normalised proton beam emittance (ϵ_p), the x, y
 635 coordinates of the proton beam beta function values at the interaction point ($\beta_{x,y}$) and the
 636 electron beam current (I_e) as

$$L = \frac{N_p \cdot \gamma}{4\pi e \epsilon_p} \cdot \frac{I_e}{\sqrt{\beta_{px} \beta_{py}}}, \quad (2.1)$$

637 with $\gamma = E_p/M_p$. The design luminosity assumes the so-called ultimate proton beam parameters
 638 for $E_p = 7$ TeV with $1.7 \cdot 10^{11}$ protons per bunch and $\epsilon_p = 3.8 \mu\text{m}$. Eq. 2.1 then corresponds to

$$L = 8.2 \cdot 10^{32} \text{cm}^{-2} \text{s}^{-1} \cdot \frac{N_p 10^{11}}{1.7} \cdot \frac{m}{\sqrt{\beta_{px} \beta_{py}}} \cdot \frac{I_e}{50 \text{mA}}, \quad (2.2)$$

639 where the electron beam current is given by

$$I_e = 0.35 \text{mA} \cdot P[\text{MW}] \cdot \left(\frac{100}{E_e[\text{GeV}]} \right)^4 \quad (2.3)$$

640 Consequently one needs to minimize the β functions and gains linearly with P and like E_e^4
 641 when decreasing the electron beam energy. With $\beta_{x(y)} = 1.8(0.5)$ m, see the optics section, one
 642 obtains a typical value of $10^{33} \text{cm}^{-2} \text{s}^{-1}$ luminosity for $E_e = 60$ GeV with 30 MW of beam power.
 643 The dependence of $L(E, P)$ is shown in Fig. 2.2 (top) for the RR configuration. While with the
 644 matching requirement for each E_e an evaluation would have to be done of the β functions, one
 645 yet recognises that the RR option has a great potential to indeed achieve very high luminosities,
 646 even exceeding $10^{33} \text{cm}^{-2} \text{s}^{-1}$ if E_e was a bit lowered and P somewhat enlarged.

647 For this design report on the LHeC a wall-plug power limit was set of 100 MW, about one
 648 fifth of what one is considering for CLIC, for example. With a 10 years running period at such
 649 a high luminosity and N_p probably enlarged, one can consider an integrated luminosity for the
 650 LHeC of $O(100) \text{fb}^{-1}$ a realistic perspective in simultaneous operation with the LHC. This
 651 is two orders of magnitude more than HERA delivered. That is necessary for exploiting the
 652 high Q^2 and large x boundaries. It means that the whole low Q^2 physics program, with the

653 exception of rare processes as DVCS and subject to trigger acceptance considerations, may yet
 654 be pursued in a rather short period of time.

655 A linear electron beam colliding with a storage ring proton beam was considered quite
 656 some time ago [?]. Its luminosity, for head-on collisions, can be obtained from the following
 657 relation [?], similar to Eq. 2.1

$$L = \frac{N_p \cdot \gamma}{4\pi e \epsilon_p} \cdot \frac{I_e}{\beta^*}, \quad (2.4)$$

658 which scales as

$$L = 8 \cdot 10^{31} \text{ cm}^{-2} \text{ s}^{-1} \cdot \frac{N_p 10^{11}}{1.7} \cdot \frac{0.2 \text{ m}}{\beta^*} \cdot \frac{I_e}{1 \text{ mA}}, \quad (2.5)$$

659 where the electron beam current is given by

$$I_e = \text{mA} \cdot \frac{P[\text{MW}]}{(1 - \eta) E_e[\text{GeV}]}. \quad (2.6)$$

660 Here η denotes the efficiency of the energy recovery process. It is easy to see that a pulsed linac
 661 without recovery is short by an order of magnitude in the luminosity to the RR configuration,
 662 even for an ambitious β^* value of 0.1 m, which is introduced in the LR section. With energy
 663 recovery, however, and an efficiency above 90 % as is expected to be realistic for the LHeC case,
 664 one obtains luminosities of similar value as in the RR case, see Fig. 2.2. The energy recovery
 665 linac (ERL) operates the cavities in CW mode at modest gradients of typically 20 MV/m.

666 The recovery of energy requires a racetrack geometry of the linac with return arcs, or possibly
 667 two linacs of opposite orientation as was originally considered [?]. This introduces synchrotron
 668 radiation losses as a parameter of concern to the LR configuration too. With the design here
 669 proposed, the arcs have a radius of xx km, which leads to a LR accelerator of about 9 km length,
 670 which is one third of the LHC circumference, and requires a small compensation stage for the
 671 energy losses in the arcs.

672 A straight high energy, pulsed linac is also considered, which at $E_e = 140 \text{ GeV}$, reaches
 673 a luminosity of about $5 \cdot 10^{31}$, the design value of the HERA upgrade phase. One can also
 674 contemplate about stages of ERL returns, which provide much higher luminosities in this case,
 675 as is briefly demonstrated in this report too.

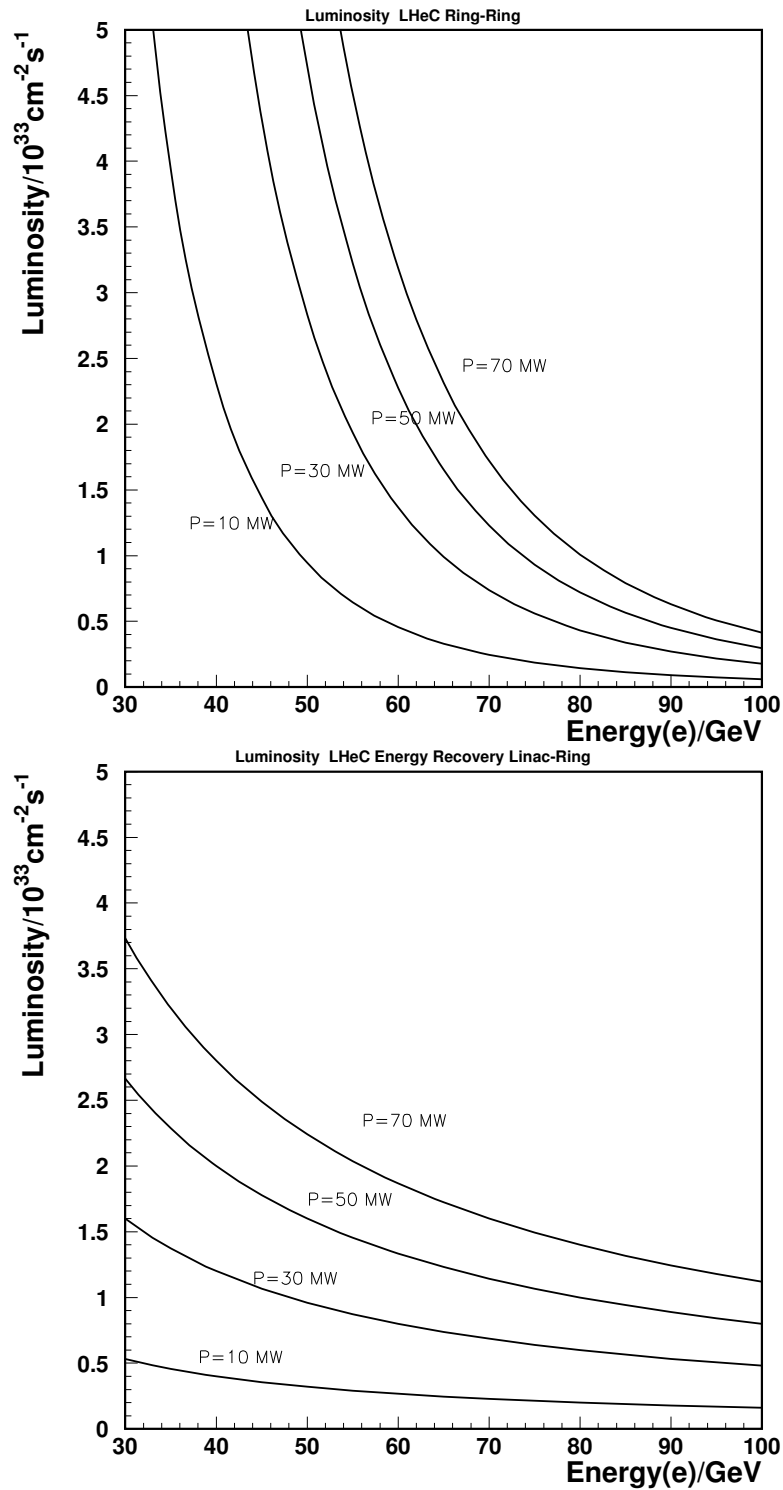


Figure 2.2: Estimated luminosity, in units of $10^{33} \text{ cm}^{-2} \text{ s}^{-1}$, for the RR configuration (top) and the LR energy recovery configuration (bottom), displayed as a function of the electron beam energy with the beam power as a parameter, see text.

⁶⁷⁶ Chapter 3

⁶⁷⁷ Executive Summary

⁶⁷⁸ The excutive summary will be added after the completion of the referee process.

679

Part II

680

Physics

Chapter 4

Precision QCD and Electroweak Physics

4.1 Inclusive Deep Inelastic Scattering

4.1.1 Cross Sections and Structure Functions

The scattering amplitude for electron-proton scattering is a product of lepton and hadron currents times the propagator characteristic of the exchanged particle, a photon or Z_0 in neutral current scattering, a W^\pm in charged current scattering. The inclusive scattering cross section therefore is given by the product of two tensors,

$$\frac{d^2\sigma}{dx dQ^2} = \frac{2\pi\alpha^2}{Q^4 x} \sum_j \eta_j L_j^{\mu\nu} W_j^{\mu\nu}, \quad (4.1)$$

where j denotes the summation over γ , Z_0 exchange and their interference for NC, and $j = W^+$ or W^- for CC. The leptonic tensor $L_j^{\mu\nu}$ is related to the coupling of the electron with the exchanged boson and contains the electromagnetic or the weak couplings, such as the vector and axial-vector electron- Z_0 couplings, v_e and a_e , in the NC case. This leptonic part of the cross section can be calculated exactly in the standard electroweak $U_1 \times SU_2$ theory. The hadronic tensor, however, describing the interaction of the exchanged boson with the proton, can only be reduced to a sum of structure functions, $F_i(x, Q^2)$, but not be fully calculated. Conservation laws reduce the number of basic structure functions in unpolarised ep scattering to $i = 1 - 3$. In perturbative QCD the structure functions are related to parton distributions f via coefficient functions C

$$[F_{1,3}, F_2] = \sum_i \int_0^1 [1, z] \frac{dz}{z} C_{1,2,3}\left(\frac{x}{z}, \frac{Q^2}{\mu_r^2}, \frac{\mu_f^2}{\mu_r^2}, \alpha_s(\mu_r^2)\right) \cdot f_i(z, \mu_f^2, \mu_r^2), \quad (4.2)$$

where i sums the quark q , anti-quark \bar{q} and gluon g contributions and $f_i(x)$ is the probability distribution of the parton of type i to carry a fraction x of the proton's longitudinal momentum. The coefficient functions are exactly calculable but depend on the factorisation and renormalisation scales μ_f and μ_r . The parton distributions are not calculable but have to be determined

704 by experiment. Their Q^2 dependence obeys evolution equations. A general factorisation the-
 705 orem, however, has proven the parton distributions to be universal, i.e. to be independent of
 706 the type of hard scattering process. This makes deep inelastic lepton-nucleon scattering a most
 707 fundamental process: the parton distributions in the proton are measured best with a lepton
 708 probe and may be used to predict hard scattering cross sections at, for example, the LHC. The
 709 parton distributions are derived from measurements of the structure functions in NC and CC
 710 scattering, as is discussed below.

711 4.1.2 Neutral Current

712 The neutral current deep inelastic ep scattering cross section, at tree level, is given by a sum
 713 of generalised structure functions according to

$$\frac{d^2\sigma_{NC}}{dx dQ^2} = \frac{2\pi\alpha^2 Y_{\pm}}{Q^4 x} \cdot \sigma_{r,NC} \quad (4.3)$$

$$\sigma_{r,NC} = \mathbf{F}_2 + \frac{Y_-}{Y_+} \mathbf{xF}_3 - \frac{y^2}{Y_-} \mathbf{FL}, \quad (4.4)$$

714 where the electromagnetic coupling constant α , the photon propagator and a helicity factor are
 715 absorbed in the definition of a reduced cross section σ_r , and $Y_{\pm} = 1 \pm (1-y)^2$. The functions
 716 \mathbf{F}_2 and \mathbf{xF}_3 depend on the lepton beam charge and polarisation (P) and on the electroweak
 717 parameters as [22]

$$\begin{aligned} \mathbf{F}_2^{\pm} &= F_2 + \kappa_Z(-v_e \mp Pa_e) \cdot F_2^{\gamma Z} + \kappa_Z^2(v_e^2 + a_e^2 \pm 2Pv_e a_e) \cdot F_2^Z \\ \mathbf{xF}_3^{\pm} &= \kappa_Z(\pm a_e + Pv_e) \cdot xF_3^{\gamma Z} + \kappa_Z^2(\mp 2v_e a_e - P(v_e^2 + a_e^2)) \cdot xF_3^Z. \end{aligned} \quad (4.5)$$

718 In the on-mass shell \overline{MS} scheme the propagator function κ_Z is given by the weak boson masses
 719 (M_Z, M_W)

$$\kappa_Z(Q^2) = \frac{Q^2}{Q^2 + M_Z^2} \cdot \frac{1}{4 \sin^2 \Theta \cos^2 \Theta} \quad (4.6)$$

720 with the weak mixing angle $\sin^2 \Theta = 1 - M_W^2/M_Z^2$. In the hadronic tensor decomposition [23]
 721 the structure functions are well defined quantities. In the Quark Parton Model (QPM) the
 722 longitudinal structure function is zero [24] and the two other functions are given by the sums
 723 and differences of quark (q) and anti-quark (\bar{q}) distributions as

$$\begin{aligned} (F_2, F_2^{\gamma Z}, F_2^Z) &= x \sum (e_q^2, 2e_q v_q, v_q^2 + a_q^2)(q + \bar{q}) \\ (xF_3^{\gamma Z}, xF_3^Z) &= 2x \sum (e_q a_q, v_q a_q)(q - \bar{q}), \end{aligned} \quad (4.7)$$

724 where the sum extends over all up and down type quarks and $e_q = e_u, e_d$ denotes the electric
 725 charge of up- or down-type quarks. The vector and axial-vector weak couplings of the fermions
 726 ($f = e, u, d$) to the Z_0 boson in the standard electroweak model are given by

$$v_f = i_f - e_f 2 \sin^2 \Theta \quad a_f = i_f \quad (4.8)$$

727 where $e_f = -1, 2/3, -1/3$ and $i_f = I(f)_{3,L} = -1/2, 1/2, -1/2$ denotes the left-handed weak
 728 isospin charges, respectively. Thus the vector coupling of the electron, for example, is very
 729 small, $v_e = -1/2 + 2 \sin^2 \Theta \simeq 0$, since the weak mixing angle is roughly equal to $1/4$.

730 At low Q^2 and low y the reduced NC cross section, Eq. 4.3, to a very good approximation is
 731 given by $\sigma_r = F_2(x, Q^2)$. At $y > 0.5$, F_L makes a sizeable contribution to $\sigma_{r,NC}$. In the DGLAP
 732 approximation of perturbative QCD, to lowest order, the longitudinal structure function is given
 733 by [25]

$$F_L(x) = \frac{\alpha_s}{4\pi} x^2 \int_x^1 \frac{dz}{z^3} \cdot \left[\frac{16}{3} F_2(z) + 8 \sum e_q^2 \left(1 - \frac{x}{z}\right) z g(z) \right], \quad (4.9)$$

734 which at low x is dominated by the gluon contribution. A measurement of F_L requires a
 735 variation of the beam energy.

736 Two further structure functions can be accessed with cross section asymmetry measure-
 737 ments, in which the charge and/or the polarisation of the lepton beam are varied. A charge
 738 asymmetry measurement, with polarisation values P_{\pm} of the e^{\pm} beam, determines the following
 739 structure function combination

$$\sigma_{r,NC}^+(P_+) - \sigma_{r,NC}^-(P_-) = -\kappa_Z a_e (P_+ + P_-) \cdot F_2^{\gamma Z} + \frac{Y_-}{Y_+} \kappa_Z a_e \cdot [2x F_3^{\gamma Z} + (P_+ - P_-) \kappa_Z a_e x F_3^Z] \quad (4.10)$$

740 neglecting terms $\propto v_e$ which can be easily obtained from Eq. 4.5. If data are taken with opposite
 741 polarisation and charge, the asymmetry represents a measurement of the difference of quark
 742 and anti-quark distributions in NC, see Eq. 4.7. In contrast to what is often stated, the charge
 743 asymmetry is a parity conserving quantity $\propto a_e a_q$. Assuming symmetry between sea and
 744 antiquarks, it is a direct measure of the valence quarks, $x F_3^{\gamma Z} = 2u_v + d_v$, in ep . This function
 745 was measured for the first time in μ^{\pm} Carbon scattering by the BCDMS Collaboration [26] at
 746 large $x > 0.2$ and for Q^2 of about 50 GeV². With the LHeC, for the first time, high precision
 747 measurements of $x F_3$ in NC become possible as is demonstrated in Sect. 4.2.2. These will access
 748 the valence quarks at low $x \lesssim 0.001$ for the first time in direct measurements.

749 A genuine polarisation asymmetry measurement, keeping the beam charge fixed, according
 750 to eqs. 4.3 and 4.5 determines a similar combination of $F_2^{\gamma Z}$ and $x F_3^{\gamma Z}$

$$\frac{\sigma_{r,NC}^{\pm}(P_L) - \sigma_{r,NC}^{\pm}(P_R)}{P_L - P_R} = \kappa_Z [\mp a_e F_2^{\gamma Z} + \frac{Y_-}{Y_+} v_e x F_3^{\gamma Z}] \simeq \mp \kappa_Z a_e F_2^{\gamma Z} \quad (4.11)$$

751 neglecting again the term $\propto v_e$. The product $a_e F_2^{\gamma Z}$ is proportional to combinations $a_e v_q$ and
 752 thus a direct measure of parity violation at very small distances.

753 The structure function $F_2^{\gamma Z}$ accesses a new combination of quark distributions and is mea-
 754 surable for the first time, and with high precision, at the LHeC, see Fig. 4.1, in which the result
 755 is shown of its possible measurement. The remarkable precision on $F_2^{\gamma Z}$ illustrates the huge
 756 potential in precision and range which the LHeC brings. For the study of electroweak effects one
 757 clearly desires to have the maximum beam energy and polarisation available as the comparison
 758 of the two results for different beam conditions but the same luminosity in Fig. 4.1 shows.

759 The polarisation asymmetry also permits a high precision measurement of the weak mixing
 760 angle at different Q^2 values, below and to much higher values than M_Z^2 , at which $\sin^2 \Theta$ was
 761 precisely measured at LEP and the SLC, see Sect. 4.6.1.

762 4.1.3 Charged Current

763 The inclusive polarised charged current $e^{\pm}p$ scattering cross section can be written as

$$\frac{d^2 \sigma_{CC}^{\pm}}{dx dQ^2} = \frac{1 \pm P}{2} \cdot \frac{G_F^2}{2\pi x} \cdot \left[\frac{M_W^2}{M_W^2 + Q^2} \right]^2 Y_{\pm} \cdot \sigma_{r,CC}. \quad (4.12)$$

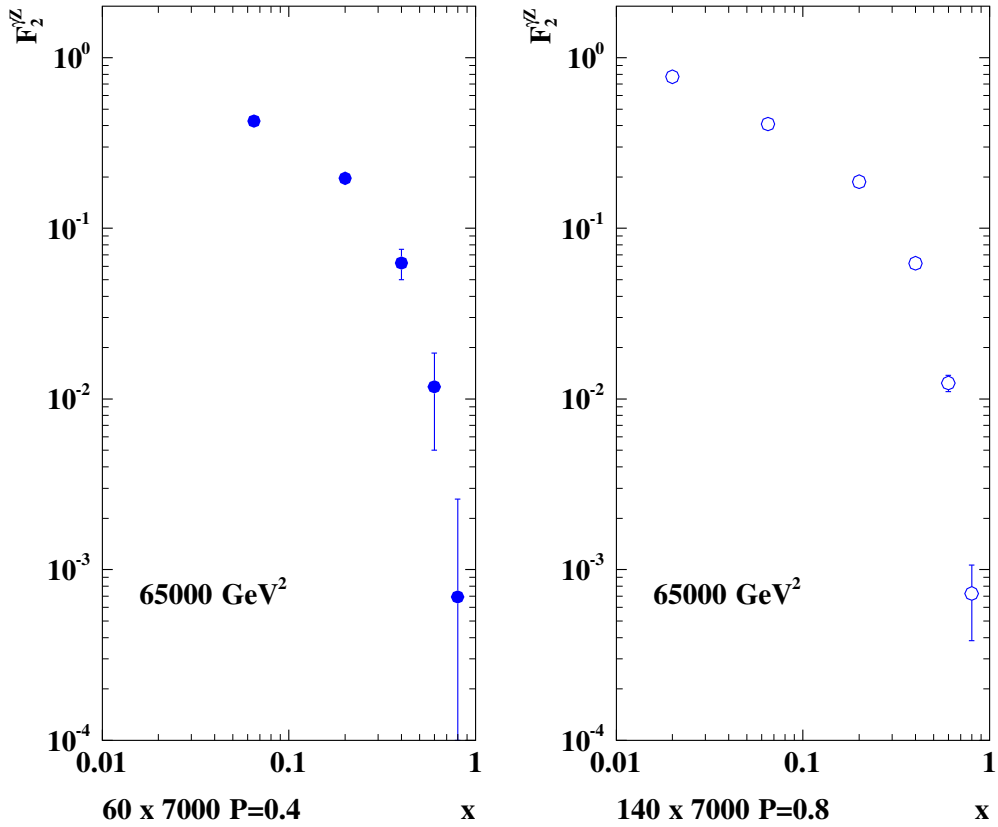


Figure 4.1: Simulation of the measurement of the γZ interference structure function $F_2^{\gamma Z}$, shown as a function of x for a typical high Q^2 value, for two LHeC configurations ($E_e = 60$ GeV and $P = \pm 0.4$, left) and ($E_e = 140$ GeV and $P = \pm 0.9$, right). The proton beam energy is 7 TeV and the luminosity assumed is 10 fb^{-1} per polarisation state. This function is a measure for parity violation and provides additional information on the quark distributions as it is proportional to $e_q v_q$ to be compared with e_q^2 in the lowest order function F_2 . Shown are statistical uncertainties only. The systematic uncertainty can be expected to be small as in the asymmetry many effects cancel and because at the LHeC such asymmetries are large, and the polarisation possibly controlled at the per mille level, as is discussed in the technical part of the CDR.

764 The reduced charged current cross section, analogous to the NC case Eq. 4.3, is a sum of
765 structure function terms

$$\sigma_{r,CC}^{\pm} = W_2^{\pm} \mp \frac{Y_-}{Y_+} xW_3^{\pm} - \frac{y^2}{Y_+} W_L^{\pm}. \quad (4.13)$$

766 In the on-mass shell scheme, the Fermi constant G_F is defined, see for example [27], using the
767 weak boson masses as

$$G_F = \frac{\pi\alpha}{\sqrt{2}M_W^2 \sin^2\theta(1 - \Delta r)} \quad (4.14)$$

768 with $\sin^2\theta = 1 - M_W^2/M_Z^2$ as above. The higher order correction term Δr can be approximated
769 [28] as $\Delta r = 1 - \alpha/\alpha(M_Z) - 0.0094(m_t/173\text{GeV})^2/\tan^2\theta$, and thus introduces a dependence
770 of the DIS cross section on the mass of the top quark. The choice of G above allows the CC
771 cross section, Eq. 4.12, to be rewritten as

$$\frac{d^2\sigma_{CC}^{\pm}}{dx dQ^2} = \frac{1 \pm P}{2} \cdot \frac{2\pi\alpha^2 Y_+}{Q^4 x} \cdot \kappa_W^2 \cdot \sigma_{r,CC}, \quad (4.15)$$

772 with

$$\kappa_W(Q^2) = \frac{Q^2}{Q^2 + M_W^2} \cdot \frac{1}{4\sin^2\theta}, \quad (4.16)$$

773 which is convenient for the consideration of NC/CC cross section ratios.

774 In the QPM (where $W_L^{\pm} = 0$), the structure functions represent beam charge dependent
775 sums and differences of quark and anti-quark distributions and are given by

$$W_2^+ = x(\bar{U} + D), \quad xW_3^+ = x(D - \bar{U}), \quad W_2^- = x(U + \bar{D}), \quad xW_3^- = x(U - \bar{D}). \quad (4.17)$$

776 Using these equations one finds

$$\sigma_{r,CC}^+ \sim x\bar{U} + (1-y)^2 xD, \quad (4.18)$$

$$\sigma_{r,CC}^- \sim xU + (1-y)^2 x\bar{D}. \quad (4.19)$$

777 Combined with Equation 4.5, which approximately reduces to

$$\begin{aligned} \sigma_{r,NC}^{\pm} &\simeq [c_u(U + \bar{U}) + c_d(D + \bar{D})] + \kappa_Z[d_u(U - \bar{U}) + d_d(D - \bar{D})] \\ c_{u,d} &= e_{u,d}^2 + \kappa_Z(-v_e \mp Pa_e)e_{u,d}v_{u,d} \quad d_{u,d} = \pm a_e a_{u,d} e_{u,d}, \end{aligned} \quad (4.20)$$

778 one finds that the NC and CC cross section measurements at the LHeC determine the complete
779 set U , D , \bar{U} and \bar{D} , i.e. the sum of up-type, of down-type and of their anti-quark-type distribu-
780 tions. Below the b quark mass threshold, these are related to the individual quark distributions
781 as follows

$$U = u + c \quad \bar{U} = \bar{u} + \bar{c} \quad D = d + s \quad \bar{D} = \bar{d} + \bar{s}. \quad (4.21)$$

782 Assuming symmetry between sea quarks and anti-quarks, the valence quark distributions result
783 from

$$u_v = U - \bar{U} \quad d_v = D - \bar{D}. \quad (4.22)$$

784 **4.1.4 Cross Section Simulation and Uncertainties**

785 The LHeC extends the kinematic range as compared to HERA in the negative momentum
 786 transfer squared Q^2 from a maximum of about 0.03 to 1 TeV² and towards low x , e.g. for
 787 $Q^2 = 3 \text{ GeV}^2$, from about $4 \cdot 10^{-5}$ to $2 \cdot 10^{-6}$. The projected increase of integrated luminosity
 788 by a factor of 100 allows to also extend the kinematic range at large x , in charged currents,
 789 from practically about 0.4 to 0.8. Due to the enlarged electron beam energy E_e the range of
 790 high inelasticity $y \simeq 1 - E'_e/E_e$ should extend closer to 1. A reduced noise in the calorimeters
 791 may allow to reach lower values of y than at HERA, also because the hadronic y is determined
 792 as the sum over $E - p_z$ divided by twice the with the LHeC enhanced electron beam energy.
 793 While these extensions of kinematic coverage and improvements of statistical precision are
 794 impressive, an estimate of the impact of LHeC NC and CC cross section measurements on
 795 derived quantities such as structure functions and parton distributions requires to also estimate
 796 the expected systematic measurement accuracy as may be achieved with the detector described
 797 in Chapter 12 below. In the following the assumptions and simulation results are presented for
 798 the NC and the CC cross sections, which are subsequently used in QCD fit and other analyses
 799 throughout this report.

800 The systematic uncertainties of the DIS cross sections have a number of sources, which at
 801 HERA have broadly been classified as uncorrelated and correlated across bin boundaries. For
 802 the NC case, the uncorrelated sources, apart from data and Monte Carlo statistics, are a global
 803 efficiency uncertainty, due to for example tracking or electron identification errors, photopro-
 804 duction background, calorimeter noise and radiative corrections. The correlated uncertainties
 805 result from imperfect energy scale and angle calibrations. In the classic kinematic reconstruc-
 806 tion methods used here, and described in Sect. ?? one uses the scattered electron energy E'_e and
 807 polar angle θ_e complemented by the energy of the hadronic final state E_h ¹. The correlated
 808 errors are due to scale uncertainties of the electron energy E'_e and of the hadronic final state
 809 energy E_h . There are also systematic errors due to an uncertainty of the measurement of the
 810 electron polar angle θ_e . The assumptions used in the simulation of pseudodata are summarised
 811 in Table 4.1.

812 In the absence of a detailed detector simulation at this stage, the systematic NC cross
 813 section uncertainties due to E'_e , θ_e and E_h are calculated, following [29], from the derivatives of the NC
 814 cross section in the chosen bins taking into account the Jacobians where needed. The results
 815 have been compared, for the HERA kinematics, with the H1 MC simulation of systematic
 816 errors [30] and found to be in very good agreement for all three sources. The resulting error
 817 depends much on the kinematics. At low Q^2 , for example, the systematic cross section error
 818 due to the uncertainty of θ_e rises because of $\delta Q^2/Q^2 = \delta E'_e/E'_e \oplus \tan(\theta_e/2) \cdot \delta\theta_e$ while at high
 819 Q^2 it is negligible. Low Q^2 is the backward region, of large electron scattering angles with
 820 respect to the proton beam direction.

821 A particular challenge is the measurement at large x because the cross section varies as

¹Basically one determines Q^2 best with the electron kinematics and determines x from $y = Q^2/sx$. At large y the inelasticity is essentially measured with the electron energy $y \simeq 1 - E'_e/E_e$. At low y one has $y = E_h \sin^2(\theta_h/2)/E_e$ with the hadronic final state energy E_h and angle θ_h which results in $\delta y/y \simeq \delta E_h/E_h$ to good approximation. There have been various refined methods proposed to determine the DIS kinematics, as the double angle method or the so-called sigma method. For the estimate of the cross section uncertainty behaviour as functions of Q^2 and x , however, the simplest method using Q_e^2, y_e at large y and Q_e^2, y_h at low y is transparent and accurate enough within better than a factor of two. In much of the phase space, moreover, it is rather the uncorrelated efficiency or further specific errors than the kinematic correlations, which dominate the cross section measurement accuracy.

source of uncertainty	error on the source or cross section
scattered electron energy scale $\Delta E'_e/E'_e$	0.1 %
scattered electron polar angle	0.1 mrad
hadronic energy scale $\Delta E_h/E_h$	0.5 %
calorimeter noise (only $y < 0.01$)	1-3 %
radiative corrections	0.5%
photoproduction background (only $y > 0.5$)	1 %
global efficiency error	0.7 %

Table 4.1: Assumptions used in the simulation of the NC cross sections on the amount of uncertainties from various sources. These assumptions correspond to the typical or best of what was achieved in the H1 experiment. Note that in the cross section measurement the energy scale and angular uncertainties are relative to the Monte Carlo and not to be confused with resolution effects which determine the purity and stability of binned cross sections. The total cross section error due to these uncertainties, e.g. for $Q^2 = 100 \text{ GeV}^2$, is about 1.2, 0.7 and 2.0 % for $y = 0.84, 0.1, 0.004$.

822 $(1-x)^c$, with $c \simeq 3$, and thus the relative error is amplified $\propto 1/(1-x)$ as x approaches
823 1. At high x the hadronic final state is scattered into the forward detector region where the
824 energy calibration becomes challenging. The calculated correlated NC cross section errors are
825 illustrated in Figs. 4.2 and 4.3 for $Q^2 = 2$ and 20000 GeV^2 , respectively. In the detector chapter
826 these calculations have been taken to define approximate requirements on the scale calibrations
827 in the different detector regions. An example for the resulting cross section measurement is
828 displayed in Fig. 4.4.

829 For the CC case, a similar simulation was done, albeit with less numeric effort. An illus-
830 tration of the high precision and large range of the inclusive CC cross section measurements
831 is presented in Fig. 4.5. The systematic cross section error, based on the H1 experience, was
832 set to 2 % and for larger $x > 0.3$ a term was added to allow the error to rise linearly to 10 %
833 at $x = 0.9$. For both NC and CC cross sections the statistical error is given by the number of
834 events but limited to 0.1 % from below. With these error assumptions a number of data sets
835 was simulated, both for NC and CC, which is summarised in Table 4.2. The energies of these
836 sets had been chosen prior to the final baseline energy choice. For the simulation of the F_L
837 measurement, described below, a separate set of beam energies is considered.

838 4.1.5 Longitudinal Structure Function F_L

839 The inclusive, deep inelastic electron-proton scattering cross section at low Q^2 ,

$$\frac{d^2\sigma}{dx dQ^2} = \frac{2\pi\alpha^2 Y_+}{Q^4 x} [F_2(x, Q^2) - f(y) \cdot F_L(x, Q^2)], \quad (4.23)$$

840 is defined by two proton structure functions, F_2 and F_L with $y = Q^2/sx$, $Y_+ = 1 + (1-y)^2$ and
841 $f(y) = y^2/Y_+$. The two functions reflect the transverse and the longitudinal polarisation state
842 of the virtual photon probing the proton structure, i.e. $F_T = F_2 - F_L$ and F_L , respectively.
843 The positivity of the transverse and longitudinal cross sections requires $0 \leq F_L \leq F_2$. Since
844 for most of the kinematic range the y dependent factor $f(y)$ is very small, there follows that

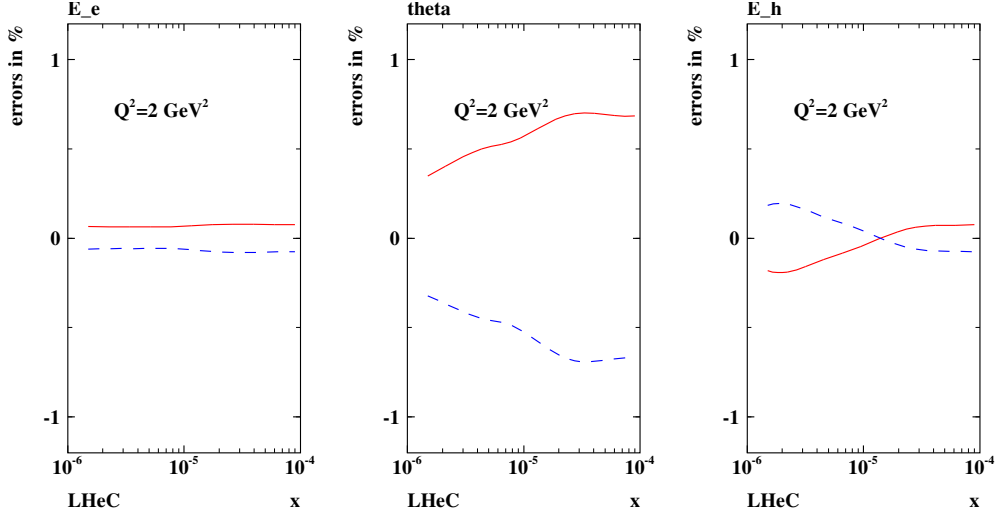


Figure 4.2: Neutral current cross section errors, calculated for $60 \times 7000 \text{ GeV}^2$, as result from scale uncertainties of the scattered electron energy $\delta E'_e/E'_e = 0.1\%$, of its polar angle $\delta\theta_e = 0.1 \text{ mrad}$ and the hadronic final state energy $\delta E_h/E_h = 0.5\%$, at low $Q^2 = 2 \text{ GeV}^2$ and correspondingly low x .

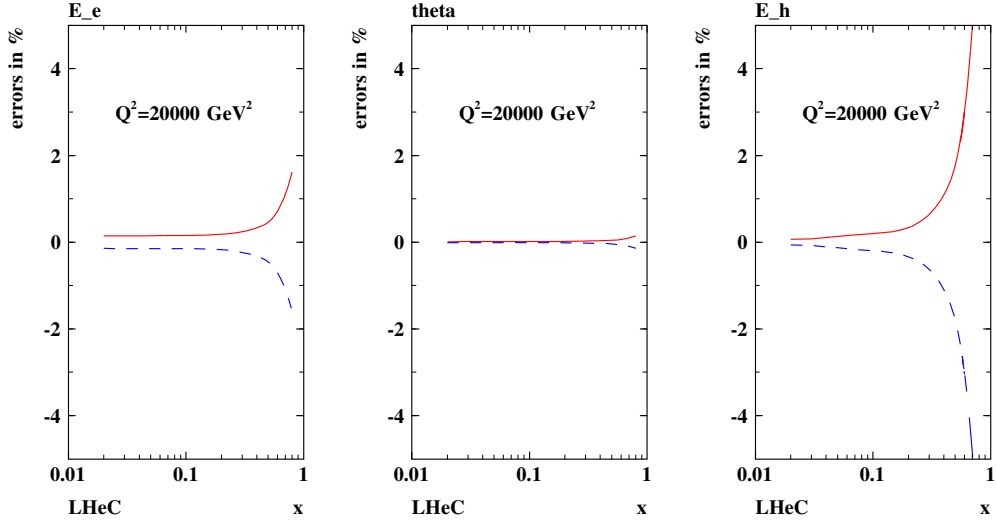


Figure 4.3: Neutral current cross section errors, calculated for $60 \times 7000 \text{ GeV}^2$ unpolarised e^-p scattering, as result from scale uncertainties of the scattered electron energy $\delta E'_e/E'_e = 0.1\%$, of its polar angle $\delta\theta_e = 0.1 \text{ mrad}$ and the hadronic final state energy $\delta E_h/E_h = 0.5\%$, at large $Q^2 = 20000 \text{ GeV}^2$ and correspondingly large x . Note that the characteristic behaviour of the relative uncertainty at large x , i.e. to diverge $\propto 1/(1-x)$, is independent of Q^2 , i.e. persistently observed at $Q^2 = 200000 \text{ GeV}^2$ for example too.

LHeC

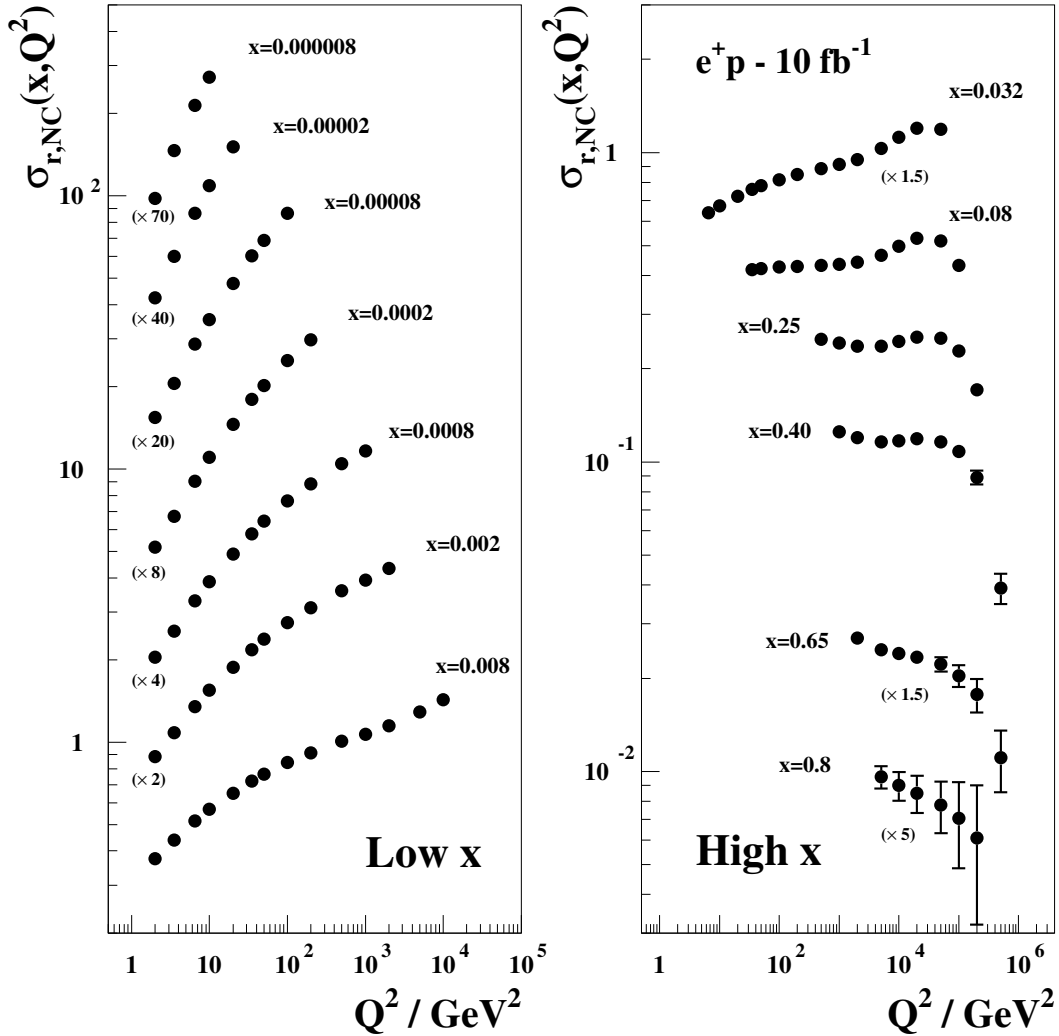


Figure 4.4: Simulated neutral current cross section measurement for an integrated luminosity of 10 fb^{-1} in unpolarised e^-p scattering at $E_e = 60$ and $E_p = 7000 \text{ GeV}$. The reduced NC cross section is measured at unprecedented precision and range. Plotted is the total uncertainty which, where visible at high x and Q^2 , is dominated by the statistical error. Similar data sets are expected with different beam polarisations and charges, and in CC scattering, for $Q^2 \geq 100 \text{ GeV}^2$. The strong variations of σ_r with Q^2 , as at $x = 0.25$, are due to the effects of Z exchange as is discussed and illustrated subsequently. Departures from the strong rise of the reduced cross section, $\sigma_r \simeq F_2$, at very low x and Q^2 are expected to appear due to non-linear gluon-gluon interaction effects in the so-called saturation region.

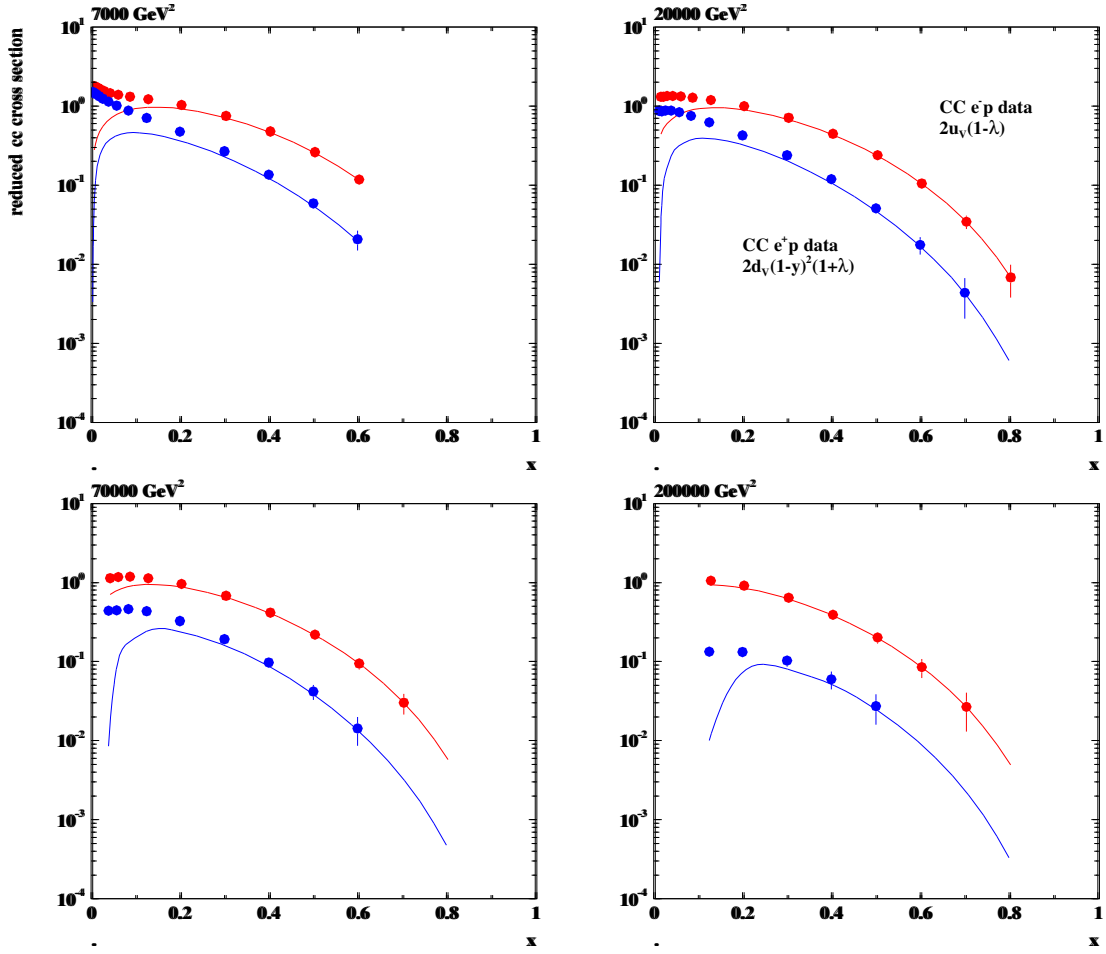


Figure 4.5: Reduced charged current cross sections with statistical uncertainties corresponding to 1 fb^{-1} electron (top data points, red) and positron (lower data points, blue) proton scattering at the LHeC. The curves are determined by the dominant valence quark distributions, u_v for e^-p and d_v for e^+p . In the simulation the lepton polarisation is taken to be zero. The valence-quark approximation of the reduced cross section is seen to hold at $x \geq 0.3$. A precise determination of the u/d ratio up to large x appears to be feasible at very high Q^2 .

Set	E_e/GeV	E_N/TeV	N	L^+/fb^{-1}	L^-/fb^{-1}	Pol
A	20	7	7	1	1	0
B	50	7	7	50	50	0.4
C	50	7	7	1	1	0.4
D	100	7	7	5	10	0.9
E	150	7	7	3	6	0.9
F	50	3.5	7	1	1	0
G	50	2.7	7	0.1	0.1	0.4
H	50	1	7	-	1	0

Table 4.2: Conditions for simulated NC and CC data sets for studies on the LHeC physics. Here, A defines a low electron beam energy option which is of interest to reach lowest Q^2 because Q_{min}^2 decreases $\propto E_e^{-2}$; B is the standard set, with a total luminosity split between different polarisation and charge states. C is a lower luminosity version which was considered in case there was a need for a dedicated low/large angle acceptance configuration, which according to more recent findings could be avoided since the luminosity in the restricted acceptance configuration is estimated, from the β functions obtained in the optics design, to be half of the luminosity in the full acceptance configuration; D is an intermediate energy linac-ring version, while E is the highest energy version considered, with the luminosities as given. It is likely that the assumptions for D and E on the positron luminosity are a bit optimistic. However, even with twenty times lower positron than electron luminosity one would have 0.5 fb^{-1} , i.e. the total HERA luminosity equivalent available in option D for example. F is the deuteron and G the lead option; finally H was simulated for a low proton beam energy configuration as is of interest to maximise the acceptance at large x .

845 F_L causes in most of the kinematic range only a small correction to the reduced cross section,
846 which is governed by F_2 , apart from the regio of maximum y . At small x , the inelasticity is
847 given as $y \simeq 1 - E'_e/E_e$. Therefore, in order to extract F_L , DIS has to be measured extremely
848 accurately at small scattered lepton energies, which is a question of how large E_e is, how to
849 trigger and how to control the background from particle production at low energies. A variation
850 of the beam energies is required to separate the two functions measured at the same x and Q^2
851 by variation of $y = Q^2/sx$.

852 A first measurement of F_L at low x at HERA has recently been performed by the ZEUS
853 Collaboration [31] and by the H1 Collaboration [32]. For the study of the gluon distribution at
854 lowest x , the H1 data are crucial as only H1 has measured F_L below Q^2 of about 10 GeV^2 owing
855 to their backward detector constellation upgraded in the nineties. The F_L measurement at
856 HERA was performed towards the end of the accelerator operation and could only extend over a
857 period of three months with about 10 pb^{-1} of integrated luminosity spent at two reduced proton
858 beam energies, 450 and 565 GeV, besides the nominal 920 GeV. The H1 result is consistent with
859 pQCD predictions. The ratio $R = F_L/(F_2 - F_L)$ has been found to be independent of x and
860 Q^2 at 20% accuracy, i.e. $R = 0.26 \pm 0.05$ [32]. This interesting relation deserves a more precise
861 investigation and may break when the region of saturation is entered at lower x than HERA
862 could access.

863 The LHeC will extend this initial measurement by using higher luminosities and dedicated

864 detector conditions into a much enlarged kinematic range. Since the LHeC is supposed to
 865 run synchronously with the LHC, the simulation presented here has been made with reduced
 866 electron beam energies keeping the proton beam energy untouched. The following set of energies
 867 and integrated luminosities: (60, 1), (30, 0.3), (20, 0.1) and (10, 0.05) (GeV, fb⁻¹). Note that
 868 the F_L measurement requires to also have data with the opposite beam charge in order to be
 869 able to reliably subtract the non DIS background which at high y is substantial. This has not
 870 been simulated here.

871 In the low x studies below a similar simulation was used for which the luminosity assumptions
 872 were similar but a set of reduced proton beam energies was considered. The advantage of
 873 lowering E_p is that the maximum y for all beam energy configurations can be high, e.g. 0.95
 874 for $E_e = 60$ GeV. When E_e is lowered instead, one has to accept a lower y_{max} as below a few
 875 GeV of energy the background is too high for a reliable measurement to be performed. The
 876 results of both F_L simulations, with reduced E_e or E_p , come out to be very similar.

877 The result of the simulation study is shown in Fig. 4.6. The technique applied is the con-
 878 ventional separation of F_2 and F_L by fitting a straight line to the various reduced cross section
 879 data points at fixed Q^2 and x with $f(y)$ as the parameter and separating the uncorrelated from
 880 the correlated systematic uncertainties which partially cancel in such an analysis. The expected
 881 accuracy on F_L is typically 4% at Q^2 of 3.5 GeV² or 7% at Q^2 of 25 GeV² at a number of points
 882 in x , with mainly similar contributions from the calculated correlated and the assumed uncor-
 883 related systematic uncertainties, and less due to statistics which yet starts to become important
 884 for $Q^2 \geq 100$ GeV². The LHeC thus will provide the first precision measurement of $F_L(x, Q^2)$
 885 ever, in a region where the behaviour of the gluon density ought to change significantly and
 886 new, non-linear laws for parton evolution should emerge.

887 A related measurement of prime interest is the determination of F_L in diffraction, as is
 888 discussed below. A pioneering measurement of F_L^D has been performed by H1 (-cite when
 889 published in July-).

890 4.2 Determination of Parton Distributions

891 Despite a series of deep inelastic scattering experiments with neutrinos, electrons and muons
 892 using stationary targets and with HERA, the knowledge of the quark distributions in the proton
 893 is still limited. It often relies on pQCD analyses using various assumptions on the Bjorken x
 894 dependence of the PDFs and their symmetries. The LHeC has the potential to put the PDF
 895 knowledge on a qualitatively and quantitatively new and superior basis. This is due to the
 896 kinematic range, huge luminosity, availability of polarised electron and positron beams, as of
 897 proton and deuteron beams, and to the anticipated very high precision of the cross section
 898 measurements as has been discussed above.

899 The LHeC has the potential to provide crucial constraints and many determinations of
 900 parton distributions completely or rather independently of the conventional QCD fitting tech-
 901 niques. For example, the valence quarks can be measured up to high x , and all heavy quarks be
 902 determined from dedicated c and b tagging analyses with unprecedented precision. Therefore,
 903 the then evolving QCD fits based on real LHeC data will be set-up with a massively improved
 904 and better constrained input data base. Their eventual effect is thus not easy to simulate now,
 905 it yet may be illustrated based on the currently used procedures.

906 The striking potential of the determination of the quark and gluon distributions will be
 907 discussed and illustrated below. For the various PDFs, the current knowledge is illustrated with

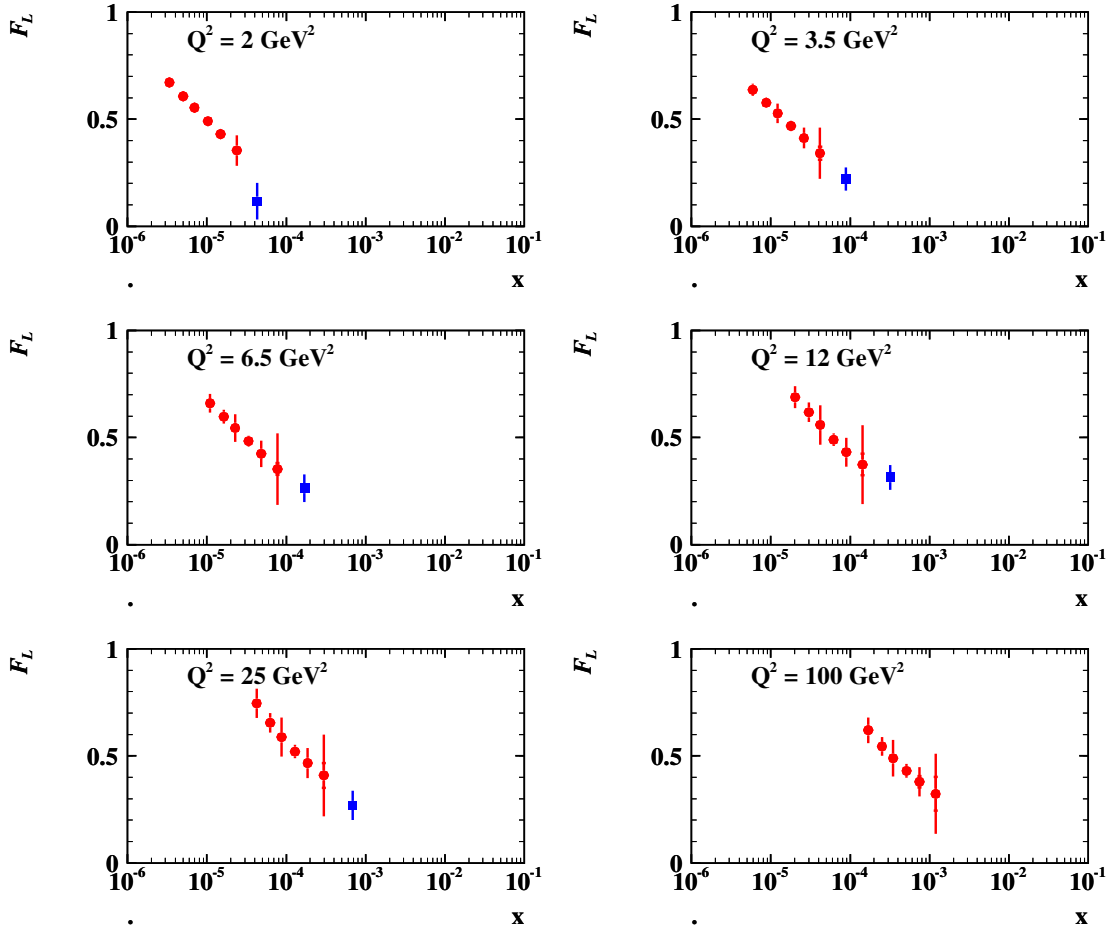


Figure 4.6: Simulated measurement of the longitudinal structure function $F_L(x, Q^2)$ at the LHeC (red closed circles) from a series of runs with reduced electron beam energy, see text. The inner error bars denote the statistical uncertainty, the outer error bars are the total errors with the additional uncorrelated and correlated systematic uncertainties added in quadrature. The blue squares denote the recently published result of the H1 Collaboration, plotting only the x averaged results as the more accurate ones, see [32]. The LHeC extends the measurement towards low x and high Q^2 (not fully illustrated here) with much improved precision.

908 a series of plots based on the world's best PDF determinations available today. Simulations of
 909 direct quark distribution measurements will be shown. Moreover, a consistent set of standard
 910 QCD fits has been performed using the simulated LHeC and further data which is first described
 911 in what follows. This is used to illustrate the effect the inclusive NC and CC data are expected
 912 to have on the PDF uncertainties.

913 Currently extensive work is being performed to test and further constrain PDFs with Drell-
 914 Yan scattering data from the LHC. This naturally focusses on the Z and W^\pm production and
 915 decay. While such tests are undoubtedly of interest, they require an extremely high level of
 916 precision as at scales $Q^2 \simeq M_{W,Z}^2$ any effect due to PDF differences at smaller scales is washed
 917 out by the overriding effect of quark-antiquark pair production from gluon emission, below
 918 the valence quark region. The present QCD fit results also use a set of simulated $W^+ - W^-$
 919 asymmetry data of ultimate precision in order to be able to estimate the effect the Drell-Yan
 920 data will have besides the LHeC in the determination of the PDF's.

921 4.2.1 QCD Fit Ansatz

922 NLO QCD fits are performed in order to study the effect of the (simulated) LHeC data on the
 923 PDF knowledge. Fits are done using the combined HERA data published and so available to date
 924 (HERA I), adding BCDMS proton data as the most accurate fixed target structure function
 925 set of importance at high x , simulated precision $W^+ - W^-$ asymmetry LHC data, using the
 926 LHeC data alone and in combination. In the fits, for the central values of the LHeC data, the
 927 Standard Model expectation is used, smeared within the uncorrelated, Gaussian distributed
 928 uncertainties and taking into account the correlated uncertainties as well.

929 The procedure used here is adopted from the HERA QCD fit analysis [10]. The QCD fit
 930 analysis to extract the proton's PDFs is performed imposing a $Q_{min}^2 = 3.5 \text{ GeV}^2$ to restrain
 931 to the region where perturbative QCD can be assumed to be valid. The fits are extended to
 932 lowest x for systematic uncertainty studies, even when at such low x values non-linear effects
 933 are expected to appear.

934 The fit procedure consists first in parametrising PDFs at a starting scale $Q_0^2 = 1.9 \text{ GeV}^2$,
 935 chosen to be below the charm mass threshold. The parametrised PDFs are the valence dis-
 936 tributions xu_v and xd_v , the gluon distribution xg , and the $x\bar{U}$ and $x\bar{D}$ distributions, where
 937 $x\bar{U} = x\bar{u}$, $x\bar{D} = x\bar{d} + x\bar{s}$. The following standard functional form is used to parameterise them

$$xf(x) = Ax^B(1-x)^C(1+Dx+Ex^2), \quad (4.24)$$

938 where the normalisation parameters (A_{uv}, A_{dv}, A_g) are constrained by quark counting and mo-
 939 mentum sum rules.

940 The parameters $B_{\bar{U}}$ and $B_{\bar{D}}$ are set equal, $B_{\bar{U}} = B_{\bar{D}}$, such that there is a single B parameter
 941 for the sea distributions, an assumption the validity of which will be settled with the LHeC.
 942 The strange quark distribution at the starting scale is assumed to be a constant fraction of
 943 \bar{D} , $x\bar{s} = f_s x\bar{D}$, chosen to be $f_s = 0.31$. In addition, to ensure that $x\bar{u} \rightarrow x\bar{d}$ as $x \rightarrow 0$,
 944 $A_{\bar{U}} = A_{\bar{D}}(1 - f_s)$. The D and E are introduced one by one until no further improvement in χ^2
 945 is found. The best fit resulted in a total of 10 free parameters [10]. As discussed above this will
 946 change considerably when the LHeC data become available and more flexible parameterisations
 947 and methods can be tested. This has been studied to some extent in the simulation for α_s
 948 presented below.

949 The PDFs are then evolved using DGLAP evolution equations [33] at NLO in the \overline{MS} scheme
 950 with the renormalisation and factorisation scales set to Q^2 using standard sets of parameters

951 as for $\alpha_s(M_Z)$. These, as well as the exact treatment of the heavy quark thresholds, are of
 952 no significant influence for the estimates of the PDF uncertainties to which the subsequent
 953 analysis is only directed. The experimental uncertainties on the PDFs are determined using
 954 the $\Delta\chi^2 = 1$ criterion.

955 4.2.2 Valence Quarks

956 The knowledge of the valence quark distributions, both at large and at low Bjorken x , as
 957 derived in the current world data QCD fit analyses is amazingly limited, as is illustrated in
 958 Fig. 4.7 from a comparison of the leading determinations of PDF sets. This has to do, at high
 959 x , with the limited luminosity, challenging systematics rising $\propto 1/(1-x)$ and nuclear correction
 960 uncertainties, and, at low x , with the smallness of the valence quark distributions as compared
 to the sea quarks. The impressive improvement expected from the LHeC is demonstrated in

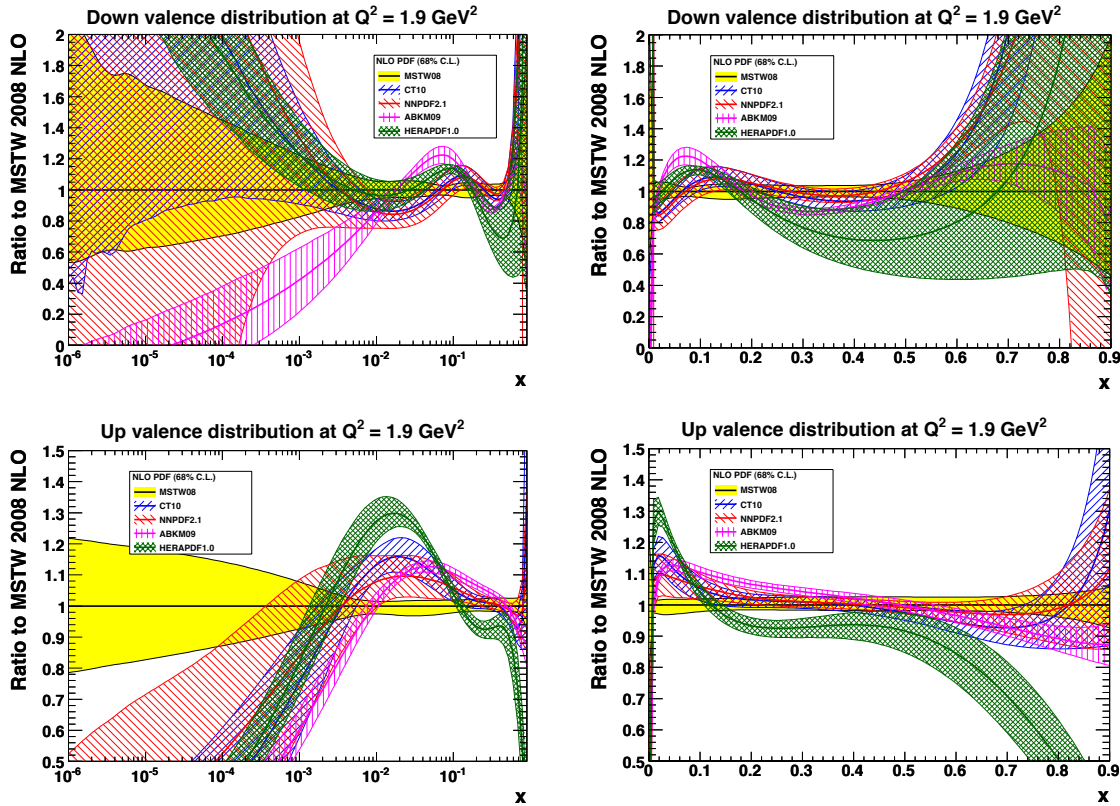


Figure 4.7: Ratios (to MSTW08) and uncertainty bands of valence quark distributions, at $Q^2 = 1.9 \text{ GeV}^2$, for most of the available recent PDF determinations. Top: up valence quark; down: down valence quark; left: logarithmic x , right: linear x .

962 Fig. 4.8. As can be seen, the uncertainty of the down valence quark distribution at, for example,
 963 $x = 0.7$ is reduced from a level of 50 – 100 % to about 5 %. The up valence quark distribution is
 964 better known than d_v , because it enters with a four-fold weight in F_2 , due to the electric quark
 965 charge ratio squared, a big improvement yet is also visible. These huge improvement effects at
 966 large x are a consequence of the high precision measurements of the NC and the CC inclusive
 967 cross sections, which at high x tend to $4u_v + d_v$ and u_v (d_v) for electron (positron) scattering,
 968 respectively. At HERA the luminosity and range had not been high enough to allow a similar
 969 measurement as will be possible for the first time with the LHeC. This is illustrated in Fig. 4.9
 970 which compares the HERA II result of the ZEUS Collaboration, H1's still to be released, on
 the CC cross section with the LHeC simulation.

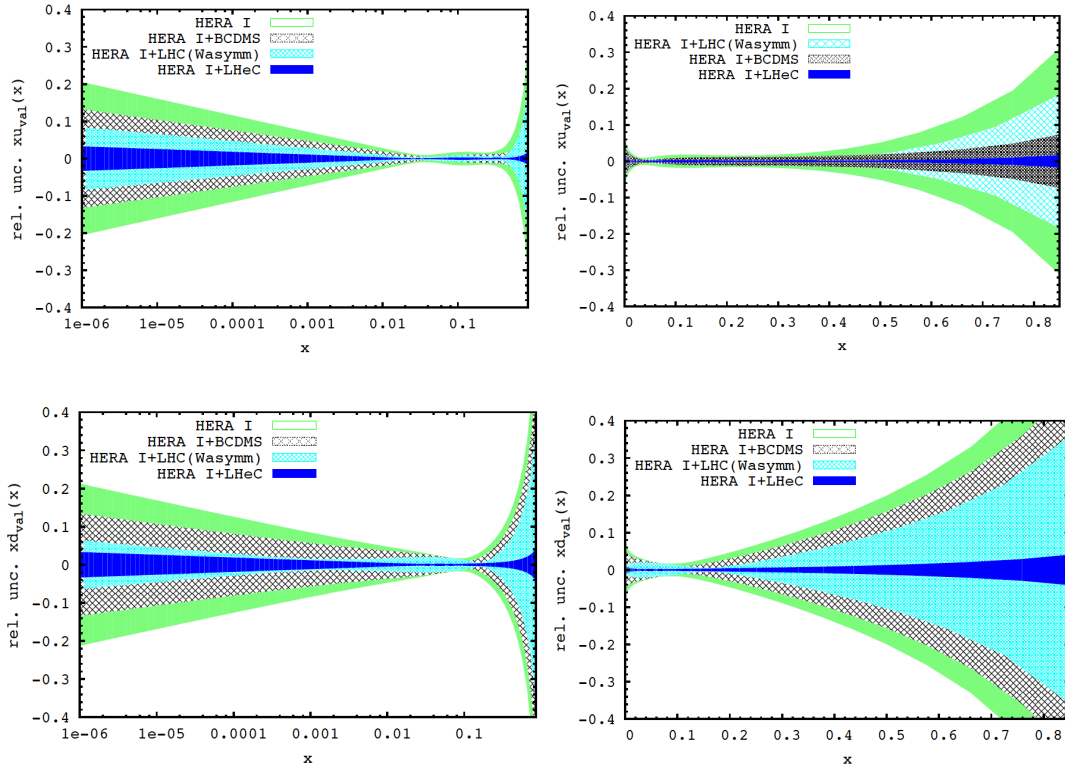


Figure 4.8: Uncertainty of valence quark distributions, at $Q^2 = 1.9 \text{ GeV}^2$, as resulting from an NLO QCD fit to HERA (I) alone (green, outer), HERA and BCDMS (crossed), HERA and LHC (light blue, crossed) and the LHeC added (blue, dark). Top: up valence quark; down: down valence quark; left: logarithmic x , right: linear x .

971

972

Access to valence quarks at low x can be obtained from the $e^\pm p$ cross section difference as

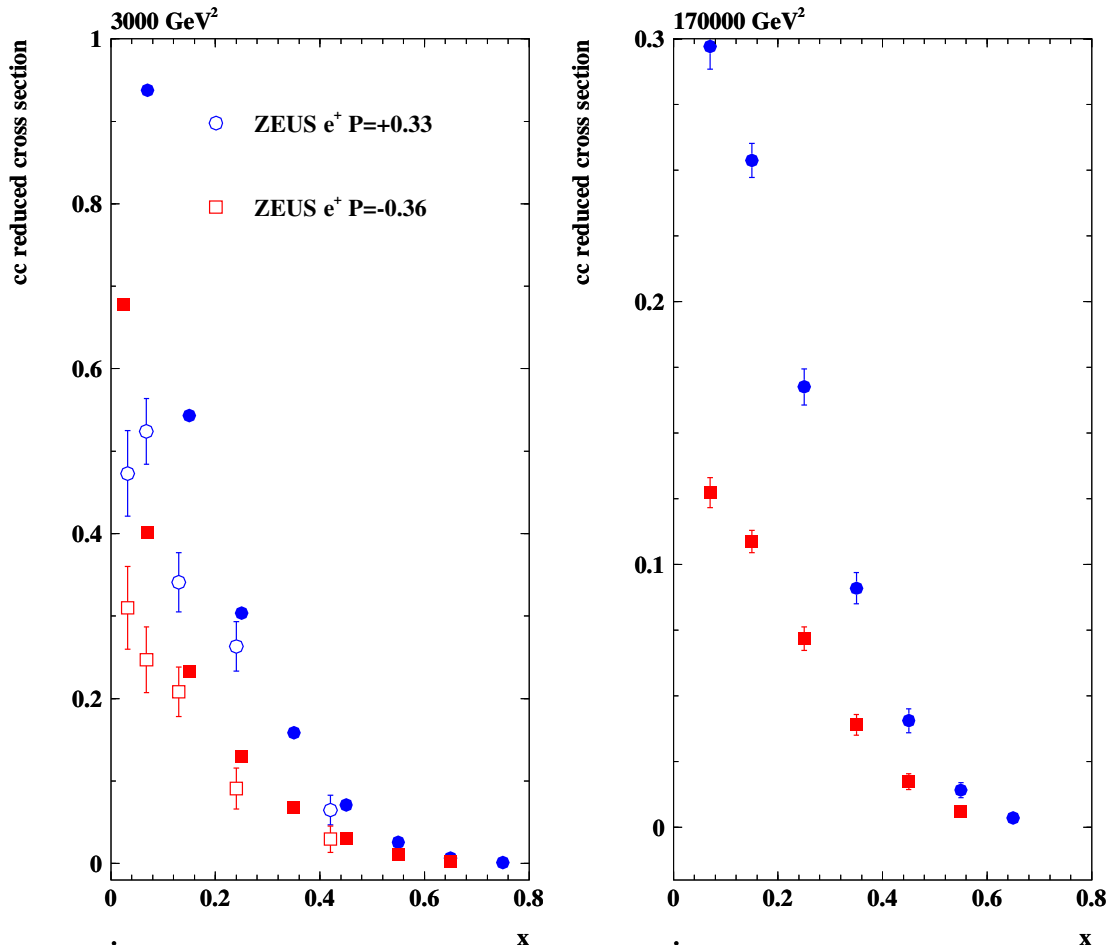


Figure 4.9: Reduced charged current e^+p scattering cross section versus Bjorken x for different polarisations $\pm P$ and values of Q^2 . Closed points: LHeC simulations for 10 fb^{-1} ; open points: ZEUS measurements based on the full HERA statistics of about 0.15 fb^{-1} per polarisation state. Note that the reduced CC cross section at fixed x and Q^2 contains an explicit dependence on the beam energy via the ratio of inelasticity dependent factors Y_-/Y_+ , which is at the origin of the simulated and measured cross section differences apparent at lower x .

973 introduced above:

$$\sigma_{r,NC}^- - \sigma_{r,NC}^+ = 2 \frac{Y_-}{Y_+} (-a_e \cdot k x F_3^{\gamma Z} + 2v_e a_e \cdot k^2 x F_3^Z). \quad (4.25)$$

974 Since the electron vector coupling, v_e , is small and k not much exceeding 1, to a very good
 975 approximation the cross section difference is equal to $-2kY_- a_e x F_3^{\gamma Z} / Y_+$. In leading order
 976 pQCD this “interference structure function” can be written as

$$x F_3^{\gamma Z} = 2x [e_u a_u (U - \bar{U}) + e_d a_d (D - \bar{D})], \quad (4.26)$$

977 with $U = u + c$ and $D = d + s$ for four flavours. The $x F_3^{\gamma Z}$ structure function thus provides
 978 information about the light-quark axial vector couplings (a_u, a_d) and the sign of the electric
 979 quark charges (e_u, e_d). Equivalently one can write

$$x F_3^{\gamma Z} = 2x [e_u a_u (u_v + \Delta_u) + e_d a_d (d_v + \Delta_d)]. \quad (4.27)$$

980 In the naive parton model as in conventional perturbative QCD, it is assumed that the differ-
 981 ences $\Delta_u = (u_{sea} - \bar{u} + c - \bar{c})$ and $\Delta_d = (d_{sea} - \bar{d} + s - \bar{s})$ are zero ². Inserting the SM charge
 982 and axial coupling values one finds

$$x F_3^{\gamma Z} = \frac{x}{3} (2u_v + d_v + \Delta) \quad (4.28)$$

983 with $\Delta = 2\Delta_u + \Delta_d$. Neglect of Δ leads to a sum rule [34], which in leading order is

$$\int_0^1 x F_3^{\gamma Z} \frac{dx}{x} = \frac{1}{3} \int_0^1 (2u_v + d_v) dx = \frac{5}{3}. \quad (4.29)$$

984 The $x F_3^{\gamma Z}$ structure function thus is determined by the valence quark distributions and pre-
 985 dicted to be only very weakly depending on Q^2 . Fig. 4.10 shows a simulation of $x F_3^{\gamma Z}$ and its
 986 comparison with the so far most accurate measurement from HERA. With such a high precision
 987 interesting tests are possible of the relation of $x F_3^{\gamma Z}$ to $x W_3$, which should only differ by the
 988 weak couplings involved in NC and CC.

989 4.2.3 Strange Quarks

990 The strange quark distribution $s(x, Q^2)$ has been very difficult to measure. In DIS some infor-
 991 mation is obtained from di-muon production in neutrino-nucleon scattering. Often s is linked
 992 to the behaviour of the sea quarks. Recently the HERMES Collaboration, from kaon multi-
 993 plicities, derived an unusual behaviour of the strange quark density as compared to previous
 994 analyses [35]. Some hints for a difference between the s and \bar{s} distributions have been discussed.
 995 The existing information on the sum of the strange and anti-strange quark distributions is plot-
 996 ted in Fig. 4.11. Obviously there is no real understanding of the strange quark distribution in
 997 the proton available. This will change with the LHeC. Here s and \bar{s} may be very well measured
 998 as a function of x and Q^2 from the $W^+ s \rightarrow c$ and $W^- \bar{s} \rightarrow \bar{c}$ processes, i.e. with charmed quark
 999 tagging in CC DIS using electron and positron beams, respectively. The precision for s which
 1000 may be obtained is illustrated in Fig. 4.12. Accurate measurements may be obtained for the
 1001 first time ever. The simulation of \bar{s} obviously leads to the same picture such that over a wide
 1002 kinematic range possible differences between s and \bar{s} may be established.

²However, in non-perturbative QCD there may occur differences, for example between the strange and anti-
 strange quark distributions, for which there are some hints in DIS neutrino nucleon di-muon data and corre-
 sponding QCD fit analyses, see below.

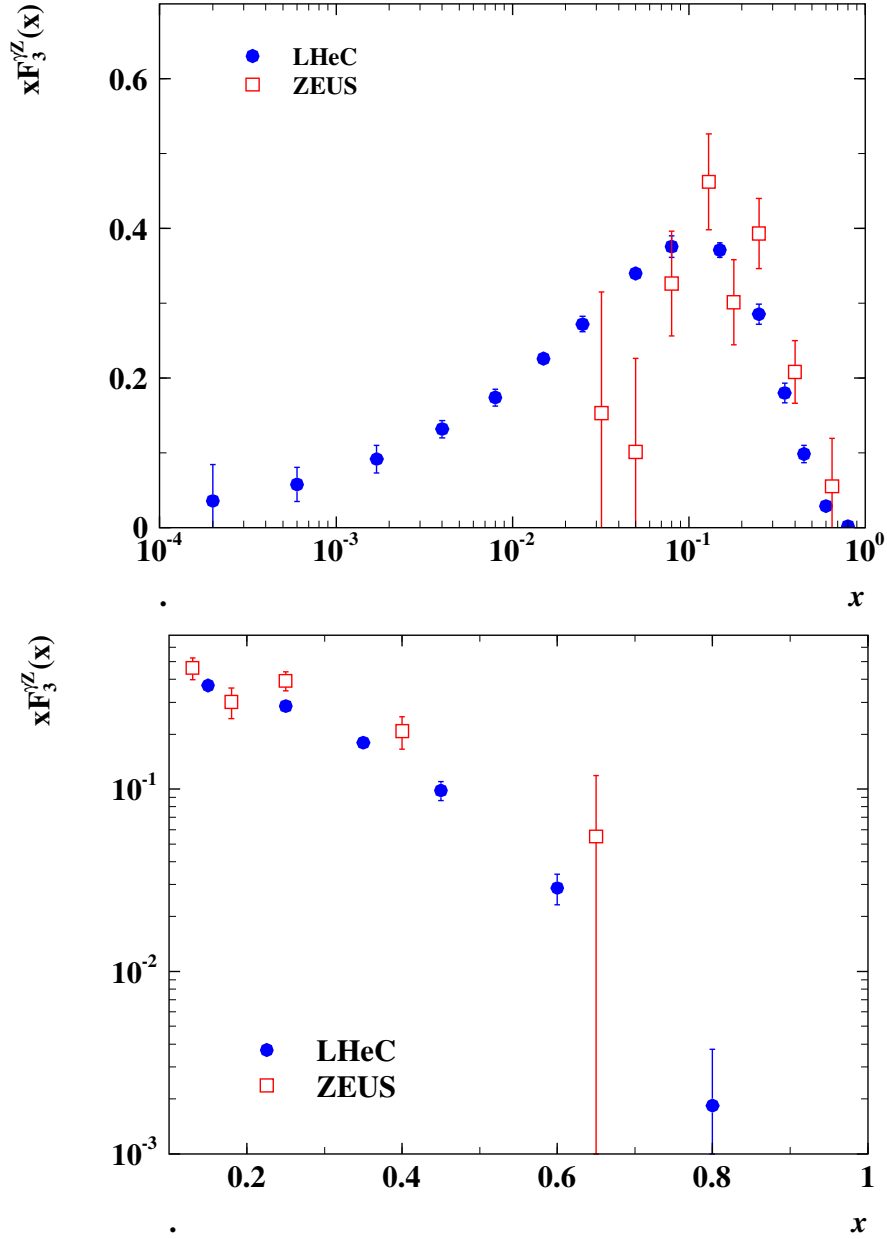


Figure 4.10: Simulation (top) of the LHeC measurement of the interference structure function $x\bar{F}_3^{\gamma Z}$ from unpolarised $e^\pm p$ scattering with 10 fb^{-1} luminosity per beam (blue, closed points) compared with the HERA II data as obtained by the ZEUS Collaboration with about 0.15 fb^{-1} luminosity per beam charge. This measurement at HERA is limited by its statistical accuracy mainly and therefore with the forthcoming H1 data added, only an about $1/\sqrt{2}$ improvement of the precision at HERA can be expected. One should notice that any significant deviation of sea from anti-quarks, see Eq. 4.27, would cause $x\bar{F}_3^{\gamma Z}$ at low x to not tend to zero. The top plot shows an average of $x\bar{F}_3^{\gamma Z}$ over Q^2 projected to a chosen Q^2 value of 1500 GeV^2 exploiting the fact that the valence quarks are approximately independent of Q^2 . The lower plot is a zoom into the high x region.

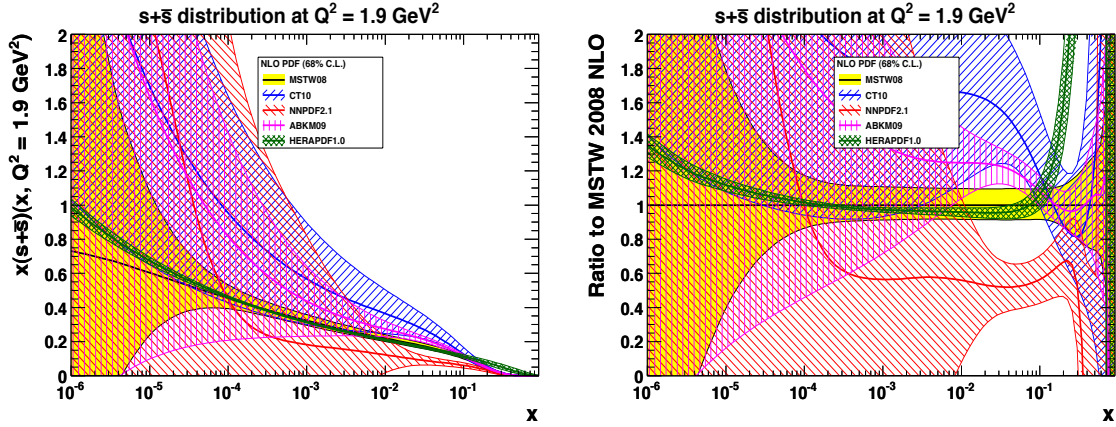


Figure 4.11: Sum of the strange and anti-strange quark distribution as embedded in the NLO QCD fit sets as noted in the legend. Left: $s + \bar{s}$ versus Bjorken x at $Q^2 = 1.9 \text{ GeV}^2$; right: ratio of $s + \bar{s}$ of various PDF determinations to MSTW08. In the HERAPDF1.0 analysis (green) the strange quark distribution is assumed to be a fixed fraction of the down quark distribution which is conventionally assumed to have the same low x behaviour as the up quark distribution, which results in a small uncertainty of $s + \bar{s}$.

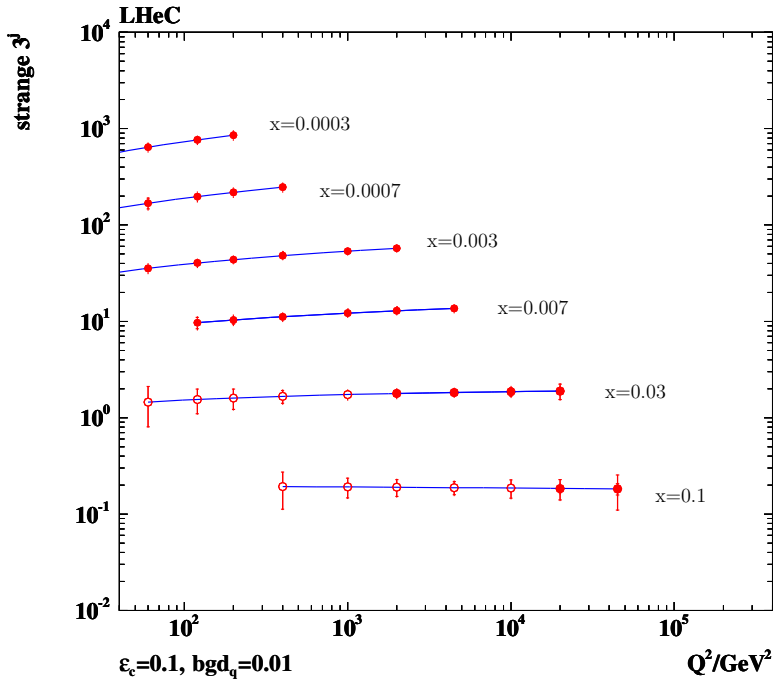


Figure 4.12: Simulated measurement of the strange quark density with the LHeC. Closed (open) points: tagging acceptance down to 10° (1°).

1003 **4.2.4 Top Quarks**

1004 The top is the heaviest of the quarks. It decays before hadrons are formed. It has not been
 1005 explored in DIS yet because the cross sections at HERA have been too small [36]. This is different
 1006 at the LHeC where top in charged currents is produced with a cross section of order 5 pb^{-1} as
 1007 can easily be estimated from the LO calculation of Wb scattering. At the LHeC therefore, for
 1008 the first time, one can study top quarks in deep inelastic scattering. Positron (electron) proton
 1009 charged current scattering provides a clear distinction between top (anti-top) quark production
 1010 in Wb to t fusion. The rates of this process are very high, as is illustrated as a function of Q^2
 in Fig. 4.13. Besides the rates and the charge tag it is notable that the absence of pile-up and

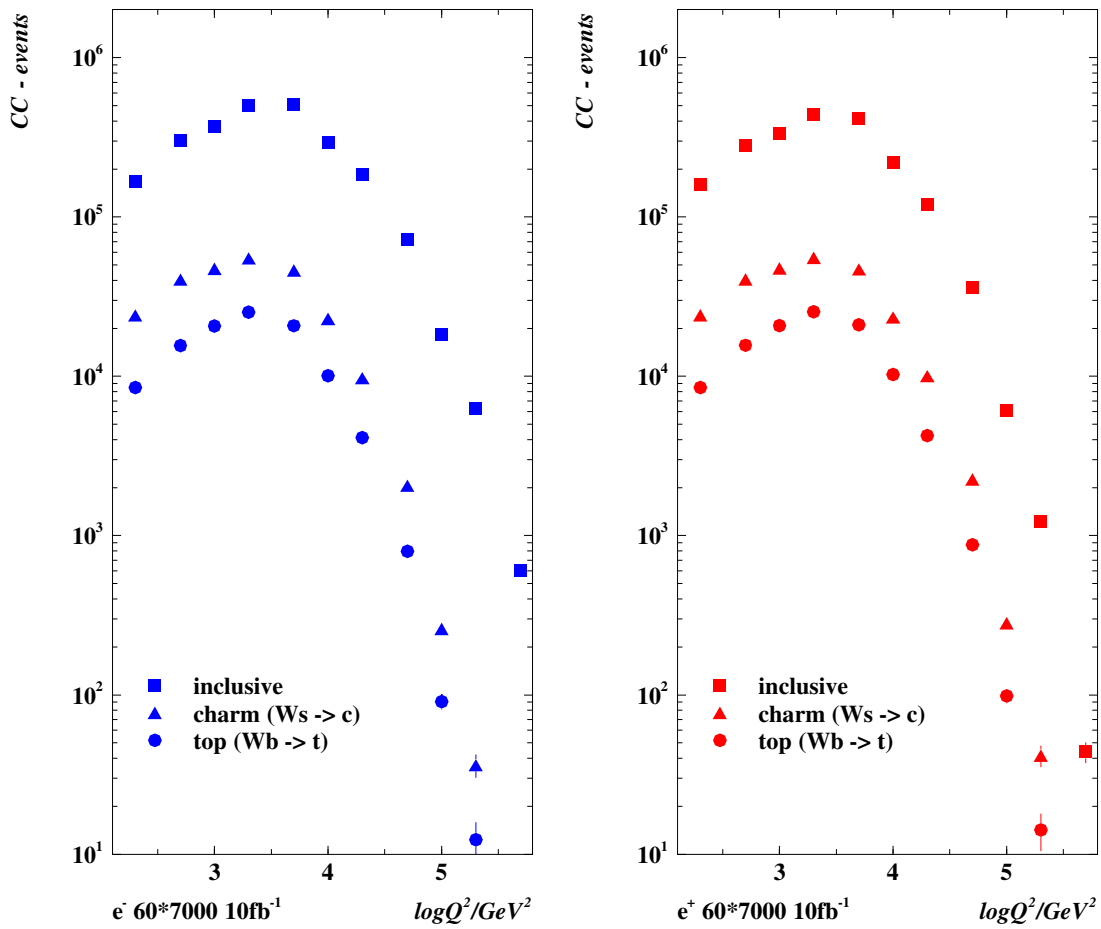


Figure 4.13: Charged current event rates for unpolarised e^-p (left) and e^+p (right) scattering in which \bar{t} and t is produced, respectively. Squares: inclusive CC rate vs. Q^2 ; triangles: charm production from Ws fusion; closed circles: top production from Wb fusion, estimated in a massless heavy flavour treatment. The rates are calculated for the default beam energies for 10 fb^{-1} of integrated luminosity. The errors are only statistical.

1012 underlying event effects, characteristic for LHC measurements, provide comfortable conditions
1013 for top quark physics at the LHeC.

1014 Due to its large mass, the top quark may very well play a role in the mechanism of elec-
1015 troweak symmetry breaking (EWSB) both in the Standard Model as well as BSM physics. In
1016 the Standard Model, a precise measurement of single top production in DIS (see for exam-
1017 ple [37]) is sensitive to the b quark content of the proton. In a BSM EWSB scenario, the top
1018 quark will couple to the new physics sector and give rise to anomalous production modes. The
1019 LHeC is expected to provide competitive sensitivity to flavor changing neutral currents (FCNC)
1020 especially anomalous $tu\gamma$ and tuZ couplings.

1021 In the SM, top is produced dominantly in gluon-boson fusion at $x \lesssim 0.1$. In CC this leads
1022 to a top-beauty final state while in NC this gives rise to pair produced top-antitop quarks, with
1023 a cross section of order 10 times lower than in CC [36]. The electron beam charge distinguishes
1024 top and anti-top quark production in CC. Thus a unique SM top physics program can be
1025 performed at the LHeC. This includes the consideration of a top-quark density which at very
1026 high scales may be considered “light”. Recently a six-flavour variable number scheme has been
1027 proposed [38], limited so far to leading order, in which it is predicted that the top contribution
1028 to proton structure has an on-set much below the threshold of its production in a massless
1029 scheme. This is illustrated in Fig. 4.14. Due to the very high Q^2 and statistics, the LHeC opens
1030 top quark PDF physics as a new field of research.

1031 Top, including anomalous couplings, has been considered for the CDR initially [39], based
1032 on some ANOTOP and PYTHIA studies at generation level. With a detector now simulated
1033 in GEANT4 and in the light of the first top results provided by the LHC experiments [40], as
1034 well as further prospects, the CC and NC top physics at the LHeC deserves a more detailed
1035 study. This shall include an analysis about the possible precision measurement of the top (and
1036 anti) top quark mass, which at the LHC may be determined with an accuracy of 1 GeV and
1037 possibly be better in ep . Independently of whether one soon finds the SM Higgs particle or it
1038 remains elusive, a high precision measurement of m_t is of prime importance.

1039 4.3 Gluon Distribution

1040 There are many fundamental reasons to understand the gluon distribution and the gluon in-
1041 teractions deeper than hitherto. Half of proton’s momentum is carried by gluons. Gluon
1042 self-interaction is responsible for the creation of baryonic mass. The Higgs particle, should it
1043 exist, is predominantly produced by gluon-gluon interactions. The rise of the gluon density
1044 towards low Bjorken x must be tamed for unitarity reasons: there is a new phase of hadronic
1045 matter to be discovered, in which gluons interact non-linearly while α_s is smaller than 1.

1046 The LHeC, with precision and range of the most appropriate process (DIS) to explore
1047 $xg(x, Q^2)$, will pin down the gluon distribution much more accurately than could be done
1048 before. This primarily comes from the extension of range and precision in the measurement
1049 of $\partial F_2 / \partial \ln Q^2$ which at small x is a measure of xg . The inclusive NC and CC measurements
1050 together provide a fully constrained data base for the determination of the quark distributions,
1051 which strongly constrains xg . The addition of precision measurements of F_L , discussed above
1052 and used in the small x chapter of this document, will unravel the saturating behaviour of
1053 xg . High precision measurements of boson-gluon fusion to heavy quark pairs will provide a
1054 complementary basis for understanding the gluon and its parton interactions.

1055 The peculiarity of the gluon density is that it is defined and observable only in the context

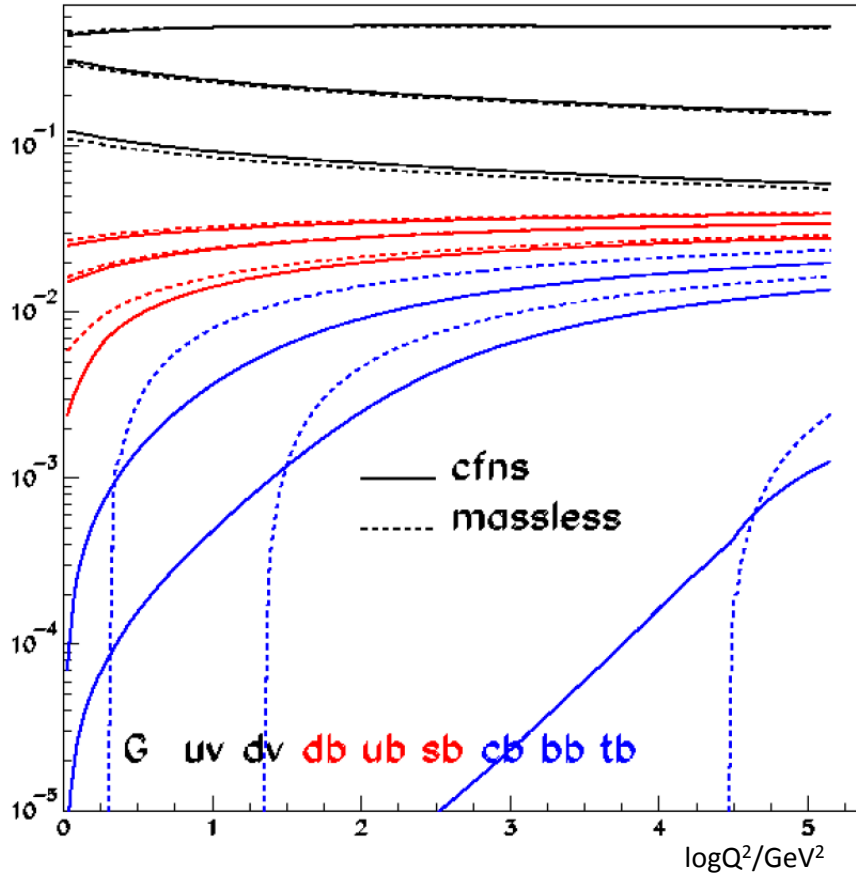


Figure 4.14: Parton momentum fractions as a function of Q^2 in a novel six-flavour variable number scheme (CFNS), solid curves, and in the massless scheme, dashed curves. At HERA one has observed beauty and charm production already below the conventional threshold of $\sqrt{Q^2} = m_Q$. The scheme of [38] suggests that there is a very early onset of top with measurable rates already at Q^2 values of only about one tenth of $m_t^2 \simeq 3 \cdot 10^4 \text{ GeV}^2$. With the LHeC the 'PDF' top physics is expected to commence.

1056 of a theory. Moreover, a crude data base and correspondingly rough fit ansatz can screen
 1057 local deviations from an otherwise preferred smooth behaviour. It has yet not been settled
 1058 whether there are gluonic “hot” spots in the proton or not. An example for possible surprises is
 1059 provided by the analysis [41], in which Chebyshev polynomials have been used to parameterise
 1060 the parton distributions in contrast to more conventional forms as in Eq. 4.24. Inspection of the
 1061 gluon distribution obtained there reveals that it seems to be vanishing at $x \simeq 0.2$, i.e. at the
 1062 point, in which scaling holds for $F_2(x, Q^2)$, which one might term a “cool” spot in the proton.
 1063 Much more is still to be learned about the gluon, even when one is disregarding the yet to be
 1064 explored role of the gluon in the theory of generalised and of unintegrated parton distributions.

1065 The current knowledge of the gluon distribution in the proton is astonishingly limited as
 1066 becomes clear from Fig. 4.15 showing the world determinations, and their uncertainties, of
 1067 $xg(x, Q^2)$ at a typical initial, low scale, and from Fig. 4.16 expressing this information with
 1068 ratios to one of the PDF sets. At low x and Q^2 most but not all of the PDF sets predict
 1069 xg to be of valence like type with very large uncertainties for x below a few times 10^{-4} . At
 1070 large x inclusive DIS has difficulties to pin down xg because the evolution of valence quarks as
 1071 non-singlet quantities in QCD is not directly coupled to the gluon and very weak. Yet, even
 1072 the information from jets, used in some of the PDF sets, does not lead to a clear understanding
 1073 of xg at large x as is illustrated too. In fact, there is a tendency of obtaining a smaller xg
 1074 at large x from HERA (I) data alone, see Fig. 4.15, as compared to the other determinations,
 albeit with large uncertainties.

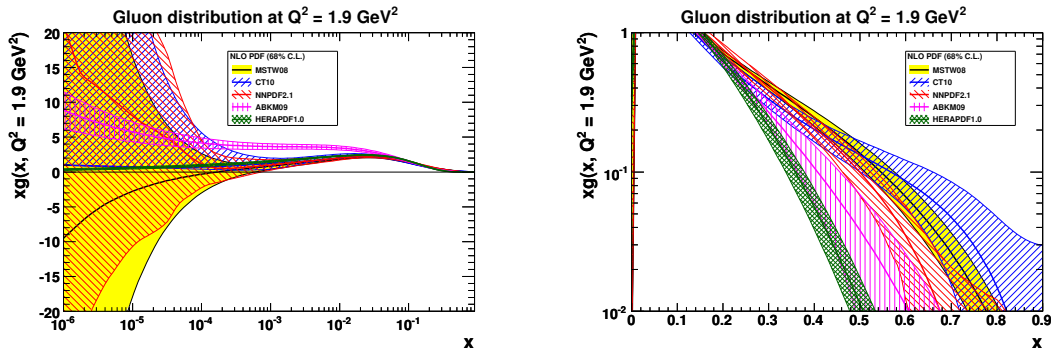


Figure 4.15: Gluon distribution and uncertainty bands, at $Q^2 = 1.9 \text{ GeV}^2$, for most of the available recent PDF determinations. Left: logarithmic x , right: linear x .

1075
 1076 The determination of xg is predicted to be radically improved with the LHeC precision
 1077 data which extend up to lowest x near to 10^{-6} and large $x \geq 0.7$. The result of the QCD fit
 1078 analysis for xg as described above in Sect. 4.2.1 is shown in Fig. 4.17. One observes a dramatic
 1079 improvement at low x , as must be expected from the extension of the kinematic range, but
 1080 also at high x , as is attributed to the high x precision measurements of the NC and CC cross
 1081 sections. At $x = 0.7$, for example, the predicted experimental uncertainty of xg is 5%, which
 1082 is about ten times more accurate than the results of MSTW08 or of the HERA fit indicate.

1083 It is worth noting that the uncertainties considered here are restricted to those related to
 1084 the genuine cross section measurement errors. There are further uncertainties, as discussed e.g.
 1085 in [10], related to the difficulty of parameterising the PDFs and choosing the optimum solution

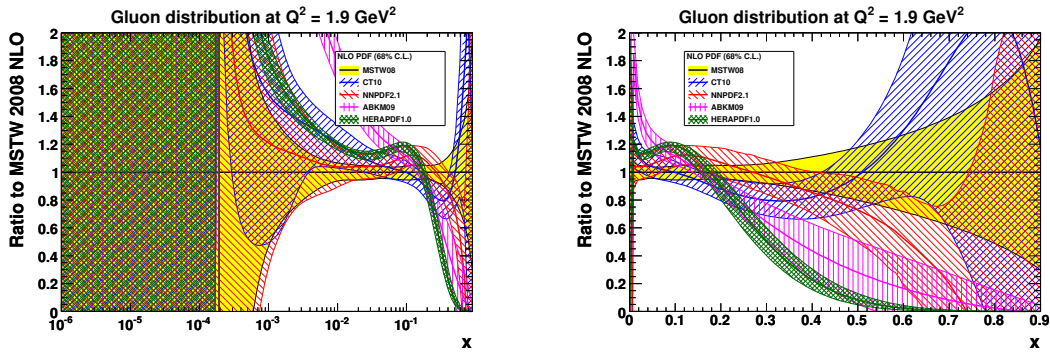


Figure 4.16: Ratios to MSTW08 of gluon distribution and uncertainty bands, at $Q^2 = 1.9 \text{ GeV}^2$, for most of the available recent PDF determinations. Left: logarithmic x , right: linear x .

1086 in such a fit analysis. These will be also considerably reduced with the LHeC extended data
 1087 base. Moreover, this analysis is not making use of the plethora of extra information on xg , which
 1088 the LHeC will provide with F_L , $F_2^{c,b}$ and jet cross section measurements. The understanding
 1089 of the gluon and its interactions is a primary task of the LHeC and undoubtedly a new horizon
 in strong interaction physics will be opened.

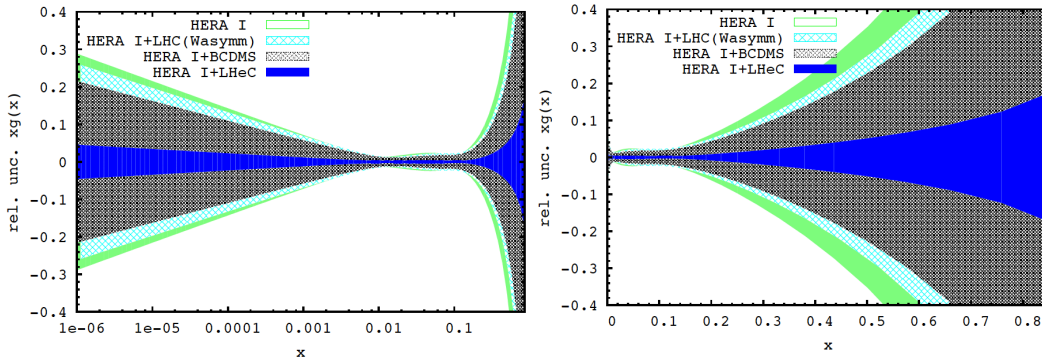


Figure 4.17: Relative uncertainty of the gluon distribution at $Q^2 = 1.9 \text{ GeV}^2$, as resulting from an NLO QCD fit to HERA (I) alone (green, outer), HERA and BCDMS (crossed), HERA and LHC (light blue, crossed) and the LHeC added (blue, dark). Left: logarithmic x , right: linear x .

1091 4.4 Prospects to Measure the Strong Coupling Constant

1092 The precise knowledge of $\alpha_s(M_Z^2)$ is of instrumental importance for the correct prediction of
1093 the electro-weak gauge boson production cross sections and the Higgs boson cross section at
1094 Tevatron and the LHC [42]. Independently of such applications, the accurate determination of
1095 the coupling constants of the known fundamental forces is of importance in the search for
1096 their possible unification within a more fundamental theory. Among the coupling constants
1097 of the forces in the Standard Model, the strong coupling α_s exhibits the largest uncertainty,
1098 which is currently of the size of $\sim 1\%$. Any future improvement of this accuracy, along with
1099 the consolidation of the genuine central value, is one of the central issues of contemporary
1100 elementary particle physics. It demands deep experimental and theoretical efforts to obtain the
1101 required precision and especially to handle all essential systematic effects.

1102 Experimentation at the LHeC will allow to measure the strong coupling constant $\alpha_s(M_Z^2)$
1103 at much higher precision than hitherto, both from the scaling violations of the deep inelastic
1104 structure functions, as will be demonstrated below, and using ep multiple jet cross sections. For
1105 the final inclusion of jet data in global pdf analyses, both from ep and from hadron colliders,
1106 their description at NNLO is required. At the LHeC, similar to HERA, the measurement of
1107 the ep jet cross sections will form important data samples ³ for the measurement of $\alpha_s(M_Z^2)$.

1108 Subsequently, a brief account will be given on the status and the complexity of determining
1109 α_s in DIS, followed by a presentation of the study of the α_s measurement uncertainty with the
1110 inclusive NC and CC data from the LHeC.

1111 4.4.1 Status of the DIS Measurements of α_s

1112 During the last 35 years the strong coupling constant has been measured with increasing ac-
1113 curacy in lepton-nucleon scattering in various experiments at CERN, FERMILAB and DESY.
1114 The precision, which has been reached currently, requires the description of the deep-inelastic
1115 scattering structure functions at $O(\alpha_s^3)$ [43–45].

³These are presented below but have not been used in this document for a determination of the strong coupling constant. One knows of course that the use of jet data in DIS helps resolving the α_s - xg correlation, especially at large x , and consequently leads to a significant reduction of the uncertainty on the coupling constant. This, however, tends to also change the central value. The LHeC as will be shown below determines α_s to permille precision already in inclusive scattering. Comparison with precise values from jets can be expected to shed light on the yet unresolved question as to whether there is a theoretical or systematic effect which leads to different values in inclusive DIS and jets or not.

	$\alpha_s(M_Z^2)$	
BBG	$0.1134^{+0.0019}_{-0.0021}$	valence analysis, NNLO [46]
GRS	0.112	valence analysis, NNLO [47]
ABKM	0.1135 ± 0.0014	HQ: FFNS $N_f = 3$ [48]
ABKM	0.1129 ± 0.0014	HQ: BSMN-approach [48]
JR	0.1124 ± 0.0020	dynamical approach [49]
JR	0.1158 ± 0.0035	standard fit [49]
MSTW	0.1171 ± 0.0014	[50]
ABM	0.1147 ± 0.0012	FFNS, incl. combined H1/ZEUS data [51]
BBG	$0.1141^{+0.0020}_{-0.0022}$	valence analysis, N ³ LO [46]
world average	0.1184 ± 0.0007	[52]

Table 4.3: Recent NNLO and N³LO determinations of the strong coupling $\alpha_s(M_Z)$ in DIS world data analyses.

As is well known [53], though also questioned [54], the fits at NLO exhibit scale uncertainties for both the renormalization and factorization scales of $\Delta_{r,f}\alpha_s(M_Z^2) \sim 0.0050$, which are too large to cope with the experimental accuracy of $O(1\%)$. Therefore, NNLO analyses are mandatory. In Table 1 recent NNLO results are summarised. NNLO non-singlet data analyses have been performed in [46, 47]. The analysis [46] is based on an experimental combination of flavor non-singlet data referring to $F_2^{p,d}(x, Q^2)$ for $x < 0.35$ and using the respective valence approximations for $x > 0.35$. The $\bar{d} - \bar{u}$ distributions and the $O(\alpha_s^2)$ heavy flavor corrections were accounted for. The analysis could be extended to N³LO effectively due to the dominance of the Wilson coefficient in this order [44] if compared to the anomalous dimension, cf. [?, 46]. This analysis led to an increase of $\alpha_s(M_Z^2)$ by $+0.0007$ if compared to the NNLO value.

A combined singlet and non-singlet NNLO analysis based on the DIS world data, including the Drell-Yan and di-muon data, needed for a correct description of the sea-quark densities, was performed in [48]. In the fixed flavor number scheme (FFNS) the value of $\alpha_s(M_Z^2)$ is the same as in the non-singlet case [46]. The comparison between the FFNS and the BSMN scheme [55] for the description of the heavy flavor contributions induces a systematic uncertainty $\Delta\alpha_s(M_Z^2) = 0.0006$. One should note that also in the region of medium and lower values of x higher twist terms have to be accounted for within singlet analyses to cover data at lower values of Q^2 . Moreover, systematic errors quoted by the different experiments usually cannot be combined in quadrature with the statistical errors, but require a separate treatment. The NNLO analyses [49] are statistically compatible with the results of [46–48], while those of [50] yield a higher value.

In [51] the combined H1 and ZEUS data were accounted for in an NNLO analysis for the first time, which led to a shift of $+0.0012$. However, running quark mass effects [56] and the account of recent F_L data reduce this value again to the NNLO value given in [48]. Other recent NNLO analyses of precision data, as the measurement of $\alpha_s(M_Z^2)$ using thrust in high energy e^+e^- annihilation data [57, 58], result in $\alpha_s(M_Z^2) = 0.1153 \pm 0.0017 \pm 0.0023$, resp. $0.1135 \pm 0.0011 \pm 0.0006$. Also the latter values are lower than the 2009 world average [52] based on NLO, NNLO and N³LO results.

1144 4.4.2 Simulation of α_s Determination

1145 Since nearly twenty years, the α_s determination in DIS is dominated by the most precise data
1146 from the BCDMS Collaboration, which hint to particularly low values of $\alpha_s(M_Z) \simeq 0.113$ [59]
1147 and exhibit some peculiar systematic error effects, when compared to the SLAC data and in
1148 the pQCD analyses as are discussed in [60, 61]. Recent analyses seem to indicate that the
1149 influence of the BCDMS data is limited, which, however, is possible only when jet and nuclear
1150 fixed target data, extending to very low Q^2 , are used. Jet data sometimes tend to increase the
1151 value of α_s and certainly introduce extra theoretical problems connected with hadronisation
1152 effects in non-inclusive measurements. The use of fixed target data poses problems due to the
1153 uncertainty of corrections from higher twists and from nuclear effects, because what is required
1154 is an extraordinary precision if indeed one wants to unambiguously determine the strong coupling
1155 constant in DIS. These problems have been discussed in detail above, and recently also in
1156 presentations by MSTW [62] and in a phenomenological study of the NNPDF group [63].

1157 The question, of how large α_s is, remains puzzling, as has been discussed at a recent work-
1158 shop [64] and requires a qualitatively and quantitatively new level of experimental input if one
1159 wants to progress in DIS.

1160 Following the description of the simulated LHeC data (Sec. 4.1.4) and the QCD fit technique
1161 (Sec. 4.2.1) a dedicated study has been performed to estimate the accuracy of an α_s measure-
1162 ment with the LHeC. In the fits, for the central values of the LHeC data, the SM expectation is
1163 used smeared within the above uncertainties assuming their Gaussian distribution and taking
1164 into account correlated uncertainties as well.

1165 The QCD fit results are summarised in Tab. 4.4. The first two lines give the result of a fit to
1166 the HERA I data. One observes that the inclusion of DIS jet data reduces the uncertainty, by a
1167 factor of two, but it also increases the central value by more than the uncertainty. The LHeC
1168 alone, in sole inclusive DIS, reaches values of better than 0.2% which when complemented
1169 with HERA data reaches a one per mille precision. From inspecting the results one finds that
1170 enlarging the Q^2 minimum still leads to an impressive precision, as of two per mille in the LHeC
1171 plus HERA case, at values which safely are in the DIS region. A Q^2 cut of for example 10 GeV²
1172 excludes also the lowest x region in which non-linear gluon interaction effects may require to
1173 change the evolution equations.

1174 It is obvious that the sole experimental uncertainty, while impressive and promising indeed,
1175 is not the only problem in such a complex analysis. That requires all relevant parameters to
1176 be correspondingly tuned and understood. For example, the charm mass has to be known at
1177 the 10 MeV level to allow an α_s uncertainty of one per mille. The question of the uncertainty
1178 of the renormalisation and factorisation scales and their effect on α_s will be posed newly and
1179 higher than NNLO approximations of pQCD appear to be necessary. However, as mentioned
1180 above there already exist first N³LO results.

1181 From an experimental and phenomenological point of view it appears extremely exciting that
1182 with the LHeC the α_s determination in DIS will be put on much more solid grounds, by the high
1183 precision and unprecedented kinematic range and but also by the resulting full constraints on the
1184 complete set of parton distributions, of light and heavy quarks, often by direct measurements,
1185 which hitherto had to be parameterised in an often crude way.

1186 In view of the importance of this result, this analysis has been performed independently
1187 twice with separately generated NC and CC pseudodata under somewhat different assumption,
1188 albeit using the same simulation program, and using different versions of the QCD fit program.
1189 The results obtained before [65] are in good agreement with the numbers presented here.

case	cut [Q^2 in GeV ²]	α_S	\pm uncertainty	relative accuracy in %
HERA only (14p)	$Q^2 > 3.5$	0.11529	0.002238	1.94
HERA+jets (14p)	$Q^2 > 3.5$	0.12203	0.000995	0.82
LHeC only (14p)	$Q^2 > 3.5$	0.11680	0.000180	0.15
LHeC only (10p)	$Q^2 > 3.5$	0.11796	0.000199	0.17
LHeC only (14p)	$Q^2 > 20.$	0.11602	0.000292	0.25
LHeC+HERA (10p)	$Q^2 > 3.5$	0.11769	0.000132	0.11
LHeC+HERA (10p)	$Q^2 > 7.0$	0.11831	0.000238	0.20
LHeC+HERA (10p)	$Q^2 > 10.$	0.11839	0.000304	0.26

Table 4.4: Results of NLO QCD fits to HERA data (top, without and with jets) to the simulated LHeC data alone and to their combination. Here 10p or 14p denotes two different sets of parametrisations, one, with 10 parameters, the minimum parameter set used in [10] and the other one with four extra parameters added as has been described VOICAWHERE. The central values of the LHeC based results are obviously of no interest. The result quoted as relative accuracy includes all the statistical and the systematic error sources taking correlations as from the energy scale uncertainties into account.

4.5 Electron-Deuteron Scattering

1190

1191 The structure of the deuteron and of the neutron are experimental unknowns over most of
1192 the kinematic region of deep inelastic scattering. The last time lepton-deuteron scattering was
1193 measured occurred in the fixed target μD experiments at CERN [66–68], while it had only been
1194 considered at HERA [69–71]. The LHeC so extends the range of these measurements by nearly
1195 four orders of magnitude in Q^2 and $1/x$, which gives rise to a most exciting programme in QCD
1196 and in experimental physics.

DIS and Partons

1197

1198 Electron-deuteron scattering complements ep scattering in that it makes possible accurate mea-
1199 surements of neutron structure in the new kinematic range accessed by the LHeC. In a collider
1200 configuration, in which the hadron “target” has momentum much larger than the lepton probe,
1201 the spectator proton can be tagged and its momentum measured with high resolution [69].
1202 The resulting neutron structure function data are then free of nuclear corrections which have
1203 plagued the interpretation of deuteron data, especially at larger x , until now [72]. At low x , for
1204 the first time, since diffraction is related to shadowing, one will be able to control the shadowing
1205 corrections at the per cent level of accuracy as is also discussed below.

1206 Accurate en cross section measurements will resolve the quark flavour decomposition of the
1207 sea, i.e. via isospin symmetry, unfolding \bar{u} from \bar{d} contributions to the rise of $F_2^p \propto x(4\bar{u} + \bar{d})$
1208 towards low x , and, from the full set of $e^\pm p$ and $e^\pm n$ charged current cross section data, a full
1209 unfolding of the flavour content of the nucleon. For the study of the parton evolution with
1210 Q^2 , the measurement of $F_2^N = (F_2^p + F_2^n)/2$ is crucial since it disentangles the evolution of the
1211 non-singlet and the singlet contributions. Down to x of about 10^{-3} the W^+/W^- LHC data
1212 will also provide important information on the up-down quark distributions, albeit at high Q^2 .

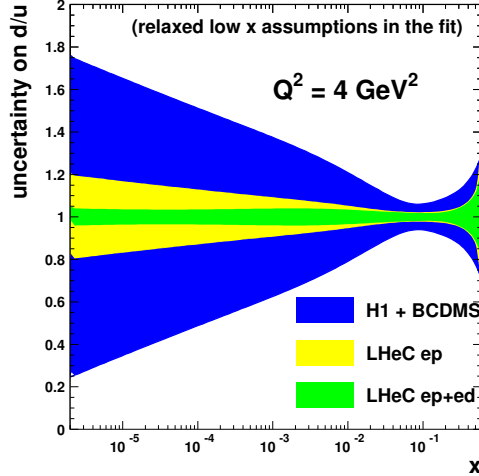


Figure 4.18: Uncertainty of the d/u ratio as a function of x from a QCD fit to H1 and BCDMS data (outer band, blue), to the LHeC proton data (middle band, yellow) and the combined simulated proton and deuteron data from the LHeC (inner band, green). In these fits the constraint of u and d to be the same at low x has been relaxed.

1213 With ep , eD and W^+/W^- data, the low x sea will be resolved for the first time, as all the low
 1214 x light quark information from HERA has been restricted to F_2^p only.

1215 A special interest in high precision neutron data at high Q^2 arises from the question of
 1216 whether there holds charge symmetry at the parton level. This, as has been discussed re-
 1217 cently [73]. It may be studied in the charged current ep and eD reactions, using both electrons
 1218 and positrons, by measuring the asymmetry ratio

$$R^- = 2 \frac{W_2^{-D} - W_2^{+D}}{W_2^{-p} + W_2^{+p}}, \quad (4.30)$$

1219 which is directly sensitive to differences of up and down quark distributions in the proton
 1220 and neutron, respectively, which conventionally are assumed to be equal. With the prospect of
 1221 directly measuring the strange and anti-strange quark asymmetry in $e^\pm p$ CC scattering and of
 1222 tagging the spectator proton and thus eliminating the Fermi motion corrections in eD , such a
 1223 measurement becomes feasible at the LHeC. It requires high luminosity of order 1 fb^{-1} in eD
 1224 scattering.

1225 Hidden Colour

1226 In nuclear physics nuclei are simply the composites of nucleons. However, QCD provides a
 1227 new perspective [74, 75]. Six quarks in the fundamental 3_C representation of $SU(3)$ color can
 1228 combine into five different color-singlet combinations, only one of which corresponds to a proton
 1229 and neutron. The deuteron wavefunction is a proton-neutron bound state at large distances,
 1230 but as the quark separation becomes smaller, QCD evolution due to gluon exchange introduces

1231 four other “hidden color” states into the deuteron wavefunction [76]. The normalization of the
 1232 deuteron form factor observed at large Q^2 [77], as well as the presence of two mass scales in the
 1233 scaling behavior of the reduced deuteron form factor [74], suggest sizable hidden-color Fock state
 1234 contributions in the deuteron wavefunction [78]. The hidden-color states of the deuteron can be
 1235 materialized at the hadron level as $\Delta^{++}(uuu)\Delta^-(ddd)$ and other novel quantum fluctuations of
 1236 the deuteron. These dual hadronic components become important as one probes the deuteron
 1237 at short distances, such as in exclusive reactions at large momentum transfer. For example,
 1238 the ratio $d\sigma/dt(\gamma d \rightarrow \Delta^{++}\Delta^-)/d\sigma/dt(\gamma d \rightarrow np)$ is predicted to increase to a fixed ratio 2 : 5
 1239 with increasing transverse momentum p_T . Similarly, the Coulomb dissociation of the deuteron
 1240 into various exclusive channels $ed \rightarrow e' + pn, pp\pi^-, \Delta\Delta, \dots$ will have a changing composition
 1241 as the final-state hadrons are probed at high transverse momentum, reflecting the onset of
 1242 hidden-color degrees of freedom. The hidden color of the deuteron can be probed at the LHeC
 1243 in electron deuteron collisions by studying reactions such as $\gamma^*d \rightarrow npX$ where the proton and
 1244 neutron emerge in the target fragmentation region at high and opposite p_T . In principle, one
 1245 can also study DIS reactions $ed \rightarrow e'X$ at very high Q^2 where $x > 1$. The production of high
 1246 p_T anti-nuclei at the LHeC is also sensitive to hidden color-nuclear components.

1247 4.6 Electroweak physics

1248 Precision electroweak measurements at low energy have played a central role in establishing the
 1249 Standard Model (SM) as the theory of fundamental interactions. More recently, measurements
 1250 at LEP, SLD, and the Tevatron have confirmed the SM at the quantum level, verifying the
 1251 existence of its higher-order loop contributions. The sensitivity of these contributions to virtual
 1252 heavy particles has allowed for an estimate of the mass of the top quark prior to its actual
 1253 discovery in 1995 by the CDF and DØ Collaborations. Now that the determination of the top
 1254 mass at the Tevatron has become quite accurate, reaching the 1% level, electroweak precision
 1255 measurements imply significant constraints on the mass of the last missing piece of the SM, the
 1256 Higgs boson. The current situation is illustrated in fig.4.6, where the Higgs mass sensitivity
 1257 of a global fit to electroweak precision observables in the SM is shown [79] (a similar analysis
 1258 has been performed in [80]). The left panel shows the $\Delta\chi^2$ of a fit to all relevant electroweak
 1259 observables, while the right panel also include information from direct searches for the Higgs
 1260 boson at LEP-2 and the Tevatron. Indeed, direct searches exclude a Higgs boson with mass
 1261 lower than 114GeV or in a narrow window around 160GeV. An important implication (at 95%
 1262 CL) is that if the SM is correct, the Higgs boson must soon be found with mass below 155GeV
 1263 either at the Tevatron or at LHC.

1264 Electroweak precision measurements are also very effective in constraining the possible ex-
 1265 tensions of the SM. In general, the observed good quality of the SM fit disfavors new physics
 1266 at an energy scale of $O(100\text{GeV})$ that modifies the Higgs mechanism in a drastic way. On the
 1267 other hand, the fit does present a few interesting deviations at the level of $2\text{-}3\sigma$. An important
 1268 one is related to the tension between the FB asymmetry of $Z \rightarrow b\bar{b}$ measured at LEP, which
 1269 favors a heavy Higgs, and the LR asymmetry in $Z \rightarrow \ell\bar{\ell}$ and the W mass, which both favors
 1270 a very light Higgs. Unfortunately, the present determination of M_H depends largely on these
 1271 conflicting information, whose origin could be either statistical or rooted in new physics around
 1272 the corner [81]. Another plausible $\sim 3\sigma$ hint of physics beyond the SM, without Higgs implica-
 1273 tions, is the discrepancy between the measured magnetic anomalous moment of the muon and
 1274 its SM prediction [82].

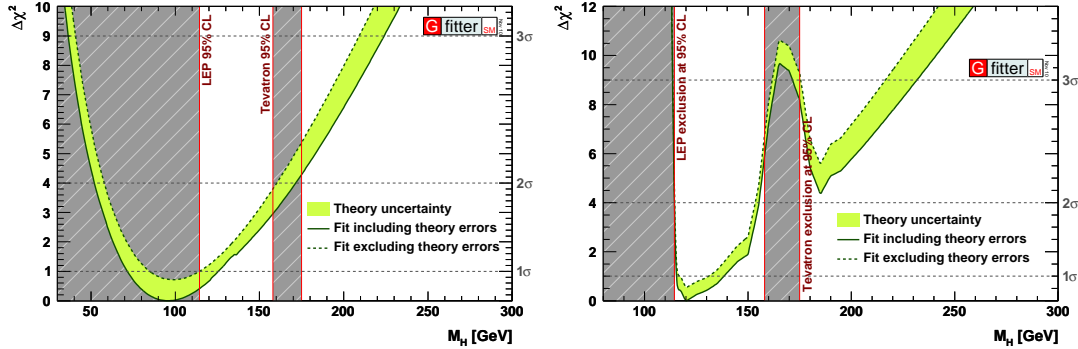


Figure 4.19: Higgs mass sensitivity of a current fit to precision electroweak observables [79]. The right panel includes the information from direct searches.

1275 It is unlikely that operating experiments will change significantly the above picture of electroweak precision measurements. The Tevatron and LHC will marginally improve the current
1276 precision on the top mass and reach a combined 15 MeV uncertainty on M_W , while LHCb
1277 might be able to achieve an interesting accuracy in the measurement of $\sin^2 \theta_W$, perhaps at the
1278 level of LEP [83,84]. Two experiments at Jefferson Lab, Q-weak [85] and (later) MOLLER [86],
1279 will measure the weak mixing angle from parity violation in $e - p$ and $e^- - e^-$ scattering at
1280 low energy: these are interesting measurements complementary to the existing ones; MOLLER,
1281 in particular, will reach an accuracy similar to that of LEP. On the other hand, it is widely
1282 expected that either the Higgs boson or new physics will be discovered at the LHC, if not both.
1283 This is the context in which precision electroweak measurements at LHeC have to be set: rather
1284 than improving bounds on the SM parameters they might help understand new physics, if that
1285 is discovered at LHC.
1286

1287 The electroweak measurements possible at LHeC are in essence the same that have already
1288 been performed at HERA (see [87, 88] for an overview), but they will greatly benefit from the
1289 higher energy and larger luminosity. A first class of measurements involves polarized charged
1290 currents (CC) only.

1291 They include a verification of the left-handedness of CC from the polarization dependence
1292 of the CC cross-section. At HERA this has led to a bound on possible right-handed currents,
1293 expressed in terms of the mass of a right-handed W_R boson that couples to quarks with the same
1294 strength as the SM one. While HERA-I result, $M_{W_R} > 210\text{GeV}$ at 95% CL, can be significantly
1295 improved at the LHeC, low-energy flavour bounds are much stronger. It is otherwise difficult to
1296 learn from CC alone. For instance, the Q^2 -dependence of the CC cross sections, proportional
1297 to $G_F^2 (M_W^2 / (M_W^2 + Q^2))^2 \phi(x, Q^2)$, allows in principle to extract the propagator mass M_W , but
1298 the residual dependence on the structure of the nucleon requires a simultaneous fit to the pdfs,
1299 which necessarily includes NC cross sections as well. In fact, the sensitivity to M_W that can
1300 be achieved in this way is rather low: at LHeC, assuming SM NC couplings, the experimental
1301 error is about 150MeV (scenario D), far from being competitive. Higher sensitivity to M_W can
1302 in principle be obtained by trading G_F for the appropriate combination of $\alpha(M_Z)$, M_W , M_Z
1303 but then the precision in luminosity and other systematics become a bottleneck and one cannot
1304 achieve an M_W determination much better than above.

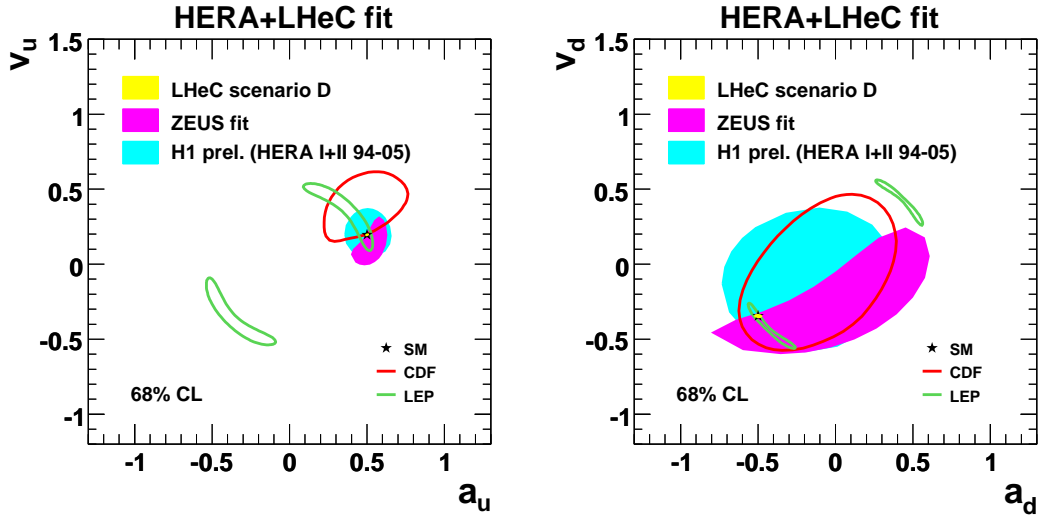


Figure 4.20: Determination of the vector and axial NC couplings of the light quarks at LEP, CDF, HERA and LHeC.

1305 *Paolo: this statement has to be checked. Using only HERA-I data H1 find an experimental*
 1306 *uncertainty of about 200MeV if data are analyzed in this way. How much can this be improved*
 1307 *at LHeC? I see a clear bottleneck: the precision in luminosity (most of the M_W sensitivity*
 1308 *comes from the overall normalization) and the model error which in H1 paper is 40MeV. All*
 1309 *other theoretical uncertainties can be brought significantly down.*

1310 On the other hand, LHeC will be able to measure at the percent level the neutral current
 1311 couplings of the light quarks. As can be seen in Fig. 4.20, LEP has been able to constrain
 1312 well only a combination of them. On the other hand, DIS experiments with polarized electron
 1313 and positron beams can completely disentangle the vector and axial couplings of up and down
 1314 type light quarks. Of course this requires a simultaneous fit to pdfs and electroweak couplings,
 1315 keeping fixed the leptonic couplings, which have been very precisely measured at LEP and SLD.
 1316 As illustrated in Fig.4.20, the preliminary results by ZEUS and H1 have improved on the LEP
 1317 determination in the case of the up quarks [88–90]. The expected resolution for scenario D of
 1318 LHeC is hardly visible on the scale of Fig. 4.20: the results for the various LHeC scenarios (and
 1319 combination thereof) are shown in Table ?? (*still to be made, see later. It should be something*
 1320 *like slide 43 of Claire’s LHeC talk*). The accuracy on the vector and axial vector couplings of
 1321 the $u, d = s$ quarks ranges, in the best possible scenario, ranges between 1 and 4%, with an
 1322 improvement wrt HERA by a factor 10 to 40. A comparison among the various LHeC scenarios
 1323 can be found in Fig. 4.21: the most interesting scenarios are B and D. (*Assuming Voica’s results*
 1324 *for scenario B*) A high degree of polarization (scenario D) can be compensated by much higher
 1325 luminosity (scenario B).

1326 A better determination of the light quark NC couplings will particularly constrain New
 1327 Physics models that modify significantly the light quark NC couplings, without affecting the
 1328 well-measured lepton and heavy quark couplings. It is not easy to realize such an exotic scenario

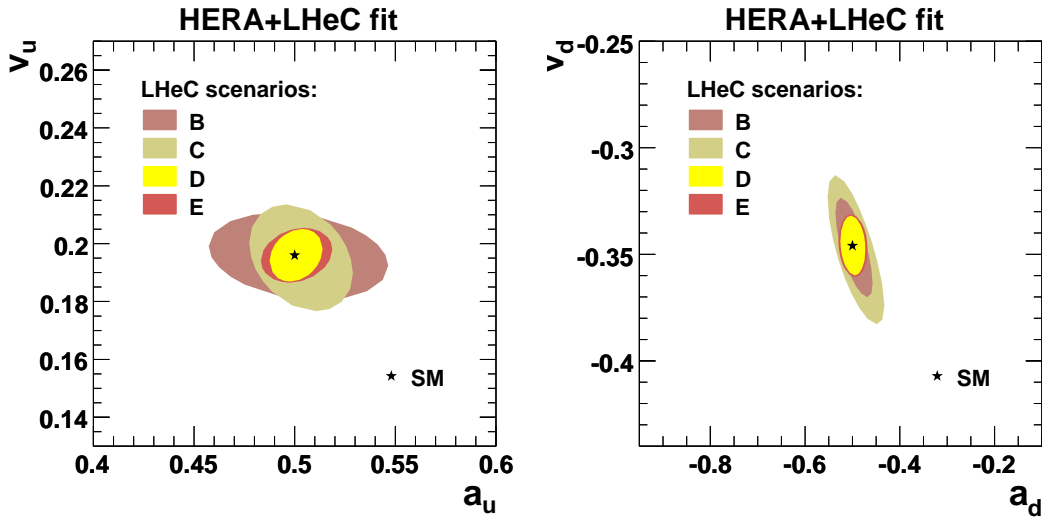


Figure 4.21: Determination of the vector and axial NC couplings of the light quarks at LHeC, comparison different scenarios. (TO BE UPDATED??)

1329 in a natural way, although family non-universal (leptophobic) Z' models (see for instance [91,92]
 1330 and refs. therein), R-parity violating supersymmetry (see [93] for a review) and leptoquarks [94]
 1331 can in principle succeed. LHeC could therefore accurately test a spectrum of interesting new
 1332 physics models. A specific linear combination of the light quark NC vector couplings (v_u and
 1333 v_d) will be soon be measured at the % level by the QWeak Collaboration [85]. Their results,
 1334 combined with existing precise measurement of Atomic Parity Violation and DIS, will provide
 1335 a percent determination of v_u and v_d [95] and test the same kind of models, but it will not
 1336 probe the axial couplings.

1337 *Additional issues concerning this fit:*

- 1338 • *Voica has shown that high precision can be obtained also in scenario B. Claire's results for*
 1339 *B are less precise, likely because of lower angular coverage (down to 10 degrees, only for*
 1340 *B). However, there are a few strange features in Voica's numbers (see my dec 10 email)*
- 1341 • *what is the effect of combining scenarios B+H and other similar combinations of scenar-*
 1342 *ios?*
- 1343 • *what is the effect on electroweak couplings of relaxing the assumptions on the sea quarks*
 1344 *(as Voica discusses on p.13 of her Chavannes slides)?*
- 1345 • *I think somebody in Chavannes asked a question on the importance of polarized positrons*
 1346 *for electroweak physics. Can we answer?*

1347 *If there is time, two easy, complementary analyses that might give a feeling of the constrain-*
 1348 *ing power in more general new physics models are the following*

- 1349 1. we express all the NC quark and lepton couplings in terms of $\sin^2\theta_W$, and fit for it. NC
1350 and CC couplings are all normalized to G_F .
- 1351 2. we express the lepton and quark couplings in terms of $G_F, \sin^2\theta_W$ and ρ (a renormaliza-
1352 tion factor in front of the NC coupling), and fit for them, see PDG.
- 1353 A fit to oblique parameters S, T, U is also possible but requires more work. Not important.

1354 4.6.1 Determination of the Weak Mixing Angle

1355 Cross Section Asymmetries and Ratios

1356 The LHeC is a unique facility for electroweak physics because of the very high luminosity, high
1357 measurement precision and the extreme range of momentum transfer Q^2 . Fig. 4.22 illustrates
1358 the reach and the size of the electroweak effects in NC scattering. Depending on the charge and
1359 polarisation of the electron beam, the contributions from γZ interference and pure Z exchange
1360 become comparable to or even exceed the photon exchange contribution, i.e. of F_2 , which has
1361 dominated hitherto all NC DIS measurements. With the availability of two charge and two
1362 polarisation states, of neutral and charged current measurements, proton and isoscalar targets,
1363 a unique menu becomes available for testing the electroweak theory, by measuring for example
1364 the light weak neutral current couplings, discussed subsequently, extracting the heavy quark
1365 contributions from γZ interference or measuring the energy dependence of the weak mixing
1366 angle, considered here.

1367 Tests of the electroweak theory in DIS require to simultaneously control the parton distri-
1368 bution effects. With the outstanding data base from the LHeC, joint QCD and electroweak fits
1369 become possible to high orders perturbation theory. Cross section asymmetries and ratios can
1370 also be used to determine electroweak parameters. Particularly useful examples are polarisation
1371 and charge asymmetries and also NC to CC cross section ratios.

1372 In NC scattering, the polarisation asymmetry

$$A^\pm = \frac{1}{P_R - P_L} \cdot \frac{\sigma_{NC}^\pm(P_R) - \sigma_{NC}^\pm(P_L)}{\sigma_{NC}^\pm(P_R) + \sigma_{NC}^\pm(P_L)} \quad (4.31)$$

1373 served for the decisive confirmation of the left handed weak neutral current doublet structure
1374 as was predicted by the GWS theory in 1979 [96]. The size of the electroweak asymmetries is
1375 given by the relative amount of Z to photon exchange $O(10^{-4}Q^2/\text{GeV}^2)$, i.e. it becomes of
1376 order 1 at high Q^2 at the LHeC.

1377 To a good approximation the asymmetry measures the structure function ratio

$$A^\pm \simeq \mp \kappa_Z a_e \frac{F_2^{\gamma Z}}{(F_2 + \kappa_Z a_e Y_- x F_3^{\gamma Z} / Y_+)} \simeq \mp \kappa_Z a_e \frac{F_2^{\gamma Z}}{F_2}. \quad (4.32)$$

1378 Thus A^+ is expected to be about equal to $-A^-$ and to be only weakly dependent on the parton
1379 distributions. The product of the axial coupling of the electron and the vector coupling of
1380 the quarks, inherent in $F_2^{\gamma Z}$, determines the polarisation asymmetry to be parity violating. A
1381 measurement of A^\pm provides a unique and precise measurement of the scale dependence of the
1382 weak mixing angle, as is discussed below (Sect. 4.6.1). At large x the polarisation asymmetry
1383 provides an NC measurement of the d/u ratio of the valence quark distributions, according to

$$A^\pm \simeq \pm \kappa \frac{1 + d_v/u_v}{4 + d_v/u_v}. \quad (4.33)$$

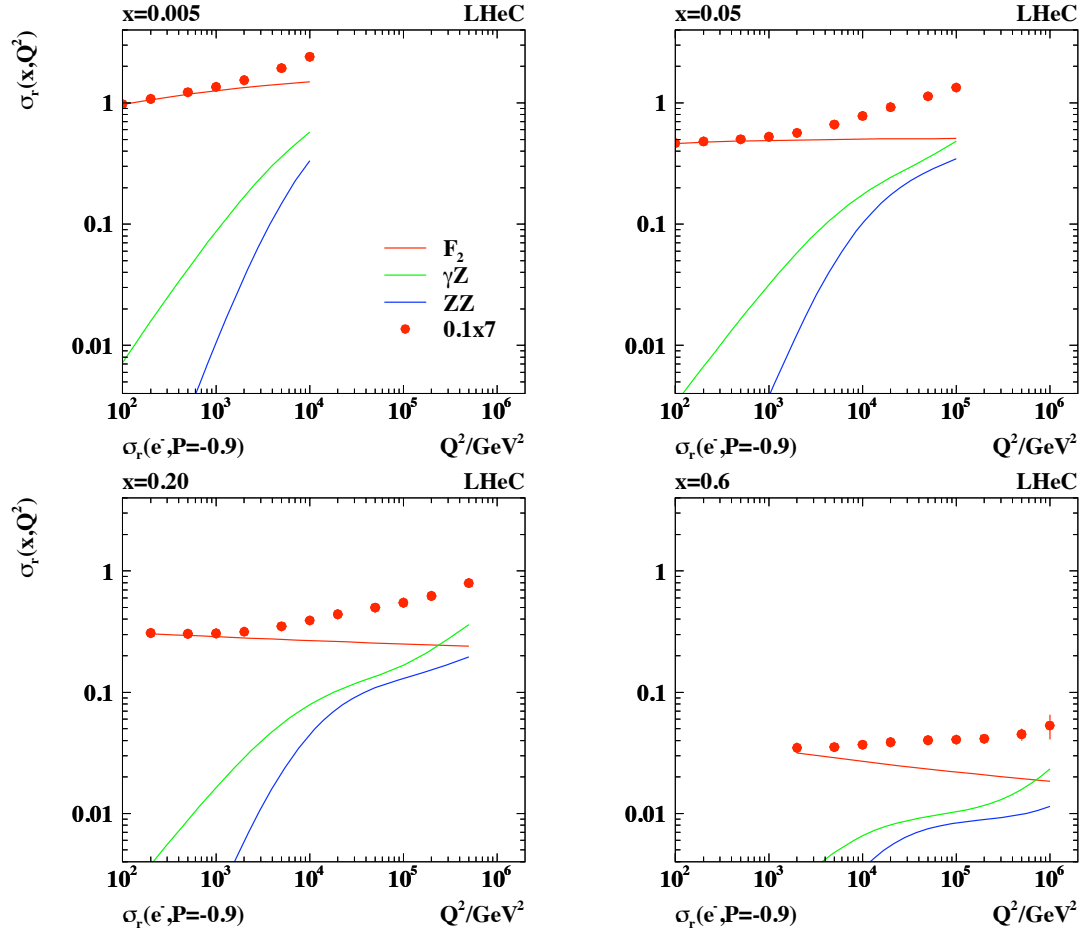


Figure 4.22: Simulated measurement of the neutral current DIS cross section (closed points) with statistical errors for 10 fb^{-1} shown as a function of Q^2 for different values of Bjorken x . The different curves represent the contributions of pure photon exchange (red), γZ interference (green) and pure Z exchange (blue) as prescribed in Eq. 4.5. Note the high precision of the reduced cross section measurement up to large x and Q^2 .

1384 Further asymmetries of NC cross sections have been discussed in [22].

1385 The neutral-to-charged current cross-section ratio

$$R^\pm = \frac{\sigma_{NC}^\pm}{\sigma_{CC}^\pm} = \frac{2}{(1 \pm P)\kappa_W^2} \cdot \frac{\sigma_{r,NC}^\pm}{\sigma_{r,CC}^\pm} \quad (4.34)$$

1386 is of interest for electroweak physics too as will be demonstrated below. At very high $Q^2 \gg M_Z^2$
 1387 and neglecting terms in the NC part proportional to v_e it becomes approximately equal to

$$R^\pm \simeq \frac{2a_e^2}{(1 \pm P)\cos^2\theta} \cdot \frac{Y_+ F_2^Z - Y_- P x F_3^Z}{Y_+ W_2^\pm + Y_- x W_3^\pm} \quad (4.35)$$

1388 which reveals the striking similarity of the neutral and charged weak interactions at high en-
 1389 ergies. One may further consider, for example, a quantity which is the eN analogon to the
 1390 Paschos-Wolfenstein relation [97] in νN scattering

$$A_{NCC} = \frac{\sigma_{NC}^+ - \sigma_{NC}^-}{\sigma_{CC}^+ - \sigma_{CC}^-}. \quad (4.36)$$

1391 The very high luminosity and Q^2 range of the LHeC as compared even to HERA will open
 1392 a completely new era of electroweak physics in DIS.

1393 Measurement of the Weak Mixing Angle

1394 Further tests of the SM at the quantum level and indirect searches for new physics require
 1395 ultimate precision. Such corrections occur in the factor $1 - \Delta r$, see Eq.4.14, which depends
 1396 on the top mass, logarithmically on the Higgs mass and possibly on new, heavy particles. A
 1397 measurement of the weak mixing angle, $\sin^2\theta$, to 0.01 % precision should fix the Higgs mass to
 1398 5 % accuracy. The so far most precise measurements of $\sin^2\theta$ have been performed at the Z pole
 1399 in e^+e^- scattering, using the very high statistics, at LEP, and in the case of the SLC, the large
 1400 beam polarisation of 75 % too. The LHeC has the potential to measure weak asymmetries and
 1401 cross section ratios at, below and beyond the M_Z scale by precisely measuring their dependence
 1402 on $\sqrt{Q^2}$.

1403 The accuracy estimated for $\sin^2\theta$ depends on its definition. The electroweak theory has
 1404 three independent parameters. In the on-mass shell scheme, these are chosen to be the fine
 1405 structure constant α and the weak boson masses, M_W and M_Z . For the subsequent study, as
 1406 in a similar study of H1 [89], the values of α and M_Z are fixed, which are best known, M_Z
 1407 0.002 %. For the estimate of the sensitivity to electroweak effects as the third parameter here
 1408 $\sin^2\theta$ is chosen, which is used, together with α and M_Z to calculate G and M_W and also occurs
 1409 in the weak neutral current couplings. This way both the NC and the CC cross sections are
 1410 sensitive to $\sin^2\theta$. Equivalently one could have expressed all parameters using α , M_Z and M_W ,
 1411 and determine M_W . Due to the relation $\sin^2\theta = 1 - M_W^2/M_Z^2$, the error of such an indirect
 1412 measurement of M_W is

$$\Delta M_W = \frac{M_W \delta \sin^2\theta}{2 \sin^2\theta}, \quad (4.37)$$

1413 i.e. a one permille accuracy on $\sin^2\theta$ corresponds to $\Delta M_W = 40$ MeV.

1414 A simulation is done of the NC and CC cross sections depending on the lepton beam charges
 1415 and polarisations based on the formulae presented above. This allows to build a variety of

1416 asymmetries and cross section ratios and derive their sensitivity to the weak mixing angle. An
 1417 example is illustrated in Fig. 4.23. Here the polarisation asymmetry (left) and the NC/CC ratio
 1418 (right) are calculated for different values of $\sin^2 \Theta$ using two recent sets of leading order parton
 1419 distributions, CTEQ6LL and MSTW08. The measurement accuracy of $\sin^2 \Theta$ has a statistical,
 1420 a polarisation, a systematic and a pdf uncertainty. One derives that the statistical precision
 1421 is about 0.1 % for the NC asymmetry A^- and even 0.05 % for the NC/CC ratio R^- for e^-p
 1422 scattering with an assumed polarisation of -0.8 and a luminosity of 10 fb^{-1} for default beam
 1423 energies.

1424 At this early stage of consideration one may not present a full error study. However, a few
 1425 first considerations are in order: The high luminosity and large Q^2 range move the electroweak
 1426 physics at this ep machine to the level of highest accuracy demands. Most of the systematic
 1427 errors cancel in asymmetry and ratio measurements. A 0.1 % electron energy scale uncertainty,
 1428 as has been achieved with H1, for example, translates at the LHeC to a 0.15 % change of A^-
 1429 and a negligible change of R^- . This measurement samples data in a region of very high cross
 1430 section accuracy and can exclude the highest x region where uncertainties grow like $1/(1-x)$.
 1431 The desired level of polarisation measurement is obviously about a permille, which seems to be
 1432 possible as is discussed in the detector chapter.

1433 The requirements for A^- and R^- are different. The asymmetry A^- requires frequent changes
 1434 of the polarisation to control the time dependence of the measurement. It measures essentially
 1435 a ratio of the structure functions $F_2^{\gamma Z}/F_2$ and therefore it is rather insensitive to uncertainties
 1436 related to the parton distributions. In fact, one observes in Fig. 4.23 that the predictions of the
 1437 two PDF sets considered differ by less than the statistical uncertainty for A^- . The NC/CC
 1438 ratio R is less sensitive to time drifts as the NC and CC data are taken simultaneously. Its
 1439 statistical power is highest, as had already been noticed for HERA [98]. It yet is sensitive to the
 1440 PDFs. For the two sets of PDFs considered here, an about two per cent difference is calculated
 1441 of the R^- ratios. This would spoil the extraction of $\sin^2 \Theta$. The high sensitivity of R to the
 1442 mixing angle can only be employed when the PDFs are much better known than so far. This,
 1443 however, is one of the major goals of the LHeC physics programme and large improvements
 1444 are to be expected as is discussed in Sec. 4.2. The potential of measuring $\sin^2 \Theta$ from NC/CC
 1445 ratios is observed to be particular striking. However, for the evaluation of the scale dependence
 1446 of $\sin^2 \Theta$ below, the results derived from A^- are used due to its much smaller PDF sensitivity.

1447 The mixing angle, similar to α_s , is predicted to vary strongly as a function of the scale
 1448 μ , which in DIS is precisely known and given as $\sqrt{Q^2}$. This dependence results from higher
 1449 order loop effects as calculated in [99]. Precise measurements to per mille uncertainty were
 1450 performed at the Z pole by SLC and LEP experiments. Recent low energy experiments have
 1451 provided measurements of $\sin^2 \Theta$ at very low Q^2 as from the parity violation asymmetry due to
 1452 polarisation conjugation in Moeller scattering at $Q^2 = 0.026 \text{ GeV}^2$ by the E158 experiment. At
 1453 scale values of about 5 GeV the NuTeV Collaboration has determined the mixing angle which
 1454 for some time created a substantial experimental and theoretical effort when it appeared to be
 1455 above the theoretical expectation by a few standard deviations. Explanations of this “anomaly”
 1456 included variations of the strange quark density, effects from QED or nuclear corrections. An
 1457 ultraprecise measurement of $\sin^2 \Theta$ is envisaged, yet still at $\mu = M_Z$, if a new Z_0 factory was
 1458 built.

1459 The current measurements are summarised in Fig. 4.24. The plot also contains projected
 1460 $\sin^2 \Theta$ uncertainty values from the LHeC, as listed in Table 4.5, which result from simulations
 1461 of the parity violation asymmetry A^- in polarised e^-p scattering, for scales between about 10
 1462 and 400 GeV. Due to the high statistics nature of the DIS NC process, the variation of $\sin^2 \Theta$ as

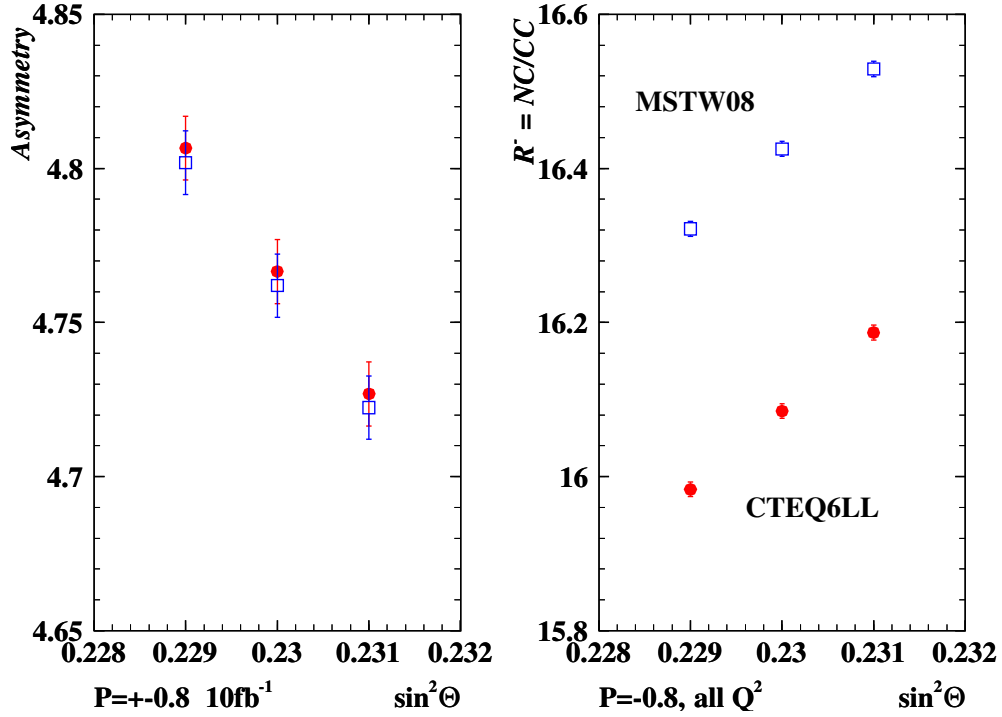


Figure 4.23: Simulated measurement of the polarisation NC cross section asymmetry A^- (left), in per cent for $P = \pm 0.8$, and the ratio of neutral-to-charged current cross sections, $R = NC/CC$ (right), for $P = -0.8$, for different values of $\sin^2 \theta$ defined in the on-mass shell scheme. The errors are statistical for luminosities of 10 fb^{-1} per beam for polarised electron scattering for $E_e = 60 \text{ GeV}$ and the nominal 7 TeV proton beam. The closed (open) symbols show the simulation for the CTEQ6LL (MSTW08) leading order parameterisations of the parton distributions. The average Q^2 is 1300 GeV^2 for the NC asymmetry A^- , while for the ratio R the average CC Q^2 is about 9500 GeV^2 . Consequently, the mean x in NC and CC differs by a factor of 6, which is at the origin of the large differences in R between the two PDF set predictions.

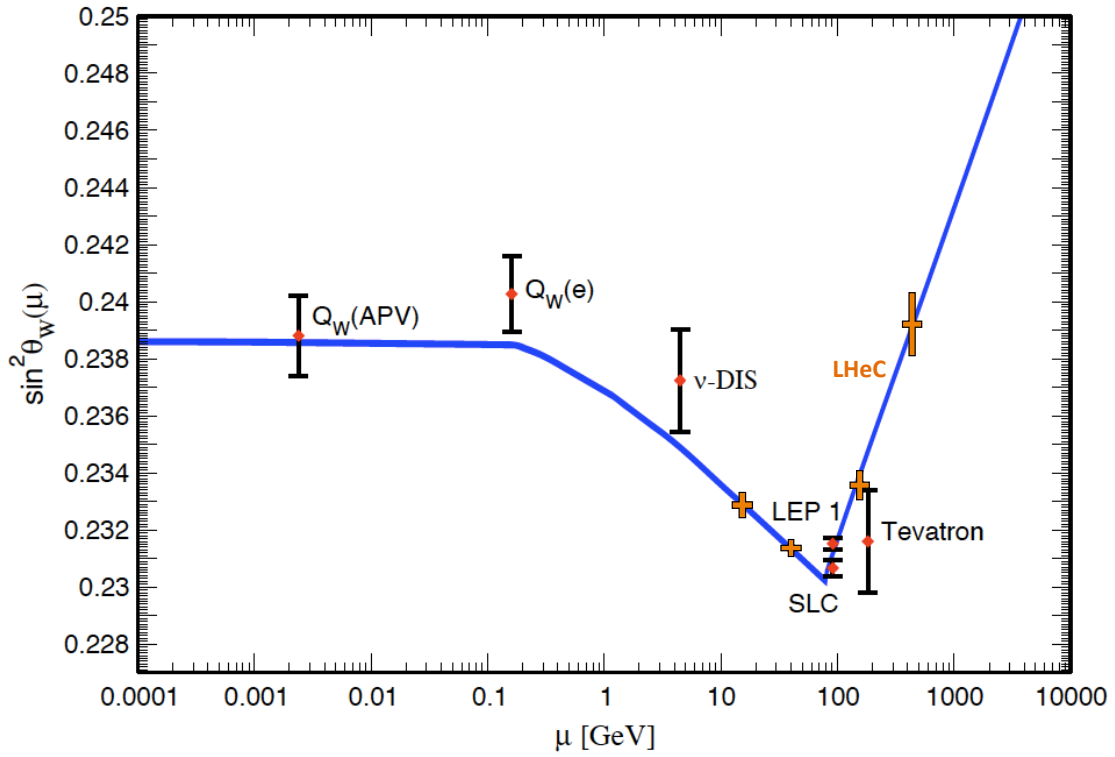


Figure 4.24: Dependence of the weak mixing angle in the on-mass shell scheme on the energy scale μ , taken from [28]. Four simulated points have been added based on the estimated measurement accuracy using the polarisation asymmetry A^- binned in intervals of $\sqrt{Q^2}$, see text.

Type	Q_1	P_1	Q_2	P_2	$\delta s(A_{12})$	$\delta s(R_1)$	$\delta s(R_2)$
e^- Polarisation Conjugation	-1.	-0.8	-1.	0.8	0.00026	0.00009	0.00024
e^+ Polarisation Conjugation	+1.	-0.8	+1.	0.8	0.00027	0.00040	0.00015
e^- Low P Conjugation	-1.	-0.4	-1.	0.4	0.00052	0.00010	0.00015
Charge Conjugation P=0	+1.	0.	-1.	0.	0.01600	0.00019	0.00012
Charge Conjugation P= \mp 0.8	+1.	-0.8	-1.	0.8	—	0.00040	0.00024
Charge Conjugation P= \pm 0.8	+1.	+0.8	-1.	-0.8	0.00790	0.00015	0.00009
e^- PC Low $Q^2 \sim 300 \text{ GeV}^2$	-1.	-0.8	-1.	0.8	0.00068	0.00029	0.00083
e^- PC Med $Q^2 \sim 1500 \text{ GeV}^2$	-1.	-0.8	-1.	0.8	0.00027	0.00012	0.00029
e^- PC High $Q^2 \sim 22000 \text{ GeV}^2$	-1.	-0.8	-1.	0.8	0.00044	0.00071	0.00055
e^- PC vHigh $Q^2 \sim 130000 \text{ GeV}^2$	-1.	-0.8	-1.	0.8	0.00170	0.00460	0.00200

Table 4.5: Estimated accuracies of the weak mixing angle, $\delta \sin^2 \Theta$, in the on-mass shell scheme, from simulated measurements of the NC asymmetry and the NC/CC cross section ratio for different beam charge and polarisation conditions.

1463 a function of $\sqrt{Q^2}$ can be measured for a large range of $\sqrt{Q^2}$. At low scales the range limited
1464 by the sensitivity to the Z exchange effects and at high scales by the kinematic limit and
1465 luminosity. It may deserve a study to understand to how low values of Q^2 the asymmetry A^-
1466 can be determined in a meaningful measurement, which is related to time drifts, polarisation
1467 flip times etc. and likely can only be answered with real data. It is to be noted that previous
1468 and planned fixed target experiments measure this asymmetry at extremely small values of Q^2
1469 as compared to the range of the LHeC.

1470 From the range considered here, with $Q^2 > 300 \text{ GeV}^2$, it can be concluded, see Fig. 4.24,
1471 that the expected measurement accuracy would lead to a decisive test of the scale dependence
1472 of $\sin^2 \Theta$.

1473 4.7 Charm and Beauty production

1474 4.7.1 Charm and Beauty production at LHeC

1475 Introduction and overview of expected highlights

1476 In this section it is shown that the measurements of charm and beauty production at LHeC
1477 provide high precision pQCD tests and are crucial to improve the knowledge of the proton
1478 structure. Historically the HERA charm and beauty studies extended by large amount results
1479 from previous fixed target experiments. This allowed a great advancement in the understand-
1480 ing of the dynamics of heavy quark production. The LHeC is the ideal machine for a further
1481 extension of similar historic importance because a higher centre of mass energy and a much
1482 larger integrated luminosity compared to HERA are available. On top of this the heavy flavour
1483 measurements will greatly benefit from the advanced detector design at LHeC with high pre-
1484 cision (Silicon or similar) trackers all over the place. At HERA the tagging was restricted to

1485 central rapidities and effective efficiencies⁴ of only 0.1% (1%) for charm (beauty) were reached.
 1486 At LHeC efficiencies of 10% (50%) should be possible for charm (beauty) and a large rapidity
 1487 range can be covered from the very backward to the very forward regions. Before further eluci-
 1488 dating the great measurement prospects the next paragraph introduces the main heavy quark
 1489 production processes, the relevant pQCD theoretical schemes and some related open questions.
 1490 In leading order, heavy quarks are produced in ep collisions via the Boson Gluon Fusion (BGF) process shown in Figure 4.25 on the left. This process provides direct access to the

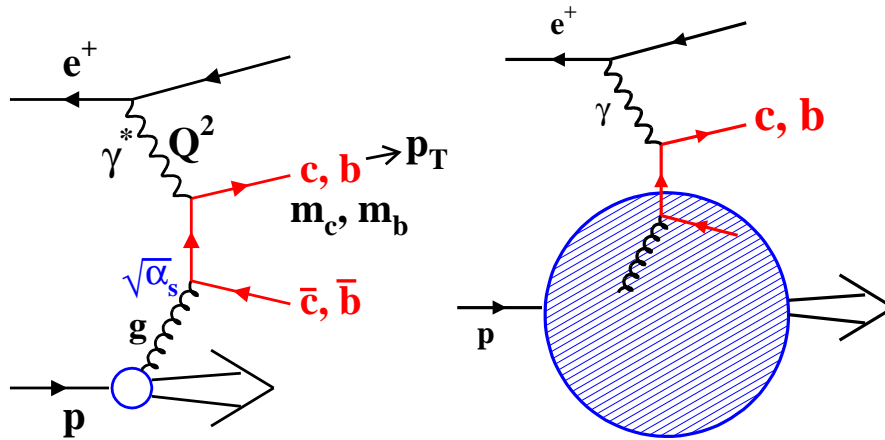


Figure 4.25: Left: Leading order Boson Gluon Fusion (BGF) diagram for charm and beauty production in ep -collisions. Right: Sketch of the leading order process in the massless approach where charm and beauty quarks are treated as massless sea quarks in the proton.

1491 gluon density in the proton. BGF type processes dominate DIS scattering towards lower x ,
 1492 due to the large gluon density. In the high Q^2 limit, the events with charm and beauty quarks
 1493 are expected to account for $\sim 36\%$ and $\sim 9\%$ of the BGF processes and hence contribute
 1494 significantly to inclusive DIS. On the theoretical side, the description of heavy quark production
 1495 in the framework of perturbative QCD is complicated due to the presence of several large scales
 1496 like the heavy quark masses, the transverse momentum p_T of the produced quarks and the
 1497 momentum transfer Q^2 . Different calculation schemes have been developed to obtain predictions
 1498 from pQCD. At low scales p_T (or Q^2) the fixed-flavour number scheme (FFNS) [100–102] is
 1499 expected to be most appropriate where the quark masses are fully accounted for. At very high
 1500 scales the NLO FFNS scheme predictions are expected to break down since large logarithms
 1501 $\ln(p_T^2/m^2)$ are neglected that represent collinear gluon radiations from the heavy quark lines.
 1502 These logarithms can be resummed to all orders in the alternative zero-mass variable flavour
 1503 number (ZM-VFNS) [103–106] schemes. Here the charm and beauty quarks are treated above
 1504 kinematic threshold as massless and appear also as active sea quarks in the proton, as depicted
 1505 in figure 4.25 in the sketch on the right. Most widely used are nowadays the so-called
 1506 generalised variable flavour number schemes (GM-VFNS) [107, 108]. These mixed schemes
 1507 converge to the massive and massless schemes at low and high kinematical scales, respectively,
 1508 and apply a suitable interpolation in the intermediate region. However, the exact modelling
 1509

⁴The effective efficiency takes the background pollution into account. It is defined as the efficiency of an equivalent background free sample with the same signal precision as that obtained in the data.

1510 of the interpolation and in general the treatment of mass dependent terms in the perturbation
 1511 series are still a highly controversial issue among the various theory groups. The different
 1512 treatments have profound implications for global PDF fits and influence the fitted densities
 1513 of gluons and other quark flavours in the proton. This has direct consequences for many
 1514 important cross section predictions at LHC, for instance for Z and W production. The value
 1515 of the charm quark mass is also an important uncertainty in the calculations. Recently the
 1516 running charm mass has been fitted [56] to fixed target and HERA charm data obtaining a
 1517 value $m_c(m_c) = 1.01 \pm 0.09(\text{exp}) \pm 0.03(\text{th})$ GeV.

1518 The following main physics highlights are expected for heavy quark production measure-
 1519 ments at LHeC:

- 1520 • *Massive vs Massless scheme:* At HERA the charm and beauty production data were found
 1521 to be well described by the NLO FFNS scheme calculations over the whole accessible phase
 1522 space, up to the highest p_T and Q^2 scales. An LHeC collider would allow to extend these
 1523 studies to a much larger kinematical phase space and thus to map the expected transition
 1524 to the massless regime. Further improvements in the determination of the charm quark
 1525 mass and in the tuning of the GM-VFNS schemes are possible and will have strong impacts
 1526 on global PDF fits.

- 1527 • *Gluon density determination:* At HERA the recorded charm data provide already some
 1528 interesting sensitivity to the gluon density in the proton. However due to the small
 1529 tagging efficiencies the precisions are far below those obtained from the scaling violations
 1530 of F_2 or those from jet data. At LHeC this situation will highly improve and it will
 1531 be possible to probe the gluon density via the BGF process down to proton momentum
 1532 fractions $x_g \leq 10^{-5}$, where it is currently not well known. At such low values of x_g the
 1533 gluon density has risen so high that non-linear effects have to occur in order to damp
 1534 the rise of the cross section to be compliant with unitarity constraints. Since the gluon
 1535 density is not directly measurable it is of particular importance that the new theory
 1536 of non-linear gluon interactions is constrained with high precision measurements of the
 1537 scaling violations of F_2 , of F_L and of the BGF process in charm and in beauty production
 1538 in DIS. In this context it is also interesting to note that in the BGF process one can
 1539 reach for charm production much smaller x_g values than with flavour inclusive jets since
 1540 experimentally one can tag charm quarks with small transverse momenta. The studies of
 1541 heavy flavour production sensitive to the gluon density can be done both in DIS and in
 1542 the photoproduction kinematic regimes.

- 1543 • *Charm and beauty densities in the proton:* In general the measurements of the structure
 1544 functions F_2^{cc} and F_2^{bb} are of highest interest for theoretical analyses of heavy flavour
 1545 production in ep collisions. These structure functions are describing the parts of F_2
 1546 which are due to events with charm or beauty quarks in the final state. At sufficiently high
 1547 $Q^2 \gg m_c^2, m_b^2$, the two structure functions can be directly related to effective densities
 1548 of charm and beauty quarks in the proton, This can be used for predictions of many
 1549 interesting processes at LHC with charm or beauty quarks in the initial state. For instance,
 1550 as discussed in [109], in the minimal supersymmetric extension of the standard model the
 1551 production of the neutral Higgs boson A is driven by $b\bar{b} \rightarrow A$ and for the calculation
 1552 of this process the PDF uncertainties dominate over the theoretical uncertainties of the
 1553 perturbative calculation. At HERA the measurements of F_2^{bb} barely reached the necessary

1554 high Q^2 regime and only with modest precision. Huge phase space extensions and precision
1555 improvements will be possible at LHeC.

- 1556 • *Intrinsic charm component:* Since long it has been suggested [18, 110–112] that the proton
1557 wave function might contain an intrinsic charm component $uudc\bar{c}$. This would show up
1558 mainly at large $x > 0.1$. Unfortunately at HERA this large x region could not be studied
1559 mainly due to the limited detector acceptance in the forward region. Due to the even larger
1560 boost in the forward direction at LHeC the situation is also not easy there. However, with
1561 a forward tracking acceptance down to small polar angles there could be a chance to study
1562 this effect, in particular with the planned proton low energy runs.
- 1563 • *Strange/antistrange densities:* Events with charm quarks in the final state can be also
1564 used as a tool for other purposes. The strange and antistrange quark densities in the
1565 proton can be analysed via the charge current process $sW \rightarrow c$, where the charm quark is
1566 tagged in the event. At HERA this was impossible due to the small cross sections, but at
1567 LHeC the cross sections for CC reactions are much higher and as noted before the other
1568 experimental conditions (luminosities, detector) will greatly improve. This leads to the
1569 first and precise measurement of both the strange and the anti-strange quark densities as
1570 is demonstrated in Sect. 4.2.
- 1571 • *Electroweak physics:* There are intriguing possibilities for LHeC electroweak physics stud-
1572 ies with charm and beauty quarks in the final state. For example one should be able to
1573 do a lepton beam polarisation asymmetry measurement for neutral current events, where
1574 the scattered quark is tagged as a beauty quark. This will provide direct access to the
1575 axial and vector couplings of the beauty quark to the Z boson. Similar measurements are
1576 possible for charm.

1577 In summary the measurements of charm and beauty at an LHeC will be extremely useful for
1578 high precision pQCD tests, in particular for the understanding of the treatment of mass terms
1579 in pQCD, to improve the knowledge of the proton PDFs: directly for g , c , b , s , \bar{s} densities
1580 and indirectly also for u and d . Furthermore they provide a great potential for electroweak
1581 physics. At the time when the LHeC will be operated, the pQCD theory calculations are
1582 expected to have advanced considerably. In particular there is hope that full massive scheme
1583 NNLO calculations of order $o(\alpha_s^3)$ will be available by then. These will allow theory to data
1584 comparisons for heavy flavour production in ep collisions with unprecedented precision.

1585 In the following subsections several dedicated simulation studies are presented which il-
1586 lustrate some of the expected highlights. First total cross sections are presented for various
1587 processes involving charm, beauty and also top quarks in the final state, showing that LHeC
1588 will be a genuine *multi heavy flavour factory*. Then the expected measurements of the structure
1589 functions F_2^{cc} and F_2^{bb} are discussed and compared to the existing HERA data. Next a study is
1590 presented of the possibility to measure intrinsic charm with dedicated low proton energy runs.
1591 Finally predictions for differential charm hadron production cross sections in the photoproduc-
1592 tion kinematic regime are presented and compared to HERA, demonstrating the large phase
1593 space extension.

1594 **Total production cross sections for charm, beauty and top quarks**

1595 This section presents total cross sections for various heavy quark processes at LHeC (with 7
1596 TeV proton beam energy) as a function of the lepton beam energy. Predictions are obtained for:

1597 charm and beauty production in photoproduction and DIS, the charged current processes $sW \rightarrow$
 1598 c and $bW \rightarrow t$ and top quark pair production in photoproduction and DIS. For comparison the
 1599 flavour inclusive charged current total cross section is also shown. Table 4.6 lists the generated
 processes, the used Monte Carlo generators and the selected parton distribution functions. The

Process	Monte Carlo	PDF
Charm γp Beauty γp tt γp	PYTHIA6.4 [113]	CTEQ6L [114]
Charm DIS Beauty DIS tt DIS	RAPGAP3.1 [115]	CTEQ5L [116]
CC e^+p CC e^-p $sW \rightarrow c$ $\bar{s}W \rightarrow \bar{c}$ $bW \rightarrow t$ $\bar{b}W \rightarrow \bar{t}$	LEPTO6.5 [117]	CTEQ5L
tt DIS	RAPGAP 3.1	CTEQ5L

Table 4.6: Used generator programmes for the predictions of total cross sections at LHeC, shown in Figure 4.26. For all processes with top quarks the top mass was set to a value of 170 GeV. For both photoproduction (labelled as γp) and DIS only direct photon processes were generated and no reactions with resolved photons.

1600
 1601 resulting cross sections are shown in Figure 4.26. For comparison also the predicted cross
 1602 sections for the HERA collider (with 920 GeV proton energy) are presented. The cross sections
 1603 at LHeC are typically about one order of magnitude larger compared to HERA. Attached to the
 1604 right of the plot are the number of events that are produced per 10 fb^{-1} of integrated luminosity.
 1605 For instance for charm more than 10 billion events are expected in photoproduction and for
 1606 beauty more than 100 million events. In DIS the numbers are typically a factor of five smaller.
 1607 The strange and antistrange densities can be probed with some hundred thousands of charged
 1608 current events with charm in the final state. The top quark production is dominated by the
 1609 single production in the charged current reaction with beauty in the initial state and about one
 1610 hundred thousands tops and a similar number of antitops are expected. In summary the LHeC
 1611 will be the first ep collider which provides access to all quark flavours and with high statistics.

1612 Charm and Beauty production in DIS

1613 This section presents predictions for charm and beauty production in neutral current DIS, for
 1614 Q^2 values of at least a few GeV^2 . The predictions are given for the structure functions $F_2^{c\bar{c}}$
 1615 and $F_2^{b\bar{b}}$ which denote the contributions from charm and beauty events to F_2 . As explained
 1616 in section 4.7.1 the two structure functions are of large interest for theoretical analyses. Ex-
 1617 perimentally they are obtained by determining the total charm and beauty cross sections in

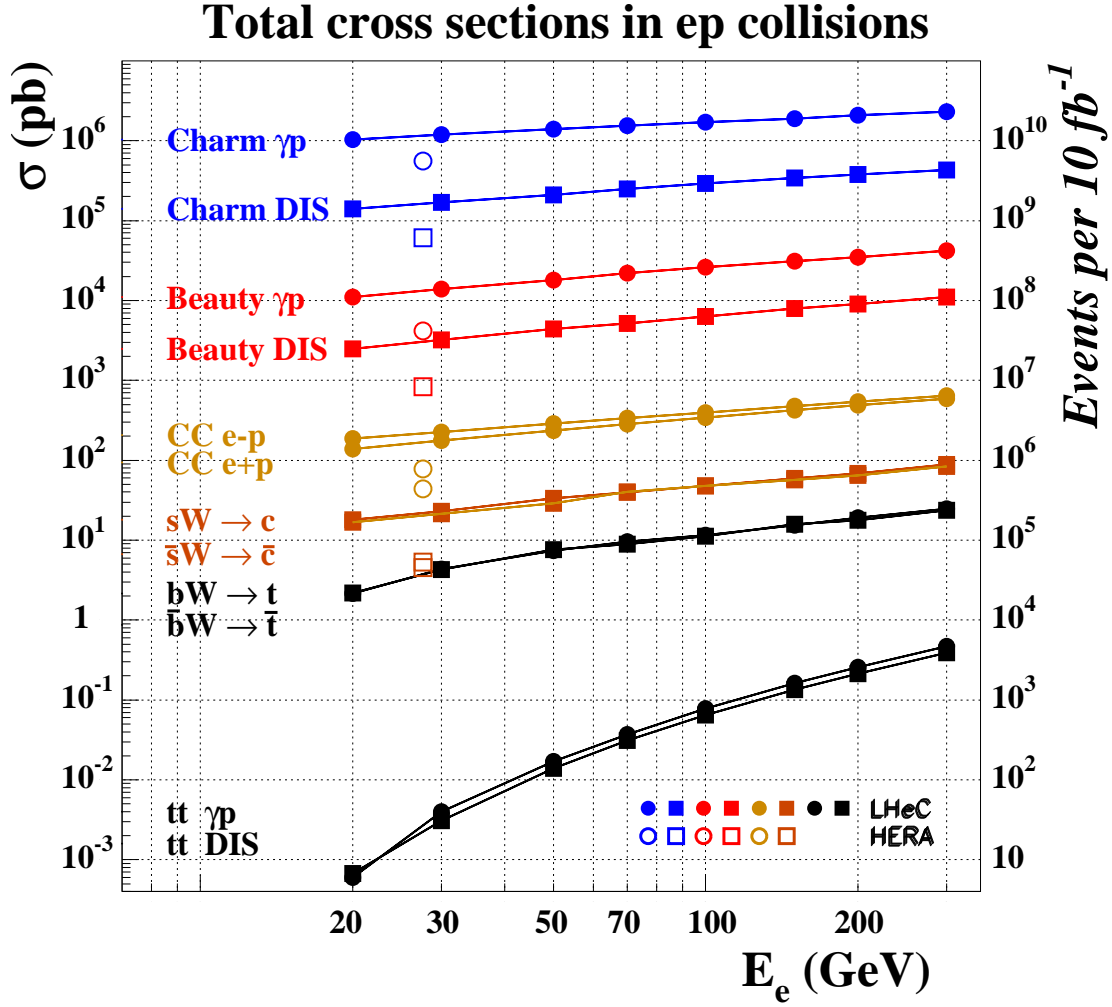


Figure 4.26: Total production cross section predictions for various heavy quark processes at the LHeC (with 7 TeV proton energy), as a function of the lepton beam energy. The following processes are covered: charm and beauty production in photoproduction and DIS, the charged current processes $sW \rightarrow c$ and $bW \rightarrow t$ and top pair production in photoproduction and DIS. The flavour inclusive charged current total cross section is also shown. All predictions are taken from Monte Carlo simulations, the details can be found in Table 4.6. For comparison also the predicted cross sections at HERA (with 920 GeV proton energy) are shown.

1618 two-dimensional bins of x and Q^2 . The LHeC projections shown here were obtained with the
 1619 Monte Carlo programme RAPGAP [115] which generates charm and beauty production with
 1620 massive leading order matrix elements supplemented by parton showers. The proton Parton
 1621 Distribution Function set CTEQ5L [116] were used and the heavy-quark masses were set to
 1622 $m_c = 1.5 \text{ GeV}$ and $m_b = 4.75 \text{ GeV}$, respectively. In general at HERA the RAPGAP predic-

1623 tions are known to provide a reasonable description of the measured charm and beauty DIS
 1624 production data. The RAPGAP data were generated for an LHeC collider scenario with 100
 1625 GeV electrons colliding with 7 TeV protons. The statistical uncertainties have been evaluated
 1626 such that they correspond to an integrated data luminosity of 10 fb^{-1} . All studies were done at
 1627 the parton level, hadronisation effects were not taken into account. Tagging efficiencies of 10%
 1628 for charm quarks and 50% for beauty quarks have been assumed, respectively. These efficiencies
 1629 are about a factor 100 larger compared to the effective efficiencies (including the dilution due to
 1630 background pollution) at HERA which may look surprisingly but is explainable. At HERA the
 1631 charm quarks were tagged either with full charm meson reconstruction or with inclusive sec-
 1632 ondary vertexing of charm hadron decays. The first method suffered from very small branching
 1633 ratios of suitable decay channels. The second technique which was also used for the beauty
 1634 tagging was affected by a large pollution from light quark background events due to the limited
 1635 detector capabilities to separate secondary from primary vertices. At LHeC one can expect a
 1636 much better secondary vertex identification and thus a very strong background reduction. It
 1637 is difficult to predict exactly how much background pollution will remain at LHeC, so for the
 1638 purpose of this simulation study it was completely neglected. Systematic uncertainties were also
 1639 neglected for the studies presented here. From the experiences at HERA the total systematic
 1640 uncertainties for charm and beauty cross sections in the visible ranges can be expected to be
 1641 of similar size as the statistical ones.

1642 Figures 4.27 and 4.28 show the resulting RAPGAP predictions at LHeC for the structure
 1643 functions F_2^{cc} and F_2^{bb} , respectively, compared to recent measurements [118] from HERA. The
 1644 data are shown as a function of x for various Q^2 values. The Q^2 values were chosen such that
 1645 they cover a large fraction of the specific values for which HERA results are available. Some
 1646 further values demonstrate the phase space extensions at LHeC. The projected LHeC data
 1647 are presented as points with error bars which (where visible) indicate the estimated statistical
 1648 uncertainties. For the open points the detector acceptance is assumed to cover the whole polar
 1649 angle range. For the grey shaded and black points events are only accepted if at least one
 1650 charm quark is found with polar angles $\theta_c > 2^0$ and $\theta_c > 10^0$, respectively. The selected results
 1651 from HERA are shown as triangles with error bars indicating the total uncertainty. The HERA
 1652 F_2^{cc} results in Figure 4.27 are those of a recent weighted average [118] of almost all available
 1653 measurements from H1 and ZEUS. In a large part of the covered phase space these results are
 1654 already rather accurate, with precisions between 5% and 10%. The overlaid LHeC projections
 1655 show a vast phase space increase to lower and larger x and also to much higher Q^2 values. In
 1656 the kinematic overlap region the expected statistical precisions at LHeC are typically a factor
 1657 ~ 40 better than at HERA which can be easily explained by the 20 times larger integrated
 1658 luminosity and the ~ 100 times better tagging efficiency. For the smaller x not covered by
 1659 HERA the precision even improves at LHeC due to the growing cross sections driven by the
 1660 rise of the gluon density. The best statistical precisions in the LHeC simulation are observed at
 1661 smallest x values and small Q^2 and reach down to 0.01%. As seen in the simulation (not shown
 1662 here) the LHeC F_2^{cc} data provide access to the gluon density in the BGF process down
 1663 to proton momentum fractions $x_g \sim 10^{-5}$. The LHeC data can also provide an substantial
 1664 extension to higher x compared to HERA where the measurements reached x values of a few
 1665 percent. As evident from the simulated points with different polar angle cuts this necessitates
 1666 an excellent forward tagging of charm quarks. In any case values of $x > 0.1$ should be accessible
 1667 in the medium and large Q^2 domain.

1668 Figure 4.28 show the RAPGAP predictions at LHeC for F_2^{bb} . Also shown are the results
 1669 from the H1 analysis [119] based on inclusive secondary vertex tagging. Clearly these results

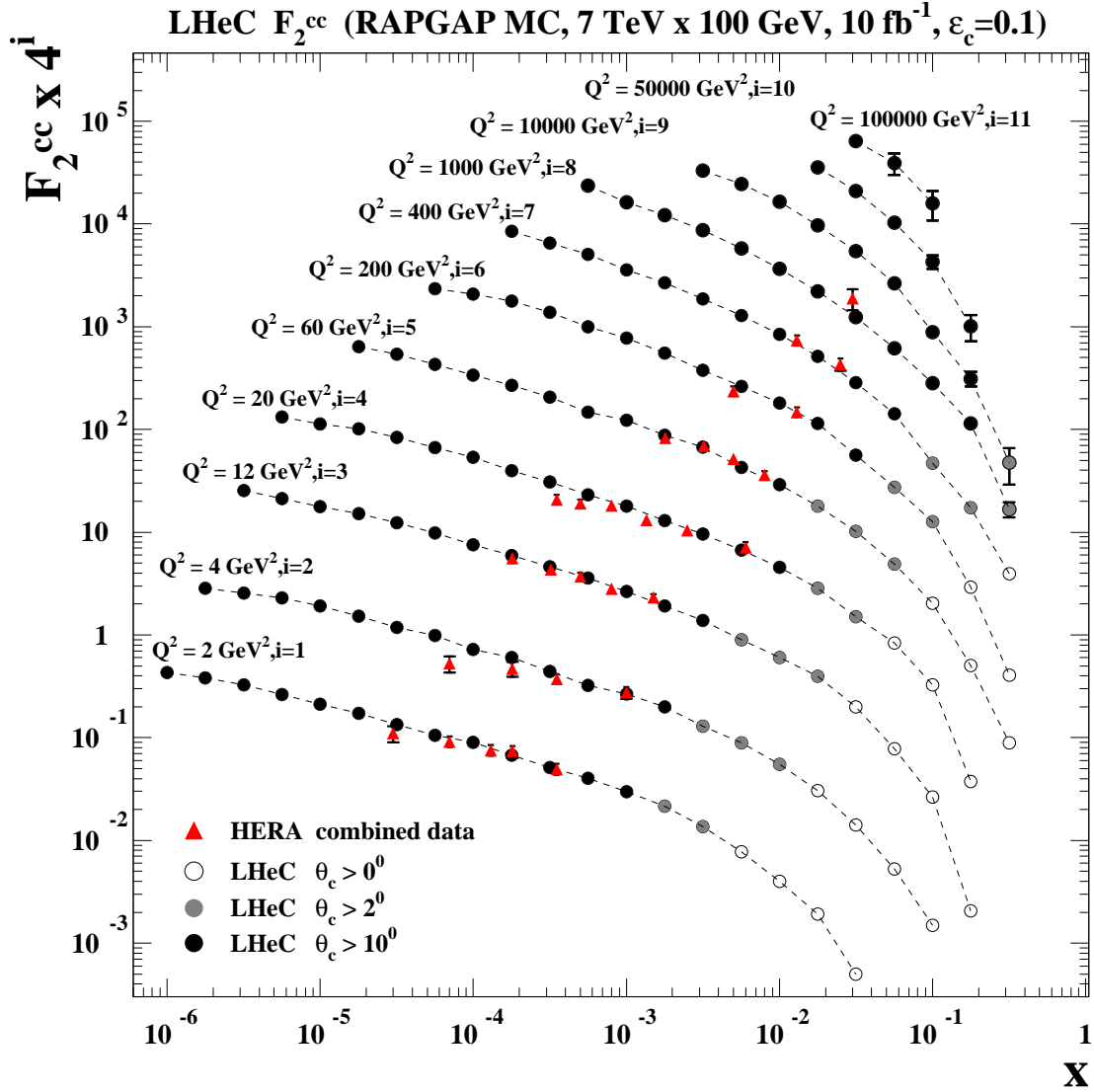


Figure 4.27: F_2^{cc} projections for LHeC compared to HERA data [118], shown as a function of x for various Q^2 values. The expected LHeC results obtained with the RAPGAP MC simulation are shown as points with error bars representing the statistical uncertainties. The dashed lines are interpolating curves between the points. For the open points the detector acceptance is assumed to cover the whole polar angle range. For the grey shaded and black points events are only accepted if at least one charm quark is found with polar angles $\theta_c > 2^\circ$ and $\theta_c > 10^\circ$, respectively. For further details of the LHeC simulation see the main text. The combined HERA results from H1 and ZEUS are shown as triangles with error bars representing their total uncertainty.

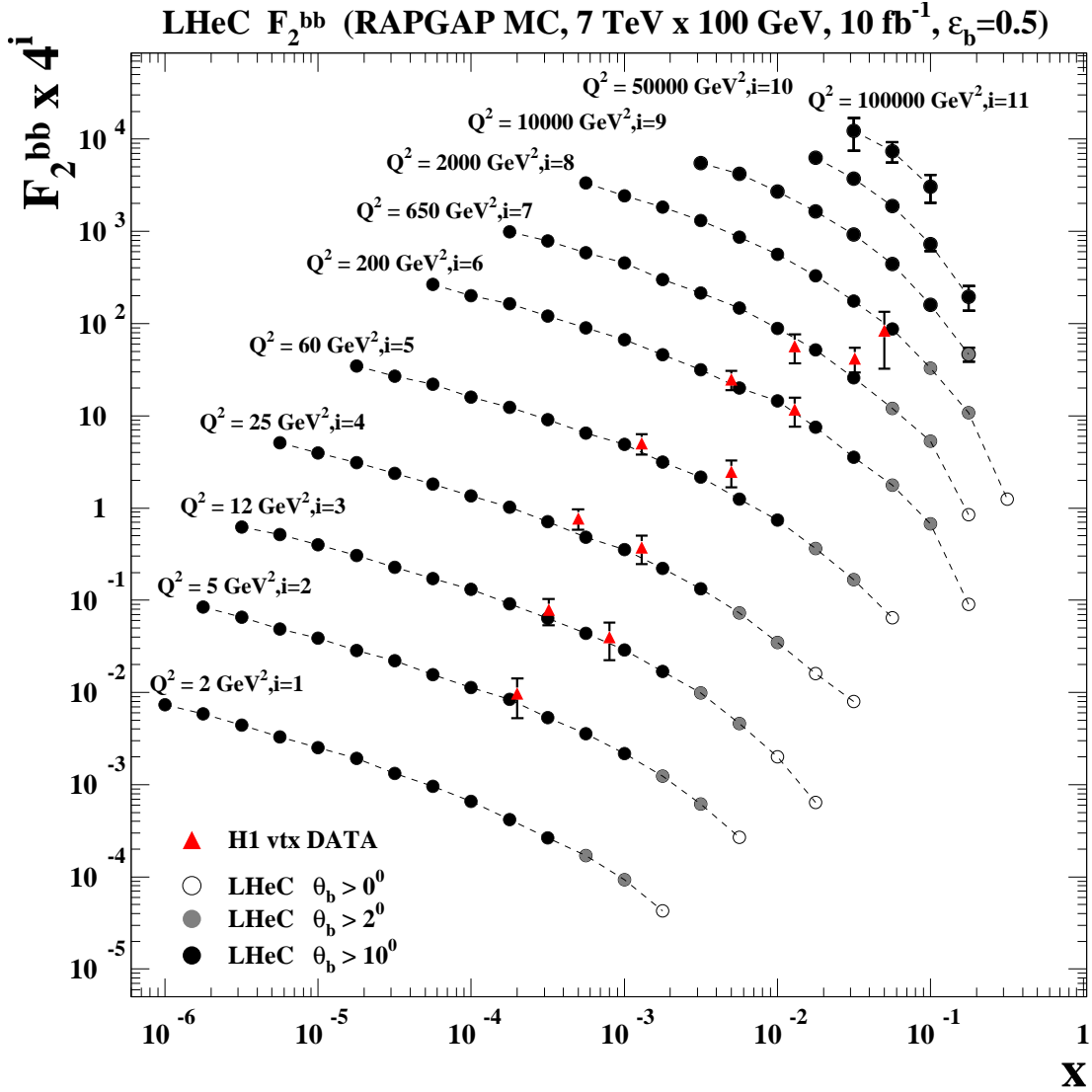


Figure 4.28: F_2^{bb} projections for LHeC compared to HERA data [119] from H1, shown as a function of x for various Q^2 values. The expected LHeC results obtained with the RAPGAP MC simulation are shown as points with error bars representing the statistical uncertainties. The dashed lines are interpolating curves between the points. For the open points the detector acceptance is assumed to cover the whole polar angle range. For the grey shaded and black points events are only accepted if at least one beauty quark is found with polar angles $\theta_b > 2^\circ$ and $\theta_b > 10^\circ$, respectively. For further details of the LHeC simulation see the main text. The HERA results from H1 are shown as triangles with error bars representing their total uncertainty.

1670 and similar ones (not shown) from ZEUS are not very precise, the typical total uncertainties are
1671 20-50%. Again, the LHeC F_2^{bb} projections demonstrate a vast phase space increase, similar as
1672 for charm. The best statistical precisions obtained at LHeC for F_2^{bb} are seen in the simulation
1673 towards low x and small and medium Q^2 and reach down to 1 permille. The measurements at
1674 LHeC will enable a precision mapping of beauty production from kinematic threshold to large
1675 Q^2 . In the context of the generalised variable flavour number schemes (GM-VFNS) this will
1676 allow to study in detail the onset of the beauty quark density in the proton and to compare
1677 it to the charm case. As mentioned in section 4.7.1, for high $Q^2 \gg m_b^2$ the F_2^{bb} results can be
1678 directly interpreted in terms of an effective beauty density in the proton. The measurement of
1679 this density is of large interest because it can be used to predict beauty quark initiated processes
1680 at the LHC. As visible in the figure, HERA covers only a small phase space in this region and
1681 with moderate precision. However, at LHeC the prospects for measuring F_2^{bb} in this region are
1682 very good.

1683 **Intrinsic Heavy Flavour**

1684 It is conventional to assume that the charm and bottom quarks in the proton structure function
1685 only arise from gluon splitting $g \rightarrow Q\bar{Q}$. In fact, the proton light-front wavefunction contains *ab*
1686 *initio* intrinsic heavy quark Fock state components such as $|uudc\bar{c}\rangle$ [18,110–112]. The intrinsic
1687 heavy quarks carry most of the proton’s momentum since this minimizes the off-shellness of
1688 the state. The heavy quark pair $Q\bar{Q}$ in the intrinsic Fock state is primarily a color-octet, and
1689 the ratio of intrinsic charm to intrinsic bottom scales as $m_c^2/m_b^2 \simeq 1/10$, as can easily
1690 be seen from the operator product expansion in non-Abelian QCD [110,112]. Intrinsic charm
1691 and bottom explain the origin of high x_F open-charm and open-bottom hadron production, as
1692 well as the single and double J/ψ hadroproduction cross sections observed at high x_F . The
1693 factorization-breaking nuclear $A^\alpha(x_F)$ dependence of hadronic J/ψ production cross sections
1694 is also explained.

1695 As emphasized recently [120], there are strong indications that the structure functions used
1696 to model charm and bottom quarks in the proton at large x have been underestimated, since they
1697 ignore intrinsic heavy quark fluctuations of hadron wavefunctions. Furthermore, the neglect of
1698 the intrinsic-heavy quark component in the proton structure function will lead to an incorrect
1699 assessment of the gluon distribution at larger x if it is assumed that sea quarks always arise
1700 from gluon splitting. The anomalous growth of the $p\bar{p} \rightarrow \gamma cX$ inclusive cross section observed
1701 by the D0 collaboration [121] at the Tevatron indicates that the charm distribution has been
1702 underestimated at $x > 0.1$.

1703 In [122] a novel mechanism for inclusive and diffractive Higgs production $pp \rightarrow pHp$ is
1704 proposed, in which the Higgs boson carries a significant fraction of the projectile proton mo-
1705 mentum. The production mechanism is based on the subprocess $(Q\bar{Q})g \rightarrow H$ where the $Q\bar{Q}$ in
1706 the $|uudQ\bar{Q}\rangle$ intrinsic heavy quark Fock state of the colliding proton has approximately 80%
1707 of the projectile protons momentum. A similar mechanism could produce the Higgs at large
1708 $x_F \sim 0.8$ in $\gamma p \rightarrow HX$ at the LHeC based on the mechanism $\gamma(Q\bar{Q}) \rightarrow H$ since the heavy
1709 quarks typically each carry light-cone momentum fractions $x \sim 0.4$ when they arise from the
1710 intrinsic heavy quark Fock states $|uudQ\bar{Q}\rangle$ of the proton.

1711 The LHeC could establish the phenomenology of the charm and bottom structure functions
1712 at larger x . In addition to DIS measurements, one can test the charm (and bottom) distributions
1713 at the LHeC by measuring reactions such as $\gamma p \rightarrow cX$ where the charm jet is produced at high
1714 p_T in the reaction $\gamma c \rightarrow cg$.

1715 In order to access the charm and bottom distributions towards larger Bjorken x , it is required
 1716 to tag heavy flavour production in the forward direction. As this is difficult in the asymmetric
 1717 electron-proton beam energy configuration such a measurement can favourably be done with
 1718 a reduced proton beam energy. Approximately, as may be derived from Eq. 11.8, the small
 1719 hadronic scattering angle, θ_h , is obtained from the relation, $\theta_h^2 \simeq 2\sqrt{Q^2}/E_p x$. Therefore a
 1720 reduction by a factor of 7 of the proton beam energy E_p enhances x by 7 at fixed Q^2 and θ_h .
 1721 One also notices that large x is reached at fixed θ_h and E_p only at high Q^2 . The attempt to access
 1722 maximum x thus requires to find an optimum of high luminosity, to reach high Q^2 , and low
 1723 proton beam energy, to access large x . Fig. 4.29 shows a simulated measurement of the charm
 1724 structure function for $E_p = 1$ TeV and a luminosity of 1 fb^{-1} . The two curves illustrate the
 1725 difference between CTEQ66 PDF sets with and without an intrinsic charm component, based
 1726 on [120]. The actual amount of intrinsic charm may be larger than in the CTEQ attempt,
 1727 it may also be smaller. One so finds that a reliable detection of an intrinsic heavy charm
 1728 component at the LHeC may be possible, but will be a challenge for forward charm detection
 1729 and requires high luminosity. The result yet may be rewarding as it would have quite some
 1730 theoretical consequences as sketched above. It would be obtained in a region of high enough
 1731 Q^2 to be able to safely neglect any higher twist effects which may mimic such an observation
 1732 at low energy experiments.

1733 D^* meson photoproduction study

1734 A study is presented of D^* meson photoproduction at LHeC compared to HERA. It is based
 1735 on NLO predictions in the so-called general-mass variable-flavour-number scheme (GM-VFNS)
 1736 [107,108] for 1-particle inclusive heavy-meson production. Both direct and resolved photon con-
 1737 tributions are taken into account. The cross section for direct photoproduction is a convolution
 1738 of the proton PDFs, the cross section for the hard scattering process and the fragmentation
 1739 functions FF for the transition of a parton to the observed heavy meson. For the resolved
 1740 contribution, an additional convolution with the photon PDFs has to be performed. For the
 1741 photoproduction predictions at the ep -colliders HERA and LHeC, the calculated photon proton
 1742 cross sections are convoluted with the photon flux using the Weizsaecker-Williams approxima-
 1743 tion.

1744 In the GM-VFNS approach the large logarithms $\ln(p_T^2/m^2)$, which appear due to the
 1745 collinear mass singularities in the initial and final state, are factorized into the PDFs and
 1746 the FFs and summed by the well known DGLAP evolution equations. The factorization is per-
 1747 formed following the usual $\overline{\text{MS}}$ prescription which guarantees the universality of both PDFs and
 1748 FFs. At the same time, mass-dependent power corrections are retained in the hard-scattering
 1749 cross sections, as in the FFNS. For the photon PDF the parametrization of Ref. [123] with
 1750 the standard set of parameter values is used and for the proton PDF the parametrization
 1751 CTEQ6.5 [124] of the CTEQ group. For the FFs the set Belle/CLEO-GM of Ref. [125] is
 1752 chosen. Various combinations of beam energies are studied. To compare with the situation at
 1753 HERA, as a reference, the values $E^p = 920$ GeV and $E^e = 27.5$ GeV for proton and electron
 1754 energies, respectively, are also included. For the LHeC the proton energy is taken to be always
 1755 $E^p = 7$ TeV and the options $E^e = 50, 100$ and 150 GeV are considered. The exchanged pho-
 1756 tons are restricted to inelasticities y in the range $0.1 < y < 0.9$. The transverse momentum p_T
 1757 and the rapidity η of the D^* -meson are varied in the kinematic ranges $5 < p_T < 20$ GeV or
 1758 $20 < p_T < 100$ and $|\eta| < 2.5$. Numerical results are shown in Fig. 4.30 for the differential cross
 1759 section $d\sigma/dp_T$ integrated over the rapidity $|\eta| \leq 2.5$ and in Fig. 4.31 for $d\sigma/d\eta$, integrated

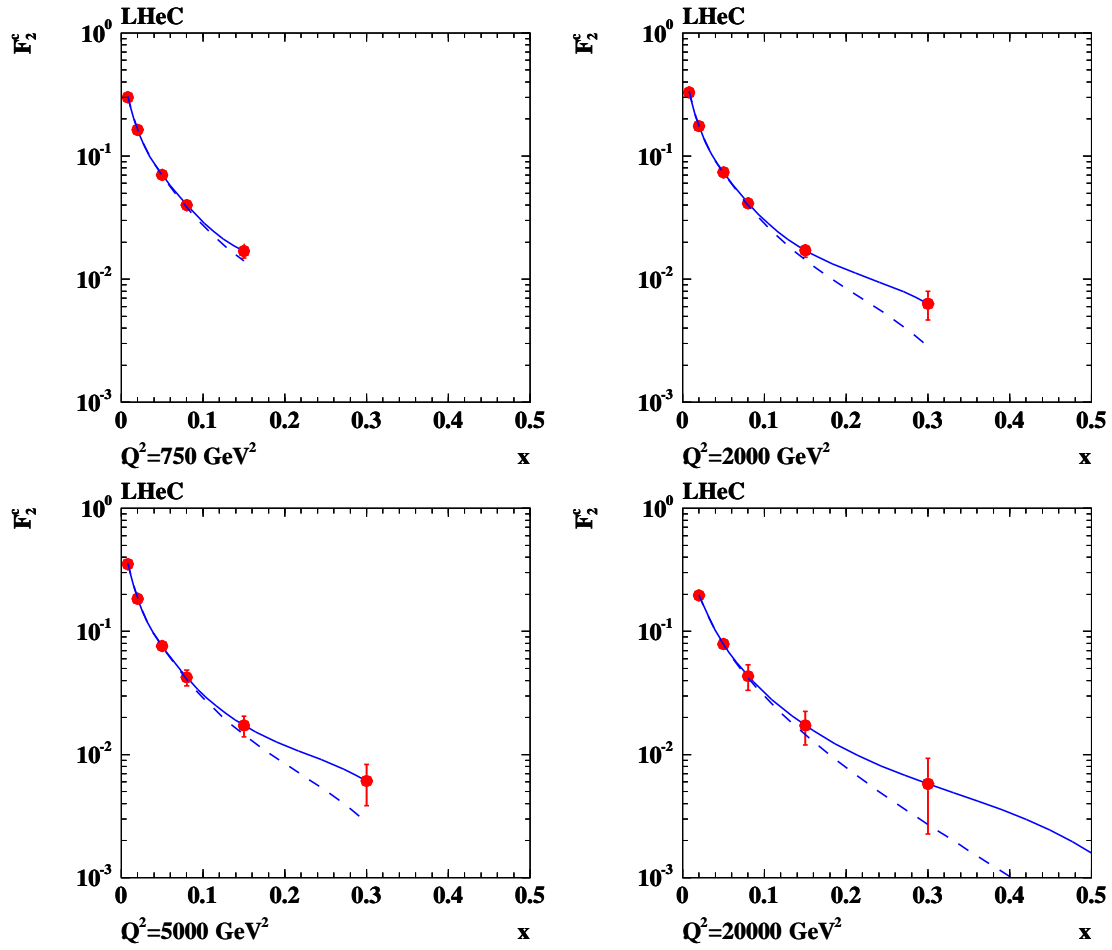


Figure 4.29: Simulation of measurement of the charm structure function at large x , see text. The errors are statistical, taking tagging and background efficiencies into account. The tagging efficiency for charm quarks was assumed to be 10% and the amount of background was estimated to be $0.01 \cdot N_{ev}$, where N_{ev} refers to the total number of expected NC events in the respective (Q^2, x) bin. Solide line: CTEQ66c predictions, including an intrinsic charm component, dashed line: ordinary CTEQ6m.

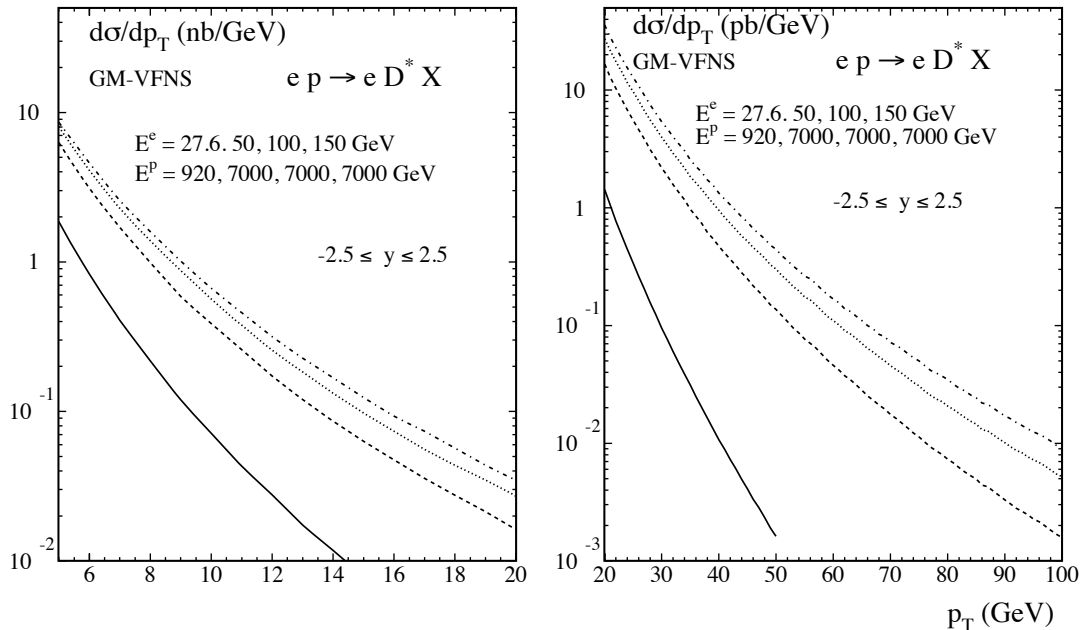


Figure 4.30: The p_T -differential cross section for the production of D^* mesons at LHeC for different beam energies integrated over rapidities $|\eta| \leq 2.5$, for the low- p_T range $5 \text{ GeV} \leq p_T \leq 20 \text{ GeV}$ (left) and for the high- p_T range $20 \text{ GeV} \leq p_T \leq 50 \text{ GeV}$ (right). The curves from bottom to top correspond to the combinations of beam energies as indicated in the figure.

1760 over the p_T -ranges $5 \leq p_T \leq 20 \text{ GeV}$ and $20 \leq p_T \leq 100 \text{ GeV}$.

1761 The higher centre-of-mass energies available at the LHeC lead to a considerable increase
 1762 of the cross sections as compared to HERA. Obviously one can expect an increase in the
 1763 precision of corresponding measurements and much higher values of p_T , as well as higher values
 1764 of the rapidity η , will be accessible. Since theoretical predictions also become more reliable at
 1765 higher p_T , measurements of heavy quark production constitute a promising testing ground for
 1766 perturbative QCD. One may expect that the experimental information will contribute to an
 1767 improved determination of the (extrinsic and intrinsic) charm content of the proton and the
 1768 charm fragmentation functions.

1769 4.8 High p_t jets

1770 4.8.1 Jets in ep

1771 The study of the jet final states in lepton-proton collisions allows the determination of aspects of
 1772 the nucleon structure which are not accessible in inclusive scattering. Moreover, jet production
 1773 allows for probing predictions of QCD to a high accuracy. Depending on the virtuality of the
 1774 exchanged photon, one distinguishes processes in photoproduction (quasi-real photon) and deep
 1775 inelastic scattering.

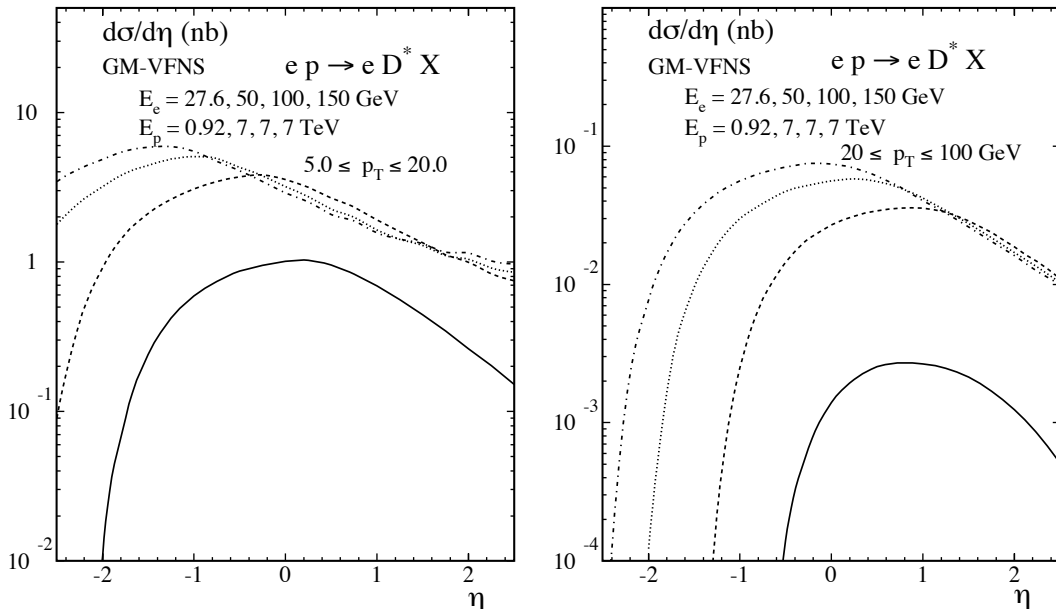


Figure 4.31: Rapidity distribution of the cross section for the production of D^* mesons at LHeC for different beam energies integrated over the low- p_T range $5 \text{ GeV} \leq p_T \leq 20 \text{ GeV}$ (left) and the high- p_T range $20 \text{ GeV} \leq p_T \leq 50 \text{ GeV}$ (right). The curves from bottom to top correspond to the combinations of beam energies as indicated in the figure.

1776 The photoproduction cross section for di-jet final states can be studied in different kinematical regions, thereby covering a wide spectrum of physical phenomena, and probing the structure of the proton and the photon. Two-jet production in deep inelastic scattering is a particularly sensitive probe of the gluon distribution in the proton and of the strong coupling constant α_s . 1777 1778 1779 1780 Both processes allow the study of potentially large enhancement effects in di-jet and multi-jet production. 1781

1782 Jet production in photoproduction proceeds via the direct processes, in which the quasi-real photon interacts as a point-like particle with the partons from the proton, and the resolved processes, in which the quasi-real photon interacts with the partons from the proton via its partonic constituents. The parton distributions in the quasi-real photon are constrained mostly from the study of processes at e^+e^- colliders, and are less well-determined than their counterparts in the proton. In both the direct and the resolved processes, there are two jets in the final state at lowest-order QCD. The jet production cross section is given in QCD by the convolution of the flux of photons in the electron (usually estimated via the Weizacker-Williams approximation), the parton densities in the photon, the parton densities in the proton and the partonic cross section (calculable in pQCD). Therefore, the measurements of jet cross sections in photoproduction provide tests of perturbative QCD and the structure of the photon and the proton. 1783 1784 1785 1786 1787 1788 1789 1790 1791 1792 1793

1794 Owing to the large size of the cross section, photoproduction of di-jets can be used for pre-

1795 cision physics in QCD. A measurement at LHeC could improve upon previous HERA results
 1796 and enter into a much larger kinematical region. In measurements made by the ZEUS collab-
 1797 oration, the available photon-proton centre-of-mass energy ranged from 142 to 293 GeV, and
 1798 jets of a transverse energy of up to 90 GeV could be observed. By comparing the measured
 1799 cross section with the theoretical prediction in NLO pQCD, a value of $\alpha_s(M_Z)$ was extracted
 1800 with a total uncertainty of $\pm 3\%$ and the running of α_s was tested over a wide range of E_t^{jet} in a
 1801 single measurement. The limiting factors in this measurement were the theoretical uncertainty
 1802 inherent to the NLO prediction (which could be improved by computing NNLO corrections
 1803 to jet photoproduction) and the experimental systematic uncertainty in the detector energy
 calibration.

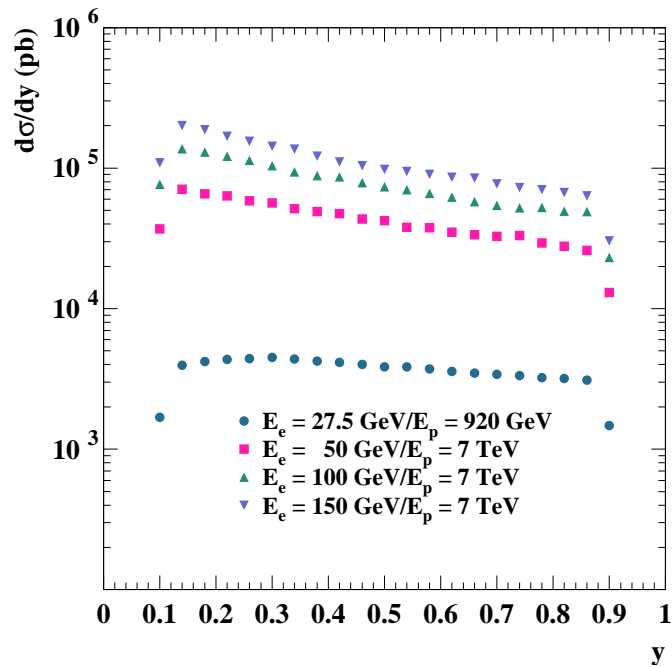


Figure 4.32: PYTHIA predictions for photoproduction cross section at HERA and for three LHeC scenarios.

1804
 1805 Another motivation for making new photoproduction experiments is to improve the knowl-
 1806 edge of the parton content of the photon. At present, most information on the photon structure
 1807 is inferred from the collision of quasi-real photons with electrons at e^+e^- colliders, resulting in
 1808 a decent determination of the total (charge weighted) quark content of the quasi-real photon.
 1809 Its gluonic content, and the quark flavour decomposition are on the other hand only loosely
 1810 constrained. Improvements to the photon structure are of crucial importance to physics studies
 1811 at a future linear e^+e^- collider like the ILC or CLIC. Such a collider, operating far above the Z -
 1812 boson resonance, will face a huge background from photon-photon collisions. This background
 1813 can be suppressed only to a certain extent by kinematical cuts. Consequently, accurate predic-
 1814 tions of it (which require an improved knowledge of the photon's parton content) are mandatory
 1815 for the reliable interpretation of hadronic final states at the ILC or CLIC. Several parametriza-

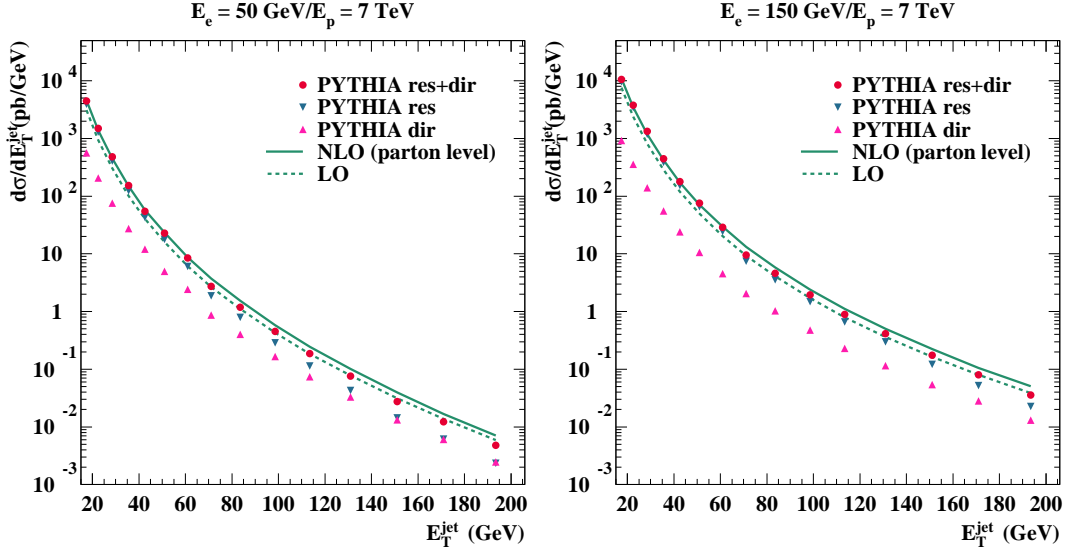


Figure 4.33: Parton level predictions for the inclusive transverse energy distribution in photoproduction.

1816 tions of the parton distributions in the photon are available. They differ especially in the gluon
 1817 content of the photon. For the studies presented here, the GRV-HO parametrization [126] is
 1818 used as default.

1819 The photoproduction studies performed at LHeC were done for three different electron
 1820 energy scenarios: $E_e=50, 100$ and 150 GeV. In all cases, the proton energy was set to 7 TeV.
 1821 PYTHIA MC samples of resolved and direct processes were generated for these three scenarios.
 1822 Jets were searched using the k_t -cluster algorithm in the kinematic region of $0.1 < y < 0.9$ and
 1823 $Q^2 < 1$ GeV². Inclusive jet cross sections were done for jets of $E_t^{\text{jet}} > 15$ GeV and $3 < \eta^{\text{jet}} < 3$.
 1824 Figure 4.32 shows the PYTHIA MC cross sections as functions of y for the three scenarios
 1825 plus the corresponding cross section for the HERA regime. It can be seen that the LHeC cross
 1826 sections are one to two orders of magnitude larger than the cross section at HERA.

1827 The full study was complemented with fixed-order QCD calculations at order α_s and α_s^2
 1828 using the program by Klasen et al. [127] with the CTEQ6.1 sets for the proton PDFs, GRV-HO
 1829 sets for the photon PDFs, $\alpha_s(M_Z) = 0.119$ and the renormalisation and factorisation scales
 1830 were set to the transverse energy of each jet.

1831 Figure 4.33 shows the inclusive jet cross sections at parton level as functions of E_t^{jet} for the
 1832 three energy scenarios for the PYTHIA res+dir (red dots), PYTHIA resolved (blue triangles)
 1833 and PYTHIA direct (pink triangles) together with the predictions from the NLO (solid curves)
 1834 and LO (dashed curves) QCD calculations. The calculations predict a sizeable rate for Etjet
 1835 of at least up to 200 GeV. Resolved processes dominate at low E_t^{jet} , but the direct processes
 1836 become increasingly more important as E_t^{jet} increases. The PYTHIA cross sections (which
 1837 have been normalised to the NLO integrated cross section) agree well in shape with the NLO
 1838 calculations. Investigating the η^{jet} distribution, we find that resolved processes dominate in the
 1839 forward region, while direct processes produce more central jets.

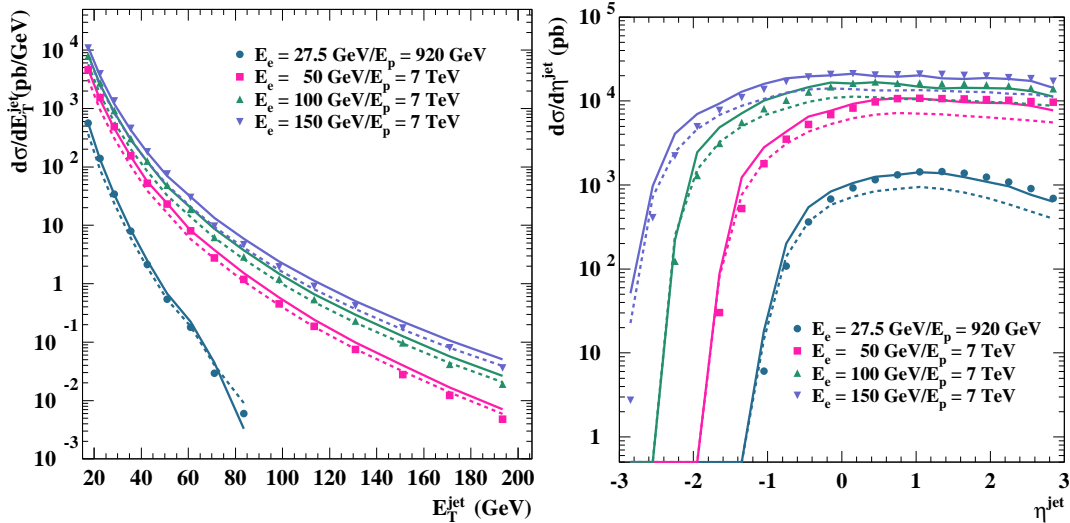


Figure 4.34: Dijet distributions in photoproduction as function of the jet transverse energy (left) and of the jet rapidity (right) for different LHeC energies compared to the HERA kinematic range.

1840 Figure 4.34 show the inclusive jet cross sections at parton level as functions of E_T^{jet} (on the
1841 left) and η^{jet} (on the right) for the PYTHIA resolved+direct (symbols) and the predictions
1842 from the NLO (solid curves) and LO (dashed curves) QCD calculations together for the three
1843 energy scenarios. For comparison, the calculations for the HERA regime are also included. It
1844 is seen that the cross sections at fixed E_T^{jet} increase and that the jets tend to go more backward
1845 as the collision energy increases. The much larger photon-proton centre-of-mass energies that
1846 could be available at LHeC provide a much wider reach in E_T^{jet} and η^{jet} compared to HERA.

1847 Hadronisation corrections for the cross sections shown were investigated. The corrections
1848 are predicted to be quite small, below +5% for the chosen scenarios. Since the hadronisation
1849 corrections are very small, the features observed at parton level remain unchanged.

1850 Inclusive-jet and dijet measurements in deep-inelastic scattering (DIS) have since long been
1851 a tool to test concepts and predictions of perturbative QCD. Especially at HERA, jets in DIS
1852 have been thoroughly studied, and the results have provided deep insights, giving for example
1853 precise values for the strong coupling constant, α_s and providing constraints for the proton
1854 PDFs.

1855 An especially interesting region for such studies has been the regime of large (for HERA) Q^2
1856 values of, for example, $Q^2 > 125 \text{ GeV}^2$. In this regime, the theoretical uncertainties, especially
1857 those due to the unknown effects of missing higher orders in the perturbative expansion, are
1858 found to be small. Recently, both the H1 and ZEUS collaborations have published measure-
1859 ments of inclusive-jet and dijet events in this kinematic regime.

1860 An extension of such measurements to the LHeC is interesting for two reasons: First, the
1861 provided high luminosity will allow measurements in already explored kinematic regions with
1862 still increased experimental precision. Second, the extension in centre-of-mass energy, \sqrt{s} , and
1863 thus in boson virtuality, Q^2 , and in jet transverse energy, $E_{T,jet}$, will potentially allow to study

1864 pQCD at even higher scales, extending the scale reach for measurements of the strong coupling
 1865 or the precision of the proton PDFs at large values of x .

1866 To explore the potential of such a measurement, we investigated DIS jet production for
 1867 the following LHeC scenario: proton beam energy 7 TeV, electron beam energy 70 GeV and
 1868 integrated luminosity 10 fb^{-1} . The study concentrates on the phase space of high boson vir-
 1869 tualities Q^2 , with event selection cuts $100 < Q^2 < 500\,000 \text{ GeV}^2$ and $0.1 < y < 0.7$, where
 1870 y is the inelasticity of the event. Jets are reconstructed using the k_T clustering algorithm in
 1871 the longitudinally invariant inclusive mode in the Breit reference frame. Jets were selected by
 1872 requiring: a jet pseudorapidity in the laboratory of $-2 < \eta_{lab} < 3$, a jet transverse energy in the
 1873 Breit frame of $E_{T,jet}^{Breit} > 20 \text{ GeV}$ for the inclusive-jet measurement and jet transverse energies
 1874 in the Breit frame of $25(20) \text{ GeV}$ for the leading and the second-hardest jet in the case of the
 1875 dijet selection.

1876 For inclusive-jet production we study cross sections in the indicated kinematic regime as
 1877 functions of Q^2 , x_{Bj} , $E_{T,jet}^{Breit}$ and η_{jet}^{lab} , the jet pseudorapidity in the laboratory frame. For dijet
 1878 production, studies are presented as functions of Q^2 , the logarithm of the proton momentum
 1879 fraction ξ , $\log_{10} \xi$, the invariant dijet mass M_{jj} , the average transverse energy of the two jets
 1880 in the Breit frame, $\overline{E_{T,jet}^{Breit}}$, and of half of the absolute difference of the two jet pseudorapidities
 1881 in the laboratory frame, η' .

1882 For the binning of the observables shown here, the statistical uncertainties for the indicated
 1883 LHeC integrated luminosity can mostly be neglected, even at the highest scales. The systematic
 1884 uncertainties were assumed to be dominated by the uncertainty on the jet energy scale which
 1885 was assumed to be known to 1% or 3% (both scenarios are indicated with different colours in
 1886 the following plots), leading to typical effects on the jet cross sections between 1 and 15%. A
 1887 further relevant uncertainty is the acceptance correction that is applied to the data which was
 1888 assumed to be 3% for all observables.

1889 The theoretical calculations were performed with the DISENT program [128] using the
 1890 CTEQ6.1 proton PDFs [114,129]. The central default squared renormalisation and factorisation
 1891 scales were set to Q^2 . The theory calculations for the LHeC scenario were corrected for the
 1892 effects of hadronisation and Z^0 exchange using Monte Carlo data samples simulated with the
 1893 LEPTO program [117].

1894 Theoretical uncertainties were assessed by varying the renormalization scale up and down
 1895 by a factor 2 (to estimate the potential effect of contributions beyond NLO QCD), by using
 1896 the 40 error sets of the CTEQ6.1 parton distribution functions, and by varying α_s using the
 1897 CTEQ6AB PDF [130]. The dominant theory uncertainty turned out to be due to the scale
 1898 variations, resulting in effects of a few to up to 20% or more, for example for low values of Q^2
 1899 or, for the case of the dijet measurement, for low values of the invariant dijet mass, M_{jj} , or the
 1900 logarithm of momentum fraction carried into the hard scattering, $\log_{10} \xi$.

1901 Note that for the inclusive-jet results also the predictions for a HERA scenario with almost
 1902 the same selection are shown in order to indicate the increased reach of the LHeC with respect
 1903 to HERA. The only change is a reduction in centre-of-mass energy to 318 GeV and a reduced
 1904 Q^2 reach, $125 < Q^2 < 45\,000 \text{ GeV}^2$. The HERA predictions shown were also corrected for
 1905 hadronisation effects and the effects of Z^0 exchange.

1906 Figure 4.35 shows the inclusive jet cross section as function of Q^2 and of the jet transverse
 1907 energy in the Breit frame, while Figure 4.36 shows the dijet cross section as function of Q^2
 1908 and of $\xi = x_{Bj}(1 + M_{jj}^2/Q^2)$. The top parts of the figures show the predicted cross sections together
 1909 with the expected statistical and (uncorrelated) experimental systematic uncertainties as errors

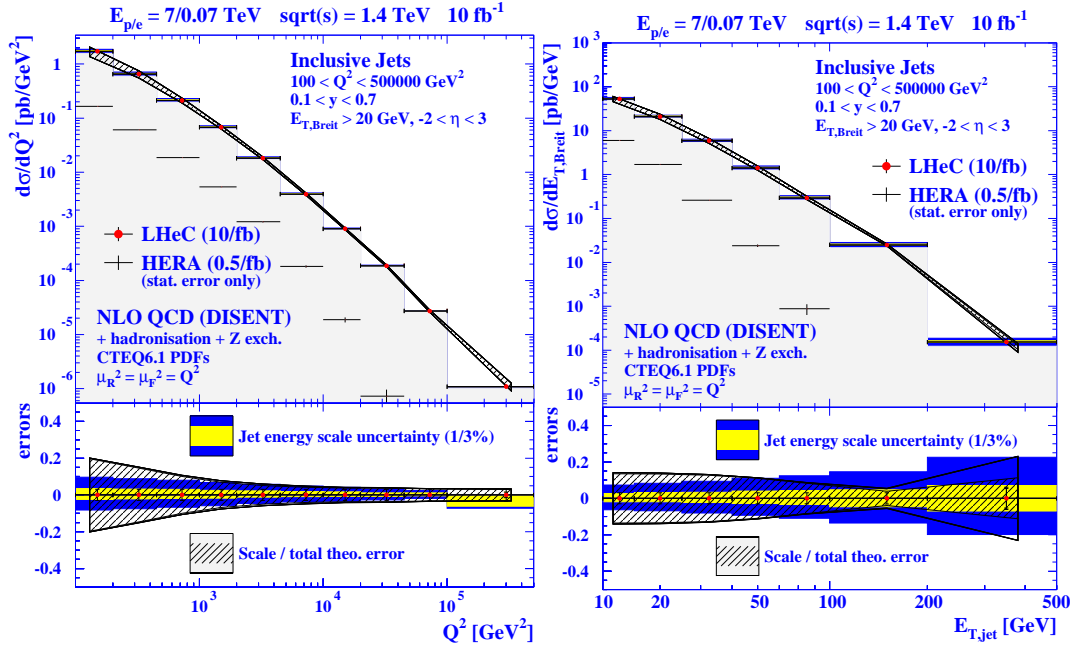


Figure 4.35: Predicted LHeC results for inclusive jet production as function of Q^2 and of E_T in the Breit frame. Predictions for HERA results are also shown.

1910 bars. The correlated jet energy scale uncertainty is indicated as a coloured band; the inner,
 1911 yellow band assumes an uncertainty of 1%, the outer, blue band one of 3%. Also shown as a
 1912 thin hashed area are the theoretical uncertainties; the width of the band indicates the size of
 1913 the combined theoretical uncertainty. In case of inclusive-jet production, also the predictions
 1914 for HERA are indicated as a thin line.

1915 The bottom parts of the figures show the relative uncertainties due to the jet energy scale
 1916 (yellow band for 1%, blue band for 3%), the statistical and uncorrelated experimental system-
 1917 atic uncertainties as inner / outer error bars, and the combined theoretical uncertainties as
 1918 hashed band. The inner part of this band indicates the uncertainty due to the variation of the
 1919 renormalisation scale.

1920 The inclusive-jet cross section as function of Q^2 shows a typical picture: In most region of
 1921 the phase space, the uncertainties are dominated by the theory uncertainties, and here mainly
 1922 by the renormalisation scale uncertainty. The typical size of experimental uncertainties is of
 1923 the order of 10%, with larger values in regions with low relevant scales — i.e. low invariant dijet
 1924 masses, low jet transverse energies or low Q^2 values. The theoretical uncertainties are typically
 1925 between 5 and 20%, with partially strong variations over the typical range of the observable in
 1926 question.

1927 A comparison with the HERA predictions for inclusive-jet production shows that the LHeC
 1928 cross sections is typically larger by 1 to 3 orders of magnitude. The dijet final state allows
 1929 for a full reconstruction of the partonic kinematics, and can thus be used to probe the parton
 1930 distribution functions in Q^2 and ξ . It can be seen that a measurement at LHeC covers a

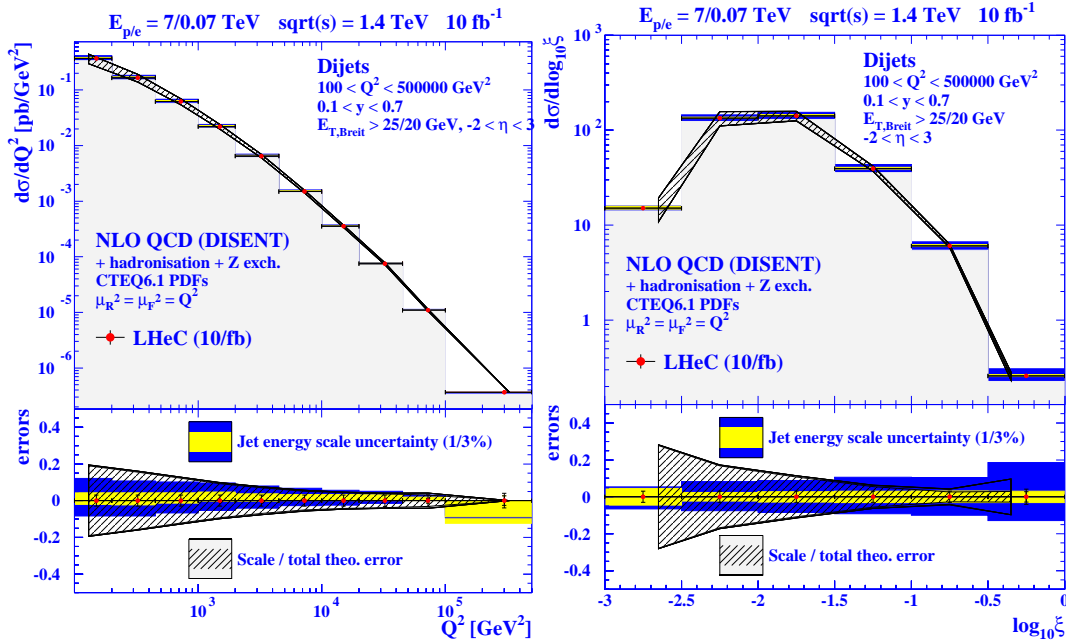


Figure 4.36: Predicted LHeC results for dijet production as function of Q^2 and of ξ .

1931 large kinematical range ranging down to $\xi \approx 10^{-3}$ and up to $Q^2 = 10^5$ GeV². Potentially
 1932 limiting factors in an extraction of parton distribution functions are especially the jet energy
 1933 scale uncertainty on the experimental side and missing higher order (NNLO) corrections on
 1934 the theory side. The jet energy scale uncertainty can be addressed by the detector design and
 1935 by the experimental setup of the measurement. NNLO corrections to dijet production in deep
 1936 inelastic scattering are already very much demanded by the precision of the HERA data, their
 1937 calculation is currently in progress [131, 132].

1938 In summary, jet final states in photoproduction and deep inelastic scattering at the LHeC
 1939 promise a wide spectrum of new results on the partonic structure of the photon and the proton.
 1940 They allow for precision tests of QCD by independent determinations of the strong coupling
 1941 constant over a kinematical range typically one to two orders of magnitude larger than what was
 1942 accessible at HERA. The resulting parton distributions will have a direct impact for precision
 1943 predictions at the LHC and a future linear collider.

1944 4.8.2 Jets in γA

1945 For photoproduction in eA collisions, jets provide an abundant yield of high-energy probes of
 1946 the nuclear medium. The expected cross sections have been computed using the calculations
 1947 in [133, 134], for an electron beam of 50 GeV colliding with the LHC beams. For the nuclear
 1948 case the same integrated luminosity (2 fb^{-1}) was assumed per nucleon as for ep . Only jets
 1949 with $E_{Tjet} > 20$ GeV are considered, and for the distribution in E_{Tjet} the pseudorapidity
 1950 acceptance is $|\eta_{jet}| < 3.1$, corresponding to $5^\circ < \theta_{jet} < 175^\circ$ in polar angle. The simulations

1951 use the Weizsäcker-Williams photon flux from the electron with the standard option in [133,
1952 134]. The chosen photon, proton and nuclear modified PDFs are taken from GRV-HO [135],
1953 CTEQ6.1M [129] and EPS09 [136], respectively - see Subsec. 6.1.4 for explanations on the
1954 nuclear modifications of PDFs. The renormalization and factorization scales are taken to be
1955 $\mu_R = \mu_F = \sum_{jets} E_{Tjet}/2$ and the inclusive k_T jet algorithm [137] is used with $D = 1$. The
1956 statistical uncertainty in the computation (i.e. in the Monte Carlo integration) is smaller than
1957 10 % for all results shown. This large statistical uncertainty is reached only for the largest E_{Tjet} ,
1958 with much smaller uncertainties at lower values of E_T . No attempt has been made to estimate
1959 the uncertainties due to the choices of photons flux, photon or proton parton densities, scales
1960 or jet algorithms (see [138,139] for such considerations at HERA). The issues of background
1961 subtraction, experimental efficiencies in the jet reconstruction or energy calibration have also
1962 yet to be addressed. The only uncertainty studied thus far is that due to the nuclear parton
1963 densities, which is extracted in the EPS09 framework [136] using the Hessian method.

1964 The results are shown in Fig. 4.37. One observes that yields of around 10^3 jets per GeV
1965 are expected with $E_{Tjet} \sim 95$ (80) GeV in ep (ePb), for $|\eta_{jet}| < 3.1$ and the considered
1966 integrated luminosity of 2 fb^{-1} per nucleon. The effects of the nuclear modification of parton
1967 densities and their uncertainties are smaller than 10 %. The two-peak structure in the η_{jet} -
1968 plot results from the sum of the direct plus resolved contributions, each of which produce a
1969 single maximum, located in opposite hemispheres. Positive η_{jet} values are dominated by direct
1970 photon interactions, whereas negative η_{jet} values are dominated by contributions from resolved
1971 photons.

1972 4.9 Total photoproduction cross section

1973 Due to the $1/Q^4$ propagator term, the LHeC ep cross section is dominated by very low Q^2
1974 quasi-real photons. With a knowledge of the effective photon flux [140], measurements in this
1975 kinematic region can be used to obtain real photoproduction (γp) cross sections. The real
1976 photon has a dual nature, sometimes interacting in a point-like manner and sometimes inter-
1977 acting through its effective partonic structure, resulting from $\gamma \rightarrow q\bar{q}$ and higher multiplicity
1978 splittings well in advance of the target [141,142], the details of which are fundamental to the
1979 understanding of QCD evolution.

1980 The behaviour of the total photoproduction cross section at high energy is a topic of a
1981 major interest. It is now firmly established experimentally that all hadronic cross sections rise
1982 with centre of mass energy for large energies. The Froissart-Martin bound has been derived
1983 for hadronic probes. It therefore remains to be seen whether this bound is applicable to γp
1984 scattering. For example in Refs. [143,144] it has been argued that the bound for real photon-
1985 hadron interactions should be of a different functional form, namely $\ln^3 s$. This would imply
1986 that the universality of the asymptotic behaviour of hadronic cross sections does not hold.
1987 Therefore the measurement of the total photoproduction cross section at high energies will
1988 bring an important insight into the problems of universality of hadronic cross sections, unitarity
1989 constraints, the role of diffraction and the interface between hard and soft physics.

1990 In Fig. 4.38, available data on the total cross section are shown [28,145–147]⁵, together with
1991 a variety of models. More specifically, the dot-dashed black line labelled ‘FF model GRS’ is a
1992 minijet model [149], the yellow band labelled ‘Godbole et al.’ is an eikonized minijet model

⁵The recent results by ZEUS [148] refer only to the energy behavior of the cross section in the range $194 < W < 296$ GeV, but do not provide absolute values.

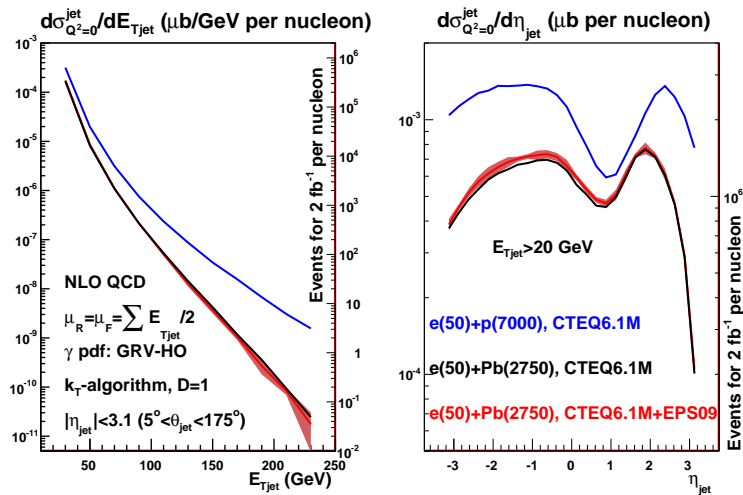


Figure 4.37: Predictions for the inclusive jet distribution in photoproduction, differential in E_{Tjet} (plot on the left) and η_{jet} (plot on the right) for $e(50)+p(7000)$ (blue lines), $e(50)+Pb(2750)$ without nuclear modification of the parton densities (black lines), and $e(50)+Pb(2750)$ with EPS09 nuclear modification of the parton densities (red lines for the central value and bands for the uncertainty coming from the nuclear modification and kinematic factors). See the text and the legends on the plots for further details of the calculations and kinematic cuts. In both plots, the axis on the left corresponds to the cross section in μb , while the axis on the right provides the number of jets expected for an integrated luminosity of 2 fb^{-1} per nucleon, per unit of E_{Tjet} (η_{jet}) in the plot on the left (right).

1993 with soft gluon resummation [149] with the band defined by different choices of the parameters in
 1994 the model, the red solid line labelled ‘Block & Halzen’ is based on a low energy parametrization
 1995 of resonances joined with Finite Energy Sum Rules and asymptotic $\ln^2 s$ -behaviour [150, 151],
 1996 and the dashed blue line labelled ‘Aspen model’ is a QCD inspired model [152].

1997 The theoretical predictions diverge at energies beyond those constrained by HERA data,
 1998 where cross sections were obtained by tagging and measuring the energies of electrons scattered
 1999 through very small angles in dedicated calorimeters located well down the beampipe in the
 2000 outgoing electron direction [145, 146]. As discussed in Chapter 13, the most promising location
 2001 for similar small angle electron detectors at the LHeC is in the region around 62 m from the
 2002 interaction point, which could be used to tag scattered electrons in events with $Q^2 < 0.01 \text{ GeV}^2$
 2003 and $y \sim 0.3$. This naturally leads to measurements of the total photoproduction cross section
 2004 at γp center-of-mass energies $W \sim 0.5\sqrt{s}$. The measurements would be strongly limited by
 2005 systematics. In the absence of a detailed simulation of an LHeC detector these uncertainties
 2006 are hard to estimate. For the simulated data in Fig. 4.38, uncertainties of 7% have been assumed,
 2007 matching the precision of the H1 and ZEUS data. This would clearly be more than adequate
 2008 to distinguish between many of the available models. The HERA uncertainties were dominated
 2009 by the invisible contributions from diffractive channels in which the diffractive masses were too
 2010 small to leave visible traces in the main detector. If detector acceptances to 1° are achieved at
 2011 the LHeC, better precision is expected to be possible.

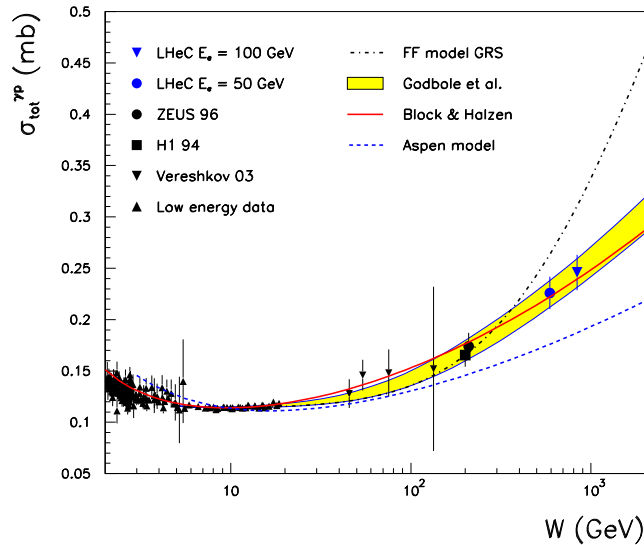


Figure 4.38: Simulated LHeC measurements of the total photoproduction cross section with $E_e = 50 \text{ GeV}$ or $E_e = 100 \text{ GeV}$, compared with previous data and a variety of models (see text for details). This is derived from a similar figure in [149].

2012 Chapter 5

2013 New Physics at Large Scales

2014 Although the LHC is expected to be the discovery machine for physics beyond the Standard
2015 Model at the TeV scale, it will not always be possible to measure with precision the parameters
2016 of the new physics. In this section, it is shown that in many cases the LHeC can probe in
2017 detail deviations from the expected electroweak interactions shared by leptons and quarks, thus
2018 adding essential information on the new physics. Previous studies [153–156] of the potential of
2019 high-energy $e - p$ colliders for the discovery of exotic phenomena have considered a number of
2020 processes, most of which are reviewed here.

2021 In some cases, Standard Model processes can also be better measured at the LHeC. Here,
2022 the charged and neutral current processes of SM Higgs production by vector boson fusion are
2023 investigated with the goal of measuring the $H - b - b$ coupling.

2024 5.1 New Physics in inclusive DIS at high Q^2

2025 The LHeC collider would enable the study of deep inelastic neutral current scattering at very
2026 high squared momentum transfers Q^2 , thus probing the structure of eq interactions at very short
2027 distances. At large scales new phenomena not directly detectable may become observable as
2028 deviations from the Standard Model predictions. A convenient tool to assess the experimental
2029 sensitivity beyond the maximal available center of mass energy and to parameterise indirect
2030 signatures of new physics is the concept of an effective four-fermion contact interaction. If the
2031 contact terms originate from a model where fermions have a substructure, a compositeness scale
2032 can be related to the size of the composite object. If they are due to the exchange of a new
2033 heavy particle, such as a leptoquark, the effective scale is related to the mass and coupling of
2034 the exchanged boson. Contact interaction phenomena are best observed as a modification of
2035 the expected Q^2 dependence and all information is essentially contained in the differential cross
2036 section $d\sigma/dQ^2$. An alternative way to parameterize the effects of fermion substructure makes
2037 use of form factors, which would also lead to deviations of $d\sigma/dQ^2$ with respect to the SM
2038 prediction. As a last example, low scale quantum gravity effects, which may be mediated via
2039 gravitons coupling to SM particles and propagating into large extra spatial dimensions, could
2040 also be observed as a modification of $d\sigma/dQ^2$ at highest Q^2 . These possible manifestations of
2041 new physics in inclusive DIS are addressed in this section.

2042 **5.1.1 Quark substructure**

2043 The remarkable similarities in the electromagnetic and weak interactions of leptons and quarks
 2044 in the Standard Model, and their anomaly cancellations in the family structure, strongly suggest
 2045 a fundamental connection. It would therefore be natural to conjecture that they could be
 2046 composed of more fundamental constituents, or that they form a representation of a larger
 2047 gauge symmetry group than that of the Standard Model, in a Grand Unified Theory.

2048 A possible method to investigate fermion substructures is to assign a finite size of radius R
 2049 to the electroweak charges of leptons and/or quarks while treating the gauge bosons γ and Z
 2050 still as pointlike particles [157]. A convenient parametrisation is to introduce ‘classical’ form
 2051 factors $f(Q^2)$ at the gauge boson–fermion vertices, which are expected to diminish the Standard
 2052 Model cross section at high momentum transfer

$$f(Q^2) = 1 - \frac{1}{6} \langle r^2 \rangle Q^2, \quad (5.1)$$

$$\frac{d\sigma}{dQ^2} = \frac{d\sigma^{SM}}{dQ^2} f_e^2(Q^2) f_q^2(Q^2). \quad (5.2)$$

2053 The square root of the mean-square radius of the electroweak charge distribution, $R =$
 2054 $\sqrt{\langle r^2 \rangle}$, is taken as a measure of the particle size. Since the pointlike nature of the elec-
 2055 tron/positron is already established down to extremely low distances in $e^+ e^-$ and $(g-2)_e$
 2056 experiments, only the quarks are allowed to be extended objects i.e. the form factor f_e can be
 2057 set to unity in the above equation.

2058 Figure.5.1 shows the sensitivity that an LHeC collider could reach on the “quark radius” [158].
 2059 Two configurations have been studied ($E_e = 70$ GeV and $E_e = 140$ GeV), and two values of
 2060 the integrated luminosity, per charge, have been assumed in each case. A sensitivity to quark
 2061 radius below 10^{-19} m could be reached, which is one order of magnitude better than the current
 2062 constraints, and comparable to the sensitivity that the LHC is expected to reach.

2063 **5.1.2 Contact Interactions**

2064 New currents or heavy bosons may produce indirect effects through the exchange of a virtual
 2065 particle interfering with the γ and Z fields of the Standard Model. For particle masses and
 2066 scales well above the available energy, $\Lambda \gg \sqrt{s}$, such indirect signatures may be investigated
 2067 by searching for a four-fermion pointlike $(\bar{e}e)(\bar{q}q)$ contact interaction. The most general chiral
 2068 invariant Lagrangian for neutral current vector-like contact interactions can be written in the
 2069 form [159–161]

$$\begin{aligned} \mathcal{L}_V = & \sum_{q=u,d} \{ \eta_{LL}^q (\bar{e}_L \gamma_\mu e_L) (\bar{q}_L \gamma^\mu q_L) + \eta_{LR}^q (\bar{e}_L \gamma_\mu e_L) (\bar{q}_R \gamma^\mu q_R) \\ & + \eta_{RL}^q (\bar{e}_R \gamma_\mu e_R) (\bar{q}_L \gamma^\mu q_L) + \eta_{RR}^q (\bar{e}_R \gamma_\mu e_R) (\bar{q}_R \gamma^\mu q_R) \}, \end{aligned} \quad (5.3)$$

2070 where the indices L and R denote the left-handed and right-handed fermion helicities and the
 2071 sum extends over *up*-type and *down*-type quarks and antiquarks q . In deep inelastic scattering
 2072 at high Q^2 the contributions from the first generation u and d quarks completely dominate and
 2073 contact terms arising from sea quarks s , c and b are strongly suppressed. Thus, there are eight
 2074 independent effective coupling coefficients, four for each quark flavour

$$\eta_{ab}^q \equiv \epsilon \frac{g^2}{\Lambda_{ab}^q{}^2}, \quad (5.4)$$

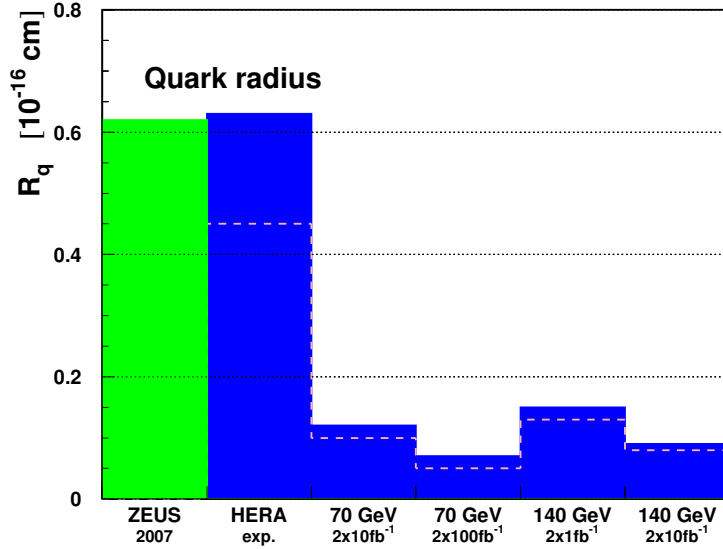


Figure 5.1: Sensitivity (95% confidence level limits) of an LHeC collider to the effective quark radius.

2075 where a and b indicate the L , R helicities, g is the overall coupling strength, Λ_{ab}^q is a scale
2076 parameter and ϵ is a prefactor, often set to $\epsilon = \pm 1$, which determines the interference sign
2077 with the Standard Model currents. The ansatz eq. (5.3) can be easily applied to any new
2078 phenomenon, *e.g.* (eq) compositeness, leptoquarks or new gauge bosons, by an appropriate
2079 choice of the coefficients η_{ab} . Scalar and tensor interactions of dimension 6 operators involving
2080 helicity flip couplings are strongly suppressed at HERA [161] and therefore not considered.

2081 Figure 5.2 shows the sensitivity that an LHeC could reach on the scale Λ , for two example
2082 cases of contact interactions [158]. In general, with 10 fb^{-1} of data, LHeC would probe scales
2083 between 25 TeV and 45 TeV, depending on the model. The sensitivity of LHC to such $eeqq$
2084 interactions, which would affect the di-electron Drell-Yan (DY) spectrum at high masses, is
2085 similar.

2086 Figure 5.3 shows how the DY cross-section at LHC would deviate from the SM value, for
2087 three examples of $eeqq$ contact interactions. In the “LL” model considered here, the sum in
2088 eq. (5.3) only involves left-handed fermions and all amplitudes have the same phase ϵ . With
2089 only pp data, it will be difficult to determine simultaneously the size of the contact interaction
2090 scale Λ and the sign of the interference of the new amplitudes with respect to the SM ones:
2091 for example, for $\Lambda = 20 \text{ TeV}$ and $\epsilon = -1$, the decrease of the cross-section with respect to
2092 the SM prediction for di-electron masses below $\sim 3 \text{ TeV}$, which is characteristic of a negative
2093 interference, is too small to be firmly established when uncertainties due to parton distribution
2094 functions are taken into account.

2095 For the same “LL” model, the sign of this interference can be unambiguously determined
2096 at LHeC from the asymmetry of σ/σ_{SM} in e^+p and e^-p data, as shown in Fig. 5.4.

2097

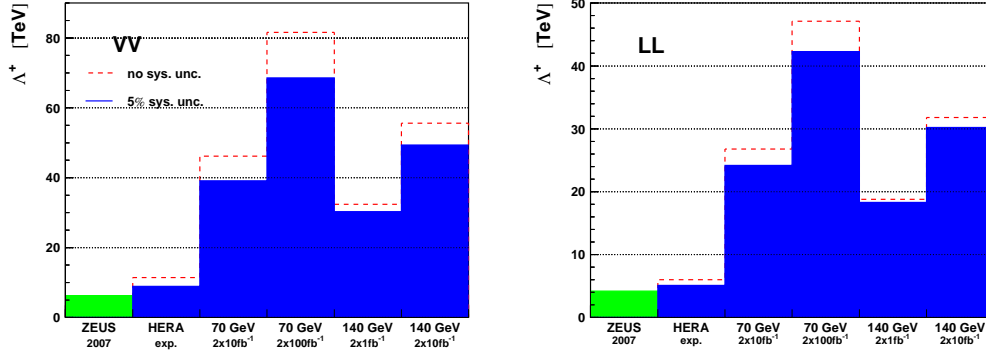


Figure 5.2: Sensitivity (95% confidence level limits) on the scale Λ for two example contact interactions.

2098 Moreover, with a polarised lepton beam, ep collisions would help determine the chiral struc-
 2099 ture of the new interaction. More generally, it is very likely that both pp and ep data would
 2100 be necessary to underpin the structure of new physics which would manifest itself as an $eeqq$
 2101 contact interaction. Such a complementarity of pp , ep (and also ee) data was studied in [162]
 2102 in the context of the Tevatron, HERA and LEP colliders.

2103 5.1.3 Kaluza-Klein gravitons in extra-dimensions

2104 In some models with n large extra dimensions, the SM particles reside on a four-dimensional
 2105 “brane”, while the spin 2 graviton propagates into the extra spatial dimensions and appears in
 2106 the four-dimensional world as a tower of massive Kaluza-Klein (KK) states. The summation
 2107 over the enormous number of Kaluza-Klein states up to the ultraviolet cut-off scale, taken as
 2108 the Planck scale M_S in the $4 + n$ space, leads to effective contact-type interactions $ff'f'f'$
 2109 between two fermion lines, with a coupling $\eta = O(1)/M_S^4$. In ep scattering, the exchange of
 2110 such a tower of Kaluza-Klein gravitons would affect the Q^2 dependence of the DIS cross-section
 2111 $d\sigma/dQ^2$. At LHeC, such effects could be observed as long as the scale M_S is below 4 – 5 TeV.
 2112 While at the LHC, virtual graviton exchange may be observed for scales up to ~ 10 TeV, and
 2113 the direct production of KK gravitons, for scales up to 5 – 7 TeV depending on n , would allow
 2114 this phenomenon to be studied further, LHeC data may determine that the new interaction
 2115 is universal by establishing that the effect in the $eq \rightarrow eq$ cross-section is independent of the
 2116 lepton charge and polarization, and, to some extent, of the quark flavor.

2117 5.2 Leptoquarks and leptogluons

2118 The high energy of the LHeC extends the kinematic range of DIS physics to much higher values
 2119 of electron-quark mass $M = \sqrt{sx}$, beyond those of present ep colliders. By providing both
 2120 baryonic and leptonic quantum numbers in the initial state, it is ideally suited to a study of the
 2121 properties of new bosons possessing couplings to an electron-quark pair in this new mass range.
 2122 Such particles can be squarks in supersymmetric models with R -parity violation (\tilde{R}_p), or first-
 2123 generation leptoquark (LQ) bosons which appear naturally in various unifying theories beyond

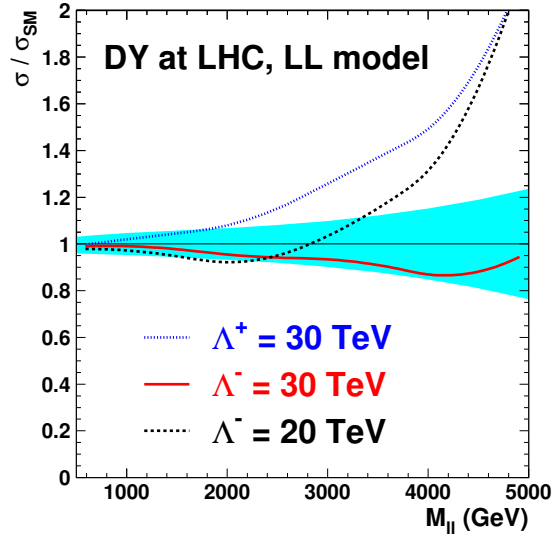


Figure 5.3: Example deviations, from its SM value, of the Drell-Yan cross-section at LHC as a function of the dilepton mass, in the presence of an $eeqq$ contact interaction. The blue band shows the relative uncertainty of the predicted SM cross-sections due to the current uncertainties of the parton distribution functions, as obtained from the CTEQ 6.1 sets.

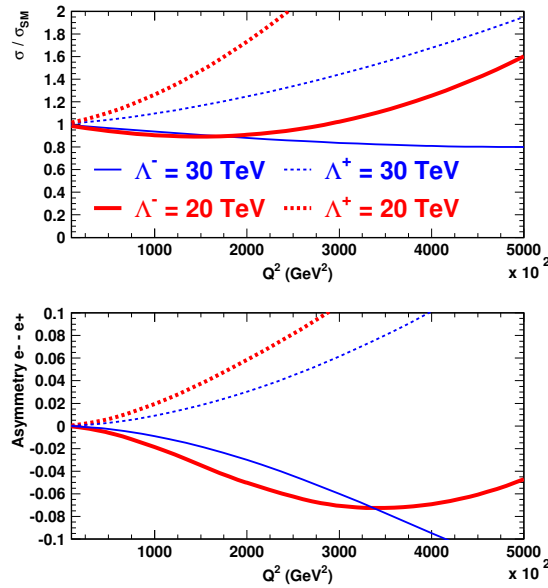


Figure 5.4: (top) Example deviations of the e^-p DIS cross-section at LHeC, in the presence of an $eeqq$ CI. The ratio of the “measured” to the SM cross-sections, $r = \sigma/\sigma_{SM}$, is shown. (bottom) Asymmetry $\frac{r(e^+) - r(e^-)}{r(e^+) + r(e^-)}$ between e^+p and e^-p measurements of σ/σ_{SM} .

2124 the Standard Model (SM) such as: E_6 [163], where new fields can mediate interactions between
 2125 leptons and quarks; extended technicolor [164, 165], where leptoquarks result from bound states
 2126 of technifermions; the Pati-Salam model [15], where the leptonic quantum number is a fourth
 2127 color of the quarks or in lepton-quark compositeness models. They are produced as single
 2128 s -channel resonances via the fusion of incoming electrons with quarks in the proton. They are
 2129 generically referred to as “leptoquarks” in what follows. The case of “leptogluons”, which could
 2130 be produced in ep collisions as a fusion between the electron and a gluon, is also addressed at
 2131 the end of this section.

2132 5.2.1 Phenomenology of leptoquarks in ep collisions

2133 In ep collisions, LQs may be produced resonantly up to the kinematic limit of $\sqrt{s_{ep}}$ via the
 2134 fusion of the incident lepton with a quark or antiquark coming from the proton, or exchanged in
 the u -channel, as illustrated in Fig. 5.5. The coupling λ at the $LQ - e - q$ vertex is an unknown

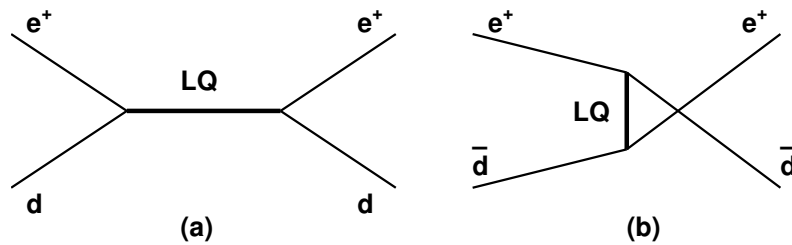


Figure 5.5: Example diagrams for resonant production in the s -channel (a) and exchange in the u -channel (b) of a LQ with fermion number $F = 0$. The corresponding diagrams for $|F| = 2$ LQs are obtained from those depicted by exchanging the quark and antiquark.

2135 parameter of the model.
 2136

2137 In the narrow-width approximation, the resonant production cross-section is proportional
 2138 to $\lambda^2 q(x)$ where $q(x)$ is the density of the struck parton in the incoming proton.

2139 The resonant production or t -channel exchange of a leptoquark gives $e + q$ or $\nu + q'$ final
 2140 states leading to individual events indistinguishable from SM NC and CC DIS respectively. For
 2141 the process $eq \rightarrow LQ \rightarrow eq$, the distribution of the transverse energy $E_{T,e}$ of the final state
 2142 lepton shows a Jacobian peak at $M_{LQ}/2$, M_{LQ} being the LQ mass. Hence the strategy to search
 2143 for a LQ signal in ep collisions is to look, among high Q^2 (i.e. high $E_{T,e}$) DIS event candidates,
 2144 for a peak in the invariant mass M of the final $e - q$ pair. Moreover, the significance of the
 2145 LQ signal over the SM DIS background can be enhanced by exploiting the specific angular
 2146 distribution of the LQ decay products (see spin determination, below).

2147 5.2.2 The Buchmüller-Rückl-Wyler Model

2148 A reasonable phenomenological framework to study first generation LQs is provided by the
 2149 BRW model [166]. This model is based on the most general Lagrangian that is invariant under
 2150 $SU(3) \times SU(2) \times U(1)$, respects lepton and baryon number conservation, and incorporates

2151 dimensionless family diagonal couplings of LQs to left- and/or right-handed fermions. Under
2152 these assumptions LQs can be classified according to their quantum numbers into 10 different
2153 LQ isospin multiplets (5 scalar and 5 vector), half of which carry a vanishing fermion number
2154 $F = 3B + L$ (B and L denoting the baryon and lepton number respectively) and couple to
 $e^+ + q$ while the other half carry $|F| = 2$ and couple to $e^+ + \bar{q}$. These are listed in Table 5.1.

$F = -2$	Prod./Decay	β_e	$F = 0$	Prod./Decay	β_e
Scalar Leptoquarks					
$^{1/3}S_0$	$e_R^+ \bar{u}_R \rightarrow e^+ \bar{u}$	1/2	$^{5/3}S_{1/2}$	$e_R^+ u_R \rightarrow e^+ u$	1
	$e_L^+ \bar{u}_L \rightarrow e^+ \bar{u}$	1		$e_L^+ u_L \rightarrow e^+ u$	1
$^{4/3}\tilde{S}_0$	$e_L^+ \bar{d}_L \rightarrow e^+ \bar{d}$	1	$^{2/3}S_{1/2}$	$e_L^+ d_L \rightarrow e^+ d$	1
$^{4/3}S_1$	$e_R^+ \bar{d}_R \rightarrow e^+ \bar{d}$	1	$^{2/3}\tilde{S}_{1/2}$	$e_R^+ d_R \rightarrow e^+ d$	1
$^{1/3}S_1$	$e_R^+ \bar{u}_R \rightarrow e^+ \bar{u}$	1/2			
Vector Leptoquarks					
$^{4/3}V_{1/2}$	$e_L^+ \bar{d}_R \rightarrow e^+ \bar{d}$	1	$^{2/3}V_0$	$e_L^+ d_R \rightarrow e^+ d$	1
	$e_R^+ \bar{d}_L \rightarrow e^+ \bar{d}$	1		$e_R^+ d_L \rightarrow e^+ d$	1/2
$^{1/3}V_{1/2}$	$e_L^+ \bar{u}_R \rightarrow e^+ \bar{u}$	1	$^{5/3}\tilde{V}_0$	$e_L^+ u_R \rightarrow e^+ u$	1
$^{1/3}\tilde{V}_{1/2}$	$e_R^+ \bar{u}_L \rightarrow e^+ \bar{u}$	1	$^{5/3}V_1$	$e_R^+ u_L \rightarrow e^+ u$	1
			$^{2/3}V_1$	$e_R^+ d_L \rightarrow e^+ d$	1/2

Table 5.1: Leptoquark isospin families in the Buchmüller-Rückl-Wyler model. For each leptoquark, the superscript corresponds to its electric charge, while the subscript denotes its weak isospin. β_e denotes the branching ratio of the LQ into $e + q$.

2155 We use the nomenclature of [167] to label the different LQ states. In addition to the
2156 underlying hypotheses of BRW, we restrict LQs couplings to only one chirality state of the
2157 lepton, given that deviations from lepton universality in helicity suppressed pseudoscalar meson
2158 decays have not been observed [168, 169].

2160 In the BRW model, LQs decay exclusively into eq and/or νq and the branching ratio $\beta_e =$
2161 $\beta(LQ \rightarrow eq)$ is fixed by gauge invariance to 0.5 or 1 depending on the LQ type.

2162 5.2.3 Phenomenology of leptoquarks in pp collisions

2163 **Pair production** In pp collisions leptoquarks would be mainly pair-produced via gg or qq
2164 interactions. As long as the coupling λ is not too strong (e.g. $\lambda \sim 0.3$ or below, corresponding
2165 to a strength similar to or lower than that of the electromagnetic coupling, $\sqrt{4\pi\alpha_{em}}$), the
2166 production cross-section is essentially independent of λ . At the LHC, LQ masses up to about
2167 1.5 to 2 TeV will be probed [170], independently of the coupling λ . However, the determination
2168 of the quantum numbers of a first generation LQ in the pair-production mode is not possible
2169 (e.g. for the fermion number) or ambiguous and model-dependent (e.g. for the spin). Single
2170 LQ production is much better suited for such studies.

2171 **Single production** Single LQ production at the LHC is also possible. So far, only the
2172 production mode $gq \rightarrow e + LQ$ (see example diagrams in Fig. 5.6a and b) has been considered

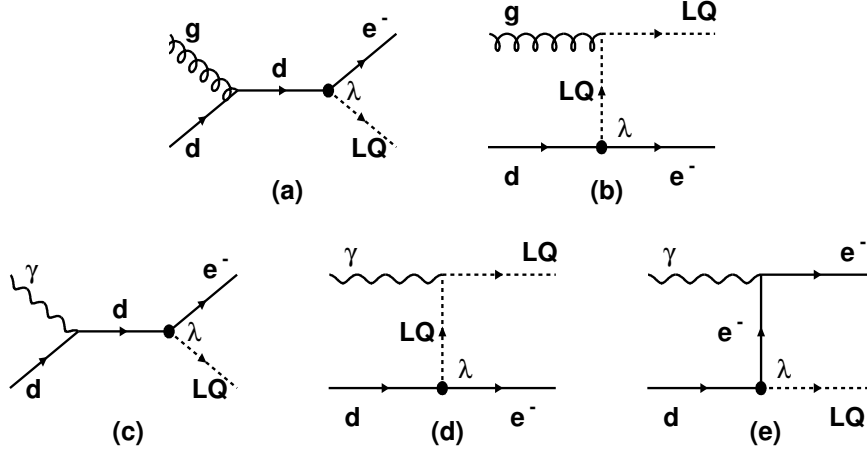


Figure 5.6: Diagrams for single LQ production in pp collisions, shown for the example case of the $\tilde{S}_{1/2}^L$ scalar leptoquark. The production may occur via qq interactions (a and b), or via $q\gamma$ interactions (c, d and e). In the latter case, the photon can be emitted by the proton (elastic regime) or by a quark coming from the proton (inelastic regime).

2173 in the literature (see e.g. [170]). In the context of this study, the additional production mode
 2174 $\gamma q \rightarrow e + LQ$ has been considered as well (see example diagrams in Fig. 5.6c, d and e). This
 2175 cross-section has been calculated by taking into account:

- 2176 • the inelastic regime, where the photon virtuality q^2 is large enough and the proton breaks
 2177 up in a hadronic system with a mass well above the proton mass. In that case, the photon
 2178 is emitted by a parton in the proton, and the process $qq' \rightarrow q + e + LQ$ is calculated.
- 2179 • the elastic regime, in which the proton emitting the photon remains intact. This calcula-
 2180 tion involves the elastic form factors of the proton.

2181 As the resonant LQ production in ep collisions, the cross-section of single LQ production in pp
 2182 collisions approximately scales with the square of the coupling, $\sigma \propto \lambda^2$. Figure 5.7 (left) shows
 2183 the cross-section for single LQ production at the LHC as a function of the LQ mass, assuming
 2184 a coupling $\lambda = 0.1$. While the inelastic part of the γq cross-section can be neglected, the elastic
 2185 production plays an important role at high masses; its cross-section is larger than that of LQ
 2186 production via gq interactions for masses above ~ 1 TeV. However, the cross-section for single
 2187 LQ production at LHC is much lower than that at LHeC, in e^+p or e^-p collisions, as shown in
 2188 Fig.5.7 (right).

2189 **The Contact Term Approach** For LQ masses far above the kinematic limit, the contraction
 2190 of the propagator in the $eq \rightarrow eq$ and $qq \rightarrow ee$ amplitudes leads to a four-fermion interaction.
 2191 Such interactions are studied in the context of general contact terms, which can be used to
 2192 parameterize any new physics process with a characteristic energy scale far above the kinematic
 2193 limit.

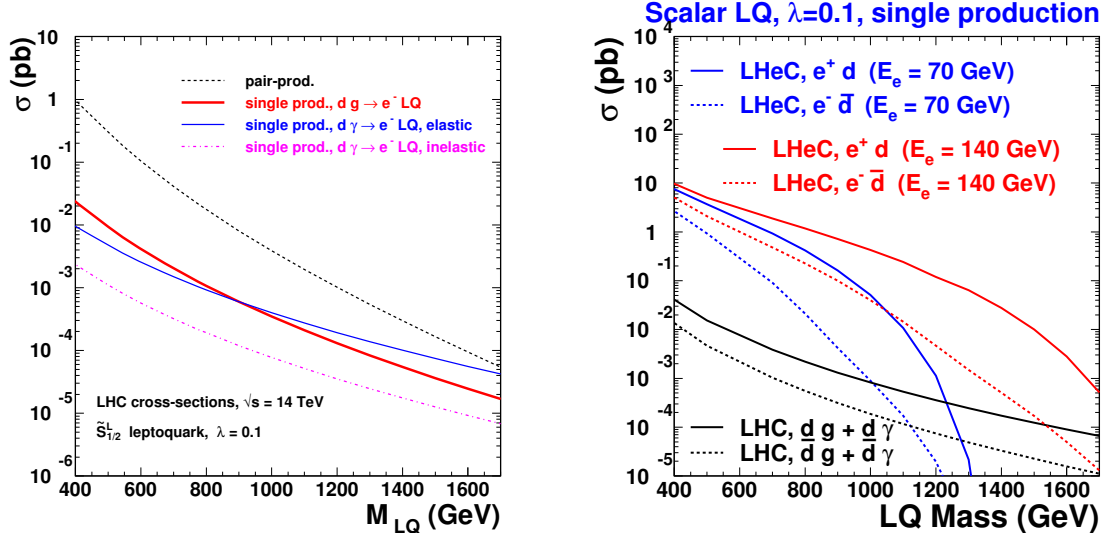


Figure 5.7: left: Single LQ production cross-section at the LHC. right: comparison of the cross-section for single LQ production, at LHC and at LHeC.

2194 In ep collisions, Contact Interactions (CI) would interfere with NC DIS processes and lead
 2195 to a distortion of the Q^2 spectrum of NC DIS candidate events. The results presented in
 2196 section 5.1 can be re-interpreted into expected sensitivities on high mass leptoquarks.

2197 5.2.4 Current status of leptoquark searches

2198 The H1 and ZEUS experiments at the HERA ep collider have constrained the coupling λ to be
 2199 smaller than the electromagnetic coupling ($\lambda < \sqrt{4\pi\alpha_{em}} \sim 0.3$) for first generation LQs lighter
 2200 than 300 GeV. The D0 and CDF experiments at the Tevatron pp collider set constraints on
 2201 first-generation LQs that are independent of the coupling λ , by looking for pair-produced LQs
 2202 that decay into eq (νq) with a branching ratio β ($1-\beta$). For a branching fraction $\beta = 1$, masses
 2203 below 299 GeV are excluded by the D0 experiment [171]. The CMS and ATLAS experiments
 2204 have recently set tighter constraints [172,173]. Fig. 5.8 shows the bounds obtained by the CMS
 2205 experiment with $\sim 32 \text{ pb}^{-1}$ collected in 2010, in the β versus M_{LQ} plane. For $\beta = 1$ ($\beta = 0.5$),
 2206 masses below 384 GeV (340 GeV) are ruled out.

2207 5.2.5 Sensitivity on leptoquarks at LHC and at LHeC

2208 **Mass - coupling reach** Fig. 5.9 shows the expected sensitivity [158] of the LHC and LHeC
 2209 colliders for scalar leptoquark production. The single LQ production cross section depends on
 2210 the unknown coupling λ of the LQ to the electron-quark pair. For a coupling λ of $\mathcal{O}(0.1)$, LQ
 2211 masses up to about 1 TeV could be probed at the LHeC. In pp interactions at the LHC, such
 2212 leptoquarks would be mainly produced via pair production, or singly produced with a much
 2213 reduced cross section.

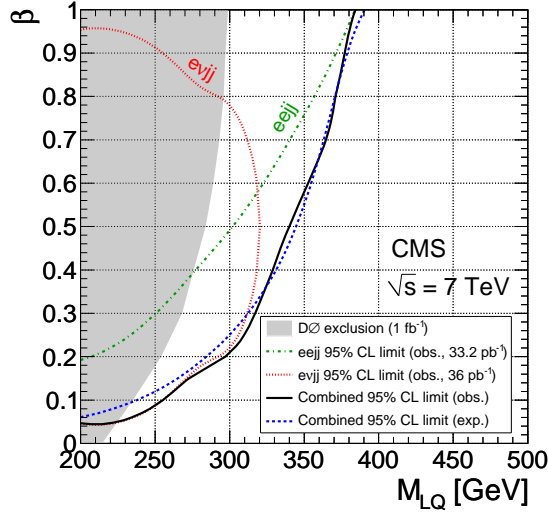


Figure 5.8: Constraints on first generation leptoquarks obtained by the CMS experiment.

2214 5.2.6 Determination of LQ properties

2215 In ep collisions LQ production can be probed in detail, taking advantage of the formation and
 2216 decay of systems which can be observed directly as a combination of jet and lepton invariant
 2217 mass in the final state. It will thereby be possible at the LHeC to probe directly and with
 2218 high precision the perhaps complex structures which will result in the lepton-jet system and to
 2219 determine the quantum numbers of new states. Examples of the sensitivity of high energy ep
 2220 collisions to the properties of LQ production follow. In particular, a quantitative comparison
 2221 of the potential of LHC and LHeC to measure the fermion number of a LQ is given.

2222

Fermion number (F) Since the parton densities for u and d at high x are much larger than those for \bar{u} and \bar{d} , the production cross section at LHeC of an $F = 0$ ($F = 2$) LQ is much larger in e^+p (e^-p) than in e^-p (e^+p) collisions. A measurement of the asymmetry between the e^+p and e^-p LQ cross sections,

$$\mathcal{A}_{ep} = \frac{\sigma_{prod}(e^+p) - \sigma_{prod}(e^-p)}{\sigma_{prod}(e^+p) + \sigma_{prod}(e^-p)}$$

thus determines, via its sign, the fermion number of the produced leptoquark. Pair production of first generation LQs at the LHC will not allow this determination. Single LQ production at the LHC, followed by the LQ decay into e^\pm and q or \bar{q} , could determine F by comparing the signal cross sections with an e^+ and an e^- coming from the resonant state. Indeed, for a $F = 0$ leptoquark, the signal observed when the resonance is made by a positron and a jet corresponds to diagrams involving a *quark* in the initial state (see Fig.5.10a). Hence the corresponding cross-section, $\sigma(e_{out}^+j)$ is larger than that of the signal observed when the resonance is made by an electron and a jet, $\sigma(e_{out}^-j)$, since a high x *antiquark* is involved in that latter case (see

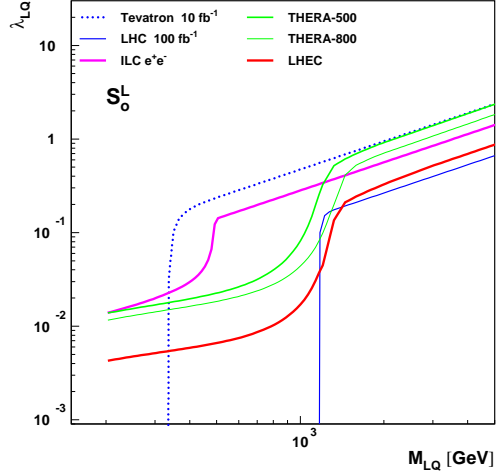


Figure 5.9: Mass-dependent upper bounds on the LQ coupling λ as expected at LHeC for a luminosity of 10 fb^{-1} (full red curve) and at the LHC for 100 fb^{-1} (full blue curve). These are shown for an example scalar LQ coupling to e^-u .

Fig.5.10b). In contrast, for a $F = 2$ LQ, $\sigma(e_{out}^+j)$ is smaller than $\sigma(e_{out}^-j)$. The measurement of (the sign of) the asymmetry

$$\mathcal{A}_{pp} = \frac{\sigma(e_{out}^+j) - \sigma(e_{out}^-j)}{\sigma(e_{out}^+j) + \sigma(e_{out}^-j)}$$

should thus provide a determination of the LQ fermion number. However, the single LQ pro-

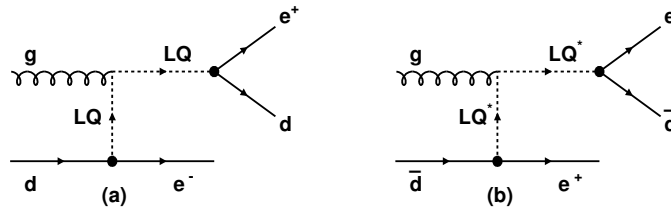


Figure 5.10: Single production of a $F = 0$ leptoquark decaying (a) into a positron and a jet and (b) into an electron and a jet. In (a) (resp. (b)), the jet comes from a quark (an antiquark); conservation of the baryon number implies that the parton involved in the initial state is a quark (an antiquark).

2223

2224

2225

duction cross section at the LHC is two orders of magnitude lower than at the LHeC (Fig. 5.7), so that the asymmetry \mathcal{A}_{pp} measured at the LHC may suffer from statistics in a large part of the

2226 parameter space. For a LQ coupling to ed and $\lambda = 0.1$, no information on F can be extracted
 2227 from 300 pb^{-1} of LHC data for a LQ mass above $\sim 1 \text{ TeV}$, while the LHeC can determine F
 2228 for LQ masses up to 1.5 TeV (Fig. 5.11 and Fig. 5.12). Details of the determination of \mathcal{A}_{pp} at
 2229 the LHC are given in the next paragraph.

2230

2231 An estimate of the precision with which the fermion number determination of a leptoquark
 2232 can be determined at the LHC was obtained from a Monte Carlo simulation. First, using the
 2233 model [174] implemented in CalcHep [175], samples were generated for the processes $g u \rightarrow$
 2234 $e^+ e^- u$ and $g \bar{u} \rightarrow e^+ e^- \bar{u}$, keeping only diagrams involving the exchange of a scalar LQ exchange
 2235 of charge $1/3$, isospin 0 and fermion number 2. This leptoquark ($^{1/3}S_0$ in the notation of
 2236 Table 5.1) couples to $e_R^- u_R$. Assuming that it is chiral, only right-handed coupling was allowed.
 2237 The $^{1/3}S_0$ leptoquark was also assumed to couple only to the first generation. Masses of 500
 2238 GeV, 750 GeV and 1 TeV were considered. The renormalization and factorization scales were
 2239 set at $Q^2 = m_{LQ}^2$ and the coupling parameter $\lambda = 0.1$. A center of mass energy of 14 TeV was
 2240 assumed at the LHC.

2241 High statistics background samples, corresponding to 150 fb^{-1} were also produced by gener-
 2242 ating the same processes $pp \rightarrow e^+ e^- + \text{jet}$, including all diagrams except those involving the
 2243 exchange of leptoquarks. Kinematic preconditions were applied at the generation level to both
 2244 signals and background: (i) $p_T(\text{jet}) > 50 \text{ GeV}$, (ii) $p_T(e^\pm) > 20 \text{ GeV}$, (iii) invariant mass of
 2245 jet- $e^+ - e^-$ system $> 200 \text{ GeV}$. The cross sections for the signals and backgrounds under these
 2246 conditions are: 19.7 fb, 3.4 fb and 0.87 fb for LQ's of mass 500 GeV, 750 GeV and 1 TeV respec-
 2247 tively, and 1780 fb for the background. These events were subsequently passed to Pythia [113]
 2248 to perform parton showering and hadronization, then processed through Delphes [176] for a fast
 2249 simulation of the ATLAS detector. Finally, considering events with two reconstructed electrons
 2250 of opposite sign and, assuming that the leptoquark has already been discovered (at the LHC),
 2251 the combination of the highest p_T jet with the reconstructed e^- or e^+ with a mass closest to
 2252 the known leptoquark mass is chosen as the LQ candidate. The following cuts for $m_{LQ} = 500$,
 2253 750 and 1000 GeV, respectively, are applied:

- 2254 • dilepton invariant mass $m_{ll} > 150, 200, 250 \text{ GeV}$. This cut rejects very efficiently the $Z+$
 2255 jets background.
- 2256 • $p_T(e_1) > 150, 200, 250 \text{ GeV}$ and $p_T(e_2) > 75, 100, 100 \text{ GeV}$, where e_1 is the reconstructed
 2257 e^\pm with higher p_T and e_2 the lower p_T electron.
- 2258 • $p_T(j_1) > 100, 250, 400 \text{ GeV}$, where j_1 is the reconstructed jet with highest p_T , used for
 2259 the reconstruction of the LQ.

2260 Table 5.2 summarizes the results of the simulation for an integrated luminosity of 300
 2261 fb^{-1} . The expected number of signal events shown in the table is then simply the number
 2262 of events due to the leptoquark production and decay, falling in the resonance peak within a
 2263 mass window of width (60, 100, 160 GeV) for the three cases studied, respectively. Although
 2264 this simple analysis can be improved by considering other less dominant backgrounds and by
 2265 using optimized selection criteria, it should give a good estimate of the precision with which
 2266 the asymmetry can be measured. This precision falls rapidly with increasing mass and, above
 2267 $\sim 1 \text{ TeV}$, it becomes impossible to observe simultaneously single production of both $^{1/3}S_0$ and
 2268 $^{1/3}\bar{S}_0$. It must be noted that the asymmetry at the LHC will be further diluted by the abundant
 2269 leptoquark pair production, not taken into account here.

LQ mass (GeV)	$1/3 S_1 \rightarrow e^+ \bar{u}$		$1/3 \bar{S}_1 \rightarrow e^- u$		Charge Asymmetry
	Signal	Background	Signal	Background	
500	121	431	771	478	0.73 ± 0.05
750	18.3	137	132	102	$0.76^{+0.16}_{-0.14}$
1000	4.9	57	44	42	$0.77^{+0.23}_{0.24}$

Table 5.2: Estimated number of events of signal and background, and the charge asymmetry measurement with 300 fb^{-1} at the LHC, for $\lambda = 0.1$.

2270 **Flavour structure of the LQ coupling** More generally, using the same charge asymmetry
2271 observable, the LHeC will be sensitive to the flavour structure of the leptoquark, through the
2272 dependence on the parton distribution functions of the interacting quark in the proton. Fig. 5.13
2273 shows the calculated asymmetry for scalar LQs. Provided that the coupling λ is not too small,
2274 the accuracy of the measurement of \mathcal{A}_{ep} at LHeC (see Fig. 5.11) would allow the various LQ
2275 types to be disentangled, as different LQs lead to values of \mathcal{A}_{ep} that differ by typically 20–30%.
2276 A similar measurement at the LHC would be possible only in a very limited part of the phase
2277 space (low masses and large couplings), where the statistics would be large enough to yield an
2278 accuracy of about 20% on the measured asymmetry \mathcal{A}_{pp} .

2279 **Spin** At the LHeC, the angular distribution of the LQ decay products is unambiguously
2280 related to its spin. Indeed, scalar LQs produced in the s -channel decay isotropically in their
2281 rest frame leading to a flat $d\sigma/dy$ spectrum where $y = \frac{1}{2}(1 + \cos\theta^*)$ is the Bjorken scattering
2282 variable in DIS and θ^* is the decay polar angle of the lepton relative to the incident proton in
2283 the LQ centre of mass frame. In contrast, events resulting from the production and decay of
2284 vector LQs would be distributed according to $d\sigma/dy \propto (1 - y)^2$. These y spectra from scalar
2285 or vector LQ production are markedly different from the $d\sigma/dy \propto y^{-2}$ distribution expected
2286 at fixed M for the dominant t -channel photon exchange in neutral current DIS events¹. Hence,
2287 a LQ signal in the NC-like channel will be statistically most prominent at high y .

2288 The spin determination will be much more complicated, even possibly ambiguous, if only
2289 the LHC leptoquark pair production data are available. Angular distributions for vector LQs
2290 depend strongly on the structure of the $g LQ \bar{L} \bar{Q}$ coupling, i.e. on possible anomalous couplings.
2291 For a structure similar to that of the γWW vertex, vector LQs produced via $q\bar{q}$ fusion are
2292 unpolarised and, because both LQs are produced with the same helicity, the distribution of
2293 the LQ production angle will be similar to that of a scalar LQ. The study of LQ spin via
2294 single LQ production at the LHC will suffer from the relatively low rates and more complicated
2295 backgrounds.

2296 **Neutrino decay modes** At the LHeC, there is similar sensitivity for LQ decay into both eq
2297 and νq . At the LHC, in pp collisions, LQ decay into neutrino-quark final states is plagued by
2298 huge QCD background. At the LHeC, production through eq fusion with subsequent νq decay
2299 is thus very important if the complete pattern of LQ decay couplings is to be determined.

¹At high momentum transfer, Z^0 exchange is no longer negligible and contributes to less pronounced differences in the y spectra between LQ signal and DIS background.

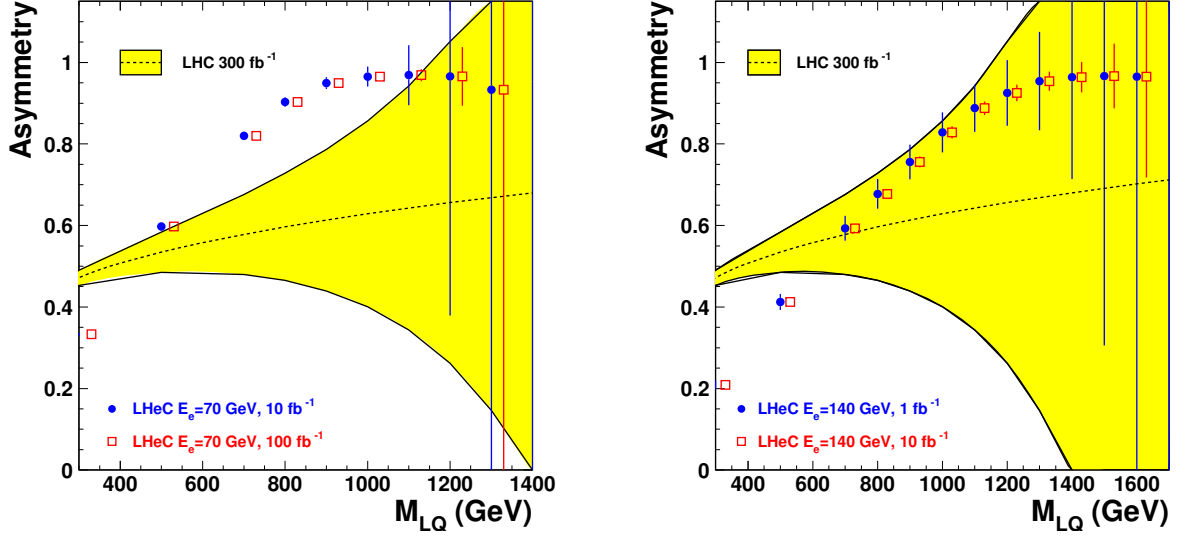


Figure 5.11: *Asymmetries which would determine the fermion number of a LQ, the sign of the asymmetry being the relevant quantity. The dashed curve shows the asymmetry that could be measured at the LHC; the yellow band shows the statistical uncertainty of this quantity, assuming an integrated luminosity of 300 fb^{-1} . The red and blue symbols, together with their error bars, show the asymmetry that would be measured at LHeC, assuming $E_e = 70 \text{ GeV}$ (left) or $E_e = 140 \text{ GeV}$ (right). Two values of the integrated luminosity have been assumed. These determinations correspond to the $\tilde{S}_{1/2}^L$ (scalar LQ coupling to $e^+ + d$), with a coupling of $\lambda = 0.1$.*

Coupling λ In the narrow-width approximation, the production cross-section of a LQ in ep collisions can be written as, depending on the LQ spin :

$$\sigma_{prod} = \frac{\lambda^2}{16\pi} q(x = M^2/s_{ep}) \quad (J = 0) \quad \text{or} \quad \sigma_{prod} = \frac{\lambda^2}{8\pi} q(x = M^2/s_{ep}) \quad (J = 1).$$

2300 At LHeC, the determination of:

- 2301 • the LQ spin, via the analysis of the angular distribution of its decay products;
- 2302 • the flavor of the quark q involved in the $e - q - LQ$ vertex, via the charge asymmetry
- 2303 described above;
- 2304 • the production cross-section, via the cross-sections measured in the eq and νq decay modes

2305 allows the value of the coupling λ to be determined, from the above formula.

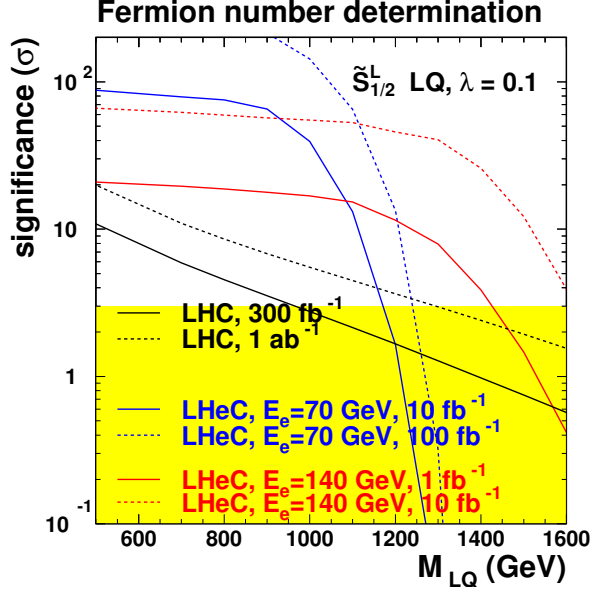


Figure 5.12: Significance of the determination of the fermion number of a LQ, at the LHC (black curve) and at the LHeC (blue and red curves). This corresponds to a $\tilde{S}_{1/2}^L$ leptoquark, assuming a coupling of $\lambda = 0.1$.

2306 **Chiral structure of the LQ coupling** Chirality is central to the SM Lagrangian. Polarised
 2307 electron and positron beams² at the LHeC will shed light on the chiral structure of the LQ-e-q
 2308 couplings. Measurements of a similar nature at LHC are impossible.

2309

2310 In summary, would a first generation leptoquark exist in the TeV mass range with a coupling
 2311 λ of $\mathcal{O}(0.1)$, the LHeC would allow a rich program of “spectroscopy” to be carried out, resulting
 2312 in the determination of most of the LQ properties.

2313 5.2.7 Leptogluons

2314 While leptoquarks and excited fermions are widely discussed in the literature, leptogluons
 2315 have not received the same attention. However, they are predicted in all models with colored
 2316 preons [177–182]. For example, in the framework of fermion-scalar models, leptons would be
 2317 bound states of a fermionic preon and a scalar anti-preon $l = (F\bar{S}) = 1 \oplus 8$ (both F and S are
 2318 color triplets), and each SM lepton would have its own colour octet partner [182].

2319 A study of leptogluons production at LHeC is presented in [183]. It is based on the following

²Whether it is possible to achieve longitudinal polarisation in a 70 GeV e^\pm beam in the LHC tunnel remains to be clarified.

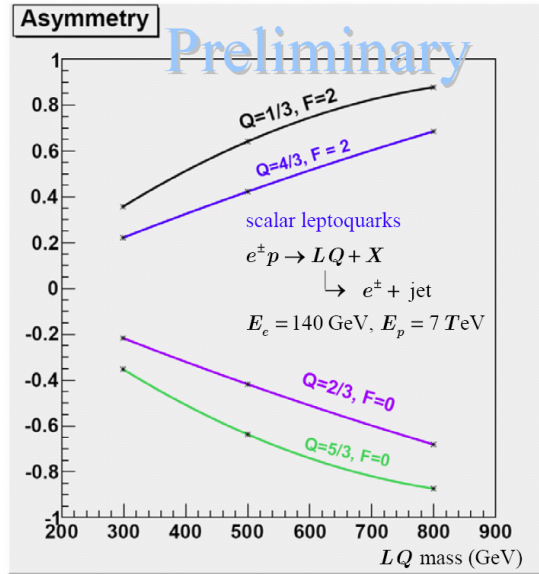


Figure 5.13: Charge asymmetry vs LQ mass for different types of scalar LQ's.

2320 Lagrangian:

$$L = \frac{1}{2\Lambda} \sum_l \{ \bar{l}_8^\alpha g_s G_{\mu\nu}^\alpha \sigma^{\mu\nu} (\eta_L l_L + \eta_R l_R) + h.c. \} \quad (5.5)$$

2321 where $G_{\mu\nu}^\alpha$ is the field strength tensor for gluon, index $\alpha = 1, 2, \dots, 8$ denotes the color, g_s is
 2322 gauge coupling, η_L and η_R are the chirality factors, l_L and l_R denote left and right spinor
 2323 components of lepton, $\sigma^{\mu\nu}$ is the anti-symmetric tensor and Λ is the compositeness scale. The
 2324 leptonic chiral invariance implies $\eta_L \eta_R = 0$.

2325 The phenomenology of leptogluons at LHC and LHeC is very similar to that of leptoquarks,
 2326 despite their different spin (leptogluons are fermions while leptoquarks are bosons) and their
 2327 different interactions. Figure 5.14 shows typical cross-sections for single leptogluon production
 2328 at the LHeC, assuming Λ is equal to the leptogluon mass. It is estimated that, for example,
 2329 a sensitivity of to a compositeness scale of 200 TeV, at 3σ level can be achieved with LHeC
 2330 having $E_e = 70$ GeV and with 1 fb^{-1} . The mass reach for M_{e8} is 1.1 TeV for $\Lambda = 10$ TeV.

2331 As for leptoquarks, would leptogluons be discovered at the LHC, LHeC data would be of
 2332 highest value for the determination of the properties of this new particle.

2333 5.3 Excited leptons and other new heavy leptons

2334 The three-family structure and mass hierarchy of the known fermions is one of the most puzzling
 2335 characteristics of the Standard Model (SM) of particle physics. Attractive explanations are
 2336 provided by models assuming composite quarks and leptons [184]. The existence of excited
 2337 states of fermions (F^*) is a natural consequence of compositeness models. More generally,
 2338 various models predict the existence of fundamental new heavy leptons, which can have similar
 2339 experimental characteristics as excited leptons. They could, for example, be part of a fourth

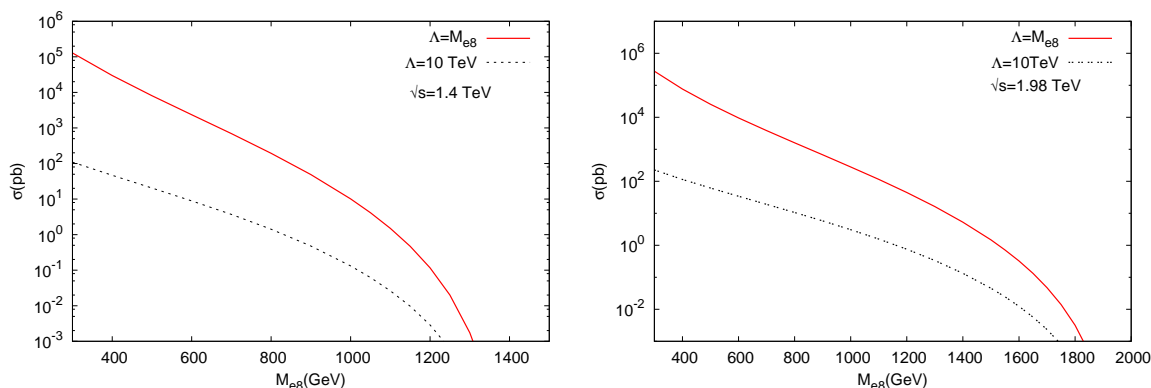


Figure 5.14: Resonant e_8 production at the LHeC, for two values of the center-of-mass energy.

2340 Standard model family. They arise also in Grand Unified Theories, and appear as colorless
 2341 fermions in technicolor models.

2342 New heavy leptons could be pair-produced at the LHC up to masses of $\mathcal{O}(300)$ GeV. As
 2343 for the case of leptoquarks, pp data from pair-production of new leptons may not allow for
 2344 a detailed study of their properties and couplings. Single production of new leptons is also
 2345 possible at the LHC, but is expected to have a larger cross-section at LHeC, via $e\gamma$ or eW
 2346 interactions. The case of excited electrons is considered in the following, with more details
 2347 being given in [185].

2348 Single production of excited leptons at the LHC (\sqrt{s} up to 14 TeV) may happen via the
 2349 reactions $pp \rightarrow e^\pm e^* \rightarrow e^+ e^- V$ and $pp \rightarrow \nu e^* + \nu^* e^\pm \rightarrow e^\pm \nu V$. The LHC should be able to tighten
 2350 considerably the current constraints on these possible new states and to probe excited lepton
 2351 masses of up to 1 TeV [186]. A sensitivity similar to the LHC could be reached at the ILC [187],
 2352 with different e^+e^- , $e\gamma$ and $\gamma\gamma$ collisions modes and a centre of mass energy of $\sqrt{s} \geq 500$ GeV.

2353 Recent results of searches for excited fermions [188–190] at HERA using all data collected
 2354 by the H1 detector have demonstrated that ep colliders are very competitive to pp or e^+e^-
 2355 colliders. Indeed limits set by HERA extend at high mass beyond the kinematic reach of LEP
 2356 searches [191, 192] and to higher compositeness scales than those obtained at the Tevatron [193]
 2357 using 1 fb^{-1} of data. Therefore a future LHeC machine, with a centre of mass energy of
 2358 $1 - 2$ TeV, much higher than at the HERA ep collider, would be ideal to search for and study
 2359 excited fermions. This has motivated us to examine excited electron production at a future
 2360 LHeC collider and compare it to the potential of other types of colliders at the TeV scale, the
 2361 LHC and the ILC.

2362

2363 5.3.1 Excited Fermion Models

2364 Compositeness models attempt to explain the hierarchy of masses in the SM by the existence
 2365 of a substructure within the fermions. Several of these models [194–196] predict excited states
 2366 of the known fermions, in which excited fermions are assumed to have spin 1/2 and isospin 1/2
 2367 in order to limit the number of parameters of the phenomenological study. They are expected
 2368 to be grouped into both left- and right-handed weak isodoublets with vector couplings. The

2369 existence of the right-handed doublets is required to protect the ordinary light fermions from
 2370 radiatively acquiring a large anomalous magnetic moment via F^*FV interaction (where V is a
 2371 γ, Z or W).

2372 Interactions between excited and ordinary fermions may be mediated by gauge bosons, as
 2373 described by the effective Lagrangian:

$$\mathcal{L}_{GM} = \frac{1}{2\Lambda} \bar{F}_R^* \sigma^{\mu\nu} \left[g f \frac{\vec{\tau}}{2} W_{\mu\nu} + g' f' \frac{Y}{2} B_{\mu\nu} + g_s f_s \frac{\vec{\lambda}}{2} G_{\mu\nu} \right] F_L + h.c., \quad (5.6)$$

2374 where Y is the weak hypercharge, g_s , $g = \frac{e}{\sin \theta_W}$ and $g' = \frac{e}{\cos \theta_W}$ are the strong and electroweak
 2375 gauge couplings, where e is the electric charge and θ_W is the weak mixing angle; $\vec{\lambda}$ and $\vec{\tau}$ are
 2376 the Gell-Mann matrices and the Pauli matrices, respectively. $G_{\mu\nu}$, $W_{\mu\nu}$ and $B_{\mu\nu}$ are the field
 2377 strength tensors describing the gluon, the $SU(2)$, and the $U(1)$ gauge fields. f_s , f and f'
 2378 are the coupling constants associated to each gauge field. They depend on the composite dynamics.
 2379 The parameter Λ has units of energy and can be regarded as the compositeness scale which
 2380 reflects the range of the new confinement force.

2381 In addition to gauge mediated (GM) interactions, novel composite dynamics may be visible
 2382 as contact interactions (CI) between excited fermions and ordinary fermions. Such interactions
 2383 can be described by an effective four-fermion Lagrangian [196]:

$$\mathcal{L}_{CI} = \frac{4\pi}{2\Lambda^2} j^\mu j_\mu, \quad (5.7)$$

2384 where Λ is here assumed to be the same parameter as in the gauge interaction Lagrangian (5.6)
 2385 and j_μ is the fermion current

$$j_\mu = \eta_L \bar{F}_L \gamma_\mu F_L + \eta'_L \bar{F}_L^* \gamma_\mu F_L^* + \eta''_L \bar{F}_L \gamma_\mu F_L + h.c. + (L \rightarrow R). \quad (5.8)$$

2386 By convention, the η factors of left-handed currents are set to ± 1 , while the factors of right-
 2387 handed currents are considered to be zero.

2389 5.3.2 Simulation and Results

2390 In the following study, excited electron (e^*) production and decays via both GM and CI are
 2391 considered. For GM interactions, the e^* production cross section under the assumption $f = -f'$
 2392 becomes much smaller than for $f = +f'$ and therefore only the case $f = +f'$ is studied.

2393 Considering pure gauge interactions, excited electrons could be produced in ep collisions at
 2394 the LHeC via a t -channel γ or Z bosons exchange. The Monte Carlo (MC) event generator
 2395 COMPOS [197] is used for the calculation of the e^* production cross section and the simulation
 2396 of signal events. The production cross sections of excited neutrinos at the LHeC is also shown
 2397 in figure 5.15. These results are obtained with the assumption $f = +f'$ and $M_{e^*} = \Lambda$ and are
 2398 compared to production cross section at HERA and also at the LHC [186]. In the mass range
 2399 accessible by the LHeC, the e^* production cross section is clearly much higher than at the LHC.

2400 Considering gauge and contact interactions together, formulae for the e^* production cross
 2401 section via CI and of the interference term between contact and gauge interactions have been
 2402 incorporated into COMPOS [188,198]. For simplicity, the relative strength of gauge and contact
 2403 interactions are fixed by setting the parameters f and f' of the gauge interaction to one.

2404 Comparisons of the e^* production cross section via only gauge interactions and via GM and
 2405 CI together, as a function of the e^* mass, are presented in figure 5.16(a) for $M_{e^*} = \Lambda$ and
 2406 figure 5.16(b) for $\Lambda = 10$ TeV, respectively. These results for the LHeC at $\sqrt{s} = 1.4$ TeV are
 2407 compared to the cross section at an LHC operating at $\sqrt{s} = 14$ TeV. These plots demonstrate
 2408 that at the LHeC the ratio of the contact and gauge cross sections (proportional to \hat{s}/Λ^4 and
 2409 $1/\Lambda^2$ respectively) decreases as Λ and M_{e^*} increase differently than for the LHC where contact
 2410 interactions may be an important source of production of excited electrons. In the mass range
 2411 accessed at the LHeC, e^* decays are dominated by gauge decays, provided that Λ is large
 2412 enough. Therefore, only gauge decays are looked for in the present study.

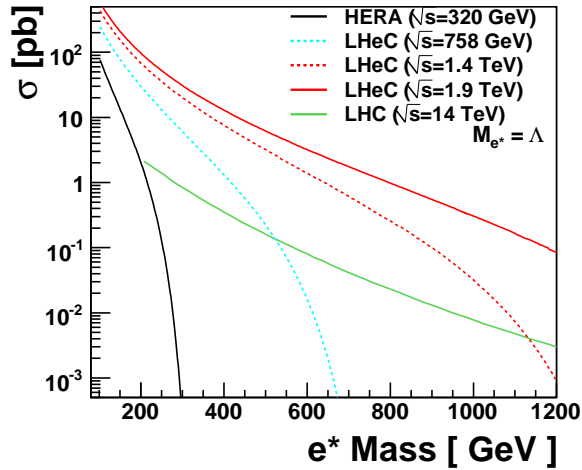


Figure 5.15: The e^* production cross section for different design scenarios of the LHeC electron-proton collider, compared to the cross sections at HERA and at the LHC.

2413 In order to estimate the sensitivity of excited electron searches at the LHeC, the e^* pro-
 2414 duction followed by its decay in the channel $e^* \rightarrow e\gamma$ is considered. This is the key channel
 2415 for excited electron searches in ep collisions as it provides a very clear signature and has a
 2416 large branching ratio. Only the main sources of backgrounds from SM processes are considered
 2417 here, namely neutral currents (NC DIS) and QED-Compton ($e\gamma$) events. Other possible SM
 2418 backgrounds are negligible. The MC event generator WABGEN [199] is used to generate these
 2419 background events. Figure 5.17 compares the e^* production cross section to the total cross
 2420 section of SM backgrounds. Background events dominate in the low e^* mass region. Hence to
 2421 enhance the signal, candidate events are selected with two isolated electromagnetic clusters with
 2422 a polar angle between 5° and 145° and transverse energies greater than 15 GeV and 10 GeV,
 2423 respectively.

2424 To translate the results into exclusion limits, expected upper limits on the coupling f/Λ are
 2425 derived at 95% Confidence Level (CL) as a function of excited electron masses.

2426 In case of gauge interaction, the attainable limits at the LHeC on the ratio f/Λ are shown in
 2427 figure 5.18 for excited electrons, for the hypothesis $f = +f'$ and different integrated luminosities
 2428 $L = 10 \text{ fb}^{-1}$ for \sqrt{s} up to 1.4 TeV and $L = 1 \text{ fb}^{-1}$ for \sqrt{s} up to 2 TeV. They are compared to
 2429 the upper limits obtained at LEP [191,192], HERA [188] and also to the expected sensitivity of

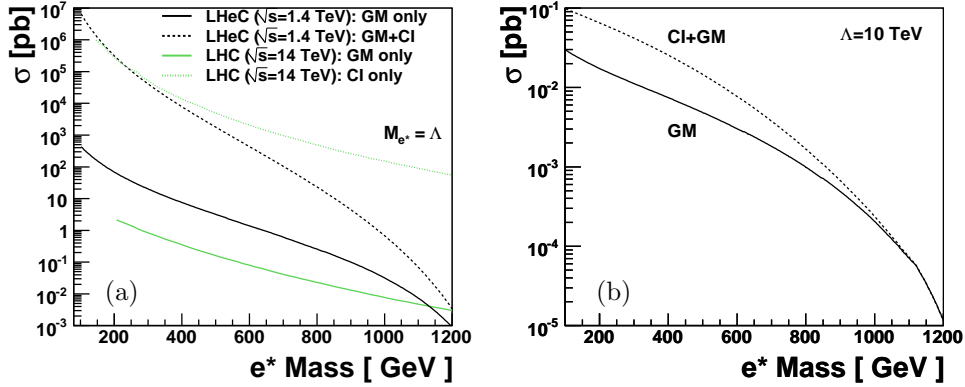


Figure 5.16: Comparison of the e^* production cross section via gauge and contact interactions. In figure (a), the results for the LHeC ($\sqrt{s} = 1.4$ TeV) and for the LHC ($\sqrt{s} = 14$ TeV) are compared. Production cross sections for a fixed Λ value of 10 TeV are shown in figure (b) for the LHeC.

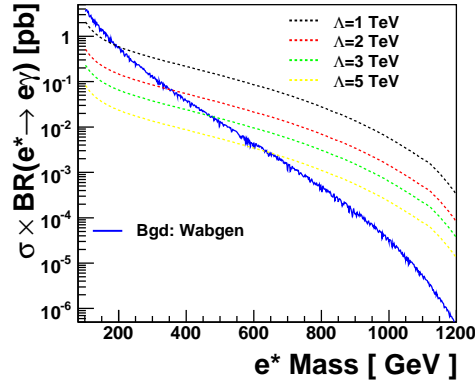


Figure 5.17: Electromagnetic production cross section for e^* ($e^* \rightarrow e\gamma$) for different values of Λ .

2430 the LHC [186]. Considering the assumption $f/\Lambda = 1/M_{e^*}$ and $f = +f'$, excited electrons with
 2431 masses up to 1.2(1.5) TeV, corresponding to centre of mass energies of $\sqrt{s} = 1.4(1.9)$ TeV of
 2432 the LHeC, are excluded. Under the same assumptions, LHC ($\sqrt{s} = 14$ TeV) could exclude e^*
 2433 masses up to 1.2 TeV for an integrated luminosity of 100 fb^{-1} . In the accessible mass range
 2434 of LHeC, the LHeC would be able to probe smaller values of the coupling f/Λ than the LHC.
 2435 Similarly to leptoquarks (see section 5.2), if an excited electron is observed at the LHC with
 2436 a mass of $\mathcal{O}(1 \text{ TeV})$, the LHeC would be better suited to study the properties of this particle,
 2437 thanks to the larger single production cross-section (see Fig. 5.15).

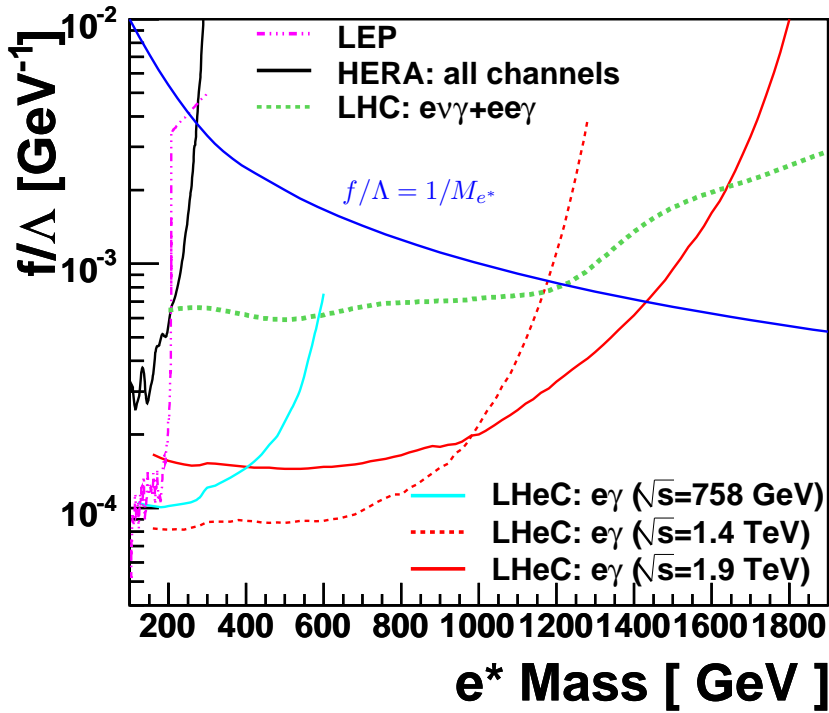


Figure 5.18: Sensitivity to excited electron searches for different design scenarios of the LHeC electron-proton collider, compared to the expected sensitivity of the LHC ($\sqrt{s} = 14$ TeV, $L = 100 \text{ fb}^{-1}$). Different integrated luminosities at the LHeC ($L = 10 \text{ fb}^{-1}$ for \sqrt{s} up to 1.4 TeV and $L = 1 \text{ fb}^{-1}$ for \sqrt{s} up to 2 TeV) are assumed. The curves present the expected exclusion limits on the coupling f/Λ at 95% CL as a function of the mass of the excited electron with the assumption $f = +f'$. Areas above the curves are excluded. Present experimental limits obtained at LEP and HERA are also represented.

2438 **5.3.3 New leptons from a fourth generation**

2439 New leptons from a fourth generation (l_4, ν_4) may have anomalous couplings to the standard
 2440 leptons, as given by the following effective Lagrangian:

$$\begin{aligned} \mathcal{L}_{nc} &= \left(\frac{\kappa_\gamma^{\ell_4 \ell_i}}{\Lambda} \right) e_\ell g_e \bar{\ell}_4 \sigma_{\mu\nu} \ell_i F^{\mu\nu} \\ &+ \left(\frac{\kappa_Z^{\ell_4 \ell_i}}{2\Lambda} \right) g_Z \bar{\ell}_4 \sigma_{\mu\nu} \ell_i Z^{\mu\nu} + \left(\frac{g_Z}{2} \right) \bar{\nu}_i \frac{i}{2\Lambda} \kappa_Z^{\nu_4 \nu_i} \sigma_{\mu\nu} q^\nu P_L \nu_4 Z^\mu + h.c. \\ \mathcal{L}_{cc} &= \left(\frac{g_W}{\sqrt{2}} \right) \bar{l}_i \left[\frac{i}{2\Lambda} \kappa_W^{\nu_4 l_i} \sigma_{\mu\nu} q^\nu \right] P_L \nu_4 W^\mu + h.c. \end{aligned}$$

2441 In that case, the single production of l_4 and ν_4 would be similar to that of excited electrons
 2442 and neutrinos. For a study of the properties and couplings of such a new lepton, an ep machine
 2443 would offer the same advantages as presented above in the case of excited electrons. A study
 2444 of the processes $ep \rightarrow l_4 X \rightarrow Ze(\gamma\mu)X$ and $ep \rightarrow \nu_4 X \rightarrow W(e, \mu)X$ at the LHeC is presented
 2445 in [200]. For example, for an anomalous coupling $\kappa/\Lambda = 1 \text{ TeV}^{-1}$, LHeC would be able to cover
 2446 l_4 masses up to $\sim 900 \text{ GeV}$.

2447 **5.4 New physics in boson-quark interactions**

2448 Several extensions of the Standard Model predict new phenomena that would be directly observ-
 2449 able in boson-quark interactions. For example, the top quark may have anomalous couplings to
 2450 gauge bosons, leading to Flavour Changing Neutral Current (FCNC) vertices $tq\gamma$, where q is a
 2451 light quark. Similarly, excited quarks (q^*) or quarks from a fourth generation (Q) could be pro-
 2452 duced via $\gamma q \rightarrow q^*$ or $\gamma q \rightarrow Q$. The transitions $\gamma q \rightarrow t, q^*, Q$ can be studied in ep collisions at
 2453 the LHeC, but a much larger cross-section would be achieved at a γp collider, due to the much
 2454 larger γp centre-of-mass energy. The single production of q^*, Q or of a top quark via anomalous
 2455 couplings is also possible at the LHC, but it involves an anomalous coupling together with an
 2456 electroweak coupling and the main background processes involve the strong interaction. The
 2457 signal to background ratio will thus be much more challenging at the LHC, and any constraints
 2458 on anomalous couplings would therefore be obtained from the decay channels of these quarks.
 2459 The example of anomalous single top production is detailed in the following.

2460 **5.4.1 An LHeC-based γp collider**

2461 The possibility to operate the LHeC as a γp collider is described in 8.1.6. If the electron beam
 2462 is accelerated by a linac, it can be converted into a beam of high energy real photons, by
 2463 backscattering off a laser pulse. The energy of these photons would be about 80% of the energy
 2464 of the initial electrons.

2465 **5.4.2 Anomalous Single Top Production at the LHeC Based γp Col-
 2466 lider**

2467 The top quark is expected to be most sensitive to physics beyond the Standard Model (BSM)
 2468 because it is the heaviest available particle of the Standard Model (SM). A precise measurement

2469 of the couplings between SM bosons and fermions provides a powerful tool for the search of
 2470 BSM physics allowing a possible detection of deviations from SM predictions [201]. Anomalous
 2471 tqV ($V = g, \gamma, Z$ and $q = u, c$) couplings can be generated through dynamical mass generation
 2472 [37], sensitive to the mechanism of dynamical symmetry breaking. They have a similar
 2473 chiral structure as the mass terms, and the presence of these couplings would be interpreted
 2474 as signals of new interactions. This motivates the study of top quark flavour changing neutral
 2475 current (FCNC) couplings at present and future colliders.

2476 Current experimental constraints at 95% C.L. on the anomalous top quark couplings are [202]:
 2477 $BR(t \rightarrow \gamma u) < 0.0132$ and $BR(t \rightarrow \gamma u) < 0.0059$ from HERA; $BR(t \rightarrow \gamma q) < 0.041$ from LEP
 2478 and $BR(t \rightarrow q\gamma) < 0.032$ from CDF. The HERA has much higher sensitivity to $u\gamma t$ than $c\gamma t$
 2479 due to more favorable parton density: the best limit is obtained from the ZEUS experiment.

2480 The top quarks will be produced in large numbers at the Large Hadron Collider (LHC),
 2481 allowing great precision measurement of the coupling. For a luminosity of 1 fb^{-1} (100 fb^{-1})
 2482 the expected ATLAS sensitivity to the top quark FCNC decay is $BR(t \rightarrow q\gamma) \sim 10^{-3}$ (10^{-4})
 2483 [203, 204]. The production of top quarks by FCNC interactions at hadron colliders has been
 2484 studied in [205–217], e^+e^- colliders in [37, 218–221] and lepton-hadron collider in [37, 222–224].
 2485 LHC will give an opportunity to probe $BR(t \rightarrow u\gamma)$ down to 5×10^{-3} [225]; ILC/CLIC has
 2486 the potential to probe $BR(t \rightarrow q\gamma)$ down to 10^{-5} [226].

2487 A linac-ring type collider presents the sole realistic way to TeV scale in γp collisions [227–
 2488 232]. Recently this opportunity has been widely discussed in the framework of the LHeC
 2489 project [233]. Two stages of the LHeC were considered: QCD Explorer ($E_e = 50 - 100 \text{ GeV}$)
 2490 and Energy Frontier ($E_e > 250 \text{ GeV}$). The potential of the LHeC as a γp collider to search
 2491 for anomalous top quark interactions has been investigated [234]. The effective Lagrangian
 2492 involving anomalous $t\gamma q$ ($q = u, c$) interactions is given by [225].

$$L = -g_e \sum_{q=u,c} Q_q \frac{\kappa_q}{\Lambda} \bar{t} \sigma^{\mu\nu} (f_q + h_q \gamma_5) q A_{\mu\nu} + h.c. \quad (5.9)$$

2493 where $A_{\mu\nu}$ is the usual photon field tensor, $\sigma_{\mu\nu} = \frac{i}{2}(\gamma_\mu \gamma_\nu - \gamma_\nu \gamma_\mu)$, Q_q is the quark charge, in
 2494 general f_q and h_q are complex numbers, g_e is the electromagnetic coupling constant, κ_q is a real
 2495 and positive anomalous FCNC coupling constant and Λ is the new physics scale. The neutral
 2496 current magnitudes in the Lagrangian satisfy $|(f_q)^2 + (h_q)^2| = 1$ for each term. The anomalous
 2497 decay width can be calculated as

$$\Gamma(t \rightarrow q\gamma) = \left(\frac{\kappa_q}{\Lambda}\right)^2 \frac{2}{9} \alpha_{em} m_t^3 \quad (5.10)$$

2498 Taking $m_t = 173 \text{ GeV}$ and $\alpha_{em} = 0.0079$, the anomalous decay width $\approx 9 \text{ MeV}$ for $\kappa_q/\Lambda = 1$
 2499 TeV^{-1} while the SM decay width is about 1.5 GeV .

2500 For numerical calculations anomalous interaction vertices are implemented into the CalcHEP
 2501 package [175] using the CTEQ6M [114] parton distribution functions. The Feynman diagrams
 2502 for the subprocess $\gamma q \rightarrow W^+ b$, where $q = u, c$ are shown in Fig. 5.19. The first three diagrams
 2503 correspond to irreducible backgrounds and the last one to the signal. The main background
 2504 comes from associated production of W boson and the light jets.

2505 The differential cross sections for the final state jets are given in Fig. 5.20 ($\kappa/\Lambda = 0.04$
 2506 TeV^{-1}) for $E_e = 70 \text{ GeV}$ and $E_p = 7000 \text{ GeV}$ assuming $\kappa_u = \kappa_c = \kappa$. It is seen that the
 2507 transverse momentum distribution of the signal has a peak around 70 GeV .

2508 Here, b-tagging efficiency is assumed to be 60% and the mistagging factors for light (u, d, s)
 2509 and c quarks are taken as 0.01 and 0.1, respectively. A p_T cut reduce the signal (by $\sim 30\%$

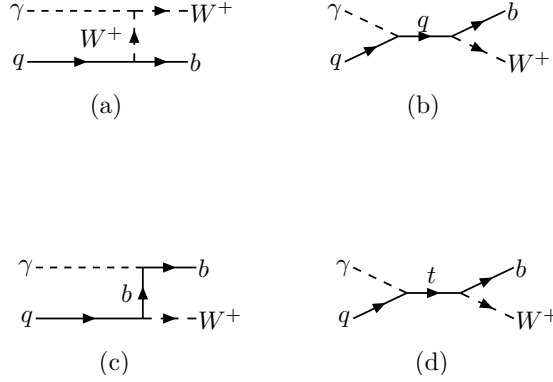


Figure 5.19: Feynman diagrams for $\gamma q \rightarrow W^+ b$, where $q = u, c$.

2510 for $p_T > 50$ GeV), whereas the background is essentially suppressed (by a factor 4-6) . In order
 2511 to improve the signal to background ratio further, one can apply a cut on the invariant mass of
 2512 $W + jet$ around top mass. In Table 5.3, the cross sections for signal and background processes
 2513 are given after having applied both a p_T and an invariant mass cuts ($M_{Wb} = 150 - 200$ GeV).

Table 5.3: The cross sections (in pb) according to the p_T cut and invariant mass interval ($M_{Wb} = 150 - 200$ GeV) for the signal and background at γp collider based on the LHeC with $E_e = 70$ GeV and $E_p = 7000$ GeV.

$\kappa/\Lambda = 0.01 \text{ TeV}^{-1}$	$p_T > 20 \text{ GeV}$	$p_T > 40 \text{ GeV}$	$p_T > 50 \text{ GeV}$
Signal	8.86×10^{-3}	7.54×10^{-3}	6.39×10^{-3}
Background: $W^+ b$	1.73×10^{-3}	1.12×10^{-3}	7.69×10^{-4}
Background: $W^+ c$	3.48×10^{-1}	2.30×10^{-1}	1.63×10^{-1}
Background: $W^+ jet$	1.39×10^{-1}	9.11×10^{-2}	6.38×10^{-2}

2514 In order to calculate the statistical significance (SS) we use following formula [235] :

$$SS = \sqrt{2 \left[(S + B) \ln\left(1 + \frac{S}{B}\right) - S \right]} \quad (5.11)$$

2515 where S and B are the numbers of signal and background events, respectively. Results are
 2516 presented in Table 5.4 for different κ/Λ and luminosity values. It is seen that even with 2 fb^{-1}
 2517 the LHeC based γp collider will provide 5σ discovery for $\kappa/\Lambda = 0.02 \text{ TeV}^{-1}$.

Table 5.4: The signal significance (SS) for different values of κ/Λ and integral luminosity for $E_e = 70$ GeV and $E_p = 7000$ GeV (the numbers in parenthesis correspond to $E_e = 140$ GeV).

SS	$L = 2 \text{ fb}^{-1}$	$L = 10 \text{ fb}^{-1}$
$\kappa/\Lambda = 0.01 \text{ TeV}^{-1}$	2.58 (2.88)	5.79 (6.47)
$\kappa/\Lambda = 0.02 \text{ TeV}^{-1}$	5.26 (5.92)	11.78 (13.25)

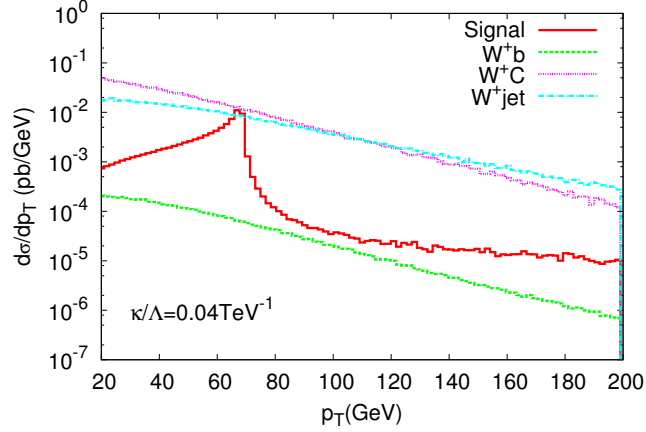


Figure 5.20: The transverse momentum distribution of the final state jet for the signal and background processes. The differential cross section includes the b -tagging efficiency and the rejection factors for the light jets. The center of mass energy $\sqrt{s_{ep}} = 1.4$ TeV and $\kappa/\Lambda = 0.04$ TeV^{-1} .

2518 Up to now, we have assumed $\kappa_u = \kappa_c = \kappa$. However, it would be interesting to analyze
 2519 the case $\kappa_u \neq \kappa_c$. Indeed, at HERA, valence u -quarks dominate whereas at LHeC energies the
 2520 c -quark and u -quark contributions become comparable. Therefore, the sensitivity to κ_c will be
 2521 enhanced at LHeC comparing to HERA. In Fig. 5.21 contour plots for anomalous couplings in
 2522 $\kappa_u - \kappa_c$ plane are presented. For this purpose, a χ^2 analysis was performed with

$$\chi^2 = \sum_{i=1}^N \left(\frac{\sigma_{S+B}^i - \sigma_B^i}{\Delta\sigma_B^i} \right)^2 \quad (5.12)$$

2523 where σ_B^i is the cross-section for the SM background in the i^{th} bin, including both b -jet and light-
 2524 jet contributions with their corresponding efficiency factors. In the σ_{S+B} calculations, we take
 2525 into account the different values for κ_u and κ_c as well as the signal-background interference.
 2526 Figs. 5.20-5.21 show that the sensitivity is enhanced by a factor of 1.5 when the luminosity
 2527 changes from 2 fb^{-1} to 10 fb^{-1} . Concerning the energy upgrade, increasing electron energy
 2528 from 70 GeV to 140 GeV results in 20% improvement for κ_c [234]. Increasing the electron energy
 2529 further (energy frontier ep collider) does not give an essential improvement in the sensitivity to
 2530 anomalous couplings [236].

2531 Table 5.4 shows that a sensitivity to anomalous coupling κ/Λ down to 0.01 TeV^{-1} could
 2532 be reached. Noting that the value of $\kappa/\Lambda = 0.01 \text{ TeV}^{-1}$ corresponds to $BR(t \rightarrow \gamma u) \approx$
 2533 2×10^{-6} which is two orders smaller than the LHC reach with 100 fb^{-1} , it is obvious that
 2534 even an upgraded LHC will not be competitive with LHeC based γp collider in the search for
 2535 anomalous $t\gamma q$ interactions. Different extensions of the SM (SUSY, technicolor, little Higgs,
 2536 extra dimensions etc.) predict branching ratio $BR(t \rightarrow \gamma q) = O(10^{-5})$, hence the LHeC will
 2537 provide an opportunity to probe these models. The top quark could provide very important
 2538 information for the Standard Model extensions due to its large mass close to the electroweak
 2539 symmetry breaking scale.

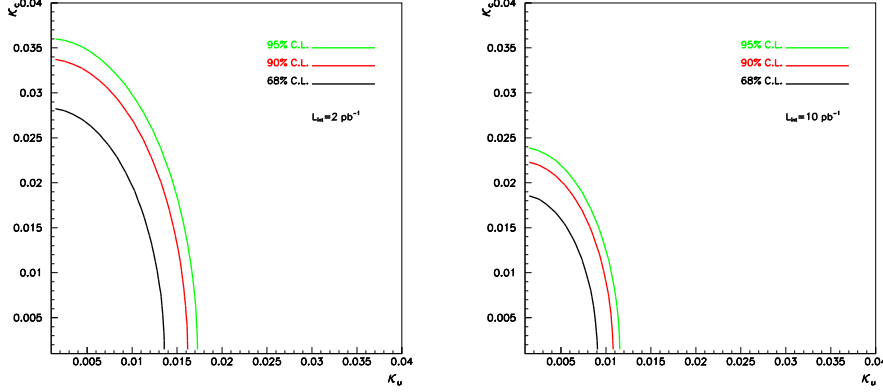


Figure 5.21: Contour plot for the anomalous couplings reachable at the LHeC based γp collider with the ep center of mass energy $\sqrt{s_{ep}} = 1.4$ TeV and integrated luminosity of $L_{int} = 2 \text{ fb}^{-1}$ (left) or $L_{int} = 10 \text{ fb}^{-1}$ (right)

5.4.3 Excited quarks in γp collisions at LHeC

Excited quarks will have vertices with SM quark and gauge bosons (photon, gluon, Z or W bosons). They can be produced at ep and γp colliders via quark photon fusion. Interactions involving excited quark are described by the Lagrangian of eq. 5.6 (where F is now a quark q)

A sizeable f_s coupling would allow for resonant q^* production at the LHC via quark-gluon fusion. In that case, the LHC would offer a large discovery potential for excited quarks and would be well suited to study the properties and couplings of these new quarks. However, if the coupling of excited quarks to gq happens to be suppressed, the LHC would mainly produce q^* via pair-production and would have little sensitivity to couplings f/Λ or f'/Λ . Such couplings would be better studied, or probed down to much lower values, via single-production of q^* at the LHeC. A study of the LHeC potential for excited quarks is presented in [237]. An example of the 3σ discovery reach, assuming $f = f' = f_s$ and setting Λ to be equal to the q^* mass, is given in Fig. 5.22. Both decays $q^* \rightarrow q\gamma$ and $q^* \rightarrow qg$ have been considered here.

5.4.4 Quarks from a fourth generation at LHeC

The case of fourth generation quarks with magnetic FCNC interactions to gauge bosons and standard quarks,

$$\mathcal{L} = \left(\frac{\kappa_\gamma^{q_4 q_i}}{\Lambda} \right) e_q g_e \bar{q}_4 \sigma_{\mu\nu} q_i F^{\mu\nu} + \left(\frac{\kappa_Z^{q_4 q_i}}{2\Lambda} \right) g_Z \bar{q}_4 \sigma_{\mu\nu} q_i Z^{\mu\nu} + \left(\frac{\kappa_g^{q_4 q_i}}{\Lambda} \right) g_s \bar{q}_4 \sigma_{\mu\nu} T^a q_i G_a^{\mu\nu} + h.c. \quad (5.13)$$

is very similar to that of excited quarks. A γp collider based on LHeC would have a better sensitivity than LHC to anomalous couplings κ_γ and κ_Z . A detailed study is presented in [200] and example results are shown in Fig. 5.23. These figures also show the clear advantage of a γp collider compared to an ep collider, for the study of new physics in γq interactions.

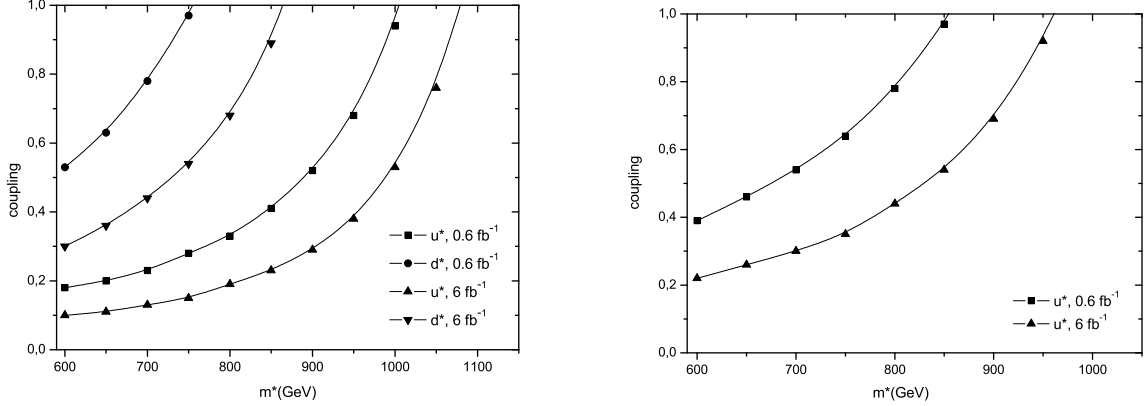


Figure 5.22: Observation reach at 3σ for coupling and excited quark mass at a γp collider with $\sqrt{s} = 1.27$ TeV from an analysis of (left) the jj channel and (right) the γj channel.

2560 5.4.5 Diquarks at LHeC

2561 The case of diquark production at LHeC has been studied in [238]. The production cross-section
 2562 can be sizeable at a high energy ep machine, especially when operated as a γp collider. The
 2563 measurement of the $\gamma p \rightarrow DQ + X$ cross-section, for a diquark DQ of known mass and known
 2564 coupling to the diquark pair³ would provide a measurement of the electric charge of the diquark.
 2565 It would thus be complementary to the pp data, which offer no simple way to access the DQ
 2566 electric charge. However, the diquark masses and couplings that could be accessible at LHeC
 2567 appear to be already excluded by the recent search for dijet resonances at the LHC [239].

2568 5.4.6 Quarks from a fourth generation in Wq interactions

2569 In case fourth generation quarks do not have anomalous interactions as in Eq. 5.13, they (or
 2570 vector-like quarks coupling to light generations [240,241]) could be produced in ep collisions by
 2571 Wq interactions provided that the V_{Qq} elements of the extended CKM matrix are not too small,
 2572 via the usual vector WqQ interactions. An example of the sensitivity that could be reached at
 2573 LHeC is presented in [242], assuming some values for the V_{Qq} parameters. Measurements of
 2574 single Q production at LHeC would provide complementary information to the LHC data, that
 2575 could help in determining the extended CKM matrix.

2576 5.5 Sensitivity to a Higgs boson

2577 Understanding the mechanism of electroweak symmetry breaking is a key goal of the LHC
 2578 physics programme. In the SM, the symmetry breaking is realized via a scalar field (the Higgs

³The LHC would observe diquark as di-jet resonances, and could easily determine its mass, width and coupling to the quark pair.

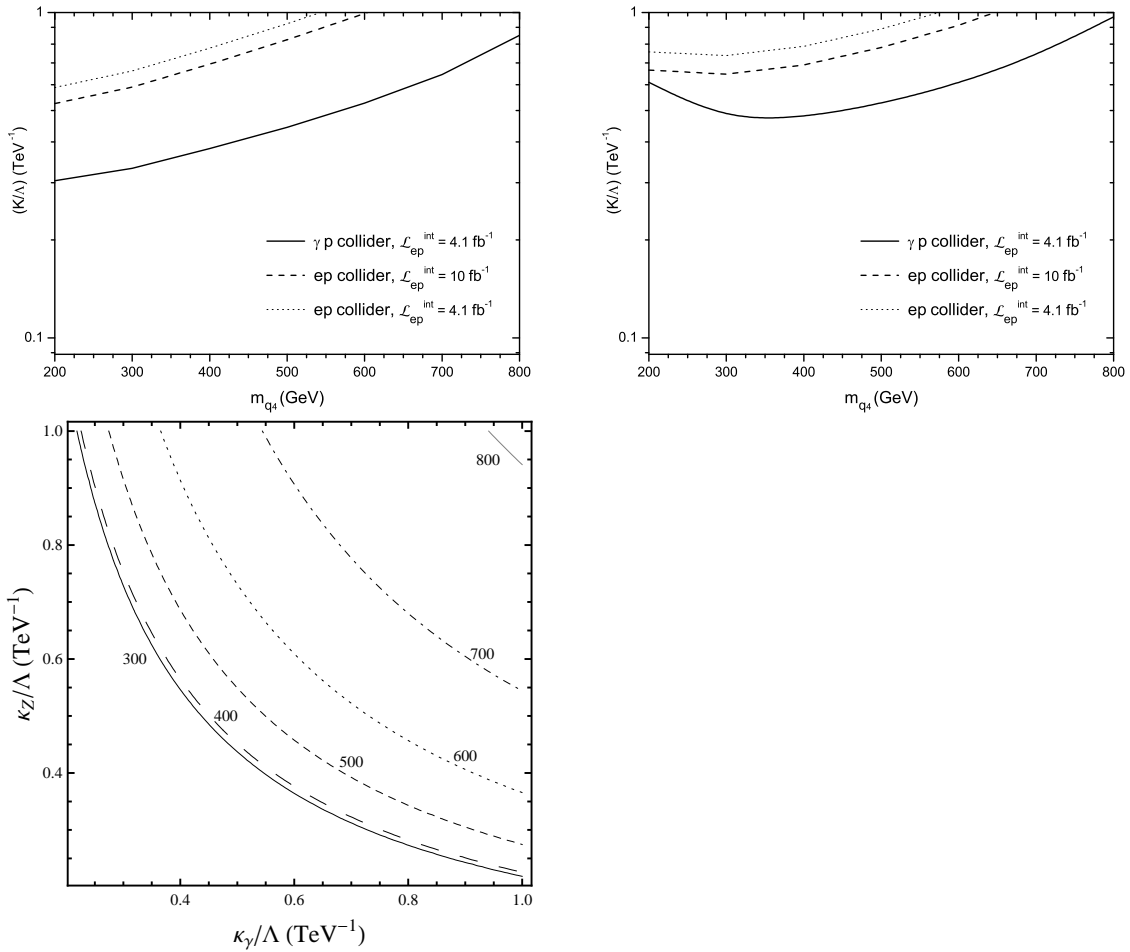


Figure 5.23: The achievable values of the anomalous coupling strength at ep and γp colliders for a) $q_4 \rightarrow \gamma q$ anomalous process and (b) $q_4 \rightarrow Zq$ anomalous process as a function of the q_4 mass; (c) the reachable values of anomalous photon and Z couplings with $L_{int} = 4.1 \text{ fb}^{-1}$.

2579 field) which, at the minimum of the potential, develops a non-zero vacuum expectation value.
 2580 The breaking of the $SU(2)_L \times U(1)_Y$ symmetry gives mass to the electroweak gauge bosons via
 2581 the Higgs mechanism while the fermions obtain their mass via Yukawa couplings with the Higgs
 2582 field. The LHC experiments should be able to discover a Higgs boson within the full allowable
 2583 mass range, with an integrated luminosity of less than 10 fb^{-1} . Following its discovery, it will
 2584 be crucial to measure the couplings of this Higgs boson to the SM particles, in particular to the
 2585 fermions, in order to:

- 2586 • establish that the Higgs field is indeed accounting for the fermion masses, via Yukawa
 2587 couplings $y_f H \bar{f} f$;
- 2588 • disentangle between the SM and (some of) its extensions. For example, despite the
 2589 richer content of the Higgs sector in the Minimal Supersymmetric Standard Model, only

2590 the light SUSY Higgs boson h would be observable at the LHC in certain regions of
 2591 parameter space. Its properties are very similar to those of the SM Higgs H , and precise
 2592 measurements of ratios $BR(\Phi \rightarrow VV)/BR(\Phi \rightarrow f\bar{f})$ will be essential in determining
 2593 whether or not the observed boson, Φ , is the SM higgs scalar.

2594 Electroweak precision measurements strongly suggest that the SM Higgs boson should be light,
 2595 in which case it would decay into a $b\bar{b}$ pair with a branching ratio of $\sim 70\%$, but a measurement
 2596 of the $Hb\bar{b}$ coupling will be very challenging at the LHC [203,235,243]. Indeed, the observation
 2597 of $H \rightarrow b\bar{b}$ in the inclusive production mode is made very difficult by the huge QCD background,
 2598 although a possible search channel would be associated WH and ZH production, with highly
 2599 boosted Higgs, leading to a high mass jet with substructure [244]. The observability of the
 2600 signal in the $t\bar{t}H$ production mode also suffers from a large background, including background
 2601 of combinatorics origin, and from experimental systematic uncertainties.

2602 The signal $H \rightarrow b\bar{b}$ may be observed in the exclusive production mode, thanks to the much
 2603 cleaner environment in a diffractive process. However, the production cross-section in this mode
 2604 suffers from large theoretical uncertainties, such that this measurement, if feasible at all, would
 2605 not translate into a precise measurement of the $Hb\bar{b}$ coupling.

2606 At the LHeC, a light Higgs boson could be produced via WW or ZZ fusion with a sizeable
 2607 cross-section. This section focusses on the observability of the signal $ep \rightarrow H + X \rightarrow b\bar{b} + X$ at
 2608 LHeC, which may be the first observation of the $H \rightarrow b\bar{b}$ decay.

2609 5.5.1 Higgs production at LHeC

2610 In ep collisions, the Higgs boson could be produced in neutral current (NC) interactions via
 2611 the ZZH coupling, and in charged current (CC) interactions via the WWH coupling. The
 2612 corresponding diagrams are shown in Fig. 5.24, and the production cross-sections, as a function
 2613 of the Higgs mass, is displayed in Fig. 5.25. The WWH production largely dominates the
 2614 total cross-section. As is the case for the inclusive CC DIS interactions, the cross-section is
 2615 much larger in e^-p collisions than in e^+p collisions, due to the more favorable density of the
 2616 valence quark that is involved (u in e^-p , d in e^+p), and to the more favorable helicity factors.
 2617 Table 5.5 shows the Higgs production cross-section (at leading order) via CC interactions in e^-p
 2618 collisions, for various values of the Higgs mass and three example values of the electron beam
 2619 energy. The scale dependency of these leading order estimate is of $\mathcal{O}(10\%)$. Next-to-leading
 2620 order corrections were calculated in [245,246]. They are small, but can affect within $\mathcal{O}(20\%)$
 2621 the shape of some kinematic distributions.

M_H in GeV :	100	120	160	200	240	280
$E_e = 50$ GeV	102	81	50	32	20	12
$E_e = 100$ GeV	201	165	113	79	55	39
$E_e = 150$ GeV	286	239	170	123	90	67

Table 5.5: Production cross-section in fb of a SM Higgs boson via charged current interactions in e^-p collisions, for three example values of the electron beam energy.

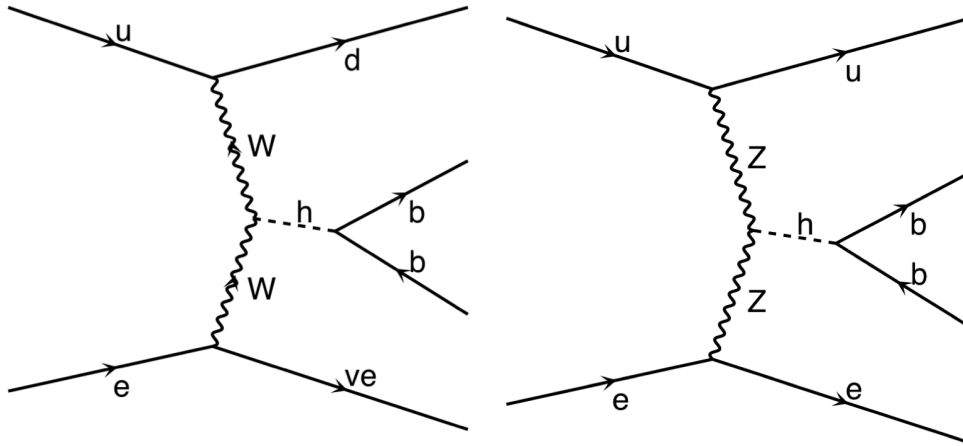


Figure 5.24: Feynman diagrams for CC(left) and NC(right) Higgs production at the LHeC.

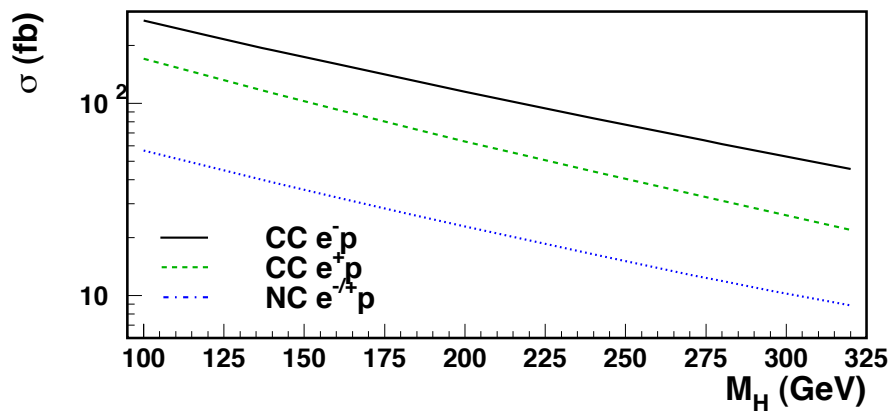


Figure 5.25: Production cross-section of a SM Higgs boson in ep collision with $E_e=150$ GeV and $E_p=7$ TeV, as a function of the Higgs mass.

2622 **5.5.2 Signal and background Monte-Carlo samples**

2623 The dominating source of background at large missing transverse energy is coming from multi-
 2624 jet production in CC DIS interactions. In particular, a good rejection of the background
 2625 coming from single top production ($e^-b \rightarrow \nu t$), where the top decays hadronically, puts severe
 2626 constraints on the acceptance and the resolution of the detector, as will be seen below. The
 2627 background due to multijet production in NC interactions is also considered.

2628 MadGraph [247] has been used to generate SM Higgs production, CC and NC DIS back-
 2629 ground events. Calculations of cross-sections and generation of final states of outgoing particles
 2630 are performed by MadGraph, given the beam parameters, considering all possible tree-level
 2631 Feynman diagrams in the SM. In the case of NC, since the cross section is very high, diverging
 2632 at low scattering angle, only processes producing two or more b quarks were generated in order
 2633 to have sufficient MC statistics. By artificially increasing the mistag probability, it was possible
 2634 to verify that, after the selection, essentially all the remaining NC background is indeed due to
 2635 events with two truly b-quark jets in the final state. Fragmentation and hadronization processes
 2636 were simulated by PYTHIA [113] with custom modifications to apply for ep collisions. Finally,
 2637 particles were passed through a generic detector using the PGS [248] fast detector simulation
 2638 tool. We assumed tracking coverage of $|\eta| < 3$ and calorimeter coverage of $|\eta| < 5$ with elec-
 2639 tromagnetic calorimeter resolution of $5\%/\sqrt{E(\text{GeV})}$ (plus 1% of constant term) and hadronic
 2640 calorimeter resolution of $60\%/\sqrt{E(\text{GeV})}$. Jets were reconstructed by a cone algorithm with a
 2641 cone size of $\Delta R = 0.7$. The efficiency of b-flavor tagging was assumed to be 60% and flat within
 2642 the calorimeter coverage, whereas mistagging probabilities of 10% and 1% for charm-quark jets
 2643 and for light-quark jets, respectively, were taken into account.

2644 We set 150 GeV of electron beam energy with 7 TeV of proton beam energy as the reference
 2645 beam configuration and assumed 120 GeV of SM Higgs boson mass in the MC simulation study.
 2646 The results were compared with those with a different beam energy and Higgs mass.

2647 **5.5.3 Observability of the signal**

2648 The following selection criteria were applied, based on observable variables generated by the
 2649 PGS detector simulation, to distinguish $H \rightarrow b\bar{b}$ from the CC and NC DIS backgrounds.

2650 **• cut (1): Primary cuts**

- 2651 – Exclude electron-tagged events
- 2652 – $E_{T,miss} > 20 \text{ GeV}$
- 2653 – $N_{jet}(P_{T,jet} > 20 \text{ GeV}) \geq 3$
- 2654 – $E_{T,total} > 100 \text{ GeV}$
- 2655 – $y_{JB} < 0.9$, where $y_{JB} = \Sigma(E - p_z)/2E_e$
- 2656 – $Q_{JB}^2 > 400 \text{ GeV}$, where $Q_{JB}^2 = E_{T,miss}^2/(1 - y_{JB})$

2657 **• cut (2): b-tag requirement**

- 2658 – $N_{b-jet}(P_{T,jet} > 20 \text{ GeV}) \geq 2$, where b-jet means a b-tagged jet

2659 **• cut (3): Higgs invariant mass cut**

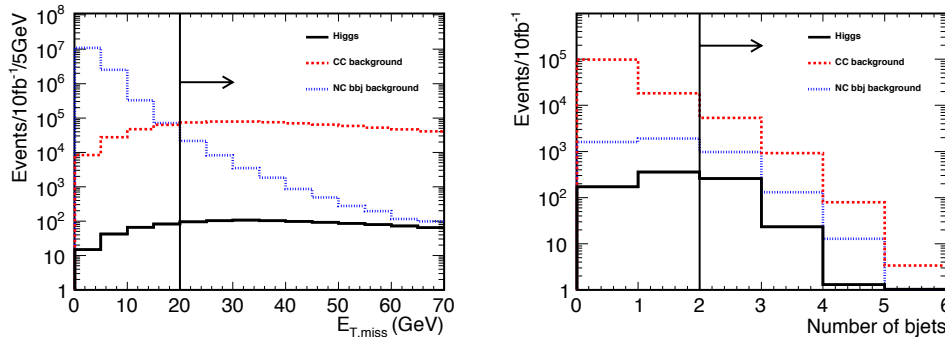


Figure 5.26: Missing E_T (left) and number of b-tagged jets (right). Solid (black), dashed (red) and dotted (blue) histograms show $H \rightarrow b\bar{b}$, CC and NC DIS background, respectively. The right plot is for events passing cut (1) in the text.

2660 – $90 < M_H < 120$ GeV; due to the energy carried by the neutrino from b decays, the
 2661 mass peaks are slightly lower than the true Higgs mass

2662 Fig. 5.26 shows the missing E_T and number of b-tagged jets for $H \rightarrow b\bar{b}$ events together with
 2663 the CC and NC DIS background. The NC background is strongly suppressed by the missing
 2664 E_T cut and electron-tag requirement. We required at least two b-tagged jets, and reconstructed
 2665 the Higgs invariant mass using the two b-tagged jets with lowest and second lowest η . After
 2666 cuts (1) + (2) + (3) were applied, 44.4% of the remaining CC background was due to single
 2667 top production. The following cuts were further applied.

2668 • **cut (4): rejection of single top production** Single top events result in a final state
 2669 with two b-jets and a W decaying into two light-quark jets. The following cuts were found
 2670 to be efficient in suppressing this background.

2671 – $M_{jjj,top} > 250$ GeV, where the three-jet invariant mass ($M_{jjj,top}$) was reconstructed
 2672 from two b-jets with the lowest η and any third jet with the lowest η regardless of
 2673 b-tag

2674 – $M_{jj,W} > 130$ GeV, where di-jet invariant mass ($M_{jj,W}$) was reconstructed from one
 2675 b-jet with the lowest η and any second jet with the lowest η regardless of b-tag but
 2676 excluding the second lowest η b-jet

2677 • **cut (5): forward jet tagging**

2678 – $\eta_{jet} > 2$ for the lowest- η jet excluding the two b-jets

2679 Fig. 5.27 shows the reconstructed three-jet ($M_{jjj,top}$) and di-jet ($M_{jj,W}$) invariant masses after
 2680 cuts (1) and (2) are applied. It is seen that, for CC background, the former peaks at the top
 2681 mass and the latter peaks at the W mass. The last cut is motivated by the fact that the jet
 2682 from light quark participating in the CC reaction for the signal is kinematically boosted to
 2683 forward rapidity (in the proton beam direction), as shown in Fig. 5.28.

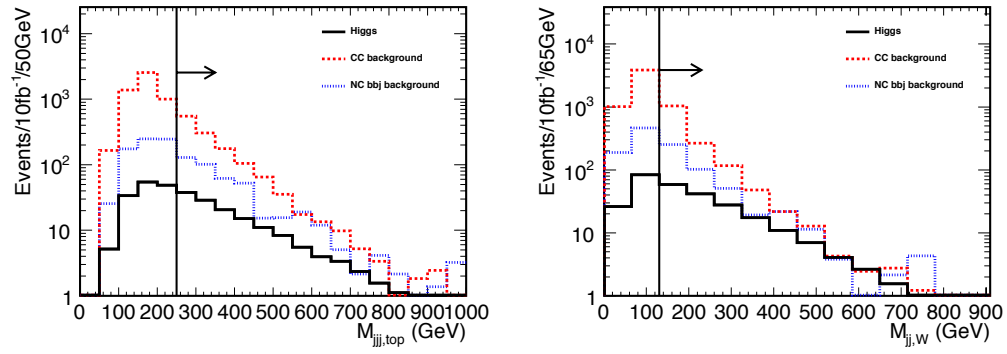


Figure 5.27: Three-jet (left) and di-jet (right) invariant masses. Solid (black), dashed (red) and dotted (blue) histograms show $H \rightarrow b\bar{b}$, CC and NC DIS background, respectively.

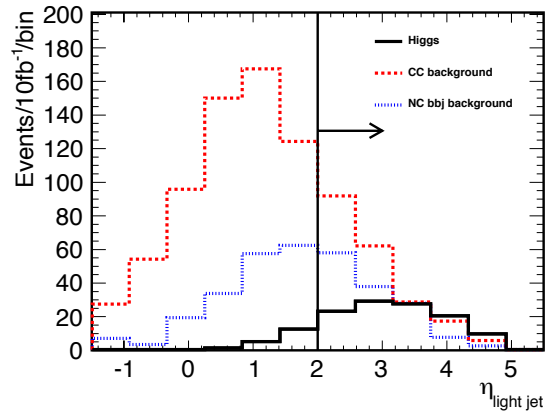


Figure 5.28: η_{jet} distribution for the lowest- η jet excluding the two b -tagged jets. Solid (black), dashed (red) and dotted (blue) histograms show $H \rightarrow b\bar{b}$, CC and NC DIS background, respectively.

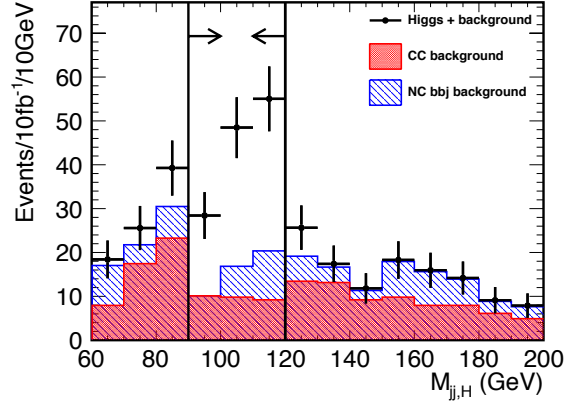


Figure 5.29: Reconstructed invariant Higgs mass after all selection criteria, except for the Higgs mass cut, have been applied. Points with error bars (black) show the $H \rightarrow b\bar{b}$ signal added to the CC (red histogram) and NC (hatched blue histogram) DIS background for an integrated luminosity of 10 fb^{-1} .

2684 Fig. 5.29 shows the reconstructed Higgs mass distribution for an integrated luminosity of
 2685 10 fb^{-1} , after all selection criteria except for the Higgs mass cut have been applied. The results
 2686 are summarized in Table 5.6. After the selection, 85 $H \rightarrow b\bar{b}$ events are expected for 10 fb^{-1}
 2687 luminosity with a 150 GeV electron beam. The signal to background ratio is 1.79 and the
 2688 significance of the signal $S/\sqrt{N} = 12.3$. For a higher Higgs mass, $m_H=150 \text{ GeV}$, the production
 2689 cross section decreases and the $b\bar{b}$ branching ratio also decreases. The expected number of signal
 2690 events becomes 25 and S/N and S/\sqrt{N} are 0.52 and 3.60, respectively. On the other hand,
 2691 with 60 GeV electron beam and five times larger luminosity (50 fb^{-1}), for 120 GeV Higgs, 124
 2692 $H \rightarrow b\bar{b}$ events are expected after the same cuts have been applied. Considering the CC and
 NC DIS background, S/N and S/\sqrt{N} are 1.05 and 11.4, respectively.

	Higgs production	CC DIS	NC bbj	S/N	S/\sqrt{N}
cut (1)	816	123000	4630	6.38×10^{-3}	2.28
cut (1) + (2) + (3)	178	1620	179	9.92×10^{-2}	4.21
All cuts	84.6	29.1	18.3	1.79	12.3

Table 5.6: Expected $H \rightarrow b\bar{b}$ signal and background events with 150 GeV electron beam for an integrated luminosity of 10 fb^{-1} . Contents of the cuts are listed in text.

2693 The results shown here are subject to large uncertainties. First, as mentioned above, the very
 2694 large NC background cross section at forward scattering angles makes it impossible to simulate a
 2695 sufficient number of events to limit the Monte Carlo statistical uncertainty. It is estimated that
 2696 the background evaluation, with the above method where only events with at least two b quarks
 2697 were simulated, has an uncertainty of about a factor 3. With a full simulation, it can be expected
 2698

2699 to be negligible when the true measurement is realized. Neglecting, therefore, this source
2700 of uncertainty, the systematic errors which will dominate are expected to be the theoretical
2701 estimates of signals and backgrounds and instrumental effects: efficiency and acceptance of
2702 lepton and jet reconstruction, b-tagging and mistagging probabilities. They are difficult to
2703 estimate without real data and a real detector. The statistical uncertainty on the cross section
2704 can, however, be estimated: 15% for the reference case of $150 \text{ GeV} \times 7 \text{ TeV}$ beams and a Higgs
2705 of mass 120 GeV . This represents a direct measure of the statistical uncertainty on the product
2706 of the squares of couplings Hbb and HWW .

Chapter 6

Physics at High Parton Densities

6.1 Physics at small x

6.1.1 Unitarity and QCD

Introduction

QCD [9] is the fundamental theory of the strong interaction that has been extensively tested in the last 38 years. Still, many open questions remain to be solved. One of them, which can be addressed at high energies, is the transition between the regimes in which the strong coupling constant is either large or small - the so-called *strong and weak coupling* regimes. In the former, standard perturbation theory techniques are not applicable and exact analytical results are not yet within the reach of current knowledge. Therefore various models, *effective* theories, whose parameters cannot yet be derived from QCD, or numerical lattice computations, have to be employed. One example of such an effective theory which has been used through the years and actually predates QCD, is the Regge-Gribov [249–251] theory.

The weak coupling regime has been well tested in high-energy experiments through a selected class of measurements - often referred to as *hard processes* - where weak and strong coupling effects can be cleanly separated. There exists a well-defined theoretical concept which has been derived from first principles and probed in the weak coupling regime, namely the collinear factorization theorem (for a comprehensive review see [252] and references therein). It allows a separation of the cross sections involving hadrons into: (i) parts that can be computed within perturbation theory, corresponding to the cross section for parton scattering, and (ii) pieces which cannot be calculated using weak coupling techniques, but whose evolution is still perturbative. The latter are universal, process-independent distributions that either characterize the partonic content of the hadron - *parton densities* on which we will mainly focus the discussion - or the eventual projection of partons onto hadrons. Together with their corresponding (DGLAP) linear evolution equations [253–255], they have been used to describe experimental data to high accuracy. Examples include total DIS cross sections, the production of jets with large transverse momenta and final states with heavy quarks.

In recent high-energy experiments have become sensitive to kinematic regions in which the coupling is small but the factorization assumption may no longer be valid. As an example, several HERA DIS measurements at small longitudinal momentum fractions x where parton

2738 densities are large, indicate deviations from the behavior expected within the standard collinear
 2739 factorization. Similarly, hadronic or nuclear collisions involving partons with small x may also
 2740 show such deviations. At the same time, in these small- x regions the cross sections grow rapidly,
 2741 so contributions from such regions dominate hadronic cross sections in sufficiently high energy
 2742 scattering. Experiments sensitive to this kinematic region thus provide a way to test QCD in
 2743 the new regime where the parton densities become very large and novel effects are expected.
 2744 We will refer to this region as the high parton density domain.

2745 From a theoretical viewpoint, this situation offers both opportunities and challenges. The
 2746 fact that, at small- x , there is no abrupt transition between the dilute and dense regimes, allows
 2747 the use of techniques which, while still being weak coupling, go beyond those used in the dilute
 2748 limit. The usual parton multiplication processes have to be supplemented by processes in which
 2749 partons recombine - thus adding non-linear terms to the evolution equations [256]. There are
 2750 deep theoretical questions arising in this new dense partonic regime of QCD. At high energies
 2751 the scattering amplitudes are close to the unitarity limit, and one expects that unitarity will be
 2752 preserved by the taming of parton densities due to recombination effects - this phenomenon is
 2753 generically referred to as *saturation*. Thus, in the weak coupling limit the physics responsible
 2754 for satisfying unitarity in QCD is expected to be describable in partonic language. Theoretical
 2755 calculations [257–260] in high-energy QCD justify these generic expectations. Furthermore,
 2756 the experimental exploration of this transition region where the standard perturbative descrip-
 2757 tion based on collinear factorization and linear evolution equations requires large corrections,
 2758 provides new possibilities of further understanding the strong coupling regime.

2759 Deep inelastic lepton-hadron scattering has already been shown to address these questions
 2760 in the most efficient manner. It provides the cleanest way of measuring the parton densities,
 2761 including the small- x region in which, as indicated above, the border between the dilute and
 2762 dense regimes of QCD should occur within the weak coupling region where calculations can be
 2763 done. Approaching this transition region from the dilute side by decreasing x or by increasing
 2764 the number of nucleons in the target, one should observe features which cannot be understood
 2765 within the framework of linear QCD evolution equations but, using more elaborate tools (non-
 2766 linear evolution equations) can still be analyzed in terms of weak coupling techniques. In fact,
 2767 within the standard framework of the leading-twist linear QCD evolution equations (DGLAP)
 2768 the parton densities are predicted to rise at small x , and this rise has been seen very clearly at
 2769 HERA. However, unitarity prevents such a rise from continuing indefinitely, leading to saturation
 2770 of gluon densities. In hadron-hadron scattering it is unitarity which limits the growth of
 2771 the total cross sections as a function of energy: according to Froissart and Martin [261, 262]

$$\sigma_{\text{tot}} \leq \text{const.} \ln^2 s/s_0 , \quad (6.1)$$

2772 where s_0 is a typical hadronic scale. This bound comes from two fundamental assumptions. The
 2773 first is that the amplitude for the scattering at fixed value of impact parameter is bounded by
 2774 unity and the second is the finite range of the strong interaction. The bound on the amplitude
 2775 has a simple physical interpretation that the probability for the interaction becomes very high,
 2776 so the target (or more precisely the interaction region) is completely absorptive. This situation
 2777 is usually referred to as a *black disk* regime. The description of this regime is very challenging
 2778 theoretically and it is expected that new phenomena will occur which are direct manifestations
 2779 of a new state in QCD which is characterized by a high parton density. The LHeC will uniquely
 2780 offer the possibility of exploring the transition towards this new state of dense QCD matter,
 2781 as it can pursue a two-pronged approach: high center-of-mass energy, extending the kinematic
 2782 range to lower x , and the possibility of deep inelastic scattering off heavy nuclei.

2783 In the rest of this section we will present the different approaches that are currently under
 2784 discussion to describe the high-energy regime of QCD. We will recall the ideas that lead from
 2785 linear evolution equations to non-linear ones. On the former, we will discuss both cases in which
 2786 the evolution equations are computed within fixed-order perturbation theory (the DGLAP
 2787 evolution equations) and where they include some kind of resummation - thus going beyond
 2788 any fixed order in the perturbative expansion in the QCD coupling constant. The most famous
 2789 example is the Balitsky-Fadin-Kuraev-Lipatov (BFKL) equation [263, 264]. Concerning the
 2790 latter, non-linear evolution leads to the phenomenon of saturation of partonic densities in the
 2791 hadron or nucleus. We will briefly review the realizations of saturation of parton densities both
 2792 at strong coupling and, mainly, at weak coupling. We will end by discussing the importance
 2793 of diffractive observables and of the use of nuclear targets for the investigation of the small- x
 2794 behavior of the hadron or nucleus wave function.

2795 **From DGLAP to non-linear evolution equations in QCD: saturation**

2796 In DIS the structure function $F_2(x, Q^2)$ is proportional to the total cross section σ_{tot} for the
 2797 scattering of a virtual photon on a hadron h , $\gamma^* h \rightarrow X$. The growth of F_2 at small x trans-
 2798 lates into the rise of σ_{tot} as a function of the energy of the virtual photon-hadron system.
 2799 Although the Froissart-Martin bound, derived for hadron-hadron scattering, cannot be applied
 2800 to a process involving a virtual photon, direct calculations based on the evaluation of the QCD
 2801 diagrams demonstrate unambiguously that, at small x , large corrections exist and need to be
 2802 resummed. These corrections suppress the leading-twist results and there is no doubt that, for
 2803 F_2 , the rise with $1/x$ predicted by DGLAP is modified by contributions which are not included
 2804 in the framework of leading-twist linear evolution equations. The corrections which become
 2805 numerically important in the small- x limit are also important for the restoration of the unitar-
 2806 ity bound. As a result of these modifications parton saturation is reached for sufficiently large
 2807 energies or small values of Bjorken- x .

2808 In deep inelastic electron-proton scattering, the virtual photon emitted by the incoming
 2809 electron interacts with partons inside the proton whose properties are specified by the kinematics
 2810 of the photon. In particular, the transverse size of the partons is (roughly) inversely proportional
 2811 to the square root of the virtuality of the photon, $\langle r_T^2 \rangle \sim 1/Q^2$. The deep inelastic cross
 2812 section, parametrized through parton densities, thus counts the numbers of quarks and gluons
 2813 per unit of phase space. For sufficiently large photon virtualities Q^2 and not too small x ,
 2814 the improved QCD parton model works well because the partons forming the hadron, on the
 2815 distance scale defined by the small photon, are in a dilute regime, and they interact only weakly.
 2816 This is a direct consequence of the property of asymptotic freedom, which makes the strong
 2817 coupling constant small. This diluteness condition is not satisfied if the density of partons
 2818 increases. This happens if either the number of partons increases (large structure function)
 2819 or the interaction between the partons becomes strong (large α_s). The former situation is
 2820 realized at small x , the latter for small photon virtuality Q^2 which sets the scale of the strong
 2821 coupling $\alpha_s(Q^2)$. This simple qualitative argument shows that corrections to the standard
 2822 QCD parton picture can be described in terms of quarks and gluons and their interactions as
 2823 long as Q^2 is not too small ($\alpha_s(Q^2) \ll 1$) and the gluon density is large (small x). Combining
 2824 these two conditions one arrives at the picture shown in Fig. 6.1: there is an approximately
 2825 diagonal line in the $\ln Q^2 - \ln 1/x$ plane below which the parton distributions are dilute, and
 2826 the standard QCD parton picture applies. In this regime linear evolution equations provide the
 2827 correct description of parton dynamics. In the vicinity of the line, non-linear QCD corrections

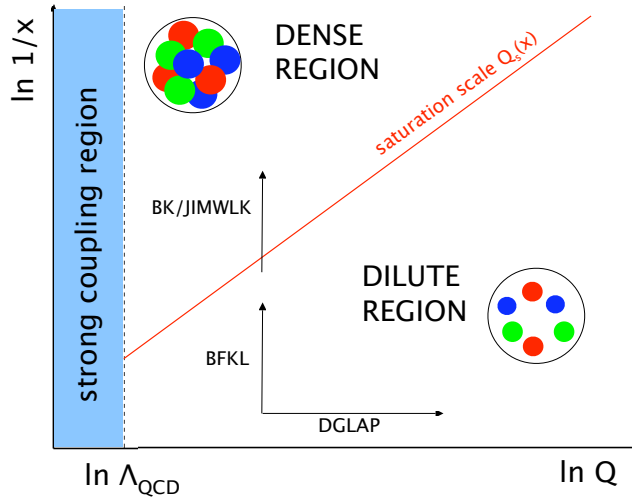


Figure 6.1: Schematic view of the different regions for the parton densities in the $\ln Q^2 - \ln 1/x$ plane. See the text for comments.

2828 become important, and above the line partons are in a high-density state. Well above the
 2829 line, interactions become strong, and standard perturbation theory is not valid. The division
 2830 between the two regimes is usually defined in terms of a saturation line, which is specified
 2831 by a dynamically generated saturation scale, growing with decreasing x . Within this picture
 2832 one easily understands which type of corrections can be expected. Once the density of gluons
 2833 increases sufficiently, it becomes probable that, prior to their interaction with the photon, gluons
 2834 undergo recombination processes.

2835 Saturation in perturbative QCD

2836 While unitarity is an unavoidable feature of any quantum field theory, the microscopic dynamics
 2837 which lead to it in QCD are not very well understood. There are several proposals to implement
 2838 unitarity in strong interactions, which can be roughly classified into those which use non-
 2839 perturbative models and those based on perturbative QCD calculations.

2840 The usual non-perturbative framework to implement unitarity are Regge-Gribov based mod-
 2841 els [21, 250, 265]. Though they are quite successful in describing existing data on inclusive and
 2842 diffractive ep and eA scattering (see e.g. [266, 267] and references therein), they lack theoretical
 2843 foundations within QCD.

2844 On the other hand, attempts have been going on for the last 30 years to implement par-
 2845 ton rescattering or recombination¹ in perturbative QCD in order to describe its high-energy

¹Note that the rescattering and recombination concepts correspond to the same physical mechanism viewed in the rest frame and the infinite momentum frame of the hadron, respectively.

2846 behaviour. In the pioneering work in [256, 268], a non-linear evolution equation in $\ln Q^2$ was
 2847 proposed to provide the first correction to the linear equations. A non-linear term appeared,
 2848 which was proportional to the local density of color charges seen by the probe (the virtual
 2849 photon).

2850 An alternative, independent approach was developed in [269], where the amplitudes for
 2851 diffractive processes in the triple Regge limit were calculated. This resulted in the extraction
 2852 of the triple Pomeron vertex in QCD at small x , which is responsible for the non-linear term
 2853 in the evolution equations.

2854 Later on these ideas were developed to include all corrections enhanced by the local density,
 2855 to constitute what is called the Color Glass Condensate (CGC) [257–260, 270–277] (see also
 2856 the most recent developments in [278–281]). The CGC provides a non-perturbative, but weak-
 2857 coupling, realization of the parton saturation ideas within QCD. The linear limit of the basic
 2858 CGC equation is the BFKL equation, which is the generally accepted linear evolution equation
 2859 for the high-energy limit. As illustrated in Fig. 6.1, the evolution in the $\ln Q^2 - \ln 1/x$ plane is
 2860 driven by both linear equations: along $\ln Q^2$ for DGLAP and along $\ln 1/x$ for BFKL.

2861 The basic framework in which saturation ideas are discussed is illustrated in Fig. 6.2.
 2862 One is considering the hadron wave function at high energy. Its partonic components can be
 2863 separated into those with a large momentum fraction x and those with small x . The large- x
 2864 components are dilute and provide color sources for the corresponding small- x components.
 2865 Due to multiple splittings of the small- x gluons, a dense system is eventually formed. One
 2866 can then construct within this formalism an evolution equation for the gluon correlators in the
 2867 hadron wave function which is a renormalization group equation with respect to the rapidity
 2868 separating large- and small- x partons. This renormalization procedure assumes perturbative
 2869 gluon emissions from the large- x partons which imply a redefinition of the source at each step
 2870 in rapidity.

2871 The mean field version of the CGC, the Balitsky-Kovchegov (BK) equation [259, 260], pro-
 2872 vides a non-linear evolution equation for unintegrated gluon densities. It turns out that the
 2873 BK approach results in a gluon density which, for a fixed resolution of the probe, is saturated
 2874 for small longitudinal momentum fractions x , whereas at large values of x , the non-linear term
 2875 is negligible. The separation between these two limits is given by a dynamically generated
 2876 saturation momentum $Q_s(x)$ which increases with decreasing x (c.f. figure 6.1), and therefore
 2877 saturation is determined by the condition $Q_s(x) > Q$. Then, for large energies or small x , the
 2878 system is in a dense regime of high gluon fields (thus non-perturbative) but the typical gluon
 2879 momentum, $\sim Q_s$, is large (thus the coupling constant which determines gluon interactions is
 2880 weak). The qualitative behavior of the saturation scale with energy and nuclear size can be
 2881 argued as follows. The transition from a dilute to a dense regime is marked by the packing
 2882 factor (in this case, the product of the density of gluons per unit transverse area times the
 2883 gluon-gluon cross section) becoming of the order unity i.e.

$$\frac{A \times xg(x, Q_s^2)}{\pi A^{2/3}} \times \frac{\alpha_s(Q_s^2)}{Q_s^2} \sim 1 \implies Q_s^2 \sim A^{1/3} Q_0^2 \left(\frac{1}{x}\right)^\lambda, \quad (6.2)$$

2884 where the growth of the gluon density at small x has been approximated by a power law,
 2885 $xg(x, Q^2) \sim x^{-\lambda}$, logarithms are neglected and the nucleus is considered a simple superposition
 2886 of independent nucleons. The exponent $\lambda \simeq 0.3$ can be derived from QCD, whereas the scale
 2887 Q_0^2 has to be taken from experiment.

2888 The BK equation was derived under several simplifying assumptions such as the scattering
 2889 of a dilute projectile on a dense target, a large number of QCD colours and the absence of

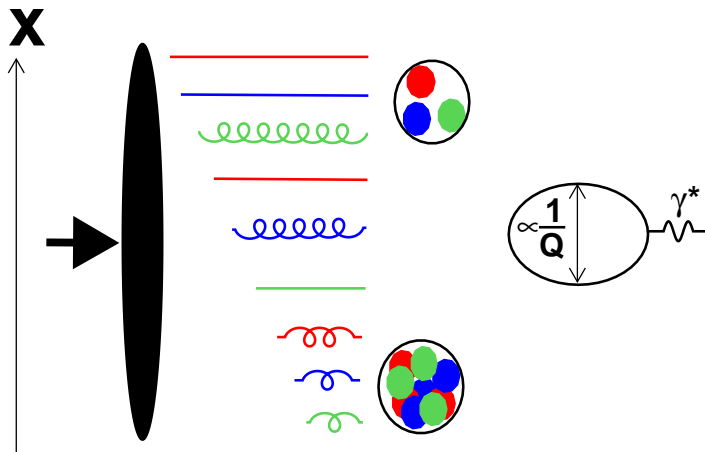


Figure 6.2: Illustration of saturation ideas. The hadron is moving very fast to the right, and its wave function contains many partonic components. Specifically, it includes partons with both large and small fractions of its longitudinal momentum x . The former are in a dilute regime, while the latter become densely packed due to multiple splitting. The photon with virtuality Q^2 is moving to the left and it constitutes a probe of the hadron wave function with a spatial resolution proportional to $1/Q$.

2890 correlations in the target. At present, the discussion is concentrated on how to overcome
 2891 these difficulties [278, 282, 283]. Possible phenomenological implications [284–286], are being
 2892 considered. Also, the proposed relation between high-energy QCD and Statistical Mechanics
 2893 [282, 287] is under investigation.

2894 In the CGC formalism, the resummed terms are those enhanced by the energy and by the
 2895 local density of partons, and the saturation scale depends on the matter (colour charge) density
 2896 at the impact parameter probed by the virtual photon. For a nucleus, the nuclear size plays
 2897 the role of an enhancement factor, see Eq. (6.2), in a manner which is analogous to impact
 2898 parameter scanning. Therefore, it is expected that when scanning the impact parameter from
 2899 the center to the periphery of the hadron at high energy, one should go from a non-linear to
 2900 a linear regime. Analogously, non-linear effects will become more important for large nuclei
 2901 than for smaller ones or for nucleons. Thus, a study of the variation of parton densities with
 2902 impact parameter and with the nuclear size, will provide an exacting test of our ideas on parton
 2903 saturation.

2904 **Resummation at low x**

2905 The generic challenges that the small- x region bears in QCD are inherently related to the
 2906 divergence of the gluon number density with decreasing values of x . As is well known, deep-
 2907 inelastic partonic cross sections and parton splitting functions receive large corrections in the

2908 small- x limit due to the presence of powers of $[\alpha_s \log x]$ to all orders in the perturbative expansion [253, 263, 264, 288, 289]. It thus suggests dramatic effects from logarithmically enhanced corrections, so the success of fixed order NLO perturbation theory at HERA has been very hard to explain in regions where x becomes small. Recently, hints have been found that indeed the DGLAP fits tend to deteriorate systematically in the region of small x and Q^2 [10, 290]. Direct calculations at next-to-leading logarithmic accuracy in the BFKL framework were performed [291, 292], and showed a slow convergence of the perturbative series in the high-energy, or small- x regime. Therefore, generically one expects deviations from fixed-order DGLAP evolution in the small- x and small- Q regime which call for resummation of higher orders in perturbation theory.

2918 Extensive analyses have been performed in the last few years [293–298], which indeed point to the importance of resummation to all orders. Resummation should embody important constraints like kinematic effects, momentum sum rules and running coupling effects.

2921 Several important questions arise here, such as the relation and interplay of the resummation and the non-linear effects, and possibly the role of resummation in the transition between the perturbative and non-perturbative regimes in QCD. Precise experimental measurements in extended kinematic regions are needed to explore the deviations from standard DGLAP evolution and to quantify the role of resummation at small x .

2926 **The importance of diffraction**

2927 It was observed at HERA that a substantial fraction, about 10%, of deep inelastic interactions are diffractive events i.e. events in which the interacting proton stays intact, despite the inelasticity of the interaction. Moreover, the proton appears well separated from the rest of the hadronic final state by a large rapidity gap. The events otherwise look similar to normal deep inelastic events.

2932 Diffraction has been extensively analyzed at HERA, with a variety of measurements in bins of x and Q^2 , as well as more differential analyses which include the dependence on the momentum transfer t . Physically, for the diffractive event to occur, there must be an exchange of a coherent, color neutral cluster of partons (a quasiparticle) which leaves the interacting proton intact. This color neutral cluster is often called the *pomeron*, and it can be characterised via a factorisation theorem [299] by a set of partonic densities analogous to those for the proton or nucleus. At lowest order, the QCD realisation of the pomeron is a pair of gluons [300, 301], which leads to enhanced sensitivity to saturation phenomena compared to the single gluon exchange in the bulk of non-diffractive processes.

2941 There are strong theoretical indications that diffraction is closely linked with the phenomenon of partonic saturation. From a wide range of calculations, mostly based on the so-called dipole model, see for example [302, 303], it is known that diffractive DIS events involve softer effective scales than non-diffractive events at the same Q^2 . Thus, the exploration of diffractive phenomena offers a unique window to analyze the transition between perturbative and non-perturbative dynamics in QCD.

2947 LHeC will provide a widely extended kinematic coverage for diffractive events. By their study one could extract diffractive parton densities for a larger range in Q^2 than at HERA, and thus provide crucial tests of parton dynamics in diffraction as well as of the factorization theorems. The high energy involved also enables the production of diffractive states with large masses which could include W and Z bosons as well as states with heavy flavours or even exotic states with quantum numbers 1^- .

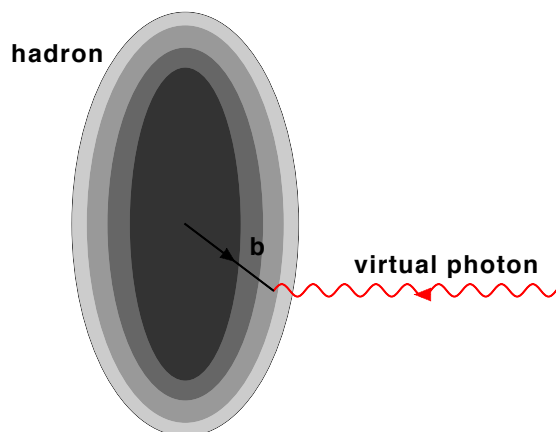


Figure 6.3: Illustration of the transverse profile of the hadron as explored by a virtual photon at impact parameter b .

2953 Of particular importance is exclusive diffractive production of vector mesons, for which
 2954 differential measurements as a function of squared four-momentum transfer, t , are most easily
 2955 performed. It has been demonstrated that in this case, information about the momentum
 2956 transfer of the cross section can be translated into the dependence of the scattering amplitude
 2957 on impact parameter. As a result, a profile in impact parameter of the interaction region,
 2958 illustrated in Fig. 6.3, can be extracted. The precise determination of the dynamics governing
 2959 the high parton density regime requires a detailed picture of the spatial distribution, in impact
 2960 parameter space, of partons in the interaction region. As mentioned previously, by selecting
 2961 small impact parameter values (large t), one is probing the regions of higher parton density
 2962 where the saturation phenomenon is more likely to occur. One can then extract the value of
 2963 the saturation scale as a function of energy and impact parameter.

2964 Even more inclusive measurements of the diffractive production of vector mesons can provide
 2965 valuable information about parton dynamics. For example, the measurement of the energy
 2966 dependence of the diffractive cross section for the production of J/ψ at the LHeC can distinguish
 2967 between different scenarios for parton evolution and thus explore parton saturation to a greater
 2968 accuracy than ever before.

2969 **The importance of nuclei**

2970 In the context of small- x physics, studying lepton-nucleus collisions has a two-fold importance:

- 2971 • On the one hand and as discussed in sections 6.1.4 and 6.2.2, the nuclear structure func-
 2972 tions and parton densities are basically unknown at small x . The main reason for this
 2973 lack of knowledge comes from the rather small area in the $\ln Q^2 - \ln 1/x$ plane covered by
 2974 presently available experimental data, see Fig. 6.4. Current theoretical and phenom-
 2975 enological analyses [304] point to the importance of non-linear dynamics in DIS off nuclei
 2976 at small and moderate Q^2 and small x , which needs to be tested experimentally. In this
 2977 respect, a relation exists, as reviewed in Sec. 6.2.4, between diffraction in lepton-proton
 2978 collisions and the small- x behavior of nuclear structure functions. Such relation relies on

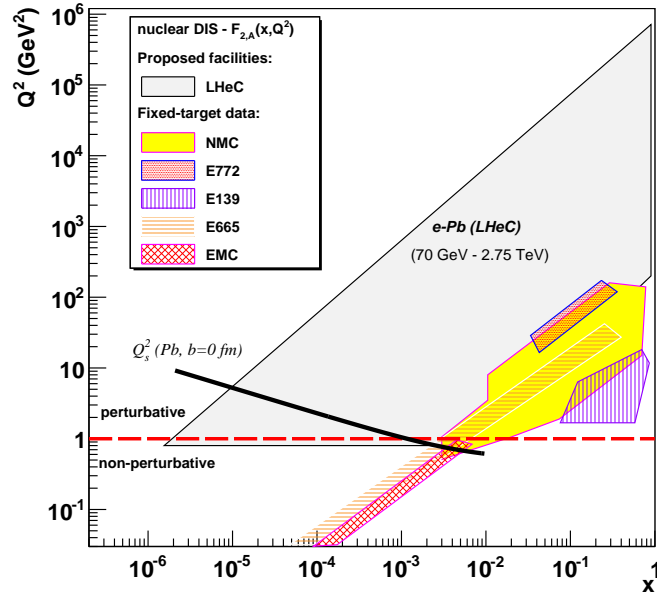


Figure 6.4: Kinematical coverage of the LHeC in the $\ln Q^2 - \ln 1/x$ plane for nuclear beams, compared with existing nuclear DIS and Drell-Yan experiments.

2979 basic properties of Quantum Field Theory and its verification provides stringent tests of
 2980 our understanding of these phenomena.

- 2981 • Non-linear effects in parton evolution are enhanced by increasing the density of partons.
 2982 Such an increase can be achieved (see Fig. 6.5) either by increasing the energy of the
 2983 collision (decreasing x), or by increasing the nuclear mass number A . The latter can be
 2984 accomplished by either using the largest nuclei possible, or by selecting subsets of collisions
 2985 with small impact parameters b (i.e. more central collisions) between the relatively light
 2986 nuclei and the virtual photon, such that more nucleons are involved. The ideal situation
 2987 would be to Map out the dependence of the saturation scale on x , b and A as fully as
 2988 possible (see Eq. (6.2). This is a key observable in formulations which resum multiple
 2989 interactions and result in parton saturation. As such it must be checked in experiment in
 2990 order to clearly settle the mechanism underlying non-linear parton dynamics.

2991 Also, the study of lepton-nucleus collisions has strong implications on the understanding
 2992 of the experimental data from ultrarelativistic nucleus-nucleus collisions, as discussed later in
 2993 Subsec. 6.1.4.

2994 6.1.2 Status following HERA data

2995 As discussed in the previous Section, in the low- x region a high parton density can be achieved
 2996 in DIS and various novel phenomena are predicted. Ultimately, unitarity constraints become
 2997 important and a ‘black disk’ limit is approached [265], in which the cross section reaches the
 2998 geometrical bound given by the transverse proton or nucleus size. When α_s is small enough for

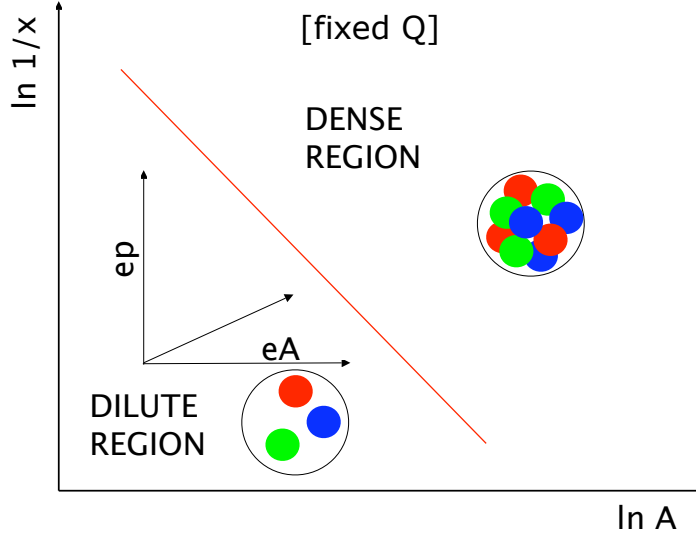


Figure 6.5: Schematic view of the different regions for the parton densities in the $\ln 1/x - \ln A$ plane, for fixed Q^2 . See the text for comments.

2999 quarks and gluons to be the right degrees of freedom, parton saturation effects are therefore
 3000 expected to occur within the theoretically controllable weak coupling regime. In this small-
 3001 x limit, many striking observable effects are predicted, such as Q^2 dependences of the cross
 3002 sections which differ fundamentally from the usual logarithmic variations, and diffractive cross
 3003 sections approaching 50% of the total [305]. This fairly good phenomenological understanding
 3004 of the onset of unitarity effects is, unfortunately, not very quantitative. In particular, the
 3005 precise location of the saturation scale line in the DIS kinematic plane (see Fig. 6.1) is to be
 3006 determined experimentally. The search for parton saturation effects has therefore been a major
 3007 issue throughout the lifetime of the HERA project.

3008 Although no conclusive saturation signals have been observed in parton density fits to ex-
 3009 isting HERA data, various hints have been obtained, for example, by studying the change in fit
 3010 quality as low- x and Q^2 data are progressively omitted, in the NNPDF [290] and HERAPDF [10]
 3011 analyses (see Subsec. 6.1.2).

3012 A more common approach is to fit the data to dipole models [302, 303, 306, 307], which
 3013 are applicable at very low Q^2 values beyond the range in which quarks and gluons can be
 3014 considered to be good degrees of freedom. The typical conclusion [307] is that HERA data
 3015 in the perturbative regime exhibit at best weak evidence for saturation. However, when data
 3016 in the $Q^2 < 1 \text{ GeV}^2$ region are included, models which include saturation effects are quite
 3017 successful in the description of the wide variety of experimental data.

3018 The ‘geometric scaling’ [308] feature of the HERA data (Fig. 6.6a) reveals that, to a good
 3019 approximation, the low- x cross section is a function of a single combined variable $\tau = Q^2/Q_s^2(x)$,
 3020 where $Q_s^2 = Q_0^2 x^{-\lambda}$ is the saturation scale, see Eq. (6.2). This parameterisation works
 3021 well for scattering off both protons and ions, as shown in Fig. 6.6b [308, 309]. Geometric

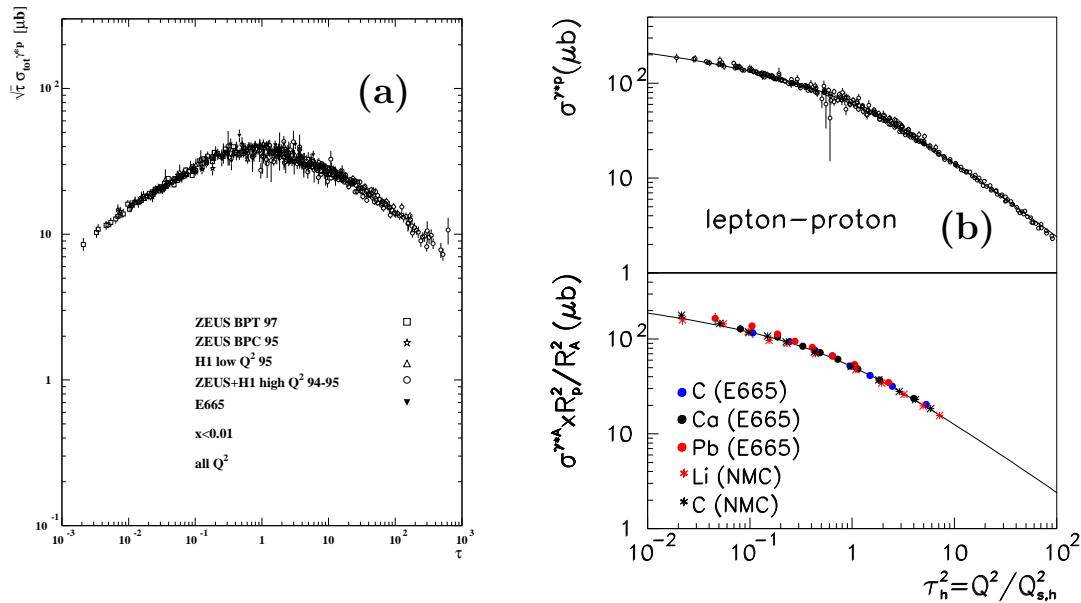


Figure 6.6: (a) Geometric scaling plot [308], in which low x data on the γ^*p cross section from HERA and E665 are plotted as a function of the dimensionless variable τ (see text). The cross sections are scaled by $\sqrt{\tau}$ for visibility. (b) Geometric scaling plot showing cross sections for electron scattering off nuclei as well as off protons [309].

3022 scaling is observed not only for the total γ^*p cross section, but also for other, more exclusive
 3023 observables in γ^*p collisions [310,311] and even in hadron production in proton-proton collisions
 3024 at the LHC [312] and nucleus-nucleus collisions at RHIC [309]. This feature supports the view
 3025 (Subsec. 6.1.1) of the cross section as being invariant along lines of constant ‘gluon occupancy’.
 3026 When viewed in detail (Fig. 6.6), there is a change in behaviour in the geometric scaling plot
 3027 near $\tau = 1$, which has been interpreted as a transition to the saturation region shown in
 3028 Fig. 6.1. However, data with $\tau < 1$ exist only at very low, non-perturbative, Q^2 values to date,
 3029 precluding a partonic interpretation. Also, the fact that the scaling extends to large values of τ
 3030 which characterize the dilute regime, has prompted theoretical explanations of this phenomenon
 3031 which do not invoke the physics of saturation [313].

3032 Dipole models

3033 As mentioned previously, one of the interesting observations at HERA is the success of the
 3034 description of many aspects of the experimental data within the framework of the so-called
 3035 dipole picture [257,314,315] with models that include unitarisation or saturation effects [316,
 3036 317]. These models are based on the assumption that the relevant degrees of freedom at
 3037 high energy are colour dipoles. Dipole models in DIS are closely related to the Good-Walker
 3038 picture [318] previously developed for soft processes in hadron-hadron collisions. In DIS, dipoles
 3039 are shown to be the eigenstates of high-energy scattering in QCD, and the photon wave function
 3040 can be expanded onto the dipole basis.

3041 The dipole factorization for the inclusive cross section in DIS is illustrated in Fig. 6.7. It
 3042 differs from the usual picture of the virtual photon probing the parton density of the target

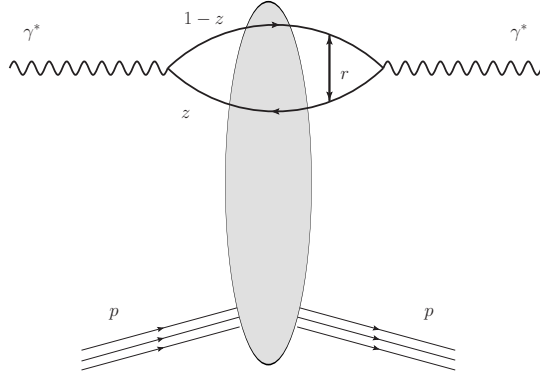


Figure 6.7: Schematic representation of dipole factorisation at small x in DIS. The virtual photon fluctuates into a quark-antiquark pair and subsequently interacts with the target. All the details of the dynamics of the interaction are encoded in the dipole scattering amplitude.

3043 in that here the partonic structure of the probed hadron is not evident. Instead, one chooses
 3044 a particular Lorentz frame where the photon fluctuates into a quark-antiquark pair with a
 3045 transverse separation r and at impact parameter b with respect to the target. For sufficiently
 3046 small $x \ll (2m_N R_h)^{-1}$, with m_N the nucleon mass and R_h the hadron or nuclear radius, the
 3047 lifetime of the $q\bar{q}$ fluctuation is much longer than the typical time for interaction with the target.
 3048 The interaction of the $q\bar{q}$ dipole with the hadron or nucleus is then described by a scattering
 3049 matrix $S(r, b; x)$ such that $|S(r, b; x)| < 1$. The unitarity constraints can be incorporated
 3050 naturally in this picture [319] by the requirement that $|S(r, b; x)| \geq 0$, with $S(r, b; x) = 0$
 3051 corresponding to the black disk limit. Integrating $1 - S(r, b; x)$ over the impact parameter b
 3052 one obtains the dipole cross section $\sigma^{q\bar{q}}(r, x)$, which depends on the dipole size and the energy
 3053 (through the dependence on $x = x_{Bj}$). The transverse size of the partons probed in this process
 3054 is roughly proportional to the inverse of the virtuality of the photon Q^2 . This statement is most
 3055 accurate in the case of a longitudinally polarized photon, while in the case of a transversely
 3056 polarized one, the distribution of the probed transverse sizes of dipoles is broadened due to the
 3057 so-called aligned jet configurations.

3058 At small values of the dipole size, such that $r \ll 1/Q$, the dipole cross section can be shown
 3059 to be related to the integrated gluon distribution function

$$\sigma^{q\bar{q}}(r, x) \sim r^2 \alpha_s(C/r^2) xg(x, C/r^2), \quad (6.3)$$

3060 where C is a constant. In this regime, where r is small, the dipole cross section is small
 3061 and consequently the amplitude is far from the unitarity limits. With increasing energy the
 3062 dipole cross section grows and saturation corrections must be taken into account in order to
 3063 guarantee the unitarity bound on $S(r, b; x)$. The transition region between the two limits is
 3064 characterised by the saturation scale $Q_s(x)$. Several models [302, 306, 320] have been proposed
 3065 which successfully describe the HERA data on the structure function F_2 .

3066 Once the dipole cross section has been constrained by the data on the inclusive structure
 3067 functions, it can be used to predict, with almost no additional parameters, the cross sections
 3068 for diffractive production at small x . Inclusive diffraction has been computed within the dipole

3069 picture in [303], and exclusive diffraction of vector mesons in [321,322]. One of the interesting
3070 aspects of these models is that they naturally lead to a constant ratio of the diffractive to total
3071 cross sections as a function of energy [303]. In models with saturation this is related to the fact
3072 that the saturation scale provides a natural x -dependent cut-off and gives the same leading-
3073 twist behavior for inclusive and diffractive cross sections. As a result the ratio of inclusive to
3074 diffractive cross sections is almost constant as a function of the energy.

3075 In spite of the fact that this approach has been able to successfully describe inclusive data
3076 and predict diffraction at small values of x , there is still important conceptual progress to
3077 be made. Certainly there are important hints from dipole models about the nature of the
3078 perturbative–non-perturbative transition in QCD. Nevertheless, dipole models should be rather
3079 regarded as effective phenomenological approaches. As such they only parametrize the essential
3080 dynamics at small x . For instance, the transverse impact parameter dependence of the dipole
3081 scattering amplitude $S(r, b; x)$ is very poorly constrained. Indeed, it is possible simultaneously
3082 to describe F_2 and F_2^D with a rather wide range of impact parameter dependences. On the
3083 theoretical side, it has not been possible so far to fully predict the realistic profile of the
3084 interaction region in transverse size. It is therefore of vital importance to measure accurately
3085 the t -dependencies of the diffractive cross sections in an extended kinematic range to pin down
3086 the impact parameter distribution of the proton at high energies.

3087 **Deviations from fixed order linear DGLAP evolution in inclusive HERA data**

3088 HERA provided extremely valuable information about the proton structure functions based
3089 on measurements of the total virtual photon-proton cross section. As discussed in previous
3090 sections, the experimental data on the inclusive structure function F_2 have been successfully
3091 described by fits which use linear fixed-order DGLAP evolution, see [114, 116, 323–329]. The
3092 current status of the calculations is fixed order at next-to-next-to-leading accuracy.

3093 There are several theoretical indications that at small x and/or at small Q^2 the fixed-order
3094 DGLAP framework needs to be extended, since in these regimes perturbative QCD predicts
3095 other relevant phenomena: linear small- x resummation, non-linear evolution and parton satu-
3096 ration or other higher-twist effects. Even if it is unclear in which kinematic regime these effects
3097 should become relevant, it is evident that at some point they will lead to deviations from fixed-
3098 order DGLAP evolution. Therefore, the important question is whether these deviations are
3099 already present in HERA data. Several analyses have been performed which aimed to address
3100 this question.

3101 In one analysis [307], the inclusive structure function $F_2(x, Q^2)$ is subjected to fits in which
3102 the dipole cross section either does not contain saturation properties, or saturates as expected in
3103 two rather different models [306,307]. All three dipole fits are able to describe the HERA data
3104 adequately in the perturbative region $Q^2 \geq 2 \text{ GeV}^2$, whereas a clear preference for the models
3105 containing saturation effects becomes evident when data in the range $0.045 < Q^2 < 1 \text{ GeV}^2$
3106 are added [307]. Due to the non-perturbative nature of this kinematic region, there is no clear
3107 interpretation in terms of parton recombination effects. Similar conclusions are drawn when
3108 the same dipole cross sections are applied to various less inclusive observables at HERA [330].

3109 In another analysis [290], possible indications of deviations from linear DGLAP evolution
3110 were discussed. It was based on an unbiased PDF analysis of the inclusive HERA data. Below,
3111 we discuss briefly the updated version of this study which uses the most precise inclusive DIS
3112 data to date, the combined HERA-I dataset [10] in the framework of the global NNPDF2.0
3113 fitting framework.

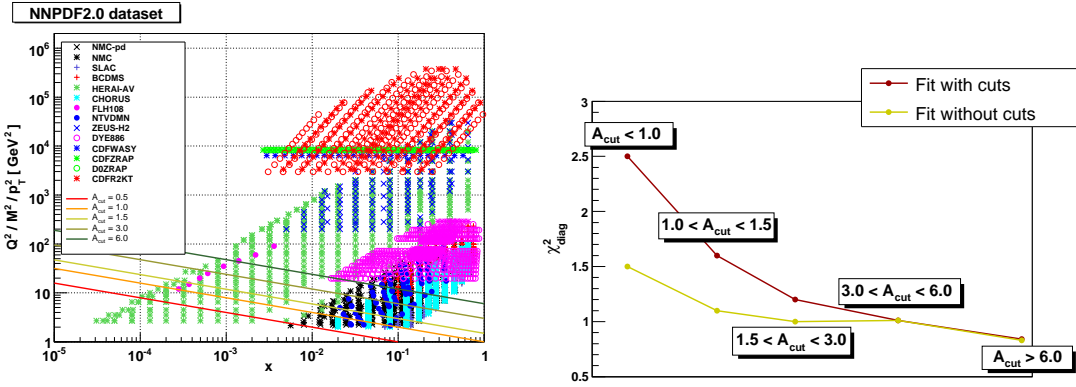


Figure 6.8: Left plot: the kinematic coverage of the data used in the NNPDF2.0 analysis, indicating the different choices of A_{cut} used to probe deviations from DGLAP. Right plot: the diagonal χ_{diag}^2 evaluated in kinematic slices corresponding to the different A_{cut} cuts, where χ_{diag}^2 has been computed using both the reference NNPDF2.0 fit without kinematic cuts (yellow line) and the NNPDF2.0 with the maximum $A_{\text{cut}} = 1.5$ cut (red line).

3114 Deviations from DGLAP evolution can be investigated by exploiting the discriminating and
 3115 sensitive framework of global PDF fits. The key idea is to perform global fits only in the large- x ,
 3116 large- Q^2 region, where NLO DGLAP is expected to be reliable. This way one can determine *safe*
 3117 parton distributions which are not contaminated by possible non-DGLAP effects. These PDFs
 3118 are then evolved backwards into the potentially *unsafe* low- x and low- Q^2 kinematic region, and
 3119 are used to compute physical observables, which are compared with data. A deviation between
 3120 the predicted and observed behavior in this region can then provide a signal for effects beyond
 3121 NLO DGLAP.

3122 The PDFs were determined within the *safe* kinematic region in which

$$Q^2 \geq A_{\text{cut}} \cdot x^{-\lambda}, \quad (6.4)$$

3123 where $\lambda = 0.3$ and A_{cut} is a variable parameter. To be precise, only data were fitted which
 3124 passed the cut Eq. (6.4) (see the left plot in Fig. 6.8). The above definition is theoretically
 3125 appealing, since it has the effective form of a saturation scale, and is also very practical, since
 3126 it does not remove moderate- Q^2 , large- x data, which are expected to be fully consistent with
 3127 DGLAP and which are very important to constrain the safe PDFs.

3128 The NNPDF2.0 analysis [329] was repeated for different choices of the kinematic cuts, one
 3129 for each choice of A_{cut} , and the results were compared with experimental data. As shown in
 3130 Fig. 6.9, at high $Q^2 = 15 \text{ GeV}^2$, one does not see any significant deviation from NLO DGLAP.
 3131 In this region all PDF sets agree with data and with one another. The only difference between
 3132 the different sets is that as A_{cut} increases the PDFs errors grow, as is statistically expected
 3133 due to the experimental information removed by the cuts. The situation is different at a lower
 3134 $Q^2 = 3.5 \text{ GeV}^2$: the prediction obtained from the backwards evolution of the data above the
 3135 cut exhibits a systematic downward trend, becoming more evident with increasing A_{cut} . It
 3136 is thus apparent that, at low- x , low- Q^2 , NLO DGLAP evolution fails to provide an accurate
 3137 description of the data. More precisely, one observes that NLO DGLAP evolves faster with Q^2
 3138 than actual data.

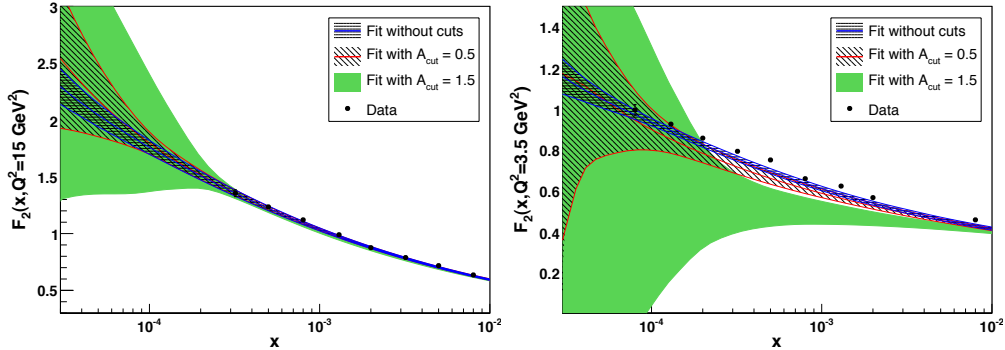


Figure 6.9: Left: the proton structure function $F_2(x, Q^2 = 15 \text{ GeV}^2)$ at small- x , computed from PDFs obtained from the NNPDF2.0 fits with different values of A_{cut} . Right: the same but at a lower $Q^2 = 3.5 \text{ GeV}^2$ scale.

3139 To be sure that one is observing a genuine small- x effect, one needs to check that it becomes
 3140 less and less relevant as x and Q^2 increase. To this aim the diagonal χ^2_{diag} was computed in
 3141 different kinematic slices, both from the fit without cuts and from that with the maximum cut
 3142 $A_{\text{cut}} = 1.5$. The expectation is that at larger x and Q^2 the difference between the two fits
 3143 becomes smaller, as deviations from NLO DGLAP should become negligible. This is exactly
 3144 what happens, as one can see from the right plot in Fig. 6.8: starting from $A_{\text{cut}} \gtrsim 1$ the statistical
 3145 features of the two fits are comparable.

3146 In summary, there is mounting evidence that the low- Q^2 -low- x region covered by HERA
 3147 is incompatible with fixed-order linear evolution. In particular, deviations from fixed order
 3148 NLO DGLAP have been found in the combined HERA-I dataset from an unbiased global PDF
 3149 analysis [331]. Similar conclusions have been reached in other independent studies like, for
 3150 example, the HERAPDF analysis [10]. Also, the fit quality to the small- Q^2 data at NNLO is
 3151 actually worse than at NLO [327] in agreement with the claims in [290] that these deviations are
 3152 consistent with either expectations from small- x resummations or saturation models, though
 3153 not from NNLO. Still, it should be noted that there is no general consensus [332]. In any case,
 3154 it is clear that this method should be used to analyse LHeC inclusive structure function data,
 3155 and would allow a detailed characterization of the new high-energy QCD dynamics unveiled
 3156 by the LHeC. The novel phenomena should be established cleanly in the high Q^2 perturbative
 3157 region where it can be understood in terms of parton degrees of freedom. This can only be
 3158 achieved by analysing DIS at lower x values than are accessible at HERA.

3159 Linear resummation schemes

3160 The deviations from DGLAP evolution could be caused by higher order effects at small x
 3161 and small Q which need to be resummed to all orders of perturbation theory. As mentioned
 3162 previously, the problem of resummation at small x has been extensively studied in recent years,
 3163 see for example [293–298]. It has been demonstrated that the small- x resummation framework
 3164 accounts for running coupling effects, kinematic constraints, gluon exchange symmetry and
 3165 other physical constraints. The results were shown to be very robust with respect to scale
 3166 changes and different resummation schemes. As a result, the effect of the resummation of

3167 terms which are enhanced at small x is perceptible but moderate - comparable in size to typical
 3168 NNLO fixed order corrections in the HERA region.

3169 A major development for high-energy resummation was presented in [295], where the full
 3170 small- x resummation of deep-inelastic scattering (DIS) anomalous dimensions and coefficient
 3171 functions was obtained including the quark contribution. This allowed for the first time a
 3172 consistent small- x resummation of DIS structure functions. These results are summarized in
 3173 Fig. 6.10, taken from Ref. [295], where the K -factors for F_2 and F_L for the resummed results are
 3174 compared. As is evident from this figure, resummation is quite important in the region of low
 3175 x for a wide range of Q^2 values. One observes, for example, that the fixed order NNLO contri-
 3176 bution leads to an enhancement of F_2 with respect to NLO, whereas the resummed calculation
 3177 leads to a suppression. This means that a truncation at any fixed order is very likely to be
 3178 insufficient for the description of the LHeC data and therefore the fixed-order perturbative ex-
 3179 pansion becomes unreliable in the low- x region, which calls for the resummation. Furthermore,
 3180 the resummation of hard partonic cross sections has been performed for several LHC processes
 3181 such as heavy quark production [333], Higgs production [334, 335], Drell-Yan [336, 337] and
 3182 prompt photon production [338, 339]. The LHC is thus likely to provide a testing ground in the
 3183 near future.

3184 We refer to the recent review in Ref. [340] as well as to the HERA-LHC workshop pro-
 3185 ceedings [341] for a more detailed summary of recent theoretical developments in high-energy
 3186 resummation.

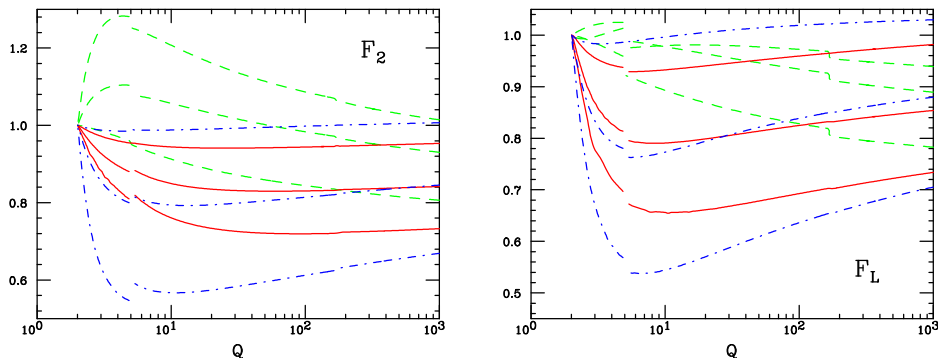


Figure 6.10: The K -factors, defined as the ratio of the fixed-order NNLO or resummed calculation to the NLO fixed-order results for the singlet F_2 and F_L structure functions, with F_2 and F_L kept fixed for all x at $Q_0 = 2$ GeV. Results are shown at fixed $x = 10^{-2}$, 10^{-4} or 10^{-6} as a function of Q in the range $Q = 2 - 1000$ GeV with α_s running and n_f varied in a zero-mass variable flavour number scheme. The breaks in the curves correspond to the b and t quark thresholds. The curves are: fixed order perturbation theory NNLO (green, dashed); resummed NLO in the $Q_0\overline{\text{MS}}$ scheme (red, solid), resummed NLO in the $\overline{\text{MS}}$ scheme (blue, dot-dashed). Curves with decreasing x correspond to those going from bottom to top for NNLO and from top to bottom in the resummed cases.

3187 To summarise, small- x resummation is becoming a very important component for precision
 3188 LHC physics, and will become a crucial ingredient of the LHeC small- x physics program [342,
 3189 343]. The LHeC extended kinematic range will enhance the differences between the resummed
 3190 predictions with respect to fixed-order DGLAP calculations.

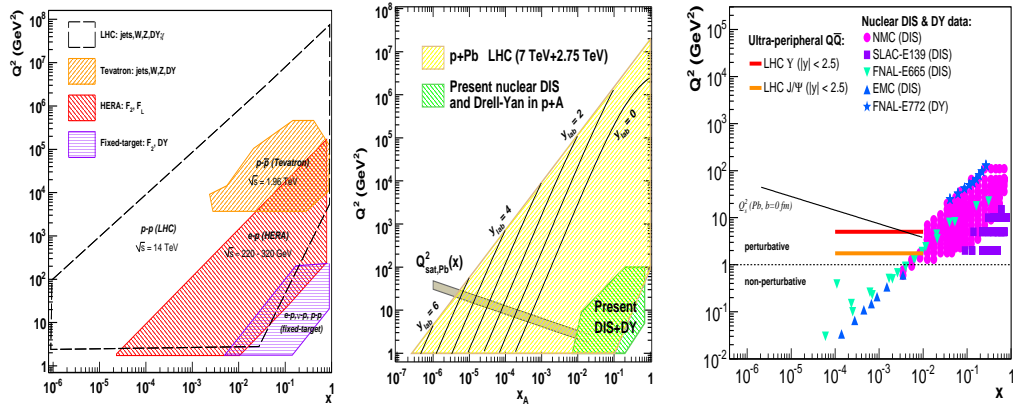


Figure 6.11: Kinematic reaches in the (x, Q^2) plane covered in proton-proton (left), proton-nucleus (center) [344] and ultraperipheral nucleus-nucleus (right) [345] collisions at the LHC. Also shown are the regions studied so far in collider and fixed-target experiments. Estimates of the saturation scale for lead are also shown.

6.1.3 Low- x physics perspectives at the LHC

The low- x regime of QCD can also be analyzed in hadron and nucleus collisions at the LHC. The experimentally accessible values of x range from $x \sim 10^{-3}$ to $x \sim 10^{-6}$ for central and forward rapidities respectively. The estimates for the corresponding saturation scale at $x \sim 10^{-3}$, based on Eq. (6.2), result in $Q_s^2 \approx 1 \text{ GeV}^2$ for proton and $Q_s^2 \approx 5 \text{ GeV}^2$ for lead.

The significant increase in the center-of-mass energy and the excellent rapidity coverage of the LHC detectors will extend the kinematic reach in the x - Q^2 plane by orders of magnitude compared to previous measurements at fixed-target and collider energies (see Fig. 6.11). Such measurements are particularly important in the nuclear case since, due to the scarcity of nuclear DIS data, the gluon PDF in the nucleus is virtually unknown at fractional momenta below $x \approx 10^{-2}$ [136]. In addition, due to the dependence of the saturation scale on the hadron transverse size, non-linear QCD phenomena are expected to play a central role in the phenomenology of collisions involving nuclei. We succinctly review here the experimental possibilities to study saturation physics in pp , pA and AA collisions at the LHC.

Low- x studies in proton-proton collisions

The LHC experiments feature detection capabilities at forward rapidities ($|\eta| \gtrsim 3$), which will allow measurements of various perturbative processes sensitive to the underlying parton structure and its dynamical evolution in the proton. The *minimum* parton momentum fractions probed in a $2 \rightarrow 2$ process with a particle of momentum p_T produced at pseudo-rapidity η is

$$x_{min} = \frac{x_T e^{-\eta}}{2 - x_T e^{\eta}}, \quad \text{where } x_T = 2p_T/\sqrt{s}, \quad (6.5)$$

i.e. x_{min} decreases by a factor ~ 10 every 2 units of rapidity. The extra e^{η} lever-arm motivates the interest in *forward* particle production measurements to study the PDFs at small values

3212 of x . From Eq. (6.5) it follows that the measurement at the LHC of particles with transverse
 3213 momentum $p_T = 10$ GeV at rapidities $\eta \approx 5$ probes x values as low as $x \approx 10^{-5}$ (Fig. 6.11,
 3214 left). Various experimental measurements have been proposed at forward rapidities at the LHC
 3215 to constrain the low- x PDFs in the proton and to look for possible evidence for non-linear QCD
 3216 effects. These include forward jets and Mueller-Navelet dijets in ATLAS and CMS [346]; and
 3217 forward isolated photons [347] and Drell-Yan (DY) [348] in LHCb.

3218 **Low- x studies in proton-nucleus collisions**

3219 Until an electron-ion collider becomes available, proton-nucleus collisions will be the best avail-
 3220 able tool to study small- x physics in a nuclear environment without the strong influence of
 3221 the final-state medium, as expected in the AA case. Though proton-nucleus collisions are not
 3222 yet scheduled at the LHC, detailed feasibility studies exist [349] and strategies to define the
 3223 accessible physics programme are being developed [344]. The pA programme at the LHC serves
 3224 a dual purpose [344]: to provide “cold QCD matter” benchmark measurements for the physics
 3225 measurements of the AA programme without significant final-state effects, and to study the
 3226 nuclear wavefunction in the small- x region. In Fig. 6.11 (center) we show how dramatically
 3227 the LHC will extend the region of phase space in the (x, Q^2) plane² by orders of magnitude
 3228 compared with those studied at present. The same figure also shows the scarcity of nuclear
 3229 DIS and DY measurements and, correspondingly, the lack of knowledge of nuclear PDFs in
 3230 the regions needed to constrain the initial state for the AA programme - there is almost no
 3231 information at present in the region $x \lesssim 10^{-2}$ [136].

3232
 3233 Nuclear PDF constraints, checks of factorization (universality of PDFs) and searches for sat-
 3234 uration of partonic densities will be performed in pA collisions at the LHC by studying different
 3235 production cross sections for e.g. inclusive light hadrons [350], heavy flavour particles [351],
 3236 isolated photons [352], electroweak bosons [353] and jets. Additional opportunities also appear
 3237 in the so-called ultra-peripheral collisions in which the coherent electromagnetic field created
 3238 by the proton or the large nucleus effectively acts as one of the colliding particles with photon-
 3239 induced collisions at centre of mass energies higher than those reached in photoproduction at
 3240 the HERA collider [354] (see next subsection).

3241 At this point it is worth mentioning that particle production in the forward (proton) rapidity
 3242 region in dAu collisions at RHIC shows features suggestive of saturation effects, although no
 3243 consensus has been reached so far, see [355–360] and references therein. The measurements at
 3244 RHIC suffer from the limitation of working at the edge of the available phase space in order to
 3245 study the small- x region in the nuclear wave function. This limitation will be overcome by the
 3246 much larger available phase space at the LHC.

3247 **Low- x studies in nucleus-nucleus collisions**

3248 Heavy-ion (AA) collisions at the LHC aim at the exploration of collective partonic behaviour
 3249 both in the initial wavefunction of the nuclei as well as in the final produced matter, the latter
 3250 being a hot and dense QCD medium (see the discussions in Subsection 6.1.4). The nuclear
 3251 PDFs at small x define the number of parton scattering centers and thus the initial conditions
 3252 of the system which then thermalises.

²Asymmetric colliding systems imply a rapidity shift in the two-in-one magnet design of the LHC. This shift has been taken into account in the figure: the quoted y values are those in the laboratory frame.

3253 A possible means of obtaining direct information on the nuclear parton distribution functions
 3254 is through the study of final state particles which do not interact strongly with the surrounding
 3255 medium, such as photons [361] or electroweak bosons [353]. Beyond this, global properties of
 3256 the collision such as the total multiplicities or the existence of long-range rapidity structures
 3257 (seen in AuAu collisions at RHIC [362] and in pp and PbPb collisions at the LHC [363,364]) are
 3258 sensitive to the saturation momentum which at the LHC is expected to be well within the weak
 3259 coupling regime [365], $Q_{\text{sat,Pb}}^2 \approx 5 - 10 \text{ GeV}^2$. CGC predictions for charged hadron multiplicities
 3260 in central Pb-Pb collisions at 5.5 TeV per nucleon are $dN_{ch}/d\eta|_{\eta=0} \approx 1500-2000$ [366]. (Note
 3261 that the predictions done before the start of RHIC in 2000 were 3 times higher). Recent data
 3262 from ALICE [367] give $dN_{ch}/d\eta|_{\eta=0} \approx 1600$ in central Pb-Pb at 2.76 TeV per nucleon, in rough
 3263 agreement with CGC expectations.

3264 As already noted for the pA case, one of the cleanest ways to study the low- x structure
 3265 of the Pb nucleus at the LHC may be via ultra-peripheral collisions (UPCs) [354] in which
 3266 the strong electromagnetic fields (the equivalent flux of quasi-real photons) generated by the
 3267 colliding nuclei can be used for photoproduction studies at maximum energies $\sqrt{s_{\gamma N}} \approx 1 \text{ TeV}$,
 3268 that is 3–4 times larger than at HERA. In particular, exclusive quarkonium photoproduction
 3269 offers an attractive opportunity to constrain the low- x gluon density at moderate virtualities,
 3270 since in such processes the gluon couples *directly* to the c or b quarks and the cross section is
 3271 proportional to the gluon density *squared*. The vector meson mass M_V introduces a relatively
 3272 large scale, amenable to a perturbative QCD treatment. In $\gamma A \rightarrow J/\psi (\Upsilon) A^{(*)}$ processes at the
 3273 LHC, the gluon distribution can be probed at values as low as $x = M_V^2/W_{\gamma A}^2 e^y \approx 10^{-4}$, where
 3274 $W_{\gamma A}$ is the γA centre of mass energy (Fig. 6.11 right). Full simulation studies [345, 368] of
 3275 quarkonium photoproduction tagged with very-forward neutrons, show that ALICE and CMS
 3276 can carry out detailed p_T, η measurements in the dielectron and dimuon decay channels.

3277 In summary, pp , pA and AA collisions at the LHC have access to the small- x regime, and will
 3278 certainly help to unravel the complex parton dynamics in this region. However, the excellent
 3279 precision of a high energy electron-proton (ion) collider cannot be matched in hadronic collisions.
 3280 The deep inelastic scattering process is much cleaner experimentally and under significantly
 3281 better theoretical control. The description of hadron-hadron and heavy ion collisions in the
 3282 regime of small x suffers from a variety of uncertainties, such as the question of the appropriate
 3283 factorization, if any, and the large indeterminacy of fragmentation functions in the relevant
 3284 kinematic region. Thus, the precise measurement of physical observables and parton densities
 3285 and their interpretation in terms of QCD dynamics is only possible at an electron-hadron (ion)
 3286 collider.

3287 6.1.4 Nuclear targets

3288 As discussed in Subsection 6.1.1, the use of nuclei offers a means of modifying the parton
 3289 density both through colliding different nuclear species and by varying the impact parameter
 3290 of the collision. Therefore, the study of DIS on nuclear targets is of the utmost importance for
 3291 our understanding of the dynamics which control the behaviour of hadron and nuclear wave
 3292 functions at small x . On the other hand, the characterization of parton densities inside nuclei
 3293 and the study of other aspects of lepton-nucleus collisions such as particle production, are of
 3294 strong interest both fundamentally and because they are crucial for a correct interpretation of
 3295 the experimental results from ultrarelativistic ion-ion collisions. In the rest of this section we
 3296 focus on these last two aspects.

3297 Additionally, nuclear effects have to be better understood in order to improve the constraints

3298 on nucleon PDF in analyses which include DIS data with neutrino beams (e.g. [327,329]). Due to
 3299 the smallness of the cross section, such neutrino experiments use nuclear targets, so corrections
 3300 for nuclear effects are a significant source of uncertainty in the extraction of parton densities
 3301 even for the proton.

3302 Comparing nuclear parton density functions

3303 The nuclear modification of structure functions has been extensively studied since the early
 3304 70's [369, 370]. It is usually characterized through the so-called nuclear modification factor
 3305 which, for a given structure function or parton density f , reads

$$R_f^A(x, Q^2) = \frac{f^A(x, Q^2)}{A \times f^N(x, Q^2)}. \quad (6.6)$$

3306 In this equation, the superscript A refers to a nucleus of mass number A , while N denotes
 3307 the nucleon (either a proton or a neutron, or their average as obtained from deuterium). The
 3308 absence of nuclear effects would result in $R = 1$.

3309 The nuclear modification factor for F_2 shows a rich structure: an enhancement ($R > 1$) at
 3310 large $x > 0.8$, a suppression ($R < 1$) for $0.3 < x < 0.8$, an enhancement for $0.1 < x < 0.3$,
 3311 and a suppression for $x < 0.1$ where isospin effects can be neglected. The latter effect is called
 3312 shadowing [304], and is the dominant phenomenon at high energies (the kinematical region
 3313 $x < 0.1$ will determine particle production at the LHC, see Sec. 6.1.3 and [371]).

3314 The modifications in each region are believed to be of different dynamical origin. In the
 3315 case of shadowing, the explanation is usually given in terms of a coherent interaction involving
 3316 several nucleons, which reduces the nuclear cross section from the totally incoherent situation,
 3317 $R = 1$, towards a region of total coherence. In the region of very small x , small-to-moderate Q^2
 3318 and for large nuclei, the unitarity limit of the nuclear scattering amplitudes is expected to be
 3319 approached and some mechanism of unitarisation such as multiple scattering should come into
 3320 play. Therefore, in this region nuclear shadowing is closely related to the onset of the unitarity
 3321 limit in QCD and the transition from coherent scattering of the probe off a single parton to
 3322 coherent scattering off many partons. The different dynamical mechanisms proposed to deal
 3323 with this problem should offer a quantitative explanation for shadowing, with the nuclear size
 3324 playing the role of a density parameter in the way discussed in Subsection 6.1.1.

3325 At large enough Q^2 the generic expectation is that the parton system becomes dilute and the
 3326 usual leading-twist linear DGLAP evolution equations should be applicable to nuclear PDFs. In
 3327 this framework, global analyses of nuclear parton densities (in exact analogy to those of proton
 3328 and neutron parton densities) have been developed up to NLO accuracy [136, 372, 373]. In
 3329 these global analyses, the initial conditions for DGLAP evolution are parametrized by flexible
 3330 functional forms but they lack theoretical motivation in terms of e.g. the dynamical mechanisms
 3331 for unitarization mentioned above. On the other hand, the relation between diffraction and
 3332 nuclear shadowing [21, 265] can in principle be employed to constrain the initial conditions for
 3333 DGLAP evolution, as has been explored previously at both LO [267] and NLO [374]³ accuracy,
 3334 see Subsec. 6.2.4. All nuclear PDF analyses [136, 372, 373] include data from NC DIS and DY
 3335 experiments, and [136] also uses particle production data at mid-rapidity in deuterium-nucleus

³In the approach in [374] predictions are provided only for sea quarks and gluons, with the valence taken from the analysis in [375].

3336 collisions at RHIC. Error sets obtained through the Hessian method are provided in [136]. CC
3337 DIS data have been considered only recently [376, 377]⁴ in this context.

3338 Results from the different nuclear PDF analyses performed at NLO accuracy are shown in
3339 Fig. 6.12, with the band indicating the uncertainty obtained using the error sets in [136]. In
3340 addition to the discrepancies concerning the existence of an enhancement/suppression at large
3341 x , the different approaches lead to clear differences at small x , both in magnitude and in shape,
3342 usually within the large uncertainty band shown. With nuclear effects vanishing logarithmically
3343 in the DGLAP analysis, the corresponding differences and uncertainties diminish, although they
3344 remain sizable until rather large Q^2 .

3345 These large uncertainties are due to the lack of experimental data on nuclear structure
3346 functions for $Q^2 > 2 \text{ GeV}^2$ and x smaller than a few times 10^{-2} . The constraints on the small
3347 x gluon are particularly poor. Particle production data at mid-rapidity coming from deuterium-
3348 nucleus collisions at RHIC offer an indirect constraint on the small- x sea and glue [136], but
3349 these data are bound to contain sizable uncertainties intrinsic to particle production in hadronic
3350 collisions at small and moderate scales. Therefore, only high-accuracy data on nuclear structure
3351 functions at smaller x , with a large lever arm in Q^2 , as is achievable at the LHeC, will be able to
3352 substantially reduce the uncertainties and clearly distinguish between the different approaches.

3353 **Requirements for the ultra-relativistic heavy ion programs at RHIC and the LHC**

3354 The LHeC will offer extremely valuable information on several aspects of high-energy hadronic
3355 and nuclear collisions. On the one hand, it will characterize hard scattering processes in nuclei
3356 through a precise determination of initial state. On the other hand, it will provide quantitative
3357 constraints on theoretical descriptions of initial particle production in ultra-relativistic nucleus-
3358 nucleus collisions and the subsequent evolution into the quark-gluon plasma, the deconfined
3359 partonic state of matter whose production and study offers key information about confinement.
3360 Such knowledge will complement that coming from pA collisions and self-calibrating hard probes
3361 in nucleus-nucleus collisions (see [344, 361, 371, 378, 379]) regarding the correct interpretation of
3362 the findings of the heavy-ion programme at RHIC (see e.g. [380, 381] and refs. therein) and at
3363 the LHC. Beyond the qualitative interpretation of such findings, the LHeC will greatly improve
3364 the quantitative characterization of the properties of QCD extracted from such studies. The
3365 relevant information can be classified into three items:

3366 a. Parton densities inside nuclei:

3367 The knowledge of parton densities inside nuclei is an essential piece of information for
3368 the analysis of the medium created in ultra-relativistic heavy-ion collisions using hard
3369 probes, i.e. those observables whose yield in nucleon-nucleon collisions can be predicted
3370 in pQCD (see [361, 371, 378, 379]). The comparison between the expectation from an
3371 incoherent superposition of nucleon-nucleon collisions and the measurement in nucleus-
3372 nucleus collision characterises the nuclear effects. However, we need to disentangle those
3373 effects which originate from the creation of a hot medium in nucleus-nucleus collisions,
3374 from effects arising only from differences in the partonic content between nucleons and
3375 nuclei.

3376 Our present knowledge of parton densities inside nuclei is clearly insufficient in the kine-
3377 matic regions of interest for RHIC and, above all, for the LHC (see [371] and Subsection

⁴The analysis in [377] shows the compatibility of the nuclear corrections as extracted in [136] with CC DIS data on nuclear targets, while in [376] some tension is found between NC and CC DIS data.

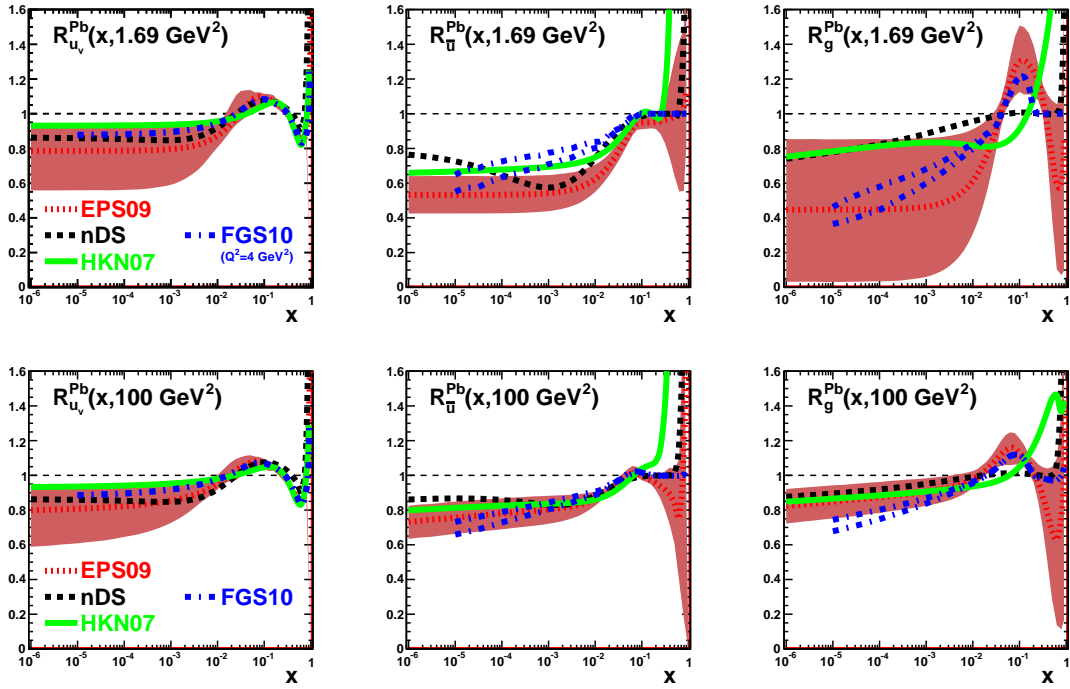


Figure 6.12: Ratio of parton densities in a bound proton in Pb to those in a free proton scaled by $A = 207$, for valence u (left), \bar{u} (middle) and g (right), at $Q^2 = 1.69$ (top) and 100 (bottom) GeV^2 . Results are shown from [372] (nDS, black dashed), [373] (HKN07, green solid), [136] (EPS09, red dotted) and [374] (FGS10, blue dashed-dotted; in this case the lowest Q^2 is 4 GeV^2 and two lines are drawn reflecting the uncertainty in the predictions). The red bands indicate the uncertainties according to the EPS09 analysis [136].

3378 6.1.3). Such ignorance reflects in uncertainties larger than a factor 3 – 4 for the calcu-
3379 lation of different cross sections in nucleus-nucleus collisions at the LHC (see Fig. 6.12
3380 and [350]), thus weakening strongly the possibility of extracting quantitative character-
3381 istics of the produced hot medium. While the pA program at the LHC will offer new
3382 constraints on the nuclear parton densities (e.g. [344, 350]), measurements at the LHeC
3383 would be far more constraining and would reduce the uncertainties in nucleus-nucleus
3384 cross sections to less than a factor two.

3385 b. Parton production and initial conditions for a heavy-ion collision:

3386 The medium produced in ultra-relativistic heavy-ion collisions develops very early a col-
3387 lective behavior, usually considered as that of a thermalized medium and describable
3388 by relativistic hydrodynamics. The initial state of a heavy-ion collision for times prior
3389 to its eventual thermalization, and the thermalisation or isotropisation mechanism, play
3390 a key role in the description of the collective behavior. Such an initial condition for
3391 hydrodynamics or transport is presently modelled and fitted to data. But it should even-
3392 tually be determined by a theoretical formalism of particle production within a saturation
3393 framework which embodies the both aspects: parton fluxes inside nuclei - discussed in the
3394 previous item, and particle production and evolution, eventually leading to isotropization.

3395 The CGC offers a well-defined framework in which the initial condition and thermalization
3396 mechanism can be computed from QCD, see Subsection 6.1.1 and e.g. [382] and refs.
3397 therein. Although our theoretical knowledge is still incomplete, electron-nucleus collisions
3398 are considerably less complex than the nucleus-nucleus collisions in which these CGC-
3399 based calculations already exist and can be tested. In this way, electron-ion collisions offer
3400 a testing ground for ideas on parton production in a dense environment, which is required
3401 for a first principles calculation of the initial conditions for the collective behavior in
3402 ultra-relativistic heavy-ion collisions. The LHeC offers the possibility of studying particle
3403 production in the kinematic region relevant for experiments at RHIC and the LHC.

3404 c. Parton fragmentation and hadronization inside the nuclear medium:

3405 The mechanism through which a highly virtual parton evolves from an off-shell coloured
3406 state to a final state consisting of colourless hadrons, is still subject to great uncertainties.
3407 Electron-ion experiments offer a testing ground for our ideas and understanding of such
3408 phenomena, see [383] and refs. therein, with the nucleus being a medium of controllable
3409 extent and density which modifies the radiation and hadronization processes.

3410 The LHeC will have capabilities for particle identification and jet reconstruction for both
3411 nucleon and nuclear targets. Its kinematic reach will allow the study of partons traveling
3412 through the nucleus from low energies, for which hadronization is expected to occur
3413 inside the nucleus, to high energies with hadronization outside the nucleus. Therefore the
3414 modification of the yields of energetic hadrons, observed at RHIC⁵ and usually attributed
3415 to in-medium energy loss - the so-called jet quenching phenomenon - will be investigated.
3416 With jet quenching playing a key role in the present discussions on the production and
3417 characterisation of the hot medium produced in ultra-relativistic heavy-ion collisions,
3418 the LHeC will offer most valuable information on effects in cold nuclear matter of great
3419 importance for clarifying and reducing the existing uncertainties.

⁵LHC experiments have already observed the jet quenching phenomenon both at the level of single-particle spectra [384] and through the study of jets [385, 386], which will play a central role in heavy-ion physics at these energies.

3420 6.2 Prospects at the LHeC

3421 6.2.1 Strategy: decreasing x and increasing A

3422 As discussed previously, in order to analyse the regime of high parton densities at small x , we
3423 propose a two-pronged approach which is illustrated in Fig. 6.5. To reach an interesting novel
3424 regime of QCD one can either decrease x by increasing the center-of-mass energy or increase
3425 the matter density by increasing the mass number A of the nucleus. In addition, we will see
3426 that diffraction, and especially exclusive diffraction, will play a special role in unravelling the
3427 new dense partonic regime of QCD.

3428 The LHeC will offer a huge lever arm in x and also a possibility of changing the matter
3429 density at fixed values of x . This will allow us to pin down and compare the small x and
3430 saturation phenomena both in protons and nuclei and will offer an excellent testing ground for
3431 theoretical predictions. Thus, in the following, LHeC simulations of electron-proton collisions
3432 are paralleled by those in electron-lead wherever possible. For a complementary perspective on
3433 the opportunities for novel QCD studies offered by the LHeC, see [54].

3434 6.2.2 Inclusive measurements

3435 Predictions for the proton

3436 The LHeC is expected to provide measurements of the structure functions of the proton with
3437 unprecedented precision, which will allow detailed studies of small- x QCD dynamics. In partic-
3438 ular, it will be highly sensitive to departures of the inclusive observables, F_2 and F_L from the
3439 fixed-order DGLAP framework, in the region of small x and Q^2 . These deviations are expected
3440 by several theoretical arguments, as discussed in detail previously.

3441 In Fig. 6.13 we show several predictions for the proton structure functions, F_2 and F_L ,
3442 in ep collisions at $Q^2 = 10 \text{ GeV}^2$ and for $10^{-6} \leq x \leq 0.01$ i.e. $F_{2(L)}(x, Q^2 = 10 \text{ GeV}^2)$.
3443 The different curves correspond to the extrapolation of models that reproduce correctly the
3444 available HERA data for the same observables in the small- x region. They are classified into two
3445 categories: those based on linear evolution approaches and those that include non-linear small-
3446 x dynamics. Among the linear approaches we include extrapolation from the NLO DGLAP
3447 fit as performed by the NNPDF collaboration [387] (solid yellow bands) and the results from
3448 a combined DGLAP/BFKL approach, which includes resummation of small- x effects [388]
3449 (black-dotted-dotted lines). The non-linear calculations shown here are all formulated within
3450 the dipole model. We distinguish two categories: those based on the eikonalization of multiple
3451 scatterings together with DGLAP evolution of the gluon distributions [320, 321] (blue dashed-
3452 dotted lines) and those relying in the Color Glass Condensate effective theory of high-energy
3453 QCD scattering (red dashed lines). The latter include calculations based on solutions of the
3454 running coupling Balitsky-Kovchegov equation [389] and other more phenomenological models
3455 of the dipole amplitude without [306], or with [322] impact parameter dependence. Finally, we
3456 also include a hybrid approach, where initial conditions based on Regge theory and including
3457 non-linearities are evolved in Q^2 according to linear DGLAP evolution [266] (green dotted line).
3458 In all cases the error bands are generated by allowing variations of the free parameters in each
3459 subset of models. The green filled squares correspond to the subset of the simulated LHeC
3460 pseudodata at $Q^2 = 10 \text{ GeV}^2$ (see subsection 4.1.4).

3461 Clearly, the accuracy of the data at the LHeC will offer huge possibilities for discriminating
3462 between different models and for constraining the dynamics underlying the small- x region.

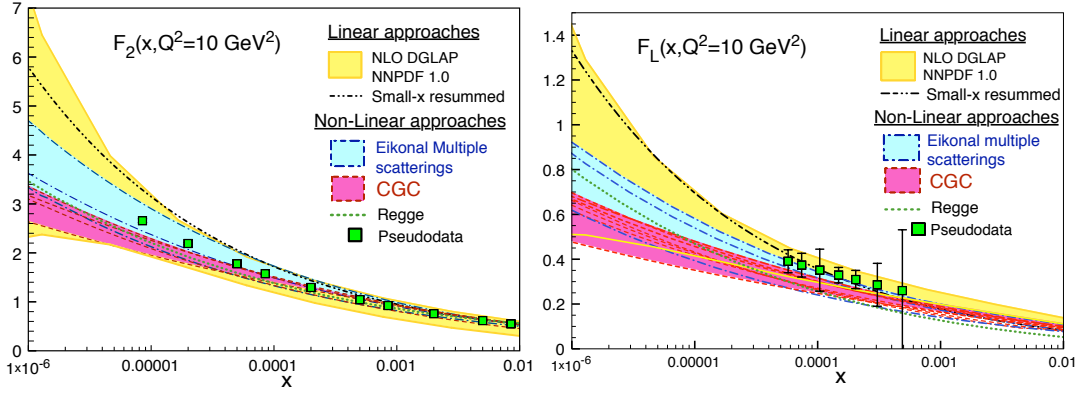


Figure 6.13: Predictions from different models for $F_2(x, Q^2 = 10 \text{ GeV}^2)$ (plot on the left) and $F_L(x, Q^2 = 10 \text{ GeV}^2)$ (plot on the right) versus x , together with the corresponding pseudodata. See the text for explanations.

3463 Constraining small- x dynamics

3464 The potential impact of the LHeC on low x parton densities within the framework of an NLO
 3465 DGLAP analysis is assessed by adding the pseudodata introduced in subsection 4.1.4 into the
 3466 NNPDF fitting analysis. The pseudodata are first generated at the extrapolated central values
 3467 according to the existing NNPDF fits.

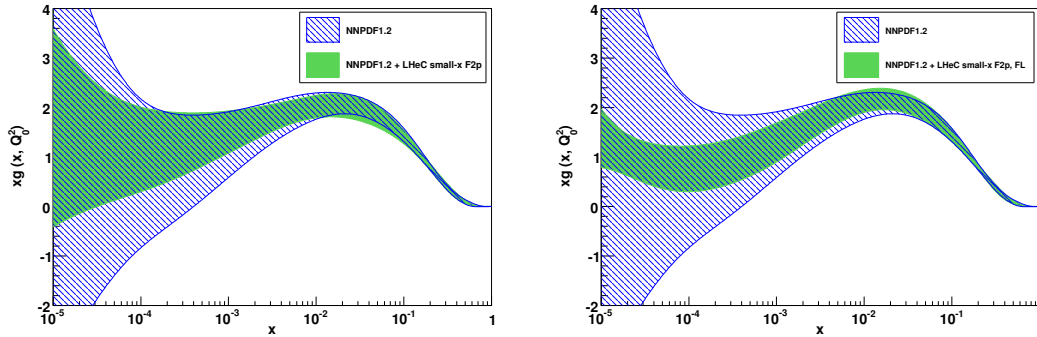


Figure 6.14: The results for the gluon distribution in the standard NNPDF1.2 DGLAP fit [387], together with the results when additionally including LHeC pseudodata for F_2 (left) and for both F_2 and F_L (right). The results are shown at the starting scale for DGLAP evolution, $Q_0^2 = 2 \text{ GeV}^2$.

3468 The extrapolated NNPDF1.2 gluon density and its uncertainty band are shown at the starting
 3469 scale for QCD evolution, $Q_0^2 = 2 \text{ GeV}^2$ in Fig. 6.14, where it can be seen that the lack
 3470 of experimental constraints for $x \lesssim 10^{-4}$ leads to an explosion in the uncertainties. When the
 3471 LHeC F_2 pseudodata are included in addition, the uncertainties improve considerably, but re-
 3472 main rather large at the lowest x values, due to the lack of a large lever-arm in Q^2 to constrain

3473 the evolution. However, when the LHeC pseudodata on the longitudinal structure function F_L
 3474 are included in addition, the additional constraints lead to a much more substantial improve-
 ment in the uncertainties on the gluon density.

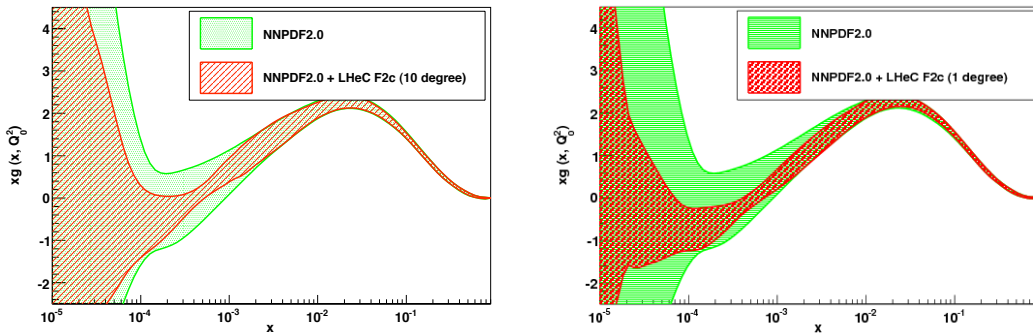


Figure 6.15: The effect on the extracted gluon distribution function of the inclusion of the LHeC pseudodata on the charmed structure function in the NNPDF global analysis. Left plot: scattered electron acceptance extending to within 10° of the beampipe. Right plot: 1° acceptance. The results are shown at the starting scale for DGLAP evolution, $Q_0^2 = 2 \text{ GeV}^2$.

3475
 3476 As is well known from experience at HERA, the measurement of the longitudinal structure
 3477 function presents many experimental challenges and involves possibly undesirable modifications
 3478 to the beam energies. An alternative constraint on the gluon density from the charmed struc-
 3479 ture function F_2^c has therefore also been investigated. As discussed in detail in Subsec. 4.7.1,
 3480 the LHeC will offer unique precision in the determination of the charm and beauty structure
 3481 functions, extending to very small x .

3482 In Fig. 6.15 the gluon distribution function is shown, as obtained from the NNPDF2.0 anal-
 3483 ysis. The green band corresponds to the standard analysis. The red band shows the modified
 3484 analysis where additionally F_2^c pseudodata from the LHeC are included, using a novel technique
 3485 based on Bayesian reweighting [390]. It is observed that the charmed structure function con-
 3486 siderably improves the constraints on the gluon density at small values of x , especially between
 3487 $3 \times 10^{-5} - 10^{-2}$, provided that the scattered electron acceptance extends to within around 1°
 3488 of the beampipe. With a sufficiently good theoretical understanding, heavy flavour production
 3489 data from the LHeC may thus offer an alternative to F_L for precision constraints on the gluon
 3490 density at all but the lowest x values.

3491 Given that for all models considered in Fig. 6.13 there are significant flexibilities in the
 3492 initial parametrisations, it is conceivable that upon suitable changes of parameters it would
 3493 be possible to obtain satisfactory fits of a wide range of models to the LHeC data. It is
 3494 therefore essential to analyse in more detail the ability of the LHeC to distinguish unambiguously
 3495 between different evolution dynamics. With this aim, a PDF analysis is performed including
 3496 LHeC pseudodata which are generated using different scenarios for small- x QCD dynamics.
 3497 Pseudodata for $F_2(x, Q^2)$ and $F_L(x, Q^2)$ at small x are considered in a scenario in which the
 3498 LHeC machine has electron energy $E_e = 70 \text{ GeV}$ and electron acceptance for $\theta_e \leq 179^\circ$, for an
 3499 integrated luminosity of 1 fb^{-1} . The study is carried out in the framework of the NNPDF1.0
 3500 analysis [391] and includes all HERA and fixed target data used in that analysis, in addition to

3501 LHeC pseudodata. The kinematics of the LHeC pseudodata included in the fit (together with
 3502 other data included in the original NNPDF1.0 analysis) are shown in Fig. 6.16. In order to avoid
 3503 correlations between low x and high x data e.g. through the momentum sum rule constraint,
 3504 only LHeC pseudodata with $x < 10^{-2}$ are considered. The average total uncertainty of the
 3505 simulated F_2 pseudodata is $\sim 2\%$, while that of F_L is $\sim 8\%$.

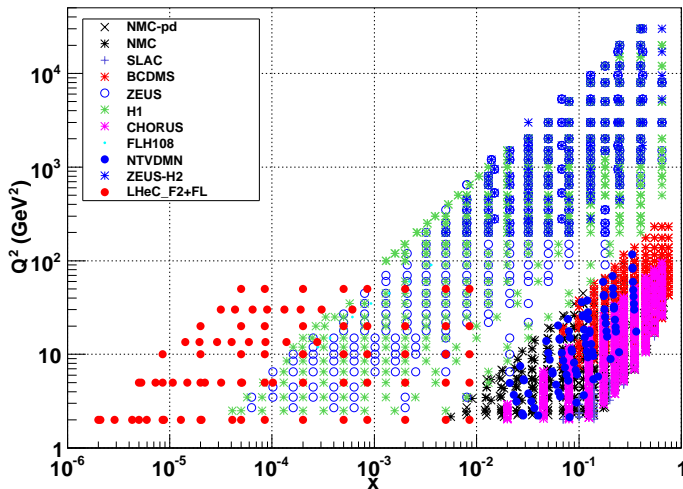


Figure 6.16: The kinematic coverage of the LHeC pseudodata used in the present studies, together with the data already included in the reference NNPDF1.0 dataset.

3506 For the NNPDF fits, the input LHeC pseudodata are generated not within the DGLAP
 3507 framework, but rather using two different models which include saturation effects in the gluon
 3508 density: the AAMS09 model [389], which is based on non-linear Balitsky-Kovchegov evolution
 3509 with a running coupling, and the FS04 dipole model [307]. Both of these models deviate
 3510 significantly from linear DGLAP evolution in the LHeC regime.

3511 The global fit using the NNPDF1.0 framework with fixed-order DGLAP evolution is re-
 3512 peated, now including LHeC pseudodata generated using the scenarios including saturation
 3513 effects. By assessing the quality of the fit with saturated LHeC pseudodata included, this study
 3514 tests the sensitivity to parton dynamics beyond fixed-order DGLAP. The conclusions are the
 3515 same for both the AAMS09 and the FS04 models. The DGLAP analysis yields an acceptable
 3516 fit when only the $F_2(x, Q^2)$ LHeC pseudodata are included. This implies that although the
 3517 underlying physical theories are different, the small- x extrapolations of AAMS09 and FS04 for
 3518 F_2 are sufficiently similar to DGLAP-based extrapolations for the differences to be absorbed
 3519 as modifications to the shapes of the non-perturbative initial conditions for the PDFs at the
 3520 starting scale Q_0^2 for DGLAP evolution. More sophisticated analyses, based for example on
 3521 sequential kinematical cuts and backwards DGLAP evolution, as presented in Subsec. 6.1.2,
 3522 could still be applied. However, it seems likely that it will not be possible unambiguously
 3523 to establish non-linear effects using LHeC data on F_2 alone.

3524 The situation is very different when data on the longitudinal structure function $F_L(x, Q^2)$

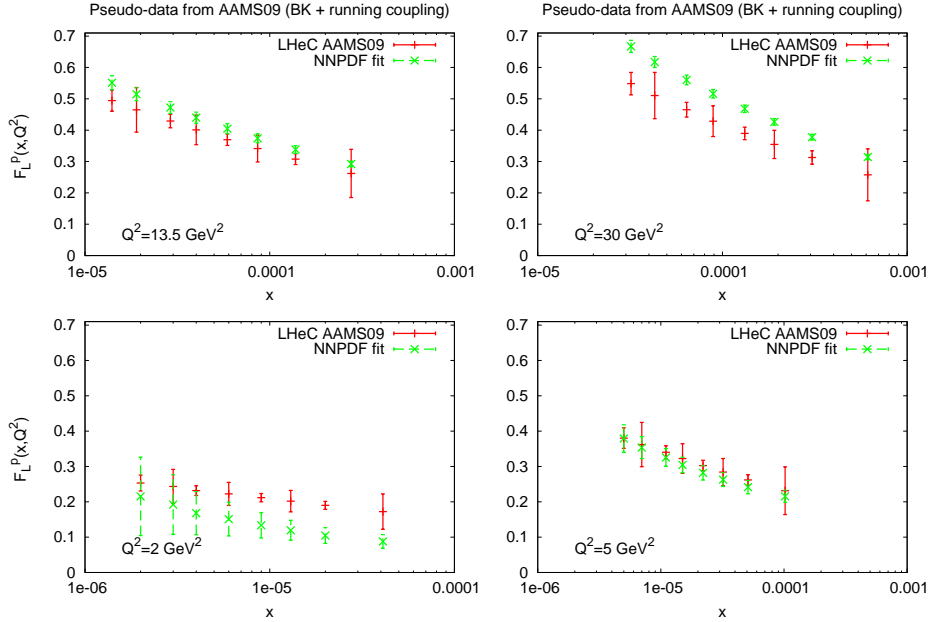


Figure 6.17: The results for F_L obtained from the best NLO DGLAP fit to the standard NNPDF1.2 data set, together with the LHeC pseudodata for $F_2(x, Q^2)$ and $F_L(x, Q^2)$ generated with the (saturating) AAMS09 model. The fit results are compared with the input AAMS09 F_L pseudodata.

3525 are included in the NNPDF fit, provided the lever-arm in Q^2 is large enough for the gluon
3526 sensitivity through the Q^2 evolution of F_2 to conflict with that through F_L . The analysis based
3527 on linear DGLAP evolution fails to reproduce simultaneously F_2 and F_L in all the Q^2 bins,
3528 and thus the overall χ^2 is very large. The effect is illustrated in Fig. 6.17, where the best fits
3529 from the NNPDF DGLAP analysis are compared with the LHeC F_L pseudodata generated
3530 from the AAMS09 model. This is a clear signal for a departure from fixed-order DGLAP of
3531 the simulated pseudodata. This analysis shows that the combined use of F_2 and F_L data is
3532 a very sensitive probe of novel small- x QCD dynamics, and that their measurement would be
3533 very likely to discriminate between different theoretical scenarios. Using F_2^c data in place of F_L
3534 may offer a similarly powerful means of establishing deviations from fixed-order linear DGLAP
3535 evolution at small x .

3536 Predictions for nuclei: impact on nuclear parton distribution functions

3537 The LHeC, as an electron-ion collider in the TeV regime, will have an enormous potential
3538 for measuring the nuclear parton distribution functions at small x . Let us start by a brief
3539 explanation of how the pseudodata for inclusive observables in e Pb collisions are obtained: To
3540 simulate an LHeC measurement of F_2 in electron-nucleus collisions, the points (x, Q^2) , generated
3541 for $e(50) + p(7000)$ collisions for a high acceptance, low luminosity scenario, as explained in
3542 subsection 4.1.4, are considered. Among them, we keep only those points at small $x \leq 0.01$

3543 and not too large $Q^2 < 1000 \text{ GeV}^2$ with $Q^2 \leq sx$, for a Pb beam energy of 2750 GeV per
 3544 nucleon. Under the assumption that the instantaneous luminosity per nucleon is the same in
 3545 ep and eA [392], the number of events is scaled by a factor $1/(5 \times 50 \times A)$, with 50 coming
 3546 from the transition from a high luminosity to a low luminosity scenario, and 5 being a crudely
 3547 estimated reduction factor accounting for the shorter running time for ions than for proton.

3548 At each point of the grid, σ_r and F_2 are generated using the dipole model of [302, 393] to
 3549 get the central value. Then, for every point, the statistical error in ep is scaled by the previously
 3550 mentioned factor $1/(5 \times 50 \times A)$, and corrected for the difference in F_2 or σ_r between the
 3551 (Glauberized) 5-flavor GBW model [393] and the model used for the ep simulation. The frac-
 3552 tional systematic errors are taken to be the same as for ep - as has been achieved in previous DIS
 3553 experiments on nuclear targets⁶. An analogous procedure is applied when obtaining the nuclear
 3554 pseudodata for F_2^c and F_2^b , considering the same tag and background rejection efficiencies as in
 3555 the ep simulation.

3556 To generate LHeC F_L pseudodata for a heavy ion target, a dedicated simulation of $e +$
 3557 $p(2750)$ collisions has been performed, at three different energies: 10, 25 and 50 GeV for the
 3558 electron, with assumed luminosities 5, 10 and 100 pb^{-1} respectively, see subsec. 4.1.5. Then,
 3559 for each point in the simulated grid, F_L values for protons and nuclei are generated using the
 3560 (Glauberized) 5-flavor GBW model [393]. The relative uncertainties are taken to be exactly
 3561 the same as in the ep simulation, as explained above.

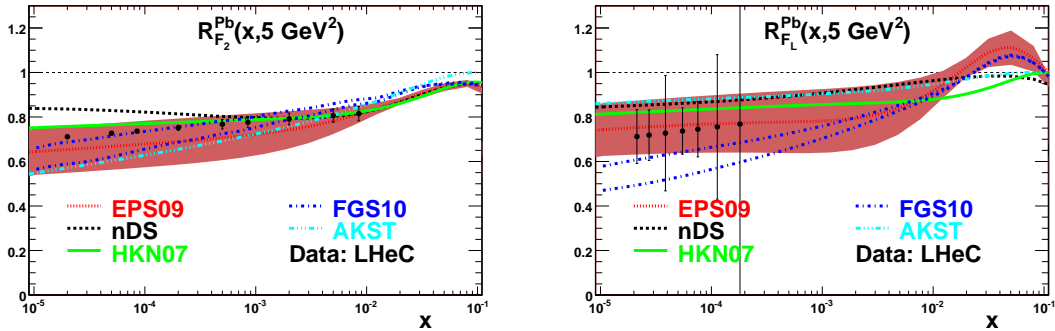


Figure 6.18: Predictions from different models for the nuclear modification factor, Eq. (6.6) for Pb with respect to the proton, for $F_2(x, Q^2 = 5 \text{ GeV}^2)$ (plot on the left) and $F_L(x, Q^2 = 5 \text{ GeV}^2)$ (plot on the right) versus x , together with the corresponding LHeC pseudodata. Dotted lines correspond to the nuclear PDF set EPS09 [136], dashed ones to nDS [372], solid ones to HKN07 [373], dashed-dotted ones to FGS10 [374] and dashed-dotted-dotted ones to AKST [267]. The band corresponds to the uncertainty in the Hessian analysis in EPS09 [136].

3562 In Fig. 6.18 we show several predictions for the nuclear suppression factor, Eq. (6.6), with
 3563 respect to the proton, for the total and longitudinal structure functions, F_2 and F_L respectively,
 3564 in $e\text{Pb}$ collisions at an example $Q^2 = 5 \text{ GeV}^2$ and for $10^{-5} < x < 0.1$. Predictions based on
 3565 global DGLAP analyses of existing data at NLO: nDS, HKN07 and EPS09 [136, 372, 373], plus
 3566 those from models using the relation between diffraction and nuclear shadowing, AKST and

⁶A significant difference in the systematics may eventually come from the different size of the QED radiative corrections for protons and nuclei, an important point which remains to be addressed in future studies.

3567 FGS10 [267, 374], are shown together with the LHeC pseudodata. Brief explanations on the
 3568 different models can be found in Subsec. 6.1.4. Clearly, the accuracy of the data at the LHeC
 3569 will offer huge possibilities for discriminating between different models and for constraining the
 3570 dynamics underlying nuclear shadowing at small x .

3571 In order to better quantify how the LHeC would improve the present situation concerning
 3572 nuclear PDFs in global DGLAP analyses (see the uncertainty band in Fig. 6.12), nuclear LHeC
 3573 pseudodata have been included in the global EPS09 analysis [136]. The DGLAP evolution
 3574 was carried out at NLO accuracy, in the variable-flavor-number scheme (SACOT prescription)
 3575 with the CTEQ6.6 [325] set for free proton PDFs as a baseline. See [136] and references
 3576 therein for further details. The only difference compared with the original EPS09 setup is that
 3577 one additional gluon parameter, x_a , has been varied (this parameter was originally frozen in
 3578 EPS09), and the only additionally weighted data set was the PHENIX data on π^0 production
 3579 at mid-rapidity [394] in dAu collisions at RHIC.

3580 Two different fits have been performed: the first one (Fit 1) includes pseudodata on the
 3581 total reduced cross section. The results of the fit are shown in Fig. 6.19 in terms of the nuclear
 3582 modification factors for the parton densities. A large improvement in the determination of sea
 3583 quark and gluon densities at small x is evident.

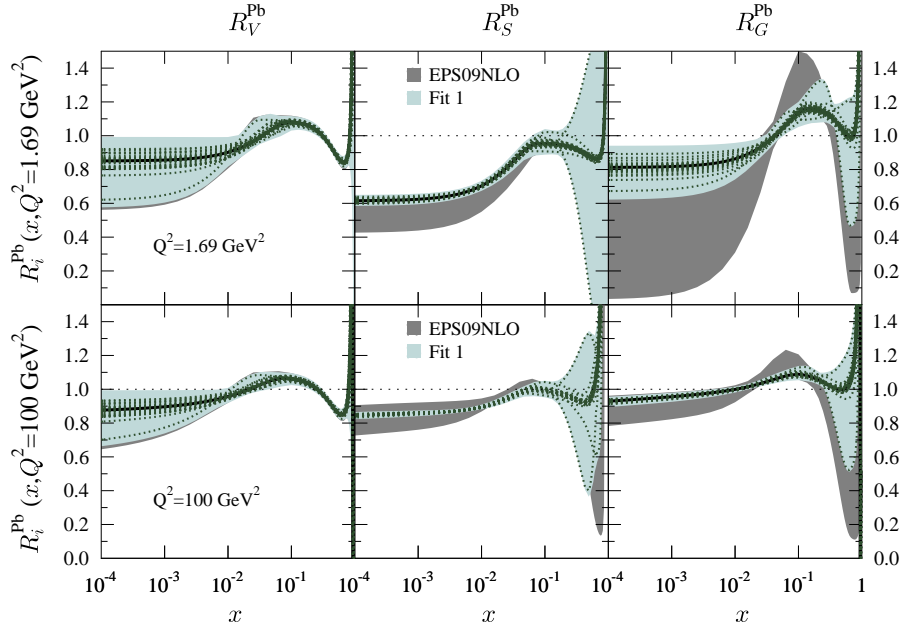


Figure 6.19: Ratio of parton densities for protons bound in Pb to those in a free proton, for valence u (left), \bar{u} (middle) and g (right), at $Q^2 = 1.69$ (top) and 100 (bottom) GeV^2 . The dark grey band corresponds to the uncertainty band using the Hessian method in the original EPS09 analysis [136], while the light blue band corresponds to the uncertainty obtained after including nuclear LHeC pseudodata on the total reduced cross sections (Fit 1). The dotted lines indicate the values corresponding to the different nPDF sets in the EPS09 analysis [136].

3584 The second fit (Fit 2) includes not only nuclear LHeC pseudodata on the total reduced cross
3585 section but also on its charm and beauty components. These data provide direct information
3586 on the nuclear effects on charm and beauty parton densities, which are generated mainly dy-
3587 namically from the gluons through DGLAP evolution. Thus, the inclusion of such pseudodata
3588 further improves the determination of the nuclear effects on the gluon at small x , as illustrated
3589 in Fig. 6.20.

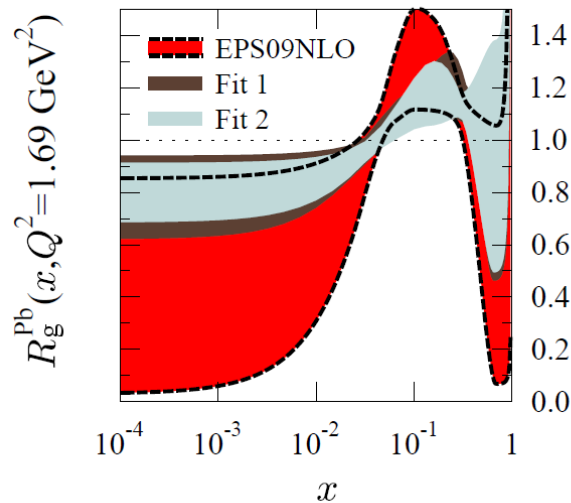


Figure 6.20: Ratio of the gluon density for protons bound in Pb to that of a free proton at $Q^2 = 1.69 \text{ GeV}^2$. The red band corresponds to the uncertainty using the Hessian method in the original EPS09 analysis [136], while the dark brown band corresponds to the uncertainty obtained after including nuclear LHeC pseudodata on the total reduced cross sections (Fit 1), and the light blue band shows the uncertainty obtained after further including pseudodata on charm and beauty reduced cross sections (Fit 2).

3590 In both Figs. 6.19 and 6.20 a sizable reduction of the uncertainties in the sea quark and
3591 gluon nuclear parton distributions at large $x > 0.1$ can also be observed. This improvement is
3592 basically due to the constraints imposed by sum rules and to the fact that DGLAP evolution
3593 links large and small x . Although the study of parton distributions at large x is not the subject
3594 of this chapter, it is worth commenting that F_2 could be measured in eA collisions at the LHeC
3595 with a statistical accuracy better than a few percent up to $x \sim 0.6$ but for large $Q^2 > 1000$
3596 GeV^2 . On the other hand, flavor decomposition will only be accessible for $x < 0.1$. Therefore,
3597 the LHeC will provide additional information on the antishadowing ($R > 1$, $0.1 < x < 0.3$)
3598 and - with less precision - on the EMC-effect ($R < 1$, $0.3 < x < 0.8$) regions. The latter is
3599 valence-dominated and there exist data from fixed target experiments, though at much smaller
3600 Q^2 , so at the LHeC the validity of leading-twist DGLAP evolution will be tested.

3601 Furthermore, the large lever-arm in Q^2 opens the possibility of measuring CC events in

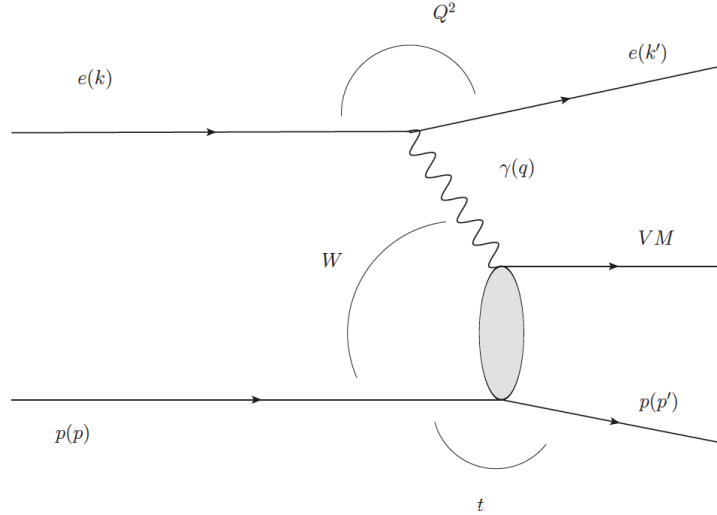


Figure 6.21: Schematic illustration of the exclusive vector meson production process and the kinematic variables used to describe it in photoproduction ($Q^2 \rightarrow 0$) and DIS (large Q^2). The outgoing particle labelled ‘VM’, may be either a vector meson with $J^{PC} = 1^{--}$ or a photon.

3602 electron scattering on nuclear targets, thus helping to improve the loose constraints on the
 3603 flavour decomposition of the nuclear parton densities coming from existing DIS and DY data.
 3604 In this respect (see the comments in Subsec. 6.1.4) the LHeC may help to clarify the issue of
 3605 the compatibility of the nuclear corrections extracted in neutrino-nucleus collisions with those
 3606 coming from electron- or muon-nucleus collisions⁷.

3607 In conclusion, the precision and large lever-arm in x and Q^2 of the nuclear data at the LHeC
 3608 will offer huge possibilities for discriminating different models and for constraining the parton
 3609 densities in global DGLAP analyses. Besides measurements of the reduced cross section, data
 3610 on its charm and bottom components and on F_L will help to constrain the nuclear effects on
 3611 PDFs, see e.g. the recent work in [396, 397].

3612 6.2.3 Exclusive Production

3613 Introduction

3614 Exclusive processes such as the electroproduction of vector mesons and photons, $\gamma^* N \rightarrow$
 3615 VN ($V = \rho^0, \phi, \gamma$), or photoproduction of heavy quarkonia, $\gamma N \rightarrow VN$ ($V = J/\psi, \Upsilon$) - see
 3616 Fig. 6.21 - provide information on nucleon structure and small- x dynamics which is comple-
 3617 mentary to that obtained in inclusive measurements [305]. The exclusive production of J/ψ
 3618 and ρ mesons in ep collisions and Deeply-Virtual Compton Scattering (DVCS, $ep \rightarrow e\gamma p$), have
 3619 been particularly prominent in the development of our understanding of HERA physics [398].

⁷Note that the nuclear modifications of the structure function F_2 in these two types of process are expected to differ due to the different coupling to quarks [395].

3620 Diffractive channels such as these are favourable, since the underlying exchange crudely
 3621 equates to a pair of gluons, making the process sensitive to the square of the gluon density [399],
 3622 in place of the linear dependence for F_2 or F_L . With a sufficiently good theoretical understand-
 3623 ing of the exclusive production mechanism, this may enhance substantially the sensitivity to
 3624 non-linear evolution and saturation phenomena. As already shown at HERA, J/Ψ production
 3625 in particular is a potentially very clean probe of the gluonic structure of the hadron [322, 399].
 3626 The same exclusive processes can be measured in deep inelastic scattering off nuclei, where the
 3627 gluon density is modified by nuclear effects [400]. In addition, exclusive processes give access to
 3628 the spatial distribution of the gluon density, parametrized by the impact parameter [401] of the
 3629 collision. The correlations between the gluons coupling to the proton contain information on the
 3630 three-dimensional structure of the nucleon or nucleus, which is encoded in the Generalised Par-
 3631 ton Densities (GPDs). The GPDs combine aspects of parton densities and elastic form factors
 3632 and have emerged as a key concept for describing nucleon structure in QCD (see [20, 402, 403]
 3633 for a review).

3634 Exclusive processes can be treated conveniently within the dipole picture described in Sub-
 3635 sec. 6.1.2. In this framework, the cross section can be represented as a product of three fac-
 3636 torisable terms: the splitting of an incoming photon into a $q\bar{q}$ dipole; the ‘dipole’ cross section
 3637 for the interaction of this $q\bar{q}$ pair with the proton and, in the case of vector mesons, a wave
 3638 function term for the projection of the dipole onto the meson. As discussed in Subsec. 6.1.2 the
 3639 dipole formalism is particularly convenient since saturation effects can be easily incorporated.

3640 Generalised Parton Densities and Spatial Structure

3641 At sufficiently large Q^2 the exclusively produced meson or photon is in a configuration of
 3642 transverse size much smaller than the typical hadronic size, $r_\perp \ll R_{\text{hadron}}$. As a result its
 3643 interaction with the target can be described using perturbative QCD [404]. A QCD factorisa-
 3644 tion theorem [405] states that the exclusive amplitudes in this regime can be factorised into a
 3645 perturbative QCD scattering process and certain universal process-independent functions des-
 3646 cribing the emission and absorption of the active partons by the target, the generalized parton
 3647 distributions (GPDs).

3648 The Fourier transform of the GPDs with respect to the transverse momentum transferred
 3649 to the nucleon describes the transverse spatial distribution of partons (illustrated in Fig. 6.3)
 3650 with a given longitudinal momentum fraction x [406]. The transverse spatial distributions
 3651 of quarks and gluons are fundamental characteristics of the nucleon, which reveal the size of
 3652 the configurations in its partonic wave function and allow the study of the non-perturbative
 3653 dynamics governing their change with x , such as Gribov diffusion, chiral dynamics, and other
 3654 phenomena. The nucleon transverse gluonic size is also an essential input in studies of saturation
 3655 at small x . It determines the initial conditions of the non-linear QCD evolution equations and
 3656 thus directly influences the impact parameter dependence of the saturation scale for the nucleon
 3657 [321, 407], which in turn predicates its nuclear enhancement [408]. Information on the nucleon
 3658 transverse quark and gluon distributions is further required in the phenomenology of high-
 3659 energy pp collisions with hard processes, including those with new particle production, where it
 3660 determines the underlying event structure (centrality dependence) in inclusive scattering [409]
 3661 and the rapidity gap survival probability in hard single diffraction [410] and central exclusive
 3662 diffraction [411, 412]. In view of its considerable interest, the transverse quark/gluon imaging of
 3663 the nucleon with exclusive processes has been recognized as an important objective of nucleon
 3664 structure and small- x physics.

3665 Mapping the transverse spatial distribution of quarks and gluons requires measurement of
 3666 the t -dependence of hard exclusive processes up to large values of $|t|$, of the order of 1 GeV^2 .
 3667 Studies of the Q^2 -dependence and comparisons between different channels provide crucial tests
 3668 of the reaction mechanism and the universality of GPDs. Vector meson production at small x
 3669 and heavy quarkonium photoproduction at high energies probe the gluon GPD of the target,
 3670 while real photon production (DVCS) involves the singlet quark as well as the gluon GPDs.
 3671 Measurements of exclusive J/ψ photo/electroproduction [413, 414] and ρ^0 and ϕ electropro-
 3672 duction at HERA have confirmed the applicability of the factorized QCD description through
 3673 several model-independent tests, and have provided basic information on the nucleon gluonic
 3674 size in the region $10^{-4} < x < 10^{-2}$ and its change with x [305]. Measurements of DVCS at
 3675 HERA [415, 416] hint that the transverse distribution of singlet quarks may extend further than
 3676 that of gluons. While these experiments have given important insight into transverse nucleon
 3677 structure, the interpretation of the HERA data is limited by the low statistics which preclude
 3678 a fully differential analysis. A major source of systematic uncertainty at larger t arises from
 3679 the lack of a complete separation between elastically scattered protons and proton excitations,
 3680 illustrating the importance of good scattered proton detection at the LHeC.

3681 As discussed in the following, the LHeC would enable a comprehensive program of gluon
 3682 and singlet quark transverse imaging through exclusive processes, with numerous applications
 3683 to nucleon structure and small- x physics. The high statistics would permit fully differential
 3684 measurements of exclusive channels, as needed to understand the reaction mechanism. For ex-
 3685 ample, measurements of the t -distributions for fixed x differentially in Q^2 are needed to confirm
 3686 the dominance of small-size configurations. The LHeC would also push such measurements
 3687 to the region $Q^2 \sim \text{few} \times 10 \text{ GeV}^2$ where finite-size (higher-twist) effects are small and the
 3688 effects of QCD evolution can be cleanly identified. Measurements of gluonic exclusive chan-
 3689 nels ($J/\psi, \phi, \rho^0$) at the LHeC would provide gluonic transverse images of the nucleon down
 3690 to $x \sim 10^{-6}$ with unprecedented accuracy, testing theoretical ideas about diffusion dynam-
 3691 ics in the wave function. Because exclusive cross sections are proportional to the square of
 3692 the gluon GPD (i.e. the gluon density), such measurements would also offer new insight into
 3693 non-linear effects in QCD evolution, and enable new tests of the approach to saturation by
 3694 measuring the impact parameter dependence of the saturation scale. Along these lines, satura-
 3695 tion effects in the exclusive vector meson production on protons and nuclei have been studied
 3696 in [400, 417–419]. Furthermore, measurements of DVCS would provide additional information
 3697 on the nucleon singlet quark size and its dependence on x . Besides its intrinsic interest for
 3698 nucleon structure and small- x physics, this information would greatly advance our theoretical
 3699 understanding of the transverse geometry of high-energy pp collisions at the LHC. We note
 3700 that these exclusive measurements at the LHeC would complement similar measurements at
 3701 moderately small x ($0.003 < x < 0.2$) with the COMPASS experiment at CERN and in the
 3702 valence region $x > 0.1$ with the JLab 12 GeV Upgrade, providing a comprehensive picture of
 3703 the nucleon spatial structure.

3704 Further interesting information comes from hard exclusive measurements accompanied by
 3705 the diffractive dissociation of the nucleon, $\gamma^* N \rightarrow V + Y$ ($Y =$ low-mass proton dissociation
 3706 state). The ratio of inelastic to elastic diffraction in these processes provides information on
 3707 the quantum fluctuations of the gluon density, which reveals the quantum-mechanical nature
 3708 of the non-perturbative colour fields in the nucleon and can be related to dynamical models
 3709 of low-energy nucleon structure [420]. HERA results are in qualitative agreement with such
 3710 model predictions but do not permit a quantitative analysis. These measurements of exclusive
 3711 diffraction at the LHeC, and similar ones for eA collisions, would allow for detailed quantitative

3712 studies of all these new aspects of nucleon and nuclear structure.

3713 Exclusive Production Formalism in the Dipole Approach

3714 For the exclusive production of vector mesons, a QCD factorization theorem has been demon-
 3715 strated (for σ_L) in [404]. The dipole model follows from this QCD factorization theorem in the
 3716 LO approximation. Within the dipole model, see Subsec. 6.1.2, the amplitude for the exclusive
 3717 diffractive production of a particle E , $\gamma^*p \rightarrow Ep$, shown in Fig. 6.22(a), can be expressed as

$$\mathcal{A}_{T,L}^{\gamma^*p \rightarrow E+p}(x, Q, \Delta) = i \int d^2\mathbf{r} \int_0^1 \frac{dz}{4\pi} \int d^2\mathbf{b} (\Psi_E^* \Psi)_{T,L} e^{-i[\mathbf{b} - (1-z)\mathbf{r}] \cdot \Delta} \frac{d\sigma_{q\bar{q}}}{d^2\mathbf{b}}. \quad (6.7)$$

3718 Here $E = V$ for vector meson production, or $E = \gamma$ for deeply virtual Compton scattering
 3719 (DVCS). In Eq. (6.7), z is the fraction of the photon's light-cone momentum carried by the
 3720 quark, $r = |\mathbf{r}|$ is the transverse size of the $q\bar{q}$ dipole, while \mathbf{b} is the impact parameter, that
 3721 is, $b = |\mathbf{b}|$ is the transverse distance from the centre of the proton to the centre-of-mass of
 3722 the $q\bar{q}$ dipole; see Fig. 6.22(a). The transverse momentum lost by the outgoing proton, Δ ,
 3723 is the Fourier conjugate variable to the impact parameter \mathbf{b} , and $t \equiv (p - p')^2 = -\Delta^2$. The
 3724 forward overlap function between the initial-state photon wave function and the final-state
 3725 vector meson or photon wave function in Eq. (6.7) is denoted $(\Psi_E^* \Psi)_{T,L}$, while the factor
 3726 $\exp[i(1-z)\mathbf{r} \cdot \Delta]$ originates from the non-forward wave function [421]. The differential cross
 3727 section for an exclusive diffractive process is obtained from the amplitude, Eq. (6.7), by

$$\frac{d\sigma_{T,L}^{\gamma^*p \rightarrow E+p}}{dt} = \frac{1}{16\pi} \left| \mathcal{A}_{T,L}^{\gamma^*p \rightarrow E+p} \right|^2, \quad (6.8)$$

3728 up to corrections from the real part of the amplitude and from skewedness ($x' \ll x \ll 1$
 3729 for the variables shown in figure 6.22a). Taking the imaginary part of the forward scattering
 3730 amplitude immediately gives the formula for the total γ^*p cross section (or equivalently, the
 3731 proton structure function $F_2 = F_T + F_L$) via the optical theorem:

$$\sigma_{T,L}^{\gamma^*p}(x, Q) = \text{Im} \mathcal{A}_{T,L}^{\gamma^*p \rightarrow \gamma^*p}(x, Q, \Delta = 0) = \sum_f \int d^2\mathbf{r} \int_0^1 \frac{dz}{4\pi} (\Psi^* \Psi)_{T,L}^f \int d^2\mathbf{b} \frac{d\sigma_{q\bar{q}}}{d^2\mathbf{b}}. \quad (6.9)$$

3732 The dipole picture therefore provides a unified description of both exclusive diffractive processes
 3733 and inclusive deep-inelastic scattering (DIS) at small x .

3734 The unknown quantity common to Eqs. (6.7) and (6.9) is the b -dependent dipole–proton
 3735 cross section,

$$\frac{d\sigma_{q\bar{q}}}{d^2\mathbf{b}} = 2 \mathcal{N}(x, r, b), \quad (6.10)$$

3736 where \mathcal{N} is the imaginary part of the dipole–proton scattering amplitude, which can vary
 3737 between zero and one, with $\mathcal{N} = 1$ corresponding to the unitarity (“black disk”) limit. The
 3738 scattering amplitude \mathcal{N} encodes the information about the details of the strong interaction
 3739 between the dipole and the target (proton or nucleus). It is generally parameterised according
 3740 to some theoretically-motivated functional form, with the parameters fitted to data. Most dipole
 3741 models assume a factorised b dependence, $\mathcal{N}(x, r, b) = T(b) \mathcal{N}(x, r)$, with $\mathcal{N}(x, r) \in [0, 1]$ and,
 3742 for example, $T(b) = \Theta(R_p - b)$, so that the b -integrated $\sigma_{q\bar{q}} = (2\pi R_p^2) \mathcal{N}(x, r)$. However, the
 3743 “saturation scale” is strongly dependent on impact parameter and the chosen of b -dependence

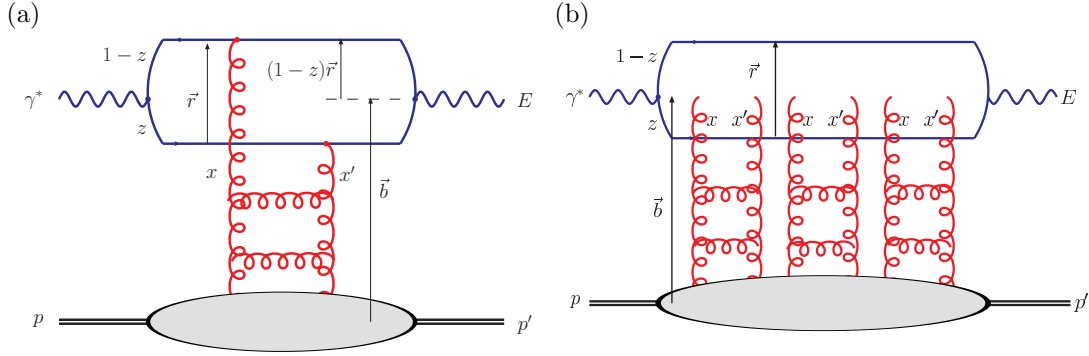


Figure 6.22: Parton level diagrams representing the γ^*p scattering amplitude proceeding via (a) single-Pomeron and (b) multi-Pomeron exchange, where the perturbative QCD Pomeron is represented by a gluon ladder. For exclusive diffractive processes, such as vector meson production ($E = V$) or DVCS ($E = \gamma$), we have $x' \ll x \ll 1$ and $t = (p - p')^2$. These diagrams are related through the optical theorem to inclusive DIS, where $E = \gamma^*$, $x' = x \ll 1$ and $p' = p$.

3744 must be made consistent with the t -dependence of exclusive diffraction at HERA. This matching
 3745 is complicated by the the non-zero effective ‘‘Pomeron slope’’ $\alpha'_{\mathbb{P}}$ measured at HERA, which
 3746 implies a correlation between the x - and b - dependences of $\mathcal{N}(x, r, b)$. Therefore, for accurate
 3747 results, $\mathcal{N}(x, r, b)$ should be determined from the simultaneous description of inclusive DIS and
 3748 exclusive diffractive processes.

3749 An impact-parameter-dependent saturation (‘‘b-sat’’) model [321, 322] has been shown to
 3750 describe very successfully a broad range of HERA data on exclusive diffractive vector meson
 3751 (J/ψ , ϕ , ρ) production and DVCS (see also the rather different approach in [422]), including
 3752 almost all aspects of the Q^2 , W and t dependence with the exception of $\alpha'_{\mathbb{P}}$, together with the
 3753 inclusive structure functions F_2 , $F_2^{c\bar{c}}$, $F_2^{b\bar{b}}$ and F_L . The ‘‘b-Sat’’ parameterisation is based on LO
 3754 DGLAP evolution of an initial gluon density, $xg(x, \mu_0^2) = A_g x^{-\lambda_g} (1 - x)^{5.6}$, with a Gaussian
 3755 impact parameter dependence, $T(b) \propto \exp(-b^2/2B_G)$. The dipole scattering amplitude is
 3756 parametrized as

$$\mathcal{N}(x, r, b) = 1 - \exp\left(-\frac{\pi^2}{2N_c} r^2 \alpha_S(\mu^2) xg(x, \mu^2) T(b)\right), \quad (6.11)$$

3757 where the scale $\mu^2 = 4/r^2 + \mu_0^2$, $B_G = 4 \text{ GeV}^{-2}$ was fixed from the t -slope of exclusive J/ψ
 3758 photoproduction at HERA, and the other three parameters ($\mu_0^2 = 1.17 \text{ GeV}^2$, $A_g = 2.55$,
 3759 $\lambda_g = 0.020$) were fitted to ZEUS F_2 data with $x_{\text{Bj}} \leq 0.01$ and $Q^2 \in [0.25, 650] \text{ GeV}^2$ [322]. The
 3760 eikonalised dipole scattering amplitude of Eq. (6.11) can be expanded as

$$\mathcal{N}(x, r, b) = \sum_{n=1}^{\infty} \frac{(-1)^{n+1}}{n!} \left[\frac{\pi^2}{2N_c} r^2 \alpha_S(\mu^2) xg(x, \mu^2) T(b) \right]^n, \quad (6.12)$$

3761 where the n -th term in the expansion corresponds to n -Pomeron exchange; for example, the
 3762 case $n = 3$ is illustrated in Fig. 6.22(b). The terms with $n > 1$ are necessary to ensure unitarity.

3763 **Simulations of LHeC Elastic J/ψ and Υ Production**

3764 Due to the extremely clean final states produced, the relatively low effective x -values ($x_{\text{eff}} \sim$
 3765 $(Q^2+m_V^2)/(Q^2+W^2)$) and scales ($Q_{\text{eff}}^2 \sim (Q^2+m_V^2)/4$) accessed [399,423], and the experimental
 3766 possibility of varying both W and t over wide ranges, J/ψ photoproduction ($Q^2 \rightarrow 0$) may offer
 3767 the cleanest available signature to study the transition between the dilute and dense regimes
 3768 of small- x partons. It should be possible to detect the muons from J/ψ or Υ decays with
 3769 acceptances extending to within 1° of the beampipe with dedicated muon chambers on the
 3770 outside of the experiment. Depending on the electron beam energy, this makes invariant photon-
 3771 proton masses W of well beyond 1 TeV accessible.

3772 For the analysis presented here we concentrate on the photoproduction limit, where the
 3773 HERA data are most precise due to the large cross sections and where unitarity effects are
 3774 most important. Studies have also been made at larger Q^2 [424], where the extra hard scale
 3775 additionally allows a perturbative treatment of exclusive light vector meson (e.g. ρ , ω , ϕ)
 3776 production. Again, perturbative unitarity effects are expected to be important for light vector
 3777 meson production when $Q^2 \gtrsim 1 \text{ GeV}^2$ is not too large.

3778 LHeC pseudodata for elastic J/ψ and Υ photoproduction and electroproduction have been
 3779 generated using the DIFFVM Monte Carlo generator [425] under the assumption of 1° ac-
 3780 ceptance and a variety of luminosity scenarios. The DIFFVM generator involves a simple
 3781 Regge-based parameterization of the dynamics and a full treatment of decay angular distribu-
 3782 tions. Statistical uncertainties are estimated for each data point. Systematic uncertainties are
 3783 hard to estimate without a detailed simulation of the muon identification and reconstruction
 3784 capabilities of the detector, but are likely to be at least as good as the 10% measurements
 3785 typically achieved for the elastic J/ψ at HERA.

3786 The plots in Fig. 6.23 show t -integrated predictions for exclusive J/ψ photoproduction
 3787 ($Q^2 = 0$) obtained from Eqs. (6.7) and (6.8), using the eikonalised “b-Sat” dipole scattering
 3788 amplitude given in Eq. (6.11) together with a “boosted Gaussian” vector meson wave func-
 3789 tion [322,426]. Also shown is the single-Pomeron exchange contribution obtained by keeping
 3790 just the first ($n = 1$) term in the expansion of Eq. (6.12), such that the scattering ampli-
 3791 tude is linearly dependent on the gluon density, without refitting any of the input parameters.
 3792 The difference between the “eikonalised” and “1-Pomeron” predictions therefore indicates the
 3793 importance of unitarity corrections, which increase significantly with rising γp centre-of-mass
 3794 energy W . The maximum kinematic limit accessible at the LHeC, $W = \sqrt{s}$, is indicated with
 3795 different options for electron beam energies (E_e) and not accounting for the angular acceptance
 3796 of the detector. The most precise HERA data [414,427] are overlaid, together with sample
 3797 LHeC pseudodata points, assuming 1° muon acceptance, with the errors (statistical only) given
 3798 by an LHeC simulation with $E_e = 150 \text{ GeV}$. The central values of the LHeC pseudodata points
 3799 were obtained from a Gaussian distribution with the mean given by extrapolating a power-law
 3800 fit to the HERA data [414,427] and the standard deviation given by the statistical errors from
 3801 the LHeC simulation. The plots in Fig. 6.23 show that the errors on the LHeC pseudodata
 3802 are much smaller than the difference between the “eikonalised” and “1-Pomeron” predictions.
 3803 Therefore, exclusive J/ψ photoproduction at the LHeC may be an ideal observable for investi-
 3804 gating unitarity corrections at a perturbative scale provided by the charm-quark mass.

3805 Similar plots for exclusive Υ photoproduction are shown in Fig. 6.24. Here, the unitar-
 3806 ity corrections are smaller than for J/ψ production due to the larger scale provided by the
 3807 bottom-quark mass and therefore the smaller typical dipole sizes r being probed. The simu-
 3808 lated LHeC pseudodata points also have larger statistical errors than for J/ψ production due

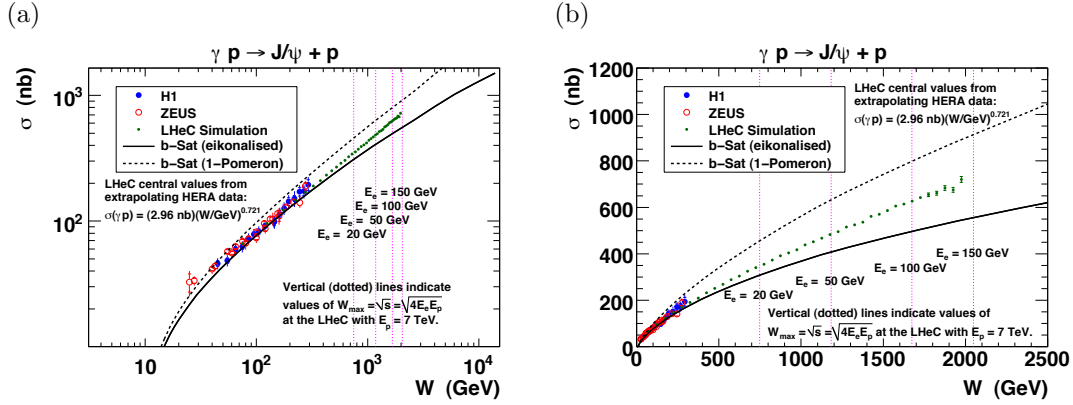


Figure 6.23: LHeC exclusive J/ψ photoproduction pseudodata, as a function of the γp centre-of-mass energy W , plotted on a (a) log–log scale and (b) linear–linear scale. The difference between the solid and dashed curves indicates the size of unitarity corrections according to the b-Sat dipole model.

3809 to the much smaller cross sections. Nonetheless, the simulations indicate that a huge improve-
 3810 ment in kinematic range and precision is possible compared with the very sparse Υ data from
 3811 HERA [428–430].

3812 In order to achieve a satisfactory description of the experimental data on exclusive Υ pho-
 3813 toproduction, an additional normalization factor of ~ 2 has to be included in the dipole calcu-
 3814 lation (a similar factor is required for other calculations using the dipole model, see for example
 3815 Ref. [431]). This normalization factor does not arise from any theoretical considerations. There-
 3816 fore, the dipole model prediction for the Υ in diffractive exclusive processes in DIS still poses
 3817 significant theoretical questions which cannot be resolved without LHeC data.

3818 The cross sections shown in Figs. 6.23 and 6.24 are integrated over $t \equiv (p - p')^2 = -\Delta^2$,
 3819 where Δ is the Fourier conjugate variable to the impact parameter \mathbf{b} . One expects that at high
 3820 center-of-mass energies (small x), saturation effects are most important close to the centre of the
 3821 proton (small b), where the interaction region is densest. This is illustrated in Fig. 6.25(a) where
 3822 the b-Sat model dipole scattering amplitude is shown as a function of b for various x values.
 3823 By measuring exclusive diffraction in bins of $|t|$ one can extract the impact parameter profile
 3824 of the interaction region. This is illustrated in Fig. 6.25(b) where the integrand of Eq. (6.7)
 3825 is shown for different values of t as a function of impact parameter. Clearly for large values
 3826 of $|t|$, small values of b are probed in the impact parameter profile., corresponding to the most
 3827 densely populated region, where saturation effects should be most clearly visible. Indeed, the
 3828 eikonalised dipole model of Eq. (6.11) leads to “diffractive dips” in the t -distribution of exclusive
 3829 J/ψ photoproduction at large $|t|$ (reminiscent of the dips seen in the t -distribution of the proton-
 3830 proton elastic cross section), departing from the exponential fall-off in the t -distribution seen
 3831 with single-Pomeron exchange [321]. The HERA experiments have only been able to make
 3832 precise measurements of exclusive J/ψ photoproduction at relatively small $|t| \lesssim 1 \text{ GeV}^2$, and
 3833 no significant departure from the exponential fall-off, $d\sigma/dt \sim \exp(-B_D|t|)$, has been observed.

3834 In Fig. 6.26, LHeC pseudodata on the differential cross section $d\sigma/dt$ is shown as a function
 3835 of the energy W in different bins of t for the case of exclusive J/Ψ production. Again two
 3836 different b-Sat model scenarios are shown, with unitarisation effects and with single Pomeron

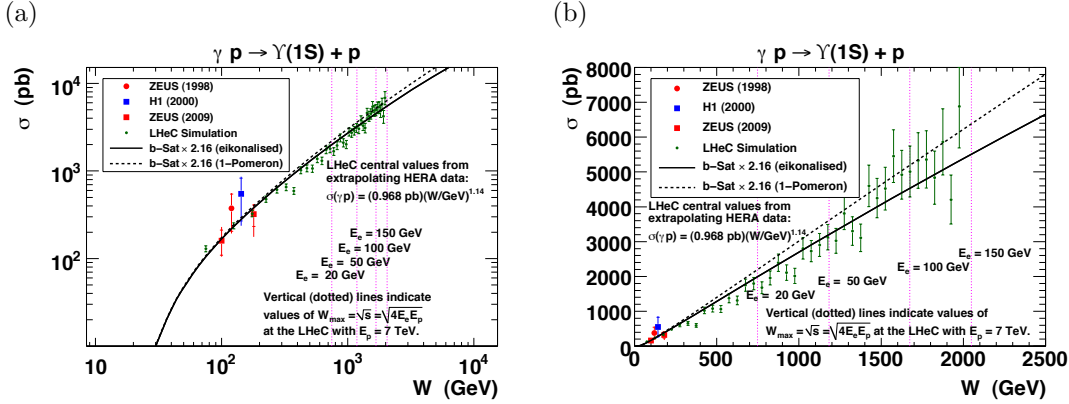


Figure 6.24: LHeC exclusive Υ photoproduction pseudodata, as a function of the γp centre-of-mass energy W , plotted on a (a) log–log scale and (b) linear–linear scale. The difference between the solid and dashed curves indicates the size of unitarity corrections according to the b-Sat model. The b-Sat theory predictions have been scaled by a factor 2.16 to best-fit the existing HERA data.

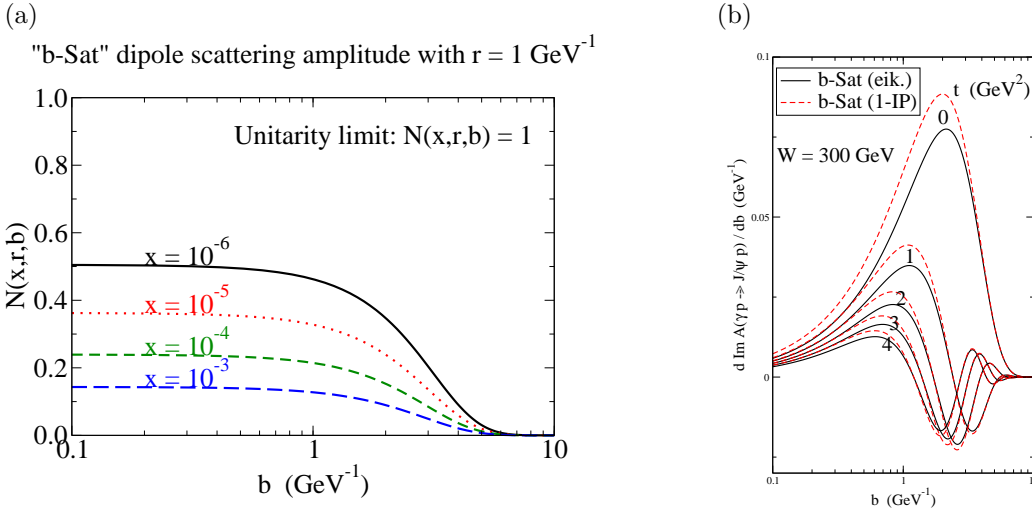


Figure 6.25: (a) The imaginary part of the dipole scattering amplitude, $\mathcal{N}(x, r, b)$, as a function of the impact parameter b , for fixed values of dipole size $r = 1 \text{ GeV}^{-1}$ (typical for exclusive J/ψ photoproduction) and different x values. (b) The $(r$ -integrated) amplitude - the integrand of Eq. (6.7) - for exclusive J/ψ photoproduction as a function of b , for $W = 300 \text{ GeV}$ and $|t| = 0, 1, 2, 3, 4 \text{ GeV}^2$.

3837 exchange. Already for small values of $|t| \sim 0.2 \text{ GeV}^2$ and low values of electron energies there is
 3838 a large discrepancy between the models. The LHeC simulated data still have very small errors
 3839 in this regime, and can clearly distinguish between the different models. The differences are of
 3840 course amplified for large t and large electron beam energies. However the precision of the data
 3841 deteriorates at large t .

3842 Summarising, it is clear that the precise measurements of large- $|t|$ exclusive J/ψ photopro-
 3843 duction at the LHeC would have significant sensitivity to unitarity effects.

3844 Simulations of Deeply Virtual Compton Scattering at the LHeC

3845 Simulations of the DVCS measurement possibilities with the LHeC have been made using the
 3846 Monte Carlo generator MILOU [432], in the ‘FFS option’, for which the DVCS cross section is
 3847 estimated using the model of Frankfurt, Freund and Strikman [433]. A t -slope of $B = 6 \text{ GeV}^{-2}$
 3848 is assumed.

3849 The $ep \rightarrow e\gamma p$ DVCS cross section is estimated in various scenarios for the electron beam
 3850 energy and the statistical precision of the measurement is estimated for different integrated
 3851 luminosity and detector acceptance choices. Detector acceptance cuts at either 1° or 10° are
 3852 placed on the polar angle of the final state electron and photon. Based on experience with
 3853 controlling backgrounds in HERA DVCS measurements [415, 416, 434], an additional cut is
 3854 placed on the transverse momentum P_T^γ of the final state photon.

3855 The kinematic limitations due to the scattered electron acceptance follow the same patterns
 3856 as for the inclusive cross section (see Subsec. 6.2.2). The photon P_T^γ cut is found to be a further
 3857 important factor in the Q^2 acceptance, with measurements at $Q^2 < 20 \text{ GeV}^2$ almost completely
 3858 impossible for a cut at $P_T^\gamma > 5 \text{ GeV}$, even in the scenario with detector acceptances reaching
 3859 1° . If this cut is relaxed to $P_T^\gamma > 2 \text{ GeV}$, it opens the available phase space towards the lowest
 3860 Q^2 and x values permitted by the electron acceptance.

3861 A simulation of a possible LHeC DVCS measurement double differentially in x and Q^2 is
 3862 shown in Fig. 6.27 for a very modest luminosity scenario (1 fb^{-1}) in which the electron beam
 3863 energy is 50 GeV , the detector acceptance extends to 1° and photon measurements are possible
 3864 down to $P_T^\gamma = 2 \text{ GeV}$. High precision is possible throughout the region $2.5 < Q^2 < 40 \text{ GeV}^2$ for
 3865 x values extending down to $\sim 5 \times 10^{-5}$. The need to measure DVCS therefore places constraints
 3866 on the detector performance for low transverse momentum photons, which in practice translates
 3867 into the electromagnetic calorimetry noise conditions and response linearity at low energies.

3868 If the detector acceptance extends to only 10° , the P_T^γ cut no longer plays such an important
 3869 role. Although the low Q^2 acceptance is lost in this scenario, the larger luminosity will allow
 3870 precise measurements for $Q^2 \gtrsim 50 \text{ GeV}^2$, a region which is not well covered in the 1° acceptance
 3871 scenario due to the small cross section. In the simulation shown in Fig. 6.28, a factor of 100
 3872 increase in luminosity is considered, resulting in precise measurements extending to $Q^2 >$
 3873 500 GeV^2 , well beyond the range explored for DVCS or other GPD-sensitive processes to date.

3874 Maximising the lepton beam energy potentially gives access to the largest W and smallest
 3875 x values, provided the low P_T^γ region can be accessed. However, the higher beam lepton en-
 3876 ergy boosts the final state photon in the scattered lepton direction, resulting in an additional
 3877 acceptance limitation.

3878 Further studies of this process will require a better understanding of the detector in order to
 3879 estimate systematic uncertainties. A particularly interesting extension would be to investigate
 3880 possible beam charge [415, 434] and polarisation asymmetry measurements at lower x or larger
 3881 Q^2 than was possible at HERA. With the addition of such information, a full study of the

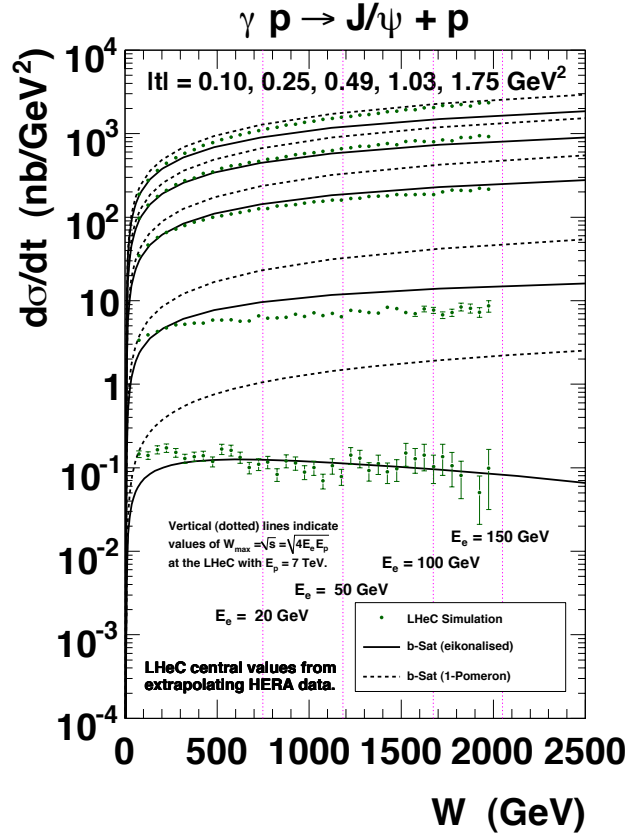


Figure 6.26: Simulated LHeC measurements of the W -dependence of exclusive J/ψ photo-production at the LHeC, differentially in bins of $|t| = 0.10, 0.20, 0.49, 1.03, 1.75$ GeV^2 . The difference between the solid and dashed curves indicates the size of unitarity corrections according to the b-Sat dipole model. The central values of the LHeC pseudodata points were obtained from a Gaussian distribution with the mean given by extrapolating a parameterization of HERA data and the standard deviation given by the statistical errors from the LHeC simulation with $E_e = 150$ GeV. The t -integrated cross section (σ) as a function of W for the HERA parameterization was obtained from a power-law fit to the data from both ZEUS [427] and H1 [414], then the t -distribution was assumed to behave as $d\sigma/dt = \sigma \cdot B_D \exp(-B_D|t|)$, with $B_D = [4.400 + 4 \cdot 0.137 \log(W/90 \text{ GeV})]$ GeV^{-2} obtained from a linear fit to the values of B_D versus W given by both ZEUS [427] and H1 [414].

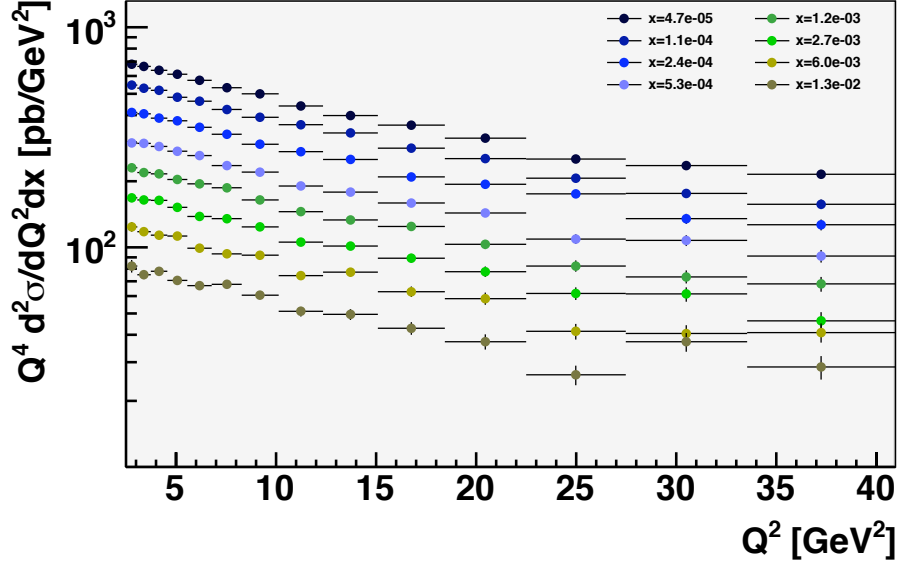


Figure 6.27: Simulated LHeC measurement of the DVCS cross section multiplied by Q^4 for different x values for a luminosity of 1 fb^{-1} , with $E_e = 50 \text{ GeV}$, and electron and photon acceptance extending to within 1° of the beampipe with a cut at $P_T^\gamma = 2 \text{ GeV}$. Only statistical uncertainties are considered.

3882 potential of the LHeC to constrain GPDs could be performed.

3883 **Diffractive Vector Meson Production off Nuclei**

3884 Exclusive diffractive processes are similarly promising as a source of information on the gluon
 3885 density in the nucleus [400]. Quasi-elastic scattering of photons from nuclei at small x can be
 3886 treated within the same dipole model framework as for ep scattering, making the comparisons
 3887 with the proton case relatively straightforward. The interaction of the dipole with the nucleus
 3888 can be viewed as a sum of dipole scatterings off the nucleons forming the nucleus. Nuclear
 3889 effects can be incorporated into the dipole cross section by modifying the transverse gluon
 3890 distribution and adding the corrections due to Glauber rescattering from multiple nucleons
 3891 [321,400]. Previous experimental data on exclusive production from nuclei exist [435,436], but
 3892 are limited in both kinematic range and precision.

3893 There is one aspect of diffraction which is specific to nuclei. The structure of incoherent
 3894 diffraction with nuclear break-up ($eA \rightarrow eXY$) is more complex than with a proton target, and it
 3895 can also be more informative. In the case of a target nucleus, we expect the following qualitative
 3896 changes in the t -dependence. First, the low- $|t|$ regime of coherent diffraction illustrated in
 3897 Fig. 6.29 left, in which the nucleus scatters elastically and remains in its ground state, will be
 3898 dominant up to a smaller value of $|t|$ (about $|t| = 0.05 \text{ GeV}^2$) than in the proton case, reflecting

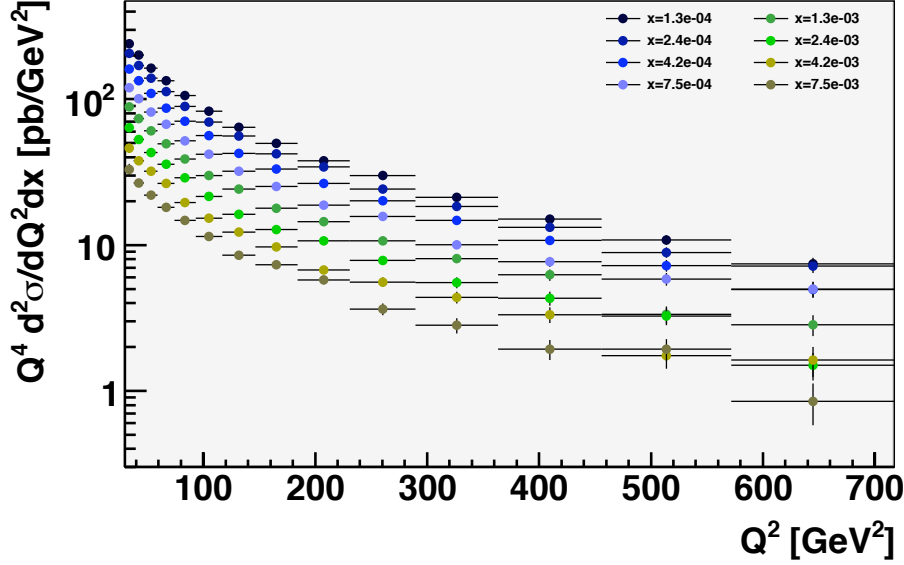


Figure 6.28: Simulated LHeC measurement of the DVCS cross section multiplied by Q^4 for different x values for a luminosity of 100 fb^{-1} , with $E_e = 50 \text{ GeV}$, and electron and photon acceptance extending to within 10° of the beampipe with a cut at $P_T^\gamma = 5 \text{ GeV}$. Only statistical uncertainties are considered.

3899 the larger size of the nucleus. The nuclear dissociation regime (incoherent case), see Fig. 6.29
 3900 right, will consist of two parts: an intermediate regime in momentum transfer up to perhaps
 3901 $|t| = 0.7 \text{ GeV}^2$, where the nucleus will predominantly break up into its constituent nucleons,
 3902 and a large- $|t|$ regime where the nucleons inside the nucleus will also break up, implying - for
 3903 instance - pion production in the Y system. While these are only qualitative expectations, it is
 3904 crucial to study this aspect of diffraction quantitatively in order to complete our understanding
 3905 of the transverse structure of nuclei.

3906 Fig. 6.30 shows the diffractive cross sections for exclusive J/Ψ production off a lead nucleus
 3907 with (b-Sat) and without (b-NonSat) saturation effects. The figure shows both the coherent
 3908 and incoherent cross sections. According to both models shown, the cross section for $t \sim$
 3909 0 is dominated by coherent production, whereas the nuclear break-up contribution becomes
 3910 dominant for $|t| \gtrsim 0.01 \text{ GeV}^2$, leading to a relatively flat t distribution. The coherent cross
 3911 section exhibits a characteristic multiple-dip structure at these relatively large t values, the
 3912 details of which are sensitive to gluon saturation effects. Resolving these dips requires a clean
 3913 separation between the coherent and nuclear break-up contributions, which may be possible
 3914 with sufficient forward instrumentation. In particular, preliminary studies suggest that the
 3915 detection of neutrons from the nuclear break-up in the Zero Degree Calorimeter (Section 13.3)
 3916 reduces the incoherent backgrounds dramatically. Assuming that it is possible to obtain a
 3917 relatively clean sample of coherent nuclear diffraction, resolving the rich structure at large t

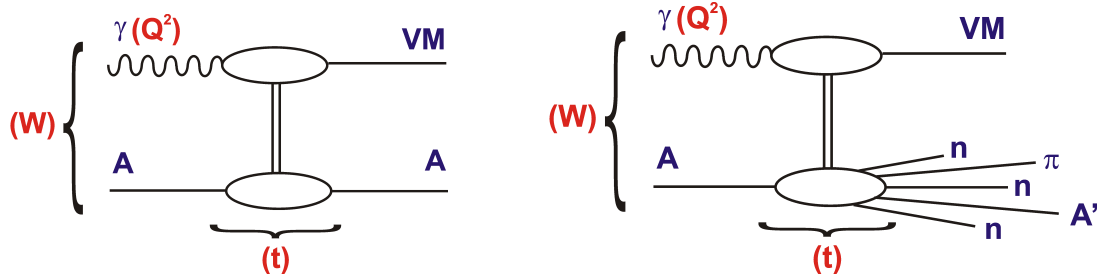


Figure 6.29: Diagrams illustrating the different types of exclusive diffraction in the nuclear case: coherent (plot on the left) and incoherent (plot on the right). While the diagrams have been drawn for the case of exclusive vector meson production, they equally apply to an arbitrary diffractively produced state.

3918 should be possible based on the measurement of the transverse momentum of the elastically
 3919 produced J/ψ according to $t = -p_T^2(J/\psi)$. The resolution on the t measurement is thus related
 3920 to that on the J/ψ by $\Delta t = 2\sqrt{-t} \Delta p_T(J/\psi)$, amounting to $\Delta t < 0.01 \text{ GeV}^2$ throughout the
 3921 range shown in Fig. 6.30 assuming $\Delta p_T(J/\psi) < 10 \text{ MeV}$, as has been achieved at HERA. The
 3922 pseudodata for the coherent process shown in the figure are consistent with this resolution and
 3923 correspond to a modest integrated luminosity of order 10 pb^{-1} .

3924 Independently of the large $|t|$ behaviour, important information can be obtained from the
 3925 low $|t|$ region alone. Coherent production for $t \sim 0$ can easily be related to the properties of
 3926 dipole-nucleon interactions, because all nuclear effects can be absorbed into the nuclear wave
 3927 functions, such that only the average gluon density of the nucleus enters the calculation. For
 3928 this forward cross section, the exact shape of the nuclear wave function is not important, in
 3929 contrast to what happens at larger $|t|$ where the distribution reflects the functional form of the
 3930 nuclear density.

3931 Saturation effects can be studied in a very clean way using the t -averaged gluon density
 3932 obtained in this way from the forward coherent cross section. Fig. 6.31 shows this cross section
 3933 for J/Ψ production as a function of W for different nuclei. The cross section varies substantially
 3934 as a function of the γ^*p centre of mass energy W and the nuclear mass number A . It is also very
 3935 sensitive to shadowing or saturation effects due to the fact that the differential cross section
 3936 at $t = 0$ has a quadratic dependence on the gluon density and A . Due to this fact, the ratios
 3937 of the cross sections for nuclei and protons are roughly proportional to the ratios of the gluon
 3938 densities squared. This has been exploited in the calculation [437] presented in Fig. 6.32, where
 3939 the nuclear modification factor R for the square of the gluon density is shown. The predictions
 3940 are consistent with those obtained from the b-Sat model (Fig. 6.31). Therefore, a precise
 3941 measurement of the J/ψ cross section around $t = 0$ is an invaluable source of information on
 3942 the gluon density and in particular on non-linear effects.

3943 Another region of interest is the measurement at larger $|t|$, $|t| \gtrsim 0.15 \text{ GeV}^2$. Here the reaction
 3944 is fully dominated by the incoherent processes in which the nucleus breaks up. The shadowing
 3945 or saturation effects should be stronger in this region than in the coherent case [408] and the
 3946 shape of the diffractive cross section should be only weakly sensitive to nuclear effects [400].
 3947 Finally, the intermediate region between $|t| \sim 0.01 \text{ GeV}^2$ and $|t| \sim 0.1 \text{ GeV}^2$ is also very
 3948 interesting because here the barely known gluonic nuclear effects can be studied.

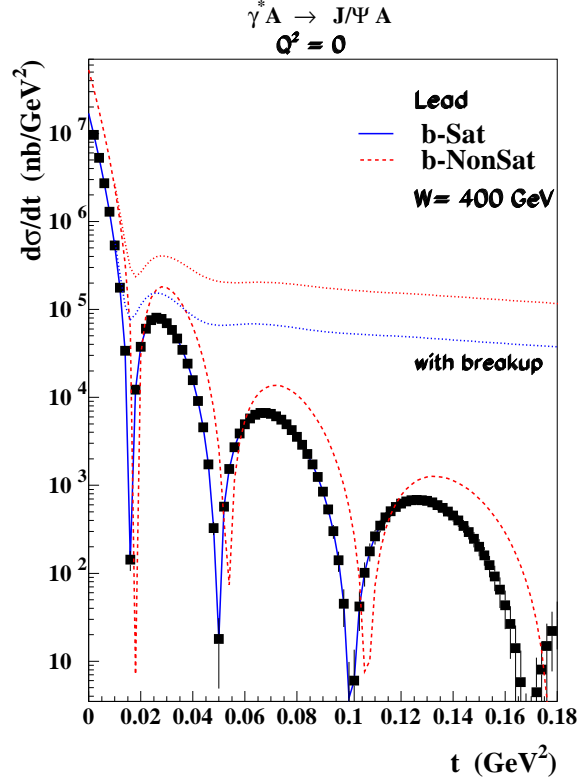


Figure 6.30: Differential cross section for the diffractive production of J/Ψ on a lead nucleus, as a function of the momentum transfer $|t|$. The dashed-red and solid-blue lines correspond to the b-Sat model predictions for coherent production without and with saturation effects, respectively. The dotted lines correspond to the predictions for the incoherent case. The pseudodata shown for the coherent case are explained in the text.

3949 Searching for the Odderon

3950 Exclusive processes in photoproduction and DIS offer unique sensitivity to rare exchanges in
 3951 QCD. One prominent example is that of exclusive pseudoscalar meson production, which could
 3952 proceed via the exchange of the Odderon. The Odderon is the postulated Reggeon which
 3953 is the C-odd partner of the Pomeron. The exchange of an Odderon should contribute with
 3954 different signs to particle-particle and particle-antiparticle scattering. Therefore, in the case of
 3955 hadron-hadron collisions it could lead, via the optical theorem, to a finite difference between
 3956 proton-proton and proton-antiproton total cross sections at high energies, provided the intercept
 3957 of the Odderon is close to unity. Despite many searches, no evidence for Odderon exchange
 3958 has been found so far, see for example [438]. Nevertheless, the existence of the Odderon is a
 3959 firm prediction of high-energy QCD, for a comprehensive review see [439]. At lowest order in
 3960 perturbation theory it can be described as a system of three non-interacting gluons. In the

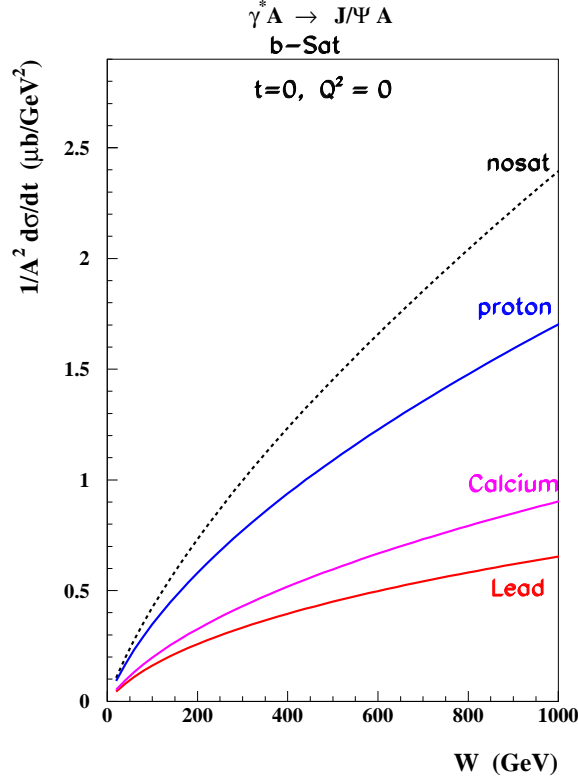


Figure 6.31: Energy dependence of the coherent photoproduction of the J/Ψ on a proton and different nuclei in the forward case $t = 0$ according to the b-Sat model. The cross sections are normalized by a factor $1/A^2$, corresponding to the dependence on the gluon density squared if no nuclear effects are present.

3961 leading logarithmic approximation in x its evolution is governed by the Bartels-Kwieciński-
 3962 Praszalowicz (BKP) equations [440–442]. Up to now, two solutions to the BKP equations are
 3963 known, one with intercept slightly below one [443] and the other with intercept exactly equal
 3964 to one [444].

3965 Several channels involving Odderon exchange are possible at the LHeC, leading to the exclu-
 3966 sive production of pseudoscalar mesons, $\gamma^{(*)}p \rightarrow Cp$, where $C = \pi^0, \eta, \eta', \eta_c \dots$. Searches for the
 3967 Odderon in the reaction $ep \rightarrow e\pi^0 N^*$ were performed by the H1 collaboration at HERA [445]
 3968 at an average γp c.m.s energy $\langle W \rangle = 215$ GeV. No signal was found and an upper limit on
 3969 the cross section was derived, $\sigma(ep \rightarrow e\pi^0 N^*, 0.02 < |t| < 0.3 \text{ GeV}^2) < 49$ nb at the 95 %
 3970 confidence level. Although the predicted cross sections for processes governed by Odderon ex-
 3971 change are rather small, they are not suppressed with increasing centre-of-mass energy and the
 3972 large luminosities offered by the LHeC may be exactly what is required for a discovery. In
 3973 addition to π^0 production, Odderon searches at the LHeC could be based on other exclusive
 3974 channels, for example with heavier mesons η_c, η_b [446]. An even more sensitive test, ideal for

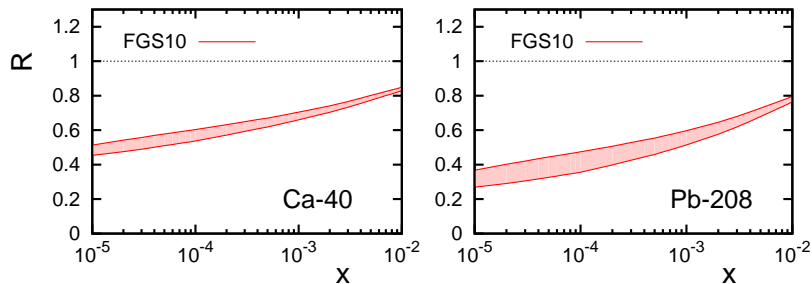


Figure 6.32: The x dependence of the nuclear modification ratio for the gluon density squared, from nuclei to protons (rescaled by A^2), for the scale corresponding to the exclusive production of the J/Ψ . Calculations obtained from the model described in [437].

3975 study at the LHeC, is the measurement of the difference between charm and anti-charm angular
 3976 or energy distributions in $\gamma^*p \rightarrow c\bar{c}N^*$. An asymmetry arises from the interference of pomeron
 3977 and Odderon exchange amplitudes [447].

3978 6.2.4 Inclusive diffraction

3979 Introduction to Diffractive Deep Inelastic Scattering

3980 Approximately 10% of low- x DIS events are of the diffractive type, $ep \rightarrow eXp$, with the proton
 3981 surviving the collision intact despite the large momentum transfer from the electron (Fig. 6.33).
 3982 This process is usually interpreted as the diffractive dissociation of the exchanged virtual photon
 3983 to produce any hadronic final state system X with mass much smaller than W and the same
 3984 net quantum numbers as the exchanged photon ($J^{PC} = 1^{--}$). Due to the lack of colour flow,
 3985 diffractive DIS events are characterised by a large gap in the rapidity distribution of final state
 3986 hadrons between the scattered proton and the diffractive final state X .

3987 As discussed in section 6.2.3, similar processes exist in electron-ion scattering, where they
 3988 can be sub-divided into fully coherent diffraction, where the nucleus stays intact ($eA \rightarrow eXA$)
 3989 and incoherent diffraction, where the nucleons within the nucleus are resolved and the nucleus
 3990 breaks up ($eA \rightarrow eXY$, Y being a system produced via nuclear or nucleon excitation, with the
 3991 same quantum numbers as A).

3992 Theoretically, rapidity gap production is usually described in terms of the exchange of a
 3993 net colourless object in the t -channel, which is often referred to as a pomeron [448, 449]. In
 3994 the simplest models [450, 451], this pomeron has a universal structure and its vertex couplings
 3995 factorise, such that it is applicable for example to proton-(anti)proton scattering as well as
 3996 DIS. One of the main achievements at HERA has been the development of an understanding
 3997 of diffractive DIS in terms of parton dynamics and QCD [452]. Events are selected using the
 3998 experimental signatures of either a leading proton [453–455] or the presence of a large rapidity
 3999 gap [454, 456]. The factorisable pomeron picture has proved remarkably successful for the
 4000 description of most of these data.

4001 The kinematic variables used to describe diffractive DIS are illustrated in Fig. 6.33. In
 4002 addition to x , Q^2 and the squared four-momentum transfer t , the mass M_X of the diffractively
 4003 produced final state provides a further degree of freedom. In practice, the variable M_X is often

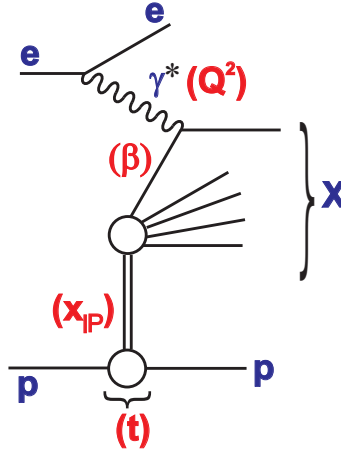


Figure 6.33: Illustration of the kinematic variables used to describe the inclusive diffractive DIS process $ep \rightarrow eXp$.

4004 replaced by

$$\beta = \frac{Q^2}{Q^2 + M_X^2 - t}. \quad (6.13)$$

4005 Small values of β refer to events with diffractive masses much bigger than the photon virtuality,
 4006 while values of β close to unity are associated with small M_X values. In models based on
 4007 a factorisable pomeron, β may be interpreted as the fraction of the pomeron longitudinal
 4008 momentum which is carried by the struck parton. The variable

$$x_{\mathbb{P}} = \frac{x}{\beta} = \frac{Q^2 + M_X^2 - t}{Q^2 + W^2 - M^2}, \quad (6.14)$$

4009 with M the nucleon mass, is then interpreted as the longitudinal momentum fraction of the
 4010 Pomeron with respect to the incoming proton or ion. It also characterises the size of the rapidity
 4011 gap as $\Delta\eta \simeq \ln(1/x_{\mathbb{P}})$.

4012 Measuring Diffractive Deep Inelastic Scattering at the LHeC

4013 Diffractive DIS (DDIS) can be studied in a substantially increased kinematic range at the LHeC,
 4014 which will allow a whole new level of investigations of the factorisation properties of inclusive
 4015 diffraction, will lead to new insights into low- x dynamics and will provide a subset of final states
 4016 with known quantum numbers for use in searches for new physics and elsewhere.

4017 As shown in [299], collinear QCD factorisation holds in the leading-twist approximation in
 4018 diffractive DIS and can be used to define diffractive parton distribution functions for the proton
 4019 or ion. That is, within the collinear framework, the diffractive structure functions [457] can
 4020 be expressed as convolutions of the appropriate coefficient functions with diffractive quark and
 4021 gluon distribution functions, which in general depend on all of β , Q^2 , $x_{\mathbb{P}}$ and t . The diffractive
 4022 parton distribution functions (DPDFs) are physically interpreted as probabilities for finding a
 4023 parton with a small fraction of the proton momentum $x = \beta x_{\mathbb{P}}$, under the condition that the
 4024 proton stays intact with a final state four-momentum which is specified up to an azimuthal angle

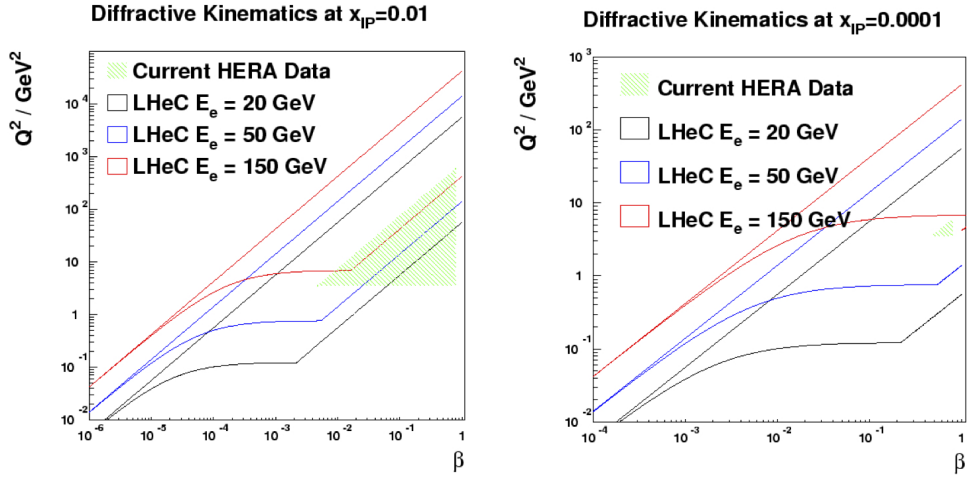


Figure 6.34: Diffractive DIS kinematic ranges in Q^2 and β of HERA and of the LHeC for different electron energies $E_e = 20, 50, 150$ GeV at $x_{\mathbb{P}} = 0.01$ (left plot), and $x_{\mathbb{P}} = 0.0001$ (right plot). In both cases, 1° acceptance is assumed for the scattered electron and the typical experimental restriction $y > 0.01$ is imposed. No rapidity gap restrictions are applied.

4025 by $x_{\mathbb{P}}$ and t . The DPDFs may then be evolved in Q^2 with the DGLAP evolution equations,
 4026 with β playing the role of the Bjorken x variable. The other two variables $x_{\mathbb{P}}$ and t play the
 4027 role of external parameters to the DGLAP evolution.

4028 In various extractions using HERA DDIS data [456, 458–460] the DPDFs have been found
 4029 to be dominated by gluons. Proton vertex factorisation holds to good approximation, such that
 4030 the DPDFs vary only in normalisation with the four-momentum of the final state proton, the
 4031 normalisation being well modelled using Regge phenomenology [449].

4032 The LHeC will offer the opportunity to study diffractive DIS in an unprecedented kinematic
 4033 range. The diffractive kinematic plane is illustrated in Fig. 6.34 for two different values of the
 4034 Pomeron momentum fraction, $x_{\mathbb{P}} = 0.01$ and $x_{\mathbb{P}} = 0.0001$. In each plot, accessible kinematic
 4035 ranges are shown for three different electron energies in collision with the 7 TeV proton beam.
 4036 Figure 6.34a corresponds to the coverage that will be possible based on leading proton detection
 4037 (see Chapter 13). Figure 6.34b is more representative of the possibilities using the large rapidity
 4038 gap technique (see the following). It is clear that the LHeC will have a much increased reach
 4039 compared with HERA towards low values of $x_{\mathbb{P}}$, where the interpretation of diffractive events
 4040 is not complicated by the presence of sub-leading meson exchanges, rapidity gaps are large and
 4041 diffractive event selection systematics are correspondingly small. The range in the fractional
 4042 struck quark momentum β extends by a factor of around 20 below that accessible at HERA.

4043 Figure 6.35 further illustrates the achievable kinematic range of diffractive DIS measure-
 4044 ments at the LHeC for the example of a 150 GeV electron beam combining large rapidity gap
 4045 and proton tagging acceptance, compared with an estimation of the final HERA performance.
 4046 For ease of illustration, a binning scheme is chosen in which the β dependence is emphasized and
 4047 very large bins in $x_{\mathbb{P}}$ and Q^2 are taken. There is a large difference between the kinematically
 4048 accessible ranges with backward acceptance cuts of 1° and 10° . Statistical uncertainties are

4049 typically much smaller than 1% for a luminosity of 2 fb^{-1} , so a much finer binning is possible,
 4050 as required. The data points are plotted according to the H1 Fit B DPDF predictions [456],
 4051 which amounts to a crude extrapolation based on dependences in the HERA range.

4052 Systematic uncertainties are difficult to estimate without a detailed knowledge of the forward
 4053 detectors and their acceptances. At HERA, sub-5% systematics have been achieved in the bulk
 4054 of the phase space and it is likely that the LHeC could do at least as well.

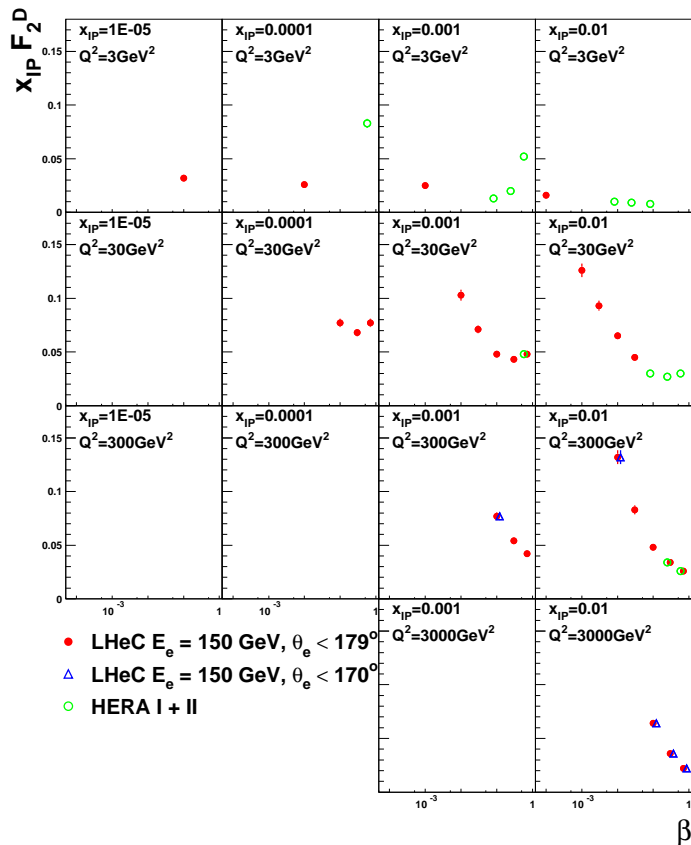


Figure 6.35: Simulation of a possible LHeC measurement of the diffractive structure function, F_2^D using a 2 fb^{-1} sample, compared with an estimate of the optimum results achievable at HERA using the full luminosity for a single experiment (500 pb^{-1}). The loss of kinematic region if the LHeC scattered electron acceptance extends to within 10° of the beam-pipe, rather than 1° is also illustrated.

4055 The limitations in the kinematic range accessible with the large rapidity gap technique are
 4056 investigated in Fig. 6.36. This shows the correlation between x_P and the pseudorapidity η_{max}
 4057 of the most forward particle in the hadronic final state system X , in simulated samples with LHeC
 4058 and HERA beam energies, according to the RAPGAP event generator [115]. This correlation
 4059 depends only on the proton beam energy and is thus the same for all LHeC running scenarios. At
 4060 HERA, a cut at $\eta_{\text{max}} \sim 3.2$ has been used to select diffractive events. Assuming LHeC forward

4061 instrumentation extending to around $\theta = 1^\circ$, a cut at $\eta_{\max} = 5$ may be possible, which would
 4062 allow measurements to be made comfortably up to $x_{\mathbb{P}} \sim 0.001$, with some limited sensitivity at
 4063 larger $x_{\mathbb{P}}$, a region where the proton tagging acceptance takes over (see Chapter 13). The two
 4064 methods are thus complementary, and offer some common acceptance in an overlap region of $x_{\mathbb{P}}$.
 4065 This redundancy could be used for cross-calibration of the two methods and their systematics,
 4066 as has been done at HERA.

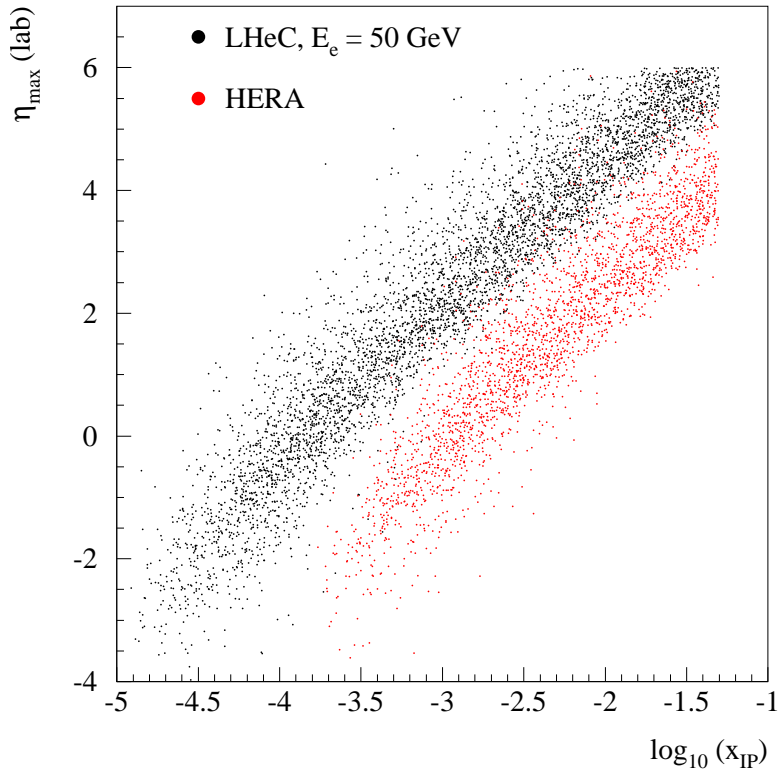


Figure 6.36: Comparison of the correlation between the rapidity gap selection variable, η_{\max} and $x_{\mathbb{P}}$ at HERA and at the LHeC, using events simulated with the RAPGAP Monte Carlo generator.

4067 **Diffractive Parton Densities and Final States**

4068 The previously unexplored diffractive DIS region of very low β is of particular interest. Here,
 4069 diffractively produced systems will be created with unprecedented invariant masses. Figure
 4070 6.37a shows a comparison between HERA and the LHeC in terms of the M_X distribution
 4071 which could be produced in diffractive processes with $x_{\mathbb{P}} < 0.05$ (using the RAPGAP Monte
 4072 Carlo model [115]). Figure 6.37a compares the expected M_X distributions for one year of run-
 4073 ning at three LHeC electron beam energy choices. Diffractive masses up to several hundred GeV
 4074 are accessible with reasonable rates, such that diffractive final states involving beauty quarks

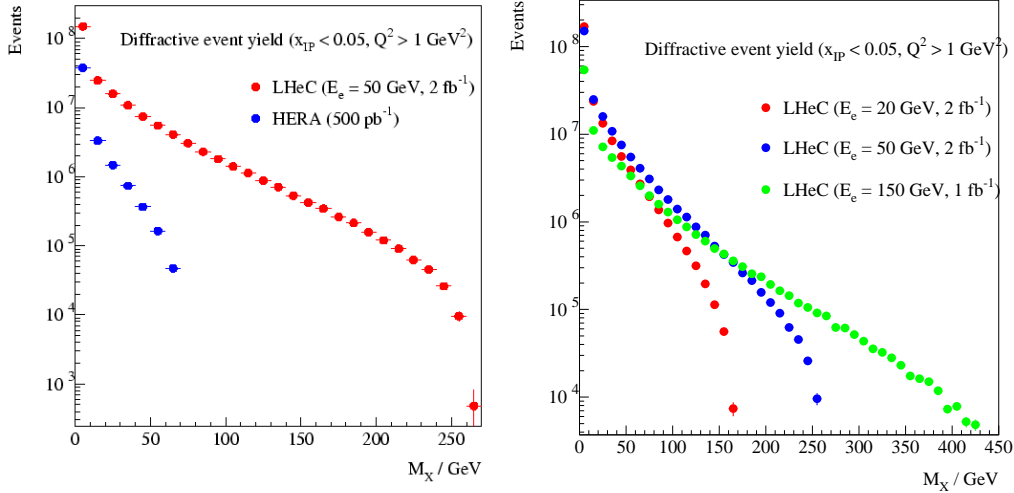


Figure 6.37: Simulated distributions in the invariant mass M_X according to the RAPGAP Monte Carlo model for samples of events obtainable with $x_{\mathbb{P}} < 0.05$ (a) One year of high acceptance LHeC running at $E_e = 50$ GeV compared with HERA (full luminosity for a single experiment). (b) Comparison between three different high acceptance LHeC luminosity and E_e scenarios.

4075 and W and Z bosons, or even exotic states with 1^- quantum numbers, could be produced.

4076 Large improvements in DPDFs are likely to be possible from NLO DGLAP fits to LHeC
 4077 diffractive structure function data. In addition to the extended phase space in β , the extension
 4078 of the kinematic range towards larger Q^2 increases the lever-arm for extracting the diffractive
 4079 gluon density and opens the possibility of significant weak gauge boson exchange, which would
 4080 allow a quark flavour decomposition for the first time.

4081 Proton vertex factorisation can be tested precisely by comparing the LHeC β and Q^2
 4082 dependences at different small $x_{\mathbb{P}}$ values in their considerable regions of overlap. The production of
 4083 dijets or heavy quarks as components of the diffractive system X will provide a means of testing
 4084 QCD collinear factorisation. These processes are driven by boson-gluon fusion ($\gamma^* g \rightarrow q\bar{q}$) and
 4085 thus provide complementary sensitivity to the diffractive gluon density to be compared with
 4086 that from the scaling violations of the inclusive cross section. Factorisation tests of this sort
 4087 have been carried out on many occasions at HERA, with NLO calculations based on DPDFs
 4088 predicting jet and heavy flavour cross sections which are in good agreement with data at large
 4089 Q^2 [461, 462]. However, due to the relatively small accessible jet transverse momenta at HERA,
 4090 the precision is limited by scale uncertainties on the theoretical predictions. At the LHeC, much
 4091 larger diffractive jet transverse momenta are measurable ($p_T \lesssim M_X/2$), which should lead to
 4092 much more precise tests [463].

4093 The simulated measurement of the longitudinal proton structure function, F_L described in
 4094 subsection 4.1.5, could also be extended to extract the diffractive analogue, F_L^D . At small β ,
 4095 where the cross section for longitudinally polarised photons is expected to be dominated by
 4096 a leading twist contribution, an F_L^D measurement provides further complementary constraints

4097 on the role of gluons in the diffractive PDFs. As $\beta \rightarrow 1$, a higher twist contribution from
 4098 longitudinally polarised photons, closely related to that driving vector meson electroproduction,
 4099 dominates the diffractive cross section in many models [464] and a measurement to even modest
 4100 precision would give considerable insight. A first measurement of this quantity has recently been
 4101 reported by the H1 Collaboration [465], though the precision is strongly limited by statistical
 4102 uncertainties. The LHeC provides the opportunity to explore it in much finer detail.

4103 In contrast to leading proton production, the production of leading neutrons in DIS ($ep \rightarrow$
 4104 eXn) requires the exchange of a net isovector system. Data from HERA have supported the
 4105 view that this process is driven dominantly by charged pion exchange over a wide range of
 4106 neutron energies [466]. With the planned emphasis on zero degree calorimetry for leading
 4107 neutron measurements (see Chapter 13), LHeC data will thus constrain the structure of the
 4108 pion at much lower x and larger Q^2 values than has been possible hitherto. Note also that
 4109 the combination of rapidity gap detection and zero degree calorimetry offers the possibility of
 4110 disentangling coherent from incoherent nuclear diffraction.

4111 **Diffractive DIS, Dipole Models and Sensitivity to Non-linear Effects**

4112 Diffractive DIS at the LHeC will give us an opportunity to test the predictions of collinear
 4113 factorisation and the possible onset of non-linear or higher-twist effects in the evolution. Of
 4114 particular importance is the semi-hard regime $Q^2 < 10 \text{ GeV}^2$ and x as small as possible. It is
 4115 possible that the non-linear saturation regime will be easier to reach with diffractive than with
 4116 inclusive measurements, since diffractive processes are mostly sensitive to quantum fluctuations
 4117 in the proton wave function that have a virtuality of order of the saturation scale Q_s^2 , instead
 4118 of Q^2 . As a result, power corrections (not the generic Λ_{QCD}^2/Q^2 corrections, but rather the
 4119 sub-class of them of order Q_s^2/Q^2) are expected to come into play starting from a higher value
 4120 of Q^2 in diffractive than in inclusive DIS. Indeed, there is already a hint of this at HERA:
 4121 collinear factorization starts to fail below about 3 GeV^2 in the case of F_2 [10], while it breaks
 4122 down already around 8 GeV^2 in the case of F_2^D [456]. This fact can alternatively be observed
 4123 in the feature that models which in principle should only work for small Q^2 , can in practice be
 4124 used up to larger Q^2 for diffractive than for inclusive observables (see e.g. [266]).

4125 With the sort of measurement precision for F_2^D possible at the LHeC, it ought to be possible
 4126 to distinguish between different models, as illustrated in Fig. 6.38. For the simulated data
 4127 shown here, a conservative situation is assumed, in which the electron beam energy is 50 GeV
 4128 and only the rapidity gap selection method is used, such that the highest x_p bin is at 0.001 .
 4129 H1 Fit B [456] extrapolations (as in Fig. 6.35) are compared with the “b-sat” [321, 322] and
 4130 bCGC [467] dipole models. As has been found to be necessary to describe HERA data, photon
 4131 fluctuations to $q\bar{q}g$ states are included in addition to the usual $q\bar{q}$ dipoles used to describe
 4132 inclusive and vector meson cross sections. Both dipole models differ substantially from the
 4133 H1 Fit B extrapolation. The LHeC simulated precision and kinematic range are sufficient to
 4134 distinguish between a range of models with and without saturation effects, and also between
 4135 different models which incorporate saturation.

4136 **Predicting nuclear shadowing from inclusive diffraction in ep**

4137 The connection between nuclear shadowing and diffraction was established a long time ago by
 4138 Gribov [265]. Its key approximation is that the nucleus can be described as a dilute system of
 4139 nucleons in the nucleus rest frame. The accuracy of this approximation for hadron-nucleus in-

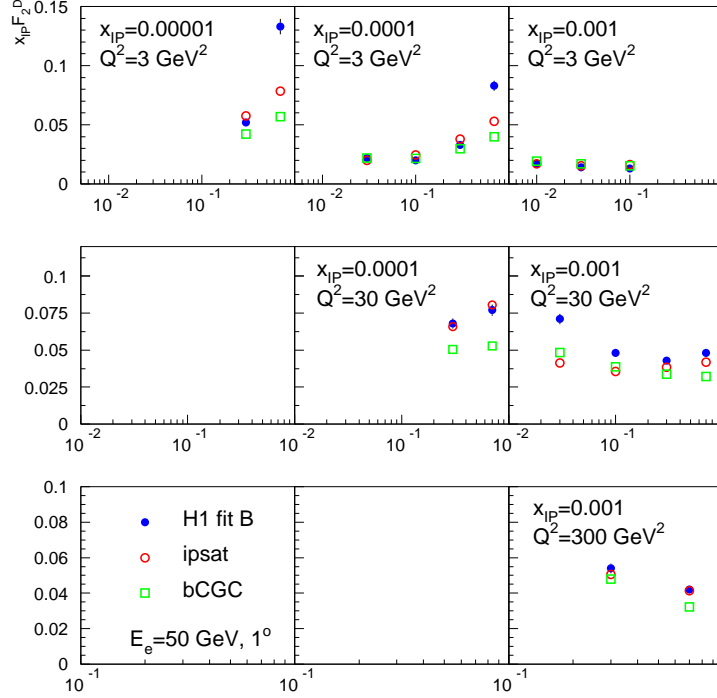


Figure 6.38: Simulated F_2^D measurements in selected $x_{\mathbb{P}}$, β and Q^2 bins. An extrapolation of the H1 Fit B DPDF fit to HERA data is compared with two different implementations of the dipole model, both of which contain saturation effects and include $q\bar{q}g$ photon fluctuations in addition to $q\bar{q}$ ones.

4140 teractions is on the level of a few %, which reflects the small admixture of non-nucleonic degrees
 4141 of freedom in nuclei and the small off-shellness of the nucleons in nuclei as compared to the
 4142 soft strong interaction scale. Gribov's result can be derived using the AGK cutting rules [468]
 4143 and hence it is a manifestation of unitarity [469, 470]. The formalism can be used to calculate
 4144 directly cross sections of $\gamma(\gamma^*)$ -nucleus scattering for the interaction with $N = 2$ nucleons, but
 4145 has to be supplemented by additional considerations to account for the contribution of the
 4146 interactions with $N \geq 3$ nucleons.

4147 In this context, nuclear PDFs at small x can be calculated [469, 470] combining unitarity
 4148 relations for different cuts of the shadowing diagrams corresponding to diffractive and inelastic
 4149 final states, with the QCD factorisation theorem for hard diffraction [299]. A *model-independent*
 4150 expression for the nuclear PDF at fixed impact parameter b , valid for the case $N = 2$ [469],
 4151 reads:

$$\begin{aligned}
 \Delta [xf_{j/A}(x, Q^2, b)] &= xf_{j/N}(x, Q^2, b) - xf_{j/A}(x, Q^2, b) \\
 &= 8\pi A(A-1) \Re e \left[\frac{(1-i\eta)^2}{1+\eta^2} \int_x^{0.1} dx_{\mathbb{P}} \beta f_j^{D(4)}(\beta, Q^2, x_{\mathbb{P}}, t_{\min}) \right. \\
 &\quad \left. \times \int_{-\infty}^{\infty} dz_1 \int_{z_1}^{\infty} dz_2 \rho_A(\vec{b}, z_1) \rho_A(\vec{b}, z_2) e^{i(z_1 - z_2)x_{\mathbb{P}}m_N} \right], \quad (6.15)
 \end{aligned}$$

4152 where $f_{j/A}(x, Q^2)$, $f_{j/N}(x, Q^2)$ are nuclear and nucleon PDFs respectively, $f_j^{D(4)}(\beta, Q^2, x_{\mathbb{P}}, t_{\min})$
4153 are diffractive nucleon PDFs, $\eta = \Re e A^{diff} / \Im m A^{diff} \approx 0.17$, $\rho_A(r)$ is the nuclear matter
4154 density, and $t_{\min} = -m_N^2 x_{\mathbb{P}}^2$ with m_N the nucleon mass. Eq. (6.15) satisfies the QCD evolution
4155 equations to all orders in α_s . Numerical studies indicate that the dominant contribution to the
4156 shadowing probed by present experiments - corresponding to not very small x - comes from
4157 the region of relatively large β , for which small- x approximations which involve resummation
4158 of $\ln x$ terms are not important.

4159 In Eq. (6.15), the interaction of different configurations of the hard probe (e.g. $q\bar{q}$, $q\bar{q}g$,
4160 vector meson resonances, ...) are encoded in $f_j^{D(4)}(\beta, Q^2, x_{\mathbb{P}}, t_{\min})$. For the case of more than
4161 $N = 2$ nucleons, there are two or more intermediate nucleon diffractive states which may
4162 be different and thus result in a different interaction between the the virtual photon and the
4163 nucleus. Therefore the interaction of the hard probe with $N \geq 3$ nucleons is sensitive to finer
4164 details of the diffractive dynamics, namely the interplay between the interactions of the hard
4165 probe with N nucleons with different cross sections. This (colour) fluctuation effect is analogous
4166 to the inelastic shadowing phenomenon for the scattering of hadrons from nuclei, with the
4167 important difference that the dispersion of the interaction cross sections for the configurations
4168 in the projectile is much smaller in the hadronic case than in DIS.

4169 In order to estimate this effect, one should note that, experimentally, the energy dependence
4170 of hard diffraction is close to that observed for soft Pomeron dynamics (the soft Pomeron
4171 intercept intercept $\alpha_{\mathbb{P}} \approx 1.11$) with the hard Pomeron contribution ($\alpha_{\mathbb{P}} \approx 1.25$) being a small
4172 correction. This fact indicates that hadron-like (aligned jet) configurations [471], evolved via
4173 DGLAP evolution to large Q^2 , dominate hard diffraction in DIS, while point-like configurations
4174 give an important, and increasing with Q^2 , contribution to small- x PDFs. This reduces the
4175 uncertainties in the treatment of $N \geq 3$ contributions [374, 437]. Calculations show that the
4176 difference between two extreme scenarios of colour fluctuations is $\leq 20\%$ for $A \sim 200$ and much
4177 smaller for lighter nuclei, see the two FGS10 curves in Figs. 6.12 and 6.18. Besides, fluctuations
4178 tend to reduce the shadowing somewhat compared with the approximations neglecting them
4179 [267, 469, 472, 473] (compare the FGS10 results in Fig. 6.18 left with those labelled AKST). The
4180 gluon density is more sensitive to the magnitude of fluctuations than F_2 , as can be inferred
4181 from Fig. 6.12 and Fig. 6.18 right.

4182 Finally, the AGK technique also allows the calculation of the nuclear diffractive PDFs, see
4183 below, and fluctuations of multiplicity in non-diffractive DIS [437, 469, 474]. Both observables
4184 turn out to be sensitive to the pattern of colour fluctuations.

4185 **Predictions for inclusive diffraction on nuclear targets**

4186 Diffractive DIS events were first discovered in ep collisions at the HERA collider. Since no eA
4187 collider has ever been built, inclusive diffraction in eA has simply never been measured. Thus,
4188 DDIS off nuclei at the LHeC will be a completely unexplored territory throughout the whole
4189 kinematic domain accessed, implying a huge discovery potential.

4190 Despite this lack of experimental information on DDIS off nuclei, we have expectations, based
4191 on our current understanding of QCD, of how it should look. For instance, the theory of nuclear
4192 shadowing allows us to construct nuclear diffractive PDFs for large Q^2 (see the previous item)
4193 while, within the Color Glass Condensate framework, nuclear diffractive structure functions can
4194 be predicted at small x . Depending on kinematics and the heavy ion species, different patterns
4195 of nuclear shadowing or antishadowing are expected as a function of β and $x_{\mathbb{P}}$. This is just
4196 one of many examples of what should be checked with an eA collider. Others are the impact

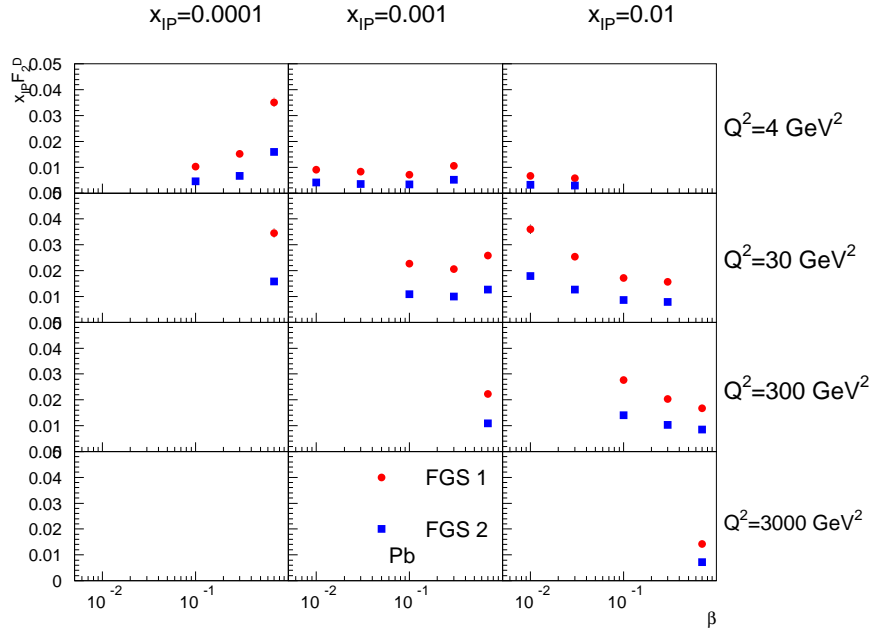


Figure 6.39: Diffractive structure function $x_{\mathbb{P}}F_2^D$ for Pb in bins of Q^2 and $x_{\mathbb{P}}$ as a function of β . Model calculations are taken from [437].

4197 parameter dependence introduced in the models, or the relation between nuclear shadowing
 4198 and diffraction in ep which relies on what we know on DDIS from HERA. Therefore, in the
 4199 larger kinematic domain accessible at the LHeC there are many things to discover about the
 4200 structure of nuclei with diffractive measurements.

4201 Predictions from a variety of models for nuclear coherent diffraction (see comments on differ-
 4202 ent types of diffractive process on nuclei in Subsection on diffractive vector meson production),
 4203 are shown in Figs. 6.39 and 6.40. The chosen models here are FGS10 [437] and KLMV [475,476].
 4204 Both plots show selected LHeC pseudodata for $x_{\mathbb{P}}F_2^D$ as a function of β in bins of Q^2 and $x_{\mathbb{P}}$.
 4205 Statistical and systematic errors are added in quadrature, with systematic errors estimated to
 4206 be at the level of 5%. The models give very different predictions both in absolute value and in
 4207 their detailed dependence on x_{IP} and Q^2 , which cannot be resolved without LHeC data.

4208 Also shown in Fig. 6.41 are predicted diffractive-to-total ratios of the structure functions as a
 4209 function of the collision energy W . It was demonstrated in [303] that the constancy with energy
 4210 of this ratio for the proton can be naturally explained in the models which include saturation

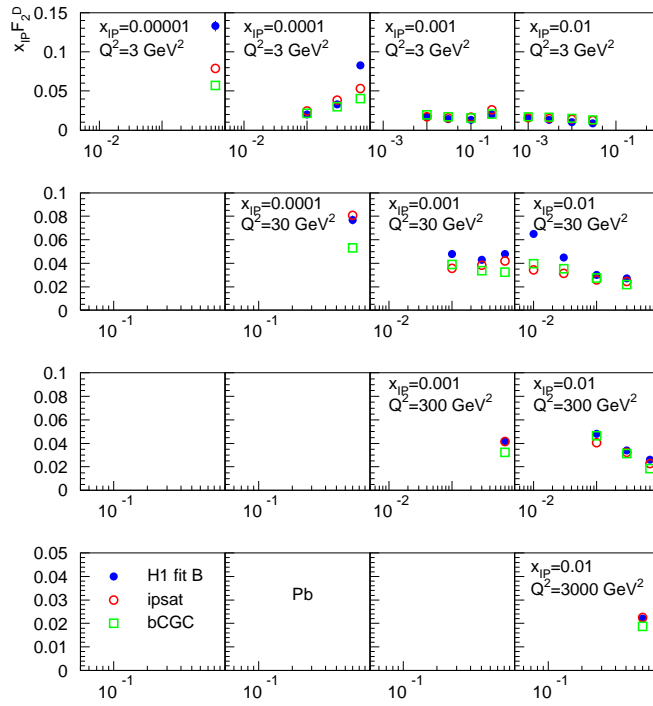


Figure 6.40: Diffractive structure function $x_{\mathbb{P}} F_2^D$ for Pb in bins of Q^2 and $x_{\mathbb{P}}$ as a function of β . Model calculations are based on the dipole framework [475, 476].

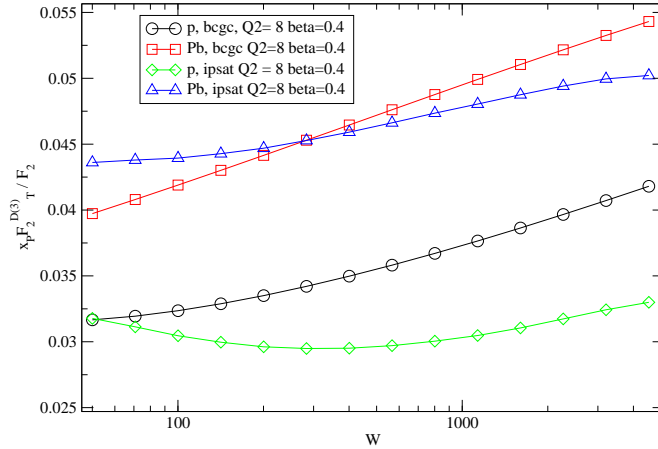


Figure 6.41: Ratio of the transversely polarised photon contribution to the diffractive structure function $x_{\mathbb{P}} F_2^{D(3)T}$ to the inclusive structure function in p and Pb for fixed values of Q^2 and β as a function of the energy W . The model calculations are based on the dipole framework [475,476].

4211 effects, because in the black disk regime the ratio of the diffractive to total cross sections tends
 4212 to a constant value. At fixed impact parameter the ratio may grow as large as 50%, but the
 4213 integration in impact parameter results in a smaller value. HERA data showed approximate
 4214 energy independence of this ratio, which could be easily obtained within the GBW saturating
 4215 dipole model [303]. Within the given energy range the models shown in figure 6.41 predict a
 4216 slight variation with energy. Note however the rather substantial difference between predictions
 4217 coming from the different models. The uncertainty in modelling the impact parameter is one
 4218 of its main sources. LHeC data are required for clarification.

4219 6.2.5 Jet and multi-jet observables, parton dynamics and fragmenta- 4220 tion

4221 Introduction

4222 Inclusive measurements provide essential information about the integrated distributions of par-
 4223 tons in a proton. However, as was discussed in previous sections, more exclusive measurements
 4224 are needed to pin down the essential details of the small- x dynamics. For example, a central
 4225 prediction of the BFKL framework at small x is the diffusion of the transverse momenta of the
 4226 emitted partons between the photon and the proton. In the standard collinear approach with
 4227 integrated parton densities the information about the transverse momentum is not accessible.
 4228 However, it can be recovered within a different framework which utilizes unintegrated parton
 4229 distribution functions, dependent on parton transverse momentum as well as x and Q^2 . Unin-
 4230 tegrated PDFs are natural in the BFKL approach to small- x physics. A general, fundamental
 4231 expectation is that as x decreases, the distribution in transverse momentum of the emitted
 4232 partons broadens, resulting in diffusion.

4233 The specific parton dynamics can be tested by a number of exclusive measurements. These
 4234 in turn can provide valuable information about the distribution of transverse momentum in the

4235 proton. As discussed in [477], for many inclusive observables the collinear approximation with
 4236 integrated PDFs is completely insufficient, and even just including parton transverse momentum
 4237 effects by hand may not be sufficient to describe many observables. In DIS, for example,
 4238 processes needing unintegrated distributions include the transverse momentum distribution of
 4239 heavy quarks. Similar problems are encountered in hadron collisions when studying heavy quark
 4240 and Higgs production. The natural framework using unintegrated PDFs gives a much more
 4241 reliable description. Furthermore, lowest-order calculations in the framework with unintegrated
 4242 PDFs provide a much more realistic description of cross sections concerning kinematics. This
 4243 may well lead to NLO and higher corrections being much smaller numerically than they typically
 4244 are at present in standard collinear factorization, since the LO description is better.

4245 This approach, however, calls for precise measurements of a variety of relatively exclusive
 4246 processes in a wide kinematic range. As discussed below, measurements of dijets, forward jets
 4247 and particles, as well as transverse energy flow, are required to constrain the unintegrated PDFs
 4248 and will give valuable information about parton dynamics at small x . While we will discuss the
 4249 case of DIS on a proton, all conclusions can be paralleled for DIS on nuclei.

4250 Unintegrated PDFs

4251 The standard integrated parton densities are functions of the longitudinal momentum fraction
 4252 of a parton relative to its parent hadron, with an integral over the parton transverse momentum.
 4253 In contrast, unintegrated, or transverse-momentum-dependent (TMD), parton densities depend
 4254 on both parton longitudinal momentum fraction and parton transverse momentum. Processes
 4255 for which unintegrated densities are natural include the Drell-Yan process (and its generalization
 4256 to Higgs production), and semi-inclusive DIS (SIDIS). In SIDIS, we need TMD fragmentation
 4257 functions as well as TMD parton densities.

4258 In the literature there are several apparently different approaches to TMD parton densities,
 4259 with varying degrees of explicitness in the definitions and derivations.

- 4260 • The CSS approach [478–481] and some further developments [482].
- 4261 • The CCFM approach [483–486] for small x .
- 4262 • Related BFKL associated works [281, 487].

4263 Central to this subject is the concrete definition of TMD densities, and complications arise
 4264 because QCD is a gauge theory. A natural initial definition uses light-front quantization: the
 4265 unintegrated density of parton j in hadron h would be

$$f_{j/h}(x, \mathbf{k}_\perp) \stackrel{?}{=} \frac{1}{2x(2\pi)^3} \sum_\lambda \frac{\langle P, h | b_{k, \lambda, j}^\dagger b_{k, \lambda, j} | P, h \rangle_c}{\langle P, h | P, h \rangle}, \quad (6.16)$$

4266 where $b_{k, \lambda, j}$ and $b_{k, \lambda, j}^\dagger$ are light-front annihilation and creation operators, j and λ label parton
 4267 flavor and helicity, while $k = (k^+, \mathbf{k}_\perp)$ is its momentum, and only connected graphs ‘c’ are
 4268 considered. The ‘?’ over the equality sign warns that the formula does not apply literally
 4269 in QCD. Expressing $b_{k, \lambda, j}$ and $b_{k, \lambda, j}^\dagger$ in terms of fields gives the TMD density as the Fourier
 4270 transform of a light-front parton correlator. For example, for a quark

$$f_j(x, \mathbf{k}_\perp) \stackrel{?}{=} \int \frac{dw^- d^2\mathbf{w}_\perp}{(2\pi)^3} e^{-ixP^+ w^- + i\mathbf{k}_\perp \cdot \mathbf{w}_\perp} \langle P | \bar{\psi}_j(0, w^-, \mathbf{w}_\perp) \frac{\gamma^+}{2} \psi_j(0) | P \rangle_c. \quad (6.17)$$

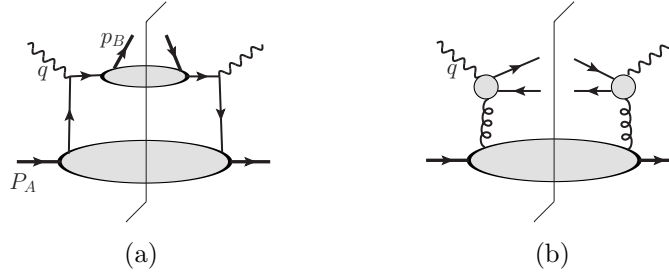


Figure 6.42: (a) Parton model factorisation for a SIDIS cross section. (b) Factorization for high-energy $q\bar{q}$ photoproduction.

4271 One can similarly define a TMD fragmentation function [479] $d_{h/j}(z, \mathbf{p}_\perp)$, for the probability
 4272 density of final-state hadron h in an outgoing parton j .

4273 The corresponding factorization formula for SIDIS $e + A(P_A) \rightarrow e + B(p_B) + X$ is [482]

$$\frac{d\sigma}{dx dQ^2 dz d^2\mathbf{P}_{B\perp}} = \sum_j \int d^2\mathbf{k}_\perp H_j f_{j/A}(x, \mathbf{k}_\perp) d_{B/j}(z, \mathbf{p}_{B\perp} + z\mathbf{k}_\perp), \quad (6.18)$$

4274 where z and $\mathbf{P}_{B\perp}$ are the fractional longitudinal momentum and the transverse momentum
 4275 of the detected hadron relative to the simplest parton-model calculation of the outgoing jet,
 4276 while H_j is the hard-scattering factor for electron-quark elastic scattering; see Fig. 6.42(a). In
 4277 the fragmentation function $d_{B/j}$ in Eq. (6.18), the use of $z\mathbf{k}_\perp$ with its factor of z is because
 4278 the transverse-momentum argument of the fragmentation function is a transverse momentum
 4279 of the outgoing hadron relative to the parton initiating the jet, whereas \mathbf{k}_\perp is the transverse
 4280 momentum of a parton relative to a hadron.

4281 The most obvious way of applying (6.17) in QCD is to define the operators in light-cone
 4282 gauge $A^+ = 0$, or, equivalently, to attach Wilson lines to the quark fields with a light-like
 4283 direction for the Wilson lines. One minor problem in QCD is that, because the wave func-
 4284 tion is infinite (see below), the exact probability interpretation of parton densities cannot be
 4285 maintained.

4286 A much harder problem occurs because QCD is a gauge theory. Evaluating TMD densi-
 4287 ties defined by (6.17) in light-cone gauge gives divergences where internal gluons have infinite
 4288 negative rapidity [478]. These cancel only in the integrated density. The physical problem is
 4289 that any coloured parton entering (or leaving) the hard scattering is accompanied by a cloud of
 4290 soft gluons, and the soft gluons of a given transverse momentum are distributed uniformly in
 4291 rapidity. A parton density defined in light-cone gauge corresponds to the asymptotic situation
 4292 of infinite available rapidity.

4293 A quark in a realisable hard scattering can be considered as having a transverse recoil against
 4294 the soft gluons, but with a physically restricted range of rapidity. So a proper definition of a
 4295 TMD density must implement a rapidity cut-off in the gluon momenta. Evolution equations
 4296 must take into account the rapidity cut-off. The CSS formalism [478] has an explicit form of the
 4297 rapidity cut-off and an equation for the dependence of TMD functions on the cut-off. But in
 4298 any alternative formalism the need in the definitions for a cut-off to avoid rapidity divergences
 4299 is non-negotiable.

4300 Parton densities and fragmentation functions are only useful because they appear in factori-
 4301 sation theorems, so a useful definition must allow useful factorisation theorems to be formulated

4302 and derived. An improved definition involving Wilson line operators has recently been given
 4303 in [488]; see also [489].

4304 A second train of argument leads to a related kind of factorisation (the so-called k_{\perp} -
 4305 factorisation) for processes at small x [288]. A classic process is photo- or electro-production of
 4306 charm pairs $\gamma(p_1) + h(p_2) \rightarrow Q(p_3) + \bar{Q}(p_4) + X$, for which k_{\perp} -factorisation has the form

$$4M^2\sigma_{\gamma g}(\rho, M^2/Q_0^2) = \int d^2\mathbf{k}_{\perp} \int_0^1 \frac{dz}{z} \hat{\sigma}(\rho/z, \mathbf{k}_{\perp}^2/M^2) f_{g/h}(x, \mathbf{k}_{\perp}), \quad (6.19)$$

4307 see Fig. 6.42(b). Here $\rho = M^2/(p_1 + p_2)^2 \ll 1$, and M is the mass of the heavy quark. The
 4308 corresponding definition of the TMD gluon density [483] is said to use light-cone gauge, but
 4309 there is in fact a hidden rapidity cut-off resulting from the use of the BFKL formalism.

4310 Although both (6.18) and (6.19) use k_{\perp} -dependent parton densities, there are important
 4311 differences. In (6.19), the hard scattering cross section $\hat{\sigma}$ has the incoming gluon *off*-shell,
 4312 whereas in (6.18), the hard scattering H_j uses on-shell partons. This is associated with a
 4313 substantial difference in the kinematics. In (6.18) for SIDIS, the transverse momenta of the
 4314 partons relative to their hadrons are less than Q , which allows the neglect of parton virtuality in
 4315 the hard scattering. This approximation fails at large partonic transverse momentum, $\mathbf{k}_{\perp} \sim Q$,
 4316 but ordinary collinear factorisation is valid in that region. So the factorisation formula is readily
 4317 corrected, by adding a suitable matching term [478].

4318 In contrast, in the small- x formula (6.19), the gluon transverse momentum is comparable
 4319 with the hard scale M . So it is not appropriate to neglect \mathbf{k}_{\perp} with respect to M , and the hard
 4320 scattering is computed with an off-shell gluon. Factorisation is actually obtained from BFKL
 4321 physics, where the gluons in Fig. 6.42(b) couple the charm quark subgraph to a subgraph where
 4322 the lines have much larger rapidity.

4323 The evolution equation of the CS-style TMD functions used in (6.18) gives the dependence
 4324 of the TMD functions on the rapidity difference between the hadron and the virtual photon
 4325 momenta. The results for TMD functions and for the cross sections can finally be obtained [482]
 4326 in terms of (a) ordinary integrated parton densities and fragmentation functions, (b) perturba-
 4327 tively calculable quantities, and (c) a restricted set of non-perturbative quantities. The most
 4328 important of these non-perturbative quantities is the distribution in recoil transverse momentum
 4329 per unit rapidity against the emission of the soft interacting gluons, which is exponentiated after
 4330 evolution. Importantly, it is independent of x and z , and it is universal between processes [490],
 4331 and different only between gluons (color octet) and quarks (color triplet). There is also what
 4332 can be characterised as a non-perturbative intrinsic transverse momentum distribution in both
 4333 parton densities and fragmentation functions. In the quark sector, all but the fragmentation
 4334 function are well measured in Drell-Yan processes [491].

4335 On the other hand, evolution for the small- x formalism in (6.19) is given by the BFKL
 4336 method.

4337 The avenues for further improvement on this subject are both theoretical and experimental.
 4338 On the theory side, these concern the relation between different formalisms for evolution [281,
 4339 478, 482, 487, 492], the extension of factorisation theorems to a larger number of particles in
 4340 the final state, and the matching to Monte Carlo generators. On the experimental side, the
 4341 sensitivity to TMD functions is linked to a sensitivity to parton transverse momentum. This
 4342 is the case of SIDIS at low transverse momentum. Another interesting process which would
 4343 enable the TMD gluon functions to be probed is $e p \rightarrow e \pi \pi X$, with the pions being in different
 4344 directions (different jets), but such that they are close to back-to-back in the (q, p_i) (the so-called
 4345 brick wall) frame.

4346 Finally, measuring SIDIS and dijet production off protons or nuclei at the LHeC will allow
 4347 detailed investigations of non-linear parton evolution in QCD. In this respect, the SIDIS cross
 4348 section [493] and dihadron production [494] have been studied in the CGC framework. It
 4349 turns out that, for small x , one is sensitive to the saturation regime of the target (proton or
 4350 nucleus) wave function if the transverse momentum of the produced hadron is of the order of
 4351 the saturation momentum.

4352 Dijet production and angular decorrelation

4353 Dijet production in high energy deep inelastic electron-proton scattering is a very valuable pro-
 4354 cess for the study of small- x behavior in QCD. The dominant process is illustrated in Fig. 6.43,
 4355 which is that of the $\gamma^*g \rightarrow q\bar{q} \rightarrow$ dijet production. The incoming gluon can have sizeable
 4356 transverse momentum accumulated from diffusion in k_T along the gluon chain. As Bjorken- x
 4357 becomes smaller, and therefore the longitudinal momentum of the gluon also decreases, larger
 4358 values of the transverse momentum k_T can be sampled. This will lead to an azimuthal decor-
 4359 relation between the jets which increases with decreasing x . The definition of $\Delta\phi$ is indicated
 4360 in Fig. 6.43. That is, the jets are no longer back-to-back since they must balance the sizable
 4361 transverse momentum k_T of the incoming virtual gluon.

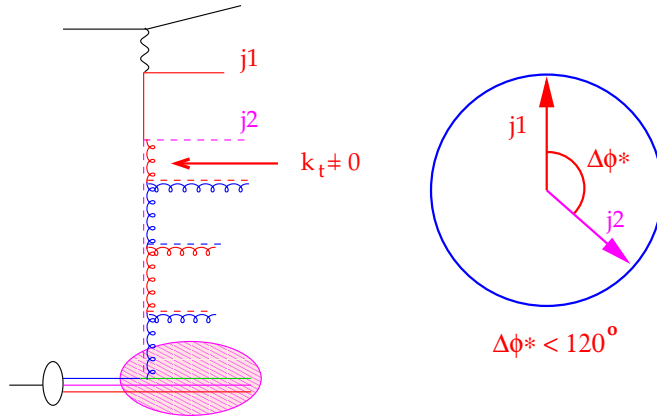


Figure 6.43: Schematic representation of the production of a system of two jets in the process of virtual photon-gluon fusion. The incoming gluon has non-vanishing transverse momentum $k_T \neq 0$ which leads to the decorrelation of the jets. $\Delta\phi$ is the angle between two jets.

4362 This picture of dijet production is to be contrasted with the conventional picture which
 4363 uses integrated parton distributions, and typically leads to a narrow distribution about the
 4364 back-to-back jet configuration. Higher orders usually broaden the distribution. However, as
 4365 shown by direct measurements of DIS dijet data [495], NLO DGLAP calculations are not able
 4366 to accommodate the pronounced effect of the decorrelation.

4367 Explicit calculations for HERA kinematics show that the models which include the resuma-
 4368 tion of powers of $\log 1/x$ compare favourably with the experimental data [496–500]. The
 4369 proposal and calculations to extend such studies to diffractive DIS also exist [501, 502].

4370 In Fig. 6.44 we show the differential cross section as a function of $\Delta\phi$ for jets in the region
 4371 $-1 < \eta_{jet} < 2.5$ with $E_{T,jet1} > 7$ GeV and $E_{T,jet2} > 5$ GeV found with the k_t jet algorithm

4372 in the kinematic range $Q^2 > 5 \text{ GeV}$, $0.1 < y < 0.6$ for different regions in x . The ‘MEPS’
 4373 prediction comes from a Monte Carlo generator [115] using $\mathcal{O}(\alpha_s)$ matrix elements with a
 4374 DGLAP-type parton shower. The ‘CDM prediction uses the same generator [115], but with
 4375 higher order parton radiation simulated with the Colour Dipole Model [503], thus effectively
 4376 including some k_t diffusion. Finally, the CASCADE Monte Carlo prediction [504], uses off-
 4377 shell matrix elements convoluted with an unintegrated gluon distribution (CCFM set A), with
 4378 subsequent parton showering according to the CCFM evolution equation.

4379 At large x all predictions agree reasonably well, in both shape and normalisation. At smaller
 4380 x the $\Delta\phi$ -distribution becomes flatter for CDM and CASCADE, indicating higher order effects
 4381 leading to a larger decorrelation of the produced jets. Whereas a decorrelation is observed,
 4382 its size depends on the details of the parton evolution and thus a measurement of the $\Delta\phi$
 4383 cross section provides a direct measurement of higher order effects which need to be taken into
 account at small x .

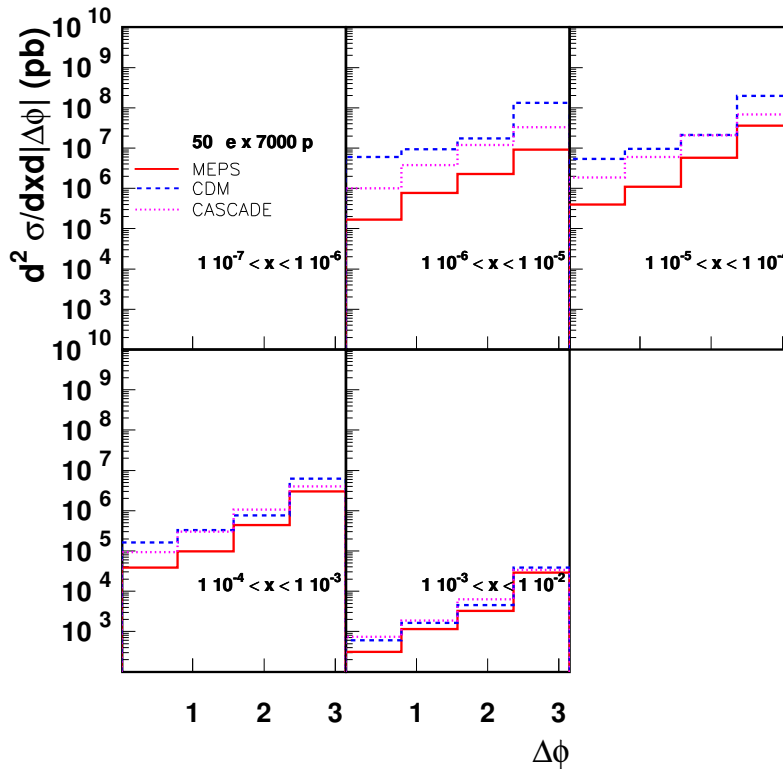


Figure 6.44: Differential cross section for dijet production as a function of the azimuthal separation $\Delta\phi$ for dijets with $E_{T,\text{jet}1} > 7 \text{ GeV}$ and $E_{T,\text{jet}2} > 5 \text{ GeV}$.

4384

4385

Thus, in principle, a measurement of the azimuthal dijet distribution offers a direct de-

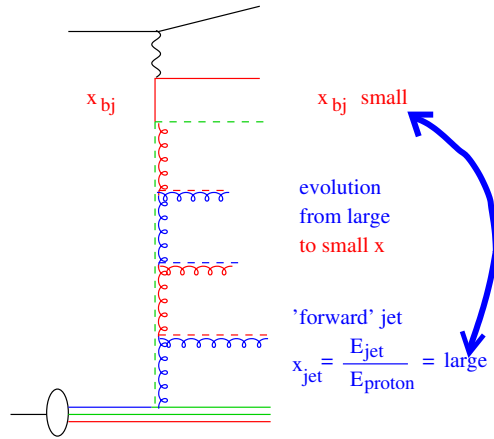


Figure 6.45: Schematic representation of the production of a high transverse momentum forward jet in DIS.

4386 termination of the k_T -dependence of the unintegrated gluon distribution. When additionally
 4387 supplemented by inclusive measurements, it can serve as an important constraint for the pre-
 4388 cise determination of the fully unintegrated parton distribution, with the transverse momentum
 4389 dynamics in the proton completely unfolded.

4390 **Forward observables**

4391 It was proposed some time ago [505, 506] that a process which would be very sensitive to the
 4392 parton dynamics and the transverse momentum distribution was the production of forward
 4393 jets in DIS. According to [505, 506], DIS events containing identified forward jets provide a
 4394 particularly clean window on small- x dynamics. The schematic view of the process is illustrated
 4395 in Fig. 6.45. The forward jet transverse momentum provides the second hard scale p_T . Hence
 4396 one has a process with two hard scales: the photon virtuality Q and the transverse momentum
 4397 of the forward jet p_T . As a result the collinear (DGLAP) configurations (with no diffusion
 4398 and strongly ordered transverse momenta) can be eliminated by choosing the scales to be of
 4399 comparable size, $Q^2 \simeq p_T^2$. Additionally, the jet is required to be produced in the forward
 4400 direction by demanding that x_J , the longitudinal momentum fraction of the produced jet, is as
 4401 large as possible, and x/x_J is as small as possible. This requirement selects events with a large
 4402 sub-energy between the jet and the virtual photon, such that the BFKL framework should be
 4403 applicable. There have been dedicated measurements of forward jets at HERA [507–512], which
 4404 demonstrated that DGLAP dynamics at NLO are indeed incompatible with the experimental
 4405 measurements. On the other hand, calculations based on resummations of powers of $\log 1/x$
 4406 (BFKL and others) [513–519] are consistent with the data. The azimuthal dependence of
 4407 forward jet production has also been studied [520, 521] as a sensitive probe of the small- x
 4408 dynamics.

4409 Another observable that provides a valuable insight into the features of small- x physics is
 4410 the transverse energy (E_T -flow) accompanying DIS events at small x . The diffusion of the
 4411 transverse momenta in this region leads to a strongly enhanced distribution of E_T at small
 4412 x . As shown in [522, 523], small- x evolution results in a broad Gaussian E_T -distribution as

4413 a function of rapidity. This should be contrasted with the much smaller E_T -flow obtained
 4414 assuming strong k_T -ordering as in DGLAP-based approaches, which give an E_T -distribution
 4415 that narrows with decreasing x , for fixed Q^2 .

4416 The first experimental measurements of the E_T -flow in small- x DIS events indicate that
 4417 there is significantly more E_T than is given by conventional QCD cascade models based on
 4418 DGLAP evolution. Instead we find that they are in much better agreement with estimates
 4419 which incorporate dynamics beyond fixed-order DGLAP [503,518,524] such as BFKL evolution.
 4420 The latter dynamics are characterized by an increase of the E_T -flow in the central region with
 4421 decreasing x .

4422 However, the experimental data from HERA do not enable a detailed analysis due to their
 4423 constrained kinematics. At the LHeC one could perform measurements with large separations
 4424 in rapidity and for different selections of the scales (Q, p_T). In particular, there is a possibility of
 4425 varying scales to test systematically the parton dynamics from the collinear (strongly ordered)
 4426 regime $Q^2 \gg p_T^2$ to the BFKL (equal scale, Regge kinematics) regime $Q^2 \simeq p_T^2$. Measurements
 4427 of the energy flow in different x -intervals, in the small- x regime, should therefore allow a defini-
 4428 tive check of the applicability of BFKL dynamics and of the eventual presence of more involved,
 4429 non-linear effects.

4430 A simulation of forward jet production at the LHeC is shown in Figs. 6.46 and 6.47. The
 4431 jets are required to have $E_T > 10$ GeV with a polar angle $\Theta_{jet} > 1^\circ$ or 3° in the laboratory
 4432 frame. Jets are found with the SISCone jet-algorithm [525]. The DIS phase space is defined by
 4433 $Q^2 > 5$ GeV, $0.05 < y < 0.85$.

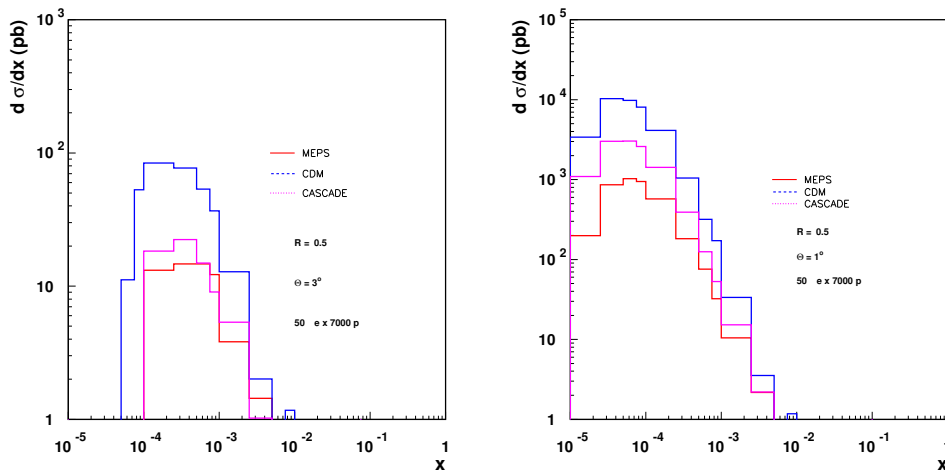


Figure 6.46: Cross section for forward jets with $\Theta_{jet} > 3^\circ$ (left) and $\Theta_{jet} > 1^\circ$ (right). Predictions from MEPS, CDM and CASCADE are shown. Jets are found with the SISCone algorithm using $R = 0.5$.

4434 In Fig. 6.46 the differential cross section is shown as a function of Bjorken x for an electron
 4435 energy of $E_e = 50$ GeV. The calculations are obtained from the MEPS [115], CDM [503] and
 4436 CASCADE [518] Monte Carlo models, as described in the previous section. Predictions for
 4437 $\Theta_{jet} > 3^\circ$ and $\Theta_{jet} > 1^\circ$ are shown. One can clearly see that the small- x range is explored

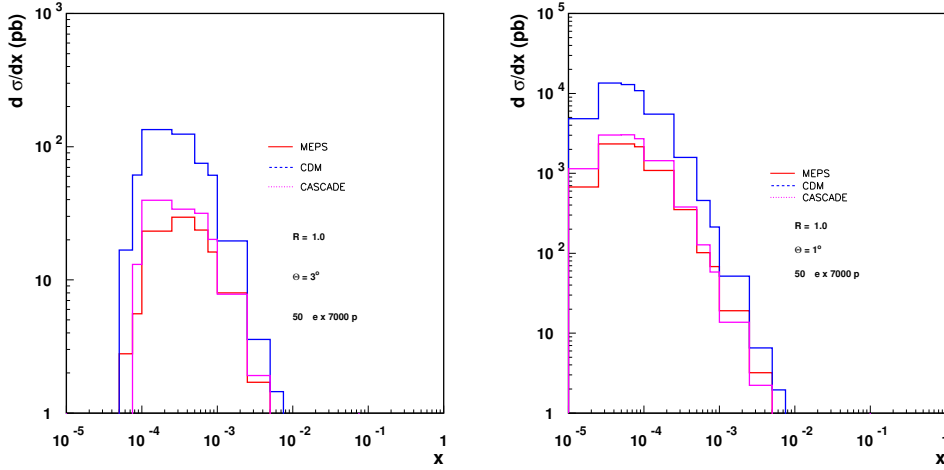


Figure 6.47: Cross section for forward jets with $\Theta_{jet} > 3^\circ$ (left) and $\Theta_{jet} > 1^\circ$ (right). Predictions from MEPS, CDM and CASCADE are shown. Jets are found with the SISCone algorithm using $R = 1.0$.

4438 in detail with the small angle scenario. In Fig. 6.47 the forward jet cross section is shown
 4439 when using $R = 1$ instead of $R = 0.5$ (Fig. 6.46). It is important to note that good forward
 4440 acceptance of the detector is crucial for the measurement of forward jets. The dependence of
 4441 the cross section on the acceptance angle is very strong as is evident from comparisons between
 4442 the cross sections for different Θ_{jet} cuts Figs. 6.46 and 6.47.

4443 A complementary reaction to that of forward jets is the production of forward π^0 mesons in
 4444 DIS. Despite having a lower rate, this process offers some advantages over forward jet produc-
 4445 tion. By looking onto single particle production the dependencies on the jet finding algorithms
 4446 can be eliminated. Also, the non-perturbative hadronisation effects can be effectively encom-
 4447 passed into fragmentation functions [514].

4448 **Perturbative and non-perturbative aspects of final state radiation and hadroniza-** 4449 **tion**

4450 The mechanism through which a highly virtual parton produced in a hard scattering gets rid of
 4451 its virtuality and colour and finally projects onto an observable final state hadron, is unknown to
 4452 a great extent (see [383] and references therein). The different postulated stages of the process
 4453 are illustrated in Fig. 6.48. The coloured parton undergoes QCD radiation before forming first
 4454 a coloured excited bound state (pre-hadron), then a colourless pre-hadron and ultimately a
 4455 final state hadron. These sub-processes are characterised by different time scales. While the
 4456 first stage can be described in perturbative QCD [526], subsequent ones require models (e.g.
 4457 the QCD dipole model for the pre-hadron stages) and non-perturbative information.

4458 The LHeC offers great opportunities to study these aspects and improve our understanding
 4459 of all of them. The energy of the parton which is struck by the virtual photon implies a Lorentz
 4460 dilation of the time scales for each stage of the radiation and hadronisation processes. All of

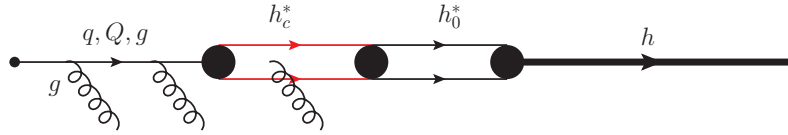


Figure 6.48: Sketch of the different postulated stages in the hadronisation of a highly virtual parton. From left to right: radiating parton; radiating coloured pre-hadron, colourless pre-hadron and final state hadron.

4461 them are influenced by the fact that they do not take place in the vacuum, but within the QCD
 4462 field created by the other components of the hadron or nucleus. While at fixed target SIDIS
 4463 or DY experiments, the lever arm in energy is relatively small (energy transfer to the struck
 4464 parton in its rest frame, $\nu < 100$ GeV), at the LHeC this lever arm will be huge ($\nu < 10^5$ GeV;
 4465 see also in Subsec. 4.8.2 the abundant yield of expected high transverse momentum jets in
 4466 photoproduction), implying that the different stages can be considered to happen in or out of
 4467 the hadron field depending on the parton energy. Furthermore, the fact that we can introduce
 4468 a piece of coloured matter of known length and density - a nucleus - by doing e Pb collisions at
 4469 different centralities, allows a controllable variation of the influence of the different processes.
 4470 The induced differences in the final distributions of hadrons, both in terms of their momenta
 4471 and of their relative abundance, will provide important information about the time scales and
 4472 the detailed physical mechanisms at work in each stage. Dramatic effects are predicted in some
 4473 models [143], with a significant suppression of the forward hadron spectra due to the creation
 4474 of the dense partonic system. Note that SIDIS experiments already provide information for the
 4475 determination of standard fragmentation functions (see [527, 528] for a recent analysis). The
 4476 other pieces of information, coming mainly from e^+e^- experiments, will not be improved until
 4477 next-generation linear colliders become available.

4478 Furthermore, these studies will shed light on two aspects already discussed in Subsec. 6.1.4,
 4479 related to the study of ultrarelativistic heavy-ion collisions: the characterization of the medium
 4480 created in such collisions through hard probes, and the details of particle production in a dense
 4481 situation which will define the initial conditions for the collective behavior of this medium.
 4482 Concerning the latter, our theoretical tools for computing particle production in eA collisions are
 4483 more advanced e.g. within the CGC framework, and on a safer ground than in nucleus-nucleus
 4484 collisions (see Subsec. 6.1.1 and e.g. [382] and refs. therein). The possibility of disentangling the
 4485 different mechanisms through which the factorisation that is used in dilute systems - collinear
 4486 factorisation [252] - becomes broken by density effects (e.g. initial and final state energy loss or
 4487 final state absorption) will be possible at the LHeC and will complement existing studies done
 4488 at much smaller energies in fixed target SIDIS and DY experiments [383].

4489 **6.2.6 Implications for ultra-high energy neutrino interactions and de-**
 4490 **tection**

The stringent constraints of the parton distributions at very small x from a future LHeC will have important implications for neutrino astronomy. Ultra-high energy neutrinos can provide important information about distant astronomical objects and the origin of the Universe. They have attracted a lot of attention during recent years, see the reviews [529, 530]. Neutrino astronomy has many advantages over conventional photon astronomy. This is due to the fact that neutrinos, unlike photons, interact only weakly, so they can travel long distances being practically undisturbed. The typical interaction lengths for neutrinos and photons at energy $E \sim 1$ TeV are about

$$\mathcal{L}_{int}^\nu \sim 250 \times 10^9 \text{ g/cm}^2, \quad \mathcal{L}_{int}^\gamma \sim 100 \text{ g/cm}^2.$$

4491 Thus, very energetic photons with energy bigger than ~ 10 TeV cannot reach the Earth from
 4492 the very distant corners of our Universe without being rescattered. In contrast, neutrinos can
 4493 travel very long distances without interacting. They are also not deflected by galactic magnetic
 4494 fields, and therefore at ultra-high energies the angular distortion of the neutrino trajectory is
 4495 very small. As a result, highly energetic neutrinos reliably point back to their sources. The
 4496 interest in the neutrinos at these high energies has led to the development of several neutrino
 4497 observatories, see [530] and references therein.

4498 For reliable observations based on neutrino detection, precise knowledge about their pro-
 4499 duction rates and interactions is essential to estimate the background, the expected fluxes and
 4500 the detection probabilities. Even though neutrinos interact only weakly with other particles,
 4501 strong interactions play an essential role in the calculations of their production rates and in-
 4502 teraction cross sections. This is due to the fact that neutrinos are produced in the decays of
 4503 various mesons such as π, K, D and even B , which are produced in high-energy proton-proton
 4504 (or proton-nucleus or nucleus-nucleus) collisions. These hadronic processes occur mainly in
 4505 the atmosphere though possibly also in the accretion discs of remote Active Galactic Nuclei.
 4506 Further, the interactions of highly energetic neutrinos with matter are dominated by the deep
 4507 inelastic cross section with nucleons or nuclei. Hence, low x information from high-energy col-
 4508 lider experiments such as HERA, Tevatron, LHC and, most importantly, the future LHeC, is
 4509 invaluable.

4510 One of the main uncertainties (if not the dominant one) in the current limits on high-energy
 4511 neutrino production is due to the neutrino-nucleon (nucleus) cross section. In fact, event rates
 4512 are proportional to the neutrino cross section in many experiments. This cross section involves
 4513 the gluon distribution probed at very small values of Bjorken x , down to even $\sim 10^{-9}$, which
 4514 corresponds to a very high centre of mass energy.

4515 To visualize the kinematic regime probed in ultra-high energy neutrino-nucleon interactions,
 4516 contour plots of the differential cross section $\frac{d^2\sigma}{d \ln 1/x d \ln Q^2/\Lambda^2}$ in the (x, Q^2) plane are shown in
 4517 Fig. 6.49. The contours enclose regions with different contributions to the total cross section
 4518 $\sigma(E_\nu)$. For very high energy $E_\nu = 10^{11}$ GeV the dominant contribution comes from the domain
 4519 $Q^2 \simeq M_W^2$ and $x_{\min} \simeq M_W^2/(2M_N E) \sim 10^{-8} - 10^{-7}$ where M_N is the nucleon mass, inaccessible
 4520 to any current or proposed accelerators. However, at lower neutrino energy $E_\nu = 10^7$ GeV the
 4521 relevant domain of (x, Q^2) could be very well covered by the LHeC, thus providing important
 4522 new constraints on the neutrino-nucleon cross section.

4523 On the other hand, another process which has been proposed for neutrino detection comes
 4524 from the discovery of neutrino flavor oscillations, which makes it possible that high rates of

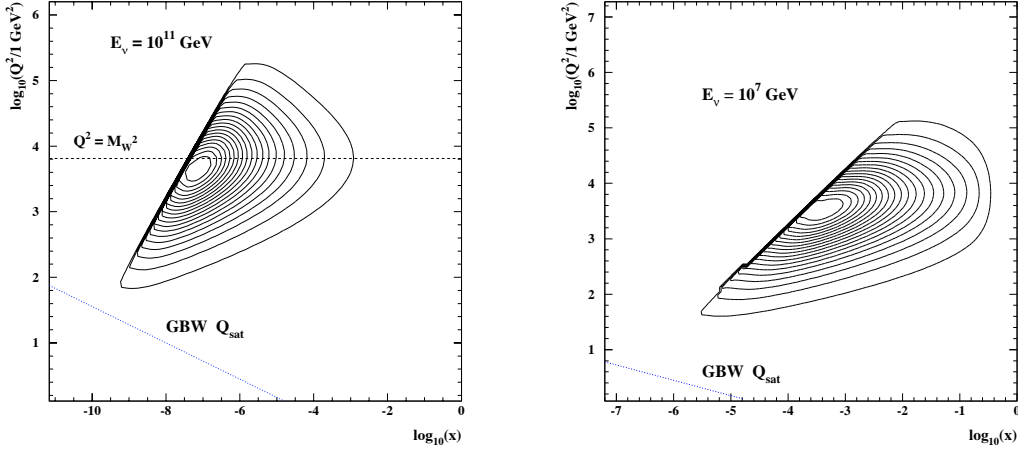


Figure 6.49: Contour plot showing the x, Q^2 domain of the dominant contribution to the differential cross section $d\sigma/d\ln(1/x)d\log Q^2$ for the total ν -nucleon interaction at neutrino laboratory energies of $E_\nu = 10^{11}$ GeV (left plot) and $E_\nu = 10^7$ GeV (right plot). The 20 contours enclose contributions of 5, 10, 15 \dots 100 % of the cross section. The saturation scale according to the model in [302] is shown as a dashed line. See the text for further explanation.

4525 τ neutrinos reach the Earth, despite being heavily suppressed in most postulated production
4526 mechanisms. The possibility to search for ν_τ 's by looking for τ leptons that exit the Earth,
4527 Earth-skimming neutrinos, has been shown to be particularly advantageous to detect neutrinos
4528 of energies in the EeV (10^{18} eV) range [531]. The short lifetime of a τ lepton originating a
4529 neutrino charged current interaction allows the τ to decay in flight while still close to the Earth's
4530 surface, producing an outgoing air shower, detectable in principle by various techniques. This
4531 channel suffers from negligible contamination for other neutrino flavors. The sensitivity to ν_τ 's
4532 through the Earth-skimming channel directly depends both on the neutrino charged current
4533 cross section and on the τ range (the energy loss) which is determined by the amount of matter
4534 with which the neutrino has to interact to produce an emerging τ . It turns out that the τ
4535 energy loss is also determined by the behavior of the proton and nucleus structure functions at
4536 very small values of x , see e.g. [532]. The average energy loss per unit depth, X , is conveniently
4537 represented by:

$$-\left\langle \frac{dE}{dX} \right\rangle = a(E) + b(E)E, \quad b(E) = \frac{N_A}{A} \int dy y \int dQ^2 \frac{d\sigma^{LA}}{dQ^2 dy}, \quad (6.20)$$

4538 where the $a(E)$ term is due to ionization, $b(E)$ is the sum of fractional losses due to e^+e^- pair
4539 production, Bremsstrahlung and photonuclear interactions, N_A is Avogadro's number and A
4540 is the mass number. The parameter $a(E)$ is nearly constant and the term $b(E)E$ dominates
4541 the energy loss above a critical energy that for τ leptons is a few TeV, with the photonuclear
4542 interaction being dominant for τ energies exceeding $E = 10^7$ GeV (as already assumed in Eq.
4543 (6.20)). In Fig. 6.50 the relative contribution to $b(E)$ of different x and Q^2 regions is shown. It
4544 can be observed that the energy loss is dominated by very small x and, in contrast to the case

of the neutrino cross section, by small and moderate $Q^2 \lesssim m_\tau^2$.

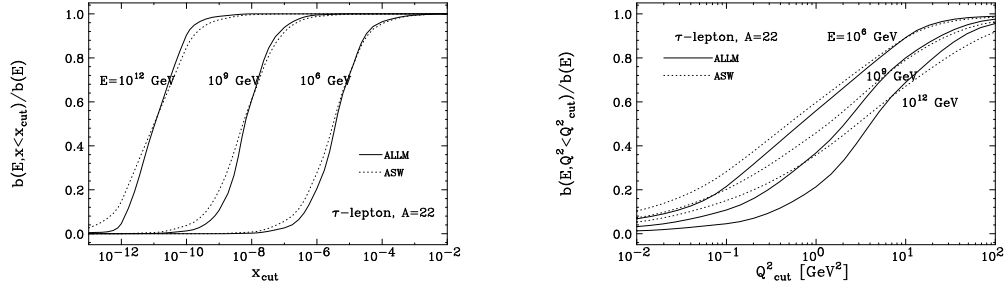


Figure 6.50: The relative contribution of $x < x_{cut}$ (plot on the left) and of $Q^2 < Q_{cut}^2$ (plot on the right) to the photonuclear energy loss rate, $b(E)$, for different neutrino energies $E = 10^6$, 10^9 and 10^{12} GeV, in two different models for the extrapolation of structure functions to very small x . See the text and [532] - from which these plots were taken - for explanations.

4545

4546

4547

4548

4549

As the LHeC will be able to explore a new regime of low x and high Q^2 and constrain the parton distributions, the measurements performed at this collider will be invaluable for the precise evaluation of the neutrino-nucleon (or nucleus) scattering cross sections and τ energy loss necessary for ultra-high energy neutrino astronomy.

4550

Part III

4551

Accelerator

4552 Chapter 7

4553 Ring-Ring Collider

4554 7.1 Baseline Parameters and Configuration

4555 7.2 Geometry

4556 All lattice descriptions in this chapter are based on the LHeC lattice Version 1.1.

4557 7.2.1 General Layout

4558 The general layout of the LHeC consists of eight arcs, six straight sections and two bypasses.
4559 The e-p collision experiment is located in Point 2, which is also the only interaction point of the
4560 beams. All straight sections except the straight sections in the bypasses have the same length
4561 as the LHC straight sections: 538.8 m at even points and 537.8 m at odd points.

4562 The insertions shared with the LHC are already used for the experiments or for LHC
4563 equipment. Therefore the RF for the electron ring is installed in the straight sections of
4564 the bypasses [?]. Out of the same reason the beam is injected in the bypass around Point
4565 1. Point 1 is preferred over Point 5 out of geological and infrastructural reasons. The overall
4566 layout of the LHeC is shown in Fig. 7.1.

4567 7.2.2 Electron Ring Circumference

4568 The LHeC electron beam collides only in one point (Point 2) with the protons of the LHC.
4569 This leaves the options to either exactly match the circumferences of the proton and electron
4570 rings or to allow a difference of a multiple of the LHC bunch spacing. In the case of different
4571 circumferences the proton beam could become unstable due to beam-beam interactions with
4572 the electrons [533]. To avoid this possible effect in the LHeC, the electron ring circumference
4573 is matched exactly to the proton ring circumference.

4574 The adjustment of the circumference can principally be achieved in two different ways:

- 4575 1. Different bypass designs, e.g. inner and outer bypass, which compensate each other in
4576 length.

4577 2. Radial displacement of the electron ring to the inside or outside of the LHC in the places
 4578 where the two rings share the same tunnel to compensate for the path length difference
 4579 caused by the bypasses.

4580 The different design possibilities for the bypasses are discussed in Sec. 7.2.4. Considering the
 4581 different bypass options and their characteristics, the best choice seems to be outer bypasses
 4582 around both experiments.

4583 7.2.3 Idealized Ring

4584 In the following the average between LHC beam 1 and beam 2 is taken as reference for the
 4585 LHC.

4586 General Layout

4587 To compensate the path length difference from the bypasses, the electron ring is placed in
 4588 average 61 cm to the inside of the LHC in the sections where both rings share the tunnel. For
 4589 this a complete ring with an ideally constant radial offset of 61 cm to the LHC was designed.
 4590 In the following we refer to this ring as the *Idealized Ring*.

4591 In addition to the horizontal displacement, the electron ring is set 1 m above the LHC in
 4592 order to minimize the interference with the LHC elements. The main remaining conflict in the
 4593 arc are then the service modules as shown in Fig. 7.11.1 and the DFBs in the insertions [?]. A
 4594 representative cross section of the LHC tunnel is shown in Fig. 7.2.

4595 In the main arcs the service modules have a length of 6.62 m and are installed at the
 4596 beginning of each LHC arc cell. The insertions host a different number of DFBs with a varying
 4597 placement and length. The idealized ring lattice is optimized in a way to avoid all service
 4598 modules in the main arcs. In order to show that it is possible to design an optics with no
 4599 e-ring elements at all DFB positions in the insertions, the dispersion suppressor of the even
 4600 respectively odd insertions was adapted to the DFB positions and lengths in IR2 respectively
 4601 IR3. For simplicity all straight sections are filled with a regular FODO cell structure.

4602 Geometry

4603 To adjust the beam optics to the regular reappearance of the service modules at the beginning
 4604 of each LHC arc cell it is suggested to use a multiple or $1/n$ th, $n \in \mathbb{N}$, of the LHC arc cell
 4605 length as LHeC FODO cell length. Beside the integration constraints, the cell has to provide
 4606 the right emittance. Taking half the LHC arc cell length as LHeC FODO cell length already
 4607 fulfils this second criterion (Sec. 7.3.1).

4608 As the LHC arc cell is symmetric, the best geometrical agreement with the LHC main arc
 4609 would be achieved, if the LHeC cell had as well a symmetrical layout. Because of the service
 4610 modules, no elements can be placed in the first approx. 6.9 m of two consecutive cells. If all
 4611 cells would have the same layout, another 6.9 m would be lost in the second FODO cell. This
 4612 would result in additional and therefore unwanted synchrotron radiation losses as the energy
 4613 loss in a dipole magnet is proportional to the inverse length of the dipole

$$U_{\text{dipole}} = \frac{C_\gamma}{2\pi} E_0^4 \frac{\theta^2}{l}, \quad C_\gamma = \frac{4\pi}{3} \frac{r_e}{(m_e c^2)^3} \quad (7.1)$$

4614 where θ is the bending angle, l the length of the dipole and E_0 the beam energy. In order
 4615 to avoid this, the LHeC arc cell is a double FODO cell, symmetric in the positioning of the
 4616 quadrupoles but asymmetric in the placement of the dipoles (Fig. 7.3).

4617 The bending angle in the arc cells and also in the DS is determined by the LHC geometry.
 4618 In the following we refer to the LHC DS as the section from the end of the arc to the beginning
 4619 of the LSS. With this definition the LHC DS consists of two cells. Keeping the same converting
 4620 rule as in the arc (one LHC FODO cell corresponds to two LHeC FODO cells), the LHeC DS
 4621 would then ideally consist of 4 equal cells. Consistently the ratio between the LHeC DS and
 4622 arc cell is the same as between the LHC DS and arc cell. For the LHC this ratio is 2/3. This
 4623 leaves the following choices for the number of dipoles in the arc and DS cell:

$$N_{\text{Dipole, arc cell}} = \frac{3}{2} N_{\text{Dipole, DS cell}} = 3, 6, 9, 12, 15 \dots \quad (7.2)$$

4624 A good compromise between a reasonable dipole length and an optimal usage of the available
 4625 space for the bending are 15 dipoles per arc cell. The dipoles are then split up in packages of
 4626 $3 + 4 + 4 + 4$ in one arc cell and $2 + 3$ in one DS cell.

4627 Beside the bending angle also the module length of the electron ring has to be matched to
 4628 the LHC geometry. As the electron ring is radially displaced to the inside of the proton ring
 4629 all e-ring modules are shorter than their proton ring equivalents (Table 7.1).

	Proton Ring	Electron Ring
Arc Cell Length	106.9 m	106.881 m
DSL Length (even points)	172.80 m	172.78 m
DSR Length (even points)	161.60 m	161.57 m
DSL Length (odd points)	173.74 m	173.72 m
DSR Length (odd points)	162.54 m	162.51 m

Table 7.1: Proton and Electron-Ring Module Lengths

4630 The above considerations already fix the bending angle of the dipoles, which leaves only
 4631 position and length as free parameters. Ideally the dipole length would be chosen as long as
 4632 possible, but due to the asymmetry of the arc cell, the dipoles have to be shortened and moved
 4633 to the right in order to fit the LHC geometry.

4634 The LHeC DS layout would ideally be similar to the LHC DS layout (Fig. 7.4), but has to
 4635 be modified in order to leave space for the DFBs in the DS region. In the final design the dipoles
 4636 are placed as symmetrically as possible between the regular arrangement of the quadrupoles
 4637 (Fig. 7.5, 7.6). The difference between the LHC proton ring and the idealized LHeC electron
 4638 ring is shown in Fig. 7.7 and 7.8.

4639 7.2.4 Different Bypass Options

4640 In the design of the e-ring geometry it is foreseen to bypass the LHC experiments at Point 1
 4641 and Point 5. The main requirements for both bypasses are, that all integration constraints are
 4642 respected, synchrotron radiation losses are not considerably increased and that the change in
 4643 circumference can be compensated by the reduction or increase of the radius of the ring.

4644 Three different options are considered as basic bypass designs:

4645 **Vertical Bypass:** A vertical bypass would have to be a vertically upward bypass as downward
4646 would imply to cross the LHC magnets and other elements. For this a separation of
4647 about 20 to 25 m is required [534]. This can only be achieved by strong additional
4648 vertical bending. In general a vertical bypass would therefore be rather long, increase the
4649 synchrotron radiation due to the additional vertical bends and decrease the polarization
4650 compared to a horizontal bypass. A vertical bypasses is therefore only considered as an
4651 option, if horizontal bypasses are not possible.

4652 **Horizontal Inner Bypass:** A horizontal inner bypass can be constructed by simply decreasing
4653 the bending radius of the main bends. Consequently the synchrotron radiation losses
4654 for an inner bypass are larger than for a comparable outer bypass. The advantage of an
4655 inner bypass is, if used in combination with an outer one, that it reduces the circumference
4656 and the two bypasses could compensate each others path length differences.

4657 **Horizontal Outer Bypass:** A horizontal outer bypass uses the existing curvature of the
4658 ring instead of additional or stronger dipoles and consequently does not increase the
4659 synchrotron radiation losses. In general this is the preferred option.

4660 7.2.5 Bypass Point 1

4661 The cavern in Point 1 reaches far to the outside of the LHC, so that a separation of about
4662 100 m would be necessary in order to fully bypass the experimental hall. For a bypass on the
4663 inside a smaller separation of about 39 m would be required. For an inner bypass with minimal
4664 separation, the bending strength in three normal arc cells would have to be doubled resulting
4665 in a bypass of more than 2 km length. A sketch of such an inner bypass is shown in Fig. 7.9.

4666 Instead of a long inner bypass, an outer bypasses using the existing survey gallery is chosen
4667 as final design. With this design the separation is brought down to 16.25 m. The RF is installed
4668 in the straight section next to the straight section of the proton ring. The electron beam is
4669 injected into the arc on the right side of the bypass. The design is shown in Fig. 7.10.

4670 7.2.6 Bypasses Point 5

4671 Due to the compact design of the cavern in Point 5 a separation of only approx. 20 m is needed
4672 to completely bypass the experiment on the outside (Fig. 7.11). The separation in the case of
4673 an inner horizontal bypass or a vertical bypass would be the same or larger and therefore, as in
4674 the case of Point 1, the horizontal outer bypass is preferred over an inner or vertical one. The
4675 RF is installed in the center straight section parallel to the proton ring.

4676 7.2.7 Matching Proton and Electron Ring Circumference

4677 Both bypasses in Point 1 and Point 5 require approximately the same separation and a similar
4678 design was chosen for both. To obtain the necessary separation Δ_{BP} a straight section of length
4679 s_{BP} is inserted into the lattice of the idealized ring (Sec. 7.2.3) in front of the last two arc cells.
4680 The separation Δ_{BP} , the remaining angle θ_{BP} and the inserted straight section s_{BP} are related
4681 by (Fig. 7.12):

$$\Delta_{BP} = s_{BP} \sin \theta_{BP} \quad (7.3)$$

4682 As indicated in Fig. 7.12 the separation could be increased by inserting a S-shaped chicane
4683 including negative bends. The advantage of additional bends would be the faster separation of

4684 the electron and proton ring. On the other hand the additional bends would need to be placed
 4685 in the LHC tunnel, the straight sections of the bypass would be reduced and the synchrotron
 4686 radiation losses increased.

4687 In the following estimates for the current bypass design, which does not include any extra
 4688 bends, are presented. Given the separation, angle and length of the inserted straight section,
 4689 the induced change in circumference is then:

$$\Delta s_{\text{BP}} = s_{\text{BP}} - x_{\text{BP}} = 2\Delta_{\text{BP}} \tan\left(\frac{\theta_{\text{BP}}}{2}\right) \quad (7.4)$$

4690 This change can be compensated by a change of radius of the idealized ring by:

$$\Delta s_{\text{BP}} = 2\pi\Delta R \quad (7.5)$$

4691 Taking the change in radius into account, the separation Δ_{BP} has to be substituted by
 4692 $\Delta_{\text{BP}} + \Delta R =: \Delta_{\text{BP,tot}}$. The radius change and the total separation are then related by:

$$\Delta R = \frac{\Delta_{\text{BP}}}{\pi \cot\left(\frac{\theta_{\text{BP}}}{2}\right) - 2}, \quad \text{with } \Delta_{\text{BP}} = \Delta_{\text{BP1}} + \Delta_{\text{BP5}} \quad (7.6)$$

4693 As the bypass in Point 1 passes through the existing survey gallery, the geometry and with it
 4694 the separation in Point 1 can not be changed. The bypass in Point 5 however is fully decoupled
 4695 from the existing LHC cavern and tunnel and is therefore used for the fine adjustment of the
 circumference. The design values of both bypasses are summarized in Table 7.2.

	Point 1	Point 5
Total bypass length	1303.3 m	1303.7 m
Separation	16.25 m	20.56 m
Dispersion free straight section	172 m	297 m
Ideal radius change of the idealized ring	61 cm	

Table 7.2: Bypass Figures

4696

4697 7.3 Layout and Optics

4698 Throughout the whole electron ring lattice, the choice of the optics is strongly influenced by
 4699 the geometrical constraints and shortage of space in the LHC tunnel. The main interference
 4700 with the LHC beside Point 1 and Point 5, which have to be bypassed, are the service modules
 4701 and DFBS in the tunnel, where no electron ring elements can be placed.

4702 7.3.1 Arc Cell Layout and Optics

4703 The LHC service modules are placed at the beginning of each LHC main arc cell. In order
 4704 to obtain a periodic solution of the lattice, the electron ring arc cell length can only be a
 4705 multiple or $1/n$ th, $n \in \mathbb{N}$, of the LHC FODO cell length. In general the emittance increases
 4706 with increasing cell length L in a FODO cell assuming the same phase advance and bending

radius. In the case of the LHeC electron ring a FODO cell length corresponding to half the LHC FODO cell length delivers an emittance close to the design value. The emittance of a cell with the full LHC FODO cell length is at least by approx. a factor of 4 too large. Choosing half the LHC FODO cell length divides the arc into 23 equal double FODO cells with a symmetric configuration of the quadrupoles and an asymmetric distribution of the dipoles, precisely 8 dipoles in the first FODO cell and 7 in the second. The dipole configuration is asymmetric in order to use all available space for the bending of the e-beam and consequently minimize the synchrotron radiation losses. With a phase advance of 180° horizontally and 120° vertically over the complete double FODO cell, which corresponds to a phase advance of $90^\circ/60^\circ$ per FODO cell, the horizontal emittance lies with 4.70 nm well below the design value of 5 nm. Because of the asymmetry of the dipole configuration, the phase advance in the horizontal plane is also not equally distributed. In the first half it is with $90.6^\circ/60^\circ$ slightly larger than in the second half with $89.4^\circ/60^\circ$. The optics of one arc cell is shown in Fig. 7.3 and the parameters listed in Table 7.3.

Beam Energy	60 GeV
Phase Advance per Cell	$180^\circ/120^\circ$
Cell length	106.881 m
Dipole Fill factor	0.75
Damping Partition $J_x/J_y/J_e$	1.5/1/1.5
Coupling constant κ	0.5
Horizontal Emittance (no coupling)	4.70 nm
Horizontal Emittance ($\kappa = 0.5$)	3.52 nm
Vertical Emittance ($\kappa = 0.5$)	1.76 nm

Table 7.3: Optics Parameters of one LHeC arc cell with a phase advance of $180^\circ/120^\circ$.

4720

4721 7.3.2 Insertion Layout and Optics

4722 For simplicity all even and all odd insertions of the electron ring have the same layout as
 4723 described in Sec. 7.2.1. Each insertion is divided in three parts: the dispersion suppressor on
 4724 the left side (DSL), the straight section and the dispersion suppressor on the right side (DSR).

4725 Dispersion Suppressor

4726 Different well known standard DS designs like the missing bend or half bend scheme exist, but
 4727 they are all based on specific placement of the dipoles. In the case of the LHeC the position
 4728 of the dipoles is strongly determined by the LHC geometry and does not match any of the
 4729 standard schemes. Therefore the matching has to be done with individual quadrupoles slightly
 4730 supported by the position of the dipoles. Each DS contains 8 matching quadrupoles. The
 4731 DS on the left side is split into two DS sections, reaching from the first DFB to the second
 4732 and from the second to the beginning of the straight section. In the DSL the quadrupoles are
 4733 distributed equally in each section. In the DSR they are placed with equal distances from each
 4734 other throughout the complete DS. This layout turned out to be better for the right side due

4735 to the different arrangement of the DFBs. The DS of the even and odd points differ slightly in
4736 their length but have in general the same layout. The length of the DS is listed in Table 7.1.
4737 The DS optics are shown in Fig. 7.5 and 7.6.

4738 **Straight Section**

4739 For simplicity the straight sections consist of a regular FODO lattice with a phase advance of
4740 $90^\circ/60^\circ$. In a later stage the lattice and optics of the straight sections will have to be adjusted
4741 to the different insertions.

4742 **7.3.3 Bypass Layout and Optics**

4743 The general layout and nomenclature of the bypasses is illustrated in Fig. 7.13. The straight
4744 sections LSSL, LSSR and IR are dispersion free sections reserved for the installation of RF,
4745 wiggler(s), injection etc. Two normal arc cells (4 FODO cells) with 8 individual quadrupoles
4746 are used as dispersion suppressor before the first straight section LSSL and after the last straight
4747 section LSSR. In the sections TLIR and TRIR the same configuration of dipoles is kept as in
4748 the idealized lattice due to geometric reasons. Between this fixed arrangement of dipoles 14
4749 matching quadrupoles per side are placed as equally as possible.

4750 The straight sections consist of a regular FODO lattice with a phase advance of $90^\circ/60^\circ$.

4751 The complete bypass optics in Point 1 and Point 5 are shown in Fig. 7.14 and 7.15.

4752 **7.3.4 Chromaticity Correction**

4753 The phase advance of one LHeC FODO cell is approximately $90^\circ/60^\circ$. The traditional choice
4754 would be to correct the chromaticity with two interleaved families in the horizontal and three in
4755 the vertical plane, but this scheme leads to one strong and one weak sextupole in the horizontal
4756 plane, which is undesirable for the suppression of resonances. An interleaved scheme with 6
4757 sextupoles yields to approximately similar strength for all sextupoles and shall therefore lead to
4758 more stability. More detailed studies have to be carried out to find the best correction scheme,
4759 but in general chromaticity correction will most probable not be a problem in this machine.

4760 **7.3.5 Working Point**

4761 Due to the bypasses and the single interaction region, the LHeC lattice has a symmetry of one.
4762 As 50% coupling are assumed also coupling resonances can be excited and must be taken into
4763 account for the choice of the working point. In addition the beam will suffer a maximal beam-
4764 beam tune shift of 0.086 in the horizontal and 0.088 in the vertical plane in the case of the 1°
4765 option and 0.085 in the horizontal and 0.090 in the vertical plane in the case of the 10° option.
4766 Taking all this into account, a possible working point could be $Q_x = 122.1/Q_y = 83.13$ for the
4767 1° optics and $Q_x = 122.1011/Q_y = 83.1283$ for the 10° optics. The working point diagrams for
4768 both cases are shown in Fig. 7.16 and 7.17.

4769 **7.3.6 Aperture**

4770 The current LHeC e-ring magnet apertures [?] are based on the experience from LEP [?] applied
4771 on the LHeC arc cells. They correspond to minimum 23.0σ hor./ 39.9σ ver. in the arc dipoles,
4772 31σ hor./ 59σ ver. in the arc quadrupoles, 9.7σ hor./ 34.3σ ver. in the insertion dipoles

4773 and 14.3σ hor./ 51.0σ ver. in the insertion quadrupoles. In the estimate all insertions were
 4774 included except the interaction region. All values are summarized in Table 7.4, 7.5, 7.6, 7.7. The
 4775 hor. aperture in the insertion dipoles could be slightly to tight, but can be probably extended
 4776 without problems over the current 20 mm half aperture. In all calculations a gaussian profile
 4777 in all three dimensions was assumed and the maximum beam size is consequently given by:

$$\sigma_{x,y} = \sqrt{\beta_{x,y}\epsilon_{x,y} + D_{x,y}^2\sigma_E^2} \quad (7.7)$$

4778 where $\epsilon_{x,y}$ are the design emittances of 5 respectively 2.5 nm.

Hor. Half Apert. Dip.	30 mm
Ver. Half Apert. Dip.	20 mm
Max. Hor. Beta Function	82.7 m
Max. Hor. Dispersion	0.51 m
Max. Ver. Beta Function	100.5 m
Max. Hor. Beam Size	0.87 mm
Max. Ver. Beam Size	0.50 mm
Hor. Apert./Max. Beam Size	34.5
Ver. Apert./Max. Beam Size	39.9

Table 7.4: Aperture and beam sizes for the arc dipoles

Hor. Half Aperture Dipole	30 mm
Ver. Half Aperture Dipole	20 mm
Max. Hor. Beta Function	126.9 m
Max. Hor. Dispersion	1.64 m
Max. Ver. Beta Function	136.2 m
Max. Hor. Beam Size	2.06 mm
Max. Ver. Beam Size	0.58 mm
Hor. Aperture/Max. Beam Size	14.6
Ver. Aperture/Max. Beam Size	34.3

Table 7.5: Aperture and beam sizes for the insertion dipoles

Apert. Radius Arc Quad.	30 mm
Max. Hor. Beta Function	99.2 m
Max. Hor. Dispersion	0.56 m
Max. Ver. Beta Function	103.3 m
Max. Hor. Beam Size	0.96 mm
Max. Ver. Beam Size	0.51 mm
Hor. Apert./Max. Beam Size	31.4
Ver. Apert./Max. Beam Size	59.0

Table 7.6: Aperture and beam sizes for the arc quadrupoles

Apert. Radius Quad.	30 mm
Max. Hor. Beta Function	141.9 m
Max. Hor. Dispersion	1.66 m
Max. Ver. Beta Function	138.4 m
Max. Hor. Beam Size	2.10 mm
Max. Ver. Beam Size	0.59 mm
Hor. Apert./Max. Beam Size	14.3
Ver. Apert./Max. Beam Size	51.0

Table 7.7: Aperture and beam sizes for the insertion quadrupoles

4779 **7.3.7 Complete Lattice and Optics**

4780 Combining all the lattice parts discussed in section 7.3.1 to 7.3.3 one obtains a lattice with the parameters listed in Table 7.8

Beam Energy	60 GeV
Numb. of Part. per Bunch	1.98×10^{10}
Numb. of Bunches	2808
Circumference	26658.8832 m
Syn. Rad. Loss per Turn	437.2 MeV
Power	43.72 MW
Damping Partition $J_x/J_y/J_e$	1.5/1/1.5
Coupling Constant κ	0.5
Damping Time τ_x	0.016 s
Damping Time τ_y	0.024 s
Damping Time τ_e	0.016 s
Polarization Time	61.7 min
Horizontal Emittance (no coupling)	5.53 nm
Horizontal Emittance ($\kappa = 0.5$)	4.15 nm
Vertical Emittance ($\kappa = 0.5$)	2.07 nm
RF Voltage V_{RF}	500 MV
RF frequency f_{RF}	721.421 MHz
Energy Spread	0.00116
Momentum Compaction	0.00008084
Synchrotron Tune	0.058
Bunch Length	6.88 mm
Max. Hor. Beta	141.94 m
Max. Ver. Beta	138.43 m
Max. Hor. Dispersion	1.66 m
Vert. Dispersion	0 m
Max. Hor. Beam Size (5/2.5 nm emittance)	2.1 mm
Max. Ver. Beam Size (5/2.5 nm emittance)	0.59 mm

Table 7.8: LHeC Optics Parameters

4781

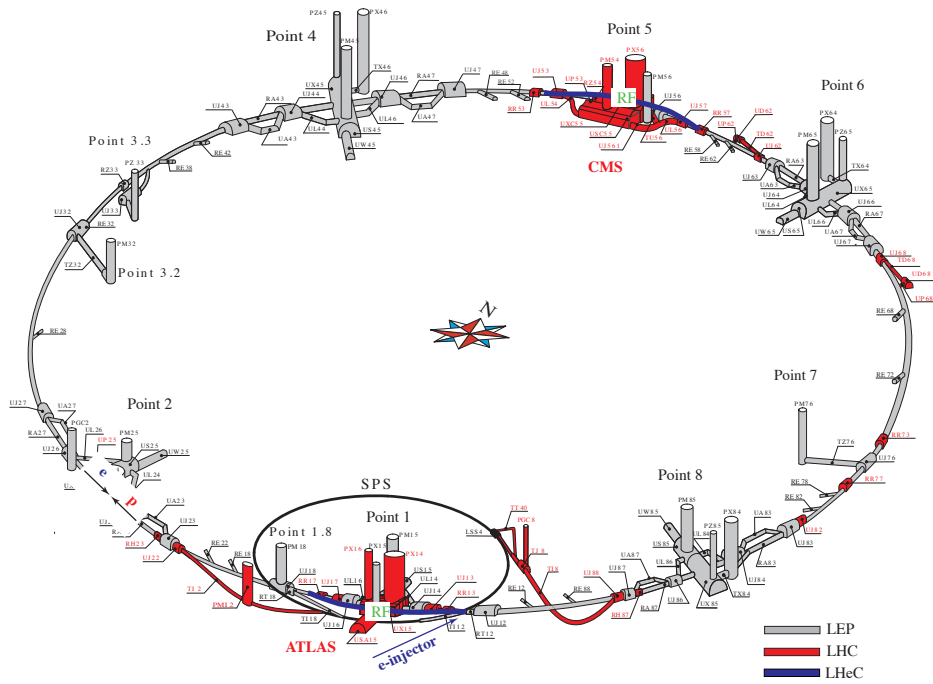


Figure 7.1: Schematic Layout of the LHeC: In grey the LEP tunnel now used for the LHC, in red the LHC extensions. The two LHeC bypasses are shown in blue. The RF is installed in the central straight section of the two bypasses. The bypass around Point 1 hosts in addition the injection.

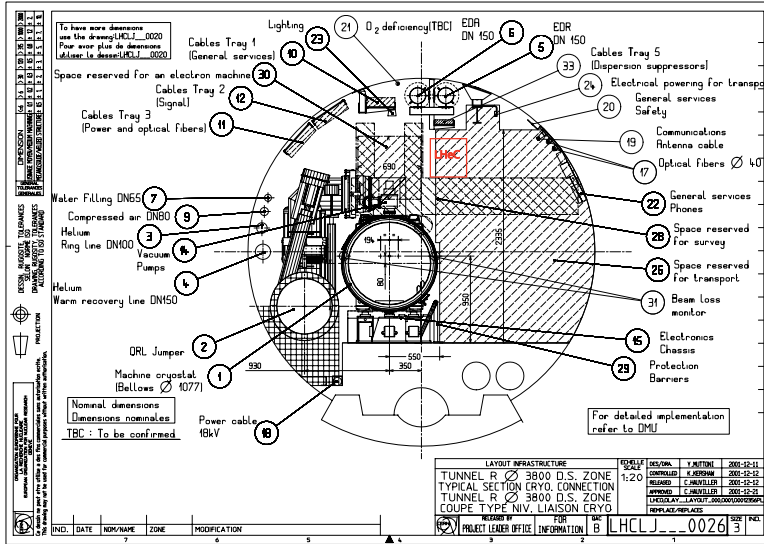


Figure 7.2: Representative cross section of the LHC tunnel. The location of the electron ring is indicated in red.

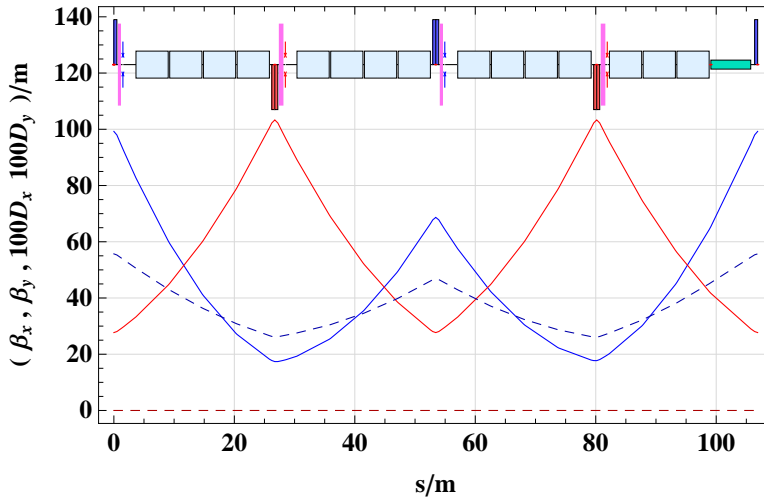


Figure 7.3: Electron ring arc cell optics. One arc cell consists of two FODO cells symmetric in the placement of the quadrupoles and asymmetric for the dipoles.

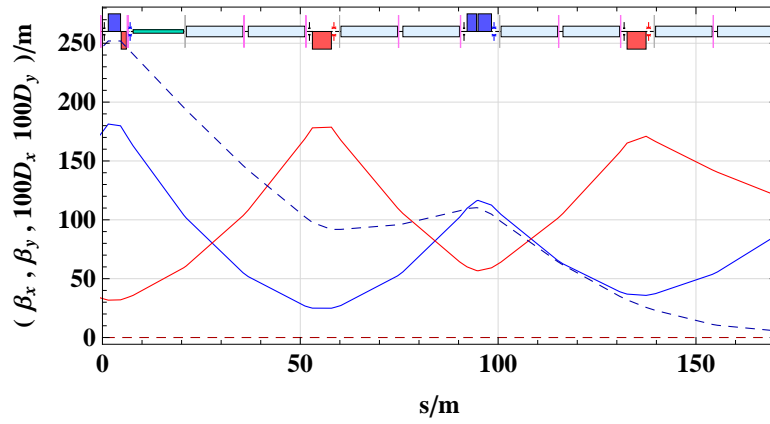


Figure 7.4: LHC DS on the left side of IP2.

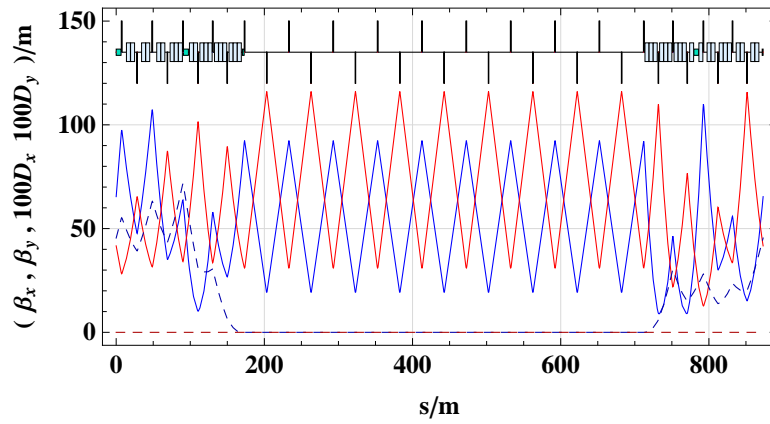


Figure 7.5: LHeC IR for even IRs, based on the DFB configuration in Point 2.

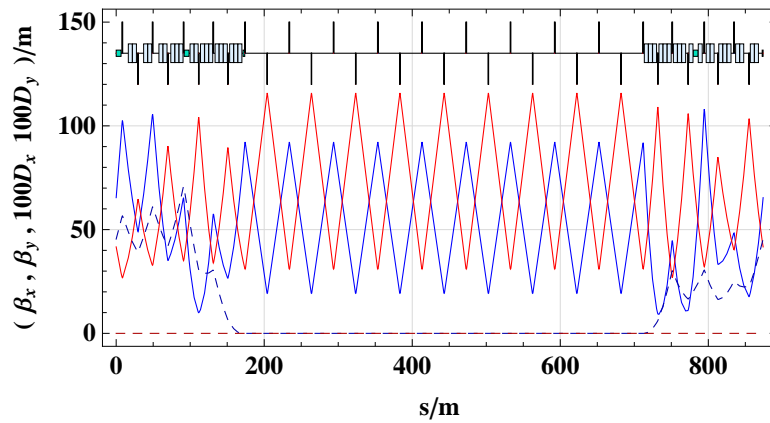


Figure 7.6: LHeC IR for odd IRs, based on the DFB configuration in Point 3.

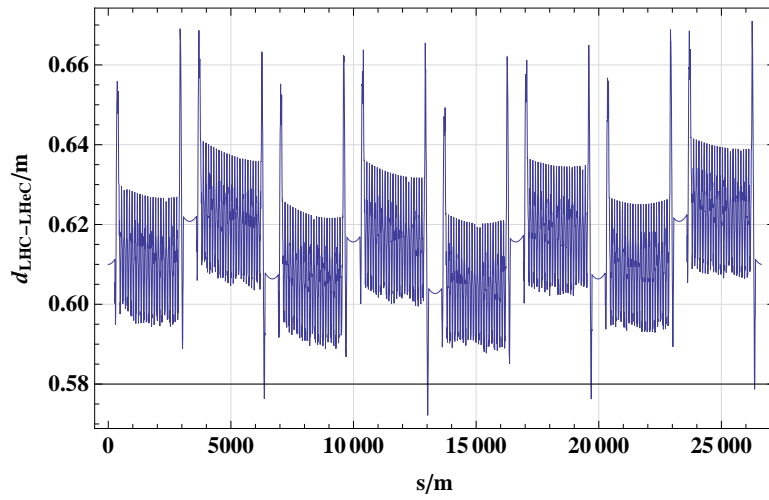


Figure 7.7: Radial distance between the idealized electron ring and the proton ring

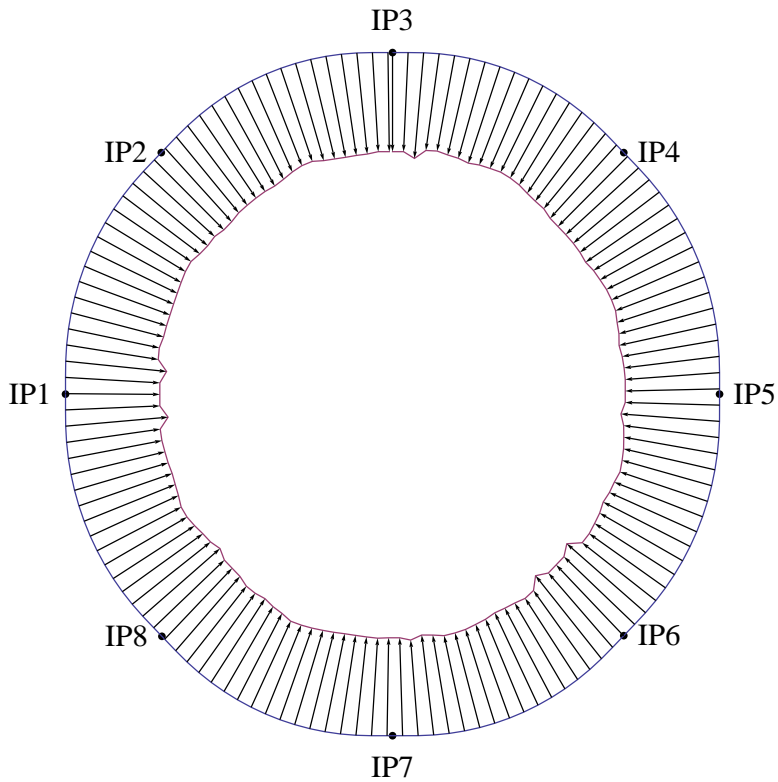


Figure 7.8: LHC and LHeC. The distance between the two rings is exaggerated by a factor 2000.

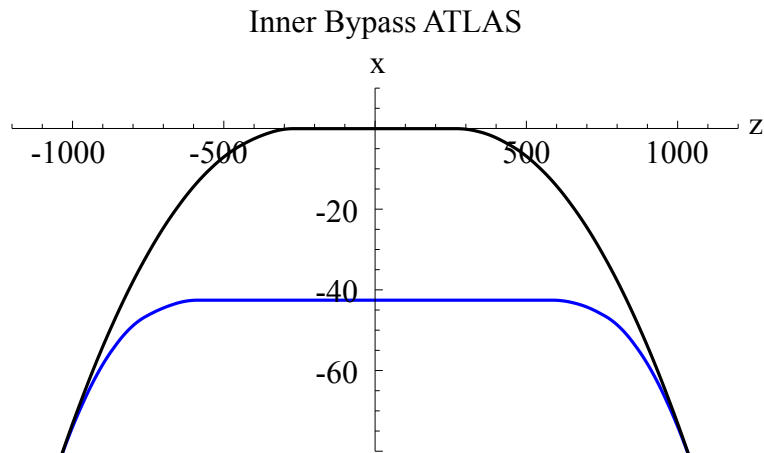


Figure 7.9: Example of an inner Bypass around Point 1. The Bypass is shown in blue, The LHC proton ring in black.

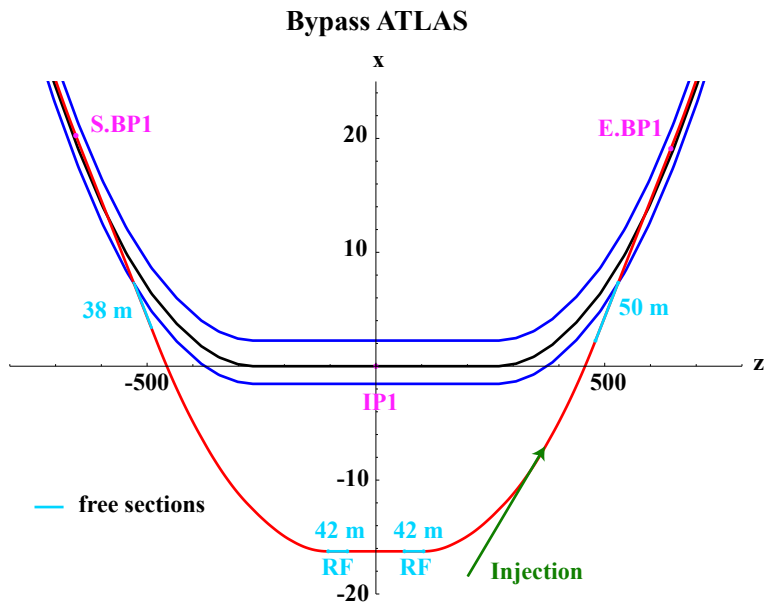


Figure 7.10: Final bypass design using the survey gallery in Point 1. The LHC proton ring is shown in black, the electron ring in red and the tunnel walls in blue. Dispersion free sections reserved for the installation of RF, wiggler(s), injection and other equipment are marked in light blue. The injection is marked in green and is located in the right arc of the bypass. Beginning and end of the bypass are marked with S.BP1 and E.BP1

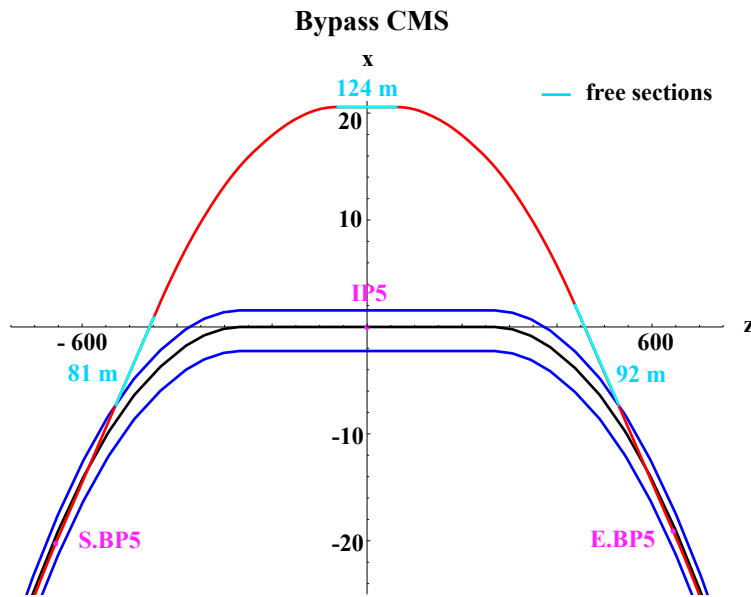


Figure 7.11: Horizontal outer bypass in Point 5. The LHC proton ring is shown in black, the electron ring in red and the tunnel walls in blue. Dispersion free sections reserved for the installation of RF, wiggler(s), injection and other equipment are marked in light blue. Beginning and end of the bypass are marked with S.BP5 and E.BP5

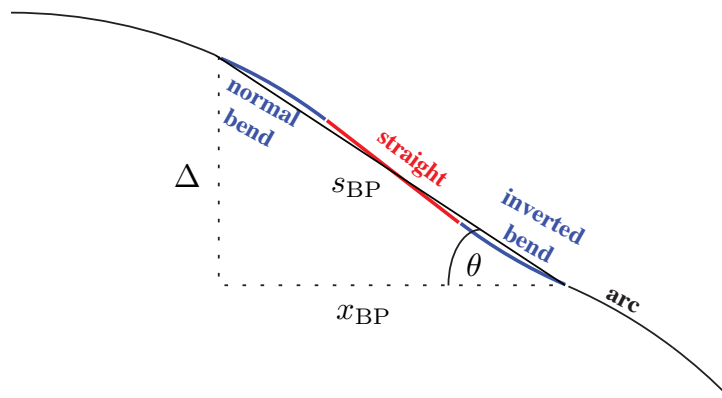


Figure 7.12: Outer bypass: a straight section is inserted to obtain the required separation. A larger separation could be achieved by inserting inverted bends.

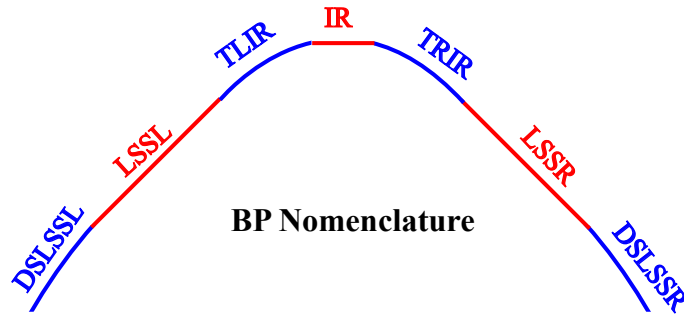


Figure 7.13: Bypass layout and nomenclature.

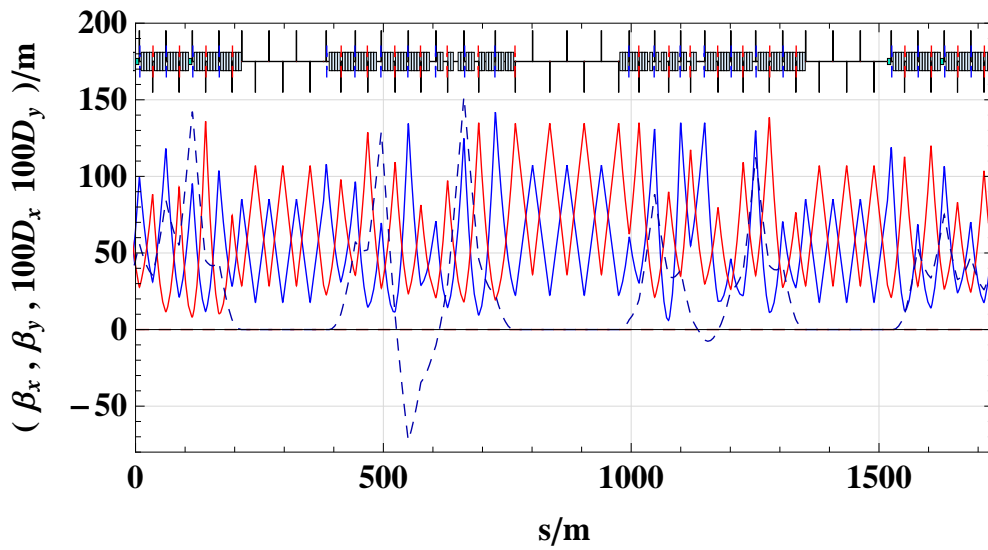


Figure 7.14: Bypass optics Point 1.

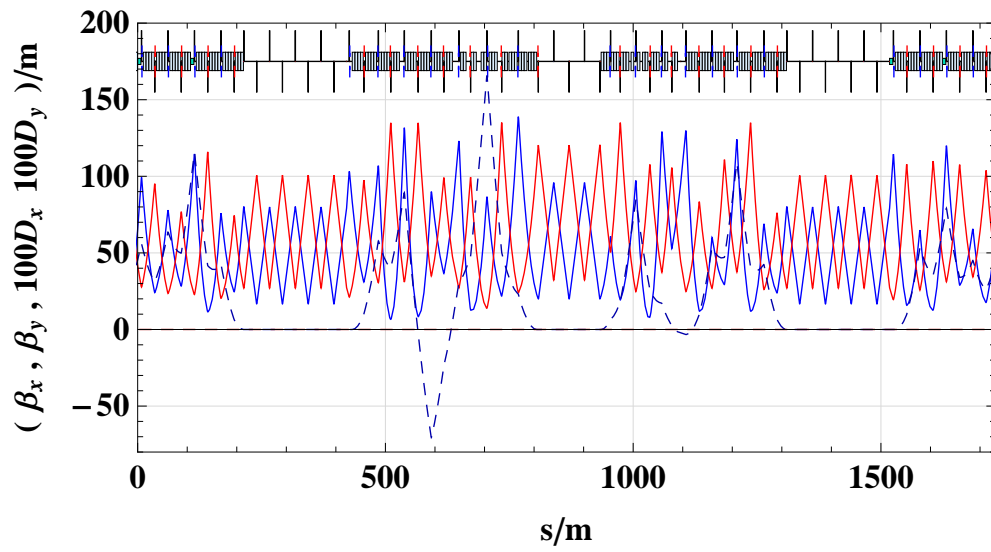


Figure 7.15: Bypass Optics Point 5.

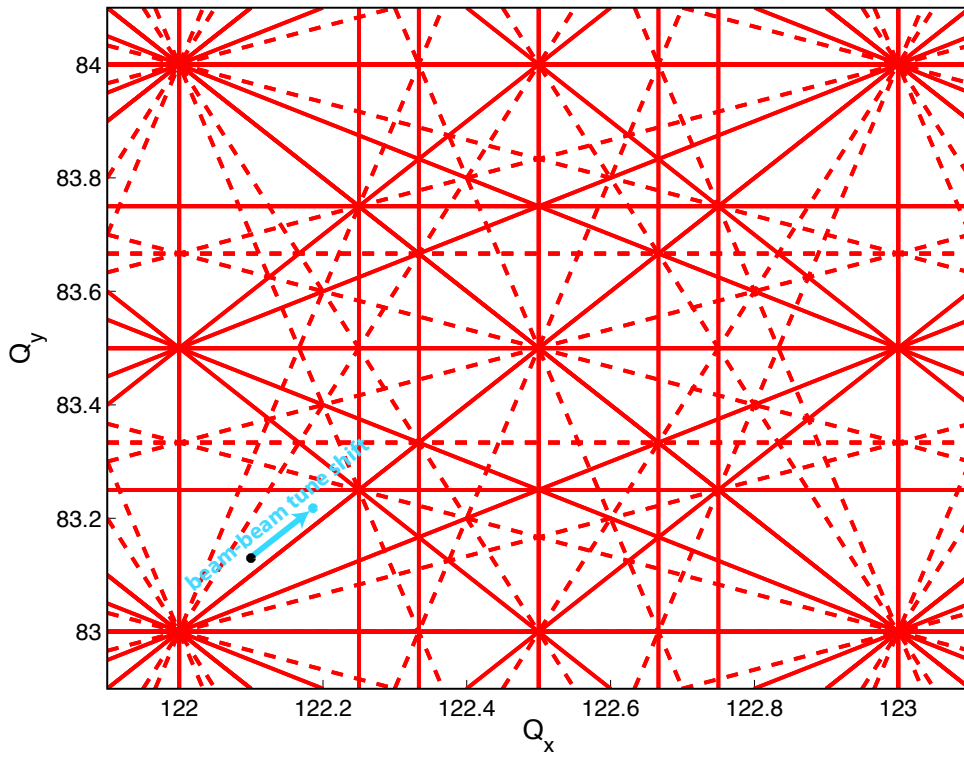


Figure 7.16: Working Point for the 1° optics. The dashed lines are the coupling resonances up to 4th order, the solid lines the constructive resonances up to 4th order. The black dot indicates the working point without beam-beam tune shift and the blue one with beam-beam tune shift.

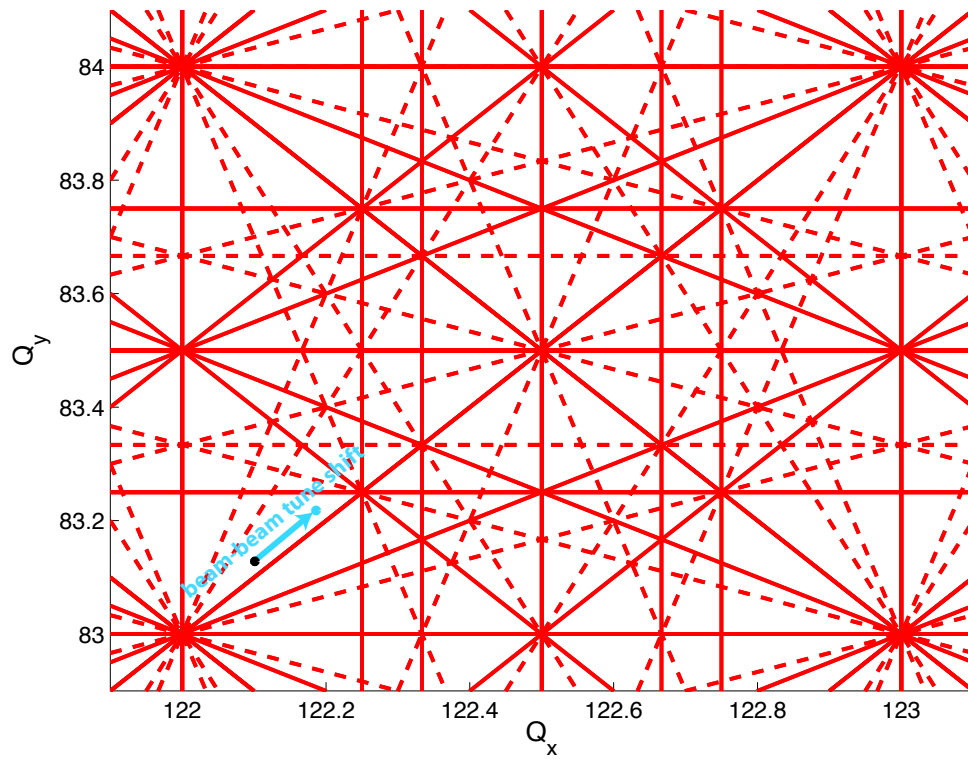


Figure 7.17: Working Point for the 10° optics. The dashed lines are the coupling resonances up to 4th order, the solid lines the constructive resonances up to 4th order. The black dot indicates the working point without beam-beam tune shift and the blue one with beam-beam tune shift.

7.4 Layout

The design of the Interaction Region (IR) of the LHeC is particularly challenging as it has to consider boundary conditions from

- The lattice design and beam optics of the electron and proton beam
- The geometry of the LHC experimental cavern and the tunnel
- The beam separation scheme which is determined by the bunch pattern of the LHC standard proton operation and related to this the optimisation of the synchrotron light emission and collimation
- The technical feasibility of the hardware.

Therefore the IR has to be optimised with respect to a well matched beam optics that adapts the optical parameters from the new electron-proton interaction point to the standard LHC proton beam optics in the arc and to the newly established beam optics of the electron ring. At the same time the two colliding beams as well as the non-colliding proton beam of LHC have to be separated efficiently and guided into their corresponding magnet lattices. As a general rule that has been established in the context of this study any modification in the standard LHC lattice and any impact on the LHC proton beam parameters had to be chosen moderately to avoid detrimental effects on the performance of the LHC proton-proton operation.

The layout and parameters of the new e/p interaction point are defined by the particle physics requirements. At present the physics programme that has been proposed for the LHeC [?] follows two themes - a high luminosity, high Q^2 programme requiring a forward and backward detector acceptance of around 10° and a low x, low Q^2 programme, which requires an increased detector acceptance in forward and backward direction of at least 1° and could proceed with reduced luminosity. Accordingly two machine scenarios have been studied for the interaction region design. Firstly, a design that has been optimised for high luminosity with an acceptance of 10° and secondly, a high acceptance design that allows for a smaller opening angle of the detector. In both cases the goal for the machine luminosity is in the range of $10^{33} \text{ cm}^{-2} \text{ s}^{-1}$ but the layouts differs in the magnet lattice, the achievable absolute luminosity and mainly the synchrotron radiation that is emitted during the beam separation process. Both options will be presented here in detail and the corresponding design luminosity, the technical requirements and the synchrotron radiation load will be compared. In both cases however, a well matched spot size of the electron and proton beam had to be established at the collision point: Experience in SPS and HERA [?], [?] showed that matched beam cross sections have to be established between the two colliding beams to guarantee stable beam conditions. Considering the different nature of the beams, namely the emittances of the electron beam in the two transverse planes, the interaction region design has to consider this boundary condition and the beam optics has to be established to achieve equal beam sizes $\sigma_x(p) = \sigma_x(e)$, $\sigma_y(p) = \sigma_y(e)$ at the IP.

The basic beam parameters however like energy, particle intensity and beam emittances are identical for both designs, determined by the electron and proton ring lattices and the pre-accelerators. They are summarised in Table 7.9.

Colliding two beams of different characteristics, the luminosity obtained is given by the equation

$$L = \sum_{i=1}^{n_b} (I_e * I_p) \frac{1}{e^2 f_0 2\pi \sqrt{\sigma_{xp}^2 + \sigma_{xe}^2} \sqrt{\sigma_{yp}^2 + \sigma_{ye}^2}}, \quad (7.8)$$

Table 7.9: Main parameters for e/p collisions.

Quantity	unit	e	p
Beam energy	GeV	60	7000
Total beam current	mA	100	860
Number of bunches		2808	2808
Particles/bunch N_b	10^{10}	2.0	17
Horiz. emittance	nm	5.0	0.5
Vert. emittance	nm	2.5	0.5
Bunch distance	ns	25	

where $\sigma_{x,y}$ denotes the beam size of the electron and proton beam in the horizontal and vertical plane and I_e, I_p the electron and proton single bunch currents. In all IR layouts the electron beam size at the IP is matched to the proton beam size in order to optimise the delivered luminosity and minimise detrimental beam beam effects.

The main difference of the IR design for the electron proton collisions with respect to the existing LHC interaction regions is the fact that the two beams of LHeC cannot be focussed and / or guided at the same time: The different nature of the two beams, the fact that the electrons emit synchrotron radiation and mainly the large difference in the particle momentum make a simultaneous focusing of the two beams impossible. The strong gradients of the proton quadrupoles in the LHC triplet structure cannot be tolerated nor compensated for the electron lattice and a stable optical solution for the electrons is not achievable under the influence of the proton magnet fields. The electron beam therefore has to be separated from the proton beam after the collision point before any strong “7 TeV like” magnet field is applied.

In order to obtain still a compact design and to optimize the achievable luminosity of the new e/p interaction region, the beam separation scheme has to be combined with the electron mini-beta focusing structure.

Figure 7.18 shows a schematic layout of the interaction region. It refers to the 10 degree option and shows a compact triplet structure that is used for early focusing of the electron beam. The electron mini beta quadrupoles are embedded into the detector opening angle and in order to obtain the required separation effect they are shifted in the horizontal plane and act effectively as combined function magnets: Thus focusing and separation of the electron beam are combined in a very compact lattice structure, which is the prerequisite to achieve luminosity values in the range of $10^{33} \text{ cm}^{-2} \text{ s}^{-1}$.

7.4.1 Beam Separation Scheme

The separation scheme of the two beams has to be optimised with respect to an efficient (i.e. fast) beam separation and a synchrotron radiation power and critical energy of the emitted photons that can be tolerated by the absorber design. Two main issues have to be accomplished: a sufficient horizontal distance between the beams has to be generated at the position of the first proton (half) quadrupole, located at a distance of $s = 22\text{m}$ from the interaction point (the nominal value of the LHC proton lattice). In addition to that, harmful beam beam effects have to be avoided at the first parasitic bunch encounters which will take place at $s = 3.75\text{m}$, as the

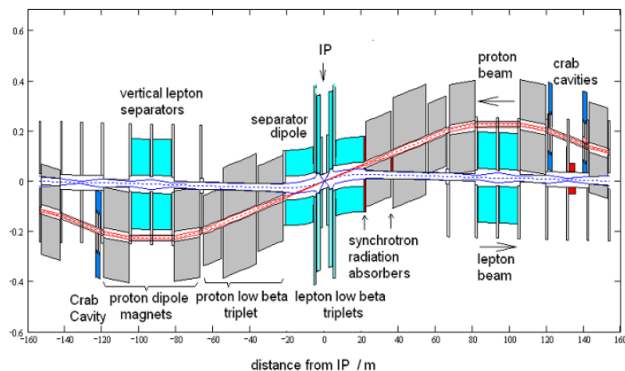


Figure 7.18: Schematic layout of the LHeC interaction region

4854 nominal bunch distance in LHC corresponds to $\Delta t = 25ns$. These so-called parasitic bunch
 4855 crossings have to be avoided as they would lead to intolerable beam-beam effects in the colliding
 4856 beams. As a consequence the separation scheme has to deliver a sufficiently large horizontal
 4857 distance between the two counter rotating bunches at these locations.

4858 To achieve the first requirement a separation effect is created inside the mini beta quadrupoles
 4859 of the electron beam: The large momentum difference of the two colliding beams provides a very
 4860 elegant way to separate the lepton and the hadron beams: Shifting the mini-beta quadrupoles
 4861 of the electron beam and installing a 15.8m long, but weak separator dipole magnet close to
 4862 the IP provides the gentle separation that is needed to keep the synchrotron radiation level in
 4863 the IR within reasonable limits.

4864 The nearest proton quadrupole to the IP is designed as a half-quadrupole to ease the extrac-
 4865 tion of the outgoing electron beam. At this location (at $s=22$ m) a minimum separation of
 4866 $\Delta x = 55mm$ is needed to guide the electron beam along the mirror plate of a sc. proton half
 4867 quadrupole [?]. A first layout of this magnet is sketched in figure 7.19

4868 The horizontal offsets of the mini beta lenses are chosen individually in such a way that
 4869 the resulting bending strength in the complete separation scheme (quadrupole triplet / doublet
 4870 and separator dipole) is constant. In this way a moderate separation strength is created with
 4871 a constant bending radius of $\rho = 6757m$ for the 10 degree option. In the case of the 1 degree
 4872 option the quadrupole lenses of the electron lattice cannot be included inside the detector de-
 4873 sign as the opening angle of the detector does not provide enough space for the hardware of
 4874 the electron ring lattice. Therefore a much larger distance between the IP and the location of
 4875 the first electron lens had to be chosen ($\Delta s = 6.2m$ instead of $\Delta s = 1.2m$). As a consequence
 4876 - in order to achieve the same overall beam separation - stronger magnetic separation fields
 4877 have to be applied resulting in a bending radius of $\rho = 4057m$ in this case. In both cases the
 4878 position of the electron quadrupoles is following the design orbit of the electron beam to avoid
 4879 local strong bending fields and keep the synchrotron radiation power to a minimum. This tech-
 4880 nique has already been succesfully applied at the layout of the HERA electron-proton collider [?].

4881

4882 Still the separation at the location of the first proton magnet is small and a half quadrupole
 4883 design for this super conducting magnet has been chosen at this point. The resulting beam

Ring-ring option half-quadrupole, 4900 A, Gradient 137 T/m,
+ 2.5 T dipole field from feeddown

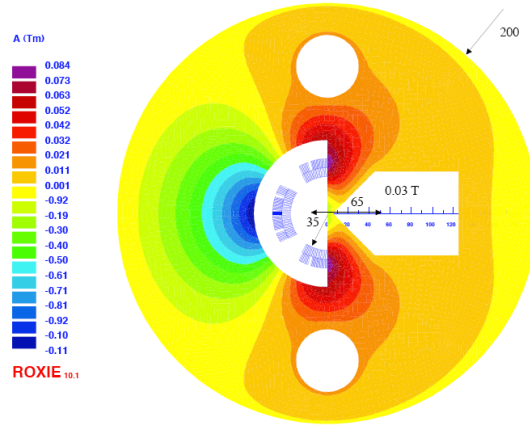


Figure 7.19: Super conducting half quadrupole in the proton lattice: The electron beam will pass on the right hand side of the mirror plate in a quasi field free region [?].

4884 parameters - including the expected luminosity for this ring ring option - are summarised in
4885 Table 2.

4886 It has to be pointed out in this context that the arrangement of the off centre quadrupoles as
4887 well as the strength of the separator dipole depend on the beam optics of the electron beam. The
4888 beam size at the parasitic crossings and at the proton quadrupole will determine the required
4889 horizontal distance between the electron and proton bunches. The strength and position of
4890 these magnets however will determine the optical parameters, including the dispersion function
4891 that is created during the separation process itself. Therefore a self-consistent layout concerning
4892 optics, beam separation and geometry of the synchrotron light absorbers has to be found.

4893 It is obvious that these boundary conditions have to be fulfilled not only during luminosity
4894 operation of the e/p rings. During injection and the complete acceleration procedure of the
4895 electron ring the influence of the electron quadrupoles on the proton beam has to be compen-
4896 sated with respect to the proton beam orbit (as a result of the separation fields) as well as to
4897 the proton beam optics: The changing deflecting fields and gradients of the electron magnets
4898 will require correction procedures in the proton lattice that will compensate this influence at
4899 any moment.

4900 7.4.2 Crossing Angle

4901 A central aspect of the LHeC IR design is the beam-beam interaction of the colliding electron
4902 and proton bunches. The bunch structure of the electron beam will match the pattern of the
4903 LHC proton filling scheme for maximal luminosity, giving equal bunch spacings of 25 ns to
4904 both beams. The IR design therefore is required to separate the bunches as quickly as possible
4905 to avoid additional bunch interactions at these positions and limit the beam-beam effect to
4906 the desired interactions at the IP. The design bunch distance in the LHC proton bunch chain
4907 corresponds to $\Delta t = 25$ ns or $\Delta s = 7.5$ m. The counter rotating bunches therefore meet after the

Table 7.10: Parameters of the mini beta optics for the 1° and 10° options of the LHeC Interaction Region.

Detector Option Quantity	unit	1°		10°	
		electrons	protons	electrons	protons
Number of bunches		2808			
Particles/bunch N_b	10^{10}	1.96	17	1.96	17
Horiz. beta-function	m	0.4	4.0	0.18	1.8
Vert. beta-function	m	0.2	1.0	0.1	0.5
Horiz. emittance	nm	5.0	0.5	5.0	0.5
Vert. emittance	nm	2.5	0.5	2.5	0.5
Distance to IP	m	6.2	22	1.2	22
Crossing angle	mrad	1.0		1.0	
Synch. Rad. in IR	kW	51		33	
absolute Luminosity	$\text{m}^{-2} \text{s}^{-1}$	$8.54 * 10^{32}$		$1.8 * 10^{33}$	
Loss-Factor S		0.86		0.75	
effective Luminosity	$\text{m}^{-2} \text{s}^{-1}$	$7.33 * 10^{32}$		$1.34 * 10^{33}$	

crossing at the interaction point at additional, parasitic collision points in a distance $s = 3.75$ m from the IP. To avoid detrimental effects from these parasitic crossings the above mentioned separation scheme has to be supported by a crossing angle that will deliver a sufficiently large horizontal distance between the bunches at the first parasitic bunch crossings. This technique is used in all LHC interaction points. In the case of the LHeC however, the crossing angle is determined by the emittance of the electron beam and the resulting beam size which is considerably larger than the usual proton beam size in the storage ring. In the case of the LHeC IR a crossing angle of $\theta = 1\text{mrad}$ is considered as sufficient in the 1° as well as in the 10° option to avoid beam-beam effects from this parasitic crossings. Figure 7.20 shows the position of the first possible parasitic encounters and the effect of the crossing angle to deliver a sufficient separation at these places.

The detailed impact of one beam on another is evaluated by a dedicated beam-beam interaction study which is included in this report, based on a minimum separation of $5\sigma_e + 5\sigma_p$ at every parasitic crossing node. Due to the larger electron emittance the separation is mainly dominated by the electron beam parameters, and as a general rule it can be stated that the rapid growth of the β -function in the drift around the IP,

$$\beta(s) = \beta^* + \frac{s^2}{\beta^*}, \quad (7.9)$$

makes it harder to separate the beams if small β^* and a large drift space s is required in the optical design.

In any design for the LHeC study, a crossing angle is used to establish an early beam separation, reduce the required strength in the separation magnets and minimise the synchrotron radiation power that is created inside the interaction region.

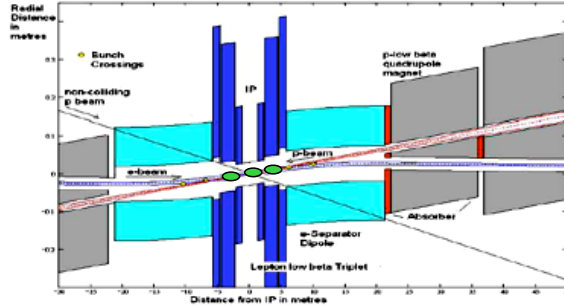


Figure 7.20: LHeC interaction region including the location of the first parasitic bunch encounters where a sufficient beam separation is achieved by a crossing angle of 1 mrad. The location of the parasitic encounters is indicated by green ovals.

4929 As a draw back however the luminosity is reduced due to the fact that the bunches will
 4930 not collide anymore head on. This reduction is expressed in a geometric luminosity reduction
 4931 factor “S”, that depends on the crossing angle θ , the length of the electron and proton bunches
 4932 σ_{ze} and σ_{zp} and the transverse beam size in the plane of the bunch crossing σ_x^* :

$$S(\theta) = \left[1 + \left(\frac{\sigma_{sp}^2 + \sigma_{se}^2}{2\sigma_x^{*2}} \right) \tan^2 \frac{\theta}{2} \right]^{-\frac{1}{2}} . \quad (7.10)$$

4933

4934

4935 Accordingly, the effective luminosity that can be expected for a given IR layout is obtained
 4936 by

$$L = S(\theta) * L_0 \quad (7.11)$$

4937

4938

4939 For the two beam optics that have been chosen for this design study (the 1° and the 10°
 4940 option) and a crossing angle of $\theta = 1\text{mrad}$ the loss factor amounts to $S = 74\%$ and $S = 85\%$
 4941 respectively.

4942 7.4.3 Beam Optics and Luminosity

4943 A special boundary condition had to be observed in the design of the proton beam optics of the
 4944 LHeC: For the layout of the four present proton-proton interaction regions in the LHC machine
 4945 an anti-symmetric option had been chosen: A solution that is appropriate for a round beam
 4946 optics ($\sigma_x^* = \sigma_y^*$). An optimised design for collisions with the flat e^\pm beams however requires
 4947 unequal β -functions for the hadron beam at the IP and the existing LHC optics can no longer
 4948 be maintained. Therefore the optical layout of the existing triplet structure in the LHC had
 4949 to be modified to match the required beta functions ($\beta_x = 1.8\text{m}$, $\beta_y = 0.5\text{m}$) at the IP to the
 4950 regular optics of the FODO structure in the arc (Figure 7.21).

4951 In the case of the electron beam optics, two different layouts of the interaction region are
 4952 considered: One optical concept for highest achievable luminosity and a solution for maximum

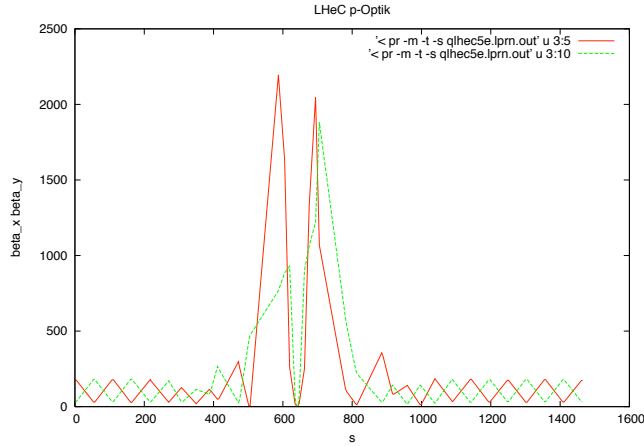


Figure 7.21: Proton optics for the LHeC interaction region. The gradients of the antisymmetric triplet lattice in the standard LHC have been modified to adopt for the requirements of the LHeC flat beam parameters.

4953 detector acceptance. In the first case an opening angle of 10° is available inside the detector ge-
 4954 ometry and allows to install an embedded magnet structure where the first electron quadrupole
 4955 lenses can be placed as close as $s = 1.2\text{m}$ from the IP. This early focusing scheme leads to
 4956 moderate values of the β function inside the mini beta quadrupoles and therefore allows for
 4957 a smaller spot size at the IP and larger luminosity values can be achieved. Still however the
 4958 quadrupoles require a compact design: While the gradients required by the optical solution are
 4959 small (for a super conducting magnet design) the outer radius of the first electron quadrupole
 4960 has been limited to $r_{max} = 210\text{mm}$.

4961 In the case of the 1° option the detector design is optimised for largest detector acceptance.
 4962 Accordingly the opening angle of the detector hardware is too small to deliver space for accelera-
 4963 tor magnets. The mini beta quadrupoles therefore have to be located outside the detector, and
 4964 a distance $s = 6\text{m}$ from the IP had to be chosen in this case. Even if the magnet dimensions
 4965 are not limited by the detector design in this case, the achievable luminosity is about a factor
 4966 of two smaller than in the 10° case.

4967 The two beam optics that are based on these considerations are discussed in detail in the next
 4968 chapter of this report. In the case of the 10° option a triplet structure has been chosen to allow
 4969 for moderate values of the beta functions inside the mini beta quadrupoles. As a special feature
 4970 of the optics that is shown in Figure 7.22 the focusing effect of the first quadrupole magnet is
 4971 moderate: Its gradient has been limited as it has to deliver mainly the first beam separation.
 4972 Table 7.10 includes as well the overall synchrotron radiation power that is produced inside the
 4973 IR. Due to the larger bending radius (i.e. smaller bending forces) in the case of the 10° option
 4974 the produced synchrotron radiation power is limited to about 30 kW, while the alternative -
 4975 high acceptance - option has to handle 50kW of synchrotron light.

4976 The details of the synchrotron light characteristics are covered in the next chapters of this

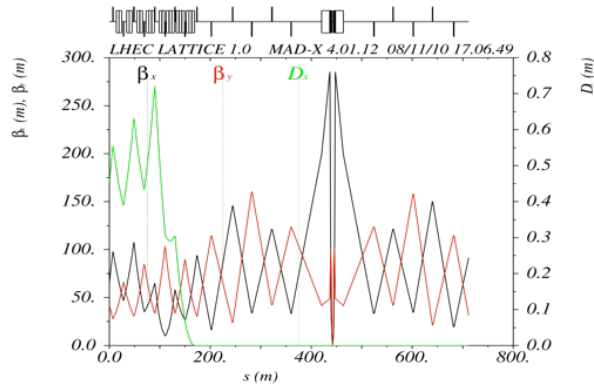


Figure 7.22: Electron optics for the LHeC interaction region. The plot corresponds to the 10 degree option where a triplet structure combined with a separation dipole has been chosen to separate the two beams.

4977 report for both cases, including the critical energies and the design of the required absorbers.
 4978 For the 1° option the mini beta focusing is based on a quadrupole doublet as the space
 4979 limitations in the transverse plane are much more relaxed compared to the alternative option
 4980 and the main issue here was to find a compact design in the longitudinal coordinate: Due to the
 4981 larger distance of the focusing and separating magnets from the IP the magnet structure has
 4982 to be more compact and the separating field stronger to obtain the required horizontal beam
 4983 distance at the location $s=22\text{m}$ of the first proton quadrupole. The corresponding beam optics
 4984 for both options are explained in full detail below.
 4985 in the 1991 Luminosity Runs of

4986 7.5 Design Requirements of the Electron Beam Optics

4987 7.5.1 Optics Matching and IR Geometry

4988 Once the beams are separated into independent beam pipes, the electron beam must be trans-
 4989 ported into the ring lattice. Quadrupoles are used in the electron machine LSS to transport the
 4990 beam from the IP to the dispersion suppressor and match twiss parameters at either end. This
 4991 matching must be smooth and not require infeasible apertures. In addition the first electron
 4992 quadrupoles will be located inside the detector hardware and therefore a compact design is
 4993 required within the limited space available.

4994 The complete design of the long straight section "LSS", that includes the mini beta inser-
 4995 tion, the matching section and the dispersion suppressor must be designed around a number
 4996 of further constraints. As well as beam separation, the electron beam must be steered from
 4997 the electron ring into the IR and back out again. The colliding proton beam must be largely
 4998 undisturbed by the electron beam. The non-colliding proton beam must be guided through the
 4999

5000 IR without interacting with either of the other beams.

5001 7.6 High Luminosity IR Layout

5002 7.6.1 Parameters

5003 Table 7.11 details the interaction point parameters and other parameters for this design. To
5004 optimise for luminosity, a small l^* is desired. An acceptance angle of 10° is therefore chosen,
5005 which gives an l^* of 1.2m for final focusing quadrupoles of reasonable size.

$L(0)$	1.8×10^{33}
θ	1×10^{-3}
$S(\theta)$	0.746
$L(\theta)$	1.34×10^{33}
β_x^*	0.18 m
β_y^*	0.1 m
σ_x^*	3.00×10^{-5} m
σ_y^*	1.58×10^{-5} m
SR Power	33 kW
E_c	126 keV

Table 7.11: Parameters for the High Luminosity IR.

5006 SR calculations are detailed in section [NATHAN]. The total power emitted in the IR is similar
5007 to that in the HERA-2 IR [reference] and as such appears to be reasonable, given enough space
5008 for absorbers.

5009 7.6.2 Layout

5010 Due to the relatively round beam spot aspect ratio of 1.8:1, a final quadrupole triplet layout
5011 has been chosen for this design. The relatively weak horizontal focussing quadrupole used as
5012 first magnet lens is mainly needed for beam separation, followed by two strong, nearly doublet
5013 like quadrupoles. The focusing strength Figure 7.23 and table 7.12 detail the layout.

5014
5015 The l^* of 1.2 m allows both strong focusing of the beam, and constant bending of the beam
5016 from 1.2 m to 21.5 m. This is achieved with offset quadrupoles and a separation dipole.

5017
5018 Figure 7.24 shows the β functions of the beam in both planes from the IP to the face of
5019 the final proton quadrupole at $s = 23$ m.

5020 7.6.3 Separation Scheme

5021 As described above a quadrupole triplet configuration is used for the first focusing of the elec-
5022 tron beam. This has the effect of generating a larger peak in β_x , between parasitic crossings but
5023 leads to smaller horizontal beam sizes at these locations and therefore reduces the necessary

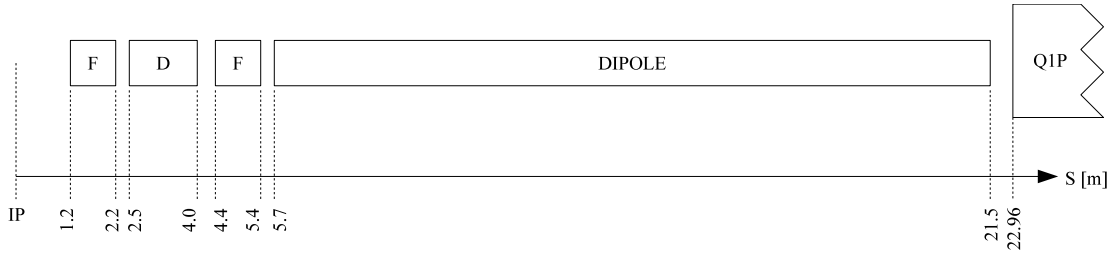


Figure 7.23: Layout of machine elements in the High Luminosity IR. Note that the left side of the IR is symmetric.

Element	S_{entry} [m]	L [m]	Gradient [T/m]	Dipole Field [T]	Offset [m]
BS.L	-21.5	15.8	-	-0.0296	-
Q3E.L	-5.4	1.0	89.09228878	-0.0296	-3.32240×10^{-4}
Q2E.L	-4	1.5	-102.2013150	-0.0296	2.89624×10^{-4}
Q1E.L	-2.2	1.0	54.34070578	-0.0296	-5.44711×10^{-4}
IP	0.0	-	-	-	-
Q1E.R	1.2	1.0	54.34070578	0.0296	5.44711×10^{-4}
Q2E.R	2.5	1.5	-102.2013150	0.0296	-2.89624×10^{-4}
Q3E.R	4.4	1.0	89.09228878	0.0296	3.32240×10^{-4}
BS.R	5.7	15.8	-	-0.0296	-

Table 7.12: Machine elements for the High Luminosity IR. S_{entry} gives the leftmost point of the idealised magnetic field of an element. Note that S is relative to the IP.

5024 beam separation. The first F quadrupole reduces β_x at $s = 3.75$ m compared to an initial D
 5025 quadrupole. The third F quadrupole then brings β_x down from the peak sufficiently to avoid
 5026 large beam-beam interactions at the second parasitic crossing, $s = 7.5$ m.

5027

5028 This is provided by the bending effect of the offset quadrupoles, and also the IP crossing
 5029 angle of 1 mrad. These elements ensure that the separation between the beams, normalised to
 5030 beam size, increases at each parasitic crossing. Note that 1 mrad is not a minimum crossing
 5031 angle required by beam-beam interaction separation criteria; it is however a chosen balance
 5032 between luminosity loss and minimising bend strength. In theory, this layout could support an
 5033 IP with no crossing angle; however the bend strength required to achieve this would generate
 5034 an undesirable level of SR power.

5035 7.6.4 Optics Matching and IR Geometry

5036 The IR is matched into the ring arc lattice by means of matching quads in the LSS. The quads
 5037 are roughly evenly placed, with sufficient space left after the IR section to accommodate the
 5038 proton optics and the remaining electron ring geometry, which has yet to be designed fully. The
 5039 solution is nearly symmetric about the IP; however due to the geometry of the LHC lattice,

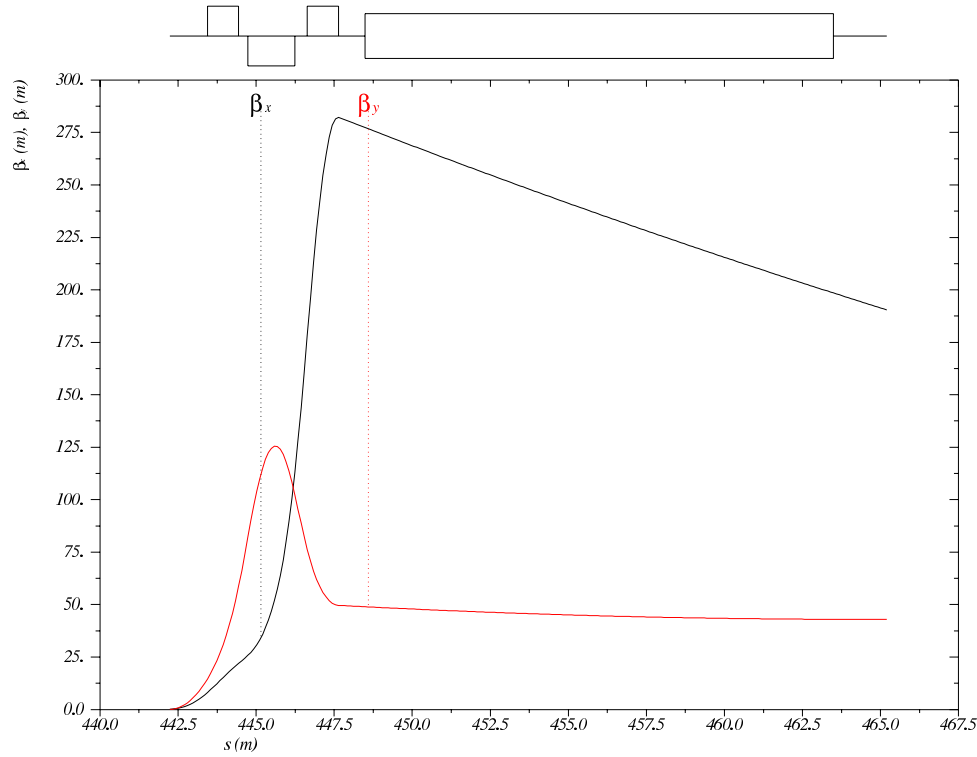


Figure 7.24: β functions in both planes for the High Luminosity IR layout, from the IP to the face of the final proton quadrupole at $s = 23$ m. Note that s is relative to the ring, which begins at the left side of the left dispersion suppressor of IP2.

5040 the electron ring itself is not exactly symmetric. As such the solution differs slightly on either
 5041 side of the LSS. Table 7.13 details the layout of machine elements in the LSS. Five matching
 5042 quadrupoles are used on either side of the IP. A sixth quadrupole is used on the left side, next
 5043 to the dispersion suppressor. Due to the asymmetric design of the dispersion suppressors, a
 5044 quadrupole (MQDSF.L2) is included at the same distance from the IP on the right side as
 5045 part of the dispersion suppressor. MQDSF.L2 is required to match the optics, but is more
 5046 constrained than the other matching quadrupoles. Figure 7.25 shows the β functions of the
 5047 matching from the IP to the dispersion suppressor, on both sides of the IP (Figure 7.26)

5048

5049 A smooth matching is obtained, where the maximum beta functions are well controlled and
 5050 continuously reduced to the values of the arc structure. The beam envelopes in the LSS are of

Element	S_{entry} [m]	L [m]	Gradient [T/m]
MQDSF.L2	-268.8944	1.0	9.611358758
MQDM5.L2	-240.5	1.0	-7.435432612
MQFM4.L2	-198.5	1.0	7.148957108
MQDM3.L2	-160.5	1.0	-6.493088294
MQFM2.L2	-120.5	1.0	6.057685328
MQDM1.L2	-82.5	1.0	-4.962254798
MQDM1.R2	81.5	1.0	-4.977379112
MQFM2.R2	119.5	1.0	6.030944724
MQDM3.R2	159.5	1.0	-6.63145508
MQFM4.R2	197.5	1.0	6.884472924
MQDM5.R2	239.5	1.0	-7.439587356

Table 7.13: Machine elements for the High Luminosity LSS layout. S_{entry} gives the leftmost point of the idealised magnetic field of an element. Note that S is relative to the IP.

5051 reasonable size and do not require excessive aperture.

5052

5053 Note that this solution is not yet matched for dispersion as the rest of the ring geometry
5054 in the LSS and IR areas is yet to be designed.

5055 Plans for the remaining IR geometry include a second horizontal dipole, and quadrupoles, on
5056 either side to turn each separation dipole into a dispersion-free S-shaped bend. This will be
5057 used to extract the beam into the electron machine.

5058 7.7 High Acceptance IR Layout

5059 7.7.1 Parameters

5060 Table 7.14 details the design parameters for this option. The chosen detector opening angle
5061 for this layout is 1° . All elements, especially the mini beta quadrupoles of the electron ring,
5062 therefore have to be placed outside the limits of the detector, at $z = \pm 6.2\text{m}$, where z the is
5063 longitudinal axis of the detector. As such, the actual acceptance of the layout is limited by the
5064 beam pipe rather than the size of machine elements. This also gives further flexibility in the
5065 strengths and designs of the final focusing quadrupoles, although this flexibility is not exploited
5066 in the design.

5067

5068 SR calculations are discussed in detail in section [NATHAN]. The total power emitted in the
5069 IR is similar to that in the HERA-2 IR [reference] and as such appears to be reasonable, given
5070 enough space for absorbers. However it is significantly higher than that in the high luminosity
5071 layout. As discussed in section [NATHAN], an option exists to reduce the total SR power by
5072 including a dipole field in the detector, thus mitigating the limitation imposed on dipole length
5073 by the larger l^* .

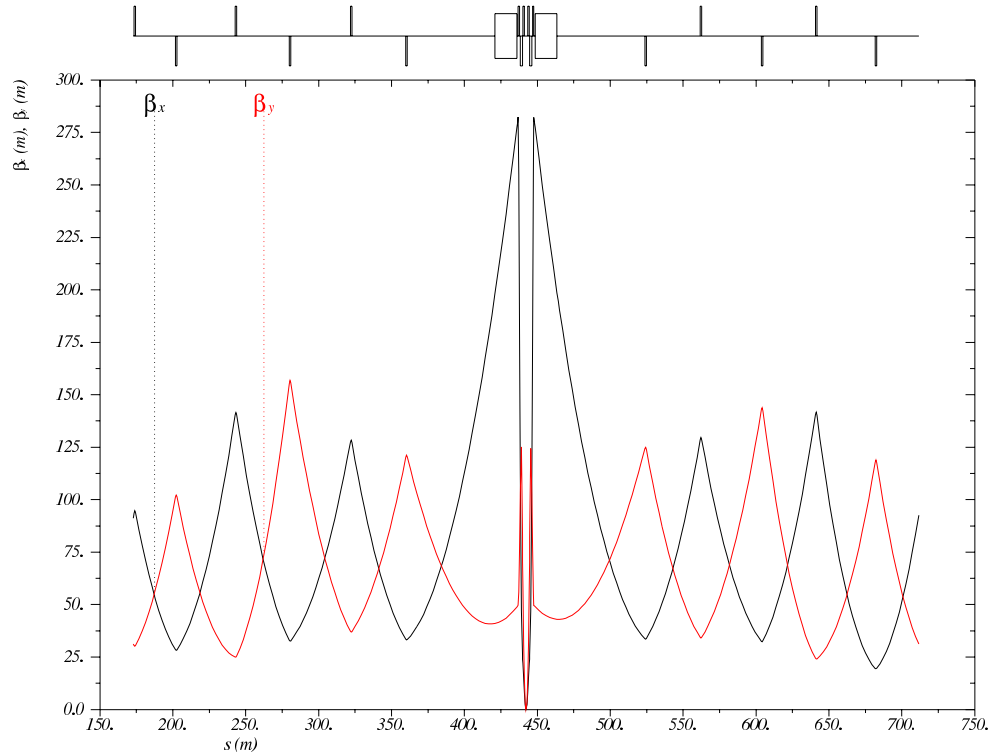


Figure 7.25: β functions in both planes for the High Luminosity IR layout, from the end of the left dispersion suppressor to the start of the right dispersion suppressor. Note that s is relative to the ring, which begins at the left side of the left dispersion suppressor of IP2.

5074 7.7.2 Layout and separation scheme

5075 A symmetric final quadrupole doublet layout has been chosen for this design. The beam spot
 5076 aspect ratio of 2:1 is marginally flatter than the High Luminosity layout, and as such a triplet
 5077 is less suitable. Figure 7.28 and table 7.15 detail the layout.

5078
 5079 The l^* of 6.2m imposes limitations on focusing and bending in this layout. Focusing is limited
 5080 by quadratic β growth through a drift space, which is increased for smaller β^* . As such, lower
 5081 instantaneous luminosity is attainable.

5082
 5083 As in the high luminosity option the beam separation will be achieved by a combination of
 5084 a adequate crossing angle and the separation fields of off-centre quadrupole magnets. However,

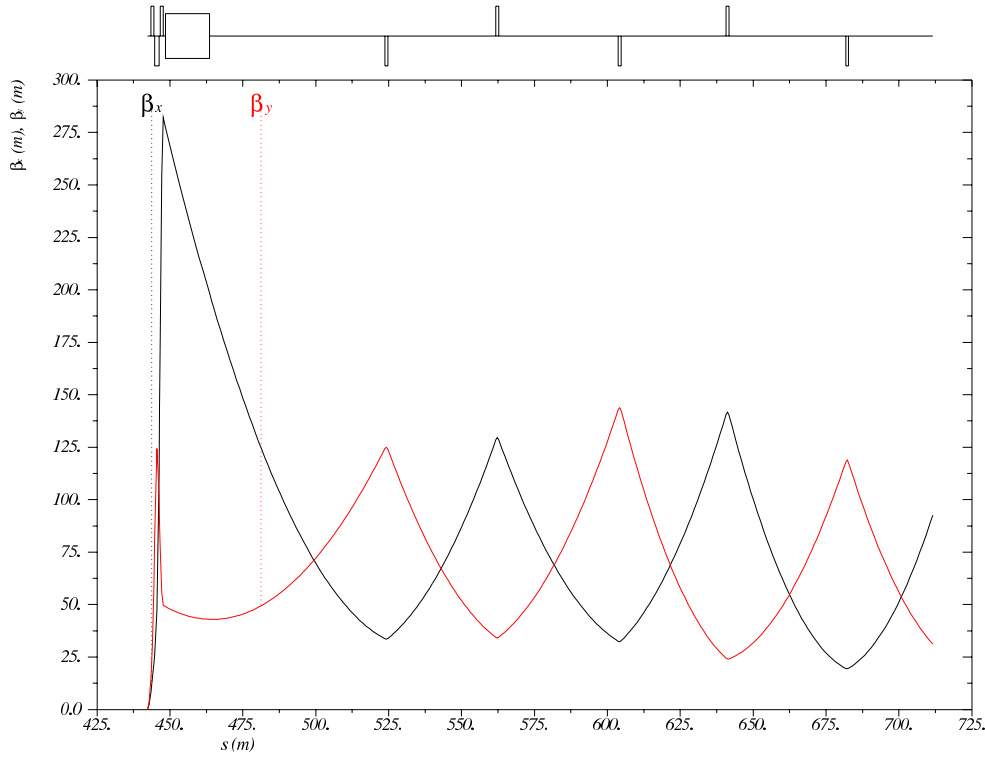


Figure 7.26: β functions in both planes for the High Luminosity IR layout, from the IP to the start of the right dispersion suppressor. Note that s is relative to the ring, which begins at the left side of the left dispersion suppressor of IP2.

5085 due to the large free space of $z=6\text{m}$ to the IP, stronger fields have to be applied to obtain the
 5086 same geometric separation at the first proton quadrupole.

5087 Figure 7.29 shows the β functions of the beam in both planes from the IP to the face of the
 5088 final proton quadrupole at $s = 23$ m.

5089 7.7.3 Optics Matching and IR Geometry

5090 The lattice that is used to match the IR optics to the periodic arc structure corresponds to
 5091 a large extent to the one presented for the high luminosity option. Figure 7.30 shows the β
 5092 functions of the matching from the IP to the dispersion suppressor, on both sides of the IP
 5093 (Figure 7.31).

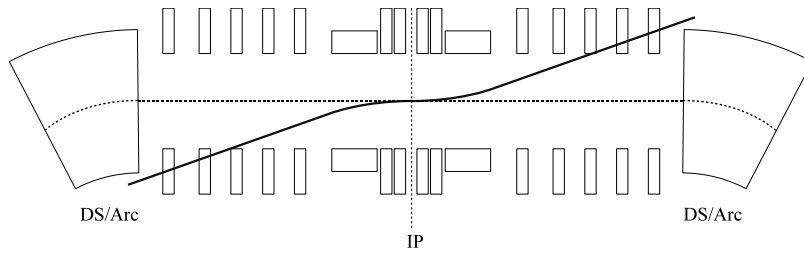


Figure 7.27: Graphical representation of misaligned LSS/IR geometry. With beam steering in the IR and no compensation in the LSS, the electron beam no longer lines up with the ring lattice reference orbit. Diagram is not to scale and does not represent the correct optical layout of the IR nor the LSS.

$L(0)$	8.54×10^{32}
θ	1×10^{-3}
$S(\theta)$	0.858
$L(\theta)$	7.33×10^{32}
β_x^*	0.4 m
β_y^*	0.2 m
σ_x^*	4.47×10^{-5} m
σ_y^*	2.24×10^{-5} m
SR Power	51 kW
E_c	163 keV

Table 7.14: Parameters for the High Acceptance IR.

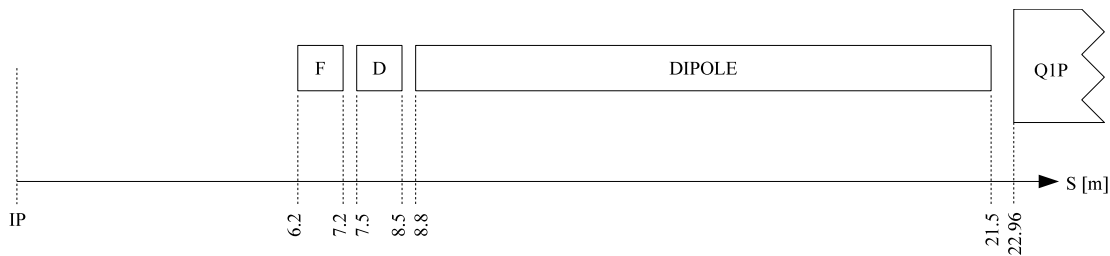


Figure 7.28: Layout of machine elements in the High Acceptance IR. Note that the left side of the IR is symmetric.

5094

5095 As with the High Luminosity layout, a smooth matching is obtained, with the IR β peaks being
 5096 brought down and controlled before being matched into the arc solution. The beam envelopes
 5097 in the LSS are of reasonable size and do not require excessive aperture.

5098

Element	S_{entry} [m]	L [m]	Gradient [T/m]	Dipole Field [T]	Offset [m]
BS.L	-21.5	12.7	-	-0.0493	-
Q2E.L	-8.5	1.0	-77.31019000	-0.0493	6.37691×10^{-4}
Q1E.L	-7.2	1.0	90.40354154	-0.0493	-5.45333×10^{-4}
IP	0.0	-	-	-	-
Q1E.R	6.2	1.0	90.40354154	0.0493	5.45333×10^{-4}
Q2E.R	7.5	1.0	-77.31019000	0.0493	-6.37691×10^{-4}
BS.R	8.8	12.7	-	0.0493	-

Table 7.15: Machine elements for the High Acceptance IR. S_{entry} gives the leftmost point of the idealised magnetic field of an element. Note that S is relative to the IP.

5099 Other geometric issues must again be addressed, which are briefly discussed in section 7.6.4.

5100 7.7.4 Comparison of Layouts

5101 Table 7.17 shows a direct comparison of various parameters of the two layouts.

5102

5103 The difference in luminosity after considering the loss factor S due to the crossing angle, is a
5104 factor of 1.8. However it should be noted that this design strives for technical feasibility and
5105 both layouts could be squeezed further to decrease β^* in both planes. The High Luminosity
5106 layout could likely be squeezed further than the High Acceptance layout due to the large dif-
5107 ference in l^* , as shown in figure 7.32 which compares the two IR layouts. At this stage both
5108 designs deliver their required IP parameters of luminosity and acceptance and appear to be
5109 feasible.

5110

5111 The High Acceptance design generates a higher level of SR power. This still appears to be
5112 within reasonable limits and is discussed in section [NATHAN]. Furthermore, an option is
5113 discussed to install a dipole magnet in the detector. This early separation would reduce the
5114 required strength of the dipole fields in the IR, significantly reducing total SR power.

5115 Synchrotron radiation and absorbers

5116 The synchrotron radiation (SR) in the interaction region has been analyzed in three ways.
5117 The SR was simulated in depth using a program made with the Geant4 (G4) toolkit. In addition
5118 a cross check of the total power and average critical energy was done in IRSYN, a Monte Carlo
5119 simulation package written by R. Appleby. [535] A final cross check has been made for the
5120 radiated power per element using an analytic method. These other methods confirmed the
5121 results seen using G4. The G4 program uses Monte Carlo methods to create gaussian spatial
5122 and angular distributions for the electron beam. The electron beam is then guided through
5123 vacuum volumes that contain the magnetic fields for the separator dipoles and electron final
5124 focusing quadrupoles.

5125 The SR is generated in these volumes using the appropriate G4 process classes. The G4
5126 SR class was written for a uniform magnetic field, and therefore the quadrupole volumes were
5127 divided such that the field remained approximately constant in each volume. This created

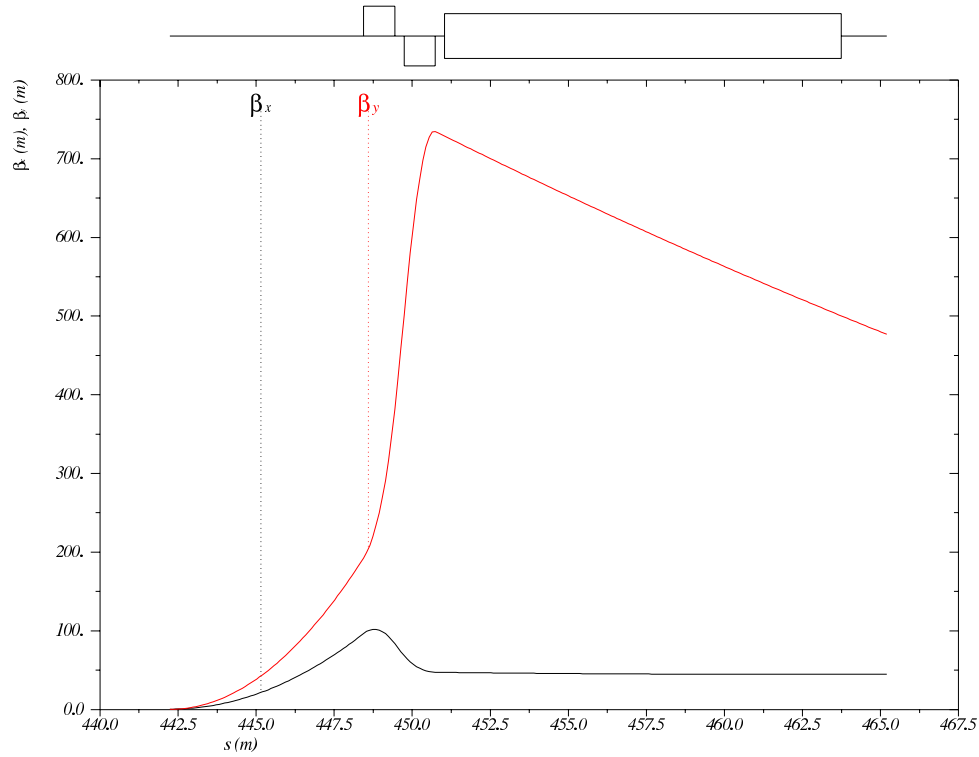


Figure 7.29: β functions in both planes for the High Acceptance IR layout, from the IP to the face of the final proton quadrupole at $s = 23$ m. Note that s is relative to the ring, which begins at the left side of the left dispersion suppressor of IP2.

5128 agreement between upstream and downstream quadrupoles since for a downstream quadrupole
 5129 the beta function at the entrance and exit are reversed from its upstream counterpart. This
 5130 agreement confirms that the field was approximately constant in each volume.

5131 The position, direction, and energy of each photon created is written as ntuples at user
 5132 defined Z values. These ntuples are then used to analyze the SR fan as it evolves in Z . The
 5133 analysis was done primarily through the use of MATLAB scripts. It was necessary to make
 5134 two versions of this program. One for the high luminosity design and one for the high detector
 5135 acceptance design.

5136 Before going further I will explain some conventions used for this section. I will refer to the
 5137 electron beam as *the beam* and the proton beams will be referred to as either the interacting
 5138 or non interacting proton beams. The beam propagates in the $-Z$ direction and the interacting

Element	S_{entry} [m]	L [m]	Gradient [T/m]
MQDSF.L2	-268.8944	1.0	9.643324144
MQFM6.L2	-237.5	1.0	-7.513288936
MQDM5.L2	-205.5	1.0	7.74537173
MQFM4.L2	-174.5	1.0	-6.18152704
MQDM3.L2	-143.5	1.0	6.475404012
MQFM2.L2	-111.5	1.0	-9.254556824
MQDM1.L2	-80.5	1.0	5.843405232
MQDM1.R2	79.5	1.0	5.843405232
MQFM2.R2	110.5	1.0	-9.254556824
MQDM3.R2	142.5	1.0	6.475404012
MQFM4.R2	173.5	1.0	-6.048380018
MQDM5.R2	204.5	1.0	7.360488416
MQFM6.R2	236.5	1.0	-7.225547436

Table 7.16: Machine elements for the High Acceptance LSS layout. S_{entry} gives the leftmost point of the idealised magnetic field of an element. Note that S is relative to the IP.

Parameter	HL	HA
$L(0)$	1.8×10^{33}	8.54×10^{32}
θ	1×10^{-3}	1×10^{-3}
$S(\theta)$	0.746	0.858
$L(\theta)$	1.34×10^{33}	7.33×10^{32}
β_x^*	0.18 m	0.4 m
β_y^*	0.1 m	0.2 m
σ_x^*	3.00×10^{-5} m	4.47×10^{-5} m
σ_y^*	1.58×10^{-5} m	2.24×10^{-5} m
SR Power	33 kW	51 kW
E_c	126 keV	163 keV

Table 7.17: Parameters for the High Luminosity IR.

5139 proton beam propagates in the +Z direction, I will use a right handed coordinate system where
5140 the X axis is horizontal and the Y axis is vertical. The beam centroid always remains in the
5141 $Y = 0$ plane. The *angle of the beam* will be used to refer to the angle between the beam
5142 centroid's velocity vector and the Z axis, in the $Y = 0$ plane. This angle is set such that the
5143 beam propagates in the -X direction as it traverses Z.

5144 The SR fans extension in the horizontal direction is driven by the angle of the beam at the
5145 entrance of the upstream separator dipole. Because the direction of emitted photons is parallel
5146 to the direction of the electron that emitted it, the angle of the beam and the distance to the
5147 absorber are both greatest at the entrance of the upstream separator dipole and therefore this

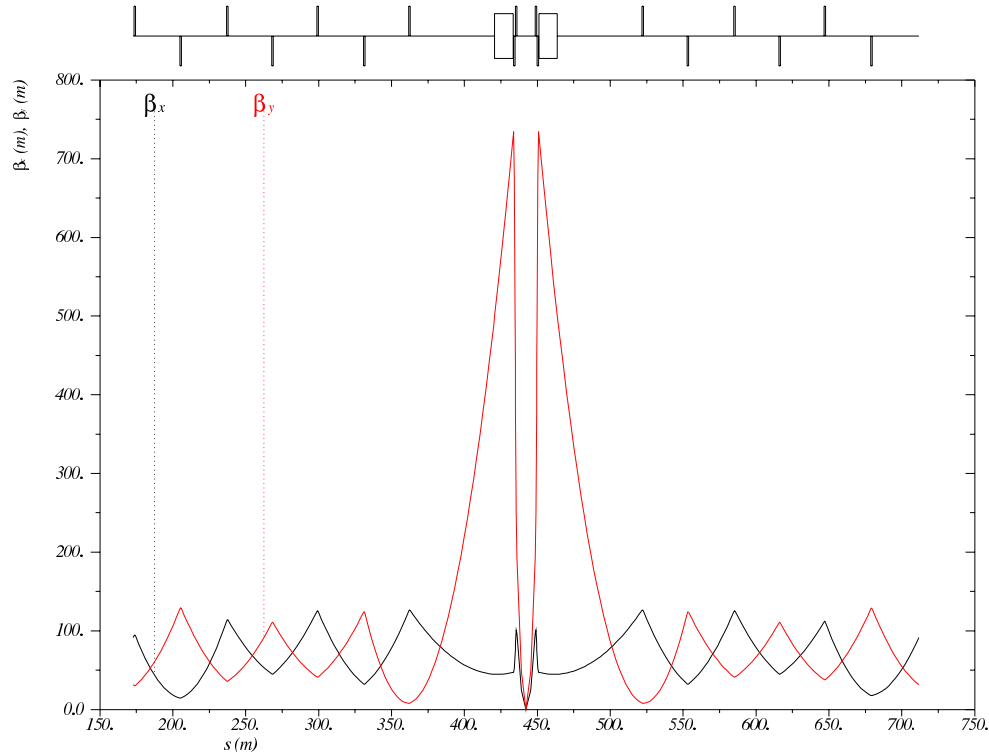


Figure 7.30: β functions in both planes for the High Acceptance IR layout, from the end of the left dispersion suppressor to the start of the right dispersion suppressor. Note that s is relative to the ring, which begins at the left side of the left dispersion suppressor of IP2.

5148 defines one of the edges of the synchrotron fan on the absorber. The other edge is defined by
 5149 the crossing angle and the distance from the IP to the absorber. The S shaped trajectory of
 5150 the beam means that the smallest angle of the beam will be reached at the IP. Therefore the
 5151 photons emitted at this point will have the lowest angle and for this given angle the smallest
 5152 distance to the absorber. This defines the other edge of the fan in the horizontal direction.

5153 The SR fans extension in the vertical direction is driven by the beta function and angular
 5154 spread of the beam. The beta function along with the emittance defines the r.m.s. spot size
 5155 of the beam. The vertical spot size defines the Y position at which photons are emitted. On
 5156 top of this the vertical angular spread defines the angle between the velocity vector of these
 5157 photons and the Z axis. Both of these values produce complicated effects as they are functions
 5158 of Z. These effects also affect the horizontal extension of the fan however are of second order

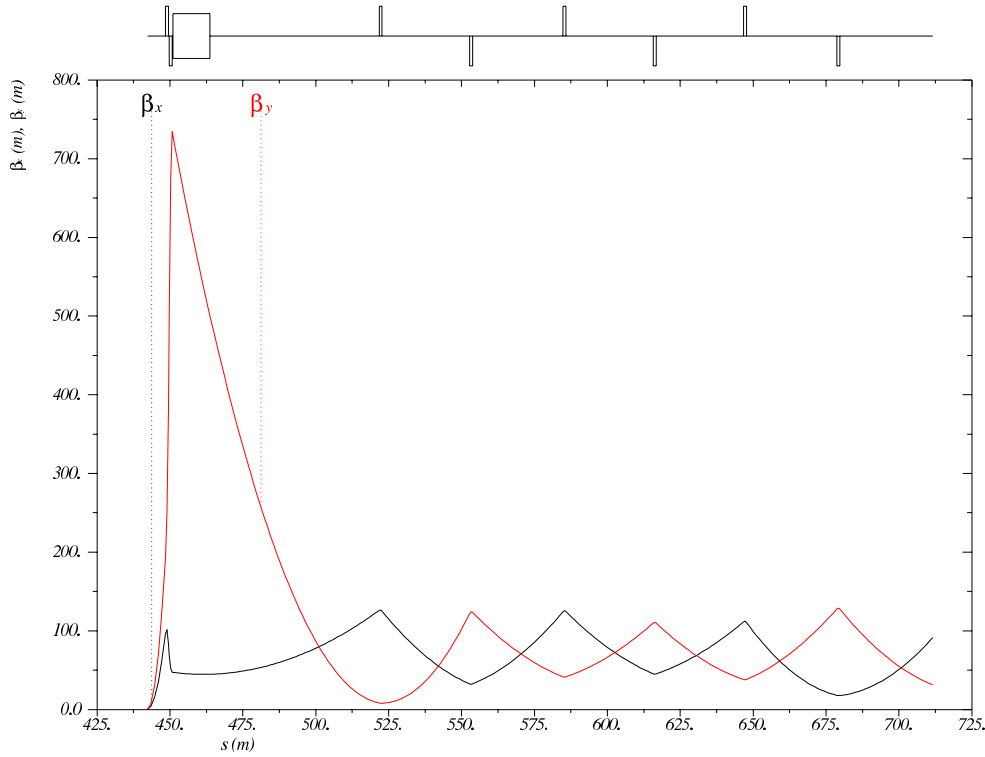


Figure 7.31: β functions in both planes for the High Luminosity IR layout, from the IP to the start of the right dispersion suppressor. Note that s is relative to the ring, which begins at the left side of the left dispersion suppressor of IP2.

5159 when compared to the angle of the beam. Since the beam moves in the $Y = 0$ plane these
 5160 effects dominate the vertical extension of the beam.

5161 The number density distribution of the fan is a complicated issue. The number density at
 5162 the absorber is highest between the interacting beams. The reason for this is that although the
 5163 separator dipoles create significantly more photons the number of photons generated per unit
 5164 length in Z is much lower for the dipoles as opposed to the quadrupoles due to the high fields
 5165 experienced in the quadrupoles. The position of the quadrupole magnets then causes the light
 5166 radiated from them to hit the absorber in the area between the two interacting beams.

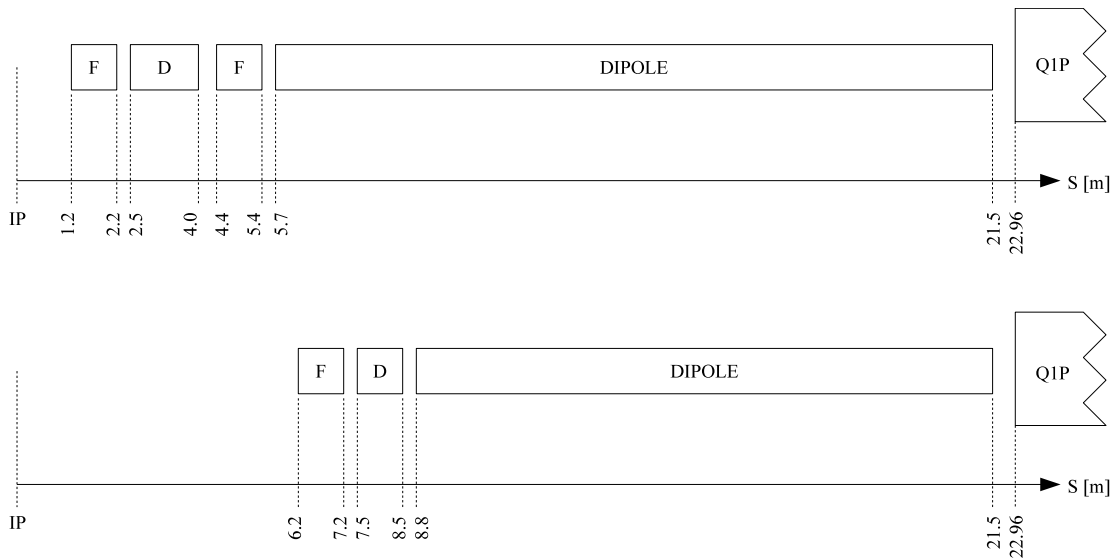


Figure 7.32: Scale comparison of the layouts for the High Luminosity and High Acceptance designs. Note the large difference in l^* .

5167 **High Luminosity**

5168 **Parameters:** The parameters for the high luminosity option are listed in Table 7.18. The
 5169 separation refers to the displacement between the two interacting beams at the face of the
 5170 proton triplet.

Characteristic	Value
Electron Energy [GeV]	60
Electron Current [mA]	100
Crossing Angle [mrad]	1
Absorber Position [m]	-21.5
Dipole Field [T]	0.0296
Separation [mm]	55
γ/s	5.39×10^{18}

Table 7.18: High Luminosity: Parameters

5171 The energy, current, and crossing angle (θ_c) are common values used in all RR calculations.
 5172 The dipole field value refers to the constant dipole field created throughout all dipole elements
 5173 in the IR. The direction of this field is opposite on either side of the IP. The quadrupole elements
 5174 have an effective dipole field created by placing the quadrupole off axis, which is the same as this
 5175 constant dipole field. The field is chosen such that 55 mm of separation is reached by the face of
 5176 the proton triplet. This separation was chosen based on S. Russenschuck's SC quadrupole design

5177 for the proton final focusing triplet. [536] The separation between the interacting beams can be
 5178 increased by raising the constant dipole field. However, for a dipole magnet $P_{SR} \propto |B^2|$, [537]
 5179 therefore an optimization of the design will need to be discussed. The chosen parameters give
 5180 a flux of 5.39×10^{18} photons per second at $Z = -21.5$ m.

5181 **Power and Critical Energy:** Table 7.19 shows the power of the SR produced by each
 5182 element along with the average critical energy produced per element. This is followed by the
 5183 total power produced in the IR and the average critical energy. Since the G4 simulations
 5184 utilize Monte Carlo, multiple runs should be made with various seeds to get an estimate for the
 5185 standard error.

Element	Power [kW]	Critical Energy [keV]
DL	6.4	71
QL3	5.3	308
QL2	4.3	218
QL1	0.6	95
QR1	0.6	95
QR2	4.4	220
QR3	5.2	310
DR	6.4	71
Total/Avg	33.2	126

Table 7.19: High Luminosity: Power and Critical Energies [Geant4]

5186 The power from the dipoles is greater than any one quadrupole however the critical energies
 5187 of the quadrupoles are significantly higher than in the dipoles. It is expected that the dipole and
 5188 quadrupole elements can create power on the same order however have very different critical
 5189 energies. This is because the dipole is an order of magnitude longer than the quadrupole ele-
 5190 ments. Since the SR power created for both the quadrupole and dipoles are linearly dependent
 5191 on length [537] one needs to have a much higher average critical energy to create comparable
 5192 amounts of power.

5193 **Comparison:** The IRSYN cross check of the power and critical energies is shown in Table
 5194 7.20. This comparison was done for the total power and the average critical energy.

	Power [kW]		Critical Energy [keV]	
	Geant4	IRSYN	Geant4	IRSYN
Total/Avg	33.2	X	126	X

Table 7.20: High Luminosity: Geant4 and IRSYN comparison

5195 A third cross check to the G4 simulations was made for the power as shown in Table
 5196 7.21. This was done using an analytic method for calculating power in dipole and quadrupole

5197 magnets. [537] This was done for every element which provides confidence in the distribution
 5198 of this power throughout the IR.

	Power [kW]	
Element	Geant4	Analytic
DL	6.4	6.3
QL3	5.3	5.4
QL2	4.3	4.6
QL1	0.6	0.6
QR1	0.6	0.6
QR2	4.4	4.6
QR3	5.2	5.4
DR	6.4	6.3
Total/Avg	33.2	33.8

Table 7.21: High Luminosity: Geant4 and Analytic method comparison

5199 **Number Density and Envelopes:** The number density of photons as a function of Z is
 5200 shown in Figure 7.33. Each graph displays the density of photons in the $Z = Z_o$ plane for
 5201 various values of Z_o . The first three figures give the growth of the SR fan inside the detector
 5202 area. This is crucial for determining the dimensions of the beam pipe. Since the fan grows
 5203 asymmetrically in the $-Z$ direction an asymmetric elliptical cone geometry will minimize these
 5204 dimensions, allowing the tracking to be placed as close to the beam as possible. The horizontal
 5205 extension of the fan in the high luminosity case is the minimum for the two Ring Ring options
 5206 as well as the Linac Ring option, which is most important inside the detector region. This is
 5207 due to the lower value of l^* . Because the quadrupoles are closer to the IP and contain effective
 5208 dipole fields the angle of the beam at the entrance of the upstream dipole can be lower as the
 5209 angle of the beam doesnt need to equal the crossing angle until $Z = l^*$. The number density of
 5210 this fan appears as expected. There exists the highest density between the two beams at the
 5211 absorber.

5212 In Figure 7.33 the distribution was given at various Z values however a continuous envelope
 5213 distribution is also important to see everything at once. This can be seen in Figure 7.34, where
 5214 the beam and fan envelopes are shown in the $Y = 0$ plane. This makes it clear that the fan is
 5215 antisymmetric which comes from the S shape of the electron beam as previously mentioned.

5216 **Critical Energy Distribution:** The Critical Energy is dependent upon the element in which
 5217 the SR is generated, and for the quadrupole magnets it is also dependent upon Z . This is a
 5218 result of the fact that the critical energy is proportional to the magnetic field component that is
 5219 perpendicular to the particle direction. i.e. $E_c \propto B_{\perp}$. [538] Since the magnitude of the magnetic
 5220 field is dependent upon x and y , then for a gaussian beam in position particles will experience
 5221 different magnetic fields and therefore have a spectrum of critical energies. In a dipole the field
 5222 is constant and therefore regardless of the position of the particles as long as they are in the
 5223 uniform field area of the magnet they have a constant critical energy. Since the magnetic field

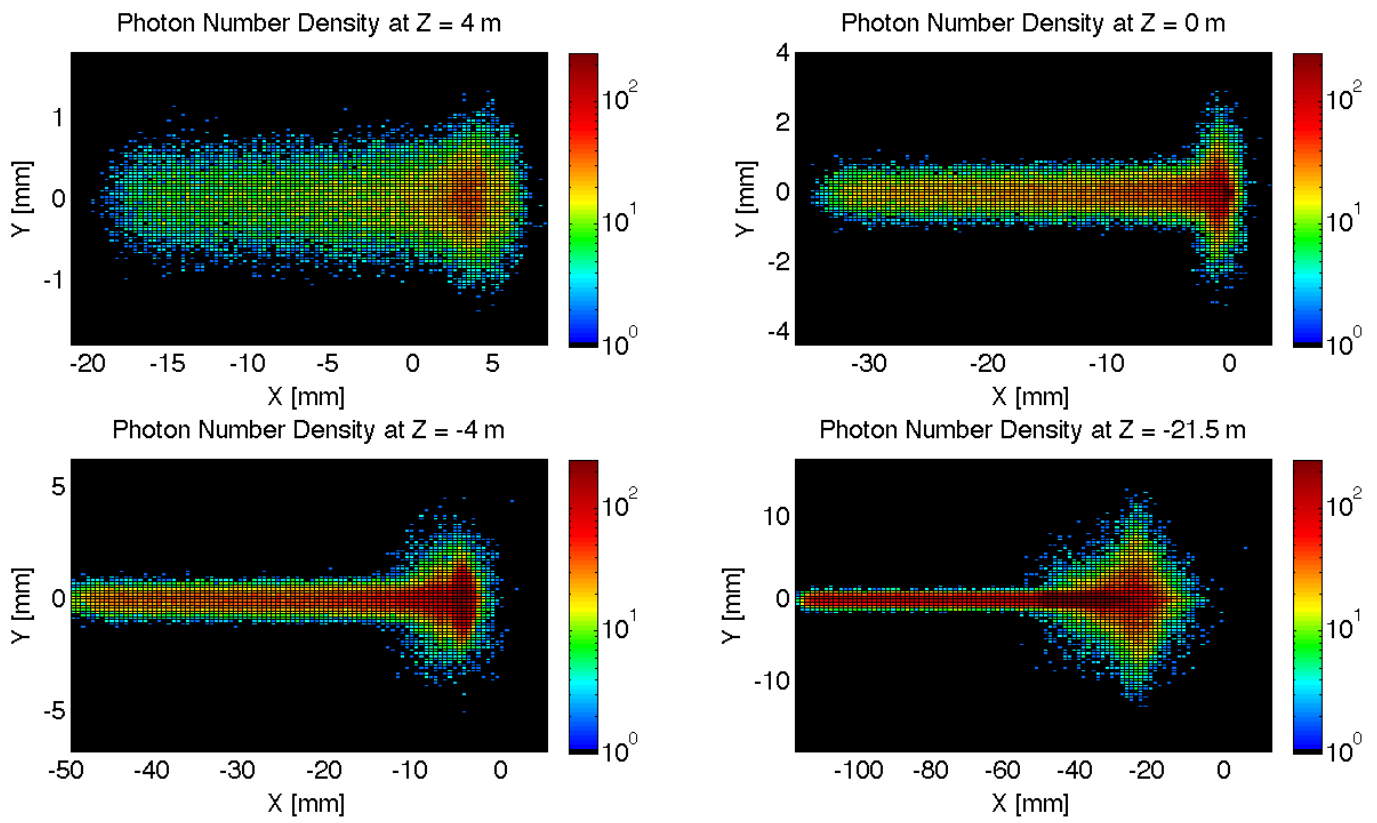


Figure 7.33: High Luminosity: Number Density Growth in Z

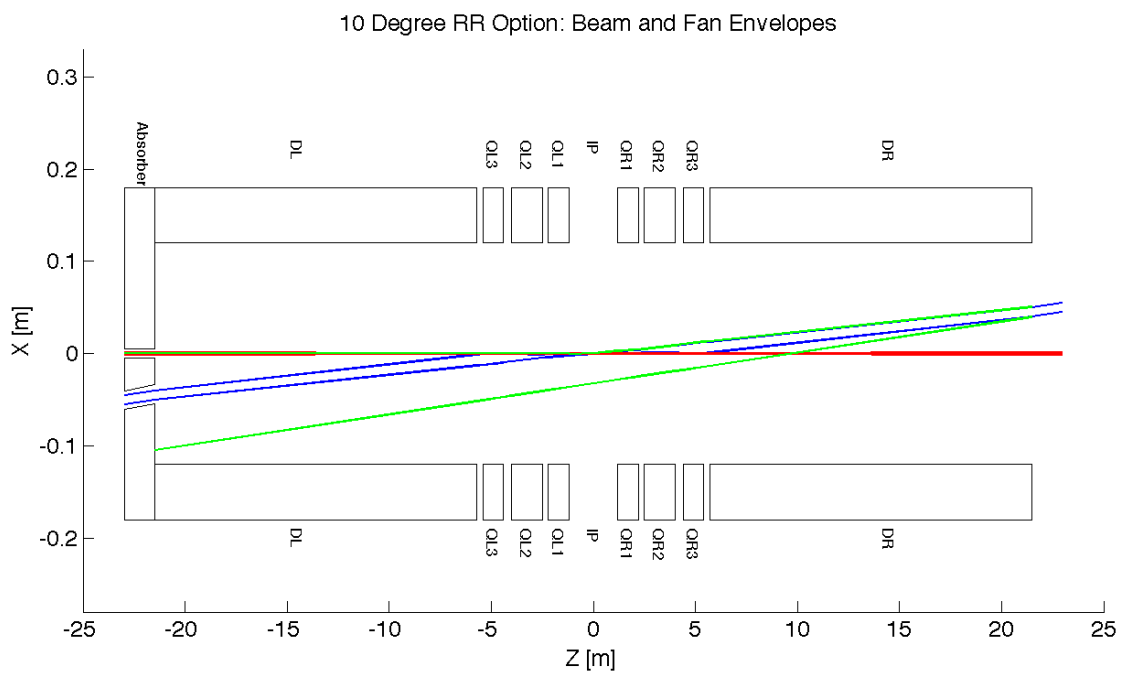


Figure 7.34: High Luminosity: Beam Envelopes in Z

5224 is dependent upon x and y it is clear that as the r.m.s. spot size of the beam decreases there
 5225 will be a decrease in critical energies. The opposite will occur for an increasing spot size. This
 5226 is evident from Figure 7.35.

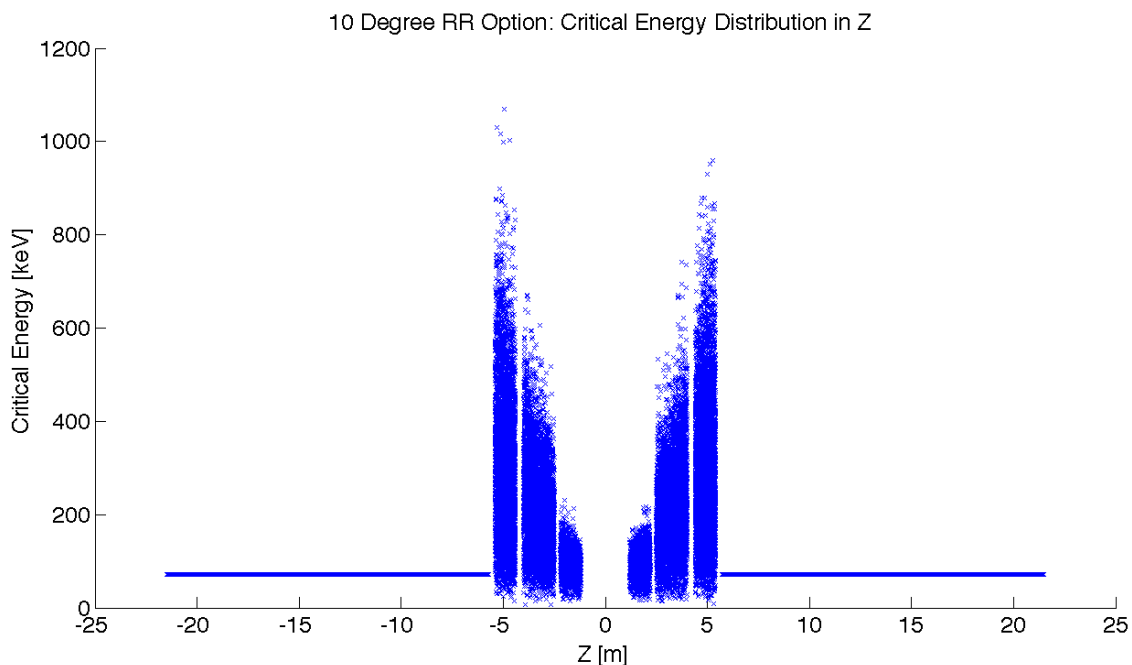


Figure 7.35: High Luminosity: Critical Energy Distribution in Z

5227 **Absorber:** The Photon distribution on the absorber surface is crucial. The distribution de-
 5228 cides how the absorber must be shaped. The shape of the absorber in addition to the distribution
 5229 on the surface then decides how much SR is backscattered into the detector region. In HERA
 5230 backscattered SR was a significant source of background that required careful attention. [539]
 5231 Looking at Figure 7.36 it is shown that for the high luminosity option 19.2 kW of power from
 5232 the SR light will fall on the face of the absorber which is 58% of the total power. This gives
 5233 a general idea of the amount of power that will be absorbed. However, backscattering and IR
 5234 photons will lower the percent that is actually absorbed.

5235 **Proton Triplet:** The super conducting final focusing triplet for the protons needs to be
 5236 protected from radiation by the absorber. Some of the radiation produced upstream of the
 5237 absorber however will either pass through the absorber or pass through the apertures for the
 5238 two interacting beams. This is most concerning for the interacting proton beam aperture which
 5239 will have the superconducting coils. A rough upper bound for the amount of power the coils
 5240 can absorb before quenching is 100 W. [540] There is approximately 217 W entering into the
 5241 interacting proton beam aperture as is shown in Figure 7.36. This doesnt mean that all this
 5242 power will hit the coils but simulations need to be made to determine how much of this will hit

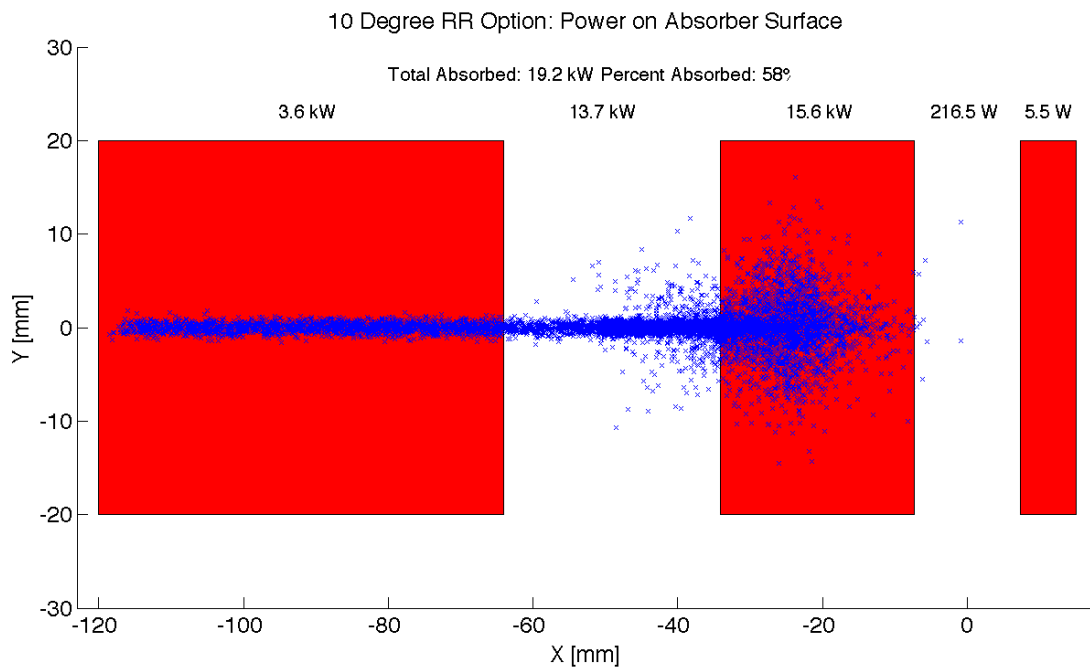


Figure 7.36: High Luminosity: Photon distribution on Absorber Surface

5243 the coils. The amount of power that will pass through the absorber can be disregarded as it is
 5244 not enough to cause any effects. The main source of power moving downstream of the absorber
 5245 will be the photons passing through the beams aperture. This was approximately 13.7 kW as
 5246 can be seen from Figure 7.36. Most of this radiation can be absorbed in a secondary absorber
 5247 placed after the first downstream proton quadrupole. Overall protecting the proton triplet is
 5248 important and although the absorber will minimize the radiation continuing downstream this
 5249 needs to be studied in depth.

5250 **Backscattering:** Another Geant4 program was written to simulate the backscattering of
 5251 photons into the detector region. The ntuple with the photon information written at the
 5252 absorber surface is used as the input for this program. An absorber geometry made of copper
 5253 is described, and general physics processes are set up. A detector volume is then described
 5254 and set to record the information of all the photons which enter in an ntuple. The first step
 5255 in minimizing the backscattering was to optimize the absorber shape. Although the simulation
 5256 didnt include a beam pipe the backscattering for different absorber geometries was compared
 5257 against one another to find a minimum. The most basic shape was a block of copper that
 5258 had cylinders removed for the interacting beams. This was used as a benchmark to see the
 5259 maximum possible backscattering. In HERA a wedge shape was used for heat dissipation and
 5260 minimizing backscattering. [539] The profile of two possible wedge shapes in the YZ plane is
 5261 shown in Figure 7.37. It was found that this is the optimum shape for the absorber. The reason
 5262 for this is that a backscattered electron would have to have its velocity vector be almost parallel
 5263 to the wedge surface to escape from the wedge and therefore it works as a trap. As can be seen
 5264 from Table 7.22 utilizing the wedge shaped absorber did not reduce the power by much. This
 5265 appears to be a statistical limitation. This needs to be redone with higher statistics to get a
 5266 better opinion on the difference between the two geometries.

5267 After the absorber was optimized it was possible to set up a beam pipe geometry. An
 5268 asymmetric elliptical cone beam pipe geometry made of beryllium was used since it would
 5269 minimize the necessary size of the beam pipe as previously mentioned. The next step was to
 5270 place the lead shield and masks inside this beam pipe. To determine placement a simulation
 5271 was run with just the beam pipe. Then it was recorded where each backscattered photon would
 5272 hit the beam pipe in Z. A histogram of this data was made. This determined that the shield
 5273 should be placed in the Z region ranging from -20 m until the absorber (-21.5 m). The shields
 5274 were then placed at -21.2 m and -20.5 m. This decreased the backscattered power to zero as
 5275 can be seen from Table 7.22. Although this is promising this number should be checked again
 5276 with higher statistics to judge its accuracy. Overall there is still more optimization that can
 5277 occur with this placement.

Absorber Type	Power [W]
Flat	22
Wedge	18.5
Wedge & Mask/Shield	0

Table 7.22: High Luminosity: Backscattering/Mask

5278 Cross sections of the beam pipe in the $Y = 0$ and $X = 0$ planes with the shields and masks
 5279 included can be seen in Figure 7.38.

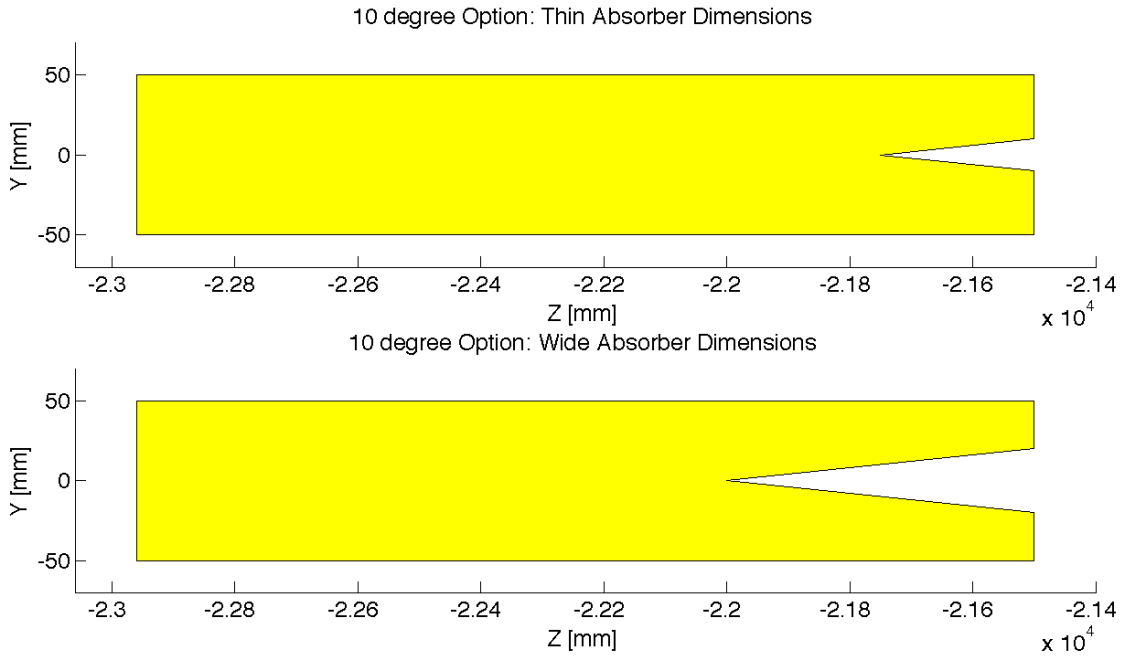


Figure 7.37: 10 deg: Absorber Dimensions

5280 **High Detector Acceptance**

5281 **Parameters:** For the Ring Ring high acceptance option the basic parameters are listed in
 5282 Table 7.23. The separation refers to the displacement between the two interacting beams at
 5283 the face of the proton triplet.

Characteristic	Value
Electron Energy [GeV]	60
Electron Current [mA]	100
Crossing Angle [mrad]	1
Absorber Position [m]	-21.5
Dipole Field [T]	0.0493
Separation [mm]	55.16
γ/s	6.41×10^{18}

Table 7.23: High Acceptance: Parameters

5284 The energy, current, and crossing angle (θ_c) are common values used in all RR calculations.
 5285 The dipole field value refers to the constant dipole field created throughout all dipole elements
 5286 in the IR. The separation is the same as in the high luminosity case and can be altered for

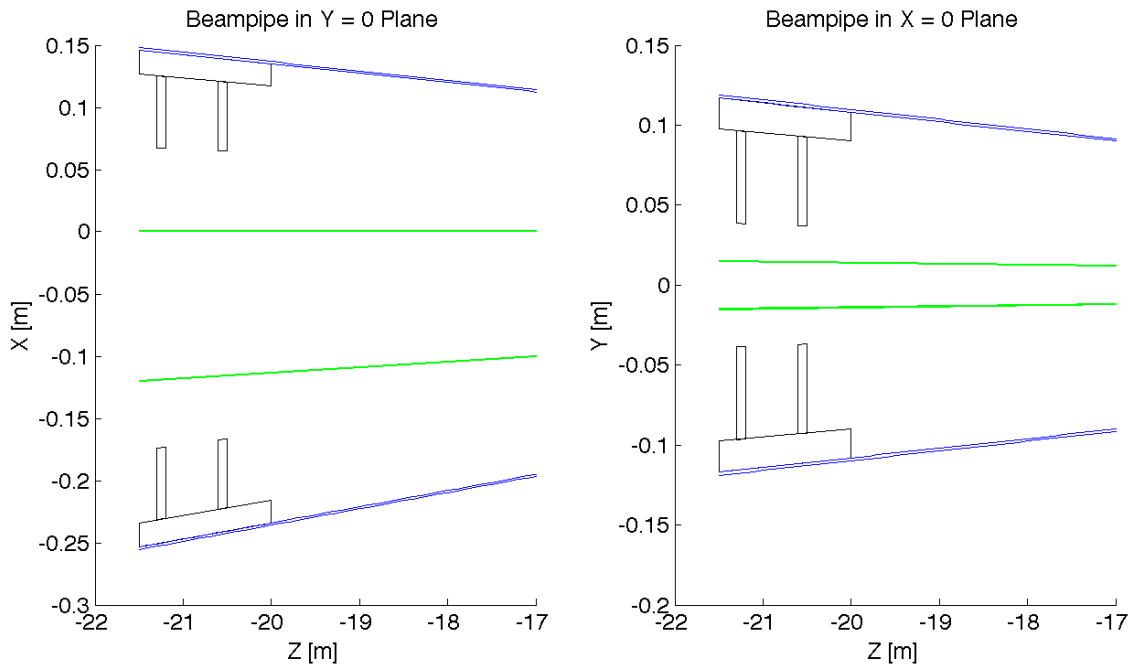


Figure 7.38: High Luminosity: Beampipe Cross Sections

5287 the same reasons with the same ramifications. The chosen parameters give a flux of 6.41×10^{18}
 5288 photons per second at $Z = -21.5$ m, which is slightly higher than in the high luminosity case.
 5289 This is expected as the fields experienced in the high acceptance case are higher.

5290 **Power and Critical Energy:** Table 7.24 shows the power of the SR produced by each
 5291 element along with the average critical energy produced per element. This is followed by the
 5292 total power produced in the IR and the average critical energy. Since the G4 simulations
 5293 utilize Monte Carlo, multiple runs should be made with various seeds to get an estimate for the
 5294 standard error.

5295 The distribution of power and critical energy over the IR elements is similar to that of the
 5296 high acceptance option with the exception of the upstream and downstream separator dipole
 5297 magnets. The power and critical energies are significantly higher than before. This is due to
 5298 the higher dipole field and the quadratic dependence of power on magnetic field and linear
 5299 dependence of critical energy on magnetic field. [538]

5300 **Comparison:** The IRSYN cross check of the power and critical energies is shown in Table
 5301 7.25. This comparison was done for the total power and the critical energy.

5302 A third cross check to the G4 simulations was also made for the power as shown in Table
 5303 7.26. This was done using an analytic method for calculating power in dipole and quadrupole
 5304 magnets. [537] This comparison provides confidence in the distribution of the power throughout
 5305 the IR.

Element	Power [kW]	Critical Energy [keV]
DL	13.9	118
QL2	6.2	318
QL1	5.4	294
QR1	5.4	293
QR2	6.3	318
DR	13.9	118
Total/Avg	51.1	163

Table 7.24: High Acceptance: Power and Critical Energies [Geant4]

	Power [kW]		Critical Energy [keV]	
	Geant4	IRSYN	Geant4	IRSYN
Total/Avg	51.1	51.3	163	162

Table 7.25: High Acceptance: Geant4 and IRSYN comparison

Element	Power [kW]	
	Geant4	Analytic
DL	13.9	14
QL2	6.2	6.2
QL1	5.4	5.3
QR1	5.4	5.3
QR2	6.3	6.2
DR	13.9	14
Total	51.1	51

Table 7.26: High Acceptance: Geant4 and Analytic method comparison

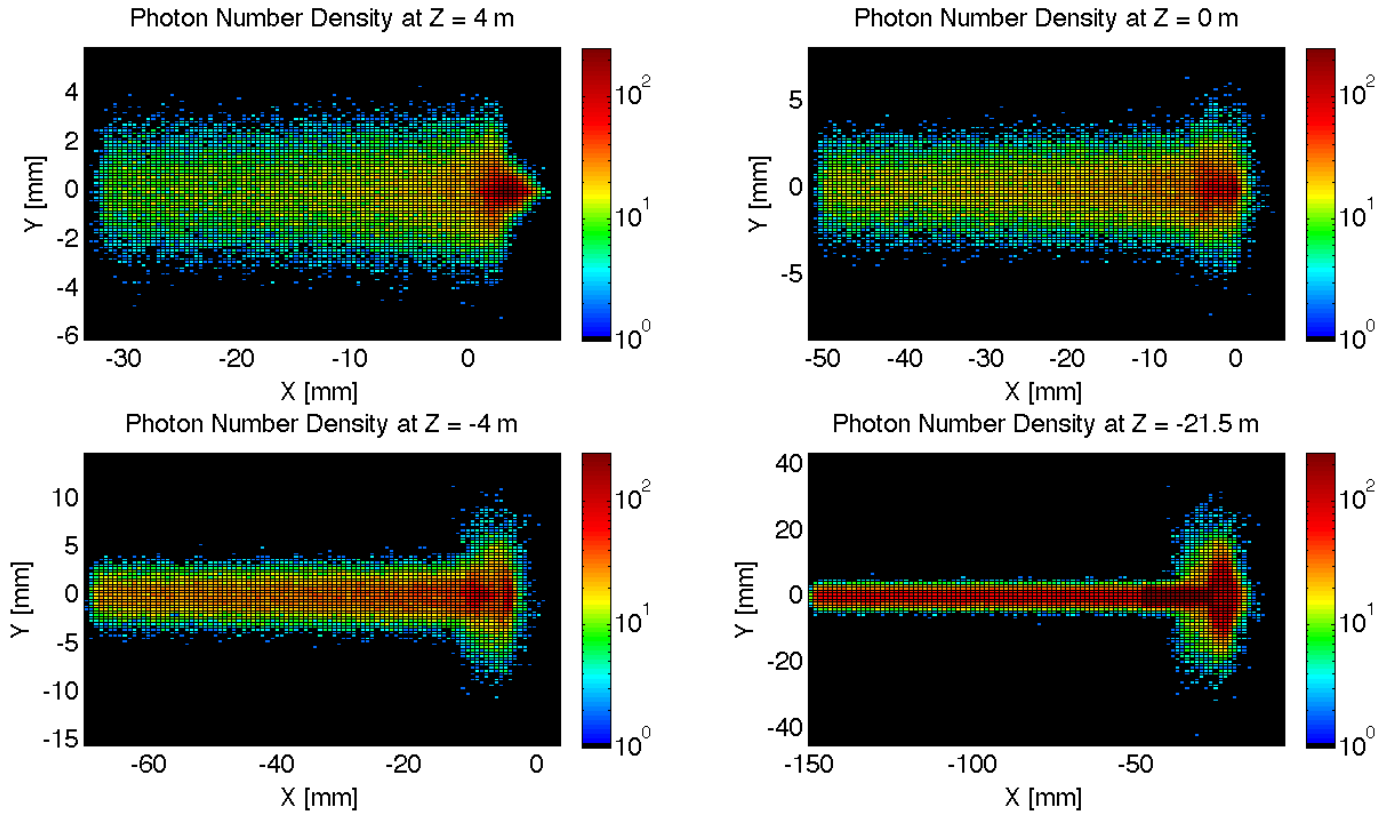


Figure 7.39: High Acceptance: Number Density Growth in Z

5306 **Number Density and Envelopes:** The number density of photons as a function of Z is
 5307 shown in Figure 7.39. The horizontal extension of the fan in the high acceptance case is larger
 5308 than in the high luminosity case however still lower than in the LR option. Since the beam
 5309 stays at a constant angle for the first 6.2 m after the IP it requires larger fields to bend in order
 5310 to reach the desired separation. This means that an overall larger angle is reached near the
 5311 absorber, and since the S shaped trajectory is symmetric in Z the angle of the beam at the
 5312 entrance of the upstream quadrupoles is also larger and therefore the fan extends further in X.

5313 The envelope of the SR fan can be seen in Figure 7.40, where the XZ plane is shown at the
 5314 value $Y = 0$. Once again the fan is antisymmetric due to the S shape of the electron beam.

5315 **Critical Energy Distribution:** The critical energy distribution in Z is similar to that of the
 5316 high luminosity case. This is due to the focusing of the beam in the IR. This is evident from
 5317 Figure 7.41.

5318 **Absorber:** Looking at Figure 7.42 it is shown that for the high acceptance option 38.5 kW
 5319 of power from the SR light will fall on the face of the absorber which is 75% of the total power.

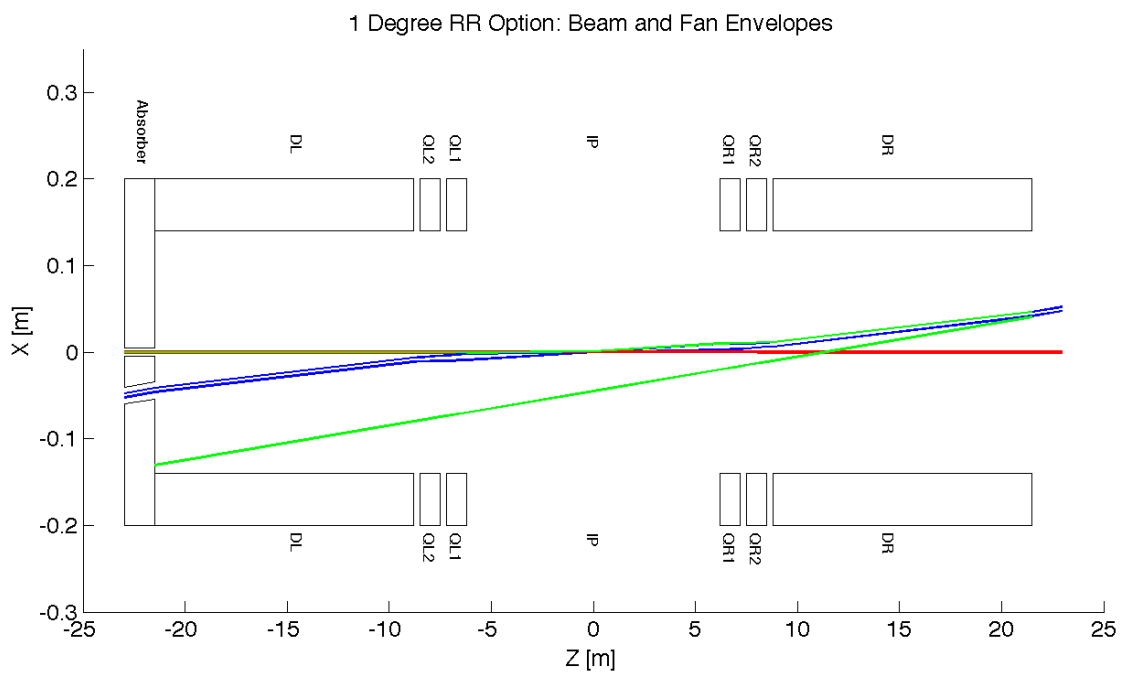


Figure 7.40: High Acceptance: Beam Envelopes in Z

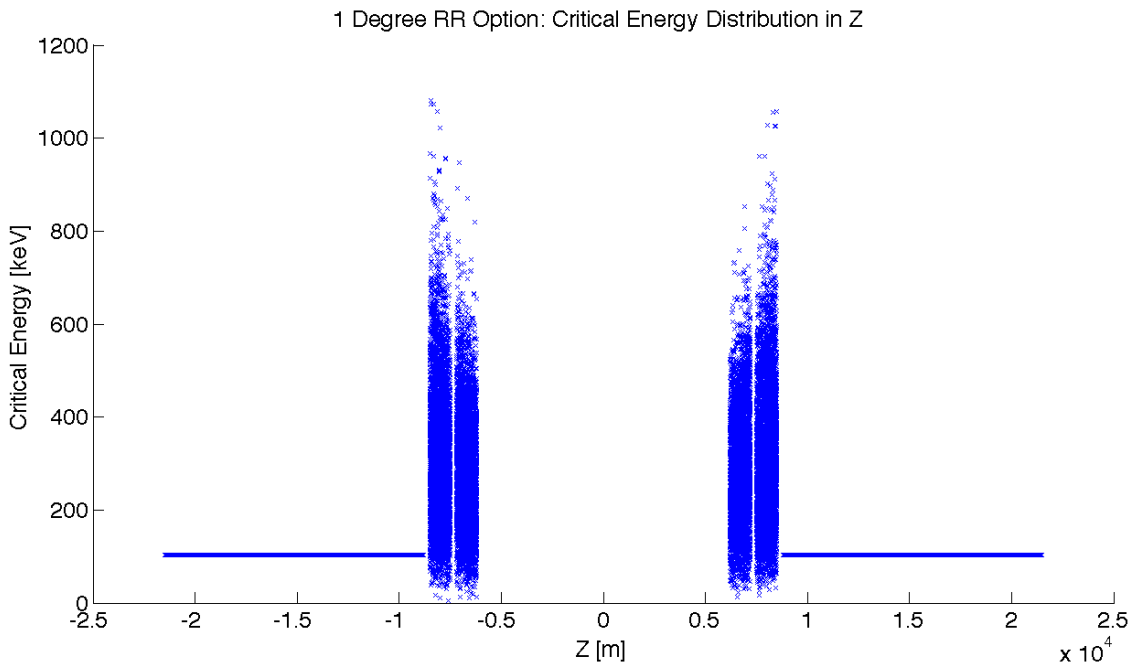


Figure 7.41: High Acceptance: Critical Energy Distribution in Z

5320 This gives a general idea of the amount of power that will be absorbed. However, backscattering
 5321 and IR photons will lower the percent that is actually absorbed.

5322 **Proton Triplet:** The super conducting final focusing triplet for the protons needs to be
 5323 protected from radiation by the absorber. Some of the radiation produced upstream of the
 5324 absorber however will either pass through the absorber or pass through the apertures for the
 5325 two interacting beams. This is most concerning for the interacting proton beam aperture which
 5326 will have the superconducting coils. A rough upper bound for the amount of power the coils can
 5327 absorb before quenching is 100 W. [540] In the high acceptance option there is approximately
 5328 0.4 W entering into the interacting proton beam aperture as is shown in Figure 7.42. Therefore
 5329 for the high acceptance option this is not an issue. The amount of power that will pass through
 5330 the absorber can be disregarded as it is not enough to cause any significant effects. The main
 5331 source of power moving downstream of the absorber will be the photons passing through the
 5332 beams aperture. This was approximately 12.7 kW as can be seen from Figure 7.42. Most of
 5333 this radiation can be absorbed in a secondary absorber placed after the first downstream proton
 5334 quadrupole. Overall protecting the proton triplet is important and although the absorber will
 5335 minimize the radiation continuing downstream this needs to be studied in depth.

5336 **Backscattering:** Another Geant4 program was written to simulate the backscattering of
 5337 photons into the detector region. The ntuple with the photon information written at the
 5338 absorber surface is used as the input for this program. An absorber geometry made of copper

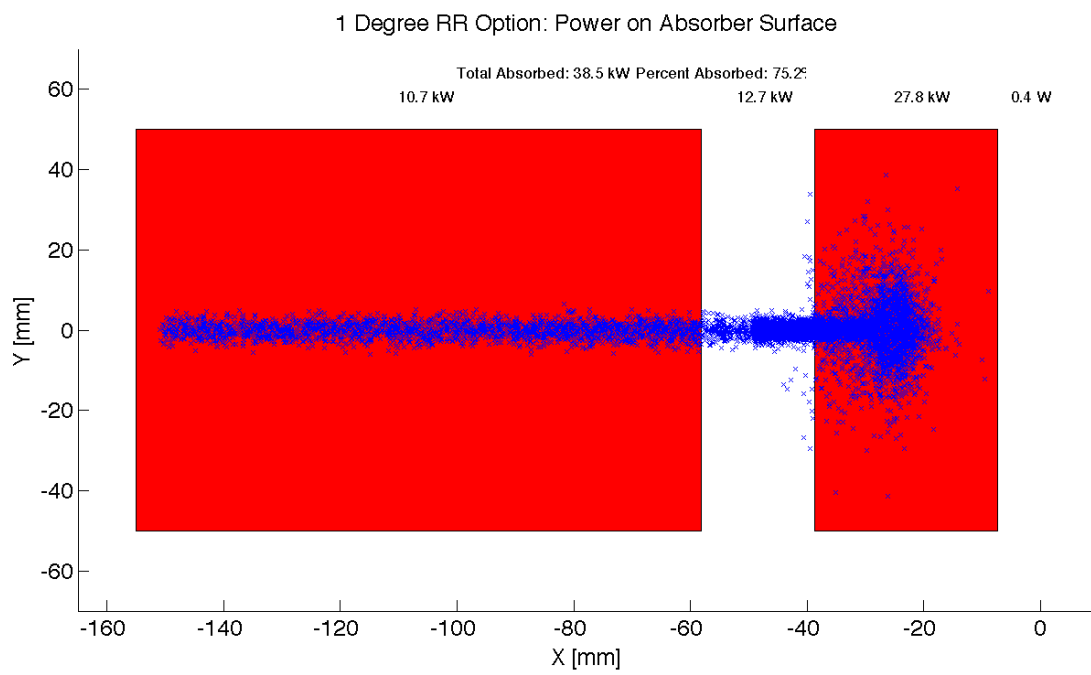


Figure 7.42: High Acceptance: Photon distribution on Absorber Surface

5339 is described, and general physics processes are set up. A detector volume is then described
 5340 and set to record the information of all the photons which enter in an ntuple. The first step
 5341 in minimizing the backscattering was to optimize the absorber shape. Although the simulation
 5342 didnt include a beam pipe the backscattering for different absorber geometries was compared
 5343 against one another to find a minimum. The most basic shape was a block of copper that
 5344 had cylinders removed for the interacting beams. This was used as a benchmark to see the
 5345 maximum possible backscattering. In HERA a wedge shape was used for heat dissipation and
 5346 minimizing backscattering. [539] The profile of two possible wedge shapes in the YZ plane is
 5347 shown in Figure 7.43. It was found that this is the optimum shape for the absorber. The reason
 5348 for this is that a backscattered electron would have to have its velocity vector be almost parallel
 5349 to the wedge surface to escape from the wedge and therefore it works as a trap. As can be seen
 5350 from Table 7.27 utilizing the wedge shaped absorber decreased the backscattered power by a
 5351 factor of 9.

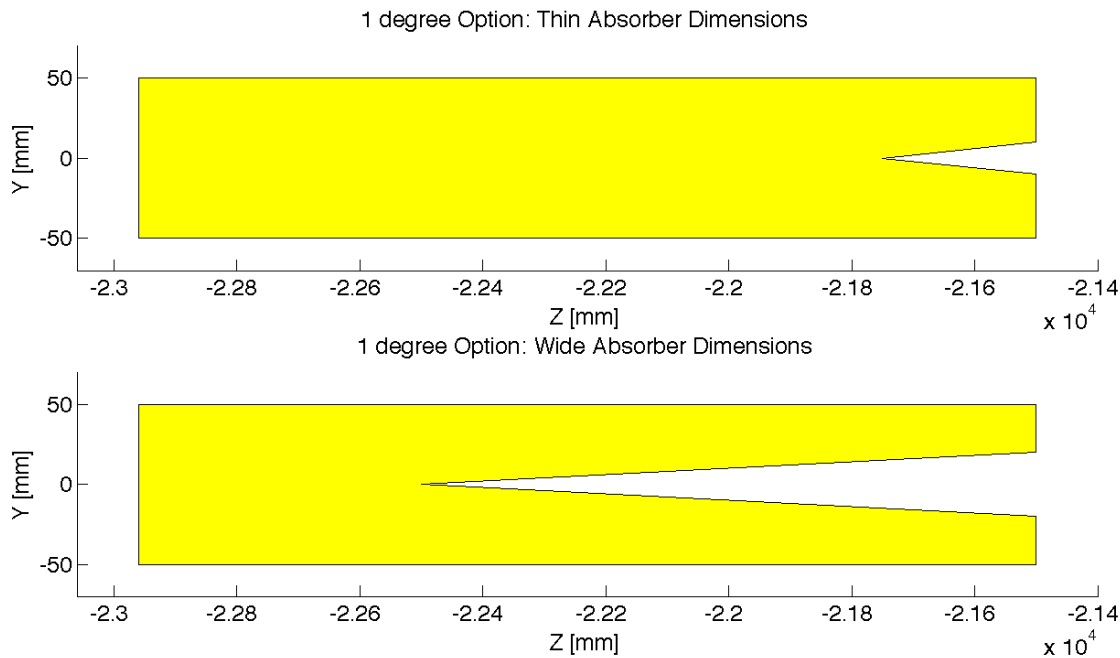


Figure 7.43: 1 deg: Absorber Dimensions

5352 After the absorber was optimized it was possible to set up a beam pipe geometry. An
 5353 asymmetric elliptical cone beam pipe geometry made of beryllium was used since it would
 5354 minimize the necessary size of the beam pipe as previously mentioned. The next step was to
 5355 place the lead shield and masks inside this beam pipe. To determine placement a simulation
 5356 was run with just the beam pipe. Then it was recorded where each backscattered photon would
 5357 hit the beam pipe in Z. This determined that the shield should be placed in the Z region ranging
 5358 from -20 m until the absorber (-21.5 m). The shields were then placed at -21.2 m and -20.6 m.
 5359 This decreased the backscattered power to zero as can be seen from Table 7.27. Although this

5360 is promising this number should be checked again with higher statistics to judge its accuracy.
 5361 Overall there is still more optimization that can occur with this placement.

Absorber Type	Power [W]
Flat	91.1
Wedge	10
Wedge & Mask/Shield	0

Table 7.27: High Acceptance: Backscattering/Mask

5362 Cross sections of the beam pipe in the $Y = 0$ and $X = 0$ planes with the shields and masks
 5363 included can be seen in Figure 7.44.

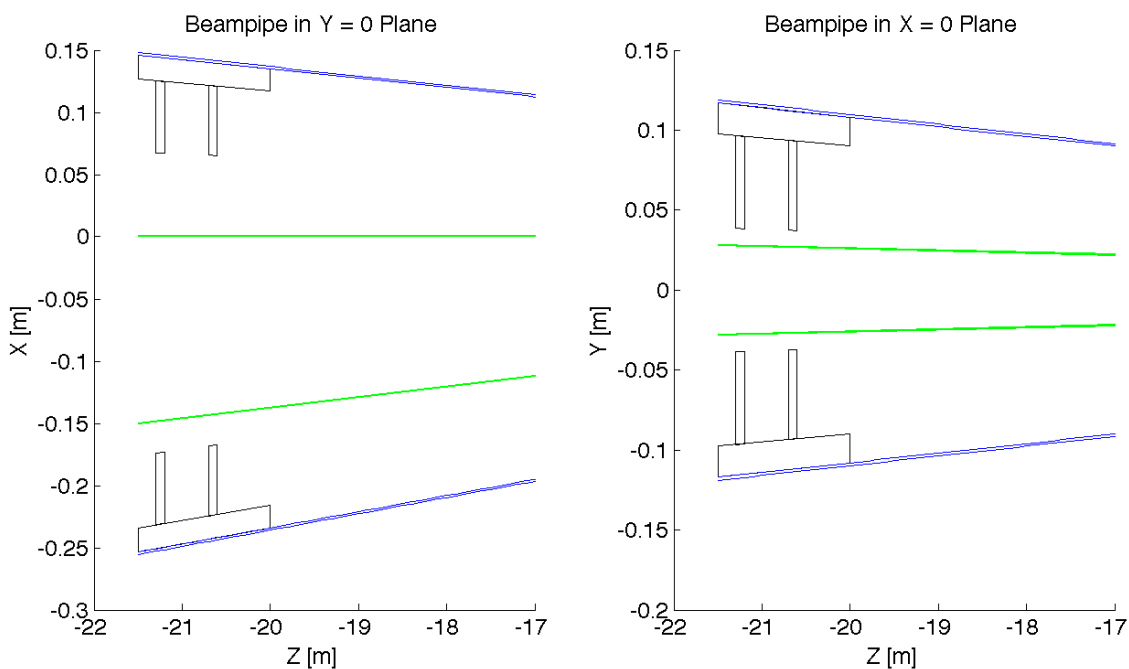


Figure 7.44: High Acceptance: Beampipe Cross Sections

5364 7.8 Beam-beam effects in the LHeC

5365 In the framework of the Large Hadron electron Collider a ring-ring option is considered where
 5366 protons of one beam collide with the protons of the second proton beam as well as with lep-
 5367 tons from the second ring. To deduce possible limitations the present knowledge of the LHC
 5368 beam-beam effects from proton-proton collisions are fundamental to define parameters of an
 5369 interaction point with electron-proton collisions. From past experience it is known that the

5370 maximum achievable luminosity in a collider is limited by beam-beam effects. These are often
 5371 quantified by the maximum beam-beam tune shifts in each of the two beams. An important
 5372 aspect in electron-proton collisions is that the proton beam, more sensitive to transverse noise,
 5373 could be perturbed by a higher level of noise in the electron beam. In this section we will
 5374 assess some limits to the possible tune shift achievable in collision based on experience from
 5375 past colliders as CESR [?] and LEP [?] and more recent ones like the LHC [?].

5376 7.8.1 Head-on beam-beam effects

5377 A first important performance issue in beam-beam interaction comes from the restricted choice
 5378 of the β -function at the interaction point to keep the transverse beam sizes equal for the two
 5379 beam since proton and electron emittances are different. The choice of beta functions at the
 5380 interaction point has to be different for the two beams in order to keep $\sigma_x^e = \sigma_x^p$ and $\sigma_y^e = \sigma_y^p$
 5381 for the reasons explained in detail in [?]. In a mismatched collision the larger bunch may suffer
 5382 more because a large part of the particle distribution will experience the non-linear beam-beam
 5383 force of the other bunch. With this in mind it is preferable to keep the electron beam slightly
 5384 larger than the proton beam since the electron beam may be less sensitive due to strong radi-
 5385 ation damping. This matching implies that the electron emittances must be controlled during
 5386 operation and kept as constant as possible (i.e. H/V coupling). For the proton beam the
 5387 beam-beam effects from the electron beam will be different for the two planes. Optical match-
 5388 ing of the beam sizes at the IP is the first constraint for any interaction region layout proposed.

5389
 5390 Another important issue is the achievable tune shift and how this relates to the linear
 5391 beam-beam parameter which is normally the parameter used to evaluate the strength of the
 5392 beam-beam interaction.

5393
 5394 The linear beam-beam parameter is defined as ξ_{bb} and is expressed for the case of round
 5395 beams like in proton-proton collision at the LHC as:

$$\xi_{bb} = \frac{Nr_p\beta^*}{4\pi\gamma\sigma^2} \quad (7.12)$$

5396 where r_p is the proton classical radius, β^* is the optical amplitude function (β -function) at the
 5397 interaction point, $\sigma = \sigma_{x,y}$ is the transverse beam size in meters at the interaction point, N_p
 5398 is the bunch intensity and γ is the relativistic factor. For proton-proton collisions where ξ_{bb} does
 5399 not reach too large values and the operational tune is far enough away from linear resonances,
 5400 this parameter is about equal to the linear tune shift ΔQ expected from the head-on beam-
 5401 beam interaction. This is the case for the LHC proton-proton collisions at IP1 and IP5 where
 5402 the linear tune shift per IP is of the order of 0.0034/0.0037 for nominal beam parameters as
 5403 summarized in Table 7.28 and corresponds to the linear beam-beam parameter ξ_{bb} . This is in
 5404 general not true for lepton colliders where the operational scenario differs from hadron colliders
 5405 and other effects become dominant and have to be taken into account.

5406 In the case of electron beams the transverse shape of the beams is normally elliptical with
 5407 $\sigma_x > \sigma_y$. In this configuration one can generalize the linear beam-beam parameter calculation
 5408 with the following formula [?]:

$$\xi_{x,y} = \frac{Nr_e\beta_{x,y}^*}{2\pi\gamma\sigma_{x,y}(\sigma_x + \sigma_y)} \quad (7.13)$$

Parameter	LEP	LHC (nominal)
Beam sizes	$160\mu\text{m} \cdot 4\mu\text{m} ?$	$16.6\mu\text{m} \cdot 16.6\mu\text{m}$
Intensity N	$4.0 \cdot 10^{11}/\text{bunch}$	$1.15 \cdot 10^{11}/\text{bunch}$
Energy	100 GeV	7000 GeV
$\beta_x^* \cdot \beta_y^*$	1.25 m · 0.05 m	0.55 m · 0.55 m
Crossing angle	0.0	0/285 μrad
Beam-beam parameter(ξ)	0.0700	0.0037/0.0034

Table 7.28: Comparison of parameters for the LEP collider and the LHC.

5409 with r_e is the electron classical radius.

5410 In the case of electron-proton collisions one has to also take into account the different species
5411 during collision and the beam-beam parameters become:

$$\xi_{(x,y),b_1} = \frac{N_{b_2} r_{b_1} \beta_{(x,y),b_1}^*}{2\pi \gamma_{b_1} \sigma_{(x,y),b_2} (\sigma_{x,b_2} + \sigma_{y,b_2})} \quad (7.14)$$

5412 Here b_1 and b_2 refer to beam 1 and beam 2 respectively. The linear beam-beam parameter
5413 ξ is often used to quantify the strength of the beam-beam interaction, however it does not
5414 reflect the non-linear nature of the electromagnetic interaction. Nevertheless, it can be used for
5415 comparison and as a scaling parameter. Since a general beam-beam limit cannot be found and
5416 will be different from one collider to the next, the interpretation should be conservative.

5417 In Table 7.28 we compare LEP and LHC beam parameters and achieved linear beam-beam
5418 parameters. Some of the differences are striking: while the beams in the LHC are round at
5419 the interaction point, they are very flat in LEP. This is due to the excitation of the beam in
5420 the horizontal plane by the strong synchrotron radiation and damping in the vertical plane.
5421 Another observation is the much larger beam-beam parameter in LEP.

5422 One reason for the larger achievable beam-beam parameter in lepton colliders is due to a
5423 significant dynamic beta effect when operating at a working point close to integer tune. This is
5424 considered more difficult with proton beams. In Equation 7.15 the perturbed β^* is expressed as
5425 a function of the beam-beam parameter and the phase advance between two interaction points
5426 $2\pi Q^i$. The tune shift becomes a function of the tune which can be chosen to keep the actual
5427 shift small.

$$\beta^*(Q) = \frac{\beta}{\sqrt{1 + 4\pi\xi(\cot(2\pi Q^i)) - 4\pi^2\xi^2}} \quad (7.15)$$

5428 From experience it is known that electrons have a bigger range for the linear head-on beam-
5429 beam parameter: LEP II has proved a beam-beam parameter of 0.07 corresponding to a mea-
5430 sured ΔQ of 0.03 as also confirmed in other lepton colliders. CESR demonstrated the possibility
5431 to achieve tune shifts of the order of 0.09. A second and most important reason for a higher
5432 acceptable tune shift in lepton colliders is the synchrotron radiation damping. Furthermore,
5433 while for lepton colliders a clear indication for a "beam-beam limit" exists, not such criteria
5434 can be easily defined for hadron machines [?]. With these brief resume on the head-on linear
5435 beam-beam parameters reached so far it is clear that the beam which will have some limits on
5436 the choice of parameters ξ_{bb} is the proton beam.

IR Option	1 degree		10 degree	
	Electrons	Protons	Electrons	Protons
Beams	Electrons	Protons	Electrons	Protons
Energy	60 GeV	7 TeV	60 GeV	7 TeV
Intensity	$2 \cdot 10^{10}$	$1.7 \cdot 10^{11}$	$2 \cdot 10^{10}$	$1.7 \cdot 10^{11}$
β_x^*	0.4 m	4.05 m	0.18 m	1.8 m
β_y^*	0.2 m	0.97 m	0.1 m	0.5 m
ϵ_x	5 nm	0.5 nm	5 nm	0.5 nm
ϵ_y	2.5 nm	0.5 nm	2.5 nm	0.5 nm
σ_x	45 μm		30 μm	
σ_y	22 μm		15.8 μm	
Cross angle	1 mrad		1 mrad	
$\xi_{bb,x}$	0.086	0.0008	0.085	0.0008
$\xi_{bb,y}$	0.088	0.0004	0.090	0.0004
Luminosity	$7.33 \cdot 10^{32} \text{ cm}^{-2} \text{ s}^{-1}$		$1.34 \cdot 10^{33} \text{ cm}^{-2} \text{ s}^{-1}$	

Table 7.29: Beam parameters for the interaction region options and the relative linear beam-beam parameter ξ .

	Nominal		Upgrade	
	Electrons	Protons	Electrons	Protons
$\xi_{bb,x}$	0.016	0.0013	0.027	0.0017
$\xi_{bb,y}$	0.018	0.0012	0.041	0.0005

Table 7.30: Linear beam-beam parameters for HERA, nominal machine and upgrade parameters.

5437 The LHC as a proton-proton collider has confirmed previous experience from SppS and
5438 Tevatron that a total linear tune shift of 0.018 (0.006 per IP) is tolerable with neither important
5439 losses nor reduction of beam lifetime during normal operation. It is generally admitted that
5440 ξ_{bb} could reach a value of 0.01 per interaction point. Recent experiments at the LHC with
5441 very high intensity beams beyond ultimate and reduced beam transverse sizes demonstrated
5442 the possibility of reaching head-on tune shifts well beyond the nominal values [?]. At the LHC
5443 tune shifts per IP close to 0.02 have been achieved. Total tune shift exceeding 0.034 have
5444 also been achieved with stable beams for two symmetric crossings at IP1 and IP5. These
5445 latest experiments demonstrate the possibility to operate with larger than nominal beam-beam
5446 parameters.

5447 The calculated beam-beam parameters for the electron and proton beams due to an electron-
5448 proton collision in the LHeC are summarized in Table 7.29 for the two interaction region options
5449 (1 Degree Option and 10 Degree Option).

5450 The two proposed interaction region options will give for the proton beams a maximum
5451 beam-beam parameter in the horizontal plane of about $8 \cdot 10^{-4}$. This effect is in the shadow of

IR Option	1 degree		10 degree	
Beams	Electrons	Protons	Electrons	Protons
β_x^*	0.4 m	4.05 m	0.18 m	1.8 m
β_y^*	0.2 m	0.97 m	0.1 m	0.5 m
ϵ_x	5 nm	0.5 nm	5 nm	0.5 nm
ϵ_y	2.5 nm	0.5 nm	2.5 nm	0.5 nm
Cross angle	1 mrad		1 mrad	
d_x	90 σ_e	8.94 σ_p	60 σ_e	6.0 σ_p

Table 7.31: Normalized distance of beam-beam long range encounter for the two interaction region options.

5452 the proton-proton collision at IP1 and IP5 which will give a beam-beam parameter of $5.5 \cdot 10^{-3}$
5453 per single IP for nominal beam emittances and assuming intensities of $1.7 \cdot 10^{11}$ protons/bunch
5454 which was already achieved during 2010 operation at the LHC with reduced emittances and
5455 nominal beam intensities. One should not expect important effects of the head-on tune shifts
5456 coming from the electron beam.

5457 For the electron beam, on the contrary, the beam-beam parameter of $8.6 \cdot 10^{-2}$ is large and
5458 represents a value at the limit of what has been achieved so far in other lepton machines (LEP
5459 at 90 GeV energy achieved a beam-beam parameter of 0.07 while KEK and HERA a maximum
5460 $\xi_{bb} = 0.04$ during operation, CESR achieved a beam-beam parameter of 0.09 for single IP but
5461 with lower luminosity). The beam-beam tuneshifts achieved at HERA for the nominal and
5462 upgrade version are summarized in Table 7.30 for comparison.

5463 7.8.2 Long range beam-beam effects

5464 So far we have discussed head-on beam-beam interactions but an important issue are the long
5465 range interactions which will occur at the electron-proton collision and their interplay with
5466 the proton-proton crossings at IP1 and IP5. The two interaction points IP1 and IP5 will give
5467 up to 60 proton-proton long-range interactions which should be added to the two interaction
5468 region options which will give two additional parasitic encounters. The beam separation at
5469 this encounters should be as large as possible to reduce any non-linear perturbation. The
5470 parasitic encounters occur every 3.75 m from the interaction point for a bunch spacing of 25
5471 ns. The proposed optics will then lead to parasitic beam-beam interactions which will occur at
5472 a transverse separation d as:

$$d(s)_{x,y} = \alpha \frac{s}{\sqrt{\epsilon_{x,y} \beta(s)_{x,y}}} \quad (7.16)$$

5473 with $\epsilon_{x,y}$ are the beam emittance in the separation plane and $\beta(s)$ is the betatron function at
5474 a distance s from the interaction point.

5475 In Table 7.31 the distances of the parasitic encounters in units of the transverse beam sizes
5476 are shown for both interaction region layouts.

5477 The 1 degree option gives long range interactions at larger separation with respect to the
5478 10 degree option which results in small separations of $\approx 6 \sigma$ for the proton beam. Particles
5479 in the tail of the proton beam particles will experience the non linearity of the electron beam

5480 electromagnetic force. The presence of two long range at 6σ separation may be acceptable
5481 since it is shown experimentally that few encounters also at smaller separation do not affect
5482 the beams dramatically [?]. However, the interplay of these two encounters with the long-
5483 range interactions from IP1 and IP5 should be studied in detail with numerical simulation
5484 to highlight possible limitations. In this framework future experiments at the LHC will help
5485 defining a possible beam parameters space for the control of the long-range effects from proton-
5486 proton collisions. If encounters at 6σ present a limitation to the collider performance then a
5487 possible cure to increase the long-range separation could be a further increase of the crossing
5488 angle and using crab cavities can recover the increased geometric luminosity reduction factor.
5489 In this case a study of the crab cavities effects on the proton beam would be essential to define
5490 the effects of transverse noise on colliding beams.

5491 For any reliable study of the LHeC project one has to address other possible beam-beam
5492 issues with extensive numerical simulations of the operational scenario of the LHeC. This is
5493 fundamental since there is no other possible simplification which can be adopted in evaluating
5494 the non-linear parts of the beam-beam forces. For this reason a detailed and full interaction
5495 layout with crossing schemes matched in thin lens version is needed. With the complete optic
5496 layout beam-beam effects which still need further studies by means of numerical simulation
5497 campaign are the following:

- 5498 • Long-range tune shifts and orbit effects.
- 5499 • Self-consistent study of the proton-proton and electron-proton beam dynamics interplay.
- 5500 • Dynamic aperture tracking studies.
- 5501 • Multi-bunch effects.

5502 The evaluation of the non-linear effects of the beam-beam interactions with self-consistent
5503 calculations will define a set of parameters for operation [?].

5504 7.9 Performance as an electron-ion collider

5505 With the first collisions of lead nuclei ($^{208}\text{Pb}^{82+}$) in 2010, the LHC has already demonstrated its
5506 capability as a heavy-ion collider and this naturally opens up the possibility of electron-nucleus
5507 (e-A) collisions in the LHeC.

5508 This mode of operation would obviously require an interruption of p-p collisions in the
5509 LHC. In principle, the CERN complex could provide A-A (or even p-A) collisions to the LHC
5510 experiments while the LHeC operates with e-A collisions. The lifetime of the nuclear beam
5511 would depend mainly on whether it was exposed to the losses from A-A luminosity in the LHC
5512 (in this case it would be at least a few hours).

5513 In the first decade or so of LHC operation, the ion injector chain is expected to provide
5514 mainly $^{208}\text{Pb}^{82+}$, but also other species such as $^{40}\text{Ar}^{18+}$ or $^{129}\text{Xe}^{54+}$, either to the LHC or from
5515 the SPS to fixed target experiments in the North Area. These beams could also be collided
5516 with electrons in the LHeC but solid intensity estimates are not yet available for the lighter
5517 ions. For simplicity, we shall estimate LHeC performance in e-Pb collisions with the design
5518 performance values of the ion injector chain as described in [?] and the assumption of a single
5519 nuclear beam in one ring of the LHC with parameters as recalled from [541] in Table 7.32.
5520 It is assumed that present uncertainties about the Pb intensity limits at full energy in the

LHC will have been resolved, if necessary, by installation of new collimators in the dispersion suppressors of the collimation insertions in the LHC. This simplifies the discussion because the design emittances of Pb and proton beams in the LHC are such that both species have the same geometric beam sizes and considerations of optics and aperture can be taken over directly. The required parameters of the Pb beam are given in .

Energy	E_{Pb}	574. TeV
Energy per nucleon	E_N	2.76 TeV
No. of bunches	n_b	592
Ions per bunch	N_{Pb}	$7. \times 10^7$
Normalised emittance	ε_n	$1.5 \mu\text{m}$

Table 7.32: Parameters for the $^{208}\text{Pb}^{82+}$ beam according to Chapter 21 of [541].

Take electron beam parameters can be taken from Table 7.8.

Assume that the injection system can create an electron bunch train matching the 592-bunch train of Pb nuclei in the LHC so that every Pb bunch finds a collision partner in the electron beam. Assuming further that the hadron optics can be adjusted to match the sizes of the electron and Pb beams the luminosity can be expressed in terms of the interaction point optical functions and emittances of the electron beam. Since the e-A physics is focused on low- x these are taken from Table 7.14 describing the High Acceptance optics, which reduces the luminosity by a factor 2 as compared with the High-Luminosity optics. Thus

$$L_{eA} = \frac{n_b f_0 N_e N_{\text{Pb}}}{4\pi \sqrt{\beta_{xe}^* \varepsilon_x} \sqrt{\beta_{ye}^* \varepsilon_y}} = 2.66 \times 10^{28} \text{ cm}^{-2} \text{ s}^{-1} \quad (7.17)$$

corresponding to an electron-nucleon luminosity of

$$L_{eN} = AL_{eA} = 5.5 \times 10^{30} \text{ cm}^{-2} \text{ s}^{-1}. \quad (7.18)$$

It should be noted that Pb single-bunch intensities have already exceeded the design values by 70-80 %, albeit only in the simplified “Early” injection mode. Moreover, by the time the LHeC comes into operation, it is not unreasonable to hope that ways to increase the number of Pb bunches and perhaps to reduce their emittance (by cooling) may be implemented. Therefore, on an optimistic view, the luminosity could be a few times higher than the value quoted here.

In addition, the 592 electron bunches only use 21 % of the power installed for 2808 bunch operation. Increasing the single bunch intensity as far as possible to exploit this would provide a further gain in luminosity. Present experience with beam-beam effects in the LHC suggests that the additional intensity would not present any problem. Indeed the optimum may be to exploit the full RF power with a smaller number of Pb bunches.

Therefore 7.18 should be considered a very conservative estimate with a further order of magnitude in e-A luminosity probably well within reach of the LHeC.

7.10 Spin polarisation – an overview

Before describing concepts for attaining electron and positron spin polarisation for the ring-ring option of the LHeC we present a brief overview of the theory and phenomenology. We can then

5550 draw on this later as required. This overview is necessarily brief but more details can be found
 5551 in [542, 543].

5552 7.10.1 Self polarisation

5553 The spin polarisation of an ensemble of spin-1/2 fermions with the same energies travelling in
 5554 the same direction is defined as

$$\vec{P} = \langle \frac{2}{\hbar} \vec{\sigma} \rangle \quad (7.19)$$

5555 where $\vec{\sigma}$ is the spin operator in the rest frame and $\langle \rangle$ denotes the expectation value for the
 5556 mixed spin state. We denote the single-particle rest-frame expectation value of $\frac{2}{\hbar} \vec{\sigma}$ by \vec{S} and
 5557 we call this the “spin”. The polarisation is then the average of \vec{S} over an ensemble of particles
 5558 such as that of a bunch of particles.

5559 Relativistic e^\pm circulating in the (vertical) guide field of a storage ring emit synchrotron
 5560 radiation and a tiny fraction of the photons can cause spin flip from up to down and vice
 5561 versa. However, the up-to-down and down-to-up rates differ, with the result that in ideal
 5562 circumstances the electron (positron) beam can become spin polarised anti-parallel (parallel)
 5563 to the field, reaching a maximum polarisation, P_{st} , of $\frac{8}{5\sqrt{3}} = 92.4\%$. This, the Sokolov-Ternov
 5564 (S-T) polarising process, is very slow on the time scale of other dynamical phenomena occurring
 5565 in storage rings, and the inverse time constant for the exponential build up is [544]:

$$\tau_{st}^{-1} = \frac{5\sqrt{3}}{8} \frac{r_e \gamma^5 \hbar}{m_e |\rho|^3} \quad (7.20)$$

5566 where r_e is the classical electron radius, γ is the Lorentz factor, ρ is the radius of curvature in
 5567 the magnets and the other symbols have their usual meanings. The time constant is usually in
 5568 the range of a few minutes to a few hours.

5569 However, even without radiative spin flip, the spins are not stationary but precess in the
 5570 external fields. In particular, the motion of \vec{S} for a relativistic charged particle travelling in
 5571 electric and magnetic fields is governed by the Thomas-BMT equation $d\vec{S}/ds = \vec{\Omega} \times \vec{S}$ where s is
 5572 the distance around the ring [543, 545]. The vector $\vec{\Omega}$ depends on the electric (\vec{E}) and magnetic
 5573 (\vec{B}) fields, the energy and the velocity (\vec{v}) which evolves according to the Lorentz equation:

$$\vec{\Omega} = \frac{e}{m_e c} \left[- \left(\frac{1}{\gamma} + a \right) \vec{B} + \frac{a\gamma}{1+\gamma} \frac{1}{c^2} (\vec{v} \cdot \vec{B}) \vec{v} + \frac{1}{c^2} \left(a + \frac{1}{1+\gamma} \right) (\vec{v} \times \vec{E}) \right] \quad (7.21)$$

$$= \frac{e}{m_e c} \left[- \left(\frac{1}{\gamma} + a \right) \vec{B}_\perp - \frac{g}{2\gamma} \vec{B}_\parallel + \frac{1}{c^2} \left(a + \frac{1}{1+\gamma} \right) (\vec{v} \times \vec{E}) \right]. \quad (7.22)$$

5574 Thus $\vec{\Omega}$ depends on s and on the position of the particle $u \equiv (x, p_x, y, p_y, l, \delta)$ in the 6-D phase
 5575 space of the motion. The coordinate δ is the fractional deviation of the energy from the energy
 5576 of a synchronous particle (“the beam energy”) and l is the distance from the centre of the bunch.
 5577 The coordinates x and y are the horizontal and vertical positions of the particle relative to the
 5578 reference trajectory and $p_x = x', p_y = y'$ (except in solenoids) are their conjugate momenta.
 5579 The quantity g is the appropriate gyromagnetic factor and $a = (g - 2)/2$ is the gyromagnetic
 5580 anomaly. For e^\pm , $a \approx 0.0011596$. \vec{B}_\parallel and \vec{B}_\perp are the magnetic fields parallel and perpendicular
 5581 to the velocity.

5582 In a simplified picture, the majority of the photons in the synchrotron radiation do not cause
5583 spin flip but tend instead to randomise the e^\pm orbital motion in the (inhomogeneous) magnetic
5584 fields. Then, if the ring is insufficiently-well geometrically aligned and/or if it contains special
5585 magnet systems like the “spin rotators” needed to produce longitudinal polarisation at a detec-
5586 tor (see below), the spin-orbit coupling embodied in the Thomas-BMT equation can cause spin
5587 diffusion, i.e. depolarisation. Compared to the S-T polarising effect the depolarisation tends to
5588 rise very strongly with beam energy. The equilibrium polarisation is then less than 92.4% and
5589 will depend on the relative strengths of the polarisation and depolarisation processes. As we
5590 shall see later, even without depolarisation certain dipole layouts can reduce the equilibrium
5591 polarisation to below 92.4 %.

5592 Analytical estimates of the attainable equilibrium polarisation are best based on the Derbenev-
5593 Kondratenko (D-K) formalism [546, 547]. This implicitly asserts that the value of the equilib-
5594 rium polarisation in an e^\pm storage ring is the same at all points in phase space and is given
5595 by

$$P_{\text{dk}} = \mp \frac{8}{5\sqrt{3}} \frac{\oint ds \left\langle \frac{1}{|\rho(s)|^3} \hat{b} \cdot \left(\hat{n} - \frac{\partial \hat{n}}{\partial \delta} \right) \right\rangle_s}{\oint ds \left\langle \frac{1}{|\rho(s)|^3} \left(1 - \frac{2}{9} (\hat{n} \cdot \hat{s})^2 + \frac{11}{18} \left| \frac{\partial \hat{n}}{\partial \delta} \right|^2 \right) \right\rangle_s} \quad (7.23)$$

5596 where $\langle \rangle_s$ denotes an average over phase space at azimuth s , \hat{s} is the direction of motion and
5597 $\hat{b} = (\hat{s} \times \dot{\hat{s}})/|\dot{\hat{s}}|$. \hat{b} is the magnetic field direction if the electric field vanishes and the motion
5598 is perpendicular to the magnetic field. $\hat{n}(u; s)$ is a unit 3-vector field over the phase space
5599 satisfying the Thomas-BMT equation along particle trajectories $u(s)$ (which are assumed to be
5600 integrable), and it is 1-turn periodic: $\hat{n}(u; s + C) = \hat{n}(u; s)$ where C is the circumference of the
5601 ring.

5602 The field $\hat{n}(u; s)$ is a key object for systematising spin dynamics in storage rings. It provides
5603 a reference direction for spin at each point in phase space and it is now called the “*invariant*
5604 *spin field*” [543, 548, 549]. At zero orbital amplitude, i.e. on the periodic (“closed”) orbit, the
5605 $\hat{n}(0; s)$ is written as $\hat{n}_0(s)$. For e^\pm rings and away from spin-orbit resonances (see below), \hat{n}
5606 is normally at most a few milliradians away from \hat{n}_0 .

5607 A central ingredient of the D-K formalism is the implicit assumption that the e^\pm polarisation
5608 at each point in phase space is parallel to \hat{n} at that point. In the approximation that the particles
5609 have the same energies and are travelling in the same direction, the polarisation of a bunch
5610 measured in a polarimeter at s is then the ensemble average

$$\vec{P}_{\text{ens,dk}}(s) = P_{\text{dk}} \langle \hat{n} \rangle_s . \quad (7.24)$$

5611 In conventional situations in e^\pm rings, $\langle \hat{n} \rangle_s$ is very nearly aligned along $\hat{n}_0(s)$. The *value* of the
5612 ensemble average, $P_{\text{ens,dk}}(s)$, is essentially independent of s .

5613 Equation 7.23 can be viewed as having three components. The piece

$$P_{\text{bk}} = \mp \frac{8}{5\sqrt{3}} \frac{\oint ds \left\langle \frac{1}{|\rho(s)|^3} \hat{b} \cdot \hat{n} \right\rangle_s}{\oint ds \left\langle \frac{1}{|\rho(s)|^3} \left(1 - \frac{2}{9} (\hat{n} \cdot \hat{s})^2 \right) \right\rangle_s} \approx \mp \frac{8}{5\sqrt{3}} \frac{\oint ds \frac{1}{|\rho(s)|^3} \hat{b} \cdot \hat{n}_0}{\oint ds \frac{1}{|\rho(s)|^3} \left(1 - \frac{2}{9} n_{0s}^2 \right)} . \quad (7.25)$$

5614 gives the equilibrium polarisation due to radiative spin flip. The quantity n_{0s} is the component
5615 of \hat{n}_0 along the closed orbit. The subscript “bk” is used here instead of “st” to reflect the fact

5616 that this is the generalisation by Baier and Katkov [550, 551] of the original S-T expression to
 5617 cover the case of piecewise homogeneous fields. Depolarisation is then accounted for by including
 5618 the term with $\frac{11}{18}|\frac{\partial \hat{n}}{\partial \delta}|^2$ in the denominator. Finally, the term with $\frac{\partial \hat{n}}{\partial \delta}$ in the numerator is the
 5619 so-called kinetic polarisation term. This results from the dependence of the radiation power on
 5620 the initial spin direction and is not associated with spin flip. It can normally be neglected but
 5621 is still of interest in rings with special layouts.

5622 In the presence of radiative depolarisation the rate in Eq. 7.20 must be replaced by

$$\tau_{\text{dk}}^{-1} = \frac{5\sqrt{3} r_e \gamma^5 \hbar}{8 m_e C} \oint ds \left\langle \frac{1 - \frac{2}{9}(\hat{n} \cdot \hat{s})^2 + \frac{11}{18}|\frac{\partial \hat{n}}{\partial \delta}|^2}{|\rho(s)|^3} \right\rangle_s . \quad (7.26)$$

5623 This can be written in terms of the spin-flip polarisation rate, τ_{bk}^{-1} , and the depolarisation rate,
 5624 τ_{dep}^{-1} , as:

$$\frac{1}{\tau_{\text{dk}}} = \frac{1}{\tau_{\text{bk}}} + \frac{1}{\tau_{\text{dep}}} , \quad (7.27)$$

5625 where

$$\tau_{\text{dep}}^{-1} = \frac{5\sqrt{3} r_e \gamma^5 \hbar}{8 m_e C} \oint ds \left\langle \frac{\frac{11}{18}|\frac{\partial \hat{n}}{\partial \delta}|^2}{|\rho(s)|^3} \right\rangle_s \quad (7.28)$$

5626 and

$$\tau_{\text{bk}}^{-1} = \frac{5\sqrt{3} r_e \gamma^5 \hbar}{8 m_e C} \oint ds \left\langle \frac{1 - \frac{2}{9}(\hat{n} \cdot \hat{s})^2}{|\rho(s)|^3} \right\rangle_s . \quad (7.29)$$

5627 The time dependence for build-up from an initial polarisation P_0 to equilibrium is

$$P(t) = P_{\text{ens,dk}} \left[1 - e^{-t/\tau_{\text{ak}}} \right] + P_0 e^{-t/\tau_{\text{ak}}} . \quad (7.30)$$

5628 In perfectly aligned e^\pm storage rings containing just horizontal bends, quadrupoles and
 5629 accelerating cavities, there is no vertical betatron motion and $\hat{n}_0(s)$ is vertical. Since the spins
 5630 do not “see” radial quadrupole fields and since the electric fields in the cavities are essentially
 5631 parallel to the particle motion, \hat{n} is vertical, parallel to the guide fields and to $\hat{n}_0(s)$ at all u
 5632 and s . Then the derivative $\frac{\partial \hat{n}}{\partial \delta}$ vanishes and there is no depolarisation. However, real rings
 5633 have misalignments. Then there is vertical betatron motion so that the spins also see radial
 5634 fields which tilt them from the vertical. Moreover, $\hat{n}_0(s)$ is also tilted and the spins can couple
 5635 to vertical quadrupole fields too. As a result \hat{n} becomes dependent on u and “fans out” away
 5636 from $\hat{n}_0(s)$ by an amount which usually increases with the orbit amplitudes. Then in general
 5637 $\frac{\partial \hat{n}}{\partial \delta}$ no longer vanishes in the dipoles (where $1/|\rho(s)|^3$ is large) and depolarisation occurs. In the
 5638 presence of skew quadrupoles and solenoids and, in particular, in the presence of spin rotators,
 5639 $\frac{\partial \hat{n}}{\partial \delta}$ can be non-zero in dipoles even with perfect alignment. The deviation of \hat{n} from $\hat{n}_0(s)$, and
 5640 the depolarisation, tend to be particularly large near to the spin-orbit resonance condition

$$\nu_0 = k_0 + k_I Q_I + k_{II} Q_{II} + k_{III} Q_{III} . \quad (7.31)$$

5641 Here $k_0, k_I, k_{II}, k_{III}$ are integers, Q_I, Q_{II}, Q_{III} are the three tunes of the synchrotron
 5642 motion and ν_0 is the spin tune on the closed orbit, i.e. the number of precessions around $\hat{n}_0(s)$ per

5643 turn, made by a spin on the closed orbit ¹. In the special case, or in the approximation, of no
5644 synchrotron coupling one can make the associations: $I \rightarrow x$, $II \rightarrow y$ and $III \rightarrow s$, where,
5645 here, the subscript s labels the synchrotron mode. In a simple flat ring with no closed-orbit
5646 distortion, $\nu_0 = a\gamma$ where γ is the Lorentz factor for the nominal beam energy. For e^\pm , $a\gamma$ in-
5647 crements by 1 for every 441 MeV increase in beam energy. In the presence of misalignments and
5648 special elements like rotators, ν_0 is usually still approximately proportional to the beam energy.
5649 Thus an energy scan will show peaks in τ_{dep}^{-1} and dips in $P_{\text{ens,dk}}(s)$, namely at around the reso-
5650 nances. Examples can be seen in figures 7.45 and 7.46 below. The resonance condition expresses
5651 the fact that the disturbance to spins is greatest when the $|\vec{\Omega}(u; s) - \vec{\Omega}(0; s)|$ along a trajectory
5652 is coherent (“in step”) with the natural spin precession. The quantity $(|k_I| + |k_{II}| + |k_{III}|)$
5653 is called the order of the resonance. Usually, the strongest resonances are those for which
5654 $|k_I| + |k_{II}| + |k_{III}| = 1$, i.e. the first-order resonances. The next strongest are usually
5655 so-called “*synchrotron sideband resonances*” of parent first-order resonances, i.e. resonances
5656 for which $\nu_0 = k_0 \pm Q_{I,II,III} + \tilde{k}_{III} Q_{III}$ where \tilde{k}_{III} is an integer and mode III is associated
5657 with synchrotron motion. All resonances are due to the non-commutation of successive spin
5658 rotations in 3-D and they therefore occur even with purely linear orbital motion.

5659 We now list some key points.

- 5660 • The approximation on the r.h.s. of Eq. 7.25 makes it clear that if there are dipole magnets
5661 with fields not parallel to \hat{n}_0 , as is the case, for example, when spin rotators are used,
5662 then P_{bk} can be lower than the 92.4% achievable in the case of a simple ring with no
5663 solenoids and where all dipole fields and $\hat{n}_0(s)$ are vertical.
- 5664 • If, as is usual, the kinetic polarisation term makes just a small contribution, the above
5665 formulae can be combined to give

$$P_{\text{ens,dk}} \approx P_{\text{bk}} \frac{\tau_{\text{dk}}}{\tau_{\text{bk}}}. \quad (7.32)$$

5666 From Eq. 7.27 it is clear that $\tau_{\text{dk}} \leq \tau_{\text{bk}}$.

- 5667 • The underlying rate of polarisation due to the S-T effect, τ_{bk}^{-1} , increases with the fifth
5668 power of the energy and decreases with the third power of the bending radii.
- 5669 • It can be shown that as a general rule the “normalised” strength of the depolarisation,
5670 $\tau_{\text{dep}}^{-1}/\tau_{\text{bk}}^{-1}$, increases with beam energy according to a tune-dependent polynomial in even
5671 powers of the beam energy. So we expect that the attainable equilibrium polarisation
5672 decreases as the energy increases. This was confirmed LEP, where with the tools available,
5673 little polarisation could be obtained at 60 GeV [552].

5674 7.10.2 Suppression of depolarisation – spin matching

5675 Although the S-T effect offers a convenient way to obtain stored high energy e^\pm beams, it is
5676 only useful in practice if there is not too much depolarisation. Depolarisation can be significant
5677 if the ring is misaligned, if it contains spin rotators or if it contains uncompensated solenoids
5678 or skew quadrupoles. Then if $P_{\text{ens,dk}}$ and/or τ_{dk} are too small, the layout and the optic must

¹In fact the resonance condition should be more precisely expressed in terms of the so-called amplitude dependent spin tune [543, 548, 549]. But for typical e^\pm rings, the amplitude dependent spin tune differs only insignificantly from ν_0 .

5679 be adjusted so that $(|\frac{\partial \hat{n}}{\partial \delta}|)^2$ is small where $1/|\rho(s)|^3$ is large. So far it is only possible to do
5680 this within the linear approximation for spin motion. This technique is called “*linear spin*
5681 *matching*” and when successful, as for example at HERA [553], it immediately reduces the
5682 strengths of the first-order spin-orbit resonances. Spin matching requires two steps: “*strong*
5683 *synchrobeta spin matching*” is applied to the optics and layout of the perfectly aligned ring and
5684 then “*harmonic closed-orbit spin matching*” is applied to soften the effects of misalignments.
5685 This latter technique aims to adjust the closed orbit so as to reduce the tilt of \hat{n}_0 from the
5686 vertical in the arcs. Since the misalignments can vary in time and are usually not sufficiently
5687 well known, the adjustments are applied empirically while the polarisation is being measured.

5688 Spin matching must be approached on a case-by-case basis. An overview can be found
5689 in [542].

5690 7.10.3 Higher order resonances

5691 Even if the beam energy is chosen so that first-order resonances are avoided and in linear
5692 approximation $P_{\text{ens,dk}}$ and/or τ_{dk} are expected to be large, it can happen that that beam energy
5693 corresponds to a higher order resonance. As mentioned above, in practice the most intrusive
5694 higher order resonances are those for which $\nu_0 = k_0 \pm Q_k + \tilde{k}_s Q_s$ ($k \equiv I, II$ or III). These
5695 synchrotron sideband resonances of the first-order parent resonances are due to modulation by
5696 energy oscillations of the instantaneous rate of spin precession around \hat{n}_0 . The depolarisation
5697 rates associated with sidebands of isolated parent resonances ($\nu_0 = k_0 \pm Q_k$) are related to the
5698 depolarisation rates for the parent resonances. For example, if the beam energy is such that
5699 the system is near to a dominant Q_y resonance we can approximate τ_{dep}^{-1} in the form

$$\tau_{\text{dep}}^{-1} \propto \frac{A_y}{(\nu_0 - k_0 \pm Q_y)^2} . \quad (7.33)$$

5700 This becomes

$$\tau_{\text{dep}}^{-1} \propto \sum_{\tilde{k}_s=-\infty}^{\infty} \frac{A_y B_y(\zeta; \tilde{k}_s)}{(\nu_0 - k_0 \pm Q_y \pm \tilde{k}_s Q_s)^2}$$

5701 if the synchrotron sidebands are included. The quantity A_y depends on the beam energy and
5702 the optics and is reduced by spin matching. The proportionality constants $B_y(\zeta; \tilde{k}_s)$ are called
5703 *enhancement factors*, and they contain modified Bessel functions $I_{|\tilde{k}_s|}(\zeta)$ and $I_{|\tilde{k}_s|+1}(\zeta)$ which
5704 depend on Q_s and the energy spread σ_δ through the *modulation index* $\zeta = (a\gamma \sigma_\delta / Q_s)^2$. More
5705 formulae can be found in [554, 555].

5706 Thus the effects of synchrotron sideband resonances can be reduced by doing the spin
5707 matches described above. Note that these formulae are just meant as a guide since they are
5708 approximate and explicitly neglect interference between the first-order parent resonances. To
5709 get a complete impression, the Monte-Carlo simulation mentioned later must be used. The
5710 sideband strengths generally increase with the energy spread and the beam energy and the
5711 sidebands are a major contributor to the increase of $\tau_{\text{dep}}^{-1} / \tau_{\text{bk}}^{-1}$ with energy.

5712 7.10.4 Spin rotators

5713 The LHeC, like all analogous projects involving spin, needs longitudinal polarisation at the
5714 interaction point. However, if the S-T effect is to be the means of producing and maintaining

5715 the polarisation, then as is clear from Eq. 7.25, \hat{n}_0 must be close to vertical in most of the
 5716 dipoles. We have seen at Eq. 7.24 that the polarisation is essentially parallel to \hat{n}_0 . So to
 5717 get longitudinal polarisation at a detector, it must be arranged that \hat{n}_0 is longitudinal at the
 5718 detector but vertical in the rest of the ring. This can be achieved with magnet systems called
 5719 spin rotators which rotate \hat{n}_0 from vertical to longitudinal on one side of the detector and back
 5720 to vertical again on the other side.

5721 Spin rotators use sequences of magnets which generate large spin rotations around different
 5722 axes and exploit the non-commutation of successive large rotations around different axes. Ac-
 5723 cording to the T-BMT equation, the rate of spin precession in longitudinal fields is inversely
 5724 proportional to the energy. However, for motion perpendicular to a magnetic field spins precess
 5725 at a rate essentially proportional to the energy: $\delta\theta_{\text{spin}} = (a\gamma + 1)\delta\theta_{\text{orb}}$ in obvious notation.
 5726 Thus for the high-energy ring considered here, spin rotators should be based on dipoles as in
 5727 HERA [553]. In that case the rotators consisted of interleaved horizontal and vertical bending
 5728 magnets set up so as to generate interleaved, closed, horizontal and vertical bumps in the design
 5729 orbit. The individual orbit deflections were small but the spin rotations were of the order of a
 5730 radian. The success in obtaining high longitudinal polarisation at HERA attests to the efficacy
 5731 of such rotators.

5732 Eq. 7.25 shows that P_{bk} essentially scales with the cosine of the angle of tilt of \hat{n}_0 from the
 5733 vertical in the arc dipoles. Thus a rotation error resulting in a tilt of \hat{n}_0 of even a few degrees
 5734 would not reduce P_{bk} by too much. However, as was mentioned above, a tilt of \hat{n}_0 in the arcs
 5735 can lead to depolarisation. In fact the calculations below show that at 60 GeV, tilts of more
 5736 than a few milliradians cause significant depolarisation. Thus well-tuned rotators are essential
 5737 for maintaining polarisation.

5738 7.10.5 Calculations of the e^\pm polarisation in the LHeC

5739 As a first step towards assessing the attainable polarisation we have considered an early version
 5740 of the LHeC lattice: a flat ring with no rotators, no interaction point and no bypasses. The
 5741 tunes are $Q_x = 123.83$ and $Q_y = 85.62$. The horizontal emittance is 8 nm which agrees well
 5742 with the on-momentum emittance calculated by MadX. The ring is therefore typical of the
 5743 designs under consideration. With perfect alignment, \hat{n}_0 is vertical everywhere and there is no
 5744 vertical dispersion. The polarisation will then reach 92.4%. At ≈ 60 GeV, $\tau_{\text{bk}} \approx 60$ minutes.

5745 For the simple flat ring these values can be obtained by hand from Eq. 7.25 and Eq. 7.29.
 5746 However, in general, e.g., in the presence of misalignments or rotators, the calculation of po-
 5747 larisation requires special software and for this study, the thick-lens code SLICKTRACK was
 5748 used [556]. This essentially consists of four sections which carry out the following tasks:

- 5749 (1) Simulation of misalignments followed by orbit correction with correction coils.
- 5750 (2) Calculation of the optical properties of the beam and the beam sizes.
- 5751 (3) Calculation of $\partial\hat{n}/\partial\delta$ for linearised spin motion with the thick-lens version (SLICK [557])
 5752 of the SLIM algorithm [542].

5753 The equilibrium polarisation is then obtained from Eq. 7.23. This provides a first impres-
 5754 sion and only exhibits the first order resonances.

- 5755 (4) Calculation of the rate of depolarisation beyond the linear approximation of item 3.

5756 In general, the numerical calculation of the integrand in Eq. 7.28 beyond first order
 5757 represents a difficult computational problem. Therefore a pragmatic approach is adopted,
 5758 whereby the rate of depolarisation is obtained with a Monte-Carlo spin-orbit tracking
 5759 algorithm which includes radiation emission. The algorithm employs full 3-D spin motion
 5760 in order to see the effect of the higher order resonances. The Monte-Carlo algorithm
 5761 can also handle the effect on the particles and on the spins of the non-linear beam-beam
 5762 forces. An estimate of the equilibrium polarisation is then obtained from Eq. 7.32.

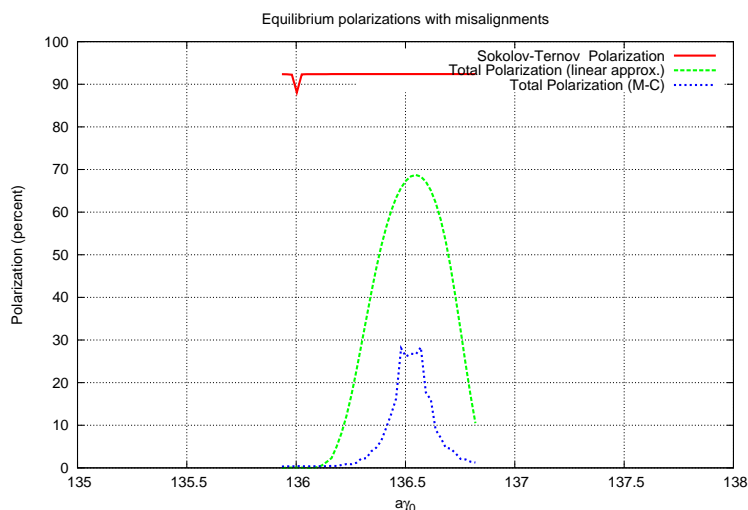


Figure 7.45: Estimated polarisation for the LHeC without spin rotators, $Q_s = 0.06$.

5763 Some basic features of the polarisation for the misaligned flat ring are shown in figures 7.45
 5764 and 7.46 where polarisations are plotted against $a\gamma$ around 60 GeV. In both cases the r.m.s.
 5765 vertical closed-orbit deviation is about $75\mu\text{m}$. This is obtained after giving the quadrupoles
 5766 r.m.s. vertical misalignments of $150\mu\text{m}$ and assigning a correction coil to every quadrupole.
 5767 The vector \hat{n}_0 has an r.m.s. tilt of about 4 milliradians from the vertical near $a\gamma = 136.5$. For
 5768 figure 7.45 the synchrotron tune, Q_s , is 0.06 so that $\xi \approx 5$. For figure 7.46, $Q_s = 0.1$ so that
 5769 $\xi \approx 1.9$.

5770 The red curves depict the polarisation due to the Sokolov-Ternov effect alone. The dip to
 5771 below 92.4 % at $a\gamma = 136$ is due to the characteristic very large tilt of \hat{n}_0 from the vertical at
 5772 an integer value of $a\gamma$. See [542].

5773 The green curves depict the equilibrium polarisation after taking into account the depolar-
 5774 isation associated with the misalignments and the consequent tilt of \hat{n}_0 . The polarisation is
 5775 calculated with the linearised spin motion as in item 3 above. In these examples the polarisation
 5776 reaches about 68 %. The strong fall off on each side of the peak is mainly due to first-order
 5777 “synchrotron” resonances $\nu_0 = k_0 \pm Q_s$. Since Q_s is small these curves are similar for the two
 5778 values of Q_s .

5779 The blue curves show the polarisation obtained as in item 4 above. Now, by going beyond
 5780 the linearisation of the spin motion, the peak polarisation is about 27 %. The fall from 68 %

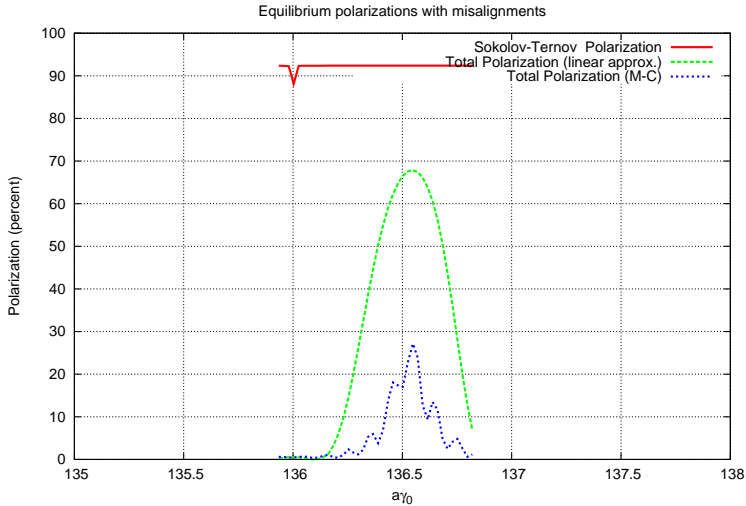


Figure 7.46: Estimated polarisation for the LHeC without spin rotators, $Q_s = 0.1$.

5781 is mainly due to synchrotron sideband resonances. With $Q_s = 0.06$ (Fig. 7.45) the resonances
 5782 are overlapping. With $Q_s = 0.1$, (Fig. 7.46) the sidebands begin to separate. In any case these
 5783 curves demonstrate the extreme sensitivity of the attainable polarisation to small tilts of \hat{n}_0
 5784 at high energy. Simulations for $Q_s = 0.1$ with a series of differently misaligned rings, all with
 5785 r.m.s. vertical closed-orbit distortions of about $75\mu\text{m}$, exhibit peak equilibrium polarisations
 5786 ranging from about about 10 % to about 40 %. Experience at HERA suggests that harmonic
 5787 closed-orbit spin matching can eliminate the cases of very low polarisation.

5788 Figure 7.47 shows a typical energy dependence of the peak equilibrium polarisation for a
 5789 fixed rf voltage and for one of the misaligned rings. The synchrotron tune varies from $Q_s = 0.093$
 5790 at 40 GeV to $Q_s = 0.053$ at 65 GeV due to the change in energy loss per turn. As expected
 5791 the attainable polarisation falls steeply as the energy increases. However, although with this
 5792 good alignment, a high polarisation is predicted at 45 GeV, τ_{bk} would be about 5 hours as at
 5793 LEP. A small τ_{bk} is not only essential for a programme of particle physics, but essential for the
 5794 application of empirical harmonic closed-orbit spin matching.

5795 As mentioned above it was difficult to get polarisation at 60 GeV at LEP. However, these cal-
 5796 culations suggest that by adopting the levels of alignment that are now standard for synchrotron-
 5797 radiation sources and by applying harmonic closed-orbit spin matching, there is reason to hope
 5798 that high polarisation in a flat ring can still be obtained.

5799 7.10.6 Further work

5800 We now list the next steps towards obtaining longitudinal polarisation at the interaction point.

- 5801 (1) A harmonic closed-orbit spin matching algorithm must be implemented for the LHeC so
 5802 try to correct the remaining tilt of \hat{n}_0 and thereby increase the equilibrium polarisation.

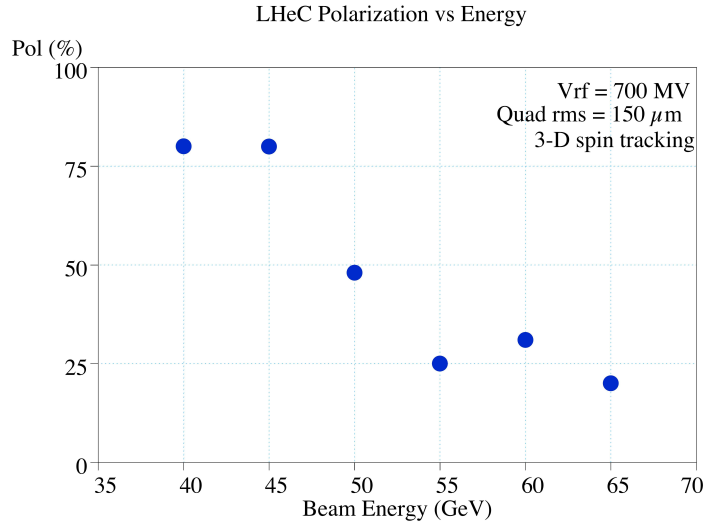


Figure 7.47: Equilibrium polarisation *vs* ring energy, full 3-D spin tracking results

5803 (2) Practical spin rotators must be designed and appropriate strong synchrobeta spin match-
 5804 ing must be implemented. The design of the rotators and spin matching are closely linked.
 5805 Some preliminary numerical investigations (below) show, as expected, that without this
 5806 spin matching, little polarisation will be obtained.

5807 (3) If synchrotron sideband resonances are still overwhelming after items 1 and 2 are imple-
 5808 mented, a scheme involving Siberian Snakes could be tried. Siberian Snakes are arrange-
 5809 ments of magnets which manipulate spin on the design orbit so that the closed-orbit spin
 5810 tune is independent of beam energy. Normally the spin tune is then $1/2$ and heuristic
 5811 arguments suggest that the sidebands should be suppressed. However, the two standard
 5812 schemes [558] either cause \hat{n}_0 to lie in the machine plane (just one snake) or ensure that it
 5813 is vertically up in one half of the ring and vertically down in the other half (two snakes). In
 5814 both cases Eq. 7.25 shows that P_{bk} vanishes. In principle, this problem can be overcome
 5815 for two snakes by again appealing to Eq. 7.25 and having short strong dipoles in the half
 5816 of the ring where \hat{n}_0 points vertically up and long weaker dipoles in the half of the ring
 5817 where \hat{n}_0 points vertically down (or vice versa). Of course, the dipoles must be chosen
 5818 so that the total bend angle is π in each half of the ring. Moreover, Eq. 7.25 shows that
 5819 the pure Sokolov-Ternov polarisation would be much less than 92.4%. One version of this
 5820 concept [559] uses a pair of rotators which together form a snake while a complementary
 5821 snake is inserted diametrically opposite to the interaction point. Each rotator comprises
 5822 interleaved strings of vertical and horizontal bends which not only rotate the spins from
 5823 vertical to horizontal, but also bring the e^\pm beams down to the level of the proton beam
 5824 and then up again. However, the use of short dipoles in the arcs increases the radiation
 5825 losses.

5826 Note that because of the energy dependence of spin rotations in the dipoles, \hat{n}_0 is vertical
5827 in the arcs at just one energy. This concept has been tested with SLICKTRACK but in
5828 the absence of a strong synchro-beta spin match, the equilibrium polarisation is very small
5829 as expected. Nevertheless the effects of misalignments and the tilt of \hat{n}_0 away from design
5830 energy, have been isolated by imposing an artificial spin match using standard facilities in
5831 SLICKTRACK. The snake in the arc has been represented as a thin element that has no
5832 influence on the orbital motion. Then it looks as if the synchrotron sidebands are indeed
5833 suppressed in the depolarisation associated with tilts of \hat{n}_0 . In contrast to the rotators in
5834 HERA, this kind of rotator allows only one helicity for electrons and one for positrons.

5835 (4) If a scheme can be found which delivers sufficient longitudinal polarisation, the effect of
5836 non-linear orbital motion, the effect of beam-beam forces and the effect of the magnetic
5837 fields of the detector must then be studied.

5838 7.10.7 Summary

5839 We have investigated the possibility of polarisation in the LHeC electron ring. At this stage of
5840 the work it appears that a polarisation of between 25 and 40% at 60 GeV can be reasonably
5841 aimed for, assuming the efficacy of harmonic closed-orbit spin matching. Attaining this degree
5842 of polarisation will require precision alignment of the magnets to better than $150\mu\text{m}$ rms, a
5843 challenging but achievable goal. The spin rotators necessary at the IP need to be properly
5844 spin matched to avoid additional depolarisation and this work is in progress. An interesting
5845 alternative involving the use of Siberian Snakes to try to avoid the depolarising synchrotron
5846 sideband resonances is being investigated. At present, this appears to potentially yield a similar
5847 degree of polarisation, at the expense of increased energy dissipation in the arcs arising from
5848 the required differences of the bending radii in the two halves of the machine.

5849 7.11 Integration and machine protection issues

5850 7.11.1 Space requirements

5851 The integration of an additional electron accelerator into the LHC is a difficult task. For
5852 once, the LEP tunnel was designed for LEP and not for the LHC, which is now using up almost
5853 all space in the tunnel. It is not evident, how to place another accelerator into the limited
5854 space. Secondly, the LHC will run for several years, before the installation of a second machine
5855 can start. Meanwhile the tunnel will be irradiated and all installation work must proceed as
5856 fast as possible to limit the collective and individual doses. The activation after the planned
5857 high-luminosity-run of the LHC and after one month of cool-down is expected to be around
5858 $0.5\text{--}1\mu\text{Sv/h}$ [?] on the proton magnets and many times more at exposed positions. Moreover
5859 the time windows for installation will be short and other work for the LHC will be going on,
5860 maybe with higher priority. Nevertheless, with careful preparation and advanced installation
5861 schemes an electron accelerator can be fitted in.

5862 So far all heavy equipment had to pass the UJ2, while entering the tunnel. There the
5863 equipment has to be moved from TI2, which comes in from the outside, to the transport zone
5864 of LHC, which is on the inner side of the ring. Clearly, everything above the cold dipoles has
5865 to be removed. The new access shafts and the smaller size of the equipment for the electron
5866 ring may render this operation unnecessary.

5867 **General** The new electron accelerator will be partially in the existing tunnel and partially in
5868 specially excavated tunnel sections and behind the experiments in existing underground areas.
5869 The excavation work will need special access shafts in the neighborhood of the experiments
5870 from where the stub-tunnels can be driven. The connection to the existing LEP tunnels will
5871 be very difficult. The new tunnel enters with a very small grazing angle, which means over a
5872 considerable length. Very likely the proton installation will have to be removed while the last
5873 meters of the new tunnel is bored.

5874 Figure 7.48 [?] shows a typical cross section of the LHC tunnel, where the two machines are
5875 together. The LHC dipole dominates the picture. The transport zone is indicated at the right
5876 (inside of the ring). The cryogenic installations (QRL) and various pipes and cable trays are on
5877 the left. The dipole cross section shows two concentric circles. The larger circle corresponds to
5878 the largest extension at the re-enforcement rings and marks a very localized space restriction on
5879 a very long object. The inner circle is relevant for items shorter than about 10 m longitudinally.
5880 A hatched square above the dipole labeled 30 indicates the area, which was kept free in the
5881 beginning for an electron machine. Unfortunately, the center of this space is right above the
5882 proton beam. Any additional machine will, however, have to avoid the interaction points 1
5883 and 5. In doing so additional length will be necessary, which can only be compensated for by
5884 shifting the electron machine in the arc about 60 cm to the inside (right). The limited space
5885 for compensation puts a constraint on the extra length created by the bypasses. The transport
5886 zone will, however, be affected. This requires an unconventional way to mount the electron
5887 machine. Nevertheless, there is clearly space to place an electron ring into the LHC, for most
5888 of the arc. Figure 7.49 gives the impression that the tunnel for most of its length is not too
5889 occupied.

5890 **In the arc** In Fig. 7.49 one sees the chain of superconducting magnets and in the far distances
5891 the *QRL Service Module* with its jumper, the cryogenic connection between the superconducting
5892 machine and the cryogenic distribution line. The service modules come always at the position
5893 of every second quadrupole and have a substantial length. The optics of the LHeC foresees
5894 no e-ring magnet at these positions. A photo of service modules in the workshop is shown in
5895 figure 7.50 (courtesy CERN). The picture 7.49, taken in sector 3, shows also the critical tunnel
5896 condition in this part of the machine. Clearly, heavy loads cannot be suspended from the tunnel
5897 ceiling. The limit is set to 100 kg per meter along the tunnel. The e-ring components have to
5898 rest on stands from the floor wherever possible. See ?? on page ?. Normally there is enough
5899 space between the LHC dipoles and the QRL to place a vertical 10 cm quadratic or rectangular
5900 support. Alternatively a steel arch bolted to the tunnel walls and resting on the floor can
5901 support the components from above. This construction is required wherever the space for a
5902 stand is not available.

5903 The electron machine, though partially in the transport zone, will be high up in the tunnel,
5904 high enough not to interfere with the transport of a proton magnet or alike. The transport
5905 of cryogenic equipment may need the full height. Transports of that kind will only happen,
5906 when part of the LHC are warmed up. This gives enough time to shift the electron ring to the
5907 outside by 30 cm, if the stands are prepared for this operation. The outside movement causes
5908 also a small elongation of the inter-magnet connections. This effect is locally so small that
5909 the expansion joints, required anyway, can accommodate it. One could even think of moving
5910 large sections of the e-machine outwards in a semi-automatic way. Thus the time to clear the
5911 transport path can be kept in the shadow of the warm-up and cool-down times.

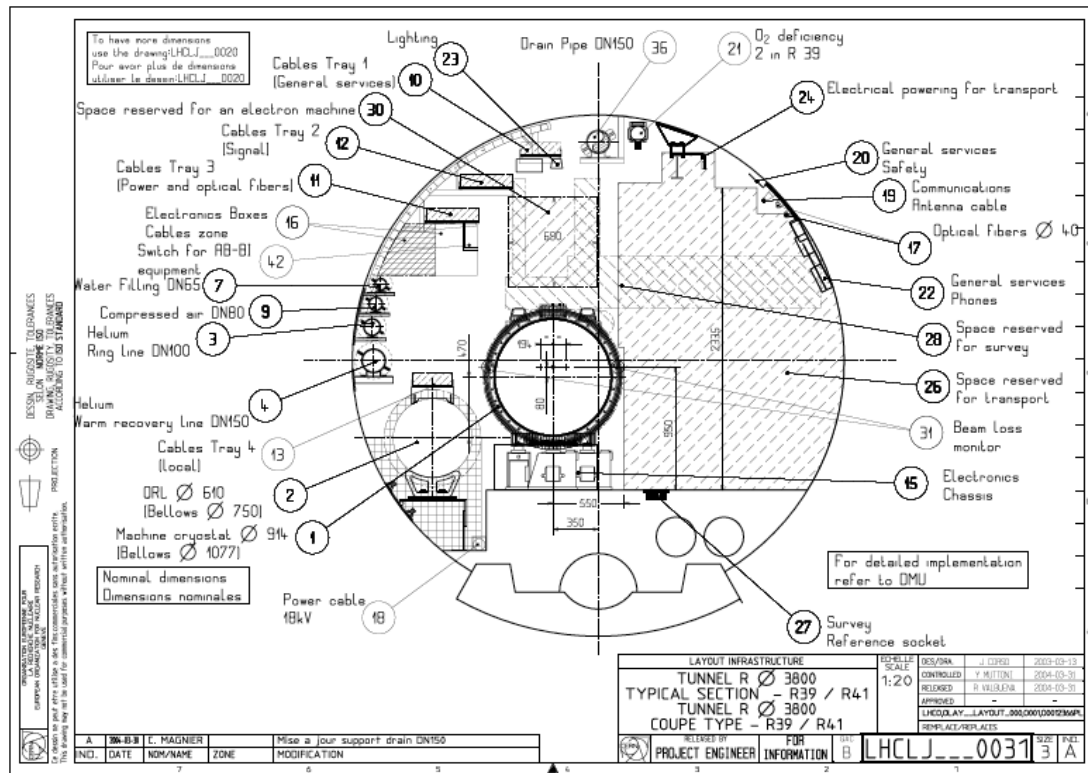


Figure 7.48: Cross-section of the LHC tunnel [?]

5912 **Dump area** The most important space constraints for the electron machine are in the proton
5913 dump area, the proton RF cavities, point 3, and in particular the collimator sections.

5914 Figure 7.51 [?] shows the situation at the dump kicker. The same area is also shown in a
5915 photo in Figure 7.52, while Figure 7.53 shows one of the outgoing dump-lines. The installation
5916 of the e-machine requires the proper rerouting of cables (which might be damaged by radiation
5917 and in need of exchange anyhow), eventually turning of pumps by 90 degrees or straight sections
5918 in the electron optics to bridge particularly difficult stretches with a beam pipe only.

5919 **Point 4, proton RF** The Figures 7.54 [?] and 7.55 illustrate the situation at the point 4,
5920 where the LHC RF is installed. Fortunately, the area is not very long. A short straight section
5921 could be created for the electron ring. This would allow to pass the area with just a shielded
5922 beam pipe.

5923 **Cryolink in point 3** The geography around point 3 did not permit to place there a cryoplant.
5924 The cryogenic cooling for the feedboxes is provided by a cryolink, as is shown in the figures
5925 7.56 and 7.57. In particular above the Q6 proton quadrupole changes have to be made. There
5926 are other interferences with the cryogenics, as for example at the DFBA's (main feedboxes). An
5927 example is shown in figure 7.58. Eventually the electron optics has to be adapted to allow the



Figure 7.49: View of sector 4.



Figure 7.50: Sideview of a QRL service module with the jumper

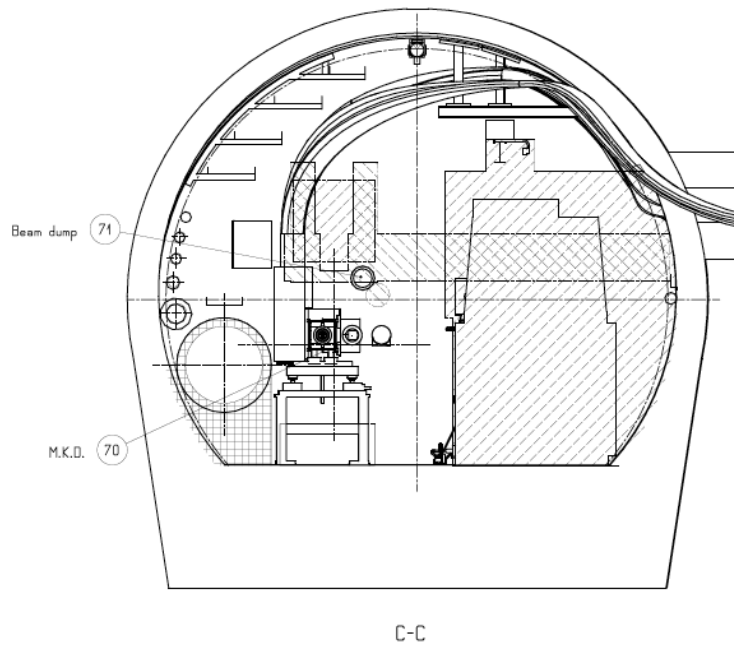


Figure 7.51: Dump kicker [?]

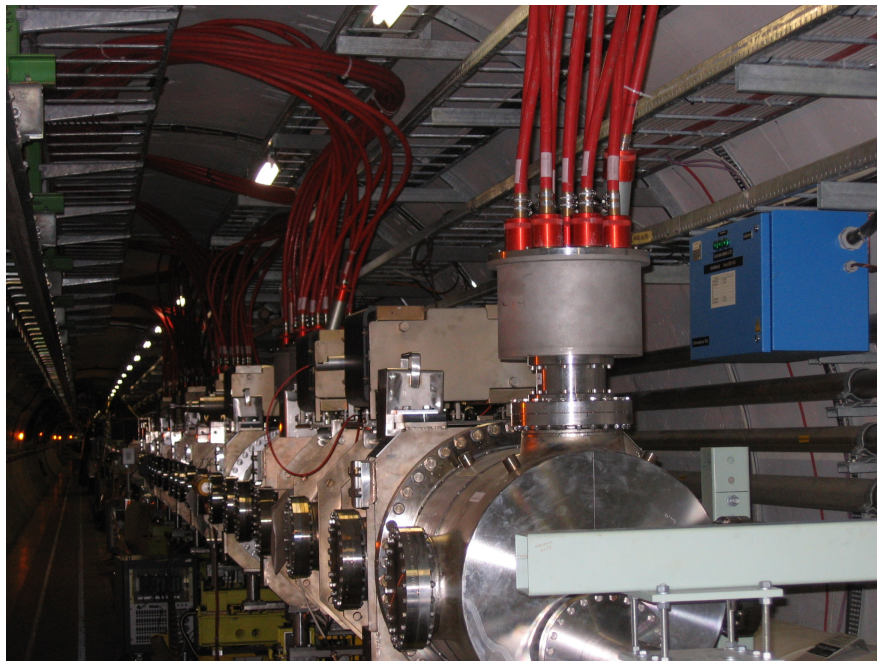


Figure 7.52: Dump kicker

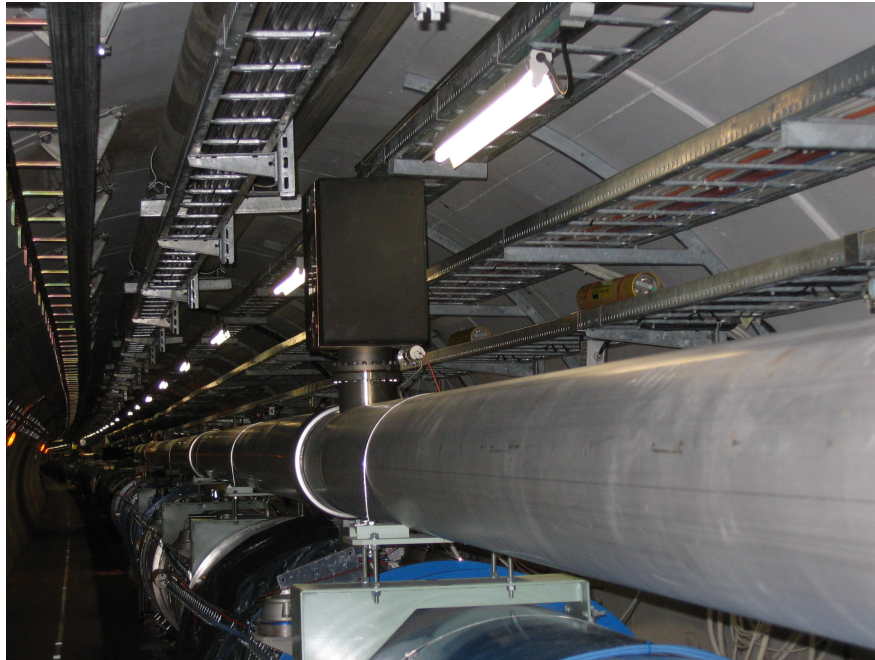
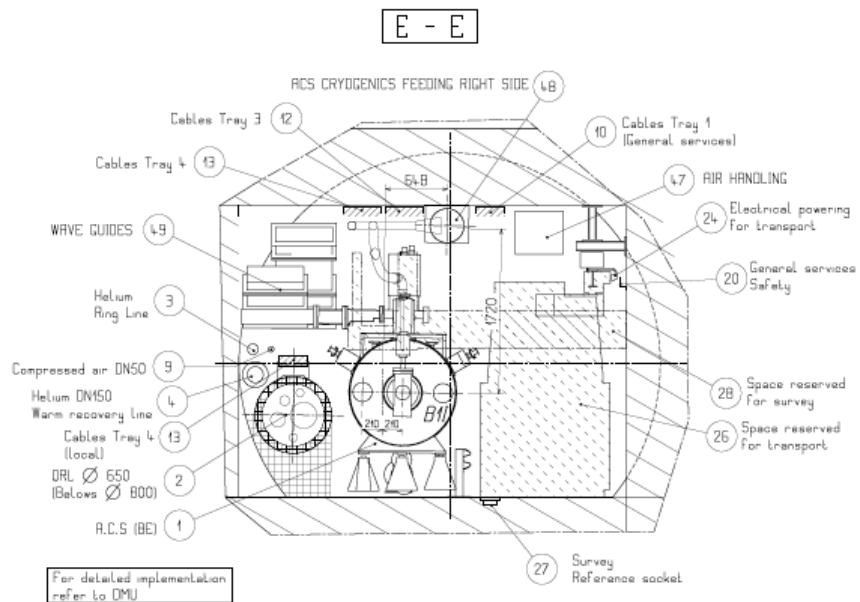


Figure 7.53: Dump line



h

Figure 7.54: Proton RF in point 4 [?]

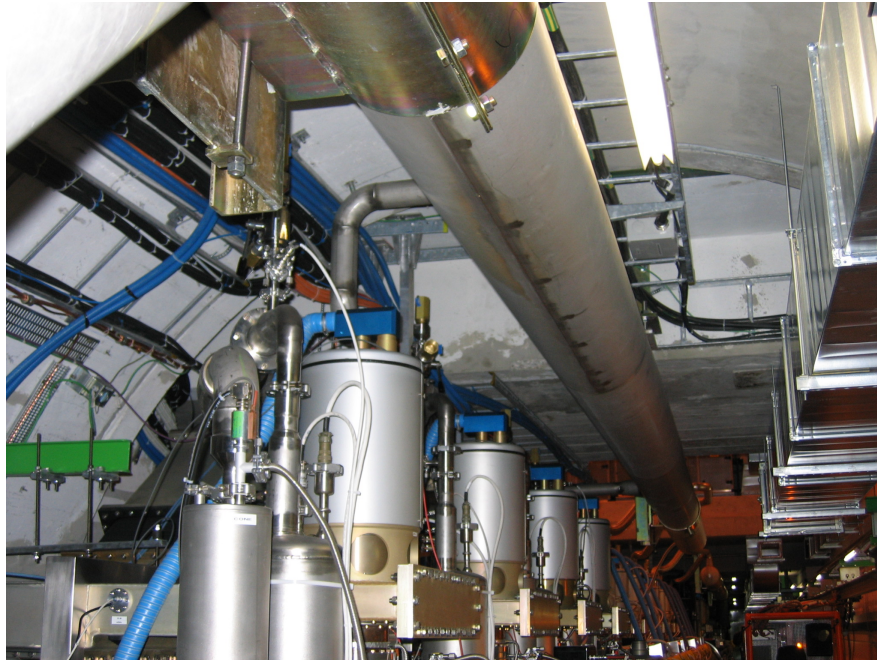


Figure 7.55: Point 4

5928 beampipe to pass the cables, which may have to be moved a bit.

5929 **Long straight section 7** An extra air duct is mounted in the long straight section 7 (LSS7)
5930 as is indicated in Fig. 7.59 avoiding the air pollution of the area above point 7. The duct
5931 occupies the space planned for the electron machine. The air duct has to be replaced by a
5932 slightly different construction mounted further outside (to the right in the figure). There are
5933 also air ducts at points 1 and 5, but they are not an issue. The electron ring is passing behind
5934 the experiments in these points

5935 **Proton collimation** The areas around point 3 (-62...+177m) and point 7 (-149...+205m) [?]
5936 are heavily used for the collimation of the proton beam. The high dose rate in the neighborhood
5937 of a collimator makes special precautions for the installation of new components or the exchange
5938 of a collimator necessary. Moreover, the collimator installation needs the full height of the tunnel.
5939 Hence, the e-installation has to be suspended from the re-enforced tunnel roof. The e-machine
5940 components must be removable and installable, easy and fast. The re-alignment must be well
5941 prepared and fast, possibly in a remote fashion. It is uncommon to identify fast mounting and
5942 demounting as a major issue. However, with sufficient emphasis during the R&D phase of the
5943 project, this problem can be solved.

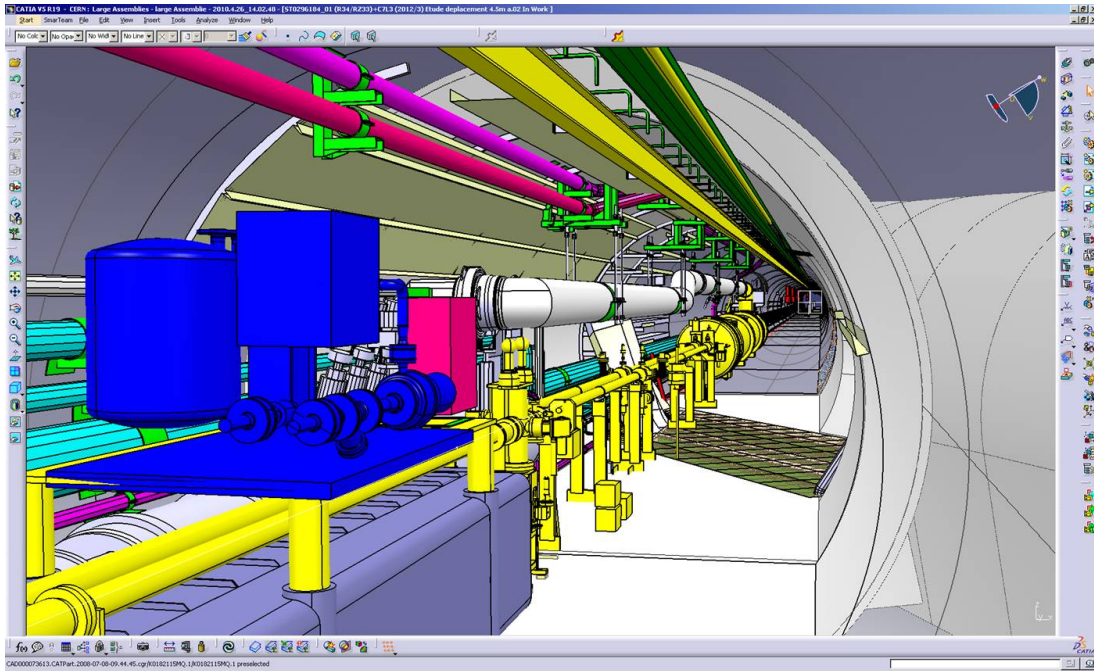


Figure 7.56: The cryogenic connection in point 3

5944 **7.11.2 Impact of the synchrotron radiation on tunnel electronics**

5945 It is assumed that the main power converters of the LHC will have been moved out of the RRs
 5946 because of the single event upsets, caused by proton losses.

5947 The synchrotron radiation has to be intercepted at the source, as in all other electron
 5948 accelerators. A few millimeter of lead are sufficient for the relatively low (critical) energies
 5949 around 100 to 200 keV. The K-edge of lead is at 88 keV, the absorption coefficient is above
 5950 80/cm at this energy [?]. One centimeter of lead is sufficient to suppress 300 keV photons by
 5951 a factor of 100. Detailed calculations of the optics will determine the amount of lead needed
 5952 in the various places. The primary shielding needs an effective water cooling to avoid partial
 5953 melting of the lead.

5954 The electronics is placed below the proton magnets. Only backscattered photons with
 5955 correspondingly lower energy will reach the electronics. If necessary, a few millimeter of extra
 5956 shielding could be added here.

5957 The risk for additional single event upsets due to synchrotron radiation is negligible.

5958 **7.11.3 Compatibility with the proton beam loss system**

5959 The proton beam loss monitoring system works very satisfactory. It has been designed to
 5960 detect proton losses by observing secondaries at the outside of the LHC magnets. The sensors
 5961 are ionization chambers. Excessive synchrotron radiation (SR) background will presumably
 5962 trigger the system and dump the proton beam. The SR background at the monitors has to
 5963 be reduced by careful shielding of either the monitors or the electron ring. Alternatively, the

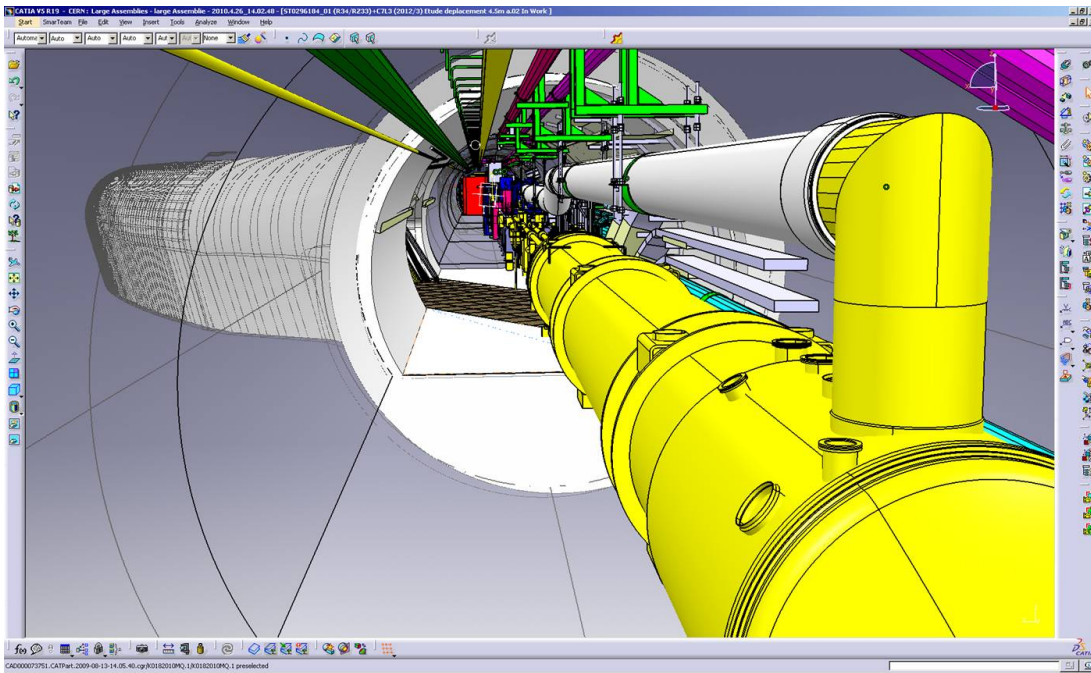


Figure 7.57: The cryogenic connection in point 3

5964 impact of the photon background can be reduced by using a new loss monitoring system which
 5965 is based on coincidences (as was done elsewhere [?]).

5966 7.11.4 Space requirements for the electron dump

5967 7.11.5 Protection of the p-machine against heavy electron losses

5968 The existing proton loss detectors are placed, as mentioned above, at the LHC magnets. The
 5969 trigger threshold requires certain number of detectors to be hit by a certain number of particles.
 5970 The assumption is that the particles come from the inside of the magnets and the particle density
 5971 there is much higher. Electron losses, creating a similar pattern in the proton loss detectors
 5972 will result in a much lower particle density in the superconducting coils. Hence, still tolerable
 5973 electron losses will unnecessarily trigger the proton loss system and dump the proton beam.
 5974 The proton losses are kept at a low level by installing an advanced system of collimators and
 5975 masks. Fast changes of magnet currents, which will result in a beam loss, are detected. A
 5976 similar system is required for the electrons. An electron loss detection system, like the one
 5977 mentioned in Ref. [?], combined with the proton loss system can be used to identify the source
 5978 of the observed loss pattern and to minimize the electron losses by improved operation. It
 5979 seems very optimistic to think of a hardware discrimination system, which determines very fast
 5980 the source of the loss and acts correspondingly. Such a system could be envisaged only after
 5981 several years of running.

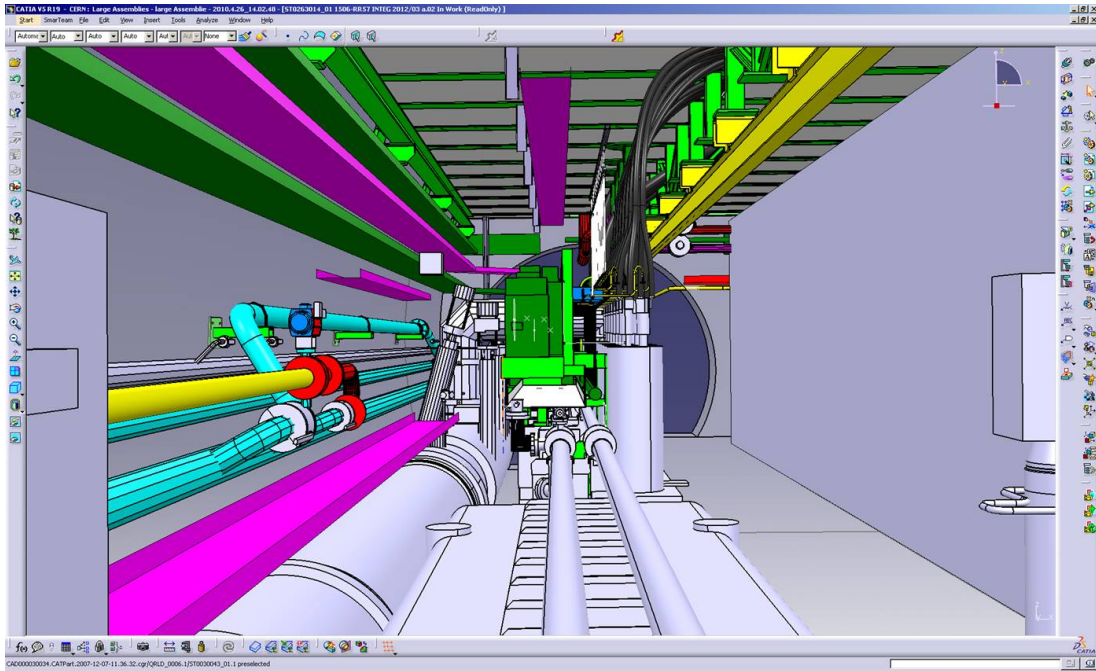


Figure 7.58: A typical big current feedbox (DFBA)

5982 **7.11.6 How to combine the Machine Protection of both rings?**

5983 The existing machine-protection system combines many different subsystems. The proton loss
 5984 system, the quench detection system, cryogenics, vacuum, access, and many other subsystems
 5985 may signal a dangerous situation. This requirement lead to a very modular architecture, which
 5986 could be expanded to include the electron accelerator.

5987 **7.12 LHeC Injector for the Ring-Ring option**

5988 Figure 10.27 shows the layout of the LPI (LEP Pre-Injector) as it was working in 2000.

5989 LPI was composed of the LIL (LEP Injector Linac) and the EPA (Electron Positron Accu-
 5990 mulator).

5991 Table 10.18 gives the beam characteristics at the end of LIL.

Beam energy	200 to 700 MeV
Charge	5×10^8 to $2 \times 10^{10} e^-$ / pulse
Pulse length	10 to 40 ns (FWHM)
Repetition frequency	1 to 100 Hz
Beam sizes (rms)	3 mm

Table 7.33: LIL beam parameters.

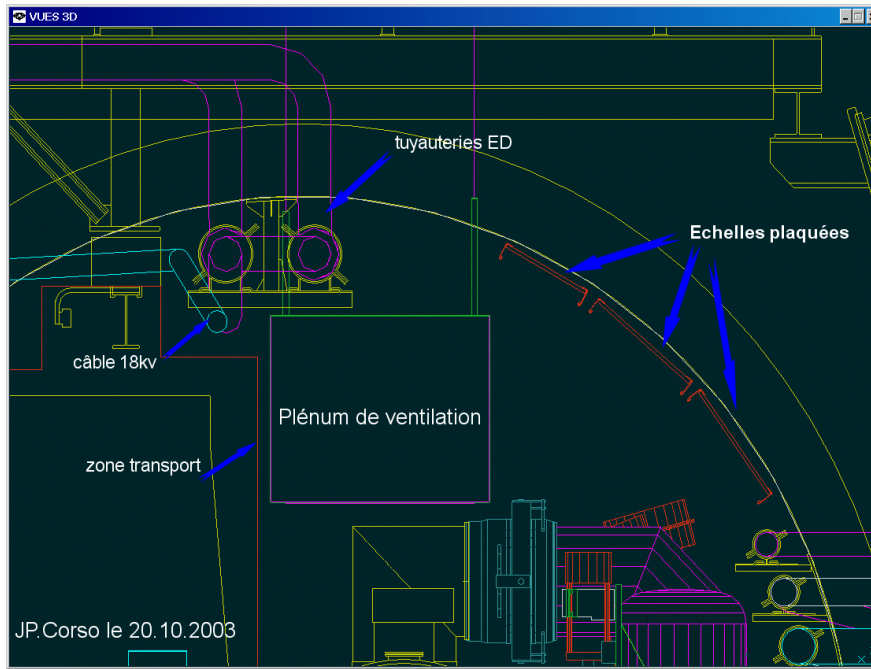


Figure 7.59: Air-duct in LSS7 [?]

5992 Figure 10.28 shows an electron beam profile at the end of LIL (500 MeV).
 5993 Table 10.19 gives the electron and positron beam parameters at the exit of EPA.

Energy	200 to 600 MeV
Charge	up to $4.5 \times 10^{11} e^{\pm}$
Intensity	up to 0.172 A
Number of buckets	1 to 8
Emittance	0.1 mm.mrad
Tune	$Q_x = 4.537, Q_y = 4.298$

Table 7.34: The electron and positron beam parameters at the exit of EPA.

5994 In summary, the LPI characteristics fulfils completely the requested performance for the
 5995 LHeC injector based on Ring-Ring option.

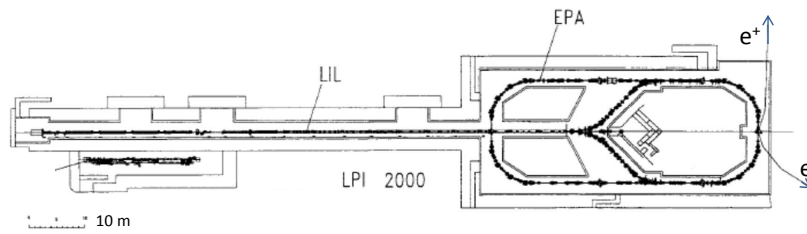


Figure 7.60: Layout of the LPI in 2000.

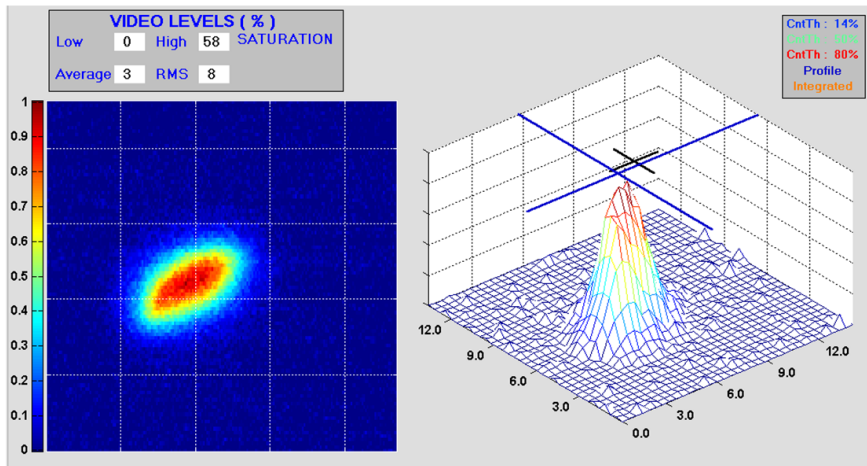


Figure 7.61: Electron beam profile at 500 MeV.

Chapter 8

Linac-Ring Collider

8.1 Basic Parameters and Configurations

8.1.1 General Considerations

A high-energy electron-proton collider can be realized by accelerating electrons (or positrons) in a linear accelerator (linac) to 60–140 GeV and colliding them with the 7-TeV protons circulating in the LHC. Except for the collision point and the surrounding interaction region, the tunnel and the infrastructure for such a linac are separate and fully decoupled from the LHC operation, from the LHC maintenance work, and from other LHC upgrades (e.g., HL-LHC and HE-LHC).

The technical developments required for this type of collider can both benefit from and be used for many future projects. In particular, to deliver a long or continuous beam pulse, as required for high luminosity, the linac must be based on superconducting (SC) radiofrequency (RF) technology. The development and industrial production of its components can exploit synergies with numerous other advancing SC-RF projects around the world, such as the DESY XFEL, eRHIC, ESS, ILC, CEBAF upgrade, CESR-ERL, JLAMP, and the CERN HP-SPL.

For high luminosity operation at a beam energy of 50–70 GeV the linac should be operated in continuous wave (CW) mode, which restricts the maximum RF gradient through the associated cryogenics power, to a value of about 20 MV/m or less. In order to limit the active length of such a linac and to keep its construction and operating costs low, the linac should, and can, be recirculating. For the sake of energy efficiency and to limit the overall site power, while boosting the luminosity, the SC recirculating CW linac can be operated in energy-recovery (ER) mode. A 60-GeV recirculating energy-recovery linac represents the baseline scenario for a linac-ring LHeC.

Electron-beam energies higher than 70 GeV, e.g. 140 GeV, can be achieved by a pulsed SC linac, similar to the XFEL, ILC or SPL. In this case the accelerating gradient can be larger than for CW operation, i.e. above 30 MV/m, which minimizes the total length, but recirculation is no longer possible at this beam energy due to prohibitively high synchrotron-radiation energy losses in any return arc of reasonable dimension. As a consequence the standard energy recovery scheme using recirculation cannot be implemented and the luminosity of such a higher-energy lepton-hadron collider would be more than an order of magnitude lower than the one of the lower-energy CW ERL machine, at the same wall-plug power. An advanced energy-recovery option for the pulsed straight linac would employ two-beam technology, as developed for CLIC,

6028 in this case based on a decelerating linac and multiple energy-transfer beams, to boost the
 6029 luminosity potentially by several orders of magnitude [560]. Such novel type of energy-recovery
 6030 linac could later be converted into a linear collider, or vice versa.

6031 While for a linac it is straightforward to deliver a 80–90% polarized electron beam, the
 6032 production of a sufficient number of positrons is extremely challenging for a linac-ring collider.
 6033 A conceivable path towards decent proton-positron luminosities would include a recycling of
 6034 the spent positrons, together with the recovery of their energy.

6035 The development of a CW SC recirculating energy-recovery linac (ERL) for LHeC would
 6036 prepare the ground, the technology and the infrastructure for many possible future projects,
 6037 e.g., for an International Linear Collider, for a Muon Collider¹, for a neutrino factory, or for
 6038 a proton-driven plasma wake field accelerator. A ring-linac LHeC would, therefore, promote
 6039 any conceivable future high-energy physics project, while pursuing an attractive forefront high-
 6040 energy physics programme in its own right.

6041 8.1.2 ERL Performance and Layout

6042 Particle physics imposes the following performance requirements. The lepton beam energy
 6043 should be 60 GeV or higher and the electron-proton luminosity of order $10^{33} \text{ cm}^{-2}\text{s}^{-1}$. Positron-
 6044 proton collisions are also required, with at least a few percent of the electron-proton luminosity.
 6045 Since the LHeC should operate simultaneously with LHC pp physics, it should not degrade
 6046 the pp luminosity. Both electron and positron beams should be polarized. Lastly, the detector
 6047 acceptance should extend down to 1° or less. In addition, the total electrical power for the
 6048 lepton branch of the LHeC collider should stay below 100 MW.

6049 For round-beam collisions, the luminosity of the linac-ring collider [561] is written as

$$L = \frac{1}{4\pi e} \frac{N_{b,p}}{\epsilon_p} \frac{1}{\beta_p^*} I_e H_{hg} H_D, \quad (8.1)$$

6050 where e denotes the electron charge, $N_{b,p}$ the proton bunch population, β_p^* the proton IP beta
 6051 function, I_e the average electron beam current, H_{hg} the geometric loss factor arising from
 6052 crossing angle and hourglass effect, and H_D the disruption enhancement factor due to the
 6053 electron pinch in collision, or luminosity reduction factor from the anti-pinch in the case of
 6054 positrons. In the above formula, it is assumed that the electron bunch spacing is a multiple of
 6055 the proton beam bunch spacing. The latter could be equal to 25, 50 or 75 ns, without changing
 6056 the luminosity value.

6057 The ratio $N_{b,p}/\epsilon_p$ is also called the proton beam brightness. Among other constraints, the
 6058 LHC beam brightness is limited by the proton-proton beam-beam limit. For the LHeC design
 6059 we assume the brightness value obtained for the ultimate bunch intensity, $N_{p,p} = 1.7 \times 10^{11}$,
 6060 and the nominal proton beam emittance, $\epsilon_p = 0.5 \text{ nm}$ ($\gamma\epsilon_p = 3.75 \text{ }\mu\text{m}$). This corresponds
 6061 to a total pp beam-beam tune shift of 0.01. More than two times higher values have already
 6062 been demonstrated, with good pp luminosity lifetime, during initial LHC beam commissioning,
 6063 indicating a potential for higher ep luminosity.

6064 To maximize the luminosity the proton IP beta function is chosen as 0.1 m. This is consider-
 6065 able smaller than the 0.55 m for the pp collisions of the nominal LHC. The reduced beta function
 6066 can be achieved by reducing the free length between the IP and the first proton quadrupole (10

¹The proposed Muon Collider heavily relies on SC recirculating linacs for muon acceleration as well as on a SC-linac proton driver.

6067 m instead of 23 m), and by squeezing only one of the two proton beams, namely the one colliding
 6068 with the leptons, which increases the aperture available for this beam in the last quadrupoles.
 6069 In addition, we assume that the final quadrupoles could be based on Nb₃Sn superconductor
 6070 technology instead of Nb-Ti. The critical field for Nb₃Sn is almost two times higher than for
 6071 Nb-Ti, at the same temperature and current density, allowing for correspondingly larger aper-
 6072 ture and higher quadrupole gradient. Nb₃Sn quadrupoles are presently under development for
 6073 the High-Luminosity LHC upgrade (HL-LHC).

6074 The geometric loss factor H_{hg} needs to be optimized as well. For round beams with $\sigma_{z,p} \gg$
 6075 $\sigma_{z,e}$ (well fulfilled for $\sigma_{z,p} \approx 7.55$ cm, $\sigma_{z,e} \approx 300$ μ m) and $\theta_c \ll 1$, it can be expressed as²

$$H_{hg} = \frac{\sqrt{\pi} z e^{z^2} \operatorname{erfc}(z)}{S}, \quad (8.2)$$

6076 where

$$z \equiv 2 \frac{(\beta_e^*/\sigma_{z,p})(\epsilon_e/\epsilon_p)}{\sqrt{1 + (\epsilon_e/\epsilon_p)^2}} S$$

6077 and

$$S \equiv \sqrt{1 + \frac{\sigma_{x,p}^2 \theta_c^2}{8\sigma_p^{*2}}}.$$

6078 Luminosity loss from a crossing angle is avoided by head-on collisions. The luminosity loss
 6079 from the hourglass effect, due to the long proton bunches and potentially small electron beta
 6080 functions, is kept small, thanks to a “small” linac electron beam emittance of 0.43 nm ($\gamma\epsilon_e =$
 6081 50 μ m). We note that the assumed electron-beam emittance, though small when compared
 6082 with a storage ring of comparable energy, is still very large by linear-collider standards.

6083 The disruption enhancement factor for electron-proton collisions is about $H_D \approx 1.35$, ac-
 6084 cording to Guinea-Pig simulations [564] and a simple estimate based on the fact that the average
 6085 rms size of the electron beam during the collision approaches a value equal to $1/\sqrt{2}$ of the pro-
 6086 ton beam size. This additional luminosity increase from disruption is not taken into account in
 6087 the numbers given below. On the other hand, for positron-proton collisions the disruption of
 6088 the positrons leads to a significant luminosity reduction, by roughly a factor $H_D \approx 0.3$, similar
 6089 to the case of electron-electron collisions [565].

6090 The final parameter determining the luminosity is the average electron (or positron) beam
 6091 current I_e . It is closely tied to the total electrical power available (taken to be 100 MW).

6092 Crossing Angle and IR Layout

6093 The colliding electron and proton beams need to be separated by 7 cm at a distance of 10 m
 6094 from the IP in order to enter through separate holes in the first proton quadrupole magnet.
 6095 This separation could be achieved with a crossing angle of 7 mrad and crab cavities. The
 6096 required crab voltage would, however, need to be of order 200 MV, which is 20–30 times the
 6097 voltage needed for pp crab crossing at the HL-LHC. Therefore, crab crossing is not considered

²The derivation of this formula is similar to the one for the LHC in Ref. [562], with the difference that here the two beams have different emittances and IP beta functions, and the electron bunch length is neglected. Curves obtained with formula (8.2) were first reported in [563].

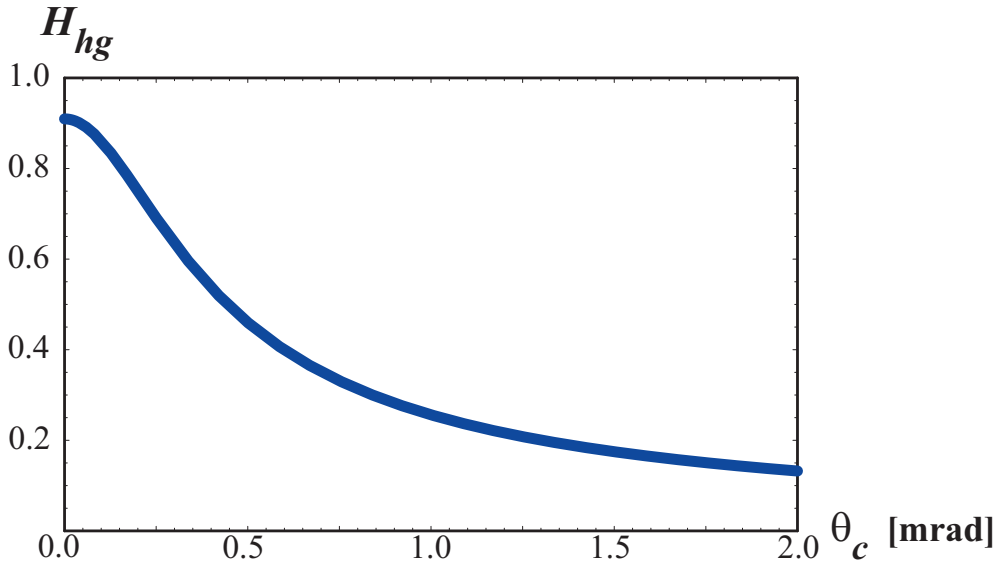


Figure 8.1: Geometric luminosity loss factor H_{hg} , (8.2), as a function of the total crossing angle

6098 an option for the L-R LHeC. Without crab cavities, any crossing angle should be smaller than
 6099 0.3 mrad, as is illustrated in Fig. 8.1. Such small a crossing angle is not useful, compared
 6100 with the 7 mrad angle required for the separation. The R-L interaction region (IR), therefore,
 6101 uses detector-integrated dipole fields around the collision point, to provide head-on ep collisions
 6102 ($\theta_c = 0$ mrad) and to separate the beams by the required amount. A dipole field of about 0.3
 6103 T over a length of ± 9 m accomplishes these goals.

6104 The IR layout with separation dipoles and crossing angle is sketched in Fig. 8.2. Significant
 6105 synchrotron radiation, with 48 kW average power, and a critical photon energy of 0.7 MeV, is
 6106 emitted in the dipole fields. A large portion of this radiation is extracted through the electron
 6107 and proton beam pipes. The SC proton magnets can be protected against the radiation heat
 6108 load by an absorber placed in front of the first quadrupole and by a liner inside the beam pipe.
 6109 Backscattering of synchrotron radiation into the detector is minimized by shaping the surface
 6110 of absorbers and by additional masking.

6111 The separation dipole fields modify, and enhance, the geometric acceptance of the detector.
 6112 Figure 8.3 illustrates that scattered electrons with energies of 10–50 GeV might be detected at
 6113 scattering angles down to zero degrees.

6114 **Electron Beam and the Case for Energy Recovery**

6115 The electron-beam emittance and the electron IP beta function are not critical, since the proton
 6116 beam size is large by electron-beam standards (namely about $7 \mu\text{m}$ rms compared with nm
 6117 beam-sizes for linear colliders). The most important parameter for high luminosity is the
 6118 average beam current, I_e , which linearly enters into the luminosity formula (8.1). In addition
 6119 to the electron beam current, also the bunch spacing (which should be a multiple of the LHC 25-
 6120 ns proton spacing) and polarization (80–90% for the electrons) need to be considered. Having
 6121 pushed all other parameters in (8.1), Fig. 8.4 illustrates that an average electron current of

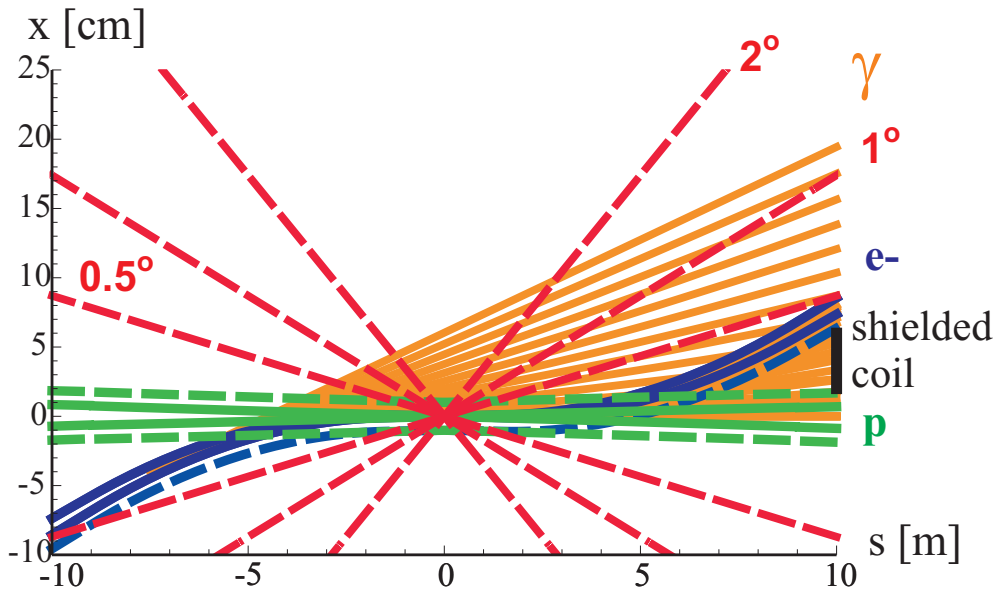


Figure 8.2: Linac-ring interaction-region layout. Shown are the beam envelopes of 10σ (electrons) [solid blue] or 11σ (protons) [solid green], the same envelopes with an additional constant margin of 10 mm [dashed], the synchrotron-radiation fan [orange], the approximate location of the magnet coil between incoming protons and outgoing electron beam [black], and a “1 degree” line.

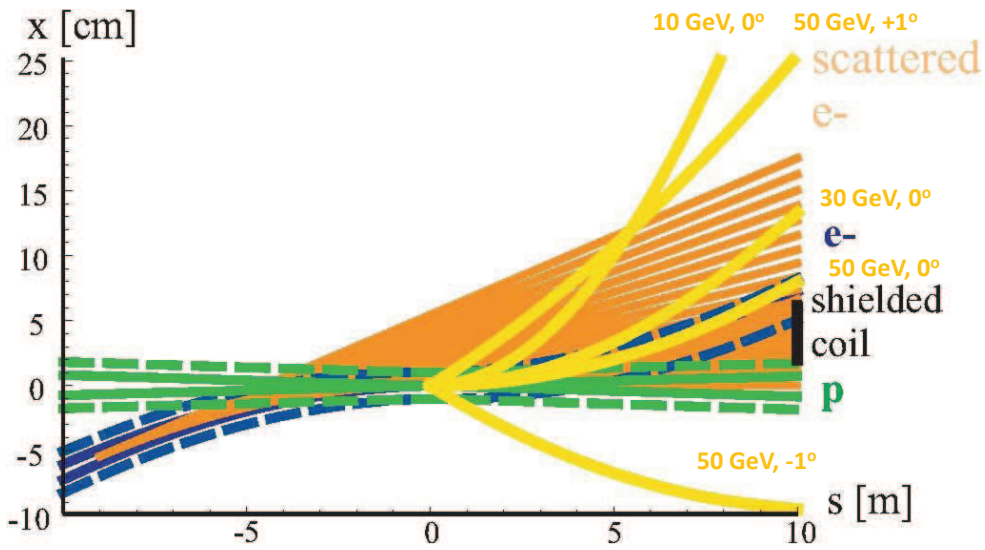


Figure 8.3: Example trajectories in the detector dipole fields for electrons of different energies and scattering angles, demonstrating an enhancement of the detector acceptance by the dipoles.

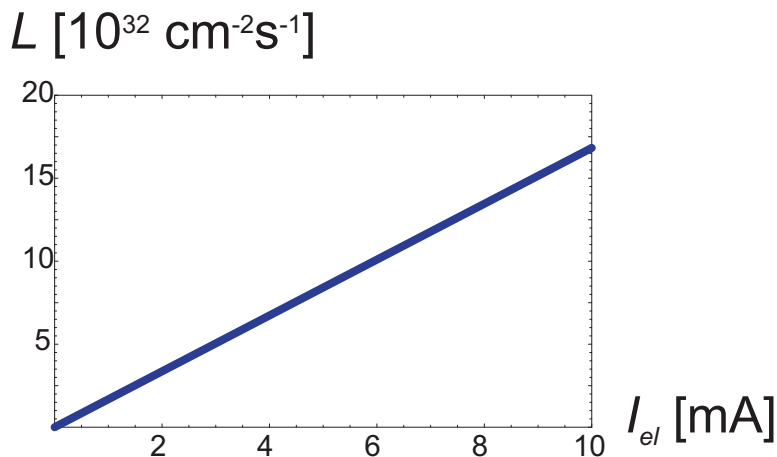


Figure 8.4: Linac-ring luminosity versus average electron beam current, according to (8.1).

6122 about 6.4 mA is required to reach the target luminosity of $10^{33} \text{ cm}^{-2} \text{ s}^{-1}$.

6123 For comparison, the CLIC main beam has a design average current of 0.01 mA [566], so
 6124 that it falls short by a factor 600 from the LHeC requirement. For other applications it has
 6125 been proposed to raise the CLIC beam power by lowering the accelerating gradient, raising the
 6126 bunch charge by a factor of two, and increasing the repetition rate up to three times, which
 6127 raises the average beam current by a factor 6 to about 0.06 mA (this type of CLIC upgrade
 6128 is described in [232]). This ultimate CLIC main beam current is still a factor 100 below the
 6129 LHeC target. On the other hand, the CLIC drive beam would have a sufficiently high current,
 6130 namely 30 mA, but at the low energy 2.37 GeV, which would not be useful for high-energy ep
 6131 physics. Due to this low an energy, also the drive beam power is still a factor of 5 smaller than
 6132 the one required by LHeC. Finally, the ILC design current is about 0.04 mA [567], which also
 6133 falls more than a factor 100 short of the goal.

6134 Fortunately, SC linacs can provide higher average current, e.g. by increasing the linac duty
 6135 factor 10–100 times, or even running in continuous wave (CW) mode, at lower accelerating
 6136 gradient. Example average currents for a few proposed designs illustrate this point: The CERN
 6137 High-Power Superconducting Proton Linac aims at about 1.5 mA average current (with 50 Hz
 6138 pulse rate) [568], the Cornell ERL design at 100 mA (cw) [569], and the eRHIC ERL at about
 6139 50 mA average current at 20 GeV beam energy (cw) [?]. All these designs are close to, or
 6140 exceed, the LHeC requirements for average beam current and average beam power (6.4 mA
 6141 at 60 GeV). It is worth noting that the JLAB UV/IR 4th Generation Light Source FEL is
 6142 routinely operating with 10 mA average current (135 pC pulses at 75 MHz) [570].

6143 The target LHeC IP electron-beam power is 384 MW. With a standard wall-plug-power to
 6144 RF conversion efficiency around 50%, this would imply about 800 MW electrical power, far
 6145 more than available. This highlights the need for energy recovery where the energy of the spent
 6146 beam, after collision, is recuperated by returning the beam 180° out of phase through the same
 6147 RF structure that had earlier been used for its acceleration, again with several recirculations.
 6148 An energy recovery efficiency η_{ER} reduces the electrical power required for RF power generation
 6149 at a given beam current by a factor $(1 - \eta_{ER})$. We need an efficiency η_{ER} above 90% or higher
 6150 to reach the beam-current goal of 6.4 mA with less than 100 MW total electrical power.

6151 The above arguments have given birth to the LHeC Energy Recovery Linac high-luminosity
6152 baseline design, which is being presented in this chapter.

6153 **Choice of RF Frequency**

6154 Two candidate RF frequencies exist for the SC linac. One possibility is operating at the ILC
6155 and XFEL RF frequency around 1.3 GHz, the other choosing a frequency of about 720 MHz,
6156 close to the RF frequencies of the CERN High-Power SPL, eRHIC, and the European Spallation
6157 Source (ESS).

6158 The ILC frequency would have the advantage of synergy with the XFEL infrastructure, of
6159 profiting from the high gradients reached with ILC accelerating cavities, and of smaller structure
6160 size, which could reduce the amount of high-purity niobium needed by a factor 2 to 4.

6161 Despite these advantages, the present LHeC baseline frequency is 720 MHz, or, more pre-
6162 cisely, 721 MHz to be compatible with the LHC bunch spacing. The arguments in favor of this
6163 lower frequency are the following:

- 6164 • A frequency of 721 MHz requires less cryo-power (about two times less than at 1.3 GHz
6165 according to BCS theory; the exact difference will depend on the residual resistance [571]).
- 6166 • The lower frequency will facilitate the design and operation of high-power couplers [572],
6167 though the couplers might not be critical [573].
- 6168 • The smaller number of cells per module (of similar length) at lower RF frequency is
6169 preferred with regard to trapped modes [574].
- 6170 • The lower-frequency structures reduce beam-loading effects and transverse wake fields.
- 6171 • The project can benefit from synergy with SPL, eRHIC and ESS.

6172 In case the cavity material costs at 721 MHz would turn out to be a major concern, they could
6173 be reduced by applying niobium as a thin film on a copper substrate, rather than using bulk
6174 niobium. The thin film technology may also enhance the intrinsic cavity properties, e.g. increase
6175 the Q value.

6176 Linac RF parameters for both 720 MHz and 1.3 GHz in CW mode as well as for a pulsed 1.3-
6177 GHz option are compared in Table 8.1. The 721 MHz parameters are derived from eRHIC [575].
6178 Pulsed-linac applications for LHeC are discussed in subsections 8.1.4 and 8.1.6.

6179 **ERL Electrical Site Power**

6180 The cryopower for two 10-GeV accelerating SC linacs is 28.9 MW, assuming pessimistically 37
6181 W/m heat load at 1.8 K and 18 MV/m cavity gradient (this is a pessimistic estimate since the
6182 heat load could be up to 3 times smaller; see Table 8.1), and 700 “W per W” cryo efficiency as
6183 for the ILC. The RF power needed to control microphonics for the accelerating RF is estimated
6184 at 22.2 MW, considering that 10 kW/m RF power may be required, as for eRHIC, with 50% RF
6185 generation efficiency. The electrical power for the additional RF compensating the synchrotron-
6186 radiation energy loss is 24.1 MW, with an RF generation efficiency of 50%. The cryo power for

¹The range of heat-load values quoted for 721 MHz reflects the measured parameters of eRHIC prototype cavity BNL-I and an extrapolation to the improved cavity BNL-III [576].

²The range of heat-load values indicated for 1.3 GHz refers to different assumptions on the cavity Q at 18 MV/m (or to two different extrapolations from [567]).

Table 8.1: Linac RF parameters for two different RF frequencies and two modes of operation.

	ERL 721 MHz	ERL 1.3 GHz	Pulsed
duty factor	CW	CW	0.05
RF frequency [GHz]	0.72	0.72	1.3
cavity length [m]	1	~1	~1
energy gain / cavity [MeV]	18	18	31.5
R/Q [100Ω]	400–500	1200	1200
Q_0 [10^{10}]	2.5–5.0	2?	1
power loss stat. [W/cav.]	5	< 0.5	< 0.5
power loss RF [W/cav.]	8–32 ¹	13–27 ²	< 10
power loss total [W/cav.]	13–37	13–27	11
“W per W” (1.8 K to RT)	700	700	700
power loss / GeV at RT [MW]	0.51–1.44	0.6–1.1	0.24
length / GeV [m] (filling=0.57)	97	97	56

6187 the compensating RF is 2.1 MW, provided in additional 1,44 GeV linacs, and the microphonics
6188 control for the compensating RF requires another 1.6 MW. In addition, with an injection energy
6189 of 50 MeV, 6.4 mA beam current, and as usual 50% efficiency, the electron injector consumes
6190 about 6.4 MW. A further 3 MW is budgeted for the recirculation-arc magnets [577]. Together
6191 this gives a grand total of 88.3 MW electrical power, some 10%.below the 100 MW limit.

6192 ERL Configuration

6193 The ERL configuration is depicted in Fig. 8.5. The shape, arc radius and number of passes
6194 have been optimized with respect to construction cost and with respect to synchrotron-radiation
6195 effects [578].

6196 The ERL is of racetrack shape. A 500-MeV electron bunch coming from the injector is
6197 accelerated in each of the two 10-GeV SC linacs during three revolutions, after which it has
6198 obtained an energy of 60 GeV. The 60-GeV beam is focused and collided with the proton beam.
6199 It is then bent by 180° in the highest-energy arc beam line before it is sent back through the
6200 first linac, at a decelerating RF phase. After three revolutions with deceleration, re-converting
6201 the energy stored in the beam to RF energy, the beam energy is back at its original value of 500
6202 MeV, and the beam is now disposed in a low-power 3.2-MW beam dump. A second, smaller
6203 (tune-up) dump could be installed behind the first linac.

6204 Strictly speaking, with an injection energy into the first linac of 0.5 GeV, the energy gain
6205 in the two accelerating linacs need not be 10 GeV each, but about 9.92 GeV, in order to reach
6206 60 GeV after three passages through each linac. Considering a rough value of 10 GeV means
6207 that we overestimate the electrical power required by about 1%.

6208 Each arc contains three separate beam lines at energies of 10, 30 and 50 GeV on one side,
6209 and 20, 40 and 60 GeV on the other. Except for the highest energy level of 60 GeV, at which
6210 there is only one beam, in each of the other arc beam lines there always co-exist a decelerating

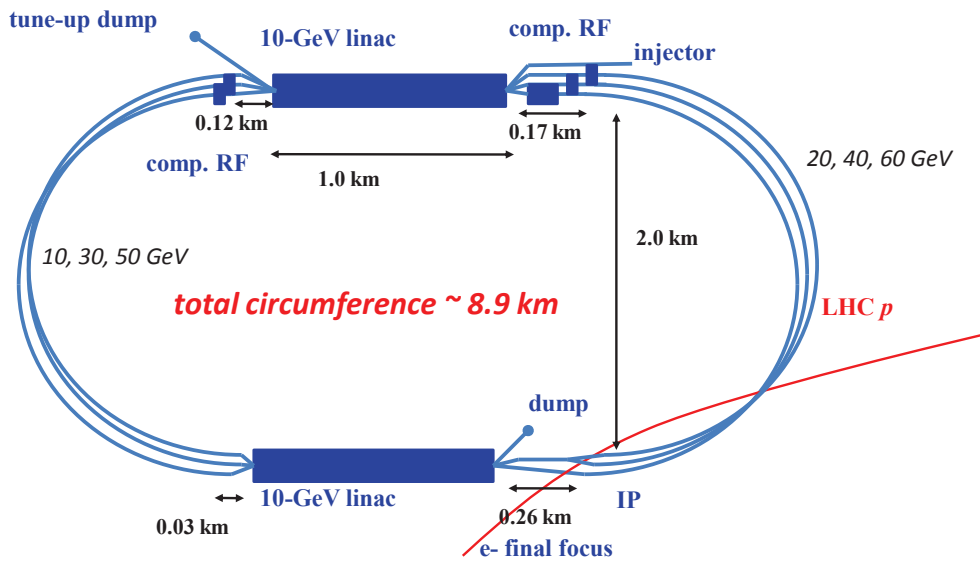


Figure 8.5: LHeC ERL layout including dimensions.

6211 and an accelerating beam. The effective arc radius of curvature is 1 km, with a dipole bending
 6212 radius of 764 m [579].

6213 The two straight sections accommodate the 1-km long SC accelerating linacs. There is
 6214 another 290 m section in each straight. In one straight of the racetrack 260 m of this additional
 6215 length is allocated for the electron final focus (plus matching and splitting), the residual 30 m on
 6216 the other side of the same straight allows for combining the beam and matching the optics into
 6217 the arc. In the second straight section the additional RF compensating for 1.44 GeV energy loss
 6218 is installed [580]. For the highest energy, 60 GeV, there is a single beam and the compensating
 6219 RF (750 MV) can have the same frequency, 721 MHz, as in the main linac [580]. For the other
 6220 energies, a higher harmonic RF system, e.g. at 1.442 GHz, can compensate the energy loss for
 6221 both decelerating and accelerating beams, which are 180° out of phase at 721 MHz. On one
 6222 side of the second straight one must compensate a total of about 907 MV ($=750+148+9$ MV,
 6223 corresponding to the energy loss at 60, 40 and 20 GeV, respectively), which should easily fit
 6224 within a length of 170 m. On the other side one has to compensate 409 MV ($=362+47$ MV),
 6225 corresponding to SR energy losses at 50 and 30 GeV), for which a length of 120 m is available.

6226 The total circumference of the ERL racetrack is chosen as 8.9 km, equal to one third of the
 6227 LHC circumference. This choice has the advantage that one could introduce ion-clearing gaps in
 6228 the electron beam which would match each other on successive revolutions (e.g. for efficient ion
 6229 clearing in the linacs that are shared by six different parts of the beam) and which would also
 6230 always coincide with the same proton bunch locations in the LHC, so that in the latter a given
 6231 proton beam would either always collide or never collide with the electrons [581]. Ion clearing
 6232 may be necessary to suppress ion-driven beam instabilities. The proposed implementation
 6233 scheme would remove ions while minimizing the proton emittance growth which could otherwise
 6234 arise when encountering collisions only on some of the turns. In addition, this arrangement can
 6235 be useful for comparing the emittance growth of proton bunches which are colliding with the

6236 electrons and those which are not.

6237 The length of individual components is as follows. The exact length of the 10-GeV linac
 6238 is 1008 m. The individual cavity length is taken to be 1 m. The optics consists of 56-m long
 6239 FODO cells with 32 cavities. The number of cavities per linac is 576. The linac cavity filling
 6240 factor is 57.1%. The effective arc bending radius is set to be 1000 m. The bending radius of
 6241 the dipole magnets is 764 m, corresponding to a dipole filling factor of 76.4% in the arcs. The
 6242 longest SR compensation linac has a length of 84 m (replacing the energy lost by SR at 60
 6243 GeV). Combiners and splitters between straights and arcs require about 20–30 m space each.
 6244 The electron final focus may have a length of 200–230 m.

6245 IP Parameters and Beam-Beam Effects

6246 Table 8.2 presents interaction-point (IP) parameters for the electron and proton beams.

Table 8.2: IP beam parameters

	protons	electrons
beam energy [GeV]	7000	60
Lorentz factor γ	7460	117400
normalized emittance $\gamma\epsilon_{x,y}$ [μm]	3.75	50
geometric emittance $\epsilon_{x,y}$ [nm]	0.,40	0.43
a IP beta function $\beta_{x,y}^*$ [m]	0.10	0.12
rms IP beam size $\sigma_{x,y}^*$ [μm]	7	7
initial rms IP beam divergence $\sigma_{x',y'}^*$ [μrad]	70	58
beam current [mA]	≥ 430	6.4
bunch spacing [ns]	25 or 50	(25 or) 50
bunch population [ns]	1.7×10^{11}	(1 or) 2×10^9

6247 Due to the low charge of the electron bunch, the proton head-on beam-beam tune shift is
 6248 tiny, namely $\Delta Q_p = +0.0001$, which amounts to only about 1% of the LHC pp design tune shift
 6249 (and is of opposite sign). Therefore, the proton-beam tune spread induced by the ep collisions is
 6250 negligible. In fact, the electron beam acts like an electron lens and could conceivably increase the
 6251 pp tune shift and luminosity, but only by about 1%. Long-range beam-beam effects are equally
 6252 insignificant for both electrons and protons, since the detector-integrated dipoles separate the
 6253 electron and proton bunches by about $36\sigma_p$ at the first parasitic encounter, 3.75 m away from
 6254 the IP.

6255 One further item to be looked at is the proton beam emittance growth. Past attempts at
 6256 directly simulating the emittance growth from ep collisions were dominated by numerical noise
 6257 from the finite number of macroparticles and could only set an upper bound [582], nevertheless
 6258 indicating that the proton emittance growth due to the pinching electron beam might be accept-
 6259 able for centered collisions. Proton emittance growth due to electron-beam position jitter and
 6260 simultaneous pp collisions is another potential concern. For a 1σ offset between the electron and
 6261 proton orbit at the IP, the proton bunch receives a deflection of about 10 nrad (approximately
 6262 $10^{-4}\sigma_{x',y'}^*$). Beam-beam simulations for LHC pp collisions have determined the acceptable level

6263 for random white-noise dipole excitation as $\Delta x/\sigma_x \leq 0.1\%$ [583]. This translates into a very
 6264 relaxed electron-beam random orbit jitter tolerance of more than 1σ . The tolerance on the
 6265 orbit jitter will then not be set by beam-beam effects, but by the luminosity loss resulting from
 6266 off-center collisions, which, without disruption, scales as $\exp(-(\Delta x)^2/(4\sigma_{x,y}^{*2}))$. The random
 6267 orbit jitter observed at the SLAC SLC had been of order $0.3\text{--}0.5\sigma$ [584, 585]. A 0.1σ offset at
 6268 LHeC would reduce the luminosity by at most 0.3%, a 0.3σ offset by 2.2%. Disruption further
 6269 relaxes the tolerance.

6270 The strongest beam-beam effect is encountered by the electron beam, which is heavily
 6271 disrupted. The electron disruption parameter is $D_{x,y} \equiv N_{b,p} r_e \sigma_{z,p} / (\gamma_e \sigma^{*2}) \approx 6$, and the
 6272 “nominal disruption angle” $\theta_0 \equiv D\sigma^*/\sigma_{z,p} = N_{b,p} r_e / (\gamma_e \sigma^*)$ [586] is about $600 \mu\text{rad}$ (roughly
 6273 $10\sigma_{x',y'}$), which is huge. Simulations show that the actual maximum angle of the disrupted
 6274 electrons is less than half θ_0 .

6275 Figure 8.6 illustrates the emittance growth and optics-parameter change for the electron
 6276 beam due to head-on collision with a “strong” proton bunch. The intrinsic emittance grows
 6277 by only 15%, but there is a 180% growth in the mismatch parameter “ B_{mag} ” (defined as
 6278 $B_{\text{mag}} = (\beta\gamma_0 - 2\alpha\alpha_0 + \beta_0\gamma)/2$, where quantities with and without subindex “0” refer to the
 6279 optics without and with collision, respectively. Without adjusting the extraction line optics to
 6280 the parameters of the mismatched beam the emittance growth will be about 200%. This would
 6281 be acceptable since the arc and linac physical apertures have been determined assuming up to
 6282 300% emittance growth for the decelerating beam [579]. However, if the optics of the extraction
 6283 line is rematched for the colliding electron beam (corresponding to an effective β^* of about 3
 6284 cm rather than the nominal 12 cm; see Fig.8.6 bottom left), the net emittance growth can be
 6285 much reduced, to only about 20%. The various optics parameters shown in Fig. 8.6 vary by no
 6286 more than 10–20% for beam-beam orbit offsets up to 1σ .

6287 Figure 8.7 presents the average electron deflection angle as a function of the beam-beam
 6288 offset. The extraction channel for the electron beam must have sufficient aperture to accom-
 6289 modate both the larger emittance due to disruption and the average trajectory change due to
 6290 off-center collisions.

6291 8.1.3 Polarization

6292 The electron beam can be produced from a polarized DC gun with about 90% polarization,
 6293 and with, conservatively, 10–50 μm normalized emittance [587]. Spin-manipulation tools and
 6294 measures for preserving polarization, like Wien filter and/or spin rotators, and polarimeters
 6295 should be included in the optics design of the injector, the final focus, and the extraction line.

6296 As for the positrons, up to about 60% polarization can be achieved either with an undulator
 6297 [588] or with a Compton-based e^+ source [589, 590]³.

6298 8.1.4 Pulsed Linacs

6299 For beam energies above about 140 GeV, due to the growing impact of synchrotron radiation,
 6300 the construction of a single straight linac is cheaper than that of a recirculating linac [578].
 6301 Figure 8.8 shows the schematic of an LHeC collider based on a pulsed straight 140-GeV linac,
 6302 including injector, final focus, and beam dump. The linac could be either of ILC type (1.3
 6303 GHz RF frequency) or operate at 721 MHz as the preferred ERL version. In both cases, ILC

³The primary challenge for positrons is to produce them in sufficient number and with a small enough emittance.

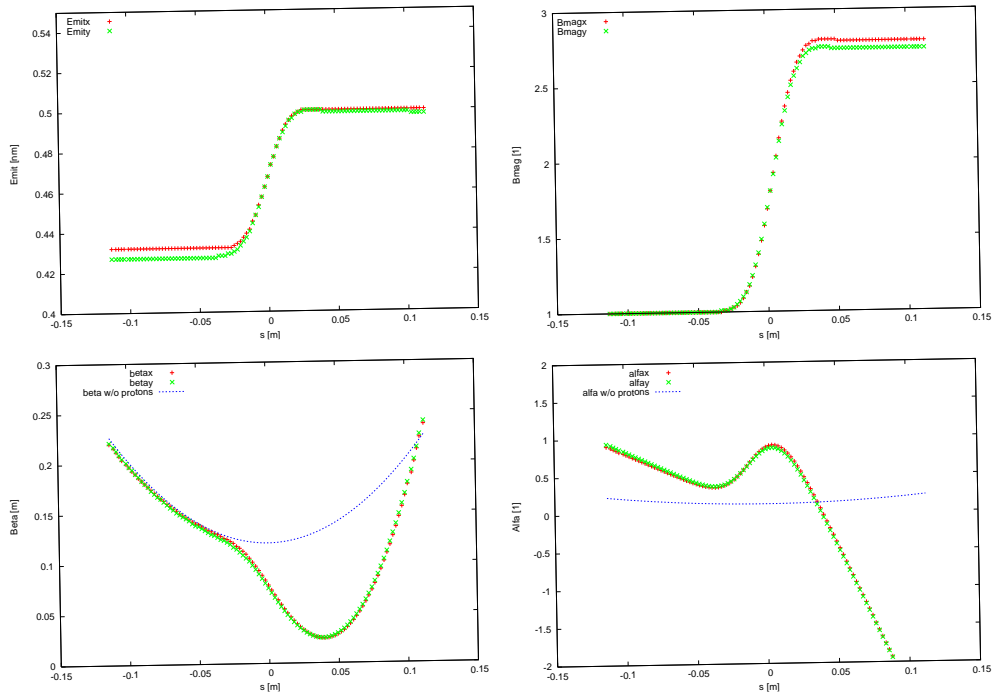


Figure 8.6: Simulated evolution of the electron beam emittance (top left), mismatch factor B_{mag} (top right) beta dfunction (bottom left) and alpha function (bottom right) during the collision with a proton bunch, as a function of distance from the IP.

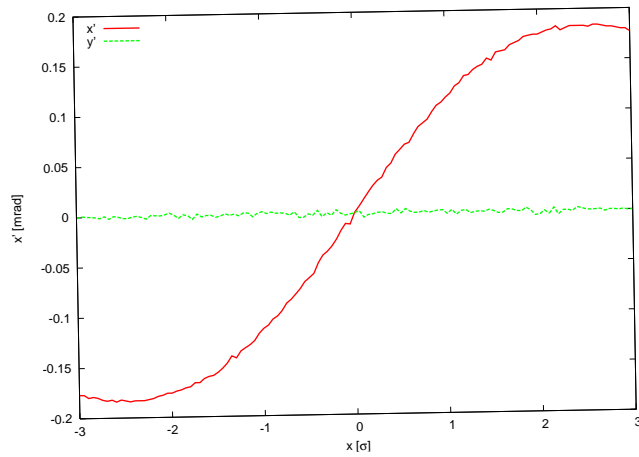


Figure 8.7: Simulated electron horizontal center-of-mass deflection angle as a function of the horizontal beam-beam offset.



Figure 8.8: Pulsed single straight 140-GeV linac for highest energy ep collisions.

6304 values are assumed for the cavity gradient (31.5 MV/m) and for the cavity unloaded Q value
 6305 ($Q_0 = 10^{10}$). This type of linac would be extendable to ever higher beam energies and could
 6306 conceivably later become part of a linear collider. In its basic, simplest and conventional version
 6307 no energy recovery is possible for this configuration, since it is impossible to bend the 140-GeV
 6308 beam around. The lack of energy recovery leads to significantly lower luminosity. For example,
 6309 with 10 Hz repetition rate, 5 ms pulse length (longer than ILC), a geometric reduction factor
 6310 $H_g = 0.94$ and $N_b = 1.5 \times 10^9$ per bunch, the average electron current would be 0.27 mA and
 6311 the luminosity $4 \times 10^{31} \text{ cm}^{-2}\text{s}^{-1}$.

6312 The construction of the 140-GeV pulsed straight linac could be staged, e.g. so as to first
 6313 feature a pulsed linac at 60 GeV, which could also be used for γ - p/A collisions (see subsection
 6314 8.1.6). The linac length decreases directly in proportion to the beam energy. For example,
 6315 at 140-GeV the pulsed linac measures 7.9 km, while at 60 GeV its length would be 3.4 km.
 6316 For a given constant wall-plug power, of 100 MW, both the average electron current and the
 6317 luminosity scale roughly inversely with the beam energy. At 60 GeV the average electron
 6318 current becomes 0.63 mA and the pulsed-linac luminosity, without any energy recovery, would
 6319 be more than $9 \times 10^{31} \text{ cm}^{-2}\text{s}^{-1}$.

6320 8.1.5 Highest-Energy LHeC ERL Option

6321 The simple straight linac layout of Fig. 8.8 can be expanded as shown in Fig. 8.9 [591]. The
 6322 main electron beam propagates from the left to the right. In the first linac it gains about
 6323 150 GeV, then collides with the hadron beam, and is then decelerated in the second linac.
 6324 By transferring the RF energy back to the first accelerating linac, with the help of multiple,
 6325 e.g. 15, 10-GeV “energy-transfer beams,” a novel type of energy recovery is realized without
 6326 bending the spent beam. With two straight linacs facing each other this configuration could
 6327 easily be converted into a linear collider, or vice versa, pending on geometrical and geographical
 6328 constraints of the LHC site. As there are no synchrotron-radiation losses the energy recovery
 6329 can be nearly 100% efficient. Such novel form of ERL could push the LHeC luminosity to the
 6330 $10^{35} \text{ cm}^{-2}\text{s}^{-1}$ level. In addition, it offers ample synergy with the CLIC two-beam technology.

6331 8.1.6 γ - p/A Option

6332 In case of a (pulsed) linac without energy recovery the electron beam can be converted into a
 6333 high-energy photon beam, by backscattering off a laser pulse, as is illustrated in Fig. 8.10. The
 6334 rms laser spot size at the conversion point should be similar to the size of the electron beam
 6335 at this location, that is $\sigma_\gamma \approx 10 \mu\text{m}$.

6336 With a laser wavelength around $\lambda_\gamma \approx 250 \text{ nm}$ ($E_{\gamma,0} \approx 5 \text{ eV}$), obtained e.g. from a Nd:YAG

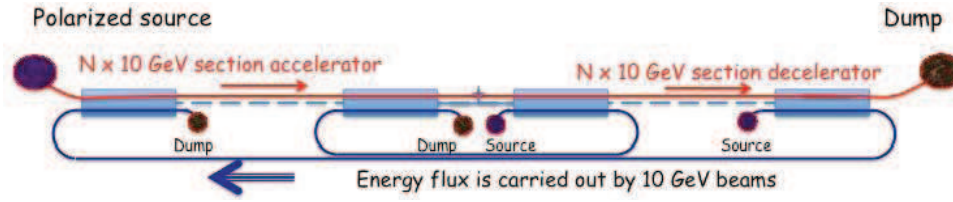


Figure 8.9: Highest-energy high-luminosity ERL option based on two straight linacs and multiple 10-GeV energy-transfer beams [591].

6337 laser with frequency quadrupling, the Compton-scattering parameter x [592, 593],

$$x \approx 15.3 \left[\frac{E_{e,0}}{\text{TeV}} \right] \left[\frac{E_{\gamma,0}}{\text{eV}} \right], \quad (8.3)$$

6338 is close to the optimum value 4.8 for an electron energy of 60 GeV (for $x > 4.8$ high-energy
 6339 photons get lost due to the creation of e^+e^- pairs). The maximum energy of the Compton
 6340 scattered photons is given by $E_{\gamma,\text{max}} = x/(x+1)E_0$, which is larger than 80% of the initial
 6341 electron-beam energy $E_{e,0}$, for our parameters. The cross section and photon spectra depend
 6342 on the longitudinal electron polarization λ_e and on the circular laser polarization P_c . With
 6343 proper orientation ($2\lambda_e P_c = -1$) the photon spectrum is concentrated near the highest energy
 6344 $E_{\gamma,\text{max}}$.

6345 The probability of scattering per individual electron is [594]

$$n_\gamma = 1 - \exp(-q) \quad (8.4)$$

6346 with

$$q = \frac{\sigma_c A}{E_{\gamma,0} 2\pi\sigma_\gamma^2}, \quad (8.5)$$

6347 where σ_c denotes the (polarized) Compton cross section and A the laser pulse energy. Using
 6348 the formulae in [?], the Compton cross section for $x = 4.8$ and $2\lambda_e P_c = -1$ is computed to be
 6349 $\sigma_c = 3.28 \times 10^{-25} \text{ cm}^2$. The pulse energy corresponding to $q = 1$, i.e. to a conversion efficiency
 6350 of 65%, is estimated as $A \approx E_{\gamma,0} 2\pi\sigma_\gamma^2 / \sigma_c \approx 16 \text{ J}$. To set this into perspective, for a $\gamma\gamma$ collider
 6351 at the ILC, Ref. [595] considered a pulse energy of 9 J at a four times longer wavelength of
 6352 $\lambda \approx 1 \mu\text{m}$.

6353 The energies of the leftover electrons after conversion extend from about 10 to 60 GeV.
 6354 This spent electron beam, with its enormous energy spread, must be safely extracted from the
 6355 interaction region. The detector-integrated dipole magnets will assist in this process. They
 6356 will also move the scattered electrons away from the interaction point. A beam dump for the
 6357 neutral photons should also be installed, behind the downstream quadrupole channel.

6358 Figure 8.11 presents an example photon energy spectrum after the conversion and a lumi-
 6359 nosity spectrum [596], obtained from a simulation with the Monte-Carlo code CAIN [597].

6360 Differently from $\gamma\gamma$ collisions at a linear collider, thanks to the much larger IP spot size
 6361 and smaller beam energy, the conversion point can be a much larger distance $\Delta s \approx \beta^* \sim 0.1 \text{ m}$
 6362 away from the interaction point, which could simplify the integration in the detector, and is
 6363 also necessary as otherwise, with e.g. a mm-distance between CP and IP, the conversion would
 6364 take place inside the proton bunch.

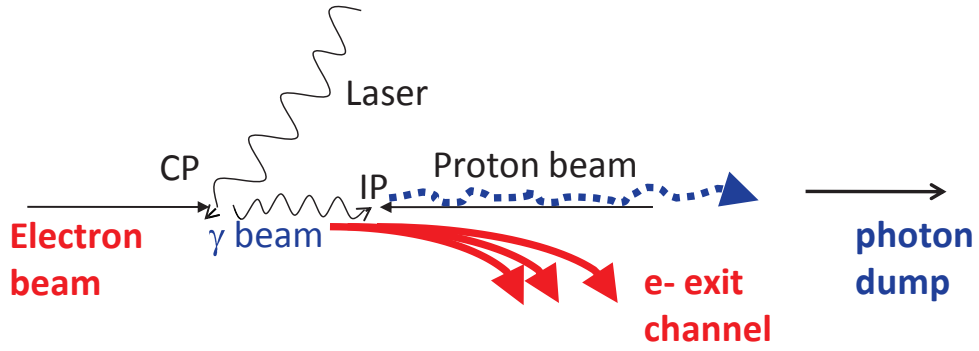


Figure 8.10: Schematic of γ - p/A collision; prior to the photon-hadron interaction point (IP), the electron beam is scattered off a several-J laser pulse at the conversion point (CP).

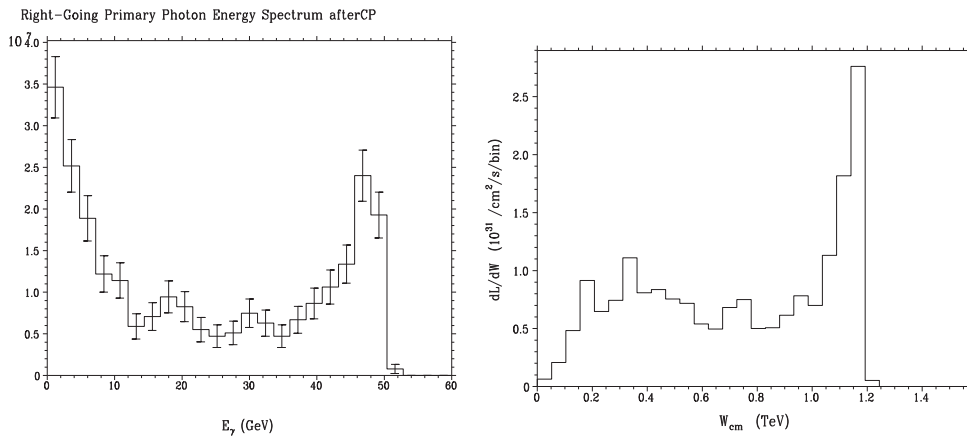


Figure 8.11: Simulated example photon spectrum after the conversion point (left) and γ - p luminosity spectrum [596].

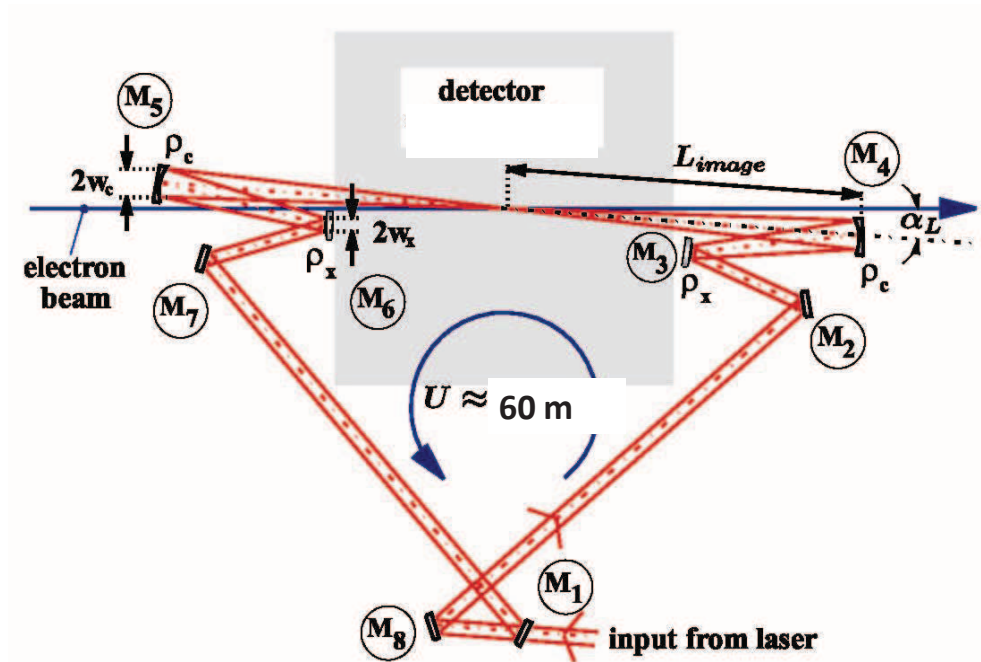


Figure 8.12: Recirculating mirror arrangement providing a laser-pulse path length of 60 m for pulse stacking synchronously with the arriving electron bunches (adapted from [595]).

6365 To achieve the required laser pulse energy, external pulses can be stacked in a recirculating
 6366 optical cavity. For an electron bunch spacing of e.g. 200 ns, the path length of the recirculation
 6367 could be 60. A schematic of a possible mirror system is sketched in Fig. 8.12 (adapted from
 6368 [595]).

6369 8.1.7 Summary of Basic Parameters and Configurations

6370 The baseline 60-GeV ERL option presented here can provide a pe luminosity of $10^{33} \text{ cm}^{-2}\text{s}^{-1}$,
 6371 at less than 100 MW total electrical power for the electron branch of the collider, and with less
 6372 than 9 km circumference. Its main hardware component is about 21 GV of SC-RF.

6373 A pulsed 140-GeV linac, without energy recovery, could achieve a luminosity of $1.4 \times$
 6374 $10^{31} \text{ cm}^{-2}\text{s}^{-1}$, at higher c.m. energy, again with less than 100 MW electrical power, and shorter
 6375 than 9 km in length. The pulsed linac can accommodate a γ - p/A option. An advanced, novel
 6376 type of energy recovery, proposed for the single straight high-energy linac case, includes a second
 6377 decelerating linac, and multiple 10-GeV “energy-transfer beams”. This type of collider could
 6378 potentially reach luminosities of $10^{35} \text{ cm}^{-2}\text{s}^{-1}$.

6379 High polarization is possible for all linac-ring options. Beam-beam effects are benign, espe-
 6380 cially for the proton beam, which will not be affected by the presence of the electron beam.

6381 Producing the required number of positrons needed for high-luminosity proton-positron
 6382 collisions is the main open challenge for a linac-ring LHeC. Recovery of the positrons together
 6383 with their energy, as well as fast transverse cooling schemes, are likely to be essential ingredients

6384 for any linac-based high-luminosity ep collider involving positrons.

6385 8.2 Interaction region

6386 This section presents a first conceptual design of the LHeC linac-ring Interaction Region (IR).
6387 The merits of the IR are a very low β^* of 0.1m with proton triplets as close as possible to
6388 the IP to minimize chromaticity. Head-on proton-electron collisions are achieved by means of
6389 dipoles around the Interaction Point (IP). The Nb₃Sn superconductor has been chosen for the
6390 proton triplets since it provides the largest gradient. If this technology proves not feasible in
6391 the timescale of the LHeC a new design of the IR can be pursued using standard technology.

6392 The main goal of this first design is to evaluate potential obstacles, decide on the needs of
6393 special approaches for chromaticity correction and evaluate the impact of the IR synchrotron
6394 radiation.

6395 8.2.1 Layout

6396 A crossing angle of 6 mrad between the non-colliding proton beams allows enough separation
6397 to place the proton triplets. Only the proton beam colliding with the electrons is focused. A
6398 possible configuration in IR2 could be to inject the electrons parallel to the LHC beam 1 and
6399 collide them head-on with beam 2, see Fig. 8.13. The signs of the separation and recombination
6400 dipoles (D1 and D2) have to be changed to allow for the large crossing angle at the IP. The
6401 new D1 has one aperture per beam and is 4.5 times stronger than the LHC design D1. The
6402 new D2 is 1.5 times stronger than the LHC design D2. Both dipoles feature about a 6 T field.
6403 The lengths of the nominal LHC D1 and D2 dipoles have been left unchanged, 23 m and 9 m,
6404 respectively. However the final IR design will need to incorporate a escape line for the neutral
6405 particles coming from the IP, probably requiring to split D1 into two parts separated by tens
6406 of meters.

6407 Bending dipoles around the IP are used to make the electrons collide head-on with beam 2
6408 and to safely extract the disrupted electron beam. The required field of these dipoles is deter-
6409 mined by the L* and the minimum separation of the electron and the focused beam at the first
6410 quadrupole (Q1). A 0.3 T field extending over 9 m allows for a beams separation of 0.07 m
6411 at the entry of Q1. This separation distance is compatible with mirror quadrupole designs
6412 using Nb₃Sn technology; see Section 10.1. The electron beam radiates 48 kW in the IR dipoles.
6413 A sketch of the 3 beams, the synchrotron radiation fan and the proton triplets is shown in
6414 Fig. 8.14.

6415 8.2.2 Optics

6416 Colliding proton optics

6417 The colliding beam triplet starts at L*=10m from the IP. It consists of 3 quadrupoles with main
6418 parameters given in Table 8.3. The quadrupole aperture is computed as $11\max(\sigma_x, \sigma_y) + 5$ mm.
6419 The 5 mm split into 1.5 mm for the beam pipe, 1.5 mm for mechanical tolerances and 2 mm
6420 for the closed orbit. The magnet parameters for the first two quadrupoles correspond to Nb₃Sn
6421 design described in Section 10.1. The total chromaticity from the two IP sides amounts to 960
6422 units. The optics functions for the colliding beam are shown in Fig. 8.15

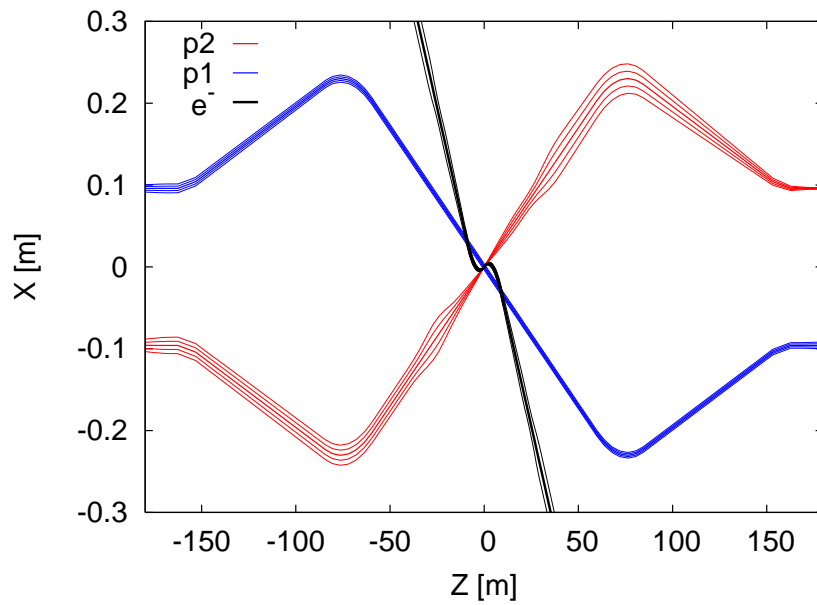


Figure 8.13: LHeC interaction region displaying the two proton beams and the electron beam trajectories with 5σ and 10σ envelopes.

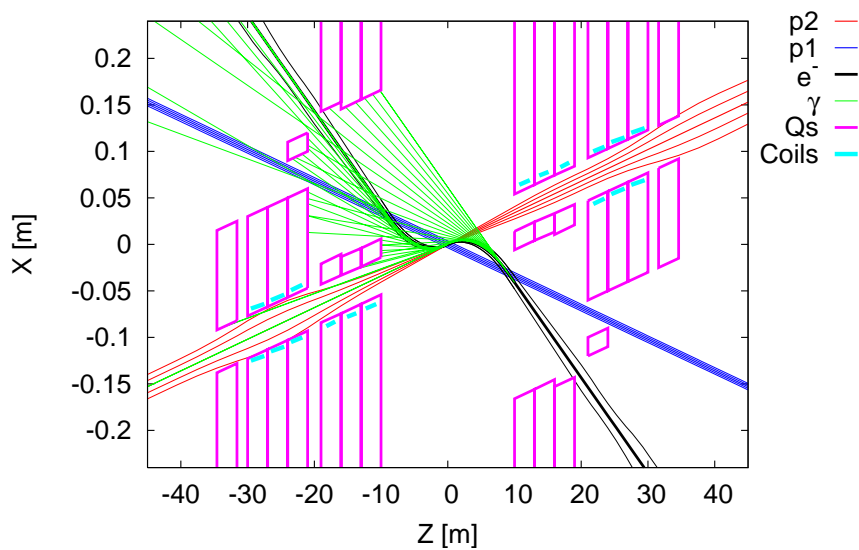


Figure 8.14: LHeC interaction region with a schematic view of synchrotron radiation. Beam trajectories with 5σ and 10σ envelopes are shown. The parameters of the Q1 and Q2 quadrupole segments correspond to the Nb_3Sn half-aperture and single-aperture (with holes) quadrupole of Fig. 10.6.

Name	Gradient [T/m]	Length [m]	Radius [mm]
Q1	187	9	22
Q2	308	9	30
Q3	185	9	32

Table 8.3: Parameters of the proton triplet quadrupoles. The radius is computed as $11\max(\sigma_x, \sigma_y) + 5$ mm.

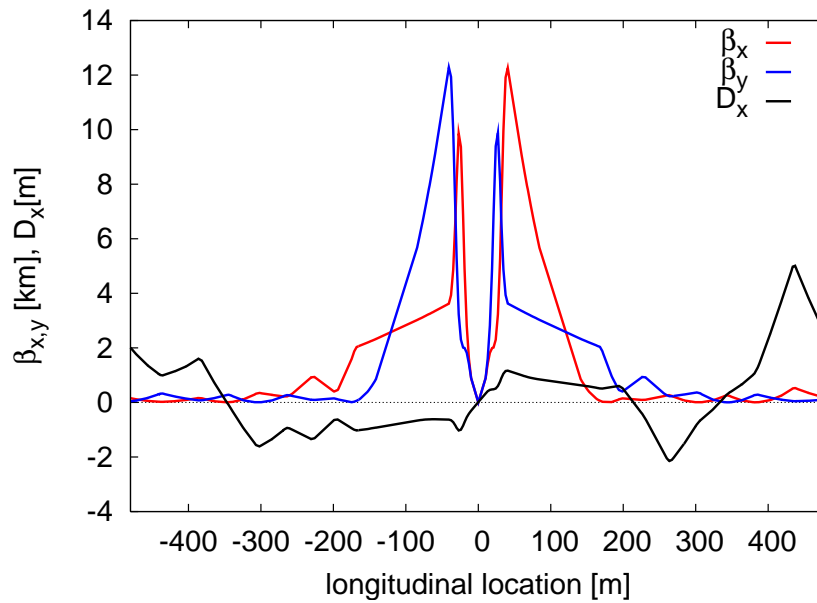


Figure 8.15: Optics functions for main proton beam.

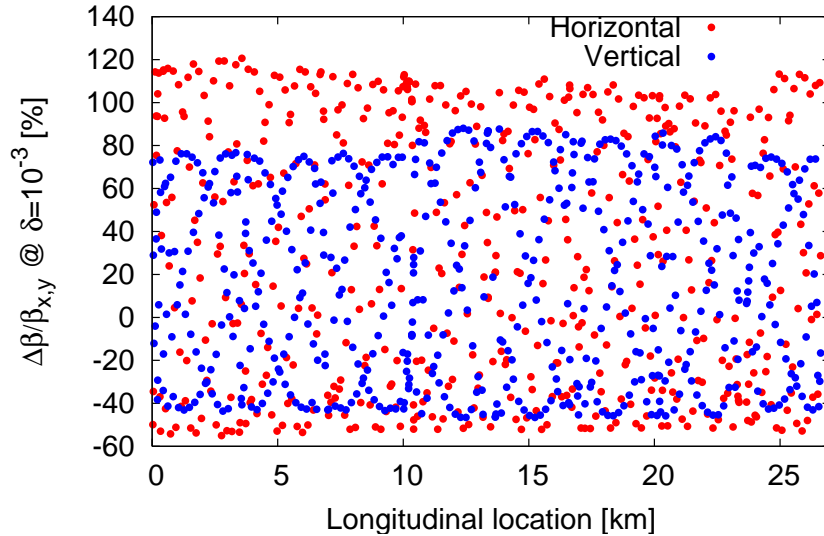


Figure 8.16: Chromatic beta-beating at $dp/p=0.001$.

6423 It was initially hoped that a compact Nb_3Sn triplet with $L^*=10m$ would allow for a normal
 6424 chromaticity correction using the arc sextupoles. However after matching this triplet to the LHC
 6425 and correcting linear chromaticity the chromatic β -beating at $dp/p=0.001$ is about 100% (see
 6426 Fig. ??). This is intolerable regarding collimation and machine protection issues. Therefore a
 6427 dedicated chromaticity correction scheme has to be adopted. A large collection of studies exist
 6428 showing the feasibility of correcting even larger chromaticities in the LHC [598–600]. Other
 6429 local chromatic correction approaches as [601], where quadrupole doublets are used to provide
 6430 the strong focusing, could also be considered for the LHeC.

6431 Since LHeC anyhow requires a new dedicated chromaticity correction scheme, current NbTi
 6432 technology could be pursued instead of Nb_3Sn and the L^* could also be slightly increased. The
 6433 same conceptual three-beam crossing scheme as in Fig. 8.13 could be kept.

6434 To achieve L^* below 23 m requires a cantilever supported on a large mass as proposed for the
 6435 CLIC QD0 [602] to provide sub-nanometer stability at the IP. The LHeC vibration tolerances
 6436 are much more relaxed, being on the sub-micrometer level.

6437 Non-colliding proton optics

6438 The non-colliding beam has no triplet quadrupoles since it does not need to be focused. The
 6439 LHC “alignment optics” [603] was used as a starting point. Figure 8.17 shows the optics
 6440 functions around the IP. The LHeC IP longitudinal location can be chosen so as to completely
 6441 avoid unwanted proton-proton collisions.

6442 The non-colliding proton beam travels through dedicated holes in the proton triplet quadrupoles,
 6443 in Q1 together with the electron beam. The Q1 hole dimensions are determined by the electron
 6444 beam, see below. By contrast, the non-colliding proton beam travels alone through the first
 6445 module of the Q2, requiring about 30 mm full aperture. No fields are assumed in these apertures
 6446 but the possible residual fields could easily be taken into account for the proton optics.

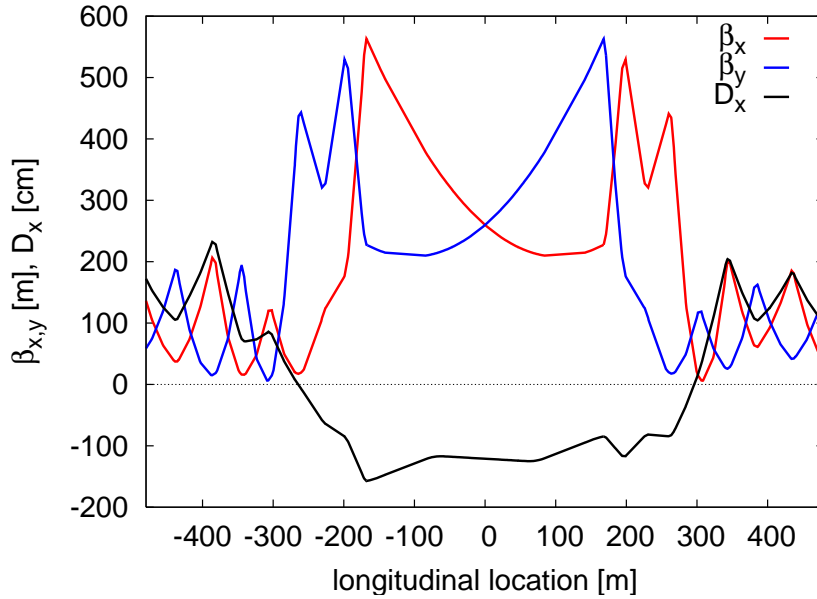


Figure 8.17: Optics functions for the non-colliding proton beam without triplets.

6447 **Electron optics**

6448 The electron $L^*=30$ m has been chosen to allow for enough separation between the proton and
 6449 the electron final focusing quadrupoles. A first design of the optics already matched to the exit
 6450 of the linac is shown in Fig. 8.18. The electron focusing quadrupoles feature moderately low
 6451 gradients as shown in Table 8.4. The IP beam size aberration versus the relative rms energy
 6452 spread of the beam is shown in Fig. 8.19. Chromatic correction is mandatory for relative
 6453 energy spreads above 3×10^{-4} . It is recommended to design a chromatic correction section.
 6454 About 200 m are available between the exit of the linac and the IP while the current electron
 6455 final focus is using only 90 m, leaving space for collimation and beam diagnostics.

6456 The electrons shares a hole with the non-colliding proton beam in the first half-quadrupole,

Name	Gradient [T/m]	Length [m]	Radius [mm]
Q1	19.7	1.34	20
Q2A	38.8	1.18	32
Q2B	3.46	1.18	20
Q3	22.3	1.34	22

Table 8.4: Parameters of the electron triplet quadrupoles. The radius is computed as $11\max(\sigma_x, \sigma_y) + 5$ mm.

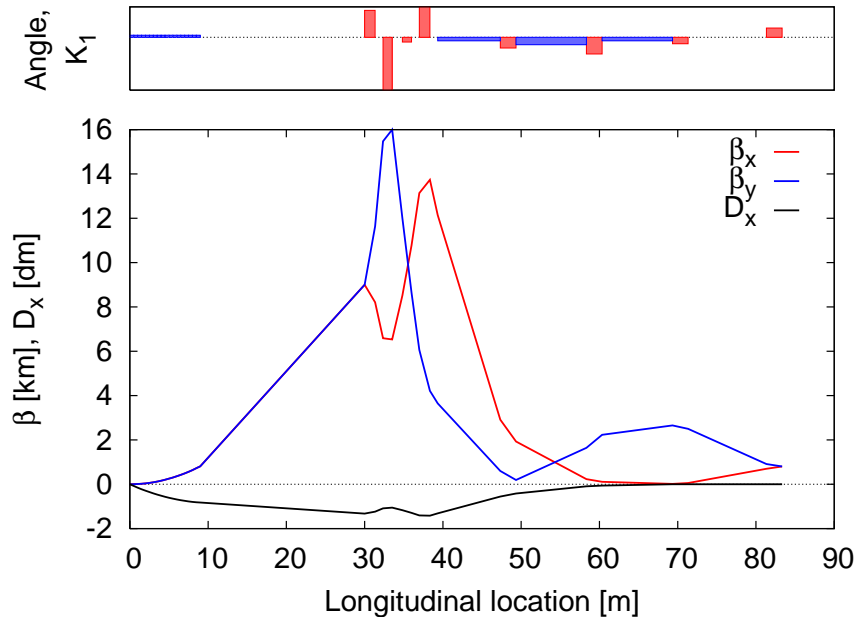


Figure 8.18: Optics of the electron beam.

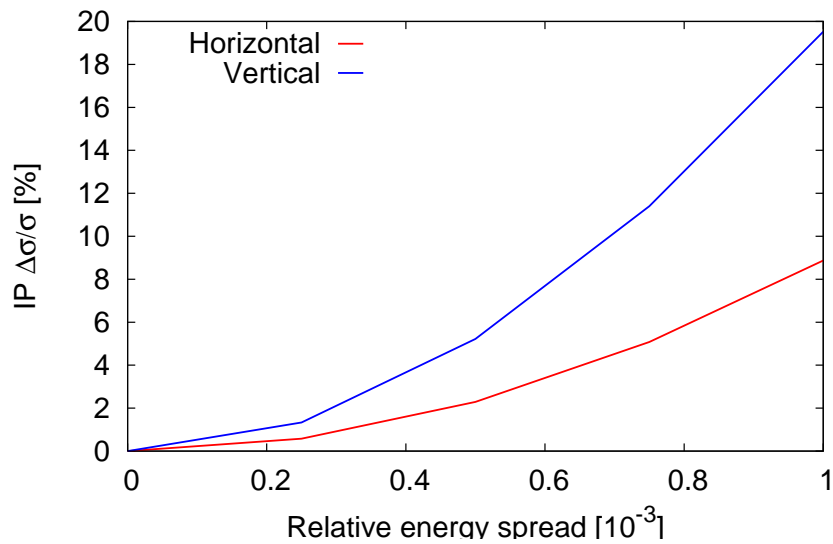


Figure 8.19: IP electron beam size versus relative energy spread of the beam.

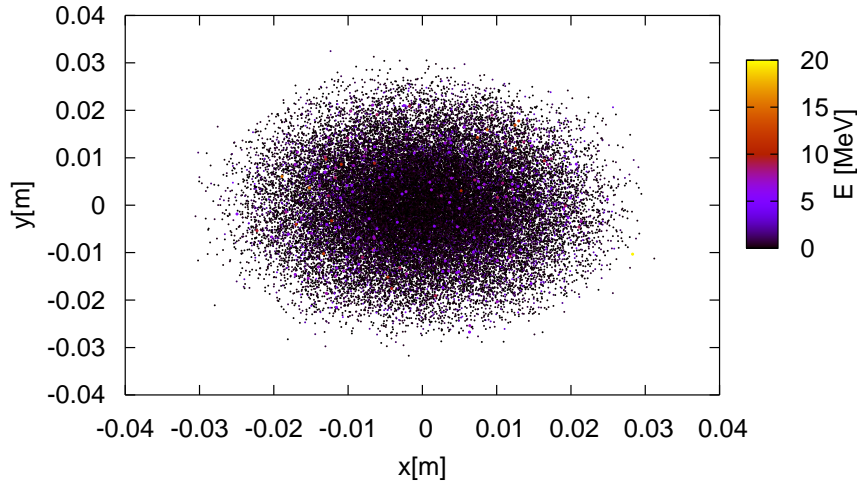


Figure 8.20: Distribution of the spent electron beam at 10 m from the IP. The Gaussian and rms sigmas are shown on the plot.

6457 Q1, and then travels through a dedicated hole in the cryostat of Q2. The common hole in the
 6458 proton Q1 must have about 160 mm full horizontal aperture to allow for the varying separation
 6459 between the electron and non-colliding proton orbit (120 mm) with the usual electron-beam
 6460 aperture assumptions (± 20 mm). First design of mirror magnets for Q1 feature a field of 0.5 T
 6461 in the electron beam pipe. This value is considered too large when compared to the IR dipole
 6462 of 0.3 T, but new designs with active isolation or dedicated coils could considerably reduce this
 6463 field. Migrating to NbTi technology would automatically reduce this field too.

6464 Spent electron beam

6465 The proton electromagnetic field provides extra focusing to the electron. This increases
 6466 the divergence of the electron. Figure 8.20 shows the horizontal distribution of the electrons
 6467 at 10 m from the IP (entry of Q1) as computed by Guineapig [604]. The contribution of
 6468 dispersion and energy spread to the transverse size of the exiting collided beam can be neglected.
 6469 Therefore, it is possible to linearly scale the sigmas at 10 m to estimate both the horizontal
 6470 and vertical sigmas at any other longitudinal location. The simulation used 10^5 particles. No
 6471 particles are observed beyond 4.5 mm from the beam centroid at 10 m from the IP and beyond
 6472 9 mm at 20 m. A radial aperture of 10 mm has been reserved for the beam size at the incoming
 6473 electron Q1 hole. The same value of 10 mm seem to be enough to also host the spent electron
 6474 beams, although it might be worth to allocate more aperture margin in the last block of Q1.

6475 8.2.3 Modifications for γp or γ -A

6476 The electron beam can be converted into photons by Compton scattering off a high-power laser
6477 pulse, as discussed Section 8.1.6. For this option a laser path and high-finesse optical cavities
6478 must be integrated into the interaction region. A multiple mirror arrangement has been sketched
6479 in Fig. 8.12. The 0.3-T dipole field after the (now) γ -p interaction point will help to separate
6480 the Compton-scattered spent electron beam from the high-energy photons. The high-energy
6481 photons propagate straight into the direction of the incoming proton beam through the main
6482 openings of Q1 and Q2, while the spent electrons will be extracted through the low-field exit
6483 holes shared with the non-colliding proton beam, as for electron-proton collisions.

6484 8.2.4 Synchrotron radiation and absorbers

6485 Introduction

6486 The synchrotron radiation (SR) in the linac-ring interaction region has been analyzed by
6487 three different approaches. The SR was simulated using a program made with the Geant4 (G4)
6488 toolkit. In addition, a cross check of the total power and average critical energy was done in
6489 IRSYN, a Monte Carlo simulation package written by R. Appleby [535]. A final cross check
6490 of the radiated power has been performed using an analytic method. The latter two checks
6491 confirmed the results obtained from G4. The G4 program uses Monte Carlo methods to create
6492 the desired Gaussian spatial and angular distributions of an electron beam. This electron beam
6493 distribution is then transported through a “vacuum system,” including the magnetic fields for
6494 the separator dipoles. In a non-zero magnetic field SR is generated using the appropriate G4
6495 process classes. The position, direction, and energy of each photon emitted is written as ntuples
6496 at user defined longitudinal positions (Z values). These ntuples are then used to analyze the
6497 SR fan as it evolves in Z . The latter analysis was done primarily through MATLAB scripts.

6498 This section uses the following conventions. The electron beam is being referred to as *the*
6499 *beam* and the proton beams will be called either the interacting or non interacting
6500 beams. The (electron) beam propagates in the $-Z$ direction and the interacting proton beam
6501 propagates in the $+Z$ direction. At the collision point both beams propagate ub the straight
6502 Z (or $-Z$) direction. A right-handed coordinate system is used where the X axis is horizontal
6503 and the Y axis vertical. The beam centroid always remains in the $Y = 0$ plane. The *angle*
6504 *of the beam* will be used to refer to the angle between the beam centroid’s direction and the
6505 Z axis, in the $Y = 0$ plane. This angle is defined such that the beam propagates in the $-X$
6506 direction when it passes through the dipole field as it moves along Z .

6507 The SR fans extension in the horizontal direction is determined by the angle of the beam
6508 at the entrance of the upstream separator dipole. Because the direction of the photons is
6509 parallel to the direction of the electron from which it is emitted, the angle of the beam and
6510 the X -distance to the interacting proton beam at the Z location of the last proton quadrupole
6511 are both greatest for photons generated at the entrance of the upstream separator dipole and,
6512 therefore, this angle defines one of the edges of the synchrotron fan on the absorber in front of
6513 the proton quadrupole. The other edge is defined by the crossing angle, which is zero for the
6514 linac-ring option. The S shaped trajectory of the beam means that the smallest angle of the
6515 beam will be reached at the IP. Therefore, the photons emitted at this point will move exactly
6516 along the Z axis. This defines the other edge of the fan in the horizontal direction.

6517 The SR fans extent in the vertical direction is determined by the beta function and angular
6518 spread of the beam. The beta function along with the emittance defines the local rms beam

6519 size. The vertical rms beam size characterizes the range of Y positions at which photons are
6520 emitted. Possibly more importantly, the vertical angular spread defines the angle between the
6521 velocity vector of these photons and the Z axis. Both of these dependencies are functions of
6522 Z . Similar effects also affect the horizontal extension of the SR fan, however, in the horizontal
6523 plane they are of second order when compared to the horizontal deflection angle in the strong
6524 dipole field.

6525 The number density distribution of the SR fan is inferred from the simulations. The number
6526 density at the location of the absorber is highest in the region between the two interacting
6527 beams. This is due to the S shaped trajectory of the beam.

6528 Parameters

6529 The parameters for the Linac Ring option are listed in Table 8.5. The separation refers to the
6530 displacement between the two interacting beams at the face of the proton triplet.

Characteristic	Value
Electron Energy [GeV]	60
Electron Current [mA]	6.6
Crossing Angle [mrad]	0
Absorber Position [m]	-9
Dipole Field [T]	0.3
Separation [mm]	75
γ/s	1.37×10^{18}

Table 8.5: LR: Parameters

6531 The energy, current, and crossing angle (θ_c) are the common values used in all LR calcula-
6532 tions. The B value refers to the constant dipole field created throughout the two dipole magnets
6533 in the IR. The direction of this field is opposite on either side of the IP. The field is chosen
6534 such that 75 mm of separation is reached by the face of the proton triplet. This separation
6535 was chosen based on S. Russenschuck's SC quadrupole design. [536] The separation between
6536 the interacting beams can be increased by raising the constant dipole field however for a dipole
6537 magnet $P_{SR} \propto |B^2|$, [537] therefore an optimization of the design will need to be discussed.
6538 The chosen parameters give a flux of 1.37×10^{18} photons per second at $Z = -9$ m.

6539 Power and Critical Energy

6540 Table 8.6 shows the power of the SR produced in the IR along with the critical energy. This is
6541 followed by the total power produced in the IR and the critical energy. Since the G4 simulations
6542 utilize Monte Carlo, multiple runs were used to provide a standard error. This only caused
6543 fluctuations in the power since the critical energy is static for a constant field and constant
6544 energy.

6545 These magnets have strong fields and therefore produce high critical energies and a sub-
6546 stantial amount of power. Although the power is similar to that of the RR design the critical
6547 energy is much larger. This comes from the linear dependence of critical energy on magnetic
6548 field (*i.e.* $E_c \propto B$). [538] With the dipole field in the LR case being an order of magnitude

Element	Power [kW]	Critical Energy [keV]
DL	24.4 +/- 0.1	718
DR	24.4 +/- 0.1	718
Total	48.8 +/- 0.1	718

Table 8.6: LR: Power and Critical Energies [Geant4]

6549 larger than the dipole fields in the RR case the critical energies from the dipole magnets are
6550 also an order of magnitude larger in the LR case.

6551 Comparison

6552 The IRSYN cross check of the power and critical energies is shown in Table 8.7. This comparison
6553 was done for the total power and the critical energy.

	Power [kW]		Critical Energy [keV]	
	Geant4	IRSYN	Geant4	IRSYN
Total	48.8 +/- 0.1	X	718	718

Table 8.7: LR: Geant4 and IRSYN comparison

6554 A third cross check to the Geant4 simulations was made for the power as shown in Table
6555 8.8. This was done using an analytic method for calculating power in dipole magnets. [537]

	Power [kW]	
Element	Geant4	Analytic
DL	24.4 +/- 0.1	24.4
DR	24.4 +/- 0.1	24.4
Total/Avg	48.8 +/- 0.1	48.8

Table 8.8: LR: Geant4 and Analytic method comparison

6556 Number Density and Envelopes

6557 The number density of photons at different Z values is shown in Figure 8.21. Each graph
6558 displays the density of photons in the $Z = Z_o$ plane for various values of Z_o . The first three
6559 graphs give the growth of the SR fan inside the detector area. This is crucial for determining the
6560 dimensions of the beam pipe inside the detector area. Since the fan grows asymmetrically in the
6561 -Z direction an asymmetric elliptical cone shaped beam pipe will minimize these dimensions,
6562 allowing the tracking to be placed as close to the beam as possible. The horizontal extension
6563 of the fan in the LR option is larger than in the RR case. This is due to the large angle of the
6564 beam at the entrance of the upstream separator dipole. As mentioned in the introduction this
6565 angle defines the fans extension, and in the LR case this angle is the largest, hence the largest

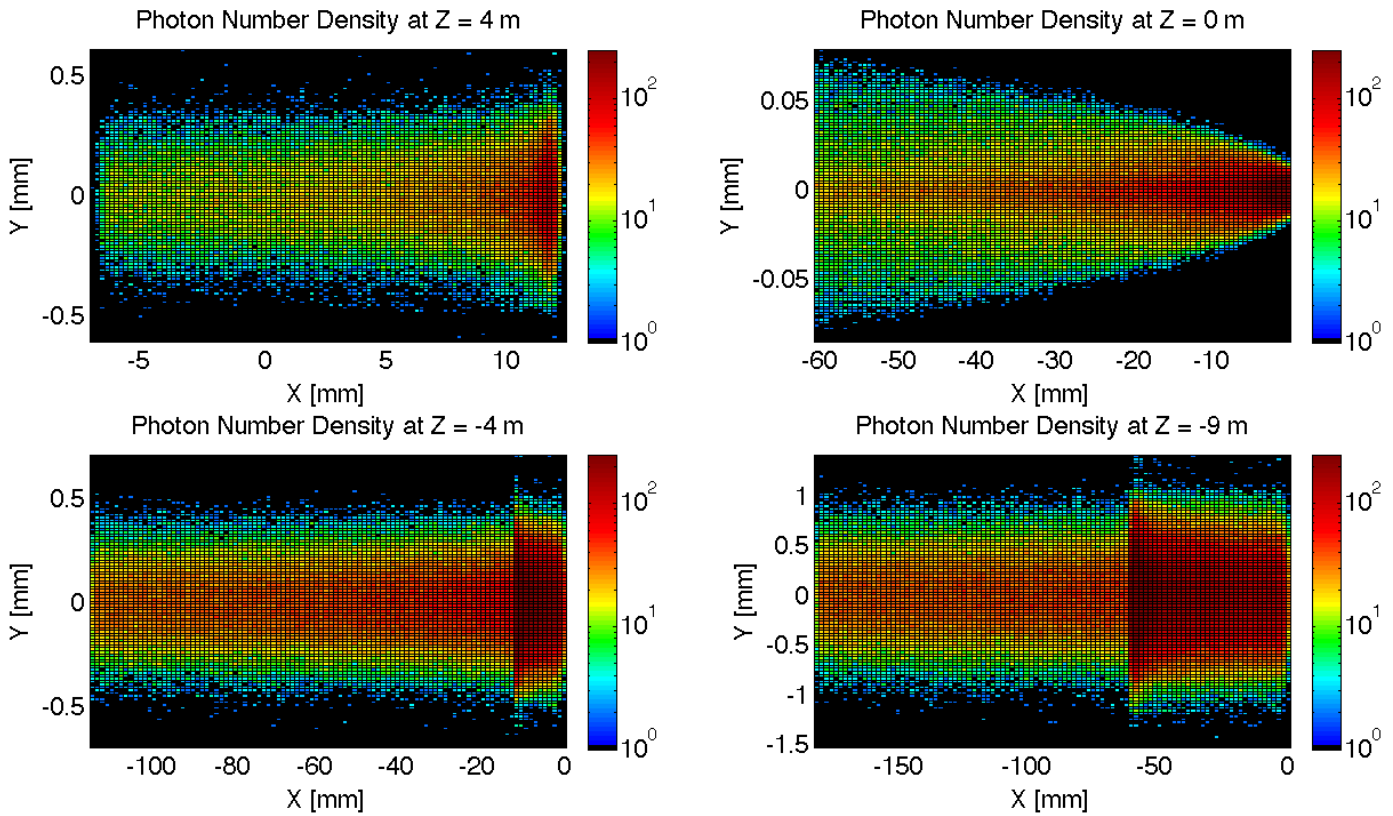


Figure 8.21: LR: Number Density Growth in Z

6566 fan. The number density of this fan appears as expected. There exists the highest density
 6567 between the two beams at the absorber.

6568 In Figure 8.21 the distribution was given at various Z values however a continuous envelope
 6569 distribution is also important to see everything at once. This can be seen in Figure 8.22, where
 6570 the beam and fan envelopes are shown in the $Y = 0$ plane. This makes it clear that the fan is
 6571 antisymmetric which comes from the S shape of the electron beam as previously mentioned.

6572 Absorber

6573 The Photon distribution on the absorber surface is crucial. The distribution decides how
 6574 the absorber must be shaped. The shape of the absorber in addition to the distribution on
 6575 the surface then decides how much SR is backscattered into the detector region. In HERA
 6576 backscattered SR was a significant source of background that required careful attention. [539]
 6577 Looking at Figure 8.23 it is shown that for the LR option 35.15 kW of power from the SR light
 6578 will fall on the face of the absorber which is 73% of the total power. This gives a general idea
 6579 of the amount of power that will be absorbed. However, backscattering and IR photons will

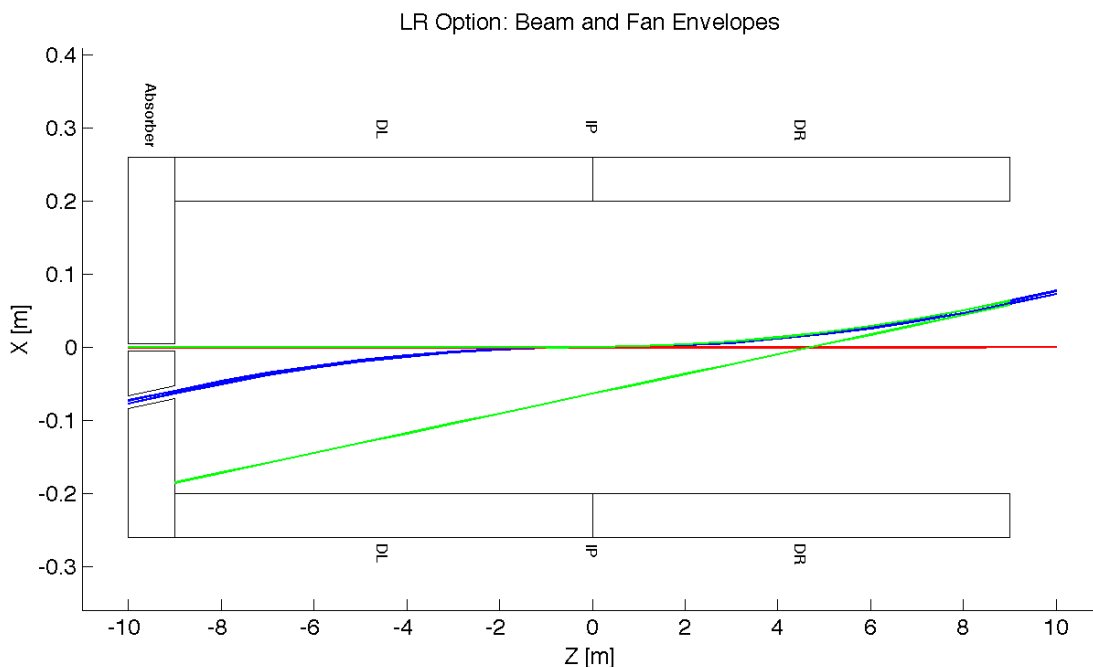


Figure 8.22: LR: Beam Envelopes in Z

6580 lower the percent that is actually absorbed.

6581 **Proton Triplet:** The super conducting final focusing triplet for the protons needs to be
 6582 protected from radiation by the absorber. Some of the radiation produced upstream of the
 6583 absorber however will either pass through the absorber or pass through the apertures for the
 6584 two interacting beams. This is most concerning for the interacting proton beam aperture which
 6585 will have the superconducting coils. A rough upper bound for the amount of power the coils
 6586 can absorb before quenching is 100 W. [540] There is approximately 2 kW entering into the
 6587 interacting proton beam aperture as is shown in Figure 8.23. This doesnt mean that all this
 6588 power will hit the coils but simulations need to be made to determine how much of this will
 6589 hit the coils. The amount of power that will pass through the absorber (0.25 W) can be
 6590 disregarded as it is not enough to cause any significant effects. The main source of power
 6591 moving downstream of the absorber will be the photons passing through the beams aperture.
 6592 This was approximately 11 kW as can be seen from Figure 8.23. Most of this radiation can be
 6593 absorbed in a secondary absorber placed after the first downstream proton quadrupole. Overall
 6594 protecting the proton triplet is important and although the absorber will minimize the radiation
 6595 continuing downstream this needs to be studied in depth.

6596 **Beamstrahlung** The beamstrahlung photons travel parallel to the proton beam until the
 6597 entrance of D1 without impacting the triplets. Figure 8.24 shows the transverse and energy
 6598 distributions of the beamstralung photons at the entry of D1 as computed with Guineapig [604].

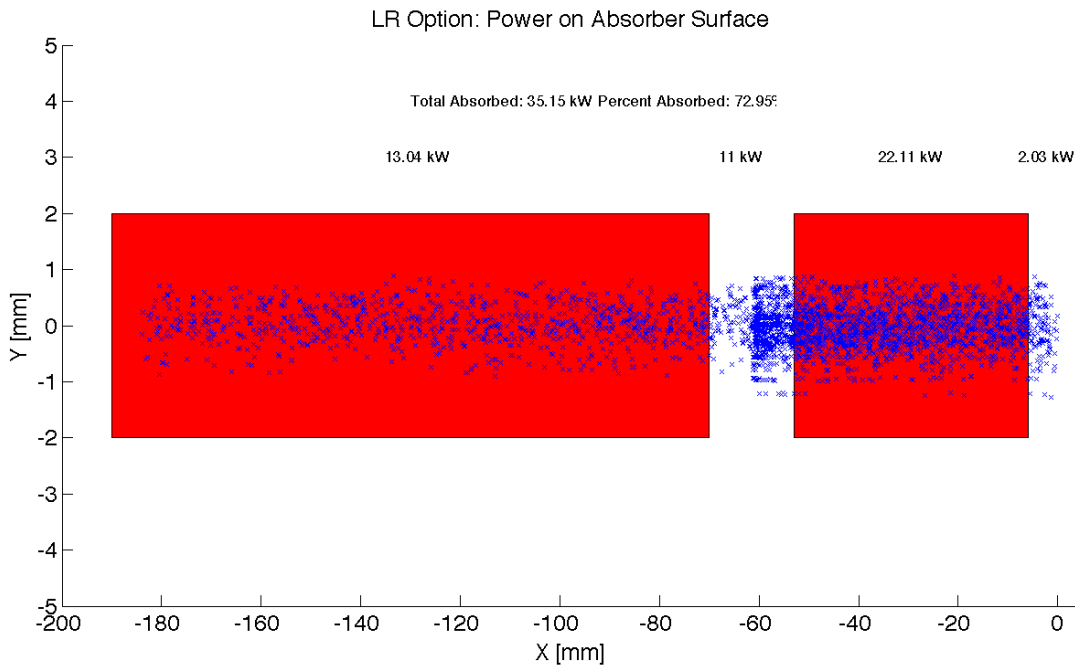


Figure 8.23: LR: Photon distribution on Absorber Surface

6599 The maximum photon energy is about 20 MeV the average photon energy is 0.4 MeV. The
 6600 beamstrahlung power is 980 W. D1 has to be designed to properly dispose the neutral debris
 6601 from the IP. Splitting D1 into two parts could allow an escape line for the neutral particles.

6602 **Backscattering** Another G4 program was written to simulate the backscattering of photons
 6603 into the detector region. The ntuple with the photon information written at the absorber
 6604 surface is used as the input for this program. An absorber geometry made of copper is de-
 6605 scribed, and general physics processes are set up. A detector volume is then described and
 6606 set to record the information of all the photons which enter in an ntuple. The first step in
 6607 minimizing the backscattering was to optimize the absorber shape. Although the simulation
 6608 didnt include a beam pipe the backscattering for different absorber geometries was compared
 6609 against one another to find a minimum. The most basic shape was a block of copper that
 6610 had cylinders removed for the interacting beams. This was used as a benchmark to see the
 6611 maximum possible backscattering. In HERA a wedge shape was used for heat dissipation and
 6612 minimizing backscattering. [539] The profile of this geometry in the YZ plane is shown in Figure
 6613 8.25. It was found that this is the optimum shape for the absorber. The reason for this is that
 6614 a backscattered electron would have to have its velocity vector be almost parallel to the
 6615 wedge surface to escape from the wedge and therefore it works as a trap. One can be seen from
 6616 Table 8.9 utilizing the wedge shaped absorber decreased the backscattered power by a factor of
 6617 4. The energy distribution for the backscattered photons can be seen in Figure 8.26.

6618 After the absorber was optimized it was possible to set up a beam pipe geometry. An

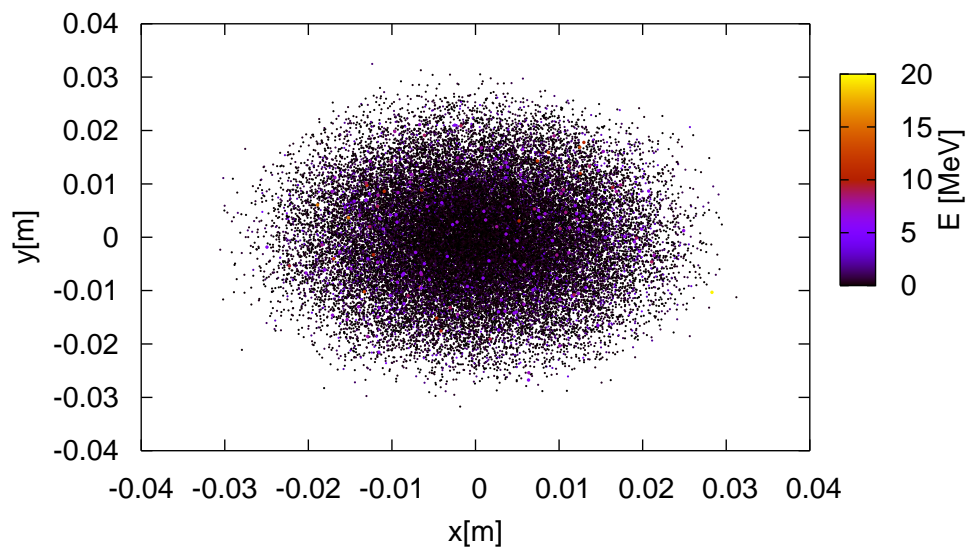


Figure 8.24: Beamstrahlung photons at the entrance of D1.

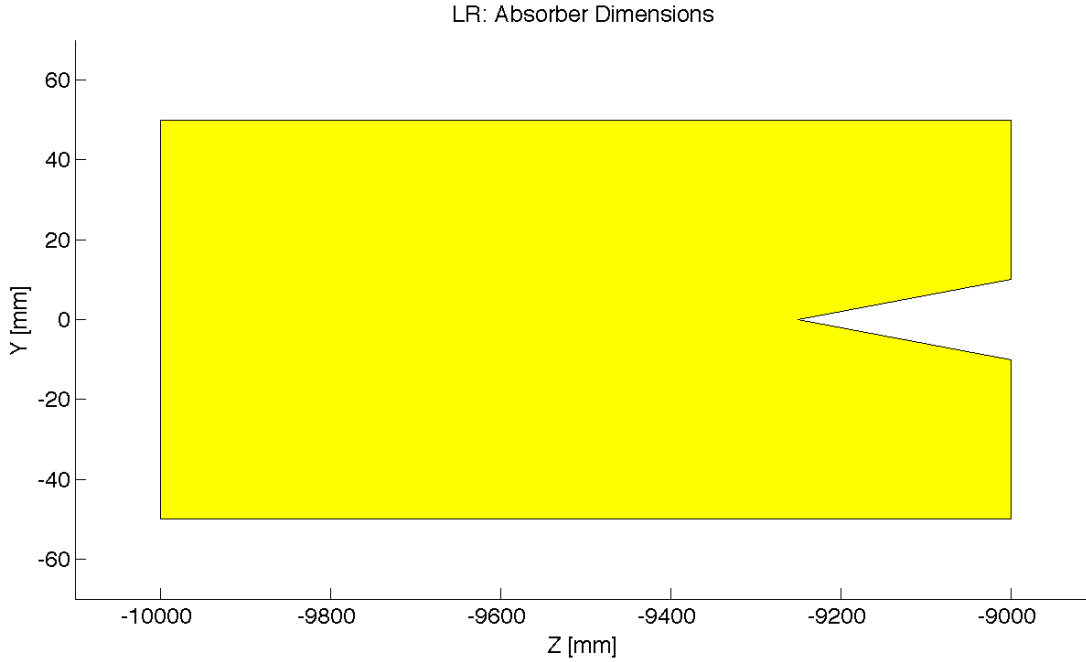


Figure 8.25: LR: Absorber Dimensions

6619 asymmetric elliptical cone beam pipe geometry made of beryllium was used since it would
 6620 minimize the necessary size of the beam pipe as previously mentioned. The next step was to
 6621 place the lead shield and masks inside this beam pipe. To determine placement a simulation
 6622 was run with just the beam pipe. Then it was recorded where each backscattered photon
 6623 would hit the beam pipe in Z. A histogram of this data was made as shown in Figure 8.27. This
 6624 determined that the shield should be placed in the Z region ranging from -8 m until the absorber
 6625 (-9 m). The masks were then placed at -8.9 m and -8.3 m. This decreased the backscattered
 6626 power by a factor of 40 as can be seen from Table 8.9. Overall there is still more optimization
 6627 that can occur with this placement.

Absorber Type	Power [W]
Flat	645.9
Wedge	159.1
Wedge & Mask/Shield	4.3

Table 8.9: LR: Backscattering/Mask

6628 Cross sections of the beampipe in the $Y = 0$ and $X = 0$ planes with the shields and masks
 6629 included can be seen in Figure 8.28.

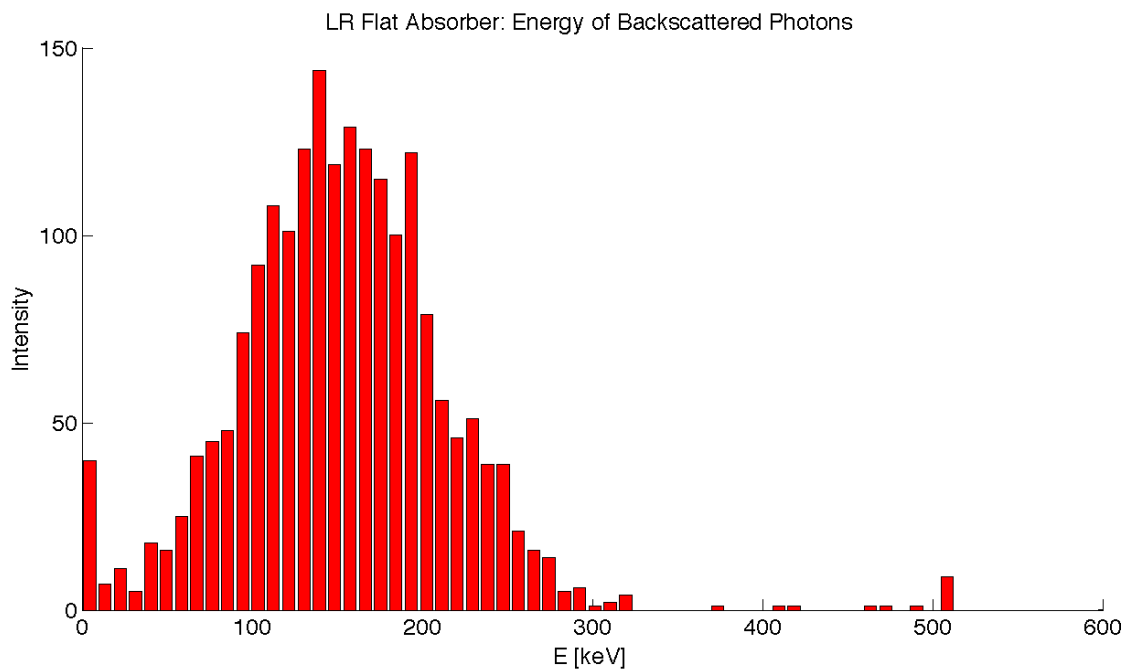


Figure 8.26: LR: Backscattered Energy Distribution

6630 8.3 Linac Lattice and Impedance

6631 8.3.1 Overall Layout

6632 The proposed layout of the recirculating linear accelerator complex (RLA) is illustrated schemat-
 6633 ically in Fig. 8.29. It consists of the following components:

- 6634 • A 0.5 GeV injector with an injection chicane.
- 6635 • A pair of 721.44MHz SCRF linacs. Each linac is one kilometer long with an energy gain
 6636 10GeV per pass.
- 6637 • Six 180° arcs. Each arc has a radius of one kilometer.
- 6638 • For each arc one re-accelerating station that compensates the synchrotron radiation emit-
 6639 ted in this arc.
- 6640 • A switching station at the beginning and end of each linac to combine the beams from
 6641 different arcs and to distribute them over different arcs.
- 6642 • An extraction dump at 0.5 GeV.

6643 After injection, the beam makes three passes through the linacs before it collides with the
 6644 LHC beam. The beam will then perform three additional turns in which the beam energy is
 6645 almost completely extracted. The size of the complex is chosen such that each turn has the same

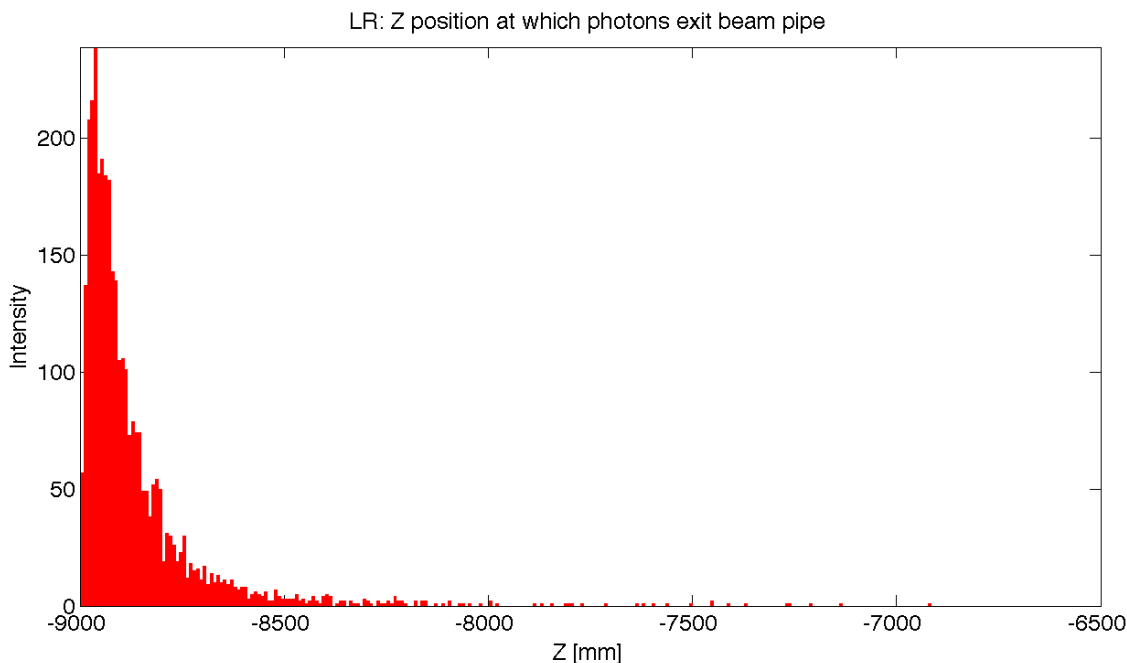


Figure 8.27: LR: Backscattered Photons Exiting the Beam Pipe

6646 length and that three turns correspond to the LHC circumference. This choice is motivated by
 6647 the following considerations:

- 6648 • To avoid the build-up of a significant ion density in the accelerator complex, clearing gaps
 6649 may be required in the beam.
- 6650 • The longitudinal position of these gaps must coincide for each of the six turns that a beam
 6651 performs. This requires that the turns have the same length.
- 6652 • Due to the gaps some LHC bunches will collide with an electron bunch but some will not.
 6653 It is advantageous to have each LHC bunch either always collide with an electron bunch
 6654 or to never collide. The choice of length for one turn in the RLA allows to achieve this.

6655 Some key beam parameters are given in table 8.10.

6656 8.3.2 Linac Layout and Lattice

6657 The key element of the transverse beam dynamics in a multi-pass recirculating linac is an
 6658 appropriate choice of multi-pass linac optics. The focusing strength of the quadrupoles along
 6659 the linac needs to be set such that one can transport the beam at each pass. Obviously, one
 6660 would like to optimize the focusing profile to accommodate a large number of passes through
 6661 the RLA. In addition, the requirement of energy recovery puts a constraint on the exit/entrance
 6662 Twiss functions for the two linacs. As a baseline we have chosen a FODO lattice with a phase

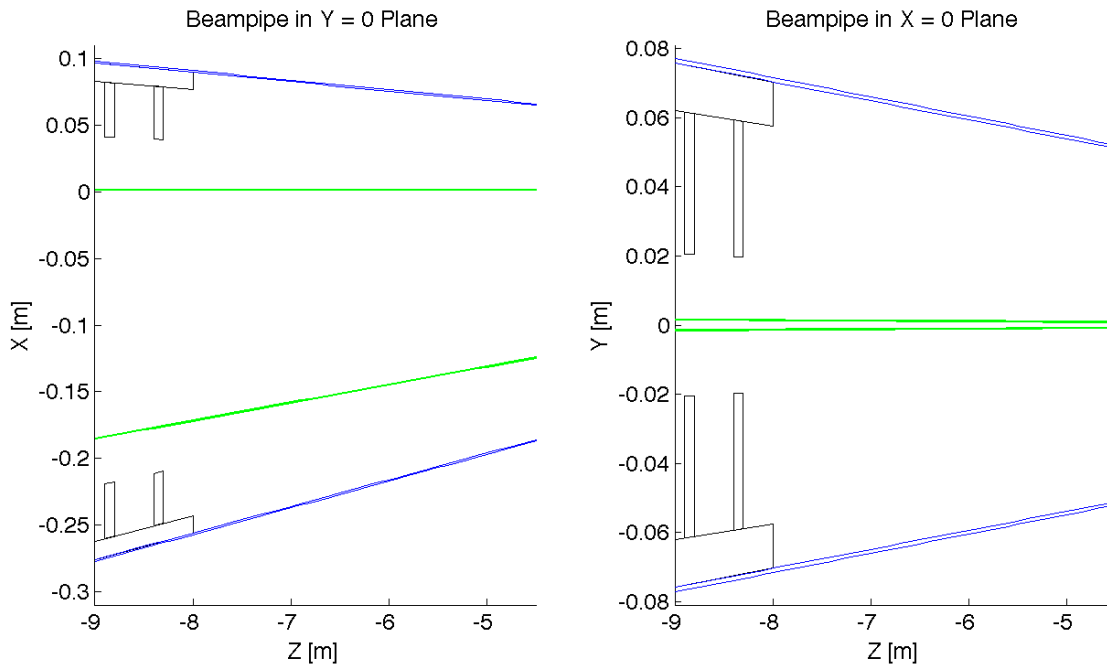


Figure 8.28: LR: Beampipe Cross Sections

6663 advance of 130° for the beam that passes with the lowest energy and a quadrupole spacing of
 6664 28m [605]. Alternative choices are possible. An example is an optics that avoids any quadrupole
 6665 in the linacs [606].

6666 Linac Module Layout

6667 The linac consists of a series of units, each consisting of two cryomodules and one quadrupole
 6668 pack. See Fig. 8.30 for the layout. Each cryomodule is 12.8m and contains eight 1m-long
 6669 accelerating cavities. The interconnect between two adjacent cryomodules is 0.8m long. The
 6670 quadrupole pack is 1.6m long, including the interconnects to the adjacent cryomodules. The
 6671 whole unit is 28m long.

6672 Each quadrupole pack contains a quadrupole, a beam position monitor and a vertical and

Parameter	Symbol	Value
Particles per bunch	N	$2 \cdot 10^9$
Initial normalised transverse emittance	ϵ_x, ϵ_y	$30\mu\text{m}$
Normalised transverse emittance at IP	ϵ_x, ϵ_y	$50\mu\text{m}$
Bunch length	σ_z	$600\mu\text{m}$

Table 8.10: Key beam parameters.

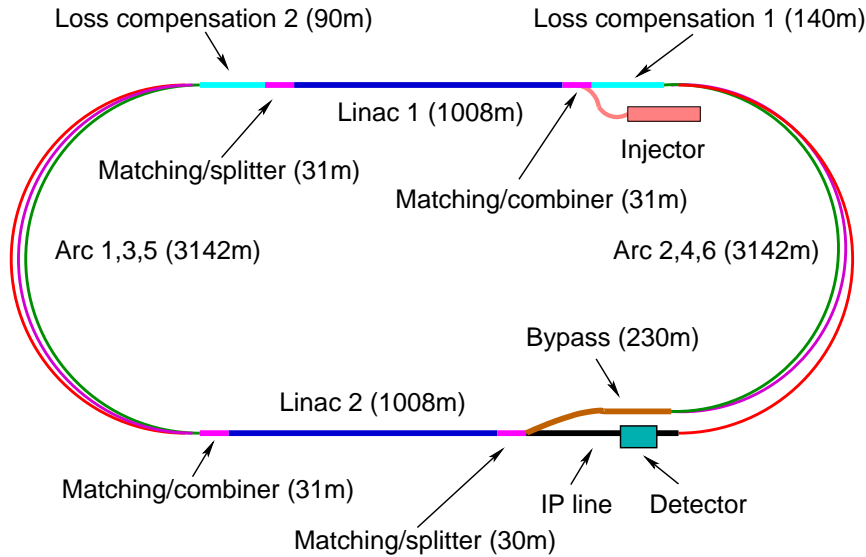


Figure 8.29: The schematic layout of the recirculating linear accelerator complex.

Figure 8.30: The schematic layout of a linac unit.

6673 horizontal dipole corrector, see section 2.9.

6674 Linac Optics

6675 The linac consists of 36 units with a total length of 1008m. In the first linac, the strength of
 6676 the quadrupoles has been chosen to provide a phase advance per cell of 130° for the beam in
 6677 its first turn. In the second linac, the strength has been set to provide a phase advance of 130°
 6678 for the last turn of the beam. The initial Twiss parameters of the beam and the return arcs are
 6679 optimised to minimise the beta-functions of the beams in the following passages. The criterium
 6680 used has been to minimise the integral

$$\int_0^L \frac{\beta}{E} ds \quad (8.6)$$

6681 Single bunch transverse wakefield effects and multi-bunch effects between bunches that have
 6682 been injected shortly after each other are proportional to this integral [607]. The final solution
 6683 is shown in Fig. 8.31. A significant beta-beating can be observed due to the weak focusing for
 6684 the higher energy beams.

6685 Return Arc Optics

6686 At the ends of each linac the beams need to be directed into the appropriate energy-dependent
 6687 arcs for recirculation. Each bunch will pass each arc twice, once when it is accelerated before
 6688 the collision and once when it is decelerated after the collision. The only exception is the arc at

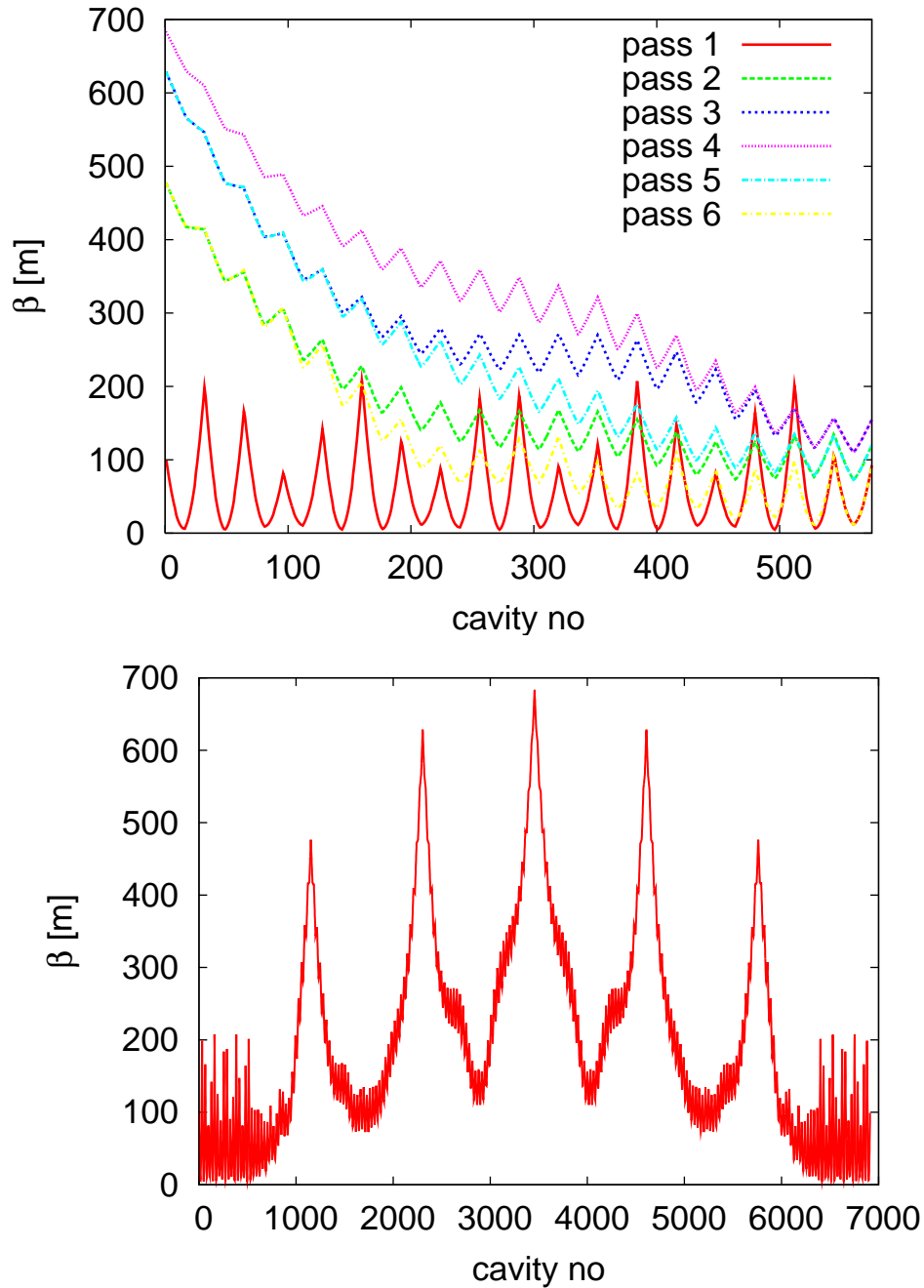


Figure 8.31: Beta-functions in the first linac. On the top, the beta-functions of the six different beam passages in the first linac are shown. On the bottom, the beta-function as seen by the beam during his stay in the linacs are shown.

turn no	E [GeV]	ΔE [MeV]	σ_E/E [%]
1	10.5	0.7	0.00036
2	20.5	10.2	0.0019
3	30.5	49.8	0.0053
4	40.5	155	0.011
5	50.5	375	0.020
6	60.5	771	0.033
7	50.5	375	0.044
8	40.5	155	0.056
9	30.5	49.8	0.074
10	20.5	10.2	0.11
11	10.5	0.7	0.216
dump	0.5	0.0	4.53

Table 8.11: Energy loss due to synchrotron radiation in the arcs as a function of the arc number. The integrated energy spread induced by synchrotron radiation is also shown.

highest energy that is passed only once. For practical reasons, horizontal rather than vertical beam separation was chosen. Rather than suppressing the horizontal dispersion created by the spreader, the horizontal dispersion can be smoothly matched to that of the arc, which results in a very compact, single dipole, spreader/recombiner system.

The initial choice of large arc radius (1 km) was dictated by limiting energy loss due to synchrotron radiation at top energy (60.5 GeV) to less than 1%. However other adverse effects of synchrotron radiation on beam phase-space such as cumulative emittance and momentum growth due to quantum excitations are of paramount importance for a high luminosity collider that requires normalized emittance of 50 mm mrad.

Three different arc designs have been developed [605]. In the design for the lowest energy turns, the beta-functions are kept small in order to limit the required vacuum chamber size and consequently the magnet aperture. At the highest energy, the lattice is optimised to keep the emittance growth limited, while the beta-functions are allowed to be larger. A cell of the lowest and one of the highest energy arc is shown in Fig. 8.32 All turns have a bending radius of 764m. The beam pipe diameter is 25mm, which corresponds to more than 12σ aperture.

An interesting alternative optics, which pushes towards a smaller beam pipe, has also been developed [606].

Synchrotron Radiation in Return Arcs

Synchrotron radiation in the arcs leads to a significant beam energy loss. This loss is compensated by the small linacs that are incorporated before or after each arc when the beams are already or still separated according to their energy, see Fig. 8.29. The energy loss at the 60GeV turn-round can be compensated by a linac with an RF frequency of 721.44MHz. The compensation at the other arcs is performed with an RF frequency of 1442.88MHz. In this way the bunches that are on their way to the collision point and the ones that already collided can

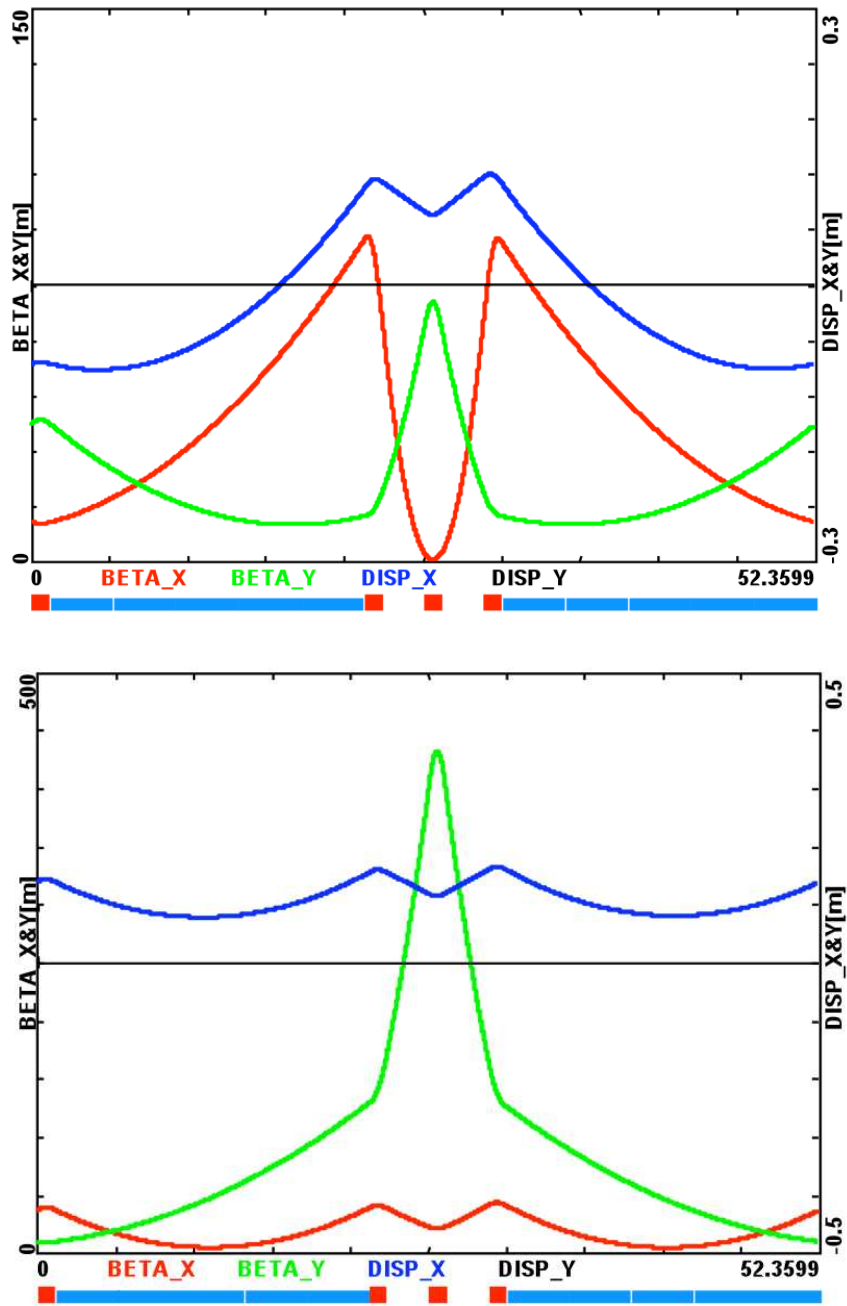


Figure 8.32: The optics of the lowest (top) and the highest (bottom) energy return arcs.

turn no	E [GeV]	$\Delta\epsilon_{arc}$ [μm]	$\Delta\epsilon_t$ [μm]
1	10.5	0.0025	0.0025
2	20.5	0.140	0.143
3	30.5	0.380	0.522
4	40.5	2.082	2.604
5	50.5	4.268	6.872
6	60.5	12.618	19.490
5	50.5	4.268	23.758
4	40.5	2.082	25.840
3	30.5	0.380	26.220
2	20.5	0.140	26.360
1	10.5	0.0025	26.362

Table 8.12: The emittance growth due to synchrotron radiation in the arcs.

6713 both be accelerated. This ensures that the energy of these bunches are the same on the way
6714 to and from the interaction point, which simplifies the optics design. If the energy loss were
6715 not compensated the beams would have a different energy at each turn, so that the number of
6716 return arcs would need to be doubled.

6717 The synchrotron radiation is also generating an energy spread of the beam. In Tab. 8.11 the
6718 relative energy spread is shown as a function of the arc number that the beam has seen. At
6719 the interaction point, the synchrotron radiation induced RMS energy spread is only 2×10^{-4} ,
6720 which adds to the energy spread of the wakefields. At the final arc the energy spread reaches
6721 about 0.22%, while at the beam dump it grows to a full 4.5%.

6722 The growth of the normalised emittance is given by

$$\Delta\epsilon = \frac{55}{48\sqrt{3}} \frac{\hbar c}{mc^2} r_e \gamma^6 I_5 \quad (8.7)$$

6723 Here, r_e is the classical electron radius, and I_5 is given by

$$I_5 = \int_0^L \frac{H}{|\rho|^3} ds = \frac{\langle H \rangle \theta}{\rho^2} \quad H = \gamma D^2 + 2\alpha DD' + \beta D'^2 \quad (8.8)$$

6724 For a return arc with a total bend angle $\theta = 180^\circ$ one finds

$$\Delta\epsilon = \frac{55}{48\sqrt{3}} \frac{\hbar c}{mc^2} r_e \gamma^6 \pi \frac{\langle H \rangle \theta}{\rho^2} \quad (8.9)$$

6725 The synchrotron radiation induced emittance growth is shown in table 8.12. Before the inter-
6726 action point a total growth of about $7\mu\text{m}$ is accumulated. The final value is $26\mu\text{m}$. While this
6727 growth is significant compared to the target emittance of $50\mu\text{m}$ at the collision point, it seems
6728 acceptable.

6729 Matching Sections and Energy Compensation

6730 Currently we do not have a design of the matching sections. However, we expect these sections
6731 to be straightforward. For the case of the linac optics without quadrupoles and the alternative
6732 return arc lattice design matching sections designs exist and exhibit no issues [606]. Also the
6733 sections that compensate the energy loss in the arcs have not been designed. But this again
6734 should be straightforward.

6735 8.3.3 Beam Break-Up

6736 Single-Bunch Wakefield Effect

6737 In order to evaluate the single bunch wakefield effects we used PLACET [608]. The full linac
6738 lattice has been implemented for all turns but the arcs have each been replaced by a simple
6739 transfer matrix, since the matching sections have not been available.

6740 Single bunch wakefields were not available for the SPL cavities. We therefore used the
6741 wakefields in the ILC/TESLA cavities [609]. In order to adjust the wakefields to the lower
6742 frequency and larger iris radius (70mm vs. 39mm for the central irises) we used the following
6743 scaling

$$W_{\perp}(s) \approx \frac{1}{(70/39)^3} W_{\perp,ILC}(s/(70/39)) \quad W_L(s) \approx \frac{1}{(70/39)^2} W_{L,ILC}(s/(70/39)) \quad (8.10)$$

6744 First, the RMS energy spread along the linacs is determined. An initial uncorrelated RMS
6745 energy spread of 0.1% is assumed. Three different bunch lengths were studied, i.e. 300 μ m,
6746 600 μ m and 900 μ m. This longest value yields the smallest final energy spread. The energy
6747 spread along during the beam life-time can be seen in Fig. 8.33. The wakefield induced energy
6748 spread is between 1×10^{-4} and 2×10^{-4} at the interaction point, $1-2 \times 10^{-3}$ at the final arc
6749 and 3.5–4.5% at the beam dump.

6750 Second, the single bunch beam-break-up is studied by tracking a bunch with an initial offset
6751 of $\Delta x = \sigma_x$. The resulting emittance growth of the bunch is very small, see Fig. 8.34.

6752 Multi-Bunch Transverse Wakefield Effects

6753 For a single pass through a linac the multi-bunch effects can easily be estimated analyti-
6754 cally [607]. Another approach exists in case of two passes through one cavity [610]. It is
6755 less straightforward to find an analytic solution for multiple turns in linacs with wakefields that
6756 vary from one cavity to the next. In this case the also phase advance from one passage through
6757 a cavity to the next passage depends on the position of the cavity within the linac.

6758 We therefore have developed a code to simulate the multi-bunch effect in the case of recir-
6759 culation and energy recovery [611]. It assumes point-like bunches and takes a number of dipole
6760 wake field modes into account. A cavity-to-cavity frequency spread of the wakefield modes can
6761 also be modeled. The arcs are replaced with simple transfer matrices. In the simulation, we
6762 offset a single bunch of a long train by one unit and determine the final position in phase space
6763 of all other bunches.

6764 We evaluated the beam stability using the wakefield modes that have been calculated for
6765 the SPL cavity design [612]. The level of the Q -values of the transverse modes is not yet known.
6766 We assume $Q = 10^5$ for all modes, which is comparable to the larger of the Q -values found in
6767 the TESLA cavities. A random variation of the transverse mode frequencies of 0.1% has been

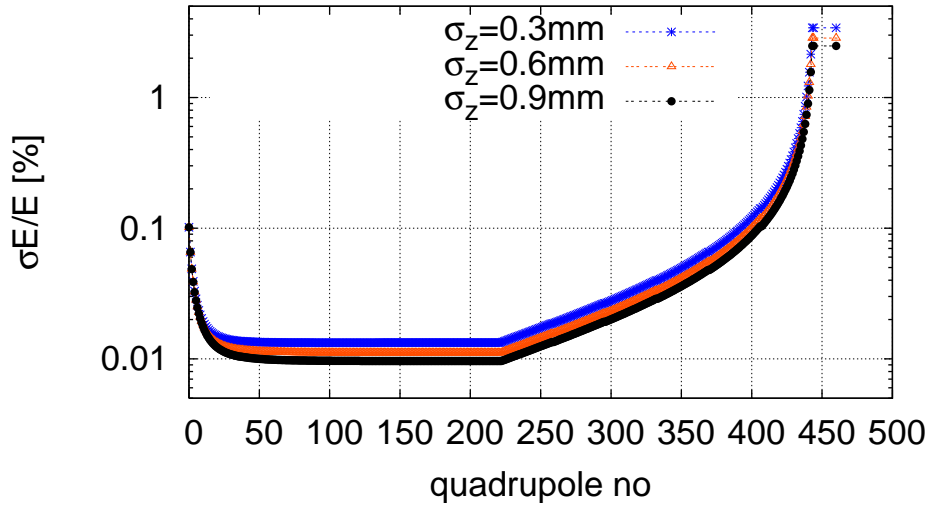


Figure 8.33: The RMS energy spread due to single bunch wakefields along the linacs. The bunch has been cut longitudinally at $\pm 3\sigma_z$ and at $\pm 3\sigma_E$ in the initial uncorrelated energy spread.

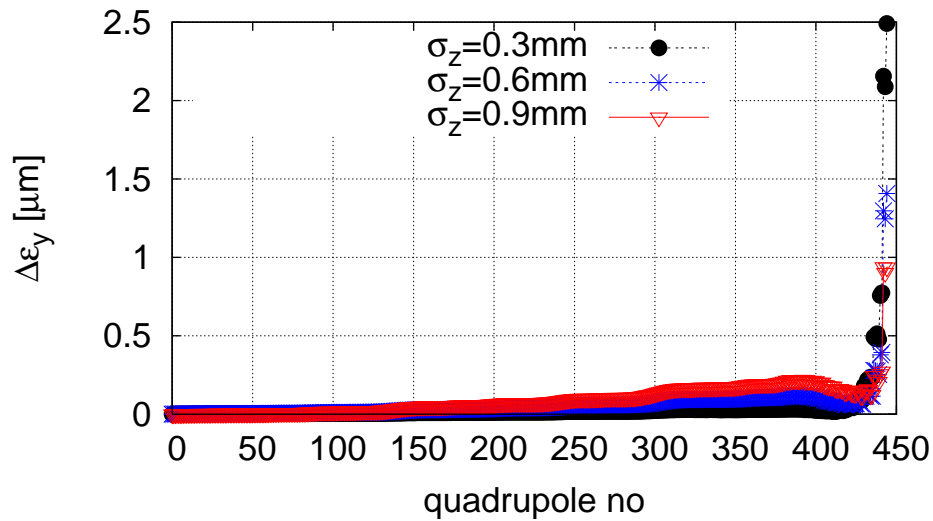


Figure 8.34: The single-bunch emittance growth along the LHeC linacs for a bunch with an initial offset of $\Delta x = \sigma_x$. The arcs have been represented by a simple transfer matrix.

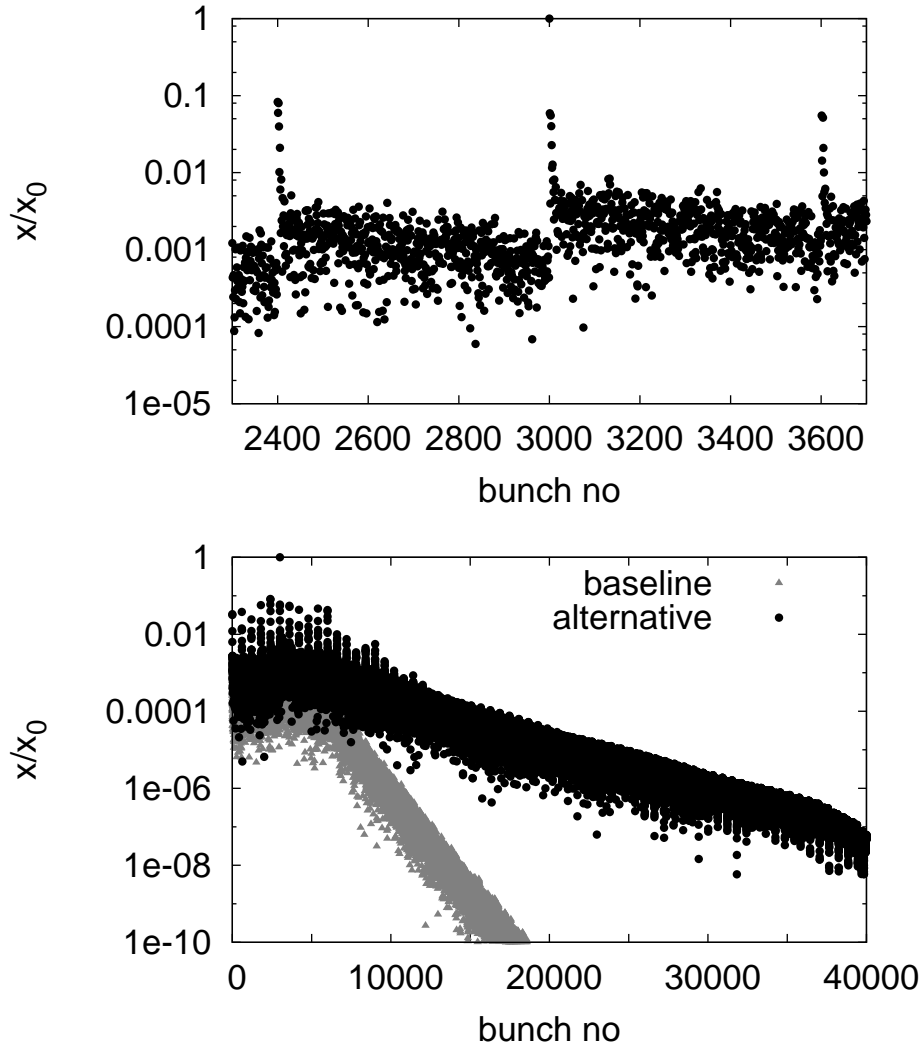


Figure 8.35: Multi-bunch beam break-up assuming the SPL cavity wakefields. One bunch has been offset at the beginning of the machine and the normalised amplitudes of the bunch oscillations are shown along the train at the end of the last turn. The upper plot shows a small number of bunches before and after the one that has been offset (i.e. bunch 3000). The lower plot shows the amplitudes along the full simulated train for the baseline lattice and the alternative design with no quadrupole focusing. One can see the fast decay of the amplitudes.

f [GHz]	k [V/pCm ²]	f [GHz]	k [V/pCm ²]
0.9151	9.323	1.675	4.160
0.9398	19.095	2.101	1.447
0.9664	8.201	2.220	1.427
1.003	5.799	2.267	1.377
1.014	13.426	2.331	2.212
1.020	4.659	2.338	11.918
1.378	1.111	2.345	5.621
1.393	20.346	2.526	1.886
1.408	1.477	2.592	1.045
1.409	23.274	2.592	1.069
1.607	8.186	2.693	1.256
1.666	1.393	2.696	1.347
1.670	1.261	2.838	4.350

Table 8.13: The considered dipole modes of the SPL cavity design.

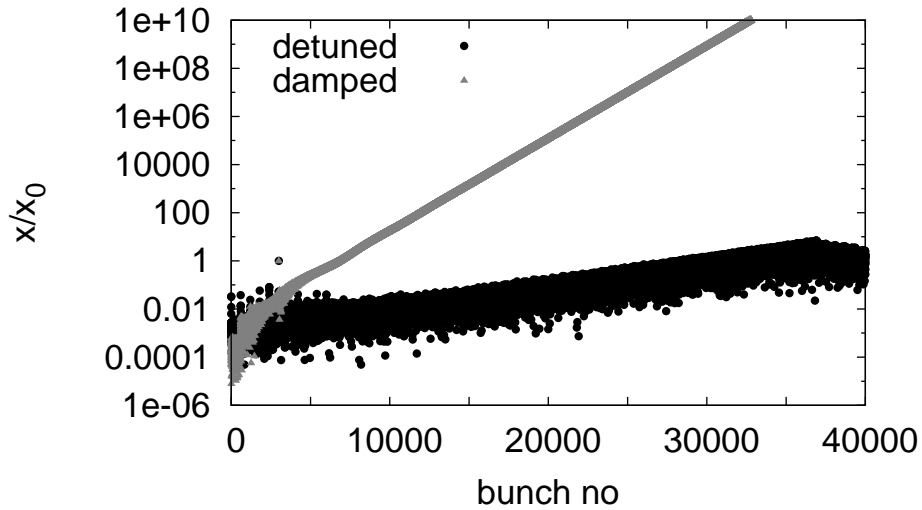


Figure 8.36: Multi-bunch beam break-up for the SPL cavities. In one case only damping, in the other case only cavity-to-cavity mode detuning is present.

6768 assumed, which corresponds to the target for ILC [609]. The results in Fig. 8.35 indicate that
 6769 the beam remains stable in our baseline design. Even in the alternative lattice with no focusing
 6770 in the linacs, the beam would remain stable but with significantly less margin.

6771 We also performed simulations, assuming that either only damping or detuning were present,
 6772 see Fig. 8.36. The beam is unstable in both cases. Based on our results we conclude

- 6773 • One has to ensure that transverse higher order cavity modes are detuned from one cavity
 6774 to the next. While this detuning can naturally occur due to production tolerances, one
 6775 has to find a method to ensure its presence. This problem exists similarly for the ILC.
- 6776 • Damping of the transverse modes is required.

6777 Further studies can give more precise limits on the maximum required Q and minimum mode
 6778 detuning.

6779 Fast Beam-Ion Instability

6780 Collision of beam particles with the residual gas in the beam pipe will lead to the production
 6781 of positive ions. These ions can be trapped in the beam. Their presence modifies the betatron
 6782 function of the beam since the ions focus the beam. They can also lead to beam break-up, since
 6783 bunches with an offset will induce a coherent motion in the ions. This can in turn lead to a
 6784 kick of the ions on following bunches.

6785 **Trapping Condition in the beam pulse** In order to estimate whether ions are trapped or
 6786 not, one can replace each beam with a thin focusing lens, with the strength determined by the
 6787 charge and transverse dimension of the beam. In this case the force is assumed to be linear
 6788 with the ion offset, which is a good approximation for small offsets.

6789 The coherent frequency f_i of the ions in the field of a beam of with bunches of similar size
 6790 is given by [613]:

$$f_i = \frac{c}{\pi} \sqrt{\frac{Q_i N r_e \frac{m_e}{A m_p}}{3 \sigma_y (\sigma_x + \sigma_y) \Delta L}} \quad (8.11)$$

6791 Here, N is the number of electrons per bunch, ΔL the bunch spacing, r_e the classical electron
 6792 radius, m_e the electron mass, Q_i the charge of the ions in units of e and A is their mass number
 6793 and m_p the proton mass. The beam transverse beam size is given by σ_x and σ_y . The ions will
 6794 be trapped in the beam if

$$f_i \leq f_{limit} = \frac{c}{4 \Delta L} \quad (8.12)$$

6795 In the following we will use $\Delta L \approx 2.5\text{m}$, i.e. assume that the bunches from the different turns
 6796 are almost evenly spaced longitudinally.

6797 In the linacs, the transverse size of the beam changes from one passage to the next while in
 6798 each of the return arcs the beams have (approximately) the same size at both passages. But
 6799 the variation from one turn to the next is not huge, so we use the average focusing strength
 6800 of the six turns. The calculation shows that ions will be trapped for a continuous beam in the
 6801 linacs. Since we are far from the limit of the trapping condition, the simplification in our model
 6802 should not matter. As can be seen in Fig. 8.37 CO_2^+ ions are trapped all along the linacs. Even
 6803 hydrogen ions H_2^+ would be trapped everywhere. If one places the bunches from the six turns
 6804 very close to each other longitudinally, the limit frequency f_{limit} is reduced. However, the ratio

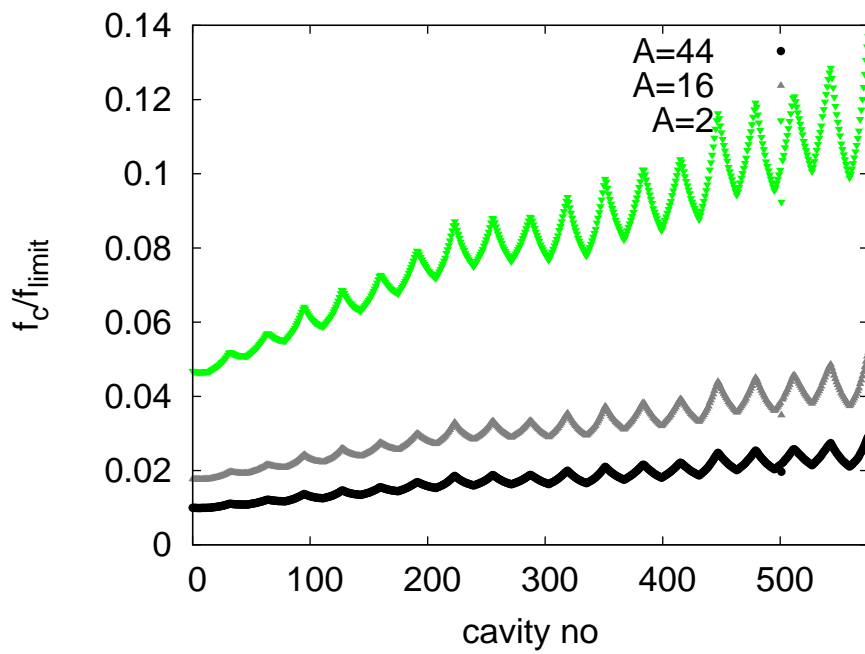


Figure 8.37: The oscillation frequency f_c of ions of different mass number A in the linacs using the average focusing strength of the bunches at different energy. The frequency is normalised to the limit frequency f_{limit} above which the ions would not be trapped any more.

6805 f_c/f_{limit} is not increased by more than a factor 6, which is not fully sufficient to remove the
 6806 H_2^+ .

6807 **Impact and Mitigation of Ion Effects** Without any methods to remove ions, a continuous
 6808 beam would collect ions until they neutralise the beam current. This will render the beam
 6809 unstable. Hence one needs to find methods to remove the ions. We will first quickly describe
 6810 the mitigation techniques and then give a rough estimate of the expected ion effect.

6811 A number of techniques can be used to reduce the fast beam-ion instability:

- 6812 • An excellent vacuum quality will slow down the build-up of a significant ion density.
- 6813 • Clearing gaps can be incorporated in the electron beam. During these gaps the ions can
 6814 drift away from the beam orbit.
- 6815 • Clearing electrodes can be used to extract the ions. They would apply a bias voltage that
 6816 lets the ions slowly drift out of the beam.

6817 **Clearing Gaps** In order to provide the gap for ion cleaning, the beam has to consist at
 6818 injection of short trains of bunches with duration τ_{beam} separated by gaps τ_{gap} . If each turn
 6819 of the beam in the machine takes τ_{cycle} , the beam parameters have to be adjusted such that
 6820 $n(\tau_{beam} + \tau_{gap}) = \tau_{cycle}$. In this case the gaps of the different turns fall into the same location
 6821 of the machine. This scheme will avoid beam loading during the gap and ensure that the gaps
 6822 are fully empty. By choosing the time for one round trip in the electron machine to be an integer
 6823 fraction of the LHC roundtrip time $\tau_{LHC} = m\tau_{cycle}$, one ensures that each bunch in the LHC
 6824 will either always collide with an electron bunch or never. We chose to use $\tau_{cycle} = 1/3\tau_{LHC}$
 6825 and to use a single gap with $\tau_{gap} = 1/3\tau_{cycle} \approx 10 \mu s$.

6826 In order to evaluate the impact of a clearing gap in the beam, we model the beam as a thick
 6827 focusing lens and the gap as a drift. The treatment follows [614], except that we use a thick
 6828 lens approach and correct a factor two in the force. The focusing strength of the lens can be
 6829 calculated as

$$k = \frac{2Nr_e m_e}{A_{ion} m_p \sigma_y (\sigma_x + \sigma_y) \Delta L} \quad (8.13)$$

6830 The ions will not be collected if the following equation is fulfilled

$$\left| 2 \cos(\sqrt{k}(L_{erl} - L_g)) - \sqrt{k} L_g \sin(\sqrt{k}(L_{erl} - L_g)) \right| \geq 2 \quad (8.14)$$

6831 Since the beam size will vary as a function of the number of turns that the beam has performed,
 6832 we replace the above defined k with the average value over the six turns using the average bunch
 6833 spacing ΔL ,

$$k = \frac{1}{n} \sum_{i=1}^n \frac{2Nr_e m_e}{A_{ion} m_p \sigma_{y,i} (\sigma_{x,i} + \sigma_{y,i}) \Delta L}. \quad (8.15)$$

6834 The results of the calculation can be found in Fig. 8.38. As can be seen, in most locations the
 6835 ions are not trapped. But small regions exist where ions will accumulate. More study is needed
 6836 to understand which ion density is reached in these areas. Longitudinal motion of the ions will
 6837 slowly move them into other regions where they are no longer trapped.

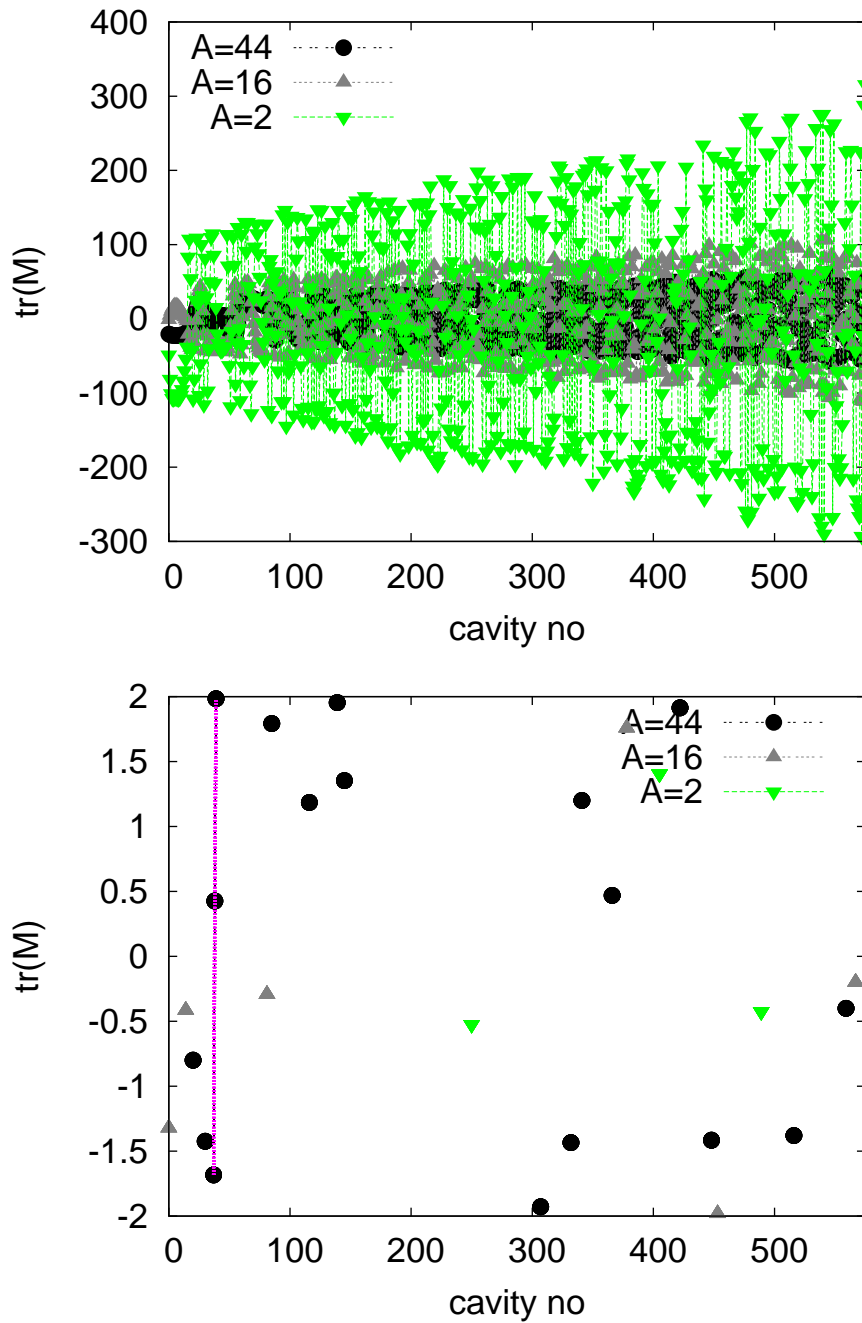


Figure 8.38: The trace of the transfer matrix for H_2^+ , CH_4^+ and CO_2^+ ions in presence of a clearing gap. Values above 2 or below -2 indicate that the ions will not be trapped.

6838 **Ion Instability** While the gap ensures that ions will be lost in the long run, they will still
6839 be trapped at least during the full train length of $20\mu\text{s}$. We therefore evaluate the impact of
6840 ions on the beam during this time. This optimistically ignores that ions will not be completely
6841 removed from one turn to the next. However, the stability criteria we employ will be pessimistic.
6842 Clearly detailed simulations will be needed in the future to improve the predictive power of the
6843 estimates.

6844 Different theoretical models exist for the rise time of a beam instability in the presence of
6845 ions. A pessimistic estimate is used in the following. The typical rise time of the beam-ion
6846 instability for the n th bunch can be estimated to be [613]

$$\tau_c = \frac{\sqrt{27}}{4} \left(\frac{\sigma_y(\sigma_x + \sigma_y)}{Nr_e} \right)^{\frac{3}{2}} \sqrt{\frac{A_{ion}m_p}{m} \frac{kT}{p\sigma_{ion}} \frac{\gamma}{\beta_y c n^2 \sqrt{L_{sep}}}} \quad (8.16)$$

6847 This estimate does not take into account that the ion frequency varies with transverse position
6848 within the bunch and along the beam line.

6849 We calculate the local instability rise length $c\tau_c$ for a pressure of $p = 10^{-11}\text{hPa}$ at the
6850 position of the beam. As can be seen in Fig. 8.39 this instability rise length ranges from a few
6851 kilometers to several hundred. One can estimate the overall rise time of the ion instability by
6852 averaging over the local ion instability rates:

$$\left\langle \frac{1}{\tau_c} \right\rangle = \frac{\int \frac{1}{\tau_c(s)} ds}{\int ds} \quad (8.17)$$

6853 For the worst case in the figure, i.e. CH_4^+ , one finds $c\tau_c \approx 14\text{ km}$ and for H_2^+ $c\tau_c \approx 25\text{km}$.
6854 The beam will travel a total of 12km during the six passes through each of the two linacs. So
6855 the typical time scale of the rise of the instability is longer than the life time of the beam and
6856 we expect no issue. This estimate is conservative since it does not take into account that ion
6857 frequency varies within the beam and along the machine. Both effects will stabilise the beam.
6858 Hence we conclude that a partial pressure below 10^{-11} hPa is required for the LHeC linacs.

6859 In the cold part of LEP a vacuum level of $0.5 \times 10^{-9}\text{hPa}$ has been measured at room
6860 temperature, which corresponds to $0.6 \times 10^{-10}\text{hPa}$ in the cold [615]. This is higher than
6861 required but this value “represents more the outgassing of warm adjacent parts of the vacuum
6862 system” [615] and can be considered a pessimistic upper limit. Measurements in the cold
6863 at HERA showed vacuum levels of 10^{-11}hPa [616], which would be sufficient but potentially
6864 marginal. Recent measurements at LHC show a hydrogen pressure of $5 \times 10^{-12}\text{hPa}$ measured
6865 at room temperature, which corresponds to about $5 \times 10^{-13}\text{hPa}$ in the cold [617]. For all other
6866 gasses a pressure of less than 10^{-13}hPa is expected measured in the warm [617], corresponding
6867 to 10^{-14}hPa in the cold. These levels are significantly better than the requirements. The
6868 shortest instability rise length would be due to hydrogen. With a length of $c\tau_c \approx 500\text{km}$ which
6869 is longer than 40 turns. Hence we do not expect a problem with the fast beam-ion instability
6870 in the linacs provided the vacuum system is designed accordingly.

6871 The effect of the fast beam-ion instability in the arcs has been calculated in a similar way,
6872 taking into account the reduced beam current and the baseline lattice for each arc. Even H_2^+
6873 will be trapped in the arcs. We calculate the instability rise length $c\tau_c$ for a partial pressure
6874 of 10^{-9} hPa for each ion mass and find $c\tau_c \approx 70\text{km}$ for H_2^+ , $c\tau_c \approx 50\text{km}$ for N_2^+ and CO^+
6875 and $c\tau_c \approx 60\text{km}$ for CO_2^+ . The total distance the beam travels in the arcs is 15km . Hence we
6876 conclude that a partial pressure below 10^{-9} hPa should be sufficient for the arcs. More detailed

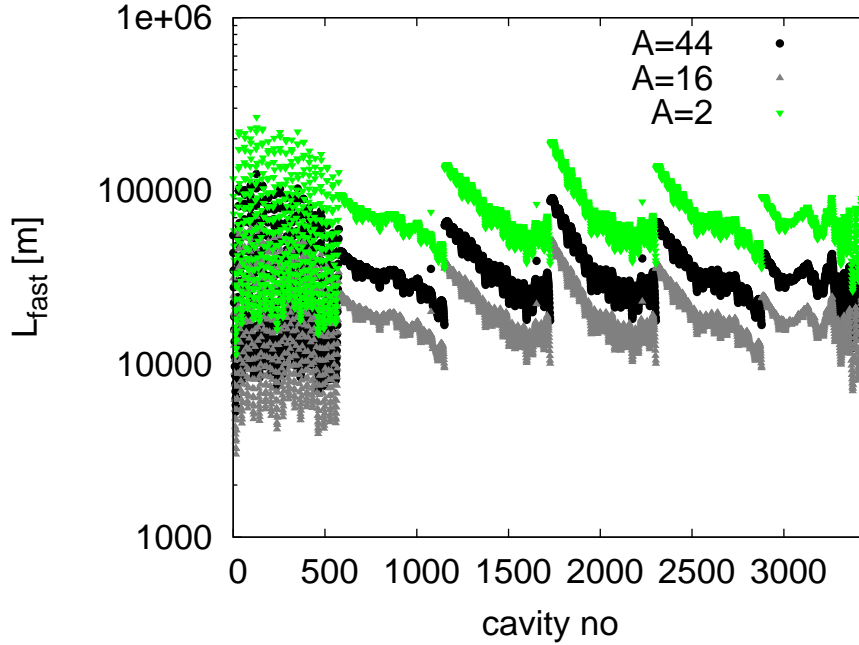


Figure 8.39: The instability length of the beam-ion instability assuming a very conservative partial pressure of 10^{-11} hPa for each gas.

6877 work will be needed in the future to fully assess the ion effects in LHeC but we remain confident
6878 that they can be handled.

Ion Induced Phase Advance Error The relative phase advance error along a beam line can be calculated using [614] for a round beam:

$$\frac{\Delta\phi}{\phi} = \frac{1}{2} \frac{Nr_e}{\Delta L \epsilon_y} \frac{\theta}{\langle \beta_y^{-1} \rangle}$$

6879 Here θ is the neutralisation of the beam by the ions. We use the maximum beta-function in
6880 the linac to make a conservative approximation $\langle \beta^{-1} \rangle = 1/700\text{m}$. At the end of the train we
6881 find $\rho \approx 3.3 \times 10^{-5}$ for $p = 10^{-11}$ hPa in the cold and $p = 10^{-9}$ hPa in the warm parts of the
6882 machine. This yields $\Delta\Phi/\Phi \approx 7 \times 10^{-4}$. Hence the phase advance error can be neglected.

6883 **Impact of the Gap on Beam Loading** It should be noted that the gaps may create some
6884 beam-loading variation in the injector complex. We can estimate the associated gradient vari-
6885 ation assuming that the same cavities and gradients are used in the injector as in the linacs.
6886 We use

$$\frac{\Delta G}{G} \approx \frac{1}{2} \frac{R}{Q} \omega \frac{\tau_{gap} \tau_{beam} I}{\tau_{gap} + \tau_{beam}} \frac{1}{G} \quad (8.18)$$

6887 In this case the $10\mu\text{s}$ gaps in the bunch train correspond to a gradient variation of about 0.6%.
6888 This seems very acceptable.

6889 8.3.4 Imperfections

6890 Static imperfections can lead to emittance growth in the LHeC linacs and arcs. However, one
6891 can afford an emittance budget that is significantly larger than the one for the ILC, i.e. $10\mu\text{m}$
6892 vs. 20nm . If the LHeC components are aligned with the accuracy of the ILC components, one
6893 would not expect emittance growth to be a serious issue. In particular in the linacs dispersion
6894 free steering can be used and should be very effective, since the energies of the different probe
6895 beams are much larger than they would be in ILC.

6896 Gradient Jitter and Cavity Tilt

Since the cavities have tilts with respect to the beam line axis, dynamic variations of the
gradient will lead to transverse beam deflections. This effect can be easily calculated using the
following expression:

$$\frac{\langle y^2 \rangle}{\sigma_y^2} = \frac{\langle (y')^2 \rangle}{\sigma_{y'}^2} = \frac{1}{2} \frac{1}{\epsilon} \int \frac{\beta}{E} ds \frac{L_{cav} \langle \Delta G^2 \rangle \langle (y'_{cav})^2 \rangle}{mc^2}$$

For an RMS cavity tilt of $300\mu\text{radian}$, an RMS gradient jitter of 1% and an emittance of $50\mu\text{m}$
we find

$$\frac{\langle y^2 \rangle}{\sigma_y^2} = \frac{\langle (y')^2 \rangle}{\sigma_{y'}^2} \approx 0.0125$$

6897 i.e. an RMS beam jitter of $\approx 0.07\sigma_y$. At the interaction point the beam jitter would be
6898 $\approx 0.05\sigma_{y'}$.

6899 8.4 Polarized-Electron Injector for the Linac-Ring LHeC

6900 We present the injector for the polarized electron beam. The issue of producing a sufficient
6901 number of polarized or unpolarized positrons is discussed in section ??.

6902 The Linac-Ring option is based on an ERL machine where the beam pattern, at IP, is shown
6903 in Figure 8.40.

6904 With this bunch spacing, one needs 20×10^9 bunches/second and with the requested bunch
6905 charge, the average beam current is $20 \times 10^9 \text{ b/s} \times 0.33 \text{ nC/b} = 6.6 \text{ mA}$.

6906 Figure 8.41 shows a possible layout for the injector complex, as source of polarized electron
6907 beam.

6908 The injector is composed of a DC gun where a photocathode is illuminated by a laser beam.
6909 Then a linac accelerates electron beam up to the requested energy before injection into the
6910 ERL. Downstream a bunch compressor system allows to compress the beam down to 1 ps and
6911 finally a spin rotator, brings the spin in the vertical plane.

6912 Assuming 90% of transport efficiency between the source and the IP, the bunch charge at the
6913 photocathode should $2.2 \times 10^9 \text{ e-/b}$. According to the laser and photocathode performance, the
6914 laser pulse width, corresponding to the electron bunch length, will be between 10 and 100 ps.

6915 Table 8.14 summarises the electron beam parameters at the exit of the DC gun.

6916 The challenges to produce the 7 mA beam current are the following:

- 6917 • a very good vacuum ($< 10^{-12}$ mbar) is required in order to get a good lifetime.

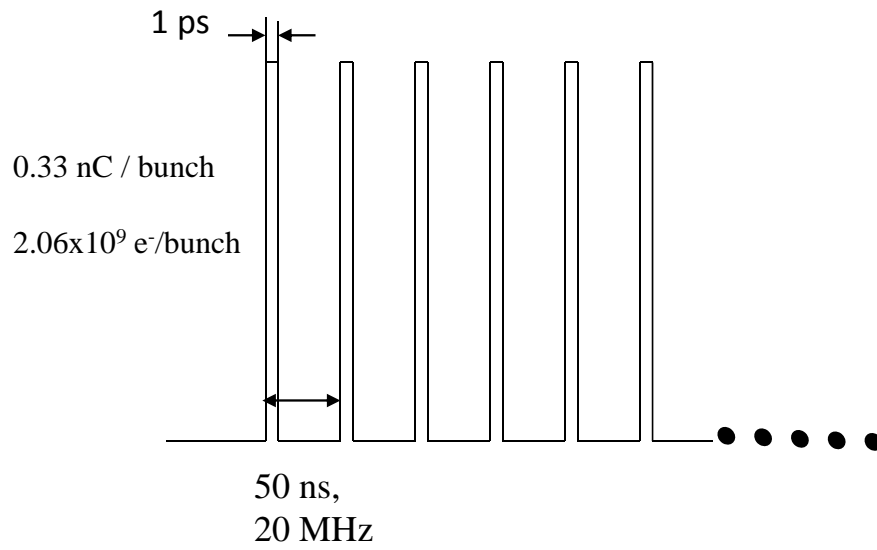


Figure 8.40: Beam pattern at IP

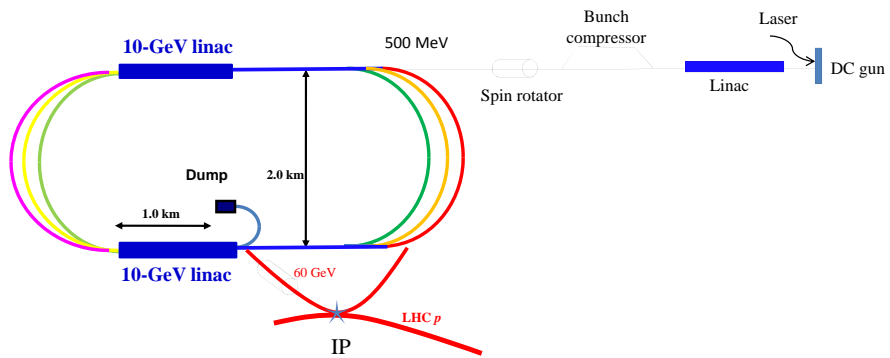


Figure 8.41: Layout of the injector (not to scale).

Parameters	60 GeV ERL
Electrons /bunch	2.2×10^9
Charge /bunch	0.35 nC
Number bunches / s	20×10^9
Bunch length	10 – 100 ps
Bunch spacing	50 ns
Pulse repetition rate	CW
Average current	7 mA
Peak current of the bunch	3.5 – 350 A
Current density (1 cm)	1.1 – 110 A/cm ²
Polarization	> 90%

Table 8.14: Beam parameters at the source.

- 6918 • the issues related to the space charge limit and the surface charge limit should be consid-
6919 ered. A peak current of 10 A with 4 ns pulse length has been demonstrated. Assuming a
6920 similar value for the DC gun, a laser pulse length of 35 ps would be sufficient to produce
6921 the requested LHeC charge.
- 6922 • the high voltage (100 kV to 500 kV) of the DC gun could induce important field emissions.
- 6923 • the design of the cathode/anode geometry is crucial for a beam transport close to 100%.
- 6924 • the quantum efficiency should be as high as possible for the photocathode ($\sim 1\%$ or more).
- 6925 • the laser parameters (300 nJ/pulse on the photocathode, 20 MHz repetition rate) will
6926 need some R&D according to what is existing today on the market.
- 6927 • the space charge could increase the transverse beam emittances.

6928 In conclusion, a tradeoff between the photocathode, the gun and the laser seems reachable
6929 to get acceptable parameters at the gun exit. A classical Pre-Injector Linac accelerates electron
6930 beam to the requested ERL energy. Different stages of bunch compressor are used to compensate
6931 the initial laser pulse and the space charge effects inducing bunch lengthening. A classical spin
6932 rotator system rotates the spin before injection into the ERL.

6933 8.5 Spin Rotator

6934 The LHeC physics requires polarized electrons with spin aligned longitudinally at the collision
6935 point [618]. In the electron accelerator of LHeC, consisting of two 10-GeV superconducting
6936 linear accelerators linked with six 180° arc paths, the depolarization due to the arcs is negligible
6937 if the spin is aligned vertically in the arcs.

6938 The motion of the spin vector \vec{S} is governed by Thomas-BMT equation [?, 619] shown in
6939 Eq. 8.19

$$\frac{d\vec{S}}{dt} = \frac{e}{m\gamma} \vec{S} \times [(1 + G\gamma)\vec{B}_\perp + (1 + G)\vec{B}_\parallel] \quad (8.19)$$

6940 where e , m and γ are the electric charge, mass and Lorentz factor of the particle. G is the
 6941 anomalous g-factor. For protons, $G = 1.7928474$ and for electrons, $G = 0.00115$. \vec{B}_\perp and \vec{B}_\parallel are
 6942 the magnetic field perpendicular and parallel to the particle velocity direction, respectively. In
 6943 Eq. 8.19, magnetic field is in the laboratory frame while the spin vector \vec{S} is in the particle's rest
 6944 frame. In a bending dipole, a spin vector precesses $G\gamma$ times of the particle's orbital rotation in
 6945 the particle's moving frame. It is also evident that solenoid field is less effective to manipulate
 6946 spin motion at high energies.

6947 For the LHeC physics program, the polarization of 60 GeV electron beam needs to be aligned
 6948 longitudinally at the collision point which is after the last arc and the acceleration. The most
 6949 economical way to control the spin direction at the collision point is to control the spin direction
 6950 of the low energy electron beam at the early stage of injector using a Wien Filter, a traditional
 6951 low energy spin rotator. Since spin vector rotates $G\gamma\pi$ each time it passes through a 180° arc,
 6952 the goal of the Wien Filter is to put the spin vector in the horizontal plane with an angle to the
 6953 direction of the particle's velocity to compensate the amount of spin rotations before collision.

6954 For the layout of LHeC, i.e. two linear accelerators linked with two arcs, spin vector rotates

$$\phi_{arc} = G\pi[\gamma_i(2n - 1) + \Delta\gamma n(2n - 1)] \quad (8.20)$$

6955 after its n th path. Here, γ_i is the initial Lorentz factor of the beam and $\Delta\gamma$ is the energy gain
 6956 of each linear accelerator. In addition, LHeC also employs two horizontal bending dipoles on
 6957 either side of the collision point to separate the electrons from the protons. Each of this bending
 6958 dipole is 0.3 T and spans 9 m from the collision point. For 60 GeV electron beam, it rotates the
 6959 spin vector by $\phi_{IP} = 104.4^\circ$. For initial energy of 10 GeV and each linear accelerator energy
 6960 gain of 10 GeV, Table 8.15 lists the amount of spin rotation through the arcs and the amount
 6961 of spin rotation through the final bending dipole at the collision point for 20 GeV, 40 GeV and
 60 GeV beam, respectively. Here, the amount of spin rotation is the net spin rotations in the

Table 8.15: total spin rotation from arcs and final bending dipole at collision point

beam energy [GeV]	# of path n	ϕ_{arc} [degrees]	ϕ_{IP} [degrees]
20	1	8101.8	34.8
40	2	36457.9	69.6
60	3	81017.6	104.4

6962 range of 2π . Since the spin rotation is proportional to beam energy, for a beam of particles
 6963 with non-zero momentum spread, different amount of spin rotation then generates a spread of
 6964 spin vector directions. This results in an effective polarization loss due to the spread of the spin
 6965 vector. Fig. 8.42 shows the angle spread of the spin vector for an off-momentum particle at
 6966 20GeV, 40GeV and 60GeV. The calculation assumes the initial energy before the electron beam
 6967 enters the arc is 10 GeV and energy gain of each linear accelerator is 10 GeV. It shows that for
 6968 60 GeV electron beam, a momentum spread of 3×10^{-4} can cause about 10% polarization loss
 6969 effectively due to the spread of the spin vectors. This may not be able to satisfy the requirement
 6970 on high polarization.
 6971

6972 In order to provide the desirable polarization direction without sacrificing polarization, one
 6973 can take the traditional approach of high energy polarized beams at HERA and RHIC, i.e. to

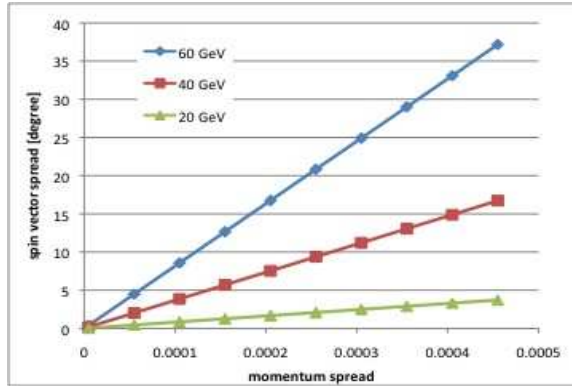


Figure 8.42: Calculated spin vector spread as function of momentum spread. The effective polarization loss is the cosine of spin vector spread angle, i.e. for an angle of 30 degrees, the effective polarization is 86% of initial beam polarization

6974 rotate the spin vector to vertical direction before it gets accelerated to high energy. Since the
 6975 spin vector aligns with the main bending magnetic fields' direction, this prevents the spread of
 6976 the spin vector due to the momentum spread. After the last arc and acceleration, at 60 GeV
 6977 beam energy, the spin vector must be rotated back so as to be longitudinally aligned at the
 6978 collision point. To this end, for the current compact LHeC design, we propose to use a RHIC
 6979 type spin rotator [?, 620] at the LHeC. Besides saving space of being compact, this approach
 6980 also provides the advantage of independent control of the spin vector orientation, as well as
 6981 nearly energy independent spin rotation for the same magnetic field. The four helical dipoles are
 6982 arranged in a similar fashion as the RHIC spin rotator, i.e. with alternating helicity. Fig. 8.43
 6983 shows the schematic layout. Each helical dipole is 3.3 m long and the helicity alternates between
 6984 right hand to left hand between each helical dipole. The two inner helical dipoles have the same
 magnetic field but opposite helicity. Same applies to the two outer helical dipoles.

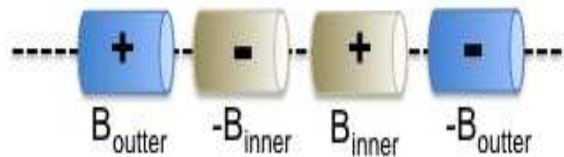


Figure 8.43: Schematic layout of LHeC spin rotator. A total of four helical dipoles with alternating helicity marked as + and -. The polarity of two outer helical dipole fields are also opposite. And so is the polarity of the two inner helical dipoles.

6985 For each helical dipole, the magnetic field is given by
 6986

$$B_x = B \cos kz; B_y = B \sin kz; B_z = 0.0 \quad (8.21)$$

6987 where, $B_{x,y,z}$ are the horizontal, vertical and longitudinal component of the magnetic field,

6988 respectively. Z is the longitudinal distance along the helical dipole axis. $|k| = \frac{2\pi}{\lambda}$ and λ are
 6989 wave number and wave length of the helical field, respectively.

6990 For spin rotator, all helical dipoles are chosen to be one period, i.e. $\lambda = L$, where L
 6991 is the length of each helical dipole. Depending on the direction of the helicity, $\frac{k}{|k|} = \pm 1$.
 6992 Fig. 8.44 shows the correlation of the magnetic field for the inner and outer helical magnets of
 6993 a spin rotator which brings the spin vector from vertical direction to be in the horizontal plane.
 6994 Fig. 8.45 shows the calculated angle of the spin vector for each outer helical magnet field. Both
 6995 plots show that this design provides a flexible choice of the direction of spin vector by adjusting
 the outer and inner helical magnetic fields respectively.

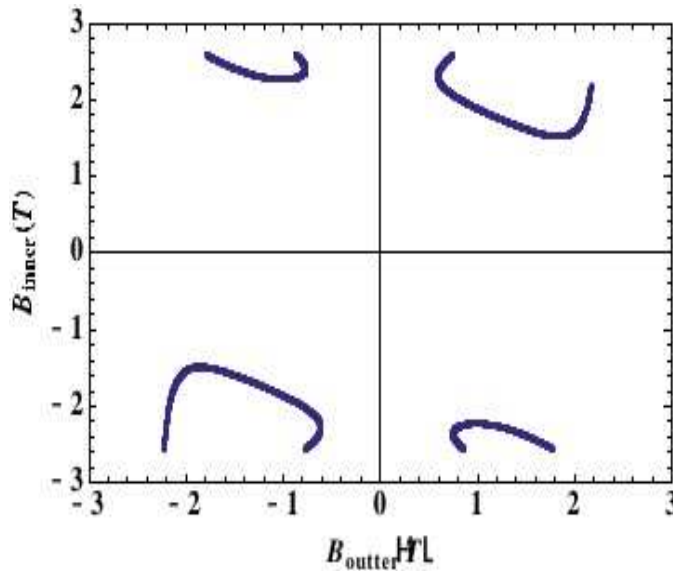


Figure 8.44: correlation of the outer and inner helical dipole magnetic field strength for a spin rotator which is designed to bring a vertically aligned spin vector to the horizontal plane.

6996
 6997 This rotator will be placed in the straight section of between LINAC and final focusing
 6998 section (FFS). This is upstream of the final bending dipole at the collision point as well as
 6999 three bends right upstream of the triplet. The 0.3 T final bending dipole rotates spin vector by
 7000 104.4 degrees for 60 GeV electron beam, while the other three bends rotates spin vector by -1.8
 7001 degrees. In order to bring the spin vector of polarized electron along longitudinal direction, it
 7002 requires that spin rotator to put the spin vector from vertical direction to the horizontal plane
 7003 with an angle of 102.6 degrees away from longitudinal direction. This requirement then yields
 7004 the magnetic field of the inner pair and outer pair to be 1.92 T and 0.93 T, respectively. The
 7005 maximum orbital excursion is 17 mm in horizontal and 8.5mm in vertical. The fine tuning of
 7006 the direction of spin vector can be achieved by empirically adjusting the helical dipole magnetic
 7007 field strength based on the measurements of the polarimeters before and after the collision
 7008 point.

7009 Detailed calculations including helical dipole design, orbital and spin tracking of spin rotator
 7010 are in working progress.

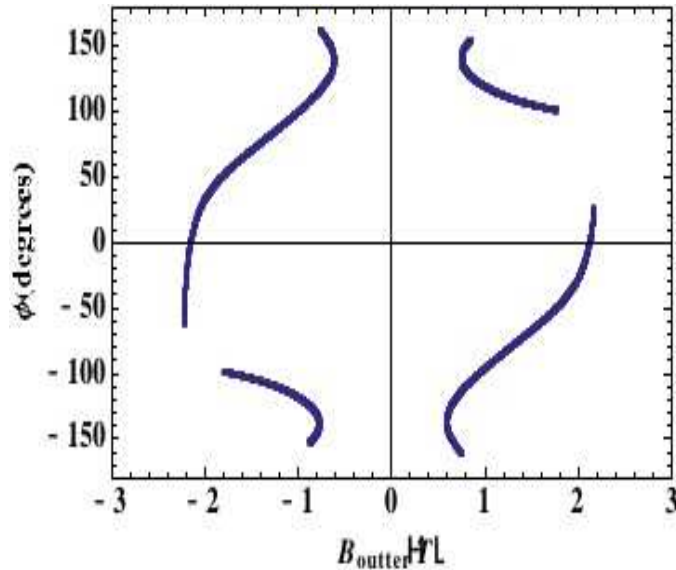


Figure 8.45: spin vector direction in the horizontal plane as function of outer helical magnet field strength

7011 8.6 Positron Options for the Linac-Ring LHeC

7012 8.6.1 Motivation

7013 To accomplish the full particle physics programme of the LHeC it is important to provide both
 7014 positron-proton (nucleon) and electron-proton (nucleon) collisions. In case of the Linac-Ring
 7015 LHeC this implies that a challenging rate of positrons must be maintained at the interaction
 7016 point.

7017 8.6.2 LHeC Linac-Ring e^+ Requirements

7018 Table 8.16 compares the e^+ beam flux foreseen for LHeC with those obtained at the SLC, and
 7019 targeted for CLIC and the ILC.

7020 The SLC (Stanford Linear Collider) was the only linear-collider type machine which has
 7021 produced e^+ for a high-energy particle physics experiment. The flux for the CLIC project (a
 7022 factor 20 compared to SLC) is already considered challenging and possible options with hybrid
 7023 targets are under investigation on paper. Even more positrons would be required for the ILC.
 7024 The requested LHeC flux for pulsed operation at 140 GeV (a factor 300 compared to SLC) could
 7025 be obtained, in a first approximation, with 10 e^+ target stations working in parallel. Several
 7026 more advanced solutions are proposed to meet the requested LHeC flux for the CW option (a
 7027 factor 7300 compared to SLC).

	SLC	CLIC (3 TeV)	ILC (500 GeV)	LHeC (p= 140)	LHeC (ERL)
Energy (GeV)	1.19	2.86	4	140	60
e^+ /bunch at IP ($\times 10^9$)	40	3.72	20	1.6	2
Norm. emittance (mm.mrad)	30 (H) 2 (V)	0.66 (H) 0.02 (V)	10 (H) 0.04 (V)	100	50
Longit. rms emittance (eV-m)	7000	5000	60000	10000	5000
e^+ /bunch after capture ($\times 10^9$)	50	7.6	30	1.8	2.2
Bunches / macropulse	1	312	2625	10^5	NA
Macropulse repetition rate	120	50	5	10	CW
Bunches / second	120	15600	13125	10^6	20×10^6
e^+ / second ($\times 10^{14}$)	0.06	1.1	3.9	18	440

Table 8.16: Comparison of the e^+ flux.

8.6.3 Mitigation Schemes

Two main approaches can be considered to reduce the rate of positrons that needs to be produced at the source, namely

- Recycling the positrons after the collision, with implied considerations on e^+ emittance after collision, emittance growth in the 60-GeV return arc due to synchrotron radiation, and the possible introduction of a cooling scheme, e.g. laser cooling à la Telnov at lower beam energy, introducing a tri-ring recovery scheme with fast laser cooling in central ring. (see below), or a using a large damping ring. If 90% of the positrons are recycled the requirement for the source drops by an order of magnitude.
- Repeated collisions on multiple turns, e.g. using a (pulsed) 180-degree phase-shift chicane in order to recover 60 GeV in the second return arc after the collision.

Reuse and Cooling of Positrons

One of the most challenging problems associated with the continuous production of positrons is cooling (damping) of the positron beam emerging from a source or recycled after the collision. The cooling process in a storage ring requires many synchrotron and betatron oscillation periods as well as the emission of many photons. The direct connection of the ERL's output and input aiming at a reuse of the positron beam does not solve the problem of beam cooling, since the electron suffers from noticeable disruption.

Beam cooling, that is at least an e-fold reduction of energy spread and transverse emittances, usually requires at least thousand turns of beam in a damping ring. The employment of a novel idea of fast cooling [?] may reduce this period, down to 200...500 turns. Even further reduction of the cooling period might be attained by designing a damping ring with multiple, S , superperiods, each of which of the double chicane scheme (to provide about $S/2$ synchrotron oscillations per full turn). In this latter case, the number of turns needed for cooling would be reduced by another factor of S .

7053 The next section present consideration on the pushed performance of a conventional damping
7054 ring, and it estimates the damping that could be obtained in a ring with the size of the SPS.
7055 An elegant complementary or alternative solution to relax the damping requirements — the
7056 tri-ring scheme — is described in the following section.

7057 Damping-Ring Considerations

7058 The main parameter driving the circumference choice of a positron damping ring for the LHeC
7059 complex is the train length (for the pulsed option) and the structure. For 10^5 bunches with
7060 separation of 25 ns the damping ring has to be unreasonably long (around 750 km). The bunch
7061 train has thus to be compressed in the damping ring and uncompressed by extracting individual
7062 bunches every 25 ns using a fast extraction kicker or RF deflector. The minimum bunch spacing
7063 in the ring is determined by the fastest achievable rise time of the extraction systems. A fast
7064 kicker can probably pulse with rise/fall times of around 2.5 ns and an RF deflector may be
7065 reduced even further (0.5 ns). Both systems have to present a stability of the order of a few
7066 10^{-4} . Given the larger emittance the kicker stability requirement may be relaxed compared with
7067 the damping rings of CLIC and ILC. Considering a 2.5-ns bunch spacing, the ring circumference
7068 can be reduced by a factor of 10 but remains still very large. A further order-of-magnitude
7069 reduction can be obtained by considering either ten times less bunches (with correspondingly
7070 higher charge) or an order of magnitude increase of the repetition rate, i.e. 100 Hz instead of
7071 10 Hz. Indeed, with a 100-Hz repetition rate, the ring becomes 7.5 km, which is very close to
7072 the circumference of the SPS of $C = 2200\pi = 6911.5$ m.

7073 In this respect, a parameter set can be deduced by taking as base a damping ring in the
7074 SPS tunnel ⁴, where a train of 9221 bunches with 2.5 ns can fit. The high repetition rate option
7075 demands that the bunches are damped and then extracted within 10 ms. Considering that at
7076 least 5 damping times are needed to reach equilibrium, the transverse damping time should be
7077 less than 2 ms. This number is assumed in the following. We note, however, that a damping
7078 time of 10 or 20 ms, with much relaxed constraints on the ring, may already be sufficient for
7079 recycling spent positrons and recovering their original emittance.

7080 The transverse damping time is given by

$$\tau_{x,y} = \frac{2EC}{cJ_{x,y}U} , \quad (8.22)$$

7081 with E the energy, $J_{x,y} \approx 1$ the damping partition numbers, c the speed of light and U the
7082 energy loss per turn:

$$U = \frac{C_\gamma E^4}{\rho} (1 + F_w) , \quad (8.23)$$

7083 with $\rho = E/(eB)$ the bending radius and F_w the wiggler damping factor:

$$F_w = \frac{L_w B_w^2}{4\pi B^2 \rho} , \quad (8.24)$$

7084 with L_w and B_w the wiggler length and field respectively. The transverse damping time can be
7085 rewritten as

$$\tau = \frac{8\pi C}{ceC_\gamma E(eB_w^2 L_w + 4\pi B E)} , \quad (8.25)$$

⁴A damping ring in the SPS tunnel has already been considered as early as 1988 by L. Evans and R. Schmidt, in CLIC Note 58, although their parameter set has been far away from present LHeC and CLIC requirements.

7086 connecting it directly with the ring energy and radiating magnet characteristics. Considering a
 7087 maximum bending field of 1.8 T and wiggler field of 1.9 T, there is a parametric interdependence
 7088 between beam energy, the total wiggler length and the damping time. Figure 8.46 shows the
 7089 dependence of the damping ring energy on the total wiggler length for a damping time of 2
 7090 ms (red curve). Without wigglers, the ring has to run at 22 GeV, whereas for around 10
 7091 GeV, wigglers with a total length of 800 m are needed. The blue curve represents the same
 7092 dependence when the low repetition rate is considered which indeed increases the damping time
 7093 by an order of magnitude. In that case, the ring energy without any wigglers can be reduced
 7094 to 7 GeV and it can be dropped to less than 4 GeV for a total wiggler length of 200 m.

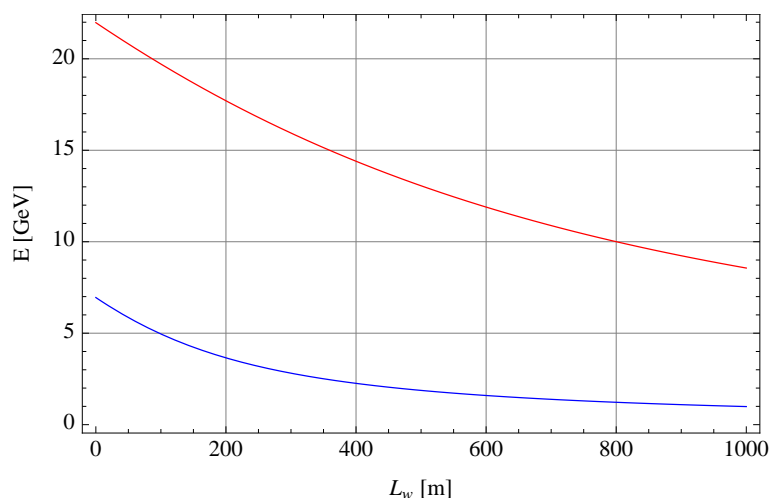


Figure 8.46: Dependence of the damping ring energy on the total wiggler length for a transverse damping time of 2 ms (red curve) and 20 ms (blue curve).

7095 A tentative parameter list for the low and high repetition rate option can be found in table
 7096 8.6.3. This example considers for both cases, 234 bending magnets of 0.5m-long dipoles with
 7097 1.8T bending field. The wiggler field of 1.9 T and a period of 5 cm is within the reach of modern
 7098 hybrid wiggler technology. A big challenge is the longitudinal parameters driven from the high
 7099 energy loss per-turn, especially in the high repetition rate case, where around 300 MV of total
 7100 RF voltage is needed to restore the high-energy loss/turn. In addition, the bunch has to be
 7101 kept short (around 5 mm) in order to achieve the longitudinal emittance target of 10 keV-m,
 7102 which necessitates a quasi-isochronous ring, with momentum compaction factor, close to 10^{-6} .
 7103 This may be a challenge for lattice design as low momentum compaction factors are achieved
 7104 for strong focusing conditions, which increase chromaticity, and necessitate strong sextupoles
 7105 with detrimental effects for the dynamic aperture of the ring. The average beam power of 25
 7106 MW indicates that the wall-plug power would be quite high and may necessitate the use of
 7107 super-conducting RF system to increase efficiency. In the low repetition case, the RF voltage
 7108 and power are an order of magnitude more relaxed.

7109 Tri-Ring Scheme

7110 A possible solution to cool down a continuous positron beam, both the recycled beam and/or
 7111 a new beam from a source, is the tri-ring scheme illustrated in Fig. 8.47.

7112 The operation cycle of the system is as follows:

- 7113 • The basic cycle lasts N turns
- 7114 – N -turn injection from ERL into the accumulating ring (bottom)
- 7115 – N -turn cooling in the cooling ring (middle); fast laser cooling may be employed here
- 7116 – N -turn slow extraction from the extracting ring (top) into rgw ERL
- 7117 • One-turn transfer from the cooling ring into the extracting ring
- 7118 • One-turn transfer from the accumulating ring into the cooling ring

7119 The average current in the cooling ring is $N \times$ average ERL current. The number of turns of the
 7120 main cycle is limited by the efficiency of multiturn injection and the maximum current wgiuch
 7121 can be stored (and cooled) in the cooling ring.

7122 Laser cooling may generate a new low-emittance positron beams to compensate for losses.and
 7123 emittance growth of the recycled beam.

7124 Reusing and/or cooling of positrons relaxes the requirements for all types of positron source
 7125 discussed in the following. The cooling period is limited by the maximal stored current in the

Table 8.17: CLIC versus NLC parameters driving the DRs design.

Parameter [unit]	High Rep-rate	Low Rep-rate
Energy [GeV]	10	7
Bunch population [10^9]	1.6	1.6
Bunch spacing [ns]	2.5	2.5
Number of bunches/train	9221	9221
Repetition rate [Hz]	100	10
Damping times trans./long. [ms]	2/1	20/10
Energy loss/turn [MeV]	230	16
Horizontal norm. emittance [μm]	20	100
Optics detuning factor	80	80
Dipole field [T]	1.8	1.8
Dipole length [m]	0.5	0.5
Wiggler field [T]	1.9	-
Wiggler period [cm]	5	-
Total wiggler length [m]	800	-
Dipole length [m]	0.5	0.5
Longitudinal norm. emittances [keV.m]	10	10
Momentum compaction factor	10^{-6}	10^{-6}
RF voltage [MV]	300	35
rms energy spread [%]	0.20	0.17
rms bunch length [mm]	5.2	8.8
average power [MW]	23.6	3.6

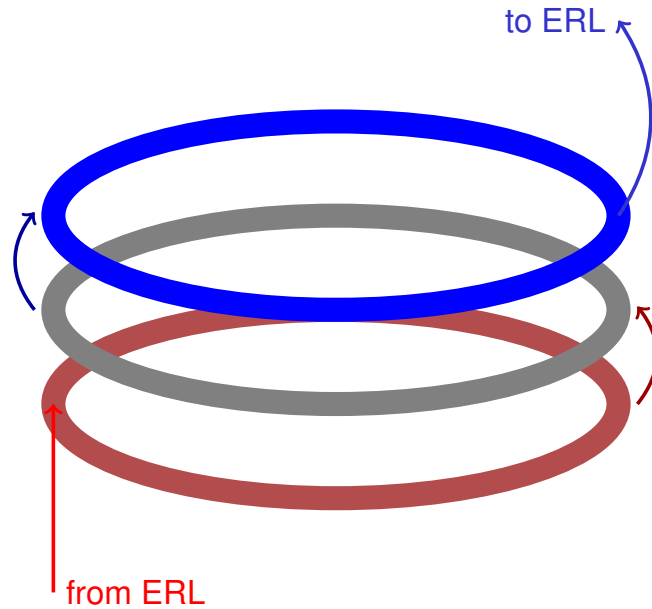


Figure 8.47: Tri-ring scheme

7126 ring and by the multiturn injection. Fast laser cooling may be employed for compensating
 7127 positron emittance growth when reusing positrons or to compensate losses (without a dedi-
 7128 cated high-current positron source). The slow extraction process is also able to further reduce
 7129 the energy spread (chromatic extraction) or, alternatively, the transverse emittance (resonant
 7130 extraction).

7131 8.6.4 Positron Production Schemes

7132 Positrons can be produced by pair creation when high-energy electrons or photons hit a target.
 7133 Conventional sources, as used at the SLC, send a high-energy electron beam on a conversion
 7134 target. Alternatively, a high-energy electron beam can first be used to create high-energy
 7135 photons, and these photons are then sent onto a target. The prior conversion into photons
 7136 reduces the heat load of the target, for a given output intensity, and it may also improve the
 7137 emittance of the generated positrons.

7138 There exist a number of schemes that can accomplish the conversion of electrons into pho-
 7139 tons. Several of them employ Compton scattering off a high-power laser pulse stacked in an
 7140 optical cavity. According to the electron-beam accelerator employed, one distinguishes Compton

7141 rings, Compton linacs, and Compton ERLs. An alternative scheme uses the photons emitted by
7142 an electron beam of very high energy (of order 100 GeV) when passing through a short-period
7143 undulator.

7144 Finally, there even exists a simpler scheme where a high-power laser pulse itself serves as
7145 the target for (coherent) pair creation.

7146 Applications of the various possible schemes to the LHeC are discussed in the following
7147 sections.

7148 8.6.5 Targets

7149 For the positron flux considered the heating and possible destruction of the target are important
7150 concerns. Different target schemes and types can address these challenges:

- 7151 • Multiple targets operating in parallel (Section 8.6.6).
- 7152 • He-cooled granular W-sphere targets (Section 8.6.6).
- 7153 • Rotating-wheel targets (Section 8.6.6).
- 7154 • Sliced-rod W tungsten conversion targets (Section 8.6.7);
- 7155 • Liquid mercury targets (Section 8.6.7).
- 7156 • Running tape with annealing process (Section 8.6.7).

7157 8.6.6 Conventional Scheme based on e^- Beam Hitting Target

7158 The LHeC ERL option requires a positron current of 6 mA or 4×10^{16} e^+ /s, with normalized
7159 emittance of ≤ 50 μm and longitudinal emittance ≤ 5 MeV-mm.

7160 For a conversion target with optimized length the power of the primary beam is converted
7161 as follows $P_{\text{primary}}(100\%) = P_{\text{thermal}}(30\%) + P_{\gamma}(50\%) + P_{e^-}(12\%) + P_{e^+}(8\%)$. The average
7162 kinetic energy of the newly generated positrons is $\langle T_{e^+} \rangle \approx 5$ MeV, which allows estimating
7163 the total power incident on the target as $P_{\text{target}} = 5 \text{ MV} \times 6 \text{ mA} / 0.08 = 375$ kW. Assuming
7164 an electron linac efficiency of $\eta_{\text{acc}} \approx 20\%$ we find $P_{\text{wall}} = P_{\text{target}}/0.2 = 1.9$ MW. This wall-plug
7165 power level looks feasible and affordable.

7166 Figure 8.48 illustrates a possible option, which alone would already meet the requirements
7167 for the 140-GeV single-linac case, where the repetition rate is 10 Hz. The idea is to use 10
7168 e^+ target stations in parallel. This implies installing 2 RF deflectors upstream and the same
7169 downstream. Experience exists for RF deflectors at 3 GHz and with operating 2 lines in parallel.
7170 Assuming that this configuration is acceptable from the beam-optics point-of-view, it would be
7171 necessary to implement a fast damping scheme because the bare emittances from the target
7172 will be too high for the injection into the ERL.

7173 Table 8.18 shows the beam characteristics at the end of the 10 GeV Primary beam Linac
7174 for electrons, before splitting the beam.

7175 Table 8.19 shows the beam parameters at each e^+ target. Energy of 5.6 kW is deposited in
7176 each target and the Peak Energy Deposition Density (PEDD) is around 30 J/g. This value has
7177 been chosen, in order to be below the breakdown limit for tungsten (W) target. It is based on
7178 recent simulations [?] with conventional W targets. A new study has been done [?], assuming
7179 a target made out of an assembly of densely packed W spheres (density about 75% of solid

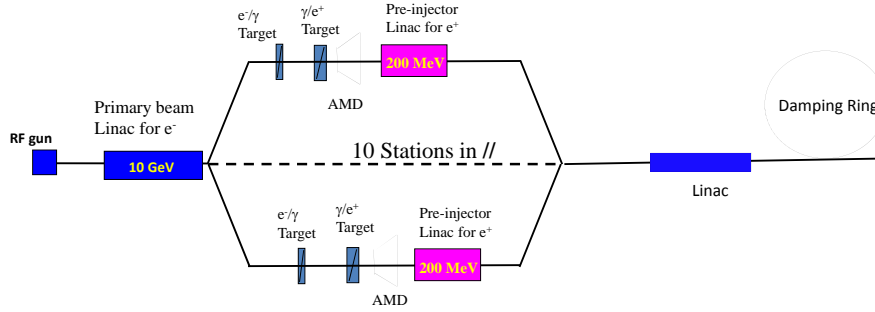


Figure 8.48: Possible layout with unpolarised e^+ for the LHeC injector (p-140 GeV).

Primary beam energy (e^-)	10 GeV
Number e^- / bunch	1.2×10^9
Number of bunches / pulse	100000
Number e^- / pulse	1.2×10^{14}
Pulse length	5 ms
Beam power	1900 kW
Bunch length	1 ps

Table 8.18: Electron beam parameters before splitting.

7180 tungsten) with diameters of 1–2 mm. The cooling is provided by blowing He-gas through the
 7181 voids between the spheres. Such He-cooled granular targets have been considered for neutrino
 7182 factories and recently for the European Spallation Source ESSS.

Yield (e^+/e^-)	1.5
Beam power (for e^-)	190 kW
Deposited power / target	5.6 kW
PEDD	30 J/g
Number e^+ / bunch	1.8×10^9
Number bunches / pulse	10,000
Number e^+ / pulse	1.8×10^{13}

Table 8.19: Beam parameters at each e^+ target.

7183 To achieve the required cooling and the corresponding mass flow of the cooling fluid, we
 7184 consider pressurized He at 10 bar entering the target volume at a velocity of 10 m/s, i.e. a
 7185 mass flow 1.8 g/s is required for each target. From this a convection coefficient of about
 7186 $\alpha = 1 \text{ W/cm}^2/\text{K}$ can be expected and a cooling time constant τ (exponential decay time after
 7187 an adiabatic temperature rise of a sphere) of 185 ms will result. Clearly, not much cooling
 7188 during a pulse of 5 ms duration will occur, but cooling will set in during the off-beam time of

7189 95 ms between the pulses. The peak temperature after each pulse will stabilize at about 500
 7190 K above that of the cooling fluid. An average exit temperature of the He-gas of about 600 °C
 7191 will have still to be added, which drives the maximum temperature of the spheres up to about
 7192 1100 °C. Although compatible with W in an inert atmosphere, it should be attempted to reach
 7193 lower temperatures. This could be achieved by increasing the He-pressure to 20 bar and the
 7194 velocity of He to 20 m/s which might reduce the maximum temperature in a sphere to 500 °C.
 7195 Thus, a He-cooled granular 10-W-target system could be a viable solution.

7196 Another approach has been considered. To achieve, as in the previous case, a reduction of
 7197 the energy deposition density by a factor of 10, a fast rotating wheel could be designed. The
 7198 beam pulse of 5 ms duration is spread over the rim of the rotating wheel and a linear velocity
 7199 of the rotating rim of 20 m/s would be required. This would lead to repetition rate of about
 7200 1000 rpm, assuming a wheel diameter of 0.4 m. Such a solution is actually under investigation
 7201 for the ILC with a rotation speed of 1800 rpm.

7202 Here tungsten spheres, again, are contained in a structure, similar to a care tyre, as is
 7203 illustrated in Fig. 8.49. The container is possibly made of light Ti-alloy where the sides, facing
 7204 the beam entrance and exit should be made of Beryllium, compatible with the beam heating.
 7205 The helium for the cooling is injected from the rotating axle through spokes into the actual
 7206 target ring and is recuperated in the same way.

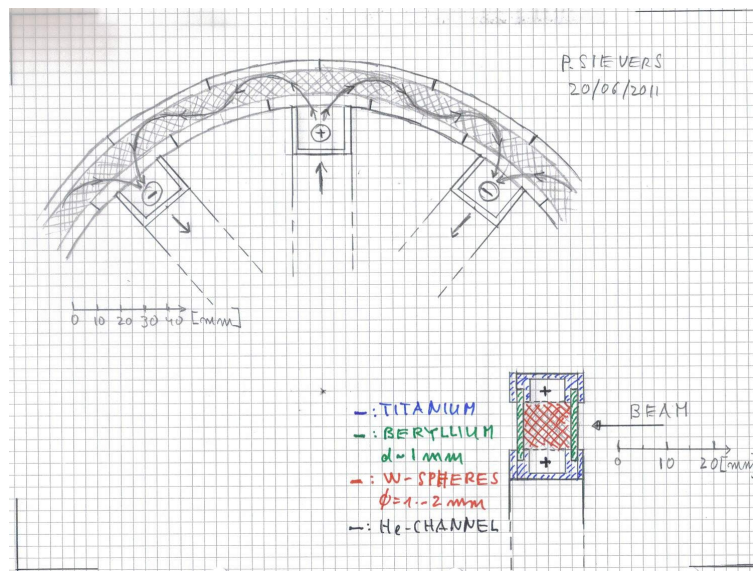


Figure 8.49: Artist's view of rotating wheel containing W spheres with He cooling.

7207 If the beam pulse duration is extended by a factor 10, i.e. 50 ms duration, maintaining of
 7208 course the same average power, then the rotation time could be reduced. The velocity of the
 7209 wheel is such that over the duration of 5 ms the rim is displaced by one beam width, i.e. 1 cm.
 7210 This leads to much reduced rotation speeds of 2 m/s, which can readily be achieved in a wheel
 7211 with a diameter of 16 cm, rotating at 240 rpm.

7212 By choosing appropriately the rotation velocity, the average time between two hits of the
 7213 same spot on the rim of the wheel, is about 0.5 s. With the aforementioned cooling time constant

7214 for the He-circuit of 185 ms, the adiabatic temperature rise during one hit over 5 ms of 211 K
 7215 will have dropped to close to zero before the next hit. Since we assume to simultaneously cool
 7216 the whole rim of the wheel, a He-flow of 90 g/s must be provided. Taking into account the
 7217 temperature increase in the cooling fluid, a maximum tungsten temperature in the W-spheres
 7218 of about 350°C can be expected, which is rather comfortable.

7219 Using a continuous D.C.-beam with no gaps will further alleviate the structure and perfor-
 7220 mance of the target wheel.

7221 The interference of the rotating wheel with the downstream flux concentrator will have to
 7222 be assessed. One may, however, expect considerably less forces than presently considered for
 7223 the ILC, due to the much lower velocity of the wheel. Moreover, proper choice of materials
 7224 with high electrical resistivity and laminating the structure may be considered.

7225 Clearly, the W-granules must be contained inside the beam vacuum within a structure which
 7226 is He-leak tight at the selected He-pressure. As material for the upstream and downstream
 7227 beam windows, Beryllium must be considered which, due to its large radiation length (34 cm
 7228 as compared to W with 0.34 cm), should resist to the thermal loads. This, however, has to be
 7229 verified.

7230 Also, radiation damage and life time issues will still have to be assessed.

7231 It is believed that rotating “Air to Vacuum” seals at 240 rpm are commercially available or
 7232 can be adapted to the radiation environment. Rotating “High Pressure He to Air” seals may
 7233 have to be developed, where small He-leaks can be tolerated.

7234 This last approach is focused on e^+ targets. Presently with conventional targets, the trans-
 7235 verse normalized rms beam emittances, in both planes, are in the range of 6000 to 10 000
 7236 mm.mrad. With the new type of target, we do not know yet by how much the transverse
 7237 emittances will be changed. In any case, a strong reduction of emittances is mandatory for the
 7238 requested LHeC performance.

7239 Assuming that large or small emittances could be recombined, Table 8.20 shows a possible
 7240 e^+ flux after recombination.

7241 Finally, if a solution is found for the emittances, it will be necessary to design and implement
 7242 a linac accelerating the positron beam up to 500 MeV, the energy for the ERL injection.

Secondary beam energy (e^+)	200 MeV
Number e^+ bunch	1.8×10^9
Number of bunches / pulse	100000
Number of e^+ / pulse	1.8×10^{14}
Bunch spacing	50 ns
Repetition rate	10 Hz

Table 8.20: Positron beam parameters after recombination.

7243 8.6.7 Compton Sources

7244 In Compton sources, (polarized) positrons are produced as a result of the following processes:

- 7245 1. Electron beam (current I_{e^-}) scatters off polarized laser photons (energy in pulse W).
- 7246 2. Gamma flux, $\sim I_{e^-} \times W$, is first collimated and then impinging on a conversion target.

7247 3. Produced positrons lose a fraction of energy while traversing the target.

7248 4. Postselection: low-energy positrons are discarded to attain the required polarization.

7249 Three principal factors limit the performance of polarized positron sources based on Compton scattering. They are:

7251 1. Limited average current of electrons scattering off laser photons (world record $I_{e^-} = 5$ A
7252 – PEP ring).

7253 2. Limited energy of pulses stored in optical resonators (fast progress, an array of resonators
7254 may be employed, 1...5 J assumed maximal accepted: higher energy of pulses violates
7255 electron dynamics).

7256 3. Limited power density of gammas, to which the conversion target is tolerable (sliced-rod
7257 convertor reduces positron losses and increases the current).

7258 The polarization degree of positrons is determined by the cut-off energy of positrons exiting from
7259 the target: the higher the polarization required the higher the energy threshold for discarding
7260 low-energy positrons (and the lower the yield). The optimal target thickness that maximizes
7261 the yield also decreases with the increase of the polarization requested, along with a decrease
7262 in the yield of positrons (but with an improved quality of the positron beam: a smaller energy
7263 spread, and a smaller transverse emittance).

7264 For a CLIC source of polarized positrons [?] (1 GeV electron energy, 1 μ m YAG laser system,
7265 and, correspondingly, 20 MeV maximal energy of the Compton spectrum) “envelopes” describ-
7266 ing the limiting number of positrons from the conversion target per scattered gamma and the
7267 associated polarization are presented in Fig. 8.50.

7268 Compton Ring

7269 A typical Compton-ring gamma source (the CLIC ring) with the parameters listed in [?], and
7270 modified to accommodate an entire array of optical resonators, namely 10 units with 50 mJ
7271 of laser energy stored in each, installed in the dispersive section, is capable of producing 0.01
7272 gammas per electron-turn. This scheme can be enhanced by increasing the laser energy by a
7273 factor of 10, up to 5 J, and by halving the collision angle, to 4 degrees, which increases the yield
7274 by an order of magnitude, up to 0.1 gammas per electron-turn.

7275 A typical tungsten convertor optimized for Compton gammas with a maximal energy of
7276 20 MeV can delivered 0.01 positrons with 60% polarization per incident scattered gamma. The
7277 convertor can be enhanced as well: a sliced-rod convertor target produces 0.07/0.13 positrons
7278 per gammas for a 1 m or 3 m long rod, respectively [?].

7279 Including a 50% overhead, for either the standard scheme and with teh two types of en-
7280 hancements, various projects require the minimal circulating currents in Compton rings listed
7281 in Table 8.21.

7282 Table 8.21 illustrates that a Compton-ring source equipped with an array of optical res-
7283 onators yielding a total laser-pulse energy of 5 Joule, together with a sliced-rod conversion
7284 raget, will produce the desired flux of polarized positrons even for the LHeC ERL option.

7285 In conclusion, according to the present understandiung and simulations, a Compton positron
7286 source may produce sufficient average positron beam current for all LHeC options. The conver-
7287 sion of gammas to positrons is a bottleneck, which requires a study and optimization of effective
7288 convertor targets such as the sliced-rod converter.

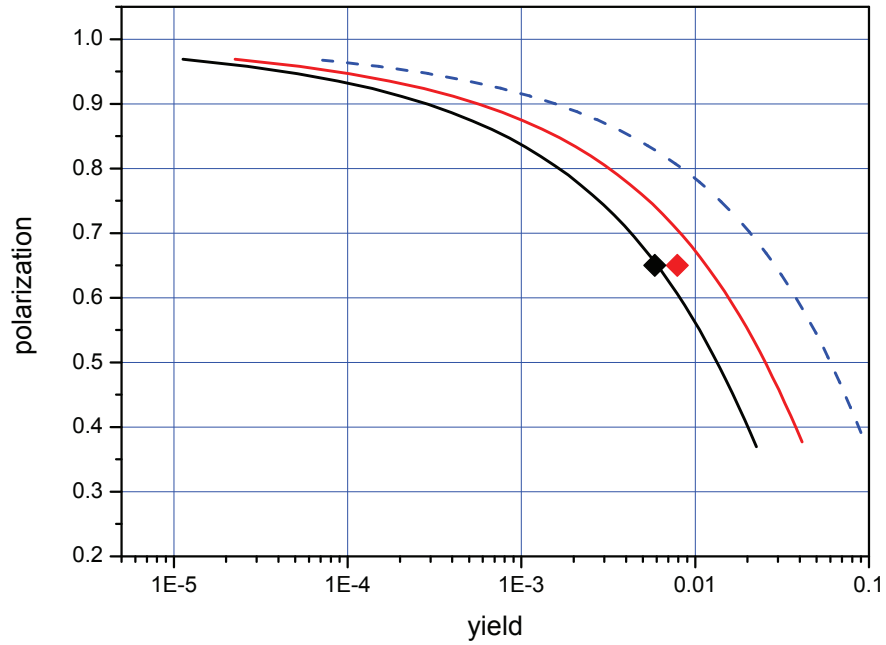


Figure 8.50: Limits for Ti (black) and W (red) conversion targets. Diamonds: simulations (A.Schalicke, S.Riemann). Blue Dashed curve: a sliced-rod conversion target.

Table 8.21: IP positron current and the implied minimum electron beam current in a Compton Ring

	unit	SLC	CLIC (3TeV)	LHeC p-140	LHeC ERL
I_{e^+} at IP	μA	0.96	18	290	7050
typical I_{e^-}	A	1.4E-2	0.26	4.3	105.7
I_{e^-} with 5 J	A	1.5E-3	2.8E-2	0.46	11.2
I_{e^-} with 5 J+1 m rod	A	2.2E-4	4.0E-3	6.5E-2	1.6

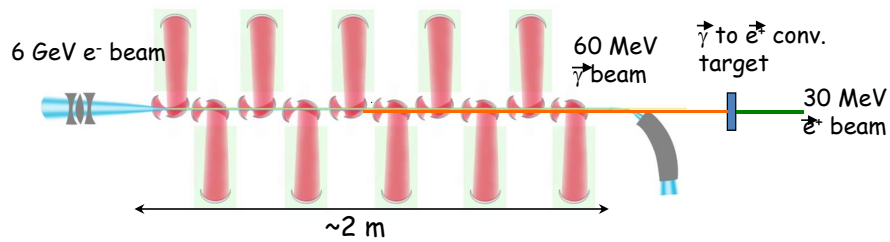


Figure 8.51: Layout based on Compton Linac.

7289 **Compton Linac**

7290 Positrons, even polarized, can be generated by the Compton scattering process of high-power
 7291 laser pulses stacked in optical cavities with a high-energy electron beam from a linac. Figure
 7292 8.51 present a possible layout for such configuration.

7293 At BNL, a ratio photon/electron close to 1 has been demonstrated. Assuming that a ratio
 7294 photon/positron close to 2% is achievable, then 50 photons are required to produce 1 e^+ . For
 7295 LHeC, one needs 0.35 nC/bunch (for the e^+ to be produced). Based on above estimations,
 7296 it implies ~ 18 nC/bunch (for the e^- beam). Then with 10 optical cavities, the requested e^-
 7297 charge is about 1.8 nC / bunch which is a reasonable value.

7298 **Power Analysis for Compton Schemes and Compton ERL**

7299 A number of pertinent technologies have been investigated, but are not yet established:

- 7300 1. 1.3 Ampere ERL (R&D at BNL)
- 7301 2. Mercury target or annealing target (Muon collider collaboration)
- 7302 3. High finesse optical stacking cavities with factor 1000 enhancement, 1 kW pump (France,
 7303 KEK, ...)

7304 This section considers different Compton-based options for an LHeC positron source including
 7305 power considerations. The following source requirements were taken into account:

- 7306 • 6mA average current or 4×10^{16} e^+ /sec
- 7307 • 2×10^7 bunches with 2×10^9 e^+ /bunch
- 7308 • Normalized rms emittance of 50 microns
- 7309 • Longitudinal emittance 5 MeV-mm or 10 mm normalized.

7310 The **power analysis** for the different schemes can be done backwards:

- 7311 1. power of the captured positron beam
- 7312 2. \rightarrow power of the gamma beam entering the conversion target and generating electron
 7313 positron pairs

7314 3. → drive electron beam generating gamma beam

7315 4. → klystron generating drive electron beam

7316 5. → wall plug power

7317 Scattering of the multi MeV gammas on the target produces the electrons and positrons. The
7318 optimal gamma beam energy range of 30-60 MeV is selected as a compromise between conversion
7319 efficiency and capture efficiency as well as longitudinal emittance. Beam power of the captured
7320 positron beam is estimated at $6 \text{ mA} \times 30 \text{ MeV}$ or 180 kW.

7321 The conversion efficiency of gamma beam into captured positrons ranges from 0.3 to 2% for
7322 different schemes of the ILC positron source. This (optimistically) sets a requirement for the
7323 gamma beam entering the target at 9 MW. A 2–6 GeV electron beam is used in different schemes
7324 to generate a gamma beam by Compton scattering of the powerful laser beam. The efficiency
7325 of electron beam power conversion is at most 10%, for the scheme with a CO2 laser. This
7326 puts a lower limit on the drive beam power at 90 MW. A CLIC type driver can optimistically
7327 generate the drive beam at approximately 50 percent efficiency and, therefore, an overall power
7328 requirement to generate a 6 mA positron beam with pulsed linac (CLIC type) and the CO2
7329 laser can be estimated at 180 MW.

7330 To summarize:

- 7331 • $6 \text{ mA} \times 30 \text{ MeV} \rightarrow 180 \text{ kW } e^+$ beam (Output of conversion target)
- 7332 • $\gamma \rightarrow e^+$ efficiency about 2% → 9 MW γ beam (conversion efficiency)
- 7333 • $e^- \rightarrow \gamma$ about 10%, 90 MW e^- beam
- 7334 • Wall → e^- about 50% or 180 MW wall power

7335 The wall plug power for the electron beam alone exceeds the limit of 100 MW set for
7336 the entire project. On the other hand, the energy spread of the circulating beam would be
7337 prohibitive in a Compton ring scheme subjected to the requirement to generate 9 MW from
7338 a 30-MeV gamma beam. Both issues can be handled by exploring the energy recovery linac
7339 option. A 3-GeV 1.3-Ampere ERL with 2 micron laser enhancement cavities has the potential
7340 of generating the required positron beam with only 50 MW of wall plug power, as follows:

- 7341 • $6 \text{ mA} \times 30 \text{ MeV} = 180 \text{ kW } e^+$ beam (Output of conversion target)
- 7342 • $\gamma \rightarrow e^+$ about 1% → 18 MW γ beam (Conversion efficiency)
- 7343 • $e^- \rightarrow \gamma$ about 0.5% 4 GW e^- beam (99.9% efficient ERL)
- 7344 • Wall → e^- about 50% of $0.001 \times 4 \text{ GW} + 18 \text{ MW}$
- 7345 • Total $\approx 50 \text{ MW}$ wall power

7346 The major challenge of a pulsed linac scheme is in the cost of driving the linac. A high
7347 wall power requirement combined with long pulse format make the CO2 laser/pulse linac com-
7348 bination an unlikely solution. The challenge of the ERL scheme lies in the development of the
7349 recirculating cavities and target/capture system that would be able to perform the CW mode
7350 of operation.

7351 **Emittances:** The upper estimate on the transverse and longitudinal emittances in the case
7352 of 2 GeV ERL for the captured positron beams can be estimated as follows:

7353 • Normalized positron beam emittance, expressed through its energy, RMS beam size and
7354 angular divergence at the target exit: $\epsilon_N \approx \gamma_{e^+} \sigma \sigma'$.

- Acquired angular spread in the length target (typically selected at 0.4 radiation length) can be estimated as

$$\sigma_{e^+} \approx \frac{1}{\sqrt{2}} \frac{14\text{MeV}}{E_{e^+}} \sqrt{\frac{L_{\text{target}}}{X_0}} \approx \frac{10}{\gamma_{e^+}} .$$

7355 • Three components contribute to the beam size:

1. Scattering in the target:

$$\sigma_{e^+,sc} \approx \frac{\sqrt{2}}{3} \sigma'_{e^+} L_{\text{target}} \approx \frac{\sqrt{2}}{3} 0.3 \cdot 1.2 \text{ mm} \approx 150 \mu\text{m} .$$

2. Beam size due to gamma beam divergence:

$$\sigma_{\gamma,div} \approx \frac{1}{2\gamma_{e^-}} \frac{L_{IR}}{\sqrt{2}} \approx \frac{1}{2 \times 4000} \frac{0.1 \text{ m}}{\sqrt{2}} \approx 15 \mu\text{m} .$$

3. and e- beam size on target:

$$\sigma_{\gamma e^-} \approx \sqrt{\frac{\epsilon_{Ne^-}}{\gamma_{e^-}} \beta_{e^-}} \approx \sqrt{\frac{10 \mu\text{m}}{4000}} 1 \text{ m} \approx 50 \mu\text{m} .$$

This results in the normalized transverse emittance of 1.5 mm. The strong magnetic field in which the target would likely be immersed will lower this estimate. The estimate for the longitudinal emittance is:

$$\epsilon_{||,N} \approx \Delta\gamma_{e^+} \sigma_{\tau e^-} \approx \frac{60 - 30}{4} 60 \mu\text{m} \approx 450 \mu\text{m} .$$

7356 **Compton-ERL Target:** Charged particle beams exiting the conversion target generate
7357 most of the heat. The deposited power can be estimated (roughly) as $6 \text{ mA} \times 5 \text{ MeV} \times 2 \times$
7358 2 , or 120 kW. 5 MeV is estimated for the energy loss and factors of 2 are attributed to equal
7359 parts of captured and non-captured low energy positrons, and to the equal number of electrons
7360 and positrons. This suggests that a liquid mercury target may be an important candidate.

7361 **Compton ERL Summary:** High current ERL seems the most promising approach, e.g.
7362 a 3-GeV 1.3-A ERL with 2-micron wavelength optical enhancement cavities.

7363 Target is going to be a very difficult consideration (candidates would be a liquid mercury
7364 target or running tape with annealing process). The desired emittances are not reached from any
7365 Compton scheme source, even if the target is immersed in a strong magnetic field. Therefore,
7366 cooling or scraping would be required.

7367 Laser Pulses and Optical Cavities

7368 Different experimental programs presently underway aim at achieving a very important photon
7369 pulse intensity by direct production in a laser system and stacking in a passive optical resonator.
7370 This laser-stacking scheme allows increasing the available average power in the optical cavity

7371 without requiring impossible performances to the drive laser system. As far as Compton-
7372 source developments are concerned, depending on the purpose of the application, the stored
7373 pulse length ranges from a few hundreds of femtoseconds to a few picoseconds, the repetition
7374 frequency (which determines the cavity length) from 20 to 200 MHz, and the wavelength from
7375 0.5 to 1.1 μm .

7376 When trying to achieve storing a very high power in a Fabry-Perot optical resonator the
7377 state of the art of the present technology has to be taken into account. As far as the laser
7378 is concerned, in the last years an impressive increase in the available average power has been
7379 provided by the development of the fiber amplifiers. The best performances have been obtained
7380 by combining the development of large core single mode photonic crystal fibers with the chirped-
7381 pulse amplification (CPA) technique. For example, a 200-fs, 1048-nm wavelength, 78-MHz
7382 oscillator pulse after a first stretching to 800 ps, has been amplified in a system composed of a
7383 two-stage double-clad photonic crystal fiber preamplifier (30 μm mode field and 170 μm pump
7384 cladding diameter) pumped at 976-nm wavelength, and a main-amplifier double-clad water
7385 cooled fibre (27- μm mode field and 500 μm air clad). After this phase a recompression of the
7386 pulse to 640 fs has yielded an “incredible” average power of 830 W and about 10 μJ per puls [?].

7387 To stack many short laser pulses in a Fabry Perot resonator, and obtain an important pulse
7388 enhancement, it is necessary to lock the cavity characteristic comb with the laser one. This
7389 implies to act on two degrees of freedom given by the repetition frequency and by the carrier to
7390 phase envelope (Φ_{ce}). In this context the Pound Driver Hall locking techniques is employed in
7391 the LAL cavity [?]. This technique has attained the best performances in gain, as far as pulses
7392 of few ps are concerned. A gain of about 10000 was achieved, storing a laser pulse of close to
7393 20 kW in a confocal two mirror cavity. However, the best result, as far as the stored power
7394 is concerned, has been achieved by the MPQ laboratory using the Hansch-Couillaud locking
7395 technique [?]. With a pulse length of 200 fs an average power of 18 kW was obtained in a
7396 78-MHz tie bow cavity with an enhancement factor of 1800. After this achievement, thermal
7397 problems were noticed due to the very high-power density of the pulse. Stretching the pulse
7398 to 2 ps the stacking process was efficient up to 72 kW with an estimated gain of 1400. In the
7399 cavity waist this corresponded to a 10^{14} W/cm² power density. At this power level the coupling
7400 between the laser power and the cavity was near 50%.

7401 In the framework of the Compton facilities another important experimental effort is carried
7402 out jointly by LAL Orsay (France) and KEK Tsukuba (Japan) [?]. In fact, to validate the
7403 use of optical passive cavities, different tests have to be performed also taking into account
7404 the reliability and the compatibility of a given optical cavity with the accelerator environment.
7405 A 176 MHz, a four-mirror vacuum-compatible optical cavity has been designed, realized and
7406 installed in the KEK-ATF ring. A four-mirror configuration was chosen instead of a two-mirror
7407 one, because with the former it is possible to achieve very small laser-waists without losing
7408 in mechanical stability. An estimated stored power of 2 kW has been achieved during the
7409 commissioning of the system at the end of 2010. A future program to explore the 100kW range
7410 is envisaged. At the ATF beam energy, Compton collision will produce gamma rays near 20
7411 MeV resulting in the world-s first beam-driven gamma factory.

7412 8.6.8 Undulator Source

7413 Another positron production option would be an undulator process, based on the main high-
7414 energy electron (or positron) beam. The LHeC undulator scheme can benefit from the pertinent
7415 development work done for the ILC. The beam energy at LHeC would be lower, e.g. 60 GeV,

7416 which might possibly be compensated by more ambitious undulator magnets, e.g. ones based
7417 on Nb₃Sn or HTS. However, the requested photon flux calls for a careful investigation. The
7418 undulator parameters needed for 60 GeV, the expected positron production rate, and technical
7419 feasibility all require further study.

7420 8.6.9 Source based on Coherent Pair Creation

7421 The normalized transverse emittance of all positrons from a target is of order $\epsilon_N \approx 1-10$ mm, to
7422 be compared with a requested emittance of $\epsilon_N = 0.05$ mm. Therefore, a factor 100 emittance
7423 reduction is required.

7424 Solution 1 would be to simply cut the phase space. However, this would give rise to an
7425 unrealistic increase of the primary beam power.

7426 Solution 2 would be to collect all positrons, accelerate them to 1 GeV and damp them for
7427 $\text{Log}(100) \sim 5$ damping times, with an implied RF power of $P_{RF} = 1 \text{ GeV} \times 5 \text{ mA} \times 5/0.6 =$
7428 60 MW , where an RF efficiency of 50% was assumed.

7429 Solution 3 would be to produce positrons in a smaller phase space volume. Indeed the
7430 inherent transverse emittance from pair production is small. The large phase space volume
7431 only comes from multiple scattering in the production target.

7432 Pair production from relativistic electrons in a strong laser field would not need any solid
7433 target, since the laser itself serves as the target, and it would not suffer from multiple scattering.
7434 This process has been studied in the 1960's and 1990's [?, ?, ?]. It should be reconsidered with
7435 2011 state of the art TiSa lasers and X-ray FELs [?].

7436 8.6.10 Conclusions

7437 The challenging requirements for the LHeC Linac-Ring positron source are relaxed if positrons
7438 can be collided several times before deceleration, if they can be reused over several acceler-
7439 ation/deceleration cycles, and/or if they can be cooled. The compact tri-ring scheme is an
7440 attractive proposal for recooling the spent and recycled positrons. A conventional damping
7441 ring in the SPS tunnel would be an alternative.

7442 Assuming some of the aforementioned measures are taken to reduce the required positron
7443 intensity, which needs to be generated, by at least an order of magnitude, and also assuming
7444 that an advanced target, e.g. W-granules, rotating wheel, sliced-rod converter, or liquid metal
7445 jet, can be used, several of the proposed source and cooling concepts could provide the intensity
7446 and the beam quality required by the LHeC ERL.

7447 For example, the Compton-ring source and the Compton ERL are viable candidates for
7448 the Linac-Ring LHeC positron source. Coherent pair production and an advanced undulator
7449 represent other possible schemes, still to be explored for LHeC in greater detail. The coherent
7450 pair production would have the appealing feature of generating positrons with an inherently
7451 small emittance.

7452 In conclusion, it does seem technically possible to meet the very demanding requirements
7453 for the LHeC positron source by a combination of approaches. A serious and concerted R&D
7454 effort will be required to determine the optimum linac-ring positron configuration.

7455 Chapter 9

7456 Civil Engineering and Services

7457 9.1 Overview

7458 Infrastructure costs for projects such as LHeC, typically represent approximately one third of
7459 the overall budget. For this reason, particular emphasis has been placed on Civil Engineering
7460 and Services studies, to ensure a cost efficient conceptual design. This chapter provides an
7461 overview of the designs adopted for the key infrastructure cost driver, namely, civil engineering.
7462 The costs for the other infrastructure items such as cooling & ventilation, electrical supply,
7463 transport & installation will be pro-rated for the CDR and studied in further detail during the
7464 next phase of the project. For the purposes of this conceptual design report, the civil engineering
7465 (CE) studies have assumed that the Interaction Region (IR) for LHeC will be at LHC Point 2,
7466 which currently houses the ALICE detector. As far as possible, any surface facilities have been
7467 situated on existing CERN land. Both the Ring-Ring and Linac-Ring underground works will
7468 be discussed in this Chapter. Surface buildings/structures have not been considered for the
7469 CDR.

7470 9.2 Location, Geology and Construction Methods

7471 This section describes the general situation and geology that can be expected for both the
7472 Ring-Ring and Linac Ring options.

7473 9.2.1 Location

7474 The proposed siting for the LHeC project is in the North-Western part of the Geneva region at
7475 the existing CERN laboratory. The proposed Interaction Region is fully located within existing
7476 CERN land at LHC Point 2, close to the village of St.Genis, in France. The CERN area is
7477 extremely well suited to housing such a large project, with the very stable and well understood
7478 ground conditions having several particle accelerators in the region for over 50 years. The civil
7479 engineering works for the most recent machine, the LHC were completed in 2005, so excellent
7480 geological records exist and have been utilised for this study to minimise the costs and risk to
7481 the project. Any new underground structures will be constructed in the stable Molasse rock
7482 at a depth of 100-150m in an area with little seismic activity. CERN and the Geneva region



Figure 9.1: Tram stop outside CERN Meyrin Site.

7483 have all the necessary infrastructure at their disposal to accommodate such a project. Due to
7484 the fact that Geneva is the home of many international organizations excellent transport and
7485 communication networks already exist. Geneva Airport is only 5km from the CERN site, with
7486 direct links and a newly constructed tramway, shown in Figure 9.1, gives direct access from the
7487 Meyrin Site to the city centre.

7488 The governments of France and Switzerland have long standing agreements concerning the
7489 support of particle accelerators in the Geneva region, which make it very likely that the land
7490 could be made available free of charge, as it was for previous CERN projects.

7491 9.2.2 Land Features

7492 The proposed location for the accelerator is situated within the Swiss midlands embedded
7493 between the high mountain chains of the Alps and the lower mountain chain of the Jura.
7494 CERN is situated at the feet of the Jura mountain chain in a plain slightly inclined towards the
7495 lake of Geneva. The surface terrain was shaped by the Rhone glacier which once extended from
7496 the Alps to the valley of the Rhone. The water of the area flows to the Mediterranean Sea. The
7497 absolute altitude of the surface ranges from 430 to 500m with respect to sea level. The physical
7498 positioning for the project has been developed based on the assumption that the maximum
7499 underground volume possible should be housed within the Molasse Rock and should avoid as

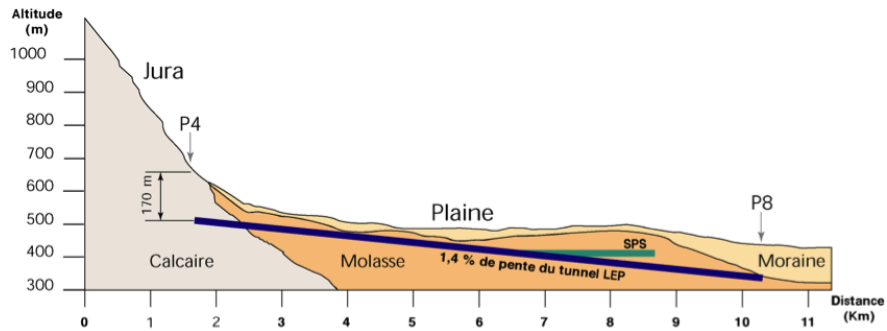


Figure 9.2: Simplified cross section of the LHC housed mostly in Molasse Rock

7500 much as possible any known geological faults or environmentally sensitive areas. The shafts
 7501 leading to any on-surface facilities have been positioned in the least populated areas, however,
 7502 as no real discussions have taken place with the local authorities, the presented layouts can
 7503 only be regarded as indicative, for costing purposes only.

7504 9.2.3 Geology

7505 The LHeC project is within the Geneva Basin, a sub-basin of the large North Alpine Foreland (or
 7506 Molasse) Basin. This is a large basin which extends along the entire Alpine Front from South-
 7507 Eastern France to Bavaria, and is infilled by Molasse deposits of Oligocene and Miocene age.
 7508 The basin is underlain by crystalline basement rocks and formations of Triassic, Jurassic and
 7509 Cretaceous age. The Molasse, comprising an alternating sequence of marls and sandstones (and
 7510 formations of intermediate compositions) is overlain by Quaternary glacial moraines related to
 7511 the Würmien and Rissien glaciations. Figure 9.2 shows a simplified layout of the LHC.

7512 9.2.4 Site Development

7513 As most of the new works are on a close to existing facilities, it is assumed for the CDR that the
 7514 existing facilities such as restaurant, main access, road network etc are sufficient and have not
 7515 been costed. However, for the parts located outside the existing fenceline, but within CERN
 7516 property, the following items will have to be included in the costs:

- 7517 • Roads and car parks
- 7518 • Drainage networks
- 7519 • Landscaping and planting
- 7520 • Spoil dumps

7521 All temporary facilities needed for the construction works have also been included in the
 7522 cost estimate.



Figure 9.3: TBM Gripper type machine used for Neutrino tunnel at CERN (left) and roadheader type machine (right).

7523 9.2.5 Construction Methods

7524 It is envisaged that Tunnel Boring Machines (TBMs) will be utilised for the main tunnel
 7525 excavation greater than approximately 2km in length. In the Molasse rock, a shielded TBM
 7526 will be utilised, with single pass pre-cast segmental lining, followed by injection grouting behind
 7527 the lining. For planning and costing exercises, an average TBM advancement of 25m per day,
 7528 or 150m per week is predicted.

7529 The second phase excavation will be executed using a roadheader type machine. Both
 7530 machines types are shown in figure 9.3. Any new shafts that have to pass through substantial
 7531 layers of water bearing moraines (for example at CMS) will have to utilize the ground freezing
 7532 technique. This involves freezing the ground with a primary cooling circuit using ammonia
 7533 and a secondary circuit using brine at -23C, circulating in vertical tubes in pre-drilled holes at
 7534 1.5 metre intervals. This frozen wall allows excavation of the shafts in dry ground conditions
 7535 and also acts as a retaining wall. Figure 9.4 shows this method being utilized for LHC shaft
 7536 excavation at CMS.

7537 9.3 Civil Engineering Layouts for Ring-Ring

7538 The Ring-Ring solution will require new bypass tunnels at both Point 1 (currently housing the
 7539 LHC Atlas detector) and Point 5 (CMS). Both of the bypass tunnels are on the outside of the
 7540 LHC ring. Figure 9.5 shows the bypass tunnel in blue needed around Point 1. This tunnel is
 7541 730m long and has an internal diameter of 4.5m. Two new 12m diameter shafts are required to
 7542 allow access to construct the underground areas with minimum disruption to LHC operations.
 7543 Underground areas are made available for RF/Cryogenic and general services. Two junction
 7544 caverns will be excavated to create a liaison with the LHC tunnel.

7545 Waveguides ducts (0.9m diameter) will connect the LHeC Bypass tunnel to the RF cavern,
 7546 as shown in Figure 9.6. In order to position the bypass as close as possible to the LHC ring, it
 7547 has been assumed that the LHeC beam pipe can be accommodated within the existing survey
 7548 gallery, and pass through the ATLAS experimental hall.

7549 The Bypass around CMS Point 5 is 1km long with an internal tunnel diameter of 4.5m.

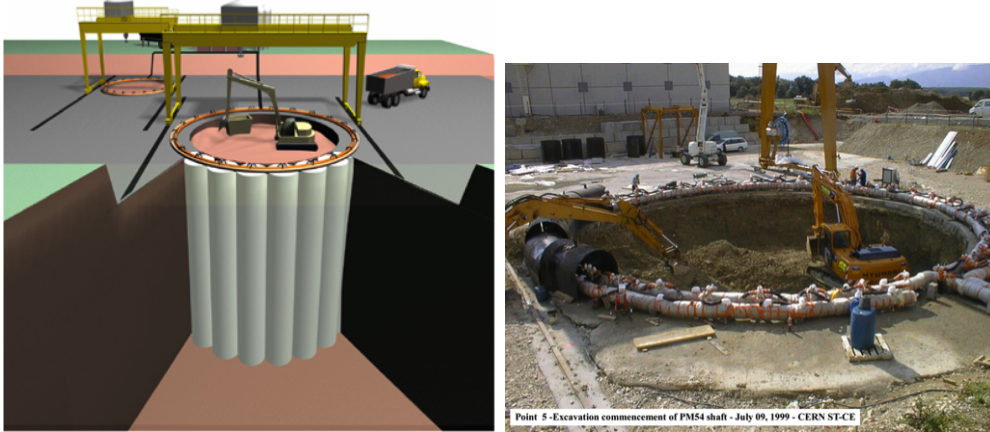


Figure 9.4: LHC Shaft PM54, linking up cylinders of ice to construct a temporary wall.

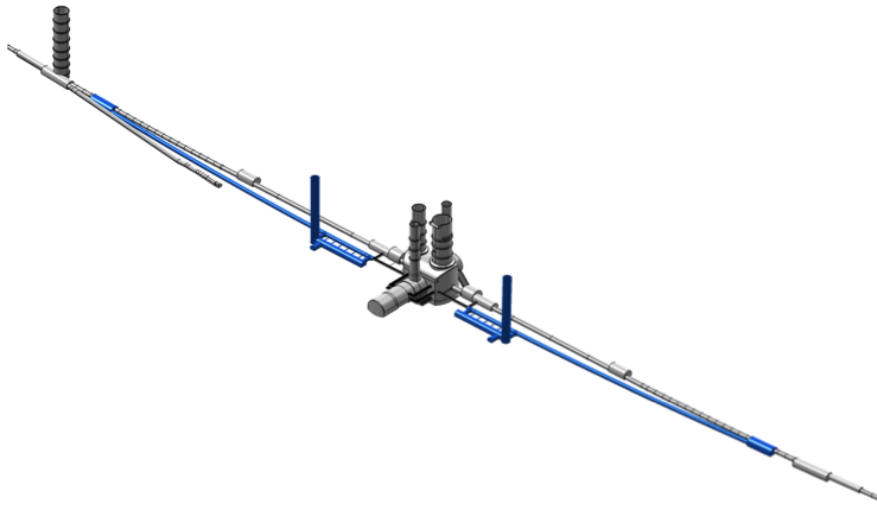


Figure 9.5: Ring-Ring Bypass around ATLAS Point 1.

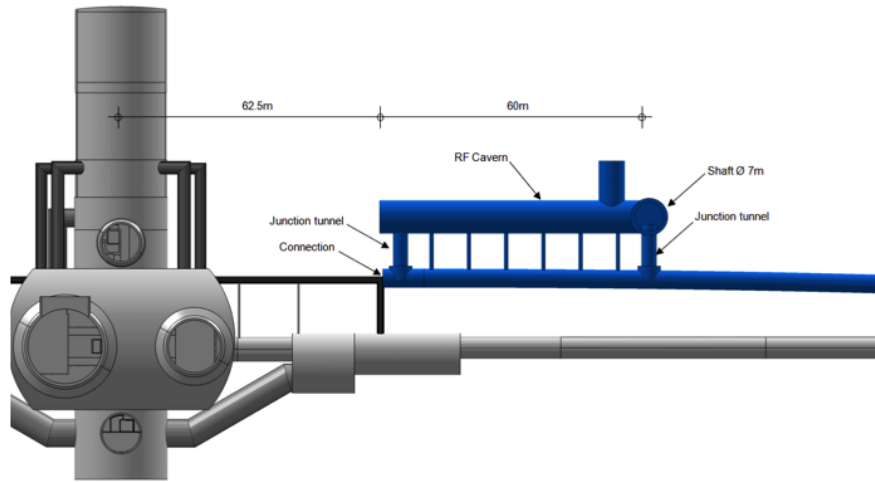


Figure 9.6: Cryo and RF Caverns at Point 1.

7550 Only one new shaft is required for excavation works. A roadheader type machine will be used
 7551 for excavation, with the new tunnel position as close as possible to the LHC tunnel as not to
 7552 induce movements or create operational problems to the existing facilities. Figure 9.7 shows
 7553 the new bypass tunnel and service cavern required around CMS.

7554 Figure 9.8 shows a 3d model of the bypass around the CMS Point 5. The new excavations
 7555 will have a minimum of 7m of Molasse rock separating the new works from existing LHC
 7556 structures. This is to avoid any unwanted deformation or vibration problems on the existing
 7557 LHC structures.

7558 9.4 Civil Engineering Layouts for Linac-Ring

7559 For the CDR it has been assumed that the 60 GeV Energy Recovery Linac (ERL) will be located
 7560 around the St.Genis area of France, injecting directly into the LHC ALICE Cavern at point
 7561 2. Approximately 10km of new tunnels (5m and 6m diameter), 2 shafts and 9 caverns will be
 7562 required. The majority of civil engineering works can be completed while LHC is operational.
 7563 Figure 9.9 highlights the area on the LHC where the new ERL will be situated.

7564 The ERL will be positioned inside the LHC Ring, in order to ensure that new surface
 7565 facilities are located, as much as possible, on existing CERN land. Secondary tunnels running
 7566 alongside the long straight sections will house RF, Cryogenic and Services for the machine. One
 7567 of the long straight sections is shown in Figure 9.10. The entire ERL will be tilted in order to
 7568 follow a suitable layer of Molasse rock. On average the ERL will be tilted approximately 1.4%,
 7569 dipping towards Lake Geneva, as per LHC.

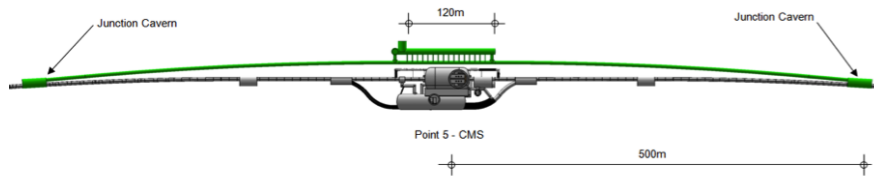


Figure 9.7: Ring-Ring Bypass around CMS Point 5.

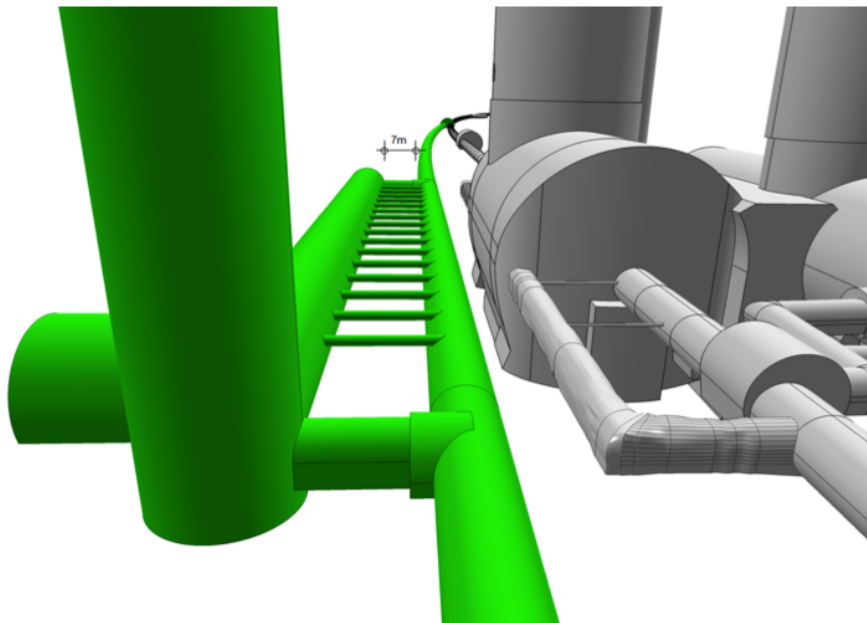


Figure 9.8: 3d model of Ring-Ring Bypass around CMS Point 5 The civil engineering for the e- injection complex for the Ring-Ring option has not been studied for the CDR.

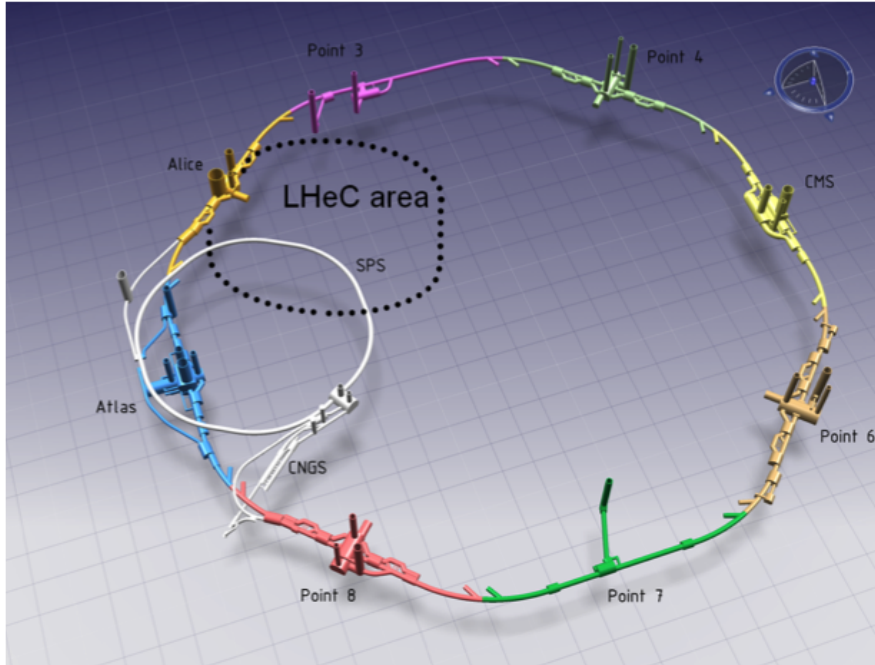


Figure 9.9: Schematic model of ERL position injecting into ALICE.

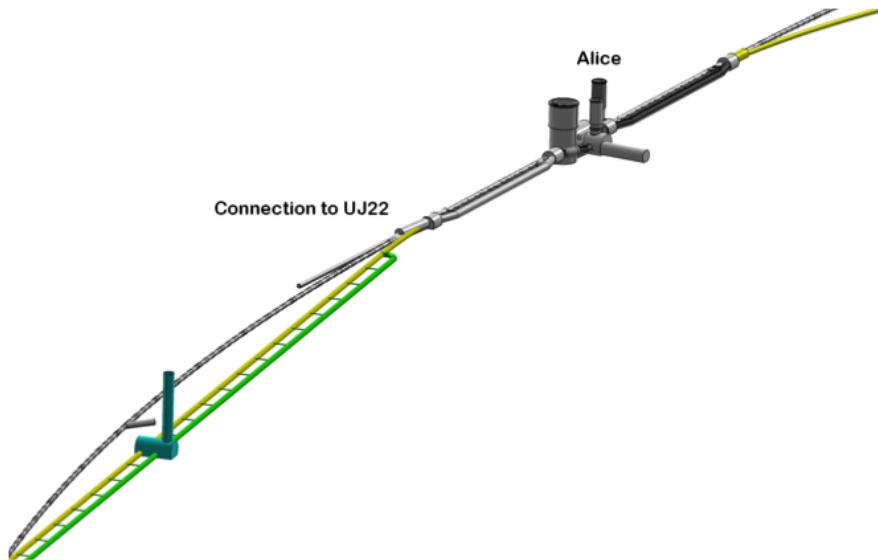


Figure 9.10: ERL Injection area into ALICE and RF/Cryo/Services Cavern (yellow & green).

7570 **9.5 Summary**

7571 From a civil engineering point of view, both the Ring-Ring and Linac-Ring options are feasible.
7572 The Ring-Ring option will provide a cheaper solution, however, with a marginally increased risk
7573 to LHC activity, due to the fact that most of the excavation works being in close proximity to
7574 the existing installations. The Linac-Ring option is the cleaner solution from a civil engineering
7575 point of view, with much less risk to LHC, but with substantial extra cost and greater time
7576 needed for environmental and building permit procedures.

7577

Chapter 10

7578

System Design

7579

10.1 Magnets for the Interaction Region

7580

10.1.1 Introduction

7581 The technical requirements for the ring-ring options are easily achieved with superconducting
7582 magnets of proven technology. It is possible to make use of the wire and cable development for
7583 the LHC inner triplet magnets. We have studied all-together seven variants of which two are
7584 selected for this CDR. Although these magnets will require engineering design efforts, there are
7585 no challenges because the mechanical design will be very similar to the MQXA [?] magnet built
7586 for the LHC [?].

7587 The requirements in terms of aperture and field gradient are much more difficult to obtain
7588 for the linac-ring option. We reverse the arguments and present the limitations for the field
7589 gradient and septum size, that is, the minimum distance between the proton and electron
7590 beams, for both Nb-Ti and Nb₃Sn superconducting technology. Here we limit ourselves to the
7591 two most promising conceptual designs.

7592

10.1.2 Magnets for the ring-ring option

7593 The interaction region requires a number of focussing magnets with apertures for the two
7594 proton beams and field-free regions to pass the electron beam after the collision point. The
7595 lattice design was presented in Section xx; the schematic layout is shown in Fig. 10.1.

7596 The field requirements for the ring-ring option (gradient of 127 T/m, beam stay clear of 13
7597 mm (12 σ), aperture radius of 21 mm for the proton beam, 30 mm for the electron beam) allow
7598 a number of different magnet designs using the well proven Nb-Ti superconductor technology
7599 and making use of the cable development for the LHC. In the simulations presented here, we
7600 have used the parameters (geometrical, critical surface, superconductor magnetization) of the
7601 cables used in the insertion quadrupole MQY of the LHC.

7602 Fig. 10.2 shows a superferric magnet as built for the KEKb facility [?]. This design comes
7603 to its limits due to the saturation of the iron poles. Indeed, the fringe field in the aperture of
7604 the electron beam exceeds the limit tolerable for the electron beam optics, and the field quality
7605 required for proton beam stability, on the order of one unit in 10^{-4} at a reference radius of $2/3$
7606 the aperture, is difficult to achieve.

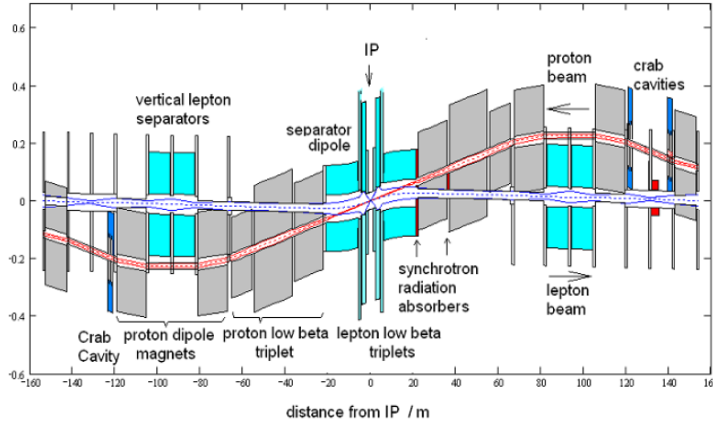


Figure 10.1: Layout of the LHeC interaction region (ring-ring option).

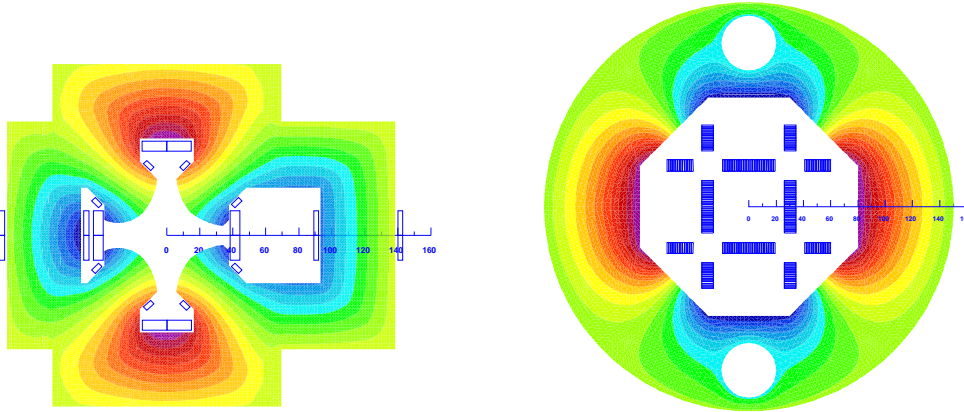


Figure 10.2: Cross-sections of insertion quadrupole magnets with iso-surfaces of the magnetic vector potential (field-lines). Left: Super-ferric, similar to the design presented in [?]. Right: Superconducting block-coil magnet as proposed in [?] for a coil-test facility.

7607 The magnetic flux density in the low-field region of the design shown in Fig. 10.2 (right)
 7608 is about 0.3 T. We therefore disregard this design as well. Moreover, the engineering design
 7609 work required for the mechanical structure of this magnet would be higher than for the proven
 7610 designs shown in Fig. 10.3.

7611 Fig. 10.3 shows the three alternatives based on LHC magnet technology. In the case of
 7612 the double aperture version the aperture for the proton beams is 21 mm in diameter, in the
 7613 single aperture version the beam pipe is 26 mm. In all cases the 127 T/m field gradient can be
 7614 achieved with a comfortable safety margin to quench (exceeding 30%) and using the cable(s) of

Table 10.1: Characteristic data for the superconducting cables and strands. OL = outer layer, IL = inner layer

Magnet	MQY (OL)	MQY (IL)
Diameter of strands (mm)	0.48	0.735
Copper to SC area ratio	1.75	1.25
Filament diameter (μ m)	6	6
B_{ref} (T) @ T_{ref} (K)	8 @ 1.9	5 @ 4.5
$J_c(B_{\text{ref}}, T_{\text{ref}})$ (A mm^{-2})	2872	2810
$-dJ_c/dB$ ($\text{A mm}^{-2} \text{T}$)	600	606
$\rho(293 \text{ K})/\rho(4.2 \text{ K})$ of Cu	80	80
Cable width (mm)	8.3	8.3
Cable thickness, thin edge (mm)	0.78	1.15
Cable thickness, thick edge (mm)	0.91	1.40
Keystone angle (degree)	0.89	1.72
Insulation thickn. narrow side (mm)	0.08	0.08
Insulation thickn. broad side (mm)	0.08	0.08
Cable transposition pitch length (mm)	66	66
Number of strands	34	22
Cross section of Cu (mm^2)	3.9	5.2
Cross section of SC (mm^2)	2.2	4.1

7615 the MQY magnet of the LHC. The operation temperature is supposed to be 1.8 K, employing
7616 superfluid helium technology. The cable characteristic data are given in Table 10.1. The outer
7617 radii of the magnet coldmasses do not exceed the size of the triplet magnets installed in the
7618 LHC (diameter of 495 mm). The fringe field in the aperture of the electron beam is in all cases
7619 below 0.05 T.

7620 Fig. 10.4 shows half-aperture quadrupoles (single and double-aperture versions for the
7621 proton beams) in a similar design as proposed in [?]. The reduced aperture requirement in
7622 the double-aperture version makes it possible to use a single layer coil and thus to reduce the
7623 beam-separation distance between the proton and the electron beams. The field-free regions is
7624 large enough to also accommodate the counter rotating proton beam. The version shown in
7625 Fig. 10.4 (left) employs a double-layer coil. In all cases the outer diameter of the coldmasses
7626 do not exceed the size of the triplet magnets currently installed in the LHC tunnel.

7627 For this CDR we retain only the single aperture version for the Q2 (shown in Fig. 10.3,
7628 left) and the half-aperture quadrupole for the Q1 (shown in Fig. 10.4, top left). The separation
7629 distance between the electron and proton beams in Q1 requires the half-aperture quadrupole
7630 design to limit the overall synchrotron radiation power emitted by bending of the 60 GeV
7631 electron beam. The single aperture version for Q2 is retained in the present layout, because
7632 the counter rotating proton beam can be guided outside the Q2 triplet magnet. The design of Q3
7633 follows closely that of Q2, except for the size of the septum between the proton and the electron

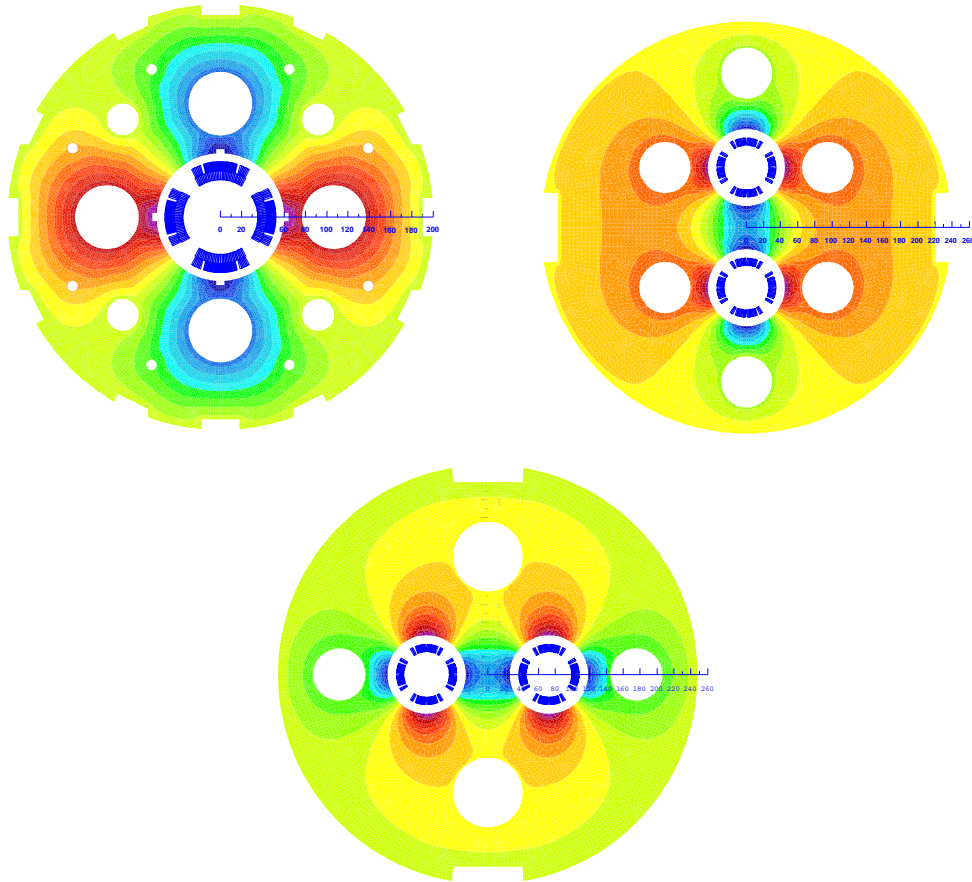


Figure 10.3: Cross-sections with field-lines of insertion quadrupole magnets. Classical designs similar to the LHC magnet technology. Top left: Single aperture with a double layer coil employing both cables listed in Table 10.1. Design chosen for Q2. Top right: Double aperture vertical. Bottom: Double aperture horizontal. The double-aperture magnets can be built with a single layer coil using only the MQY inner layer cable; see the right column of Table 10.1.

7634 beams.

7635 The coils in all three triplet magnets are made from two layers, using both Nb-Ti composite
 7636 cables as specified in Table 10.1. The layers are individually optimized for field quality. This
 7637 reduces the sensitivity to manufacturing tolerances and the effect of superconductor magneti-
 7638 zation [?]. The mechanical design will be similar to the MQXA magnet where two kinds of
 7639 interleaved yoke laminations are assembled under a hydraulic press and locked with keys in
 7640 order to obtain the required pre-stress of the coil/collar structure. The main parameters of the
 7641 magnets are given in Table 10.2.

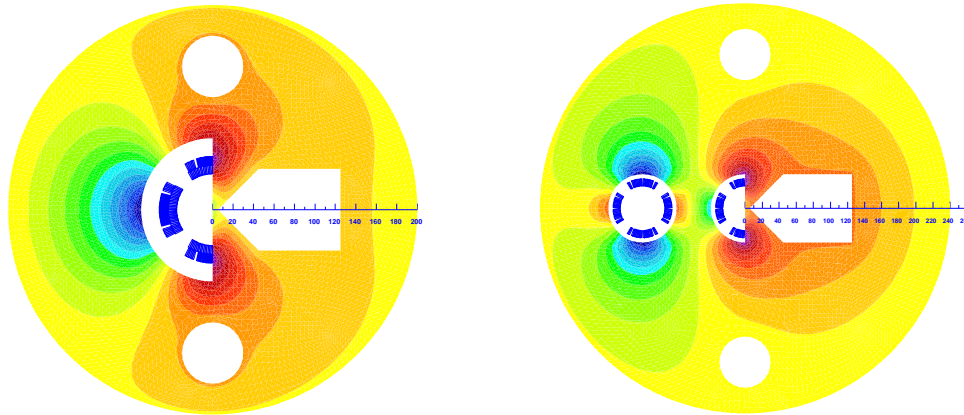


Figure 10.4: Cross-sections of insertion quadrupole magnets with field-lines. Left: Single half-aperture quadrupole with field-free domain [?]; design selected for Q1. Right: Double-aperture magnet composed of a quadrupole and half quadrupole.

7642 10.1.3 Magnets for the linac-ring option

7643 The requirements in terms of aperture and field gradient are more difficult to obtain for the
 7644 linac-ring option. Consequently we present the limitations for the field gradient and septum size
 7645 achievable with both Nb-Ti and Nb₃Sn superconducting technologies. We limit ourselves to the
 7646 two conceptual designs already chosen for the ring-ring option. For the half quadrupole, shown
 7647 in Fig. 10.6 (right), the working points on the load-line are given for both superconducting
 7648 technologies in Fig. 10.5.

7649 However, the conductor size must be increased and in case of the half quadrupole, a four
 7650 layer coil must be used; see Fig. 10.6. The thickness of the coil is limited by the flexural
 7651 rigidity of the cable, which will make the coil-end design difficult. Moreover, a thicker coil will
 7652 also increase the beam separation between the proton and the electron beams. The results
 7653 of the field computation are given in Table 10.2, column 3 and 4. Because of the higher iron
 7654 saturation, the fringe fields in the electron beam channel are considerably higher than in the
 7655 magnets for the ring-ring option.

7656 For the Nb₃Sn option we assume composite wire produced with the internal Sn process (Nb
 7657 rod extrusions), [?]. The non-Cu critical current density is 2900 A/mm² at 12 T and 4.2 K.
 7658 The filament size of 46 μm in Nb₃Sn strands give rise to higher persistent current effects in the
 7659 magnet. The choice of Nb₃Sn would impose a considerable R&D and engineering design effort,
 7660 which is however, not more challenging than other accelerator magnet projects employing this
 7661 technology [?].

7662 Fig. 10.7 shows the conceptual design of the mechanical structure of these magnets. The
 7663 necessary prestress in the coil-collar structure, which must be high enough to avoid unloading
 7664 at full excitation, cannot be exerted with the stainless-steel collars alone. For the single ap-
 7665 erture magnet as shown in Fig. 10.7 left, two interleaved sets of yoke laminations (a large one
 7666 comprising the area of the yoke keys and a smaller, floating lamination with no structural func-
 7667 tion) provide the necessary mechanical stability of the magnet during cooldown and excitation.

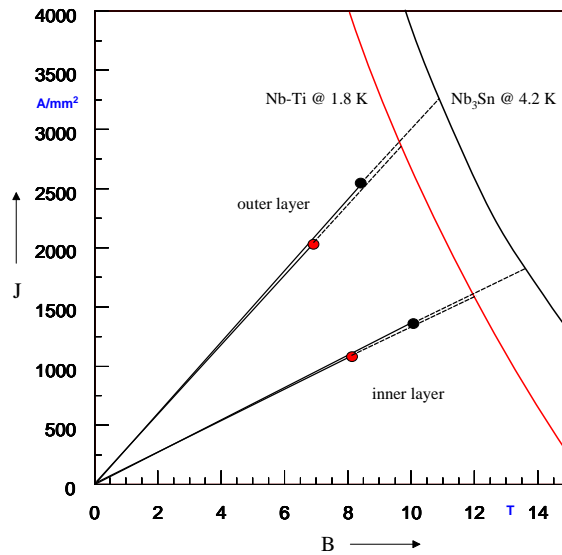


Figure 10.5: Working points on the load-line for both Nb-Ti and Nb₃Sn variants of the half quadrupole for Q1.

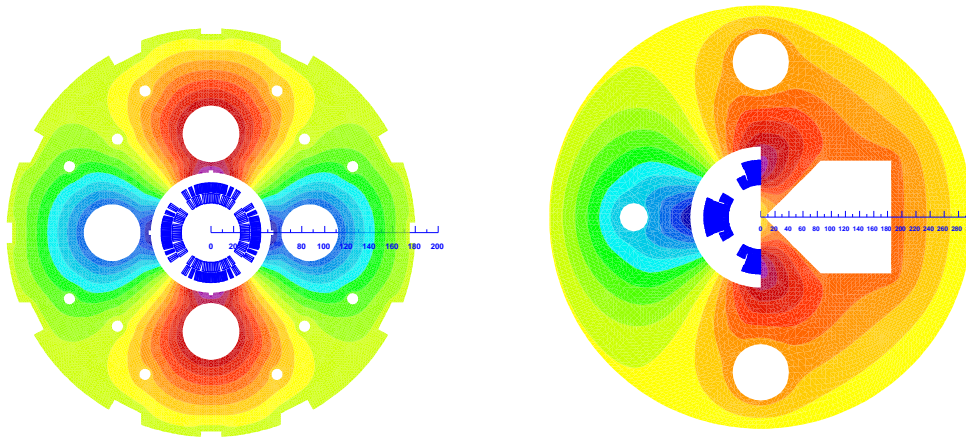


Figure 10.6: Cross-sections of the insertion quadrupole magnets for the linac-ring option. Left: Single aperture quadrupole. Right: Half quadrupole with field-free region.

7668 Preassembled yoke packs are mounted around the collars and put under a hydraulic press, so
 7669 that the keys can be inserted. The sizing of these keys and the amount of prestress before the
 7670 cooldown will have to be calculated using mechanical FEM programs. This also depends on
 7671 the elastic modulus of the coil, which has to be measured with a short-model equipped with

Table 10.2: SC = type of superconductor, g = field gradient, R = radius of the aperture (without coldbore and beam-screen), LL = operation percentage on the load line of the superconductor material, I_{nom} = operational current, B_0 = main dipole field, S_{beam} = beam separation distance, B_{fringe} = fringe field in the aperture for the electron beam, g_{fringe} = gradient field in the aperture for the electron beam.

Type		Ring-ring single aperture	Ring-ring half-quad	Linac-ring single aperture	Linac-ring half-quad
Function		Q2	Q1	Q2	Q1
SC		Nb-Ti at 1.8 K			
R	mm	36	35	23	46
I_{nom}	A	4600	4900	6700	4500
g	T/m	137	137	248	145
B_0	T	-	2.5	-	3.6
LL	%	73	77	88	87
S_{beam}	mm	107	65	87	63
B_{fringe}	T	0.016	0.03	0.03	0.37
g_{fringe}	T/m	0.5	0.8	3.5	18
SC		Nb ₃ Sn at 4.2 K			
I_{nom}	A			6700	4500
g	T/m			311	175
B_0	T			-	4.7
LL	%			83	82
B_{fringe}	T			0.09	0.5
g_{fringe}	T/m			9	25

7672 pressure gauges. Special care must be taken to avoid nonallowed multipole harmonics because
7673 the four-fold symmetry of the quadrupole will not entirely be maintained.

7674 The mechanical structure of the half-quadrupole magnet is somewhat similar, however,
7675 because of the left/right asymmetry four different yoke laminations must be produced. The
7676 minimum thickness of the septum will also have to be calculated with structural FEM programs.

7677 10.1.4 Dipole Magnets

7678 Two different types of bending magnets are considered in this document: the ones for the LR
7679 Option, used in the arcs of the recirculator, and the ones for the RR Option, to be installed in
7680 the LHC ring.

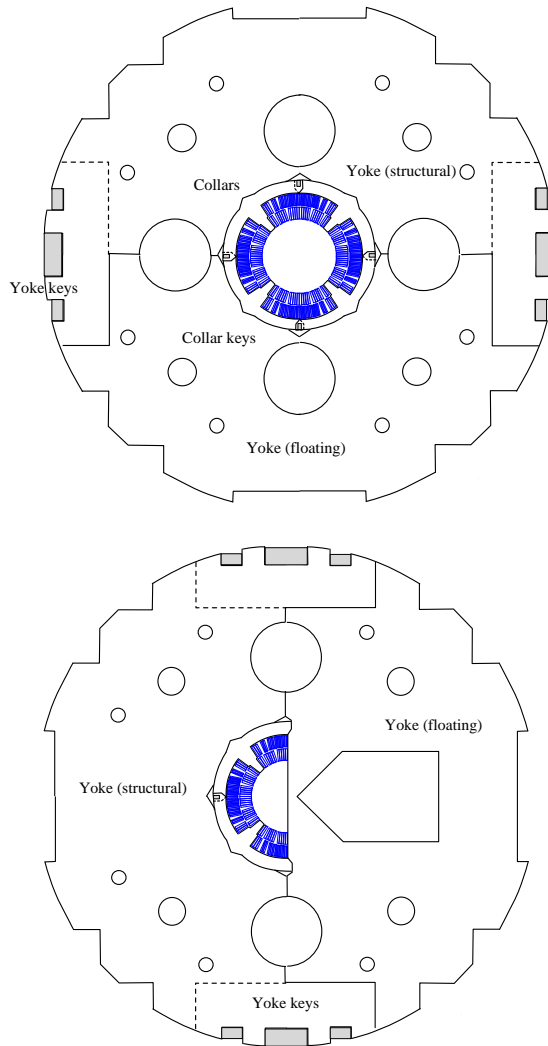


Figure 10.7: Sketch of the mechanical structure. Left: Single aperture magnet. Right: Half quadrupole with field-free region.

7681 **Dipole Magnets for the LR Option**

7682 Each of the 6 arcs of the recirculator needs 600 four-meter-long bending magnets, providing a
 7683 magnetic field from 0.046 T to 0.264 T depending on the arc energy from 10.5 GeV to 60.5
 7684 GeV.

7685 Considering the relatively low field strength required even for the highest energy arc, and
 7686 the small required physical aperture of 25 mm only, it is proposed here to adopt the same cross
 7687 section for all magnets, possibly with smaller conductors for the lowest energies.

7688 This allows the design of very compact and relatively cheap magnets, running at low current
 7689 densities to minimize the power consumption.

7690 Table 10.3 summarizes the main parameters of the proposed magnet design illustrated in
 7691 Figure 10.8.

Parameter	Value	Units
Beam Energy	10.5-60.5	GeV
Magnetic Length	4.0	Meters
Magnetic Field	0.046-0.264	Tesla
Number of magnets	6 x 600 = 3600	
Vertical aperture	25	mm
Pole width	80	mm
Number of turns	2	
Current @ 0.264 T	2200	Ampere
Conductor material	copper	
Magnet inductance	0.10	milli-Henry
Magnet resistance	0.10	milli-Ohm
Power @ 10.5 GeV	15	Watt
Power @ 20.5 GeV	55	Watt
Power @ 30.5 GeV	125	Watt
Power @ 40.5 GeV	225	Watt
Power @ 50.5 GeV	350	Watt
Power @ 60.5 GeV	500	Watt
Total power consumption 10-60 GeV	762	kW
Cooling	air or water	depends on energy

Table 10.3: Main parameters of bending magnets for the LR recirculator. Resistance and power refer to the same conductor size, however for the lowest energies conductors may be smaller.

7692 Dipole Magnets for the RR Option

7693 3040 bending magnets, 5.35-meter-long each, are needed in the LHC tunnel for the RR option.
 7694 They shall provide a magnetic field ranging from 0.0127 T at 10 GeV to 0.0763 T at 60 GeV.
 7695 Additionally, about 40 magnets will be needed in the Interaction Regions totalling about 3080
 7696 magnets. The main issues in the design of these magnets are:

- 7697 • the field range, situated in low field region, and in particular the very low injection field
 7698 constitute a challenge for achieving a satisfactory field reproducibility from cycle to cycle
 7699 and for making field quality relatively constant during the field ramp. These specific issues
 7700 will be discussed further in the paragraphs dealing with the experimental work carried
 7701 out at BINP and at CERN
- 7702 • compactness, to fit in the present LHC

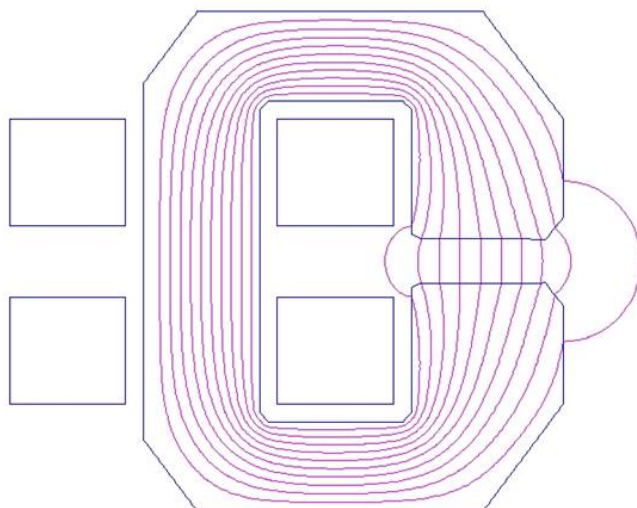


Figure 10.8: Bending magnets for the LR recirculator

- compatibility with synchrotron radiation power

The proposed design is constituted by compact C-Type dipoles, with the C-aperture on the external side of the ring to possibly allow the use of a vacuum pre-chamber and in any case to avoid the magnet intercepts the synchrotron radiation. The unusual poles shape allows minimizing the difference of flux lines length over the horizontal aperture, making magnetic field quality less dependent on the iron characteristics than in a C-type dipole of conventional shape. The coils are constituted by solid single bars of conductor, which after insulation are individually slit inside the magnet. The conductor can be in aluminium or in copper depending from economical reasons coming from a correct balance between investment cost and operation. The present design is based on an aluminium conductor, which among other has the advantage of making the magnet lighter than with a copper conductor. The conductor size is sufficiently large to reduce the dissipated power within levels which can be dealt by ventilation in the LHC tunnel: this is a considerable advantage in terms of simplicity of magnet manufacture, connections, reliability and of course of avoiding the installation of a water cooling circuit in the LHC arcs.

Table 10.4 summarizes the main parameters of the proposed magnet design illustrated in Figure 10.9.

10.1.5 BINP Model

Two different types of models have been manufactured, both aiming at demonstrating that a cycle-to-cycle reproducibility of the relatively low injection field (only 127 Gauss at an injection energy of 10 GeV) better than 0.1 Gauss can be achieved. Both models, pictured in Figure 10.10, showed a magnetic field reproducibility at injection field within ± 0.075 Gauss when cycled between injection and maximum field. To achieve such results both models make use of the same iron laminations, which are 3408 type silicon steel grain oriented 0.35 mm thick.

Parameter	Value	Units
Beam Energy	10-60	GeV
Magnetic Length	5.35	Meters
Magnetic Field	0.0127-0.0763	Tesla
Number of magnets	3080	
Vertical aperture	40	mm
Pole width	150	mm
Number of turns	2	
Current @ 0.763 T	1300	Ampere
Conductor material	copper	
Magnet inductance	0.15	milli-Henry
Magnet resistance	0.16	milli-Ohm
Power @ 60 GeV	270	Watt
Total power consumption @ 60 GeV	0.8	MW
Cooling	air or water	depends on tunnel ventilation

Table 10.4: Main parameters of bending magnets for the RR Option.

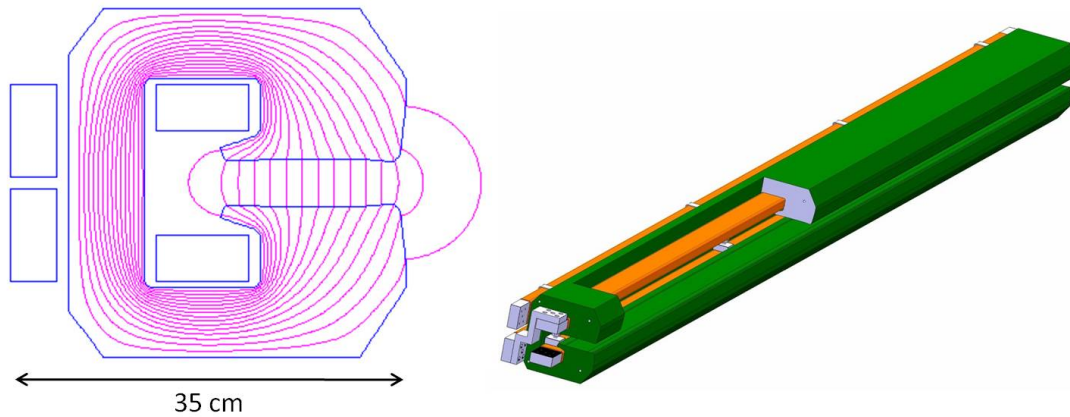


Figure 10.9: Bending magnets for the RR Option

7727 Their coercive force in the direction of the orientation is about 6 A/m, and perpendicular to
7728 the direction of the orientation remains relatively low at about 22 A/m. The C-type model
7729 has been assembled in two variants, with the central iron part with grains oriented vertically
7730 and with grain oriented horizontally (both blocks are as shown in the picture). The relevant
7731 magnetic measurements did not show differences between the two versions.

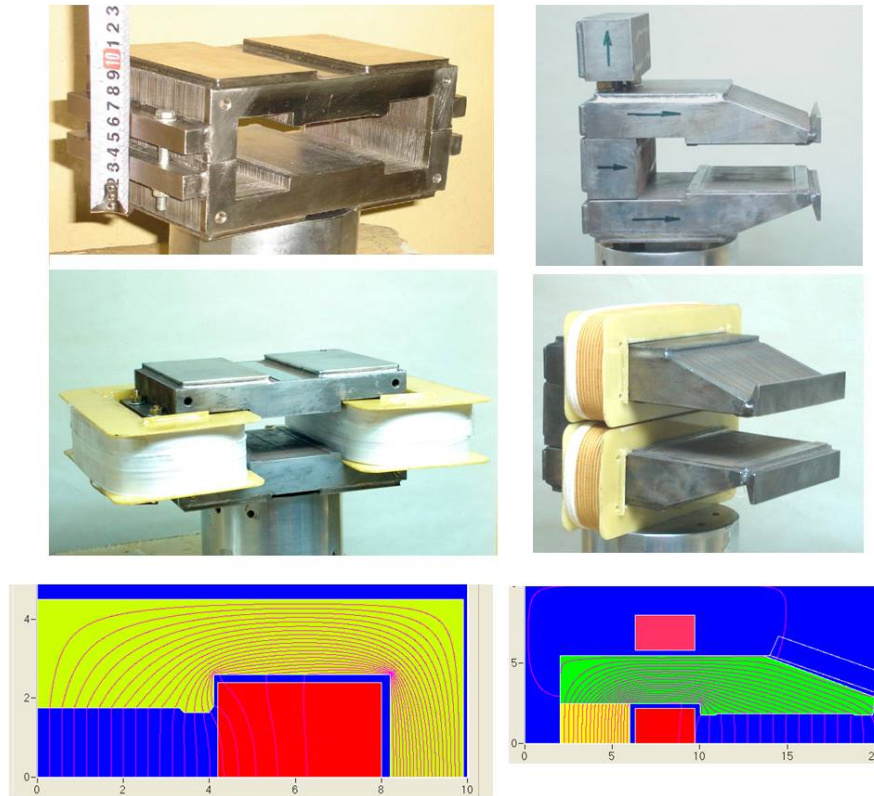


Figure 10.10: H and C-Type model magnets made by BINP

7732 10.1.6 CERN Model

7733 As a complementary study to the one made by BINP, the CERN model explores the man-
 7734 ufacture of lighter magnets, with the yoke made by interleaved iron and plastic laminations.
 7735 The magnetic flux produced in the magnet aperture is concentrated in the iron only, with a
 7736 thickness ratio between plastic and iron of about 2:1 the magnetic field in the iron is about 3
 7737 times that in the magnet gap. In addition to a lighter assembly, this solution has the advantage
 7738 of increasing the magnetic working point of the iron at injection fields, thus being less sensitive
 7739 to the quality of the iron and in particular to the coercive force. To explore the whole potential
 7740 of this solution three different lamination materials have been explored: an expensive NiFe 50
 7741 steel (H_c 3A/m) which will act as reference, a conventional grain oriented steel with similar
 7742 characteristics as the one used by BINP, and a conventional low carbon steel with H_c 70 A/m.
 7743 The model cross section reproduces the reference one described for the RR dipoles.

7744 10.1.7 Quadrupole and Corrector Magnets

7745 In case of the RR option we need, in the LHC tunnel:

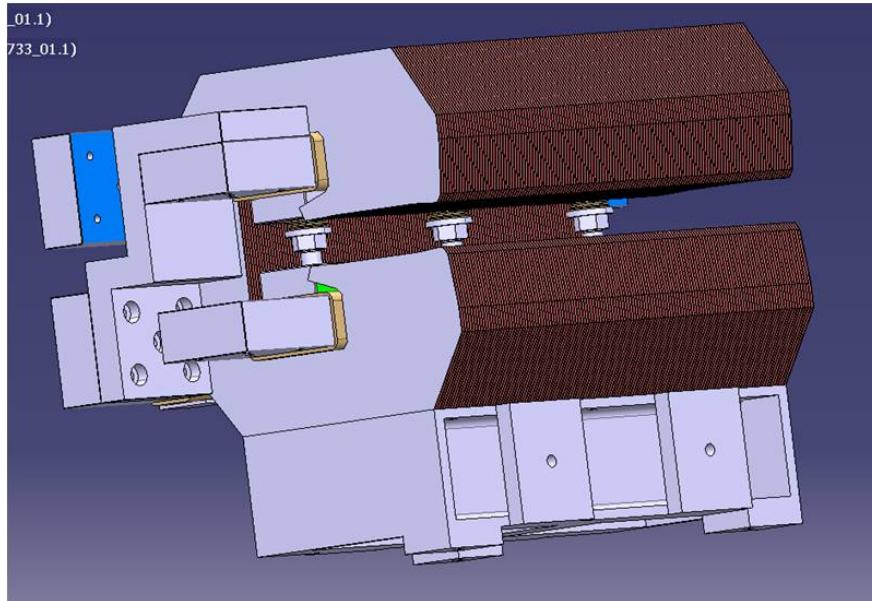


Figure 10.11: 400 mm long RR dipole model with interleaved laminations

7746 • in the arcs, 336 QF each providing 10.28T integrated strength, and 336 QD each providing
7747 8.40T integrated strength

7748 • in the insertion and by-pass, 97 QF each providing 18T integrated strength, and 97 QD
7749 each providing 12.6T integrated strength

7750 In case of the LR option we need:

7751 • in the two 10 GeV linacs, 37+37 quadrupoles each providing 2.5T integrated strength

7752 • again in the two 10 GeV linacs, 37+37 correctors each providing 10mTm integrated
7753 strength in both vertical and horizontal direction

7754 • in the recirculator arcs 4 different quadrupole types, the Q0, Q1 and Q3 each providing
7755 about 35 T integrated strength, and the Q2 each providing about 50T integrated strength

7756 **RR: 336+336 quadrupoles in the arcs**

7757 Considering the integrated strength of QD and QF are not much different, we propose having
7758 the same type of magnets: the relevant parameters are summarized in Table 10.5 and the cross
7759 section is illustrated in Figure 10.12.

7760 **RR: 148 + 148 quadrupoles in the insertion and by-pass**

7761 In total 148 QF and 148 QD quadrupoles are needed in the insertion and by-pass. The required
7762 integrated strength is 18T for the QF and 13T for the QD. We propose having the same magnet
7763 cross section with two different length, 1.0 m the QF and 0.7 m the QD, capable of producing a

Parameter	Value	Units
Beam Energy	10-60	GeV
Magnetic Length	1.0	Meters
Field gradient @ 60 GeV	10.28 (QF) - 8.40 (QD)	T/m
Number of magnets	336 + 336	
Aperture radius	30	mm
Total length	1.2	meters
Weight	700	kg
Number of turns/pole	10	
Current @ 10.28 T/m	390	Ampere
Conductor material	copper	
Current density	4	A/mm ²
Magnet inductance 3	milli-Henry	
Magnet resistance	16	milli-Ohm
Power @ 60 GeV	2500	Watt
Cooling	water	

Table 10.5: Main parameters of arc quadrupole magnets for the RR Option.

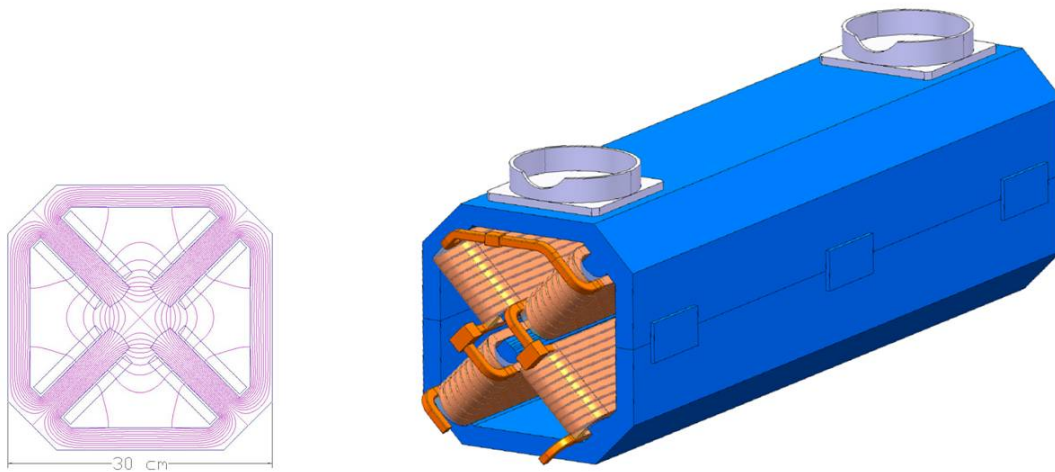


Figure 10.12: Arc quadrupole magnets for the RR Option

7764 gradient of up to 19 T/m. The relevant parameters are summarized in table 10.9 and the cross
7765 section is illustrated in Figure 10.13.

Parameter	Value	Units
Beam Energy	10-60	GeV
Magnetic Length (QD/QF)	1.0/0.7	Meters
Field gradient @ 60 GeV	19	T/m
Number of magnets (QD+QF)	148 + 148	
Aperture radius	30	mm
Total length (QD/QF)	1.2/0.9	meters
Weight (QD/QF)	700/500	kg
Number of turns/pole	17	
Current @ 19 T/m	410	Ampere
Conductor material	copper	
Current density	5	A/mm ²
Magnet inductance (QD/QF)	12/9	milli-Henry
Magnet resistance (QD/QF)	40/30	milli-Ohm
Power @ 60 GeV (QD/QF)	7/5	kWatt
Cooling	water	

Table 10.6: Main parameters of insertion and by-pass quadrupole magnets for the RR Option.

7766 **LR: 37 + 37 quadrupoles for the two 10 GeV Linacs**

7767 The present design solution considers 70 mm aperture radius magnets to be compatible with
7768 any possible aperture requirement. The relevant parameters are summarized in table ?? and
7769 the cross section is illustrated in Figure 10.14.

7770 **LR: 37 + 37 correctors for the two 10 GeV Linacs**

7771 The combined function correctors shall provide an integrated field of 10 mTm in an aperture
7772 of 140 mm. The relevant parameters are summarized in table 10.8 and the cross section is
7773 illustrated in Figure 10.15.

7774 **LR: 360 Q0 + 360 Q1+ 360 Q2 + 360 Q3 quadrupoles for the recirculator arcs**

7775 In each of the 6 arcs there are 4 types of quadrupoles, each type in 60 units, making 240
7776 quadrupoles per arc. The required integrated strength can be met with one type of quadrupole
7777 manufactured in two different length: 1200 mm the Q2 and 900 mm the Q0-Q1-Q3. The
7778 quadrupoles of the low energy arcs may use a smaller conductor or less turns or the same
7779 conductor as the higher energy quadrupoles showing then ecological friendly power consump-
7780 tion. The relevant parameters are summarized in table ?? and the cross section is illustrated
7781 in Figure 10.16.

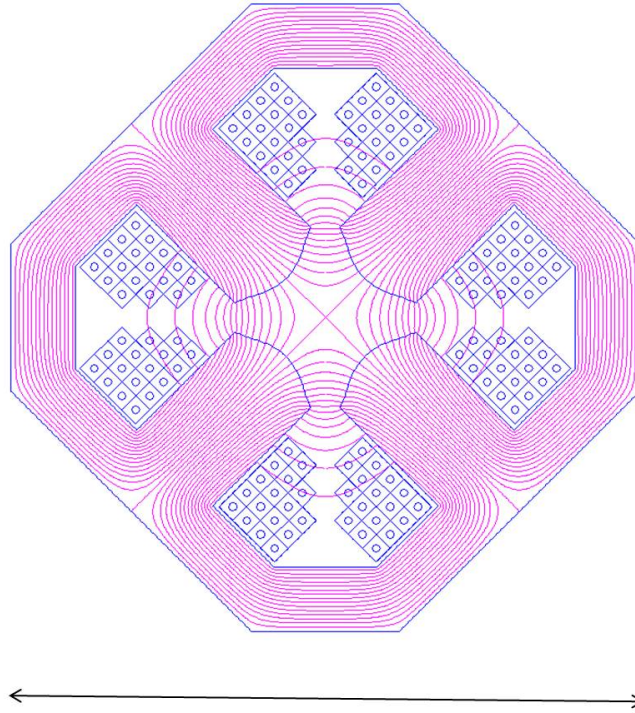


Figure 10.13: Insertion and by-pass quadrupole magnets for the RR Option

Parameter	Value	Units
Magnetic Length	250	mm
Field gradient	10	T/m
Number of magnets	37 + 37	
Aperture radius	70	mm
Weight (QD/QF)	300	kg
Number of turns/pole	44	
Current @ 10 T/m	500	Ampere
Conductor material	copper	
Current density	5	A/mm ²
Magnet inductance	12	milli-Henry
Magnet resistance	24	milli-Ohm
Power @ 500 A	6	kWatt
Cooling	water	

Table 10.7: Main parameters of quadrupoles for the 10 GeV linacs of the LR option

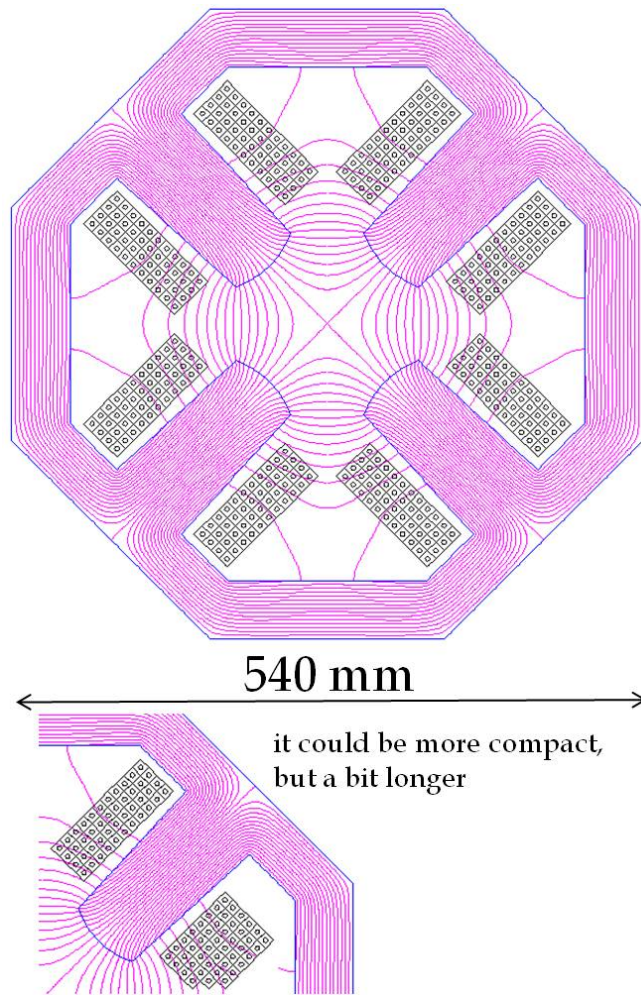


Figure 10.14: Quadrupoles for the 10 GeV linacs of the LR option

7782 10.2 Ring-Ring RF Design

7783 10.2.1 Design Parameters

7784 The RF system parameters for the e-ring are listed in Table 10.10. For a beam energy of 60 GeV
 7785 the synchrotron losses are 437 MeV/turn. With a nominal beam current of 100 mA the rather
 7786 significant amount power of 47.3 MW is lost due to synchrotron radiation. For the voltages
 7787 needed superconducting RF is the only choice.

Parameter	Value	Units
Magnetic Length	400	mm
Field induction	25	mT
Number of magnets (QD+QF)	37 + 37	
Free aperture	140 x 140	mm x mm
Yoke length	250	mm
Total length	350	mm
Weight	100	kg
Number of turns/circuit	2x100	
Current	40	Ampere
Conductor material	copper	
Current density	1.5	A/mm ²
Magnet inductance per circuit	10	milli-Henry
Magnet resistance per circuit	0.1	Ohm
Power per circuit	160	Watt
Cooling	air	

Table 10.8: Main parameters of combined function corrector magnets for the LR Option.

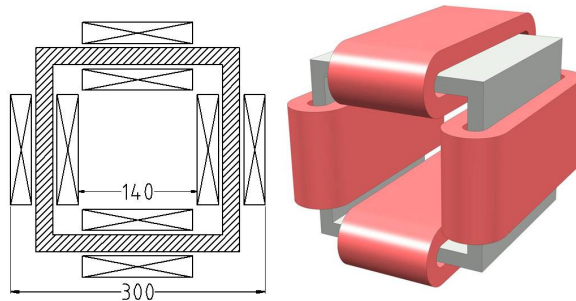


Figure 10.15: Combined function corrector magnets for the LR Option

7788 10.2.2 Cavities and klystrons

7789 Cavity design

7790 The most important issue determining the RF design is not so much in achieving high accel-
7791 erating gradient but rather the need to handle large powers through the power coupler. The
7792 choice of RF frequency is based on relatively compact cavities which are able to handle the
7793 relatively high beam intensities and allowing fitting of power couplers of sufficient dimensions
7794 to handle the RF power. A frequency in the range 600 to 800 MHz is the most appropriate.
7795 Cavities of frequency of 704 MHz are currently being developed at CERN in the context of the
7796 study of a Superconducting Proton Linac (SPL) [?] [?] [?]. The same frequency is also used
7797 at BNL for ERL cavities for the RHIC upgrade project [?]. Both cavities are 5-cell and can

Parameter	Value	Units
Beam Energy	10-60	GeV
Magnetic Length	0.9/1.2	Meters
Field gradient	41	T/m
Number of magnets (Q0+Q1+Q2+Q3)	1440	
Aperture radius	20	mm
Weight (QD/QF)	550/750	kg
Number of turns/pole	17	
Current @ 41 T/m	410	Ampere
Conductor material	copper	
Current density	5	A/mm ²
Magnet inductance	15/20	milli-Henry
Magnet resistance	30/40	milli-Ohm
Power @ 410 A	5/7	kWatt
Cooling	water	

Table 10.9: Main parameters of quadrupoles for the recirculators of the LR option

7798 achieve gradients greater than 20 MV/m. For the present study we take an RF frequency of
7799 721.42 MHz, which is compatible with LHC \tilde{O} s minimum 25 ns bunch spacing. An RF voltage of
7800 500 MV gives a quantum lifetime of 50 hours; this is taken as the minimum operating voltage.
7801 An RF voltage of 560 MV gives infinite quantum lifetime and a margin of 60 MV which permits
7802 feedback system voltage excursions and provides tolerance to temporary failure of part of the
7803 RF system without beam loss.

7804 5-cell cavities would require too much RF power transferred through the power coupler,
7805 therefore we use 2-cell cavities here in keeping the cell shape. Then with a total of 112 cavities,
7806 the power per cavity supplied to the beam to compensate the synchrotron radiation losses is
7807 390 kW. This level of power handling is only just reached for the power couplers of the larger
7808 400 MHz cavities of the LHC. It is therefore proposed to use two power couplers per cavity and
7809 split the power. In terms of voltage, only 5 MV per cavity is required to make 560 MV, hence
7810 it is sufficient to use cavities with two cells instead of five. The resulting cavity active length
7811 is 0.42 m and the gradient is a conservative 11.9 MV/m. Under these conditions the matched
7812 loaded Q is $2.8 \cdot 10^5$. Over-coupling by 50 % to $1.9 \cdot 10^5$ provides a stability margin and incurs
7813 relatively small power overhead. Under this condition the average forward power through the
7814 coupler is just under 200 kW. This nevertheless remains challenging for the design of power
7815 coupler.

7816 Cryomodule layout

7817 With 8 cavities per cryomodule there are a total of 14 cryomodules. The estimated cryomodule
7818 length, scaled from the 8 5-cell cavity of SPL to two cells per cavity is 10 m. There are 8
7819 double cell cavities in 14 10m cryomodules, the total RF cryomodule length is therefore 140
7820 m, but space must be allowed for quadrupoles, vacuum equipment and beam instrumentation.

Energy	GeV	60
Beam current	mA	100
Synchrotron losses	MeV/turn	437
Power loss to synchrotron radiation	MW	43.70
Bunch frequency (25 ns spacing)	MHz	40.08
Multiplying factor		18
RF frequency	MHz	721.42
Harmonic number		64152
RF Voltage for 50 hour quantum lifetime	MV	500.00
Nominal RF voltage (MV)	MV	560.00
Synchronous phase angle	degrees	129
Quantum lifetime at nominal RF voltage	hrs	infinite
Number of cavities		112
Number of 8-cavity cryomodules		14
Power couplers per cavity		2
Average RF power to beam per power coupler	kW	195
Voltage per cavity at nominal voltage	MV	5.00
Cells per cavity		2
Cavity active length	m	0.42
Cavity R/Q		114
Cavity Gradient	MV/m	11.90
Cavity loaded Q (Matched)		$2.8 \cdot 10^5$
Cavity forward power (nom. current, nom. voltage) for matched condition	kW	390
Nominal cavity loaded Q (matched for 50 % more beam)		$1.9 \cdot 10^5$
Cavity forward power (nominal current, voltage & loaded Q)	kW	406
Forward power per coupler	kW	203
Number of cavities per klystron		2
Waveguide losses	%	7
Klystron output power	kW	870
Feedbacks & detuning power margins	%	15
Klystron rated power	kW	1000
Total number of klystrons		56
Total average operating klystron RF power	MW	49
DC power to klystrons assuming 65% klystron efficiency	%	75
Grid power for RF, assuming 95% efficiency of power converters	MW	79

Table 10.10: RF system parameters for the electron ring.

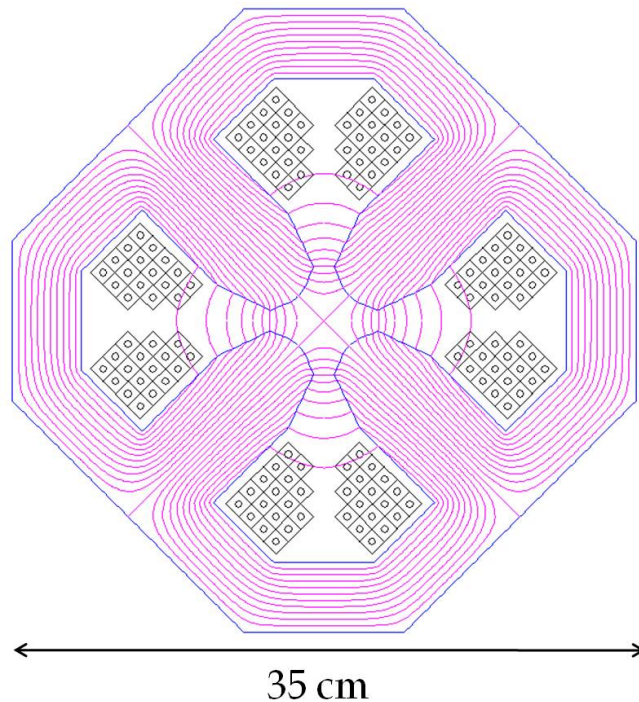


Figure 10.16: Quadrupoles for the recirculators of the LR option

7821 A total of 208 m is available in the by-passes: 124 m at CMS and 2 x 42m at ATLAS. Eight
 7822 cryomodules can therefore be installed in the CMS bypass and six, three on each side, in the
 7823 ATLAS by-passes. The distance between the modules can be taken as 3 m to allow space for
 7824 the other equipment. The positioning of the RF tunnels in the CMS and ATLAS bypasses is
 7825 shown in Figure 10.17.

7826 **RF Power System**

7827 The configuration for powering of one eight cavity cryomodule is shown in figure 10.18. Each
 7828 klystron feeds two cavities with power being split near the cavity to its two couplers. Taking
 7829 two cavities per klystron with an estimated 7 % losses in the waveguide system gives a mean
 7830 required klystron output power of 870 kW. A 15 % margin for the feedbacks gives a klystron
 7831 rated power of 1 MW. The total number of klystrons is 56, delivering an average total RF power
 7832 of 49 MW. Taking 65 % klystron efficiency and 95 % efficiency in the power converters gives
 7833 roughly 79 MW grid power needed for the RF power system.

7834 **RF Power System Layout**

7835 The klystrons are installed in the additional tunnels parallel to the by-passes. An estimated
 7836 surface area of 100m² is needed for the two klystrons, circulators, HV equipment and Low Level
 7837 RF and controls racks for each 8 cavity module in adjacent RF gallery. This defines the tunnel

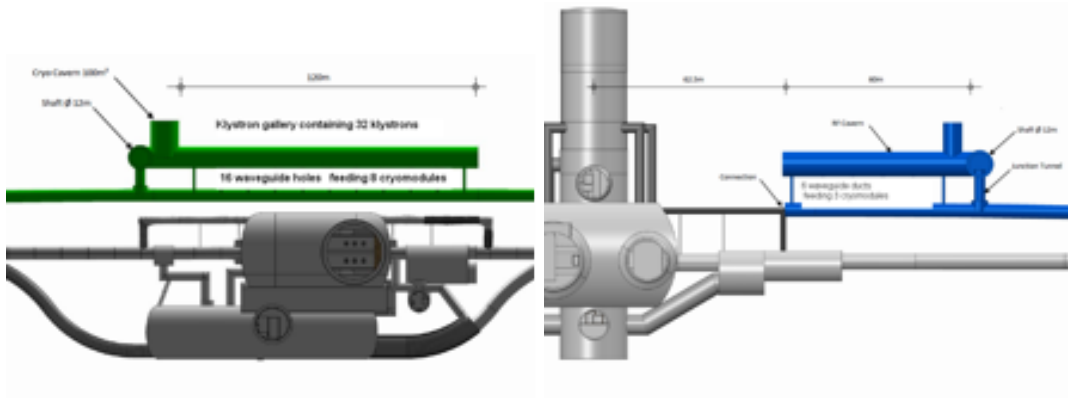


Figure 10.17: RF tunnel Layouts at CMS and ATLAS bypasses. Note only the right hand side at ATLAS shown.

7838 width over the 13 m module interval (length + spacing) to be 8 m. Waveguide ducts are needed
 7839 between the by-passes and the RF tunnels. With one waveguide per klystron into the tunnel,
 7840 and two waveguides per duct, there are 16 ducts in the CMS tunnels, spaced roughly 6.5 m
 7841 apart. At ATLAS there would be six ducts on either side with the same spacing. The required
 7842 diameter of the duct tunnel is 90cm.

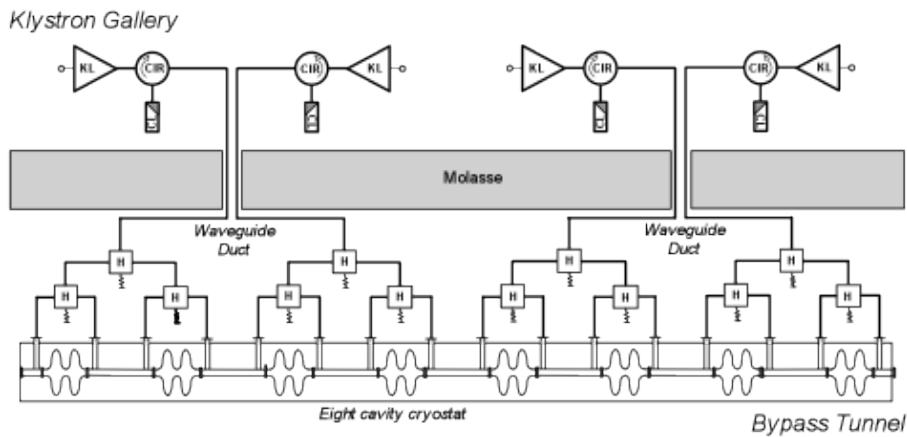


Figure 10.18: Layouts of RF power equipment in bypass and in RF gallery for one cryomodule.

7843 **Surface Installations**

7844 One HV Power Converter rated at 6 MVA is needed per 4 klystrons. These are housed in
 7845 surface buildings: eight converters at CMS, and six at ATLAS.

Arc	Arc energy [GeV]	Energy loss per arc passage [MeV]	Number of passages	Total energy loss per arc [MeV]
6	60	570.0	1	570.0
5	50	275.0	2	550.0
4	40	115.0	2	230.0
3	30	35.0	2	70.0
2	20	7.0	2	14.0
1	10	0.4	2	0.8
				1434.8

Table 10.11: Energy losses in the arcs on a half circle of 1 km radius

7846 Conclusions

7847 721.4 MHz RF systems can be just fitted in the two bypasses nearest ATLAS and CMS. Detailed
7848 studies need to be done on the optimization of the cavity geometry for the high beam current
7849 and ensuring acceptable transverse impedance. The RF power system is large. Further work
7850 is needed on integration to exactly define tunnel and cavity cavern layouts and quantify the
7851 space requirements. Phased installation with gradual energy build-up, as was done for LEP, is
7852 an interesting possibility. The power needed for RF is 79 MW. To this must be added power
7853 for RF controls, for power converters, cryogenics and all other machine equipment.

7854 10.3 Linac-Ring RF Design

7855 10.3.1 Design Parameters

7856 The ERL design [?] [?] [?] is based on two 10 GeV linacs, with 0.3 GeV injection and 6 linac
7857 passes to reach 60 GeV. This is shown in Figure ??.

7858 The overall parameters are given in table [Frank]. With a beam current of 6.6 mA produced,
7859 there are currents of nearly 20 mA in both directions in the linacs. Significant power, greater
7860 than the injection energy, is lost in the passages though the arcs due to synchrotron radiation
7861 as shown in Table 10.11.

7862 The energy loss in the arcs can be compensated by independent RF systems operating at
7863 twice the normal RF frequency. As proposed by [?] it could be envisaged to let the main linacs
7864 replace the energy lost to synchrotron radiation. However, this scheme significantly restricts
7865 operational freedom and is not tested yet. Therefore we keep it only as one possible option.
7866 For the present report both options are presented - Case 1 for additional RF systems in the
7867 arcs to compensate synchrotron losses and Case 2 for this energy supplied by the linacs.

7868 Linac design

7869 High accelerating gradient is needed. First tests on cavities at similar frequency at BNL have
7870 already reached 20 MV at Q_0 of $1 \cdot 10^{10}$. Improved cavity design and careful cavity processing

7871 should allow meeting the specifications. The optimum number of cavities and the gradient is an
7872 overall compromise taking into account cost, cryogenics consumption and operational reliability.
7873 The RF power system needs to compensate energy loss and non-ideal energy recovery due to
7874 beam losses, phasing errors, transients, ponderomotive effects and noise. It also needs to allow
7875 testing and processing of the cavities at full gradient without circulating beam. The main RF
7876 parameters are given in Table 10.12, for the two cases described above.

7877 The linac RF design is based on 5-cell cavities operating at 721.42 MHz, this frequency
7878 being compatible with 25 ns bunch spacing in LHC, as for the electron ring option. A gradient
7879 of 20 MV/m can be taken. This is a conservative estimate based on SPL type cavities presently
7880 being developed, with a design aim of 25 MV/m. The unloaded Q (Q_0) is taken as $2.5 \cdot 10^{10}$.
7881 This is presently a challenging figure, but recent tests on cavities at this frequency for e-RHIC
7882 have been very encouraging. With an active cavity length of 1.06 m the voltage is 21.2 MV
7883 per cavity. This requires 944 cavities in total, or 472 cavities per linac. The cavity external
7884 Q (Q_{ext}) is derived from optimum coupling to the required beam power to compensate the 4
7885 energy losses in Case 1 and this plus the synchrotron radiation losses in the arcs in Case 2. It
7886 should be noted that the 300 MeV injection linac, with nearly 2 MW beam power will also take
7887 grid power of between 3 and 4 MW.

7888 10.3.2 Layout and RF powering

7889 Cryomodule and RF power system layout

7890 With eight cavities in a cryomodule of 14 m length, there are 59 cryomodules per linac. Allowing
7891 a further 2 m per cryomodule for other linac equipment the total linac length is 944 m. This is
7892 summarized in table 10.13.

7893 RF power system

7894 Assuming optimum coupling the forward power per cavity is approximately 17.9 kW and
7895 28.7 kW for Cases 1 and 2 respectively. The available power per cavity must be somewhat
7896 higher to allow margin for operation of RF the feedback systems; i.e. 21 kW and 33 kW per
7897 cavity. These levels can certainly be achieved with solid state amplifiers, avoiding the need for
7898 high voltage power supplies and associated protection equipment. The grid to RF conversion
7899 efficiency is also somewhat higher; 70 % can be taken. The total supplied average RF powers are
7900 approximately 17 MW and 27 MW for the two cases and the grid power required for powering
7901 of the linacs is 24 MW and 39 MW respectively.

7902 RF Power system layout

7903 The RF amplifiers and RF feedback and controls racks are housed in a separate parallel pow-
7904 ering gallery. There is one RF amplifier per cavity, the power being fed by WR1150 standard
7905 waveguides, each 11.5 inches by 5.75 inches (30 cm by 15 cm). The number of holes between
7906 the powering and linac tunnels can be limited to one per four cavities, i.e. two per cryomodule,
7907 spaced 8 m apart giving 118 holes per linac. The diameter is 90cm. The diameters could be
7908 reduced if half height waveguides or coax lines are used.

Parameter	Unit	Separate Arc RF	No Arc RF
Beam energy	GeV	60.0	60.0
Injection energy	GeV	0.3	0.3
Average beam current out	mA	6.6	6.6
Av. accelerated beam current in linacs	mA	19.8	19.8
Required total voltage in both linacs	GV	20.0	20.0
Energy recovery efficiency	%	96	96
Total power needed to compensate recovery losses	MW	15.8	15.8
Total energy loss per cycle in arcs	MeV	1434.8	1434.8
Total power needed to compensate arc losses	MW	0.0	9.5
RF frequency	MHz	721.42	721.42
Gradient	MV/m	20	20
Cells per cavity		5	5
Cavity length	m	1.06	1.06
Cavity voltage	MV	21.2	21.2
Number of cavities		944	944
Power to compensate recovery losses per cavity	kW	16.8	16.8
Power to compensate synch. rad. losses per cavity	kW	0.0	10.0
Cavity R/Q	circuit Ω	285	285
Cavity unloaded Q [Q_o]	10^{10}	2.5	2.5
Loaded Q [Q_{ext}]	10^6	47	29
Cavity forward power	kW	16.8	26.8
Cavity forward power - no beam		4.2	6.7
Number of cavities per solid state amp.		1	1
Transmission losses	%	7	7
Amplifier output power per cavity	kW	17.9	28.7
Feedbacks power margin	%	15	15
Amplifier rated power	kW	21	33
Total number of amplifiers		944	944
Total average amplifier output power	MW	17	27
Assumed overall conversion efficiency grid to amplifier RF output	%	70	70
Grid power for linacs RF	MW	24	39

Table 10.12: Linac RF parameters.

Parameter	Unit	Value
Cavities per cryomodule		8
Number of cavities		472
Number of cryomodules per linac		59
Cryomodule length	m	14
Spacing of cryomodules	m	2
Linac length	m	944

Table 10.13: ERL cryomodule numbers, length and spacing.

Parameter	Unit	Value
Total energy loss in 20-60GeV arcs	MeV	1434
Power loss in 20-60GeV arcs	MW	9.5
Arc RF frequency	MHz	1442/721
Number of cavities		49/28
Number of klystrons		25/7
Total average supplied klystron RF power	MW	10.8
Assumed overall conversion efficiency - grid to klystrons RF out	%	60
Grid power for arc RF systems	MW	18

Table 10.14: Arc RF systems overall parameters.

7909 10.3.3 Arc RF systems

7910 Table 10.11 shows the synchrotron radiation losses in the arcs; they are negligible in the 10 GeV
7911 arc. In the 20, 30, 40 and 50 GeV arc both the accelerated and decelerated beams pass the same
7912 arc RF system with 180° phase shift at the basic frequency of 721.42 MHz; hence to accelerate
7913 both beams, the arc RF system is operated at twice the frequency, i.e. at 1442.82 MHz. The
7914 60 GeV arc carries only the decelerated beam and there one can use the linac RF cavities at
7915 721.42 MHz. However, since here the required power per cavity is much larger the solid state
7916 amplifiers of the main linac cannot be used but a klystron or IOT must be applied. Overall
7917 parameters for these RF systems are given in Table 10.14.

7918 The arc systems provide very different voltages. Parameters for the individual systems
7919 are given in table 10.15. Use of cavities and cryostats scaled to those in the linacs is assumed;
7920 however short cryostats containing four cavities could be used in the 20 and 40 GeV arc systems.
7921 Powering would be by klystrons, a total of 36 rated at a maximum of 360 kW, with one klystron
7922 supplying up to four cavities.

7923 It can be noted that the overall grid power is less if the arc energy recovery is supplied by
7924 the main linacs. (39 MW compared to 24 plus 18 = 42 MW). This is partly due to the assumed
7925 higher efficiency of the solid state amplifiers in the linacs compared to the klystrons in the arc
7926 RF systems.

Parameter	Unit	Arc 2	Arc 3	Arc 4	Arc 5	Arc 6	Totals
Arc energy	GeV	20	30	40	50	60	
Energy lost per arc passage	MeV	7	35	115	275	570	
Number of passes		2	2	2	2	1	
Total energy loss in arc	MeV	14	70	230	550	570	1434
Power loss in arc	MW	0.1	0.5	1.5	3.6	3.8	9.5
RF frequency 1442 MHz	MHz	x	x	x	x		
RF frequency 721 MHz	MHz					x	
Cavities at 1442 MHz		1	4	12	32		49
Cavities at 721 MHz						28	28
Required voltage/cavity	MV	7.2	9.1	9.9	8.9	21.1	
RF Power/cavity	kW	92	116	127	113	134	
Nominal RF power/cavity	kW	96	120	132	118	140	
Klystron output power/cavity	kW	103	129	141	126	150	
Kl. rated power/cavity	kW	120	150	170	150	180	
Cavities/klystron		1	2	2	2	4	
Klystron rated power	kW	120	300	340	300	720	
Klystrons at 1442 MHz		1	2	6	16		25
Klystrons at 721 MHz						7	7
Total average supplied klystron RF power	MW	0.1	0.5	1.7	4.0	4.2	10.5
Assumed overall conversion efficiency grid to klystrons total RF power	%	60	60	60	60	60	
Grid power arc RF systems	MW	0.2	0.9	2.8	6.7	7.0	18

Table 10.15: Parameters of the individual arc RF systems.

7927 10.4 Crab crossing for the LHeC

7928 Due to the very high electron beam energies for the LHeC, the required RF power and the
7929 interaction region design due to synchrotron radiation are challenging. The IR layout for the
7930 RR option consists of a crossing angle to mitigate parasitic interactions and allows for a simple
7931 scheme to accommodate the synchrotron radiation fan. A crab crossing scheme for the proton
7932 beam is highly desirable to recover the geometric luminosity loss due to this crossing angle. The
7933 complex interaction region in the LHeC and the issues associated with the synchrotron radiation
7934 can be relaxed with an implementation of crab crossing. In addition to the luminosity gain, the
7935 issues associated with the synchrotron radiation can be relaxed with an implementation of crab
7936 crossing near the IR. It is also a natural knob to regulate the beam-beam parameter if desired.
7937 Although the linac-ring option plans to employ separation dipoles and mirrors for synchrotron
7938 radiation, crab crossing can prove to be a simpler option if the technology is viable.

7939 10.4.1 Luminosity Reduction

7940 In the nominal LHC with proton-proton collision, the two beams share a common vacuum
7941 chamber for approximately a 100m from the IP. Therefore, a crossing angle is required in the
7942 IRs to avoid parasitic interactions. Consequently, the luminosity is reduced by a geometrical
7943 reduction factor which can be expressed as

$$R = \frac{1}{\sqrt{1 - \Phi^2}} \quad (10.1)$$

7944 where $\Phi = \sqrt{\theta\sigma_z/2\sigma_x}$ is the Piwinski parameter, which is proportional to ratio of the longitudinal
7945 and transverse beam sizes in the plane of the crossing.

7946 With reducing β^* for the upgrade and a constant beam-to-beam separation in the IRs
7947 ($\sim 10\sigma$), the luminosity reduction factor becomes significant. To compensate this crossing angle,
7948 a crab crossing scheme is proposed and R&D is moving rapidly to realize the technology [?, ?].
7949 In addition to crossing angle compensation, it allows a natural knob to regulate the beam-beam
7950 parameter which can be valuable while operating close to the beam-beam limit.

7951 For the electron-proton collisions, the Piwinski parameter can be redefined as

$$\Phi_p = \frac{\theta_c}{2\sqrt{2}\sigma_x^*} \sqrt{\sigma_{z,p}^2 + \sigma_{z,e}^2} \quad (10.2)$$

7952 where $\sigma_{z,p}$ and $\sigma_{z,e}$ are the proton and electron bunch lengths. Table 10.16 lists the relevant
7953 parameters of the crossing schemes in the LHeC as compared to some other machines.

7954 10.4.2 Crossing Schemes

7955 Since the bunch length of the electrons are significantly smaller (at least factor 10) than that
7956 of the protons, the geometrical overlap due to crossing angle is mainly dominated by the angle
7957 of the proton bunches. Four different cases (see Fig. 10.19) were simulated to determine the
7958 luminosity gain in the different cases with crab cavities and comparing it to the nominal case
7959 (see Table 10.17).

7960 The luminosity gains strongly depend on the choice of RF frequency as the reduction factor
7961 due to the RF curvature at frequencies of interest (0.4-0.8 GHz) is non-negligible.

Table 10.16: Relevant parameters of the crossing schemes in the LHeC compared to LHC, KEK-B and eRHIC. Note † corresponds to electrons and * corresponds vertical plane.

	KEK-B	LHC		LHeC		eRHIC
		Nominal	Upgrade	RR	LR	
θ_c [mrad]	22.0	0.285	0.4-0.6	1.0	0.0 (4.0)	0.0 (5.0)
σ_z [cm]	0.7	7.55		7.55 (0.7†)		20/1.2†
σ_x^* [μm]	103	16.6	11.2	30 (15.8*)	-	32
Φ	0.75	0.64	1-1.4	0.9 (1.6*)	0.0	0.0 (11.0)

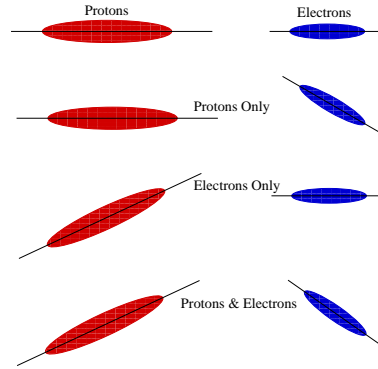


Figure 10.19: Schematic of different crossing schemes using crab cavities on either proton or electron beams as compared to the head-on collision.

7962 10.4.3 RF Technology

7963 The cavity voltage required for can be calculated using

$$V_{crab} = \frac{2cE_0 \tan(\theta_c/2) \sin(\mu_x/2)}{\omega_{RF} \sqrt{\beta_{crab} \beta^*} \cos(\psi_{cc \rightarrow ip}^x - \mu_x/2)} \quad (10.3)$$

7964 where E_0 is the beam energy, ω_{RF} is the RF frequency of the cavity, β_{crab} and β^* are the beta-
7965 functions at the cavity and the IP respectively, $\psi_{cc \rightarrow ip}^x$ is the phase advance from the cavity
7966 to the IP and μ_x is the betatron tune. The nominal scenarios for both proton-proton and
7967 electron-proton IRs are anticipated to have local crab crossing with two cavities per beam to
7968 create a local crab-bump within the IR. Since the β -functions are typically large in the location
7969 of the crab cavities, a voltage of approximately 20 MV should suffice for crossing angles of
7970 approximately 1-2 mrad. The exact voltage will depend on the final interaction region optics
7971 of the both the proton and the electron beams.

7972 To accomodate the crab cavities within the IR region, deflecting structures with a compact
7973 footprint are required. Conventional pill-box type elliptical cavities at frequencies of 400 MHz
7974 are too large to fit within the LHC interaction region constraints. The effort to compress the
7975 cavity footprint recently resulted in several TEM type deflecting mode geometries [?]. Apart

Table 10.17: Luminosity gains computed for different crossing schemes with crab cavities and a crossing angle of 1 mrad.

Scenario	L/L ₀	
	400 MHz	800 MHz
X-Angle (1 mrad)	1.0	
Uncross both e^- and p^+	1.88%	1.48
Uncross only e^-	1.007	
Uncross only p^+	1.88	1.48

7976 from being significantly smaller than its elliptical counterpart, the deflecting mode is the primary
7977 mode thus giving paving way to a new class of cavities at lower frequencies (400 MHz) which
7978 is preferred from the RF curvature point of view

7979 Demonstration of novel RF concepts providing high kick gradients and robust operation
7980 within the LHC constraints are mandatory to realize the benefits of crab crossing. R&D on
7981 novel concepts are already underway for the LHC upgrade. The issues of impedance, collimation
7982 and machine protection are similar to that of the implementation of the proton-proton IRs.

7983 10.5 Vacuum

7984 10.5.1 Vacuum requirements

7985 In particle accelerators, beams are travelling under vacuum to reduce beam-gas interactions i.e.
7986 the scattering of beam particles on the molecules of the residual gas. The beam-gas interaction
7987 is dominated by the bremsstrahlung on the nuclei of gas molecules therefore depends on partial
7988 pressure, weight of the gas species and radiation length [g/cm²]. In presence of a photon-
7989 stimulated desorption, the residual gas is dominated by hydrogen (75%) followed by CO/CO₂
7990 (24%) and 1% CH₄. Argon normally represents less than 1% of the residual gas if welding best
7991 practice for UHV applications is applied. To be noted that Argon is 67 times more harmful
7992 than hydrogen (H₂), CO₂, CO and N₂ are about 30 times worst and is 10 times worst.

7993 The beam-gas interactions are responsible for machine performance limitations such as re-
7994 duction of beam lifetime (nuclear scattering), machine luminosity (multiple coulomb scattering),
7995 intensity limitation by pressure instabilities (ionisation) and for positive beams only, electron
7996 (ionisation) induced instabilities (beam blow up). The heat load induced by scatted protons
7997 and ions can also be an issue for the cryomagnets since local heat loads can lead to a magnet
7998 quench i.e. a transition from the superconducting to the normal state. The heavy gases are
7999 the most dangerous because of their higher ionisation cross-sections. In the case of the LHeC,
8000 this limitation exists only in the experimental areas where the two beams travel in the same
8001 beampipe. The beam-gas interactions can also increase the background to the detectors in the
8002 experimental areas (non-captured particles or nuclear cascade generated by the lost particles
8003 upstream the detectors) and the radiation dose rates in the accelerator tunnels. Thus, leading
8004 to material activation, dose rates to intervention crews, premature degradation of tunnel in-
8005 frastructures like cables and electronics and finally higher probability of electronic single events
8006 induced by neutrons which can destroy the electronics in the tunnel but also in the service

8007 galleries.

8008 The design of the vacuum system is also driven by severe additional constraints which
8009 have to be considered at the design stage since retrofitting mitigation solutions is often im-
8010 possible or very expensive. Among them, the vacuum system has to be designed to minimise
8011 beam impedance and higher order modes (HOM) generation while optimising beam aperture
8012 in particular in the magnets. It has to provide also enough ports for the pumps and vacuum
8013 diagnostics. For accelerators with cryogenic magnets, the beampipe has to be designed to in-
8014 tercept heat loads induced by synchrotron radiation, energy loss by nuclear scattering, image
8015 currents, energy dissipated during the development of electron clouds, the later building up
8016 only in presence of positively charged beams.

8017 The integration of all these constraints often lead to a compromise in performances and in
8018 the case of the LHeC, the compromise will differ between the Linac-Ring and the Ring-Ring
8019 options.

8020 10.5.2 Synchrotron radiation

8021 The presence of a strong synchrotron radiation has two major implications for the vacuum sys-
8022 tem: it has to be designed to operate under the strong photon-induced stimulated desorption
8023 while being compatible with the significant heat loads onto the beampipes. In the common
8024 beampipe, the photo-electrons generated by the synchrotron radiation will dramatically en-
8025 hanced the electron cloud build-up and mitigation solutions shall be included at the design
8026 stage.

8027 Synchrotron radiation power

8028 The synchrotron radiation power is an issue for the heat load deposited on the beampipes
8029 and for its evacuation and will be the driving factor for the mechanical engineering of the
8030 beampipes. Indeed, the heated surfaces will have a higher outgassing rates, the increase being
8031 exponentially dependent with the surface temperature (factor 10 for a $\Delta T = 50^\circ\text{C}$ increase).
8032 The synchrotron radiation power can be calculated with equation 10.4. Since scaling linearly
8033 with the beam intensity, I , with the power of 4 for energy, E , and inversely to power of 2 of
8034 the bending radius, the synchrotron radiation power in the Ring-Ring option is expected to
8035 be 45 times higher than LEP and locally at the by-passes, the power can be about 180 times
8036 higher. To be compared with the factor 10 expected in the bending and injection sections of
8037 the Linac-Ring option.

$$P[\text{W}/\text{m}] = 1.24 \times 10^3 \frac{E^4 I}{\rho^2} \quad (10.4)$$

8038 Photon-induced desorption

8039 The desorption rate depends on critical energy of the synchrotron light, ϵ_c , the energy which
8040 divides in two the emitted power. For most materials, the desorption rates vary quasi linearly
8041 with the critical energy (equation 10.5).

$$\epsilon_c(\text{eV}) = \frac{3 \cdot 10^{-7}}{R} \left(\frac{E_B}{E_0} \right)^3 \quad (10.5)$$

8042
8043
8044
8045
8046
8047
8048

$E_0 = 5.10^{-4}$ GeV for electrons, E_B is the energy of the beam and R the bending radius.

For the LHeC, the beam energies will be equivalent to the LEP at start. Then, a similar value of the critical energy can be assumed allowing the comparison with LEP pressure observations. Figure 10.20 shows typical photo-desorption yields measured on copper and stainless steel samples. But the beam intensities being by far larger, the linear photon flux which scales linearly (equation 3) with energy and intensity and inversely with bending radius will increase significantly.

$$\Gamma[\text{photons}/s/m] = 7 \times 10^{19} \frac{EI}{\rho} \quad (10.6)$$

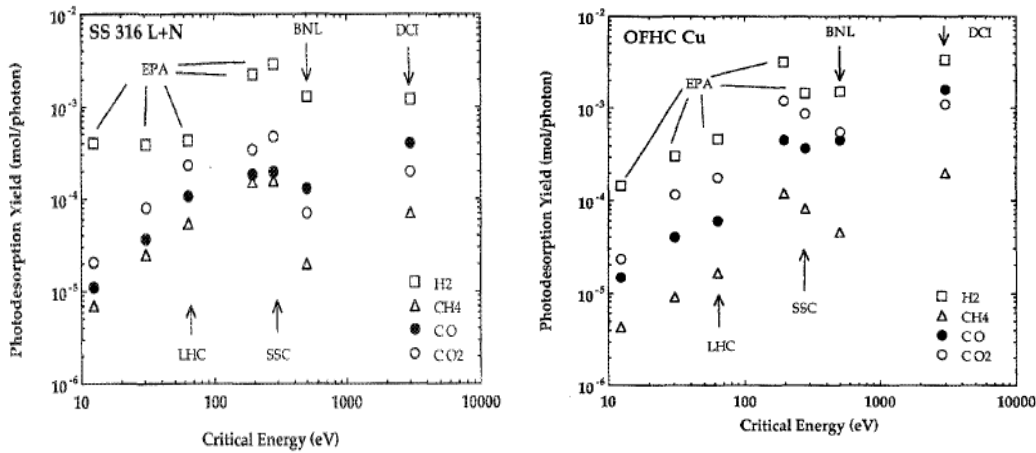


Figure 10.20: Photodesorption yields measured on copper and stainless steel surfaces. To be noted that the desorption yields of methane, η_{CH_4} , is 50 times lower than η_{H_2} .

8049
8050
8051
8052
8053
8054
8055
8056

For the Ring-Ring option (bending sections and by-passes), the linear photon flux is expected to be 45 times larger than in LEP, to be compared to the factor 5 expected for the Linac-Ring option.

The photon stimulated pressure rise, ΔP , depends linearly on the critical energy, on the beam energy and beam intensity as shown by equation 10.7. The temperature affecting the dependence of the desorption yield (equation 10.8 and 10.9), η , to the critical energy, ϵ_c the pressure rises will differ between surfaces at ambient temperature (equation 10.8) and at cryogenic temperature (equation 10.9).

$$\Delta P \propto \eta(\epsilon_c)EI \quad (10.7)$$

$$\text{at room temperature : } \eta \propto \epsilon_c \text{ and } \epsilon_c \propto E^3 \text{ such that } \Delta P \propto E^4I \quad (10.8)$$

$$\text{at cryogenic temperature : } \eta \propto \epsilon_c^{2/3} \text{ and } \epsilon_c \propto E^3 \text{ such that } \Delta P \propto E^3I \quad (10.9)$$

8057
8058

Therefore, the photon stimulated pressure rise is expected to be 45 times higher than LEP for the Ring-Ring option, to be compared with the factor 30 for the Linac-Ring option.

8059 Vacuum cleaning and beam scrubbing

8060 The dynamic pressure i.e. the pressure while operating the accelerator with beams will be
8061 dominated by the beam-induced dynamic effects like stimulated desorption due to beam losses
8062 or synchrotron radiations or by electron stimulated desorption in case an electron cloud is
8063 building-up.

8064 In presence of synchrotron radiation, the vacuum cleaning process which characterises the
8065 reduction of the desorption yields (η) of a surface resulting from the bombardment of the
8066 surface by electrons, photons or ions, significantly decreases the induced gas loads (3 – 4 orders
8067 of magnitude observed in LEP) improving the dynamic pressure at constant pumping speed.
8068 This results in a progressive increase of the beam lifetime.

8069 In presence of an electron cloud, the beam scrubbing which characterises the reduction
8070 of the secondary electron yield (SEY, δ) of a surface resulting from the bombardment of the
8071 surface by electrons, photons or ions, significantly decreases the induced gas loads (2 – 3 orders
8072 of magnitude observed in SPS) improving the dynamic pressure at constant pumping speed.
8073 Similarly to what happens with the vacuum cleaning, this results also in a progressive increase
8074 of the beam lifetime.

8075 By default and mainly driven by costs and integration issues, the vacuum system of an ac-
8076 celerator dominated by beam-induced dynamic effects is never designed to provide the nominal
8077 performances as from “day 1”. Indeed, vacuum cleaning and beam scrubbing are assumed to
8078 improve the beampipe surface characteristics while the beam intensity and beam energy are
8079 progressively increased during the first years of operation.

8080 This implies accepting a shorter beam lifetime or reduced beam current during the initial
8081 phase; about 500 h of operation with beams were required for LEP to achieve the nominal
8082 performances. New technical developments such as Non-Evaporable Coatings (NEG) shall be
8083 considered since significantly decreasing the time required to achieve the nominal performances
8084 (Figures 10.21 and 10.22).

8085 10.5.3 Vacuum engineering issues

8086 The engineering of the vacuum system has to be integrated right from the beginning of the
8087 project. This becomes imperative for the Ring-Ring option since it has to take into account
8088 the constraints of the LHC and allow for future consolidations and upgrades. For the Linac-
8089 Ring option, the tangential injection and dump lines will be in common with the LHC beam
8090 vacuum over long distances. The experience has shown that the vacuum engineering shall
8091 proceed in parallel on the following topics: expertise provided to beam-related components
8092 (magnets, beam instrumentation, radio-frequency systems, etc.), engineering of vacuum related
8093 components (beampipes, bellows, pumping ports, etc.) and machine integration including the
8094 cabling and the integration of the services.

8095 Basically, the vacuum system is designed to interconnect the beam related equipments in-
8096 stalled on the beam line (magnets, kickers, RF cavities, beam absorbers, beam instrumentation,
8097 etc.) and to provide the adequate pumping speed and vacuum instrumentation. The vacuum
8098 components are often composed by vacuum pipes, interconnection bellows, diagnostics, pump-
8099 ing ports and sector valves. The number of pumps, vacuum diagnostics, bellows and ports will
8100 differ significantly between the two options discussed in this CDR and also between vacuum
8101 sectors of the same accelerator.

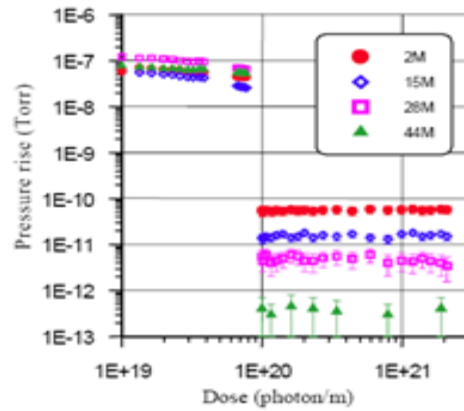
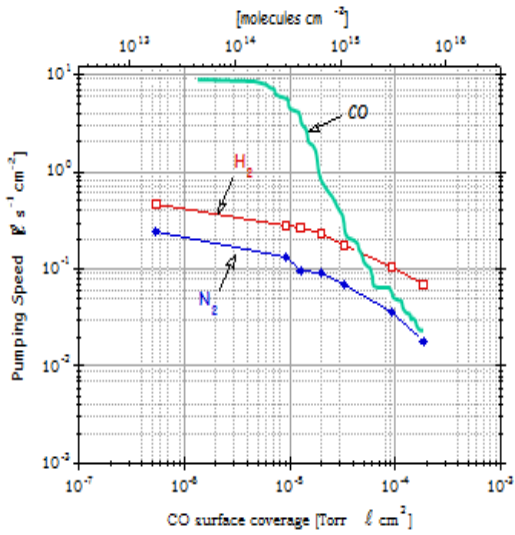
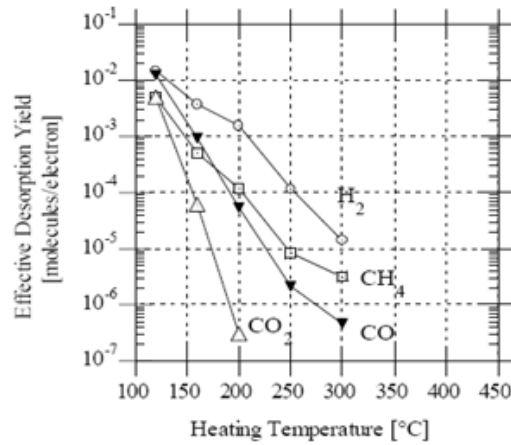


Figure 2: Pressure rise measured in the centre of the TiZrV coated test chamber before activation ($<1 \cdot 10^{20}$ photons/m) and after activation ($>1 \cdot 10^{20}$ photons/m).

Figure 10.21: NEG pumping speed for different gas species and pressure rises measured in presence of a photon flux before and after NEG activation.

Table 2: Summary of results from the activated test chamber

Gas	Sticking probability	Photodesorption yield (molecules/photon)
H ₂	~0.007	$\sim 1.5 \cdot 10^{-5}$
CH ₄	0	$2 \cdot 10^{-7}$
CO (28)	0.5	$< 1 \cdot 10^{-5}$
C _x H _y (28)	0	$< 3 \cdot 10^{-8}$
CO ₂	0.5	$< 2 \cdot 10^{-6}$



© Benvenuti et al. J.Vac Sci Technol A 16(1) 1998

Figure 10.22: Photon (left) and Electron (right) desorption yields.

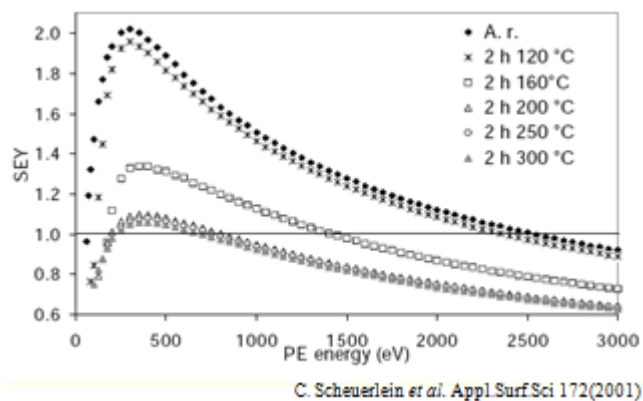


Figure 10.23: Reduction of the secondary electron yield (SEY, δ) by Photons a) and Electron b) desorption yields.

8102 **Vacuum pumping**

8103 The vacuum system of the LHeC will be mainly operated at ambient temperature. These
 8104 systems rely more and more on NEG coatings since they provide a distributed pumping and huge
 8105 pumping speed (Fig.2) and capacity and reduce the outgassing and desorption yields (Fig.3-
 8106 4). These coatings are compatible with copper, aluminium and stainless steel beampipes. An
 8107 alternative could be to use the LEP configuration with NEG strips. This alternative solution
 8108 has only the advantage of avoiding the bake out constraints for the activation of the NEG
 8109 coatings. A configuration of a distributed ion pumps is not considered since less performing
 8110 and only applicable in dipole magnets i.e. bending sections. In any case, ion pumps are
 8111 required as a complement of the NEG coatings to pump the noble gasses and methane to avoid
 8112 the ion beam-induced instability. Sublimation pumps are not excluded in case of local huge
 8113 outgassing rates, NEG cartridges being an interesting alternative since recent developments
 8114 made by manufacturers include an ion pump and a NEG cartridge in the same body.

8115 The roughing from atmosphere down to the UHV range will be obtained using mobile
 8116 turbomolecular pumping stations. These pumps are dismantled prior to beam circulations.

8117 The part of the vacuum system operated at cryogenic temperature, if any, could rely on
 8118 gas condensation if the operating temperatures are below 2 K. Additional cryosorbing material
 8119 could be required if an important hydrogen gas load is expected. This issue still needs to be
 8120 addressed. As made for the LHC, the parts at cryogenic temperature must be isolated from
 8121 the NEG coated part by sector valves when not at their operating temperature to avoid the
 8122 premature saturation of the NEG coatings.

8123 The pumping layout will be simpler for the Ring-Ring option since more space is available
 8124 around the beampipes. The tighter tolerances for the Linac-Ring option make the integration
 8125 and pumping layout more delicate. However, the vacuum stability will be easier to ensure in
 8126 the Linac-Ring option since only the bending sections are exposed to the synchrotron radiation.

8127 **Vacuum Diagnostics**

8128 For both options, the radiation level expected will be too high to use pressure sensors with
8129 onboard electronics. Therefore, passive gauges shall be used, inducing additional cabling costs
8130 and need for gauge controllers.

8131 **Vacuum Sectorisation**

8132 The sectorisation of the beam vacuum system results from the integration of various constraints,
8133 the major being: venting and bake-out requirements, conditioning requirements (RF and HV
8134 devices), protection of fragile and complex systems (experimental areas and ceramic chambers),
8135 decoupling of vacuum parts at room temperature from upstream and downstream parts at
8136 cryogenic temperature thus non-baked, radiation issues, etc.

8137 For UHV beam vacuum systems, all-metal gate valves shall be preferred in order to allow
8138 for bake-out at temperature above 250°C. VITON-sealed valves even though the VITON has
8139 been submitted to a special treatment are not recommended nearby NEG coatings or NEG
8140 pumps since minor outgassing of Fluor will degrade the pump characteristics.

8141 In the injection and extraction regions, the installation of the sector valves will lead to inte-
8142 gration issues since the space left between the beampipes with a tangential injection/extraction
8143 and the circulating beams is often limited. This could result in a long common beam vacuum
8144 which implies that the LHC beam vacuum requirements will apply to the LHeC part shared
8145 with LHC.

8146 **Vacuum protection**

8147 The distribution of the vacuum sector valves will be made in order to provide the maximum
8148 protection to the beam vacuum in case of failure (leak provoked or not). Interlocking the
8149 sector valves is not an obvious task. Indeed, increasing the number of sensors will provide more
8150 pressure indications but often results in a degradation of the overall reliability. The protection
8151 at closure (pressure rise, leaks) is treated differently from the protection while recovering from
8152 a technical stop with parts of the accelerator beampipe vented or being pumped down.

8153 The vacuum protections of the common beampipes between LHeC and LHC shall fulfill the
8154 strong LHC requirements. Indeed, any failure in the LHeC propagating to the LHC could lead
8155 to long machine downtime (several months) in case of an accidental venting of an LHC beam
8156 vacuum sector.

8157 **HOM and Impedance implications**

8158 The generation and trapping of higher order mode (HOM) resulting from the changes in
8159 beampipe cross-sections are severe issues for high intensity electron machines. Thus, the en-
8160 gineering design of LHeC must be inspired on new generation of synchrotron radiation light
8161 sources instead of the simple LEP design. All bellows and gaps shall be equipped with opti-
8162 mised RF fingers, designed to avoid sparking resulting from bad electrical continuity. Indeed,
8163 these effects could induce pressure rises and machine performance limitations.

8164 **Bake-out of vacuum system**

8165 An operating pressure in the UHV range (10^{-10} Pa) will be required for both options. This
8166 implies the use of a fully baked-out beam vacuum system. Two options are possible: permanent

8167 and dismantlable bake out. The permanent solution could be an option for the Linac-Ring
8168 but has to be excluded for the Ring-Ring option for cost reasons. As done for the dipole
8169 chambers (bending sections) of LEP, hot pressurised water can be used but the limit at 150°C
8170 is a constraint for the activation of NEG coatings. Developments are being carried on at CERN
8171 to lower the activation temperature from 180°C down to 150°C but this technology is not yet
8172 available.

8173 **Shielding issues**

8174 The synchrotron radiation power is an engineering challenge for the beampipes. Indeed, 50% of
8175 the radiation power hitting the vacuum chamber is absorbed in the beampipe chamber (case of
8176 LEP aluminum chamber). The remainder 50%, mainly the high-energy part of the spectrum,
8177 escapes into the tunnel and creates severe problems like degradation of organic material and
8178 electronics due to high dose rates and formation of ozone and nitric acid could lead to severe
8179 corrosion problems in particular with aluminum and copper materials.

8180 In this respect, the Ring-Ring option is less favorable since the synchrotron radiation will
8181 be localised at the plane of the existing LHC cable trays and electrical distribution boxes in the
8182 tunnel. Similar constraints exist also for the Linac-Ring option but these zones are localised at
8183 the bending sections of the LHeC.

8184 Detailed calculations are still to be carried on but based on LEP design, a lead shielding
8185 of 3 to 8 mm soldered directly on the vacuum chamber would be required for 70 GeV beams.
8186 Higher energies could require more thickness. The evacuation of the synchrotron radiation
8187 induced heat load on the beampipe wall and on lead shielding is a critical issue which needs
8188 to be studied. In case of insufficient heat propagation and cooling, the lead will get melted as
8189 observed in LEP in the injection areas. The material fatigue shall also be investigated since
8190 running at much higher beam current as compared to LEP, will increase the induced stress to
8191 the material and welds of the beampipes.

8192 As made in LEP, the best compromise to fulfill the above mentioned constraints is the use
8193 of aluminum beampipes, covered by a lead shielding layer. The complex beampipe cross-section
8194 required to optimise the water cooling of the beampipe and shielding is feasible by extrusion of
8195 aluminum billets and the costs are acceptable for large productions. The large heat conductivity
8196 helps also the heat exchange. However, extruded aluminum beampipes induce limitations for the
8197 maximum bake out temperature and therefore for the NEG coatings activation. Special grades
8198 of aluminum shall be used. The reliability of vacuum interconnections based on aluminum
8199 flanges is a concern at high temperature (>150°C) and corrosion issues shall be addressed. The
8200 stainless steel beampipes do not have these limitations but they have poorer heat conductivity
8201 and they are more difficult and costly to machine and shape.

8202 The LEP 110 GeV operation has shown the criticality of unexpected synchrotron radia-
8203 tions heating vacuum components and in particular the vacuum connections between pipes or
8204 equipments. Indeed, the flanges, by “offering” a thick path, are behaving as photon absorbers
8205 and heat up very quickly. Hence, at cool down and due to the differential dilatation, leaks are
8206 opening. In LEP, these unexpected SR induced heat loads resulted from orbit displacement in
8207 quadrupoles during the ramp in energy and of the use of the wigglers also during the ramp. In
8208 LHeC, resulting from the much higher beam current, these issues shall be carefully studied.

8209 Corrosion issues

8210 In vacuum systems, feedthroughs and bellows are particularly exposed to corrosion. The
8211 feedthroughs, particularly those of the ion pumps where high voltage is permanently present,
8212 are critical parts. A demonstrated and cheap solution to prevent the risk of corrosion consists
8213 in heating directly the protective cover to reduce the relative humidity around the feedthrough.

8214 The bellows are critical due to their thickness, often between 0.1 – 0.15 mm. PVC material
8215 must be prohibited in the tunnel. Indeed, in presence of radiations, it can generate hydrochloric
8216 acid (HCl) which corrodes stainless steel materials. This corrosion has the particularity to
8217 be strongly penetrating, once seen at the surface, it is often too late to mitigate the effects.
8218 Aluminum bellows are exposed to corrosion by nitric acid (HNO₃) which is generated by the
8219 combination of O₃ and NO.

8220 Humidity is the driving factor and shall be kept 50%. However, in the long term, accidental
8221 spillage can compromise locally the conditions and therefore, corrosion-resistant design are
8222 strongly recommended.

8223 10.6 Beam Pipe Design

8224 10.6.1 Requirements

8225 The vacuum system inside the experimental sector has a number of different and sometimes
8226 conflicting requirements. Firstly, it must allow normal operation of the LHC with two circu-
8227 lating beams in the chamber. This implies conformity with aperture, impedance, RF, machine
8228 protection as well as dynamic vacuum requirements. The addition of the incoming electron
8229 beam adds constraints in terms of geometry for the associated synchrotron radiation (SR) fan
8230 and the addition of SR masks in the vacuum. Finally, optimization of the surrounding detec-
8231 tor for high acceptance running means that all materials for chambers, instrumentation and
8232 supports must be optimized for transparency to particles and the central chamber must be as
8233 small and well aligned as possible to allow detectors to approach the beam aperture limit at
8234 the interaction point.

8235 10.6.2 Choice of Materials for beampipes

8236 LHC machine requirements imply an inner beampipe wall that has low impedance (good electri-
8237 cal conductivity) along with low desorption yields for beam stimulated emissions and resistance
8238 to radiation damage.

8239 Ideal materials for transparency to particles have low radiation length (Z) and hence low
8240 atomic mass. These materials either have poor (i.e. high) desorption yields (eg. aluminium,
8241 beryllium) or are not vacuum and impedance compatible (eg. carbon). Solutions to this problem
8242 typically include thin film coatings to improve desorption yields and composite structures to
8243 combine good mechanical properties with vacuum and electrical properties.

8244 The LHC experimental vacuum systems, along with most other colliders currently use
8245 metallic beryllium vacuum chambers around the interaction points due to a very favourable
8246 combination of Z , electrical conductivity, vacuum tightness, radiation resistance, plus mechan-
8247 ical stiffness and strength. High desorption yields are suppressed by a thin film TiNiV non-
8248 evaporable getter (NEG) coating. This coating also gives a high distributed vacuum pumping
8249 speed, allowing long, small aperture vacuum chambers to be used that would otherwise be

8250 conductance-limited. Activation of this coating requires periodic heating of the chamber to
 8251 $180 - 220^{\circ}\text{C}$ under vacuum for a few hours. This means that the chamber and environment
 8252 must be designed for these temperatures. This activation is scheduled in annual LHC shut-
 8253 downs. Long-term development is in progress for low desorption yield coatings that do not
 8254 require high temperature activation [621]. These may have applications for LHeC.

8255 Production technology developed for the LHC uses beryllium sections machined from hot-
 8256 pressed blocks and electron beam welded to produce chambers. This has the advantage that a
 8257 wide range of vacuum chamber forms can be manufactured. Cylindrical and conical chamber
 8258 sections are installed in the LHC experiments.

8259 Disadvantages of beryllium include high cost, fragility and toxicity in the powder form, as
 8260 well as limited availability. For this reason, long-term development of other technologies for
 8261 experimental beampipes is under way at CERN which may yield applications for LHeC.

8262 Composite beampipe structures made from carbon and other low-Z materials have been
 8263 developed for colliders. These typically use a thin inner membrane to comply with vacuum
 8264 and impedance requirements. Composite structure pipes were eventually rejected for LHC
 8265 application for reasons of temperature and radiation resistance and the risk of delamination
 8266 due to mismatch of thermal expansion coefficients. Lower luminosity in LHeC experiments
 8267 combined with new low temperature coatings may allow these materials to be re-evaluated.

8268 10.6.3 Beampipe Geometries

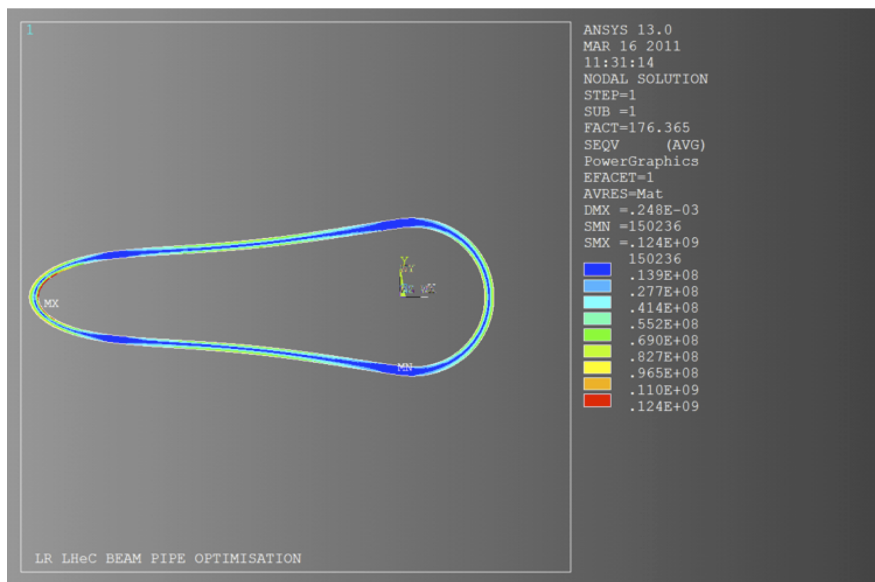


Figure 10.24: Section through the LR geometry showing contours of Von Mises equivalent stress (Pa).

8269 The proposed geometry has a cross section composed of a half-circle intersecting with a half-
 8270 ellipse. Cylindrical cross-sections under external pressure fail by elastic instability (buckling)
 8271 whereas elliptical sections can (depending on the geometry) fail by plastic collapse (yielding).

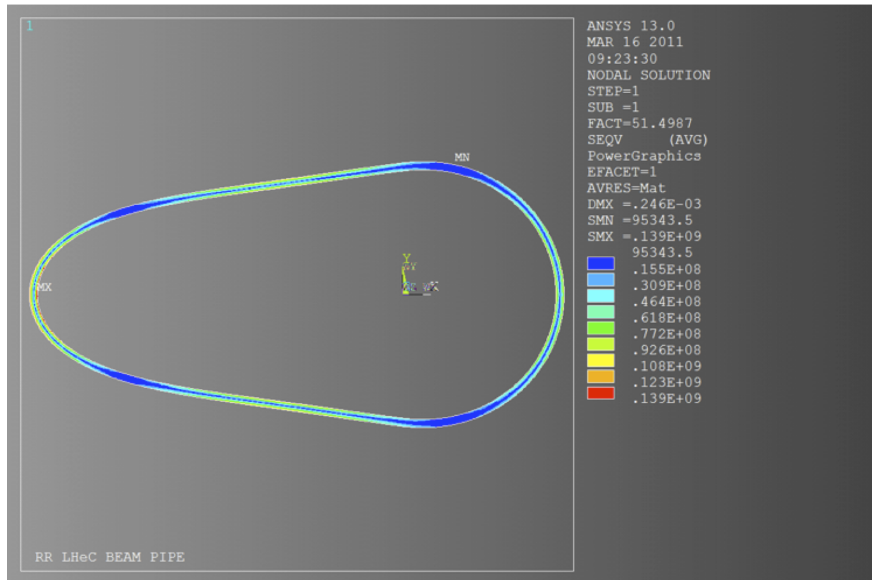


Figure 10.25: Section through the RR geometry showing contours of Von Mises equivalent stress (Pa).

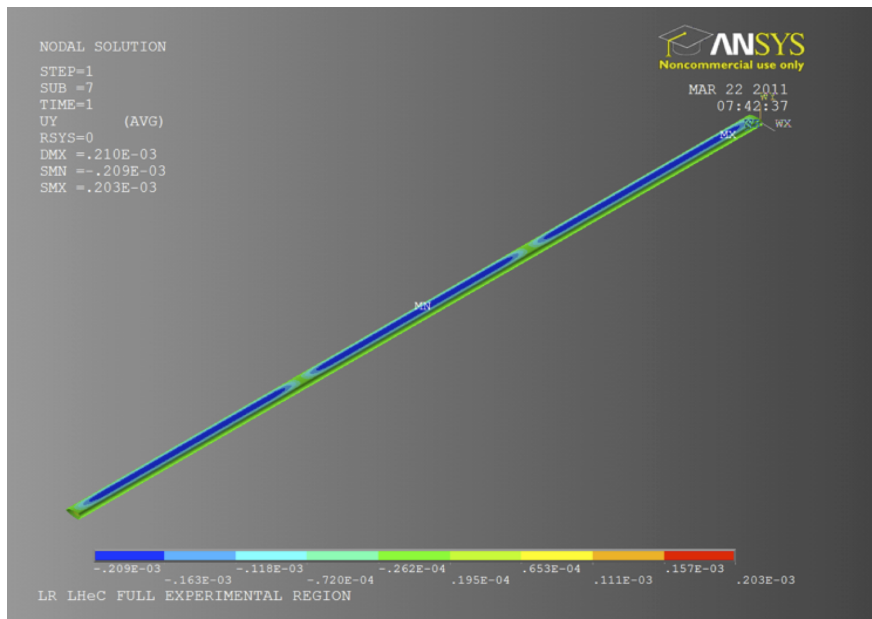


Figure 10.26: 3-D view of the LR geometry showing contours of bending displacement [m].

8272 Figure 10.24 and 10.25 show optimizations of the proposed geometries for the LINAC-Ring
8273 (LR) and Ring-Ring (RR) beampipes assuming a long chamber of constant cross section made
8274 from beryllium metal. Preliminary analyses have been performed using the ANSYS finite
8275 element code. The wall thickness was minimized for the criteria of yield strength and buckling
8276 load multiplier. The LR geometry considered has a circular section radius of 22 mm and
8277 elliptical major radius of 100 mm. The RR geometry has a circular section radius of 22 mm
8278 and elliptical major radius of 55 mm. This preliminary analysis suggests that a constant wall
8279 thickness of 2.5 – 3 mm for the LR and 1.3 to 1.5 mm for the RR would be sufficient to resist
8280 the external pressure. Failure for both of these sections would be expected to occur by plastic
8281 collapse.

8282 At this stage of the project, these geometries represent the most optimized forms that fulfill
8283 the LHC machine requirements. However, for 1 degree tracks this corresponds to $X/X_0 \approx$
8284 21-25% for the LR and \approx 41-49% for the RR designs. This suggests that additional effort
8285 must be put into beampipe geometries optimized for low angles. Composite beampipe concepts
8286 suggested for machines such as the LEP [622] should be re-considered in the light of advances
8287 in lightweight materials and production techniques.

8288 The optimized section of the experimental chamber is 6.1 m in length. This length will
8289 require a number of optimized supports. These supports function to reduce bending deflection
8290 and stresses to within acceptable limits and to control the natural frequency of chamber vibra-
8291 tion. The non-symmetric geometry will lead to a torsional stress component between supports
8292 which must be considered in their design. Figure 10.26 shows a preliminary analysis of bend-
8293 ing displacement for the LR chamber geometry. With 2 intermediate supports the maximum
8294 calculated displacement (without bakeout equipment) is 0.21 mm.

8295 10.6.4 Vacuum Instrumentation

8296 If, as assumed, this chamber is coated with a NEG film on the inner surfaces, then a high
8297 pumping speed of chemically active gasses will be available. Additional lumped pumps will be
8298 required for non-gettered gasses such as CH_4 and noble gasses; however, outgassing rates for
8299 these gasses are typically very low.

8300 The vacuum sector containing the experiment will be delimited from the adjacent machine
8301 by sector valves. These will be used to allow independent commissioning of machine and
8302 experiment vacuum. The experimental vacuum sector will require pressure gauges covering the
8303 whole range from atmospheric to UHV, these are used both for monitoring the pressure in the
8304 experimental chamber and as interlocks for the machine control system.

8305 10.6.5 Synchrotron Radiation Masks

8306 LHeC experimental sector will require a moveable SR mask upstream of the interaction. From
8307 the vacuum perspective, this implies a system for motion separated from atmosphere by UHV
8308 bellows. The SR flux on the mask will generate a gas load that should be removed by a local
8309 pumping system dedicated to the mask. As the load due to thermally stimulated desorption
8310 increases exponentially with the temperature, cooling may be required. However, cooling the
8311 mask would significantly complicate the vacuum system design. The generation of photo-
8312 electrons must also be avoided since these photo-electrons can interact with the proton beam
8313 and lead to an electron cloud build-up.

8314 **10.6.6 Installation and Integration**

8315 The installation of the vacuum system is closely linked to the detector closure sequence. There-
8316 fore, the design has to be validated in advance to prevent integration issues which would lead
8317 to significant delay and increase of costs. Temporary supports and protections are required
8318 at each stage of the installation. Indeed, as compared to the size of the detectors, the beam
8319 pipe are small, fragile and need to be permanently supported and protected while moving the
8320 detector components. Leak tightness and bake-out testing are compulsory at each step of the
8321 installation since all vacuum systems are subsequently enclosed in the detector, preventing any
8322 access or repair. Their reliability is therefore critical. Precise survey procedures must also be
8323 developed and incorporated in the beampipe design to minimize the mechanical component
8324 of the beam aperture requirement. Engineering solutions for bakeout also has to be studied
8325 in details since the equipment (heaters, probes and cables) must fit within the limited space
8326 available between beampipes and the detector components.

8327 **10.7 Cryogenics**

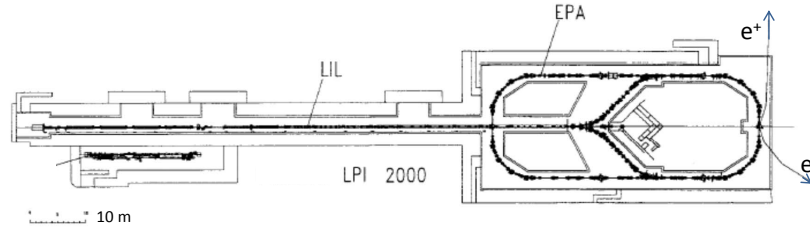


Figure 10.27: Layout of the LPI in 2000.

10.8 Positron P for the Linac-Ring option

Figure 10.27 shows the layout of the LPI (LEP Pre-Injector) as it was working in 2000.

LPI was composed of the LIL (LEP Injector Linac) and the EPA (Electron Positron Accumulator).

Table 10.18 gives the beam characteristics at the end of LIL.

Beam energy	200 to 700 MeV
Charge	5×10^8 to $2 \times 10^{10} e^-$ / pulse
Pulse length	10 to 40 ns (FWHM)
Repetition frequency	1 to 100 Hz
Beam sizes (rms)	3 mm

Table 10.18: LIL beam parameters.

Figure 10.28 shows an electron beam profile at the end of LIL (500 MeV).

Table 10.19 gives the electron and positron beam parameters at the exit of EPA.

Energy	200 to 600 MeV
Charge	up to $4.5 \times 10^{11} e^\pm$
Intensity	up to 0.172 A
Number of buckets	1 to 8
Emittance	0.1 mm.mrad
Tune	$Q_x = 4.537, Q_y = 4.298$

Table 10.19: The electron and positron beam parameters at the exit of EPA.

In summary, the LPI characteristics fulfils completely the requested performance for the LHeC injector based on Ring-Ring option.

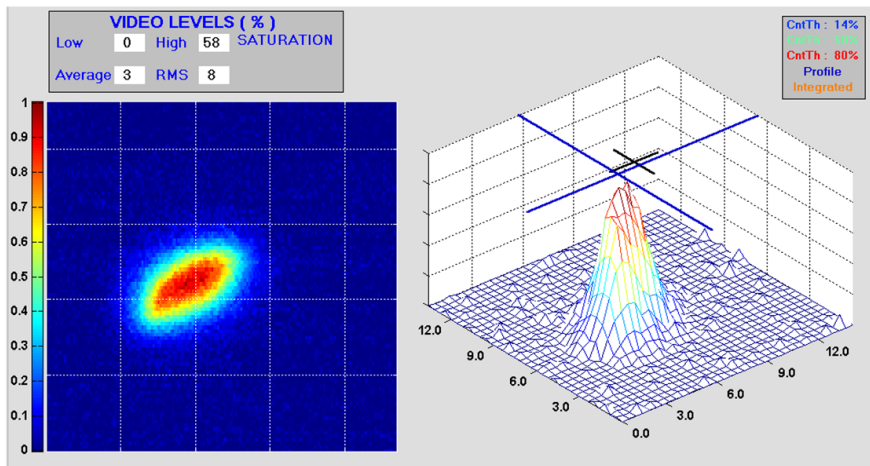


Figure 10.28: Electron beam profile at 500 MeV.

8337 10.9 Beam dumps

8338 Beam Dump

8339 10.10 Post collision line for 140 GeV option

8340 The post collision line for the 140 GeV Linac option has to be designed taking care of minimising
8341 beam losses and irradiation. The production of beamsstrahlung photons and e^-e^+ pairs is
8342 negligible and the energy spread limited to 2×10^{-4} . A standard optics with FODO cells and
8343 a long field-free region allowing the beam to naturally grow before reaching the dump can be
8344 foreseen. The aperture of the post collision line is defined by the size of the spent beam and,
8345 in particular, by its largest horizontal and vertical angular divergence (to be calculated). A
8346 system of collimators could be used to keep losses below an acceptable level. Strong quadrupoles
8347 and/or kickers should be installed at the end of the line to dilute the beam in order to reduce
8348 the energy deposition at the dump window. Extraction line requirements:

- 8349 • Acceptable radiation level in the tunnel
- 8350 • Reasonably big transverse beam size at the dump window and energy dilution
- 8351 • Beam line aperture big enough to host the beam: beta function and energy spread must
8352 be taken into account
- 8353 • elements of the beam line must have enough clearance.

8354 10.11 Absorber for 140 GeV option

8355 Nominal operation with the 140 GeV Linac foresees to dump a 50 MW beam. This power
8356 corresponds to the average energy consumption of 69000 Europeans. An *Eco Dump* could be
8357 used to recover that energy; detailed studies are needed and are not presented here. Another
8358 option is to start from the concept of the ILC water dump and scale it linearly to the LHeC
8359 requirements. The ILC design is based on a water dump with a vortex-like flow pattern and
8360 is rated for 18 MW beam of electrons and positrons [623]. Cold pressurized water (18 m³
8361 at 10 bar) flows transversely with respect to the direction of the beam. The beam always
8362 encounters fresh water and dissipates the energy into it. The heat is then transmitted through
8363 heat exchangers. Solid material plates(Cu or W) are placed beyond the water vessel to absorb
8364 the tail of the beam energy spectrum and reduce the total length of the dump. This layer is
8365 followed by a stage of solid material, cooled by air natural convection and thermal radiation to
8366 ambient, plus several meters of shielding. The size of the LHeC dump, including the shielding,
8367 should be 36 m longitudinally and 21 m transversely and it should contain 36 m³ of water.
8368 The water is separated from the vacuum of the extraction line by a thin Titanium Alloy (Ti-
8369 6Al-4V) window which has high temperature strength properties, low modulus of elasticity and
8370 low coefficient of thermal expansion. The window is primarily cooled by forced convection to
8371 water in order to reduce temperature rise and thermal stress during the passage of the beam.
8372 The window must be thin enough to minimise the energy absorption and the beam spot size
8373 of the undisturbed beam must be sufficiently large to prevent window damage. A combination
8374 of active dilution and optical means, like strong quadrupoles or increased length of the transfer
8375 line, can be use on this purpose. Further studies and challenges related to the dump design are:

- 8376 • pressure wave formation and propagation into the water vessel
- 8377 • remotely operable window exchange
- 8378 • handling of tritium gas and tritiated water.

8379 10.11.1 Energy deposition studies

8380 Preliminary estimates, of the maximum temperature increase in the water and at the dump
 8381 window, have been defined according to FLUKA simulation results performed for the ILC
 8382 dump [624]. A 50 MW steady state power should induce a maximum temperature increase ΔT
 8383 of 90° corresponding to a peak temperature of 215° . The water in the vessel should be kept at
 8384 a pressure of about 35 bar in order to insure a 25° margin from the water boiling point.

8385 FLUKA studies have been carried out for a 1 mm thick Ti window with a hemispherical
 8386 shape. The beam size at the ILC window is $\sigma_x = 2.42$ mm and $\sigma_y = 0.27$ mm; an extraction
 8387 line with 170 m drift and 6 cm sweep radius for beam dilution have been considered. A beam
 8388 power of 25 W with a maximum heat source of 21 W/cm^3 deposited on the window have been
 8389 calculated. This corresponds to a maximum temperature of 77° for the minimum ionisation
 8390 particle ($dE/dx = 2 \text{ MeV} \times \text{cm}^2/\text{g}$), no shower is produced because the thickness of the window
 8391 is significantly smaller than the radiation length. A maximum temperature lower than 100°
 8392 would require a minimum beam size of $\sigma_{x,y} = 1.8$ mm. A minimum β function of 8877 m would
 8393 be needed being the beam emittance $\varepsilon_{x,y} = 0.37$ nm for the undisturbed beam. The radius of
 8394 the dump window depends on the size of the disrupted beam. The emittance of the disrupted
 8395 beam is $\varepsilon_{x,y} = 0.74$ nm corresponding to a beam size $\sigma_{x,y}$ of 2.56 mm (for $\beta = 8877$ m); a
 8396 radius $R = 5$ cm could then fit a 10σ envelope. The yield strength of the Ti alloy used for the
 8397 window is $\sigma_{Ti} = 830$ MPa, this, according to the formula:

$$\sigma_{Ti} = 0.49 \times \Delta P \frac{R^2}{d^2} \quad (10.10)$$

8398 where $\Delta P = 3.5$ MPa, imposes that the thickness of the window d is bigger than 2.3 mm.
 8399 Length of the transfer line drift space and possible dilution have to be estimated together
 8400 with possible cooling.

8401 10.12 Beam line dump for ERL Linac-Ring option

8402 The main dump for the ERL Linac-ring option will be located downstream of the interaction
 8403 point. Splitting magnets and switches have to be installed in the extraction region and the
 8404 extracted beam has to be tilted away from the circulating beam by 0.03 rad to provide enough
 8405 clearance for the first bending dipole of the LHeC arc (see Fig. 10.29). A 90 m transfer line,
 8406 containing two recombination magnets and dilution kickers, is considered to be installed between
 8407 the LHeC and the LHC arcs(see Fig. 10.30). The beam dump will be housed in a UD62/UD68
 8408 like cavern at the end of the TL and the option of having service caverns for water treatment
 8409 and heat exchange is explored. An additional dump, and its extraction line, could be installed
 8410 at the end of the first linac(see Fig. 10.30) for beam setup purposes at intermediate energy. The
 8411 same design as for the nominal dump and extraction line would be applied.

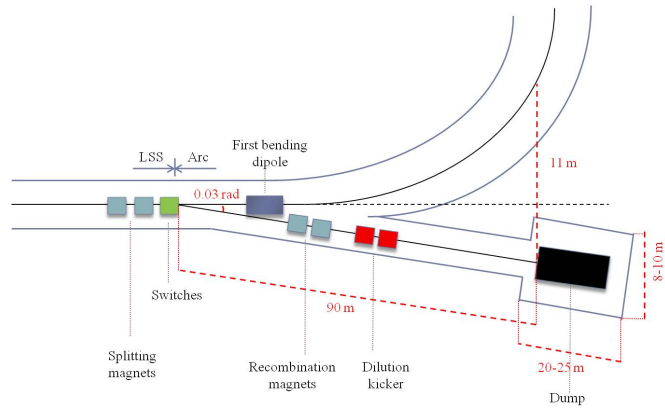


Figure 10.29: Scheme of the transfer line from end of long straight section of the linac and beam dump.

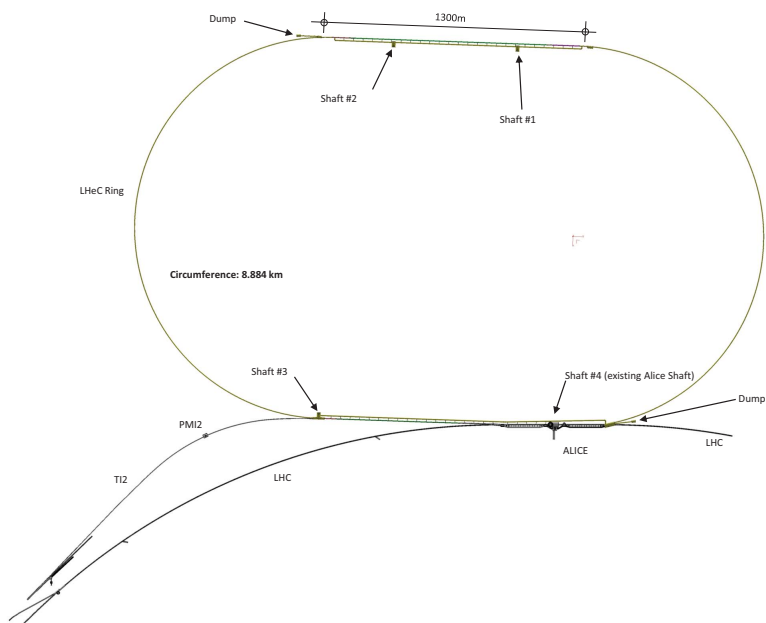


Figure 10.30: Two beam dumps are installed 90 m downstream the end of the long straight section of each linac for nominal operation and beam setup.

8412 **10.13 Absorber for ERL Linac-Ring option**

8413 During nominal operation a 0.5 GeV beam has to be dumped with a current of 6.6 mA. The
8414 setup beam will have a maximum current of 0.05 mA and an energy varying from 10 GeV to
8415 60 GeV (10 GeV step size). Globally, a maximum beam power of 3 MW has to be dumped.
8416 The same design as for the 140 GeV option can be used by scaling linearly. In this case, a
8417 3 m^3 water dump (0.5 m diameter and 8 m length) with a $3 \text{ m} \times 3 \text{ m} \times 10 \text{ m}$ long shielding
8418 has to be implemented. No show stopper has been identified for the 18 MW ILC dump, same
8419 considerations are valid in this less critical case.

8420 **10.14 Injection Region Design for Ring-Ring Option**

8421 A 10 GeV recirculating Linac will be used to inject the electrons in the LHeC. This will be
8422 built on the surface or underground and a transfer line will connect the linac to the LHeC
8423 injection region. At this stage a purely horizontal injection is considered, since this will be
8424 easier to integrate into the accelerator. The electron beam will be injected in the bypass
8425 around ATLAS, with the baseline being injection into a dispersion free region (at the right
8426 side of ATLAS). Bunch-to-bucket injection is planned, as the individual bunch intensities are
8427 easily reachable in the injector and accumulation is not foreseen. Two options are considered:
8428 a simple septum plus kicker system where single bunches or short trains are injected directly
8429 onto the closed orbit; and a mismatched injection, where the bunches are injected with either
8430 a betatron or dispersion offset.

8431 **10.14.1 Injection onto the closed orbit**

8432 The baseline option is injection onto the orbit, where a kicker and a septum would be installed in
8433 the dispersion free region at the right side of ATLAS bypass (see Fig. 10.31). Injecting the beam
8434 onto the closed orbit has the advantage that the extra aperture requirements around the rest
8435 of the machine from injection oscillations or mismatch are minimised. The kicker and septum
8436 can be installed around a Defocusing quadrupole to minimise the kicker strength required. The
8437 kicker-septum phase advance is 75° .

8438 Some assumptions made to define the required element apertures are made in Table 10.20.

8439 For the septum, an opening between injected and circulating beam of 47 mm is required,
8440 taking into account some pessimistic assumptions on orbit, tolerances and with a 4 mm thick
8441 septum. This determines the kicker strength of about 1 mrad.

8442 The septum strength should be about 33 mrad to provide enough clearance for the injected
8443 beam at the upstream lattice quadrupole, the yoke of which is assumed to have a full width of
8444 0.6 m. This requires about 1.1 T m, and a 3.0 m long magnet at about 0.37 T is reasonable, of
8445 single turn coil construction with a vertical gap of 40 mm and a current of 12 kA.

8446 The RF frequency of the linac is 1.3 GHz and a bunch spacing of 25 ns is considered, as the
8447 LHeC electron beam bunch structure is assumed to match with the LHC proton beam structure.
8448 Optimally a train of 72 bunches would be injected, which would require a $1.8 \mu\text{s}$ flattop for the
8449 kickers and a very relaxed $0.9 \mu\text{s}$ rise time (as for the LHC injection kickers [625]). However,
8450 this train length is too long for the recirculating linac to produce, and so the kicker rise time
8451 and fall time requirements are therefore assumed to be about 23 ns, to allow for the bunch
8452 length and some jitter.

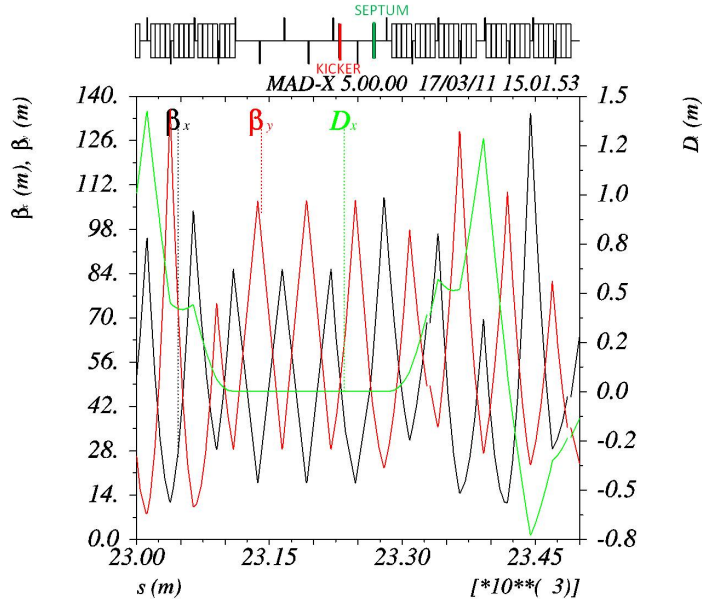


Figure 10.31: Injection optics is shown. The sequence starts ($s=0$) at the beginning of the dispersion suppressor at the left side of IP2 and proceeds clockwise, while the electron beam rotates counterclockwise (from right to left in the figure). The injection kicker and septum are installed in the dispersion free region of the bypass at the right side of ATLAS.

8453 For a rise time $t_m = 23$ ns, a system impedance Z of 25Ω is assumed, and a rather
 8454 conservative system voltage U of 60 kV.

8455 Assuming a full vertical opening h of 40 mm, and a full horizontal opening w of 60 mm
 8456 (which allow $\pm 6 \sigma$ beam envelopes with pessimistic assumptions on various tolerances and
 8457 orbit), the magnetic length l_m of the individual magnets is:

$$l_m = ht_m Z / \mu_0 w = 0.31 \text{ m}$$

8458 For a terminated system the gap field B is simply:

$$B = \frac{\mu_0 U}{2hZ} = 0.037 \text{ T}$$

8459 As 0.03 Tm are required, the magnetic length should be 0.8 m, which requires 3 magnets.
 8460 Assuming each magnet is 0.5 m long, including flanges and transitions the total installed kicker
 8461 length is therefore about 1.5 m.

8462 10.14.2 Mismatched injection

8463 A mismatched injection is also possible, Figure 10.32 with a closed orbit bump used to bring the
 8464 circulating beam orbit close to the septum, and then switched off before the next circulating
 8465 bunch arrives.

Orbit variation	± 4 mm
Injection precision	± 3 mm
Mechanical/alignment tolerance	± 1 mm
Horizontal normalised emittance $\varepsilon_{n,x}$	0.58 mm
Vertical normalised emittance $\varepsilon_{n,y}$	0.29 mm
Injection mismatch (on emittance)	100 %
β_x, β_y @ Kicker	61.3 m, 39.7 m
β_x, β_y @ Septum	57.3 m, 42.3 m
σ_x, σ_y @ Kicker and Septum	0.8 mm, 0.4 mm

Table 10.20: Assumptions for beam parameters used to define the septum and kicker apertures

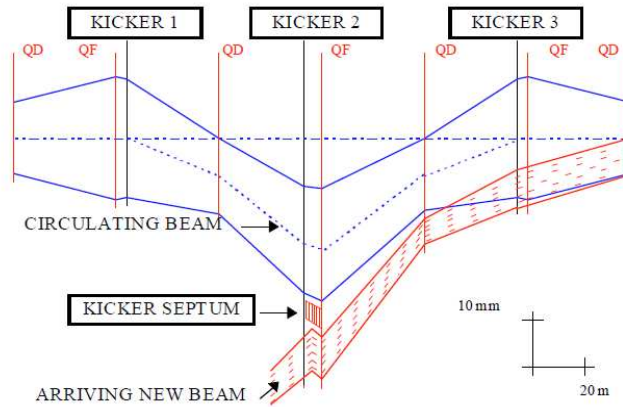


Figure 10.32: layout of mismatched injection system. To minimise kicker strengths the magnets are located near focusing quadrupoles.

8466 The injected beam then performs damped betatron or synchrotron oscillations, depending
8467 on the type of mismatch used. In LHeC the damping time is about 3 seconds, so that to achieve
8468 the suggested 0.2 s period between injections, a damping wiggler would certainly be needed -
8469 the design of such a wiggler needs to be investigated.

8470 Three kickers (KICKER 1, KICKER 2 and KICKER 3 in Fig. 10.32) are used to generate a
8471 closed orbit bump of 20 mm at the injection point. The kicker parameters are summarized in
8472 table 10.21. In case of betatron mismatch, the bumpers can be installed in the dispersion free
8473 region considered for the injection onto the closed orbit case discussed in the previous section
8474 (see Fig. 10.33). The installed magnet lengths of the kickers should be 2 m, 3.5 m and 1 m
8475 respectively, for the kickers size, Z and U parameters given above. Overall the kicker system is
8476 not very different to the system needed to inject onto the orbit.

8477 To allow for the possibility of synchrotron injection, the injection kicker-septum would need
8478 to be located where the horizontal dispersion D_x is large. The beam is then injected with a

Magnet	θ_x [mrad]	B dl [Tm]
KICKER1	1.35	0.04
KICKER2	2.37	0.08
KICKER3	0.55	0.02

Table 10.21: Kickers strength and integrated magnetic field needed to generate an orbit bump of 20 mm at the injection point.

8479 position offset x and a momentum offset δp , such that:

$$x = D_x \delta p$$

8480 The beam then performs damped synchrotron oscillations around the ring, which can have an
8481 advantage in terms of faster damping time and also smaller orbit excursions in the long straight
8482 sections, particularly experimental ones, where the dispersion functions are small.

8483 As an alternative to the fast (23 ns rise time) kicker for both types of mismatched injection,
8484 the kicker rise- and fall-time could be increased to almost a full turn, so that the bump is off when
8485 the mismatched bunch arrives back at the septum. This relaxes considerably the requirements
8486 on the injection kicker in terms of fall time. However, this does introduce extra complexity in
8487 terms of synchronizing the individual kicker pulse lengths and waveform shapes, since for the
8488 faster kicker once the synchronization is reasonably well corrected only the strengths need to
8489 be adjusted to close the injection bump for the single bunch.

8490 10.14.3 Injection transfer line

8491 The injection transfer line from the 10 GeV injection recirculating linac is expected to be
8492 straightforward. A transfer line of about 900 m, constituted by 15 FODO cells, has been
8493 considered. The phase advance of each cell corresponds to about 100° .

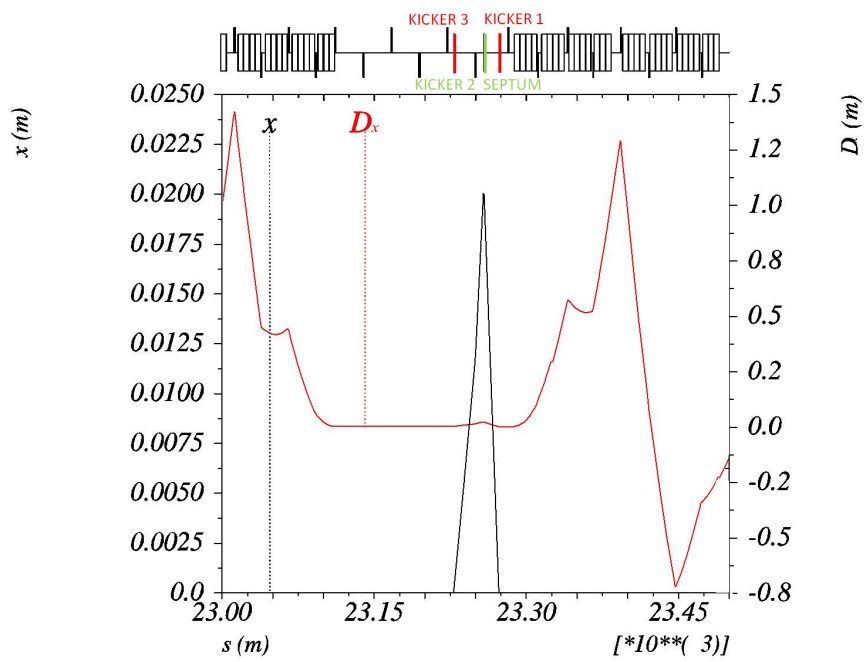


Figure 10.33: A closed orbit bump of 20 mm is generated by three kickers installed in the dispersion free region located at the right side of the bypass around ATLAS (electron beam moves from right to left in the Figure).

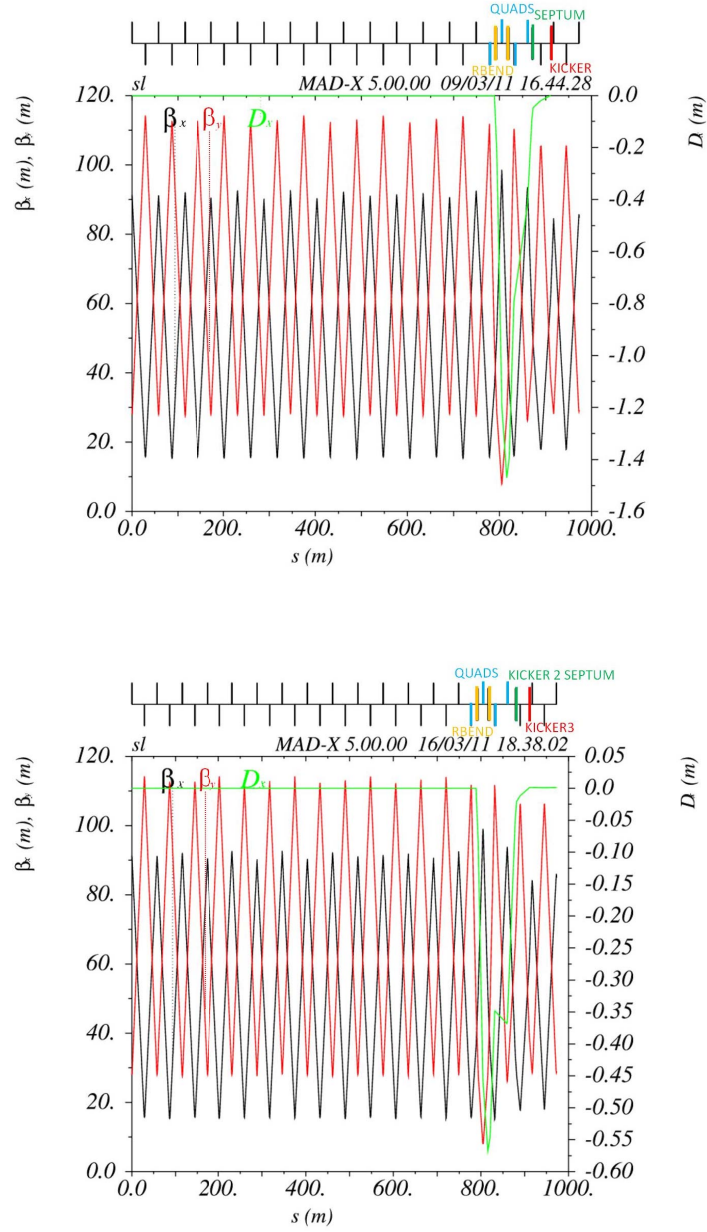


Figure 10.34: Transfer line optics for the injection onto orbit case (top) and mismatched injection case (bottom).

8494 The last two cells are used for optics matching. In particular, four quadrupoles, 1 m long
8495 each, are used for β_x and β_y matching, while two rectangular bending magnets, 5 m long
8496 each, are used for matching the horizontal dispersion D_x to 0 (maximum $D_x = -1.48$ m for
8497 the injection onto closed orbit case and maximum $D_x = -0.57$ m for the mismatched injection
8498 case). The “good field region” for a 6σ beam envelope requires a minimum half-aperture, in
8499 the matching insertion, of 15 mm and 10 mm for the focusing and defocusing quadrupoles
8500 respectively, corresponding to a pole tip field of about 0.02 T. The maximum strength of the
8501 bending magnets, which are used for dispersion matching, corresponds to about 39 mrad. This
8502 requires 1.3 T m and a maximum field of 0.3 T. A single turn coil of 9.5 kA with a vertical gap
8503 of 40 mm could be used.

8504 10.15 60 GeV internal dump

8505 An internal dump will be needed for electron beam abort. The design for LEP [626] consisted
8506 of a boron carbide spoiler and an Aluminum alloy (6% copper, low magnesium) absorbing block
8507 (0.4 m \times 0.4 m \times 2.1 m long). A fast kicker was used to sweep eight bunches, of 8.3×10^{11}
8508 electrons at 100 GeV, onto the absorber. The first bunch was deflected by 65 mm and the last
8509 by 45 mm, inducing a temperature increase ΔT of 165° .

8510 The bunch intensity for the LHeC is about a factor of 20 lower than for LEP and beam size
8511 is double ($\sigma = 0.5$ mm in LEP and $\sigma = 1$ mm in LHeC).

8512 The lower energy (60 GeV) and energy density permit to dump 160 bunches in 20 mm
8513 to obtain the same ΔT as for LEP. However, in total LHeC will be filled with 2808 bunches,
8514 which means that significant additional dilution will be required. A combination of a horizontal
8515 and a vertical kicker magnet can be used, as an active dilution system, to paint the beam on
8516 the absorber block and increase the effective sweep length. The kickers and the dump can be
8517 located in the bypass around CMS, in a dispersion free region (see fig. 10.35).

8518 It is envisaged to use Carbon-composite for the absorber block, since this has much better
8519 thermal and mechanical properties than aluminum. The required sweep length is then assumed
8520 to be about 100 mm, from scaling of the LEP design. The minimum sweep speed in this case
8521 is about 0.6 mm per μs , which means about 54 bunches per mm. Taking into account the
8522 energy and the beam size, this represents less than a factor 2 higher energy density on the
8523 dump block, compared to the average determined by the simple scaling, that should be feasible
8524 using carbon. More detailed studies are required to optimise the diluter and block designs.
8525 Vacuum containment, shielding and a water cooling system has to be incorporated. A beam
8526 profile monitor can be implemented in front of each absorber to observe the correct functioning
8527 of the beam dump system.

8528 The vertical kicker would provide a nominal deflection of about 55 mm (see fig. 10.36), mod-
8529 ulated by $\pm 13\%$ for three periods during the 100 μs abort (see fig. 10.37), while the horizontal
8530 kicker strength would increase linearly from zero to give a maximum deflection at the dump
8531 of about 55 mm (see Fig. 10.36 and Fig. 10.37). This corresponds to system kicks of 2.7 and
8532 1.6 mrad respectively.

8533 Parameters characterizing the kicker magnets are presented in Table 10.22.

8534 In the present lattice the dump is placed ~ 30 m downstream of the kickers, corresponding
8535 to a phase advance of about 63° in the horizontal plane and 35° in the vertical plane. The
8536 minimum horizontal and vertical aperture at the dump are 26 mm and 22 mm respectively
8537 (at the dump: $\beta_x = 37$ m and $\beta_y = 55$ m, using the same beam and machine parameter

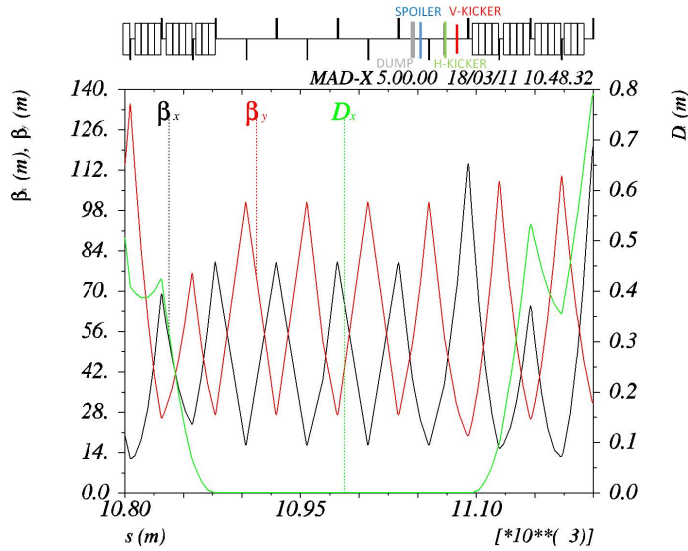


Figure 10.35: The optics in the region of the CMS bypass where the beam dump system could be installed is shown. The system consists of two kickers, one spoiler and a Carbon-composite absorber which are installed in the dispersion free region of the bypass at the right side of CMS (beam proceeds from right to left in the Figure).

8538 assumptions, as presented in Table 10.20). The kicker system field rise time is assumed to be
 8539 at most $3 \mu\text{s}$ (abort gap) and the kicker field flat-top at least $90 \mu\text{s}$ as for the LHC proton
 8540 beam. Same design as for the LHC dump kicker magnets MKD can be used: a steel yoke with
 8541 a one-turn HV winding. These magnets can provide a magnetic field in the gap of 0.34 T. For
 8542 a magnetic length of 0.31 m ($Z = 25 \Omega$ and $U = 60 \text{ kV}$), a total installed kicker length of 1.5 m
 8543 for the horizontal system and 2.5 m for the vertical system has to be considered.

	MKDV	MKDH
Length [m]	2.5	1.5
Maximum angle [mrad]	2.7	1.6
Maximum field [T]	0.34	0.34
Rise/Fall time [ns]	800	800
Flat top length [μs]	90	90

Table 10.22: Parameters characterising vertical and horizontal kicker magnets of the extraction system.

8544 A spoiler (one-side single graphite block: $0.3 \text{ m} \times 0.10 \text{ m} \times 0.5 \text{ m}$ long) can be installed
 8545 5 m upstream of the dump at the extraction side to provide further dilution.

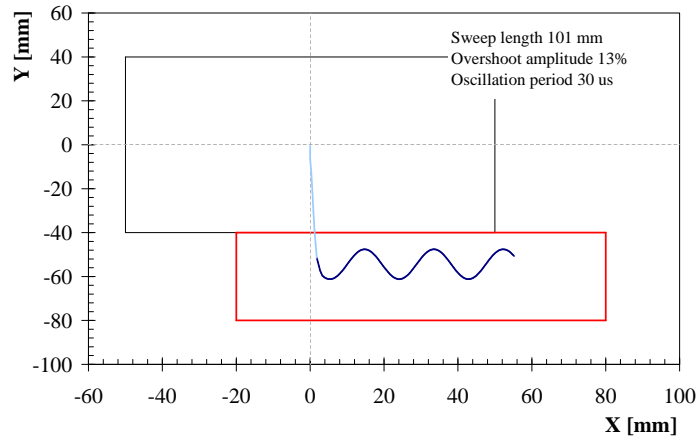


Figure 10.36: A vertical and a horizontal kicker are used to dilute the beam on the dump absorbing block.

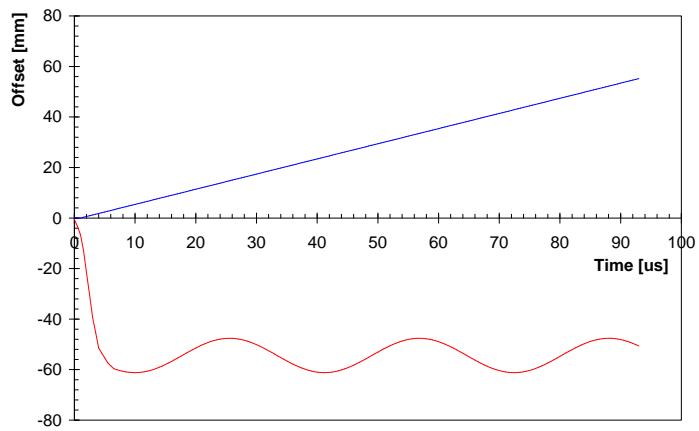


Figure 10.37: The strength of the vertical kicker oscillates in time by $\pm 13\%$ around its nominal value. The deflection provided by the horizontal kicker increases almost linearly in time.

8546

Part IV

8547

Detector

8548 Chapter 11

8549 Detector Requirements

8550 11.1 Requirements on the LHeC Detector

8551 The new ep/A detector at the LHeC has to basically be a precision instrument of maximum
8552 acceptance. The physics program depends on a high level of precision, as for the measurement
8553 of α_s , and in the reconstruction of complex final states, like the charged current single top
8554 production and decay or the precision measurement of the b -quark density. The acceptance has
8555 to extend as close as possible to the beam axis because of the interest in the physics at low and
8556 at large Bjorken x . The dimensions of the detector are constrained by the radial extension of
8557 the beam pipe in combination with maximum polar angle coverage¹, desirably down to about
8558 1° and 179° for forward going final state particles and backward scattered electrons at low Q^2 ,
8559 respectively. A further general demand is a high modularity enabling much of the detector
8560 construction to be performed above ground for keeping the installation time at a minimum,
8561 and to be able to access inner detector parts within reasonable shut down times.

8562 The time schedule of the project demands to have a detector ready within about ten years.
8563 This prevents any significant R&D program to be performed. The choice of components for-
8564 tunately can rely on the vast experience obtained at HERA, the LHC, including its detector
8565 upgrades to come, and on ILC detector development studies. The next few sections outline
8566 the acceptance and measurement requirements on the detector in detail. Then follow more de-
8567 tailed technical considerations, including alternative solutions, which taken together illustrate
8568 the feasibility of experimentation at the LHeC.

8569 11.1.1 Installation and Magnets

8570 The LHeC project represents an upgrade of the LHC. The experiment would be the fifth large
8571 experiment, and the detector the third multi-purpose 4π acceptance detector. It requires a
8572 cavern, which for the purpose of the design study has been considered to be the ALICE cavern

¹This CDR adopts the HERA convention of the coordinate system, which has been defined with the z axis given by the proton beam direction. This implies that Rutherford "backscattering" of the electron is viewed as scattering into small angles. When the partons are essentially at rest, at very small x , the electrons are scattered "forward" as in fixed target forward spectrometers. The somewhat unfortunate HERA convention calls this backwards. The x and y coordinates are defined such that there is a right handed coordinate system formed with y pointing upwards and x to the center of the proton ring.

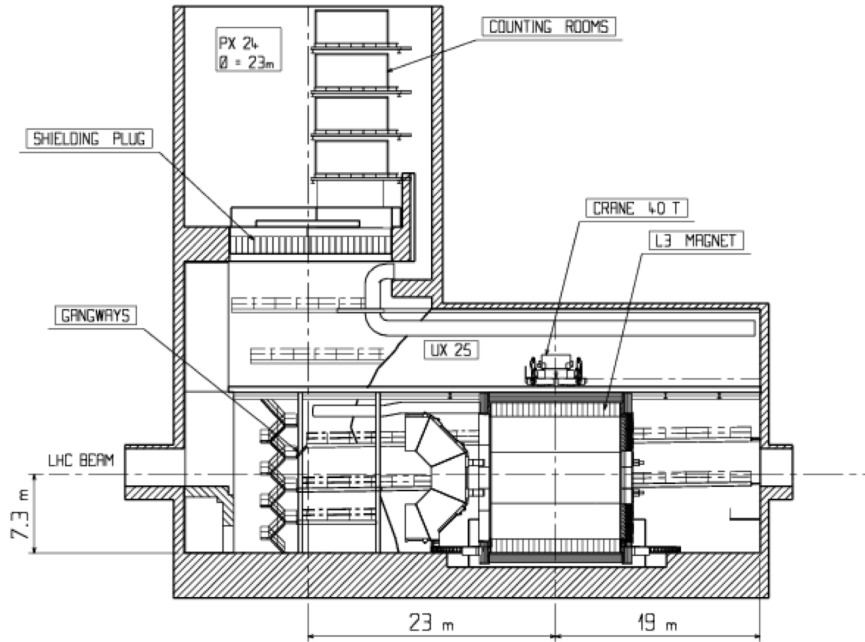


Figure 11.1: Cross section of the IP2 cavern with the ALICE detector inside the L3 magnet. Round access shaft of 23m diameter, cavern about 50m along the beam-line.

8573 in IP2, see Fig. 11.1. The installation of the detector has to proceed as fast as possible in order
 8574 not to introduce large extra delays to the LHC program. High modularity and pre-assembly
 8575 above ground are therefore inevitable demands for the design.

8576 The cost has to be limited in order for the project to be fundable in parallel to when
 8577 the large upgrade investments are presumably made for the ATLAS and CMS detectors in
 8578 the high luminosity phase of the LHC. The cost is related to technology choices, the detector
 8579 granularity and its size. Crucial parameters of the detector are the beam pipe dimensions,
 8580 when combined with the small angle acceptance constraint, see below, and the parameters of
 8581 the solenoid. The cost C of a solenoid can be represented as a function of the energy density,
 8582 ρ_E , $C \simeq 0.5(\rho_E/MJ)^{0.66}$ [28], which is determined as

$$\rho_E = \frac{1}{2\mu_0} \cdot \int B^2 dV \simeq \frac{1}{2\mu_0} \cdot \pi r^2 \cdot l \cdot B^2. \quad (11.1)$$

8583 From these relations one derives roughly that the solenoid cost scales linearly with the radius
 8584 r and field strength B and with the length l to the power 0.66. The solenoid radius influences
 8585 the track length in the transverse plane, which determines $\propto r^{-2}$ the transverse momentum
 8586 resolution whereas field strength enters linearly $\propto B^{-1}$.

8587 The Linac-Ring version of the LHeC requires to put an extended dipole field of 0.3 T into
 8588 the detector for ensuring head-on ep collisions and for separating the beams.

8589 A balance between a strong magnetic field for optimal tracking resolution and an affordable
 8590 sized magnet has to be found, knowing that the magnets themselves represent one source of

8591 inactive material and that the energy stored in the magnets and their return flux require an
 8592 outer shielding proportional to the field and to the square of the solenoid radius.

8593 In the current design the solenoid is placed in between the electromagnetic and the hadron
 8594 calorimeter² at a radius of about 1 m. The field strength is set to 3.5 T in order to compensate
 8595 the small radial extension of the tracker, the focus of which in the LHeC environment is on
 8596 the forward direction. The chosen design position with dipoles and solenoid placed outside
 8597 the electromagnetic calorimeter ensures good electromagnetic calorimetry and high dipole field
 8598 quality near to the beam line. Fig. 11.2 shows such the magnet arrangement inside the detector
 volume schematically. The total material budget of the solenoid and the dipole, at perpendicular

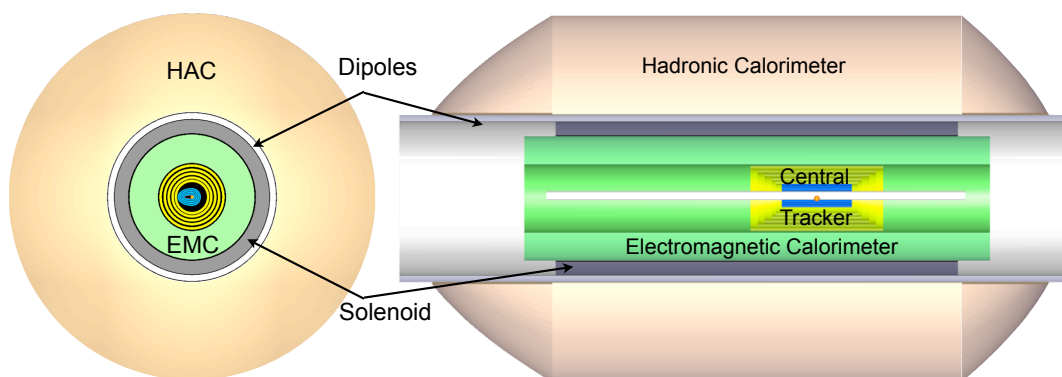


Figure 11.2: Schematic xy and rz views of the magnets and barrel calorimeter arrangement for the baseline layout.

8599 crossing, may be represented by about $\mathcal{O}(\infty)$ cm of Aluminum, corresponding to about one
 8600 quarter of an interaction length (λ_I) and about 1 radiation length (X_0). This further supports
 8601 the choice of the magnets located outside of the electromagnetic calorimeter, yet placed before
 8602 the hadronic calorimeter in order to limit the radial dimensions. More details on the design
 8603 study of the detector magnets are addressed in Sect.12.3.

8605 11.1.2 Kinematic reconstruction

8606 The inclusive ep DIS kinematics are defined by the negative four-momentum transfer squared,
 8607 Q^2 , and Bjorken x . Both are related to the cms energy squared s via the inelasticity y through
 8608 the relation $Q^2 = sxy$, which implies $Q^2 \leq s$. The energy squared s is determined by the
 8609 product of the beam energies, $s = 4E_p E_e$, for head-on collisions and large energies compared
 8610 to the proton mass.

8611 The kinematics are determined from the scattered electron with energy E'_e and polar angle
 8612 θ_e and from the hadronic final state of energy E_h and scattering angle θ_h . The variables Q^2

²An option is also considered of placing the solenoid outside the calorimeters, at about 2.5 m radius, combined with a second, bigger solenoid for the flux return, with the muon detector in between. A two-solenoid solution was considered already in the fourth detector concept for the ILD [627].

8613 and y can be calculated from the scattered electron kinematics as

$$\begin{aligned} Q_e^2 &= 4E_e E'_e \cos^2\left(\frac{\theta_e}{2}\right) \\ y_e &= 1 - \frac{E'_e}{E_e} \sin^2\left(\frac{\theta_e}{2}\right) \end{aligned} \quad (11.2)$$

8614 and from the hadronic final state kinematics as

$$\begin{aligned} Q_h^2 &= \frac{1}{1 - y_h} \cdot E_h^2 \sin^2(\theta_h) \\ y_h &= \frac{E_h}{E_e} \sin^2\left(\frac{\theta_h}{2}\right) \end{aligned} \quad (11.3)$$

8615 and x is given as Q^2/sy . The kinematic reconstruction in neutral current scattering therefore is
 8616 redundant, which is one reason why DIS experiments at ep colliders are precise. An important
 8617 example is the calibration of the electromagnetic energy scale from the measurements of the
 8618 electron and the hadron scattering angles. At HERA, this led to energy calibration accuracies
 8619 for E'_e at the per mil level. In a large part of the phase space, around $x = E_e/E_p$, the scattered
 8620 electron energy is approximately equal to the beam energy, $E'_e \simeq E_e$, which causes a large
 8621 “kinematic peak” in the scattered electron energy distribution. The hadronic energy scale can
 8622 be obtained from the transverse momentum balance in neutral current scattering, $p_t^e \simeq p_t^h$. It
 8623 is determined to about 1% at HERA.

8624 Following Eq.11.3, the kinematics in charged current scattering is reconstructed from the
 8625 transverse and longitudinal momenta and energy of the final state particles according to

$$\begin{aligned} Q_h^2 &= \frac{1}{1 - y_h} \sum p_t^2 \\ y_h &= \frac{1}{2E_e} \sum (E - p_z). \end{aligned} \quad (11.4)$$

8626 There have been many refinements used in the reconstruction of the kinematics, as discussed
 8627 e.g. in [628], which for the principle design considerations, however, are of less importance.

8628 11.1.3 Acceptance regions - scattered electron

8629 The positions of isolines of constant energy and angle of the scattered electron in the (Q^2, x)
 8630 plane are given by the relations:

$$\begin{aligned} Q^2(x, E'_e) &= sx \cdot \frac{E_e - E'_e}{E_e - xE_p} \\ Q^2(x, \theta_e) &= sx \cdot \frac{E_e}{E_e + xE_p \tan^2(\theta_e/2)}. \end{aligned} \quad (11.5)$$

8631 Following these relations, an acceptance limitation of the scattered electron angle, as due to
 8632 the beam pipe or focussing magnets, to a maximum value θ_e^{max} defines a constant minimum
 8633 Q^2 which independently of E_p is given as

$$Q_{min}^2(x, \theta_e^{max}) \simeq [2E_e \cot(\theta_e^{max}/2)]^2. \quad (11.6)$$

LHeC - electron kinematics

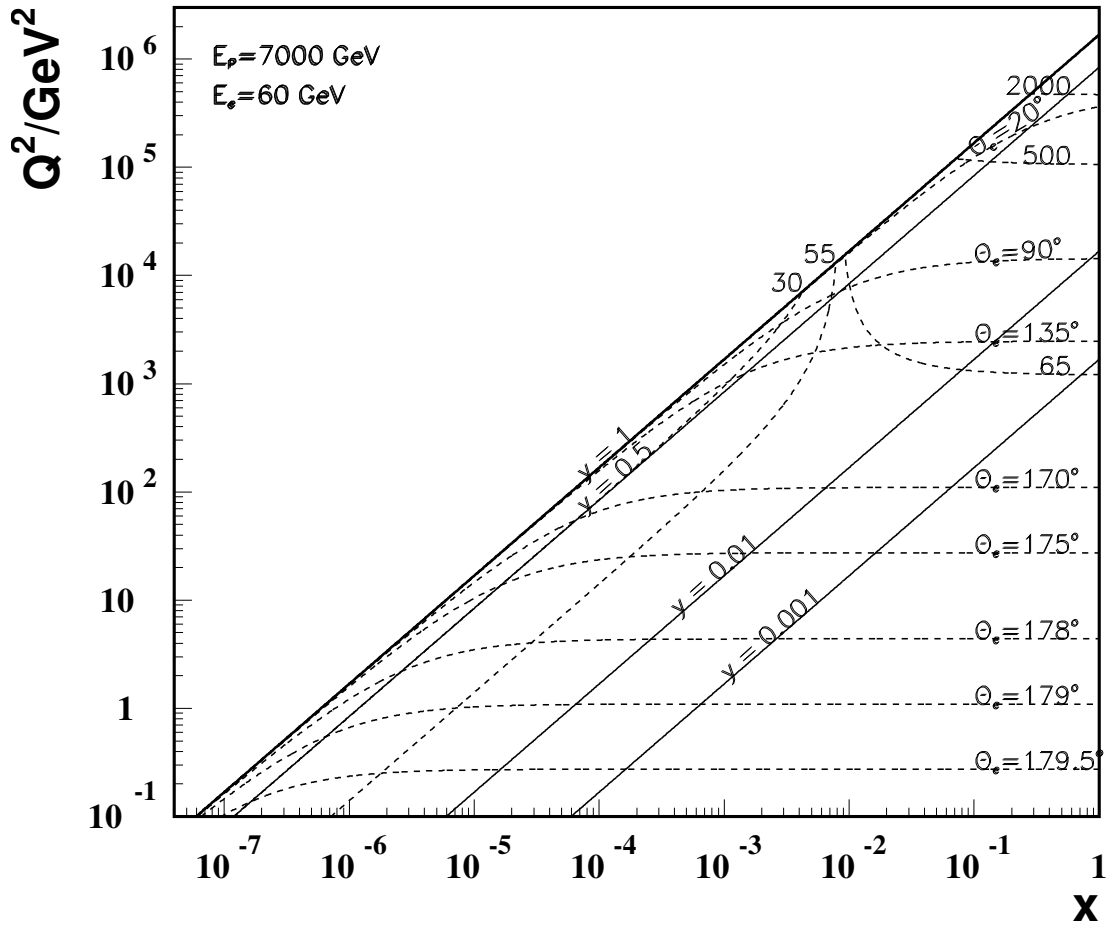


Figure 11.3: Kinematics of electron detection at the LHeC. Lines of constant scattering angle θ_e and energy, in GeV, are drawn. The region of low $Q^2 \lesssim 10^2$ GeV², comprising the lowest x region, requires to measure electrons scattered backwards with energies not exceeding E_e . At small energies, for $y \lesssim 0.5$ a good e/h separation is important to suppress hadronic background, as from photoproduction. The barrel calorimeter part, of about $90 \pm 45^\circ$, measures scattered electrons of energy not exceeding a few hundreds of GeV, while the forward calorimeter has to reconstruct electron energies of a few TeV. Both the barrel and the forward calorimeters measure the high x part, which requires very good scale calibration as the uncertainties diverge $\propto 1/(1-x)$ towards large x .

8634 apart from the smallest x . This is illustrated in Fig. 11.3. There follows that a 179° (170°)
 8635 angular cut corresponds to a minimum Q^2 of about 1 (100) GeV^2 at nominal electron beam
 8636 energy. One easily recognizes in Fig. 11.3 that the physics at low x and Q^2 requires to measure
 8637 electrons scattered backwards from about 135° up to 179° . Their energy in this θ_e region does
 8638 not exceed E_e significantly. At lower x to very good approximation $y = E'_e/E_e$ (as can be seen
 8639 from the lines $y = 0.5$ and $E'_e = 30 \text{ GeV}$ in Fig. 11.3).

8640 Following Eq. 11.6, Q_{min}^2 varies $\propto E_e^2$. It thus is as small as 0.03 GeV^2 for $E_e = 10 \text{ GeV}$,
 8641 the injection energy of the ring accelerator but increases to 6.0 GeV^2 for $E_e = 140 \text{ GeV}$, the
 8642 maximum electron beam energy considered in this design report, apart from smallest x , if
 8643 $\theta_e^{max} = 179^\circ$. While Q_{min}^2 decreases $\propto E_e^2$, the acceptance loss towards small x is only $\propto E_e$.
 8644 The measurement of the transition region from hadronic to partonic behavior, from 0.1 to
 8645 10 GeV^2 , therefore requires to take data at lower electron beam energies³. These variations are
 8646 illustrated in Fig. 11.4 for an electron beam energy of 10 GeV , the injection energy for the ring
 8647 and a one-pass linac energy, and for the highest E_e of 140 GeV considered in this report.

8648 Electrons scattered forward correspond to scattering at large $Q^2 \geq 10^4 \text{ GeV}^2$, as is illustrated
 8649 in the zoomed kinematic region plot Fig. 11.5. The energies in the very forward region, $\theta_e \lesssim 10^\circ$,
 8650 exceed 1000 GeV . For large E_e and x , Eq. 11.5 simplifies to $Q^2 \simeq 4E_e E'_e$, i.e. a linear relation
 8651 of Q^2 and E'_e which is independent of x and of E_p , apart from the fact that $Q_{max}^2 = s$.

8652 11.1.4 Acceptance regions - hadronic final state

8653 The positions of isolines in the (Q^2, x) plane of constant energy and angle of the hadronic final
 8654 state, approximated here by the current jet or struck quark direction, are given by the relations:

$$\begin{aligned}
 Q^2(x, E_h) &= sx \cdot \frac{x E_p - E_h}{x E_p - E_e} \\
 Q^2(x, \theta_h) &= sx \cdot \frac{x E_p}{x E_p + E_e \cot^2(\theta_h/2)}
 \end{aligned}
 \tag{11.7}$$

8655 and are illustrated in Fig. 11.6. At low $x \lesssim 10^{-4}$, the hadronic final state is emitted backwards,
 8656 $\theta_h > 135^\circ$, with energies of a few GeV to a maximum of E_e . Lines at constant y at low x are
 8657 approximately at $y = 1 - E'_e/E_e$ and $E'_e + E_h = E_e$, i.e. $y = E_h/E_e$. Final state physics at
 8658 lowest $x \lesssim 3 \cdot 10^{-6}$ requires access to the backward region within a few degrees of the beam pipe
 8659 (Fig. 11.6). This is the high y region in which the longitudinal structure function is measured.

³The requirement of acceptance up to 179° determines the length of the backward detector. It could be tempting to utilize this E_e dependence in the design: if one limited the backward electron acceptance to for example 178° instead of 179° this would reduce the backward detector extension in $-z$. With data taken at reduced E_e one would come back to lower Q^2 . From Eq. 11.6 one derives that $E_e = 30 \text{ GeV}$ and 178° is leading to the same Q_{min}^2 of about 1.1 GeV^2 , at not extremely small x , as is $E_e = 60 \text{ GeV}$ and 179° . However, one would loose in acceptance to the lowest x , linearly with E_e . Moreover, for the present design the (inner) beam pipe radius in vertical direction is 2.2 cm . This results in an extension of about 1.5 m for the first tracker plane to register an electron scattered at 179° . If one adds about 1 m for the tracker length, and 1 m for the backward calorimeter following the tracker, one arrives at about 3.5 m backward detector length. Obviously for 178° one could reduce the first 1.5 m to say 80 cm but one would still like to have a sizable tracker length for achieving some sagitta to determine the charge of the scattered electron and perhaps arrive at an overall backward detector length of about 2.5 m . While this is an interesting reduction one loses the lowest x corner which opens $\propto E_e$. The access to lowest x in the DIS region is a fundamental part of the LHeC physics program and thus the about 179° design requirement has been kept. There are reasons to take data with reduced E_e as for F_L , thus the LHeC detector will access the region below 1 GeV^2 too.

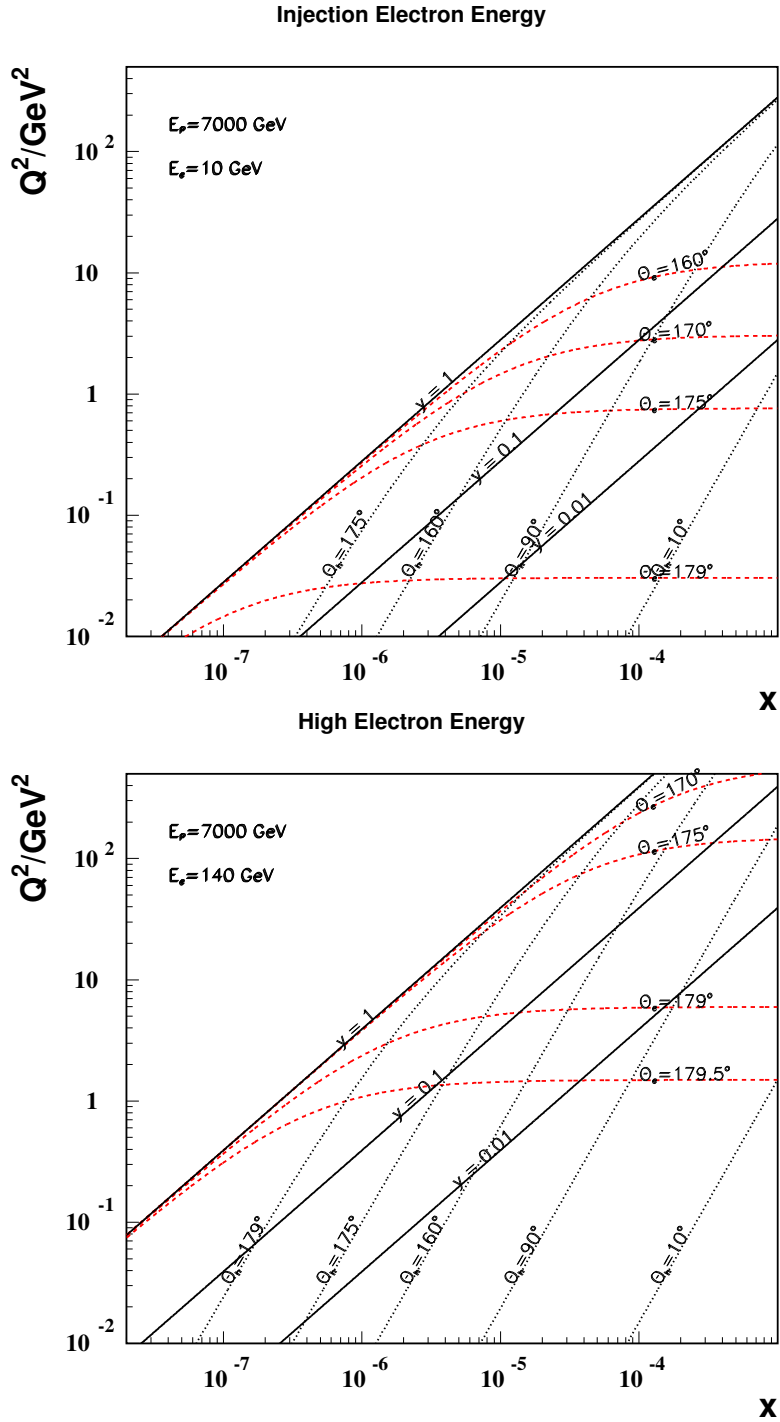


Figure 11.4: Kinematics at low x and Q^2 of electron and hadronic final state detection at the LHeC with an electron beam energy of 10 GeV (top) as compared to 140 GeV (bottom). At larger x , the iso- θ_e lines are at about constant $Q^2 \propto E_e^2$. At low x , the scattered energies, not drawn here, are approximately at $E'_e \simeq (1 - y) \cdot E_e$, and at lower Q^2 and x one has $E_h \simeq E_e - E'_e \simeq y \cdot E_e$. At very high E_e part of the very low Q^2 region may be accessible with the electron tagged along the e beam direction, outside the central detector, and the kinematics measured with the hadronic final state.

LHeC - electron kinematics

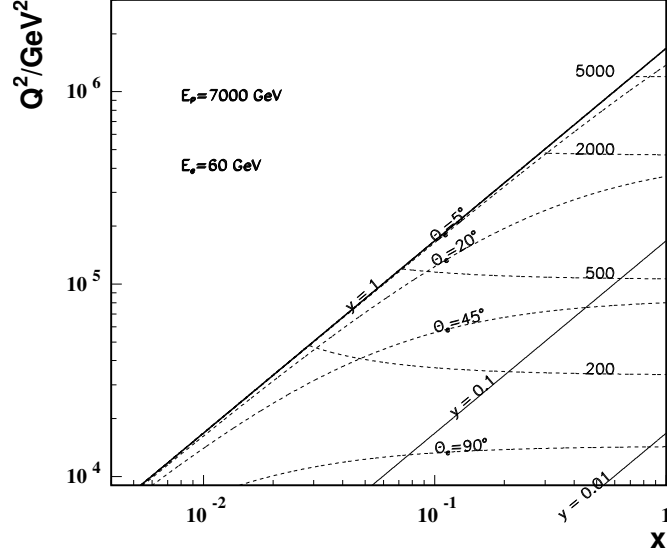


Figure 11.5: Kinematics of electron detection in the forward detector region corresponding to large $Q^2 \geq 10^4 \text{ GeV}^2$. The energy values are given in GeV. At very high Q^2 the iso- E'_e lines are rather independent of x , i.e. $Q^2(x, E'_e) \simeq 4E_e E'_e$.

8660 The x range accessed with the barrel calorimeter region, of θ_h between 135° and 45° , is
 8661 typically around 10^{-4} and smaller than a decade for each Q^2 , as can be seen in Fig. 11.6. The
 8662 hadronic energies in this part do not exceed typically 200 GeV. The detector part which covers
 8663 this region is quite large but the requirements are modest. One might even be tempted to
 8664 consider a two-arm spectrometer only. However, the measurement of missing transverse energy
 8665 and the importance of using the longitudinal momentum conservation for background and
 8666 radiative correction reductions, with the $E - p_z$ criterion, demand the detector to be hermetic
 8667 and complete.

8668 For the measurement of the hadronic final state the forward detector is most demanding.
 8669 Due to the high luminosity, the large x region will be populated and a unique physics program
 8670 at large x and high Q^2 may be pursued. In this region the relative systematic error increases
 8671 like $1/(1-x)$ towards large x , see below. At high x and not extreme Q^2 the $Q^2(x, E_h)$ line
 8672 degenerates to a line $x = E_h/E_p$ as can be derived from Eq. 11.7 and be seen in Fig. 11.6. High
 8673 x coverage thus demands the registration of up to a few TeV of energy close to the beam pipe,
 8674 i.e. a dedicated high resolution calorimeter is mandatory for the region below about $5 - 10^\circ$
 8675 extending to as small angles as possible. A minimum angle cut $\theta_{h,min}$ in the forward region,
 8676 the direction of the proton beam, would exclude the large x region from the hadronic final state
 8677 acceptance (Fig. 11.6), along a line

$$Q^2(x, \theta_{h,min}) \simeq [2E_p x \tan^2(\theta_{h,min}/2)]^2, \quad (11.8)$$

8678 which is linear in the $\log Q^2, \log x$ plot and depends on E_p only. Thus at $E_p = 7 \text{ TeV}$ the
 8679 minimum Q^2 is roughly $(1000[100]x)^2$ at a minimum angle of $10[1]^\circ$. Since the dependence in

LHeC - hadronic final state kinematics

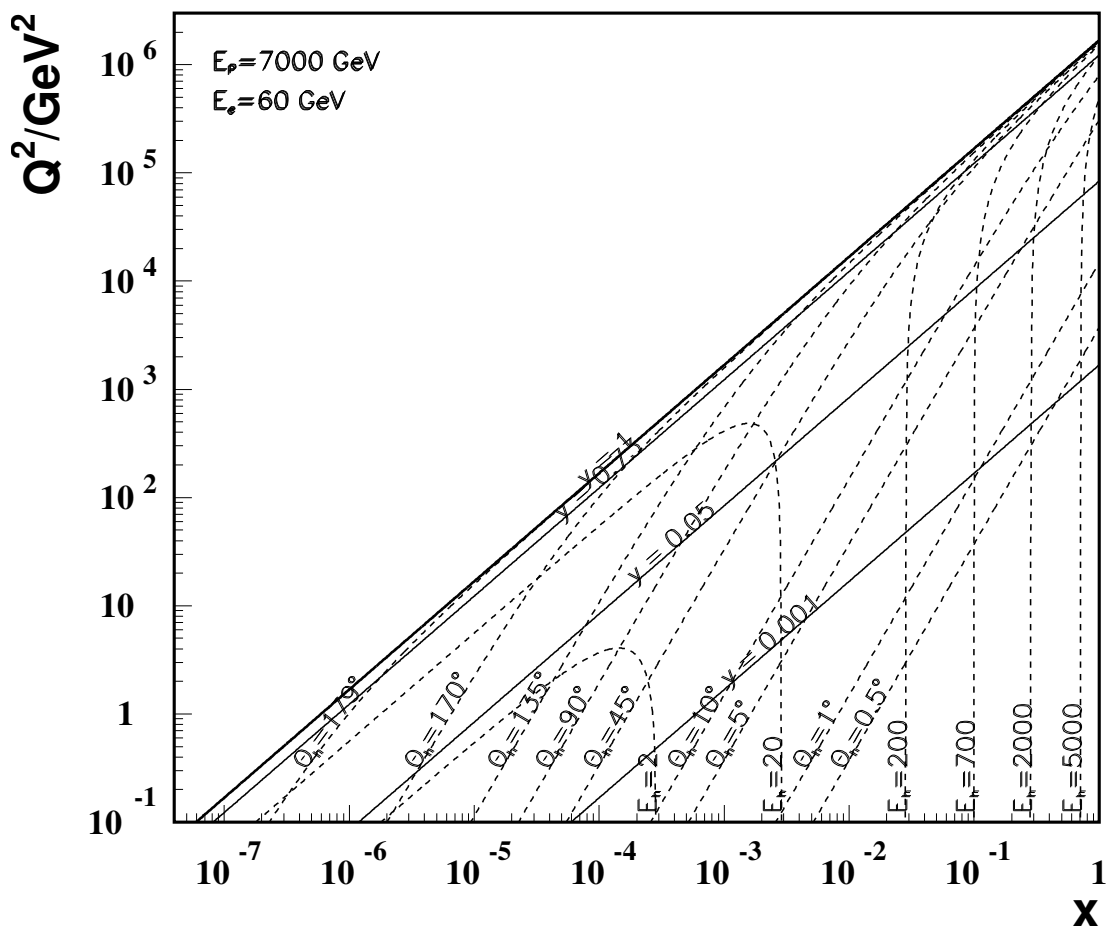


Figure 11.6: Kinematics of hadronic final state detection at the LHeC. Lines of constant energy and angle of the hadronic final state are drawn, as represented by simple kinematics of the struck quark. One easily recognizes that the most demanding region is the large x domain, where very high energetic final state particles are scattered close to the (forward) direction of the proton beam. The barrel region, of about $90 \pm 45^\circ$, is rather modest in its requirements. At low x the final state is not very energetic, $E_h + E'_e \simeq E_e$, and scattered into the backward detector region.

Eq. 11.8 is quadratic with E_p , lowering the proton beam energy is of considerable interest for reaching the highest possible x and overlapping with the large x data of previous experiments or searches for specific phenomena as intrinsic heavy flavour.

11.1.5 Acceptance at the High Energy LHC

Presently one considers to build a high energy (HE) LHC in the thirties with proton beam energies of 16 TeV [629]. Such an accelerator would better be combined with an electron beam of energy exceeding the 60 GeV, considered as default here, in order to profit from the doubled proton beam energy and to limit the asymmetry of the two beam energies. Choosing the 140 GeV beam mentioned above as an example, Figure 11.7 displays the kinematics and acceptance regions for given scattering angles and energies of the electron (dashed green and red) and of the hadronic final state (black, dotted and dashed dotted). The cms energy in this case is enhanced by about a factor of five. The maximum Q^2 reaches 10 TeV², which is 10⁶ times higher than the typical momentum transfer squared covered by the pioneering DIS experiment at SLAC. The kinematic constraints in terms of angular acceptance would be similar to the present detector design as can be derived from the Q^2, x plot. At very high x (Q^2) the energy E_h (E'_e) to be registered would be doubled. With care in the present design, one would probably be able to use the main LHeC detector components also in the HE phase of the LHC.

11.1.6 Energy Resolution and Calibration

The LHeC detector is dedicated to most accurate measurements of the strong and electroweak interaction and to the investigation of new phenomena. The calorimetry therefore requires:

- Optimum scale calibrations, as for the measurement of the strong coupling constant. This is much helped by the redundant kinematic reconstruction and kinematic relations, as $E'_e \simeq E_e$ at low Q^2 , $E'_e + E_h \simeq E_e$ at small x , the double angle reconstruction [630] of E'_e and the transverse momentum balance of p_T^e and p_T^h . From the experience with H1 and the much increased statistics it is assumed that E'_e may be calibrated to 0.1 – 0.5 % and E_h to 1 – 2 % accuracy. The latter precision will be most crucial in the forward, high x part of the calorimeter because the uncertainties diverge $\propto 1/(1-x)$ towards large x .
- High resolution, for the reconstruction of multi-jet final states as from the $H \rightarrow b\bar{b}$ decay. This is a particular challenge for the forward calorimeter. While detailed simulations are still ongoing one may assume that $(10 - 15)/\sqrt{E/GeV}$ % resolutions for E'_e and $(40 - 50)/\sqrt{E/GeV}$ % for E_h are appropriate, with small linear terms. These requirements are very similar to the ATLAS detector which quotes electromagnetic resolutions of $10/\sqrt{E/GeV} \oplus 0.007$ % and hadronic energy resolutions of $50/\sqrt{E/GeV} \oplus 0.03$ %. The basic electromagnetic calorimeter choice for the LHeC can be for Liquid Argon (LAr)⁴. The hadronic calorimeter is outside the magnets and serving also for the magnetic flux return may be built as a tile calorimeter with the additional advantage of supporting the whole detector. The first year of operating the ATLAS combined LAr/TileCal calorimeter has been encouraging. Some special calorimeters are needed in the small angle forward

⁴In H1 very good experience has been collected with the longterm stability of the LAr calorimeter. A special demand is the low noise performance because the measurements at small inelasticity y are crucial for reaching large Bjorken x . In this region a small misidentified deposition of energy in the backward part of the detector can spoil the measurement at low $y \lesssim 0.01$, as can be seen from Eq. 11.4.

Kinematics at HE-LHeC

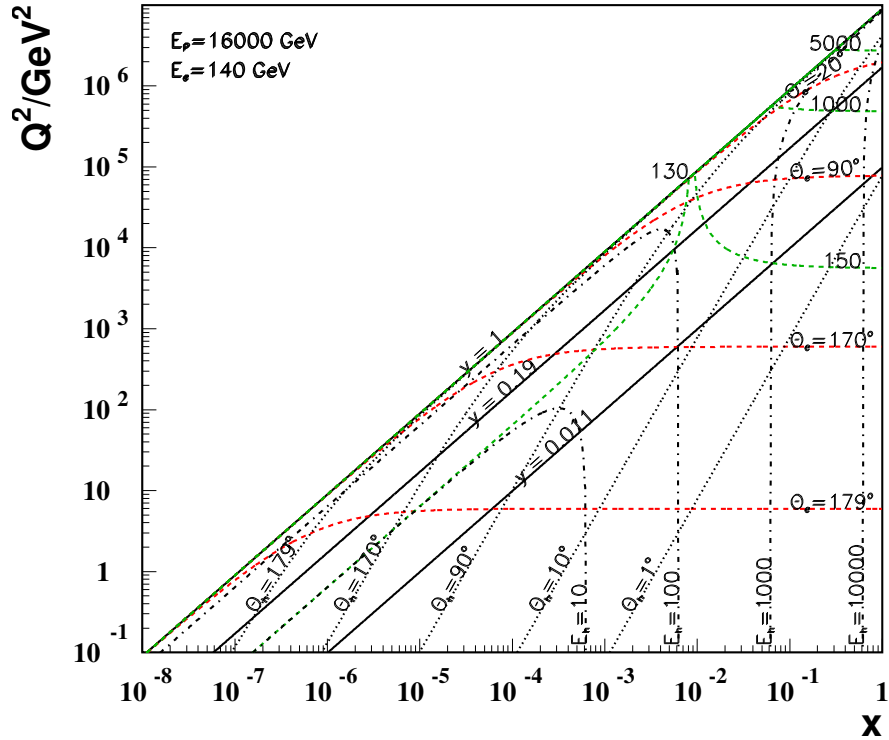


Figure 11.7: Scattered electron and hadronic final state kinematics for the HE-LHC at $E_p = 16$ TeV coupled with a 140 GeV electron beam. Lines of constant scattering angles and energies are plotted. The line $y = 0.011$ defines the edge of the HERA kinematics and $y = 0.19$ defines the edge of the default machine considered in this report ($E_e = 60$ GeV and $E_p = 7$ TeV).

8718 region ($\theta \lesssim 5^\circ$) where the deposited energies are extremely large, and also in the backward
8719 region ($\theta \geq 135^\circ$) where the electron detection of modest energy is a special task.

- 8720 • Good electron-hadron separation, as for the electron identification at high y and low Q^2
8721 (backwards) or high Q^2 (in the extreme forward direction). This is a requirement on the
8722 segmentation of the calorimeters and on building trackers in front also of the forward and
8723 backward calorimeters to support the energy measurements and the electron identification
8724 in particular.

8725 Obviously the calorimetry needs to be hermetic for the identification of the charged current pro-
8726 cess and good measurement of $E_{T,miss}$. These considerations are also summarised in Tab. 11.1.
8727

8728 11.1.7 Tracking Requirements

8729 The tracking detector has to enable

region of detector	backward	barrel	forward
approximate angular range / degrees	179 - 135	135 -45	45-1
scattered electron energy/GeV	3-100	10-400	50-5000
x_e	$10^{-7} - 1$	$10^{-4} - 1$	$10^{-2} - 1$
elm scale calibration in %	0.1	0.2	0.5
elm energy resolution $\delta E/E$ in % $\cdot \sqrt{E/GeV}$	10	15	15
hadronic final state energy/GeV	3-100	3-200	3-5000
x_h	$10^{-7} - 10^{-3}$	$10^{-5} - 10^{-2}$	$10^{-4} - 1$
hadronic scale calibration in %	2	1	1
hadronic energy resolution in % $\cdot \sqrt{E/GeV}$	60	50	40

Table 11.1: Summary of calorimeter kinematics and requirements for the default design energies of $60 \times 7000 \text{ GeV}^2$, see text. The forward (backward) calorimetry has to extend to $1^\circ(179^\circ)$.

- 8730 • Accurate measurements of the transverse momenta and polar angles
- 8731 • Secondary vertexing in a maximum polar angle acceptance range
- 8732 • Resolution of complex, multiparticle and highly energetic final states in forward direction
- 8733 • Charge identification of the scattered electron
- 8734 • Distinction of neutral and charged particle production
- 8735 • Measurement of vector mesons, as the J/ψ or Υ decay into muon pairs

8736 The transverse momentum resolution in a solenoidal field can be approximated by

$$\frac{\delta p_T}{p_T^2} = \frac{\Delta}{0.3BL^2} \cdot \sqrt{\frac{720}{N+4}} \quad (11.9)$$

8737 where B is the field strength, Δ is the spatial hit resolution and L the track length in the
8738 plane transverse to the beam direction, and N being the number of measurements on a track,
8739 which enters as prescribed in [631]. As an example, for $B = 3.5 \text{ T}$, $\Delta = 10 \mu\text{m}$, $N = 4 + 5$ and
8740 $L = 0.42 \text{ m}$ one obtains a transverse momentum measurement accuracy of about $3 \cdot 10^{-4}$. A
8741 simulation, using the LICTOY program [632], of the transverse momentum, transverse impact
8742 parameter and polar angle resolutions is shown in Fig.11.8. One can see that the estimate
8743 following Eq. 11.9 is approximately correct for larger momenta where the multiple scattering
8744 becomes negligible. This momentum resolution, in terms of $\delta p_T/p_T^2$ is about ten times better
8745 than the one achieved with the H1 central drift chamber. It is similar to the ATLAS momentum
8746 resolution for central tracks and thus considered to be adequate for the enlarged momenta at
8747 LHeC as compared to HERA and the goal of high precision vertex tagging. One finds that the
8748 impact parameter resolution, for high momenta, is a factor of eight improved over the H1 or
8749 ZEUS result.

8750 In backward direction, a main tracking task is to determine the charge of the scattered
8751 electron or positron, which has momenta $E'_e \leq E_e$, down to a few GeV for DIS at high $y \simeq$
8752 $1 - E'_e/E_e$. With a beam spot as accurate as about $10 \times 30 \mu\text{m}^2$ and the beam pipe radius

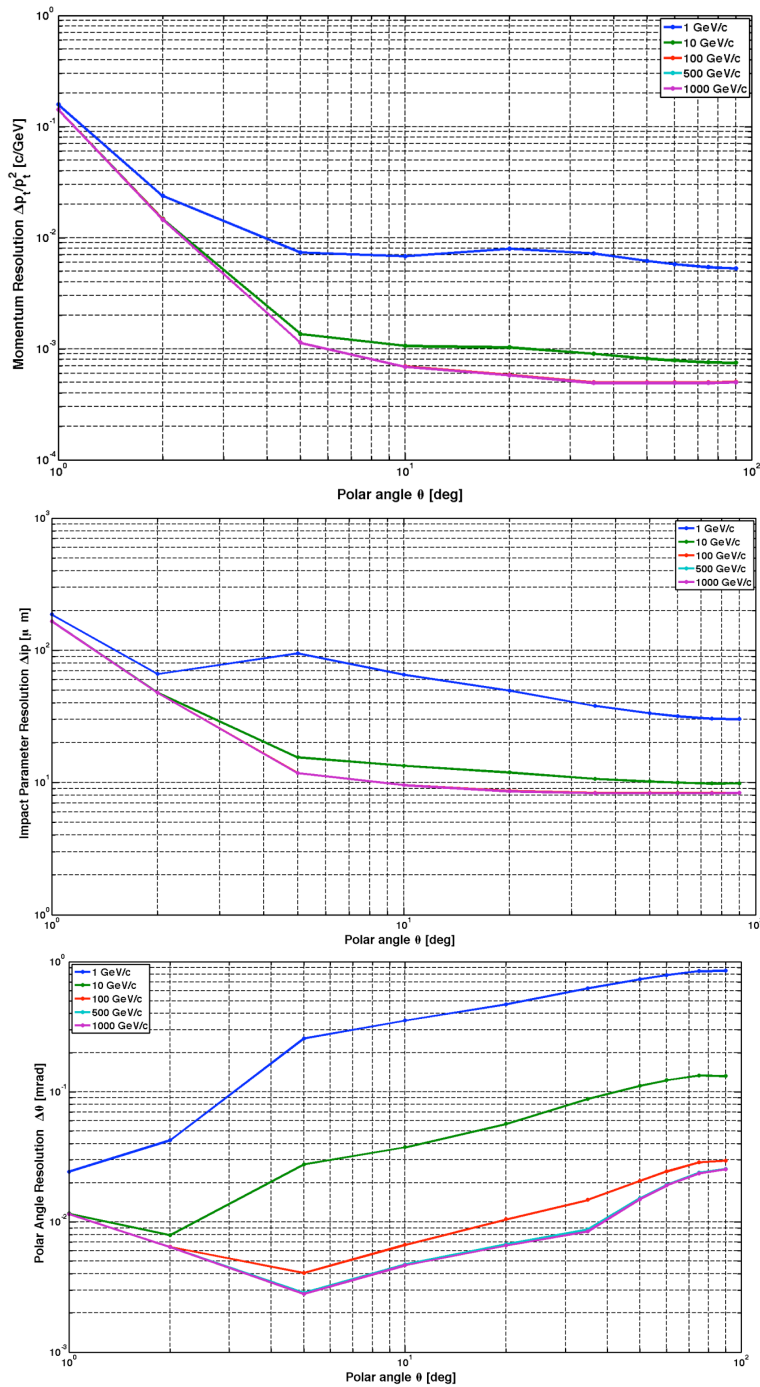


Figure 11.8: Transverse momentum (top), impact parameter (middle) and polar angle (bottom) measurement resolutions as function of the polar angle for the default detector design for four values of track transverse momentum.

8753 of a few cm only, the backward Silicon strip tracker will allow a precise E/p determination
8754 when combined with the backward calorimeter, even better than has been achieved with the
8755 H1 backward silicon detector [32].

8756 In the forward region, $\theta < 5^\circ$, as may be deduced from Figs. 11.5, 11.6, the hadronic final
8757 state, for all Q^2 , and the scattered electron, when scattered "back" at high Q^2 , are very ener-
8758 getic. This requires a dedicated calorimeter. Depending on the track path and momentum, the
8759 track sagitta becomes very small, for example about $10 \mu\text{m}$ for a 1 TeV track momentum and
8760 a 1 m track length. In such extreme cases of high momenta, the functionality of the tracker
8761 will be difficult to achieve: the sagitta becoming small means that there will be limits to the
8762 transverse momentum measurement while the ability to distinguish photons and electrons will
8763 be compromised by the high probability of showering and conversion when the pipe is passed
8764 under very small angles. A forward tracker yet is considered to be useful down to small angles
8765 for the reconstruction of the event structure, the rejection of beam induced background and
8766 the reconstruction of forward going muons. This region requires detailed simulation studies in
8767 a next phase of the project.

8768 11.1.8 Particle Identification Requirements

8769 The requirements on the identification of particles focus on the identification of the scattered
8770 electron, a reliable missing energy measurement and precision tracking for measuring the decay
8771 of charm and beauty particles, the latter rather on a statistical basis than individually. Classic
8772 measurements as the identification of the D meson from the $K\pi\pi$ decay with a slow pion or
8773 the identification of B production from high p_T leptons require a very precise track detector.
8774 The tracker should determine some dE/dX properties but there is no attempt to distinguish
8775 strange particles, as kaons from pions, as the measurement of the strange quark distribution
8776 is traced back to charm tagging in CC events. The identification of muons, apart from some
8777 focus on the forward and backward direction, is similar to that of pp detectors. In addition a
8778 number of taggers is foreseen to tag

- 8779 • electrons scattered near the beam pipe in backward direction to access low Q^2 events and
8780 control the photoproduction background;
- 8781 • photons scattered near the beam pipe in backward direction to measure the luminosity
8782 from Bethe Heitler scattering;
- 8783 • protons scattered in forward direction to measure diffractive DIS in ep scattering and to
8784 tag the spectator proton in en scattering in electron-deuteron runs;
- 8785 • neutrons scattered in forward direction to measure pion exchange in ep scattering and to
8786 tag the spectator neutron in ep scattering in electron-deuteron runs;
- 8787 • deuterons scattered in forward direction in order to discover diffraction in lepton-nucleus
8788 scattering.

8789 From the perspective of particle identification therefore no unusual requirements are derived.
8790 One needs a state of the art tracker with a very challenging forward part and a tagger system
8791 with the deuteron as a new component in forward direction.

8792 11.1.9 Summary of the Requirements on the LHeC Detector

8793 The above considerations along with the constraints from machine operation and the physics
8794 program can be summarized in the following detector requirements.

- 8795 1. The LHeC experiment has to be operated in parallel to the other LHC experiments and
8796 has to be set up in accordance to CERN regulations.
- 8797 2. The detector realization requires a modular design and construction with the assembly
8798 process done in parallel partly at surface level and partly in the experimental area following
8799 the LHC machine running and maintenance periods.
- 8800 3. The beam pipe will host the electron beam along with the two LHC counter rotating
8801 proton beams. The non interacting proton/ion beam has to bypass the IP region guided
8802 through the same beam pipe housing the electron and interacting proton/ion beam (see
8803 chapter ??).
- 8804 4. The detector should be modular and flexible to accommodate the high acceptance as
8805 well as the high luminosity running foreseen for the two main physics programs. The
8806 flexibility should accommodate reducing/enhancing the energy asymmetry of the beams
8807 - chapter 12.4.
- 8808 5. The detector design can profit from the experience at HERA and the LHC and will be
8809 based on the recent detector developments in order to meet the ambitious physics require-
8810 ments, summarized in previous chapter, using settled technology, avoiding extended R&D
8811 programs and being of comparatively reasonable cost.
- 8812 6. Mechanics/services have to be optimized minimizing the amount of material in sensitive
8813 regions of the experimental setup.
- 8814 7. The detector has to be operated in a high luminosity environment L . High \bar{L} is anticipated
8815 with small beam spot sizes ($\sigma_x \approx 30\mu m$, $\sigma_y \approx 16\mu m$), small β^* and relatively large IP
8816 angles (see acc. part). On the other hand β^* has to be chosen to eliminate effects of
8817 parasitic bunch crossings. The machine and detector requirements near the IP is an
8818 optimization problem.
- 8819 8. The detector must experience acceptable backgrounds. The design has to be background
8820 insensitive as far as possible and the machine has to incorporate masks, shielding's and an
8821 appropriate optics design that minimizes background sources and a vacuum profile that
8822 reduces backgrounds.
- 8823 9. It might be necessary to have insertable/removable shielding protecting the detector
8824 against injection and poor machine performance.
- 8825 10. Special Interaction Region (IR) instrumentation for tuning of the machine with respect
8826 to background and luminosity is needed. Radiation detectors e.g. near mask and tight
8827 apertures are useful for fast identification of background sources. Fast bunch related
8828 informations are useful for beam optimization in that context.
- 8829 11. Good vertex resolution for decay particle secondary vertex tagging is required, which
8830 implies a small radius and thin beam pipe optimized in view of synchrotron radiation and
8831 background production - see section 10.6.

- 8832 12. The detector will have one solenoid in its default version building a homogenous field
8833 in the tracking area of 3.5 T extending over $z = +370\text{cm}, -200\text{cm}$. Solenoid options are
8834 described in section 12.3.
- 8835 13. The tracking and calorimetry in the forward and backward direction has to be set up
8836 such that the extreme asymmetry of the production kinematics are taken into account
8837 by layout and choice of technology for the detector design and ensure high efficiency
8838 measurements. The detectors have to be radiation hard.
- 8839 14. Very forward/backward detectors have to be set up to access the diffractive produced
8840 events and measuring the luminosity with high precision, respectively - section ??.

8841 Chapter 12

8842 Central Detector

8843 12.1 Basic Detector Description

8844 Following the considerations of the physics requirements and the technical and operational
8845 constraints outlined above, a detector design for high precision and large acceptance Deep
8846 Inelastic Scattering is presented. The detectors for the Linac-Ring or the Ring-Ring options
8847 are nearly identical: the two notable differences are the dipoles in the Linac-Ring case for
8848 separating the e and the p beams and the larger beam pipe due to the wider synchrotron
8849 radiation fan. For practical reasons of this report the more complicated Linac-Ring detector
8850 has been chosen as the baseline, termed version A. This evidently affects the solenoid-dipole
8851 configuration and the inner shape of the tracker but is of no severe concern. For the Ring-Ring
8852 case the luminosity may be maximised by inserting focussing quadrupoles near to the IP. This
8853 causes the inner detector to be designed modular such that a transition could be made between
8854 the two phases, with the quadrupoles to achieve maximum luminosity and without, to ensure
8855 maximum polar angle acceptance ¹.

8856 The LHeC detector is asymmetric in design, reflecting the beam energy asymmetry and
8857 reducing cost. It is a general purpose 4π detector, which consists of an inner silicon tracker,
8858 with extended forward and backward parts, surrounded by an electromagnetic calorimeter,
8859 which is separated from the hadronic calorimeter by a solenoid with 3.5 T field incorporating
8860 dipoles, in the Linac-Ring case, Fig. 12.1, or not, in the Ring-Ring case, Fig. 12.2. The hadron
8861 calorimeter is enclosed in a muon tracker system, not shown here but discussed below. The
8862 main detector is complemented by hadron tagging detectors in the forward direction and a
8863 polarimeter and luminosity measurement system backwards, as is also presented below. Its
8864 longitudinal extension is determined by the need to cover polar angles down to 1° at the given
8865 beam pipe dimension. Its radial size is mainly determined by the requirement of full energy
8866 containment of hadronic showers in the calorimeter.

8867 The dipoles for the Linac-Ring IR cannot be of a too large radius to act on the beam and be

¹The very recent optics design results suggest that there is only a factor of two difference between the luminosity achievable with and without the quadrupoles. That is not enough to justify considering two measurement phases, in particular having in mind that such a transition, as happened at HERA, may take much more time than one would estimate beforehand. If the Ring-Ring solution was chosen, therefore, it would most likely only require one unchanged main detector configuration. The baseline considered here would be fully adequate for this case, with less complication of the magnets and a narrower pipe.

8868 affordable. Their bulk material should also not compromise tracking and electromagnetic energy
 8869 measurements and thus have to be placed outside the electromagnetic calorimeter, chosen to be
 8870 Liquid Argon. The solenoid cost scales, as discussed above, approximately with its radius which
 8871 in absolute allows some ten millions CHF to be economised, with the solenoid placed inside
 8872 the hadronic calorimeter ². In order to minimize cost and material, it appears appropriate to
 8873 foresee a single cryostat housing the electromagnetic calorimeter and the solenoid and dipole
 8874 magnets. This leads also to some modification of the forward and backward calorimeter inserts,
 8875 which can be seen comparing the Linac-Ring Fig. 12.1 with the Ring-Ring Fig. 12.2.

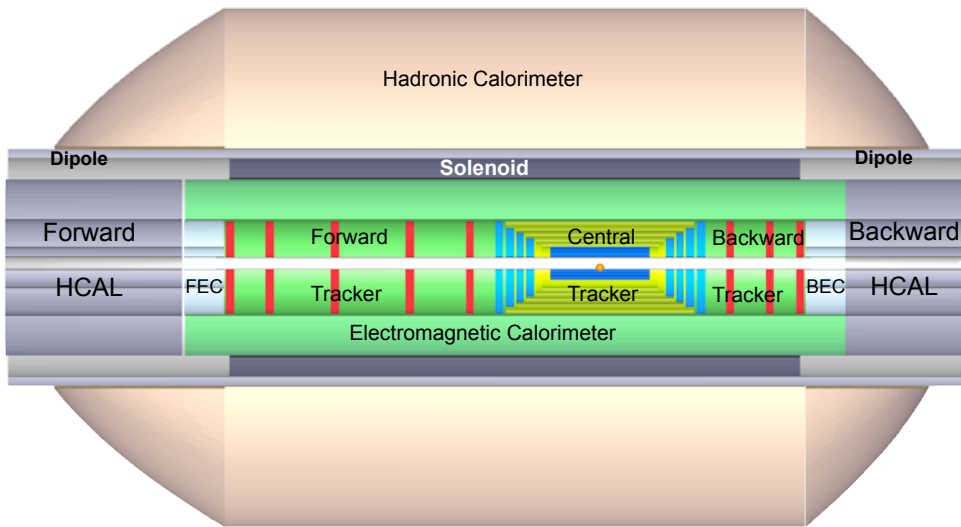


Figure 12.1: Schematic rz view of the detector design for the Linear-Ring machine option showing the characteristic dipole and solenoid placement between the electromagnetic and the hadronic calorimeters. The proton beam, from the right, collides with the electron beam, from the left, at the IP which is surrounded by a central tracker system complemented by large forward and backward tracker telescopes followed by sets of calorimeters. The detector as sketched here, i.e. without the muon tracking system, has a radius of 2.6 m and extends from about $z = -3.6$ m to $z = +5.9$ m in the direction of the proton beam.

8876 The Ring-Ring configuration possibly requires separate data taking phases with maximum
 8877 polar angle acceptance, for physics at low and high x , and with ultimate luminosity, for elec-
 8878 troweak physics and the search for rare phenomena. Correspondingly, the LHeC inner detector
 8879 is designed here with a modular structure as is illustrated in Figs. 12.3 and 12.4 which show the
 8880 detector without and with the low β quadrupoles inserted to accomodate for either configura-
 8881 tion, respectively. This requires the removal of the forward/backward tracking setup (shown in
 8882 red in Fig. 12.3) and the subsequent reinstallation of the external forward/backward electro-
 8883 magnetic and hadronic calorimeter plugins near to the vertex. The high luminosity apparatus
 8884 would have a polar angle acceptance coverage of about 8° - 172° for an estimated gain in lumi-

²Since for the physics performance it is evidently advantageous to place the solenoid outside the hadronic calorimeter, this option, termed B, has also been studied and is discussed below. The radius of the large coil would be about 2.5 m which still compares well with for example the H1 and the CMS coils.

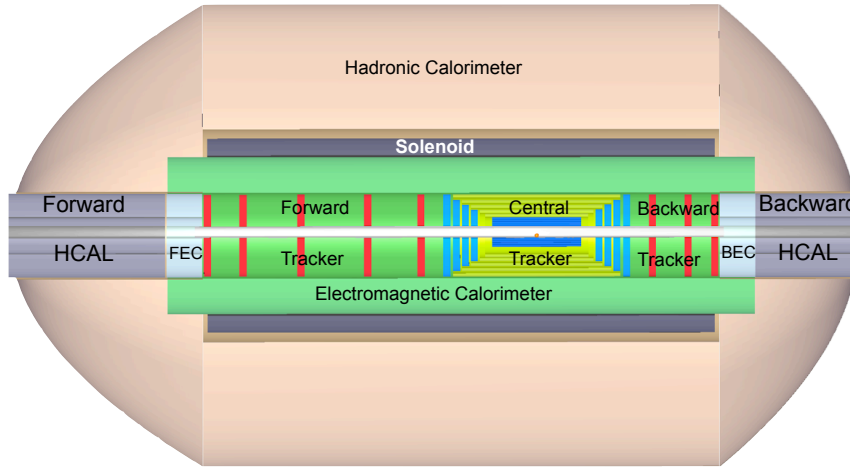


Figure 12.2: Schematic rz view of the detector design for the Ring-Ring machine option. Note that the outer part of the forward and backward calorimeters ends at smaller radii, as compared to the Linac-Ring case, since there are no dipole magnets foreseen.

8885 nosity of slightly higher than a factor of two with respect to the large acceptance configuration.

8886

8887 The Ring-Ring and Linac-Ring detectors also differ due to the different optics and the beam
8888 pipe geometry.

8889 In the Ring-Ring design the e and p/A beams collide with a small non-zero crossing angle,
8890 large enough to avoid parasitic crossings, which for a 25 ns bunch crossing occur at ± 3.75 m
8891 from the IP. Additional masks are used to shield the inner part of the detector from synchrotron
8892 radiation generated upstream of the detector.

8893 For the Linac-Ring design, the dipole field in the detector area which allow for head-on
8894 collisions and provide the required separation, produces additional synchrotron radiation which
8895 has to pass through the interaction region requiring a larger beam pipe. This difference results
8896 in a factor of two wider extension of the horizontal beam pipe in the outer region in the Linac-
8897 Ring case, which in this regard is the unfavourable solution. The radius of the circular part has
8898 been chosen according to tentative choices of the LHC upgrade beam pipe dimensions.

8899 According to a first estimate of the synchrotron radiation and an initial placement of masks,
8900 shielding the Ring-Ring detector from direct and backscattered photons, the beam pipe geometries
8901 have been chosen as shown in Fig. 12.5 for the Ring-Ring case and in Fig. 12.6 for the
8902 Linac-Ring case.

8903 As already mentioned, the necessity to register particle production down to 1 and 179°
8904 poses severe constraints on the material and the thickness of the pipe. In the design as shown
8905 here, a beryllium pipe would have 3.0 (1.5) mm thickness in the Linac-Ring (Ring-Ring) case.
8906 An extensive R&D program is needed aiming for higher stability of the beam pipe at given
8907 dimensions and for thinner/lighter beam wall construction resulting in higher transparency for
8908 all final state particles. This R&D program is necessary regardless of which machine option for
8909 the LHeC facility is selected. It may also turn out to be advantageous to use a trumpet shaped
8910 beam pipe when this problem gets revisited in a more advanced phase of the LHeC design when

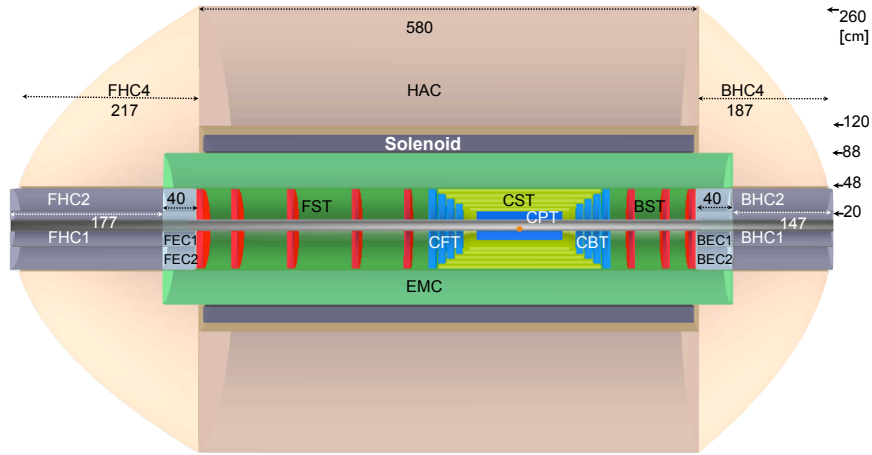


Figure 12.3: An rz cross section and dimensions of the main detector (muon detector not shown) for the Ring-Ring detector version (no dipoles) extending the polar angle acceptance to about 1° in forward and 179° in backward direction.

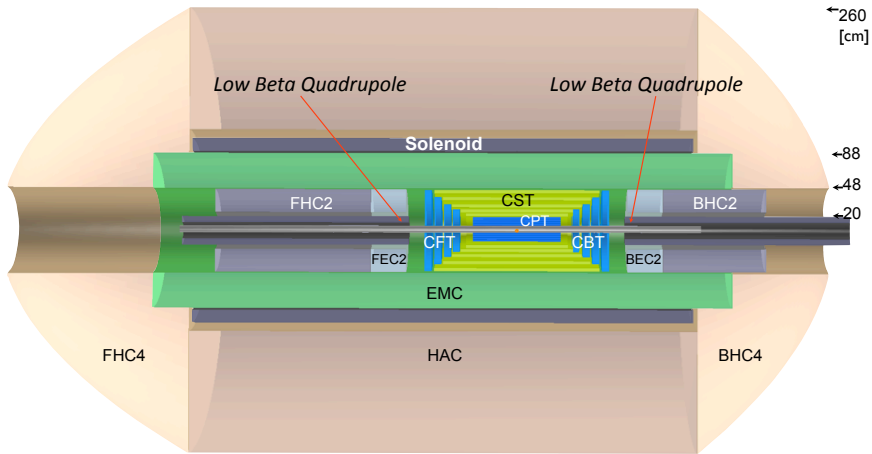


Figure 12.4: An rz cross section and dimensions of the main detector (muon detector not shown) for the Ring-Ring detector version (no dipoles) in which the luminosity is maximised by replacing the forward and backward tracker telescopes by focusing, low β quadrupole magnets at ± 1.2 m away from the nominal interaction point. The polar angle acceptance is thus reduced to about $8 - 172^\circ$. As compared to the high acceptance detector (Fig. 12.3), the outer forward/backward calorimeter inserts have been moved nearer to the interaction point.

RR - Inner Dimensions
Circular(x)=2.2cm; Elliptical(-x)=-5.5, y=2.2cm

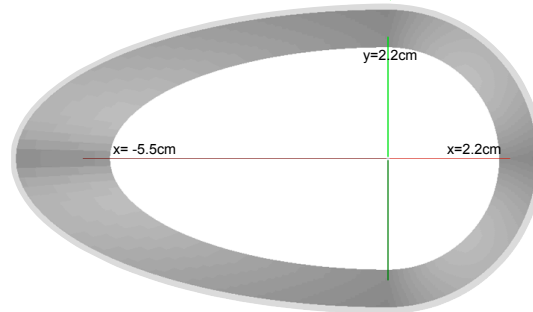


Figure 12.5: Perspective drawing of the beam pipe and its dimensions in the ring-ring configuration. The dimensions consider a 1 cm safety margin around the synchrotron radiation envelope with masks (not shown) for primary synchrotron radiation suppression placed at $z = 6, 5, 4$ m.

LR - Inner Dimensions
Circular(x)=2.2cm; Elliptical(-x)=-10., y=2.2cm

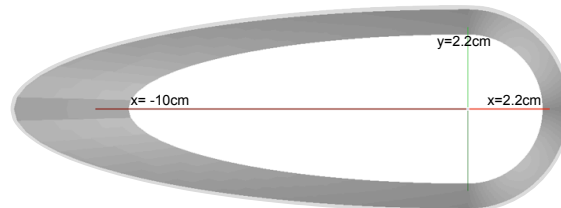


Figure 12.6: Perspective drawing of the beam pipe and its dimensions in the linac-ring configuration. The dimensions consider a 1 cm safety margin around the synchrotron radiation envelope.

8911 more detailed simulations will be available and results of pipe material developments become
 8912 known.

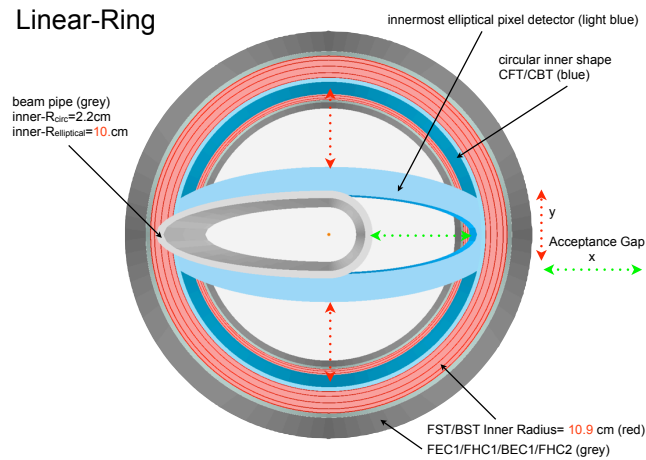


Figure 12.7: Linac-Ring beam pipe design and acceptance gap's due to deviations of inner shapes of the forward/backward tracking detectors FST/BST (circular) and the innermost central pixel detector layer (elliptical) from the pipe shape.

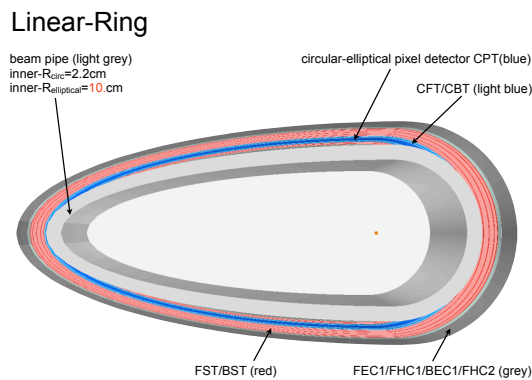


Figure 12.8: Beam pipe design for Linac-Ring and optimized circular-elliptical shape following the beam pipe for all adjacent detector parts.

8913 In order to ensure optimal polar angle acceptance coverage, the innermost subdetector
 8914 dimensions have to be adapted to the beam pipe shape. Fig.12.7 illustrates the disposition
 8915 that a circular silicon tracker would imply and the corresponding acceptance losses. These can
 8916 be reduced as is shown in Fig. 12.8 if the detector acceptance follows as close as possible the
 8917 elliptic-circular shape of the pipe. Electrons scattered at high polar angle, corresponding to
 8918 small $Q^2 \sim 1 \text{ GeV}^2$, will only be registered in the inner part of the azimuthal angle region for
 8919 the nominal electron beam energy. As had been shown above, the lowering of the electron beam
 8920 energy effectively reduces the strong requirement of measuring up to about 179° , at the expense

8921 however, of a somewhat reduced acceptance towards lowest Bjorken x .

8922 The optimum configuration of the inner detector will be revisited when the choice between
 8923 the Linac-Ring and the Ring-Ring option is made. It represents in any case one of the most
 8924 challenging problems to be solved for the LHeC.

8925 12.2 Baseline Detector Layout

8926 The baseline configuration (A) of the main detector has the solenoid in between the two
 8927 calorimeters, combined with a dipole field in the Linac-Ring case. It is subdivided into a
 8928 central barrel and the forward and backward end-cap regions, which differ in their design be-
 8929 cause the forward region sees the remnant and the highly energetic ($E_h \lesssim E_p$) jet from the
 8930 struck quark while the backward region sees the scattered electron of energy $E'_e \leq E_e$. The de-
 8931 tector configuration is sketched in Fig. 12.9 with component abbreviations and some dimensions
 given. More detailed dimensions are given in Fig. 12.10.

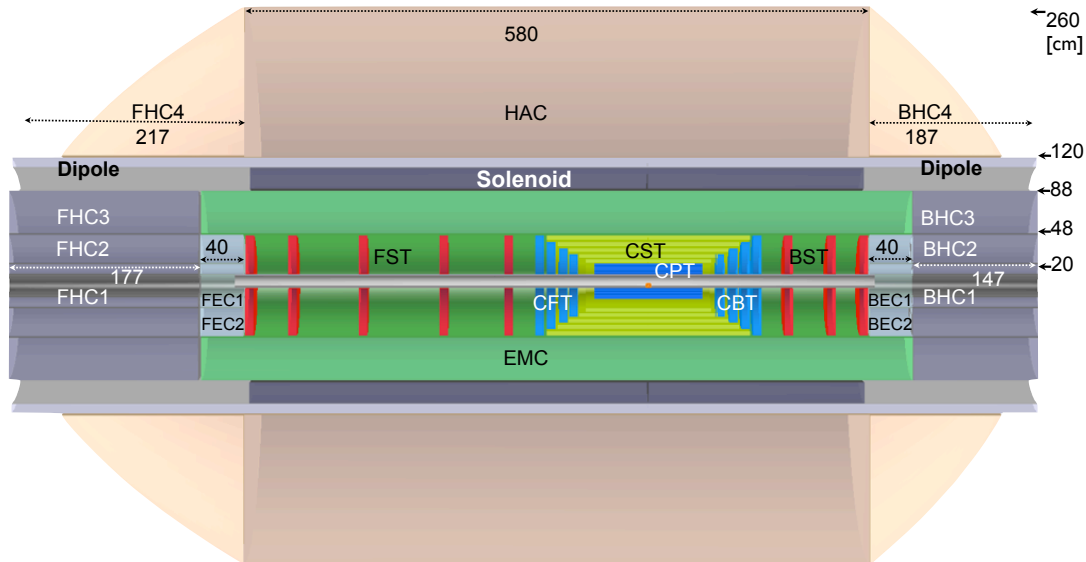


Figure 12.9: An rz cross section of the LHeC detector, in its baseline configuration (A). In the central barrel, the following components are considered: a central Silicon pixel detector (CPT); silicon tracking detectors (CST,CFT/CBT) of different technology; an electromagnetic calorimeter (EMC) surrounded by the magnets and followed by a hadronic calorimeter (HAC). Not shown is the muon detector. The electron at low Q^2 is scattered into the backward silicon tracker (BST) and its energy measured in the BEC and BHC calorimeters. In the forward region similar components are placed for tracking (FST) and calorimetry (FEC, FHC).

8932 For the purpose of this design, technologies had to be chosen in line with the detector
 8933 requirements, see Sect. ??, and based on an evaluation of the technologies available or under
 8934 development for the LHC experiments or foreseen for a linear collider detector. The complete
 8935 inner tracker is considered to be made of Silicon. This enables to keep the radius of the
 8936

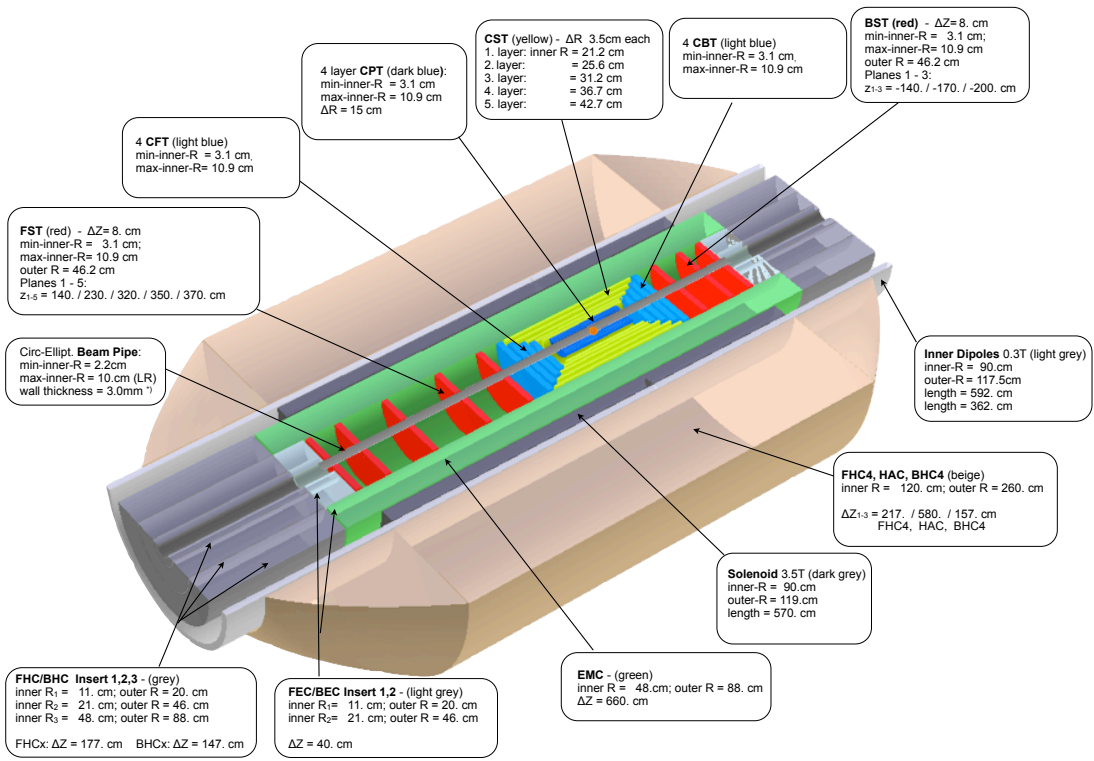


Figure 12.10: View of the baseline detector configuration (A) with some dimensions for each of the main detector components.

magnets small, at about 1 m. Based on experience with H1 and ATLAS the EMC is chosen to be a Liquid Argon (LAr) Calorimeter. The super conducting dipoles (light grey in Fig. 12.9) are placed in a common cryostat with the detector solenoid (dark grey) and the LAr EMC (green). The common cryostat is optimum for reducing the amount of material present in front of the hadronic barrel calorimeter. The HAC is an iron-scintillator tile calorimeter, which also guides the return flux of the magnetic field, as in ATLAS [633,634]. In the baseline design (A) the muon detectors are placed outside of the magnetic field with the function of tagging muons, the momentum of which is determined by the inner tracker.

For the Ring-Ring machine, in order to maximize the luminosity, extra focusing magnets must be placed near to the interaction point ³. This would mean replacing the FST and the BST tracking detectors by the low- β quadrupoles (see Fig. 12.4), at the expense of losing about 8° of polar angle acceptance. The modular design of the forward and backward trackers and the corresponding calorimeter modules allow the trackers to be mounted/unmounted and the calorimeter inserts to be moved in and out of position as required. The inner electromagnetic and hadronic endcap inserts, FEC1/BEC1 and FHC1/BHC1, respectively, will be removed allowing the insertion of the low β -magnets and only partially put back in. Particular attention is needed for the mechanical support structures of the quadrupoles. The structure must ensure the stability of reproducible beam steering, while interfering as little as possible with the detector. The presence of strong focussing magnets close to the interaction point was one issue experienced during HERA2 running [635].

12.2.1 An Alternative Solenoid Placement - Option B

The configuration A is determined by the intention to keep the detector ‘small’: it uses the HAC as flux return for an inside solenoid which, for the Linac-Ring case, is combined with long dipoles. This is not ideal for the hadronic energy measurement. Therefore a second configuration (B) has been considered, to much less detail, in which the solenoid is placed outside the HAC. Option B might be of interest only for the Ring-Ring case as otherwise, the requirement of the bending dipoles to be placed right after the EMC would anyhow compromise the design requiring anyhow similar cryogenics and support structures as in option A.

In considering a solenoid around the HAC one finds, as from the CMS geometry, that the return iron would be massive, of order 10000 tons [HERMANN??], and extend by several meters further out in radius, which may pose problems when one has the IP2 cavern in mind. One then is lead to consider using a second solenoid for an active flux return, which gives a good muon momentum reconstruction. A strong magnetic field of 3.5 T covering the barrel calorimeter (HAC) leads to a better separation of charged hadron induced showers in the HAC area compared to the sole fringe field effect in case of the inner solenoid baseline design A. The HAC would have to be designed very carefully as there would be no muon-iron return yoke following for catching shower tails. A warm EMC design with no need for a cryostat would become an option worth considering. Also extending the tracker by an extra more conventional layer of tracking chambers in front of the EMC would be an interesting possibility, with which the amount and radius of the Silicon detector may be somewhat reduced.

An overview of the detector configuration B is given in Fig. 12.11. A two solenoid configuration is the 4th Concept for an ILC Detector [627]. The second outer solenoid keeps the overall dimensions of the detector limited. A detailed consideration of option B has not been intended

³See above for an evaluation of that possibility.

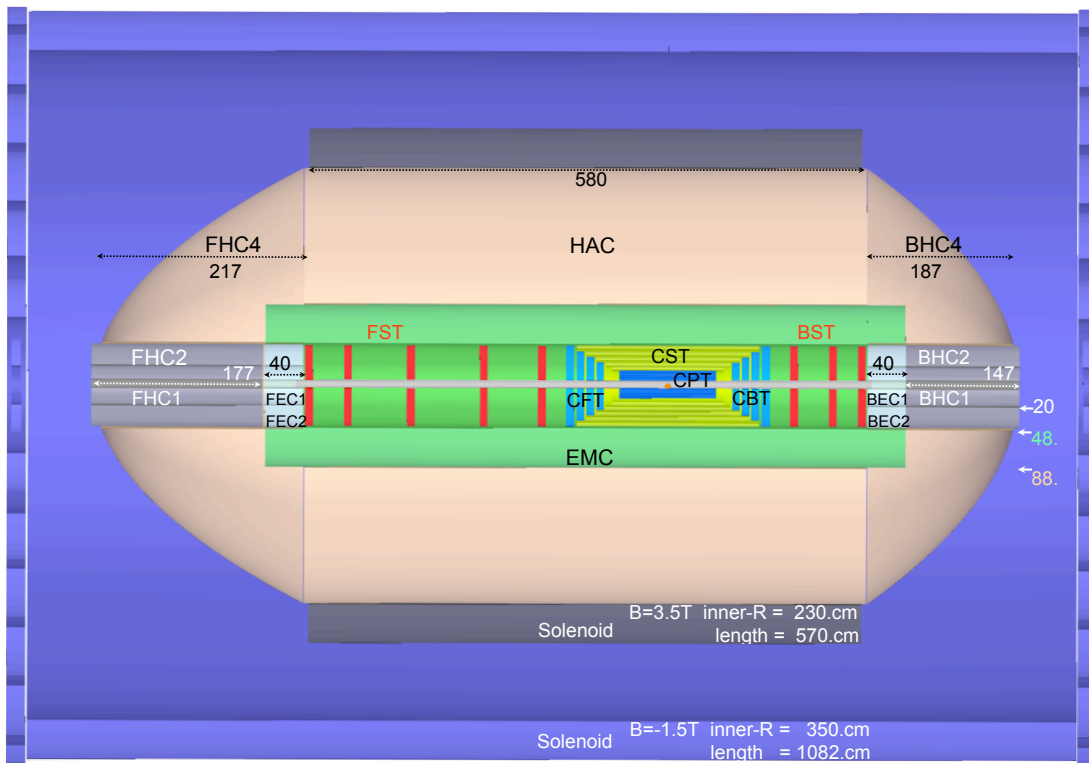


Figure 12.11: An rz cross section of the LHeC detector, option B, in which the solenoid is placed outside the HAC. A compensating larger solenoid is considered, see text. The muon detector is not shown but would be placed inside the second solenoid. The overall dimensions of this detector configuration are about 10 m length and 8 m diameter.

8980 at this stage of the project.

8981 12.3 Magnet Design

Option	Solenoid	Dipole	Cryostat(s)
	$B = 3.5T$ Length = 570cm	$B = 0.3T$ $L_{+z} = 600cm, L_{-z} = 370cm$	Length = 1020 cm
A	$R_{min} = 90cm$	$R_{min} = 90cm$ $R_{outCryostat} = 117.5cm$	EMC, Solenoid, Dipoles $R_{in} = 48cm, R_{out} = 117.5cm$
B	$R_{min}^1 = 230cm$	$\Delta R_{Cryo-Sol_{out}}$ - not defined	1 st -Solenoid 2 nd -Solenoid

Table 12.1: Magnet dimensions and characteristics of the two options A and B (no dipoles in case of Ring-Ring machine and in case B).

8982 The main properties of the different magnet designs are summarized in Tabl. 12.1.
8983 Text beeing written by H.T.Kate, A.Dudarev - describing design properties etc.

8984 12.4 Tracking Detector

8985 12.4.1 Tracking Detectors Layout - Baseline Detector

8986 The tracking detectors (Fig.12.13) inside the electromagnetic calorimeter are Si-sensor only
8987 devices. The tracker system has to provide precise tracking, momentum determination as far
8988 as possible, vertex reconstruction and pattern recognition. It covers the pseudorapidity range
8989 $-4.8 < \eta < 5.5$ and is located inside the solenoidal field of 3.5T. Additionally a dipole field of
8990 0.3T is superposed resulting from the beam steering dipoles housed inside the same cryostat as
8991 the solenoid. For 1° tracks the bending solenoidal field component (0.36T) is of the same order
8992 as the dipole field and the resulting track Sagitta reaches the [mm] range when particles of
8993 momentum $< 100GeV$ pass 250cm (track length measured) Fig. 12.13. The tracker described
8994 here (FST) measure 1° tracks over a distance of $\approx 180cm$ (forward direction). Therefore a
8995 momentum determination for $\approx 1^\circ$ and high momentum tracks is unlikely but with precision
8996 tracking the analysis will rely on the tagged energy measurement. The backward measurement
8997 is characterised by even shorter track length's. There the analysis will rely on the energy
8998 measurement in calorimeters combined with a well defined track definition. That approach
8999 is supported by the fact that the particle flux in backward compared to forward direction is
9000 lower due to kinematics. The well separated charged tracks in backward direction are usually
9001 easier to measure and will allow the precision tagging of corresponding calorimeter signals.
9002 Very low Q^2 /low x processes will be better accessible by reducing the electron beam energy thus

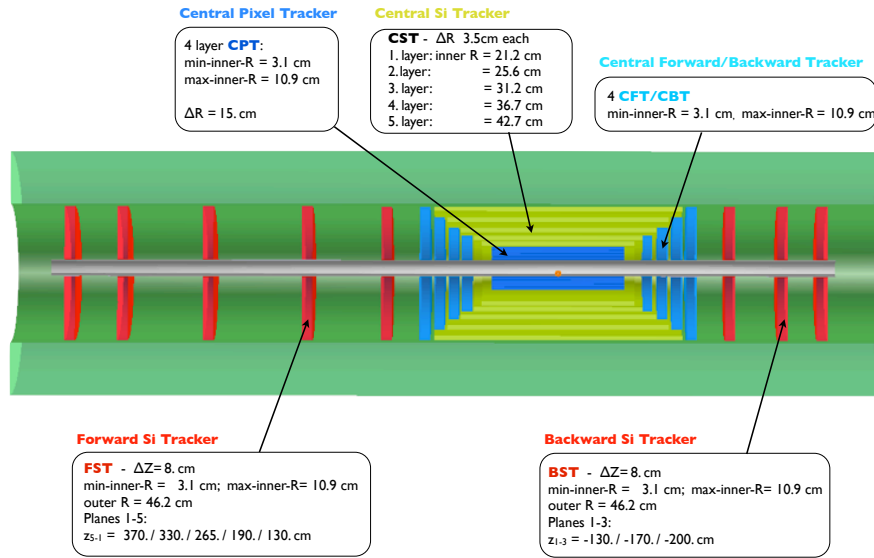


Figure 12.12: Tracker and barrel Electromagnetic-Calorimeter rz view of the baseline detector (Linac-Ring case).

9003 measured at larger angles in backward direction (see Fig. 11.3 and Fig. 11.4 and discussion in
 9004 chapter ??).

9005 The tracker is subdivided into central (CPT, CST, CFT/CBT) and forward/backward parts
 9006 (FST, BST). Fig. 12.13 shows the tracker configuration for the high acceptance running of
 9007 solution (A) of the detector design. More details are summarized in Tab. 12.2 ⁴.

9008 Acceptance coverage down to 1° and 179° , respectively, and the tagging of secondary vertices
 9009 originating from the decay of heavy particles over a wide range of $|\eta|$ are requirements vital for
 9010 the physics program for the LHeC experiment. Measuring close to the beam line for maximal
 9011 polar angle coverage and to the vertex are major requests. The shape of the CPT and the
 9012 inner dimensions of all near-beam detectors have been chosen accordingly (Fig. 12.14 show the
 9013 xy view of the circular-elliptical CPT and the cylindrical CST detectors).

9014 The *All-Silicon* based tracking devices allow high resolution track space points measurement
 9015 and hence sufficient pattern recognition even at both angle acceptance limits in forward and
 9016 in backward direction, respectively. The expected jet angular and energy distribution for some
 9017 selected physics processes simulated using *RAPGAP* (Ref. [115]) is shown in Fig. 12.15. That
 9018 figures illustrate once again the importance of the forward acceptance down to 1° .

9019

9020 Some results of preliminary tracker performance simulations using the LicToy-2.0 program
 9021 [632] for the tracker setup (see table 12.2 and Fig. 12.16), are summarized in Fig. 12.17. The
 9022 geometrical arrangement of the tracking detectors together with the pre-defined resolution

⁴The item *project area* in table 12.2 describes the area which has to be equipped with appropriate Si-sensors (e.g. single-sided or double-sided sensors). An alternative would be the usage of Si-Gas detectors providing track segment information instead of track points, e.g. in the CST cylinders (Ref. [636], [637], [638])

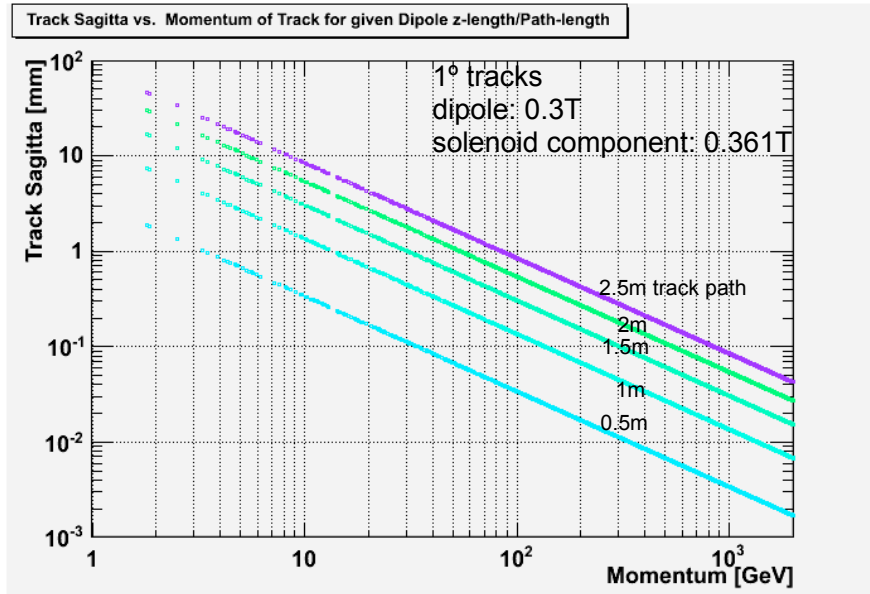


Figure 12.13: Track Sagitta vs. Momentum of 1° tracks in a superposed dipole/solenoidal field.

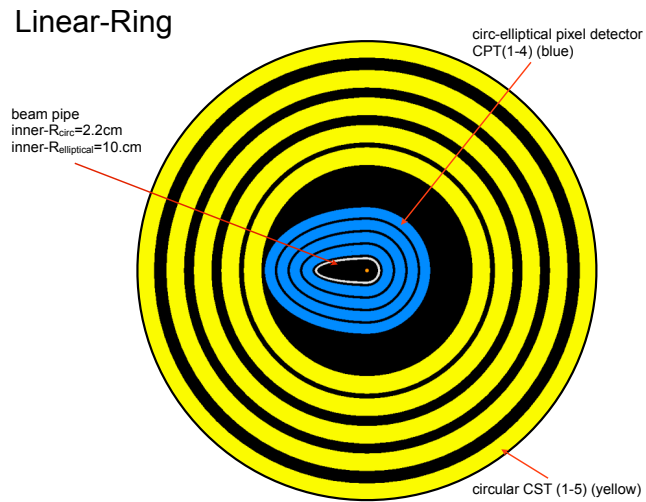


Figure 12.14: XY cut away view of the Central Pixel (CPT) and Central Strixel Tracker (CST) (Linac-Ring layout).

Central Barrel	CPT1	CPT2	CPT3	CPT4	CST1	CST2	CST3	CST4	CST5
Min. Radius R [cm]	3.1	5.6	8.1	10.6	21.2	25.6	31.2	36.7	42.7
Min. Polar Angle θ [°]	3.6	6.4	9.2	12.0	20.0	21.8	22.8	22.4	24.4
Max. $ \eta $	3.5	2.9	2.5	2.2	1.6	1.4	1.2	1.0	0.8
ΔR [cm]	2	2	2	2	3.5	3.5	3.5	3.5	3.5
$\pm z$ -length [cm]	50	50	50	50	58	64	74	84	94
Project Area [m ²]	1.4				8.1				
Central Endcaps	CFT4	CFT3	CFT2	CFT1		CBT1	CBT2	CBT3	CBT4
Min. Radius R [cm]	3.1	3.1	3.1	3.1		3.1	3.1	3.1	3.1
Min. Polar Angle θ [°]	1.8	2.0	2.2	2.6		177.4	177.7	178	178.2
at z [cm]	101	90	80	70		-70	-80	-90	-101
Max./Min. η	4.2	4.0	3.9	3.8		-3.8	-3.9	-4.0	-4.2
Δz [cm]	7	7	7	7		7	7	7	7
Project Area [m ²]	1.8					1.8			
Fwd/Bwd Planes	FST5	FST4	FST3	FST2	FST1		BST1	BST2	BST3
Min. Radius R [cm]	3.1	3.1	3.1	3.1	3.1		3.1	3.1	3.1
Min. Polar Angle θ [°]	0.48	0.54	0.68	0.95	1.4		178.6	178.9	179.1
at z [cm]	370	330	265	190	130		-130	-170	-200
Max./Min. η	5.5	5.4	5.2	4.8	4.5		-4.5	-4.7	-4.8
Outer Radius R [cm]	46.2	46.2	46.2	46.2	46.2		46.2	46.2	46.2
Δz [cm]	8	8	8	8	8		8	8	8
Project Area [m ²]	3.3						2.0		

Table 12.2: Summary of tracker dimensions.

The 4 Si-Pixel-Layers CPT1-CPT4 (resolution of $\sigma_{\text{pix}} \approx 8\mu\text{m}$) positioned as close to the beam pipe as possible.

Si-strixel (CST1-CST5) (resolution of $\sigma_{\text{strixel}} \approx 12\mu\text{m}$) forming the central barrel layers. An alternative is the of 2_in_1 single sided Si-strip solution for these barrel cylinders ($\sigma_{\text{strip}} \approx 15\mu\text{m}$) (Ref. [639]).

The endcap Si-strip detectors CFT/CBT(1-4) complete the central tracker.

The tracker inserts, 5 wheels of Si-Strip detectors in forward direction (FST) and 3 wheels in backward direction (BST), are based on single sided Si-strip detectors of 2_in_1-design ($\sigma_{\text{strip}} \approx 15\mu\text{m}$). They have to be removed in case of high luminosity running for the Ring-Ring option of the accelerator configuration see Fig. 12.4.

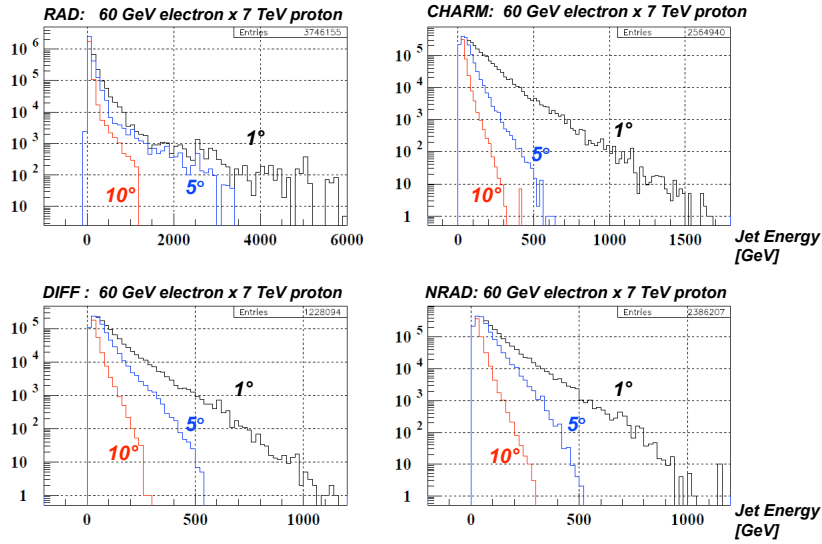


Figure 12.15: Radiative, diffractive, charm and non-radiative Jet production for polar angle $\theta = 1^\circ, 5^\circ$ and 10° .

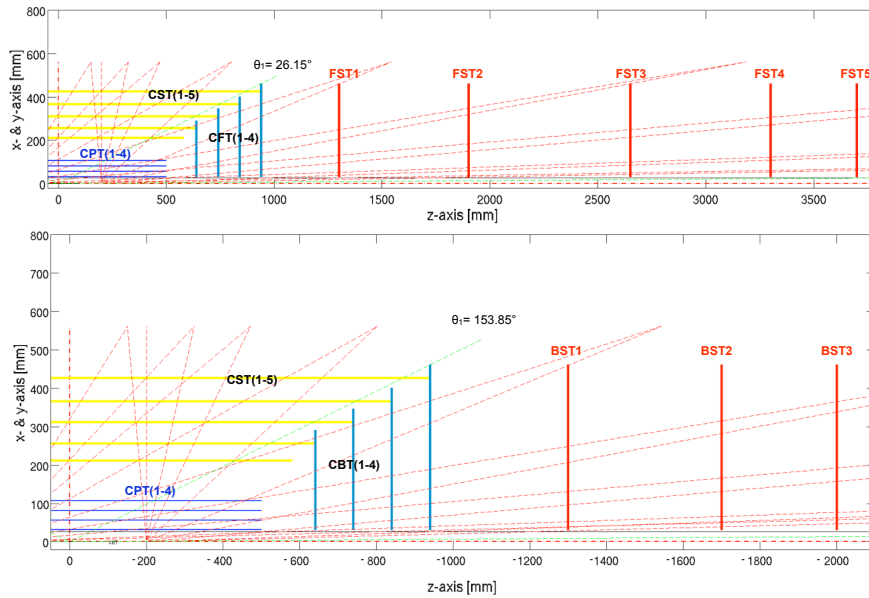


Figure 12.16: LicToy2.0 tracker design of the central/forward FST(top) and central/backward direction BST(bottom).

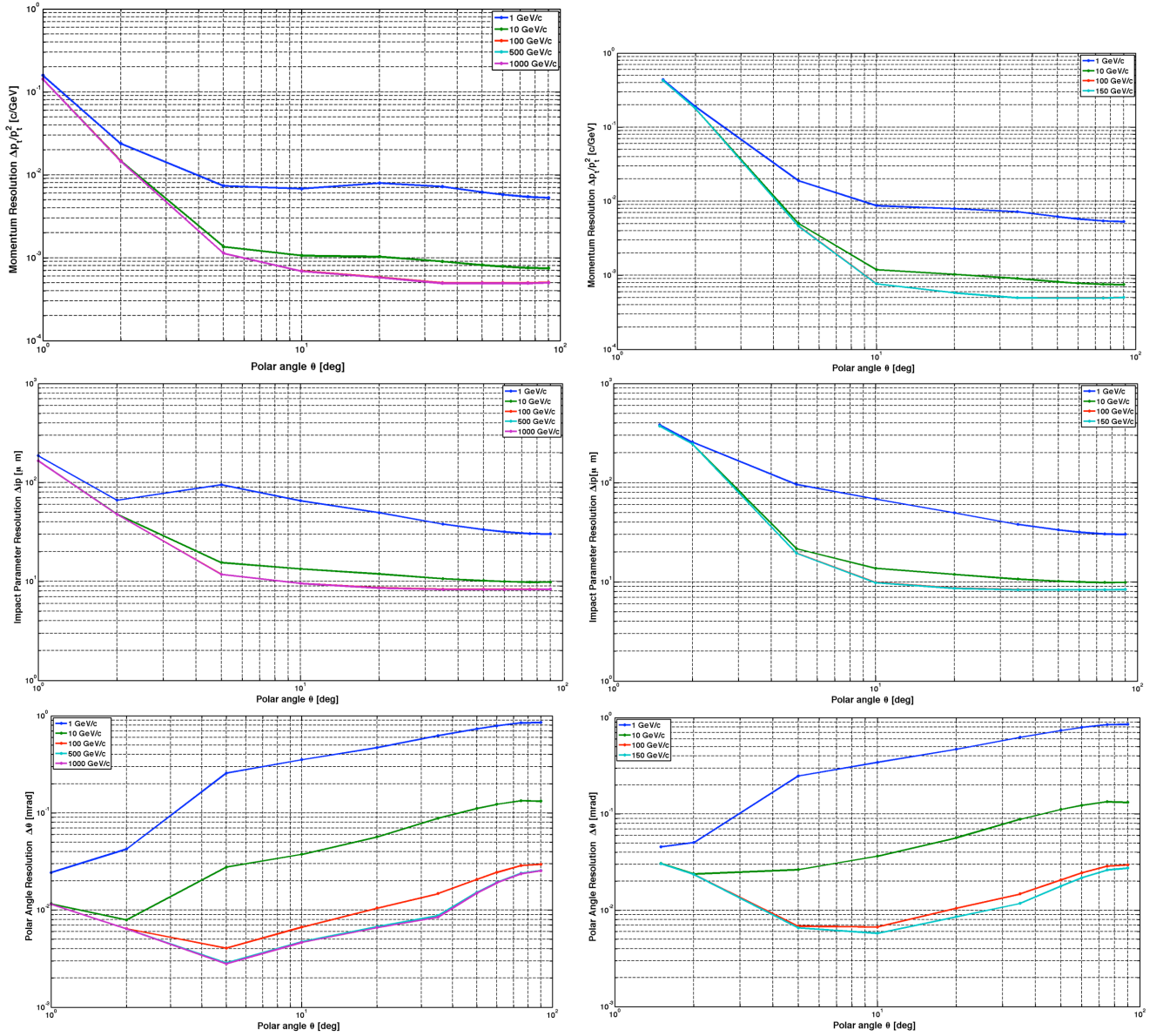


Figure 12.17: Scaled momentum, impact parameter and polar angle resolution as function of polar angle θ resulting from tracker design simulation using LiCToy2 for the FST(left) and BST(right) side. Tracker setup used as shown in Fig. 12.16,

Basic parameters:

$B=3.5T$, $X/X_0^{\text{beam pipe}} = 0.002$, $X/X_0^{\text{det-parts}} = 0.005$, efficiency=0.99%, Resolutions(σ):

$\sigma_{\text{CPT}} = 8\mu\text{m}$, $\sigma_{\text{CST,CFT,CBT}} = 12\mu\text{m}$, $\sigma_{\text{FST,BST}} = 15\mu\text{m}$, minimal inner radius
 $R_{\text{min}}^{\text{CPT,CFT,CBT,FST,BST}} = 3.15\text{cm}$.

9023 settings for those parts, perform as expected at least within that simplified framework.

9024 12.4.2 Tracking Detector Design Criteria and possible Solutions

9025 The experience of former attempts for an optimal detector setup suggest that some criteria
9026 should be discussed as early as possible.

9027 Some arguments for the design will predominantly be (see Ref. [640], [641]):

- 9028 • Optimizing of cost for all components. Making use of technology developments for HL-
9029 LHC/ILC experiments (Ref. [642], [643], [644], [645], [646], [647], [648], [649], [650], [651],
9030 [652], [653], [654], [655]) but rely on technologies available today because of time con-
9031 straints. Today's accessible sensors, integrated electronics, readout/trigger circuitry, me-
9032 chanics, cooling etc. have to be used to meet the goal: installation in the 2020's.
- 9033 • The default tracker setup is based on the silicon microstrip detector technology developed
9034 for the big experiments at LHC, ILC, TEVATRON, b-factories, etc. within the last 20
9035 years. The decisions for sensor types (pixel, strip, strip) operation depend on many
9036 factors and will be taken according to its functionality finally:

9037 The expected radiation load is defined and influenced by the interaction rate (25ns),
9038 luminosity ($\approx 10^{33} \text{cm}^{-2} \text{s}^{-1}$), particle rate per angle interval, fluence n_{eq} and ionisation
9039 dose over 1 year running. Some data will be better defined after evaluation of more
9040 detailed simulations. Specifically the radiation impact on tracker wheels, calorimeter
9041 inserts and inner pixel-barrel layer has to be studied. The tools for those simulations are
9042 being prepared. Very first estimates will be discussed in section 12.5 in more detail, but no
9043 indication for extremely high radiation load into the detectors adjacent to the beam pipe
9044 have been obtained so far. The expected levels are far below what the LHC experiments
9045 have to sustain.

9046 A side remark is related to the active parts of the forward/backward calorimeter. For
9047 safety reasons those calorimeter inserts should be equipped with radiation hard Si-based
9048 sensors according to LHC/HL-LHC standards. Relatively small in volume but still large in
9049 terms of layer area (m^2), the equipment of calo-inserts Si-strip/Si-pad based is a sizeable
9050 investment but might be needed for safety reasons. A final decision will be possible after
9051 more cross checks (some FLUKA simulations are pending).⁵

9052 Decisions have to define the trigger capabilities/options, here in the context of track-
9053 ing only, which have a direct impact on sensor choice, arrangement and attached electron-
9054 ics. It might be that very recent developments of 3D integration semiconductor layers
9055 interconnected to form monolithic unities of sensor&electronic circuitry are in time for the
9056 installation in the 2020's but conventional wire bonded or bump bonded solutions may
9057 be more cost efficient and rely on components available today. E.g. using the 2_in_1
9058 strip sensor design as p_t -trigger discussed by the CMS upgrade design group Fig. 12.18,
9059 Refs. [639] will have, e.g., direct impact on a muon-trigger definition. The sensor, hybrid
9060 and readout modules are available and interconnected by wire bonds. On the other hand
9061 the 2_in_1 sensor design is a very elegant way saving resources when setting up a tracker
9062 (CMS design Fig. 12.19, Refs. [639]).

⁵On physics event generation level appropriate instruments are missing or of limited use; e.g. ep interactions are not incorporated into PYTHIA8 currently

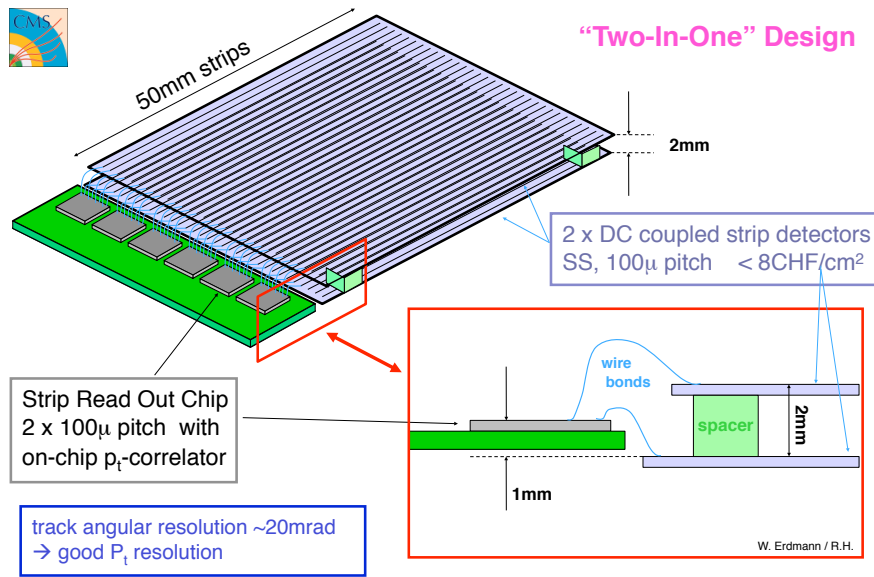


Figure 12.18: Layout of the 2_in_1 strip sensor design used as p_t -trigger setup for the CMS experiment.

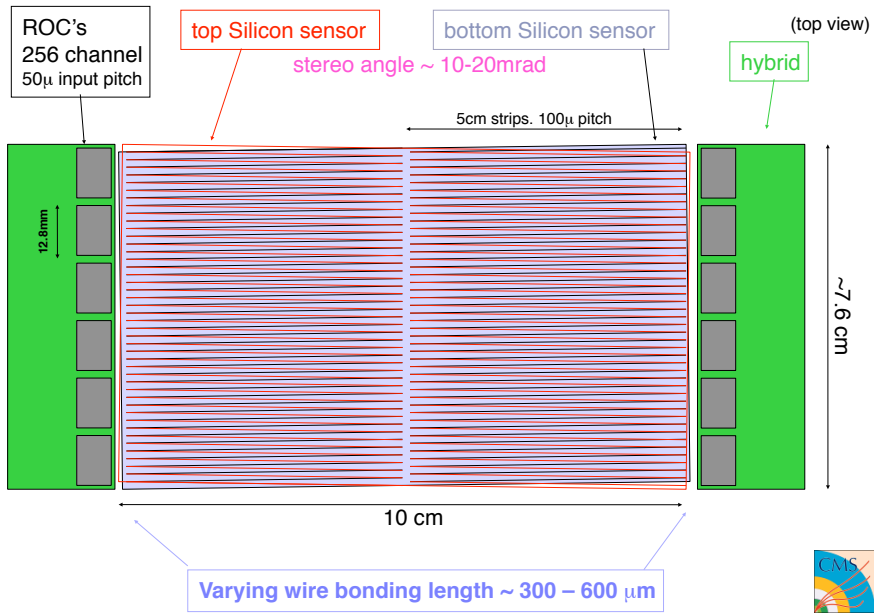


Figure 12.19: Layout of the 2_in_1 strip sensor design used as tracker module. Double use of e.g. power and cooling.

9063 Candidates of readout chips attached to the sensors are e.g. the ATLAS FE-I4
 9064 ($50\mu m \times 250\mu m$) and CMS ROC ($100\mu m \times 150\mu m$) (see Refs. [641], [642]). The sensor
 9065 pitch has to be matched and the electronics scheme defined before.

- 9066 • The size of the largest stave structure to be installed (half z-length $\approx 94cm$) is smaller
 9067 than the stave length used e.g. by ATLAS ($\approx 120cm$). Powering and in that respect
 9068 cooling per stave are therefore less demanding than for the current LHC installations.
 9069 Minimization of cooling effort reduces the material budget directly; cooling is related to
 9070 power consumption issues and it might be a criterion for technology selection. A decision
 9071 on powering concept is needed (serial, parallel powering). It will depend on the template
 9072 chosen for readout and services. The obvious suggestion is to re-apply one scheme used by
 9073 a current LHC experiment inline with the sensor & electronic & readout option selected.

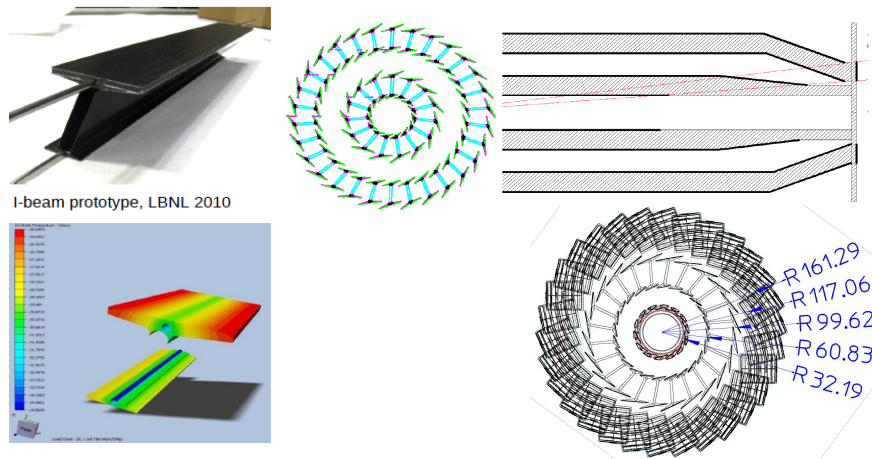


Figure 12.20: Proposed mechanics and sensor layout for the ATLAS pixel upgrade.

- 9074 • The mechanical support and cooling elements have to be chosen to minimize the material
 9075 budget of the setup and hence to diminish the impact of Coulomb multiple-scattering
 9076 on track resolution by the tracker material. The HL-LHC upgrade developments of e.g.
 9077 ATLAS and CMS show the relevance of that topic for the future physics program at the
 9078 second phase of LHC. Rigid but very light mechanics in connection with improved sensor
 9079 arrangement, incorporation of cooling systems and all other services into the support
 9080 structure are the main design criteria for HL-LHC and should be for LHeC as well. In
 9081 Figs. 12.20, 12.21 and 12.22 are possible mechanical solutions for the ATLAS and CMS
 9082 tracker upgrade in the barrel as well as in the forward/backward tracker region shown
 9083 (Refs. [656], [639], [641]). Those designs may well serve as templates for the LHeC experiment.
 9084 An artist view in Fig. 12.23 shows the implementation of the double-I ATLAS pixel
 9085 arrangement into the 4 layer pixel structure of the LHeC experiment. That could be an
 9086 installation template. The goal is the design of a tracker which is transparent enough and
 9087 reaches in terms of radiation length thickness the range $\approx 1.5 - 2\% X_0$. Possible paths
 9088 (orange) for the IN/OUT services of the tracking detectors are sketched in Fig. 12.24.
 9089 The cables and tubes are as far as possible integrated into the support structures of the

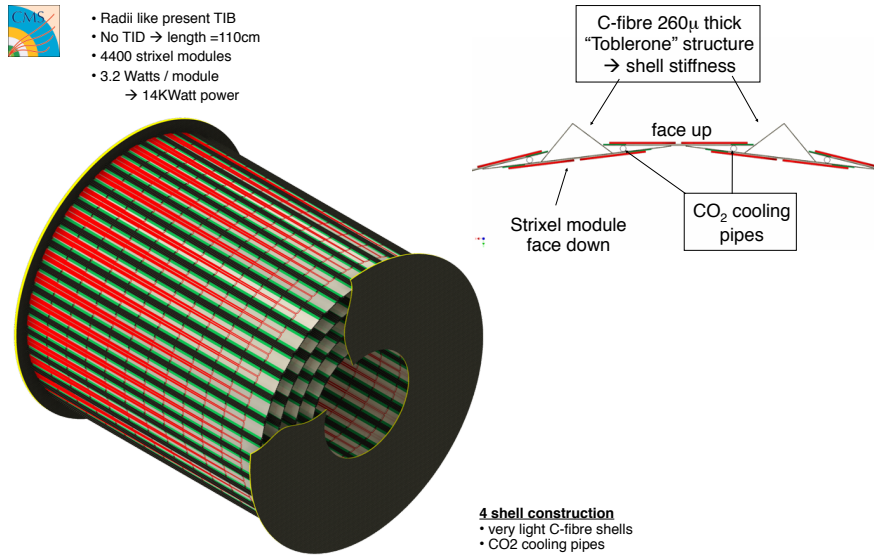


Figure 12.21: Proposed mechanics layout for the CMS inner barrel tracker upgrade.

Mechanics of Disks



Inner & outer ring of blades

CO₂ tubes embedded in half disk support:

- support cylinder:
 - Carbon carbon
 - Grooves for cooling tube
 - Stainless steel tube:
 - 1.8mm OD, 100 μ m wall

Blades:

- all identical
- Rotated by 20° radial
- Tilted by 12° (inner ring)
- 2 modules per blade (ϕ overlap)
- individually replaceable

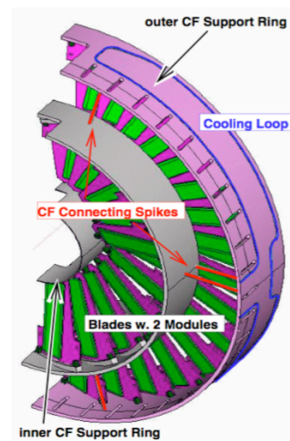
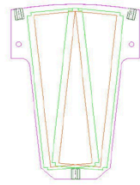


Figure 12.22: Proposed mechanics layout for the CMS tracker wheel upgrade.

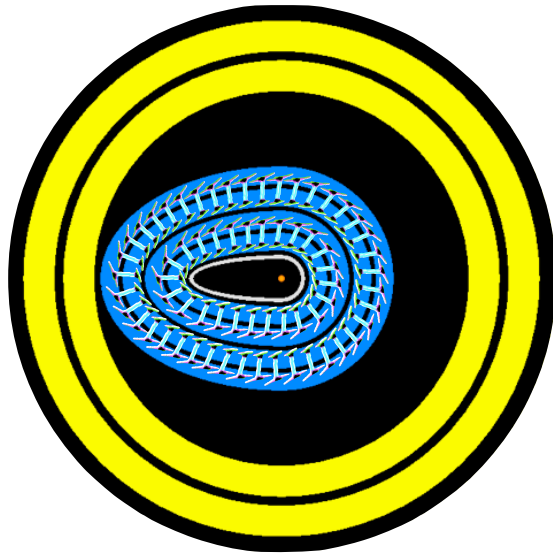


Figure 12.23: Artist view of the pixel sensor arrangement using the double-I ATLAS layout as template (Fig. 12.20).

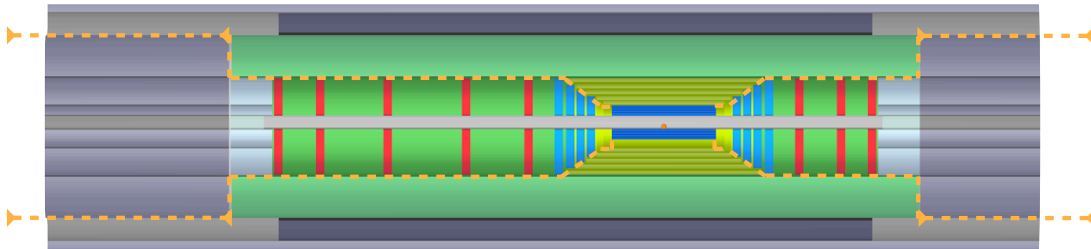


Figure 12.24: Path of services for all tracking detectors (orange). The services are integrated into support structures whenever possible

9090 sub-detectors.

- 9091 • Optimization of detector Read-Out reducing the cost and material impact of cables. An
9092 example is discussed in detail for the ATLAS/CMS HL-LHC opto-link upgrade in Ref.
9093 [657]. The front end electronics buffer depth will depend on bunch crossing rate (25ns)
9094 and trigger/readout speed capability.
- 9095 • Special Interaction Region instrumentation for tuning of the machine minimizing the
9096 background and optimizing the luminosity is needed. Radiation detectors e.g. near mask
9097 and tight apertures are useful for fast identification of background sources. Fast bunch
9098 related informations are collected efficiently e.g. by dedicated diamond detectors (like for
9099 CMS: [658], [659], [660], [661]).

9100 First and preliminary **GEANT4** studies using minimum bias events generated with **Pythia6**
9101 (Ref. [113]) will be discussed in the following section. The simulation of detector responds is
9102 important because it may have impact on technology decisions and will be evaluated further.
9103 A more refined simulation will provide, a more differential picture of the detector responds. Of
9104 course the performance of the detector in line with the software algorithms used define how
9105 accurate the particle flow tracking in jets, the reseed after interactions and conversions can
9106 be solved. That implies that the software solutions play a major role to come up with the
9107 optimized detector finally.

9108 12.5 Geant4 Event Simulations - General Detector De- 9109 scription

9110 12.5.1 Introduction

9111 Minimum bias events in the LHeC Detector have been simulated using the **GEANT4**
9112 Toolkit [662]. In addition **ROOT** [663], **GDML** [664], **AIDA** [665] and **Pythia6** [113] have
9113 also been incorporated. A **ROOT** macro has been written which gives a general description of
9114 the LHeC Detector geometry and materials. This description is then transported from **ROOT**
9115 to **GEANT4** in XML format via **GDML**. A **Pythia6** program has also been used to create
9116 minimum bias ep events. **Pythia6** outputs the events in HEPEVT format. This is then run
9117 through a subroutine to produce a format readable by **GEANT4**. The actual simulations are
9118 completed natively in **GEANT4** once the geometry, materials and events are loaded. The
9119 Analysis is done with **ROOT** (and the Java Analysis Studio **JAS** [665]) which is interfaced to
9120 **GEANT4** via **AIDA**. The flow of these simulations is outlined in Figure 12.25.

9121 12.5.2 Pythia6

9122 The **Pythia6** event used in the **GEANT4** simulations contains γ^*P interactions convoluted with
9123 the γ/e^- flux. This setup contains non vanishing cross sections including semihard QCD, elastic
9124 scattering, single/double diffractive among others (The listed interactions dominate σ_{tot}). In
9125 order for the events to be minimum bias no restrictions are placed on the W or Q^2 range.

9126 Table 12.3 gives the **Pythia6** parameters used for the minimum bias events. The logarithm
9127 of the variables W and Q^2 are given. Since these variables obey amplitudes given by $P(x) \propto \frac{1}{x^2}$

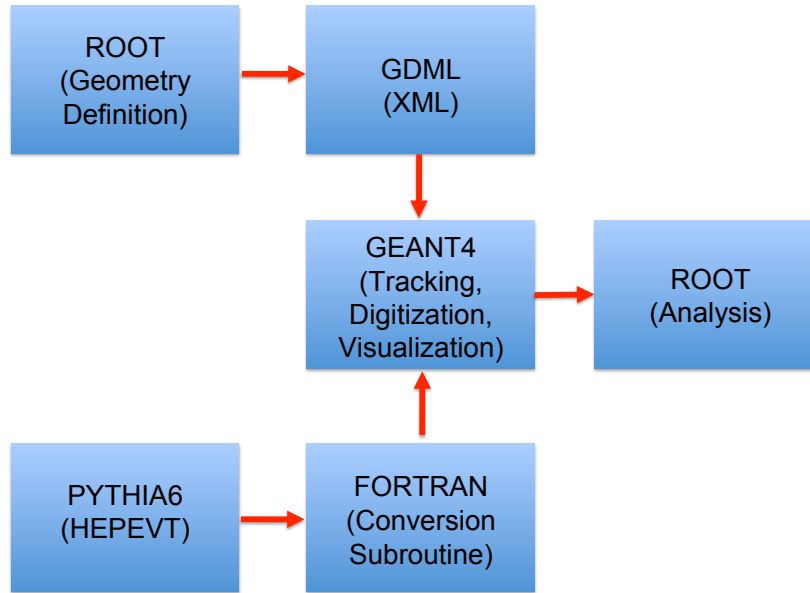


Figure 12.25: Simulation Framework Flow Chart

9128 then $P(\text{Log}(x)) \propto e^{-x^2}$ showing that $\text{Log}(x)$ produces mean and rms values following normal
 9129 statistics.

9130 The tools available for ep event generation are not current. The frontier of high energy
 9131 physics is focused on hadron collisions due to the LHC. The numerous problems present in a
 9132 new energy scale require developers to focus in this area. This results in a lack of development
 9133 of event generation tools for a new energy scale of ep collisions. This is the reason we are using
 9134 **Pythia6** as opposed to its C++ successor. Although it works fine for an approximation it would
 9135 be advantageous to have development here.

Characteristic	Value
$\text{Log}(W)_{mean}$ [GeV]	2.09
$\text{Log}(W)_{rms}$ [GeV]	0.55
$\text{Log}(Q^2)_{mean}$ [GeV^2]	-4.98
$\text{Log}(Q^2)_{rms}$ [GeV^2]	3.15
Electron Energy [GeV]	60
Proton Energy [GeV]	7000

Table 12.3: Pythia6 Parameters

9136 The parameters used to scale the results of the simulation in order to find annual quantities
 9137 are given in Table 12.4.

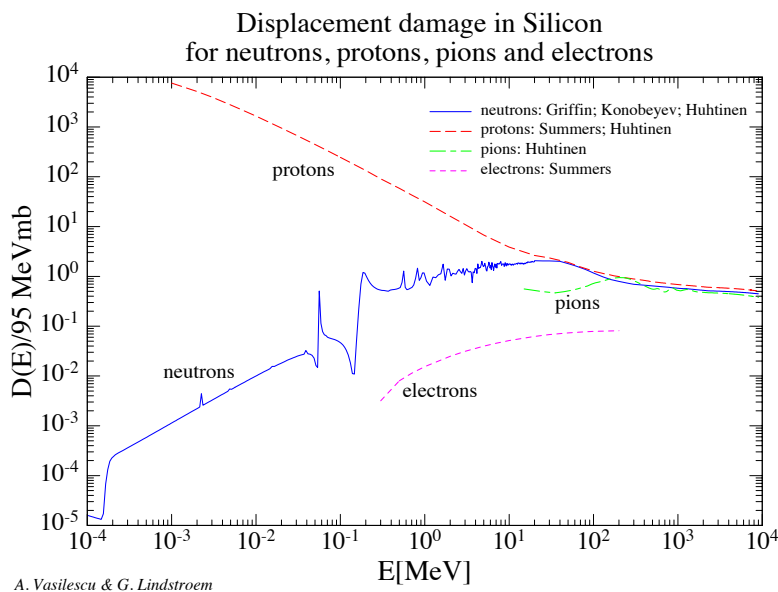
Characteristic	Value
Total Cross Section [mb]	0.0686
Luminosity [$mb^{-1}s^{-1}$]	10^6
$\frac{dN}{dt}$ [int/yr]	2.57×10^{12}

Table 12.4: Scaling Parameters

9138 **12.5.3 1 MeV Neutron Equivalent**

9139 **NEIL Scaling**

9140 In order to find the 1 MeV Neutron Equivalent one must find the appropriate displacement
 9141 damage functions $[D(E)]$ for the particles. By scaling the damage functions by the reciprocal
 9142 of $D(n, 1 \text{ MeV})$ one arrives at a weight which will turn a fluence of random particles into the 1
 9143 MeV Neutron Equivalent fluence. $D(E)$ is not only dependent on particle type but also on the
 9144 material in which the particles are traversing. The $D(E)$ functions used in the simulations can
 9145 be found in Figure 12.26 [666].



A. Vasilescu & G. Lindstroem

Figure 12.26: Displacement Damage for various particles in Silicon

9146 **Scoring**

9147 In order to find the 1 MeV Neutron Equivalent fluence through the tracking portion of the
 9148 detector scoring was incorporated into the **GEANT4** simulations. A user defined scorer was
 9149 used that would calculate the number of hits on the surface of a detector component, weight

9150 the hits according to the appropriate damage functions and finally divide the sum of these
9151 weighted hits by the inner surface area of the detector component. The flux was then scaled
9152 by the number of events per year using the mentioned scaling parameters given in Table 12.4.
9153 The total 1 MeV Neutron Equivalent fluences are given in Table 12.5.

Central Barrel			
Region	ΔZ [cm]	R_{min} [cm]	Fluence [$\frac{N}{cm^2 yr}$]
CPT1	100	3.1	1.38×10^{10}
CPT2	100	5.6	9.99×10^9
CPT3	100	8.1	8.26×10^9
CPT4	100	10.6	7.25×10^9
CST1	116	21.2	6×10^9
CST2	128	25.6	5.66×10^9
CST3	148	31.2	5.38×10^9
CST4	168	36.7	5.25×10^9
CST5	188	42.7	5.16×10^9
Central Endcaps			
Region	Z [cm]	ΔR [cm]	Fluence [$\frac{N}{cm^2 yr}$]
CFT1	70	26	8×10^9
CFT2	80	31.6	7.42×10^9
CFT3	90	37.1	7.08×10^9
CFT4	101	43.1	6.93×10^9
CBT1	-70	26	2.77×10^9
CBT2	-80	31.6	2.48×10^9
CBT3	-90	37.1	2.26×10^9
CBT4	-101	43.1	2.09×10^9
Fwd/Bwd Planes			
Region	Z [cm]	ΔR [cm]	Fluence [$\frac{N}{cm^2 yr}$]
FST1	130	43.1	8.2×10^9
FST2	190	43.1	1.14×10^{10}
FST3	265	43.1	1.63×10^{10}
FST4	330	43.1	2.29×10^{10}
FST5	370	43.1	2.75×10^{10}
BST1	-130	43.1	1.96×10^9
BST2	-170	43.1	1.91×10^9
BST3	-200	43.1	1.99×10^9

Table 12.5: 1 MeV Neutron Equivalent Fluence

9154 **Histogramming**

9155 A different approach was used in order to find the 1 MeV Neutron Equivalent fluence distribution
 9156 in R_{polar} and Z . In order to retain data generated on the event level instead of the run level a
 9157 set up of Sensitive Detectors [SD] must be initialized that will measure user defined quantities
 9158 for traversing particles. The entire tracking region was set as one SD, with each hit containing
 9159 the position information, and the current $D(E)$ value of the given track. A 2D histogram
 9160 is generated for the variables R_{polar} and Z . The intensity (each hit weighted by its $D(E)$ value)
 9161 is then scaled by the number of events in the run, the number of events per year, and a fluence
 9162 weighting function. This function divides the number of entries in each bin by the average
 9163 surface area the bin represents (i.e. $2\pi R_{mean}\Delta Z$ where R_{mean} is the mean R value which the
 9164 bin spans and ΔZ is the width of the Z bins). By this weighting process the resulting 2D
 9165 histogram (Figure 12.27) displays the 1 MeV Neutron Equivalent Fluence in $\frac{cm^{-2}}{year}$.

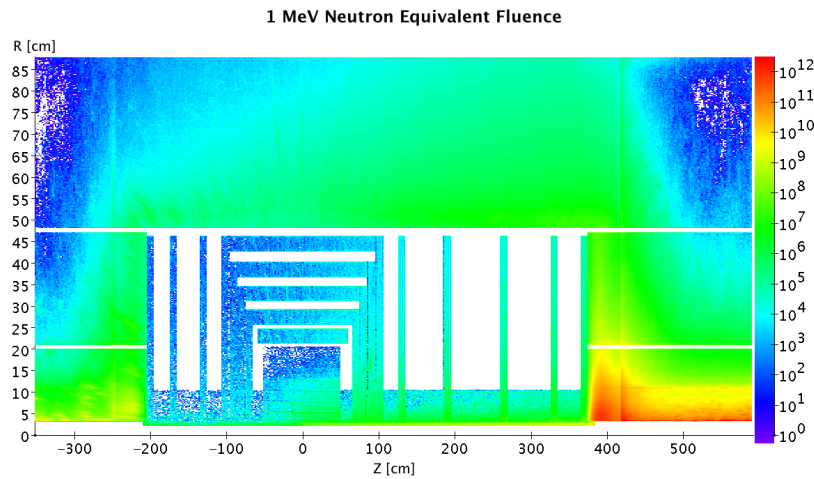


Figure 12.27: 1 MeV Neutron Equivalent Fluence [$cm^{-2}/year^{-1}$].

9166 **12.5.4 Nearest Neighbor**

Tracking Component	Hits under $10 \mu m$ [%]
CFT1	0.18
CFT4	0.23
FST1	0
FST5	0.1

Table 12.6: Nearest Neighbor under $10 \mu m$

9167 The **Geant4** simulations were also used to find the resolution required in the forward track-
 9168 ing. Firstly, the flux through the surface of CFT1, CFT4, FST1, and FST5 was found. A

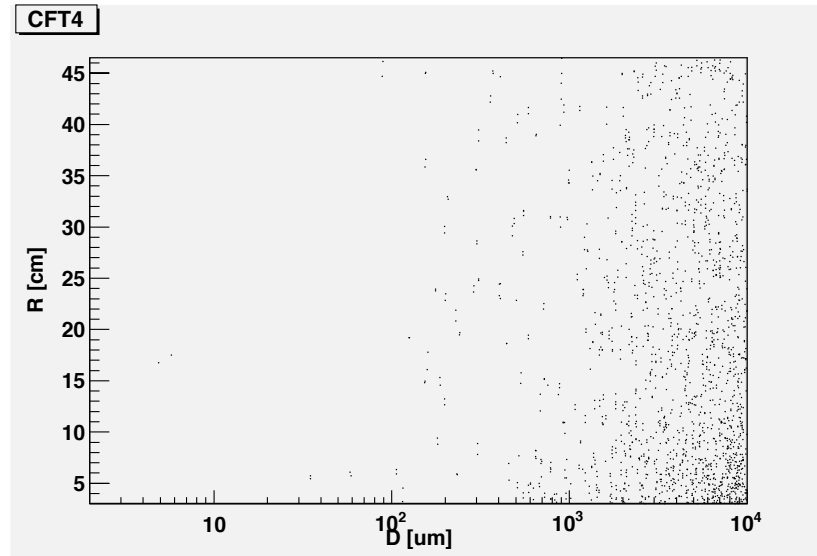


Figure 12.28: Nearest Neighbor distribution for CFT4

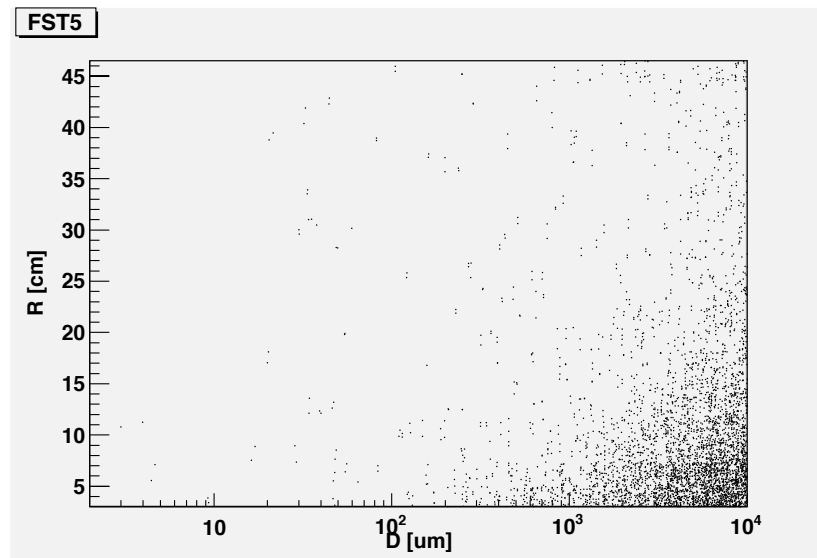


Figure 12.29: Nearest Neighbor distribution for FST5

9169 minimization algorithm is then used to find the nearest neighboring hit at the $Z = \text{constant}$
 9170 surface for each hit. This distance scale is characteristic of the resolution required for the
 9171 tracking component in question. The nearest neighboring hit distribution is calculated on the
 9172 event level. This implies that only the hits from the same event are compared. This will have
 9173 to be studied further to take pileup into account, however information on the event level is a
 9174 nice approximation. The nearest neighbor distribution for CFT4 is shown in Figure 12.28 and
 9175 for FST5 in Figure 12.29. The x axis contains the value of the nearest neighbor for each hit in
 9176 terms of μm while the y axis contains R in terms of cm. A required resolution of 10 or less μm
 9177 would require pixel detectors instead of strip detectors. The CFT4 and FST5 Figures display a
 9178 very low hit density in this area. The percentage of hits with $D < 10 \mu\text{m}$ for the four tracking
 9179 components in question are given in Table 12.6.

9180 12.5.5 Cross Checking

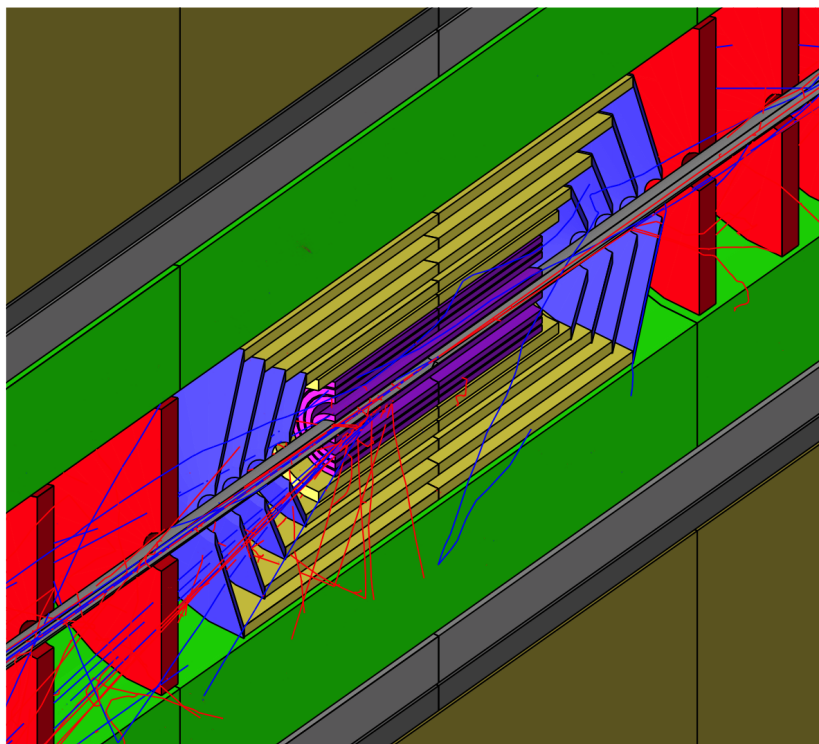


Figure 12.30: G4 Event

9181 DAWN was used for visualization of the detector. This was able to produce clear pictures
 9182 which was one way to make sure the translation of geometry from **ROOT** to **GEANT4** went
 9183 as expected. An event in the central tracking region is presented in Figure 12.30.

9184 In addition to the minimum bias events, **Pythia6** was also used to create some Leptoquark
 9185 events. This was one method of checking the **Pythia6** input (i.e. that the events produced
 9186 describe the given kinematic range and cross sections available). However it was also utilized to

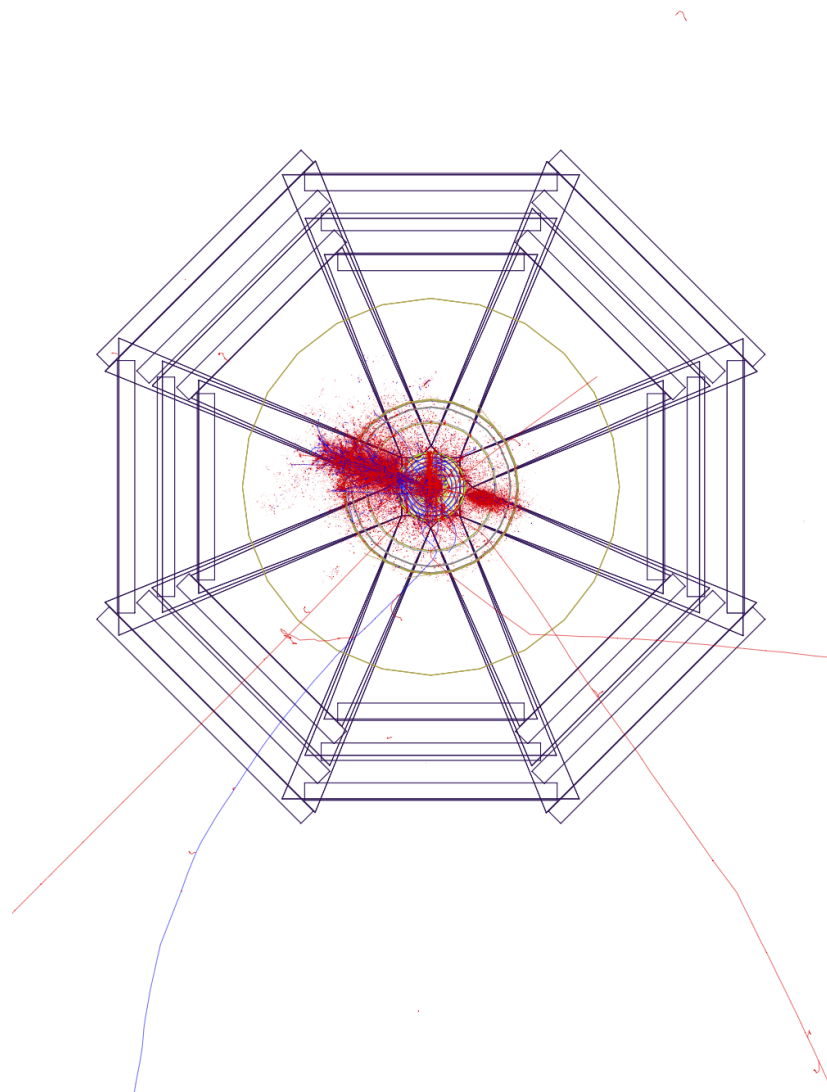


Figure 12.31: Leptoquark Event XY

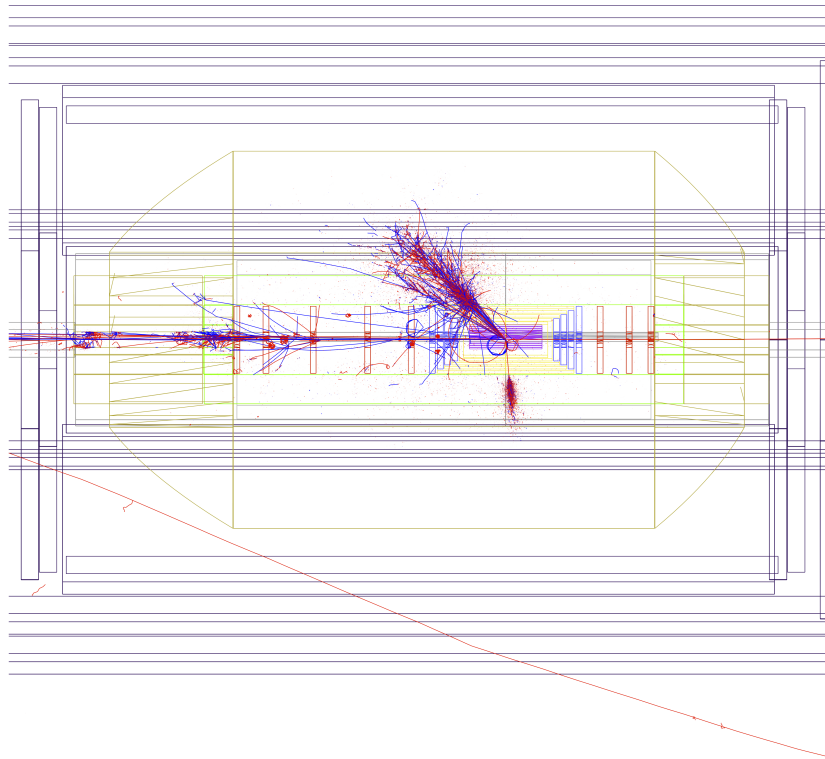


Figure 12.32: Leptoquark Event RZ

9187 determine the detector response at various kinematic ranges. Since $\sigma_{EM} \propto \frac{1}{Q^4}$ The minimum
9188 bias events have very low Q^2 and therefore very forward jets, which leaves almost no activity
9189 in the barrel HCAL. By looking at some high Q^2 events it is possible to see the response of the
9190 hadronic calorimetry in the barrel region, making sure it is showering correctly. Some pictures
9191 of the Leptoquark events are given in Figure 12.31 and Figure 12.32.

9192 12.5.6 Future Goals

9193 There are many goals still to be accomplished by the LHeC Detector Simulations. The set up
9194 needs to be modified to include a detailed calorimeter description. Currently the calorimeter
9195 volumes contain a mixture of FR4, Krypton, Active and Passive material which is weighted
9196 according to a realistic set up. This design must be replaced with a realistic setup of the
9197 calorimeters. This also needs to be done for the tracking which is currently composed of single
9198 silicon pieces instead of smaller modules. The majority of the work in making these changes
9199 comes from the required read out geometry and sensitive detector set up that would be required
9200 for analysis of a complicated geometrical structure. This also might require a restructuring of
9201 the simulation package. Since the detector description was done first in **ROOT**, **GDML** was
9202 an option to allow utilizing **GEANT4** without recoding the geometry. However if the geometry
9203 will significantly change then this might benefit from being done natively in **GEANT4**. Of
9204 course the Geometry needs to be iterated until it actually describes the exact detector (service
9205 pipes, read out, etc...). However this will come with the TDR.

9206 Finally the stability of the simulations needs to be assessed. Eventually a complex multi-
9207 functional detector simulation package needs to be produced. This is best done by wrapping
9208 numerous simulation toolkits into a single package utilizing **ROOT**, such as **AliROOT** [667],
9209 [668], [669] or **ILCROOT** [670]. The LHeC simulations at some point need to make a shift
9210 towards creating a package like this, in order to promote greater functionality and greater
9211 accessibility.

9212 12.6 Calorimetry

9213 The LHeC calorimetry has to fulfill the requirements described in ???. The goal is a powerful
9214 level 1 trigger and detector able to resolve shower development in 3D space with no or minimal
9215 punch through. High transverse and longitudinal segmentation are necessary along with a good
9216 matching to tracking devices for particle identification and separation of neutral and charged
9217 particles. The calorimetry needs to be hermetic for the identification of the charged current
9218 process and good measurement of E_T^{miss} . These considerations are summarized in Tab. 11.1.

9219 The baseline design foresees a modular structure of independent electromagnetic and hadronic
9220 calorimeter components. A high segmentation and minimal dead material between the tracking
9221 and the calorimetry will allow a precise energy measurement and identification or separation
9222 of charged and neutral particles. In order to fully contain electromagnetic showers a thickness
9223 of about $25 \sim 30X_0$ is required. The design of the EMC modules will vary when moving from
9224 the very forward region, where energies up to $\mathcal{O}(1\text{TeV})$ are expected to the barrel and the rear
9225 region where the detection of the scattered low energy electron has to be precisely tagged and
9226 measured.

9227 Following the option A of baseline design, the EMC is surrounded by the coil providing the
9228 magnetic field for momentum measurement in the tracking.

9229 The hadronic calorimetry, naturally surrounding the EMC is also foreseen to have a sufficient
9230 depth and a projective modular design to precisely measure over the full energy range high
9231 energetic jets and provide a granularity such to faithfully separate multiple jet events. Given
9232 the energies available at the LHeC, the forward part will be much more extended (up to $10\lambda_I$)
9233 for full containment of energies up to few TeV.

9234 In the next sections the baseline design for the EMC and HAC components is presented
9235 and discussed along with a comparison of technologies and the experience from other HEP
9236 detectors. A brief outlook towards ongoing and new technologies R&D which would even
9237 extend the precision and the scope of the detector are briefly addressed.

9238 12.6.1 The Barrel Electromagnetic Calorimeter

9239 Due to the very asymmetric energy and particle multiplicity distribution over the azimuthal
9240 angle, the detector baseline design foresees a composite electromagnetic calorimeter which includes
9241 a Liquid Argon Calorimeter in the barrel region. For the endcaps very diverse requirements are
9242 pushing the design toward different technical choices.

9243 Liquid argon (LAr) based calorimetry is a well established technology in HEP. LAr sampling
9244 calorimeter technique with “accordion-shaped” electrodes is used in ATLAS for all electromag-
9245 netic calorimetry covering the pseudorapidity interval $2.8 < \eta < -2.4$. The choice of liquid
9246 Argon calorimetry follows from its intrinsic excellent linearity, stability in time and radiation
9247 tolerance ([671], [672], [673], [674], [675], [676], [677], [678]).

9248 At the LHeC, LAr would provide the required energy resolution, detector granularity and
9249 projective design. The detector with an outer diameter of 88 cm would share the same cryostat
9250 of the main solenoid which in case of a Linac-Ring design would include the bending dipoles.
9251 Size and construction details of the cryogenics are described in ???. At larger radii, where most
9252 of the calorimeter weight is located and where the radiation levels are low, a less expensive
9253 technology based on absorber-scintillator hadronic calorimeter can be used. The performance
9254 of the LAr calorimetry system has been extensively addressed [679] and here only specific design
9255 issues and detector simulation will be discussed.

9256 Fig. 12.33 shows a x - y and r - z view of the LHeC Barrel EM calorimeter. As for the ATLAS
9257 LAr Calorimeter, the detector volume is filled with a projective accordion structure based on
9258 lead absorber. This layout allows for the extraction of the detector signals without significantly
9259 degrading the high-frequency components which are vital for fast shaping. The flexibility in
9260 the longitudinal and transverse segmentation, and the possibility of implementing a section
9261 with narrow strips to measure the shower shape in its initial part, represent additional advan-
9262 tages. It is worth noticing that due to the asymmetric design, the projective structure is not
9263 fully symmetric as the calorimeter and the solenoid center are shifted forward with respect
9264 to the interaction point. Fig. 12.34 shows a detail of the accordion-electrode structure. The
9265 layout, adapted from the ATLAS LAr Calorimeter [679], has been faithfully implemented in
9266 a **GEANT4** simulation. Several aspects considerations and design choices were inherited and
9267 adapted to the LHeC design. Their merits were then compared for several critical performance
9268 issues, such as energy resolution, accuracy in position and angular measurements and particle
9269 identification, and balanced against arguments of reliability and cost.

9270 The readout granularity has been subdivided in 3 cylindrical sections of increasing size in
9271 $\Delta\eta \times \Delta\phi$. As in Fig. 12.35, the first sampling section of the electromagnetic calorimeter
9272 has a very fine granularity ($\Delta\eta \times \Delta\phi = 0.003 \times 0.1$), to optimize the ability to separate photons
9273 from π^0 energy deposits. The second sampling section, mainly devoted to energy measurement,

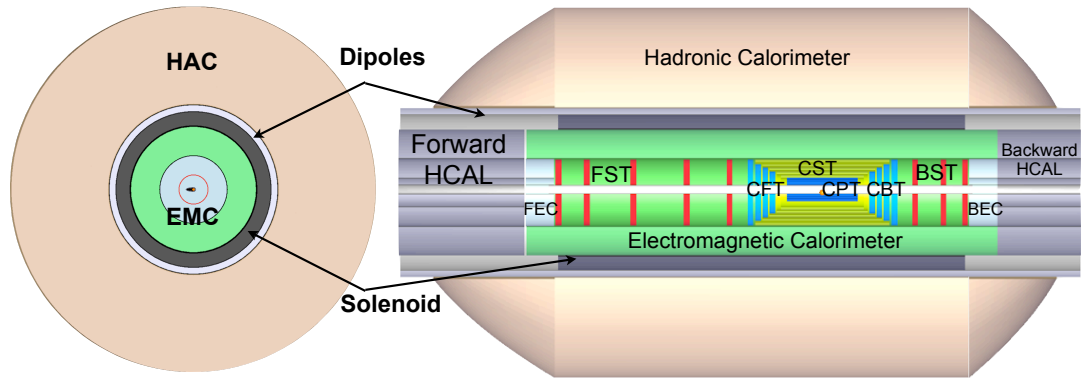


Figure 12.33: x - y and r - z view of the LHeC Barrel EM calorimeter (green).

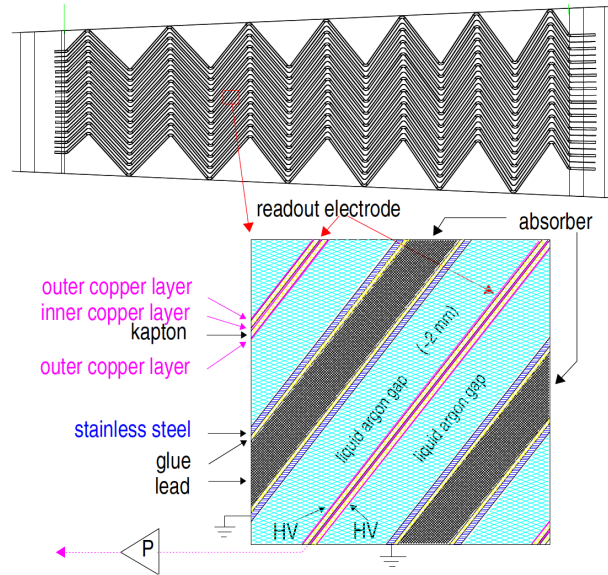


Figure 12.34: Longitudinal view of the accordion structure of the ATLAS LAr Calorimeter

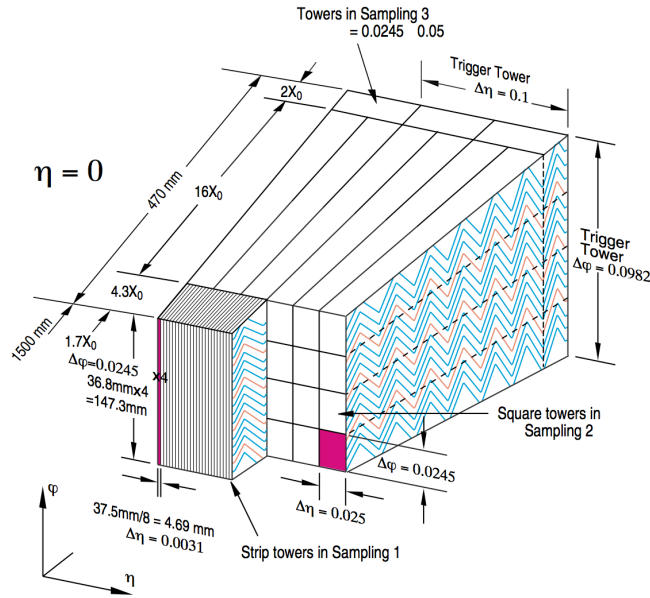


Figure 12.35: 3D view of the accordion structure of the ATLAS LAr Calorimeter

9274 has a granularity of 0.025×0.025 , and the back sampling has a slightly coarser granularity of
 9275 $\Delta\eta \times \Delta\phi = 0.050 \times 0.025$.

9276 A basic cell consists of an absorber plate, a liquid argon gap, a readout electrode and a
 9277 second liquid argon gap. The mean thickness of the liquid argon gap is constant (2.1mm) along
 9278 the whole barrel and along the calorimeter depth (more details see [679]).

9279 12.6.2 The Hadronic Barrel Calorimeter

9280 In the barrel region a sampling device made out of steel and scintillating tiles, as absorber
 9281 and active material is foreseen as baseline design. The detector would provide the required
 9282 mechanical stability for the inner LAr and Magnet cryostat along with the iron required for the
 9283 return flux of the solenoidal field.

9284 The simple and very well proven idea of calorimetry is particularly suited for the LHeC en-
 9285 vironment since also in use in ATLAS [679]. The absorber structure is a laminate of steel plates
 9286 of various dimensions, connected to a massive structural element referred to as a girder. The
 9287 highly periodic structure of the system allows the construction of a large detector by assembling
 9288 smaller sub-modules together. Since the mechanical assembly is completely independent from
 9289 the optical instrumentation, the design becomes simple and cost effective. Simplicity has been
 9290 the guideline for the light collection scheme used as well: the fibers are coupled radially to the
 9291 tiles along the outside faces of each module. The laminated structure of the absorber allows for
 9292 channels in which the fibers run. The use of fibers for the readout allows to define a tridimen-
 9293 sional cell read-out, creating a projective geometry for triggering and energy reconstruction. A
 9294 compact electronics read-out is housed in the girder of each module. Finally, the read-out of

9295 the two sides of each of the scintillating tiles into two separate photomultipliers provides the
 9296 redundancy needed during the expected period of operation.

IE-Calo Parts	FEC1	FEC2		EMC		BEC2	BEC1
Min. Inner Radius R [cm]	3.1	21		48		21	3.1
Min. Polar Angle θ [°]	0.48	3.2		6.6/168.9		174.2	179.1
Max. Pseudorapidity η	5.5	3.6		2.8/-2.3		-3.	-4.8
Outer Radius [cm]	20	46		88		46	20
z-length [cm]	40	40		660		40	40
Volume [m^3]	0.3			11.3		0.3	
H-Calo Parts barrel			FHC4	HAC	BHC4		
Inner Radius [cm]			120	120	120		
Outer Radius [cm]			260	260	260		
z-length [cm]			217	580	157		
Volume [m^3]			121.2				
H-Calo Parts Inserts	FHC1	FHC2	FHC3		BHC3	BHC2	BHC1
Min. Inner Radius R [cm]	11	21	48		48	21	11
Min. Polar Angle θ [°]	0.43	2.9	6.6		169.	175.2	179.3
Max/Min Pseudorapidity η	5.6	3.7	2.9		-2.4	-3.2	-5.
Outer Radius [cm]	20	46	88		88	46	20
z-length [cm]	177	177	177		117	117	117
Volume [m^3]	4.2				2.8		

Table 12.7: Summary of calorimeter dimensions.

The electromagnetic barrel calorimeter is currently represented by the barrel part EMC (LAr-Pb module); the setup reaches $X_0 \approx 25$ radiation length) and the movable inserts forward FEC1, FEC2 (Si-W modules ($X_0 \approx 30$) and the backward BEC1, BEC2 (Si-Pb modules; $X_0 \approx 25$).

The hadronic barrel parts are represented by FHC4, HAC, BHC4 (forward, central and backward - Scintillator-Fe Tile modules; $\lambda_I \approx 8$ interaction length) and the movable inserts FHC1, FHC2, FHC3 (Si-W modules; $\lambda_I \approx 10$), BHC1, BHC2, BHC3 (Si-Cu modules, $\lambda_I \approx 8$) see Fig. 12.9.

9297 In the baseline design the calorimeter consists of a cylindrical structure with inner and
 9298 outer radius of 120 and 260 cm respectively (Tab. 12.7). The central HAC barrel part is 580 cm
 9299 in length along the beam axis. Endcaps extend the calorimetry further in the forward and
 9300 backward direction in order to guarantee full energy containment. The detector cylinder would
 9301 be likely built of several independent wedges along the azimuthal direction while the modularity
 9302 and segmentation might vary depending on the adopted machine design (Ring-Ring or Linac-
 9303 Ring). The Tile Calorimeter forms the shell of the inner part of the LHeC detector. Within its
 9304 volume, once the barrel and the extended barrels are assembled, all the sub-detectors, except
 9305 the muon system, will be placed. The massive iron structure is rigid enough to support their

9306 weight, with the such important components being the full Liquid Argon cryostat and the
9307 solenoid.

9308 The main function of the Tile Calorimeter is to contribute to the energy reconstruction of the
9309 jets produced in $e-p$ interactions and, with the addition of the end-cap and forward calorimeters,
9310 to provide a good p_T^{miss} measurement. Achieving this at the LHeC is not so straightforward as
9311 the large proton beam energy and the electron proton energy imbalance center requires good
9312 performance over an extremely large dynamic range extending from a few GeV up to several
9313 TeV.

9314 The guidelines for the design of this device are derived from the required overall physics
9315 performance which call for an intrinsic resolution for jets in the barrel region of $50\% \cdot \sqrt{E/GeV}$
9316 with a segmentation of $\Delta\eta \times \Delta\phi = 0.1 \times 0.1$ (11.1).

9317 The granularity of the Tile Calorimeter is important to finely match the electromagnetic
9318 LAr calorimeter in front and correct for the dead material of the magnet complex. The pro-
9319 posed hadronic segmentation for the cells behind the electromagnetic section, will allow an
9320 efficient hadron leakage cut, needed for electron and photon identification. A reasonable longi-
9321 tudinal segmentation, especially around the maximum depth of the shower, favours an appro-
9322 priate weighting technique to restore, at the level of 1-2%, the linearity of the energy response
9323 to hadrons, which is intrinsically non-linear because of the non-compensating nature of the
9324 calorimeter. At the highest energies expected, the resolution of the calorimetry is dominated
9325 by the constant term, for which the largest contribution comes from the detector non-linearity
9326 and from the calibration. An attempt is made to keep the constant term below the 2% level. For
9327 the measurement P_T^{miss} a large contribution comes from the overall acceptance of the detector.

9328 To improve the energy measurement in the barrel/end-cap region, it will be evaluated in
9329 detail where a presampler system with the same granularity as the corresponding calorimeter
9330 region has to be implemented in front of the barrel/end-cap systems. Such presampler has a
9331 limited active thickness (≈ 5 mm) and does not really matter in terms of material impact and
9332 space requirements.

9333 12.6.3 Endcap Calorimeters

9334 Calorimetry in the forward and backward direction at the LHeC is of extreme importance: in the
9335 forward region highest energy deposits require high granularity and very good scale calibration,
9336 in the backward region high sensitivity to low energy electrons and a good e/h separation is
9337 important to suppress hadronic background.

9338 As seen from Fig. 12.27 the very forward and to less extend also the backward parts of the
9339 calorimeter are specifically exposed to dense particle radiation and have to be radiation hard
9340 by design. Synchrotron radiation and any further background radiation has to be tolerated
9341 additionally.

9342 Fig. 12.9 shows in detail the encap calorimeters for the Ring-Ring design. The two-phase
9343 experimental program requires the endcaps to be modular as these components will be either
9344 moved along the beam line or removed to allow the placement of the strong focussing magnets
9345 for the high energy run. Relevant dimensions and specifications are summarised in Tab. 12.7

9346 For the Linac-Ring design, where no additional magnets along the beampipe will be required,
9347 the subcomponents FHC2/FHC3 and BHC2/BHC3, can be unified in single modules for the
9348 forward and backward direction, respectively.

9349 We envisage excellent performance regarding:

- 9350 • electron identification in jets (tagging and e from heavy quark production); precision
9351 measurement of showers,
- 9352 • identifying heavy flavour production by partial reconstruction,
- 9353 • good γ separation by identified impact, thus discriminating γ/π^0
- 9354 • hadronic and electromagnetic signatures, also in case of e^\pm -*Ion* interactions
- 9355 • jet finding, jet energy and impact position measurements
- 9356 • Level one triggering

9357 The tight geometry of the insert calorimeters require a non conventional and challenging
9358 design based on former developments [680], [681], [682], [683], [684], [685], [686], [687]. The
9359 choice of a tungsten absorber specifically for the forward inserts is driven by its very short
9360 radiation length and a large absorption to radiation length ratio. About 26 cm of tungsten
9361 will absorb the electromagnetic showers completely and will contain the hadronic shower to a
9362 large extent and over a large range of energy ($\approx 30X_0 + \approx 10\lambda_I$). The electromagnetic as the
9363 hadronic part can be combined even in the same compartment to minimize boundary effects.

9364 An alternative to the tungsten hadronic absorber is copper (*Cu*). Simulations have been
9365 performed to compare the different absorbers. Since the backward inserts have more relaxed
9366 requirements, the absorber chosen are lead *Pb* for the electromagnetic part and *Cu* for the
9367 hadronic one. For the Ring-Ring option, where no dipole field along the beampipe is required a
9368 further and more economical choice instead of *Cu* could be steel *Fe*. The active signal sensors
9369 for both the forward as the backward calorimeter arrangements have been chosen to be Si-strip
9370 (electromagnetic fwd/bwd parts) and Si-pad (hadronic fwd/bwd parts), respectively.

9371 12.7 Calorimeter Simulation

9372 This sections summarizes some first simulations describing the barrel calorimeters, endcap
9373 calorimeters default setups as well as some alternative sampling arrangements. The calorimeter
9374 components presented have been simulated using **GEANT4.9.2** [662] with single and multiple
9375 particle events along with full e - p events from the **QGSP-3.3** [688] physics list. The Quark-
9376 Gluon String Precompound (**QGSP**) is based on theory-driven models and uses the quark-
9377 gluon-string model for interactions and a pre-equilibrium decay model for fragmentation.

9378 The detector raw structure, including the various layers of active, absorbing and support
9379 material were coded and inserted in the simulation. Energy resolutions for electromagnetic and
9380 hadronic deposits were studied along with concepts for optimal trigger and signal reconstruc-
9381 tion. Particular attention was put into the key features and the construction constraints of
9382 the detector, namely the beam optics and the magnets (solenoid and the Linac-Ring dipoles).
9383 Where a similar design from an existing or developing detector was available, the results are
9384 presented complemented by referenced studies.

9385 The energy resolution of a calorimeter is parameterized by the following quadratic sum:
9386
9387

$$\frac{\sigma_E}{E} = \frac{a}{\sqrt{E}} \oplus b \quad (12.1)$$

9388 where E is the particle energy in GeV , a is the stochastic term, which is arising from fluctuations
9389 in the number of signal producing processes, b is the constant term, which includes
9390 imperfections in calorimeter construction, fluctuations in longitudinal energy containment, non-
9391 uniformities in signal collection etc. A third term c is often also added which would represent
9392 the noise in experimental data description. The energy deposition of primary and secondary
9393 particles in the calorimeter was obtained using **GEANT4**, and fitted to extract a and b . Effects
9394 including the readout process were not considered at this stage.

9395

9396 **12.7.1 Liquid Argon Barrel Calorimeter Simulation**

9397 The parallel geometry accordion calorimeter was simulated with accordion shapes absorbers
9398 and LAr. Absorber sheets are 2.2mm thick lead and LAr gaps are 3.8mm. Both absorber
9399 and LAr gap have accordion fold length of 40.1mm and 13 bend angles of 90° . A total of 62
9400 absorber sheets each 250 cm wide in the z -direction were simulated (Fig. 12.36). An example
9401 of a 20 GeV incident single electron is shown in Fig. 12.37. The energy resolution for electrons
9402 was obtained from ratio of the mean and the standard deviation of the electron response, both
9403 obtained by fitting a gaussian to the energy spectrum. Figure 12.38 shows the energy resolution
9404 for electrons of energy between 10 and 400 GeV. These results are in agreement with [678]. In
9405 the simulation the energy deposited in the active material is normalized to the energy of the
9406 incident particle.

9407 The simulation has also been performed to see the energy resolution variations of combined
9408 system (accordion and tile calorimeter) with and without a thick Aluminium layer in between
9409 simulating the effect of the magnet complex. The study has been performed with particles in
9410 a wide range of energy and incident angle in order to simulate the detector behaviour at for
9411 particle entering the calorimeters at different z . The Aluminium layer of 16cm represent the
9412 solenoid/dipole/cryostat system between the EMC and HAC calorimeters.

9413 Hadronic shower simulations have been obtained for the energies from 3 to 200 GeV. The ob-
9414 tained energy resolutions as a function of energy for pions are shown in Fig. 12.39 and Fig. 12.39.

9415 **12.7.2 Electromagnetic (warm) and Hadronic Barrel (tile) Calorimeter Simulation**

9417 Beside the default LAr calorimeter setup comprising the magnet system and the electromag-
9418 netic calorimeter in one cryostat a warm EMC calorimeter has been considered and simulation
9419 performed which are summarized in the following. The barrel part of the warm electromagnetic
9420 (EMC) calorimeter module consist of a lead-scintillator sampling calorimeter, with 20 layers of
9421 0.85 cm Pb sheets interspaced by 4 mm plastic scintillator plates. Thus the radiation length of
9422 the EMC test module correspond to $30X_0$ ($X_0(\text{Pb})=0.56\text{cm}$). All dimensions of the calorimeter
9423 has been kept according to the default solution summarized in Tab. 12.7. For the simulation
9424 the Pb-scintillator EMC was placed 30 cm in front of the Hadronic Calorimeter (HAC). An
9425 aluminum block of 16 cm was placed between EMC and HAC as illustrated in Fig. 12.40. The
9426 sketched module would be one out of 6 azimuthal segments of the complete barrel EMC and
9427 HAC.

9428 The HAC is an ATLAS type scintillator-steel tile calorimeter and made out of 4 mm thick
9429 steel plates sandwiched by 3 mm thick scintillator tiles. The tiles are placed in planes perpen-
9430 dicular to the z -direction. The absorber structure consist of 262 repeated period, each of which

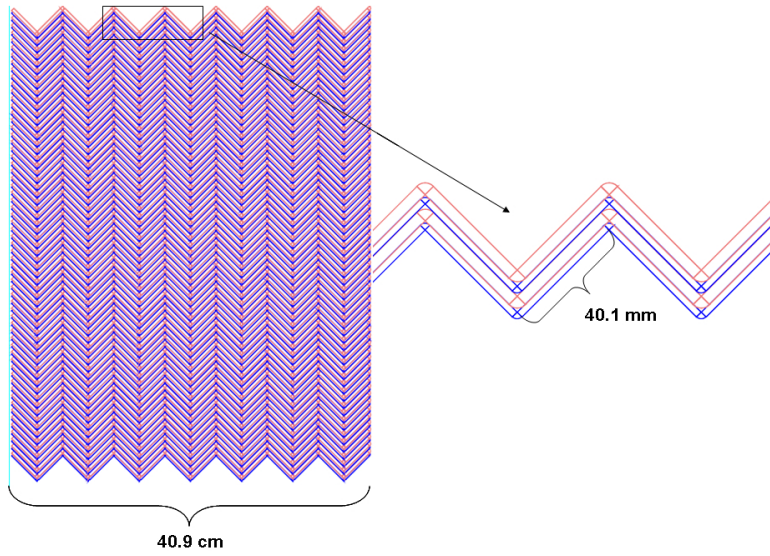


Figure 12.36: View of the parallel geometry accordion calorimeter.

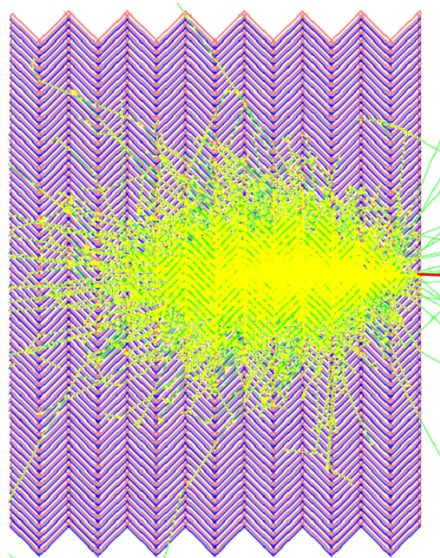


Figure 12.37: Simulation of the single electron energy with 20 GeV.

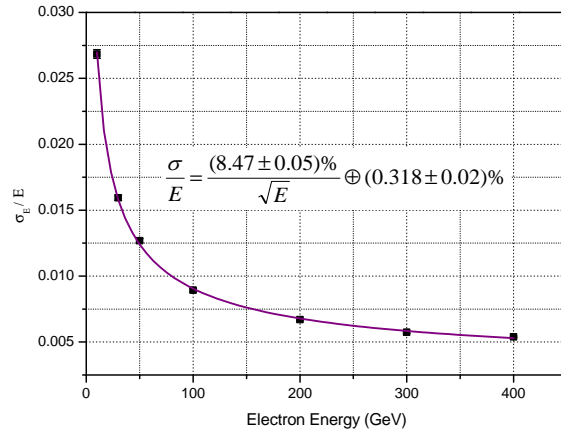


Figure 12.38: Accordion Calorimeter energy resolution for electrons between 10 and 400 GeV.

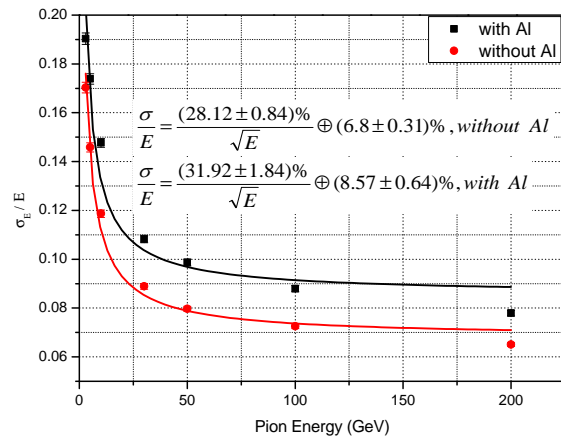


Figure 12.39: Accordion and Tile Calorimeter energy resolution for pions with and without 16cm Al block.

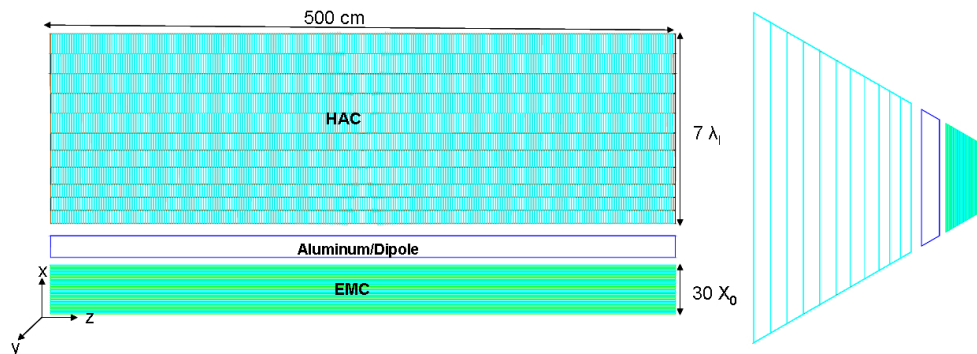


Figure 12.40: Simulation - barrel calorimeter module EMC/solenoid-dipole-system(16cm Al-block)/HAC.

9431 spans 19 mm in z and consist of 16 mm of steel and 3 mm of scintillator tile. 11 transverse rows
 9432 of tiles are used in a module. The tile rows are numbered from inner to outer radius. The total
 9433 interaction depth of the HAC prototype correspond to $\lambda_I = 7$. The longitudinal segmentation
 of the HAC module is described in Tab. 12.8.

Tile Rows	Height of Tiles in Radial Direction	Scintillator Thickness
1-3	97 mm	3 mm
4-6	127 mm	3 mm
7-11	147 mm	3 mm

Table 12.8: Longitudinal (into x-direction) segmentation of the hadronic tile calorimeter HAC.

9434

9435 **GEANT4-4.9.2** [662] was used with the **QGSP-3.3** [688] physics list for the simulations.
 9436 The **QGSP** physics list is based on theory-driven models: it uses the quark-gluon-string model
 9437 for interactions and a pre-equilibrium decay model for fragmentation. The energy distribution
 9438 was fitted with a Gaussian, $\pm 2\sigma$ from the mean, and the resolution was calculated for each
 9439 point. An example of the energy distribution and Gaussian fit is shown in Fig. 12.41. The a
 9440 and b parameters are calculated from the fit of σ/E .

9441

9442 The energy resolution of the Pb-scintillator sampling EM-Calorimeter has been calculated
 9443 for electrons within the energy range 10-400 GeV (Fig. 12.42). In **GEANT4** the energy deposited
 9444 in the active material is normalized to the energy of the incident simulated particle.
 9445 The performance of the Hadron Calorimeter in a standalone mode has been investigated. The
 9446 energy resolution of the tile Calorimeter was simulated for electrons and pions within the energy
 9447 range 3-200 GeV (Fig. 12.43 and 12.44). The obtained stochastic term values are consistent
 9448 with [678]. The response to electrons has been studied to understand the properties of the tile
 9449 calorimeter.

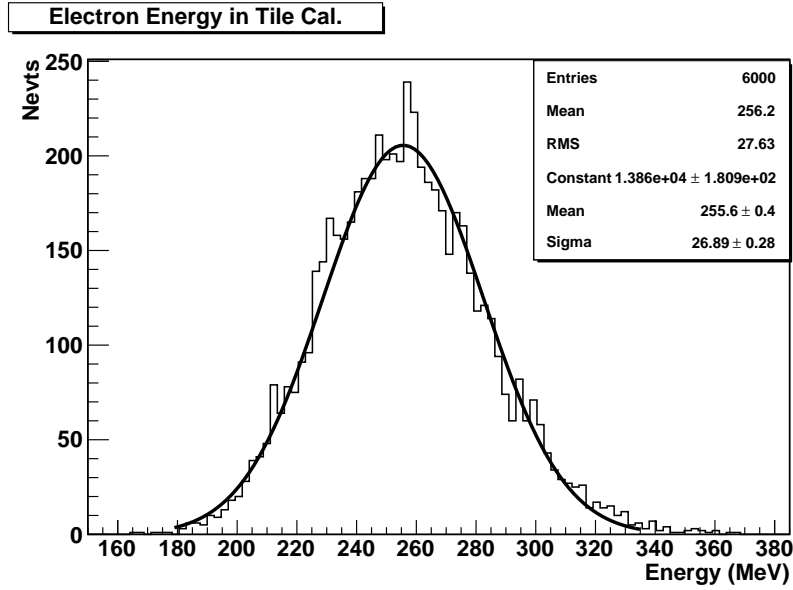


Figure 12.41: Example of the pion energy distribution and the Gaussian fit to obtain σ and mean values (Run taken at $\theta = 70^\circ$ and 10 GeV).

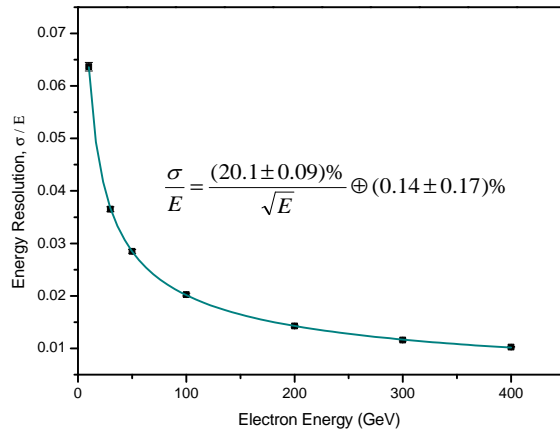


Figure 12.42: EM-Calorimeter energy resolution for electrons at $\theta = 90^\circ$.

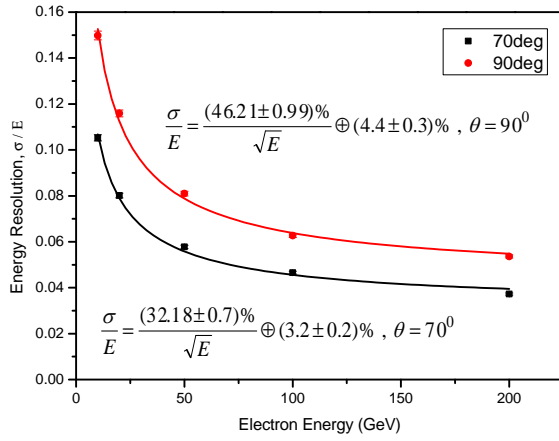


Figure 12.43: Tile Calorimeter energy resolution for electrons at $\theta = 70^\circ$ and 90° .

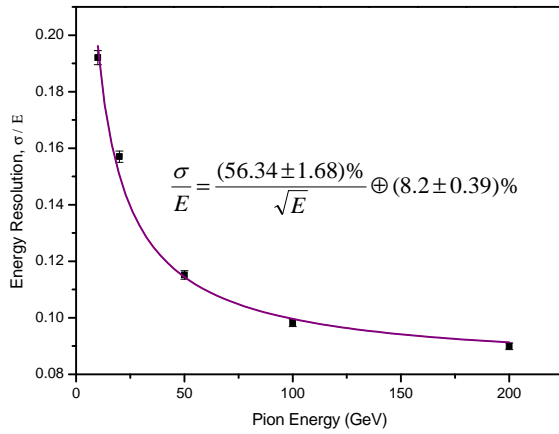


Figure 12.44: Tile Calorimeter energy resolution for pions at $\theta = 90^\circ$.

9450 **12.7.3 Energy Resolution of the Combined Calorimeter System**

9451 The simulation has also been performed to see the energy resolution variations of the combined
9452 system as a function of incident particle angles. Fig.12.45 shows the simulated calorimeter
9453 geometry for incident particles at the different θ angles. Hadronic shower simulations have
9454 been obtained for the incident pion angles ranged from 30° to 90° and the energies from 3 to
9455 200 GeV. As an example, the **GEANT4** simulation for the 50 GeV incident single pion at
9456 $\theta = 90^\circ$ can be seen in Fig.12.46. The obtained energy resolutions as a function of energy for
9457 pions at different θ angles are shown in Fig.12.47. The calculated a and b parameters at the
different angles are given in Tabl.12.9.

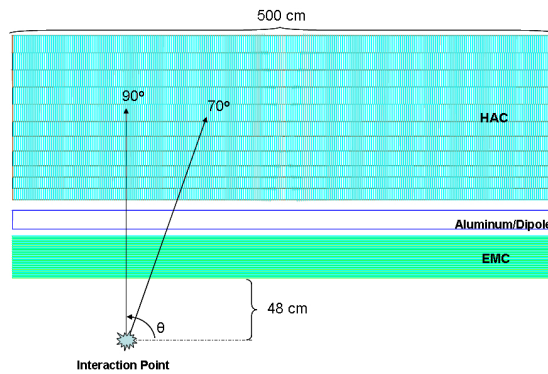


Figure 12.45: The simulated calorimeter geometry for different incident particle angle.

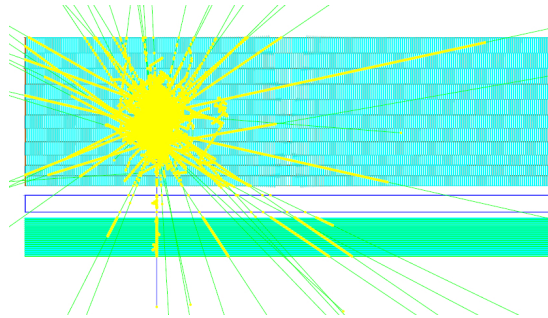


Figure 12.46: Simulation of the single pion energy with 50 GeV at $\theta = 90^\circ$.

9458 As the incident particle angle decreases, the total deposited energy and sigma will decrease
9459 and the energy resolution improves.
9460

9461 **12.7.4 Longitudinal Shower Profiles**

9462 Electrons and pions develop showers at very different depth on average. In order to derive
9463 longitudinal shower development information from calorimeter system, incident particles send
9464 to the calorimeter perpendicular to beam axis. The longitudinal length of the EMC is 37 cm and

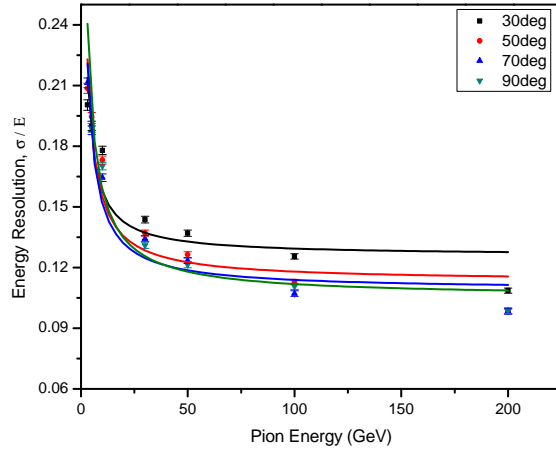


Figure 12.47: EMC+HAC energy resolution for different incident angles of pions.

	30°	50°	70°	90°
a(stoch.)%	29.93±2.96	33.28±2.62	33.28±1.98	37.44±2.5
b(const.)%	12.59±0.79	11.32±0.80	10.89±0.62	10.54±0.58

Table 12.9: Stochastic and constant terms of the pion energy resolution for different incident angles.

9465 HAC varies from 67 cm to 207 cm. The simulated longitudinal shower profiles for electrons and
 9466 pions are presented in Fig. 12.48, Fig. 12.49 and Fig. 12.50. They represent the mean deposited
 9467 energy as a function of the depth. The longitudinal shower profile of electrons is shorter as of
 9468 pions. The energy deposition of the electrons has its maximum in the EMC (Fig. 12.48). Pions,
 9469 normally, penetrate deeper into the calorimeter. So the maximum of energy deposition of the
 9470 pions are seen in the HAC (Fig. 12.50). Less energy deposition occurs between 37 and 67 cm
 9471 because of the Al block representing the cryostat-wall, solenoid and dipole magnet structures.

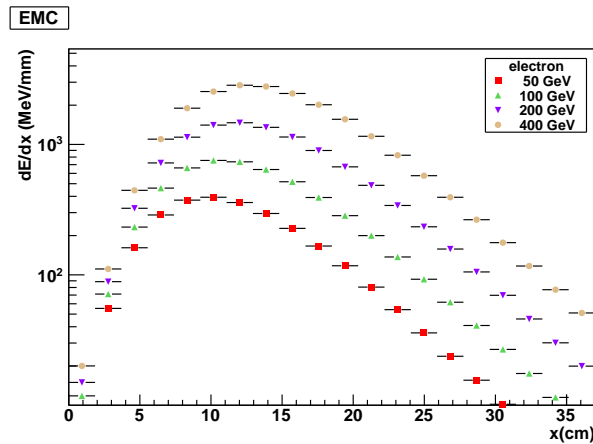


Figure 12.48: Electron longitudinal shower profile for EMC at various energies. Only statistical uncertainties are shown.

9472

9473 12.7.5 Transverse Shower Profiles

9474 Transverse profiles are usually expressed as a function of the transverse coordinates, not the
 9475 radius, and are integrated over the other coordinate. Figs. 12.51 and 12.52 show the transverse
 9476 shower profiles for electrons and pions. Since the electromagnetic showers are compact, the
 9477 electromagnetic energy is deposited relatively close to the core of the shower. As expected the
 9478 hadronic transversal shower spreads are much larger than for the electromagnetic showers.

9479 12.8 Electromagnetic and Hadronic Forward/Backward 9480 Insert Calorimeter Simulation for the LHeC Detec- 9481 tor

9482 12.8.1 The Forward and Backward Calorimeter Construction

9483 The forward electromagnetic calorimeter (FEC) inserts (i.e. FEC1 and FEC2) are tungsten-
 9484 silicon sampling calorimeters. The simulated FEC consists of consecutive layers of Tungsten
 9485 (W) absorber, a Silicon (Si) active layer, a silicon support circuit (FR4), and circuit kapton in
 9486 the listed order. The depth of each layer is given by the thickness of the W plate used in the

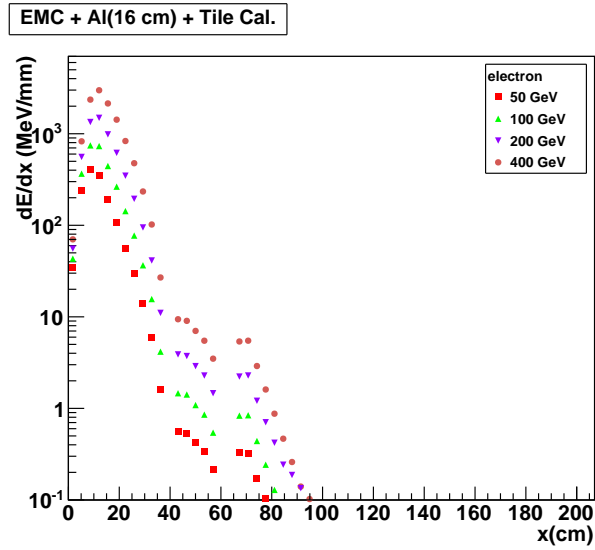


Figure 12.49: Electron longitudinal shower profile for EMC/solenoid-dipole-system (Al-block)/HAC at various energies.

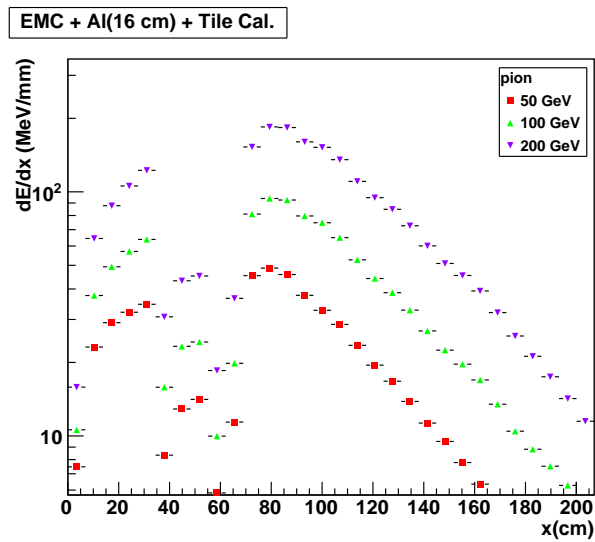


Figure 12.50: Pion longitudinal shower profile for EMC/solenoid-dipole-system (Al-block)/HAC at various energies.

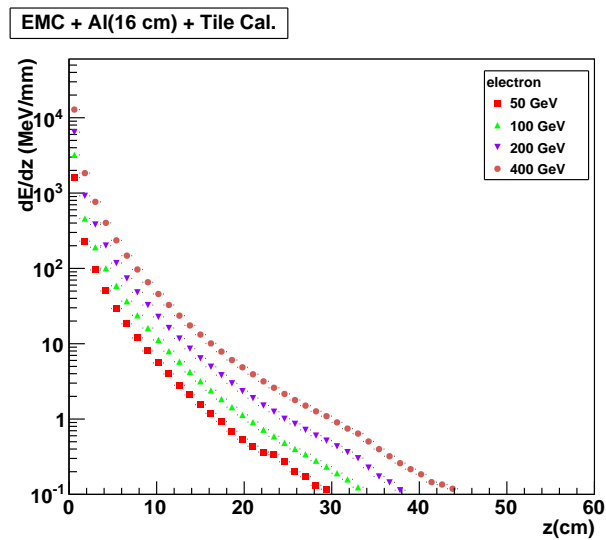


Figure 12.51: Transverse shower profiles for electron induced interactions.

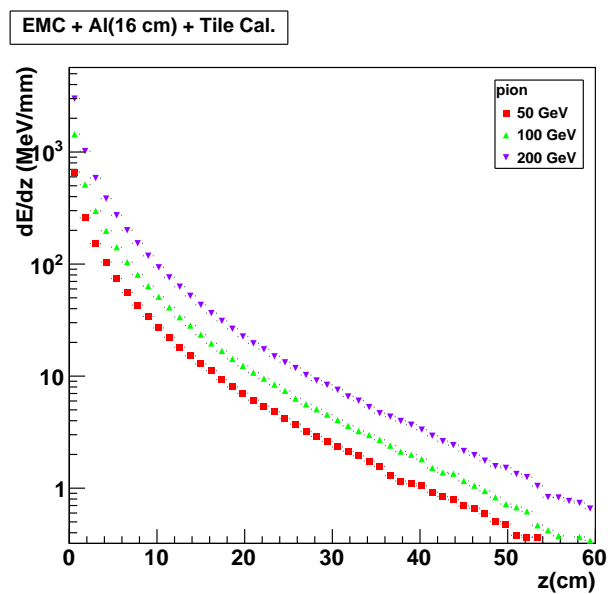


Figure 12.52: Transverse shower profiles for pion induced interactions.

9487 layer plus 5 mm for the other components. The absorber length of the FEC prototype is 10.5 cm,
 9488 which corresponds to a radiation length of $\approx 30X_0(X_0(W) = 0.3504 \text{ cm})$. The total depth of the
 9489 FEC is 35.5 cm. The thickness of all FEC layers is given in Table 12.10.

	Nb of Layers	Absorber	Silicon	Silicon support circuit (FR4)	Circuit kapton
	FEC 1-25	1.4 mm	525 μm	0.65 mm	1.15 mm
	FEC 26-50	2.8 mm	525 μm	0.65 mm	1.15 mm

Table 12.10: Longitudinal segmentation of $\text{FEC}_{(W-Si)}$.

9490 the forward hadronic calorimeter (FHC) inserts (i.e. FHC1, FHC2 and FHC3) have been
 9491 simulated using two different absorber materials, Copper (Cu) and Tungsten (W). The ac-
 9492 tive layers, FR4, and circuit kapton follow the same dimensions as given by the FEC. In
 9493 the Cu-Si case, the nuclear interaction length of the FHC prototype corresponds to $\approx 10\lambda_I$
 9494 ($\lambda_I(\text{Cu})=15.06 \text{ cm}$). The total depth of $\text{FHC}_{(Cu-Si)}$ is 165 cm. The thickness of all $\text{FHC}_{(Cu-Si)}$
 9495 layers are given in Table 12.11.

	Nb of Layers	Absorber	Silicon	Silicon support circuit (FR4)	Circuit kapton
	FHC 1-10	2.5 cm	525 μm	0.65 mm	1.15 mm
	FHC 11-20	5 cm	525 μm	0.65 mm	1.15 mm
	FHC 21-30	7.5 cm	525 μm	0.65 mm	1.15 mm

Table 12.11: Longitudinal segmentation of $\text{FHC}_{(Cu-Si)}$.

9496 In the W-Si case, the nuclear interaction length of FHC prototype corresponds to $\approx 10\lambda_I$
 9497 ($\lambda_I(\text{W})=9.946 \text{ cm}$). Also in the W-Si case the space between absorber plates is 14 mm unlike
 9498 the $\text{FHC}_{(Cu-Si)}$ or FEC. Total depth of $\text{FHC}_{(W-Si)}$ is 165 cm. The thickness of all $\text{FHC}_{(W-Si)}$
 9499 layers are given in Table 12.12.

	Nb of Layers	Absorber	Silicon	Silicon support circuit (FR4)	Circuit kapton
	FHC 1-15	1.2 cm	525 μm	0.65 mm	1.15 mm
	FHC 16-31	1.6 cm	525 μm	0.65 mm	1.15 mm
	FHC 32-46	3.8 cm	525 μm	0.65 mm	1.15 mm

Table 12.12: Longitudinal segmentation of $\text{FHC}_{(W-Si)}$.

9500 The longitudinal segmentation of the FHC and FEC is given in Figure 12.53. The absorber
 9501 of the FHC is in blue. The absorber of the FEC is in pink. Finally the silicon detectors, silicon
 9502 support circuits and circuit kapton of FEC and FHC are in brown, green and gray respectively.

9503 The backward electromagnetic calorimeter (BEC) inserts (i.e. BEC1 and BEC2) are lead-
 9504 silicon sampling calorimeters. The simulated BEC consists of consecutive layers of Lead (Pb)
 9505 absorber, a Silicon (Si) active layer, a silicon support circuit (FR4), and circuit kapton in the
 9506 listed order. The depth of each layer is given by the thickness of the Pb plate used in the
 9507 layer plus 5 mm for the other components. The absorber length of the BEC prototype is 14 cm,

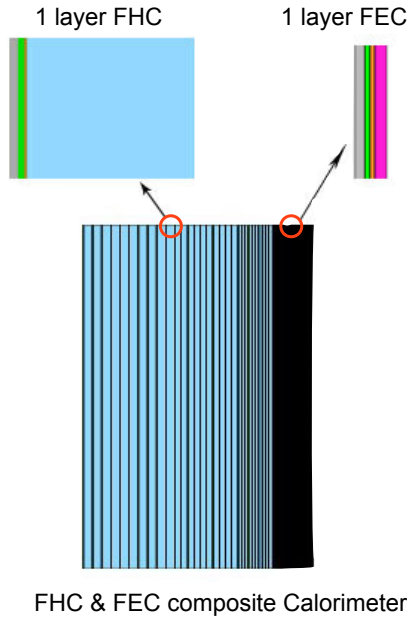


Figure 12.53: Cross section in rz of FHC+FEC.

9508 which corresponds to a radiation length of $\approx 25X_0$ ($X_0(\text{Pb}) = 0.5612 \text{ cm}$). The total depth of
 9509 the BEC is 39 cm. The thickness of all BEC layers is given in Table 12.13.

	Nb of Layers	Absorber	Silicon	Silicon support circuit (FR4)	Circuit kapton
	BEC 1-25	1.8 mm	525 μm	0.65 mm	1.15 mm
	BEC 26-50	3.8 mm	525 μm	0.65 mm	1.15 mm

Table 12.13: Longitudinal segmentation of (Pb-Si) BEC.

9510 the backward hadronic calorimeter (BHC) inserts (i.e. BHC1, BHC2 and BHC3) are iron-
 9511 silicon sampling calorimeters. The active layers, FR4, and circuit kapton follow the same
 9512 dimensions as given by the BEC. The Absorber length of the BHC prototype is 132.5 cm, which
 9513 corresponds to the nuclear interaction length of the $7.9\lambda_I$ ($\lambda_I(\text{Fe})=16.77 \text{ cm}$) The total depth
 9514 of the BHC is 145 cm. The thickness of all BHC layers are given in Table 12.14.

9515 The overall structure of the BEC, BHC and BEC+BHC composite calorimeter are like their
 9516 forward electromagnetic and hadronic calorimeter counterparts shown in Figure 12.53.

9517 **FEC Simulation Results**

9518 All of the FEC simulations were done with a radiation length of $\approx 30X_0(W)$.

	Nb of Layers	Absorber	Silicon	Silicon support circuit (FR4)	Circuit kapton
	BHC 1-7	2.5 cm	525 μ m	0.65 mm	1.15 mm
	BHC 8-15	5 cm	525 μ m	0.65 mm	1.15 mm
	BHC 16-25	7.5 cm	525 μ m	0.65 mm	1.15 mm

Table 12.14: Longitudinal segmentation of (Fe-Si) BHC.

$$\frac{\sigma_E}{E} = \frac{(14.0 \pm 0.16)\%}{\sqrt{E}} \oplus (5.3 \pm 0.049)\% \quad (12.2)$$

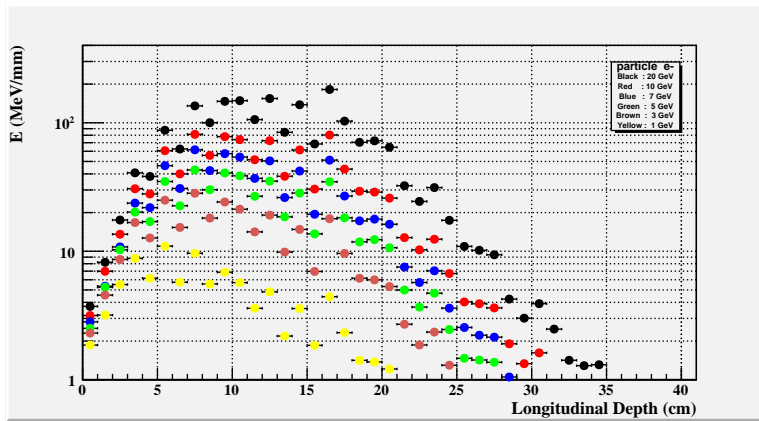


Figure 12.54: Average energy deposition as a function of depth for electrons with energy in range 1 GeV-20 GeV incident on the FEC.

9519 **FEC+FHC Composite Calorimeter Simulation Results**

9520 **GEANT4** simulations were performed in order to determine the shower development profiles
 9521 and the energy resolutions of the FEC+FHC_(Cu-Si) and FEC+FHC_(W-Si) combined systems
 9522 for 50 GeV-1 TeV pions. All the simulations of the FEC + FHC composite system were done
 9523 for the radiation length of $\approx 30X_0(W)$ for the FEC and the nuclear interaction length of $\approx 10\lambda_I$
 9524 for the FHC.

9525 Cu-Si case of FHC:

$$\frac{\sigma_E}{E} = \frac{(46.0 \pm 1.7)\%}{\sqrt{E}} \oplus 6.1 \pm 0.073)\% \quad (12.3)$$

9526 W-Si case of FHC:

$$\frac{\sigma_E}{E} = \frac{(45.4 \pm 1.7)\%}{\sqrt{E}} \oplus (4.8 \pm 0.086)\% \quad (12.4)$$

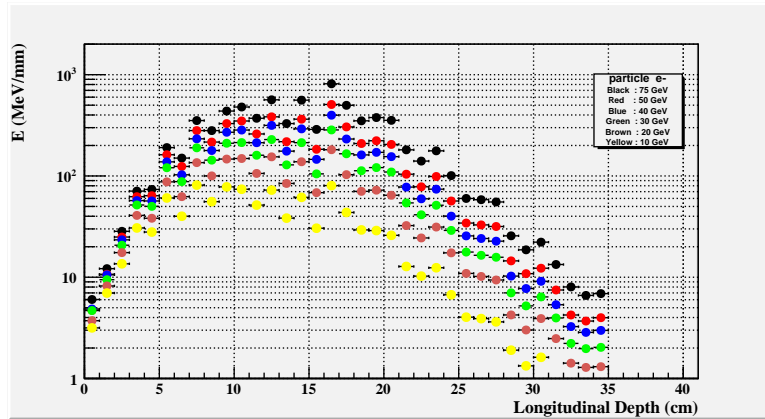


Figure 12.55: Average energy deposition as a function of depth for electrons with energy in range 10 GeV-75 GeV incident on the FEC.

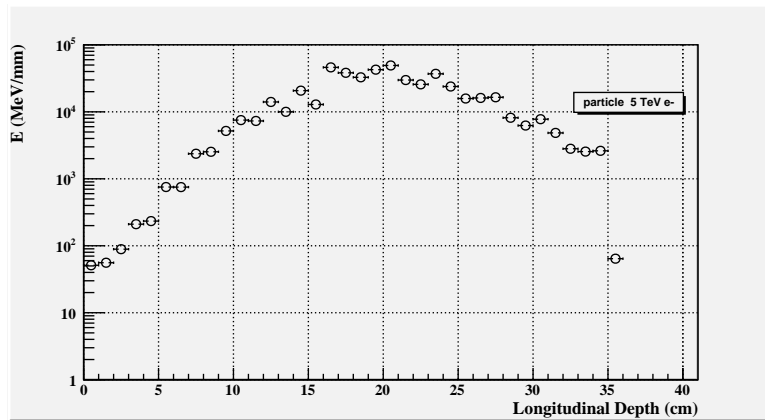


Figure 12.56: Average energy deposition as a function of depth for electrons with energy 5 TeV incident on the FEC

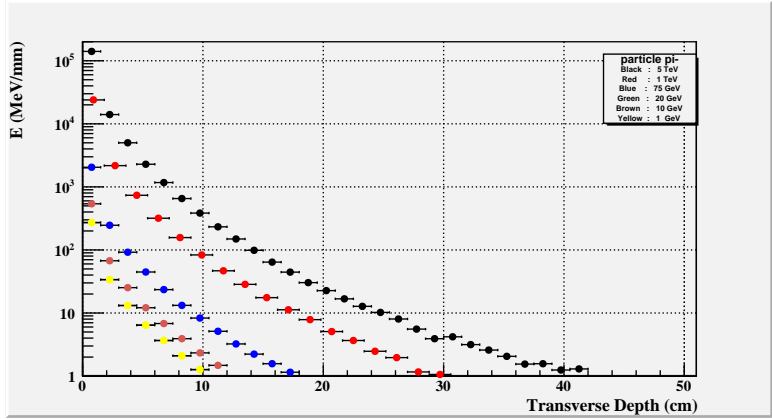


Figure 12.57: Transverse shower profiles for electrons with energy in range 1 GeV-5 TeV in the FEC.

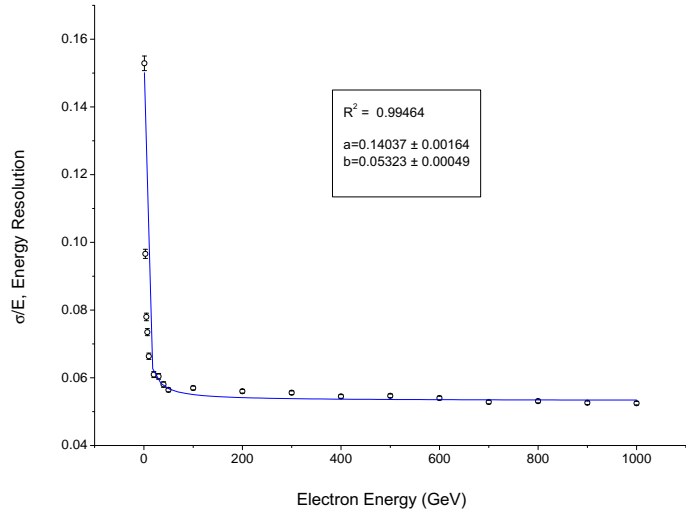


Figure 12.58: Energy Resolution spectra for electrons with energy in range 1 GeV-1 TeV in the FEC.

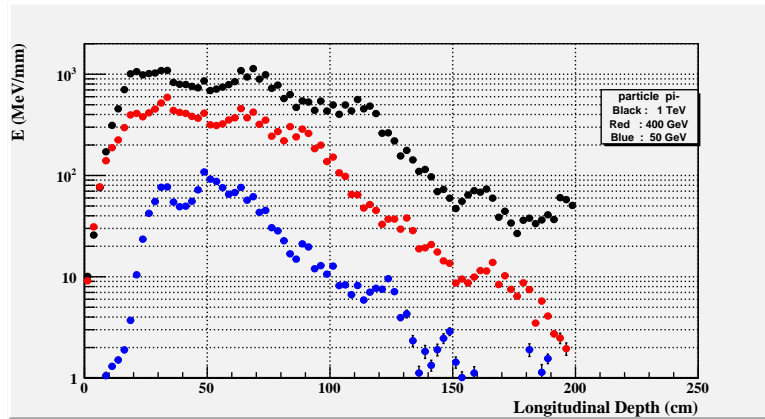


Figure 12.59: Average energy deposition as a function of depth for pions with energy in range $50\text{ GeV} - 1\text{ TeV}$ in the FEC1+FEC2 + (copper-silicon) FHC1+FHC2+FHC3 composite system.

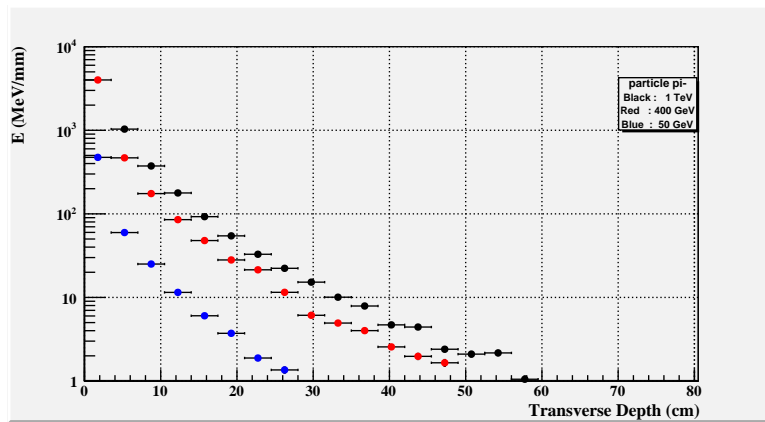


Figure 12.60: Transverse shower profiles for pions with energy in range $50\text{ GeV} - 1\text{ TeV}$ in the FEC1+FEC2 + (copper-silicon) FHC1+FHC2+FHC3 composite system.

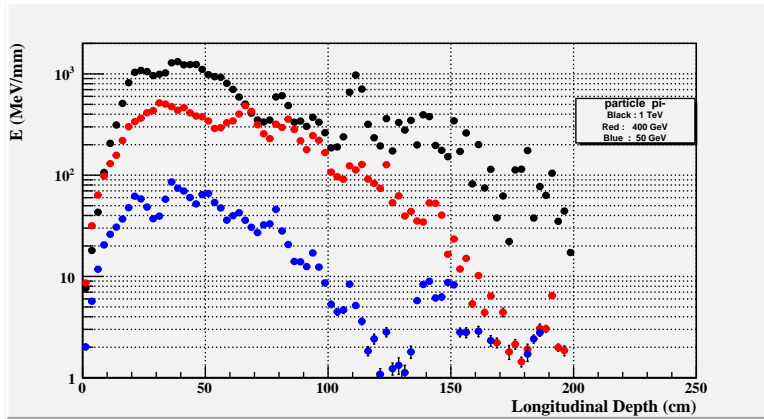


Figure 12.61: Average energy deposition as a function of depth for pions with energy in range $50\text{ GeV} - 1\text{ TeV}$ in the FEC1+FEC2 + (tungsten-silicon) FHC1+FHC2+FHC3 composite system.

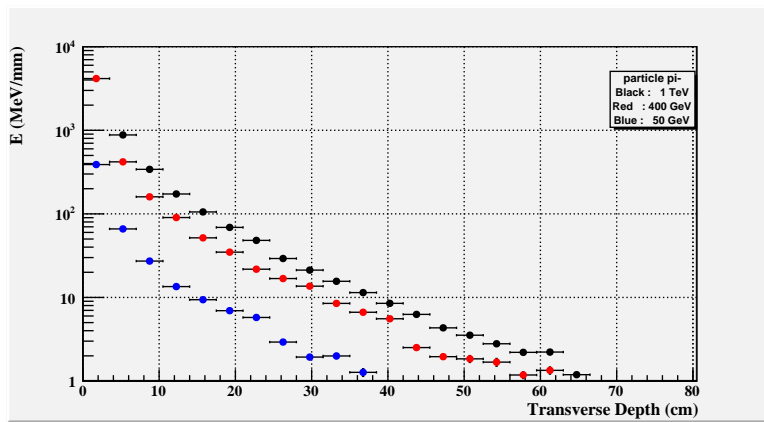


Figure 12.62: Transverse shower profiles for pions with energy in range $50\text{ GeV} - 1\text{ TeV}$ in the FEC1+FEC2 + (tungsten-silicon) FHC1+FHC2+FHC3 composite system.

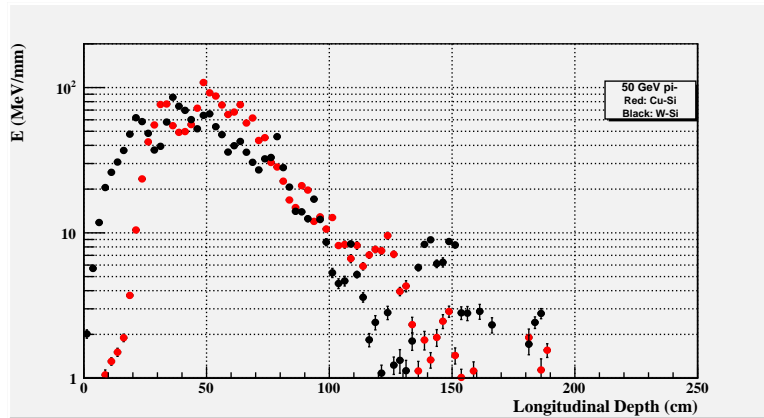


Figure 12.63: Comparison of average energy deposition as a function of depth for pions with energy 50 GeV in cases of the (copper-silicon) and (tungsten-silicon) of the FHC in FEC+FHC composite system.

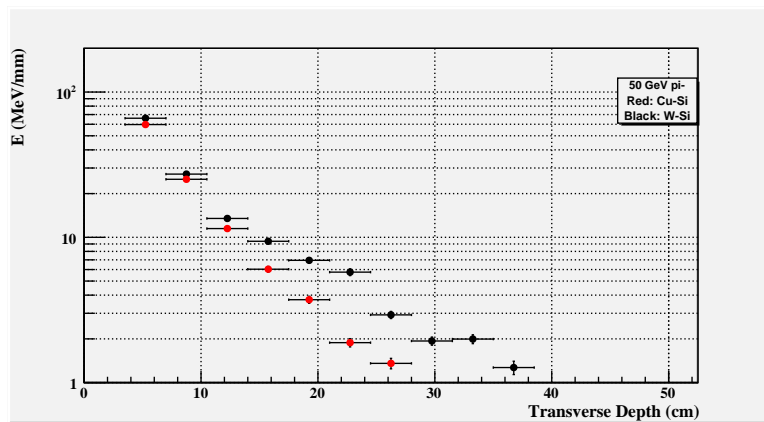


Figure 12.64: Comparison of transverse shower profiles for pions with energy 50 GeV in cases of the (copper-silicon) and (tungsten-silicon) of the FHC in the FEC+FHC composite system.

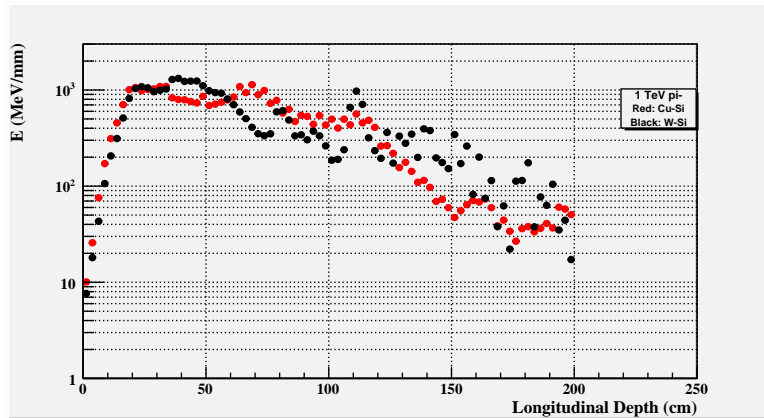


Figure 12.65: Comparison of average energy deposition as a function of depth for pions with energy 1 TeV in cases of the (copper-silicon) and (tungsten-silicon) of the FHC in FEC+FHC composite system.

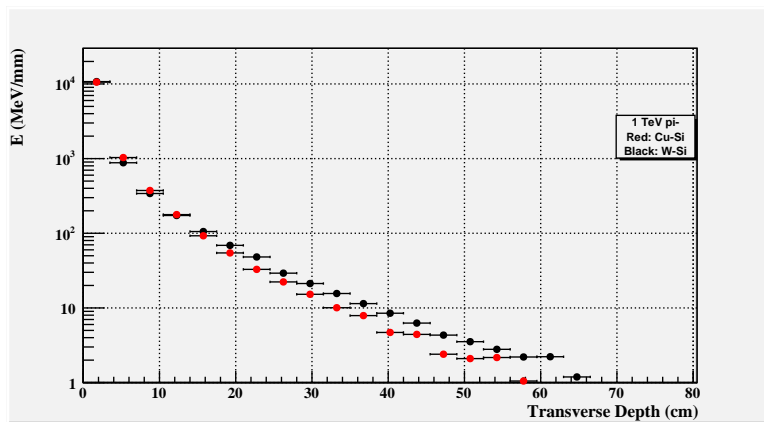


Figure 12.66: Comparison of transverse shower profiles for pions with energy 1 TeV in cases of the (copper-silicon) and (tungsten-silicon) of the FHC in FEC+FHC composite system.

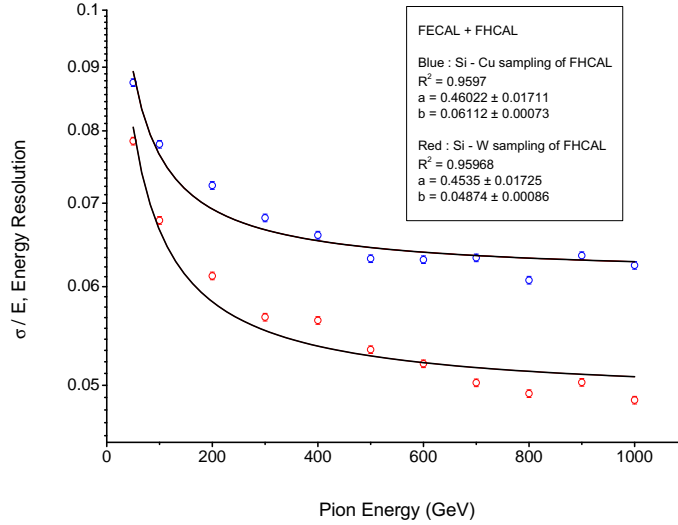


Figure 12.67: Comparison of energy resolution spectrums for pions with energy in range 50 GeV - 1 TeV in cases of the (copper-silicon) and (tungsten-silicon) of the FHC in FEC+FHC composite system.

9527 BEC Simulation Results

9528 All of the BEC simulations were done for a radiation length of $\approx 25X_0(\text{Pb})$, and incident elec-
9529 trons.

9530 Pb-Si case of BEC:

$$\frac{\sigma_E}{E} = \frac{(11.4 \pm 0.5)\%}{\sqrt{E}} \oplus (6.3 \pm 0.1)\% \quad (12.5)$$

9531 BEC+BHC Composite Calorimeter Simulation Results

9532 All the simulations for the BEC (radiation length of $\approx 25X_0(\text{Pb})$) and BHC (nuclear interaction
9533 length of $\approx 8\lambda_I$), were done for incident pions.

9534 Energy resolution for the BEC+BHC composite system:

$$\frac{\sigma_E}{E} = \frac{(21.6 \pm 1.9)\%}{\sqrt{E}} \oplus (9.6 \pm 0.4)\% \quad (12.6)$$

9535 12.8.2 Calorimeter Simulation Conclusion

9536 Lateral development of the electromagnetic showers initiated by electrons or photons scales with
9537 the Moliere radius. The Moliere Radii of tungsten and lead are 0.9327 cm and 1.602 cm [28],
9538 respectively. The surface area of the calorimeters (Forward and Backward) is 300 cm \times 300 cm,

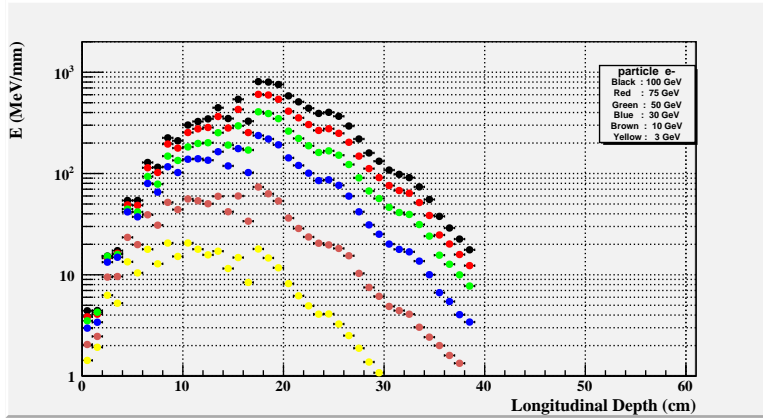


Figure 12.68: Average energy deposition as a function of depth for electrons with energy in range $3\text{ GeV} - 100\text{ GeV}$ incident on the BEC.

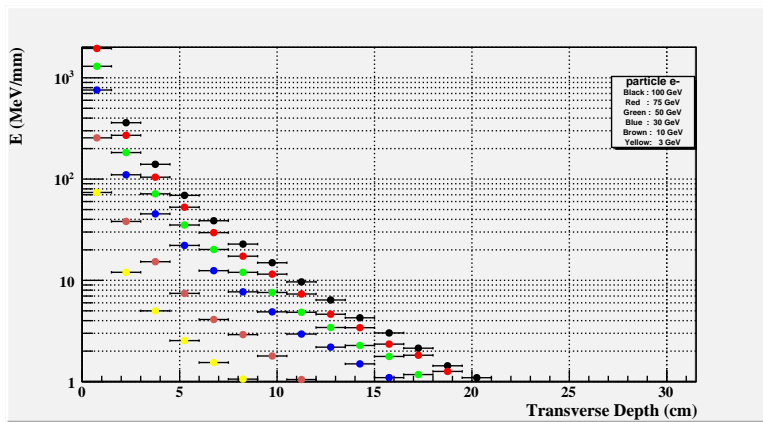


Figure 12.69: Transverse shower profiles for electrons with energy in range $3\text{ GeV} - 100\text{ GeV}$ incident on the BEC.

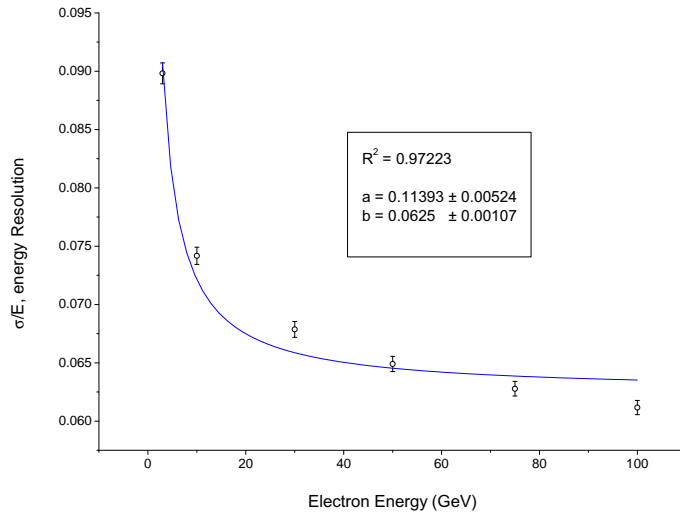


Figure 12.70: Energy resolution spectrum for electrons with energy in range 3 GeV - 100 GeV in the BEC.

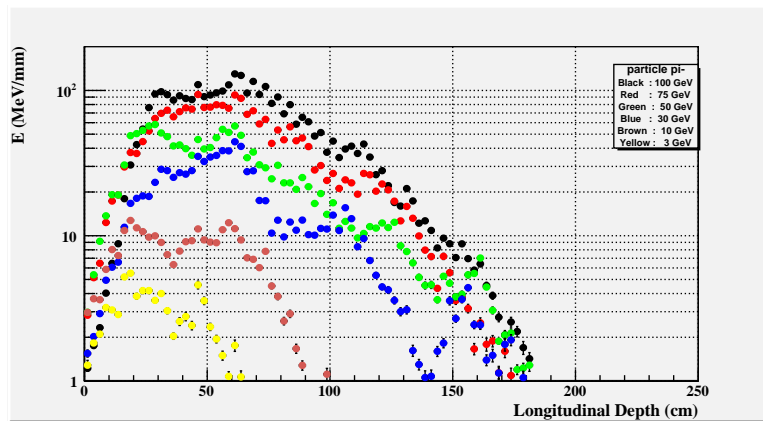


Figure 12.71: Average energy deposition as a function of depth for pions with energy in range 3 GeV - 100 GeV incident on the BEC+BHC composite system.

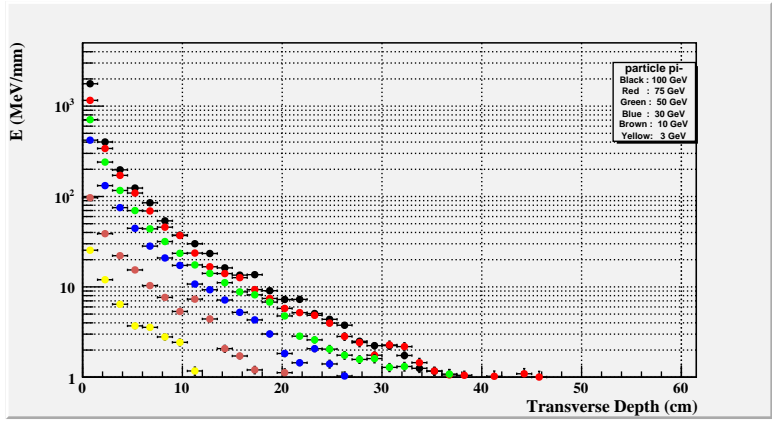


Figure 12.72: Transverse shower profiles for pions with energy in range 3 GeV-100 GeV incident on the BEC+BHC composite system.

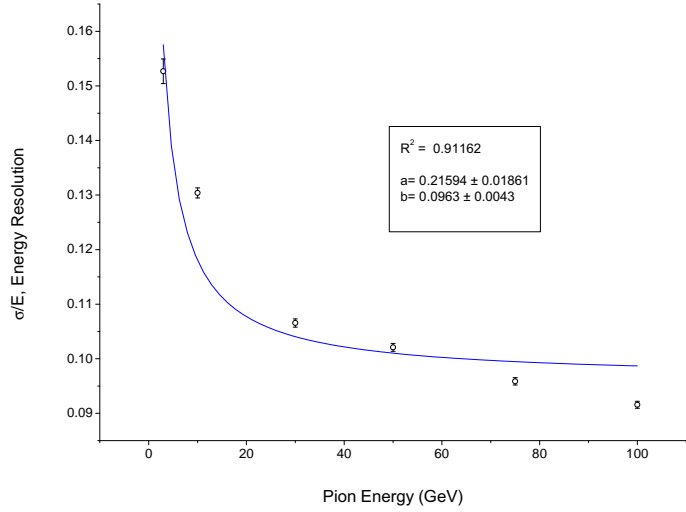


Figure 12.73: Energy resolution spectrum for pions with energy in range 3 GeV-100 GeV in the BEC+BHC composite system.

9539 which is larger than Moliere radii, so that the whole shower is contained in the FEC or BEC
 9540 transversely. The simulated maximum longitudinal shower profile for electrons in the FEC and
 9541 BEC is in agreement with literature [689]. Avaraged 99.4 and 98.8 percent of the incident
 9542 energy for electron energies in ranges of 1 GeV-1 TeV for FEC and 3 GeV-100 GeV for BEC
 9543 are deposited in the electromagnetic calorimeter in the simulation, respectively. The relation
 9544 between the depth of the shower maximum and amount of the deposited energy in the FEC or
 9545 BEC is acceptable in the simulation. Also, we observed that the FEC and BEC show a linearity
 9546 with 72% and 100% respectively. But, as can be seen from Fig 12.54, Fig 12.55 and Fig 12.56
 9547 for the FEC and from Fig 12.68 for BEC, it is obvious that there will be the problem of shower
 9548 leakage for these incident electron energies and higher electron energies in case of the radiation
 9549 lengths of $\approx 30X_0(W)$ and $\approx 25X_0(Pb)$ for the FEC and BEC, respectively. Incoming electron
 9550 energy to the front surface of FEC or BEC increases, an increase in the shower leakages were
 9551 observed. The FEC and BEC have the stochastic terms of $(14.0 \pm 0.16\%)$ and $(11.4 \pm 0.5\%)$
 9552 and the constant terms of $(5.3 \pm 0.049\%)$ and $(6.3 \pm 0.1\%)$, respectively. If the variations in the
 9553 energy leakage from the FEC or BEC via back surfaces can be prevented, the constant terms
 9554 will be smaller than these values.

9555 Longitudinal distribution of the hadronic calorimeters and shower maximum of the longitu-
 9556 dinal distrubition are scaled with λ_I . Nuclear interaction length of the copper is bigger $\approx 51\%$
 9557 than tungsten one. Accordingly, we observed that the shower maximum of the $FHC_{(W-Si)}$
 9558 is in the smaller depth. Avaraged 82.6% and 85.5% of pion's energy is deposited in the
 9559 $FEC+FHC_{(Cu-Si)}$ and the $FEC+FHC_{(W-Si)}$ combined systems and the combined systems
 9560 have linearities with percentages 83.5% and 84%, respectively. Both of the combined systems
 9561 have some leakages as can see in Fig 12.59 and Fig 12.61 in the higher pion's energies. In case
 9562 of (W-Si) sampling, the leakage from $FEC+FHC$ combined system is smaller 3% than (Cu-
 9563 Si) sampling (see Fig 12.63). In the simulation, stochastic terms of the energy resolutions in
 9564 both cases have the similar values, but the constant value of the $FEC+FHC_{(W-Si)}$ are smaller
 9565 by 21.3% than $FEC+FHC_{(Cu-Si)}$ one. This means that if the $FEC+FHC_{(W-Si)}$ combined
 9566 calorimeter is used, the leakges will be smaler.

9567 We observed that avaraged deposited pion's energy is 77.5% of the incident pion's energy
 9568 in the $BEC+BHC$ combined system and the linearity of the combined system has a percentage
 9569 72.8%. It is obvious that there are some leakages for the backward combined system according
 9570 to the simulation.

9571 12.9 Further Option

- 9572 • detector design B. - No solenoid within the calorimetry.

9573 12.10 Calorimeter Summary

- 9574 • Validation of present simulation
- 9575 • Alternative Calorimeter Design toward New Technologies
- 9576 • Discussion : what makes sense, what not. A word on PFA etc.
- 9577 • Technologies and timescale: a dual readout fully active calorimetry.

9578 • RPC based Digital readout, integrated calorimeter and muon detector.

9579 12.11 Muon Detector

9580 Fig. 12.74.

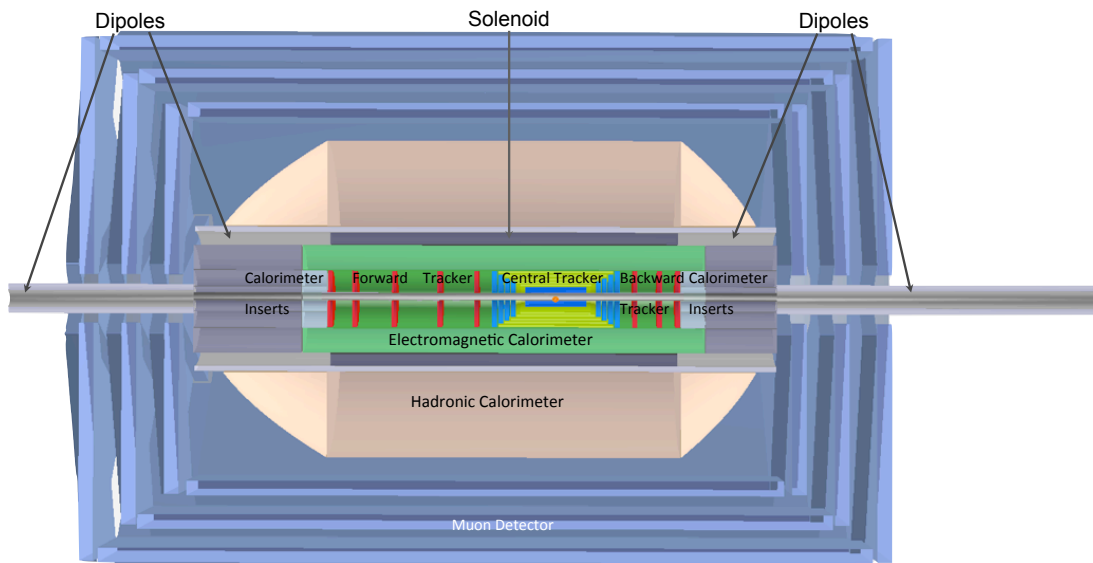


Figure 12.74: A full view of the baseline detector in the r-z plane with all components shown. The detector dimensions are ≈ 14 m in z with a diameter of ≈ 9 m.

Chapter 13

Forward and Backward Detectors

13.1 Luminosity Measurement and Electron Tagging

Luminosity measurement is an important issue for any collider experiment. At the LHeC, where precision measurements constitute a significant part of the physics programme, the design requirement is $\delta\mathcal{L} = 1\%$.

In addition to an accurate determination of integrated luminosity, \mathcal{L} , for the normalisation of physics cross sections, the luminosity system should allow for fast beam monitoring with a typical statistical precision of 1%/sec for tuning and optimisation of ep -collisions and to provide good control of the mid-term variations of instantaneous luminosity, L .

Rich experience gained by H1 [690, 691] and ZEUS [692, 693] Collaborations at HERA was used in the design studies of the luminosity system for the LHeC. In particular, one important lesson to be learnt from HERA is to prepare several alternative methods for luminosity determination.

For the LHeC we consider both Linac-Ring (LR) and Ring-Ring (RR) options as well as high Q^2 ($10^\circ - 170^\circ$ acceptance) and low Q^2 ($1^\circ - 179^\circ$ acceptance) detector setups. This spans over a wide range of instantaneous luminosity¹ $L = (10^{32} - 2 \cdot 10^{33})\text{cm}^{-2}\text{s}^{-1}$. Hence suitable processes for the three tasks outlined above should have the following minimal visible cross sections²:

- fast monitoring ($\delta\mathcal{L} = 1\%/ \text{sec} \Rightarrow 10 \text{ kHz}$) – $\sigma_{\text{vis}} \gtrsim 100\mu\text{b}$,
- mid-term control ($\delta\mathcal{L} = 0.5\%/ \text{hour} \Rightarrow 10 \text{ Hz}$) – $\sigma_{\text{vis}} \gtrsim 100\text{nb}$,
- physics sample normalisation ($\delta\mathcal{L} = 0.5\%/ \text{week} \Rightarrow 0.1 \text{ Hz}$) – $\sigma_{\text{vis}} \gtrsim 1\text{nb}$.

The best candidate for luminosity determination is the purely electromagnetic *bremsstrahlung* reaction $ep \rightarrow e\gamma + p$ shown in Figure 13.1a, which has a large and precisely known cross section. Depending on the photon emission angle it is called either Bethe-Heitler process (collinear emission) or QED Compton scattering (wide angle bremsstrahlung). In addition, Neutral Current DIS events in a well understood (x, Q^2) range can be used for the *relative* normalisation and mid-term yield control.

¹This also takes into account exponential reduction of L during the data taking in every luminosity fill.

²Statistical error has to be small in comparison with total error δL_{tot} in order not to spoil overall accuracy.

9609 While QED Compton and NC DIS processes can be measured in the main detector dedi-
 9610 cated ‘tunnel detectors’ are required to register Bethe-Heitler events. For the latter, additional
 9611 challenges as compared to HERA are related to the LHeC specifics: non-zero beam crossing
 9612 angle in IP for RR option, and severe aperture limitation for LR option. Finally, for the high
 9613 luminosity LHeC running one should not forget about significant pileup (L/bunch is $\sim 2 - 3$
 9614 times bigger as compared to HERA-II running).

9615 13.1.1 Options

9616 The huge rate of ‘zero angle’ electrons and photons from Bethe-Heitler reaction³ makes a
 9617 dedicated luminosity system in the tunnel ideal for fast monitoring purposes. However, it is
 9618 usually very sensitive to the details of the beam optics at the IP, may suffer from synchrotron
 9619 radiation (SR) and requires, for accurate absolute normalisation, a large and precisely known
 9620 geometrical acceptance which is often difficult to ensure. On the contrary, the main detector
 9621 has stable and well known acceptance and is safely shielded against SR. Therefore, although
 9622 QED Compton events in the detector acceptance have significantly smaller rates they may be
 9623 better suited for overall global normalisation of the physics samples. Thus the two methods are
 9624 complementary, having very different systematics and providing useful redundancy and cross
 9625 check for the luminosity determination.

9626 To evaluate the main LHeC detector acceptance for NC DIS events and for the elastic QED
 9627 Compton process DJANGO [694] and COMPTON [695] event generators were used respectively.
 9628 Different options for dedicated luminosity detectors in the LHC tunnel have been studied with
 9629 help of the special H1LUMI program package [696], which contains Monte Carlo generation of
 9630 the ‘collinear’ photons and electrons from various processes (Bethe-Heitler reaction, quasi-real
 9631 photoproduction, e-beam scattering on the rest gas) as well as a simple tracking through the
 9632 beamline.⁴

9633 13.1.2 Use of the Main LHeC Detector

9634 To estimate visible cross sections for NC DIS and elastic QED Compton events a typical HERA
 9635 analysis strategy was used. That is: safe fiducial cuts against energy leakage over the backward
 9636 calorimeter boundaries at small radii, safe (Q^2, y) cuts for NC DIS events to restrict measure-
 9637 ment to the phase space where F_2 is known to good precision of $1 - 2\%$ and the F_L contribution
 9638 is negligible, and elasticity cuts for QEDC events to reject the less precisely known inelastic
 9639 contribution. In addition basic cuts against major backgrounds were applied (photoproduction
 9640 in case of NC DIS and DVCS, elastic VM production and low mass diffraction in case of QED
 9641 Compton).

9642 The visible NC DIS cross section, $\sigma_{\text{vis}}^{\text{DIS}}(Q^2 > 10\text{GeV}^2, 0.05 < y < 0.6) \simeq 10$ nb for 10°
 9643 setup and $\simeq 150$ nb for 1° setup. This corresponds to a $10 - 15$ Hz rate which is comfortable
 9644 enough for mid-term yield control.

9645 For elastic QED Compton events, the visible cross section, $\sigma_{\text{vis}}^{\text{QEDC}} \simeq 0.03$ nb for 10° setup
 9646 and $\simeq 3.5$ nb for 1° setup. Hence while for the latter sufficiently high rate is possible even for
 9647 $L = 10^{32}\text{cm}^{-2}\text{s}^{-1}$, in case of ‘high Q^2 ’ setup the QEDC event rate is $4 - 5$ times smaller, thus
 9648 only providing acceptable statistical precision for large samples, of the order 0.5% /month.

³Total cross section, $\sigma_{BH} \simeq 870$ mb for 60×7000 GeV² ep collisions at the LHeC.

⁴The tracking has been performed by interfacing H1LUMI to GEANT3 [697] having LHeC beamline imple-
 mented up to $\sim 110\text{m}$ from the IP.

9649 In order to improve this a special small dedicated calorimeter could eventually be added
 9650 after the strong focusing quadrupole, at $z = -6\text{m}$. Such ‘QEDC tagger’ should consist of
 9651 two movable stations approaching the beam-pipe from the top and the bottom in the vertical
 9652 direction, as sketched in Figure 13.1b. This way detector sections will be safe with respect to
 9653 SR fan confined in the median plane. The visible elastic QED Compton cross section for such
 9654 a device is $4.3 \pm 0.2 \text{ nb}$ which significantly improves statistics for the luminosity measurement.
 9655 The angular acceptance of the ‘QEDC tagger’ corresponds to the range $\theta = 0.5^\circ - 1^\circ$ which
 9656 lies outside the tracking acceptance. Therefore calorimeter sections should be supplemented by
 9657 small silicon detectors in order to make it possible to reconstruct the event vertex from the final
 9658 state containing only one electron and one photon. These silicon trackers are also useful for
 9659 e/γ separation and rejection of the potential background. Actual dimensions and parameters
 9660 of this optional ‘QEDC tagger’ requires extra design studies.

9661 13.1.3 Dedicated Luminosity Detectors in the tunnel

9662 In case of the RR-option which implies non-zero crossing angle for early e/p beam separation,
 9663 the dominant part of the Bethe-Heitler photons will end up at $z \simeq -22\text{m}$, between electron
 9664 and proton beam-pipes (see Figure 13.1c). This is the hottest place where also a powerful SR
 9665 flux must be absorbed. On the first glance this makes luminosity monitoring based upon the
 9666 bremsstrahlung photons impossible.

9667 There is however an interesting possibility. SR absorber needs good cooling system. The
 9668 most natural cooling utilises circulating water. This cooling water can be used at the same
 9669 time as an active media for Čerenkov radiation from electromagnetic showers initiated by the
 9670 energetic Bethe-Heitler photons. The idea is based on two facts:

- 9671 1. The dominant part of the SR spectrum lies below the Čerenkov threshold for water,
 9672 $E_{\text{thr}} = 260 \text{ keV}$, and hence will not produce light signal. Low intensity tail of the energetic
 9673 synchrotron photons can be further suppressed by few radiation lengths of the absorber
 9674 material in front of the water volume.
- 9675 2. Water is absolutely radiation resistant media and hence such simple Čerenkov counter
 9676 can stand any dose without performance deterioration.

9677 The Čerenkov light can be collected and read out by two photo-multipliers as sketched on
 9678 Figure 13.1d. The geometric acceptance depends on the details of the e -beam optics. For the
 9679 actual RR design with the crossing angle $\sim 1 \text{ mrad}$ the acceptance to the Bethe-Heitler photons
 9680 is up to 90%, thus allowing fast and reliable luminosity monitoring with 3 – 5% systematic
 9681 uncertainty.

9682 Of course, such an active SR absorber is not a calorimeter with good energy resolution,
 9683 but just a simple counter. It is worth noting, that similar water Čerenkov detector has been
 9684 successfully used in the H1 Luminosity System during HERA-I operation.

9685 In case of LR-option, electrons collide with protons head-on, with zero crossing angle. This
 9686 makes the situation very similar to HERA, where Bethe-Heitler photons travel along the proton
 9687 beam direction and can be caught at around $z = -120\text{m}$, after the first proton bending dipole.
 9688 Essential difference is that unlike HERA, LHC protons are deflected horizontally at this place
 9689 rather than vertically. Thus the luminosity detector should be placed in the median plane next
 9690 to the interacting proton beam, p_1 , as shown on Figure 13.1e. In this case energy measurement
 9691 with good resolution is not a problem, so major uncertainty will come from the knowledge of the

9692 limited geometric acceptance. This limitation is defined by the proton beam-line aperture, in
 9693 particular by the aperture of the quadrupoles Q1-Q3 of the low-beta proton triplet. Moreover,
 9694 it might be necessary to split D1 dipole into two parts in order to provide escape path for the
 9695 photons with sufficient aperture. First estimates show that the geometric acceptance of the
 9696 Photon Detector up to 95% is possible at the nominal beam conditions. HERA experience
 9697 tells, that the uncertainty can be estimated as $\delta A = 0.1 \cdot (1 - A)$ leading to the total luminosity
 9698 error of $\delta L = 1\%$ in this case.

9699 13.1.4 Small angle Electron Tagger

9700 The Bethe-Heitler reaction can be tagged not only by detecting a final state photon, but also
 9701 by detecting the outgoing electron. Since all other competing processes have much smaller
 9702 cross sections measuring inclusive rate of the scattered electrons under zero angle will provide a
 9703 clean enough sample for luminosity monitoring. The remaining small background (mainly due
 9704 to off-momentum electrons from e -beam scattering on the rest gas) can be precisely controlled
 9705 and statistically subtracted using non-colliding (*pilot*) electron bunches.

9706 In order to determine the best positions for the Electron taggers the LHeC beamline simu-
 9707 lation has been performed in the vicinity of the Interaction Region for the RR-option. Several
 9708 positions for the e -tagger stations were tried:⁵ $z = -14\text{m}$, -22m and -62m . As one can see on
 9709 the top part of Figure 13.2 all places provide reasonable acceptances, reaching approximately
 9710 (20 – 25)% at the maximum. However, $z = -14\text{m}$ and $z = -22\text{m}$ most likely will suffer from
 9711 SR flux, making e -tagger operation problematic at those positions.

9712 The most promising position for the Electron tagger is at $z = -62\text{m}$. The actual acceptance
 9713 strongly depends both on the distance of the sensitive detector volume from the e -beam axis
 9714 and on the details of the electron optics at the IP, such as beam tilt or small trajectory offset,
 9715 as illustrated on the bottom part of Figure 13.2. Therefore a precise independent monitoring of
 9716 beam optics and accurate position measurement of the e -tagger are required in order to control
 9717 geometrical acceptance to a sufficient precision. For example, instability in the horizontal
 9718 trajectory offset at IP, x_{off} , of $\pm 20\mu\text{m}$ leads to the systematic uncertainty of 5% in the visible
 9719 cross section, $\sigma_{\text{vis}}(\text{ET62})$.

9720 It is fair to note, that the magnetic field of the main LHeC detector was not taken into
 9721 account in the simulation. The influence of this field is expected to be very small and will not
 9722 alter basic conclusions of this section. Also, for the LR-option a similar acceptance is expected,
 9723 although it may differ in shape somewhat.

9724 In order to demonstrate that the ideas described in Sec. 13.1.3 and 13.1.4 are realistic a
 9725 typical example of the online rates variations for the H1 Luminosity System at HERA is shown
 9726 on Figure 13.3. The system utilised all three types of the detectors discussed above: a total
 9727 absorption electromagnetic calorimeter for the Bethe-Heitler photons (PD), a water Čerenkov
 9728 counter (VC) and the Electron tagger (ET6). One can see, that online luminosity estimate by
 9729 every of those detectors is well within 5% in spite of significant changes in the acceptance due
 9730 to electron beam tilt jumps and adjustments at the IP.

⁵For the station at $z = -14\text{m}$ the electron dipole magnet should be split into two parts, while the region around $z = -62\text{m}$ has sufficiently comfortable place for the Electron tagger, before the e -beam is bended vertically.

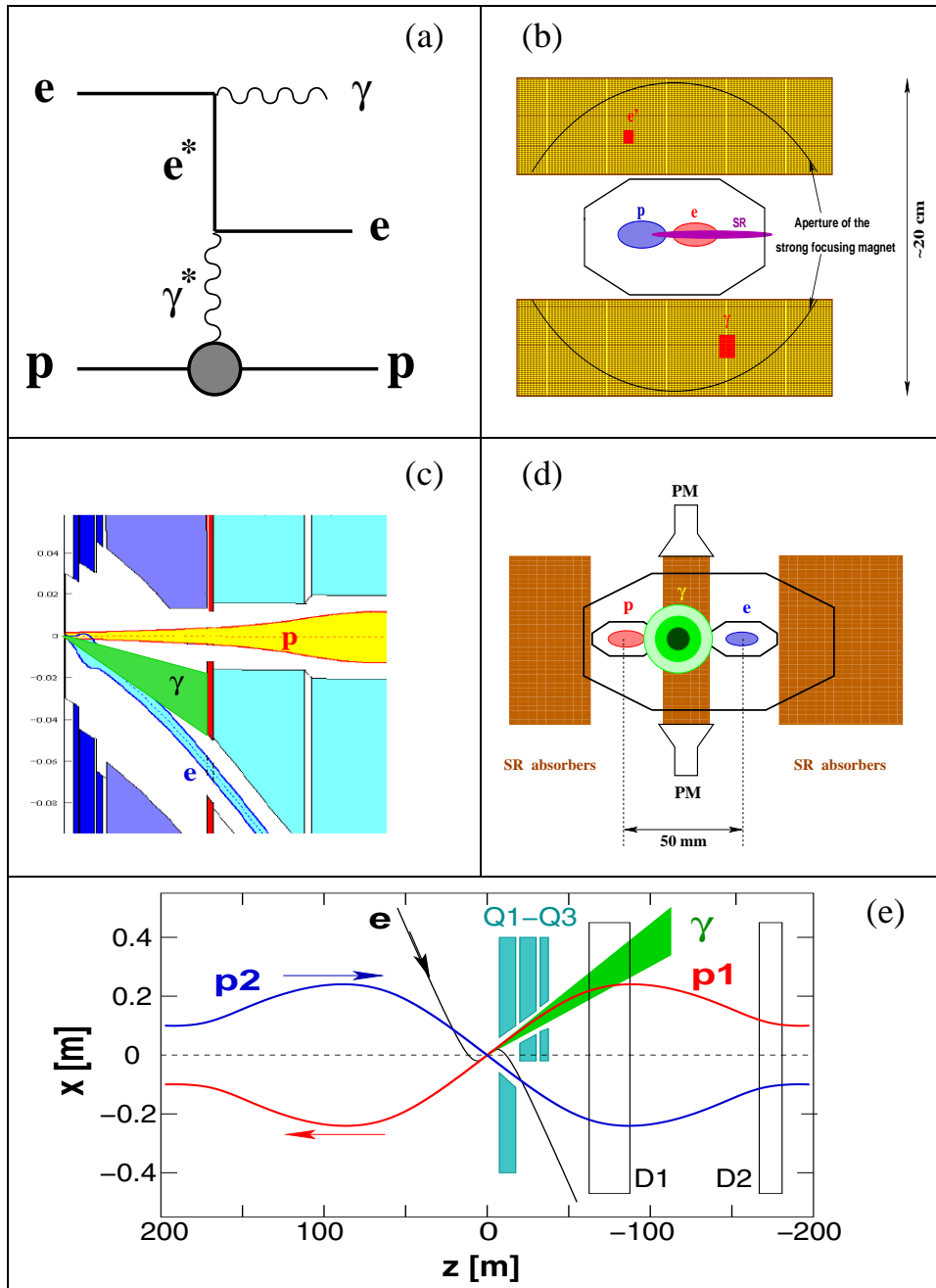


Figure 13.1: Options for the luminosity monitoring at the LHeC. (a) Feynman diagram for QEDC (γ^* pole) or BH (γ^* , e^* poles) processes; (b) QEDC tagger at $z = -6\text{m}$; (c,d) active SR absorber at $z = -22\text{m}$ for RR-option (circles show 1-, 2- and 3- σ contours for BH photons); (e) schematic view for the LR-option with 3- σ fan of BH photons.

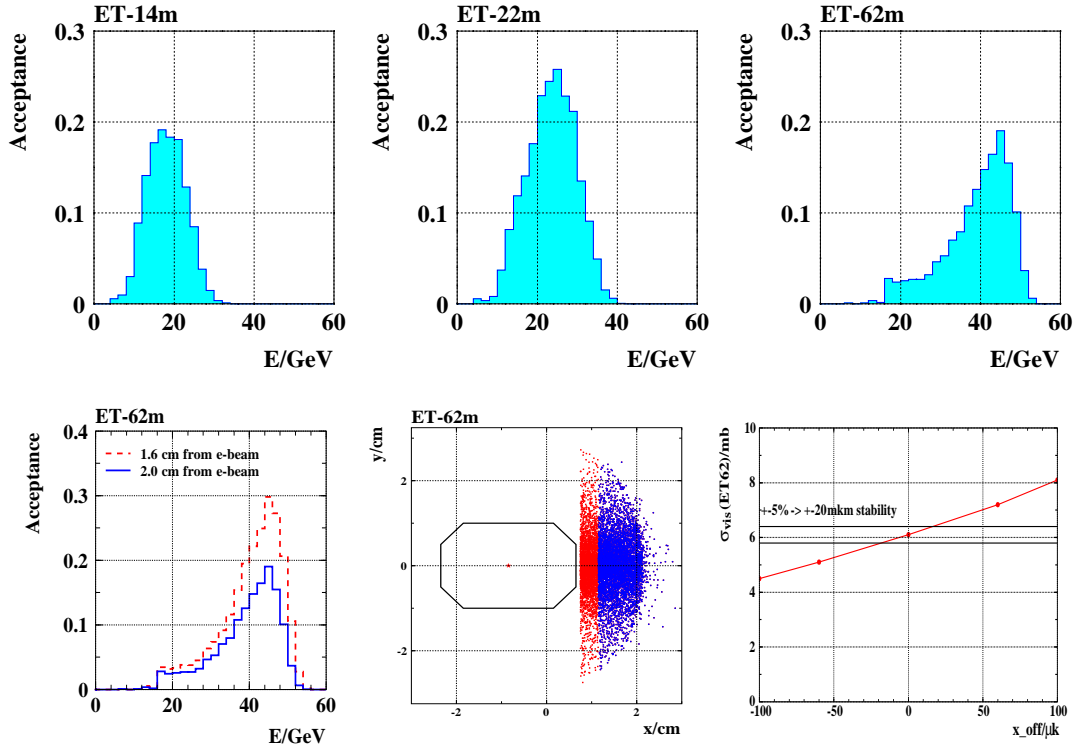


Figure 13.2: Top: acceptances of the e -taggers for Bethe-Heitler events at different z -positions from IP (RR-option). Bottom: variations in the acceptance of the e -tagger at $z = -62\text{m}$ as a function of its position with respect to the e -beam axis and on the horizontal offset of the beam orbit at the IP.

9731 13.1.5 Summary and Open Questions

9732 Accurate luminosity measurement at the LHeC is highly non-trivial task. As follows from
 9733 HERA experience unexpected surprises are possible, hence it is important to consider several
 9734 scenarios from the beginning and to prepare alternative methods for luminosity determination.

9735 Statistical precision and systematic uncertainties for different methods of luminosity mea-
 9736 surement are summarised in Table 13.1.

9737 Precise determination of integrated luminosity, \mathcal{L} , is possible with the main detector utilising
 9738 the QEDC process. $\delta\mathcal{L} = 1.5 - 2\%$ is within reach. Further improvement requires in particular
 9739 more accurate theoretical calculation of the elastic QED Compton cross section, with $\delta\sigma_{\text{el}}^{\text{QEDC}} \lesssim$
 9740 0.5% . To enhance statistical precision a dedicated QEDC tagger at $z = -6\text{m}$ might be useful.
 9741 This device could also be used to access very low Q^2 region, interpolating between DIS and
 9742 photoproduction regimes.

9743 Fast instantaneous luminosity monitoring is challenging, but several options do exist which
 9744 are based upon detection of the photons and/or electrons from the Bethe-Heitler process.

- 9745 • Photon Detector at $z = 110\text{m}$ for LR option requires properly shaped proton beam-pipe

Method	Stat. error	Syst.error	Systematic error components	Application
BH (γ)	0.05%/sec	1–5%	$\sigma(E \gtrsim 10\text{GeV})$ acceptance, A E -scale, pileup	0.5% 10%(1– A) 0.5 – 4% Monitoring, tuning, short term variations
BH (e)	0.2%/sec	3–6%	$\sigma(E \gtrsim 10\text{GeV})$ acceptance background E -scale	0.5% 2.5 – 5% 1% 1% Monitoring, tuning, short term variations
QEDC	0.5%/week	1.5%	σ (el/inel) acceptance vertex eff. E -scale	1% 1% 0.5% 0.3% Absolute \mathcal{L} , global normalisation
NC DIS	0.5%/h	2.5%	σ ($y < 0.6$) acceptance vertex eff. E -scale	2% 1% 1% 0.3% Relative \mathcal{L} , mid-term variations

Table 13.1: Dominant systematics for various methods of luminosity measurement.

9746 at $z = -68 - 120\text{m}$ from IP2.

9747 • In case of RR option Bethe-Heitler photons can be detected using a water Čerenkov
9748 counter integrated with SR absorber at $z = -22\text{m}$.

9749 • Electron tagger at $z = -62\text{m}$ is very promising for both LR and RR schemes. It can
9750 be used not only for luminosity monitoring, but also to enhance photoproduction physics
9751 capabilities and to provide extra control of the γp background to DIS, by tagging quasi-
9752 real photoproduction events.

9753 Good monitoring of the e -optics at the IP is required to control acceptances of the tunnel
9754 detectors to a level of 2 – 5%.

9755 13.2 Polarimeter

The most powerful technique to measure the polarisation of the electrons and positrons of LHeC is Compton polarimetry. At high electron beam energies, this technique has been successfully used in the past at SLC [?] and at HERA [?] for example. The experimental setup consists of a laser beam which provides the electron/positron beam, and a calorimeter to measure the scattered gamma ray. At SLC, the scattered electron was also measured in a dedicated spectrometer. From the kinematics of Compton scattering one can get the expression for the maximum scattered photon energy:

$$E_{\gamma,max} \approx E_0 \frac{x}{1+x}$$

and the minimum scattered electron energy

$$E_{e,min} \approx E_0 \frac{1}{1+x},$$

9756 where E_0 is the electron/positron beam energy and $x = 4kE_0/m_e^2$ with k being the laser photon
9757 beam energy. At LHeC and for a $\approx 1\mu\text{m}$ laser beam wavelength, one gets $E_{\gamma,max} \approx 29\text{GeV}$ and
9758 $E_{e,min} \approx 31\text{GeV}$. Providing that the laser beam is circularly polarised, the electron/positron
9759 beam longitudinal polarisation is obtained from a fit to the scattered photon and/or to the
9760 electron energy spectrum. From an experimental point of view, both measurements can be
9761 complementary since the high energy region of the scattered photon energy spectrum is sensitive
9762 to the electron/positron beam longitudinal polarisation, whereas it is the opposite for the
9763 scattered electron/positron energy spectrum. Indeed, the high measurement precision of SLC
9764 was achieved thanks to the measurement of the scattered electrons. The measurement of both
9765 scattered photon and electron/positron spectra was therefore foreseen for a very high precision
9766 polarimetry at future electron-positron high energy colliders [?,?].

9767 For LHeC, we may follow the work done for the future linear colliders [?]. In order to reach
9768 the per mille level on the longitudinal polarisation measurement, one may measure both the
9769 scattered photon and electron energy spectrum.

9770 13.2.1 Polarisation from the scattered photons

9771 The photons are scattered within a very narrow cone of half aperture $\approx 1/\gamma$. It is therefore
9772 impossible to distinguish the photons reaching the calorimeter. As for the extraction of the
9773 longitudinal polarisation from the scattered photon beam energy, one may then distinguishes
9774 three dynamical regimes [?]. The single and few scattered photons regimes, where one can
9775 extract the polarisation from a first principle fit to the scattered photon energy spectrum; the
9776 multi-photon regime where the central limit theorem holds for the energy spectra and where the
9777 longitudinal polarisation is extracted from an asymmetry between the average scattered energies
9778 corresponding to a circularly left and right laser beam polarisation [?]. Both regimes have
9779 positive and negative experimental features. In the single and few photon regimes the energy
9780 spectra exhibits kinematical edges which allow an in situ calibration of the detector energy
9781 response but the physical accelerator photon background which is difficult to model precisely,
9782 e.g. synchrotron radiation, limits the final precision on the polarisation measurement [?]. In
9783 the multi-photon regime, the background is negligible since it is located at low energy but
9784 one cannot measure the energy calibration of the detector in situ and one must rely on some
9785 high energy extrapolation of calibrations obtained at low energy [?] (e.g. for 100 scattered
9786 photon/bunch the deposited energy in the calorimeter would be more than 1TeV at LHeC).
9787 However, the laser technology has improved in the last ten years and one can consider at present
9788 a very stable pulsed laser beam with adjustable pulse energy allowing to operate in single, few
9789 and multi photon regimes. In this way, one can calibrate the calorimeter in situ and optimise
9790 the dynamical regime, a multi-photon regime as close as possible to the few photon regime, in
9791 order to minimise the final uncertainty on the polarisation measurement.

9792 13.2.2 Polarisation from the scattered electrons

9793 The nice feature of the scattered electron/positron is that one can use a magnetic spectrometer
9794 to distinguish them from each other. Following [?] one may carefully design a Compton inter-

9795 action region in order to implement a dedicated electron spectrometer followed by a segmented
9796 electron detector in order to measure the scattered electron angular spectrum, itself related
9797 to the electron energy spectrum. A precise particle tracking is needed but this experimental
9798 method also allows a precise control of the systematic uncertainties [?].

9799 Common to both techniques is the control and measurement of the laser beam polarisation.
9800 it was shown in [?] that a few per mille precision can be achieved in an accelerator environment.
9801 Therefore, with a redundancy in measuring the electron/positron beam longitudinal polarisation
9802 from both the electron and photon scattered energy spectra, a final precision at the per mille
9803 level will be reachable at LHeC.

9804 13.3 Zero Degree Calorimeter

9805 The goal of Zero Degree Calorimeter (ZDC) is to measure the energy and angles of very forward
9806 particles. At HERA experiments, H1 and ZEUS, the forward neutral particles scattered at polar
9807 angles below 0.75 mrad have been measured in the dedicated Forward Neutron Calorimeters
9808 (FNC) [466, 698]. The LHC experiments, CMS, ATLAS, ALICE and LHCf, have the ZDC
9809 calorimeters for detection of forward neutral particles, ALICE has also the ZDC calorimeter for
9810 the measurements of spectator protons [699–703].

9811 The ZDC calorimeter will be an important addition to the future LHeC experiment as many
9812 physics measurements in ep , ed and eA collisions can be made possible with the installation of
9813 ZDC.

9814 13.3.1 ZDC detector design

9815 The position of the Zero Degree Calorimeter in the tunnel and the overall dimensions depend
9816 mainly on the space available for the installation. At the LHC the beams are deflected by two
9817 separating dipoles. These dipoles also deflect the spectator protons, separating them from the
9818 neutrons and photons, which scatter at $\sim 0^\circ$.

9819 The ZDC detector will be made of two calorimeters: one for the measurement of neutral
9820 particles at 0° and another one positioned externally to the outgoing proton beam for the
9821 measurement of spectator protons from eD and eA scattering. The geometry, technical speci-
9822 fications and proposed design of ZDC detectors are to large extent similar to the ZDCs of the
9823 LHC experiments. There the ZDC calorimeter for detection of neutral particles are placed at
9824 $z = 115 - 140$ m in a 90 mm narrow space between two beam pipes. (The photo of neutron
9825 calorimeter of ALICE experiment [699, 700] is shown in Figure 13.4). In the case of the LHeC,
9826 the ZDC calorimeter can be placed in the space available at about 90 – 100 m next to the
9827 interacting proton beam pipe, as indicated in Figure 13.5.

9828 Below the general considerations for the design are presented. In order to finalise the study
9829 of the geometry of detectors, a detailed simulation of the LHeC interaction region and the
9830 beamline must be performed.

9831 13.3.2 Neutron Calorimeter

9832 The design of ZDC has to satisfy various technical issues. Detector has to be capable of detecting
9833 neutrons and photons produced with scattering angles up to 0.3 mrad or more and energies
9834 between some hundreds GeV to the proton beam energy (7 TeV) with a reasonable resolution

9835 of few percents. It should be able to distinguish hadronic and electromagnetic showers (i.e.
9836 separate neutrons from photons) and to separate showers from two or more particle entering
9837 the detector (i.e. needs position resolution of $\mathcal{O}(1\text{mm})$ or better).

9838 The condition, that at least 95% of hadronic shower of $\mathcal{O}(\text{TeV})$ is contained within the
9839 calorimeter, requires 9.5–10 nuclear interaction lengths of absorber. The neutron ZDC will
9840 be made of two sections. The front part of calorimeter (electromagnetic section) with 1.5-2 λ
9841 length and fine granularity is needed for precise determination of the position of impact point,
9842 discrimination of electromagnetic and hadronic showers and separation of showers from two or
9843 more particles entering the detector. The hadronic section of the ZDC can be built with coarser
9844 sampling, which gives an increase of average density and, consequently, the increase of effective
9845 nuclear interaction length. The ZDC will be operating in a very hard radiation environment,
9846 therefore it has to be made of radiation resistant materials. Since the different parts of calorime-
9847 ter undergo different intensity of radiation (higher for front part), it is advantageous to have
9848 longitudinal segmentation of 4-5 identical sections, which will allow to control the change of
9849 energy response due to radiation damage. Comparison of the energy spectrum from the showers
9850 which start in different sections can be used for correction of changes in energy response.

9851 A possible solution to build a compact device with good radiation resistance is to use
9852 spaghetti calorimeter with tungsten absorbers and quartz fibres. The principle of operation is
9853 based on the detection of Cherenkov light produced by the shower's charged particles in the
9854 fibres. These detectors are proven to be fast (\sim few ns), radiation hard and have good energy
9855 resolution. Using tungsten as a passive material allows the construction of compact devices.
9856 One can also consider option to use thick gaseous electron multipliers (THGEM) [704, 705] as
9857 active media.

9858 13.3.3 Proton Calorimeter

9859 In analogy to ALICE experiment, the second ZDC for detection of spectator protons can be
9860 positioned at about a same distance from IP as neutron ZDC [699, 700]. The size of proton
9861 ZDC has to be small, due to the few cm small size of spectator proton spot, but sufficient to
9862 obtain shower containment. This calorimeter will be made with same technique as the neutron
9863 ZDC.

9864 13.3.4 Calibration and monitoring

9865 After initial calibration of the ZDCs with test-beams, it is essential to have regular online and
9866 offline control of the stability of the response, in particular due to hard radiation and temper-
9867 ature environment. The stability of the gain of the PMTs and the radiation damage in fibres
9868 can be monitored using the laser or LED light pulses. The stability of absolute calibration
9869 can be monitored using the interactions of the proton beam and residual gas molecules in the
9870 beam-pipe and comparison with the results of Monte Carlo simulation based on pion exchange,
9871 as used at HERA [466, 698]. A useful tool for absolute energy calibration will be the recon-
9872 struction of invariant masses, e.g. $\pi^0 \rightarrow 2\gamma$ or $\Lambda, \Delta \rightarrow n\pi^0$, with decay particles produced at
9873 very small opening angles and reconstructed in ZDC. This will however require the possibility
9874 to reconstruct several particles in the ZDC within one event.

13.4 Forward Proton Detection

In diffractive interactions between protons or between an electron and a proton, the proton may survive a hard collision and be scattered at a low angle θ along the beam line while losing a small fraction ξ ($\sim 1\%$) of its energy. The ATLAS and CMS collaborations have investigated the feasibility to install detectors along the LHC beam line to measure the energy and momentum of such diffractively scattered protons [?]. Since the proton beam optics is primarily determined by the shape of the accelerator - which will not change for proton arm of the LHeC - the conclusions reached in this R&D study are still relevant for an LHeC detector.

In such a setup, diffractively scattered protons are separated from the nominal beam when traveling through dipole magnets with a slightly lower momentum. This spectroscopic behavior of the accelerator is described by the energy dispersion function, D_x , which, when multiplied with the actual energy loss, ξ , gives the additional offset of the trajectory followed by the off-momentum proton:

$$x_{\text{offset}} = D_x \times \xi.$$

The acceptance window in ξ is therefore determined by the closest possible approach of the proton detectors to the beam for low ξ and by the distance of the beam pipe walls from the nominal proton trajectory for high ξ . The closest possible approach is often taken to be equal to 12σ with σ equal to the beam width at a specific point. At the point of interest, 420m from the interaction point, the beam width is approximately equal to $250 \mu\text{m}$. On the other hand, the typical LHC beam pipe radius at large distances from the interaction point is approximately 2 cm. Even protons that have lost no energy, will eventually hit the beam pipe wall if they are scattered at large angles. This therefore fixes the maximally allowed fourmomentum-transfer squared t , which is approximately equal to the square of the transverse momentum p_T of the scattered proton at the interaction point.

At 420 m from the interaction point, the dispersion function at the LHC reaches 1.5 m, which results in an optimal acceptance window for diffractively scattered protons (roughly $0.002 < \xi < 0.013$). The acceptance as function of ξ and t is shown in Fig. 13.6, using the LHC proton beam optics [?]. The small corrections to be applied for the LHeC proton beam optics are not considered to be relevant for the description of the acceptance.

When the proton's position and angle w.r.t. the nominal beam can be accurately measured by the detectors, it is in principle possible to reconstruct the initial scattering angles and momentum loss of the proton at the interaction point. Even with an infinitesimally small detector resolution, the intrinsic beam width and divergence will still imply a lower limit on the resolution of the reconstructed kinematics. As the beam is typically maximally focussed at the interaction point in order to obtain a good luminosity, it will be the beam divergence that dominates the resolution on reconstructed variables.

Figure 13.7 show the relation of position and angle w.r.t. the nominal beam and the proton scattering angle and momentum loss in both the horizontal and vertical plane as obtained from the LHC proton beam optics [?]. Clearly, in order to distinguish angles and momentum losses indicated by the curves in Fig. 13.7, the detector must have a resolution better than the distance between the curves.

As stated above, protons with the same momentum loss and scattering angles will still end up at different positions and angles due to the intrinsic width and divergence of the beam. Lower limits on the resolution of reconstructed kinematics can therefore be determined. These are typically of the order of 0.5% for ξ and $0.2 \mu\text{rad}$ for the scattering angle θ . Figure 13.8 show the main dependences of the resolution on ξ , t and the azimuthal scattering angle ϕ .

9915 A crucial issue in the operation of near-beam detectors is the alignment of the detectors
9916 w.r.t. the nominal beam. Typically, such detectors are retracted when beams are injected and
9917 moved close to the beam only when the accelerator conditions are declared to be stable. Also
9918 the beam itself, may not always be reinjected at the same position. It is therefore important to
9919 realign the detectors at for each accelerator run and to monitor any drifts during the run. At
9920 HERA, a kinematic peak method section was used for alignment: as the reconstructed scattering
9921 angles depend on the misalignment, one may extract alignment constants by required that the
9922 observed cross section is maximal for forward scattering. In addition, this alignment procedure
9923 may be cross-checked by using a physics process with a exclusive system produced in the central
9924 detector such that the proton kinematics is fixed by applying energy-momentum conservation
9925 to the full set of final state particles. The feasibility of various alignment methods at the LHeC
9926 remains to be studied.

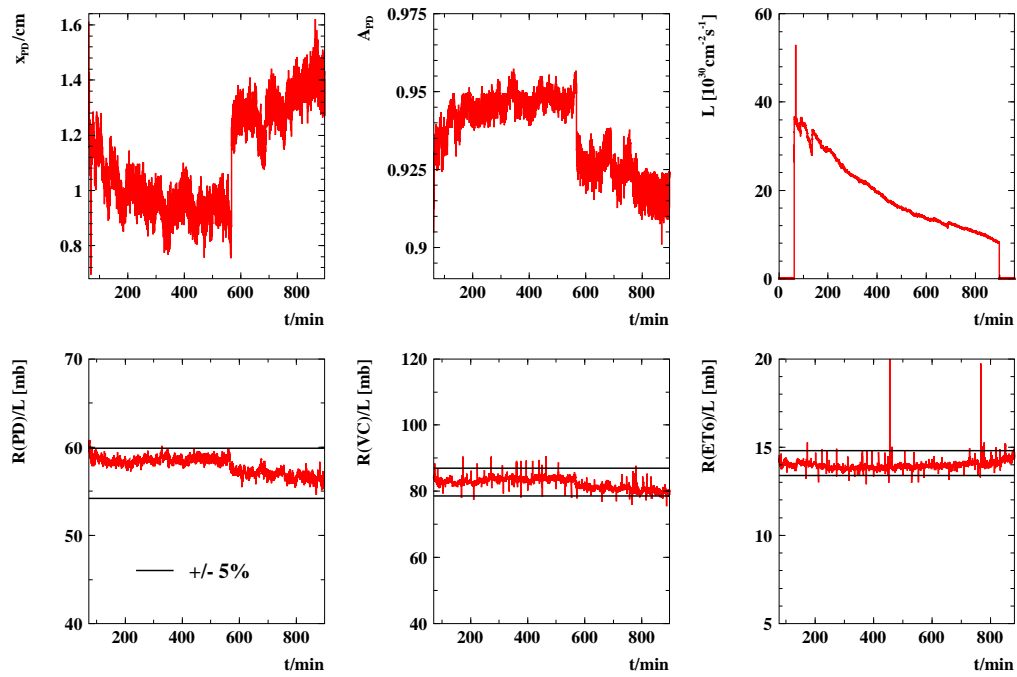


Figure 13.3: Online H1 Lumi System acceptance and rates variations in a typical HERA luminosity fill.

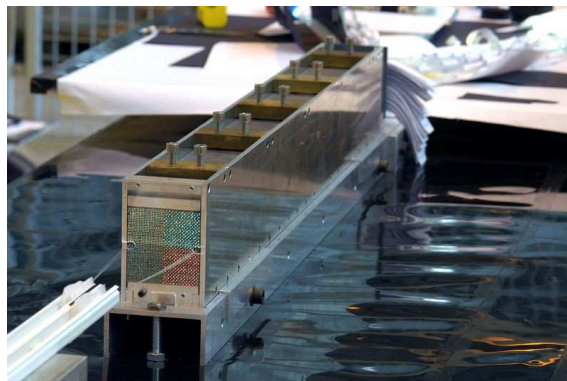


Figure 13.4: Photo of the Zero Degree Neutron Calorimeter (ZN) of ALICE experiment.

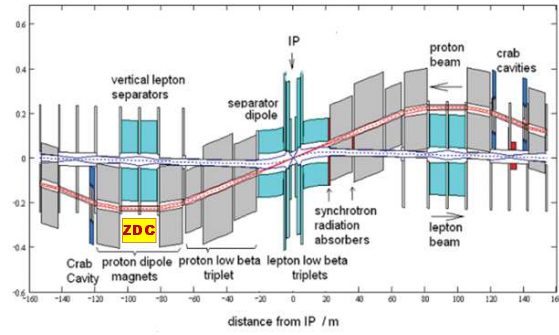


Figure 13.5: Schematic layout of the LHeC interaction region. The possible position of the ZDC is indicated.

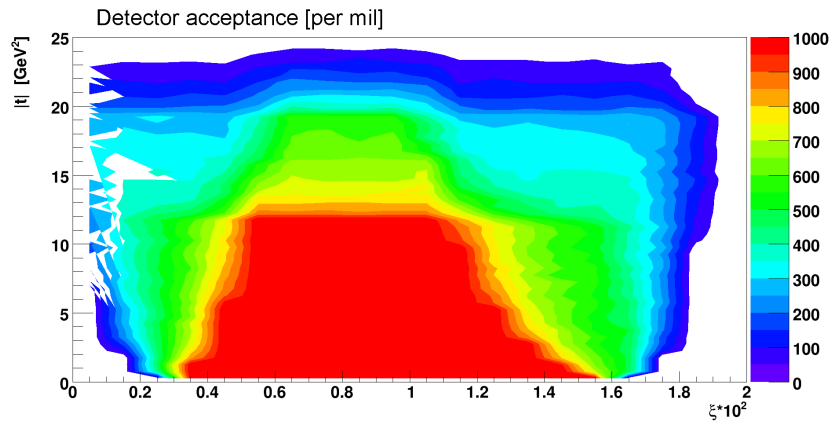


Figure 13.6: The acceptance for a proton detector placed at 420m from the interaction point is shown as function of the momentum loss ξ and the fourmomentum-transfer squared t . The color legend runs from 0‰(no acceptance) to 1000‰(full acceptance).

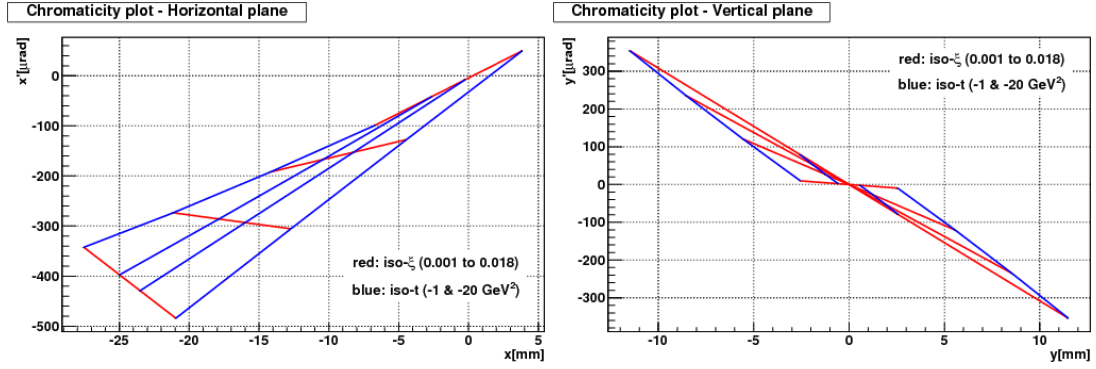


Figure 13.7: Lines of constant ξ and $t \approx (1 - \xi)E_{\text{beam}}\theta^2$ are shown in the plane of proton position and angle w.r.t. the nominal proton beam in the horizontal (left) and vertical (right) plane.

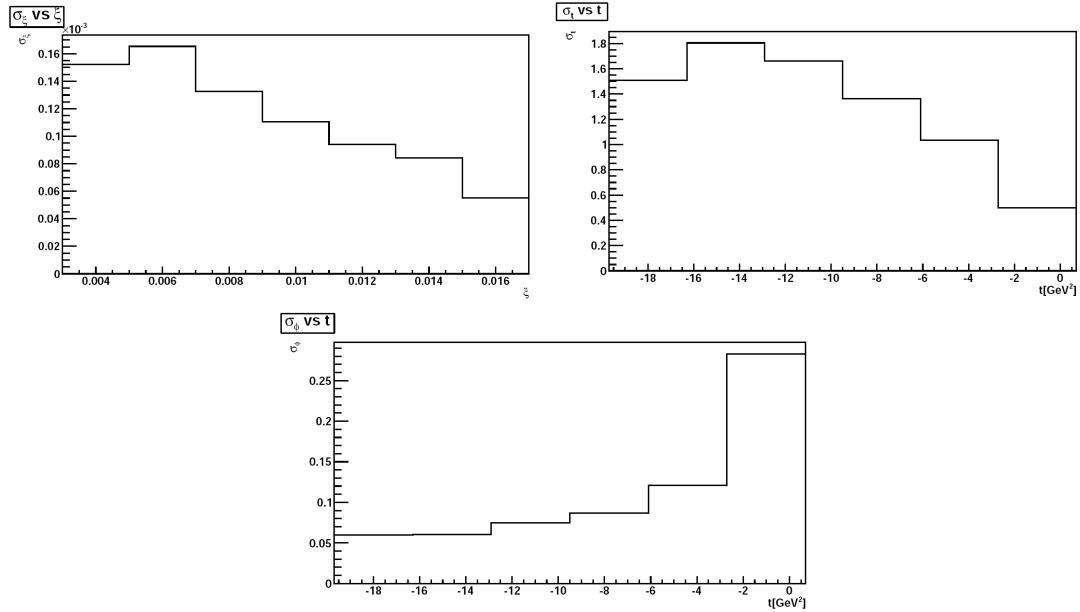


Figure 13.8: The lower limit due to the intrinsic beam width and divergence on the resolution of kinematic variables is shown for ξ as function ξ (top left), t as function t (top right) and ϕ as function of t (bottom).

9927

Part V

9928

Summary

9929 Acknowledgement

9930 Many thanks to many

9931 We express our gratitude to E. Avsar, W. K. Brooks, J. R. Forshaw, K. Golec-Biernat, K.
9932 Kutak, J. G. Milhano, G. Pancheri, T. C. Rogers and T. Teubner for discussions, information
9933 on their work and presentations at the LHeC workshops.

Bibliography

- 9935 [1] H. Geiger and E. Marsden, *On a Diffuse Reflection of the α Particles*, Proc. Royal
9936 Society **A82** (1909) 495–500.
- 9937 [2] E. Rutherford, *The scattering of the α and β Particles by Matter and the Strcuture of*
9938 *the Atom*, Philosophical Magazine, Series 6 **21** (1911) 669–688.
- 9939 [3] R. Hofstadter and R. McAllister, *ELECTRON SCATTERING FROM THE PROTON*,
9940 Phys.Rev. **98** (1955) 217–218.
- 9941 [4] E. D. Bloom, D. Coward, H. DeStaebler, J. Drees, G. Miller, et al., *High-Energy*
9942 *Inelastic $e p$ Scattering at 6-Degrees and 10-Degrees*, Phys.Rev.Lett. **23** (1969) 930–934.
- 9943 [5] M. Breidenbach, J. I. Friedman, H. W. Kendall, E. D. Bloom, D. Coward, et al.,
9944 *Observed Behavior of Highly Inelastic electron-Proton Scattering*, Phys.Rev.Lett. **23**
9945 (1969) 935–939.
- 9946 [6] D. J. Gross and F. Wilczek, *ULTRAVIOLET BEHAVIOR OF NON-ABELIAN*
9947 *GAUGE THEORIES*, Phys. Rev. Lett. **30** (1973) 1343–1346.
- 9948 [7] H. D. Politzer, *RELIABLE PERTURBATIVE RESULTS FOR STRONG*
9949 *INTERACTIONS?*, Phys. Rev. Lett. **30** (1973) 1346–1349.
- 9950 [8] R. Feynman, *Photon-hadron interactions*, . 1973.
- 9951 [9] H. Fritzsch, M. Gell-Mann, and H. Leutwyler, *Advantages of the Color Octet Gluon*
9952 *Picture*, Phys.Lett. **B47** (1973) 365–368.
- 9953 [10] H1 and ZEUS Collaboration, F. Aaron et al., *Combined Measurement and QCD*
9954 *Analysis of the Inclusive $e^+ p$ Scattering Cross Sections at HERA*, JHEP **1001** (2010)
9955 109, [arXiv:0911.0884](https://arxiv.org/abs/0911.0884) [[hep-ex](#)].
- 9956 [11] A. De Rujula, *Charm is found*, . Proceedings of XVIII ICHEP Conference, Tbilissi,
9957 1976.
- 9958 [12] A. Salam, *The Unconfined Quarks and Gluons*, . Proceedings of XVIII ICHEP
9959 Conference, Tbilissi, 1976.
- 9960 [13] weissnicht, *E6*, . 1976.
- 9961 [14] weissnicht, *RPV SUSY*, . 1976.

- 9962 [15] J. C. Pati and A. Salam, *Lepton Number as the Fourth Color*, Phys. Rev. **D10** (1974)
9963 275–289.
- 9964 [16] B. Andersson, G. Gustafson, G. Ingelman, and T. Sjostrand, *Parton Fragmentation and*
9965 *String Dynamics*, Phys. Rept. **97** (1983) 31–145.
- 9966 [17] J. Kuti and V. F. Weisskopf, *Inelastic lepton - nucleon scattering and lepton pair*
9967 *production in the relativistic quark parton model*, Phys.Rev. **D4** (1971) 3418–3439.
- 9968 [18] S. Brodsky, P. Hoyer, C. Peterson, and N. Sakai, *The Intrinsic Charm of the Proton*,
9969 Phys.Lett. **B93** (1980) 451–455.
- 9970 [19] D. Mueller, D. Robaschik, B. Geyer, F. M. Dittes, and J. Horejsi, *Wave functions,*
9971 *evolution equations and evolution kernels from light-ray operators of QCD*, Fortschr.
9972 Phys. **42** (1994) 101, [arXiv:hep-ph/9812448](#).
- 9973 [20] A. V. Belitsky and A. V. Radyushkin, *Unraveling hadron structure with generalized*
9974 *parton distributions*, Phys. Rept. **418** (2005) 1–387, [arXiv:hep-ph/0504030](#).
- 9975 [21] V. N. Gribov, *Interaction of gamma quanta and electrons with nuclei at high-energies*,
9976 Sov. Phys. JETP **30** (1970) 709–717.
- 9977 [22] M. Klein and T. Riemann, *ELECTROWEAK INTERACTIONS PROBING THE*
9978 *NUCLEON STRUCTURE*, Z.Phys. **C24** (1984) 151.
- 9979 [23] E. Derman, *Tests for a weak neutral current in lN to $l+$ anything at high energy*,
9980 Phys.Rev. **D7** (1973) 2755–2775.
- 9981 [24] J. Callan, Curtis G. and D. J. Gross, *High-energy electroproduction and the constitution*
9982 *of the electric current*, Phys.Rev.Lett. **22** (1969) 156–159.
- 9983 [25] G. Altarelli and G. Martinelli, *Transverse Momentum of Jets in Electroproduction from*
9984 *Quantum Chromodynamics*, Phys.Lett. **B76** (1978) 89.
- 9985 [26] A. Argento, A. Benvenuti, D. Bollini, G. Bruni, T. Camporesi, et al., *MEASUREMENT*
9986 *OF THE INTERFERENCE STRUCTURE FUNCTION $xG(3)(x)$ IN MUON -*
9987 *NUCLEON SCATTERING*, Phys.Lett. **B140** (1984) 142.
- 9988 [27] A. Arbuzov, D. Y. Bardin, J. Blumlein, L. Kalinovskaya, and T. Riemann, *Hector 1.00:*
9989 *A Program for the calculation of QED, QCD and electroweak corrections to $e p$ and*
9990 *lepton+- N deep inelastic neutral and charged current scattering*,
9991 Comput.Phys.Commun. **94** (1996) 128–184, [arXiv:hep-ph/9511434](#) [hep-ph].
- 9992 [28] Particle Data Group Collaboration, K. Nakamura, *Review of particle physics*, J. Phys.
9993 **G37** (2010) 075021.
- 9994 [29] J. Blumlein and M. Klein, *On the cross calibration of calorimeters at $e p$ colliders*, Nucl.
9995 Instrum. Meth. **A329** (1993) 112–116.
- 9996 [30] M. Klein, *Scenarios and Measurements with the LHeC*, Talk given at the LHeC Meeting
9997 at DIS 2009, Madrid, Spain, April 2009.

- 9998 [31] ZEUS Collaboration, S. Chekanov et al., *Measurement of the Longitudinal Proton*
9999 *Structure Function at HERA*, Phys.Lett. **B682** (2009) 8–22, arXiv:0904.1092
10000 [hep-ex].
- 10001 [32] F. Aaron, C. Alexa, V. Andreev, S. Backovic, A. Baghdasaryan, et al., *Measurement of*
10002 *the Inclusive $e\pm p$ Scattering Cross Section at High Inelasticity y and of the Structure*
10003 *Function FL* , Eur.Phys.J. **C71** (2011) 1579, arXiv:1012.4355 [hep-ex].
- 10004 [33] M. Botje, *QCDNUM manual*. <http://www.nikhef.nl/~h24/qcdnum/>.
10005 <http://www.nikhef.nl/~h24/qcdnum/>.
- 10006 [34] E. Rizvi and T. Sloan, *$x F^{**}(\gamma Z)(3)$ in charged lepton scattering*,
10007 Eur.Phys.J.direct **C3** (2001) N2, arXiv:hep-ex/0101007 [hep-ex].
- 10008 [35] HERMES Collaboration, A. Airapetian et al., *Measurement of Parton Distributions of*
10009 *Strange Quarks in the Nucleon from Charged-Kaon Production in Deep-Inelastic*
10010 *Scattering on the Deuteron*, Phys. Lett. **B666** (2008) 446–450, arXiv:0803.2993
10011 [hep-ex].
- 10012 [36] U. Baur and J. van der Bij, *TOP QUARK PRODUCTION AT HERA*, Nucl.Phys.
10013 **B304** (1988) 451.
- 10014 [37] H. Fritzsche and D. Holtmannspotter, *The Production of single t quarks at LEP and*
10015 *HERA*, Phys. Lett. **B457** (1999) 186–192, arXiv:hep-ph/9901411.
- 10016 [38] C. Pascaud, *CFNS*, Talk given at DIS 2011, Newport News, USA, April 2011.
- 10017 [39] G. Brandt, *Single top production of diquarks at LHeC*, Talk given at the 1st
10018 CERN-ECFA Workshop on the LHeC, Divonne-les-Bains, France, 1-3 September 2008.
- 10019 [40] CMS Collaboration, S. Chatrchyan et al., *Measurement of the t -channel single top quark*
10020 *production cross section in pp collisions at $\sqrt{s} = 7$ TeV*, arXiv:1106.3052
10021 [hep-ex]. * Temporary entry *.
- 10022 [41] A. Glazov, S. Moch, and V. Radescu, *Parton Distribution Uncertainties using*
10023 *Smoothness Prior*, Phys.Lett. **B695** (2011) 238–241, arXiv:1009.6170 [hep-ph].
- 10024 [42] S. Alekhin, J. Blumlein, P. Jimenez-Delgado, S. Moch, and E. Reya, *NNLO Benchmarks*
10025 *for Gauge and Higgs Boson Production at TeV Hadron Colliders*, Phys. Lett. **B697**
10026 (2011) 127–135, arXiv:1011.6259 [hep-ph].
- 10027 [43] S. Moch, J. Vermaseren, and A. Vogt, *The Three loop splitting functions in QCD: The*
10028 *Nonsinglet case*, Nucl.Phys. **B688** (2004) 101–134, arXiv:hep-ph/0403192 [hep-ph].
- 10029 [44] J. A. M. Vermaseren, A. Vogt, and S. Moch, *The third-order QCD corrections to*
10030 *deep-inelastic scattering by photon exchange*, Nucl. Phys. **B724** (2005) 3–182,
10031 arXiv:hep-ph/0504242.
- 10032 [45] I. Bierenbaum, J. Blumlein, and S. Klein, *Mellin Moments of the $O(\alpha^{**3}(s))$ Heavy*
10033 *Flavor Contributions to unpolarized Deep-Inelastic Scattering at $Q^{**2} \gg m^{**2}$ and*
10034 *Anomalous Dimensions*, Nucl.Phys. **B820** (2009) 417–482, arXiv:0904.3563
10035 [hep-ph].

- 10036 [46] J. Blumlein, H. Bottcher, and A. Guffanti, *Non-singlet QCD analysis of deep inelastic*
10037 *world data at $O(\alpha(s)^{**3})$* , Nucl.Phys. **B774** (2007) 182–207,
10038 arXiv:hep-ph/0607200 [hep-ph].
- 10039 [47] M. Gluck, E. Reya, and C. Schuck, *Non-singlet QCD analysis of $F(2)(x, Q^{**2})$ up to*
10040 *NNLO*, Nucl.Phys. **B754** (2006) 178–186, arXiv:hep-ph/0604116 [hep-ph].
- 10041 [48] S. Alekhin, J. Blumlein, S. Klein, and S. Moch, *The 3, 4, and 5-flavor NNLO Parton*
10042 *from Deep-Inelastic-Scattering Data and at Hadron Colliders*, Phys.Rev. **D81** (2010)
10043 014032, arXiv:0908.2766 [hep-ph].
- 10044 [49] P. Jimenez-Delgado and E. Reya, *Dynamical NNLO parton distributions*, Phys. Rev.
10045 **D79** (2009) 074023, arXiv:0810.4274 [hep-ph].
- 10046 [50] A. D. Martin, W. J. Stirling, R. S. Thorne, and G. Watt, *Uncertainties on α_s in*
10047 *global PDF analyses and implications for predicted hadronic cross sections*, Eur. Phys.
10048 J. **C64** (2009) 653–680, arXiv:0905.3531 [hep-ph].
- 10049 [51] S. Alekhin, J. Blumlein, and S.-O. Moch, *Update of the NNLO PDFs in the 3-, 4-, and*
10050 *5-flavour scheme*, PoS **DIS2010** (2010) 021, arXiv:1007.3657 [hep-ph].
- 10051 [52] S. Bethke, *The 2009 World Average of $\alpha(s)$* , Eur.Phys.J. **C64** (2009) 689–703,
10052 arXiv:0908.1135 [hep-ph].
- 10053 [53] J. Blumlein, S. Riemersma, W. van Neerven, and A. Vogt, *Theoretical uncertainties in*
10054 *the QCD evolution of structure functions and their impact on $\alpha-s$ ($M(Z)^{**2}$)*,
10055 Nucl.Phys.Proc.Suppl. **51C** (1996) 97–105, arXiv:hep-ph/9609217 [hep-ph].
- 10056 [54] S. J. Brodsky, *Novel QCD Phenomenology at the LHeC*, arXiv:1106.5820 [hep-ph].
10057 LHeC-Note-2011-002 PHY and SLAC-PUB-14487.
- 10058 [55] M. Buza, Y. Matiounine, J. Smith, and W. van Neerven, *Charm electroproduction*
10059 *viewed in the variable flavor number scheme versus fixed order perturbation theory*,
10060 Eur.Phys.J. **C1** (1998) 301–320, arXiv:hep-ph/9612398 [hep-ph].
- 10061 [56] S. Alekhin and S. Moch, *Heavy-quark deep-inelastic scattering with a running mass*,
10062 Phys. Lett. **B699** (2011) 345–353, arXiv:1011.5790 [hep-ph].
- 10063 [57] T. Gehrmann, M. Jaquier, and G. Luisoni, *Hadronization effects in event shape*
10064 *moments*, Eur.Phys.J. **C67** (2010) 57–72, arXiv:0911.2422 [hep-ph].
- 10065 [58] R. Abbate, M. Fickinger, A. H. Hoang, V. Mateu, and I. W. Stewart, *Thrust at N^3LL*
10066 *with Power Corrections and a Precision Global Fit for $\alpha_s(m_Z)$* , Phys.Rev. **D83**
10067 (2011) 074021, arXiv:1006.3080 [hep-ph].
- 10068 [59] M. Virchaux and A. Milsztajn, *A Measurement of $\alpha-s$ and higher twists from a QCD*
10069 *analysis of high statistics $F-2$ data on hydrogen and deuterium targets*, Phys.Lett. **B274**
10070 (1992) 221–229.
- 10071 [60] H1 Collaboration, C. Adloff et al., *Deep-inelastic inclusive $e p$ scattering at low x and a*
10072 *determination of $\alpha(s)$* , Eur. Phys. J. **C21** (2001) 33–61, arXiv:hep-ex/0012053.

- 10073 [61] R. Wallny, *A Measurement of the Gluon Distribution in the Proton and of the Strong*
10074 *Coupling Constant α_s from Inclusive Deep-Inelastic Scattering*, H1 PhD Thesis
10075 2001, Zurich, Switzerland, 2001.
- 10076 [62] A. Martin, W. Stirling, R. Thorne, and G. Watt, *alphas in MSTW Analyses*, Talk given
10077 in [64], February 2011.
- 10078 [63] S. Lionetti, R. D. Ball, V. Bertone, F. Cerutti, L. Del Debbio, et al., *Precision*
10079 *determination of α_s using an unbiased global NLO parton set*, [arXiv:1103.2369](#)
10080 [hep-ph].
- 10081 [64] S. Bethke et al., *Workshop on Precision Measurements on alphas*, MPI Munich,
10082 Germany, February, 2011.
- 10083 [65] T. Kluge, *Prospects of alphas Determinations in DIS*, Talks given at the
10084 CERN-ECFA-NuPECC Workshops on the LHeC, Divonne-les-Bains, France, September
10085 2008/09.
- 10086 [66] BCDMS Collaboration, A. Benvenuti et al., *A COMPARISON OF THE STRUCTURE*
10087 *FUNCTIONS F_2 OF THE PROTON AND THE NEUTRON FROM DEEP*
10088 *INELASTIC MUON SCATTERING AT HIGH Q^{*2}* , Phys.Lett. **B237** (1990) 599.
- 10089 [67] BCDMS Collaboration, A. C. Benvenuti et al., *A HIGH STATISTICS*
10090 *MEASUREMENT OF THE DEUTERON STRUCTURE FUNCTIONS $F_2(x, Q^{*2})$*
10091 *AND R FROM DEEP INELASTIC MUON SCATTERING AT HIGH Q^{*2}* , Phys.
10092 Lett. **B237** (1990) 592.
- 10093 [68] European Muon Collaboration, J. Aubert et al., *Measurements of the nucleon structure*
10094 *functions F_{2n} in deep inelastic muon scattering from deuterium and comparison with*
10095 *those from hydrogen and iron*, Nucl.Phys. **B293** (1987) 740.
- 10096 [69] T. A. et al., *eD Scattering with H1, A Letter of Intent DESY 03-194*, .
- 10097 [70] T. A. et al., *A New experiment For HERA, MPP-2003-62*, .
- 10098 [71] T. Greenshaw and M. Klein, *The Future of lepton nucleon scattering: A Summary of*
10099 *the Durham Workshop, December 2001*, J.Phys.G **G28** (2002) 2503–2508,
10100 [arXiv:hep-ex/0204032](#) [hep-ex].
- 10101 [72] I. Schienbein, J. Yu, K. Kovarik, C. Keppel, J. Morfin, et al., *PDF Nuclear Corrections*
10102 *for Charged and Neutral Current Processes*, Phys.Rev. **D80** (2009) 094004,
10103 [arXiv:0907.2357](#) [hep-ph].
- 10104 [73] T. Hobbs, J. Londergan, D. Murdock, and A. Thomas, *Testing Partonic Charge*
10105 *Symmetry at a High-Energy Electron Collider*, Phys.Lett. **B698** (2011) 123–127,
10106 [arXiv:1101.3923](#) [hep-ph].
- 10107 [74] S. J. Brodsky and B. Chertok, *The Asymptotic Form-Factors of Hadrons and Nuclei and*
10108 *the Continuity of Particle and Nuclear Dynamics*, Phys.Rev. **D14** (1976) 3003–3020.
- 10109 [75] V. A. Matveev and P. Sorba, *Is Deuteron a Six Quark System?*, Lett.Nuovo Cim. **20**
10110 (1977) 435.

- 10111 [76] S. J. Brodsky, C.-R. Ji, and G. Lepage, *Quantum Chromodynamic Predictions for the*
10112 *Deuteron Form-Factor*, Phys.Rev.Lett. **51** (1983) 83.
- 10113 [77] R. Arnold, B. Chertok, E. Dally, A. Grigorian, C. Jordan, et al., *Measurement of the*
10114 *electron-Deuteron Elastic Scattering Cross-Section in the Range 0.8 GeV**2 ; q**2 ; 6*
10115 *GeV**2*, Phys.Rev.Lett. **35** (1975) 776.
- 10116 [78] G. R. Farrar, K. Huleihel, and H.-y. Zhang, *Deuteron form-factor*, Phys.Rev.Lett. **74**
10117 (1995) 650–653.
- 10118 [79] H. Flacher, M. Goebel, J. Haller, A. Hocker, K. Monig, et al., *Gfitter - Revisiting the*
10119 *Global Electroweak Fit of the Standard Model and Beyond*, Eur.Phys.J. **C60** (2009, see
10120 <http://gfitter.desy.de/>) 543–583, arXiv:0811.0009 [hep-ph].
- 10121 [80] J. Erler, *The Mass of the Higgs Boson in the Standard Electroweak Model*, Phys.Rev.
10122 **D81** (2010) 051301, arXiv:1002.1320 [hep-ph].
- 10123 [81] P. Gambino, *The top priority: Precision electroweak physics from low to high energy*,
10124 Int. J. Mod. Phys. **A19** (2004) 808–820, arXiv:hep-ph/0311257.
- 10125 [82] M. Davier, A. Hoecker, B. Malaescu, and Z. Zhang, *Reevaluation of the Hadronic*
10126 *Contributions to the Muon $g-2$ and to $\alpha(MZ)$* , Eur.Phys.J. **C71** (2011) 1515,
10127 arXiv:1010.4180 [hep-ph].
- 10128 [83] S. Haywood, P. Hobson, W. Hollik, Z. Kunszt, G. Azuelos, et al., *Electroweak physics*,
10129 *hep-ph/0003275*, arXiv:hep-ph/0003275 [hep-ph].
- 10130 [84] K. Rabbertz, *QCD and Electroweak Physics at LHC*, PoS **RADCOR2009** (2010) 016,
10131 arXiv:1002.3628 [hep-ph].
- 10132 [85] S. <http://www.jlab.org/qweak/>, , .
- 10133 [86] S. <http://hallaweb.jlab.org/12GeV/Moller/>, , .
- 10134 [87] R. Cashmore, E. Elsen, B. A. Kniehl, and H. Spiesberger, *Electroweak physics at HERA:*
10135 *Introduction and summary*, arXiv:hep-ph/9610251 [hep-ph].
- 10136 [88] H1 and ZEUS Collaboration, Z. Zhang, *Electroweak and beyond the Standard Model*
10137 *results from HERA*, Nucl.Phys.Proc.Suppl. **191** (2009) 271–280, arXiv:0812.4662
10138 [hep-ex].
- 10139 [89] H1 Collaboration, A. Aktas et al., *A Determination of electroweak parameters at*
10140 *HERA*, Phys.Lett. **B632** (2006) 35–42, arXiv:hep-ex/0507080 [hep-ex].
- 10141 [90] H1 Collaboration, Z.-Q. Zhang, *Combined electroweak and QCD fits including NC and*
10142 *CC data with polarised electron beam at HERA-2*, PoS **DIS2010** (2010) 056.
- 10143 [91] E. Salvioni, A. Strumia, G. Villadoro, and F. Zwirner, *Non-universal minimal Z'*
10144 *models: present bounds and early LHC reach*, JHEP **1003** (2010) 010,
10145 arXiv:0911.1450 [hep-ph].
- 10146 [92] J. Erler and P. Langacker, *Indications for an extra neutral gauge boson in electroweak*
10147 *precision data*, Phys.Rev.Lett. **84** (2000) 212–215, arXiv:hep-ph/9910315 [hep-ph].

- 10148 [93] R. Barbier, C. Berat, M. Besancon, M. Chemtob, A. Deandrea, et al., *R-parity violating*
10149 *supersymmetry*, Phys.Rept. **420** (2005) 1–202, arXiv:hep-ph/0406039 [hep-ph].
- 10150 [94] M. Carpentier and S. Davidson, *Constraints on two-lepton, two quark operators*,
10151 Eur.Phys.J. **C70** (2010, and refs. therein) 1071–1090, arXiv:1008.0280 [hep-ph].
- 10152 [95] J. Erler, A. Kurylov, and M. J. Ramsey-Musolf, *The Weak charge of the proton and new*
10153 *physics*, Phys.Rev. **D68** (2003) 016006, arXiv:hep-ph/0302149 [hep-ph].
- 10154 [96] C. Prescott, W. Atwood, R. Cottrell, H. DeStaebler, E. L. Garwin, et al., *Further*
10155 *Measurements of Parity Nonconservation in Inelastic electron Scattering*, Phys.Lett.
10156 **B84** (1979) 524.
- 10157 [97] E. A. Paschos and L. Wolfenstein, *Tests for neutral currents in neutrino reactions*,
10158 Phys. Rev. **D7** (1973) 91–95.
- 10159 [98] J. Blumlein, M. Klein, and T. Riemann, *TESTING THE ELECTROWEAK*
10160 *STANDARD MODEL AT HERA*, .
- 10161 [99] A. Czarnecki and W. J. Marciano, *Polarized Moller scattering asymmetries*,
10162 Int.J.Mod.Phys. **A15** (2000) 2365–2376, arXiv:hep-ph/0003049 [hep-ph].
- 10163 [100] B. W. Harris and J. Smith, *Charm quark and D^{*+-} cross sections in deeply inelastic*
10164 *scattering at HERA*, Phys. Rev. **D57** (1998) 2806–2812, arXiv:hep-ph/9706334.
- 10165 [101] S. Frixione, M. L. Mangano, P. Nason, and G. Ridolfi, *Total Cross Sections for Heavy*
10166 *Flavour Production at HERA*, Phys. Lett. **B348** (1995) 633–645,
10167 arXiv:hep-ph/9412348.
- 10168 [102] S. Frixione, P. Nason, and G. Ridolfi, *Differential distributions for heavy flavor*
10169 *production at HERA*, Nucl. Phys. **B454** (1995) 3–24, arXiv:hep-ph/9506226.
- 10170 [103] J. Binnewies, B. A. Kniehl, and G. Kramer, *Inclusive B meson production in $e^+ e^-$ and*
10171 *p anti- p collisions*, Phys. Rev. **D58** (1998) 034016, arXiv:hep-ph/9802231.
- 10172 [104] J. Binnewies, B. A. Kniehl, and G. Kramer, *Coherent description of D^{*+-} production in*
10173 *$e^+ e^-$ and low- Q^{*2} $e p$ collisions*, Z. Phys. **C76** (1997) 677–688,
10174 arXiv:hep-ph/9702408.
- 10175 [105] B. A. Kniehl, G. Kramer, and M. Spira, *Large $p(T)$ photoproduction of D^{*+-} mesons in*
10176 *$e p$ collisions*, Z. Phys. **C76** (1997) 689–700, arXiv:hep-ph/9610267.
- 10177 [106] M. Cacciari and M. Greco, *Charm Production via Fragmentation*, Z. Phys. **C69** (1996)
10178 459–466, arXiv:hep-ph/9505419.
- 10179 [107] G. Kramer and H. Spiesberger, *Inclusive photoproduction of D^* mesons with massive*
10180 *charm quarks*, Eur. Phys. J. **C38** (2004) 309–318, arXiv:hep-ph/0311062.
- 10181 [108] B. A. Kniehl, G. Kramer, I. Schienbein, and H. Spiesberger, *Inclusive D^{*+-} production*
10182 *in p anti- p collisions with massive charm quarks*, Phys. Rev. **D71** (2005) 014018,
10183 arXiv:hep-ph/0410289.

- 10184 [109] A. Belyaev, J. Pumplin, W.-K. Tung, and C. P. Yuan, *Uncertainties of the inclusive*
10185 *Higgs production cross section at the Tevatron and the LHC*, JHEP **01** (2006) 069,
10186 arXiv:hep-ph/0508222.
- 10187 [110] S. J. Brodsky, J. C. Collins, S. D. Ellis, J. F. Gunion, and A. H. Mueller, *INTRINSIC*
10188 *CHEVROLETS AT THE SSC*, .
- 10189 [111] B. Harris, J. Smith, and R. Vogt, *Reanalysis of the EMC charm production data with*
10190 *extrinsic and intrinsic charm at NLO*, Nucl.Phys. **B461** (1996) 181–196,
10191 arXiv:hep-ph/9508403 [hep-ph].
- 10192 [112] M. Franz, M. V. Polyakov, and K. Goeke, *Heavy quark mass expansion and intrinsic*
10193 *charm in light hadrons*, Phys.Rev. **D62** (2000) 074024, arXiv:hep-ph/0002240
10194 [hep-ph].
- 10195 [113] T. Sjostrand, S. Mrenna, and P. Z. Skands, *PYTHIA 6.4 Physics Manual*, JHEP **05**
10196 (2006) 026, arXiv:hep-ph/0603175.
- 10197 [114] J. Pumplin et al., *New generation of parton distributions with uncertainties from global*
10198 *QCD analysis*, JHEP **07** (2002) 012, arXiv:hep-ph/0201195.
- 10199 [115] H. Jung, *Hard diffractive scattering in high-energy $e p$ collisions and the Monte Carlo*
10200 *generator RAPGAP*, Comp. Phys. Commun. **86** (1995) 147–161.
- 10201 [116] CTEQ Collaboration, H. L. Lai et al., *Global QCD analysis of parton structure of the*
10202 *nucleon: CTEQ5 parton distributions*, Eur. Phys. J. **C12** (2000) 375–392,
10203 arXiv:hep-ph/9903282.
- 10204 [117] G. Ingelman, A. Edin, and J. Rathsman, *LEPTO 6.5 - A Monte Carlo Generator for*
10205 *Deep Inelastic Lepton-Nucleon Scattering*, Comput. Phys. Commun. **101** (1997)
10206 108–134, arXiv:hep-ph/9605286.
- 10207 [118] H1 and Z. Collaborations, *Combination of F_2^{cc} from DIS measurements at HERA,*
10208 *Preliminary measurements H1prelim-09-171,ZEUS-prel-09-015.*
- 10209 [119] H1 Collaboration, F. D. Aaron et al., *Measurement of the Charm and Beauty Structure*
10210 *Functions using the H1 Vertex Detector at HERA*, Eur. Phys. J. **C65** (2010) 89–109,
10211 arXiv:0907.2643 [hep-ex].
- 10212 [120] J. Pumplin, H. L. Lai, and W. K. Tung, *The charm parton content of the nucleon*, Phys.
10213 Rev. **D75** (2007) 054029, arXiv:hep-ph/0701220.
- 10214 [121] D0 Collaboration, V. Abazov et al., *Measurement of $\gamma + b + X$ and $\gamma + c$*
10215 *+ X production cross sections in p anti- p collisions at $s^{*(1/2)} = 1.96$ -TeV,*
10216 Phys.Rev.Lett. **102** (2009) 192002, arXiv:0901.0739 [hep-ex].
- 10217 [122] S. J. Brodsky, B. Kopeliovich, I. Schmidt, and J. Soffer, *Diffractive Higgs production*
10218 *from intrinsic heavy flavors in the proton*, Phys.Rev. **D73** (2006) 113005,
10219 arXiv:hep-ph/0603238 [hep-ph].
- 10220 [123] P. Aurenche, M. Fontannaz, and J. P. Guillet, *New NLO parametrizations of the parton*
10221 *distributions in real photons*, Eur. Phys. J. **C44** (2005) 395–409,
10222 arXiv:hep-ph/0503259.

- 10223 [124] W. K. Tung et al., *Heavy quark mass effects in deep inelastic scattering and global QCD*
10224 *analysis*, JHEP **02** (2007) 053, arXiv:hep-ph/0611254.
- 10225 [125] T. Kneesch, B. A. Kniehl, G. Kramer, and I. Schienbein, *Charmed-Meson*
10226 *Fragmentation Functions with Finite-Mass Corrections*, Nucl. Phys. **B799** (2008)
10227 34–59, arXiv:0712.0481 [hep-ph].
- 10228 [126] M. Gluck, E. Reya, and A. Vogt, *Photonic parton distributions*, Phys. Rev. **D46** (1992)
10229 1973–1979.
- 10230 [127] M. Klasen and G. Kramer, *Inclusive two-jet production at HERA: Direct and resolved*
10231 *cross sections in next-to-leading order QCD*, Z. Phys. **C76** (1997) 67–74,
10232 arXiv:hep-ph/9611450.
- 10233 [128] S. Catani and M. H. Seymour, *A general algorithm for calculating jet cross sections in*
10234 *NLO QCD*, Nucl. Phys. **B485** (1997) 291–419, arXiv:hep-ph/9605323.
- 10235 [129] D. Stump et al., *Inclusive jet production, parton distributions, and the search for new*
10236 *physics*, JHEP **10** (2003) 046, arXiv:hep-ph/0303013.
- 10237 [130] J. Pumplin, A. Belyaev, J. Huston, D. Stump, and W. K. Tung, *Parton distributions and*
10238 *the strong coupling: CTEQ6AB PDFs*, JHEP **02** (2006) 032, arXiv:hep-ph/0512167.
- 10239 [131] T. Gehrmann and E. W. N. Glover, *Two-Loop QCD Helicity Amplitudes for (2+1)-Jet*
10240 *Production in Deep Inelastic Scattering*, Phys. Lett. **B676** (2009) 146–151,
10241 arXiv:0904.2665 [hep-ph].
- 10242 [132] A. Daleo, A. Gehrmann-De Ridder, T. Gehrmann, and G. Luisoni, *Antenna subtraction*
10243 *at NNLO with hadronic initial states: initial-final configurations*, JHEP **01** (2010) 118,
10244 arXiv:0912.0374 [hep-ph].
- 10245 [133] S. Frixione, Z. Kunszt, and A. Signer, *Three jet cross-sections to next-to-leading order*,
10246 Nucl. Phys. **B467** (1996) 399–442, arXiv:hep-ph/9512328.
- 10247 [134] S. Frixione, *A General approach to jet cross-sections in QCD*, Nucl. Phys. **B507** (1997)
10248 295–314, arXiv:hep-ph/9706545.
- 10249 [135] M. Gluck, E. Reya, and A. Vogt, *Parton structure of the photon beyond the leading*
10250 *order*, Phys. Rev. **D45** (1992) 3986–3994.
- 10251 [136] K. J. Eskola, H. Paukkunen, and C. A. Salgado, *EPS09 - a New Generation of NLO*
10252 *and LO Nuclear Parton Distribution Functions*, JHEP **04** (2009) 065, arXiv:0902.4154
10253 [hep-ph].
- 10254 [137] S. D. Ellis and D. E. Soper, *Successive combination jet algorithm for hadron collisions*,
10255 Phys. Rev. **D48** (1993) 3160–3166, arXiv:hep-ph/9305266.
- 10256 [138] H1 Collaboration, C. Adloff et al., *Measurement of inclusive jet cross-sections in*
10257 *photoproduction at HERA*, Eur. Phys. J. **C29** (2003) 497–513, arXiv:hep-ex/0302034.
- 10258 [139] S. Frixione and G. Ridolfi, *Jet photoproduction at HERA*, Nucl. Phys. **B507** (1997)
10259 315–333, arXiv:hep-ph/9707345.

- 10260 [140] V. M. Budnev, I. F. Ginzburg, G. V. Meledin, and V. G. Serbo, *The Two photon*
10261 *particle production mechanism. Physical problems. Applications. Equivalent photon*
10262 *approximation*, Phys. Rept. **15** (1975) 181–281.
- 10263 [141] T. H. Bauer, R. D. Spital, D. R. Yennie, and F. M. Pipkin, *The Hadronic Properties of*
10264 *the Photon in High-Energy Interactions*, Rev. Mod. Phys. **50** (1978) 261.
- 10265 [142] J. M. Butterworth and M. Wing, *High energy photoproduction*, Rept. Prog. Phys. **68**
10266 (2005) 2773–2828, [arXiv:hep-ex/0509018](#).
- 10267 [143] L. Frankfurt, V. Guzey, M. McDermott, and M. Strikman, *Revealing the black body*
10268 *regime of small x DIS through final state signals*, Phys. Rev. Lett. **87** (2001) 192301,
10269 [arXiv:hep-ph/0104154](#).
- 10270 [144] T. C. Rogers and M. I. Strikman, *Hadronic interactions of ultra-high energy photons*
10271 *with protons and light nuclei in the dipole picture*, J. Phys. **G32** (2006) 2041–2063,
10272 [arXiv:hep-ph/0512311](#).
- 10273 [145] ZEUS Collaboration, S. Chekanov et al., *Measurement of the photon proton total cross*
10274 *section at a center-of-mass energy of 209-GeV at HERA*, Nucl. Phys. **B627** (2002)
10275 3–28, [arXiv:hep-ex/0202034](#).
- 10276 [146] H1 Collaboration, S. Aid et al., *Measurement of the total photon-proton cross-section*
10277 *and its decomposition at 200-GeV center-of-mass energy*, Z. Phys. **C69** (1995) 27–38,
10278 [arXiv:hep-ex/9509001](#).
- 10279 [147] G. M. Vereshkov, O. D. Lalakulich, Y. F. Novoseltsev, and R. V. Novoseltseva, *Total*
10280 *cross section for photon nucleon interaction in the energy range $\sqrt{s} = 40\text{-GeV} -$*
10281 *250-GeV*, Phys. Atom. Nucl. **66** (2003) 565–574.
- 10282 [148] Z. Collaboration, *Measurement of the energy dependence of the total photon-proton cross*
10283 *section at HERA*, Phys.Lett. **B697** (2011) 184–193, [arXiv:1011.1652 \[hep-ex\]](#). *
10284 Temporary entry *.
- 10285 [149] R. M. Godbole, A. Grau, G. Pancheri, and Y. N. Srivastava, *Total photoproduction*
10286 *cross-section at very high energy*, Eur. Phys. J. **C63** (2009) 69–85, [arXiv:0812.1065](#)
10287 [\[hep-ph\]](#).
- 10288 [150] M. M. Block and F. Halzen, *Evidence for the saturation of the Froissart bound*, Phys.
10289 Rev. **D70** (2004) 091901, [arXiv:hep-ph/0405174](#).
- 10290 [151] M. M. Block and F. Halzen, *New evidence for the saturation of the Froissart bound*,
10291 Phys. Rev. **D72** (2005) 036006, [arXiv:hep-ph/0506031](#).
- 10292 [152] M. M. Block, E. M. Gregores, F. Halzen, and G. Pancheri, *Photon - proton and*
10293 *photon-photon scattering from nucleon- nucleon forward amplitudes*, Phys. Rev. **D60**
10294 (1999) 054024, [arXiv:hep-ph/9809403](#).
- 10295 [153] J. A. Bagger and M. E. Peskin, *EXOTIC PROCESSES IN HIGH-ENERGY $e p$*
10296 *COLLISIONS*, Phys. Rev. **D31** (1985) 2211.

- 10297 [154] G. Altarelli, B. Mele, and R. Ruckl, *PHYSICS OF $e p$ COLLISIONS IN THE TeV*
 10298 *ENERGY RANGE*, . Presented at ECFA-CERN Workshop on Feasibility of Hadron
 10299 Colliders in LEP Tunnel, Lausanne and Geneva, Switzerland, Mar 26-27, 1984.
- 10300 [155] R. J. Cashmore et al., *EXOTIC PHENOMENA IN HIGH-ENERGY $E P$*
 10301 *COLLISIONS*, Phys. Rept. **122** (1985) 275–386.
- 10302 [156] G. Jarlskog, (Ed.) and D. Rein, (Ed.), *ECFA Large Hadron Collider Workshop,*
 10303 *Aachen, Germany, 4-9 Oct 1990: Proceedings.1*, . CERN-90-10-V-1.
- 10304 [157] G. Kopp, D. Schaile, M. Spira, and P. M. Zerwas, *Bounds on radii and magnetic dipole*
 10305 *moments of quarks and leptons from LEP, SLC and HERA*, Z. Phys. **C65** (1995)
 10306 545–550, [arXiv:hep-ph/9409457](#).
- 10307 [158] A. F. Zarnecki, *Leptoquarks and Contact Interactions at LeHC*, [arXiv:0809.2917](#)
 10308 [[hep-ph](#)].
- 10309 [159] E. Eichten, K. D. Lane, and M. E. Peskin, *New Tests for Quark and Lepton*
 10310 *Substructure*, Phys. Rev. Lett. **50** (1983) 811–814.
- 10311 [160] R. Ruckl, *PROBING LEPTON AND QUARK SUBSTRUCTURE IN POLARIZED*
 10312 *$e + N$ SCATTERING*, Nucl. Phys. **B234** (1984) 91.
- 10313 [161] P. Haberl, F. Schrempp, and H. U. Martyn, *Contact interactions and new heavy bosons*
 10314 *at HERA: A Model independent analysis*, . In *Hamburg 1991, Proceedings, Physics at
 10315 HERA, vol. 2* 1133-1148. (see HIGH ENERGY PHYSICS INDEX 30 (1992) No.
 10316 12988).
- 10317 [162] A. F. Zarnecki, *Global analysis of $eeqq$ contact interactions and future prospects for*
 10318 *high-energy physics*, Eur. Phys. J. **C11** (1999) 539–557, [arXiv:hep-ph/9904334](#).
- 10319 [163] J. L. Hewett and T. G. Rizzo, *Low-Energy Phenomenology of Superstring Inspired $E(6)$*
 10320 *Models*, Phys. Rept. **183** (1989) 193.
- 10321 [164] E. Farhi and L. Susskind, *Technicolor*, Phys. Rept. **74** (1981) 277.
- 10322 [165] C. T. Hill and E. H. Simmons, *Strong dynamics and electroweak symmetry breaking*,
 10323 Phys. Rept. **381** (2003) 235–402, [arXiv:hep-ph/0203079](#).
- 10324 [166] W. Buchmuller, R. Ruckl, and D. Wyler, *Leptoquarks in lepton quark collisions*, Phys.
 10325 Lett. **B191** (1987) 442–448.
- 10326 [167] B. Schrempp, *Leptoquarks and leptogluons at HERA: Theoretical perspectives*, . In
 10327 *Hamburg 1991, Proceedings, Physics at HERA, vol. 2* 1034-1042. (see HIGH
 10328 ENERGY PHYSICS INDEX 30 (1992) No. 12988).
- 10329 [168] S. Davidson, D. C. Bailey, and B. A. Campbell, *Model independent constraints on*
 10330 *leptoquarks from rare processes*, Z. Phys. **C61** (1994) 613–644, [arXiv:hep-ph/9309310](#).
- 10331 [169] M. Leurer, *A Comprehensive study of leptoquark bounds*, Phys. Rev. **D49** (1994)
 10332 333–342, [arXiv:hep-ph/9309266](#).

- 10333 [170] A. Belyaev, C. Leroy, R. Mehdiyev, and A. Pukhov, *Leptoquark single and pair*
10334 *production at LHC with CalcHEP/CompHEP in the complete model*, JHEP **09** (2005)
10335 005, arXiv:hep-ph/0502067.
- 10336 [171] D0 Collaboration, V. M. Abazov et al., *Search for pair production of first-generation*
10337 *leptoquarks in $p\bar{p}$ collisions at $\sqrt{s}=1.96$ TeV*, Phys. Lett. **B681** (2009) 224–232,
10338 arXiv:0907.1048 [hep-ex].
- 10339 [172] T. A. Collaboration, *Search for pair production of first or second generation leptoquarks*
10340 *in proton-proton collisions at $\sqrt{s}=7$ TeV using the ATLAS detector at the LHC*,
10341 arXiv:1104.4481 [hep-ex]. * Temporary entry *.
- 10342 [173] CMS Collaboration, S. Chatrchyan et al., *Search for First Generation Scalar*
10343 *Leptoquarks in the $e\nu j j$ channel in pp collisions at $\sqrt{s} = 7$ TeV*, arXiv:1105.5237
10344 [hep-ex]. * Temporary entry *.
- 10345 [174] A. Belyaev and A. Pukhov.
- 10346 [175] A. Pukhov, *Calcchep 2.3: MSSM, structure functions, event generation, 1, and*
10347 *generation of matrix elements for other packages*, arXiv:hep-ph/0412191.
- 10348 [176] S. Ovyn, X. Rouby, and V. Lemaitre, *Delphes, a framework for fast simulation of a*
10349 *generic collider experiment*, arXiv:0903.2225 [hep-ph].
- 10350 [177] H. Harari, *A Schematic Model of Quarks and Leptons*, Phys. Lett. **B86** (1979) 83.
- 10351 [178] H. Fritzsch and G. Mandelbaum, *Weak Interactions as Manifestations of the*
10352 *Substructure of Leptons and Quarks*, Phys. Lett. **B102** (1981) 319.
- 10353 [179] O. W. Greenberg and J. Sucher, *A Quantum Structure Dynamic Model of Quarks,*
10354 *Leptons, Weak Vector Bosons, and Higgs Mesons*, Phys. Lett. **B99** (1981) 339.
- 10355 [180] R. Barbieri, R. N. Mohapatra, and A. Masiero, *Compositeness and a Left-Right*
10356 *Symmetric Electroweak Model Without Broken Gauge Interactions*, Phys. Lett. **B105**
10357 (1981) 369–374.
- 10358 [181] U. Baur and K. H. Streng, *COLORED LEPTON MASS BOUNDS FROM p anti- p*
10359 *COLLIDER DATA*, Phys. Lett. **B162** (1985) 387.
- 10360 [182] A. Celikel, M. Kantar, and S. Sultansoy, *A search for sextet quarks and leptogluons at*
10361 *the LHC*, Phys. Lett. **B443** (1998) 359–364.
- 10362 [183] S. S. M. Sahin and S. Turkoz, *Resonant production of color octet electrons at the LHeC,*
10363 . CERN-LHeC-Note-2010-015 PHY.
- 10364 [184] H. Harari, *COMPOSITE MODELS FOR QUARKS AND LEPTONS*, Phys. Rept. **104**
10365 (1984) 159.
- 10366 [185] N. T. E. Sauvan, *Single production of excited fermions at LHeC,*
10367 . CERN-LHeC-Note-2010-011 PHY.
- 10368 [186] O. J. P. Eboli, S. M. Lietti, and P. Mathews, *Excited leptons at the CERN Large*
10369 *Hadron Collider*, Phys. Rev. **D65** (2002) 075003, arXiv:hep-ph/0111001.

- 10370 [187] E. M. Gregores, M. C. Gonzalez-Garcia, and S. F. Novaes, *Discriminating new physics*
10371 *scenarios at NLC: The Role of polarization*, Phys. Rev. **D56** (1997) 2920–2927,
10372 [arXiv:hep-ph/9703430](#).
- 10373 [188] H1 Collaboration, F. D. Aaron et al., *Search for Excited Electrons in ep Collisions at*
10374 *HERA*, Phys. Lett. **B666** (2008) 131–139, [arXiv:0805.4530 \[hep-ex\]](#).
- 10375 [189] H1 Collaboration, F. D. Aaron et al., *A Search for Excited Neutrinos in e-p Collisions*
10376 *at HERA*, Phys. Lett. **B663** (2008) 382–389, [arXiv:0802.1858 \[hep-ex\]](#).
- 10377 [190] H1 Collaboration, F. D. Aaron et al., *Search for Excited Quarks in ep Collisions at*
10378 *HERA*, Phys. Lett. **B678** (2009) 335–343, [arXiv:0904.3392 \[hep-ex\]](#).
- 10379 [191] OPAL Collaboration, G. Abbiendi et al., *Search for charged excited leptons in e+ e-*
10380 *collisions at $s^{*(1/2)} = 183\text{-}209\text{-GeV}$* , Phys. Lett. **B544** (2002) 57–72,
10381 [arXiv:hep-ex/0206061](#).
- 10382 [192] DELPHI Collaboration, J. Abdallah et al., *Determination of the e+ e- \rightarrow γ γ*
10383 *(γ) cross- section at LEP 2*, Eur. Phys. J. **C37** (2004) 405–419,
10384 [arXiv:hep-ex/0409058](#).
- 10385 [193] D0 Collaboration, V. M. Abazov et al., *Search for excited electrons in $p\bar{p}$ collisions at*
10386 *$\sqrt{s} = 1.96\text{-TeV}$* , Phys. Rev. **D77** (2008) 091102, [arXiv:0801.0877 \[hep-ex\]](#).
- 10387 [194] K. Hagiwara, D. Zeppenfeld, and S. Komamiya, *Excited Lepton Production at LEP and*
10388 *HERA*, Z. Phys. **C29** (1985) 115.
- 10389 [195] F. Boudjema, A. Djouadi, and J. L. Kneur, *Excited fermions at e+ e- and e P colliders*,
10390 Z. Phys. **C57** (1993) 425–450.
- 10391 [196] U. Baur, M. Spira, and P. M. Zerwas, *EXCITED QUARK AND LEPTON*
10392 *PRODUCTION AT HADRON COLLIDERS*, Phys. Rev. **D42** (1990) 815–824.
- 10393 [197] T. Kohler, *Exotic processes at HERA: The Event generator COMPOS*, . In *Hamburg
10394 1991, Proceedings, Physics at HERA, vol. 3* 1526-1541. (see HIGH ENERGY
10395 PHYSICS INDEX 30 (1992) No. 12988).
- 10396 [198] M. Spira. private communication.
- 10397 [199] C. Berger and P. Kandel, *A new generator for wide angle bremsstrahlung*, . Prepared for
10398 Workshop on Monte Carlo Generators for HERA Physics (Plenary Starting Meeting),
10399 Hamburg, Germany, 27-30 Apr 1998.
- 10400 [200] A. C. et al., *Production of the Fourth SM Family Fermions at the Large Hadron*
10401 *Electron Collider*, . CERN-LHeC-Note-2010-016 PHY.
- 10402 [201] J. A. Aguilar-Saavedra, *A minimal set of top anomalous couplings*, Nucl. Phys. **B812**
10403 (2009) 181–204, [arXiv:0811.3842 \[hep-ph\]](#).
- 10404 [202] Particle Data Group Collaboration, C. Amsler et al., *Review of particle physics*, Phys.
10405 Lett. **B667** (2008) 1.

- 10406 [203] The ATLAS Collaboration, G. Aad et al., *Expected Performance of the ATLAS*
10407 *Experiment - Detector, Trigger and Physics*, arXiv:0901.0512 [hep-ex].
- 10408 [204] *ATLAS detector and physics performance. Technical design report. Vol. 2, .*
10409 CERN-LHCC-99-15.
- 10410 [205] T. Han, K. Whisnant, B. L. Young, and X. Zhang, *Searching for $t \rightarrow c g$ at the Fermilab*
10411 *Tevatron*, Phys. Lett. **B385** (1996) 311–316, arXiv:hep-ph/9606231.
- 10412 [206] E. Malkawi and T. M. P. Tait, *Top-Charm Strong Flavour-Changing Neutral Currents*
10413 *at the Tevatron*, Phys. Rev. **D54** (1996) 5758–5762, arXiv:hep-ph/9511337.
- 10414 [207] T. M. P. Tait and C. P. Yuan, *Anomalous t - c - g coupling: The connection between single*
10415 *top production and top decay*, Phys. Rev. **D55** (1997) 7300–7301,
10416 arXiv:hep-ph/9611244.
- 10417 [208] T. Han, M. Hosch, K. Whisnant, B.-L. Young, and X. Zhang, *Single top quark*
10418 *production via FCNC couplings at hadron colliders*, Phys. Rev. **D58** (1998) 073008,
10419 arXiv:hep-ph/9806486.
- 10420 [209] T. M. P. Tait and C. P. Yuan, *Single top quark production as a window to physics*
10421 *beyond the standard model*, Phys. Rev. **D63** (2001) 014018, arXiv:hep-ph/0007298.
- 10422 [210] J. J. Liu, C. S. Li, L. L. Yang, and L. G. Jin, *Single top quark production via*
10423 *SUSY-QCD FCNC couplings at the CERN LHC in the unconstrained MSSM*, Nucl.
10424 Phys. **B705** (2005) 3–32, arXiv:hep-ph/0404099.
- 10425 [211] J. J. Liu, C. S. Li, L. L. Yang, and L. G. Jin, *Next-to-leading order QCD corrections to*
10426 *the direct top quark production via model-independent FCNC couplings at hadron*
10427 *colliders*, Phys. Rev. **D72** (2005) 074018, arXiv:hep-ph/0508016.
- 10428 [212] J.-j. Cao, G.-l. Liu, J. M. Yang, and H.-j. Zhang, *Top-quark FCNC productions at LHC*
10429 *in topcolor-assisted technicolor model*, Phys. Rev. **D76** (2007) 014004,
10430 arXiv:hep-ph/0703308.
- 10431 [213] J. J. Cao et al., *SUSY-induced FCNC top-quark processes at the Large Hadron Collider*,
10432 Phys. Rev. **D75** (2007) 075021, arXiv:hep-ph/0702264.
- 10433 [214] P. M. Ferreira, R. B. Guedes, and R. Santos, *Combined effects of strong and electroweak*
10434 *FCNC effective operators in top quark physics at the CERN LHC*, Phys. Rev. **D77**
10435 (2008) 114008, arXiv:0802.2075 [hep-ph].
- 10436 [215] J. M. Yang, *Probing New Physics from Top Quark Processes at LHC: A Mini Review*,
10437 Int. J. Mod. Phys. **A23** (2008) 3343, arXiv:0801.0210 [hep-ph].
- 10438 [216] X.-F. Han, L. Wang, and J. M. Yang, *Top quark FCNC decays and productions at LHC*
10439 *in littlest Higgs model with T -parity*, arXiv:0903.5491 [hep-ph].
- 10440 [217] J. Cao, Z. Heng, L. Wu, and J. M. Yang, *R -parity violating effects in top quark FCNC*
10441 *productions at LHC*, Phys. Rev. **D79** (2009) 054003, arXiv:0812.1698 [hep-ph].

- 10442 [218] V. F. Obraztsov, S. R. Slabospitsky, and O. P. Yushchenko, *Search for anomalous top*
10443 *quark interaction at LEP-2 collider*, Phys. Lett. **B426** (1998) 393–402,
10444 arXiv:hep-ph/9712394.
- 10445 [219] T. Han and J. L. Hewett, *Top charm associated production in high-energy e^+e^-*
10446 *collisions*, Phys. Rev. **D60** (1999) 074015, arXiv:hep-ph/9811237.
- 10447 [220] J.-j. Cao, Z.-h. Xiong, and J. M. Yang, *SUSY-induced top quark FCNC processes at*
10448 *linear colliders*, Nucl. Phys. **B651** (2003) 87–105, arXiv:hep-ph/0208035.
- 10449 [221] J. A. Aguilar-Saavedra, *Top flavor-changing neutral interactions: Theoretical*
10450 *expectations and experimental detection*, Acta Phys. Polon. **B35** (2004) 2695–2710,
10451 arXiv:hep-ph/0409342.
- 10452 [222] A. T. Alan and A. Senol, *Single top production at HERA and THERA*, Europhys. Lett.
10453 **59** (2002) 669–673, arXiv:hep-ph/0202119.
- 10454 [223] A. A. Ashimova and S. R. Slabospitsky, *The Constraint on FCNC Coupling of the Top*
10455 *Quark with a Gluon from ep Collisions*, Phys. Lett. **B668** (2008) 282–285,
10456 arXiv:hep-ph/0604119.
- 10457 [224] H1 Collaboration, F. D. Aaron et al., *Search for Single Top Quark Production at HERA*,
10458 Phys. Lett. **B678** (2009) 450–458, arXiv:0904.3876 [hep-ex].
- 10459 [225] O. Cakir and S. A. Cetin, *Anomalous single top quark production at the CERN LHC*, J.
10460 Phys. **G31** (2005) N1–N8.
- 10461 [226] G. A. Moortgat-Pick et al., *The role of polarized positrons and electrons in revealing*
10462 *fundamental interactions at the linear collider*, Phys. Rept. **460** (2008) 131–243,
10463 arXiv:hep-ph/0507011.
- 10464 [227] S. Sultansoy, *Linac-ring type colliders: Second way to TeV scale*, Eur. Phys. J. **C33**
10465 (2004) s1064–s1066, arXiv:hep-ex/0306034.
- 10466 [228] S. F. Sultanov, *Prospects of the future $e p$ and gamma p colliders: Luminosity and*
10467 *physics*, . IC/89/409.
- 10468 [229] S. I. Alekhin et al., *PHYSICS AT gamma p COLLIDERS OF TeV ENERGIES*, Int. J.
10469 Mod. Phys. **A6** (1991) 21–40.
- 10470 [230] A. K. Ciftci, S. Sultansoy, S. Turkoz, and O. Yavas, *Main parameters of TeV energy*
10471 *gamma p colliders*, Nucl. Instrum. Meth. **A365** (1995) 317–328.
- 10472 [231] A. K. Ciftci, S. Sultansoy, and O. Yavas, *TESLA*HERA based gamma p and gamma A*
10473 *colliders*, Nucl. Instrum. Meth. **A472** (2001) 72–78, arXiv:hep-ex/0007009.
- 10474 [232] H. Aksakal, A. K. Ciftci, Z. Nergiz, D. Schulte, and F. Zimmermann, *Conversion*
10475 *efficiency and luminosity for gamma proton colliders based on the LHC-CLIC or*
10476 *LHC-ILC QCD Explorer scheme*, Nucl. Instrum. Meth. **A576** (2007) 287–293,
10477 arXiv:hep-ex/0612041.
- 10478 [233] J. B. Dainton, M. Klein, P. Newman, E. Perez, and F. Willeke, *Deep inelastic electron*
10479 *nucleon scattering at the LHC*, JINST **1** (2006) P10001, arXiv:hep-ex/0603016.

- 10480 [234] I. T. Cakir, O. Cakir, and S. Sultansoy, *Anomalous Single Top Production at the Large*
10481 *Hadron electron Collider Based gamma p Collider*, Phys. Lett. **B685** (2010) 170–173,
10482 arXiv:0911.4194 [hep-ph].
- 10483 [235] CMS Collaboration, G. L. Bayatian et al., *CMS technical design report, volume II:*
10484 *Physics performance*, J. Phys. **G34** (2007) 995–1579.
- 10485 [236] O. Cakir, *Anomalous production of top quarks at CLIC + LHC based γp colliders*, J.
10486 Phys. **G29** (2003) 1181–1192, arXiv:hep-ph/0301116.
- 10487 [237] R. Ciftci, *Production of Excited Quark at γp Collider Based on the Large Hadron*
10488 *Electron Collider*, . CERN-LHeC-Note-2010-017 PHY.
- 10489 [238] O. Çakır and M. Şahin, *Diquarks in γp Collisions at LHeC*, .
10490 CERN-LHeC-Note-2010-012 PHY.
- 10491 [239] CMS Collaboration, V. Khachatryan et al., *Search for Dijet Resonances in 7 TeV pp*
10492 *Collisions at CMS*, Phys. Rev. Lett. **105** (2010) 211801, arXiv:1010.0203 [hep-ex].
- 10493 [240] A. Atre, M. Carena, T. Han, and J. Santiago, *Heavy Quarks Above the Top at the*
10494 *Tevatron*, Phys. Rev. **D79** (2009) 054018, arXiv:0806.3966 [hep-ph].
- 10495 [241] A. Atre et al., *Model-Independent Searches for New Quarks at the LHC*,
10496 arXiv:1102.1987 [hep-ph].
- 10497 [242] O.Cakir, *Single Production of Fourth Family Quarks at LHeC*, .
10498 CERN-LHeC-Note-2010-013 PHY.
- 10499 [243] M. Dührssen, *Measurement of Higgs boson parameters at the LHC*, Czech. J. Phys. **55**
10500 (2005) B145–B152.
- 10501 [244] J. M. Butterworth, A. R. Davison, M. Rubin, and G. P. Salam, *Jet substructure as a*
10502 *new Higgs search channel at the LHC*, Phys. Rev. Lett. **100** (2008) 242001,
10503 arXiv:0802.2470 [hep-ph].
- 10504 [245] B. Jager, *Next-to-leading order QCD corrections to Higgs production at a future*
10505 *lepton-proton collider*, Phys.Rev. **D81** (2010) 054018, arXiv:1001.3789 [hep-ph].
- 10506 [246] J. Blumlein, G. van Oldenborgh, and R. Ruckl, *QCD and QED corrections to Higgs*
10507 *boson production in charged current e p scattering*, Nucl.Phys. **B395** (1993) 35–59,
10508 arXiv:hep-ph/9209219 [hep-ph].
- 10509 [247] J. Alwall et al., *MadGraph/MadEvent v4: The New Web Generation*, JHEP **09** (2007)
10510 028, arXiv:0706.2334 [hep-ph].
- 10511 [248] PGS. [http:](http://www.physics.ucdavis.edu/~conway/research/software/pgs/pgs4-general.htm)
10512 [//www.physics.ucdavis.edu/~conway/research/software/pgs/pgs4-general.htm](http://www.physics.ucdavis.edu/~conway/research/software/pgs/pgs4-general.htm).
- 10513 [249] T. Regge, *Introduction to complex orbital momenta*, Nuovo Cim. **14** (1959) 951.
- 10514 [250] V. N. Gribov, *A REGGEON DIAGRAM TECHNIQUE*, Sov. Phys. JETP **26** (1968)
10515 414–422.

- 10516 [251] H. D. I. Abarbanel, J. B. Bronzan, R. L. Sugar, and A. R. White, *Reggeon Field Theory: Formulation and Use*, Phys. Rept. **21** (1975) 119–182.
- 10517
- 10518 [252] J. C. Collins, D. E. Soper, and G. F. Sterman, *Factorization of Hard Processes in QCD*, Adv. Ser. Direct. High Energy Phys. **5** (1988) 1–91, [arXiv:hep-ph/0409313](#).
- 10519
- 10520 [253] V. N. Gribov and L. N. Lipatov, *Deep inelastic ep scattering in perturbation theory*, Sov. J. Nucl. Phys. **15** (1972) 438–450.
- 10521
- 10522 [254] G. Altarelli and G. Parisi, *Asymptotic Freedom in Parton Language*, Nucl. Phys. **B126** (1977) 298.
- 10523
- 10524 [255] Y. L. Dokshitzer, *Calculation of the Structure Functions for Deep Inelastic Scattering and e^+e^- Annihilation by Perturbation Theory in Quantum Chromodynamics*, Sov. Phys. JETP **46** (1977) 641–653.
- 10525
- 10526
- 10527 [256] L. V. Gribov, E. M. Levin, and M. G. Ryskin, *Semihard Processes in QCD*, Phys. Rept. **100** (1983) 1–150.
- 10528
- 10529 [257] A. H. Mueller, *Small x Behavior and Parton Saturation: A QCD Model*, Nucl. Phys. **B335** (1990) 115.
- 10530
- 10531 [258] J. Jalilian-Marian, A. Kovner, A. Leonidov, and H. Weigert, *The Wilson renormalization group for low x physics: Towards the high density regime*, Phys. Rev. **D59** (1999) 014014, [arXiv:hep-ph/9706377](#).
- 10532
- 10533
- 10534 [259] I. Balitsky, *Operator expansion for high-energy scattering*, Nucl. Phys. **B463** (1996) 99–160, [arXiv:hep-ph/9509348](#).
- 10535
- 10536 [260] Y. V. Kovchegov, *Small- x F_2 structure function of a nucleus including multiple pomeron exchanges*, Phys. Rev. **D60** (1999) 034008, [arXiv:hep-ph/9901281](#).
- 10537
- 10538 [261] M. Froissart, *Asymptotic behavior and subtractions in the Mandelstam representation*, Phys. Rev. **123** (1961) 1053–1057.
- 10539
- 10540 [262] A. Martin, *Unitarity and high-energy behavior of scattering amplitudes*, Phys. Rev. **129** (1963) 1432–1436.
- 10541
- 10542 [263] E. A. Kuraev, L. N. Lipatov, and V. S. Fadin, *The Pomeron Singularity in Nonabelian Gauge Theories*, Sov. Phys. JETP **45** (1977) 199–204.
- 10543
- 10544 [264] I. I. Balitsky and L. N. Lipatov, *The Pomeron Singularity in Quantum Chromodynamics*, Sov. J. Nucl. Phys. **28** (1978) 822–829.
- 10545
- 10546 [265] V. N. Gribov, *Glauber corrections and the interaction between high-energy hadrons and nuclei*, Sov. Phys. JETP **29** (1969) 483–487.
- 10547
- 10548 [266] N. Armesto, A. B. Kaidalov, C. A. Salgado, and K. Tywoniuk, *A unitarized model of inclusive and diffractive DIS with Q^2 -evolution*, Phys. Rev. **D81** (2010) 074002, [arXiv:1001.3021 \[hep-ph\]](#).
- 10549
- 10550

- 10551 [267] N. Armesto, A. B. Kaidalov, C. A. Salgado, and K. Tywoniuk, *Nuclear shadowing in*
10552 *Glauber-Gribov theory with Q^2 - evolution*, Eur. Phys. J. **C68** (2010) 447–457,
10553 arXiv:1003.2947 [hep-ph].
- 10554 [268] A. H. Mueller and J.-w. Qiu, *Gluon Recombination and Shadowing at Small Values of x* ,
10555 Nucl. Phys. **B268** (1986) 427.
- 10556 [269] J. Bartels and M. Wusthoff, *The Triple Regge limit of diffractive dissociation in deep*
10557 *inelastic scattering*, Z. Phys. **C66** (1995) 157–180.
- 10558 [270] L. D. McLerran and R. Venugopalan, *Computing quark and gluon distribution functions*
10559 *for very large nuclei*, Phys. Rev. **D49** (1994) 2233–2241, arXiv:hep-ph/9309289.
- 10560 [271] L. D. McLerran and R. Venugopalan, *Gluon distribution functions for very large nuclei*
10561 *at small transverse momentum*, Phys. Rev. **D49** (1994) 3352–3355,
10562 arXiv:hep-ph/9311205.
- 10563 [272] L. D. McLerran and R. Venugopalan, *Green's functions in the color field of a large*
10564 *nucleus*, Phys. Rev. **D50** (1994) 2225–2233, arXiv:hep-ph/9402335.
- 10565 [273] J. Jalilian-Marian, A. Kovner, and H. Weigert, *The Wilson renormalization group for*
10566 *low x physics: Gluon evolution at finite parton density*, Phys. Rev. **D59** (1999) 014015,
10567 arXiv:hep-ph/9709432.
- 10568 [274] A. Kovner, J. G. Milhano, and H. Weigert, *Relating different approaches to nonlinear*
10569 *QCD evolution at finite gluon density*, Phys. Rev. **D62** (2000) 114005,
10570 arXiv:hep-ph/0004014.
- 10571 [275] H. Weigert, *Unitarity at small Bjorken x* , Nucl. Phys. **A703** (2002) 823–860,
10572 arXiv:hep-ph/0004044.
- 10573 [276] E. Iancu, A. Leonidov, and L. D. McLerran, *Nonlinear gluon evolution in the color glass*
10574 *condensate. I*, Nucl. Phys. **A692** (2001) 583–645, arXiv:hep-ph/0011241.
- 10575 [277] E. Ferreiro, E. Iancu, A. Leonidov, and L. McLerran, *Nonlinear gluon evolution in the*
10576 *color glass condensate. II*, Nucl. Phys. **A703** (2002) 489–538, arXiv:hep-ph/0109115.
- 10577 [278] T. Altinoluk, A. Kovner, M. Lublinsky, and J. Peressutti, *QCD Reggeon Field Theory*
10578 *for every day: Pomeron loops included*, JHEP **03** (2009) 109, arXiv:0901.2559
10579 [hep-ph].
- 10580 [279] F. Gelis, E. Iancu, J. Jalilian-Marian, and R. Venugopalan, *The Color Glass*
10581 *Condensate*, Ann.Rev.Nucl.Part.Sci. **60** (2010) 463–489, arXiv:1002.0333 [hep-ph].
- 10582 [280] Y. V. Kovchegov and H. Weigert, *Triumvirate of Running Couplings in Small- x*
10583 *Evolution*, Nucl.Phys. **A784** (2007) 188–226, arXiv:hep-ph/0609090 [hep-ph].
- 10584 [281] I. Balitsky and G. A. Chirilli, *Next-to-leading order evolution of color dipoles*, Phys.
10585 Rev. **D77** (2008) 014019, arXiv:0710.4330 [hep-ph].
- 10586 [282] E. Iancu, A. Mueller, and S. Munier, *Universal behavior of QCD amplitudes at high*
10587 *energy from general tools of statistical physics*, Phys.Lett. **B606** (2005) 342–350,
10588 arXiv:hep-ph/0410018 [hep-ph].

- 10589 [283] Y. V. Kovchegov, J. Kuokkanen, K. Rummukainen, and H. Weigert, *Subleading- $N(c)$*
10590 *corrections in non-linear small- x evolution*, Nucl.Phys. **A823** (2009) 47–82,
10591 [arXiv:0812.3238](#) [hep-ph].
- 10592 [284] A. Dumitru and J. Jalilian-Marian, *Forward dijets in high-energy collisions: Evolution*
10593 *of QCD n -point functions beyond the dipole approximation*, Phys.Rev. **D82** (2010)
10594 074023, [arXiv:1008.0480](#) [hep-ph].
- 10595 [285] C. Marquet and H. Weigert, *New observables to test the Color Glass Condensate beyond*
10596 *the large- N_c limit*, Nucl.Phys. **A843** (2010) 68–97, [arXiv:1003.0813](#) [hep-ph].
- 10597 [286] Y. Hatta, E. Iancu, C. Marquet, G. Soyez, and D. Triantafyllopoulos, *Diffusive scaling*
10598 *and the high-energy limit of deep inelastic scattering in QCD at large $N(c)$* , Nucl.Phys.
10599 **A773** (2006) 95–155, [arXiv:hep-ph/0601150](#) [hep-ph].
- 10600 [287] S. Munier, *Quantum chromodynamics at high energy and statistical physics*, Phys.Rept.
10601 **473** (2009) 1–49, [arXiv:0901.2823](#) [hep-ph]. * Temporary entry *.
- 10602 [288] S. Catani, M. Ciafaloni, and F. Hautmann, *High-energy factorization and small x heavy*
10603 *flavor production*, Nucl. Phys. **B366** (1991) 135–188.
- 10604 [289] S. Catani and F. Hautmann, *High-energy factorization and small x deep inelastic*
10605 *scattering beyond leading order*, Nucl. Phys. **B427** (1994) 475–524,
10606 [arXiv:hep-ph/9405388](#).
- 10607 [290] F. Caola, S. Forte, and J. Rojo, *Deviations from NLO QCD evolution in inclusive*
10608 *HERA data*, Phys. Lett. **B686** (2010) 127–135, [arXiv:0910.3143](#) [hep-ph].
- 10609 [291] V. S. Fadin and L. N. Lipatov, *BFKL pomeron in the next-to-leading approximation*,
10610 Phys. Lett. **B429** (1998) 127–134, [arXiv:hep-ph/9802290](#).
- 10611 [292] M. Ciafaloni and G. Camici, *Energy scale(s) and next-to-leading BFKL equation*, Phys.
10612 Lett. **B430** (1998) 349–354, [arXiv:hep-ph/9803389](#).
- 10613 [293] G. Altarelli, R. D. Ball, and S. Forte, *An anomalous dimension for small x evolution*,
10614 Nucl. Phys. **B674** (2003) 459–483, [arXiv:hep-ph/0306156](#).
- 10615 [294] G. Altarelli, R. D. Ball, and S. Forte, *Perturbatively stable resummed small x evolution*
10616 *kernels*, Nucl. Phys. **B742** (2006) 1–40, [arXiv:hep-ph/0512237](#).
- 10617 [295] G. Altarelli, R. D. Ball, and S. Forte, *Small x Resummation with Quarks: Deep-Inelastic*
10618 *Scattering*, Nucl. Phys. **B799** (2008) 199–240, [arXiv:0802.0032](#) [hep-ph].
- 10619 [296] M. Ciafaloni, D. Colferai, G. P. Salam, and A. M. Stasto, *Renormalisation group*
10620 *improved small- x Green’s function*, Phys. Rev. **D68** (2003) 114003,
10621 [arXiv:hep-ph/0307188](#).
- 10622 [297] M. Ciafaloni, D. Colferai, G. P. Salam, and A. M. Stasto, *The gluon splitting function at*
10623 *moderately small x* , Phys. Lett. **B587** (2004) 87–94, [arXiv:hep-ph/0311325](#).
- 10624 [298] M. Ciafaloni, D. Colferai, G. P. Salam, and A. M. Stasto, *A matrix formulation for*
10625 *small- x singlet evolution*, JHEP **08** (2007) 046, [arXiv:0707.1453](#) [hep-ph].

- 10626 [299] J. C. Collins, *Proof of factorization for diffractive hard scattering*, Phys. Rev. **D57**
10627 (1998) 3051–3056, [arXiv:hep-ph/9709499](#).
- 10628 [300] F. Low, *A Model of the Bare Pomeron*, Phys. Rev. **D12** (1975) 163.
- 10629 [301] S. Nussinov, *Colored Quark Version of Some Hadronic Puzzles*, Phys. Rev. Lett. **34**
10630 (1975) 1286.
- 10631 [302] K. J. Golec-Biernat and M. Wusthoff, *Saturation effects in deep inelastic scattering at*
10632 *low Q^{*2} and its implications on diffraction*, Phys. Rev. **D59** (1998) 014017,
10633 [arXiv:hep-ph/9807513](#).
- 10634 [303] K. J. Golec-Biernat and M. Wusthoff, *Saturation in diffractive deep inelastic scattering*,
10635 Phys. Rev. **D60** (1999) 114023, [arXiv:hep-ph/9903358](#).
- 10636 [304] N. Armesto, *Nuclear shadowing*, J. Phys. **G32** (2006) R367–R394,
10637 [arXiv:hep-ph/0604108](#).
- 10638 [305] L. Frankfurt, M. Strikman, and C. Weiss, *Small- x physics: From HERA to LHC and*
10639 *beyond*, Ann. Rev. Nucl. Part. Sci. **55** (2005) 403–465, [arXiv:hep-ph/0507286](#).
- 10640 [306] E. Iancu, K. Itakura, and S. Munier, *Saturation and BFKL dynamics in the HERA data*
10641 *at small x* , Phys. Lett. **B590** (2004) 199–208, [arXiv:hep-ph/0310338](#).
- 10642 [307] J. R. Forshaw and G. Shaw, *Glucion saturation in the colour dipole model?*, JHEP **12**
10643 (2004) 052, [arXiv:hep-ph/0411337](#).
- 10644 [308] A. M. Stasto, K. J. Golec-Biernat, and J. Kwiecinski, *Geometric scaling for the total*
10645 *gamma* p cross-section in the low x region*, Phys. Rev. Lett. **86** (2001) 596–599,
10646 [arXiv:hep-ph/0007192](#).
- 10647 [309] N. Armesto, C. A. Salgado, and U. A. Wiedemann, *Relating high-energy lepton hadron,*
10648 *proton nucleus and nucleus nucleus collisions through geometric scaling*, Phys. Rev.
10649 Lett. **94** (2005) 022002, [arXiv:hep-ph/0407018](#).
- 10650 [310] C. Marquet and L. Schoeffel, *Geometric scaling in diffractive deep inelastic scattering*,
10651 Phys. Lett. **B639** (2006) 471–477, [arXiv:hep-ph/0606079](#).
- 10652 [311] V. Goncalves and M. Machado, *Geometric scaling in inclusive charm production*,
10653 Phys.Rev.Lett. **91** (2003) 202002, [arXiv:hep-ph/0307090](#) [hep-ph].
- 10654 [312] L. McLerran and M. Praszalowicz, *Saturation and Scaling of Multiplicity, Mean p_T and*
10655 *p_T Distributions from 200 GeV to \sqrt{s} to 7 TeV*, Acta Phys.Polon. **B41** (2010)
10656 1917–1926, [arXiv:1006.4293](#) [hep-ph].
- 10657 [313] F. Caola and S. Forte, *Geometric Scaling from GLAP evolution*, Phys. Rev. Lett. **101**
10658 (2008) 022001, [arXiv:0802.1878](#) [hep-ph].
- 10659 [314] N. N. Nikolaev and B. G. Zakharov, *Colour transparency and scaling properties of*
10660 *nuclear shadowing in deep inelastic scattering*, Z. Phys. **C49** (1991) 607–618.
- 10661 [315] N. Nikolaev and B. G. Zakharov, *Pomeron structure function and diffraction*
10662 *dissociation of virtual photons in perturbative QCD*, Z. Phys. **C53** (1992) 331–346.

- 10663 [316] A. H. Mueller and B. Patel, *Single and double BFKL pomeron exchange and a dipole*
 10664 *picture of high-energy hard processes*, Nucl. Phys. **B425** (1994) 471–488,
 10665 [arXiv:hep-ph/9403256](#).
- 10666 [317] A. H. Mueller, *Unitarity and the BFKL pomeron*, Nucl. Phys. **B437** (1995) 107–126,
 10667 [arXiv:hep-ph/9408245](#).
- 10668 [318] M. L. Good and W. D. Walker, *Diffraction dissociation of beam particles*, Phys. Rev.
 10669 **120** (1960) 1857–1860.
- 10670 [319] A. H. Mueller, *Parton saturation: An overview*, [arXiv:hep-ph/0111244](#).
- 10671 [320] J. Bartels, K. J. Golec-Biernat, and H. Kowalski, *A modification of the saturation*
 10672 *model: DGLAP evolution*, Phys. Rev. **D66** (2002) 014001, [arXiv:hep-ph/0203258](#).
- 10673 [321] H. Kowalski and D. Teaney, *An impact parameter dipole saturation model*, Phys. Rev.
 10674 **D68** (2003) 114005, [arXiv:hep-ph/0304189](#).
- 10675 [322] H. Kowalski, L. Motyka, and G. Watt, *Exclusive diffractive processes at HERA within*
 10676 *the dipole picture*, Phys. Rev. **D74** (2006) 074016, [arXiv:hep-ph/0606272](#).
- 10677 [323] A. D. Martin, R. G. Roberts, W. J. Stirling, and R. S. Thorne, *Uncertainties of*
 10678 *predictions from parton distributions. I: Experimental errors. ((T))*, Eur. Phys. J. **C28**
 10679 (2003) 455–473, [arXiv:hep-ph/0211080](#).
- 10680 [324] A. D. Martin, W. J. Stirling, R. S. Thorne, and G. Watt, *Update of Parton Distributions*
 10681 *at NNLO*, Phys. Lett. **B652** (2007) 292–299, [arXiv:0706.0459 \[hep-ph\]](#).
- 10682 [325] P. M. Nadolsky et al., *Implications of CTEQ global analysis for collider observables*,
 10683 Phys. Rev. **D78** (2008) 013004, [arXiv:0802.0007 \[hep-ph\]](#).
- 10684 [326] G. Watt, A. D. Martin, W. J. Stirling, and R. S. Thorne, *Recent Progress in Global*
 10685 *PDF Analysis*, [arXiv:0806.4890 \[hep-ph\]](#).
- 10686 [327] A. Martin, W. Stirling, R. Thorne, and G. Watt, *Parton distributions for the LHC*,
 10687 Eur.Phys.J. **C63** (2009) 189–285, [arXiv:0901.0002 \[hep-ph\]](#).
- 10688 [328] H.-L. Lai, J. Huston, Z. Li, P. Nadolsky, J. Pumplin, et al., *Uncertainty induced by QCD*
 10689 *coupling in the CTEQ global analysis of parton distributions*, Phys.Rev. **D82** (2010)
 10690 054021, [arXiv:1004.4624 \[hep-ph\]](#).
- 10691 [329] R. D. Ball et al., *A first unbiased global NLO determination of parton distributions and*
 10692 *their uncertainties*, Nucl. Phys. **B838** (2010) 136–206, [arXiv:1002.4407 \[hep-ph\]](#).
- 10693 [330] J. R. Forshaw, R. Sandapen, and G. Shaw, *Further success of the colour dipole model*,
 10694 JHEP **11** (2006) 025, [arXiv:hep-ph/0608161](#).
- 10695 [331] F. Caola, S. Forte, and J. Rojo, *HERA data and DGLAP evolution: theory and*
 10696 *phenomenology*, [arXiv:1007.5405 \[hep-ph\]](#).
- 10697 [332] H.-L. Lai, M. Guzzi, J. Huston, Z. Li, P. M. Nadolsky, et al., *New parton distributions*
 10698 *for collider physics*, Phys.Rev. **D82** (2010) 074024, [arXiv:1007.2241 \[hep-ph\]](#).

- 10699 [333] R. D. Ball and R. K. Ellis, *Heavy quark production at high-energy*, JHEP **05** (2001) 053,
10700 arXiv:hep-ph/0101199.
- 10701 [334] S. Marzani, R. D. Ball, V. Del Duca, S. Forte, and A. Vicini, *Higgs production via*
10702 *gluon-gluon fusion with finite top mass beyond next-to-leading order*, Nucl. Phys. **B800**
10703 (2008) 127–145, arXiv:0801.2544 [hep-ph].
- 10704 [335] S. Marzani, R. D. Ball, V. Del Duca, S. Forte, and A. Vicini, *Finite-top-mass effects in*
10705 *NNLO Higgs production*, Nucl. Phys. Proc. Suppl. **186** (2009) 98–101,
10706 arXiv:0809.4934 [hep-ph].
- 10707 [336] S. Marzani and R. D. Ball, *High Energy Resummation of Drell-Yan Processes*, Nucl.
10708 Phys. **B814** (2009) 246–264, arXiv:0812.3602 [hep-ph].
- 10709 [337] S. Marzani and R. D. Ball, *Drell-Yan processes in the high-energy limit*,
10710 arXiv:0906.4729 [hep-ph].
- 10711 [338] G. Diana, *High-energy resummation in direct photon production*, Nucl. Phys. **B824**
10712 (2010) 154–167, arXiv:0906.4159 [hep-ph].
- 10713 [339] G. Diana, J. Rojo, and R. D. Ball, *High energy resummation of direct photon production*
10714 *at hadronic colliders*, Phys.Lett. **B693** (2010) 430–437, arXiv:1006.4250 [hep-ph].
- 10715 [340] S. Forte, G. Altarelli, and R. D. Ball, *Can we trust small x resummation?*, Nucl. Phys.
10716 Proc. Suppl. **191** (2009) 64–75, arXiv:0901.1294 [hep-ph].
- 10717 [341] M. Dittmar et al., *Parton Distributions*, arXiv:0901.2504 [hep-ph].
- 10718 [342] J. Rojo, G. Altarelli, R. D. Ball, and S. Forte, *Towards small x resummed DIS*
10719 *phenomenology*, arXiv:0907.0443 [hep-ph].
- 10720 [343] J. Rojo and F. Caola, *Parton distributions and small- x QCD at the Large Hadron*
10721 *Electron Collider*, arXiv:0906.2079 [hep-ph].
- 10722 [344] C. Salgado, J. Alvarez-Muniz, F. Arleo, N. Armesto, M. Botje, et al., *Proton-Nucleus*
10723 *Collisions at the LHC: Scientific Opportunities and Requirements*, arXiv:1105.3919
10724 [hep-ph]. * Temporary entry *.
- 10725 [345] D. G. d’Enterria, *Quarkonia photoproduction at nucleus colliders*,
10726 Nucl.Phys.Proc.Suppl. **184** (2008) 158–162, arXiv:0711.1123 [nucl-ex].
- 10727 [346] D. d’Enterria, *Forward jets physics in ATLAS, CMS and LHCb*, arXiv:0911.1273
10728 [hep-ex].
- 10729 [347] R. Ichou and D. d’Enterria, *Sensitivity of isolated photon production at TeV hadron*
10730 *colliders to the gluon distribution in the proton*, Phys.Rev. **D82** (2010) 014015,
10731 arXiv:1005.4529 [hep-ph].
- 10732 [348] LHCb Collaboration, F. de Lorenzi et al. Proceedings of DIS2010.
- 10733 [349] J. M. Jowett, *The LHC as a Nucleus-Nucleus Collider*, J.Phys.G **G35** (2008) 104028,
10734 arXiv:0807.1397 [nucl-ex]. * Temporary entry *.

- 10735 [350] P. Quiroga-Arias, J. G. Milhano, and U. A. Wiedemann, *Testing nuclear parton*
10736 *distributions with pA collisions at the TeV scale*, Phys.Rev. **C82** (2010) 034903,
10737 arXiv:1002.2537 [hep-ph].
- 10738 [351] K. Eskola, V. Kolhinen, and R. Vogt, *Obtaining the nuclear gluon distribution from*
10739 *heavy quark decays to lepton pairs in pA collisions*, Nucl.Phys. **A696** (2001) 729–746,
10740 arXiv:hep-ph/0104124 [hep-ph].
- 10741 [352] F. Arleo and T. Gousset, *Measuring gluon shadowing with prompt photons at RHIC and*
10742 *LHC*, Phys.Lett. **B660** (2008) 181–187, arXiv:0707.2944 [hep-ph].
- 10743 [353] H. Paukkunen and C. A. Salgado, *Constraints for the nuclear parton distributions from*
10744 *Z and W production at the LHC*, JHEP **1103** (2011) 071, arXiv:1010.5392 [hep-ph].
- 10745 [354] A. Baltz, G. Baur, D. d’Enterria, L. Frankfurt, F. Gelis, et al., *The Physics of*
10746 *Ultraperipheral Collisions at the LHC*, Phys.Rept. **458** (2008) 1–171, arXiv:0706.3356
10747 [nucl-ex].
- 10748 [355] BRAHMS Collaboration, I. Arsene et al., *On the evolution of the nuclear modification*
10749 *factors with rapidity and centrality in d + Au collisions at $s(NN)^{1/2} = 200$ -GeV*,
10750 Phys.Rev.Lett. **93** (2004) 242303, arXiv:nucl-ex/0403005 [nucl-ex].
- 10751 [356] B. Kopeliovich, J. Nemchik, I. Potashnikova, M. Johnson, and I. Schmidt, *Breakdown of*
10752 *QCD factorization at large Feynman x*, Phys.Rev. **C72** (2005) 054606,
10753 arXiv:hep-ph/0501260 [hep-ph].
- 10754 [357] STAR Collaboration, E. Braidot, *Suppression of Forward Pion Correlations in d+Au*
10755 *Interactions at STAR*, arXiv:1005.2378 [hep-ph].
- 10756 [358] L. Frankfurt and M. Strikman, *Energy losses in the black disc regime and correlation*
10757 *effects in the STAR forward pion production in d Au collisions*, Phys.Lett. **B645** (2007)
10758 412–421, arXiv:nucl-th/0603049 [nucl-th].
- 10759 [359] J. L. Albacete and C. Marquet, *Azimuthal correlations of forward di-hadrons in d+Au*
10760 *collisions at RHIC in the Color Glass Condensate*, Phys.Rev.Lett. **105** (2010) 162301,
10761 arXiv:1005.4065 [hep-ph].
- 10762 [360] PHENIX Collaboration, A. Adare et al., *Suppression of back-to-back hadron pairs at*
10763 *forward rapidity in d+Au Collisions at $\sqrt{s_{NN}} = 200$ GeV*, arXiv:1105.5112
10764 [nucl-ex]. * Temporary entry *.
- 10765 [361] F. Arleo et al., *Photon physics in heavy ion collisions at the LHC*,
10766 arXiv:hep-ph/0311131.
- 10767 [362] STAR Collaboration, B. Abelev et al., *Three-particle coincidence of the long range*
10768 *pseudorapidity correlation in high energy nucleus-nucleus collisions*, Phys.Rev.Lett. **105**
10769 (2010) 022301, arXiv:0912.3977 [hep-ex].
- 10770 [363] CMS Collaboration, V. Khachatryan et al., *Observation of Long-Range Near-Side*
10771 *Angular Correlations in Proton-Proton Collisions at the LHC*, JHEP **1009** (2010) 091,
10772 arXiv:1009.4122 [hep-ex].

- 10773 [364] CMS Collaboration, S. Chatrchyan et al., *Long-range and short-range dihadron angular*
10774 *correlations in central PbPb collisions at a nucleon-nucleon center of mass energy of*
10775 *2.76 TeV*, arXiv:1105.2438 [nucl-ex]. * Temporary entry *.
- 10776 [365] A. Dumitru, K. Dusling, F. Gelis, J. Jalilian-Marian, T. Lappi, et al., *The Ridge in*
10777 *proton-proton collisions at the LHC*, Phys.Lett. **B697** (2011) 21–25, arXiv:1009.5295
10778 [hep-ph].
- 10779 [366] N. Armesto, *Predictions for the heavy-ion programme at the Large Hadron Collider*,
10780 arXiv:0903.1330 [hep-ph].
- 10781 [367] ALICE Collaboration, K. Aamodt et al., *Charged-particle multiplicity density at*
10782 *mid-rapidity in central Pb-Pb collisions at $\sqrt{s_{NN}} = 2.76$ TeV*, Phys.Rev.Lett. **105**
10783 (2010) 252301, arXiv:1011.3916 [nucl-ex]. * Temporary entry *.
- 10784 [368] ALICE Collaboration, J. Nystrand, *Photon-Induced Physics with Heavy-Ion Beams in*
10785 *ALICE*, Nucl.Phys.Proc.Suppl. **179-180** (2008) 156–161, arXiv:0807.0366 [nucl-ex].
- 10786 [369] M. Arneodo, *Nuclear effects in structure functions*, Phys. Rept. **240** (1994) 301–393.
- 10787 [370] D. F. Geesaman, K. Saito, and A. W. Thomas, *The nuclear EMC effect*, Ann. Rev.
10788 Nucl. Part. Sci. **45** (1995) 337–390.
- 10789 [371] A. Accardi et al., *Hard probes in heavy ion collisions at the lhc: pdfs, shadowing and pa*
10790 *collisions*, arXiv:hep-ph/0308248.
- 10791 [372] D. de Florian and R. Sassot, *Nuclear parton distributions at next to leading order*, Phys.
10792 Rev. **D69** (2004) 074028, arXiv:hep-ph/0311227.
- 10793 [373] M. Hirai, S. Kumano, and T. H. Nagai, *Determination of nuclear parton distribution*
10794 *functions and their uncertainties at next-to-leading order*, Phys. Rev. **C76** (2007)
10795 065207, arXiv:0709.3038 [hep-ph].
- 10796 [374] V. Guzey and M. Strikman, *Color fluctuation approximation for multiple interactions in*
10797 *leading twist theory of nuclear shadowing*, Phys. Lett. **B687** (2010) 167–173,
10798 arXiv:0908.1149 [hep-ph].
- 10799 [375] K. J. Eskola, V. J. Kolhinen, and C. A. Salgado, *The scale dependent nuclear effects in*
10800 *parton distributions for practical applications*, Eur. Phys. J. **C9** (1999) 61–68,
10801 arXiv:hep-ph/9807297.
- 10802 [376] K. Kovarik, I. Schienbein, F. Olness, J. Yu, C. Keppel, et al., *Nuclear corrections in*
10803 *neutrino-nucleus DIS and their compatibility with global NPDF analyses*, Phys.Rev.Lett.
10804 **106** (2011) 122301, arXiv:1012.0286 [hep-ph].
- 10805 [377] H. Paukkunen and C. A. Salgado, *Compatibility of neutrino DIS data and global analyses*
10806 *of parton distribution functions*, JHEP **07** (2010) 032, arXiv:1004.3140 [hep-ph].
- 10807 [378] A. Accardi et al., *Hard probes in heavy ion collisions at the LHC: Jet physics*,
10808 arXiv:hep-ph/0310274.
- 10809 [379] M. Bedjidian et al., *Hard probes in heavy ion collisions at the LHC: Heavy flavor*
10810 *physics*, arXiv:hep-ph/0311048.

- 10811 [380] M. Gyulassy and L. McLerran, *New forms of QCD matter discovered at RHIC*, Nucl.
10812 Phys. **A750** (2005) 30–63, [arXiv:nucl-th/0405013](#).
- 10813 [381] D. G. d’Enterria, *Quark-gluon matter*, J. Phys. **G34** (2007) S53–S82,
10814 [arXiv:nucl-ex/0611012](#).
- 10815 [382] T. Lappi, *Initial conditions of heavy ion collisions and high energy factorization*, Acta
10816 Phys. Polon. **B40** (2009) 1997–2012, [arXiv:0904.1670](#) [hep-ph].
- 10817 [383] A. Accardi, F. Arleo, W. K. Brooks, D. D’Enterria, and V. Muccifora, *Parton
10818 Propagation and Fragmentation in QCD Matter*, Riv. Nuovo Cim. **032** (2010) 439–553,
10819 [arXiv:0907.3534](#) [nucl-th].
- 10820 [384] ALICE Collaboration, K. Aamodt et al., *Suppression of Charged Particle Production at
10821 Large Transverse Momentum in Central Pb–Pb Collisions at $\sqrt{s_{NN}} = 2.76$ TeV*,
10822 Phys.Lett. **B696** (2011) 30–39, [arXiv:1012.1004](#) [nucl-ex]. * Temporary entry *.
- 10823 [385] Atlas Collaboration, G. Aad et al., *Observation of a Centrality-Dependent Dijet
10824 Asymmetry in Lead-Lead Collisions at $\sqrt{s(NN)} = 2.76$ TeV with the ATLAS
10825 Detector at the LHC*, Phys.Rev.Lett. **105** (2010) 252303, [arXiv:1011.6182](#) [hep-ex].
10826 * Temporary entry *.
- 10827 [386] CMS Collaboration, S. Chatrchyan et al., *Observation and studies of jet quenching in
10828 PbPb collisions at nucleon-nucleon center-of-mass energy = 2.76 TeV*,
10829 [arXiv:1102.1957](#) [nucl-ex]. * Temporary entry *.
- 10830 [387] The NNPDF Collaboration, R. D. Ball et al., *Precision determination of electroweak
10831 parameters and the strange content of the proton from neutrino deep-inelastic scattering*,
10832 Nucl. Phys. **B823** (2009) 195–233, [arXiv:0906.1958](#) [hep-ph].
- 10833 [388] K. Golec-Biernat and A. M. Stasto, *F_L proton structure function from the unified
10834 DGLAP/BFKL approach*, Phys. Rev. **D80** (2009) 014006, [arXiv:0905.1321](#) [hep-ph].
- 10835 [389] J. L. Albacete, N. Armesto, J. G. Milhano, and C. A. Salgado, *Non-linear QCD meets
10836 data: A global analysis of lepton- proton scattering with running coupling BK evolution*,
10837 Phys. Rev. **D80** (2009) 034031, [arXiv:0902.1112](#) [hep-ph].
- 10838 [390] The NNPDF Collaboration, and others, *Reweighting NNPDFs: the W lepton
10839 asymmetry*, [arXiv:1012.0836](#) [hep-ph].
- 10840 [391] NNPDF Collaboration, R. D. Ball et al., *A determination of parton distributions with
10841 faithful uncertainty estimation*, Nucl. Phys. **B809** (2009) 1–63, [arXiv:0808.1231](#)
10842 [hep-ph].
- 10843 [392] J. Jowett. Private communication.
- 10844 [393] N. Armesto, *A simple model for nuclear structure functions at small x in the dipole
10845 picture*, Eur. Phys. J. **C26** (2002) 35–43, [arXiv:hep-ph/0206017](#).
- 10846 [394] PHENIX Collaboration, S. S. Adler et al., *Centrality dependence of π^0 and η
10847 production at large transverse momentum in $s(NN)^{1/2} = 200$ -GeV $d + Au$
10848 collisions*, Phys. Rev. Lett. **98** (2007) 172302, [arXiv:nucl-ex/0610036](#).

- 10849 [395] S. J. Brodsky, I. Schmidt, and J.-J. Yang, *Nuclear antishadowing in neutrino deep*
10850 *inelastic scattering*, Phys.Rev. **D70** (2004) 116003, arXiv:hep-ph/0409279 [hep-ph].
- 10851 [396] E. R. Cazaroto, F. Carvalho, V. P. Goncalves, and F. S. Navarra, *Constraining the*
10852 *nuclear gluon distribution in eA processes at RHIC*, Phys. Lett. **B669** (2008) 331–336,
10853 arXiv:0804.2507 [hep-ph].
- 10854 [397] N. Armesto, H. Paukkunen, C. A. Salgado, and K. Tywoniuk, *Nuclear effects on the*
10855 *longitudinal structure function at small x*, Phys.Lett. **B694** (2010) 38–43,
10856 arXiv:1005.2035 [hep-ph].
- 10857 [398] A. Bruni, X. Janssen, and P. Marage, *Exclusive Vector Meson Production and Deeply*
10858 *Virtual Compton Scattering at HERA*, Proceedings of the HERA-LHC Workshops,
10859 2006-8, eds. Jung, de Roeck, DESY-PROC-2009-02 (2009) 427, 2009.
- 10860 [399] A. D. Martin, C. Nockles, M. G. Ryskin, and T. Teubner, *Small x gluon from exclusive*
10861 *J/psi production*, Phys. Lett. **B662** (2008) 252–258, arXiv:0709.4406 [hep-ph].
- 10862 [400] A. Caldwell and H. Kowalski, *Investigating the gluonic structure of nuclei via J/psi*
10863 *scattering*, Phys. Rev. **C81** (2010) 025203.
- 10864 [401] S. Munier, A. M. Stasto, and A. H. Mueller, *Impact parameter dependent S-matrix for*
10865 *dipole proton scattering from diffractive meson electroproduction*, Nucl. Phys. **B603**
10866 (2001) 427–445, arXiv:hep-ph/0102291.
- 10867 [402] K. Goeke, M. V. Polyakov, and M. Vanderhaeghen, *Hard Exclusive Reactions and the*
10868 *Structure of Hadrons*, Prog. Part. Nucl. Phys. **47** (2001) 401–515,
10869 arXiv:hep-ph/0106012.
- 10870 [403] M. Diehl, *Generalized parton distributions*, Phys. Rept. **388** (2003) 41–277,
10871 arXiv:hep-ph/0307382.
- 10872 [404] S. J. Brodsky, L. Frankfurt, J. F. Gunion, A. H. Mueller, and M. Strikman, *Diffractive*
10873 *leptoproduction of vector mesons in QCD*, Phys. Rev. **D50** (1994) 3134–3144,
10874 arXiv:hep-ph/9402283.
- 10875 [405] J. C. Collins, L. Frankfurt, and M. Strikman, *Factorization for hard exclusive*
10876 *electroproduction of mesons in QCD*, Phys. Rev. **D56** (1997) 2982–3006,
10877 arXiv:hep-ph/9611433.
- 10878 [406] M. Burkardt, *Impact parameter dependent parton distributions and off- forward parton*
10879 *distributions for zeta \rightarrow 0*, Phys. Rev. **D62** (2000) 071503, arXiv:hep-ph/0005108.
- 10880 [407] T. Rogers, V. Guzey, M. Strikman, and X. Zu, *Determining the proximity of gamma* N*
10881 *scattering to the black body limit using DIS and J/psi production*, Phys. Rev. **D69**
10882 (2004) 074011, arXiv:hep-ph/0309099.
- 10883 [408] H. Kowalski, T. Lappi, and R. Venugopalan, *Nuclear enhancement of universal*
10884 *dynamics of high parton densities*, Phys. Rev. Lett. **100** (2008) 022303,
10885 arXiv:0705.3047 [hep-ph].

- 10886 [409] L. Frankfurt, M. Strikman, and C. Weiss, *Dijet production as a centrality trigger for pp*
10887 *collisions at CERN LHC*, Phys. Rev. **D69** (2004) 114010, arXiv:hep-ph/0311231.
- 10888 [410] H1 Collaboration, F. D. Aaron et al., *Diffraction Dijet Photoproduction in ep Collisions*
10889 *at HERA*, Eur. Phys. J. **C70** (2010) 15–37, arXiv:1006.0946 [hep-ex].
- 10890 [411] L. Frankfurt, C. E. Hyde, M. Strikman, and C. Weiss, *Generalized parton distributions*
10891 *and rapidity gap survival in exclusive diffractive pp scattering*, Phys. Rev. **D75** (2007)
10892 054009, arXiv:hep-ph/0608271.
- 10893 [412] M. Deile et al., *13th International Conference on Elastic and Diffractive Scattering*
10894 *(Blois Workshop) - Moving Forward into the LHC Era*, arXiv:1002.3527 [hep-ph].
- 10895 [413] ZEUS Collaboration, S. Chekanov et al., *Exclusive electroproduction of J/psi mesons at*
10896 *HERA*, Nucl. Phys. **B695** (2004) 3–37, arXiv:hep-ex/0404008.
- 10897 [414] H1 Collaboration, A. Aktas et al., *Elastic J/psi production at HERA*, Eur. Phys. J. **C46**
10898 (2006) 585–603, arXiv:hep-ex/0510016.
- 10899 [415] H1 Collaboration, F. D. Aaron et al., *Measurement of Deeply Virtual Compton*
10900 *Scattering and its t-dependence at HERA*, Phys. Lett. **B659** (2008) 796–806,
10901 arXiv:0709.4114 [hep-ex].
- 10902 [416] ZEUS Collaboration, S. Chekanov et al., *A measurement of the Q², W and t*
10903 *dependences of deeply virtual Compton scattering at HERA*, JHEP **05** (2009) 108,
10904 arXiv:0812.2517 [hep-ex].
- 10905 [417] C. Marquet and B. Wu, *Exclusive vs. diffractive vector meson production in DIS at*
10906 *small x or off nuclei*, arXiv:0908.4180 [hep-ph].
- 10907 [418] T. Lappi and H. Mantysaari, *Incoherent diffractive J/Psi-production in high energy*
10908 *nuclear DIS*, (2010) , arXiv:1011.1988 [hep-ph].
- 10909 [419] W. Horowitz, *Measuring the Gluon Density in e + A Collisions: KLN CGC, DGLAP*
10910 *Glauber, or Neither?*, arXiv:1102.5058 [hep-ph]. * Temporary entry *.
- 10911 [420] L. Frankfurt, M. Strikman, D. Treleani, and C. Weiss, *Evidence for color fluctuations in*
10912 *the nucleon in high- energy scattering*, Phys. Rev. Lett. **101** (2008) 202003,
10913 arXiv:0808.0182 [hep-ph].
- 10914 [421] J. Bartels, K. J. Golec-Biernat, and K. Peters, *On the dipole picture in the nonforward*
10915 *direction*, Acta Phys. Polon. **B34** (2003) 3051–3068, arXiv:hep-ph/0301192.
- 10916 [422] C. Marquet, R. B. Peschanski, and G. Soyez, *Exclusive vector meson production at*
10917 *HERA from QCD with saturation*, Phys.Rev. **D76** (2007) 034011,
10918 arXiv:hep-ph/0702171 [HEP-PH].
- 10919 [423] M. G. Ryskin, *Diffractive J / psi electroproduction in LLA QCD*, Z. Phys. **C57** (1993)
10920 89–92.
- 10921 [424] P. Newman, *Low x and Diffractive Physics at a Large Hadron electron Collider*, . In
10922 *Proceedings of the 13th International (Blois) Conference on Elastic and Diffractive*
10923 *Scattering*, EDS'09, CERN, 2009, p182.

- 10924 [425] B. List and A. Mastroberardino, *DIFFVM: A Monte Carlo generator for diffractive*
10925 *processes in ep scattering*, Proceedings of the Workshop on Monte Carlo Generators for
10926 HERA Physics, DESY-PROC-1992-02 (1999) 396, 1999.
- 10927 [426] J. R. Forshaw, R. Sandapen, and G. Shaw, *Colour dipoles and rho, Phi*
10928 *electroproduction*, Phys. Rev. **D69** (2004) 094013, arXiv:hep-ph/0312172.
- 10929 [427] ZEUS Collaboration, S. Chekanov et al., *Exclusive photoproduction of J/psi mesons at*
10930 *HERA*, Eur. Phys. J. **C24** (2002) 345–360, arXiv:hep-ex/0201043.
- 10931 [428] ZEUS Collaboration, J. Breitweg et al., *Measurement of elastic Upsilon photoproduction*
10932 *at HERA*, Phys. Lett. **B437** (1998) 432–444, arXiv:hep-ex/9807020.
- 10933 [429] H1 Collaboration, C. Adloff et al., *Elastic photoproduction of J/psi and Upsilon mesons*
10934 *at HERA*, Phys. Lett. **B483** (2000) 23–35, arXiv:hep-ex/0003020.
- 10935 [430] ZEUS Collaboration, S. Chekanov et al., *Exclusive photoproduction of upsilon mesons at*
10936 *HERA*, Phys. Lett. **B680** (2009) 4–12, arXiv:0903.4205 [hep-ex].
- 10937 [431] B. E. Cox, J. R. Forshaw, and R. Sandapen, *Diffractive upsilon production at the LHC*,
10938 *JHEP* **06** (2009) 034, arXiv:0905.0102 [hep-ph].
- 10939 [432] E. Perez, L. Schoeffel, and L. Favart, *MILOU: A Monte-Carlo for deeply virtual*
10940 *Compton scattering*, arXiv:hep-ph/0411389 [hep-ph].
- 10941 [433] L. Frankfurt, A. Freund, and M. Strikman, *Diffractive exclusive photoproduction in DIS*
10942 *at HERA*, Phys.Rev. **D58** (1998) 114001, arXiv:hep-ph/9710356 [hep-ph].
- 10943 [434] H1 Collaboration, F. Aaron et al., *Deeply Virtual Compton Scattering and its Beam*
10944 *Charge Asymmetry in e+- Collisions at HERA*, Phys.Lett. **B681** (2009) 391–399,
10945 arXiv:arXiv:0907.5289 [hep-ex].
- 10946 [435] Fermilab Tagged Photon Spectrometer Collaboration, M. D. Sokoloff et al., *An*
10947 *Experimental Study of the a-Dependence of J/psi Photoproduction*, Phys. Rev. Lett. **57**
10948 (1986) 3003.
- 10949 [436] E665 Collaboration, M. R. Adams et al., *Measurement of nuclear transparencies from*
10950 *exclusive rho0 meson production in muon - nucleus scattering at 470-GeV*, Phys. Rev.
10951 Lett. **74** (1995) 1525–1529.
- 10952 [437] L. Frankfurt, V. Guzey, and M. Strikman, *Leading twist nuclear shadowing phenomena*
10953 *in hard processes with nuclei*, arXiv:1106.2091 [hep-ph].
- 10954 [438] B. Nicolescu, *Recent advances in odderon physics*, arXiv:hep-ph/9911334 [hep-ph].
- 10955 [439] C. Ewerz, *The Odderon in quantum chromodynamics*, arXiv:hep-ph/0306137
10956 [hep-ph].
- 10957 [440] J. Bartels, *High-Energy Behavior in a Nonabelian Gauge Theory. 1. T(n,m) in the*
10958 *Leading Log Normal S Approximation*, Nucl.Phys. **B151** (1979) 293.
- 10959 [441] J. Bartels, *High-Energy Behavior in a Nonabelian Gauge Theory. 2. First Corrections to*
10960 *T(n,m) Beyond the Leading LNS Approximation*, Nucl.Phys. **B175** (1980) 365.

- 10961 [442] J. Kwiecinski and M. Praszalowicz, *Three Gluon Integral Equation and Odd c Singlet*
10962 *Regge Singularities in QCD*, Phys.Lett. **B94** (1980) 413.
- 10963 [443] R. Janik and J. Wosiek, *Solution of the odderon problem*, Phys.Rev.Lett. **82** (1999)
10964 1092–1095, [arXiv:hep-th/9802100](#) [hep-th].
- 10965 [444] J. Bartels, L. Lipatov, and G. Vacca, *A New odderon solution in perturbative QCD*,
10966 Phys.Lett. **B477** (2000) 178–186, [arXiv:hep-ph/9912423](#) [hep-ph].
- 10967 [445] H1 Collaboration, C. Adloff et al., *Search for odderon induced contributions to exclusive*
10968 *π^0 photoproduction at HERA*, Phys.Lett. **B544** (2002) 35–43, [arXiv:hep-ex/0206073](#)
10969 [hep-ex].
- 10970 [446] J. Czyzewski, J. Kwiecinski, L. Motyka, and M. Sadzikowski, *Exclusive $\eta(c)$*
10971 *photoproduction and electroproduction at HERA as a possible probe of the odderon*
10972 *singularity in QCD*, Phys.Lett. **B398** (1997) 400–406, [arXiv:hep-ph/9611225](#)
10973 [hep-ph].
- 10974 [447] S. J. Brodsky, J. Rathsmann, and C. Merino, *Odderon-Pomeron interference*, Phys.Lett.
10975 **B461** (1999) 114–122, [arXiv:hep-ph/9904280](#) [hep-ph].
- 10976 [448] A. Kaidalov, *Diffraction Production Mechanisms*, Phys.Rept. **50** (1979) 157–226.
- 10977 [449] K. A. Goulianos, *Diffraction Interactions of Hadrons at High-Energies*, Phys. Rept. **101**
10978 (1983) 169.
- 10979 [450] G. Ingelman and P. E. Schlein, *Jet Structure in High Mass Diffractive Scattering*, Phys.
10980 Lett. **B152** (1985) 256.
- 10981 [451] A. Donnachie and P. V. Landshoff, *Diffractive Deep Inelastic Lepton Scattering*, Phys.
10982 Lett. **B191** (1987) 309.
- 10983 [452] G. Wolf, *Review of High Energy Diffraction in Real and Virtual Photon Proton*
10984 *scattering at HERA*, Rept. Prog. Phys. **73** (2010) 116202, [arXiv:0907.1217](#) [hep-ex].
- 10985 [453] H1 Collaboration, A. Aktas et al., *Diffractive deep-inelastic scattering with a leading*
10986 *proton at HERA*, Eur. Phys. J. **C48** (2006) 749–766, [arXiv:hep-ex/0606003](#).
- 10987 [454] ZEUS Collaboration, S. Chekanov et al., *Deep inelastic scattering with leading protons*
10988 *or large rapidity gaps at HERA*, Nucl. Phys. **B816** (2009) 1–61, [arXiv:0812.2003](#)
10989 [hep-ex].
- 10990 [455] F. Aaron et al., *Measurement of the Diffractive Deep-Inelastic Scattering Cross Section*
10991 *with a Leading Proton at HERA*, [arXiv:1010.1476](#) [hep-ex].
- 10992 [456] H1 Collaboration, A. Aktas et al., *Measurement and QCD analysis of the diffractive*
10993 *deep- inelastic scattering cross-section at HERA*, Eur. Phys. J. **C48** (2006) 715–748,
10994 [arXiv:hep-ex/0606004](#).
- 10995 [457] J. Blumlein and D. Robaschik, *On the scaling violations of diffractive structure*
10996 *functions: Operator approach*, Phys. Lett. **B517** (2001) 222–232,
10997 [arXiv:hep-ph/0106037](#).

- 11098 [458] H1 Collaboration, A. Aktas et al., *Dijet Cross Sections and Parton Densities in*
11099 *Diffraction DIS at HERA*, JHEP **10** (2007) 042, arXiv:0708.3217 [hep-ex].
- 11000 [459] ZEUS Collaboration, S. Chekanov et al., *A QCD analysis of ZEUS diffractive data*,
11001 Nucl. Phys. **B831** (2010) 1–25, arXiv:0911.4119 [hep-ex].
- 11002 [460] A. D. Martin, M. G. Ryskin, and G. Watt, *Diffractive parton distributions from*
11003 *perturbative QCD*, Eur. Phys. J. **C44** (2005) 69–85, arXiv:hep-ph/0504132.
- 11004 [461] H1 Collaboration, A. Aktas et al., *Tests of QCD factorisation in the diffractive*
11005 *production of dijets in deep-inelastic scattering and photoproduction at HERA*, Eur.
11006 Phys. J. **C51** (2007) 549–568, arXiv:hep-ex/0703022.
- 11007 [462] H1 Collaboration, A. Aktas et al., *Diffractive open charm production in deep-inelastic*
11008 *scattering and photoproduction at HERA*, Eur. Phys. J. **C50** (2007) 1–20,
11009 arXiv:hep-ex/0610076.
- 11010 [463] P. Newman, *Deep Inelastic Scattering at the TeV Energy Scale and the LHeC Project*,
11011 Nucl. Phys. Proc. Suppl. **191** (2009) 307–319, arXiv:0902.2292 [hep-ex].
- 11012 [464] J. Bartels, J. R. Ellis, H. Kowalski, and M. Wusthoff, *An analysis of diffraction in*
11013 *deep-inelastic scattering*, Eur. Phys. J. **C7** (1999) 443–458, arXiv:hep-ph/9803497.
- 11014 [465] H. Collaboration, *Measurement of the Diffractive Longitudinal Structure Function at*
11015 *HERA*, . in litt.
- 11016 [466] H1 Collaboration, F. D. Aaron et al., *Measurement of Leading Neutron Production in*
11017 *Deep- Inelastic Scattering at HERA*, Eur. Phys. J. **C68** (2010) 381–399,
11018 arXiv:1001.0532 [hep-ex].
- 11019 [467] G. Watt and H. Kowalski, *Impact parameter dependent colour glass condensate dipole*
11020 *model*, Phys. Rev. **D78** (2008) 014016, arXiv:0712.2670 [hep-ph].
- 11021 [468] V. A. Abramovsky, V. N. Gribov, and O. V. Kancheli, *CHARACTER OF INCLUSIVE*
11022 *SPECTRA AND FLUCTUATIONS PRODUCED IN INELASTIC PROCESSES BY*
11023 *MULTI - POMERON EXCHANGE*, Yad. Fiz. **18** (1973) 595–616.
- 11024 [469] L. Frankfurt and M. Strikman, *Diffraction at HERA, color opacity and nuclear*
11025 *shadowing*, Eur. Phys. J. **A5** (1999) 293–306, arXiv:hep-ph/9812322.
- 11026 [470] L. Frankfurt, V. Guzey, and M. Strikman, *Leading twist nuclear shadowing: A user’s*
11027 *guide*, Phys. Rev. **D71** (2005) 054001, arXiv:hep-ph/0303022.
- 11028 [471] H. Abramowicz, L. Frankfurt, and M. Strikman, *Interplay of hard and soft physics in*
11029 *small x deep inelastic processes*, ECONF **C940808** (1994) 033, arXiv:hep-ph/9503437.
- 11030 [472] N. Armesto, A. Capella, A. Kaidalov, J. Lopez-Albacete, and C. Salgado, *Nuclear*
11031 *structure functions at small x from inelastic shadowing and diffraction*, Eur.Phys.J.
11032 **C29** (2003) 531–540, arXiv:hep-ph/0304119 [hep-ph].
- 11033 [473] K. Tywoniuk, I. Arsene, L. Bravina, A. Kaidalov, and E. Zabrodin, *Gluon shadowing in*
11034 *the Glauber-Gribov model at HERA*, Phys. Lett. **B657** (2007) 170–175,
11035 arXiv:0705.1596 [hep-ph].

- 11036 [474] L. Frankfurt, V. Guzey, and M. Strikman, *Leading twist coherent diffraction on nuclei*
 11037 *in deep inelastic scattering at small x and nuclear shadowing*, Phys. Lett. **B586** (2004)
 11038 41–52, [arXiv:hep-ph/0308189](#).
- 11039 [475] C. Marquet, *A Unified description of diffractive deep inelastic scattering with*
 11040 *saturation*, Phys.Rev. **D76** (2007) 094017, [arXiv:0706.2682 \[hep-ph\]](#).
- 11041 [476] H. Kowalski, T. Lappi, C. Marquet, and R. Venugopalan, *Nuclear enhancement and*
 11042 *suppression of diffractive structure functions at high energies*, Phys. Rev. **C78** (2008)
 11043 045201, [arXiv:0805.4071 \[hep-ph\]](#).
- 11044 [477] J. Collins and H. Jung, *Need for fully unintegrated parton densities*,
 11045 [arXiv:hep-ph/0508280](#).
- 11046 [478] J. C. Collins and D. E. Soper, *Back-To-Back Jets in QCD*, Nucl. Phys. **B193** (1981)
 11047 381.
- 11048 [479] J. C. Collins and D. E. Soper, *Parton Distribution and Decay Functions*, Nucl. Phys.
 11049 **B194** (1982) 445.
- 11050 [480] J. C. Collins, *What exactly is a parton density?*, Acta Phys. Polon. **B34** (2003) 3103,
 11051 [arXiv:hep-ph/0304122](#).
- 11052 [481] J. Collins, *Rapidity divergences and valid definitions of parton densities*, PoS **LC2008**
 11053 (2008) 028, [arXiv:0808.2665 \[hep-ph\]](#).
- 11054 [482] X.-d. Ji, J.-p. Ma, and F. Yuan, *QCD factorization for semi-inclusive deep-inelastic*
 11055 *scattering at low transverse momentum*, Phys. Rev. **D71** (2005) 034005,
 11056 [arXiv:hep-ph/0404183](#).
- 11057 [483] M. Ciafaloni, *Coherence Effects in Initial Jets at Small q^{*2} / s* , Nucl. Phys. **B296**
 11058 (1988) 49.
- 11059 [484] S. Catani, F. Fiorani, and G. Marchesini, *QCD Coherence in Initial State Radiation*,
 11060 Phys.Lett. **B234** (1990) 339.
- 11061 [485] S. Catani, F. Fiorani, and G. Marchesini, *Small x Behavior of Initial State Radiation in*
 11062 *Perturbative QCD*, Nucl.Phys. **B336** (1990) 18.
- 11063 [486] G. Marchesini, *QCD coherence in the structure function and associated distributions at*
 11064 *small x* , Nucl.Phys. **B445** (1995) 49–80, [arXiv:hep-ph/9412327 \[hep-ph\]](#).
- 11065 [487] I. Balitsky, *High-energy QCD and Wilson lines*, [arXiv:hep-ph/0101042](#).
- 11066 [488] J. C. Collins, *Foundations of Perturbative QCD*. Cambridge University Press,
 11067 Cambridge, 2011. To be published.
- 11068 [489] S. Aybat and T. C. Rogers, *TMD Parton Distribution and Fragmentation Functions*
 11069 *with QCD Evolution*, [arXiv:1101.5057 \[hep-ph\]](#). * Temporary entry *.
- 11070 [490] J. C. Collins and A. Metz, *Universality of soft and collinear factors in hard- scattering*
 11071 *factorization*, Phys. Rev. Lett. **93** (2004) 252001, [arXiv:hep-ph/0408249](#).

- 11072 [491] F. Landry, R. Brock, P. M. Nadolsky, and C. P. Yuan, *Tevatron Run-1 Z boson data*
11073 *and Collins-Soper-Sterman resummation formalism*, Phys. Rev. **D67** (2003) 073016,
11074 [arXiv:hep-ph/0212159](#).
- 11075 [492] J. C. Collins, D. E. Soper, and G. F. Sterman, *Transverse Momentum Distribution in*
11076 *Drell-Yan Pair and W and Z Boson Production*, Nucl. Phys. **B250** (1985) 199.
- 11077 [493] C. Marquet, B.-W. Xiao, and F. Yuan, *Semi-inclusive Deep Inelastic Scattering at small*
11078 *x*, Phys. Lett. **B682** (2009) 207–211, [arXiv:0906.1454 \[hep-ph\]](#).
- 11079 [494] F. Dominguez, B.-W. Xiao, and F. Yuan, *kt-factorization for Hard Processes in Nuclei*,
11080 Phys. Rev. Lett. **106** (2011) 022301, [arXiv:1009.2141 \[hep-ph\]](#).
- 11081 [495] H1 Collaboration, A. Aktas et al., *Inclusive dijet production at low Bjorken-x in deep*
11082 *inelastic scattering*, Eur. Phys. J. **C33** (2004) 477–493, [arXiv:hep-ex/0310019](#).
- 11083 [496] A. J. Askew, D. Graudenz, J. Kwiecinski, and A. D. Martin, *Dijet production at HERA*
11084 *as a probe of BFKL dynamics*, Phys. Lett. **B338** (1994) 92–97, [arXiv:hep-ph/9407337](#).
- 11085 [497] J. Kwiecinski, A. D. Martin, and A. M. Stasto, *Predictions for dijet production in DIS*
11086 *using small x dynamics*, Phys. Lett. **B459** (1999) 644–648, [arXiv:hep-ph/9904402](#).
- 11087 [498] A. Szczurek, N. N. Nikolaev, W. Schafer, and J. Speth, *Mapping the proton unintegrated*
11088 *gluon distribution in dijets correlations in real and virtual photoproduction at HERA*,
11089 Phys. Lett. **B500** (2001) 254–262, [arXiv:hep-ph/0011281](#).
- 11090 [499] M. Hansson and H. Jung, *Towards precision determination of uPDFs*,
11091 [arXiv:0707.4276 \[hep-ph\]](#).
- 11092 [500] F. Hautmann and H. Jung, *Angular correlations in multi-jet final states from kt-*
11093 *dependent parton showers*, JHEP **10** (2008) 113, [arXiv:0805.1049 \[hep-ph\]](#).
- 11094 [501] J. Bartels, C. Ewerz, H. Lotter, and M. Wusthoff, *Azimuthal distribution of quark -*
11095 *anti-quark jets in DIS diffractive dissociation*, Phys.Lett. **B386** (1996) 389–396,
11096 [arXiv:hep-ph/9605356 \[hep-ph\]](#).
- 11097 [502] J. Bartels, H. Jung, and M. Wusthoff, *Quark - anti-quark gluon jets in DIS diffractive*
11098 *dissociation*, Eur.Phys.J. **C11** (1999) 111–125, [arXiv:hep-ph/9903265 \[hep-ph\]](#).
- 11099 [503] L. Lonnblad, *ARIADNE version 4: A Program for simulation of QCD cascades*
11100 *implementing the color dipole model*, Comput.Phys.Commun. **71** (1992) 15–31.
- 11101 [504] H. Jung et al., *The CCFM Monte Carlo generator CASCADE 2.2.0*, Eur. Phys. J. **C70**
11102 (2010) 1237–1249, [arXiv:1008.0152 \[hep-ph\]](#).
- 11103 [505] A. H. Mueller, *Parton distributions at very small x values*, Nucl. Phys. Proc. Suppl.
11104 **18C** (1991) 125–132.
- 11105 [506] A. H. Mueller, *Jets at LEP and HERA*, J. Phys. **G17** (1991) 1443–1454.
- 11106 [507] H1 Collaboration, S. Aid et al., *Transverse energy and forward jet production in the low*
11107 *x regime at HERA*, Phys. Lett. **B356** (1995) 118–128, [arXiv:hep-ex/9506012](#).

- 11108 [508] H1 Collaboration, C. Adloff et al., *Forward jet and particle production at HERA*, Nucl.
11109 Phys. **B538** (1999) 3–22, [arXiv:hep-ex/9809028](#).
- 11110 [509] H1 Collaboration, A. Aktas et al., *Forward jet production in deep inelastic scattering at*
11111 *HERA*, Eur. Phys. J. **C46** (2006) 27–42, [arXiv:hep-ex/0508055](#).
- 11112 [510] ZEUS Collaboration, J. Breitweg et al., *Forward jet production in deep inelastic*
11113 *scattering at HERA*, Eur. Phys. J. **C6** (1999) 239–252, [arXiv:hep-ex/9805016](#).
- 11114 [511] ZEUS Collaboration, J. Breitweg et al., *Measurement of the $E(T, \text{jet})^{**2}/Q^{**2}$*
11115 *dependence of forward- jet production at HERA*, Phys. Lett. **B474** (2000) 223–233,
11116 [arXiv:hep-ex/9910043](#).
- 11117 [512] ZEUS Collaboration, S. Chekanov et al., *Forward jet production in deep inelastic $e p$*
11118 *scattering and low- x parton dynamics at HERA*, Phys. Lett. **B632** (2006) 13–26,
11119 [arXiv:hep-ex/0502029](#).
- 11120 [513] J. Kwiecinski, S. C. Lang, and A. D. Martin, *Single particle spectra in deep inelastic*
11121 *scattering as a probe of small x dynamics*, Eur. Phys. J. **C6** (1999) 671–680,
11122 [arXiv:hep-ph/9707240](#).
- 11123 [514] J. Kwiecinski, A. D. Martin, and J. J. Outhwaite, *Small x QCD effects in DIS with a*
11124 *forward jet or a forward π^0* , Eur. Phys. J. **C9** (1999) 611–622, [arXiv:hep-ph/9903439](#).
- 11125 [515] G. Bottazzi, G. Marchesini, G. P. Salam, and M. Scorletti, *Small- x one-particle-inclusive*
11126 *quantities in the CCFM approach*, JHEP **12** (1998) 011, [arXiv:hep-ph/9810546](#).
- 11127 [516] H. Jung, *CCFM prediction on forward jets and F_2 : Parton level predictions and a new*
11128 *hadron level Monte Carlo generator CASCADE*, [arXiv:hep-ph/9908497](#).
- 11129 [517] H. Jung, *CCFM prediction for F_2 and forward jets at HERA*, Nucl. Phys. Proc. Suppl.
11130 **79** (1999) 429–431, [arXiv:hep-ph/9905554](#).
- 11131 [518] H. Jung and G. P. Salam, *Hadronic final state predictions from CCFM: The hadron-*
11132 *level Monte Carlo generator CASCADE*, Eur. Phys. J. **C19** (2001) 351–360,
11133 [arXiv:hep-ph/0012143](#).
- 11134 [519] O. Kepka, C. Royon, C. Marquet, and R. B. Peschanski, *Next-leading BFKL effects in*
11135 *forward-jet production at HERA*, Phys. Lett. **B655** (2007) 236–240,
11136 [arXiv:hep-ph/0609299](#).
- 11137 [520] J. Bartels, V. Del Duca, and M. Wusthoff, *Azimuthal dependence of forward jet*
11138 *production in DIS in the high-energy limit*, Z.Phys. **C76** (1997) 75–79,
11139 [arXiv:hep-ph/9610450](#) [hep-ph].
- 11140 [521] A. Sabio Vera and F. Schwennsen, *Azimuthal decorrelation of forward jets in Deep*
11141 *Inelastic Scattering*, Phys. Rev. **D77** (2008) 014001, [arXiv:0708.0549](#) [hep-ph].
- 11142 [522] J. Kwiecinski, A. D. Martin, P. J. Sutton, and K. J. Golec-Biernat, *QCD predictions for*
11143 *the transverse energy flow in deep inelastic scattering in the HERA small x regime*,
11144 Phys. Rev. **D50** (1994) 217–225, [arXiv:hep-ph/9403292](#).

- 11145 [523] K. J. Golec-Biernat, J. Kwiecinski, A. D. Martin, and P. J. Sutton, *Transverse energy*
11146 *flow at HERA*, Phys. Lett. **B335** (1994) 220–225, arXiv:hep-ph/9405400.
- 11147 [524] N. H. Brook et al., *A comparison of deep inelastic scattering Monte Carlo event*
11148 *generators to HERA data*, arXiv:hep-ex/9912053.
- 11149 [525] G. P. Salam and G. Soyez, *A practical Seedless Infrared-Safe Cone jet algorithm*, JHEP
11150 **05** (2007) 086, arXiv:0704.0292 [hep-ph].
- 11151 [526] Y. L. Dokshitzer, V. A. Khoze, A. H. Mueller, and S. I. Troyan, *Basics of perturbative*
11152 *QCD*, . Editions Frontieres 1991, 274p.
- 11153 [527] D. de Florian, R. Sassot, and M. Stratmann, *Global analysis of fragmentation functions*
11154 *for pions and kaons and their uncertainties*, Phys.Rev. **D75** (2007) 114010,
11155 arXiv:hep-ph/0703242 [HEP-PH].
- 11156 [528] D. de Florian, R. Sassot, and M. Stratmann, *Global analysis of fragmentation functions*
11157 *for protons and charged hadrons*, Phys.Rev. **D76** (2007) 074033, arXiv:0707.1506
11158 [hep-ph].
- 11159 [529] A. M. Stasto, *Physics of ultrahigh energy neutrinos*, Int. J. Mod. Phys. **A19** (2004)
11160 317–340, arXiv:astro-ph/0310636.
- 11161 [530] J. K. Becker, *High-energy neutrinos in the context of multimessenger physics*, Phys.
11162 Rept. **458** (2008) 173–246, arXiv:0710.1557 [astro-ph].
- 11163 [531] E. Zas, *Neutrino Detection with Inclined Air Showers*, New J. Phys. **7** (2005) 130,
11164 arXiv:astro-ph/0504610.
- 11165 [532] N. Armesto, C. Merino, G. Parente, and E. Zas, *Charged Current Neutrino Cross*
11166 *Section and Tau Energy Loss at Ultra-High Energies*, Phys. Rev. **D77** (2008) 013001,
11167 arXiv:0709.4461 [hep-ph].
- 11168 [533] K. Hirata and E. Keil, *Barycentre motion of beams due to beam-beam interaction in*
11169 *asymmetric ring colliders*, Nuclear Instruments and Methods in Physics Research
11170 Section A: Accelerators, Spectrometers, Detectors and Associated Equipment **292**
11171 (1990) no. 1, 156 – 168. [http://www.sciencedirect.com/science/article/](http://www.sciencedirect.com/science/article/B6TJM-470F1H3-M/2/ff1b42fa7c847256a9e6c3245d3335d5)
11172 [B6TJM-470F1H3-M/2/ff1b42fa7c847256a9e6c3245d3335d5](http://www.sciencedirect.com/science/article/B6TJM-470F1H3-M/2/ff1b42fa7c847256a9e6c3245d3335d5).
- 11173 [534] *Private Communication with Sylvain Weisz*, .
- 11174 [535] R. Appleby, *IRSYN*, (2010) .
- 11175 [536] S. Russenschuck, *Magnet Options for Q1 and Q2 (Ring-Ring and Linac-Ring, 3rd*
11176 *CERN-ECFA-NuPECC Workshop on the LHeC* (2010) .
- 11177 [537] N. Bernard, *Analytic Method to Calculate the Power Produced by Synchrotron Radiation*
11178 *in a Quadrupole Magnet*, CERN LHeC Note 2 (2010) .
- 11179 [538] H. Wiedemann, *Synchrotron Radiation*, Springer-Verlag Berlin Heidelberg (2003) .
- 11180 [539] I. B. et al., *Study of beam-induced backgrounds in the ZEUS detector from 2002 HERA*
11181 *running*, (2002) .

- 11182 [540] S. Russenschuck, *Private Communication*, (2010) .
- 11183 [541] O. S. Bruning, (Ed.) et al., *LHC design report. Vol. I: The LHC main ring*, .
11184 CERN-2004-003-V-1.
- 11185 [542] D. Barber and G. Ripken in *Handbook of Accelerator Physics and Engineering*, A. Chao
11186 and M. Tigner, eds. World Scientific, first ed., 2006. third printing.
- 11187 [543] D. Barber et al., *Several articles*, in *Proc. ICFA Workshop on Quantum Aspects of*
11188 *Beam Physics*. World Scientific, Monterey, CA, USA, 1999.
- 11189 [544] A. Sokolov and I. Ternov Sov. Phys. Dokl. **8** (1964) no. 12, 1203.
- 11190 [545] J. Jackson, *Classical Electrodynamics*. Wiley & Sons, third ed., 1998.
- 11191 [546] Y. Derbenev and A. Kondratenko Sov. Phys. JETP **37** (1973) 968.
- 11192 [547] S. Mane Phys. Rev. **A36** (1987) 105–130.
- 11193 [548] G. Hoffstätter, M. Vogt, and D. Barber Phys. Rev. ST Accel. Beams **11** (1999) no. 2,
11194 114001.
- 11195 [549] D. Barber, G. Hoffstätter, and M. Vogt in *Proc. 14th Int. Spin Physics Symp. AIP*
11196 *Conf. Proc.* 570 (2001), 2000.
- 11197 [550] V. Baier and V. Katkov Sov. Phys. JETP **25** (1967) 944.
- 11198 [551] V. Baier, V. Katkov, and V. Strakhovenko Sov. Phys. JETP **31** (1970) 908.
- 11199 [552] R. Assmann et al. in *Proc. Part. Accel. Conf.*, p. 2999 and page 3002. New York, NY,
11200 USA, 1999.
- 11201 [553] D. Barber et al. Phys. Lett. **343B** (1995) 436.
- 11202 [554] S. Mane Nucl.Inst.Meth. **A292** (1990) 52.
- 11203 [555] S. Mane Nucl.Inst.Meth. **A321** (1992) 21.
- 11204 [556] D. Barber. SLICKTRACK is the extended version of SLICK [557] which includes
11205 Monte-Carlo spin-orbit tracking using the mathematical structures of SLICK.
- 11206 [557] D. Barber. SLICK is a thick lens version of SLIM [542] by D.P. Barber using the
11207 formalism of [706].
- 11208 [558] B. Montague Physics Reports **113** (1984) .
- 11209 [559] Y. Derbenev and H. Grote Tech. Rep. SL/Note 95-37, CERN, 1995.
- 11210 [560] V. Litvinenko, *LHeC with 100% Energy Recovery Linac*, 2nd CERN-ECFA-NuPECC
11211 Workshop on the LHeC, Divonne-les-Bains, 1–3 September 2009 (2009) .
- 11212 [561] P. Grosse-Wiesmann, *Colliding a Linear Electron Beam with a Storage Ring Beam*, NIM
11213 **A 274** (1989) 21.

- 11214 [562] F. Ruggiero and F. Zimmermann, *Luminosity Optimization near the Beam-Beam Limit*
11215 *by Increasing Bunch Length or Crossing Angle*, PRST-AB **5** (2002) 061101.
- 11216 [563] F. Zimmermann et al., *Linac-LHC ep Collider Options*, Proc. EPAC'08 Genoa (2008)
11217 2847–2849.
- 11218 [564] D. Schulte, *LHeC Ring-Linac Lattice and Beam Dynamics*, 3rd CERN-ECFA-NuPECC
11219 LHeC Workshop Chavannes-de-Bogis, December 2010 (2010) .
- 11220 [565] F. Zimmermann, K. Thompson, and R. Helm, *Electron-Electron Luminosity in the Next*
11221 *Linear Collider*, Int. J. Mod. Phys. A **13** (1998) 2443–2454.
- 11222 [566] H. Braun et al., *CLIC 2008 Parameters*, CLIC-Note-764 (2008) .
- 11223 [567] N. Phinney, N. Toge, and N. Walker, *LC Reference Design Report Volume 3 -*
11224 *Accelerator*, (2007) , [arXiv:0712.2361](https://arxiv.org/abs/0712.2361) [[physics.acc-ph](https://arxiv.org/abs/0712.2361)].
- 11225 [568] F. Gerigk et al., *Conceptual Design of the SPL II*, CRN-2006-006 (2006) .
- 11226 [569] C. Mayes and G. Hoffstaetter, *Cornell Energy Recovery Linac Lattice and Layout*,
11227 Proc. IPAC'10 Kyoto (2010) .
- 11228 [570] G. Neil, *Free Electron Lasers from THz to X-rays*, Invited Talk at UPHUK4, Bodrum,
11229 Turkey, 30 August 2010 (2010) .
- 11230 [571] Linnecar, T. and Tückmantel, J., , Private communication, 28 May 2008 (2008) .
- 11231 [572] O. Napoly, , Private communication, 6th EuCARD Steering Meeting, Malta, 12–13
11232 October 2010. (2010) .
- 11233 [573] E. Ciapala, *RF for the LHeC*, 3rd CERN-ECFA-NuPECC LHeC Workshop
11234 Chavannes-de-Bogis, December 2010 (2010) .
- 11235 [574] J. Tuckmantel, , Comment at 2nd RFTech meeting, PSI, Villigen, 2–3 December 2010
11236 (2010) .
- 11237 [575] V. Litvinenko and I. Ben-Zvi, , Private communications (2010) .
- 11238 [576] I. Ben-Zvi, , Private communications, 16 November 2010 (2010) .
- 11239 [577] D. Tommasini, *RR+RL Magnets*, 3rd CERN-ECFA-NuPECC LHeC Workshop
11240 Chavannes-de-Bogis, December 2010 (2010) .
- 11241 [578] J. Skrabacz, *Optimizing Cost and Minimizing Energy Loss in the Recirculating*
11242 *Race-Track Design of the LHeC Electron Linac*, CERN-AB-Note-2008-043 (2008) .
- 11243 [579] A. Bogacz, *LHeC Recirculator with Energy Recovery – Beam Optics Choices*,
11244 JLAB-TN-10-040 (2010) .
- 11245 [580] D. Schulte and F. Zimmermann, , Private discussions (2010) .
- 11246 [581] D. Schulte, , Private communication (2010) .

- 11247 [582] D. Schulte and F. Zimmermann, *QCD Explorer Based on LHC and CLIC-1*,
11248 Proc. EPAC'04, Lucerne, CERN-AB-2004-079, and CLIC Note 608 (2004) .
- 11249 [583] K. Ohmi, R. Calaga, W. Hofle, R. Tomas, and F. Zimmermann, *Beam-Beam Effects*
11250 *with External Noise in LHC*, Proc. PAC07, Albuquerque (2007) 1496.
- 11251 [584] F. Zimmermann et al., *First Bunch Length Studies in the SLC South Final Focus*,
11252 Proc. EPAC 1998 Stockholm (1998) 487.
- 11253 [585] C. Adolphsen et al., *Pulse-to-Pulse Stability Issues at the SLC*, Proc. IEEE PAC 1995
11254 Dallas (1995) .
- 11255 [586] P. Chen and K. Yokoya, *Disruption Effects from the Interaction of Round $e+e-$ Beams*,
11256 Phys. Rev. D **38** (1988) 987.
- 11257 [587] M. Yamamoto, M. and Kuwahara, *Superlattice Photocathode Development for Low*
11258 *Emittance*, Photocathode Physics for Photoinjectors Workshop, BNL, October 2010
11259 (2010) .
- 11260 [588] I. Bailey, *A Helical Undulator Based Positron Source for the International Linear*
11261 *Collider*, Proc. PoS HEP2005 (2006) 368.
- 11262 [589] S. Araki et al., *Conceptual Design of a Polarised Positron Source Based on Laser*
11263 *Compton Scattering*, CARE/ELAN-Document-2005-013, CLIC Note 639, KEK Preprint
11264 2005-60, LAL 05-94 (2005) , physics/0509016.
- 11265 [590] F. Zimmermann et al., *Stacking Simulations for Compton Positron Sources of Future*
11266 *Linear Colliders*, Proc. PAC'09 Vancouver (2009) .
- 11267 [591] V. Litvinenko, *Recirculating Linac*, 2nd CERN-ECFA-NuPECC workshop on LHeC,
11268 Divonne-les-Bains (2009) .
- 11269 [592] I. Ginzburg, G. Kotkin, V. Serbo, and V. Telnov, *Colliding γe and $\gamma\gamma$ Beams Based on*
11270 *the Single Pass Accelerators (of VLEPP Type)*, Nucl. Instr. & Meth. **205** (1983) 47.
- 11271 [593] H. Burkhardt and V. Telnov, *CLIC 3-TeV Photon Collider Options*,
11272 CERN-SL-2002-013-AP, CLIC-Note-508 (2002) .
- 11273 [594] T. N. D. Group, *NLC Zeroth-Order Design Report for the Next Linear Collider*,
11274 *Appendix B*, LBNL-5424, SLAC-474, Appendix B (1996) .
- 11275 [595] Klemz, G. and Mönig, K. and Will, I. , *Design Study of an Optial Cavity for a Future*
11276 *Photon-Collider at ILC*, NIM A **564** (2006) 212.
- 11277 [596] H. Aksakal, Z. Nergiz, et al., *γp Option for LHeC*, Draft Note, October 2010 (2010) .
- 11278 [597] K. Yokoya, *CAIN: A Computer Simulation Code for the Interaction of Electron,*
11279 *Positron, Gamma Beams and Strong Lasers*, available at
11280 <http://ldev.kek.jp/yokoya/CAIN> (2010) .
- 11281 [598] C. Johnstone, *Local chromaticity correction of the LHC*, PAC97 (1997) .

- 11282 [599] S. Fartoukh, *Optics Challenges and Solutions for the LHC Insertion Upgrade Phase I*,
11283 LHC Project Report 0038 (2010) .
- 11284 [600] S. Fartoukh, *Towards the LHC Upgrade using the LHC well-characterized technology*,
11285 LHC Project Report 0049 (2010) .
- 11286 [601] P. Raimondi and A. Seryi, *Novel Final Focus Design for Future Linear Colliders*, Phys.
11287 Rev. Lett. **86** (2001) .
- 11288 [602] A. Gaddi, *Passive isolation*, Presented in IWLC 2010 (2010) .
- 11289 [603] A. Verdier, *Alignment optics for LHC*, LHC Project Note 325 (2003) .
- 11290 [604] D. Schulte, *Beam-Beam Simulations with GUINEA-PIG*, ICAP98 (1998) .
- 11291 [605] A. Bogacz, *LHeC Recirculator with Energy Recovery Beam Optics Choices*,
11292 CERN-LHeC-Note-2010-009 ACC, JLAB-TN-10-040 (2010) .
- 11293 [606] Y. Hao, K. D., V. Litvinenko, V. Ptitsyn, D. Trbojevic, and N. Tsoupas, *ERL Option
11294 for LHeC*, CERN-LHeC-Note-2010-010 ACC (2010) .
- 11295 [607] D. Schulte, *Multi-bunch calculations in the CLIC main linac*, PAC2009 Vancouver
11296 (2009) .
- 11297 [608] D. Schulte, *Simulation package based on PLACET*, Proceedings PAC01, Chicago
11298 (2001) .
- 11299 [609] *International Linear Collider Reference Design Report*, ILC-Report-2007-001 (2007) .
- 11300 [610] I. Bazarov and G. Hoffstaetter, *Multi-pass Beam-breakup: Theory and Calculation*,
11301 EPAC2004 Lucerne (2004) .
- 11302 [611] D. Schulte, , to be published .
- 11303 [612] M. Schuh, , private communication .
- 11304 [613] F. Zimmermann, J. Byrd, A. Chao, S. Heifets, M. Minty, T. Raubenheimer, J. Seeman,
11305 S. G., and J. Thomson, *Experiments on the fast beam-ion instability at the ALS*, Report
11306 SLAC-PUB-7617 (1997) .
- 11307 [614] G. Hoffstaetter and M. Liepe, , NIM A **557** (2006) 205–212.
- 11308 [615] N. Hilleret, , Private communication .
- 11309 [616] B. Holzer, , Private communication .
- 11310 [617] V. Baglin, , Private communication .
- 11311 [618] F. Zimmermann et al., *CAIN: A Computer Simulation Code for the Interaction of
11312 Electron, Positron, Gamma Beams and Strong Lasers*, 3rd CERN-ECFA-NuPECC
11313 Workshop on the LHeC, <http://www.lhec.org.uk>, Nov. 12-13, 2010. (2010) .
- 11314 [619] L. Thomas, , Phil. Mag, **3** (1927) 1.

- 11315 [620] V. Ptitsin, *Symmetric Designs for Helical Spin Rotators at RHIC*, AGS/RHIC/SN No.
11316 5 (1996) .
- 11317 [621] C. Yin Vallgren, A. Ashraf, S. Calatroni, P. Chiggiato, P. Costa Pinto, et al., *Low*
11318 *Secondary Electron Yield Carbon Coatings for Electron-cloud Mitigation in Modern*
11319 *Particle Accelerators*, .
- 11320 [622] C. Hauviller, *DEVELOPMENT OF COMPOSITE TUBES FOR EXPERIMENTAL*
11321 *VACUUM CHAMBERS OF COLLIDERS*, .
- 11322 [623] R. Appleby, L. Keller, T. W. Markiewicz, A. Seryi, D. Walz, et al., *The International*
11323 *linear collider beam dumps*, [arXiv:physics/0601103](#) [physics].
- 11324 [624] J. Amann, R. Arnold, A. Seryi, D. Walz, K. Kulkarni, et al., *Design of an 18 MW Beam*
11325 *Dump for 500 GeV Electron/Positron Beams at an ILC*, .
- 11326 [625] M. Barnes, F. Caspers, L. Ducimetiere, N. Garrel, and T. Kroyer, *The beam screen for*
11327 *the LHC injection kicker magnets*, .
- 11328 [626] E. Carlier, U. Jansson, R. Jung, V. Mertens, S. Péraire, et al., *The LEP beam dumping*
11329 *system*, .
- 11330 [627] A. Mazzacane, *The 4th concept detector for the ILC*, Nucl.Instrum.Meth. **A617** (2010)
11331 173–176.
- 11332 [628] M. Klein and R. Yoshida, *Collider Physics at HERA*, Prog.Part.Nucl.Phys. **61** (2008)
11333 343–393, [arXiv:0805.3334](#) [hep-ex].
- 11334 [629] e. Pire, Bernard, e. Cirelli, Marco, e. Colas, Paul, e. Djouadi, Abdelhak, e. Lounis,
11335 Abdenour, et al., *High energy physics. Proceedings, 35th International Conference,*
11336 *ICHEP 2010, Paris, France, July 22-28, 2010*, .
- 11337 [630] e. Buchmuller, W. and e. Ingelman, G., *Physics at HERA. Proceedings, Workshop,*
11338 *Hamburg, Germany, October 29-30, 1991. Vol. 1-3*, .
- 11339 [631] R. Gluckstern, *Uncertainties in track momentum and direction, due to multiple*
11340 *scattering and measurement errors*, Nucl.Instrum.Meth. **24** (1963) 381–389.
- 11341 [632] M. Regler, W. Mitaroff, M. Valentan, R. Fruhwirth, and R. Hofler, *The 'LiC Detector*
11342 *Toy' program*, J.Phys.Conf.Ser. **119** (2008) 032034.
- 11343 [633] P. Adragna, C. Alexa, K. Anderson, A. Antonaki, A. Arabidze, et al., *Measurement of*
11344 *pion and proton response and longitudinal shower profiles up to 20 nuclear interaction*
11345 *lengths with the ATLAS tile calorimeter*, Nucl.Instrum.Meth. **A615** (2010) 158–181.
- 11346 [634] ATLAS Collaboration, G. Aad et al., *The ATLAS Experiment at the CERN Large*
11347 *Hadron Collider*, JINST **3** (2008) S08003.
- 11348 [635] B. Holzer, , Private communication .
- 11349 [636] E. Koffeman, *Gossip: Gaseous pixels*, Nucl.Instrum.Meth. **A582** (2007) 858–860.

- 11350 [637] H. van der Graaf, "Gossip and GridPix at LHeC", talk at 3rd CERN-ECFA-NuPECC
 11351 Workshop on LHeC, Chavannes-de-Bogis, Switzerland, 12. November 2010.
 11352 [http://indico.cern.ch/materialDisplay.py?contribId=51&sessionId=9\](http://indico.cern.ch/materialDisplay.py?contribId=51&sessionId=9&materialId=slides&confId=105142)
 11353 [&materialId=slides&confId=105142.](http://indico.cern.ch/materialDisplay.py?contribId=51&sessionId=9&materialId=slides&confId=105142)
- 11354 [638] H. van der Graaf, *Gaseous detectors*, Nucl.Instrum.Meth. **A628** (2011) 27–30.
- 11355 [639] R.Horrisberger, "Tracking at Phase II, Pixel, Strixel & Strips", CMS Tracker Week, La
 11356 Biodola, Isola d'Elba 27. May 2010.
- 11357 [640] R. Horrisberger, "Considerations for future Large Pixel Systems", talk CMS Pixel
 11358 Detector Upgrade Workshop, FNAL 10. October 2006.
- 11359 [641] P. Allport, "Conventional Silicon Pixel/Strip Tracker", talk at 3rd
 11360 CERN-ECFA-NuPECC Workshop on LHeC, Chavannes-de-Bogis, Switzerland, 12.
 11361 November 2010. [http://indico.cern.ch/getFile.py/access?contribId=50\](http://indico.cern.ch/getFile.py/access?contribId=50&sessionId=9&resId=0&materialId=slides&confId=105142)
 11362 [&sessionId=9&resId=0&materialId=slides&confId=105142.](http://indico.cern.ch/getFile.py/access?contribId=50&sessionId=9&resId=0&materialId=slides&confId=105142)
- 11363 [642] J. Brau, *The Science and Challenges for Future Detector Development in High Energy*
 11364 *Physics*, .
- 11365 [643] N. Wermes, "Silicon Pixel Detectors for Tracking", talk at 1st CERN-ECFA Workshop
 11366 on LHeC, Divonne-les-Bains, France, 1-3 September 2008. [http://indico.cern.ch/](http://indico.cern.ch/contributionDisplay.py?sessionId=19&contribId=63&confId=31463)
 11367 [contributionDisplay.py?sessionId=19&contribId=63&confId=31463.](http://indico.cern.ch/contributionDisplay.py?sessionId=19&contribId=63&confId=31463)
- 11368 [644] ATLAS and CMS Collaboration, N. Hessey, *Overview and electronics needs of ATLAS*
 11369 *and CMS high luminosity upgrades*, . [http://indico.cern.ch/getFile.py/access?](http://indico.cern.ch/getFile.py/access?contribId=140&sessionId=21&resId=0&materialId=paper&confId=21985)
 11370 [contribId=140&sessionId=21&resId=0&materialId=paper&confId=21985.](http://indico.cern.ch/getFile.py/access?contribId=140&sessionId=21&resId=0&materialId=paper&confId=21985)
- 11371 [645] M. Nessi, "The Detector Upgrade and the Requirements on the Upgrade Scenarios".
 11372 [http://cdsweb.cern.ch/record/1304568.](http://cdsweb.cern.ch/record/1304568)
- 11373 [646] C. Haber, "Lecture Silicon Detectors: Principles and Technology", talk at TIPP,
 11374 Chicago, USA, June 2011. [https://indico.cern.ch/getFile.py/access?](https://indico.cern.ch/getFile.py/access?contribId=529&sessionId=25&resId=0&materialId=slides&confId=102998)
 11375 [contribId=529&sessionId=25&resId=0&materialId=slides&confId=102998.](https://indico.cern.ch/getFile.py/access?contribId=529&sessionId=25&resId=0&materialId=slides&confId=102998)
- 11376 [647] D. Christian, "Semiconductor Detectors Overview", talk at TIPP, Chicago, USA, June
 11377 2011. [https://indico.cern.ch/getFile.py/access?contribId=527&sessionId=](https://indico.cern.ch/getFile.py/access?contribId=527&sessionId=22&resId=1&materialId=slides&confId=102998)
 11378 [22&resId=1&materialId=slides&confId=102998.](https://indico.cern.ch/getFile.py/access?contribId=527&sessionId=22&resId=1&materialId=slides&confId=102998)
- 11379 [648] S. Cihanger, "Silicon sensor R&D for an upgraded CMS Tracker in HL-LHC", talk at
 11380 TIPP, Chicago, USA, June 2011. [https://indico.cern.ch/getFile.py/access?](https://indico.cern.ch/getFile.py/access?contribId=107&sessionId=22&resId=0&materialId=slides&confId=102998)
 11381 [contribId=107&sessionId=22&resId=0&materialId=slides&confId=102998.](https://indico.cern.ch/getFile.py/access?contribId=107&sessionId=22&resId=0&materialId=slides&confId=102998)
- 11382 [649] A. Affolder, "Silicon Strip Detectors for the ATLAS sLHC Upgrade", talk at TIPP,
 11383 Chicago, USA, June 2011. [https://indico.cern.ch/getFile.py/access?](https://indico.cern.ch/getFile.py/access?contribId=31&sessionId=22&resId=1&resmaterialId=slides&confId=102998)
 11384 [contribId=31&sessionId=22&resId=1&resmaterialId=slides&confId=102998.](https://indico.cern.ch/getFile.py/access?contribId=31&sessionId=22&resId=1&resmaterialId=slides&confId=102998)
- 11385 [650] A. Macchiolo, "Performance of Silicon n-in-p Pixel Detectors irradiated up to 5^{15}
 11386 n_{eq}/cm^2 for the future ATLAS Upgrades", talk at TIPP, Chicago, USA, June 2011.
 11387 [https://indico.cern.ch/getFile.py/access?contribId=33&sessionId=22\](https://indico.cern.ch/getFile.py/access?contribId=33&sessionId=22&resId=0&materialId=slides&confId=102998)
 11388 [&resId=0&materialId=slides&confId=102998.](https://indico.cern.ch/getFile.py/access?contribId=33&sessionId=22&resId=0&materialId=slides&confId=102998)

- 11389 [651] U. Parzefall, "Silicon for High-Luminosity Tracking Detectors - Recent RD50 Results",
 11390 talk at TIPP, Chicago, USA, June 2011.
 11391 [https://indico.cern.ch/getFile.py/access?contribId=203&sessionId=22\](https://indico.cern.ch/getFile.py/access?contribId=203&sessionId=22&resId=3&materialId=slides&confId=102998)
 11392 [&resId=3&materialId=slides&confId=102998](https://indico.cern.ch/getFile.py/access?contribId=203&sessionId=22&resId=3&materialId=slides&confId=102998).
- 11393 [652] I. Rubinskiy, "An EUDET/AIDA pixel beam telescope for detector development", talk at
 11394 TIPP, Chicago, USA, June 2011. [https://indico.cern.ch/getFile.py/access?](https://indico.cern.ch/getFile.py/access?contribId=25&sessionId=22&resId=0&materialId=slides&confId=102998)
 11395 [contribId=25&sessionId=22&resId=0&materialId=slides&confId=102998](https://indico.cern.ch/getFile.py/access?contribId=25&sessionId=22&resId=0&materialId=slides&confId=102998).
- 11396 [653] M. Bomben, "Recent progress of the ATLAS Planar Pixel Sensor R&D Project", talk at
 11397 TIPP, Chicago, USA, June 2011. [https://indico.cern.ch/getFile.py/access?](https://indico.cern.ch/getFile.py/access?contribId=436&sessionId=22&resId=0&materialId=slides&confId=102998)
 11398 [contribId=436&sessionId=22&resId=0&materialId=slides&confId=102998](https://indico.cern.ch/getFile.py/access?contribId=436&sessionId=22&resId=0&materialId=slides&confId=102998).
- 11399 [654] M. Mikuz, "Diamond for high energy radiation and particle detection", talk at TIPP,
 11400 Chicago, USA, June 2011. [https://indico.cern.ch/getFile.py/access?](https://indico.cern.ch/getFile.py/access?contribId=463&sessionId=22&resId=1&materialId=slides&confId=102998)
 11401 [contribId=463&sessionId=22&resId=1&materialId=slides&confId=102998](https://indico.cern.ch/getFile.py/access?contribId=463&sessionId=22&resId=1&materialId=slides&confId=102998).
- 11402 [655] A. Mac Raighne, "3D pixel devices; design, production and characterisation in test
 11403 beams", talk at TIPP, Chicago, USA, June 2011.
 11404 [https://indico.cern.ch/getFile.py/access?contribId=249&sessionId=22\](https://indico.cern.ch/getFile.py/access?contribId=249&sessionId=22&resId=1&materialId=slides&confId=102998)
 11405 [&resId=1&materialId=slides&confId=102998](https://indico.cern.ch/getFile.py/access?contribId=249&sessionId=22&resId=1&materialId=slides&confId=102998).
- 11406 [656] M. Garcia-Sciveres, "ATLAS pixels for 2017/18", talk at ACES 2011 Workshop, CERN
 11407 9. March 2011.
- 11408 [657] K.K.Gan, F.Vasey, T.Weidberg "Lessons Learned and to be Learned from LHC", talk at
 11409 Joint ATLAS-CMS Working Group on Opto-Electronics for SLHC, Report from
 11410 Sub-Group A, Joint ATLAS/CMS NOTE, ATL-COM-ELEC-2007-001.
 11411 <https://edms.cern.ch/document/882775/3.8>.
- 11412 [658] A. Bell, E. Castro, R. Hall-Wilton, W. Lange, W. Lohmann, et al., *Fast Beam*
 11413 *Conditions Monitor BCM1F for the CMS Experiment*, Nucl.Instrum.Meth. **A614**
 11414 (2010) 433–438, arXiv:0911.2480 [physics.ins-det].
- 11415 [659] L. Fernandez Hernando, D. Chong, R. Gray, C. Ilgner, A. Macpherson, et al.,
 11416 *Development of a CVD diamond beam condition monitor for CMS at the Large Hadron*
 11417 *Collider*, Nucl.Instrum.Meth. **A552** (2005) 183–188.
- 11418 [660] A. Macpherson, *Beam Condition Monitoring and radiation damage concerns of the*
 11419 *experiment, talk at ICHEP 2010, Paris, France, .*
- 11420 [661] D. Chong, L. Fernandez-Hernando, R. Gray, C. J. Ilgner, A. Oh, et al., *Validation of*
 11421 *synthetic diamond for a beam condition monitor for the Compact Muon Solenoid*
 11422 *experiment*, IEEE Trans.Nucl.Sci. **54** (2007) 182–185.
- 11423 [662] GEANT4 Collaboration, S. Agostinelli et al., *GEANT4: A Simulation toolkit*,
 11424 Nucl.Instrum.Meth. **A506** (2003) 250–303.
- 11425 [663] R. Brun and F. Rademakers, *ROOT - An Object Oriented Data Analysis Framework*,
 11426 *Proceedings AIHENP'96 Workshop, Lausanne, Sep. 1996*, Nucl. Inst. & Meth. in Phys.
 11427 Res. A 389 (1997) 81–86.

- 11428 [664] R. Chytracsek, J. McCormick, W. Pokorski, and S. G., *Geometry Description Markup*
 11429 *Language for Physics Simulation and Analysis Applications*, IEEE Trans. Nucl. Sci.
 11430 **Vol. 53, Issue: 5, Part 2** 2892–2896.
- 11431 [665] V. V. Serbo, *Status of AIDA and JAS 3*, Nuclear Instruments and Methods in Physics
 11432 Research Section A: Accelerators, Spectrometers, Detectors and Associated Equipment
 11433 **502** (2003) no. 2-3, 663 – 665.
 11434 <http://www.sciencedirect.com/science/article/pii/S0168900203005370>.
 11435 Proceedings of the VIII International Workshop on Advanced Computing and Analysis
 11436 Techniques in Physics Research.
- 11437 [666] A. Vasilescu and L. G., *Displacement damage in Silicon for neutrons, protons, pions,*
 11438 *and electrons*, . <http://sesam.desy.de/members/gunnar/NIEL-allr.ps>.
- 11439 [667] F. Carminati and A. Morsch, *Simulation in ALICE*, [arXiv:physics/0306092](https://arxiv.org/abs/physics/0306092)
 11440 [physics]. On behalf of the ALICE Offline Project.
- 11441 [668] ALICE Collaboration, I. Hrivnacova et al., *The Virtual Monte Carlo*,
 11442 [arXiv:cs/0306005](https://arxiv.org/abs/cs/0306005) [cs-se].
- 11443 [669] ALICE Collaboration, I. Gonzalez Caballero, F. Carminati, A. Morsch, and
 11444 I. Hrivnacova, *ALICE experience with GEANT4*, [arXiv:physics/0306025](https://arxiv.org/abs/physics/0306025) [physics].
- 11445 [670] J. Hauptman, *Particle Identification in 4th*, [arXiv:0812.3571](https://arxiv.org/abs/0812.3571) [hep-ex].
- 11446 [671] H1 Collaboration, A. Babaev, *Performance of the H1 liquid argon calorimeter*, .
- 11447 [672] H1 Collaboration, I. Abt et al., *The H1 detector at HERA*, Nucl.Instrum.Meth. **A386**
 11448 (1997) 310–347.
- 11449 [673] M. Fleischer, M. Keller, K. Meier, O. Nix, G. Schmidt, et al., *Performance and upgrade*
 11450 *of H1 calorimeters: LAr calorimeter, SpaCal and VLQ*, .
- 11451 [674] C. Issever, *The calibration of the H1 liquid argon calorimeter*, .
- 11452 [675] H1 collaboration Collaboration, C. Schwanenberger, *The Jet calibration in the H1 liquid*
 11453 *argon calorimeter*, [arXiv:physics/0209026](https://arxiv.org/abs/physics/0209026) [physics].
- 11454 [676] J. Seehafer, *Simulation of hadronic showers in the H1 liquid argon calorimeter with the*
 11455 *simulation programs GHEISHA and CALOR*, .
- 11456 [677] C. Kiesling, A. Dubak, and B. Olivier, *The liquid argon jet trigger of the H1 experiment*
 11457 *at HERA*, Nucl.Instrum.Meth. **A623** (2010) 513–515.
- 11458 [678] ATLAS Electromagnetic Barrel Liquid Argon Calorimeter Group Collaboration,
 11459 B. Aubert et al., *Construction, assembly and tests of the ATLAS electromagnetic barrel*
 11460 *calorimeter*, Nucl.Instrum.Meth. **A558** (2006) 388–418.
- 11461 [679] ATLAS Collaboration, A. Airapetian et al., *ATLAS calorimeter performance Technical*
 11462 *Design Report*, .
- 11463 [680] I. Golutvin, B. Borgia, F. Carminati, M. Della Negra, S. Giani, et al., *A Silicon hadron*
 11464 *calorimeter module operated in a strong magnetic field with VLSI readout for LHC*, .

- 11465 [681] OPAL Collaboration, B. Anderson et al., *The OPAL silicon - tungsten calorimeter front*
11466 *end electronics*, IEEE Trans.Nucl.Sci. **41** (1994) 845–852.
- 11467 [682] J. Adams, G. Bashindzhagian, V. Zatsepin, M. Merkin, M. Panasyuk, et al., *The silicon*
11468 *matrix as a charge detector for the ATIC experiment*, Instrum.Exp.Tech. **44** (2001)
11469 455–461.
- 11470 [683] V. Zatsepin, J. Adams, H. Ahn, G. Bashindzhagian, K. Batkov, et al., *Experience of*
11471 *application of silicon matrix as a charge detector in the ATIC experiment*, .
- 11472 [684] V. Bonvicini, M. Boezio, E. Haslum, D. Matveev, M. Pearce, et al., *New concepts in*
11473 *silicon calorimetry for space experiments*, Nucl.Instrum.Meth. **A518** (2004) 186–187.
- 11474 [685] V. Bonvicini, A. Vacchi, V. Dzhordzhadze, R. Seto, E. Kistenev, et al., *Silicon-tungsten*
11475 *calorimeter for the forward direction in the PHENIX experiment at RHIC*, IEEE
11476 Trans.Nucl.Sci. **52** (2005) 874–878.
- 11477 [686] D. Strom "Silicon Tungsten Calorimetry", talk at SLAC Meeting, 8 January 2004.
- 11478 [687] D. M. Strom, R. Frey, M. Breidenbach, D. Freytag, N. Graf, et al., *Fine grained*
11479 *silicon-tungsten calorimetry for a linear collider detector*, IEEE Trans.Nucl.Sci. **52**
11480 (2005) 868–873.
- 11481 [688] A. Kaidalov and K. Ter-Martirosian, *Pomeron as Quark-Gluon Strings and Multiple*
11482 *Hadron Production at SPS Collider Energies*, Phys.Lett. **B117** (1982) 247–251.
- 11483 [689] M. Barbi "Calorimetry - 3rd course", talk at TRIUMF Summer Institute, July 2007.
- 11484 [690] H1 Collaboration, T. Ahmed et al., *Experimental Study of Hard Photon Radiation*
11485 *Processes at HERA*, Z. Phys. **C66** (1995) 529–542.
- 11486 [691] V. Andreev et al., *The new H1 luminosity system for HERA II*, Nucl. Instrum. Meth.
11487 **A494** (2002) 45–50.
- 11488 [692] ZEUS Luminosity Group Collaboration, J. Andruszkow et al., *Luminosity measurement*
11489 *in the ZEUS experiment*, Acta Phys. Polon. **B32** (2001) 2025–2058.
- 11490 [693] ZEUS Collaboration, S. D. Paganis, *The upgraded luminosity system for the ZEUS*
11491 *experiment*, Int. J. Mod. Phys. **A16S1C** (2001) 1147–1149.
- 11492 [694] G. A. Schuler and H. Spiesberger, *DJANGO: The Interface for the event generators*
11493 *HERACLES and LEPTO*, . In *Hamburg 1991, Proceedings, Physics at HERA, vol. 3*
11494 1419-1432. (see HIGH ENERGY PHYSICS INDEX 30 (1992) No. 12988).
- 11495 [695] A. Courau and P. Kessler, *QED Compton scattering in high-energy electron - proton*
11496 *collisions*, Phys. Rev. **D46** (1992) 117–124.
- 11497 [696] S. Levonian, *H1LUMI - A Fast Simulation Package for the H1 Luminosity System*, . H1
11498 internal note h1-0493-287 (1993);
11499 <http://www.desy.de/~levonian/papers/H1lumi.pdf>.

- 11500 [697] R. Brun, M. Caillat, M. Maire, G. N. Patrick, and L. Urban, *THE GEANT3*
11501 *ELECTROMAGNETIC SHOWER PROGRAM AND A COMPARISON WITH THE*
11502 *EGS3 CODE*, . CERN-DD/85/1.
- 11503 [698] ZEUS FNC Group Collaboration, S. Bhadra et al., *Design and test of a forward neutron*
11504 *calorimeter for the ZEUS experiment*, Nucl. Instrum. Meth. **A394** (1997) 121–135,
11505 arXiv:hep-ex/9701015.
- 11506 [699] R. Arnaldi et al., *The Zero Degree Calorimeters for the ALICE Experiment*, Nucl.
11507 Instrum. Meth. **A581** (2007) 397–401.
- 11508 [700] ALICE Collaboration, N. De Marco et al., *Commissioning and calibration of the zero*
11509 *degree calorimeters for the ALICE experiment*, J. Phys. Conf. Ser. **160** (2009) 012060.
- 11510 [701] A. Collaboration, *Zero degree calorimeters for ATLAS*, . CERN-LHCC-2007-01.
- 11511 [702] O. Grachov et al., *Commissioning of the CMS zero degree calorimeter using LHC beam*,
11512 arXiv:1008.1157 [physics.ins-det].
- 11513 [703] LHCf Collaboration, O. Adriani et al., *The LHCf detector at the CERN Large Hadron*
11514 *Collider*, JINST **3** (2008) S08006.
- 11515 [704] A. Breskin et al., *The THGEM: A thick robust gaseous electron multiplier for radiation*
11516 *detectors*, Nucl. Instrum. Meth. **A623** (2010) 132–134.
- 11517 [705] V. Inshakov et al., *Development of detector active element based on thgem*,
11518 arXiv:0906.4441 [physics.ins-det].
- 11519 [706] H. Mais and G. Ripken Tech. Rep. 83-62, DESY, 1983. Modern notation: replace \vec{n} by
11520 \vec{n}_0 .

11521 **Appendix 1**

11522 **Tasks for a Technical Design Report**

11523 **Building and Operating the LHeC**

11524 **Appendix 2**

11525 **Scientific Advisory Committee**

- 11526 Guido Altarelli (Roma)
- 11527 Sergio Bertolucci (CERN)
- 11528 Stan Brodsky (SLAC)
- 11529 Allen Caldwell (MPI Muenchen)
- 11530 Swapan Chattopadhyay (Cockcroft Institute)
- 11531 John Dainton (Liverpool)
- 11532 John Ellis (CERN)
- 11533 Jos Engelen (NWO)
- 11534 Joel Feltesse (Saclay)
- 11535 Roland Garoby (CERN)
- 11536 Rolf Heuer (CERN)
- 11537 Roland Horisberger (PSI)
- 11538 Young-Kee Kim (Fermilab)
- 11539 Aharon Levy (Tel Aviv)
- 11540 Lev Lipatov (St. Petersburg)
- 11541 Karlheinz Meier (Heidelberg)
- 11542 Richard Milner (MIT)
- 11543 Joachim Mnich (DESY)
- 11544 Steve Myers (CERN)
- 11545 Guenther Rosner (Glasgow)
- 11546 Alexander N. Skrinsky (INP Novosibirsk)
- 11547 Anthony Thomas (JLab)
- 11548 Steve Vigdor (Brookhaven)
- 11549 Ferdinand Willeke (Brookhaven)
- 11550 Frank Wilczek (MIT)
- 11551

11552 **Steering Committee**

- 11553 Oliver Bruning(CERN)
- 11554 John Dainton (Liverpool)
- 11555 Albert De Roeck (CERN)
- 11556 Stefano Forte (Milano)
- 11557 Max Klein (Liverpool)
- 11558 Paul Laycock (Liverpool)
- 11559 Paul Newman (Birmingham)
- 11560 Emmanuelle Perez (CERN)
- 11561 Wesley Smith (Wisconsin)
- 11562 Bernd Surrow (MIT)
- 11563 Katsuo Tokushuku (KEK)
- 11564 Urs Wiedemann (CERN)
- 11565 Frank Zimmermann (CERN)

11566 **Working Group Convenors**

11567 **Accelerator Design**

11568 Oliver Brüning (CERN)
11569 John Dainton (Liverpool)
11570

11571 **Interaction Region and Fwd/Bwd**

11572 Bernhard Holzer (CERN)
11573 Uwe Schneekloth (DESY)
11574 Pierre van Mechelen (Antwerpen)
11575

11576 **Detector Design**

11577 Peter Kostka (DESY)
11578 Alessandro Polini (Bologna)
11579 Rainer Wallny (Zurich)
11580

11581 **New Physics at Large Scales**

11582 Georges Azuelos (Montreal)
11583 Emmanuelle Perez (CERN)
11584 Georg Weiglein (Hamburg)
11585

11586 **Precision QCD and Electroweak**

11587 Olaf Behnke (DESY)
11588 Paolo Gambino (Torino)
11589 Thomas Gehrmann (Zurich)
11590 Claire Gwenlan (Oxford)
11591

11592 **Physics at High Parton Densities**

11593 Néstor Armesto (Santiago de Compostela)
11594 Brian A. Cole (Columbia)
11595 Paul R. Newman (Birmingham)
11596 Anna M. Stasto (PennState)
11597

11598 **CERN Referees**

11599 **Accelerator Design - Ring Ring**

11600 Kurt Huebner
11601 Alexander N. Skrinsky (INP Novosibirsk)
11602 Ferdinand Willeke (Brookhaven)
11603

11604 **Accelerator Design - Linac Ring**

11605 Reinhard Brinkmann (DESY)
11606 Andy Wolski (STFC)
11607 Kaoru Yokoya (KEK)
11608

11609 **Accelerator Design - Energy Recovery**

11610 Georg Hoffstaetter
11611 Ilan Ben Zvi (BNL)
11612

11613 **Accelerator Design - Magnets**

11614 Neil Marks(STFC)
11615 Martin Wilson
11616

11617 **Interaction Region and Fwd/Bwd**

11618 Daniel Pitzl (DESY)
11619 Mike Sullivan (SLAC)
11620

11621 **Detector Design**

11622 Philippe Bloch (CERN)
11623 Roland Horisberger (PSI)
11624

11625 **Installation and Infrastructure**

11626 Sylvain Weisz (CERN)
11627

11628 **New Physics at Large Scales**

11629 Cristinel Diaconu (IN2P3 Marseille)

11630 Gian Giudice (CERN)

11631 Michelangelo Mangano (CERN)

11632

11633 **Precision QCD and Electroweak**

11634 Guido Altarelli (Roma)

11635 Vladimir Chekelian

11636 Alan Martin (Durham)

11637

11638 **Physics at High Parton Densities**

11639 Alfred Mueller (Columbia)

11640 Raju Venugopalan (BNL)

11641 Michele Arneodo (INFN Torino)

11642